NANOSTRUCTURE SCIENCE AND TECHNOLOGY
Series Editor: David J. Lockwood

Nanostructured Coatings

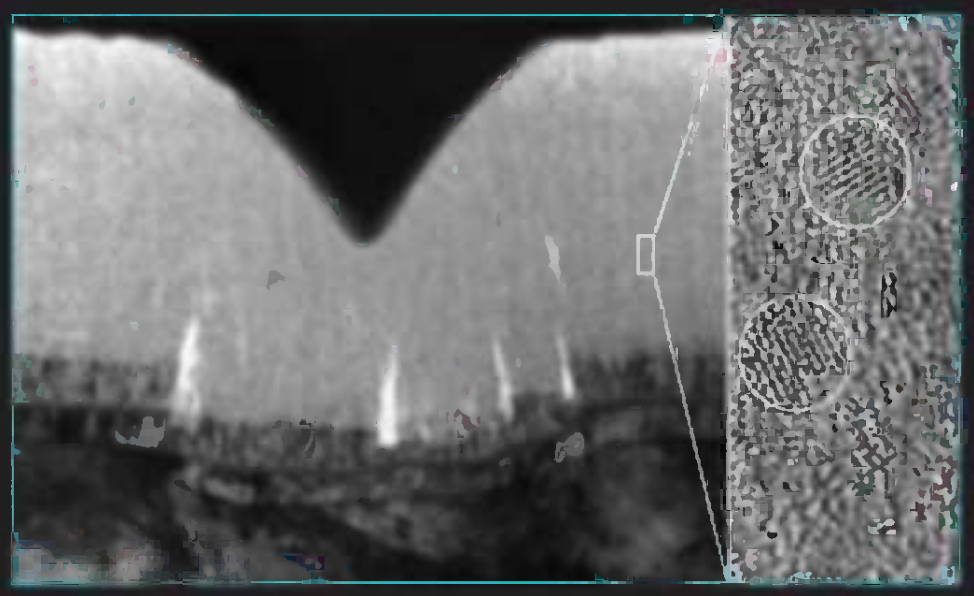

Edited by
Albano Cavaleiro and Jeff Th. M. De Hosson

Nanostructured Coatings

Nanostructure Science and Technology

Series Editor: David J. Lockwood, FRSC
National Research Council of Canada
Ottawa, Ontario, Canada

Nanostructured Coatings
Edited by Albano Cavaleiro and Jeff Th. M. De Hosson

Nanotechnology in Catalysis, Volume 3
Edited by Bing Zhou, Scott Han, Robert Raja, and Gabor A. Somorjai

Light Scattering and Nanoscale Surface Roughness
Edited by Alexei A. Maradudin

Controlled Synthesis of Nanoparticles in Microheterogeneous Systems
Vincenzo Turco Liveri

Nanoscale Assembly Techniques
Edited by Wilhelm T.S. Huck

Ordered Porous Nanostructures and Applications
Edited by Ralf B. Wehrspohn

Surface Effects in Magnetic Nanoparticles
Dino Fiorani

Alternative Lithography: Unleashing the Potentials of Nanotechnology
Edited by Clivia M. Sotomayor Torres

Interfacial Nanochemistry: Molecular Science and Engineering
at Liquid–Liquid Interfaces
Edited by Hitoshi Watarai

Introduction to Nanoscale Science and Technology, Vol. 6
Massimiliano Di Ventra, Stephane Evoy, and James R. Heflin Jr.

Nanoparticles: Building Blocks for Nanotechnology
Edited by Vincent Rotello

Self-Assembled Nanostructures
Jin Z. Zhang, Zhong-lin Wang, Jun Liu, Shaowei Chen, and Gang-yu Liu

Semiconductor Nanocrystals: From Basic Principles to Applications
Edited by Alexander L. Efros, David J. Lockwood, and Leonid Tsybeskov

Nanostructured Coatings

edited by

Albano Cavaleiro
Universidade de Coimbra
Pinhal de Marrocos, Coimbra, Portugal

and

Jeff Th. M. De Hosson
University of Groningen
Groningen, The Netherlands

Springer

Albano Cavaleiro
Depto. Eng. Mecanica
University de Coimbra
Pinhal Marrocos
Columbra 3030 Portugal
albano.cavaleiro@dem.uc.pt.

Jeff Th. M. De Hosson
Department of Applied Physics
University of Groningen
4 Nijenborgh
Groningen 9747 AG
The Netherlands
j.t.m.de.hosson@rug.nl

Cover Illustration: Cross-sectional transmission electron micrograph of a nc-Ti/a- C:H nanocomposite coating after nanoindentation (Yutao Pei, Damiano Galvan, Jeff Th. M. De Hosson, University of Groningen, The Netherlands)

Library of Congress Control Number: 2006925865

ISBN-10: 0-387-25642-3
ISBN-13: 978-0387-25642-9

Printed on acid-free paper.

9 8 7 6 5 4 3 2 1

springer.com

Contributors

Nuno J. M. Carvalho, Department of Applied Physics, Materials Science Center and Netherlands Institute for Metals Research, University of Groningen, Nijenborgh 4, 9747 AG Groningen, The Netherlands

Albano Cavaleiro, ICEMS, Mechanical Engineering Department, Faculty of Sciences and Technology, University of Coimbra, Portugal

Thomas Chudoba, ASMEC Advanced surface mechanics GmbH, Rossendorf, Germany

Ming Dao, Massachusetts Institute of Technology, Cambridge, MA, USA

Peter M. Derlet, Paul Scherrer Institut, NUM/ASQ, Villigen, Switzerland

Damiano Galvan, Department of Applied Physics, Materials Science Center and Netherlands Institute for Metals Research, University of Groningen, Nijenborgh 4, 9747 AG Groningen, The Netherlands

Abdellatif Hasnaoui, Paul Scherrer Institut, NUM/ASQ, Villigen, Switzerland

Jeff T. M. De Hosson, Department of Applied Physics, Materials Science Centre and the Netherlands Institute for Metals Research, University of Groningen, Nijenborgh 4, 9747 A. G. Groningen, The Netherlands

P. Eh. Hovsepian, Nanotechnology Centre for PVD Research, Materials and Engineering Research Institute of Sheffield Hallam University, Sheffield S1 1WB, UK

Lars Hultman, Department of Physics and Measurement Technology (IFM), Linköping University, S-581 83 Linköping, Sweden

Adrian Leyland, Department of Engineering Materials, The University of Sheffield, Sheffield, UK

Allan Matthews, Department of Engineering Materials, The University of Sheffield, Sheffield, UK

Christian Mitterer, Department of Physical Metallurgy and Materials Testing, University of Leoben, Franz-Josef-Strasse 18, A-8700 Leoben, Austria

Benedikt Moser, Massachusetts Institute of Technology, Cambridge, MA, USA

W.-D. Münz, Nanotechnology Centre for PVD Research, Materials and Engineering Research Institute of Sheffield Hallam University, Sheffield S1 1WB, UK

J. Musil, Department of Physics, University of West Bohemia, Plzeň, Czech Republic; Institute of Physics, Academy of Sciences of the Czech Republic, Praha, Czech Republic

Ilya A. Ovid'ko, Institute of Problems of Mechanical Engineering, Russian Academy of Sciences, St. Petersburg, Russia

Yutao Pei, Department of Applied Physics, Materials Science Center and Netherlands Institute for Metals Research, University of Groningen, Nijenborgh 4, 9747 AG Groningen, The Netherlands

Ruth Schwaiger, Massachusetts Institute of Technology, Cambridge, MA, USA

Helena Van Swygenhoven, Paul Scherrer Institut, NUM/ASQ, Villigen, Switzerland

Bruno Trindade, ICEMS, Mechanical Engineering Department, Faculty of Sciences and Technology, University of Coimbra, Portugal

Stan Veprek, Institute for Chemistry of Inorganic Materials, Technical University Munich, Lichtenbergstr. 4, D-85747 Garching b. Munich

Maritza G.J. Veprek-Heijman, Institute for Chemistry of Inorganic Materials, Technical University Munich, Lichtenbergstr. 4, D-85747 Garching b. Munich

Maria Teresa Vieira, ICEMS, Mechanical Engineering Department, Faculty of Sciences and Technology, University of Coimbra, Portugal

Foreword

Controlling the performance of structures and components of all sizes and shapes through the use of engineered coatings has long been a key strategy in materials processing and technological design. The ever-increasing sophistication of engineered coatings and the rapid trend toward producing increasingly smaller devices with greater demands on their fabrication, properties and performance have led to significant progress in the science and technology of coatings, particularly in the last decade or two. Nanostructured coatings constitute a major area of scientific exploration and technological pursuit in this development. With characteristic structural length scales on the order of a few nanometers to tens of nanometers, nanostructured coatings provide potential opportunities to enhance dramatically performance by offering, in many situations, extraordinary strength and hardness, unprecedented resistance to damage from tribological contact, and improvements in a number of functional properties. At the same time, there are critical issues and challenges in optimizing these properties with flaw tolerance, interfacial adhesion and other nonmechanical considerations, depending on the coating systems and applications.

Nanostructured coatings demand study in a highly interdisciplinary research arena which encompasses:

- surface and interface science
- study of defects
- modern characterization methodologies
- cutting-edge experimental developments to deposit,synthesize, consolidate, observe as well as chemically and mechanically probe materials at the atomic and molecular length scales
- state-of-the-art computational simulation techniques for developing insights into material behaviour at the atomic scale which cannot be obtained in some cases from experiments alone

The interdisclipinary nature of the subject has made it a rich playing field for scientific innovation and technological progress.

Albano Cavaleiro and Jeff De Hosson have edited an outstanding volume on nanostructured coatings which provides an excellent snapshot of the state-of-the-art in this important topic. They have assembled as contributors to this volume an

impressive group of research teams who have participated in the rapid progress this area has seen in the recent past. The volume provides a very balanced picture of the broad scope of the field, while at the same time capturing the rich details associated with the various topics covered. The community will benefit greatly from the hard work of the editors and authors of this volume, and I expect this volume to have a significant impact on research and practice involving nanostructured coatings.

SUBRA SURESH
Ford Professor of Engineering
Massachusetts Institute of Technology
Cambridge, Massachusetts

Acknowledgments

The editors are grateful to the team of experts that took care of the peer-review of the chapters, consisting of Prof. Jorgen Bottiger, Prof. Steve Bull, Dr. Peter Hatto, Dr. Nigel Jenett, Prof. Francis Levy, Dr. Joerg Patscheider, Prof. Jean-François Pierson, Prof. Yves Pauleau, Prof. Carlos Tavares, Prof. Carl Thompson, Prof. Filipe Vaz, Prof. Atul Chokshi, and Prof. Dirk van Dyck.

Contents

1

Galileo Comes to the Surface!

Jeff T. M. De Hosson[1] and Albano Cavaleiro[2]

[1]Department of Applied Physics, Materials Science Centre and the Netherlands Institute for Metals Research, University of Groningen, Nijenborgh 4, 9747 A. G. Groningen, The Netherlands

[2]Departamento de Engenharia Mecanica, FCTUC, Universidade de Coimbra Pinhal de Marrocos, 3030 Coimbra, Portugal

1. INTRODUCTION

The year was 1635: Galileo completed his "Dialogues concerning *new* sciences."[1] The science listed first was his study of "*what holds solids together*?" and "*why do they fall apart*?" It is fair to say that since his "Dialogues," the former question has developed to the core of interests in condensed matter physics, whereas the latter became an important branch of engineering. After the introduction of quantum mechanics, about 300 years later, the question "what holds solids together?" became based on collective excitations. These concepts were very successful in explaining functional properties of materials. In contrast, a similar success was not achieved in explaining the mechanical properties and the second question of Galileo, namely "why do solids fall apart?" could not be properly answered. Mechanical properties are determined by the collective behavior of defects rather than by the bonding between atoms and electrons. Even the behavior of one singular defect is often irrelevant. For instance, there exists a vast amount of microscopy analyses on *ex situ* deformed solids that try to link observed defect patterns to the mechanical behavior characterized by stress–strain curves. However, in spite of the enormous effort that has been put in both theoretical and experimental works, a clear physical picture that could even predict one stress–strain curve and failure by crack propagation of a coating is still lacking. The reason is quite obvious: in plastic deformation and in fracture we are faced with very nonlinear effects. These phenomena are irreversible and far from equilibrium and consequently cannot be treated by common solid-state physics approaches. As a result, this area of research has largely been ignored by condensed matter physics. The problem was too tough to be "cracked,"

so to speak. However, like in all sciences, he who would eat the kernel must crack the nut.

Luckily enough the tide is turning for two reasons. The first reason lies in new instrumental developments, which permit microstructural control on a nanometer scale, often by sophisticated processing. Alongside these developments in processing, it became possible to do *in situ* mechanical experiments under controlled conditions in conjunction with microscopy analyses, for both structural and chemical information. These developments became particularly relevant for the design of novel coatings in the field of surface engineering.

2. COATINGS

The surface of a component is usually the most important engineering factor. While it is in use it is often the surface of a workpiece that is subjected to wear and corrosion. The complexity of the tribological properties of materials and the economic aspects of friction and wear justify an increasing research effort. In industrialized countries some 30% of all energy generated is ultimately lost through friction. In the highly industrialized countries losses due to friction and wear are put at between 1 and 2% of gross national product. To an increasing degree therefore, the search is on for surface modification techniques, which can increase the wear resistance of materials. Unfortunately, there exists an almost bewildering choice of surface treatments that cover a wide range of thickness. The choice has to be such that the surface treatment does not impair too much the properties of the substrate for which it was originally chosen; that is to say, it should not reduce the load-bearing overlooked capabilities, for example. This aspect of the substrate has been overlooked frequently in surface engineering, with emphasis put rather more on the protective coating itself. Equally, the surface treatment chosen should be suitably related to the problem to be solved.[2,3] If a thin protective layer may do the job, it does not make much sense in concentrating on processing of a thick layer on top of a substrate. It is worth noting here that wear resistance is a property not of materials but of systems, since the material of the workpiece always wears against some other medium. It is its relation to its environment (e.g., lubrication and speed of sliding/rotation) that determines the wear resistance of the material in a given construction. As a general rule, wear is determined by the interplay of two opposing properties: ductility and hardness. Wear can be reduced by modifying the surface layer in such a way that it acquires higher ductility, so that greater plastic deformation can occur without particles breaking off. Soft surface layers can be very effective in reducing wear due to delamination. Resistance to wear by abrasion, on the other hand, is then low. However, wear can also be reduced by making the surface layer harder. Then again, increasing hardness also means an increase in the elasticity strain limit and a reduction in ductility, leading to a lowering of fatigue resistance and hence to brittle failure. The characteristics of the system (i.e., whether the wear

is caused by delamination or abrasion) determine which of the surface engineering methods should be chosen. An interesting approach is decreasing the grain size, which could lead to both an increase in mechanical strength and fracture toughness.

The enormous advantages for materials properties by decreasing the grain size down to the nanometric level were very rapidly extended into the field of mechanical applications. The enthusiasm to manipulate the structure of the deposited films by playing with the binomial feature size/phases distribution was contagious. The deposition of metastable phases either of high-temperature type or with extreme shifts far from stoichiometric chemical composition led to unexpected phases, quasi-amorphous structures, and nano-sized grains. In fact, the knowledge transfer from bulk materials to coatings led to extensive studies on ceramic materials, in particular oxides, carbides, and nitrides, due to their excellent performance concerning very high hardness, chemical and thermal stability, and, in many cases, good tribological characteristics. These coatings are known as "hard coatings". Traditionally, the term *hard coatings* refers to the property of high hardness in the mechanical sense with good tribological properties, although it can be extended to other areas (optical, optoelectronics) where a system operates satisfactorily in a given environment.[4] Although for a long time, hardness has been regarded as a primary material property affecting wear resistance, the elastic strain to failure, which is related to the H/E ratio, is a more suitable parameter for predicting wear resistance.[5] The parameter H refers to hardness and the parameter E represents the Young's modulus. Within a linear elastic approach, this is understandable according to the relations that the yield stress of contact is proportional to (H^3/E^2) and the equation $G_c = \pi a \sigma_c^2/E$, with a being the crack length and σ_c the critical stress at failure. It indicates that the fracture toughness of coatings defined by the so-called critical strain energy release rate G_c would be improved by both a low Young's modulus and a high hardness.

Immediately after the first results on hard coatings, it was concluded that their final properties were outstanding compared to the corresponding bulk materials with similar chemical compositions. Among the several suggested explanations for the difference in this mechanical performance, the much lower grain size was the preferred one. However, most of the time, only empirical relationships were established without any deep understanding of what was going on. The well-known Hall–Petch relationship was frequently applied, without a critical sense that could comprise all the other cases where such a relation was not respected. This period coincided with the first steps in systematic studies in nanocrystalline materials.

Roughly speaking surface modification techniques fall into two groups[6]:

- *Processes for applying protective coatings*, e.g., plating, electrolytic galvanization, physical vapor deposition (PVD), chemical vapor deposition (CVD), and laser cladding.

- *Processes designed to modify the material of the existing surface* by altering its structure or composition. Recent developments in structural manipulation comprise laser hardening, electron beam hardening, and shot peening, whereas thermochemical treatments include nitriding, boriding, carburizing, and ion implantation.

There are two main reasons that provided an impetus for bridging the fields of nanostructured materials and coatings: (1) in various coating systems deposited by PVD or CVD, the final structures consist very often of grain sizes much smaller than obtained with traditional processing techniques; (2) the versatility of deposition techniques allows the production of materials over a large range of chemical compositions, structures, and functional properties. Many of the difficulties in processing nanocrystalline bulk materials (such as fully dense microstructures), control of phase distribution, and control of grain size and its homogeneity can be easily overcome with deposition techniques.

3. CHALLENGES AND OPPORTUNITIES

3.1. Wear: The Role of Interfaces in Nanostructured Materials

Making an appropriate microstructure of a nanostructured coating is an epitome in materials design. This is so because the concentration of lattice defects and the details of the numerous interfaces, including the topology of the triple junctions between the interfaces, determine the overall mechanical response. The overarching challenge is therefore the design of a nanostructured coating that is free of defects that degrade the structural and functional behavior. As will be discussed in various chapters in this book, from experimental and theoretical analyses, one can conclude, with a certain confidence, that deformation in nanocrystalline materials, in particular metals, is at least partially carried by dislocation activity for grain sizes above a critical value around 10–15 nm. Below that critical value, plastic deformation is mostly carried by grain boundary processes. Nevertheless, in many investigations it has been overlooked quite often that several deformation processes might act simultaneously. This means that even though dislocations are observed above the critical grain size and less below the critical grain size, various grain boundary processes are likely to occur at the same time. In evaluating the performance of a nanostructured coating, it is essential to examine the defect content as well as the microstructural features,[7,8] in particular, grain-size dispersion, distribution of interface misorientation angles, and internal strains. It can be anticipated that control of the grain-size dispersion is extremely important in the experimental design of these nanostructured coatings. A nanostructured material with a broad grain-size dispersion will exhibit a lower overall flow stress than a material with the same average grain size but with a much smaller grain-size distribution. Consequently, experimental control over the grain-size distribution is important to investigate concepts in materials design of nanostructured coatings.

Diffusion-, time-, and temperature-dependent processes play an important role in nanocrystalline materials.

In the materials design of a coating for specific mechanical applications, i.e., hard versus tough,[9–21] one has to make a distinction between crack nucleation and crack propagation. Grain-size effects can be considered as follows. Whether the material exhibits intergranular fracture can be estimated from the stress of a pileup of dislocations in a particular grain, τ^*, that is required to activate dislocations in the next grain at a distance r. The stress concentration from the dislocation pileup increases with the number of dislocations in the pileup. The latter increases with the grain size d,[22–24] and dislocation activation in the next grain occurs when

$$\tau^* = (\tau_a - \tau_0)\sqrt{\frac{d}{4r}} \tag{1.1}$$

where τ_a is the applied shear stress and τ_0 is the intrinsic, frictional shear stress, resisting dislocation motion inside the grain. Suppose that intergranular fracture occurs along the grain boundary, i.e., r in Eq. (1.1) becomes of the order of the interatomic spacing a_0, and that the effective tensile stress $\sigma^*(\cong 2\tau^*)$ becomes as large as the theoretical strength σ_{th}. The latter can be described by the decohesion of two atomic planes of surface energy γ, on which the atoms are arranged periodically. Hooke's law is assumed for the initial part of the stress–displacement curve, yielding a theoretical strength σ_{th} equal to $\sqrt{E\gamma/a_0}$. Equation (1.1) yields for crack nucleation, with $\gamma \cong Ea_0/40$,

$$\sigma_{nuc} > \sigma_0 + \frac{1}{3}E\sqrt{\frac{a_0}{d}} \tag{1.2}$$

Whether or not flow initiation is concurrent with fracture depends on the value of σ_0 in comparison with the fracture stress σ_F. When σ_0 is larger than σ_F, cracks will nucleate and the microcracks thus formed propagate along the boundary, leading to more or less brittle failure. From Eq. (1.2), it can be concluded that with decreasing grain size, the stress necessary for crack nucleation increases. The ultimate case is found in amorphous materials where crack nucleation is effectively suppressed. It does not mean that an amorphous coating would be the best choice for a tough coating because crack propagation is enhanced and purely amorphous materials are intrinsically very brittle under tension. An amorphous material shows a certain density distribution caused by localized defects having either severe shear or hydrostatic stress field components.[25] The hydrostatic stress field component, actually representing a free volume, can be annealed out but localized defects with shear stress components cannot. The latter trigger the formation of shear localization leading to enhanced crack propagation. One way of improving the materials design of an amorphous coating, keeping the suppression of crack nucleation, is to spread the localization of shear in a delocalized state by the introduction of particles in an amorphous matrix. The ductility and therefore the toughness will be enhanced provided the particles become of the same size as the width of the shear localization, i.e., $s \approx d$ in Fig. 1.1. Of course this physical picture applies

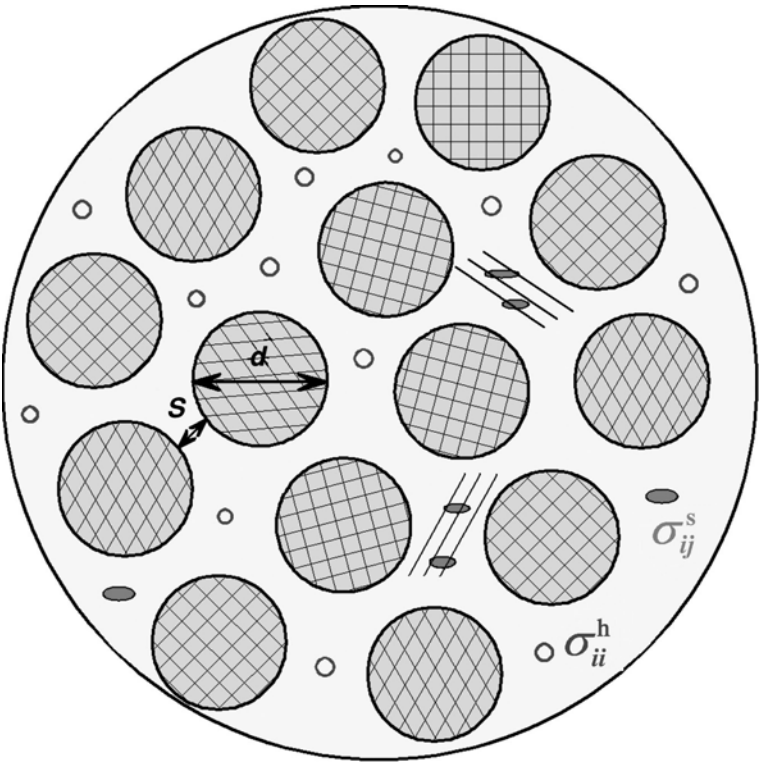

FIGURE 1.1. Nanocrystallites of diameter d separated at a distance s and embedded in an amorphous matrix. Inside the amorphous matrix, density fluctuations lead to a distribution of defects characterized by shear σ_{ij}^{s} and hydrostatic σ_{ii}^{h} stresses.

more to metallic systems than to covalent bonded amorphous materials. Although locally the mechanical response of the directionality of the bonds in amorphous carbon differs from an amorphous metal, the basic description will stay the same. For hard coatings the key challenge is to avoid grain boundary sliding, leaving grain rotation as the deformation mechanism, i.e., $s \ll d$ in Fig. 1.1. As far as toughness is concerned, more compliant (amorphous) boundary layers might be more beneficial. This was experimentally confirmed in the case of TiC/a-C:H nanocomposite coatings (Fig. 1.2). Indeed according to this physical picture, the coating with $s \approx d$ (Fig. 1.2c) showed a substantially lower wear rate compared to the situation when $s \ll d$ (Fig. 1.2a), i.e., $3 \times 10^{-17}\mathrm{m}^3/(\mathrm{N\,m\,lap})$ versus $2 \times 10^{-15}\mathrm{m}^3/(\mathrm{N\,m\,lap})$, respectively.

In most cases, as will be illustrated in the various chapters the experimental and theoretical analyses of nanostructured coatings assume that internal interfaces are free of impurities and segregation. However, segregation to interfaces may have both beneficial and detrimental effects on the mechanical performance of

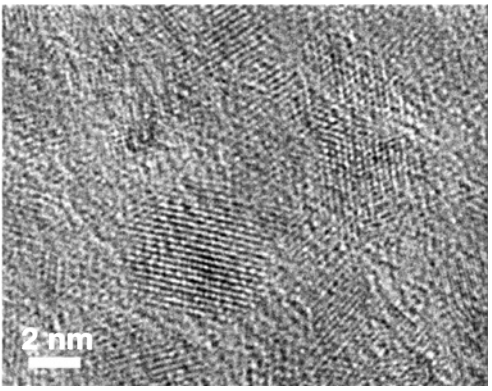

(a)

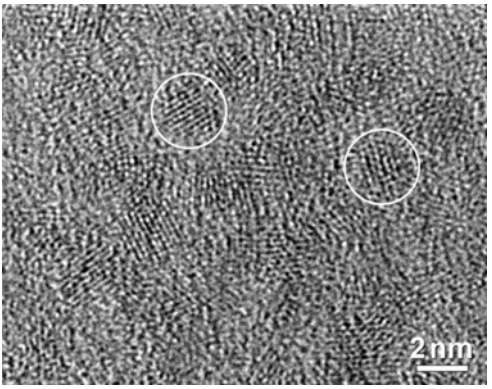

(b)

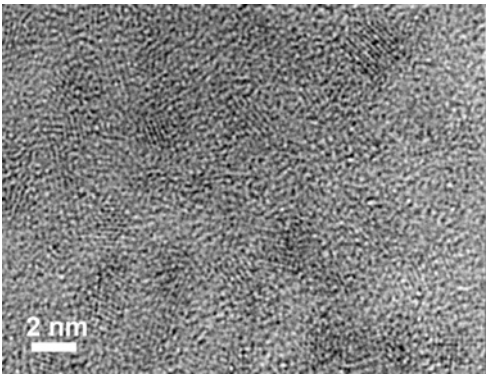

(c)

FIGURE 1.2. HRTEM micrographs showing TiC nanocrystallites embedded in an a-C:H matrix in nc-TiC/a-C:H nanocomposite: (a) $d = 4.5$ nm and $s = 0.3$ nm; (b) $d = 2.2$ nm and $s = 0.7$ nm; and (c) $d = 2.2$ nm and $s = 1.8$ nm, where d is the mean particles size and s is the mean particle spacing.

coatings. The importance of segregation to interfaces is determined primarily by the inherent inhomogeneity of interfaces, i.e., the fact that physical and chemical properties may change dramatically at or near the interface itself. The accumulation of impurity atoms at grain boundaries and surfaces leads to the formation of a very narrow zone, of the order of a few lattice spacings, with different chemical compositions. As a result of sharp concentration gradients, an isotropic bulk solid may change locally into a highly anisotropic medium. Very small bulk concentrations of impurity atoms can lead to significant amounts of those atoms at the grain boundary and interphase interfaces. This can drastically change the response of a material on loading and can eventually lead to brittle failure of an otherwise ductile material. Although embrittlement by impurity segregation is frequently observed, interface segregation can also have a ductilizing effect on brittle materials, depending on both impurity and matrix elements. Even small amounts of oxygen can contribute to interface embrittlement and the fracture mode of the material may change from cleavage to intergranular, with the fracture path closely following the interfaces. This behavior is typical of materials that have undergone certain types of heat treatments when impurities are present. The effect of segregation on surface and interfacial energies is well established.[26] It has been shown that the surface or interface energy is reduced by segregants and that those segregants that are highly surface active lead to the most drastic reduction. The effects of segregants on interface cohesion have been the subject of many discussions. Calculations for segregants in all matrices in the ideal solution approximation have given an indication of the influence of segregation on the interface cohesion.[27] However, an increase in cohesion cannot be related directly to a decrease in the propensity of intergranular fracture. The temperature at which fracture takes place may influence the fracture process. Effects of segregation on mechanical properties can be presented within a thermodynamic framework,[28] where the embrittlement of grain boundaries by solute segregation is formulated in terms of the ideal work of interfacial separation $2\gamma_{\text{int}}$. The control of γ interfacial separation

$$2\gamma_{\text{int}} = (2\gamma_{\text{int}})_0 - \left(\Delta G^0_{\text{int}} - \Delta G^0_{\text{FS}}\right) \Gamma \tag{1.3}$$

where $(2\gamma_{\text{int}})_0$ is the work of separation of a fully clean interface and Γ is the excess interfacial solute coverage (concentration per unit area), is the most appropriate way of enhancing interfacial resistance to fracture. ΔG^0_{int} and ΔG^0_{FS} are usually negative and represent the free energies of segregation to the interface and free surface, respectively, evaluated at the same temperature. Embrittlement (or ductilization) by solute segregation can now be explained with Eq. (1.3) in terms of $2\gamma_{\text{int}}$: a segregating solute with a greater free energy of segregation to a free surface compared with ΔG^0_{int} (i.e., more negative) will embrittle because $2\gamma_{\text{int}}$ will be reduced. In contrast, a lower free energy at an interface compared with ΔG^0_{FS} will enhance interfacial cohesion, i.e., $2\gamma_{\text{int}}$ increases. However, even more important than these brittle fracture modes is the effect of segregation on the ductile–brittle transition temperature (DBTT). Above that temperature a material is ductile, whereas it becomes brittle when the temperature decreases below the

DBTT. An otherwise ductile material becomes brittle because the DBTT is raised. The effects of segregants have been reported generally as variations in DBTT, i.e., δDBTT, associated with a variation in solute coverage, $\delta\Gamma$:

$$\delta\text{DBTT} \propto \delta\Gamma \tag{1.4}$$

According to Eq. (1.3) solute segregation influences the DBTT via the effect on $2\gamma_{\text{int}}$ and

$$\frac{\delta\text{DBTT}}{\delta\Gamma} \propto \left(\Delta G^0_{\text{int}} - \Delta G^0_{\text{FS}}\right) \tag{1.5}$$

In some cases, the DBTT has been observed to be inversely related to the impact fracture toughness, K_{IC}, and K_{IC}^{-1} versus Γ should be approximately linear.[29] When there is no redistribution of the segregants, the reduction in the ideal work of fracture, namely

$$\Delta 2\gamma_{\text{int}} = -\int_0^{\Gamma_{\text{GB}}} \left\{ \left[\frac{\delta G_{\text{GB}}(\Gamma)}{\delta n_i}\right]_{P,T,n_j} - \left[\frac{\delta G_{\text{FS}}(\Gamma)}{\delta n_i}\right]_{P,T,n_j} \right\} \mathrm{d}\Gamma \tag{1.6}$$

where $\left[\frac{\delta G(\Gamma)}{\delta n_i}\right]_{P,T,n_j}$ is the chemical potential of solute n_i in equilibrium with Γ at the boundary or free surface, leads in the dilute limit to Eq. (1.3). Segregants may offset the total embrittling effect described by Eq. (1.5) because of their contribution to the ease of dislocation emission at the crack tip.

It is quite obvious that all these processes at the interface have to be understood in order to tailor nanostructured coatings with a desirable set of physical and chemical properties for structural applications. The impossibility in many cases of demonstrating, experimentally, the theories that could support the particular characteristics and properties of nanocrystalline materials constituted the driving force for the huge amount of research work on the modeling of the deformation response of these materials when externally loaded. Molecular dynamics (MD) modeling has been very instrumental in the understanding of mechanical deformation mechanism of such materials, which are not accessible by experimental means.[30,31] Expressions such as "grain boundary sliding," "grain boundary diffusion," "inverse Hall–Petch relationship," "triple junctions," and "disclinations" now make part of the current terminology in our field.[32] These efforts are being directed, not only to the complete understanding of the more simple metallic materials, but also to much more structurally complex materials such as those of ceramic type. Unfortunately, the extrapolation of the knowledge already concerning nanocrystalline metals to ceramic materials is still in a very embryonic state.

3.2. Friction: Size Effects in Nanostructured Coatings

Challenging experimental and theoretical studies that have not received much attention are size effects on friction.[33] The question is whether there is a critical size below which the friction becomes negligibly small. This holds particular pertinence

in explaining the effect of the thickness of the so-called transfer layer on the counterpart during wear and the optimal size of wear debris creating the transfer layer. In DLCs (diamond-like carbons), adhesive interactions are responsible for friction and the commonly accepted idea is that covalent bonding between unoccupied states and dangling σ bonds attributes to a high friction coefficient.[34] Of course, this will dramatically change in hydrogenated DLC films and a much lower friction coefficient is observed. In fact, this crude idea is influenced greatly by the operative environment and the friction coefficient of hydrogenated DLC films increases with 2 orders of magnitude up to 0.1 when moisture and oxygen are present. In essence a-C:H represents an amorphous network composed of carbon and hydrogen. This network consists of strongly cross-linked carbon atoms with mainly sp^2 (graphite-like) and sp^3(diamond-like) bonds. Hydrogen may either bond to carbon atoms to form H-terminated carbon bonds or stay unbonded in hydrogen reservoirs. In fact, hydrogen acts as a promoter or stabilizer of the sp^3-bonded carbon phase. It is generally speculated that the low friction of most carbon films is largely because these materials are chemically inert and consequently they exert very little adhesive force during sliding against other materials. The major friction-controlling mechanisms have been suggested as the following: (1) Build-up of a transfer film on the surface of the counterpart, which permits easy shear within the interfacial materials and protects the counterpart against wear. However, the shear strength strongly depends on the tribochemical reaction with the surrounding gases present in the contact. (2) The ability to form graphitic surface layer under most tribological conditions. The wear-induced surface graphitization of DLC films consists of two steps: first hydrogen release causes relaxations and then shear deformation promotes a graphitic structure at the surface. (3) Hydrogen passivation of the dangling carbon bonds on the surface, permitting only weak interactions between the DLC film and the sliding counterpart. The friction of DLCs can be lowered by controlling the availability of hydrogen, either through incorporating hydrogen in the films or by adding hydrogen to the surrounding atmosphere. In the absence of hydrogen measurement data, it is difficult to judge the contribution of hydrogen passivation on the reduction of friction in the case of TiC/a-C:H nanocomposite coatings. However, the effect of the transfer films are clearly revealed with the *in situ* monitoring of the wear depth (actually the thickness of the transfer films) and the simultaneous recording of the coefficient of friction curves during the tribotests, together with the microscopic observations on the wear scar of the balls as will be shown in the following.

Friction can be regarded as a conversion of translational motion of the solids, with respect to each other, into vibrational energy.[35,36] It is significant to recall that, for infinite systems, the phonon spectrum consists of a continuum of vibrational modes and phonon damping can be easily realized because, due to anharmonicity, energy can be easily transferred from one mode to the other. As a matter of course, this is not the case in a finite system in which all the modes are discrete and only a certain combination of modes can carry the phonon damping. In principle, it implies that the smaller the system, the smaller is the friction and, in the limit below

a critical size, the system becomes frictionless. Surroundings will also contribute to anharmonicity and possibilities of dissipation, but the contribution to the phonon damping is still considered to be small for smaller sized systems. In the case of nanocomposite coatings, as schematically displayed in Fig. 1.1, we are facing density fluctuations that can be described as a distribution of stress fields having different character. In fact, the phonons are scattered by anharmonicities due to the strain field of these defects. In this mechanism, a translational motion interacts with phonons via scattering accompanying momentum transfer. The starting point in our description is therefore the total momentum of the phonon gas,

$$\vec{p} = \sum \hbar \vec{k} N(\vec{k}) \tag{1.7}$$

where $N(\vec{k})$ is the number of phonons in a vibrational mode $\{\vec{k}\}$. Because of the interaction, phonons are interchanged between the various modes, which leads to a variation of the occupation number $N(\vec{k})$. The average retarding force is then

$$\vec{f} = -\sum \hbar \vec{k}\, \dot{\overline{N}}(\vec{k}) \tag{1.8}$$

The rate of change of the average numbers of phonons $\overline{N}(\vec{k})$ in mode $\{\vec{k}\}$ can be expressed in a general form[37]

$$\dot{\overline{N}}(\vec{k}) = \sum W(\vec{k}, -\vec{k}')[\overline{N}(\vec{k}') - \overline{N}(\vec{k})] + \cdots \tag{1.9}$$

The sum in Eq. (1.9) represents the increase per unit of time of the average number of phonons in mode $\{\vec{k}\}$, and $W(\vec{k}, -\vec{k}')$ is the probability rate for the scattering of a phonon from mode $\{\vec{k}\}$ to $\{\vec{k}'\}$. Next, we assume, for the sake of simplicity, that the energy of the phonon gas is also conserved in three-phonon collisions, and $W(\vec{k}, -\vec{k}', -\vec{k}'')$ vanishes.

For static defects one finds, according to Fermi's golden rule,

$$W_{\text{static}}(\vec{k}, -\vec{k}') = w_{\text{static}}(\vec{k}, -\vec{k}')\delta(\omega(\vec{k}) - \omega(\vec{k}')) \tag{1.10}$$

with

$$w_{\text{static}}(\vec{k}, -\vec{k}') = 2\pi \left[\frac{(2\pi)^3}{\Omega_0 \rho_0}\right]^2 \frac{|V_1(\vec{k}, -\vec{k}')|^2}{\omega(\vec{k})\omega(\vec{k}')} \tag{1.11}$$

The δ function in Eq. (1.10) means that the energy of the phonons is conserved in collisions with *static* defects. W contains the basic physics of the description by V_1, which is the coupling between the vibrational modes, represented by $\{\vec{k}\}$, their polarization vectors $\vec{e}\,(\vec{k})$, and the defects (see Fig. 1.1), which are represented by the Fourier transforms $\Im(\varepsilon)$ of their strain fields ε. A typical element of V_1 has the form

$$V_1 = A_1(\vec{e} \cdot \vec{k})(\vec{e}' \cdot \vec{k}')\, \Im(\varepsilon)(\vec{q}) + \cdots \tag{1.12}$$

with $\vec{q} = (q_1,\ q_2,\ q_3)$. V_1 vanishes unless $\vec{k} + \vec{k}' + \vec{q} = 0$, meaning that the momentum of the phonon is changed in collisions with the defects.

In our case of a *uniformly moving* system, a standard, time-dependent, perturbation treatment yields the probability rate

$$W_{\text{moving}}(\vec{k}, -\vec{k}') = w_{\text{moving}}(\vec{k}, -\vec{k}')\,\delta(\omega(\vec{k}) - \omega(\vec{k}') - (\vec{k} - \vec{k}') \cdot \vec{v}) \tag{1.13}$$

The latter reflects in the δ function [compare Eq. (1.10)] that after the interactions not only the *momentum* changes, but also the *energy*. We assume that the time the system needs to travel a distance of the order of the phonon mean free path is *large* compared to the phonon relaxation time; i.e., the phonon distribution is then, on average, equal to the distribution in thermal equilibrium. The phonon relaxation time τ_{phonon} can be estimated from the thermal conductivity $K = c_{\text{V}}\rho v l/3$, with c_{V} being the specific heat and ρ the material density. For v we take the maximum shear wave velocity equal to $\sqrt{\mu/\rho}$, where μ is the shear modulus. Considering DLC amorphous carbon with $K = 1$ W/(m K), $c_{\text{V}} = 0.8$ J/(g K),[38,39] $\rho = 1.8 \times 10^6$ g/m^3, the phonon mean free path becomes $l_{\text{C}} \cong 0.5$ nm, yielding a relaxation time $\tau_{\text{phonon}} = l_{\text{C}}/v \cong 10^{-13}$s. The thermal conductivity of the composite can be calculated based on an effective medium theory,[40,41] but in the present case with a volume fraction of 20% of TiC it leads to a small deviation in τ_{phonon} [the thermal conductivity approaches 2 W/(m K)]. Indeed, at experimental velocities the phonon distribution is in equilibrium; i.e.,

$$\overline{\overline{N}}_k^j = \left[\exp\left(\frac{\hbar\omega_k^j}{kT}\right) - 1\right]^{-1} \tag{1.14}$$

where k is Boltzmann's constant and T represents the absolute temperature. If the system velocity approaches the sound velocity, the phonon distribution is *not* at equilibrium and actually a severe heat current will arise from the deviations $\overline{N}(\vec{k}) - \overline{\overline{N}}(\vec{k})$. This is basically also the difference between the thermal heat conduction that can only exist provided $\overline{N}(\vec{k}) \neq \overline{\overline{N}}(\vec{k})$ and the phonon drag that can exist even when $\overline{N}(\vec{k}) = \overline{\overline{N}}(\vec{k})$.

It is rather difficult to work out analytical equations for the phonon interactions in case the phonon distribution is not in thermal equilibrium. In general, to study the dissipative properties of a system, it is convenient to apply the quantum-mechanical technique of nonequilibrium statistical mechanics. The dissipation of energy per unit time t can be written as the product of the time derivative of the phonon Hamiltonian $H(t)$ and the deviation of the so-called density matrix, $\exp[-H(t)/T]/\text{Tr}\{\exp[-H(t)/T]\}$, from its equilibrium value. The latter can be expressed as a time-dependent integral equation and accordingly the anharmonicity drag becomes time dependent. However, in the following we will assume only interactions with a phonon gas in thermodynamic equilibrium, independent of t.

Within this theoretical framework, friction is possible only if the inverse of the phonon lifetimes are larger than the spacing of the vibrational modes.[42]

The latter depends on the size and increases with decreasing size. In a harmonic approximation, the spacing is determined by the spring constant α and the mass m. Friction will occur if

$$\frac{1}{\tau_{\text{ph}}} \geq \frac{\pi}{N}\sqrt{\frac{\alpha}{m}} \tag{1.15}$$

where N represents the number of vibrational units involved. The spring constant of C—H and C—C bonds is about 500 N/m, leading to the prediction, based on Eq. (1.15), that for N smaller than 50 unit cells, i.e., 20–30 nm, the friction becomes negligibly small. For a metal like Cu the critical thickness will be about 40 nm. It means that generating wear debris of these dimensions in the beginning is the best.

An example of the wear behavior and friction coefficient as a function of laps is shown in Fig. 1.3 for the TiC/a-C:H nanocomposite coating of Fig. 1.2c. Tribo-tests were performed on a CSM tribometer with a ball-on-disc configuration at 0.1 m/s sliding speed and 2 or 5 N normal load. The wear depth/height of the coating sample (disc) and the counterpart (6-mm-diameter ball) was monitored *in situ* with a resolution of 0.02 μm by an RVDT sensor during the tribo-tests, which allowed *in situ* measurement of the thickness of the transfer films on the surface of the counterpart in contact. The coating shows a very low steady-state friction coefficient, but also a quick drop from an initially high value of about 0.2 at the beginning of sliding until the transition point where the steady state is reached. Such a behavior is attributed to the gradual formation of a transfer film on the counterpart surface during the early stage of a tribo-test, which makes the contact in between two, basically similar, hydrophobic a-C:H surfaces that contribute to self-lubrication. Against different counterparts, i.e., sapphire, alumina, and bearing steel balls, only slight differences in the friction coefficient are observed on the coatings that self-lubricate. It may imply that the interfacial sliding actually takes place between the transfer films on the ball and the surface of the coating, rather than sliding between the surfaces of the counterpart and the coating. To prove that the self-lubrication is induced by the formation of transfer films, the wear depth was *in situ* monitored with the RVDT sensor during the tribo-tests. As marked by the arrows in Fig. 1.3, segments with a negative slope were observed in the depth versus laps graph and indicated a significant growth of the transfer film on the ball surface, rather than a real reduction in the depth of the wear track on the coatings. Correspondingly, substantial decreases in the friction coefficient were detected. The maximum growth amplitude in the thickness of the transfer films was measured at about 100 nm and the minimum at the level of 10 nm. Once the transfer film stopped growing, the coefficient of friction could not decrease further and started to fluctuate. Because the transfer film covered the ball surface in contact, the wear rate of the coating diminished at that moment and resulted in less debris formed. As a result, the transfer film became thinner with sliding distance until it broke down fully, leading to a sudden rise in the friction coefficient. Sliding at higher friction coefficient may generate more debris, which in turn provided the

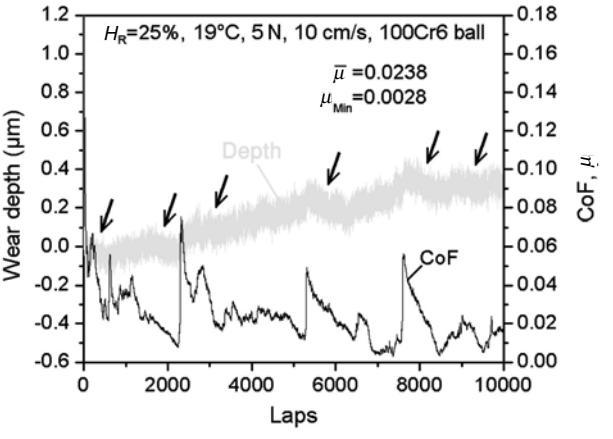

(a)

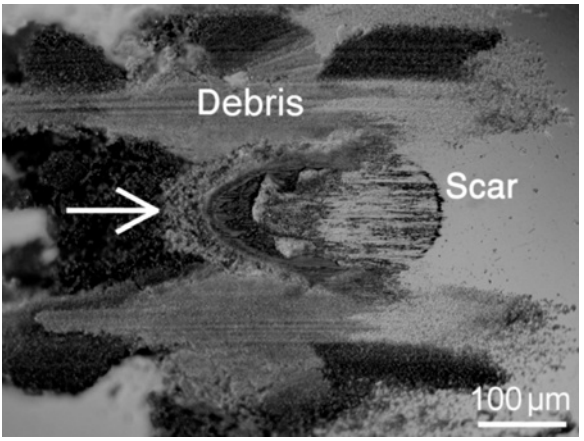

(b)

FIGURE 1.3. (a) Dynamic frictional behavior of coating sliding in air of 25% relative humidity, and (b) wear scar of 100Cr6 steel ball. (An arrow indicating the sliding direction of the coating in contact is inserted.). CoF, coefficient of friction.

necessary materials for the growth of new transfer film. Thereafter, this dynamic friction process was observed to be cyclical. Figure 1.3b shows the wear scar of the 100Cr6 ball covered with transfer films, as well as the wear debris collected in front of, and at the flanks of, the wear scar.

To understand the behavior of the coefficient of friction in the framework of size effects, the following analysis is made: For an elastic contact of a 6-mm-diameter steel ball pressed against a coating of 150-GPa elastic modulus, with a

load of 5 N, a circular contact area of 100-μm diameter will develop, corresponding to a maximum contact pressure p_0 of about 950 MPa. As a consequence of the applied load, shear stresses will develop beneath the surface, with a maximum of about 0.3-GPa shear stress 20 μm below the surface, i.e., far below the interface between the thin coating and the substrate. A typical steel substrate is able to withstand this shear stress level. The shear stress gradually decreases going toward the surface, and only low shear strength materials will be able to fail locally, with the development of debris that will ensure that a thin transfer layer will form for the reduction of friction. This is the reason why commonly lamellar, low shear strength materials such as graphite and MoS_2 are employed as solid lubricants.[43] DLC coatings suit very well this proposed framework for low friction. They are hard and stiff materials with a typically amorphous structure. A distinction must be made between hydrogenated (a-C:H) and H-free (a-C) amorphous carbons. Under contact their surface undergoes a phase transition with the local formation of aromatic structures (for a-C:H) or graphite (for a-C). These phases are characterized by low shear strengths, which will cause the formation of wear debris. Because of the low shear strength of graphitized a:C (of the order of 10–100 MPa) wear debris will be formed, the thickness of which is related to the thickness of the graphitized layer under the surface, i.e., of the order of nanometers. It leads to very low friction in agreement with the predictions based on Eq. (1.15). In the present case (Figs. 1.1–1.3) the material will yield when the contact pressure $p = \sigma_Y/\mu$, where σ_Y and μ represent the yield stress and coefficient of friction, respectively. The point of yielding is easily reached because of the low shear strength of graphitized a-C and is expected[44] to lie beneath the contact if $\mu \leq 0.3$, which is the case at the onset of the friction coefficient in the experiment (see Fig. 1.3).

Chemical effects should be considered if the influence of the atmosphere on the coefficient of friction must be explained. For a-C:H a low humidity atmosphere is the preferred condition for low friction. The H-terminated surfaces of both counterparts ensure their contact occurs under low adhesion, so that the transfer layer will be kept at the optimal thickness. The presence of humidity influences the surface properties of the counterparts, increasing their adhesion. Under these conditions the thickness of the transfer layer will vary under sliding contact, with subsequent increase of friction, which will increase wear, modifying the transfer layer thickness and leading to an unstable situation that will finally lead to high-friction sliding. For H-free a-C the situation is different, in that in this case the transfer layer formation is "dynamic," with graphite plates continuously transferring between coating and ball, because of the low shear rate along the basal planes of graphite. The ease of mutual sliding of the graphite basal planes can be improved with the presence of intercalated water molecules, giving a very different behavior as compared to a-C:H. Also in this case, when the transfer layer thickness has reached an optimum thickness there will be a stable situation, as the corresponding low friction will ensure that no further modifications of its thickness will occur. In this case sliding in vacuum or inert atmosphere leads to an

unstable high-friction state. Under vacuum sliding the p_z orbitals of each graphite atom will be dangling on the unsaturated surface, which will increase the adhesion between two such surfaces enormously, leading to high friction and wear and no possibility for transfer layer formation. Chemical effects are probably the reason why lamellar, low shear strength materials such as Ti_3SiC_2 do not exhibit low friction following the formation of a transfer layer,[45,46] which is in contrast with the classical theory of low friction, which states that a low shear strength material on top of a hard substrate is the desired low-friction configuration. To further support the theoretical framework presented here the behavior of polymers such as HDPE (high-density polyethylene) and PTFE (polytetrafluoroethylene) sliding against glass can be mentioned.[47] These polymers form a transfer layer on the hard counterpart, but their initial coefficients of friction remain around 0.2–0.3, while the transfer layers are micrometers thick. As the sliding progresses the transfer layers become much thinner, and only then coefficients of friction as low as 0.05 are measured (for PTFE).

The physical picture is that a wear debris of nanometer thickness is formed, reducing the friction according to Eq. (1.15). The wear debris is collected during the sliding process with the ball to produce a compacted transfer layer. In getting the wear debris and transfer layer in the first place the starting roughness of the ball may play a decisive role. Commonly the roughness is around 40 nm, creating high local shear stresses around the asperities that in the beginning contribute to the formation of the wear debris and the formation of the transfer layer.

3.3. Tribological Properties: The Role of Roughness

Clearly, from the last section, roughness may have a crucial influence on the attachment and detachment of layers from a substrate. Despite its importance, the effects of roughness on tribological properties have been somewhat overlooked from a research perspective in the chapters to come. Therefore, some new ideas and developments will be presented herein. This topic was studied initially by Fuller and Tabor,[48] and it was shown that a relatively small surface roughness could diminish or even remove the adhesion. In their model a Gaussian distribution of asperity heights was considered with all asperities having the same radius of curvature. The contact force was obtained by applying the contact theory of Johnson *et al.*[49] to each individual asperity. However, this approach considers surface roughness over a single lateral length scale. The maximum pull-off, or detachment, force is expressed as a function of a single parameter that determines (the statistically averaged) competition between the compressive forces from higher asperities that try to pull the surfaces apart and the adhesive forces from lower asperities that try to hold the surfaces together.

On the other hand, randomly rough surfaces, which are commonly encountered for solid surfaces,[50,51] possess roughness over many different length scales

rather than a single one. This case was considered by Persson and Tosatti[52] for the case random self-affine rough surfaces. It was shown that when the local fractal dimension D is larger than 2.5, the adhesive force may vanish or at least be reduced significantly. Because $D = 3 - H$ the roughness effect becomes more prominent for roughness exponents $H < 0.5 (D > 2.5)$. The parameter H represents the roughness exponent (not to be confused with hardness H in this chapter) that characterizes the degree of surface irregularity. Upon decreasing H the surface becomes more irregular at short length scales.

These predictions were limited to the case of small surface roughness and the calculations were performed using power law approximations for the self-affine roughness spectrum, which are valid for lateral roughness wavelengths $q\xi > 1$, with ξ being the in-plane roughness correlation length. Extension for the case of arbitrary roughness, including contributions from roughness wavelengths $q\xi < 1$, was presented in Ref. 53. Although the effect of various roughness parameters on the detachment force was partially analyzed, a more detailed study is necessary in order to provide a complete picture of the effect of various detailed self-affine roughness parameters. In the following description the rough interface either refers to the substrate/coating system or to the coating/transfer layer on a sliding ball.

We assume that the substrate surface roughness is described by the single-valued random roughness fluctuation function $h(\vec{r})$, with $\vec{r} = (x, y)$ being the in-plane position vector, such that $\langle h(\vec{r}) \rangle = 0$. The adhesive energy is given by

$$U_{\text{ad}} = -\Delta\gamma \int \mathrm{d}^2 r \sqrt{1 + \vec{\nabla} h \cdot \vec{\nabla} h} \tag{1.16}$$

Assuming Gaussian random roughness fluctuations yields after ensemble averaging over possible random roughness configuration, with γ being the surface energy,

$$U_{\text{ad}} = -\Delta\gamma A_{\text{flat}} \left\langle \sqrt{1 + \vec{\nabla} h \cdot \vec{\nabla} h} \right\rangle \tag{1.17}$$

where

$$\left\langle \sqrt{1 + \vec{\nabla} h . \vec{\nabla} h} \right\rangle = \int_0^{+\infty} \mathrm{d}u \left(\sqrt{1 + \rho^2 u} \right) e^{-u} \tag{1.18}$$

where A_{flat} is the average macroscopic flat contact area, $\rho = \sqrt{\langle (\nabla h)^2 \rangle}$ represents the average local surface slope of the substrate rough surface, and $-\Delta\gamma$ is the change of the local surface energy upon contact due to film–substrate interaction. Substituting in $\rho = (\langle |\vec{\nabla} h|^2 \rangle)^{1/2}$ the Fourier transform of the surface height $h(\vec{q}) = (2\pi)^{-2} \int h(\vec{r})\, e^{-i\vec{q}\cdot\vec{r}}\, \mathrm{d}^2\vec{r}$, with $\vec{r} = (x, y)$ being the in-plane position vector and

assuming $\langle h(\vec{q})h(\vec{q}')\rangle = \delta^2(\vec{q}' + \vec{q})\langle h(\vec{q})h(-\vec{q})\rangle$ (i.e., translation invariance), the rms local slope ρ is given by

$$\rho^2 = \int q^2 \langle |h(\vec{q})|^2 \rangle \, \mathrm{d}^2\vec{q} = \int q^2 C(q) \, \mathrm{d}^2\vec{q} \tag{1.19}$$

where $C(q)$ is the Fourier transform of the substrate height–height correlation function $\vec{r}C(r) = \langle h(\vec{r})h(0)\rangle$ that characterizes the substrate roughness. Furthermore, the elastic energy stored in the film of elastic modulus E and Poisson's ratio v is given by

$$U_{\mathrm{el}} = -\frac{1}{2} \int \mathrm{d}^2 r \, \langle h(\vec{r})\sigma_z(\vec{r})\rangle \tag{1.20}$$

assuming that the normal displacement field of the film equals $h(\vec{r})$. Since in Fourier space we have $h(\vec{q}) = M_{zz}(\vec{q})\sigma_z(\vec{q})$ with $M_{zz}(\vec{q}) = -2(1 - v^2)/Eq$[52] and $h(\vec{q}) = (2\pi)^{-2} \int h(\vec{r}) \, e^{-i\vec{q}\cdot\vec{r}} \, \mathrm{d}^2\vec{r}$, we obtain after substitution into Eq. (1.20)

$$U_{\mathrm{el}} = A_{\mathrm{flat}} \frac{E}{4(1 - v^2)} \int q C(q) \, \mathrm{d}^2 q \tag{1.21}$$

Notably, Eq. (1.21) is valid for relatively weak roughness or small local surface slopes, $\rho = \langle (\nabla h)^2 \rangle < 1$.

A wide variety of surfaces/interfaces are well described by a kind of roughness associated with self-affine fractal scaling.[50] For self-affine surface roughness $C(q)$ scales as a power law $C(q) \propto q^{-2-2H}$ if $q\xi \gg 1$ and $C(q) \propto$ const if $q\xi \ll 1$. The roughness exponent H is a measure of the degree of surface irregularity, such that small values of H characterize more jagged or irregular surfaces at short length scales ($< \xi$). This scaling behavior is satisfied by a simple Lorentzian form $C(q)$.[53] For other self-affine roughness correlation models, see Ref. 51. Simple analytical expressions of $\rho = \langle (\nabla h)^2 \rangle$ for the local surface slope yields can be derived,[53,54] and Fig. 1.4 shows calculations of the local surface slope. Clearly a strong influence of the roughness exponent H is observed.

The change in the total free energy, when the thin layer is in contact with the rough substrate, is given by the sum of the adhesive and elastic energy such that

$$U_{\mathrm{ad}} + U_{\mathrm{el}} = -A_{\mathrm{flat}} \Delta\gamma_{\mathrm{eff}} \tag{1.22}$$

where $\Delta\gamma_{\mathrm{eff}}$ is the effective change in surface free energy due to substrate surface roughness. For $\Delta\gamma_{\mathrm{eff}}$ the main roughness contribution comes from the local surface slope ρ especially at absence of interfacial elastic energy stored in the system. Moreover, since $C(q) \propto w^2$, the influence of the rms roughness amplitude w on $\Delta\gamma_{\mathrm{eff}}$ is rather simple ($\Delta\gamma_{\mathrm{eff}} \propto w^2$) for small w (for large w the contribution to adhesion is proportional to w), while any complex dependence on the substrate surface roughness will arise solely from the roughness parameters H and ξ.

Considering a uniform slab of thickness d that undergoes a displacement $\tilde{u}$ upon the action of a force F, we can calculate the necessary force F to delaminate

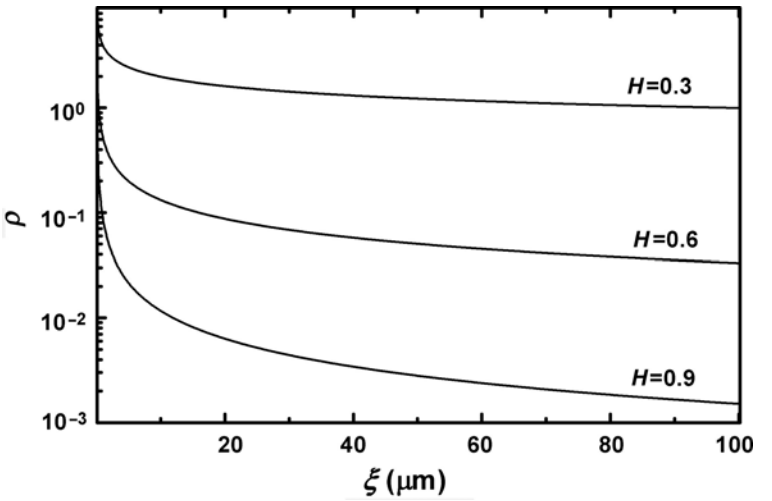

FIGURE 1.4. Local surface slope ρ as a function of the in-plane roughness correlation length ξ for $w = 10$ nm and various roughness exponents H.

the film from the substrate by equalizing the elastic energy $A_{\text{flat}} d(1/2) E(\tilde{u}/L)^2$ with the effective adhesion energy $A_{\text{flat}} \Delta\gamma_{\text{eff}}$, which is actually a Griffith calculation in fracture mechanics. Therefore, since $F = A_{\text{flat}} E(\tilde{u}/L)$, we obtain

$$F = F_{\text{flat}} \left[\int_0^{+\infty} \mathrm{d}u \, (1 + \rho u)^{1/2} \, e^{-u} - \frac{\pi E}{2(1 - \nu^2)\Delta\gamma} \int_{Q_{\text{L}}}^{Q_{\text{c}}} q^2 C(q) \, \mathrm{d}q \right]^{1/2} \tag{1.23}$$

with $F_{\text{flat}} = A_{\text{flat}}(2\Delta\gamma E/L)^{1/2}$. For small local surface slopes such that $\rho < 1$, we can rewrite the integral for the adhesive term [Eq. (1.17)] in a closed integral form and for the elastic term the analytic expression only for roughness exponents $H = 0$, $H = 0.5$, and $H = 1$ can be found.[53]

Figure 1.5 shows that the force required to detach the film increases with increasing roughness at long wavelengths or increasing ratio w/ξ, and low values of the elastic modulus E. In this case, the increment of the surface area dominates the contribution of the elastic energy. However, with increasing elastic modulus E, a maximum for the detachment force is reached, beyond which it starts to decrease rather fast and becomes even lower than the detachment force for a flat surface (elastic energy assisted detachment regime). Notably, the maximum is more pronounced for relatively low values of the elastic modulus E, so that $F_{\text{rough}} > F_{\text{flat}}$ over a significant range of roughness ratios w/ξ. The maximum indicates that the detachment can be a *multivalued* function of the ratio w/ξ, which makes the interpretation of the roughness influence more complex. The detachment force

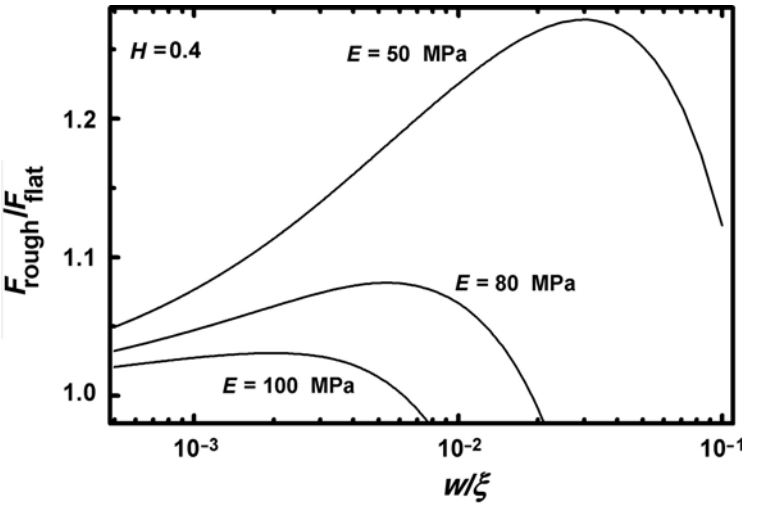

FIGURE 1.5. Detachment force $F_{\text{rough}}/F_{\text{flat}}$ versus roughness ratio w/ξ for roughness exponent $H = 0.4$, $w = 10$ nm, and various elastic moduli E.

shows a maximum with increasing roughness ratio w/ξ as long as $H < 0.5$. The detachment force decreases with increasing H at a faster rate and magnitude for $H > 0.5$ and decreasing ratio w/ξ (see also Fig. 1.6).[53,55] Up to now we assumed complete contact between the thin film and the substrate. If, however, only partial

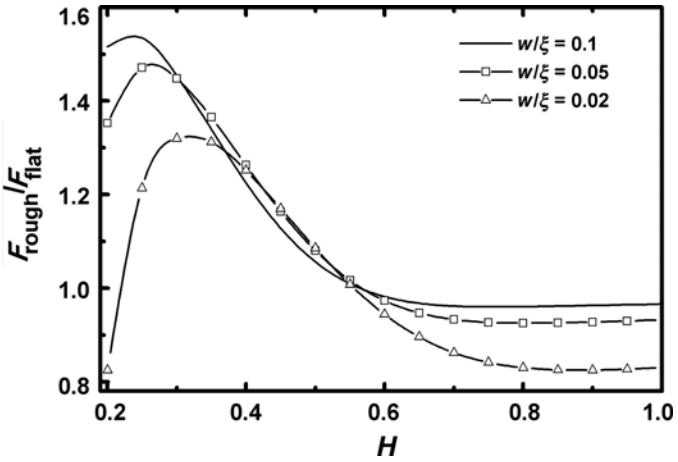

FIGURE 1.6. Detachment force $F_{\text{rough}}/F_{\text{flat}}$ versus roughness exponent H.

contact occurs at a lateral length scale λ, then the real contact area $A(\lambda)$ (if the surface was smooth on all length scales shorter than λ; or apparent area of contact on the length scale λ) is related to the macroscopic nominal contact area $A(L) = A_{\text{flat}}(\approx L^2, L \gg \xi)$.[54–56] In conclusion, it is shown that the self-affine roughness at the junction of an elastic film and a substrate influences its detachment force in a way that the detachment force can be smaller than that of a flat surface for relatively high elastic modulus E, depending also on the specific roughness details. When the surface becomes rougher at long wavelengths, i.e., with increasing ratio w/ξ, the effect of elastic energy becomes more dominant, leading to a detachment force that shows a maximum after which it decreases and becomes lower than that of a flat surface. Similar is the case of partial contact, where the detachment force also increases as the contact length increases up to a maximum for contact lengths larger than the roughness correlation length ξ. It further decreases and is followed by saturation. The multivalued behavior around the maximum further complicates the interpretation of the roughness influence. These results clearly indicate that the roughness has to be precisely quantified in fraction and wear studies. So far, we should note that our analytic calculations are strictly valid for elastic solids and more research is needed to include plasticity.

4. LEITMOTIV AND OBJECTIVE

The empirical knowledge brought by the study of many complex systems showed the importance of managing the structure of the deposited materials at different levels, including the size of the crystallites. The experience accumulated led to the development of theories based on fundamentals in materials science, which could help to explain the unusual values found for the combinations of mechanical strength and fracture toughness that some coatings could exhibit. These theories were in many cases too speculative and only very recently the use of powerful analyzing techniques is being introduced to confirm their validity. However, there are so many interrelated factors affecting the formation of a thin coating that the theories have to be progressively adapted to the arising "new" results of the characterizing experimental techniques. Without being exhaustive, and giving a simple example such as the deposition of carbon and the use of only one processing technique (e.g., sputtering), it is possible to deposit from the graphitic form up to a high degree of diamond type with sp^3/sp^2 ratios from almost 0 to almost 1 and a panoply of mechanical properties, such as hardness in the range from 1 to 80 GPa. The coatings are often deposited in a reactive mode with hydrogen contents that can reach values of 50%. The presence of other impurities resulting from the process itself, such as argon, introduces one more variable. The challenge now is to correlate all these factors, either with the microstructure (type of phases, grain sizes, phase distribution, residual stresses) or with the processing parameters (partial pressure of reactive gas, discharge pressure, input of energy in the growing film), to understand the

processing–structure–property relationships. If a ternary system is being treated, the complexity increases considerably. The possibility to form different mixtures of phases, all of them in different thermodynamic states, with several structural parameters, still justifies an empirical approximation. It must be remarked that many of the actual industrially used hard coatings belong to these ternary systems, e.g., Ti–Al–N coatings.

The synergy of knowledge acquired already by materials scientists on nanocrystalline materials and by materials engineers on the deposition and characterization of coatings is extremely important for the future development of advanced coatings. This was the leitmotiv of this book. It intends to be a text focusing on the latest developments in the interpretation of the mechanical behavior of nanocrystalline materials, in the form of both bulk and thin film. The state of the art presented in the different chapters is concentrated in the subjects that, in each field, are judged to allow being integrated in common future research studies. For materials scientists, it demonstrates a collection of experimental cases that can stimulate the interest of their unique character, in relation to the nanocrystalline nature. For the materials engineers, this book is a source of information that can bring new scents for further analysis of the experimental results. In summary, the impetus for this book revolves around the fundamental basis for the understanding of the mechanical behavior of nanostructured materials and their differences in relation to traditionally processed ones. The state-of-the-art deposition and characterization techniques for hard nanostructured coatings for mechanical applications are also proposed and reviewed.

This particular approach is quite different from the extensive literature available in both fields of nanostructured materials and hard coatings. Excellent review books, papers, and special issues of scientific journals have been published in recent years, on either the study of the mechanical behavior of nanostructured materials, supported by the results of powerful techniques of analysis, or the deposition of coatings for tribological applications by using different kinds of processing techniques, including PVD and CVD methods. Many of these references are available in the chapters of this book.

The guidelines followed for the selection of the themes were pointed on the words "mechanical behavior," in particular hardness and toughness. In all cases, special attention was paid to the relationship between the hardness and the structural/microstructural features. Two main parts can be considered in the book, the first one dealing with what can be called "fundamental principles," i.e., a close insight of the understanding of the mechanical behavior of nanostructured materials. It includes a sequence comprising bulk materials and films deposited on substrates with the necessary complement by MD simulation results for validation of the experimental results. Two main characterization techniques capable of validating the experimental microstructure–hardness relationship are also reviewed in this section. These are, namely, electron microscopy techniques with all the complementary accessories for chemical composition, bond type and structural

analyses, and depth-sensing indentation for the elastic and plastic characterization of the materials, with an emphasis on those deposited under the form of thin films. This is in most of the cases the unique suitable technique for the mechanical characterization of a coated material.

In the second part, selected hard coatings are outlined, either under development or already in industrial applications. The first restriction used in this part was the processing technique; only coatings deposited by PVD or CVD methods were considered. Furthermore, taking into account the importance of the microstructure–structure/hardness relationship in nanostructured films for the aim of this book, no contributions on intrinsically super-hard coatings were selected. Boron nitride/carbide-based films (DLC and diamond) are not treated in this book. It should be remarked that with nanocomposite structures, very interesting results are now being obtained with self-lubricating coatings, which combine their self-lubricating character to hardness values as high as 20 GPa. Two chapters were dedicated to the influence that the addition of a third element can have in the structure and functional properties of transition metal nitrides and carbides. These materials are the most widely studied and used hard coatings since the beginning of their development in the latter part of the 1960s. These chapters point at the cases where single-phase films are deposited, although the problem of phase separation has already been touched upon. The transition metal nitrides serve as a common base in most of the other chapters. Two of them deal with nanocomposite coatings: one from the materials point of view and the other on the influence of the processing parameters required to achieve this type of nanostructure. The thermal stability and the conditions for optimizing the tribological behavior of these nanostructured coatings are treated in separate chapters. Finally, the book ends with two chapters dedicated to one particular type of nanocomposite coating—the low-period multilayers. The first of these deals with the more fundamental concepts on the interaction in multilayers, whereas the last chapter gives the "happy end" to the book, presenting an extensive review of industrial applications of these kinds of coatings, particularly for multilayer films. Galileo would have appreciated it.

ACKNOWLEDGMENTS

Financial support from the foundation Fundamental Research on Matter (Physics division Netherlands Organization for Scientific Research, The Hague), TNO Institute of Industrial Technology, the Netherlands Institute for Metals Research is gratefully acknowledged. Thanks are due to Yutao Pei, Damiano Galvan, Dave Matthews, George Palasantzas, Redmer van Tijum, Willem-Pier Vellinga, Dimitri van Agterveld, and Arjen Roos for discussions on various aspects in this chapter.

REFERENCES

1. Galileo, *Discorsi e Dimonstrazioni Matematiche* (Leyden, The Netherlands, 1635) (See also: http://galileoandeinstein.phys.virginia.).
2. K. Holmberg and A. Matthews, Coatings tribology, in *Tribology Series 28*, edited by D. Dowson (Elsevier, Amsterdam, 1994).
3. K. N. Strafford, P. K. Datta, and J. S. Gray, *Surface Engineering Practice* (Ellis Horwood, New York, 1990).
4. R. F. Bunshah, Introduction, in *Handbook of Hard Coatings: Deposition Technologies, Properties and Applications*, edited by R. F. Bunshah (Noyes Publications, New Jersey, 2001), Chapter 1.
5. A. Leyland and A. Matthews, On the significance of the H/E ratio in wear control: A nanocomposite coating approach to optimized tribological behavior, *Wear* **246**, 1 (2000).
6. T. S. Sudarshan, and M. Jeandin (eds.), *Surface Modification Technologies*, Series of the Institute of Materials, vols. 1–18 (Institute of Materials, London, 1988–2004).
7. K. J. Van Vliet, J. Li, T. Zhu, S. Yip, and. S. Suresh, Quantifying the early stages of plasticity through nanoscale experiments and simulations, *Phys. Rev.B* **67**, 104105 (1999).
8. J. R. Weertman, D. Farkas, H. Kung, M. Mayo, R. Mitra, and H. Van Swygenhoven, Structure and mechanical behavior of bulk nanocrystalline materials, *MRS Bull.* **24**, 44 (1999).
9. S. Veprek, P. Nesladek, A. Niederhofer, F. Glatz, M. Jilek, and M. Sima, Recent progress in the superhard nanocrystalline composites: Towards their industrialization and understanding of the origin of the superhardness, *Surf. Coat. Technol.* **108**, 138 (1998).
10. J. Patscheider, T. Zehnder, and M. Diserens, Structure performance relations in nanocomposite coatings, *Surf. Coat. Technol.* **146**, 201 (2001).
11. F. Vaz, L. Rebouta, S. Ramos, M. F. da Silva, and J. C. Soares, Physical, structural and mechanical characterization of $Ti_{1-x}Si_xN_y$ films, *Surf. Coat. Technol.* **108**, 236 (1998).
12. T. Zehnder and J. Patscheider, Nanocomposite TiC/a-C:H hard coatings deposited by reactive PVD, *Surf. Coat. Technol.* **133**, 138 (2000).
13. A. A. Voevodin and J. S. Zabinski, Supertough wear-resistante coatings with "chameleon" surface adaptation, *Thin Solid Films* **370**, 223 (2000).
14. J. E. Kranowski and S. H. Koutzaki, Mechanical properties of sputter-deposited titanium–silicon carbon films, *J. Am. Ceram. Soc.* **84**, 672 (2001).
15. Y. T. Pei, D. Galvan, and J. Th. De Hosson, Nanostructure and properties of TiC/a-C:H composite coatings, *Acta Mater.* **53**, 4505 (2005).
16. S. Veprek and A. S. Argon, Towards the understanding of mechanical properties of super and ultrahard nanocomposites, *J. Vac. Sci. Technol. B* **20**, 650 (2002).
17. A. Cavaleiro and C. Louro, Nanocrystalline structure and hardness of thin films, *Vacuum* **64**, 211 (2002).
18. J. Patscheider, Nanocomposite hard coatings for wear protection, *MRS Bull.* **28**, 180 (2003).
19. M. Nastasi, P. Kodali, K. C. Walter, J. D. Embury, R. Raj, and Y. Nakamura, Fracture thoughness on diamond like carbon coatings *J. Mater. Res.* **14**, 2173 (1999).
20. N. J. M. Carvalho and J. T. M. De Hosson, Microstructure investigation of magnetron sputtered, *Thin Solid Films* **388**, 150 (2001).
21. N. J. M. Carvalho, E. Zoestbergen, B. J. Kooi, and J. T. M. De Hosson, Stress analysis and microstructure of PVD monolayer TiN and multilayer TiN/(Ti,Al)N coatings, *Thin Solid Films* **429**, 179 (2003).
22. J. P. Hirth and J. Lothe, *Theory of Dislocations* (McGraw-Hill, New York, 1968).
23. J. D. Embury, Strengthening by dislocation substructures, in *Strengthening Methods in Crystals*, edited by A. Kelly and R. B. Nicholson (Wiley, New York, 1971).
24. T. H. Courtney, *Mechanical Behavior of Materials* (McGraw-Hill, New York, 1990).
25. V. Vitek, *Modeling of the Structure and Properties of Amorphous Materials* (The Metallurgical Society of AIME, New York, 1983).
26. E. D. Hondros and D. McLean, *Monograph 28* (Society of Chemical Industry, London, 1968).

27. M. P. Seah, Grain-boundary segregation and T-T dependence of temper brittleness, *Acta Metall.* **25**, 345 (1977).
28. J. R. Rice and J. S. Wang, Embrittlement of interfaces by solute segregation, *Mater. Sci. Eng. A* **107**, 23 (1989).
29. J. P. Hirth and J. R. Rice, On the thermodynamics of adsorption at interfaces as it influences decohesion, *Metall. Trans A*. 11 **9**, 1501 (1980).
30. H. Van Swygenhoven, D. Farkas, and A. Caro, Grain boundary structures in polycrystalline metals at the nonoscale, *Phys. Rev. B* **62**, 831 (2000).
31. H. Van Swygenhoven and P. M. Derlet, Grain-boundary sliding in nanocrystalline fcc metals, *Phys. Rev. B* **64**, 224105/1–9 (2001).
32. M. Y. Gutkin and L. A. Ovid'ko, *Plastic Deformation in Nanocrystalline Materials* (Springer, Berlin, 2004).
33. S. M. Hsu, Nano-lubrication: Concept and design, *Tribol. Int.* **37**, 537 (2004).
34. A. Erdimir, Design criteria for superlubricity in carbon films and related microstructures, *Tribol. Int.* **37**, 577 (2004).
35. J. B. Sokoloff, Theory of atomic level sliding friction between ideal crystal interfaces, *J. Appl. Phys.* **72**, 1262 (1992).
36. P. P. Gruner, Phonon scattering, in *Fundamental Aspects of Dislocation Theory*, edited by J. A. Simmons, R. de Wit, and R. Bullough (National Bureau of Standards, USA,1970), Special Publications 317 and 363.
37. P. G. Klemens, Thermal conductivity and lattice vibration modes, in *Solid State Physics No. 7*, edited by F. Seitz, and D. Turnbull (Academic Press, New York, 1958).
38. C. J. Morath, H. J. Maris, J. J. Cuomo, D. L. Pappas, A. Grill, V. V. Patel, J. P. Doyle, and K. L. Saenger, Picosecond optical studies of amorphous diamond like carbon: Thermal conductivity and longitudinal sound velocity, *J. Appl. Phys.* **76**, 2636 (1994).
39. A. J. Bullen, K. O'Hara, D. G. Cahill, O. Monteiro, and A. Von Keudell, Thermal conductivity of amorphous carbon thin films, *J. Appl. Phys.* **88**, 6317 (2005).
40. R. Landauer, The electric resistance of binary metallic mixtures, *J. Appl. Phys.* **23**, 779 (1952).
41. F. W. Smith, Optical-constants of a hydrogenated amorphous carbon film, *J. Appl. Phys.* **55**, 764 (1984).
42. J. B. Sokoloff, Possible nearly frictionless sliding for mesoscopic solids, *Phys. Rev. Lett.* **71**, 3450 (1993).
43. I. L.Singer, R. N. Bolster, J. Wegand, S. Fayeulle, and B. C. Stupp, Hertzian stress contribution to low friction behavior of film MoS_2 coatings, *Appl. Phys. Lett.* **57**, 995 (1990).
44. K. L. Johnson, *Contact Mechanics* (Cambridge University Press, Cambridge, UK, 1999).
45. T. El-Raghy, P. Blau, and M. W. Barsoum, Effect of grain size on friction and wear behaviour of Ti_3SiC_2, *Wear* **238**, 125 (2000).
46. T. Zehnder, J. Matthey, P. Schwaller, A. Klein, P.-A. Steinmann, and J. Patscheider, Wear protective coatings consisting of TiC–SiC–a-C:H deposited by magnetron sputtering, *Surf. Coat. Technol.* **163**, 238 (2003).
47. I. M. Hutchings, *Tribology: Friction and Wear of Engineering Materials* (Edward Arnold, UK, co-published by CRC Press, Boca Raton, FL, 1992).
48. K. N. G. Fuller and D. Tabor, Effect of surface roughness on adhesion of elastic solids, *Proc. R. Soc. Lond. A* **345**, 327 (1975).
49. K. L. Johnson, K. Kendall, and A. D. Roberts, Surface energy and contact of elastic solids, *Proc. R. Soc. Lond. A* **234**, 3018 (1971).
50. P. Meakin, *Fractals, Scaling, and Growth Far from Equilibrium* (Cambridge University Press, Cambridge, UK, 1998).
51. Y. P. Zhao, G. C. Wang, and T. M. Lu, Characterization of amorphous and crystalline rough surfaces—principles and applications, in *Experimental Methods in the Physical Science*, Vol. 37 (Academic Press, New York, 2000).

52. B. N. J. Persson and E. Tosatti, The effect of surface roughness on the adhesion of elastic solids, *J. Chem. Phys.* **115**, 5597 (2001).
53. G. Palasantzas and J. T. M. De Hosson, Influence of surface roughness on the adhesion of elastic films, *Phys. Rev. E* **67**, 021604/1–6 (2003).
54. J. Krim and G. Palasantzas, Experimental observation of self-affine scaling and kinetic roughening at submicron lengthscales, *Int. J. Mod. Phys. **B*** **9**, 599 (1995).
55. G. Palasantzas and J. T. M. De Hosson, Evolution of normal stress and surface roughness in buckled thin films, *J. Appl. Phys.* **93**, 893 (2003).
56. B. N. Persson, Elastoplastic contact between randomly rough surfaces, *J. Phys. Rev. Lett.* **87**, 11161 (2001).

2

Size Effects on Deformation and Fracture of Nanostructured Metals

Benedikt Moser[1], Ruth Schwaiger[2], and Ming Dao[3]

[1]EMPA Materials Science and Technology, Thun, Switzerland

[2]Forschungszentrum Karlsruhe, Karlsruhe, Germany

[3]Massachusetts Institute of Technology, Cambridge, MA, USA

1. INTRODUCTION

Material properties undergo significant changes as some characteristic length scales approach the nanometer regime. In what follows, we will focus on the mechanical properties of nanostructured metals. In our understanding, the term "nanostructured metals" comprises systems with at least one characteristic length scale smaller than 100 nm. This could be the grain size (referred to as "microstructural constraint"), as well as the specimen size or film thickness in a film–substrate system (referred to as "dimensional constraint").[1] Properties of such materials cannot simply be extrapolated from the properties of conventional samples. The extensive use of thin films in the production of microelectronic devices or in corrosion protection and of bulk nanostructured materials in wear-intense applications has stimulated considerable interest in their mechanical properties and significant research efforts in both the scientific community and the industry.

In the further discussion, we use the term "nanocrystalline" (nc) for metals with an average grain size and range of grain sizes smaller than 100 nm. "Ultrafine crystalline" (ufc) metals are those with a grain size in the 100–1000 nm range, and their "microcrystalline" (mc) counterparts have an average grain size of a micrometer or larger.

We will start with a brief overview of mechanical testing techniques (Section 2) that are typically used for testing nanostructured materials. In Sections 3 and 4, we will continue with a description of the current understanding of deformation (monotonic and cyclic) and fracture in nanostructured metals and related size effects. A short section (Section 3.2) will highlight some results on amorphous metals that are relevant for our understanding of deformation mechanisms in nc

metals. In the course of this essay, we will emphasize size effects and distinguish between effects related to microstructural or dimensional constraint.

2. MECHANICAL TESTING OF NANOSTRUCTURED BULK AND THIN FILM MATERIALS

The determination of mechanical properties of nanoscaled materials as well as the investigation of size-related effects often require mechanical testing of small-volume specimens. In some cases, the reason is the limited availability of materials; in other cases, it is the inherently small scale of one or several dimensions such as film thickness in thin films or diameter in nanowires. Many conventional testing techniques have simply been scaled down, but novel techniques such as bulge testing, nanoindentation, and microbeam deflection have been developed as well. These techniques aim at determining material properties such as Young's modulus, yield strength, strain-rate sensitivity, strain-hardening rate, and tensile or fracture strength in small volumes. In addition, the question about governing deformation mechanisms has driven the development of new ways of testing. Methods relevant to testing of nanostructured metals will be briefly described in the following sections.

2.1. Tensile and Compression Testing

For conventional elastoplastic materials, tensile testing is the most important and desirable testing method, mainly because of the specimen's uniaxial stress state, yielding the highly useful stress–strain curve. Compression testing, although often involving a more complicated stress state due to friction at the loading surface and resulting barreling, is in certain cases preferable due to the more stable deformation particularly for materials with limited ductility. When tensile failure due to porosity or other material flaws is a problem, substantial plastic deformation can often be reached by compression testing, which is less affected by defects.[2,3]

Tensile testing of conventional materials is standardized and regulated in several testing norms.[4,5] If the material's availability is limited and the specimen geometry requirement cannot be fulfilled, the specimen geometry should be scaled down in a self-similar manner in order to maintain a uniaxial stress state in the gauge section. Special care is required in order to avoid scaling-related measurement *artifact*s:

- Geometry measurement has to be done with a higher absolute precision in the case of smaller specimens. Measuring a standard tensile testing specimen with a caliper might be adequate, but measuring submillimeter cross-sectional dimensions might require a micrometer screw.
- Surface preparation is more critical for smaller specimens; a better surface finish can significantly increase the tensile strength.[6] Even native oxide

layers can in some cases influence the tensile testing results of very small specimens.[7]

- The use of conventional strain measurement equipment, such as miniaturized clip-on extensometers or glued strain gauges, may introduce a considerable stiffening of the miniature specimen.

In addition to downscaling of conventional standardized tensile testing, novel microtensile testing systems have been developed (e.g., Refs. 8 and 9). The size of the specimens used in these systems renders conventional strain measurement techniques impossible; noncontact strain measurement with video- or laser extensometers can be employed instead. However, these methods still require a certain minimum specimen size because, in general, a marker has to be placed on the specimen surface. For micron-sized specimens, special vision algorithms have been developed, extracting strain information from an optical microscope video capture of the specimen during the test.[10] Furthermore, micro electro mechanical system (MEMS) testing devices, especially suited for freestanding thin films and samples with submicron dimensions, have been developed (cf. Fig. 2.1).[11–16] These testing devices may contain actuator and sensor on one chip[13]; in other cases, the actuation is done by a piezo crystal.[16] In the case of freestanding thin films, the specimen can even be fabricated together with the test chip.[12] Displacement and load resolutions of MEMS testing devices are high; however, calibrations are

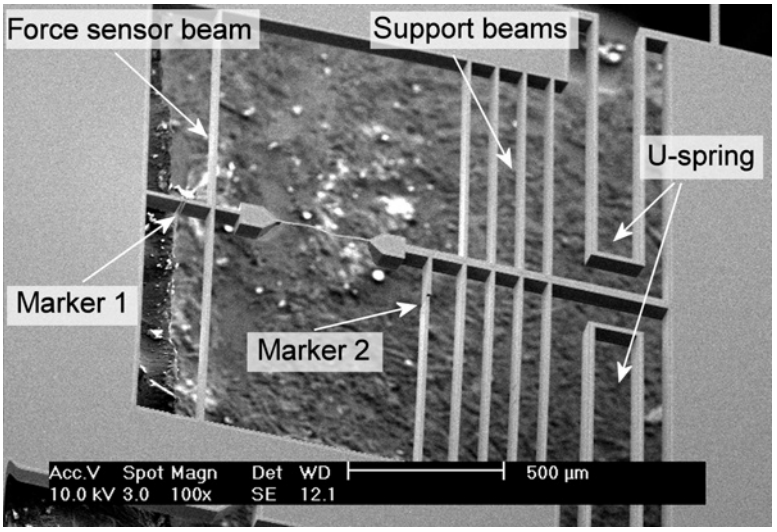

FIGURE 2.1. Test chip for the testing of a freestanding thin film in the scanning electron microscope. The chip includes the specimen, a force sensor beam, displacement measurements markers, and several alignment springs. Actuation is done externally (e.g., by a piezo crystal). (Courtesy of T. Saif, University of Illinois at Urbana—Champaign, Urbana, IL.)

often indirectly done through calculations or additional experiments after the test, which reduces the accuracy of results.

Alternatively, thin films can be tested in tension while resting on an elastically or plastically deformable soft substrate. The film stress can either be inferred by measuring the response of the substrate alone and subtracting it from the measured response of the film–substrate system[17] or by X-ray measurement of the film stress–strain.[18] Using a purely elastic substrate such as polyimide, the metal thin film deforms plastically and can be tested in compression simply by unloading, as the total strain on the film–substrate system is still tensile and buckling is not an issue.[19] This method has successfully been used to study the fatigue behavior of Cu thin films.[20] Thermal cycling is another method used to investigate the stress–strain behavior of a thin film on a substrate. This method is based on the thermal mismatch between film and substrate, resulting in a curvature of the specimen and strain in the film. For a thorough description of thin film testing techniques, see for instance Refs. 21 and 22.

2.2. Indentation Testing: Experimental Technique and Computations

The determination of hardness has a long tradition in materials testing.[23,24] In conventional hardness testing, a hard tip is pressed into the material and the residual indentation size is measured optically. The size of such an indentation mark has to be in the range of micrometers in order to be measurable in an optical microscope. For nanostructured materials, the size of such an indent could exceed the specimen size or the film thickness. Thus, a variety of depth-sensing hardness testing systems have been developed (see Ref. 25, pp. 142–158, for a brief overview of commercially available instruments). During the past decade, interest in indentation has increased significantly; first, because of its simplicity of sample preparation, and second, because of the noticeable improvement of indentation equipment. It is now possible to monitor with high precision both load and displacement of an indenter during indentation experiments in the micro-Newton and nanometer ranges, respectively. The high spatial resolution and accurate positioning also add to the popularity of nanoindentation methods; indentation systems frequently offer the possibility to image the sample surface prior to testing, to choose the position of the indentation with high lateral accuracy, and also to image the residual imprint afterwards. Furthermore, the tested material volume is easily scalable by changing the load on the indenter, which makes this method particularly useful to determine length-scale effects, such as film thickness and grain size effects, in nanostructured materials.

During the indentation process, a load P is applied to the tip, and the tip penetration h into the material is measured. For nanoindentation, Berkovich tips, which are sharp three-sided diamond pyramids, are commonly used. The contact stiffness between the tip and the specimen is then determined either from the peak load and the initial slope of the unloading curves[26,27] or dynamically during the loading portion.[26,28] The dynamic measurement is accomplished by superimposing a small oscillation to the load on the indenter tip and measuring the resulting displacement

of the tip with a lock-in amplifier. By this technique, truly instantaneous values of the stiffness can be obtained for all penetration depths.

Using the contact stiffness, hardness and Young's modulus may be calculated when the tip shape and consequently the contact area are known. Methods to do so have long been established by Doerner and Nix[27] and Oliver and Pharr.[26] The determination of the elastic modulus and the hardness depends strongly on an accurate measurement of the contact area. However, this is not always straightforward, particularly for metals, because material may pileup or sink-in in the vicinity of the indentation, resulting in under- or overestimation of the contact area, respectively.[29] A quantitative measurement of the surface topography allows to determine the true contact area of the indent and gives a more accurate result for elastic modulus and hardness.[30]

Today, a comprehensive framework of theoretical and computational studies exists, elucidating the contact mechanics and deformation mechanisms in order to systematically extract material properties from P–h curves obtained from instrumented indentation (e.g., Refs. 26, 27, and 31–36).

In what follows, we will focus on fundamental studies of contact mechanics during the indentation process, enabling an accurate estimation of elastic *and* plastic properties of the indented material.

The elastic and plastic properties may be computed from the indentation response, following a procedure proposed by Giannakopoulos and Suresh[34]; the residual stresses may be extracted by the method described in Ref. 33. Using the concept of self-similarity, simple but general results of elastoplastic indentation response have been obtained. Recently, scaling functions were applied to study bulk[37] and coated material systems.[38] Despite these advances, an accurate characterization method to extract plastic properties remains elusive. This issue was addressed by Dao *et al*.,[31] who constructed a set of universal dimensionless functions in order to describe the indentation response of a power law elastoplastic material. Figure 2.2 shows the typical P–h response of an elastoplastic material to sharp indentation. In the absence of an indentation size effect,[39] the loading portion of the indentation response generally follows the relation described by Kick's law,

$$P = Ch^2 \tag{2.1}$$

where C is the loading curvature. The average contact pressure $p_{\text{ave}} = P_{\text{m}}/A_{\text{m}}$ (A_{m} is the true projected contact area measured at the maximum load P_{m}) can be identified with the hardness of the indented material. The maximum indentation depth h_{m} occurs at P_{m}, and the initial unloading slope is defined as $\frac{\mathrm{d}P_{\text{u}}}{\mathrm{d}h}\big|_{h_{\text{m}}}$, where P_{u} is the unloading force. In Fig. 2.2, W_{t} is the total work done by the load P during loading, W_{e} is the released (elastic) work during unloading, and $W_{\text{p}} = W_{\text{t}} - W_{\text{e}}$ the stored (plastic) work. The residual indentation depth after complete unloading is h_{r}.

As discussed by Giannakopoulos and Suresh,[34] C, $\frac{\mathrm{d}P_{\text{u}}}{\mathrm{d}h}\big|_{h_{\text{m}}}$, and $\frac{h_{\text{r}}}{h_{\text{m}}}$ are three independent quantities that may be directly obtained from a single P–h curve. Dao *et al*.[31] proposed a set of reverse algorithms to use these three

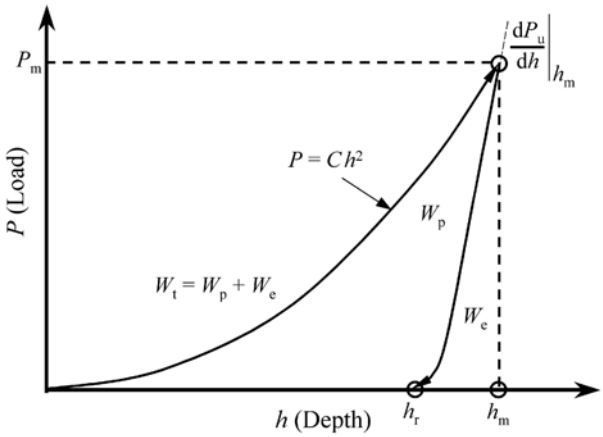

FIGURE 2.2. Schematic illustration of a typical *P–h* response of an elastoplastic material to instrumented sharp indentation.[31]

indentation parameters to extract three (unknown) mechanical properties: reduced modulus E^*, yield strength σ_y, and hardening exponent n. The so-called reverse algorithms enable the extraction of elastoplastic properties from a given set of indentation data, whereas the forward algorithms allow for the calculation of a unique indentation response for a given set of elastoplastic properties. For a Berkovich or Vickers indenter, a representative strain ε_r was identified at 3.3%.[31] It was further demonstrated that within the same theoretical framework, the apparent disparities between the value of 3.3% identified and the values of 8%[23,40] and 29%[34,41] proposed in the literature stem from the different functional definitions used to obtain these values, rather than from any intrinsic differences in mechanistic interpretations.[31] Various authors discussed the important issue of sensitivity,[31,42,43] and realized that within certain parameter ranges the reverse analysis results are sensitive to experimental scatter.

More recently, a systematic methodology[44,45] and experimental verifications[45] of dual indentation algorithms were proposed by Bucaille *et al.*[44] and Chollacoop *et al.*[45] The computational as well as experimental results showed that the dual indentation method can significantly improve the accuracy of the extracted plastic property.[44–46]

The presented computational models are valid only in the absence of an indentation size effect (i.e., at large enough indentation depths). At small indentation depths of the order of 100 nm to 1 μm, an increase in hardness with decreasing indentation depth is often observed.[39,47–49] This phenomenon is generally believed to be related to geometric necessary dislocations due to the sharp strain gradients imposed by the indenter tip.[39,47–49] How to effectively describe the indentation size effect and how to extract mechanical properties from small indents affected by that effect is still an open question and needs further careful studies.

Another important phenomenon that can complicate the above-mentioned computational analysis of P–h curves is the frequently observed discontinuities (also called pop-ins) in these curves for indentation depths smaller than roughly 100 nm in crystalline materials.[32,50] It was proposed that these pop-ins are triggered by the homogeneous nucleation of dislocations under the indenter.[32,50–52] The phenomenon is normally associated with single crystals and mc metals. It is unclear to what extent the small grain size in ufc and nc metals is affecting or even suppressing this behavior.

2.3. Cantilever Bending

Another technique to study elasticity and plasticity of thin films and nanostructured materials using nanoindentation equipment is the deflection of microbeams.[53–55] The volume tested during microbeam deflection is somewhat larger than in nanoindentation experiments. The microbeams are micromachined applying lithography and etching techniques and have typical dimensions of about 100-μm length, 10–20-μm width, and a few micrometers thickness. This rather extensive sample preparation cannot be applied to all materials and structures.

Nanoindentation systems have been used for several beam deflection studies on single-layer and bilayer beams.[53–57] In the case of bilayer beams, the substrate beams are generally made of Si or SiO_2. Then, a thin metal film is deposited onto the beams. The beams are deflected using a nanoindenter and the P–h behavior is recorded. A schematic of this experiment is shown in Fig. 2.3. For rectangular beams, strain distribution and deformation in the thin metal film are not homogeneous; hence, it is not straightforward to obtain the stress–strain behavior of the thin film material. This problem can be avoided by using beams of triangular shape,[56,57] which results in a constant bending moment per unit width. Consequently, the strain on top of the beam is constant and the thin film on the surface is homogeneously deformed.

Both methods, nanoindentation and microbeam deflection, are suitable for characterizing plastic behavior, but do not give direct results for the yield or tensile strength, the elongation to failure, or hardening rate. Due to the complex loading conditions, more sophisticated analysis methods are required to extract the

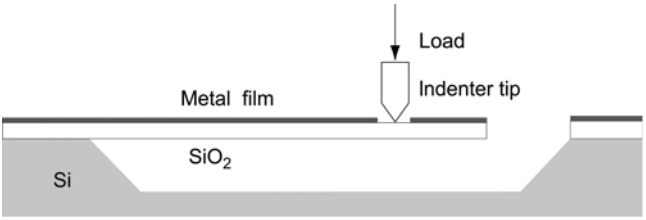

FIGURE 2.3. Schematic of beam deflection experiment. In this edge view, the SiO_2 beam extends over an etch pit in the underlying Si substrate. A thin film can be deposited on the microfabricated beams. (Adapted from Ref. 58.)

materials parameters. A comprehensive study was undertaken by Schwaiger and Kraft[57] to identify the extent to which the mechanical properties of thin metal films on substrates could be determined quantitatively from nanoindentation and microbeam deflection. Thin Cu films on substrates were tested and the mechanical behavior was described using finite elements with a simple bilinear constitutive law. The results from finite element modeling of nanoindentation and microbeam deflection were quite different. Microbeam deflection experiments appeared to be more sensitive to the elastic–plastic transition, whereas the nanoindentation results described the mechanical behavior at larger plastic strains more accurately.

At this point we want to mention that MEMS-based bending tests have been developed recently.[13] For this type of experiment, an electrostatic comb drive actuator was used to generate the load. The actuator had a probe to apply a point load on the cantilever specimen. In this particular case, a 100-nm-thick freestanding Al film was tested. These novel design and testing methods show that some powerful tools are available to investigate fundamental mechanical properties in nanostructured materials.

2.4. *In Situ* Testing Technique

In situ experiments with direct observation in an optical or electron microscope can reveal important information about deformation mechanisms in materials. Microtensile and cantilever bending experiments are well suited for *in situ* studies in a transmission (TEM) or scanning (SEM) electron microscope.[59–63] Often MEMS tensile devices are used in a SEM or TEM.[12,15,64] Furthermore, a nanoindenter for *in situ* TEM studies has recently been developed and successfully used to indent Al thin films.[65,66]

Observations during *in situ* experiments need to be judged with care. The correct interpretation of the results has to take possible artifacts into account. TEM specimens are very thin and the observed material behavior could be influenced by the close proximity of the surface. During *in situ* SEM studies the behavior only at the surface, not necessarily representative for the bulk, can be observed.

3. DEFORMATION AND FRACTURE UNDER MICROSTRUCTURAL CONSTRAINT

3.1. Crystalline Materials

3.1.1. Microstructure

Ultrafine crystalline and nanocrystalline metals can be produced by a number of different methods that can roughly be divided into four groups: cryomilling and compaction,[67–69] severe plastic deformation,[70] gas condensation and consolidation,[71–73] and electrodeposition.[74,75] The microstructure of the produced metals is closely related to the manufacturing process. The first two methods produce

reasonable amounts of bulk material and yield grain sizes in the ufc regime (100–1000 nm). The latter two yield nc materials with grain sizes below 100 nm, but quantity is very limited. Both compaction processes suffer from some porosity and/or unwanted grain growth during the compaction process (particularly when the process is thermally assisted). Ultrafine crystalline metals produced by repeated severe plastic deformation are 100% dense and exhibit high dislocation density. Their microstructure usually consists of a few larger grains containing a clear subgrain structure. Electrodeposition enables the processing of nc metals with grain sizes down to a few nanometers and a narrow grain size distribution.[76,77] The material usually exhibits a 100% density, although some nanoporosity in electrodeposited Ni has been detected by Van Petegem *et al*.[78] using TEM and positron annihilation lifetime measurements. The chemical purity is normally relatively high compared to materials produced by other processing routes. However, so far only sheet material with a thickness of a few hundred micrometers can be produced with high quality. A short overview of the different processing routes with information on the resulting microstructure can be found in Ref. 79.

The structure of grain boundaries in nc metals has been under debate for a long time. Earlier studies suggested that an amorphous layer existed at the grain boundaries exhibiting a high degree of disorder.[80] There is, however, growing evidence from high-resolution TEM studies that grain boundaries in nc materials are very similar to grain boundaries in mc materials.[59,81] Crystallinity is usually maintained up to the grain boundaries and the intercrystalline density is found to be very close to the density of the respective single crystals.[82] Recent molecular dynamics (MD) studies have corroborated these results.[83,84]

It is generally accepted that nc metals are thermodynamically unstable. Critical temperatures for normal and abnormal grain growth have been determined[85–89] and alloying is generally found to inhibit grain growth to a certain extent and make the structure stable to higher temperatures.[90,91]

Quite a few experimental studies have been performed on electrodeposited, fully dense, high-purity Ni. Since it is relevant to the subsequent discussion, the microstructure of this material (procured from Integran Technologies Inc., Canada) will be described in greater detail at this point. Figure 2.4 shows the microstructures of differently grain-sized specimens. The microstructure of nc Ni (Fig. 2.4a) has been thoroughly characterized by Kumar *et al*.[59] The average grain size was determined from transmission electron micrographs to be about 40 nm, with a fairly narrow grain size distribution and the largest grain diameters smaller than 100 nm. This is an important point because a few large grains can dominate the deformation behavior of the material and determine its performance. The grains have a considerable aspect ratio; however, the major axis length is insignificant compared to the specimen thickness. The material contains a considerable number of growth twins. The grain interior was generally found to be clean and free of dislocations. The grain boundaries showed no evidence of second-phase particles or films or any amorphous grain boundary layer; crystallinity is maintained up to the grain boundary. Occasional low-angle grain boundaries are present in this material.

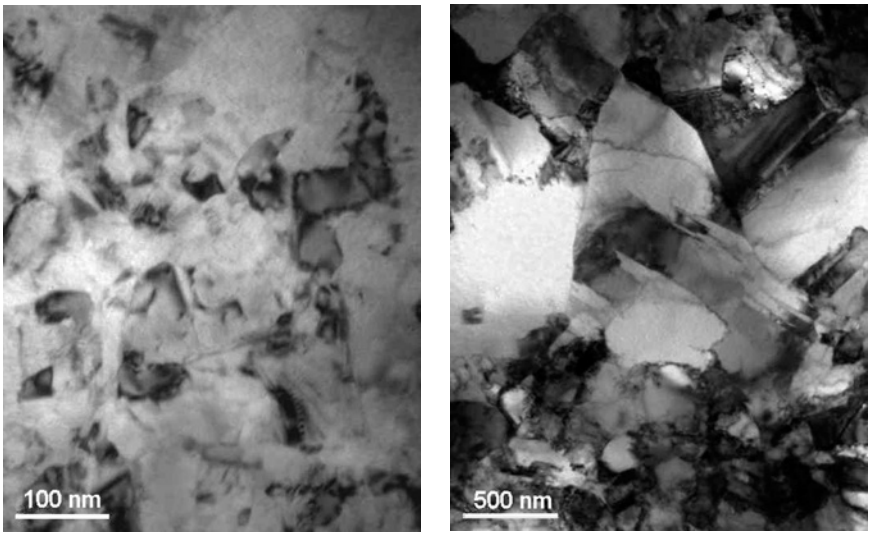

(a) (b)

FIGURE 2.4. Transmission electron micrographs of electrodeposited (a) nc and (b) ufc Ni. (Courtesy of S. Kumar, Brown University, Providence, RI.)

The ufc Ni (Fig. 2.4b) was found to have a roughly bimodal grain size distribution.[92] The average grain size was 300–400 nm, but larger grains with diameters exceeding 1000 nm were found frequently. Due to the larger grain size, grains with several dislocations were found occasionally.[93] X-ray diffraction using θ–2θ scans showed that the materials exhibited a certain texture.[92]

3.1.2. Monotonic Deformation

Monotonic deformation yields important basic information for engineering purposes as well as valuable information to link the mechanical behavior to the microstructure. As illustrated by several review articles over the last few years, the scientific interest clearly lies in elucidating the governing deformation mechanisms.[3,79,94,95] Padmanabhan[96] emphasizes the importance of microstructural defects of the currently available nc materials. Data obtained from different materials are often difficult to compare and have led to a lot of controversy in the past.

3.1.2a. Elastic Response of Nanocrystalline Metals. An early point of discussion was the apparently reduced Young's modulus of nc materials. Early studies on nc Cu and Pd produced by inert gas condensation and compaction reported a considerably lower value compared to coarse-grained materials.[6] Large variations in the elastic properties have been found in another study on the same

materials.[97] But already in these studies the results were deemed doubtful and mostly attributed to insufficient sensitivity of the strain measurement, sample porosity, or microcracks in the specimens. In more recent studies, elastic properties mostly independent of grain size have been found down to the nanograin size in nc AlZr alloys and in nc Cu.[9,98–100] However, in some cases there is still a reduced Young's modulus measured for nc materials.[73,77,101] Sanders *et al.*[73] established an experimental correlation between the specimen's density and the Young's modulus for inert gas condensation processed nc Pd and nc Cu. This correlation would fully account for the Young's modulus deviation in the case of nc Pd; however, in the case of nc Cu there is still a discrepancy. The authors postulated that this was a texture effect. In the majority of the very recent studies, however, it has been found that the elastic properties are not at all or negligibly affected by the grain size down to very small grain sizes of a few nanometers, consistent with theoretical predictions.[102,103] Atomistic simulations[104] showed a slight decrease in Young's modulus for grain sizes below 20 nm, in agreement with a rule-of-mixtures model for composite material.[102] Erb *et al.*[77,101] found the Young's modulus in electrodeposited nc metals with near 100% theoretical density to be almost unaffected, whereas nc metals processed by powder consolidation usually exhibit a decrease in elastic modulus together with an increase in the thermal expansion coefficient. This is believed to be a consequence of the higher porosity in the consolidated materials.

3.1.2b. Plastic Response of Nanocrystalline Materials. The significantly increased yield strength of nc materials is the most obvious advantage of these materials.[71,105,106] Figure 2.5 shows the uniaxial tensile response of pure Ni with three different grain sizes. It can clearly be seen that the yield stress as well as the tensile strength are significantly improved by the grain size reduction. It has generally been found in nc materials that the hardness can be increased more than fivefold compared to conventional mc materials, by reducing the average grain size to less than 100 nm.[106] In metallic materials this increase in hardness is often accompanied by a decrease in ductility, as can be seen in Fig. 2.5. The increase in yield strength with decreasing grain size can be expected according to the well-known Hall–Petch relationship (cf. Ref. 107, pp. 270–273). Yield strengths near the theoretical value would be expected for grain sizes of a few nanometers, if this relation is valid down to these grain sizes. But the basic concept of dislocations piled up against grain boundaries, often invoked as the physical basis for the Hall–Petch equation, does obviously lose its foundation below a certain grain size. A dislocation pileup can no longer form in nanometer-sized grains. It is therefore interesting to find out whether the material does continue to harden down to such small grain sizes and what the relevant mechanisms are. The first question leads to the very vivid discussion about Hall–Petch breakdown, often also called "inverse Hall–Petch effect."

It has been found experimentally that below a certain critical grain size, Hall–Petch hardening ceases and the material softens with further decreasing grain size

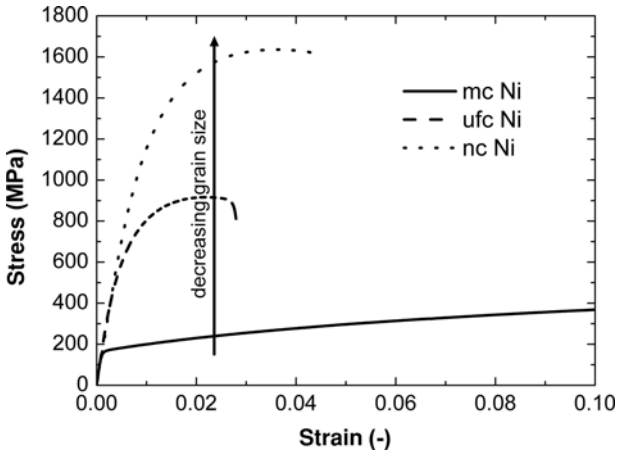

FIGURE 2.5. Uniaxial tensile response of Ni with different grain sizes at a strain rate of 3×10^{-4}.

(see, e.g., Refs. 73, 108, and 109). Values between 30 and 3 nm have been identified as this critical grain size; however, there is some controversy about the validity of some of the results, as described below.

Weertman *et al.*[97] pointed out that softening with decreasing grain size could be an artifact related to the specimen-processing method used. Hardening down to very small grain sizes was most often observed when individually produced specimens were tested in the as-produced condition, whereas softening was found when specimens with different grain sizes were produced through annealing of samples originally consisting of very small grains. Indeed, it was found that short annealing without or with only limited grain growth can actually increase the material's hardness.[97] Further grain growth eventually leads to a decreasing hardness again. These results have been corroborated by a number of other researchers.[110,111]

At this point, we would like to briefly mention results from other experiments that might originate from the same underlying phenomenon. Bonetti *et al.*[112] performed mechanical spectroscopy on nc Fe and Ni specimens produced by mechanical attrition and consolidation. They found that stress relaxation was much faster in the as-prepared samples and slower in the annealed ones, although the grain size was nearly identical in the two samples. Hadian and Gabe[113] produced nc Ni and nc NiFe alloys by two different electrodeposition methods: pulsed and direct current electrodeposition. These two techniques lead to different levels of residual stresses in the materials, with the pulsed current deposited samples exhibiting markedly smaller residual stresses. Interestingly, this material is constantly harder than the direct current deposited material. Recently, Hasnaoui *et al.*[114] have performed MD calculations and found that after annealing, the amount of plastic strain is reduced,

and the material indeed behaved stronger. From all these observations it can be concluded that nonequilibrium grain boundaries together with local residual stresses are present in most as-prepared nc metals. These grain boundaries and stresses lead to a slightly reduced hardness of the material. The grain boundaries can be transformed into a state closer to equilibrium by low-temperature annealing without promoting excessive grain growth. This results in a slight strength increase.

Although in some cases the observed softening with decreasing grain size might be an artifact related to processing (as explained above), more and more researchers agree that there seems to be a genuine effect of grain size softening. Chokshi *et al.*[108] did a careful study of nc Cu and Pd and found a negative Hall–Petch slope below 25 nm. A positive Hall–Petch relation has been observed in nc Cu produced by inert gas condensation and subsequent compaction down to a grain size of 5 nm,[97] while a deviation from Hall–Petch at a grain size of about 15 nm has been found for a similar material.[73] Softening in electrodeposited fully dense nc Ni and Ni alloys has been found in a number of studies, below a grain size of around 15 nm.[101,115,116] In Ref. 109 a breakdown of the grain size hardening was found in mechanically alloyed FeAl alloys at a grain size of about 40 nm. Khan *et al.*[117] found grain softening in nc Fe and nc Cu (produced by ball milling) below a grain size of 23 nm. In a recent study on electrodeposited nc NiW alloys, Schuh *et al.*[118] found indications of Hall–Petch breakdown around 9 nm. Their findings were in line with a compilation of other data for nc Ni alloys in the same article.[118]

The reason for a potential breakdown of the Hall–Petch relationship at very small grain sizes is discussed controversially in the literature. Grain boundary sliding was suggested as the major mechanism contributing to softening, by Hahn *et al.*[119] The authors argue that in the course of deformation a mesoscopic glide plane is formed, which is easier at a smaller grain size because steric hindrance is reduced. Using this description, they were able to explain experimental data obtained from nc TiAl from Ref. 120. Furthermore, large-scale three-dimensional MD simulations on nc Ni with an average grain size of 5 nm containing 125 grains at 800 K indicated emerging shear planes.[121] At relatively high deformations of up to 4% plastic strain, three different deformation mechanisms related to the formation of such shear planes have been identified: grain boundary migration, intragranular slip, and rotation and coalescence of grains. These simulations are indeed corroborated by experiments: nc and ufc metals tend to deform and fail by plastic instabilities such as shear bands.[122,123]

Although this is a pretty clear picture supported by modeling and experiments, other models can also explain grain size softening. A phase mixture model was introduced by Kim *et al.*,[124] modeling the grain boundary phase as a diffusional flow of matter through the grain boundary. Fedorov *et al.*[125] explains softening by a competition between conventional dislocational slip, grain boundary diffusional creep (Coble creep), and triple-junction diffusional creep.

Common to most of these physically meaningful models is that they predict a change in deformation mechanisms, as also predicted in MD simulations. Molecular dynamics simulations of nc Cu and Ni indicate that a change from an

intragrain deformation by traveling partial dislocations above a critical grain size to grain boundary sliding below this grain size takes place.[126] The critical grain size depends on the stacking fault of the material and is around 8 nm for Cu and around 12 nm for Ni. Furthermore, it has been pointed out that this behavior depends on the structure of the grain boundaries.[127,128] High-angle grain boundaries are more likely to cause grains sliding against each other whereas low-angle grain boundaries are more prone to emit partial dislocations.

Recently, the Bragg–Nye bubble raft was employed to visualize deformation mechanisms during the indentation process and revealed very interesting insight into the phenomenon of the Hall–Petch breakdown (Fig. 2.6). Van Vliet *et al.*[135] performed indentation experiments in a two-dimensional face-centered cubic (fcc) bubble raft polycrystal. This setup has been used before to simulate indentation in a two-dimensional single crystal to show the validity of analytical models of

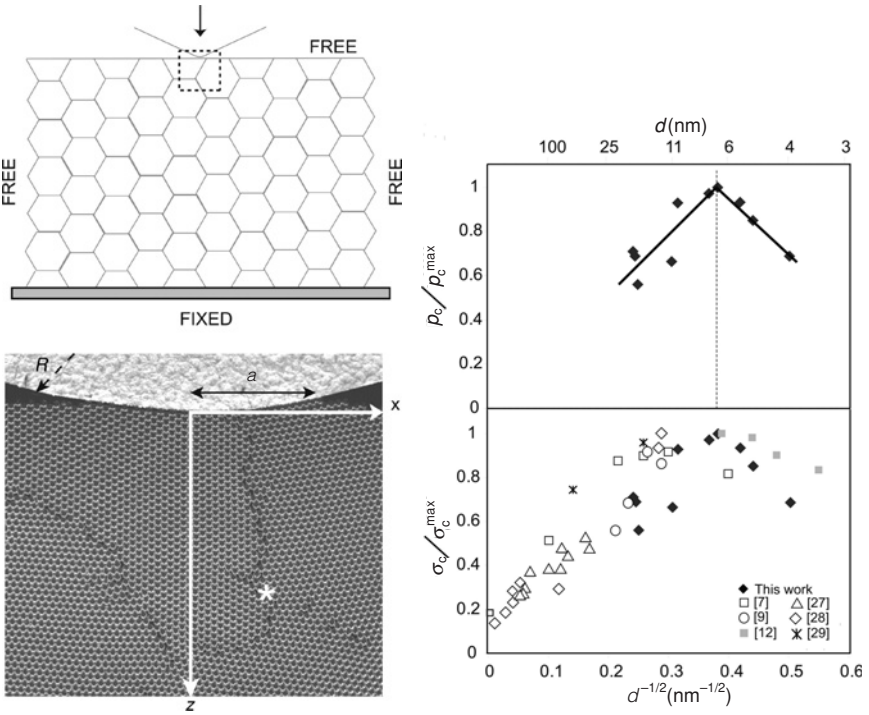

FIGURE 2.6. (a) Schematic (top) and actual (bottom) macrograph of the indentation experiment in a polycrystalline bubble raft. (b) Critical shear stress necessary to initiate the first plastic event (defect nucleation) in a polycrystal in the bubble raft experiment in comparison with other results from the literature ([7] from Ref. 129, [9] from Ref. 130, [12] from Ref. 131, [27] from Ref. 132, [28] from Ref. 133, and [29] from Ref. 134.) (Reprinted with permission from Ref. 135.)

homogeneous dislocation nucleation under an indenter[51,136] and was then extended to investigate two-dimensional polycrystals. About 150 000 soap bubbles with a diameter of 1 mm in different rafts (i.e., grains) have been aggregated to form polycrystals with average grain sizes between 4 and 37 nm and a narrow grain size distribution (assuming the analogy that one bubble of 1-mm diameter is the equivalent of an atom with roughly 0.3-nm diameter). Indentations using a tip with a tip radius of 28 nm have been performed and the deformation of the raft has been recorded using a high-speed camera. Contrary to what was found in experiments on single crystals,[51,52,136] no defect nucleation was observed inside the grains (i.e., no homogeneous dislocation nucleation) but all defects nucleated from grain boundaries and triple junctions.[135] As the load on the indenter cannot directly be measured in this experiment, the critical resolved shear stress at the point of the first defect nucleation is inferred from the contact radius just before the defect nucleates (assuming fully elastic deformation at this point) via Hertzian contact mechanics (cf. Ref. 137, pp. 84–106). This stress was found to significantly depend on the grain size, namely to increase with decreasing grain size at an average grain size greater than 7 nm, but to decrease with decreasing grain size for grains smaller than 7 nm. This critical stress is certainly not generalized yielding and cannot be viewed as a yield strength of the material. However, since defect nucleation is a prerequisite for dislocational yielding, it contributes to a better understanding of plastic deformation. It is also interesting to note that the maximum value of this critical stress determined from the bubble raft is still more than 7% below the critical stress necessary for dislocation nucleation in a defect-free single crystal. Thus, the grain boundaries facilitate defect nucleation in nc materials. The observed Hall–Petch breakdown was accompanied by a change in deformation mechanism. Above 7 nm, deformation is mainly accommodated by dislocations emitted from triple junctions and sometimes from simple grain boundaries. Below this value, grain boundary migration through the collective motion of atoms and vacancies seems to be the governing mechanism.

3.1.2c. Rate-Sensitive Mechanical Behavior: Experiments. The strain- or load-rate sensitivity of nc metals is a topic that is currently of great interest. It has been known for a while now that nc ceramics exhibit a higher strain-rate sensitivity than do the coarse-grained ones,[138,139] and also metals were observed to show interesting trends. Numerous studies explore the dynamic properties of nc and ufc metals by a wide variety of techniques. The most important experimental findings will be described below.

Sanders *et al.*[99] reported strain-rate sensitive behavior in nc Cu. However, the trends shown are ambiguous due to experimental scatter, and furthermore, a comparison with coarse-grained copper has not been made. Wang *et al.*[115] studied electrodeposited Ni and found a significant load-rate sensitivity. In the respective study, the width of the stress–strain loop in a dynamic creep experiment became significantly larger as the load rate became smaller; a smaller load rate, thus, results in a lower yield stress. The authors conclude that some dynamic processes are

operative upon loading and unloading. However, also in this study, no comparison with coarse-grained material was presented.

Most studies take recourse to dynamic testing methods such as split Hopkinson bar technique[117,140] and compare these results with quasistatic tests. These very different loading conditions together with very different sample geometries and stress states make it difficult to distinguish between experimental artifacts and intrinsic material behavior. Nevertheless, Mukai *et al.*,[141] by compiling experimental results from various sources, established a general trend for nc fcc metals to exhibit a higher strain-rate sensitivity compared with their coarse-grained counterparts.

Lu *et al.*[142] reported an unusual rate-sensitive behavior for electrodeposited nc Cu. The yield stress depended only weakly on the strain rate (similar to coarse-grained Cu), whereas the tensile strength and particularly the fracture strain exhibited a very pronounced positive strain-rate dependence (i.e., increased ductility with increasing strain rate), in contrast to conventional Cu. The Cu samples investigated in this study mainly consisted of nano-sized grains separated by low-angle grain boundaries. In another study, Jia *et al.*[143] tested nc Cu in compression at both quasistatic and dynamic strain rates. Also in this case, the yield stress depended only weakly on the strain rate, but the strain-hardening rate seemed to slightly increase with increasing strain rate. This is similar to what Mukai *et al.*[141] had found on electron-beam-deposited Al–Fe alloys. However, in Ref. 143, the authors compared nc and coarse-grained Cu. They found that at lower strain rates the strain-rate sensitivity of the flow stress at 15% strain was similar for the two materials, whereas at high strain rates nc Cu exhibited a lower rate sensitivity than did the coarse-grained material.

A number of high-strain-rate deformation experiments have been performed on fine-grained Fe.[2,144] For grain sizes ranging from 20 μm to 80 nm, it was found that the normalized rate sensitivity decreased with decreasing grain size.[2,144] The strain-hardening rate of the material was close to zero, which means that the material exhibited a nearly elastic—perfectly plastic behavior. These findings may have significant implications for the stability of plastic deformation, because a high-rate sensitivity stabilizes plastic deformation and is usually a prerequisite for superplastic deformation (Ref. 107, pp. 580–591). Indeed, it has been found that Fe with ufc or nc grain structure deforms and fails by shear banding, which is a form of plastic instability.[2] A decreased strain-rate sensitivity of the flow stress and tensile instability with decreasing grain size has also been found in ufc Ti.[145]

As mentioned above, an increased strain-rate sensitivity in nc metals is closely related to possible low-temperature superplasticity. A significant amount of literature is available on this topic but a discussion of the numerous findings is beyond the scope of this study. For more information, see, for instance, Ref. 146.

It is important to note that results on the strain-rate dependence yield valuable information on the mechanisms governing the deformation of nc metals. However, "clean" results obtained from high-purity, defect-free materials are necessary. This problem was addressed recently by Schwaiger *et al.*[92] They performed a systematic study on the rate-sensitive deformation behavior of electrodeposited nc Ni, using two independent experimental methods, namely tensile testing and indentation.

The deformation behavior of nc, ufc, and mc Ni was compared. The microstructure of the material used in this study has been described in detail in Section 3.1.

Microcrystalline and ufc Ni exhibited essentially rate-independent plastic flow in the range from 3×10^{-4} to 3×10^{-1}/s, whereas nc Ni exhibited a marked rate sensitivity in the same range. As shown in Fig. 2.7a the flow stress clearly increases with increasing tensile strain rate. The same behavior has been found in nano- and micro-indentation as shown in Fig. 2.7b. It is important to note that this

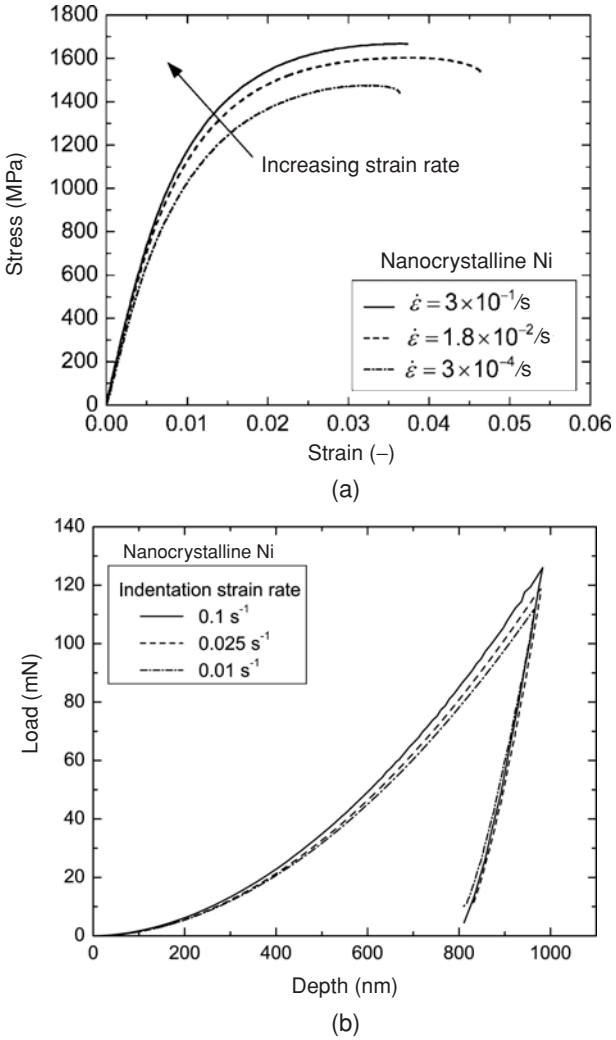

FIGURE 2.7. Strain-rate sensitivity of nc Ni in a (a) uniaxial tensile test and (b) depth-sensing indentation experiment with constant indentation strain rate. (Reprinted from Ref. 92.)

behavior did not depend on the indentation depth. During the continuous hardness measurement[26] a strain-rate effect on the hardness was obvious already at the early stage of loading. Measurements on the ufc and mc Ni showed no evidence of rate-sensitive behavior for the strain- and load rates employed in this study. Large scatter was observed during nanoindentation in the ufc Ni, and one could argue that the number of grains sampled was too small to investigate rate-sensitive deformation behavior. However, the test volume was large enough during microindentation and also during tensile testing, and still no evidence of a rate sensitivity was observed. As the ufc Ni was produced by the same electrodeposition technique, nc Ni processing artifacts can be ruled out. Moreover, it can be concluded that the observed rate-sensitive deformation behavior is a genuine effect related to the reduced grain size.

3.1.2d. Rate-Sensitive Mechanical Behavior: A Simple Computational Model. The results on pure Ni that have been discussed in the preceding section[92] clearly show an effect of the grain size on the rate sensitivity of deformation in pure Ni. In order to interpret these findings, Schwaiger et al.[92] presented a simple computational model assuming the existence of a grain boundary affected zone (GBAZ). The proposed model is based on recent TEM studies and MD simulations that are summarized as follows: (i) transmission electron microscopy on nc Ni showed that grain boundaries are atomically sharp without an amorphous layer (see Section 3.1.1. for a more detailed description); (ii) *in situ* experiments in the TEM revealed dislocation activity during deformation inside grains as small as 30 nm[59]; (iii) MD simulations[147–149] suggest that grainboundary atoms as well as atoms up to 7–10 lattice parameters away from the grain boundary are heavily involved in plastic deformation; and (iv) it was further suggested that atoms within a certain distance to the grain boundary are easier to move and that the deformation mechanisms near grain boundaries are likely to be rate sensitive.[147,148] With this in mind, the suggested GBAZ can be seen as a region adjoining the grain boundaries in nc metals, in which the crystalline lattice is elastically strained despite the ostensible absence of any defects.

The GBAZ model proposed by Schwaiger *et al.*[92] assumes the following: (i) A GBAZ in a nc or ufc material spans a distance of about 7–10 lattice parameters away from the grain boundary; (ii) the GBAZ is plastically much softer than the grain interior and deforms with a positive rate sensitivity; and (iii) under tensile loading conditions, a strain-based damage criterion captures the onset and progression of failure. Figure 2.8a schematically shows the unit cell model, including geometry and mesh used in the finite element simulation. Computational parametric studies were then performed using a simple linear hardening constitutive behavior for both the grain interior and the GBAZ (see Fig. 2.8b); Fig. 2.8c shows the computational results, using a volume fraction of GBAZ at 25% (representing nc Ni with a grain size of 30–40 nm).[92] The continuum mechanics results compare well with experimental results shown in Fig. 2.5. Furthermore, using the same model to predict the properties of the ufc Ni (with a volume of GBAZ of 3%) the

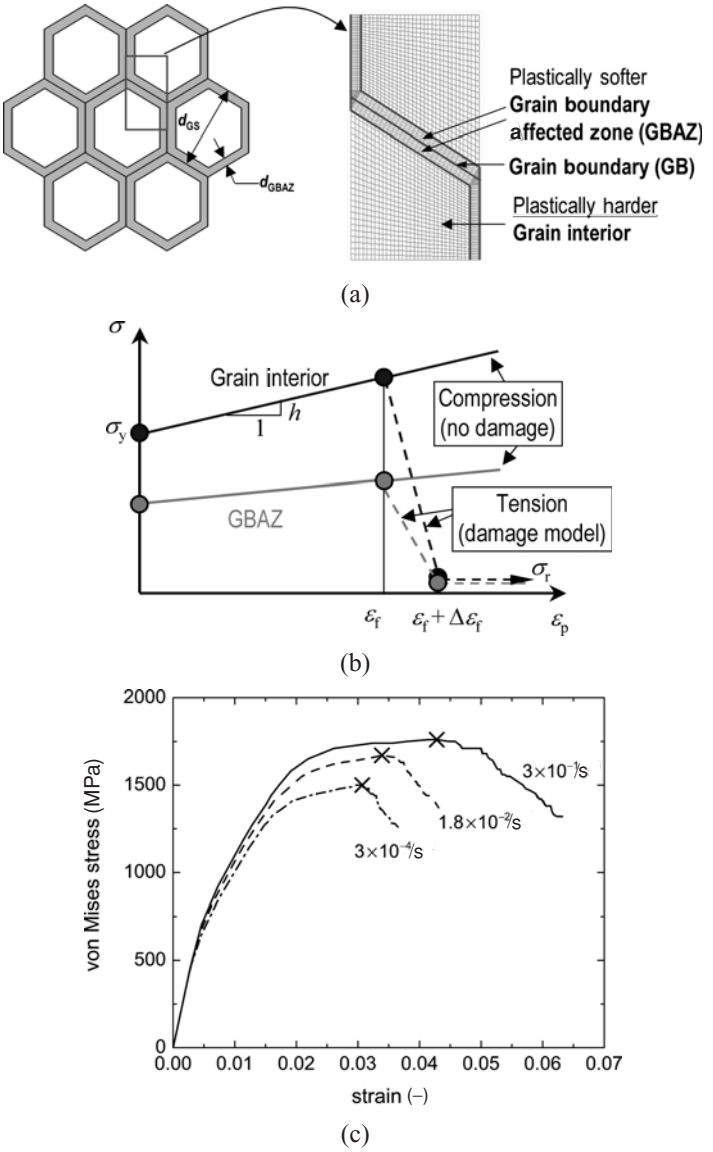

FIGURE 2.8. Grain boundary affected zone (GBAZ) model and computational results.[92] (a) Two-dimensional grains of hexagonal shape separated by the GBAZ preserving crystallinity to the atomically sharp grain boundary. Periodic boundary conditions were applied and a unit cell model was used in the computations. (b) Linear-hardening constitutive behavior for the grain interior and the GBAZ with the initial yield stress σ_y and a strain-hardening rate θ. Material failure/damage under tension is assumed to initiate from $\epsilon_p = \epsilon_f$, and the material strength drops linearly to a residual strength of σ_r (0) within an additional strain of $\delta\epsilon$. (c) Finite element results using a GBAZ volume fraction of 25% (representing nc Ni with a grain size of 30–40 nm).

strain-rate effect was observed to be negligible, which also matches the experimental observations. Regarding the structure of the model, this result is not surprising because the thickness of the GBAZ is a constant value, independent of the grain size, and thus leads to a larger volume fraction of the rate-sensitive GBAZ for smaller grains.

3.1.2e. Deformation Mechanisms of Nanocrystalline Metals. The discussion on deformation mechanisms in nc materials is strongly linked to the discussions on Hall–Petch breakdown and strain-rate sensitivity, which might cause some repetitions in the paragraphs to come. However, we believe that it is essential to repeat the necessary information. It will not be discussed as thoroughly as above though, and the reader is referred to the preceding sections for more details. We will limit the discussion mostly to nc Ni, but whenever necessary we will draw upon results from other fcc metals or make comparisons with bcc and hcp metals.

Three observations form the basis for the following discussion:

1. Although nc metals generally deform in a macroscopically brittle manner with only limited elongation to failure (compared to their coarse-grained counterparts) the stress–strain curve is considerably nonlinear (see Fig. 2.7) and fractography indicates considerable microductility during failure (dimple structure on fracture surfaces, see Fig. 2.9 and Section 3.1.3).[59,92]

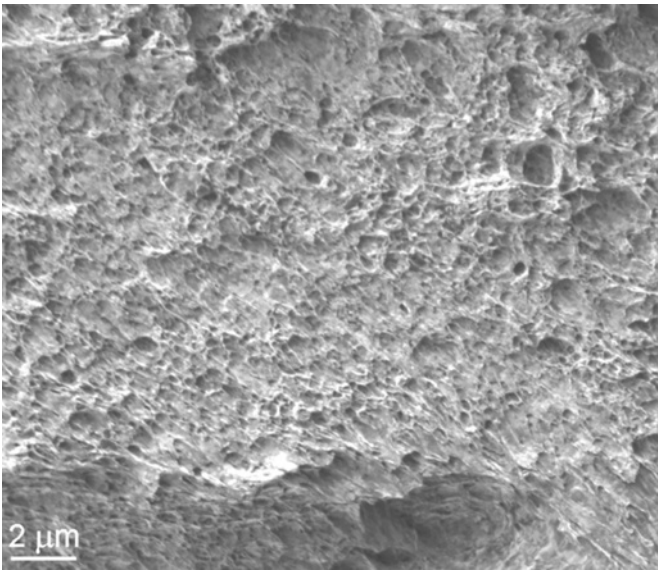

FIGURE 2.9. Fracture surface of an electrodeposited nc Ni after a monotonic tensile test. The ductile dimple rupture is clearly visible.

2. Grains with a diameter of 50 nm and below are too small to contain active dislocation sources such as Frank–Read sources (value for Cu from Ref. 1).
3. In general, *ex situ* TEM examinations of deformed specimens do not show any dislocation debris. The grains are mostly clean and free of dislocations.[59]

Only the combination of results obtained using different investigation techniques can lead to a comprehensive picture of active deformation mechanisms. In particular, creep and stress-relaxation tests, as well as cyclic loading or elevated temperature testing, can yield valuable information about time-dependent and thermally activated processes. Furthermore, fractography can teach us a lot about the governing mechanisms involved in the failure process. Indispensible information comes from *ex situ* and *in situ* TEM studies. Computational experiments represent another tool: atomistic simulations such as MD or MS (molecular statics) simulations give very interesting insights, despite their own limitations. Another interesting "low-tech" simulation consists in two-dimensional Bragg–Nye bubble raft experiments mentioned earlier.

We will now review the most important results and describe our conclusions regarding the current understanding of deformation mechanisms.

- *Mechanical testing:* Generally nc metals have been found to have considerably reduced elongation to failure compared with their coarse-grained counterparts. Maximum elongation at failure is usually below 10%, often only 3–4%.[92,99,150,151] In some cases, a distinct yield stress is visible in the stress–strain curve; in other cases a yield stress can be defined only as an offset yield stress.[92,142] The information on hardening behavior described in the literature is also ambiguous. In some experiments almost perfectly plastic behavior (no strain hardening) has been found,[152] whereas in other experiments the materials showed strong strain hardening almost up to the point of failure.[92,142]

  Most nc metals exhibit considerable creep rates even at room temperature.[115,146,153] This clearly indicates that time-dependent processes are important and have to be considered in a discussion of deformation mechanisms. Several studies describe the activation energy of the deformation processes determined via mechanical testing.[95,112,132,154] It is very difficult to draw unambiguous conclusions for the governing deformation mechanisms from these measurements, but one finds growing evidence that more than one deformation mechanisms are acting simultaneously.[112] Generally, activation energies close to the values for grain boundary self-diffusion are found.[95,112,154] However, there is still some controversy whether grain boundary diffusivity in nc metals is enhanced compared to coarse-grained materials or not.[155,156] Knowing that the grain boundary microstructure of nc metals is similar to that of their mc counterparts,[59,81,83,84] there is no obvious reason why the grain boundary diffusivity should be enhanced.

Most studies are performed on pure nc metals, although alloying effectively reduces grain growth, improves the thermal stability, and make it possible to perform mechanical tests at moderately elevated temperatures without unwanted grain growth during testing. Schuh *et al.*[118] investigated electrodeposited nc Ni–W alloys and found that the solid solution hardening expected from the addition of W to Ni could not account for the considerable increase in hardness observed in their experiments. The authors conclude that this hardness increase was mainly due to the reduced grain size achieved by W addition. Increasing Fe content in electrodeposited Ni–Fe was also found to decrease the grain size and increase the hardness.[157] Again, grain size and alloying effects could not be separated from each other. One could expect that solute atoms along the grain boundary would influence the diffusional material flow necessary for grain boundary sliding. But experimental evidence of a reduced strain-rate sensitivity or similar effects are, to the best knowledge of the authors, so far missing. Further research in this area would be required.

- *In situ and ex situ TEM observations: Ex situ* TEM investigations have been conducted on deformed nc metals, but the dislocation debris known from deformation studies on coarse-grained specimens was not found.[59,151] Early *in situ* TEM straining experiments on nc Au showed no evidence of dislocation activity,[61] but formation and growth of nanopores was observed. This fact together with the observation of extensive grain boundary grooving suggested that diffusion plays an important role in the plastic deformation of nc Au. The absence of dislocation activity could be explained by the fact that high-resolution images were probably taken while the deformation was stopped and not continuously recorded. Later, deformation experiments on nc Cu have shown numerous rapid contrast changes in nc grains together with some clearly identified single dislocation events.[63,158] It was not clear from this study whether the rapid contrast changes in the grains originated from dislocation activity or from grain boundary sliding and grain rotation.

  Kumar *et al.*[59] performed extensive *ex situ* and *in situ* experiments on electrodeposited nc Ni. In *ex situ* TEM investigations in deformed nc Ni, some dislocation debris was found; however, these few dislocations could not account for the large amount of plastic deformation observed in mechanical testing. During *in situ* deformation, grains with rapidly changing contrast were observed and the front of contrast change moving through the grain was recorded on videotape. These contrast changes occurred repeatedly in the same grains and were claimed to be caused by moving dislocations. The reason why only few dislocations have been seen during *ex situ* investigations is found in the fact that image forces are strong enough to pull dislocations from the grain interior to the grain boundaries.[159] Toward the end of the deformation process, when necking down to a single chisel point occurs, twin formation and even gliding along twin boundaries were

observed.[59] This is probably a phenomenon not particular to nc materials but simply a small volume effect.

Recent *ex situ* TEM studies on nc Al have shown a considerable amount of stacking faults and twins due to the deformation process.[160] These observations corroborate the importance of dislocations for the plastic deformation of nc fcc metals and support the postulate from the MD community that partial dislocations are emitted from grain boundaries, travel through the grain, and are absorbed from the opposite grain boundary leaving behind a stacking fault. Such a large number of twins has not been found in nc Ni so far, which could be related to the higher stacking fault energy in Ni compared to Al. It has to be noted, however, that a very severe deformation mode by grinding the specimen surface was imposed on the Al.[160]

- *Atomistic simulations:* Atomistic simulations give very illustrative insights into possible deformation mechanisms. Recent increase in computation capacities and the small grain size of nc materials make large-scale simulations of realistic polycrystalline samples possible. These simulations confirmed a number of hypotheses that have been established from experimental results. The plastic deformation process of nc metals is found to be a competition between grain boundary sliding and dislocation-mediated processes.[149] Whether the dislocation process or grain boundary sliding dominates the plastic deformation depends on grain size,[84] stacking fault energy,[126] grain boundary structure (low-angle versus high-angle grain boundary),[127] and possibly on the imposed strain rate.[147] At grain sizes below 10 nm all dislocation activity ceases and deformation is carried exclusively by grain boundary sliding, grain rotation, and diffusional processes. At larger grain sizes, atomic rearrangements in the grain boundaries lead to the emission of partial dislocations that travel through the grains. These partial dislocations are finally absorbed in the opposite grain boundary, leaving behind a stacking fault in the grain.[161] There is no evidence so far for a trailing partial dislocation to be emitted at the same place.[161] In the comparison of nc Ni and nc Cu, Van Swygenhoven *et al.*[126] found that the dislocation activity ceases at larger grain sizes for Ni (12 nm) compared with Cu (8 nm). They conclude that this is related to the eightfold higher stacking fault energy in Ni. Diffusional processes and grain boundary sliding are more likely to happen in a specimen with predominantly high-angle grain boundaries.[127] In specimens containing mostly low-angle grain boundaries, more stacking faults are found after deformation.

  Experiments on two-dimensional bubble rafts have been presented above (see Section 3.1.2.). Nucleation of dislocations at grain boundaries as well as grain boundary sliding have been observed in these experiments depending on the grain size.[135]

  At this point, the authors would like to add a word of caution concerning the comparison of results from simulation and experiments. Although

results of atomistic simulations are very illustrative and revealing, the several orders of magnitude shorter timescale compared with experiments may introduce artifacts. Limitations of computational capacity require extremely high strain- or load rates. These rates are several orders of magnitude lower in experiments. Hence, time-dependent mechanisms might be artificially suppressed in the atomistic simulation.

- *Conclusions:* From all this information we can conclude with confidence that deformation in nc metals is at least partially carried by dislocation activity for grain sizes above a critical value around 15 nm. Below that critical value, plastic deformation is mostly carried by grain boundary processes. There is increasing evidence that several deformation processes might act simultaneously. This means that even though dislocations are observed above the critical grain size, grain boundary processes are likely to occur at the same time. This is also caused by the presence of a certain grain size distribution combined with the mentioned size dependence of the predominant mechanism. Diffusion and time- and temperature-dependent processes play an important role in nc materials. However, further research is necessary to better understand the deformation mechanisms in these materials.

3.1.3. Monotonic Fracture

Studies of the fracture behavior of nc materials are mostly limited to the investigation of fracture surfaces from monotonic tensile tests. The fracture surfaces exhibit clear signs of ductility.[79] The globally flat fracture surface has a classical dimple structure. The dimple size was found to be clearly bigger than the grain size. These dimples indicate plasticity at least at the microscale during the failure event.

Fracture toughness measurements are difficult to perform due to the limited availability of high-quality nc materials. Often, the specimen geometry required by the testing standards cannot be fulfilled. Mirshams *et al.*[162] measured the *R*-curve behavior on nc Ni and C-doped nc Ni. Specimen limitations necessitated the use of a specially designed "antibuckling" fixture for the compact tension specimens and quantitative conclusions are difficult. However, it can be said that in most of the cases the fracture surface showed dimples indicating ductile failure and that the *R*-curve behavior was influenced by the annealing temperature and time.

Farkas *et al.*[163] studied the fracture behavior of nc Ni by MD simulations. With grain sizes in the range between 5 and 12 nm, they found, independent of grain size, intergranular fracture behavior with only limited dislocation activity. Unfortunately, their results cannot be directly compared with experimental results, as nc Ni with such small grain sizes is not readily available.

Overall, there is only little information on the fracture behavior of nc metals and more research is necessary in order to understand the fundamental properties.

3.1.4. Cyclic Deformation

Understanding the cyclic deformation behavior of nc metals is crucial for potential applications as structural materials or as coatings in engineering components. This includes the resistance to crack initiation and crack growth under cyclic loading conditions, as well as the stress- and strain-based fatigue life.

A considerable amount of experimental information on the fatigue response of mc metals and alloys is available, but little is known about the fatigue characteristics of ufc and nc metals. This is due to the fact that processing methods typically used to produce ufc and nc materials, such as electrodeposition and e-beam deposition, generally yield only thin foils (about 100 μm thick). The small thickness makes it difficult to perform valid experiments to extract crack propagation or fatigue properties. Problems encountered are, for instance, gripping the specimen, imposing controlled small loads and measuring the strain, out-of-plane bending, or buckling. However, there are methods that produce sufficiently thick samples, i.e., equal channel angular pressing or mechanical consolidation. The drawback of these processing routes is the inhomogeneous microstructure, a high defect density, as well as large variations in grain size. Furthermore, these materials are generally not nc but ufc.

Several studies have examined the total fatigue life of ufc metals produced by equal channel angular pressing.[164–166] In these experiments, repeated loading resulted in pronounced cyclic softening and a reduced low cycle fatigue resistance was found. These trends have also been seen in mc metals and alloys where, in general, initially soft microstructures cyclically harden and initially hard microstructures (such as those produced by severe cold working) soften.[167] However, the studies mentioned above[164–166] have also shown that the total fatigue life of ufc metals is enhanced compared to that of their mc counterparts, as reflected in their relatively high fatigue endurance limit values.

A low cycle fatigue life prediction model for ufc metals was proposed by Ding *et al*.[168] The microstructure is treated as a composite, consisting of the "soft" grain interior and the "harder" grain boundaries. The authors assume in their model, which is essentially a fatigue crack propagation model, that damage takes place in a localized zone ahead of the crack tip. Under large strains, the stress level in this damage zone approaches the tensile strength of the material. The strain localization in the material is caused by a dislocation sliding-off process. The authors compared the results obtained from the model with experimental findings obtained from tests on ufc Cu and found good agreement. Moreover, the model was also found to describe the fatigue behavior in the high cycle fatigue regime reasonably well. This result was rather surprising because the model does not account for fatigue crack initiation, which usually occupies a large fraction of the high cycle fatigue life.

Another interesting point was addressed by Thiele *et al*.[169] They fatigue tested the ufc Ni produced by equal channel angular pressing and investigated the influence of the grain size on the formation of typical fatigue-induced dislocation

structures, such as veins, ladder and cell structures, and the cyclic stress–strain curve. The average grain sizes of their samples were between 500 nm and 5 μm. They found a lower threshold grain size of about 1 μm that was necessary for the formation of dislocation structures. No grain size effect on the cyclic stress–strain curve was observed for grain sizes larger than 3 μm, whereas for smaller grain sizes the stress level of the cyclic stress–strain curves appeared to follow a Hall–Petch relation.

To the authors' knowledge there is only one published report so far on the fatigue life and fatigue crack growth characteristics of a fully dense high-purity nc metal with a narrow grain size range below 100 nm. Hanlon *et al.*[170] studied the fatigue response of electrodeposited pure Ni and of a cryomilled ufc Al–Mg alloy. In particular they compared the fatigue response under stress control of electrodeposited nc Ni with an average grain size of 30 nm with that of a similarly produced ufc Ni having an average grain size of 300 nm and of a conventionally produced mc Ni. They performed zero-tension fatigue experiments (i.e., load ratio $R = 0$). The load was applied sinusoidally at a frequency of 1 Hz.

Grain refinement was observed to have a significant effect on the fatigue life under constant stress amplitude. The endurance limit (defined at 2×10^6 cycles) of nc Ni was higher compared to that of the ufc Ni. Both nc and ufc Ni had a significantly improved fatigue endurance limit compared to that of the mc metal.

Hanlon *et al.*[170] also conducted fatigue crack growth experiments on nc Ni using edge-notched specimens that were subjected to cyclic tension at different R ratios. The rate of fatigue crack growth was faster with decreasing grain size in the regime investigated. Figure 2.10 shows the constant load amplitude fatigue crack growth data for pure Ni as a function of grain size. A grain size reduction from the micrometer to the nanometer scale resulted in up to an order of magnitude increase in fatigue crack growth rates in the intermediate regime of fatigue fracture. Such trends are fully consistent with the mechanistic expectations of fatigue fracture based on results available for mc alloys. These new results show that nc materials that might have an improved total fatigue life may have a reduced resistance to subcritical crack growth under constant strain amplitude fatigue.

The trends seen in pure nc Ni appear to carry over to the more complex situation involving commercially produced ufc alloys where conventional fatigue fracture studies were conducted using standard experimental techniques widely used for mc metals. Constant amplitude fatigue crack growth experiments on cryomilled Al–7.5wt %Mg alloy with equiaxed grains and an average grain size of approximately 300 nm have shown a relatively faster crack growth rate (by a factor of 10 in the intermediate regime of fatigue crack growth) when compared with a commercial aluminum alloy with a similar composition.[171] Furthermore, the finer grained alloy has a lower fatigue crack growth threshold stress-intensity factor range.

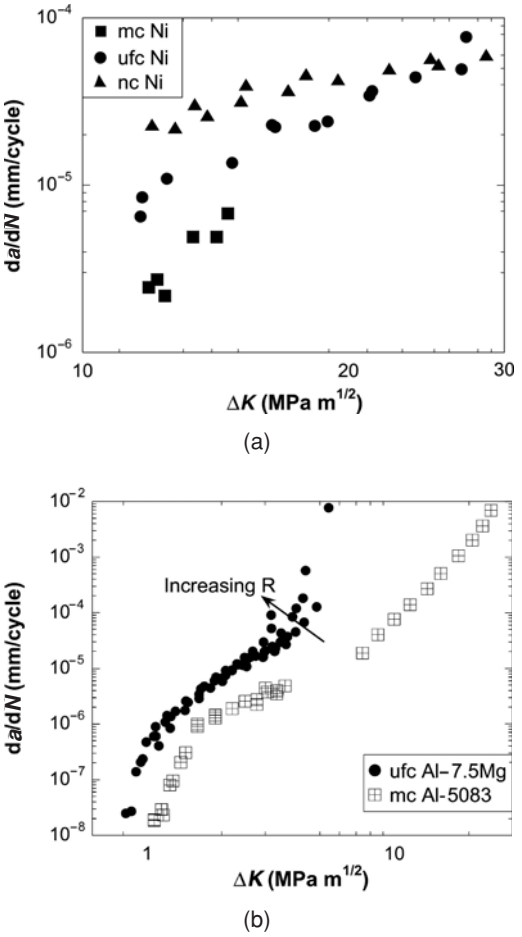

FIGURE 2.10. (a) Variation of fatigue crack growth rate, da/dN, as a function of the stress-intensity factor range, ΔK, for mc pure Ni and for electrodeposited ufc and nc pure Ni at $R = 0.3$ at a frequency of 10 Hz at room temperature. (b) Variation of fatigue crack growth rate, da/dN, as a function of the stress-intensity factor range, ΔK, for acryomilled Al–7.5 Mg at $R = 0.1$–0.5 at a fatigue frequency of 10 Hz at room temperature. Also shown are the corresponding crack growth data for a commercial mc aluminium alloy (5083) at $R = 0.22$. (Reprinted with permission from Ref. 170.)

3.2. Amorphous Materials

Bulk metallic glasses attracted considerable scientific interest since their discovery back in the 1960s (e.g., Ref. 172). These materials represent the limiting case of nc materials with infinitely small grain size. Studying their behavior can help in some cases to understand the behavior of nc materials. Recently, Lund and Schuh[173]

have pointed out important similarities in the plasticity of nc and amorphous metals.

The fact that controlled crystallization of bulk metallic glasses is one possible technique to produce nc materials is another important aspect of amorphous metals in the present context. The technique has been demonstrated for a wide range of alloys including Al-based,[174] Mg-based,[175] Fe-based,[176] and Zr-based[177] alloys. Through controlled nucleation, nano-sized (about 20 nm) quasicrystals can be produced from the amorphous matrix resulting in enhanced strengthening[178] and ductility. The principal advantage of using amorphous alloys over heavily deformed materials is that grain growth is relatively sluggish in these alloys. However, it has to be mentioned that often a remnant amorphous matrix surrounds the nc grains.

3.2.1. Yield Function

To study the deformation mechanisms as well as to understand the proper constitutive description that is consistent with its multiaxial deformation behavior, several recent studies used nanoindentation techniques (see, e.g., Ref. 179 for a recent review). A number of earlier studies postulated that the von Mises yield criterion adequately models the deformation characteristics of bulk metallic glasses,[180] i.e.,

$$(\sigma_1 - \sigma_2)^2 + (\sigma_2 - \sigma_3)^2 + (\sigma_3 - \sigma_1)^2 = 6k^2 = 2\sigma_y^2 \tag{2.2}$$

where σ_1, σ_2, and σ_3 are the principal stresses and $k = \sigma_y/\sqrt{3}$, where σ_y is the yield strength measured in a uniaxial tension test. Alternatively, the Mohr–Coulomb criterion, where the plastic flow is assumed to be influenced by the local normal stress, is generally written for metallic glasses as[181,182]

$$\tau_c = k_0 - \alpha - \sigma_n \tag{2.3}$$

where τ_c is the shear stress on the slip plane at yielding, k_0 and α are constants, and σ_n is the stress component in the direction normal to the slip plane. Figure 2.11 shows the results of nanoindentation experiments by Vaidyanathan *et al.*[183] where a metallic glass (nominal composition $Zr_{41.25}Ti_{13.75}Cu_{12.5}Ni_{10}Be_{22.5}$ in at %) was indented to depths of 5 and 9 μm in two sets of indentation tests. The unloading portion of the load–depth response is also shown and the penetration depth is large enough to eliminate tip imperfection effects. Using known elastic properties and yield strength data for the metallic glass used in these experiments (i.e., elastic modulus of 96 GPa, Poisson's ratio of 0.36, and tensile yield strength of 1.9 GPa), finite element simulations were carried out to generate predictions of indentation load versus penetration depth curves, assuming either the von Mises or the Mohr–Coulomb yield criteria. For the latter, the constants were established so as to satisfy macroscopic tensile yielding at 1.9 GPa while varying the value of α [see Eq. (2.3)]. Numerical predictions of the complete indentation

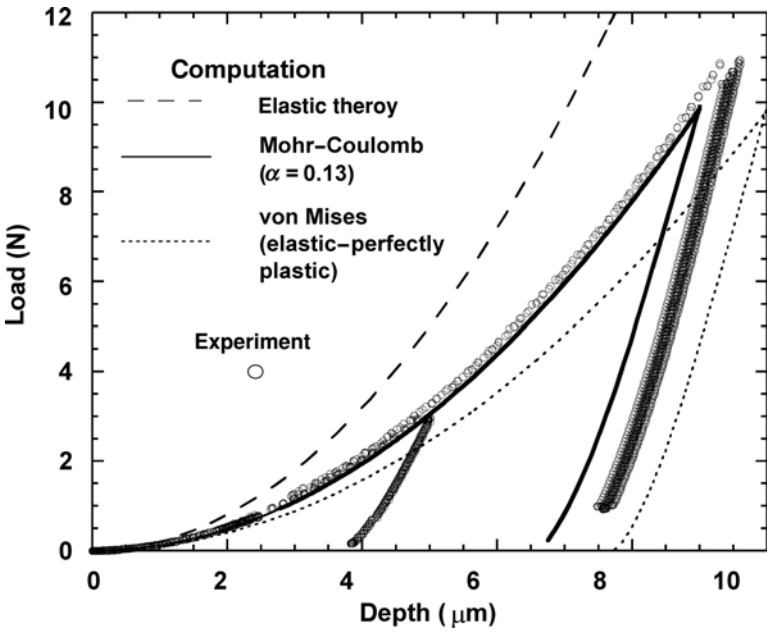

FIGURE 2.11. Microindentation response of a metallic glass (nominal composition $Zr_{41.25}Ti_{13.75}Cu_{12.5}Ni_{10}Be_{22.5}$ in at%) during loading and unloading. Two series of experiments to depths of 5 and 9 μm, consisting of five and eight indivivdual indents, respectively, are shown.[183]

load–displacement curves (loading and unloading portions) for the elastic deformation as well as the elastoplastic deformation, extracted by assuming either the von Mises or Mohr–Coulomb criteria, are superimposed on the experimental data in Fig. 2.11. It appears from this figure that the metallic glass does not follow the von Mises criterion. The load–depth prediction using a Mohr–Coulomb criterion (with $\alpha = 0.13$) follows the experimental results more closely, suggesting the influence of a normal stress component on yielding.[183] This value of $\alpha = 0.13$ used in the finite element simulation compares well with the value of 0.11 ± 0.05 previously reported by Donovan[181] for $Pd_{40}Ni_{40}P_{20}$ metallic glass.

Schuh and Lund[184,185] performed molecular simulations of multiaxial deformation in a model metallic glass, using a 0 K energy minimization technique. A significant asymmetry between the tensile and compressive yield stresses was found, with the uniaxial compressive strength approximately 24% higher. By exploring a variety of biaxial stress states, the Mohr–Coulomb yield criterion, which includes an additional normal stress term, was found to describe the molecular simulation data quite well, using the value of $\alpha = 0.123 \pm 0.004$.[184] These results provided an atomistic basis for the plastic yield criterion of metallic glass.

Additionally, for Tresca or von Mises yielding of a compression specimen, the shear band angle under uniaxial compression would be expected to lie at $\theta = 45^\circ$ go the compression axis, whereas the Mohr–Coulomb criterion predicts a smaller angle given by[183]

$$\alpha = \frac{\cos(2\theta)}{\sin(2\theta)} \tag{2.4}$$

When $\alpha = 0.13$, Eq. (2.4) predicts a compressive shear angle of $\theta = 41.3^\circ$,[183] and when $\alpha = 0.123 \pm 0.004$,[184] $\theta = 41.5 \pm 0.15^\circ$. These values are in good agreement with previous experimental results of $\theta = 39.5 - 43.7^\circ$ for a number of different metallic glass compositions.[186]

3.2.2. Serrated Flow in Bulk Metallic Glasses

Not only the overall yield behavior of bulk metallic glasses differs from that of metals but also their microscopic deformation mechanisms are distinct. Plastic deformation governed by several discrete events (i.e., serrated flow) has been observed in numerous studies (e.g., Ref. 181 and 187–189). It was found that plastic deformation is highly inhomogeneous in these materials. Several models have been proposed to describe this discrete plasticity.

Instrumented indentation can be used to detect discrete deformation modes in crystalline materials[32,50] as well as in amorphous materials.[179] It has been found that amorphous alloys display pop-ins during indentation (see, e.g., Ref. 190 and 191). These events have been correlated with the motion of individual shear bands through the specimen.[192] Wright *et al.*[192] found that the first pop-in event marked the transition from the elastic to the plastic deformation regime and that the critical stress related to this transition is well characterized using the Mohr–Coulomb yield criterion rather than the maximum shear stress criterion. Golovin *et al.*[191] observed a correlation between the number of pop-ins in the P–h curve and the shear bands found at the surface of the specimen, which strongly suggests that each pop-in corresponds to one individual shear band. Shuh *et al.*[193] reported that the magnitude of the pop-in displacements increased roughly linearly with indentation depth. This linear dependence is a direct consequence of the self-similar indenter geometry, and suggests that each shear band may approximately carry the same amount of strain but the displacement needed to achieve that strain is proportional to the indentation depth.[179]

Recently, Schuh *et al.*[193–195] studied the effect of strain rate on the serrated flow of bulk metallic glasses. They found that discrete plasticity events can be effectively suppressed during indentation with sufficiently high load rates. It was also shown that at small indentation load rates the discrete plastic events (pop-ins) would account for most of the plastic strain and that upon manual removal of these events from the experimental measurement, the curve favorably compares with the prediction for a purely elastic contact.[195]

3.2.3. Stress-Induced Nanocrystallization

A recent study by Kim *et al.*[196] on a Zr–17.9Cu–14.6Ni–10Al–5Ti metallic glass showed that nanocrystallization can be induced locally by severe plastic deformation. It is known that nanocrystallites can form in shear bands produced during severe bending or high-energy ball milling of thin metallic glass ribbons.[197–199] For the first time, however, direct experimental evidence was obtained that highly confined and controlled local contact at the ultrafine scale in the form of quasistatic nanoindentation of a bulk metallic glass at room temperature can also cause nanocrystallization.[196] Atomic force microscopy and transmission electron microscopy results show that nanocrystallites nucleate in and around the shear bands produced near indents and that they are the same as crystallites formed during annealing without deformation at 783 K (see Fig. 2.12). Analogous to results from recent experiments with glassy polymers,[200] the nanocrystallites were argued to be the result of flow dilatation inside the shear bands and of the attendant, radically enhanced, atomic diffusional mobility inside actively deforming shear bands.[196]

4. DEFORMATION UNDER DIMENSIONAL CONSTRAINT

Thin films are by definition the materials in which the dimension in the "thickness" direction is significantly smaller than the other two. In this case it can be expected that the dimensional constraint, i.e., the film thickness, rather than the microstructural constraint, i.e., the grain size (see Section 3), will control the mechanical properties. However, it is important to note that in polycrystalline thin films the dimensional constraint often causes an additional microstructural constraint: normal grain growth usually stagnates when the grain size is comparable to the film thickness.[201] Consequently, thin films generally consist of relatively small grains, unless they are heat treated in a way to encourage abnormal grain growth.[202] In terms of micromechanisms, thin film plasticity is influenced by both the dimensional and the microstructural constraint on dislocation motion, which result in a pronounced size effect.

A large variety of experimental techniques can be applied to study the deformation behavior of thin films. The most prominent ones have been described in Section 3. In this section we will give an overview of important experimental findings using different techniques and describe theoretical models and dislocation mechanisms that control the deformation of thin metal films.

4.1. Yield Stress and Hardening

The yield stress of thin films has been studied extensively during the last decade because it is crucial for the reliability of thin film components. For example, for interconnects, typically pure metals with high electrical conductivities such as Al

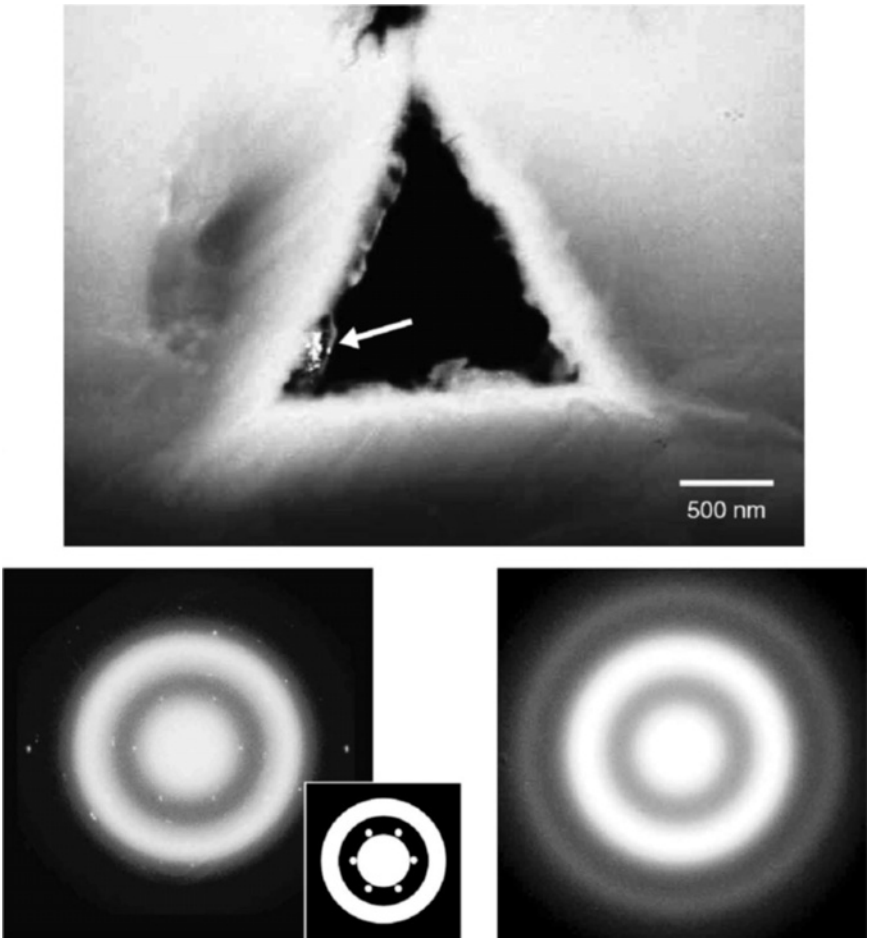

FIGURE 2.12. Dark-field TEM image obtained from a back-edged indent in a Zr–17.0Cu–14.6Ni–10Al–5Ti metallic glass, and selected area diffraction (SAD) patterns obtained in a region located at a small distance outside of the indent (bottom right) and from the indent (bottom left, and schematic). In the dark-field image, the arrow indicates clustered nanocrystallites at the edge of the dark triangular zone, which is a hole made by the backside thinning through the indent impression. Six spots around the transmitted beam in the schematic, which are close to the exact Bragg condition, were analyzed and found to be associated with the (111) plane of tetragonal Zr_2Ni (space group $14/mcm$, $a = 6.49$ Å, $c = 5.28$ Å). Halo rings of the bottom-right SAD pattern without spots indicate the fully amorphous structure of metallic glass in a region that is not affected by the indentation. (Reprinted with permission from Ref. 196.)

or Cu are used. These metals are inherently soft and deform plastically in service as well as during device fabrication, although the plastic strains that are imposed might be small. It has long been known that the strength of thin metal films on substrates exceeds the strength of their bulk counterparts by up to an order of magnitude (for an early reference, see Ref. 203). Moreover, both theoretical and experimental studies of thin metal films on a substrate, mainly via substrate curvature and X-ray diffraction methods, have shown that a thinner film is plastically stronger than a thicker one. However, a common basic understanding of thin film plasticity has not yet been obtained, neither experimentally nor theoretically.

Different theoretical models based on energy-balance arguments[204–206] have been proposed. Common to these models is the idea that the energy cost of geometrically necessary interfacial dislocation segments must be balanced by the work done by an external stress upon glide. In the model proposed by Nix,[204] plastic yielding is accomplished by threading dislocations. Yielding is impeded by dislocation segments deposited at the film–substrate interface and at a possible film–passivation interface. These interfacial dislocation segments resemble misfit dislocations in heteroepitaxial films. The geometry for constrained dislocation motion is shown in Fig. 2.13. The stress needed to move a dislocation in a thin film on a substrate is approximately inversely proportional to the film thickness. This provides a basis for understanding the strong dependence of the film strength on film thickness.

The predicted reciprocal film thickness dependence was indeed found experimentally by Keller *et al*.,[207] but the yield stresses of the Cu thin films tested were

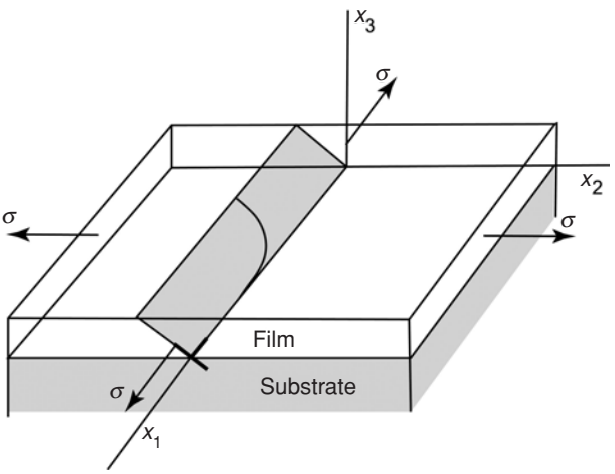

FIGURE 2.13. Geometry for constrained dislocation motion in a film on a rigid substrate. (Adapted from Ref. 204.)

significantly higher than calculated using the Nix model. The authors reported a room temperature yield stress of 280 MPa for a 1-μm-thick unpassivated Cu film; the yield stress for the same film calculated with the Nix model is only 45 MPa. This discrepancy is not surprising because the Nix model considers only the movement of a single dislocation, ignoring the interaction between dislocations. The authors pointed out that the high flow stresses of metal films seem to be the result of the superposition of different strengthening mechanisms including strain hardening in addition to the constraining of dislocation motion by the finite film thickness and grain size. Nix[205] incorporated strain hardening into this model. The author calculated the elastic interaction of moving threading dislocations with the interface dislocations. Strain hardening was accounted for by the narrowing of the channels through which dislocations in a thin film can move.

Thompson[206] extended the Nix model for the case of the deposition of dislocation segments at the grain boundaries. In his description the yield stress varies not only with the reciprocal film thickness but also with the reciprocal grain size. This dependency was experimentally found by Venkatraman and Bravman[208] for the yield stress of Al thin films, in which grain size and film thickness had been varied independently by applying a back-etch technique. Venkatraman and Bravman determined stress variations with temperature as a function of film thickness by the substrate curvature method for a fixed grain size in pure Al and Al–0.5%Cu films on Si substrates. They found that the film strength varied inversely with film thickness, and examined their results in the context of the classical Hall–Petch relationship (see Ref. 107, pp. 270–273) for the effect of grain size on strength. They found that the data for thin films followed a $(\textit{grain size})^{-1}$ variation instead of the $(\textit{grain size})^{-1/2}$ functional form for bulk materials, which on the other hand was found by Keller *et al.*[207] In general, the grain size dependence of the yield stress in bulk metals has been found to follow a $(\textit{grain size})^{-1/2}$ relationship which was attributed to the formation of dislocation pileups (see Ref. 107, pp. 270–273). Using the argument of strain hardening due to geometrically necessary dislocations, Ronay[209] has predicted a $(\textit{film thickness})^{-1/2}$ and $(\textit{grain size})^{-1/2}$ dependence. The importance of very strong kinematic strain hardening effects has been pointed out by Shen *et al.*[210]

In a recent study, Hommel and Kraft[211] studied the deformation behavior of thin Cu films with thicknesses between 0.4 and 3.2 μm on polyimide substrates, by tensile testing. In these experiments, the substrate strain is transferred to the film during the test and the film stress is measured by *in situ* X-ray diffraction. Simultaneously, the dislocation density that is related to the width of the measured peaks was characterized as a function of plastic strain. The X-ray measurements were performed in different texture components. The observed stress–strain behavior was found to consist of three regimes, i.e., elastic, plastic with strong strain hardening, and plastic with weak hardening. The flow stresses and the hardening rate were about two times higher in (111)-grains compared to the (100)-grains. The peak width in the X-ray measurements increased continuously in the second and third regime, indicating a steady increase of the dislocation density or

inhomogeneous micro-stresses. The flow stresses and the strain-hardening rate in the second deformation regime increased with decreasing film thickness and/or grain size.

Another model for the strengthening of thin polycrystalline films subjected to a thermal mismatch strain was presented by Choi and Suresh.[212] Instead of a single dislocation or dislocation loop, they considered arrays of circular dislocation loops that were equally spaced and confined within the slip planes of a grain. The generation of each dislocation loop in the set consecutively relaxed the elastic thermal strain arising from thermal mismatch between the thin film and the substrate during thermal cycling. The authors evaluated the total energy of the system as the sum of the energies stored in dislocation loops, the interaction energies among the loops, and the elastic energy of the grain and calculated the time-independent equilibrium strains and stresses sustained by the metal film. Through comparison of experimental data for Al and Cu films (with different thickness and grain size) on Si substrates, the stress–temperature curves of those films upon cooling from a high temperature could be estimated without considering the possibility of rate-dependent processes such as diffusional creep.[213] Since the model predicts that dislocation densities of thin films increase as the film thickness and grain size decrease, strain hardening due to high dislocation densities can be considered as an important source of thin film strengthening. However, thermally activated processes leading to stress relaxation should be taken into account in order to broaden the scope of this model and to describe those metal films that are not covered by a native oxide or effective passivation layer.

The plasticity of thin films can also be studied by measuring the indentation hardness as a function of indentation depth. But it has to be noted that determination of mechanical properties of thin films on substrates has always been difficult because of the influence of the substrate on the measured properties. Several studies, both experimental and numerical ones, have investigated the influence of substrates on the nanoindentation responses of thin films.[214–216] The major objective of these investigations has been the estimation of hardness and modulus of films, independent of the substrate, employing continuum analysis. The standard methods that are generally used for extracting properties from the measured load–displacement (P–h) data were developed primarily for monolithic materials but are also applied to film–substrate systems, without explicit consideration of how the substrate influences the measurements. However, these methods do not account for pileup of material around the indenter tip. Consequently, the contact area is underestimated, resulting in errors in the measured hardness. Additional errors are produced by inaccuracies in the measurement of contact stiffness caused by substrate effects on the shape of the unloading curve and creep in the film.[215] Collectively, these errors may result in an overestimation of the hardness by as much as 100%.

Figure 2.14 shows the hardness of Al thin films, 500 nm thick, on various substrates.[217] The increasing hardness with decreasing depth at very small indentation depths has been attributed to the hardening effect of sharp strain gradients that are created in such small indentations (also referred to as indentation size

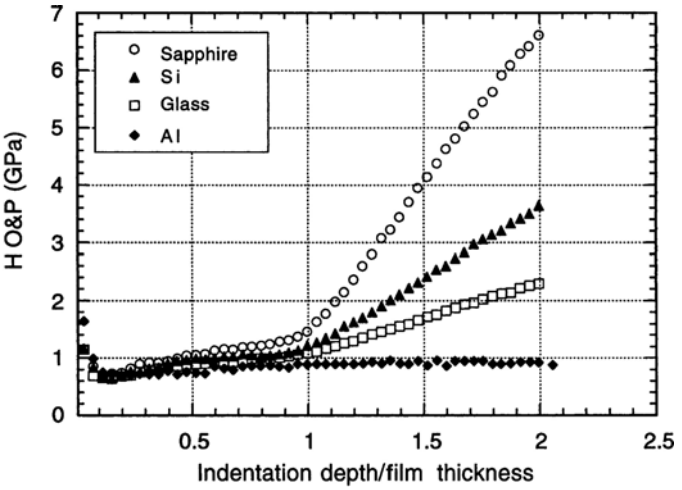

FIGURE 2.14. Hardness of an Al thin film, 0.5 μm in thickness on different substrates, as a function of indentation depth relative to the film thickness. The hardness was determined continuosly as described in Ref. 26. (Reprinted with permission from Ref. 217.)

effect).[39] With increasing depth the hardness rises gradually before rising sharply when the indenter begins to penetrate the substrate. The gradual rise is partly an artifact of the contact area determination; it is caused mainly by the pileup of material on the sides of the indenter neglected in the analysis of Oliver and Pharr.[26] The dramatic increase in hardness observed when the indenter reaches the film–substrate interface is expected, because these substrate materials are much harder than the Al film. It was found for indentation depths less than the film thickness that the substrate properties did not influence the measured film properties when the true contact area was determined and pileup was taken into account. For the case of a hard film on a soft substrate, substrate hardness was observed to affect film hardness because the substrate yields at indentation depths less than the film thickness.

Not only the film thickness but also lateral dimensions were observed to influence the early stages of plastic deformation. Choi and Suresh[218] and Choi *et al.*[219] performed nanoindentation studies on continuous films and unidirectionally patterned lines on substrates and investigated the effects of film thickness and linewidth. In this study a systematic investigation of size-scale effects on the early stages of nanoindentation-induced plasticity has been conducted via experiments and computation. The authors did not observe a size effect on the elastic P–h responses. Beyond the onset of plasticity, however, the two size scales (film thickness and linewidth) exhibited distinct effects, depending on their geometric constraints, which can be seen in Fig. 2.15. For a given load, the indentation depth decreased as the film thickness decreased, whereas the depth increased as the linewidth decreased in case of the patterned lines.[219] In the early stages of the

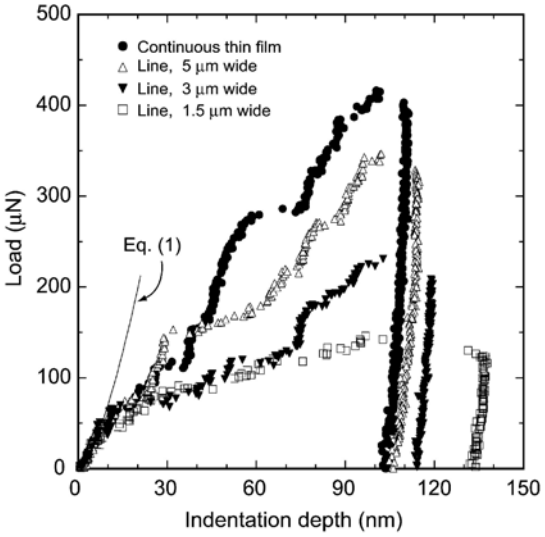

FIGURE 2.15. *P–h* response of polycrystalline Al thin film and lines of 1.5-, 3.0-, and 5.0-μm linewidths. The solid line denotes the elastic response on aluminium of a spherical diamond indenter with $R = 500$ nm. (Reprinted with permission from Ref. 218.)

indentation process, in both continuous films and patterned lines, a significant number of discontinuities, which are related to the discrete motion of dislocations,[32,51] were observed. Finite element modeling results indicated that the continuum approach has a limited use in rationalizing nanoindentation experiments in which discrete discontinuities are dominant, whereas MD simulations could describe the general trends observed experimentally. The results indicate that individual defects and their interaction with boundary conditions become important in small-scale deformation.

4.2. Cyclic Deformation

Recent studies on fatigue in thin metal films have shown that their fatigue behavior differs from that of bulk materials.[20,58,220–224] It is widely accepted that fatigue damage evolution in bulk ductile metals involves the formation of well-defined dislocation structures, such as veins, persistent slip bands (PSB), cells, and labyrinth structures, as well as the formation of surface extrusions and intrusions. Generally, the characteristic dimensions of these dislocation structures and extrusions are on the micron scale. For example, in Cu the wall spacing within a PSB is about 1.3 μm and the extrusions on the sample surface are several microns high.[225] These dimensions are comparable with the physical dimensions and grain sizes of thin films, making it questionable whether fatigue dislocation structures can be generated in thin films.[169]

Systematic experimental investigations of fatigue damage and corresponding dislocation structures in thin Cu films as a function of film thickness have been reported.[20,224] In a recent study on fatigue damage in Cu films with a thickness of a few microns or less, a careful attempt was made to look for dislocation structures using cross-sectional transmission electron microscopy (TEM).[20] Although evidence for ordering of the dislocations was found, no clearly defined dislocation structures were observed. In a follow-up study, plan-view TEM allowing for a more careful investigation of dislocation structures in the same fatigued Cu films revealed dislocation wall and cell structures in thick films and grains of at least 3.0 μm diameter.[224] In contrast, in thin films or in small-diameter grains no clearly defined dislocation structures, but rather tangled individual dislocations, were present. The surface structure after fatigue also showed pronounced differences. The thick films and large grains showed rather coarse surface extrusions, whereas in thinner films and smaller grains finer, very localized extrusions were found (see Fig. 2.16). The authors of that study suggest that a crystal volume with a characteristic dimension of 3.0 μm or larger is necessary for dislocation ordering and dislocation structure formation. This minimum required dimension, either geometric or microstructural, may be caused by constrained dislocation motion in small dimensions. Assuming that extrusions and dislocation structures are the result of large accumulated plastic strains, the finer, more localized extrusions and the tangled individual dislocations typical of the thinner films should result from smaller accumulated plastic strains. Thus, a trend of increasing fatigue life with decreasing film thickness and/or grain size can be expected and has indeed been observed in several thin film systems.[20,21,58,221,222]

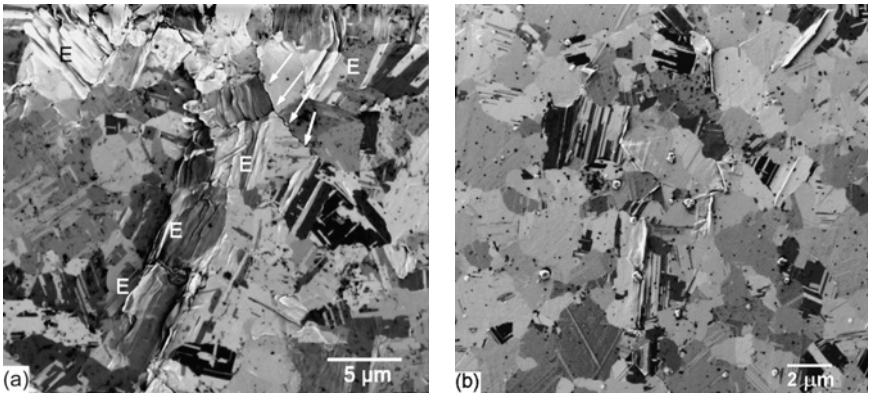

FIGURE 2.16. Extrusions at the surfaces of the fatigued Cu thin films imaged by focused ion beam microscopy: (a) a film 0.3 μm thick after 5×10^3 cycles, and (b) a film 0.4 μm thick after 1×10^4 cycles. The tensile axis is the horizontal direction.[20]

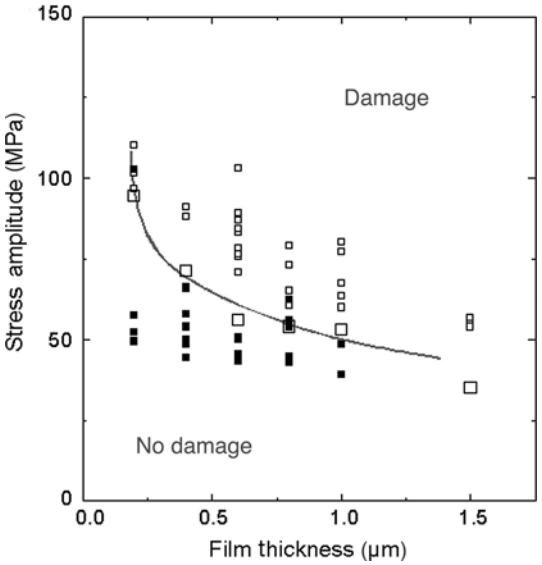

FIGURE 2.17. Damage map showing the stress amplitude versus. the film thickness. Test conditions in the upper-right part of the map led to fatigue damage within 3.8×10^6 cycles, whereas no damage was found for conditions in the lower-left corner. Damaged beams are denoted by open symbols, those that were not damaged by full ones. Note that the 1.5 μm thick film damage was always observed after 3.8×10^6 cycles. The critical stress amplitude above which damage occured is indicated by large square symbols for each film thickness.[58]

For thin Ag films between 1.5 and 0.2 μm thick on SiO_2 microbeams, a clear size effect has been found in the high cycle fatigue regime,[58] which is illustrated in Fig. 2.17. The films were subjected to 3.8×10^6 loading cycles with a constant stress amplitude and were then investigated for microstructural changes. The 1.5-μm-thick films showed fatigue damage even for a stress amplitude as low as 30 MPa. In contrast, a stress amplitude of about 100 MPa was required to produce fatigue damage in the thinnest films.

The cyclic deformation behavior of thin Cu films was also studied through tensile testing. The films on polyimide substrates were tested in the low cycle fatigue regime and exhibited a fatigue behavior that varied strongly with the film thickness.[20,222] This is shown in Fig. 2.18. The lifetimes determined for 3.1 μm thick films (A in Fig. 2.18) follow the Coffin–Manson law (cf. Ref. 226, pp. 256–260) with a fatigue exponent of about −0.5 and a fatigue ductility of about 20%.[227] As indicated by the dashed line in Fig. 2.18, this behavior is comparable to the fatigue lifetime of fine-grained bulk Cu.[228] The 0.4-μm-thick films with a grain size of about 0.3 μm (full circles) show improved lifetimes compared to the 0.4-μm-thick films with larger grains (full squares), or compared to the 3.1-μm-thick films with a grain size of 0.8 μm (open circles). The shortest lifetime was observed for

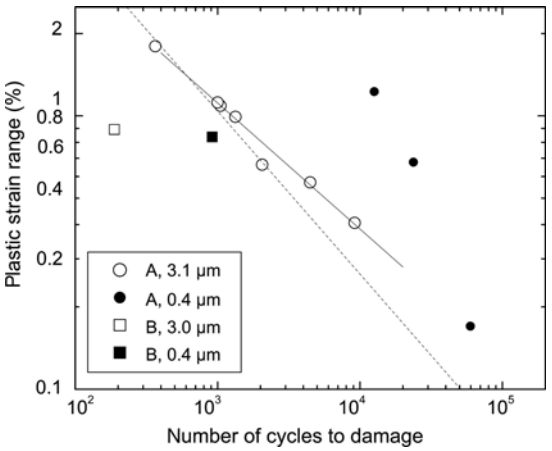

FIGURE 2.18. Plastic strain range versus fatigue lifetime for Cu films of thicknesses $h = 0.4$ μm (filled symbols) and $h = 3$μm (open symbols) and different grain sizes. The dashed line indicates the lifetime of bulk mc Cu with grain size of 25 μm.[227]

the 3.0-μm-thick film with a grain size of 1.5 μm (open squares). This suggests that the lifetime is influenced more strongly by the grain size than by the film thickness.

The origin of this fatigue size-effect may be the same that is responsible for the strengthening observed in thin films during monotonic loading. This strengthening is generally attributed to the inhibition of dislocation motion in thin films. In particular, "dislocation channeling" due to the film thickness constraint[204,205] and grain size strengthening in thin films[207,211] have been proposed as mechanisms to explain this decrease in dislocation mobility (see also Section 4.1.). Another possible explanation for the fatigue size-effect may be the activation of dislocation sources and sinks, which might depend on film thickness and grain size. The formation of voids at the film–substrate interface (see Fig. 2.19) under extrusions in these samples has been proposed as evidence of the activity of dislocation sources and sinks.[20]

5. CONCLUDING REMARKS

Large research efforts during the past years on the mechanical behavior of nanostructured materials have yielded a wealth of information and deepened our understanding of deformation mechanisms and the structure–property relationship. However, a number of issues remain unsolved despite these advances.

- Although evidence for dislocation activity during deformation has been found in nanostructured materials, no dislocation debris or stable dislocation structures postmortem have been found so far. With this in mind, the strain hardening mechanism cannot be explained satisfactorily. Since

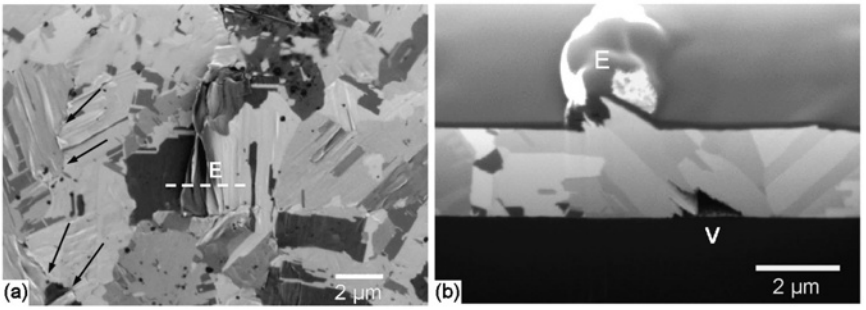

FIGURE 2.19. Fatigue damage of a 3.0- μm- thick Cu film: (a), and (b) Extrusions (marked as "E") at the film surface and cracks along the grain boundaries (marked by arrows). (b) Void (marked as "V") close to the film–substrate interface. The cross- section was prepared by FIB milling at the position indicated in (a) and imaged at a tilt angle of 45°. [20]

the importance of grain boundaries for the observed dislocation activity has been illustrated by atomistic simulations, it is conceivable that grain boundaries play an important role for strain hardening as well.

- We showed that microstructural as well as dimensional constraints have a considerable influence on the mechanical performance of materials during cyclic loading. Although the deformation mechanisms responsible for fatigue in mc bulk materials are well documented and understood, a comprehensive description and understanding of fatigue in nanostructured materials is missing.
- Up to now, most research efforts concentrated on pure metals or commercial alloys (in the case of materials produced by severe plastic deformation). Studies on clean binary or ternary alloy systems may give further insight into the influence of alloying elements at these reduced length scales.
- Many of today's nanostructured metals behave macroscopically brittle but are microscopically ductile. This may be related to plastic instability in the material. For structural applications, it is crucial to understand and control this plastic instability.
- The strong influence of microstructural length scales on the mechanical properties offers new possibilities to locally tailor mechanical properties by changing the microstructure. Plastically graded materials, for instance, could improve the wear properties. Hence, understanding of the indentation and scratch responses of graded materials at nano-length scales is necessary.

REFERENCES

1. E. Arzt, Overview No. 130—Size effects in materials due to microstructural and dimensional constraints: A comparative review, *Acta Mater.* **46**, 5611–5626 (1998).

2. D. Jia, K. T. Ramesh, and E. Ma, Effects of nanocrystalline and ultrafine grain sizes on constitutive behavior and shear bands in iron, *Acta Mater*. **51**, 3495–3509 (2003).
3. H. Hahn and K. A. Padmanabhan, Mechanical response of nanostructured materials, *Nanostruct. Mater*. **6**, 191–200 (1995).
4. *Standard Test Methods for Tension Testing of Metallic Materials*, ASTM E8-03 (ASTM International, 2003).
5. *Standard Test Methods for Tension Testing of Metallic Materials* (metric), ASTM E8M-03 (ASTM International, 2003).
6. G. W. Nieman, J. R. Weertman, and R. W. Siegel, Mechanical behavior of nanocrystalline Cu and Pd, *J. Mater. Res*. **6**, 1012–1027 (1991).
7. M. T. A. Saif, S. Zhang, A. Haque, and K. J. Hsia, Effect of native Al_2O_3 on the elastic response of nanoscale Al films, *Acta Mater*. **50**, 2779–2786 (2002).
8. W. N. Sharpe and R. O. Fowler, Novel miniature tension test machine, in *Proceedings of the Symposium on Small Specimen Test Techniques Applied to Nuclear Reactor Vessel Thermal Annealing and Plant Life Extension*, New Orleans, LA, January 29–31, 1992, pp. 386–401, 1993.
9. M. Legros, K. J. Hemker, D. A. LaVan, W. N. Sharpe, Jr., M. N. Rittner, and J. R. Weertman, Microtensile testing of nanocrystalline Al/Zr alloys, in *Materials Research Society Symposium*, 1997, pp. 273–278.
10. E. Mazza, G. Danuser, and J. Dual, Light optical deformation measurements in microbars with nanometer resolution, *Microsyst. Technol*. **2**, 83–91 (1996).
11. M. A. Haque and M. T. A. Saif, A review of MEMS-based microscale and nanoscale tensile and bending testing, *Exp. Mech*. **43**, 248–255 (2003).
12. M. A. Haque and M. T. A. Saif, *In situ* tensile testing of nanoscale specimens in SEM and TEM, *Exp. Mech*. **42**, 123–128 (2002).
13. M. A. Haque and M. T. A. Saif, Microscale materials testing using MEMS actuators, *J. Microelectromech. Syst*. **10**, 146–152 (2001).
14. M. A. Haque and M. T. A. Saif, Mechanical behavior of 30–50 nm thick aluminum films under uniaxial tension, *Scr. Mater*. **47**, 863–867 (2002).
15. A. Haque and T. Saif, *In situ* mechanical characterization of a freestanding 100 nanometer thick aluminum film in SEM using MEMS sensors, in *Thin Films: Stresses and Mechanical Properties IX*, Boston, MA, November 26–30, 2001, pp. 361–364 (2002).
16. M. A. Haque and M. T. A. Saif, Application of MEMS force sensors for *in situ* mechanical characterization of nanoscale thin films in SEM and TEM, *Sensors Actuators A* **3245**, 1–7 (2002).
17. Y.-S. Kang and P. S. Ho, Thickness dependent mechanical behavior of submicron aluminum films, *J. Electron. Mater*. **26**, 805–813 (1997).
18. L. Schadler and I. C. Noyan, Quantitative measurement of the stress transfer function in nickel/polyimide thin film/copper thin film structures, *Appl. Phys. Lett*. **66**, 22–24 (1995).
19. M. Hommel, O. Kraft, and E. Arzt, A new method to study cyclic deformation of thin films in tension and compression, *J. Mater. Res*. **14**, 2373–2376 (1999).
20. R. Schwaiger, G. Dehm, and O. Kraft, Cyclic deformation of polycrystalline Cu films, *Phil. Mag. A* **83**, 693–710 (2003).
21. O. Kraft and C. A. Volkert, Mechanical testing of thin films and small structures, *Adv. Eng. Mater*. **3**, 99–110 (2001).
22. L. B. Freund and S. Suresh, *Thin Film Materials Stress, Defect Formation, and Surface Evolution* (Cambridge University Press, New York, 2003).
23. D. Tabor, *Hardness of Metals* (Clarendon Press, Oxford, UK, 1951).
24. D. Tabor, The hardness of solids, *Rev. Phys. Technol*. **1**, 145–179 (1970).
25. A. C. Fischer-Cripps, *Nanoindentation* (Springer, New York, 2002).
26. W. C. Oliver and G. M. Pharr, An improved technique for determining hardness and elastic modulus using load and displacement sensing indentation experiments, *J. Mater. Res*. **7**, 1564–1583 (1992).

27. M. F. Doerner and W. D. Nix, A method for interpreting the data from depth-sensing indentation instruments, *J. Mater. Res*. **1**, 601–609 (1986).
28. X. Li and B. Bhushan, A review of nanoindentation continuous stiffness measurement technique and its application, *Mater. Charact*. **48**, 11–36 (2002).
29. A. Bolshakov and G. M. Pharr, Influences of pileup on the measurement of mechanical properties by load and depth sensing indentation techniques, *J. Mater. Res*. **13**, 1049–1058 (1998).
30. N. X. Randall, Direct measurement of residual contact area and volume during the nanoindentation of coated materials as an alternative method of calculating hardness, in *Second International Indentation Workshop*, Cambridge, UK, July 15–20, 2002.
31. M. Dao, N. Chollacoop, K. J. Van Vliet, T. A. Venkatesh, and S. Suresh, Computational modeling of the forward and reverse problems in instrumented sharp indentation, *Acta Mater*. **49**, 3899–3918 (2001).
32. A. Gouldstone, H. J. Koh, K. Y. Zeng, A. E. Giannakopoulos, and S. Suresh, Discrete and continuous deformation during nanoindentation of thin film, *Acta Mater*. **48**, 2277–2295 (2000).
33. S. Suresh and A. E. Giannakopoulos, A new method for estimating residual stresses by instrumented sharp indentation, *Acta Mater*. **46**, 5755–5767 (1998).
34. A. E. Giannakopoulos and S. Suresh, Determination of elastoplastic properties by instrumented sharp indentation, *Scr. Mater*. **40**, 1191–1198 (1999).
35. Y. T. Cheng and C. M. Cheng, Relationships between hardness, elastic modulus, and the work of indentation, *Appl. Phys. Lett*. **73**, 614–616 (1998).
36. Y. T. Cheng and C. M. Cheng, Can stress–strain relationships be obtained from indentation curves using conical and pyramidal indenters? *J. Mater. Res*. **14**, 3493–3496 (1999).
37. Y. T. Cheng and C. M. Cheng, Scaling approach to conical indentation in elastic–plastic solids with work hardening, *J. Appl. Phys*. **84**, 1284–1291 (1998).
38. K. Tunvisut, N. P. O'Dowd, and E. P. Busso, Use of scaling functions to determine mechanical properties of thin coatings from microindentation tests, *Int. J. Solids Struct*. **38**, 335–351 (2001).
39. W. D. Nix and H. Gao, Indentation size effects in crystalline materials: A law for strain gradient plasticity, *J. Mech. Phys. Solids* **46**, 411–425 (1998).
40. K. L. Johnson, The correlation of indentation experiments, *J. Mech. Phys. Solids* **18**, 115–126 (1970).
41. A. E. Giannakopoulos, P. L. Larsson, and R. Vestergaard, Analysis of Vickers indentation, *Int. J. Solids Struct*. **31**, 2679–2708 (1994).
42. T. A. Venkatesh, K. J. Van Vliet, A. E. Giannakopoulos, and S. Suresh, Determination of elastoplastic properties by instrumented sharp indentation: Guidelines for property extraction, *Scr. Mater*. **42**, 833–839 (2000).
43. T. W. Capehart and Y. T. Cheng, Determining constitutive models from conical indentation: Sensitivity analysis, *J. Mater. Res*. **18**, 827–832 (2003).
44. J. L. Bucaille, S. Stauss, E. Felder, and J. Michler, Determination of plastic properties of metals by instrumented indentation using different sharp indenters, *Acta Mater*. **51**, 1663–1678 (2003).
45. N. Chollacoop, M. Dao, and S. Suresh, Depth-sensing instrumented indentation with dual sharp indenters, *Acta Mater*. **51**, 3713–3729 (2003).
46. Y. P. Cao and J. Lu, Depth-sensing instrumented indentation with dual sharp indenters: Stability analysis and corresponding regularization schemes, *Acta Mater*. **52**, 1143–1153 (2004).
47. Y. Huang, Z. Xue, H. Gao, W. D. Nix, and Z. C. Xia, A study of microindentation hardness tests by mechanism-based strain gradient plasticity, *J. Mater. Res*. **15**, 1786–1796 (2000).
48. J. Y. Shu and N. A. Fleck, The prediction of a size effect in microindentation, *Int. J. Solids Struct*. **35**, 1363–1383 (1998).
49. T. Y. Zhang, W. H. Xu, and M. H. Zhao, The role of plastic deformation of rough surfaces in the size-dependent hardness, *Acta Mater*. **52**, 57–68 (2004).
50. S. Suresh, T. G. Nieh, and B. W. Choi, Nanoindentation of copper thin films on silicon substrates, *Scr. Mater*. **41**, 951–957 (1999).

51. A. Gouldstone, K. J. Van Vliet, and S. Suresh, Nanoindentation—Simulation of defect nucleation in a crystal, *Nature* **411**, 656 (2001).
52. J. Li, K. J. Van Vliet, T. Zhu, S. Yip, and S. Suresh, Atomistic mechanisms governing elastic limit and incipient plasticity in crystals, *Nature* **418**, 307–310 (2002).
53. O. Kraft, R. Schwaiger, and W. D. Nix, Measurement of mechanical properties in small dimensions by microbeam deflection, in *Proceedings of the 1998 MRS Spring Symposium*, San Francisco, CA, April 15–16, 1998, pp. 39–44.
54. T. P. Weihs, S. Hong, J. C. Bravman, and W. D. Nix, Mechanical deflection of cantilever microbeams—A new technique for testing the mechanical properties of thin films, *J. Mater. Res.* **3**, 931–942 (1998).
55. S. P. Baker and W. D. Nix, Mechanical properties of compositionally modulated Au–Ni thin films—Nanoindentation and microcantilever deflection experiments, *J. Mater. Res.* **9**, 3131–3145 (1994).
56. J. N. Florando and W. D. Nix, Study of the yielding and strain hardening behavior of a copper thin film on a silicon substrate using microbeam bending, in *Dislocations and Deformation Mechanics in Thin Films and Small Structures*, San Francisco, CA, April 17–19, 2001, pp. 1–9.
57. R. Schwaiger and O. Kraft, Analyzing the mechanical behavior of thin films using nanoindentation, cantilever microbeam deflection, and finite element modeling, *J. Mater. Res.* **19**, 315–324 (2004).
58. R. Schwaiger and O. Kraft, Size effects in the fatigue behavior of thin Ag films, *Acta Mater.* **51**, 195–206 (2003).
59. K. S. Kumar, S. Suresh, M. F. Chisholm, J. A. Horton, and P. Wang, Deformation of electrodeposited nanocrystalline nickel, *Acta Mater.* **51**, 387–405 (2003).
60. M. Taher, A. Saif, and A. Haque, Bending response of a 100 nm thick free standing aluminum cantilever beam, in *Materials Research Society Symposium—Proceedings, Thin Films-Stress and Mechanical Properties VIII*, Boston, MA, USA, November 29–December 3, 1999, Vol. 594, pp. 207–211, 2000.
61. W. W. Milligan, S. A. Hackney, M. Ke, and E. C. Aifantis, *In situ* studies of deformation and fracture in nanophase materials, *Nanostruct. Mater.* **2**, 267–276 (1993).
62. S. X. McFadden, A. V. Sergueeva, T. Kruml, J. L. Martin, and A. K. Mukherjee, Superplasticity in nanocrystalline Ni_3Al and Ti alloys, in *Materials Research Society Symposium*, 2001, pp. B1.3.1–B1.3.6.
63. C. J. Youngdahl, J. R. Weertmann, R. C. Hugo, and H. H. Kung, Deformation behavior in nanocrystralline copper, *Scr. Mater.* **44**, 1475–1478 (2001).
64. M. P. de Boer, B. D. Jensen, and F. Bitsie, A small area *in situ* MEMS test structure to measure fracture strength by electrostatic probing, in *Proceedings of the SPIE—The International Society for Optical Engineering, Materials and Device Characterization in Micromachining II*, Santa Clara, CA, USA, September 20–21, 1999, Vol. 3875, pp. 97–103.
65. A. M. Minor, J. W. Morris, and E. A. Stach, Quantitative *in situ* nanoindentation in an electron microscope, *Appl. Phys. Lett.* **79**, 1625–1627 (2001).
66. E. A. Stach, T. Freeman, A. M. Minor, D. K. Owen, J. Cumings, M. A. Wall, T. Chraska, R. Hull, J. W., Morris, Jr., A. Zettl, and U. Dahmen, Development of a nanoindenter for *in situ* transmission electron microscopy, *Microsc. Microanal.* **7**, 507–517 (2001).
67. C. C. Koch, Synthesis of nanostructured materials by mechanical milling: Problems and opportunities, *Nanostruct. Mater.* **9**, 13–22 (1997).
68. X. Zhang, H. Wang, R. O. Scattergood, J. Narayan, and C. C. Koch, Evolution of microstructure and mechanical properties of *in situ* consolidated bulk ultra-fine-grained and nanocrystalline Zn prepared by ball milling, *Mater. Sci. Eng. A* **344**, 175–181 (2003).
69. F. Zhou, X. Z. Liao, Y. T. Zhu, S. Dallek, and E. J. Lavernia, Microstructural evolution during recovery and recrystallization of a nanocrystalline Al–Mg alloy prepared by cryogenic ball milling, *Acta Mater.* **51**, 2777–2791 (2003).

70. R. Z. Valiev, R. K. Islamgaliev, and I. V. Alexandrov, Bulk nanostructured materials from severe plastic deformation, *Prog. Mater. Sci*. **45**, 103–189 (2000).
71. H. Gleiter, Nanocrystalline materials, *Prog. Mater. Sci*. **33**, 223–315 (1989).
72. P. G. Sanders, G. E. Fougere, L. J. Thompson, J. A. Eastman, and J. R. Weertman, Improvements in the synthesis and compaction of nanocrystalline materials, *Nanostruct. Mater*. **8**, 243–252 (1997).
73. P. G. Sanders, J. A. Eastman, and J. R. Weertman, Elastic and tensile behavior of nanocrystalline copper and palladium, *Acta Mater*. **45**, 4019–4025 (1997).
74. U. Erb, Electrodeposited nanocrystrals: Synthesis, properties and industrial applications, *Nanostruct. Mater*. **6**, 533–538 (1995).
75. F. Ebrahimi, Q. Zhai, and D. Kong, Deformation and fracture of electrodeposited copper, *Scr. Mater*. **39**, 315–321 (1998).
76. A. M. El-Sherik and U. Erb, Synthesis of bulk nanocrystalline nickel by pulsed electrodeposition, *J. Mater. Sci*. **30**, 5743–5749 (1995).
77. U. Erb, G. Palumbo, B. Szpunar, and K. T. Aust, Electrodeposited versus consolidated nanocrystals: Differences and similarities, *Nanostruct. Mater*. **9**, 261–270 (1997).
78. S. Van Petegem, F. Dalla Torre, D. Segers, and H. Van Swygenhoven, Free volume in nanostructured Ni, *Scr. Mater*. **48**, 17–22 (2003).
79. K. S. Kumar, H. Van Swygenhoven, and S. Suresh, Mechanical behavior of nanocrystalline metals and alloys, *Acta Mater*. **51**, 5743–5774 (2003).
80. P. Keblinski, D. Wolf, S. R. Phillpot, and H. Gleiter, Structure of grain boundaries in nanocrystalline palladium by molecular dynamics simulation, *Scr. Mater*. **41**, 631–636 (1999).
81. S. Ranganathan, R. Divakar, and V. S. Raghunathan, Interface structures in nanocrystalline materials, *Scr. Mater*. **44**, 1169–1174 (2001).
82. T. R. Haasz, K. T. Aust, G. Palumbo, A. M. El-Sherik, and U. Erb, Intercrystalline density of nanocrystalline nickel, *Scr. Mater*. **32**, 423–426 (1995).
83. H. Van Swygenhoven, D. Farkas, and A. Caro, Grain boundary structures in polycrystalline metals at the nanoscale, *Phys. Rev. B* **62**, 831–838 (2000).
84. H. Van Swygenhoven, A. Caro, and D. Farkas, A molecular dynamics study of polycrystalline fcc metals at the nanoscale: Grain boundary structure and its influence on plastic deformation, *Mater. Sci. Eng. A* **309–310**, 440–444 (2001).
85. F. Dalla Torre, H. Van Swygenhoven, M. Victoria, R. Schaeublin, and W. Wagner, Mechanical properties of nanocrystalline Ni in relation to its microstructure, in *Materials Research Society Symposium*, 2001, pp. B2.8.1–B2.8.6.
86. S. X. McFadden, A. P. Zhilyaev, R. S. Mishra, and A. K. Mukherjee, Observations of low-temperature superplasticity in electrodeposited ultrafine grained nickel, *Mater. Lett*. **45**, 345–349 (2000).
87. R. Klemm, E. Thiele, C. Holste, J. Eckert, and N. Schell, Thermal stability of grain structure and defects in submicrocrystalline and nanocrystalline nickel, *Scr. Mater*. **46**, 685–690 (2002).
88. H. Natter, M. Schmelzer, and R. Hempelmann, Nanocrystalline nickel and nickel–copper alloys: Synthesis, characterization, and thermal stability, *J. Mater. Res*. **13**, 1186–1197 (1998).
89. G. D. Hibbard, J. L. McCrea, G. Palumbo, K. T. Aust, and U. Erb, An initial analysis of mechanisms leading to late stage abnormal grain growth in nanocrystalline Ni, *Scr. Mater*. **47**, 83–87 (2002).
90. C. Xiao, R. A. Mirshams, S. H. Whang, and W. M. Yin, Tensile behavior and fracture in nickel and carbon doped nanocrystalline nickel, *Mater. Sci. Eng. A* **301**, 35–43 (2001).
91. R. Suryanarayanan Iyer, C. A. Frey, S. M. Sastry, B. E. Waller, and W. E. Buhro, Plastic deformation of nanocrystalline Cu and Cu–0.2 wt.% B, *Mater. Sci. Eng. A* **264**, 210–214 (1999).
92. R. Schwaiger, B. Moser, M. Dao, N. Chollacoop, and S. Suresh, Some critical experiments on the strain-rate sensitivity of nanocrystalline nickel, *Acta Mater*. **51**, 5159–5172 (2003).
93. K. S. Kumar, unpublished research (2003).

94. S. Cheng, J. A. Spencer, and W. W. Milligan, Strength and tension/compression asymmetry in nanostructured and ultrafine-grain metals, *Acta Mater*. **51**, 4505–4518 (2003).
95. J. D. Embury and D. J. Lahaie, The mechanical properties of fine scale metallic materials, in *NATO Advanced Study Institute on Mechanical Properties and Deformation Behavior of Materials Having Ultra-Fine Microstructures*, Porto Novo, Portugal, June 28–July 10, 1992, pp. 287–301, 1993.
96. K. A. Padmanabhan, Mechanical properties of nanostructured materials, *Mater. Sci. Eng. A* **304–306**, 200–205 (2001).
97. J. R. Weertman, M. Niedzielka, and C. Youngdahl, Hall–Petch behavior in nanocrystalline metals, in *NATO Advanced Study Institute on Mechanical Properties and Deformation Behavior of Materials Having Ultra-Fine Microstructures*, Porto Novo, Portugal, June 28–July 10, 1992, pp. 241–254, 1993.
98. M. N. Rittner, J. R. Weertman, J. A. Eastman, K. B. Yoder, and D. S. Stone, Microhardness and elastic modulus of nanocrystalline Al–Zr, in *Processing and Properties of Nanocrystalline Materials*, Cleveland, OH, USA, October 29–November 2, 1995, pp. 399–405, 1996.
99. P. G. Sanders, J. A. Eastman, and J. R. Weertman, Tensile behavior of nanocrystalline copper, in *Processing and Properties of Nanocrystalline Materials*, Cleveland, OH, USA, October 29–November 2, 1995, pp. 379–386, 1996.
100. H. S. Cao, R. Bonnet, J. J. Hunsinger, and O. Elkedim, Determination of elastic properties of consolidated nanocrystalline alloys iron–copper by means of acoustic echography and interferometry, *Scr. Mater*. **48**, 531–537 (2003).
101. U. Erb, G. Palumbo, R. Zugic, and K. T. Aust, Structure–property relationships for electrodeposited nanocrystals, in *Materials Week*, Cleveland, OH, October 29–November 2, 1995, pp. 93–111, 1996.
102. T. D. Shen, C. C. Koch, T. Y. Tsui, and G. M. Pharr, On the elastic moduli of nanocrystalline Fe, Cu, Ni, and Cu–Ni alloys prepared by mechanical milling/alloying, *J. Mater. Res*. **10**, 2892–2896, (1995).
103. H. S. Kim and M. B. Bush, The effects of grain size and porosity on the elastic modulus of nanocrystalline materials, *Nanostruct. Mater*. **11**, 361–367 (1999).
104. A. Latapie and D. Farkas, Effect of grain size on the elastic properties of nanocrystalline alpha-iron, *Scr. Mater*. **48**, 611–615 (2003).
105. C. Suryanarayana, Nanocrystalline materials, *Int. Mater. Rev*. **40**, 41–64 (1995).
106. R. A. Masumura, P. M. Hazzledine, and C. S. Pande, Yield stress of fine grained materials, *Acta Mater*. **46**, 4527–4534 (1998).
107. M. A. Meyers and K. K. Chawla, *Mechanical Behavior of Materials* (Prentice Hall, Upper Saddle River, NJ, 1999).
108. A. H. Chokshi, A. Rosen, J. Karch, and H. Gleiter, On the validity of the Hall–Petch relationship in nanocrystalline materials, *Scr. Mater*. **23**, 1679–1684 (1989).
109. M. A. Morris-Munoz, A. Dodge, and D. G. Morris, Structure, strength, and toughness of nanocrystalline FeAl, *Nanostruct. Mater*. **11**, 873–885 (1999).
110. T. Volpp, E. Goering, W. M. Kuschke, and E. Arzt, Grain size determination and limits to Hall–Petch behavior in nanocrystalline NiAl powders. *Nanostruct. Mater*. **8**, 855–865 (1998).
111. M. S. Choudry, M. Dollar, and J. A. Eastman, Nanocrystalline NiAl-processing, characterization, and mechanical properties, *Mater. Sci. Eng. A* **256**, 25–33 (1998).
112. E. Bonetti, E. G. Campari, L. D. Bianco, L. Pasquini, and E. Sampaolesi, Mechanical behaviour of nanocrystalline iron and nickel in the quasistatic and low frequency anelastic regime, *Nanostruct. Mater*. **11**, 709–720 (1999).
113. S. E. Hadian and D. R. Gabe, Residual stresses in electrodeposits of nickel and nickel–iron alloys, *Surf. Coat. Technol*. **122**, 118–135 (1999).
114. A. Hasnaoui, H. Van Swygenhoven, and P. M. Derlet, On nonequilibrium grain boundaries and their effect on thermal and mechanical behaviour: A molecular dynamics computer simulation, *Acta Mater*. **50**, 3927–3939 (2002).

115. N. Wang, Z. Wang, K. T. Aust, and U. Erb, Room temperature creep behavior of nanocrystalline nickel produced by an electrodeposition technique, *Mater. Sci. Eng. A* **237**, 150–158 (1997).
116. K. T. Aust, U. Erb, and G. Palumbo, Interfacial effects in nanocrystalline metals, in *Materials Week '95*, Cleveland, OH, October 29–November 2, 1995, pp. 11–22, 1996.
117. A. S. Khan, H. Zhang, and L. Takacs, Mechanical response and modeling of fully compacted nanocrystalline iron and copper, *Int. J. Plast.* **16**, 1459–1476 (2000).
118. C. A. Schuh, T. G. Nieh, and H. Iwasaki, The effect of solid solution W additions on the mechanical properties of nanocrystalline Ni, *Acta Mater.* **51**, 431–443 (2003).
119. H. Hahn, P. Mondal, and K. A. Padmanabhan, Plastic deformation of nanocrystalline materials, *Nanostruct. Mater.* **9**, 603–306 (1997).
120. H. Chang, C. J. Altstetter, and R. S. Averback, Characteristics of nanophase TiAl produced by inert gas condensation, *J. Mater. Res.* 7(11), 2962–2970 (1992).
121. A. Hasnaoui, H. Van Swygenhoven, and P. M. Derlet, Cooperative processes during plastic deformation in nanocrystalline fcc metals: A molecular dynamics simulation, *Phys. Rev. B.* **66**, 184112-1-8 (2002).
122. Q. Wei, D. Jia, K. T. Ramesh, and E. Ma, Evolution and microstructure of shear bands in nanostructured Fe, *Appl. Phys. Lett.* **81**, 1240–1242 (2002).
123. E. Ma, Instabilities and ductility of nanocrystalline and ultrafine-grained metals, *Scr. Mater.* **49**, 663–668 (2003).
124. H. S. Kim, Y. Estrin, and M. B. Bush, Plastic deformation behavior of fine-grained materials, *Acta Mater.* **48**, 493–504 (2000).
125. A. A. Fedorov, M. Y. Gutkin, and I. A. Ovid'ko, Triple junction diffusion and plastic flow in fine-grained materials, *Scr. Mater.* **47**, 51–55 (2002).
126. H. Van Swygenhoven, M. Spaczer, and A. Caro, Microscopic description of plasticity in computer generated metallic nanophase samples: A comparison between Cu and Ni, *Acta Mater.* **47**, 3117–3126 (1999).
127. H. Van Swygenhoven, M. Spaczer, and A. Caro, Role of low and high angle grain boundaries in the deformation mechanism of nanophase Ni: A molecular dynamics simulation study, *Nanostruct. Mater.* **10**, 819–828 (1998).
128. H. Van Swygenhoven, M. Spaczer, D. Farkas, and A. Caro, The role of grain size and the presence of low and high angle grain boundaries in the deformation mechanism of nanophase Ni: A molecular dynamics computer simulation, *Nanostruct. Mater.* **12**, 323–326 (1999).
129. U. Erb, A. M. El-Sherik, G. Palumbo, and K. T. Aust, Synthesis, structure and properties of electroplated nanocrystalline materials, *Nanostruct. Mater.* **2**, 383–390 (1993).
130. C. A. Schuh, T. G. Nieh, and T. Yamasaki, Hall–Petch breakdown manifested in abrasive wear resistance of nanocrystalline nickel, *Scr. Mater.* **46**, 735–740 (2002).
131. J. Schiøtz, F. D. Di Tolla, and K. W. Jacobson, Softening of nanocrystalline metals at very small grain sizes, *Nature* **391**, 561–563 (1998).
132. F. Ebrahimi, G. R. Bourne, M. S. Kelly, and T. E. Matthews, Mechanical properties of nanocrystalline nickel produced by electrodeposition, *Nanostruct. Mater.* **11**, 343–350 (1999).
133. G. D. Hughes, S. D. Smith, C. S. Pande, H. R. Johnson, and R. W. Armstrong, Hall–Petch strengthening for the microhardness of 12 nanometer grain diameter electrodeposited nickel, *Scr. Metal.* **20**, 93–97 (1986).
134. C. A. Schuh, unpublished research.
135. K. J. Van Vliet, S. Tsikata, and S. Suresh, Model experiments for direct visualization of grain boundary deformation in nanocrystalline metals, *Appl. Phys. Lett.* **83**, 1441–1443 (2003).
136. K. J. Van Vliet, J. Li, T. Zhu, S. Yip, and S. Suresh, Quantifying the early stages of plasticity through nanoscale experiments and simulations, *Phys. Rev. B.* **67**, 1–15 (2003).
137. K. L. Johnson, *Contact Mechanics* (Cambridge University Press, Cambridge, UK, 1985).
138. M. J. Mayo, R. W. Siegel, Y. X. Liao, and W. D. Nix, Nanoindentation of nanocrystalline ZnO, *J. Mater. Res.* **7**, 973–979 (1992).

139. M. J. Mayo, R. W. Siegel, A. Narayanasamy, and W. D. Nix, Mechanical properties of nanophase TiO_2 as determined by nanoindentation, *J. Mater. Res.* **5**, 1073–1082 (1990).
140. T. Mukai, M. Kawazoe, and K. Higashi, Dynamic mechanical properties of a near-nano aluminum alloy processed by equal-channel-angular-extrusion, *Nanostruct. Mater.* **10**, 755–765 (1998).
141. T. Mukai, S. Suresh, K. Kita, H. Sasaki, N. Kobayashi, K. Higashi, and A. Inoue, Nanostructured Al–Fe alloys produced by e-beam deposition: Static and dynamic tensile properties, *Acta Mater.* **51**, 4197–4208 (2003).
142. L. Lu, S. X. Li, and K. Lu, An abnormal strain rate effect on tensile behavior in nanocrystalline copper, *Scr. Mater.* **45**, 1163–1169 (2001).
143. D. Jia, K. T. Ramesh, E. Ma, L. Lu, and K. Lu, Compressive behavior of an electrodeposited nanostructured copper at quasistatic and high strain rates, *Scr. Mater.* **45**, 613–620 (2001).
144. D. Jia, K. T. Ramesh, and E. Ma, Failure mode and dynamic behavior of nanophase iron under compression, *Scr. Mater.* **42**, 73–78 (1999).
145. D. Jia, Y. M. Wang, K. T. Ramesh, and E. Ma, Deformation behavior and plastic instabilities of ultrafine-grained titanium, *Appl. Phys. Lett.* **79**, 611–613 (2001).
146. F. A. Mohamed and Y. Li, Review—Creep and superplasticity in nanocrystalline materials: Current understanding and future prospects, *Mater. Sci. Eng. A* **298**, 1–15 (2001).
147. V. Yamakov, D. Wolf, S. R. Phillpot, and H. Gleiter, Grain-boundary diffusion creep in nanocrystalline palladium by molecular-dynamics simulation, *Acta Mater.* **50**, 61–73 (2002).
148. J. Schiøtz, T. Vegge, F. D. Di Tolla, and K. W. Jacobsen, Atomic-scale simulations of the mechanical deformation of nanocrystalline metals, *Phys. Rev. B* **60**, 11971–11983 (1999).
149. H. Van Swygenhoven, M. Spaczer, A. Caro, and D. Farkas, Competing plastic deformation mechanisms in nanophase metals, *Phys. Rev. B* **60**, 22–25 (1999).
150. F. Dalla Torre, H. Van Swygenhoven, and M. Victoria, Nanocrystalline electrodeposited Ni: Microstructure and tensile properties, *Acta Mater.* **50**, 3957–3970 (2002).
151. M. Legros, B. R. Elliott, M. N. Rittner, J. R. Weertman, and K. J. Hemker, Microsample tensile testing of nanocrystalline metals, *Phil. Mag. A* **80**, 1017–1026 (2000).
152. Y. Champion, C. Langlois, S. Guérin-Mailly, P. Langlois, J.-L. Bonnentien, and M. J. Hÿtch, Near-perfect elastoplasticity in pure nanocrystalline copper, *Science* **300**, 310–311 (2003).
153. W. M. Yin, S. H. Whang, R. Mirshams, and C. H. Xiao, Creep behavior of nanocrystalline nickel at 290 and 373 K, *Mater. Sci. Eng. A* **301**, 18–22 (2001).
154. X. Zhang, H. Wang, R. O. Scattergood, J. Narayan, C. C. Koch, A. V. Sergueeva, and A. K. Mukherjee, Studies of deformation mechanisms in ultra-fine-grained and nanostructured Zn, *Acta Mater.* **50**, 4823–4830 (2002).
155. Y. R. Kolobov, G. P. Grabovetskaya, M. B. Ivanov, A. P. Zhilyaev, and R. Z. Valiev, Grain boundary diffusion characteristics of nanostructured nickel, *Scr. Mater.* **44**, 873–878 (2001).
156. B. S. Bokstein, H. D. Brose, L. I. Trusov, and T. P. Khvostantseva, Diffusion in nanocrystalline nickel, *Nanostruct. Mater.* **6**, 873–876 (1995).
157. C. Cheung, F. Djuanda, U. Erb, and G. Palumbo, Electrodeposition of nanocrystalline Ni–Fe alloy, *Nanostruct. Mater.* **5**, 513–523 (1995).
158. C. J. Youngdahl, R. C. Hugo, H. Kung, and J. R. Weertman, TEM observation of nanocrystalline copper during deformation, in *Materials Research Society Symposium*, 2001, pp. B1.2.1–B1.2.6.
159. L. Priester and O. Khalfallah, Image force on a lattice dislocation due to a grain-boundary in anisotropic fcc materials, *Phil. Mag. A* **69**, 471–484 (1994).
160. M. Chen, E. Ma, K. J. Hemker, H. Sheng, Y. Wang, and X. Cheng, Deformation twinning in nanocrystalline aluminum, *Science* **300**, 1275–1277 (2003).
161. H. Van Swygenhoven, P. M. Derlet, and A. Hasnaoui, Atomic mechanism for dislocation emission from nanosized grain boundaries, *Phys. Rev. B.* **66**, 024101-1-8 (2002).
162. R. A. Mirshams, C. H. Xiao, S. H. Whang, and W. M. Yin, *R*-curve characterization of the fracture toughness of nanocrystalline nickel thin sheets, *Mater. Sci. Eng. A* **315**, 21–27 (2001).
163. D. Farkas, H. Van Swygenhoven, and P. M. Derlet, Intergranular fracture in nanocrystalline metals, *Phys. Rev. B* **66**, 060101-1-4 (2002).

164. S. R. Agnew and J. R. Weertman, Cyclic softening of ultrafine grain copper, *Mater. Sci. Eng. A* **244**, 145–153 (1998).
165. S. R. Agnew, A. Y. Vinogradov, S. Hashimoto, and J. R. Weertman, Overview of fatigue performance of Cu processed by severe plastic deformation, *J. Electron. Mater.* **28**, 1038–1044 (1999).
166. H. Mughrabi and H. W. Hoeppel, Cyclic deformation and fatigue properties of ultrafine grain size materials: Current status and some criteria for improvement of the fatigue resistance, in *Materials Research Society Symposium*, 2001, pp. B2.1.1–B2.1.12.
167. C. E. Feltner and C. Laird, Cyclic stress–strain response of fcc metals and alloys—I: Phenomenological experiments, *Acta Metall.* **15**, 1621–1632 (1967).
168. H. Z. Ding, H. Mughrabi, and H. W. Höppel, A low-cycle fatigue life prediction model of ultrafine-grained metals, *Fatigue Fract. Eng. Mater. Struct.* **25**, 975–984 (2002).
169. E. Thiele, C. Holste, and R. Klemm, Influence of size effect on microstructural changes in cyclically deformed polycrystalline nickel, *Z. Met. kd.* **93**, 730–736 (2002).
170. T. Hanlon, Y.-N. Kwon, and S. Suresh, Grain size effects on the fatigue response of nanocrystalline metals, *Scr. Mater.* **49**, 675–680 (2003).
171. B. Q. Han, Z. Lee, S. R. Nutt, E. J. Lavernia, and F. A. Mohamed, Mechanical properties of an ultrafine-grained Al–7.5 pct Mg alloy, *Metall. Mater. Trans. A* **34**, 603–613 (2003).
172. W. Klement, R. H. Willens, and P. Duwez, Noncrystalline structure in solidified gold–silicon alloys, *Nature* **187**, 869–870 (1960).
173. A. C. Lund and C. A. Schuh, Plasticity in nanocrystalline and amorphous metals: Similarities at the atomic scale, in *Materials Research Society Symposium*, Boston, MA, 2004, pp. MM7.4.1–MM7.4.6.
174. C. S. Kiminami, N. D. Basim, M. J. Kaufman, M. F. Amateau, T. J. Eden, and J. M. Galbraith, Challenges in the development of aluminum-based bulk amorphous alloys, *Key Eng. Mater.* **189–191**, 503–508 (2001).
175. W. S. Liu and W. L. Johnson, Precipitation of bcc nanocrystals in bulk Mg–Cu–Y amorphous alloys, *J. Mater. Res.* **11**, 2388–2392 (1996).
176. A. Inoue, A. Makino, and T. Masumoto, Soft-magnetic properties of Cu-free Fe-based nanocrystalline alloys, *Mat. Sci. Forum* **179–181**, 497–505 (1995).
177. C. Fan, A. Takeuchi, and A. Inoue, Preparation and mechanical properties of Zr-based bulk nanocrystalline alloys containing compound and amorphous phases, *Mater. Trans. JIM* **40**, 42–51 (1999).
178. A. Inoue, H. M. Kimura, K. Sasamori, and T. Masumoto, Synthesis and high mechanical strength of Al-based alloys consisting mainly of nanogranular amorphous particles, *Mater. Sci. Eng. A* **217**, 401–406 (1996).
179. C. A. Schuh and T. G. Nieh, A survey of instrumented indentation studies on metallic glasses, *J. Mater. Res.* **19**, 46–57 (2004).
180. H. A. Bruck, T. Christman, A. J. Rosakis, and W. L. Johnson, Quasistatic constitutive behavior of Zr41.25Ti13.75Ni10Cu12.5Be22.5 bulk amorphous-alloys, *Scr. Metall. Mater.* **30**, 429–434 (1994).
181. P. E. Donovan, A yield criterion for Pd40Ni40P20 metallic glass, *Acta Metall.* **37**, 445–456 (1989).
182. P. Lowhaphandu, S. L. Montgomery, and J. J. Lewandowski, Effects of superimposed hydrostatic pressure on flow and fracture of a Zr–Ti–Ni–Cu–Be bulk amorphous alloy, *Scr. Mater.* **41**, 19–24 (1999).
183. R. Vaidyanathan, M. Dao, G. Ravichandran, and S. Suresh, Study of mechanical deformation in bulk metallic glass through instrumented indentation, *Acta Mater.* **49**, 3781–3789 (2001).
184. C. A. Schuh and A. C. Lund, Atomistic basis for the plastic yield criterion of metallic glass, *Nat. Mater.* **2**, 449–452 (2003).
185. A. C. Lund and C. A. Schuh, Yield surface of a simulated metallic glass, *Acta Mater.* **51**, 5399–5411 (2003).

186. Z. F. Zhang, J. Eckert, and L. Schultz, Difference in compressive and tensile fracture mechanisms of Zr59Cu20Al10Ni8Ti3 bulk metallic glass, *Acta Mater*. **51**, 1167–1179 (2003).
187. C. A. Pampillo and H. S. Chen, Comprehensive plastic deformation of a bulk metallic glass, *Mater. Sci. Eng*. **13**, 181–188 (1974).
188. H. Kimura and T. Masumoto, A model of the mechanics of serrated flow in an amorphous alloy, *Acta Metall*. **31**, 231–240 (1983).
189. W. J. Wright, R. B. Schwarz, and W. D. Nix, Localized heating during serrated plastic flow in bulk metallic glasses, *Mater. Sci. Eng. A* **319–321**, 229–232 (2001).
190. J. G. Wang, B. W. Choi, T. G. Nieh, and C. T. Liu, Crystallization and nanoindentation behavior of a bulk Zr–Al–Ti–Cu–Ni amorphous alloy, *J. Mater. Res*. **15**, 798–807 (2000).
191. Y. I. Golovin, V. I. Ivolgin, V. A. Khonik, K. Kitagawa, and A. I. Tyurin, Serrated plastic flow during nanoindentation of a bulk metallic glass, *Scr. Mater*. **45**, 947–952 (2001).
192. W. J. Wright, R. Saha, and W. D. Nix, Deformation mechanisms of the Zr40Ti14Ni10Cu12Be24 bulk metallic glass, *Mater. Trans*. **42**, 642–649 (2001).
193. C. A. Schuh, A. S. Argon, T. G. Nieh, and J. Wadsworth, The transition from localized to homogeneous plasticity during nanoindentation of an amorphous metal, *Phil. Mag. A* **83**, 2585–2597 (2003).
194. C. A. Schuh, T. G. Nieh, and Y. Kawamura, Rate dependence of serrated flow during nanoindentation of a bulk metallic glass, *J. Mater. Res*. **17**, 1651–1654 (2002).
195. C. A. Schuh and T. G. Nieh, A nanoindentation study of serrated flow in bulk metallic glasses, *Acta Mater*. **51**, 87–99 (2003).
196. J. J. Kim, Y. Choi, S. Suresh, and A. S. Argon, Nanocrystallization during nanoindentation of a bulk amorphous metal alloy at room temperature, *Science* **295**, 654–657 (2002).
197. H. Chen, Y. He, G. J. Shiflet, and S. J. Poon, Deformation-induced nanocrystal formation in shear bands of amorphous alloys, *Nature* **367**, 541–543 (1994).
198. Y. He, G. J. Shiflet, and S. J. Poon, Ball milling-induced nanocrystal formation in aluminum-based metallic glasses, *Acta Metall. Mater*. **43**, 83–91 (1995).
199. K. Lu, Nanocrystalline metals crystallized from amorphous solids: Nanocrystallization, structure, and properties, *Mater. Sci. Eng. R* **16**, 161–221 (1996).
200. Q. Y. Zhou, A. S. Argon, and R. E. Cohen, Enhanced case-II diffusion of diluents into glassy polymers undergoing plastic flow, *Polymer* **42**, 613–621 (2001).
201. W. W. Mullins, The effect of thermal grooving on grain boundary motion, *Acta Metall*. **6**, 414–427 (1958).
202. C. V. Thompson, Grain growth in thin films, *Ann. Rev. Mater. Sci*. **20**, 245–268 (1990).
203. C. A. Neugebauer, J. B. Newkirk, and D. A. Vermilyea, eds., *International Conference on Structure and Properties of Thin Films* (Bolton Landing, Wiley NY, September 9–11, 1959).
204. W. D. Nix, Mechanical properties of thin films, *Metall. Trans. A* **20**, 2217–2245 (1989).
205. W. D. Nix, Yielding and strain hardening of thin metal films on substrates, *Scr. Mater*. **39**, 545–554 (1998).
206. C. V. Thompson, The yield stress of polycrystalline thin films, *J. Mater. Res*. **8**, 237–238 (1993).
207. R. M. Keller, S. P. Baker, and E. Arzt, Quantitative analysis of strengthening mechanisms in thin Cu films: Effects of film thickness, grain size, and passivation, *J. Mater. Res*. **13**, 1307–1317 (1998).
208. R. Venkatraman and J. C. Bravman, Separation of film thickness and grain boundary strengthening effects in Al thin films on Si, *J. Mater. Res*. **7**, 2040–2048 (1992).
209. M. Ronay, Yield stress of thin fcc polycrystalline metal films bonded to rigid substrates, *Phil. Mag. A*- **40**, 145–160 (1979).
210. Y. L. Shen, S. Suresh, M. Y. He, A. Bagchi, O. Kienzle, M. Ruhle, and A. G. Evans, Stress evolution in passivated thin films of Cu on silica substrates, *J. Mater. Res*. **13**, 1928–1937 (1998).
211. M. Hommel and O. Kraft, Deformation behavior of thin copper films on deformable substrates, *Acta Mater*. **49**, 3935–3947 (2001).

212. Y. Choi and S. Suresh, Size effects on the mechanical properties of thin polycrystalline metal films on substrates, *Acta Mater*. **50**, 1881–1893 (2002).
213. D. Weiss, H. Gao, and E. Arzt, Constrained diffusional creep in UHV-produced copper thin films, *Acta Mater*. **49**, 2395–2403 (2001).
214. A. K. Bhattacharya and W. D. Nix, Analysis of elastic and plastic deformation associated with indentation testing of thin films on substrates, *Int. J. Solids Struct*. **24**, 1287–1298 (1998).
215. T. Y. Tsui and G. M. Pharr, Substrate effects on nanoindentation mechanical property measurement of soft films on hard substrates, *J. Mater. Res*. **14**, 292–301 (1999).
216. X. Chen and J. J. Vlassak, Numerical study on the measurement of thin film mechanical properties by means of nanoindentation, *J. Mater. Res*. **16**, 2974–2982 (2001).
217. R. Saha and W. D. Nix, Effects of the substrate on the determination of thin film mechanical properties by nanoindentation, *Acta Mater*. **50**, 23–38 (2002).
218. Y. Choi and S. Suresh, Nanoindentation of patterned metal lines on a Si substrate, *Scr. Mater*. **48**, 249–254 (2003).
219. Y. Choi, K. J. Van Vliet, J. Li, and S. Suresh, Size effects on the onset of plastic deformation during nanoindentation of thin films and patterned lines, *J. Appl. Phys*. **94**, 6050–6058 (2003).
220. S. Hong and R. Weil, Low cycle fatigue of thin copper foils, *Thin Solid Films* **283**, 175–181 (1996).
221. R. Schwaiger and O. Kraft, High cycle fatigue of thin silver films investigated by dynamic microbeam deflection, *Scr. Mater.* **41**, 823–829 (1999).
222. O. Kraft, P. Wellner, M. Hommel, R. Schwaiger, and E. Arzt, Fatigue behavior of polycrystalline thin copper films, *Z. Met. kd* **93**, 392–400 (2002).
223. D. T. Read, Tension–tension fatigue of copper thin films, *Int. J. Fatigue* **20**, 203–209 (1998).
224. 224.G. P. Zhang, R. Schwaiger, C. A. Volkert, and O. Kraft, Effect of film thickness and grain size on fatigue-induced dislocation structures in Cu thin films, *Phil. Mag. Lett*. **83**, 477–483 (2003).
225. J. C. Grosskreutz and H. Mughrabi, Description of the work-hardened structure at low temperature in cyclic deformation, in *Constitutive Equations in Plasticity*, edited by A. S. Argon (The MIT Press, Cambridge, MA, 1975), pp. 251–325.
226. S. Suresh, *Fatigue of Materials*, 2nd edn (Cambridge University Press, New York, 1998).
227. O. Kraft, R. Schwaiger, and P. Wellner, Damage formation in Cu thin films due to mechanical fatigue, in *Fatigue 2002*, Stockholm, Sweden, 2002, pp. 2225–2232.
228. H. Mughrabi and R. Wang, Cyclic stress–strain response and high-cycle fatigue behavior of copper polycrystals, in *Basic Mechanisms in Fatigue of Metals, Proceedings of the International Colloquium*, Brno, Czechoslovakia, April 12–14, 1988, pp. 1–13.

3

Defects and Deformation Mechanisms in Nanostructured Coatings

Ilya A. Ovid'ko

Institute of Problems of Mechanical Engineering, Russian Academy of Sciences, St. Petersburg, Russia

1. INTRODUCTION

Nanostructured (nanocrystalline, nanocomposite, multilayer) coatings (Fig. 3.1) exhibit outstanding physical, mechanical, and chemical properties, opening a range of new applications in high technologies (see, e.g., Refs. 1–5). These outstanding properties are due to the interface and nanoscale effects associated with structural peculiarities of nanostructured coatings where the volume fraction of the interfacial phase is extremely high, and crystallite size d does not exceed 100 nm. In general, the interface effect comes into play because a large fraction of atoms of a nanostructured coating are located at interfaces (grain and interphase boundaries), where their behavior is different from that in the bulk. The nanoscale effect occurs because many fundamental processes in solids are associated with length scales of around a few nanometers.

Of special importance from both fundamental and applied viewpoints are the unique mechanical properties of nanostructured coatings (e.g., Refs. 5–16). These properties are strongly influenced by the interface and nanoscale effects and are essentially different from those of conventional coatings with the coarse-grained polycrystalline and/or microscale composite structure. In particular, nanostructured coatings exhibit the superhardness and enhanced tribological characteristics[6–10,12] highly desirable for applications. The superhardness and high wear resistance of nanostructured coatings in many respects are related to the role of interfaces as effective obstacles for lattice dislocation slip, the dominant deformation mechanism in conventional coarse-grained polycrystalline and microscale composite coatings. Also, the image forces acting in nanometer-sized crystallites of nanostructured coatings cause the difficulty in forming lattice dislocations in such nanocrystallites.[17,18] With these interface and nanoscale effects, the conventional

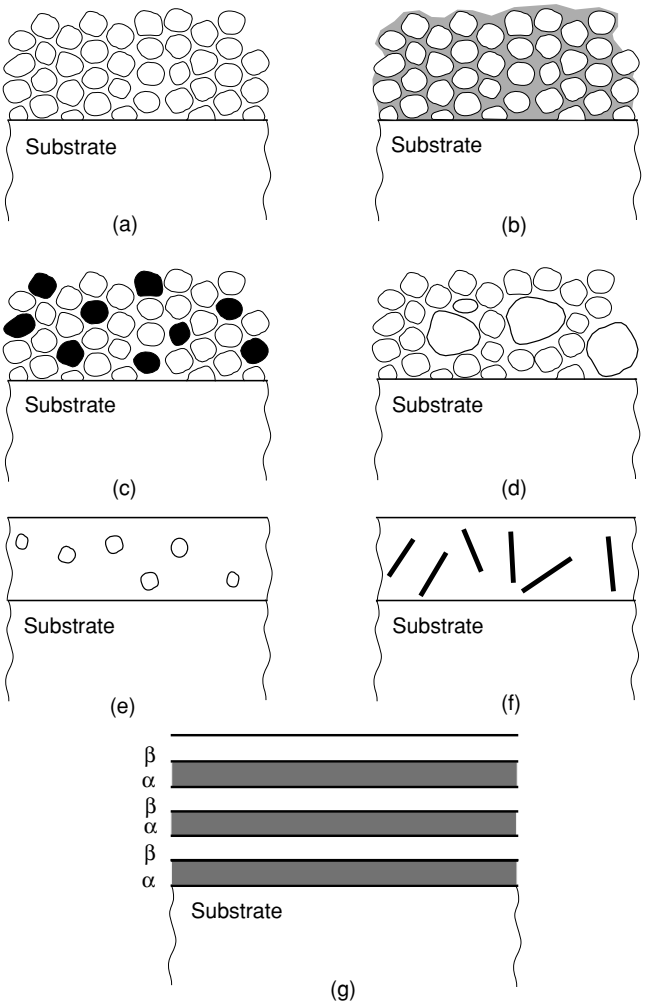

FIGURE 3.1. Typical nanostructured coatings: (a) Nano–nano single-phase coating consists of tentatively equiaxed nanograins of the same phase. (b) Nano–nanolayer composite coating consists of tentatively equiaxed nanograins of one phase, divided by intergranular nanolayers of the second phase. (c) Nano–nano composite coating consists of tentatively equiaxed nanograins of two (or more) phases. (d) Nano–micro coating consists of micrometer-size grains embedded into a nanocrystalline matrix. (e, f) Micro–nano composite coatings consist of either (e) nanoparticles or (f) nanofibers (nanotubes) of the second phase embedded into a single-crystalline matrix with micrometer size thickness. (g) Nanoscale multilayer coating consists of nanoscale layers of two (or more) phases.

lattice dislocation slip is hampered in nanostructured coatings. At the same time, interfaces in nanostructured coatings provide the effective action of deformation mechanisms being different from the conventional lattice dislocation slip. As a corollary, the crystallite refinement leads to the competition between the lattice dislocation slip and deformation mechanisms associated with the active role of interfaces.

The competition between different deformation mechanisms is viewed to be responsible for the unique mechanical properties of nanocrystalline solids.[19–32] In this context, identification of effective deformation mechanisms and their contributions to plastic flow is very important for understanding the fundamentals of the mechanical behavior of nanostructures as well as development of technologies based on use of nanocrystalline coatings. However, in many cases, the deformation mechanisms in nanocrystalline coatings cannot be unambiguously identified with the help of contemporary experimental methods, because of high-precision demands on experiments at the nanoscale. In these circumstances, theoretical modeling of plastic deformation processes represents a very important constituent of both fundamental and applied research of nanocrystalline coatings. In this chapter, we give a brief overview of theoretical models that describe deformation mechanisms and defects being carriers of plastic flow in nanocrystalline coatings (see Sections 2–7). For brevity, we will concentrate our consideration on final results of theoretical models, while their mathematical details will be omitted.

The outstanding physical, mechanical, and chemical properties of nanostructured coatings are highly sensitive to internal stresses in such coatings. The internal stresses are generated at interphase boundaries, in particular, at coating–substrate boundaries due to lattice parameter mismatch, elastic modulus mismatch, thermal coefficient of expansion mismatch, and plastic flow mismatch between the adjacent phases (e.g., Ref. 33). The relaxation of internal stress in nanostructured coatings occurs through the formation and evolution of defects, structural transformations of interfaces, and phase transitions. These structural and phase transformations strongly affect functional characteristics of nanostructured coatings and exhibit the specific peculiarities caused by the nanoscale and interface effects in such coatings. In Section 8 of this chapter, we will discuss theoretical models focused on relaxation mechanisms for internal stresses in nanostructured coatings, with the special attention being paid to the nanoscale and interface effects on stress relaxation processes.

2. DEFORMATION MECHANISMS IN NANOCRYSTALLINE COATINGS: GENERAL VIEW

Let us consider plastic deformation mechanisms in nanocrystalline coatings, that is, coatings composed of tentatively equiaxed nanograins (nanocrystallites). This widespread class of nanostructured coatings includes, in particular, single-phase nanocrystalline coatings, nano–nanolayer composite coatings, and

nano–nano composite coatings. Single-phase nanocrystalline coatings (Fig. 3.1a) are aggregates of tentatively equiaxed nanograins of the same phase. Neighboring nanograins are characterized by different orientations of the crystal lattice and divided by grain boundaries. The nanograins and grain boundaries have the same chemical composition.

In terms of classification[34] of nanocomposite structures, nano–nanolayer composite nanocrystalline coatings (Fig. 3.1b) are defined as aggregates of tentatively equiaxed nanograins of the same phase, divided by intergranular layers (grain boundaries) whose chemical composition is different from that of nanograins. Such intergranular layers (grain boundaries) are treated as layers of the second phase and often are amorphous.

In terms of classification,[34] nano–nano composite coatings (Fig. 3.1c) are aggregates of tentatively equiaxed nanograins of two or more phases. Neighboring nanograins of the same phase are divided by grain boundaries. Neighboring nanograins of different phases are divided by interphase boundaries.

Nanocrystalline coatings show very high mechanical characteristics[9–12] that are definitely related to the action of the specific deformation mechanisms in these coatings. This causes interest in understanding the specific deformation mechanisms operating due to the nanocrystalline structure. Notice that most theoretical representations on the deformation mechanisms in the nanocrystalline matter are primarily developed in efforts to explain the outstanding mechanical behavior of bulk nanocrystalline materials (see, e.g., Refs. 19–32). However, the intrinsic deformation mechanisms operating in nanocrystalline coatings and bulk nanocrystalline materials are very similar or even the same. The difference in such external factors as mechanical loading conditions, sample geometry, and the substrate effects between the bulk materials and coatings leads to the difference in their macroscopic mechanical characteristics, but hardly influences the intrinsic deformation mechanisms caused by the nanostructure in both coatings and bulk materials. In this context, the following discussion of plastic deformation mechanisms operating in nanocrystalline coatings is mostly based on theoretical models describing plastic flow and fracture in nanocrystalline bulk materials.

The specific deformation behavior of nanocrystalline bulk materials and coatings, in particular, is exhibited in the so-called abnormal Hall–Petch effect, which manifests itself as either the saturation or the decrease of the yield stress of a material with reduction in the grain size d[35,36] in the range of very small grains. Most theoretical models relate the abnormal Hall–Petch dependence to the competition between deformation mechanisms in nanocrystalline bulk materials and coatings (e.g., Refs. 19–32). In the framework of this approach, the conventional dislocation slip dominates in crystalline materials in the grain size range $d > d_c$, where the critical grain size d_c is about 10–30 nm, depending on material and structural parameters. With the well-known strengthening effect of grain boundaries,[37] the yield stress and associated mechanical characteristics of these materials grow with diminishing grain size in the range of $d > d_c$. The deformation mechanisms associated with the active role of grain boundaries dominate in nanocrystalline

bulk materials and coatings in the range of very small grains ($d < d_c$). These deformation mechanisms provide either saturation or a decrease of the yield stress (or strength) with diminishing grain size d in the range of $d < d_c$. Therefore, a possible strategy in reaching maximum strength characteristics of nanocrystalline coatings is to fabricate coatings with the mean grain size being close to d_c. However, the action of deformation mechanisms associated with the active role of grain boundaries in nanocrystalline materials is not well understood; it is the subject of controversial discussions (see, e.g., Refs. 19–32). In these circumstances, there is a potential to optimize the strength and other mechanical characteristics of nanocrystalline coating materials through an adequate theoretical description of grain-boundary-conducted deformation mechanisms and use of this knowledge in fabrication and processing of nanocrystalline coatings with the desired structure and mechanical properties. This motivates high interest in theoretical models of plastic flow mechanisms and their interaction in nanocrystalline solids.

In general, according to contemporary representations on plastic flow processes in the nanocrystalline matter,[19–32,38–41] the following deformation mechanisms operate in nanocrystalline bulk materials and coatings:

- lattice dislocation slip
- grain boundary sliding
- grain boundary diffusional creep (Coble creep)
- triple junction diffusional creep
- rotational deformation occurring via movement of grain boundary disclinations
- twin deformation conducted by partial dislocations emitted from grain boundaries.

In the next sections, we will consider in detail the deformation mechanisms, their interaction and competition, and their role in plastic flow processes in nanocrystalline bulk materials and coatings.

3. LATTICE DISLOCATION SLIP

As noted previously, the conventional dislocation slip dominates in crystalline materials in the grain size range $d > d_c$, where the critical grain size d_c is about 10–30 nm, depending on material and structural parameters. In traditional coarse-grained polycrystalline materials with grain size d being about 1 μm or more, the lattice dislocation slip occurs in the conventional way, causing the classical Hall–Petch dependence of the yield stress on grain size[37]:

$$\tau = \tau_0 + kd^{-1/2} \tag{3.1}$$

with τ_0 and k being constant parameters. The classical Hall–Petch relationship [Eq. (3.1)] in coarse-grained polycrystals is traditionally described in terms of a dislocation pileup model. These are reviewed in detail by Li and Chou.[42] In

deriving the Hall–Petch relation, the role of grain boundaries as barriers to the dislocation motion is considered in various models. In one type of the models,[43] a grain boundary acts as a barrier to pileup the dislocations, causing stresses to concentrate and activating dislocation sources in the neighboring grains, thus initiating the slip from grain to grain. In the other type of the models,[44,45] the grain boundaries are regarded as dislocation barriers limiting the mean free path of the dislocations, thereby increasing strain hardening, resulting in a Hall–Petch-type relation. A review of the various competing theories of strengthening by grain refinement has been discussed by several workers. For a more recent survey, see Ref. 37.

With grain refinement, the lattice dislocation slip shows some specific features owing to the interface and nanoscale effects. In particular, following the dislocation model of Pande and Masumura,[46] the classical Hall–Petch dislocation pileup model is still dominant in nanocrystalline solids with the sole exception that the analysis must take into account the fact that in the nanometer-size grains, the number of dislocations within a grain cannot be very large. Further, at still smaller grain sizes, this mechanism should cease when there are only two dislocations in the pileup. In the framework of the dislocation model,[46] the dependence of the yield stress τ on d deviates from the classical Hall–Petch relationship; τ saturates in the range of small grain sizes d being of the order of 10 nm. This model recovers the classical Hall–Petch relation at large grain sizes but for smaller grain sizes the τ levels off. This model therefore cannot explain a drop in τ.

Nazarov *et al.*,[47] Nazarov,[48] and Lian *et al.*[49] have developed the models similar to that of Pande and Masumura,[46] focusing on the influence of the grain size d on the parameters of lattice dislocation pileups in grain interiors. Malygin[50] has suggested a theory based on a lattice dislocation mechanism, with the effects of grain boundaries taken into account. The dislocation density $\rho(d)$ at any grain size d is related in the usual fashion to the square of yield stress, and an expression is obtained that connects ρ to the grain size. The expression is based on the assumption that grain boundaries act predominantly as sinks for dislocations (just the opposite to that used by Li,[51] who postulated that grain boundaries could be sources for dislocation generation). In Malygin's model, as the grains become finer and finer, more and more dislocations are absorbed by the grain boundaries, leading ultimately to a drop in dislocation density and hence in the flow stress, since the two are directly related as mentioned above. The model is attractive, and should be considered further. At present, we merely point out two problems with the model. First, it is doubtful if the dislocations play the same role whether the grains are large or small. It is more likely that dislocations in ultrafine grains, if present at all, are confined to grain boundaries.[52] Second, in Malygin's model,[50] the stress calculated is a work-hardened flow stress rather than a yield stress.

Lu and Sui[53] assume that both the energy and free volume of grain boundaries decrease with a reduction of the grain size d. This gives rise to an enhancement of lattice dislocation penetration through the grain boundaries and the corresponding softening of nanocrystalline materials. Following Scattergood and Koch,[54] the

yield stress of fine-grained materials is controlled by the intersection of mobile lattice dislocations with the dislocation networks at grain boundaries. In this context, with the dislocation line tension assumed to be size dependent, there is a critical grain size that corresponds to a transition from cutting to Orowan bypassing of the dislocation network. This critical grain size characterizes the experimentally detected transition from the conventional to inverse Hall–Petch relationship, with reduction in the grain size d.

Despite of the good correspondences between theoretically predicted $\tau(d)$ dependences and experimental data, all the above models based on the representations on the lattice dislocation mechanism of plastic flow in nanocrystalline materials meet the question if the lattice dislocations exist and play the same role in nanograin interiors as with conventional coarse grains. As pointed out in papers,[17,18,55] the existence of lattice dislocations in either free nanoparticles or nanograins composing nanocrystalline aggregate is energetically unfavorable, if their characteristic size, nanoparticle diameter, or grain size is lower than some critical size which depends on such material characteristics as the shear modulus and the resistance to dislocation motion. The dislocation instability in nanovolumes is related to the effect of the so-called image forces occurring due to the elastic interaction between dislocations and either free surface of nanoparticle or grain boundaries adjacent to a nanograin.[17,18,55] The paucity of mobile dislocations in nanograins has been welldocumented in electron microscopy experiments.[55,56] The above question arises in the namely case of $d < d_c = 30$ nm, where the abnormal Hall–Petch relationship comes into play. However, the models based on the lattice dislocation slip are effective in explaining the deformation behavior of nanocrystalline materials with grain size $d > d_c = 30$ nm.

Recently, Cheng *et al.*[32] have suggested a very interesting classification of polycrystalline and nanocrystalline materials, based on the specific features of the lattice dislocation slip and the role of grain boundaries in the lattice dislocation generation. Materials are divided into four categories as shown below[32]:

1. Traditional materials with grain size d being larger than tentatively 1 μm. In these materials, the lattice dislocation slip is dominant with carriers—perfect lattice dislocations—being generated by mostly dislocation sources (like Frank–Read sources) located in grain interiors.
2. Fine-grained materials with grain size d being in the range from tentatively 30 nm to 1 μm. In these materials, the lattice dislocation slip is dominant with carriers—perfect lattice dislocations—being generated by mostly dislocation sources located at grain boundaries.
3. Nano II materials with grain size d being in the range from tentatively 10 to 30 nm. In these materials, the basic carriers of plastic flow are partial lattice dislocations generated by mostly dislocation sources located at grain boundaries. Since these mobile lattice dislocations are partial, their movement is accompanied by the formation of stacking faults and deformation twins.

4. Nano I materials with grain size d being lower than tentatively 10 nm. In these materials, grain boundary sliding and other deformation mechanisms conducted by grain boundaries are dominant.

Cheng *et al.*[32] emphasized that grain size ranges used in their classification scheme are very approximate; they can be very different in various materials. In the context of this chapter, it should be noted that the classification[32] indirectly takes into account different forms of the interaction between the lattice dislocation slip and grain-boundary-conducted deformation modes. In this interpretation, grain-boundary-conducted deformation modes provide the generation of either perfect (unit) or partial dislocations from grain boundaries in fine-grained and nano II solids. The classification[32] is relevant to both nanocrystalline bulk materials and coatings.

It is important to note that the most intriguing mechanical behavior is exhibited by nano I coatings, that is, nanocrystalline coatings with very small grains. In these coating materials, plastic flow occurs mostly through grain-boundary-conducted deformation mechanisms, in particular, grain boundary sliding, which will be discussed in the next section.

4. GRAIN BOUNDARY SLIDING

Grain boundary sliding is well known as the dominant deformation mechanism in conventional microcrystalline materials exhibiting superplasticity (see, e.g., Refs. 57 and 58). Carriers of grain boundary sliding are treated to be grain boundary dislocations with small Burgers vectors being tentatively parallel with grain boundary planes.[59] (These small vectors are those of the displacement-shift-complete lattices characterizing grain boundary translational symmetries.)[59] In the theory of superplasticity of conventional microcrystalline materials, characteristics of superplastic flow are caused by mechanisms that accommodate grain boundary sliding (see, e.g., Refs. 57 and 58). The same is true in the situation with nanocrystalline materials deformed through grain boundary sliding, in which case, however, the interface and nanoscale effects modify the action of grain boundary sliding and its accommodating mechanisms.

Hahn with coworkers[60,61] have suggested a model describing the grain boundary migration as the accommodation mechanism whose combined action with grain boundary sliding gives rise to plastic flow localization in nanostructured bulk materials and coatings. The model[60,61] suggests that grain boundary migration occurs during plastic deformation and results in the formation of a zone where all grain boundary planes are tentatively parallel to each other (Fig. 3.2a,b). The grain boundary sliding is enhanced in this zone which, therefore, develops into a shear band where plastic flow is localized. At the same time, however, the model[60,61] does not identify a mechanism for the specific grain boundary migration which makes grain boundary planes to be parallel to each other.

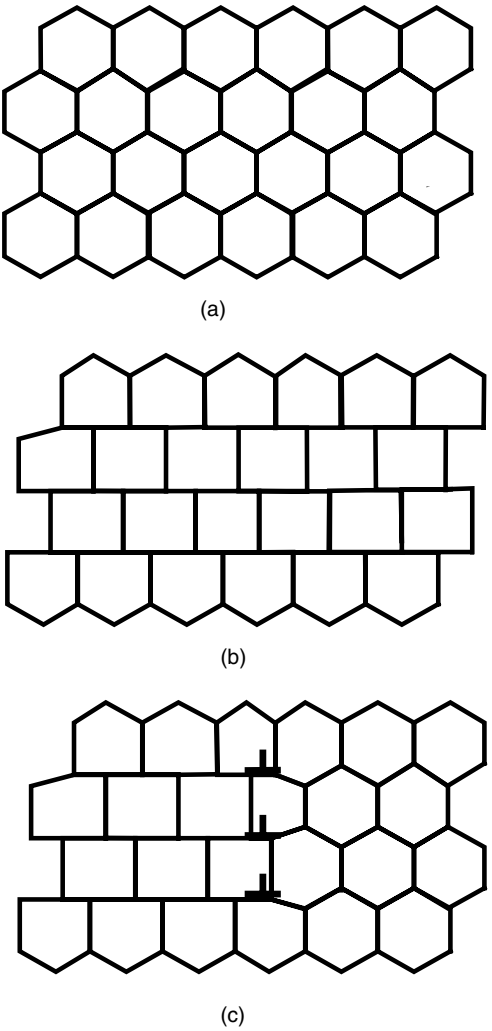

FIGURE 3.2. Plastic flow localization. (a) Nondeformed state of a nanocrystalline specimen modeled as a regular two-dimensional array of hexagons (nanograins). (b) Local migration of grain boundaries gives rise to the formation of a local zone where grain boundaries are parallel each other and intensive plastic shear through grain boundary sliding occurs. (c) The formation of a local zone where grain boundaries are parallel to each other results from movement of partial cellular dislocations.

Representations of the model[60,61] have been recently extended in two ways. First, the formation of a zone where all grain boundary planes are tentatively parallel to each other has been recently described as resulting from movement of partial cellular dislocations (Fig. 3.2c), defects in arrays of nanograins (cells) of a deformed nanocrystalline sample.[62] It is a large-scale description of plastic flow localization at the grain ensemble level.

Second, a theoretical model[63,64] has been suggested which focuses on nanoscale peculiarities of grain boundary sliding and transformations of defect structures near triple junctions of grain boundaries. With results of the nanoscale analysis, the model[63,64] also describes the experimentally detected[65–72] strengthening and softening phenomena in nanocrystalline materials under high-strain-rate superplastic deformation. In the framework of this model, superplastic deformation, occurring mostly by grain boundary sliding in nanocrystalline materials, is characterized by both strengthening due to transformations of gliding grain boundary dislocations at triple junctions and softening due to local migration of triple junctions and adjacent grain boundaries (Fig. 3.3a–g). A theoretical analysis[64] of the energy characteristics of the transformations indicates that the transformations of grain boundary dislocations at triple junctions are energetically favorable in certain ranges of parameters of the defect configuration. The corresponding flow stress is highly sensitive to both the level of plastic strain and the triple junction geometry. Sessile dislocations at triple junctions elastically interact with gliding grain boundary dislocations. This interaction hampers grain boundary sliding.[64] Thus, the storage of sessile grain boundary dislocations at triple junctions (Fig. 3.3) causes a strengthening effect that dominates at the first long stage of superplastic deformation. At the same time, the movement of grain boundary dislocations across triple junctions can be accompanied with either grain boundary migration (Fig. 3.3a–g)[64] or the formation of a triple junction nanocrack (Fig. 3.3h,i),[73] depending on parameters of the defect system. Let us consider the former way of defect structure evolution, that is, the action of grain boundary migration as the accommodation mechanism for grain boundary sliding (Fig. 3.3a–g). As a result of numerous acts of movement of grain boundary dislocations across triple junctions and the accompanying grain boundary migration, the grain boundary planes temporarily become parallel to each other at the shear surface (Fig. 3.3a–g). In these circumstances, triple junctions stop being geometric obstacles for the movement of new grain boundary dislocations, which, therefore, is enhanced along the shear surface (Fig. 3.3h). This scenario quantitatively explains the softening effect experimentally observed[65–72] at the second stage of superplastic deformation in nanocrystalline materials. The discussed representations[64] on the softening mechanism related to local migration of grain boundaries are supported by experimental observation[74–80] of plastic flow localization in nanocrystalline bulk materials and coatings. Following electron microscopy experiments,[79,80] shear bands where superplastic flow is localized in nanocrystalline materials contain brick-like grains with grain boundaries being parallel and perpendicular to the shear direction. It

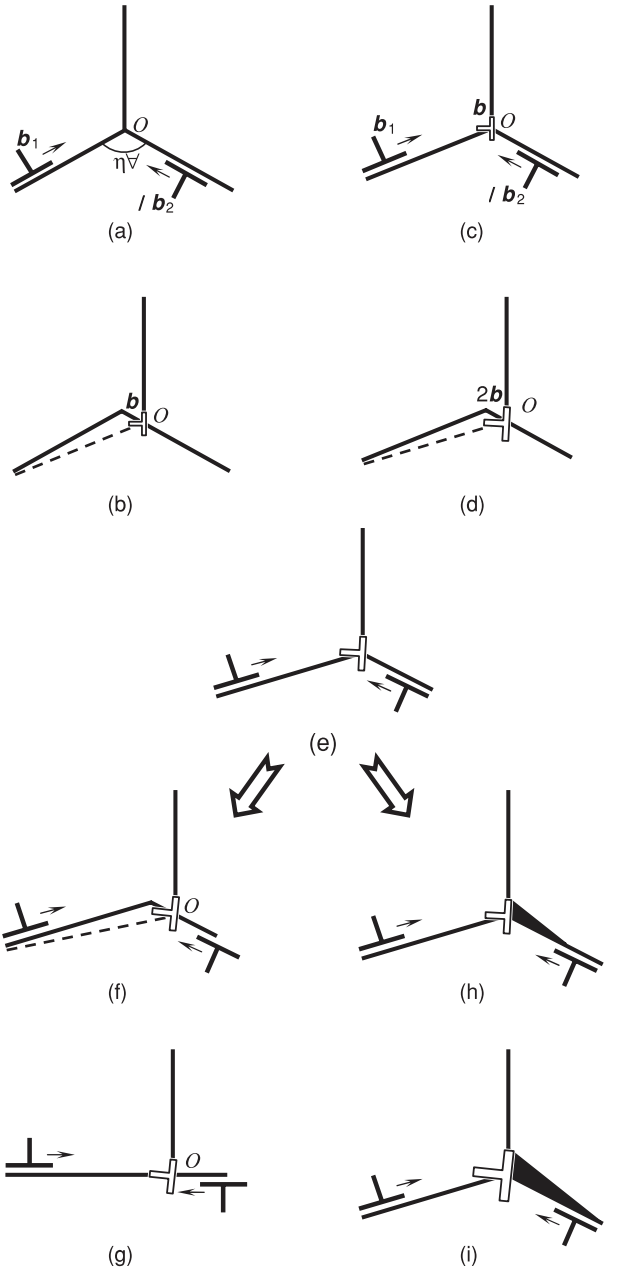
b1
O
η∀
/ b2
(a)
b1
b
O
/ b2
(c)
b
O
(b)
2b
O
(d)
(e)
O
(f)
(h)
O
(g)
(i)

is effectively and naturally interpreted as a result of the grain boundary migration (Fig. 3.3a–g) accompanying grain boundary sliding across triple junctions.

Thus, in nanocrystalline solids deformed through grain boundary sliding, there are both the strengthening and the softening effects occurring due to transformations of grain boundary dislocations at triple junctions and the accompanying local migration of grain boundaries, respectively. The competition between the strengthening and the softening effects is capable of crucially influencing the deformation behavior of nanocrystalline bulk materials and coatings. In particular, superplastic deformation regime is realized if the strengthening dominates over the softening during the first extensive stage of deformation. This strengthening is responsible for an increase of the flow stress that drives the movement of grain boundary dislocations and prevents plastic flow localization. With rising plastic strain, local grain boundary migration (Fig. 3.3a–h) makes grain boundary planes to be tentatively parallel to each other in some local regions of a loaded sample. As a result, local softening becomes substantial, which causes gradual macroscopic softening of nanocrystalline coating material. At some level of plastic strain, the softening becomes dominant over the strengthening. At this point, the movement of new grain boundary dislocations is dramatically enhanced along the shear surfaces where grain boundary planes temporarily become parallel to each other due to the movement of previous grain boundary dislocations across their junctions. As a corollary, the softening effect leads to plastic flow localization often followed by failure.

5. ROTATIONAL DEFORMATION MECHANISMS

Now let us turn to a discussion of a rotational deformation mechanism in nanocrystalline coatings, that is, plastic deformation accompanied by crystal lattice rotation.

←

FIGURE 3.3. Grain boundary sliding and transformations of defect structures near a triple junction of grain boundaries. (a) Initial state of defect configuration in a deformed nanocrystalline coating. Two gliding grain boundary dislocations with Burgers vectors $\mathbf{b_1}$ and $\mathbf{b_2}$ move towards the triple junction O. (b) Sessile dislocation (open dislocation sign) with the Burgers vector $\mathbf{b}$ is formed. Triple junction is displaced by the vector $\mathbf{b_2}$ from its initial position shown in Fig. 3.3a. (c) Generation of two new gliding grain boundary dislocations that move towards the triple junction. (d) Convergence of two gliding dislocations results in increase of Burgers vector magnitude of sessile dislocation. Also, the triple junction is transferred by the vector $2\mathbf{b_2}$ from its initial position shown in Fig. 3.3a. (e) Generation of two new gliding grain boundary dislocations that move towards the triple junction. (f, g) Numerous acts of transfer of grain boundary dislocations across a triple junction and accompanying local migration of grain boundaries make grain boundary planes (adjacent to the triple junction) to be temporarily parallel to each other. This process enhances grain boundary sliding across the triple junction. An alternative way of defect structure evolution involves (h) generation and (i) growth of a triple junction nanocrack in the stress field of the sessile dislocation.

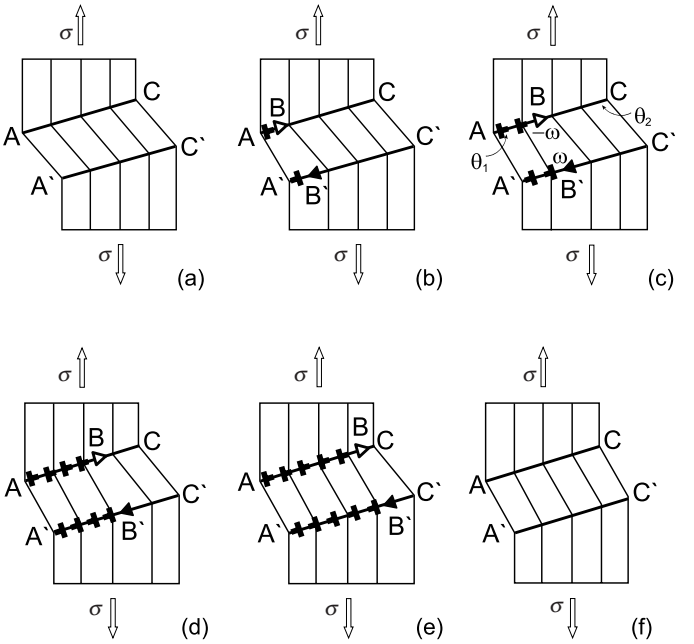

FIGURE 3.4. (a)–(f) Rotational deformation occurs through movement of a dipole of grain boundary disclinations (schematically). A grain boundary disclination line is treated as that terminating a wall of grain boundary dislocations. Grain boundary fragments separated by disclination of strength ω are characterized by misorientation parameters θ_2 and θ_1, where $\omega = \theta_2 - \theta_1$; see Fig. 3.4c.

Electron microscopy experiments are indicative of the essential role of the rotational plastic flow in deformed nanocrystalline bulk materials[72,81] and films,[76] as with conventional coarse-grained materials under high-strain deformation (for a review, see Refs. 82 and 83). This causes high interest to a theoretical description of the rotational deformation mode in the nanocrystalline matter.

The primary carriers of the rotational plastic deformation in solids are believed to be dipoles of grain boundary disclinations (Fig. 3.4).[82,83] A grain boundary disclination represents a line defect that separates two grain boundary fragments with different misorientation parameters (for illustration, see Fig. 3.4c). That is, grain boundary misorientation exhibits a jump at disclination line. A wedge disclination line is also treated as that terminating a finite wall of grain boundary dislocations (Fig. 3.4).[83,84] For instance, dislocations at grain boundary fragment AB (A′B′, respectively) shown in Fig.3.4c provide the difference in the tilt misorientation between the dislocated grain boundary fragment AB (A′B′, respectively) and nondislocated fragment BC (B′C′, respectively). A disclination dipole consists of two grain boundary disclinations having disclination strength values of opposite signs (Fig. 3.4). Movement of a disclination dipole causes plastic deformation

accompanied by crystal lattice rotation (Fig. 3.4). It is called as the rotational deformation mode.

The rotational deformation is capable of being very intensive in nanocrystalline coatings.[25–27,84,85] Actually, the volume fraction of grain boundaries is extremely high in nanocrystalline coatings, in which case grain boundary disclinations can be formed, roughly speaking, in every point of a mechanically treated coating material. In addition, the elastic energy of a disclination dipole rapidly diverges on increasing the distance between disclinations.[82] Therefore, such dipoles are energetically permitted mostly for grain boundary disclinations that are close to each other. It is the, namely, case of nanocrystalline coatings where the interspacings between neighboring grain boundaries are extremely small. Finally, nanocrystalline coatings contain high-density ensembles of triple junctions where the crossover from the conventional grain boundary sliding to the rotational deformation effectively occurs. Below, we will discuss this phenomenon serving as a remarkable illustration of the interaction between different deformation mechanisms operating in the nanocrystalline matter.

The grain boundary sliding treated as the dominant mode of superplasticity in nanocrystalline materials occurs via motion of gliding grain boundary dislocations. They have Burgers vectors that are parallel with corresponding grain boundary planes along which these dislocations glide. Triple junctions of grain boundaries, where grain boundary planes change their orientations, serve as obstacles for the grain boundary dislocation motion. In these circumstances, splitting of gliding grain boundary dislocations can occur at triple junctions, resulting in the formation of sessile dislocations and gliding dislocations providing the further grain boundary sliding along the adjacent grain boundaries (Fig. 3.3).[63,64,86] However, in general, grain boundary dislocations stopped at a triple junction are also capable of being split into climbing grain boundary dislocations (Fig. 3.5). When this process repeatedly occurs at a triple junction, it results in the formation of two walls of dislocations climbing along the grain boundaries adjacent to the triple junction[25,27] (Fig. 3.5). The finite walls of climbing dislocations are terminated by two disclinations that form a dipole and cause the rotational deformation (Fig. 3.5).

Thus, the crossover occurs through the splitting of a pileup of gliding grain boundary dislocations into climbing dislocation walls that provide crystal lattice rotation in a nanograin as a whole. In doing so, the crossover is sensitive to geometric parameters of the defect structure. As shown in Ref. 27 the crossover from the grain boundary sliding to the rotational mode of plastic flow in nanocrystalline materials effectively occurs at triple junctions with low values of the triple junction angle ϕ (see Fig. 3.5). It is contrasted to the previously considered situation in Section 3 with grain boundary sliding which effectively occurs (changing its direction) at triple junctions with large values of the triple junction angle (ϕ) (Fig. 3.3). In these circumstances, grain boundary sliding and rotational mode act as alternative deformation mechanisms at triple junctions with different geometric parameters (ϕ). The experimentally detected[72,76,81] grain rotations

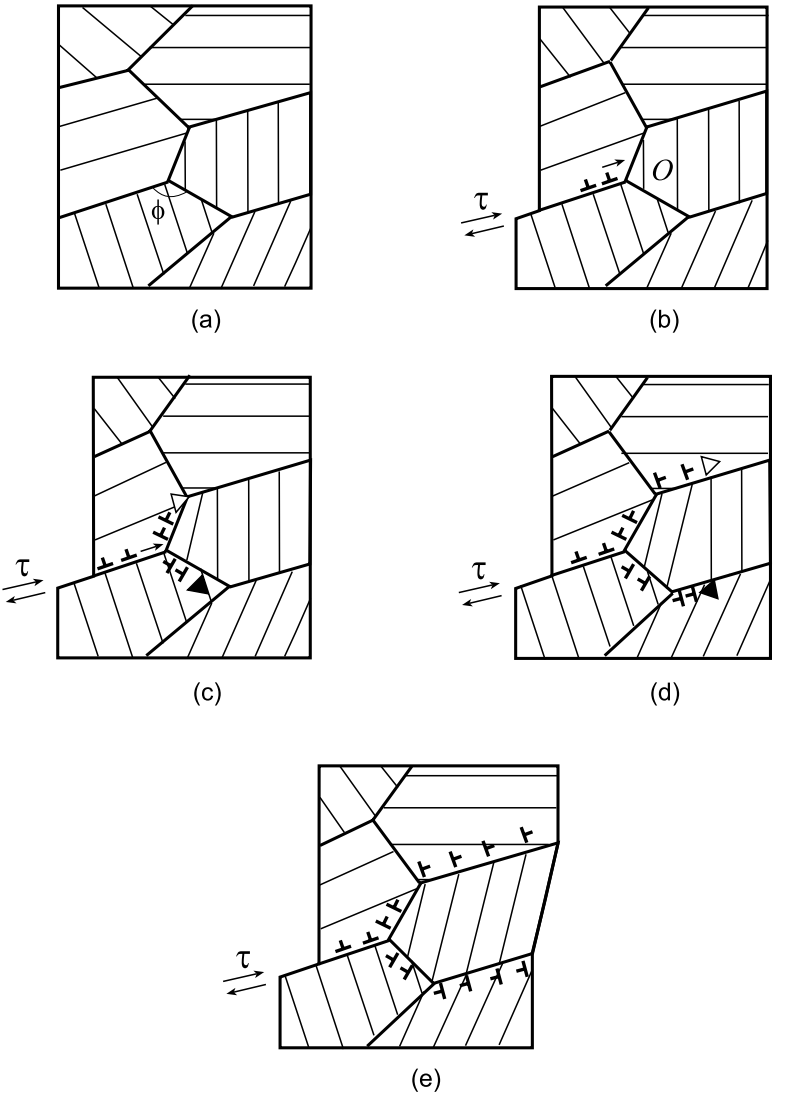

FIGURE 3.5. Crossover from grain boundary sliding to rotational deformation mode. (a) Nanocrystalline specimen in a nondeformed state. (b) Grain boundary sliding occurs via motion of gliding grain boundary dislocations under shear stress action. (c) Gliding dislocations split at triple junction O of grain boundaries into climbing dislocations. (d, e) The splitting of gliding grain boundary dislocations repeatedly occurs causing the formation of walls of grain boundary dislocations. The climb of grain boundary dislocation walls is equivalent to movement of disclination dipole and causes plastic deformation accompanied by crystal lattice rotation in a grain.

in superplastically deformed nano- and microcrystalline materials where grain boundary sliding is the dominant deformation mechanism support the theoretical model.[27]

6. GRAIN BOUNDARY DIFFUSIONAL CREEP (COBLE CREEP) AND TRIPLE JUNCTION DIFFUSIONAL CREEP

Besides grain boundary sliding and rotational deformation mechanism, grain boundary diffusional creep (Coble creep) and triple junction diffusional creep are capable of essentially contributing to plastic flow in nanocrystalline coating materials with very small grains. The role of these deformation mechanisms increases on increasing the volume fractions of the grain boundary and triple junction phases. Of particular importance are the diffusional creep modes in those nanocrystalline solids with very small grains in which grain boundary sliding is suppressed. For instance, it is the case of superhard nano–nanolayer composite coatings (Fig. 3.2b) where intergranular boundaries are often amorphous[9,10,12] and thereby do not conduct the conventional grain boundary sliding. Also, nanocrystalline solids after thermal treatment do not contain mobile grain boundary dislocations that carry grain boundary sliding. In these circumstances, Coble creep and triple junction diffusional creep (whose carriers are point defects, mostly vacancies) are treated to effectively operate in mechanically loaded nanocrystalline bulk materials and coatings.[25]

Coble creep is well described in the classical theory of creep of conventional microcrystalline materials, where this plastic flow mechanism plays an important role (see, e.g., Ref. 71). In contrast, representations on the triple junction diffusional creep are not well known. However, in recent years, triple junctions of grain boundaries have been recognized as defects with the structure and properties being essentially different from those of grain boundaries that they adjoin.[87] For instance, from experimental data and theoretical models it follows that triple junctions play the role of enhanced diffusion tubes,[88,89] nuclei of the enhanced segregation of the second phase,[90] strengthening elements and sources of lattice dislocations[91,92] during plastic deformation, and drag centers of grain boundary migration during recrystallization processes.[93] Also, as it has been shown in experiments,[88] creep associated with enhanced diffusion along triple junctions contributes to plastic flow of coarse-grained polycrystalline aluminum. Actually, since triple junction diffusion coefficient D_{tj} highly exceeds grain boundary diffusion coefficient D_{gb},[88,89] enhanced diffusional mass transfer along triple junction tubes occurs under mechanical stresses and contributes to plastic forming of a mechanically loaded material.

To characterize contributions of bulk diffusional creep, grain boundary diffusional creep, and triple junction diffusional creep to plastic deformation of a nanocrystalline coating, of crucial importance are dependences of plastic strain

rate on grain size d, inherent to these deformation modes. Grain size exponent is -4 in the case of the triple junction diffusional creep,[88] in contrast to grain boundary diffusional creep (Coble creep) and bulk diffusional creep characterized by grain size exponents of -3 and -2, respectively:

$$\dot{\varepsilon}_{\mathrm{tj}} \propto D_{\mathrm{tj}} d^{-4} \tag{3.2}$$

$$\dot{\varepsilon}_{\mathrm{gb}} \propto D_{\mathrm{gb}} d^{-3} \tag{3.3}$$

$$\dot{\varepsilon}_{\mathrm{bulk}} \propto D_{\mathrm{bulk}} d^{-2} \tag{3.4}$$

Here $\dot{\varepsilon}_{\mathrm{tj}}$, $\dot{\varepsilon}_{\mathrm{gb}}$, and $\dot{\varepsilon}_{\mathrm{bulk}}$, are plastic strain rates that correspond to triple junction diffusional creep, grain boundary diffusional creep, and bulk diffusional creep, respectively. D_{bulk} denotes the bulk self-diffusion coefficient. In these circumstances, grain refinement enhances plastic flow occurring via Coble creep and especially triple junction difusional creep.

To describe the dependence of the yield stress on grain size d in a wide range (including the anomalous Hall–Petch relationship at small grain sizes),[35,36] Masumura *et al.*[19] suggested a model based on the idea of competition between lattice dislocation slip, grain boundary diffusional creep (Coble creep), and bulk diffusional creep. They assumed that polycrystals with a relatively large average grain size obey the classical Hall–Petch relation [Eq. (3.1)]. At the other extreme, for very small grain sizes, it is assumed that Coble creep operates. Also, it is assumed that a grain size d^* exists at which value the classical Hall–Petch mechanism switches to the Coble creep mechanism. The model by Masumura *et al.*[19] effectively explains the deformation behavior of materials with the mean grain size in the 5–200-nm range, including the transition regime between the Hall–Petch and Coble-creep-like behavior. The transition regime is effectively described with a distribution of grain size taken into account. Thus, Masumura *et al.*[19]provided a unified model and developed an analytical expression for the yield stress τ as a function of the inverse square root of d in a simple and approximate manner that could be compared with experimental data over a wide range of grain sizes. This model has been extended by several authors[22,94] to involve grain boundary sliding into consideration. In addition, recent results[95] of computer modeling are in agreement with the idea of Coble creep as the effective deformation mechanism operating in nanocrystalline bulk materials and coatings with very small grains.

Recently, Fedorov *et al.*[23] have suggested a theoretical model describing the yield stress dependence on grain size in fine-grained materials, based upon competition between conventional dislocation slip, grain boundary diffusional creep, and triple junction diffusional creep. It has been shown that the contribution of triple junction diffusional creep increases with reduction of grain size, causing a negative slope of the Hall–Petch dependence in the range of very small grains. The results of the model[23] are compared with experimental data[96–99] from copper and shown to be in rather good agreement.

7. INTERACTION BETWEEN DEFORMATION MODES IN NANOCRYSTALLINE COATING MATERIALS: EMISSION OF DISLOCATIONS FROM GRAIN BOUNDARIES

Nanocrystalline coating materials (Fig. 3.1a–c) are aggregates of nano-sized grains in which different deformation mechanisms can strongly influence each other. That is, there is a kind of effective interaction between deformation modes in the nanocrystalline matter. In this context, the theory of plastic deformation processes should involve into consideration the combined action of interacting deformation modes that enhance each other. Interaction between deformation modes strongly depends on characteristics of grain boundary structures, grain size distribution, triple junction geometry, and grain boundary defects. These parameters, in their turn, are sensitive to fabrication of nanocrystalline coatings. Therefore, the theoretical approach focused on the interaction between different deformation mechanisms is potentially capable of effectively explaining "fabrication–structure–properties" relationships that are responsible for the macroscopic deformation behavior of nanocrystalline coating materials.

An example of interacting deformation modes is the grain boundary sliding enhanced due to lattice dislocation slip. Lattice dislocation moving in grain interiors come to grain boundaries where they split into grain boundary dislocations that carry intense grain boundary sliding.[100] This kind of interaction between deformation modes is well known in the theory of superplasticity of conventional microcrystalline materials and definitely plays a significant role in nanocrystalline materials with grain size $d > 30$ nm, in which lattice dislocation slip is intense. Another case of interacting deformation modes is the crossover from grain boundary sliding to the rotational deformation in nanocrystalline materials (see Section 3 and Ref. 27).

In nanocrystalline materials characterized by a high-volume fraction of the grain boundary phase, grain boundaries also intensively emit lattice dislocations, but not only absorb. This phenomenon has been observed in direct experiments[71,72,101] and indirectly confirmed by experimental data[38–41] indicating twin deformation conducted by partial lattice dislocations in nanograins.

The theoretical model[86] describes emission of perfect and partial lattice dislocations as a process induced by the preceding grain boundary sliding. It is a manifestation of interaction between grain boundary sliding and lattice dislocation slip, which is realized as follows: A pileup of grain boundary dislocations is generated under the action of mechanical load in a grain boundary in a plastically deformed nanocrystalline sample. Mechanical-load-induced motion of the grain boundary dislocation pileup is stopped by a triple junction of grain boundaries. There are several ways of evolution of the grain boundary dislocation pileup, including emission of either perfect (Fig. 3.6a) or partial (Fig. 3.6b) dislocations from the triple junction.[86] In the second case, stacking faults are formed behind the moving partial dislocations (Fig. 3.6b).

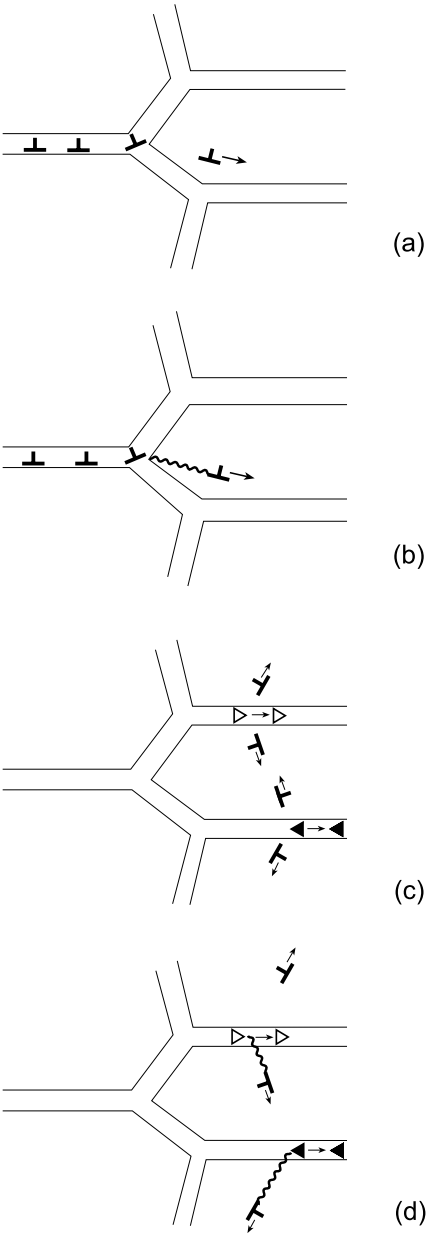

FIGURE 3.6. Emission of lattice dislocations from grain boundaries in deformed nanocrystalline coating materials. (a) Perfect lattice dislocation is emitted from a triple junction of grain boundaries. (b) Partial lattice dislocation is emitted from a triple junction of grain boundaries. Stacking fault (wavy line) is formed behind the moving partial dislocation. (c) Movement of a dipole of grain boundary disclinations is accompanied by emission of perfect lattice dislocations into grain interiors. (d) Movement of a dipole of grain boundary disclinations is accompanied by emission of partial lattice dislocations into grain interiors. Stacking faults (wavy lines) are formed behind the moving partial dislocations.

Emission of lattice dislocations by grain boundaries effectively occurs also as a process accompanying rotational deformation in nanocrystalline materials. Rotational deformation mode—plastic deformation accompanied by crystal lattice rotations—occurs through movement of grain boundary disclination dipoles and is capable of effectively contributing to plastic flow in nanocrystalline materials (see Section 5 and Refs. 25–27, 84, and 85). It is confirmed by experimental observations of disclination dipoles and grain rotations in mechanically loaded bulk nanocrystalline materials and films.[72,76,81] Movement of grain boundary disclinations in plastically deformed solids is commonly treated as being associated with absorption of lattice dislocations (that are generated and move in grains under the action of mechanical load) by grain boundaries.[102] This micromechanism, according to Ref. 102, is responsible for experimentally observed grain rotations in polycrystalline materials during (super)plastic deformation. Recently, a theoretical model[25,84,103] has been suggested to describe the rotational deformation in nanocrystalline solids as the processes occurring mostly via the motion of grain boundary disclinations and their dipoles, associated with the emission of lattice dislocations from grain boundaries into the adjacent grain interiors (Fig. 3.6c,d). It is an example of interacting deformation modes in which the rotational deformation and lattice dislocation slip support each other.

Grain-boundary-conducted plastic deformation creates stress inhomogeneities in vicinities of grain boundaries, which thereby serve as preferable places for the generation of nanocracks. For instance, grain boundary sliding leads to the formation of sessile triple junction dislocations whose stresses relax through the generation of nanocracks near triple junctions of grain boundaries[73] (Fig. 3.3h,i). Also, grain boundary disclinations—carriers of rotational deformation—create stress fields capable of causing the generation and growth of nanocracks along grain boundaries in deformed poly- and nanocrystalline materials.[25,104] These examples illustrate interaction between plastic deformation and fracture modes in nanocrystalline coating materials.

8. DEFECTS AND PLASTIC DEFORMATION RELEASING INTERNAL STRESSES IN NANOSTRUCTURED FILMS AND COATINGS

Let us discuss the role of defects and plastic deformation in the internal stress relaxation in nanostructured films and coatings. In general, an interphase coating–substrate boundary serves as a source of internal stresses occurring due to lattice parameter mismatch, thermal expansion mismatch, elastic modulus mismatch, and plastic flow mismatch between the adjacent phases. The internal stresses strongly influence the structure and functional properties of nanostructured coatings. In particular, defect structures, phase content, and mechanical, magnetic, and diffusional properties of films and coatings are very sensitive to the internal stresses (see, e.g.,

Refs. 6–11 and 105–112). Therefore, it is very important to identify mechanisms for internal stress relaxation in nanostructured coatings.

The internal stresses in conventional single crystalline thin films and nanoscale multilayer coatings (Fig. 3.1g) relax mostly through the generation of misfit dislocations that form dislocation rows in interphase boundary planes or more complicately arranged configurations (see, e.g., experimental and theoretical works).[105–107,113–117] Generally speaking, the formation of misfit dislocation rows at interphase boundaries is either desirable or disappointing, from an applications viewpoint, depending on the roles of films, nanoscale coating layers (Fig. 3.1g), and interphase boundaries in applications. So, if the properties of a film or nanoscale coating layers are exploited, the formation of misfit dislocation rows commonly is desirable, as it results in a (partial) compensation of misfit stresses in the film. If the properties of an interphase boundary are exploited, the formation of misfit dislocation rows commonly is undesirable, since the formed misfit dislocation cores violate the preexistent ideal (coherent) structure of the interphase boundary.

The structure and the properties of nanocrystalline coatings are different from those of single crystalline thin films and nanolayers of multilayer coatings. Therefore, relaxation of misfit stresses in nanocrystalline films, in general, can occur via mechanisms that are different from the standard mechanism, the formation of rows of perfect misfit dislocations at interphase boundaries. In particular, due to the existence of high-density ensembles of grain boundaries, relaxation of internal stresses in nanocrystalline films and coatings effectively occurs via the formation of grain boundary dislocations and disclinations as misfit defects (Fig. 3.7).[118–120] These grain boundary dislocations and disclinations induce stress fields that compensate for, in part, misfit stresses and are located at grain boundaries and their triple junctions (Fig. 3.7). The formation of grain boundary dislocations and disclinations as misfit defects does not induce any extra violations of coherency of interphase boundaries and, therefore, does not lead to degradation of their functional properties used in applications.

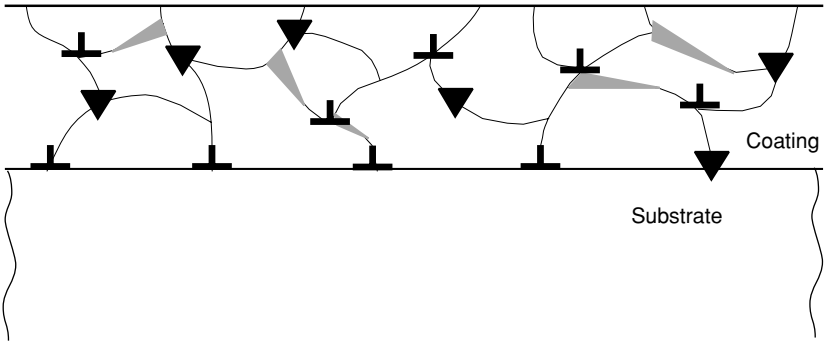

FIGURE 3.7. Relaxation of internal stresses in nanocrystalline films and coatings effectively occurs through the formation of grain boundary dislocations and disclinations. Their stress fields induce the generation of stable nanocracks.

Let us discuss briefly a scenario for the formation of grain boundary dislocations and disclinations as misfit defects. Nanocrystalline coatings are often synthesized at highly nonequilibrium conditions, in which case grain boundaries in these coatings are highly defected. Grain boundaries contain "nonequilibrium" or extrinsic grain boundary dislocations and disclinations.[100,118,119] In the absence of long-range stress fields, "nonequilibrium" dislocations and disclinations in a grain boundary, after some relaxation time interval, disappear via entering to a free surface of a solid and/or via annihilation of defects. The internal stresses generated at the coating–substrate boundary cause many "nonequilibrium" grain boundary dislocations to keep existing, even after relaxation, as misfit defects compensating for these internal stresses in nanocrystalline coatings. High-density ensembles of "nonequilibrium" grain boundary dislocations and disclinations are capable of providing a very effective relaxation of the internal stresses in nanocrystalline coatings. For instance, as it has been noted in Ref. 121, residual stresses are low in nanocrystalline cermet coatings (fabricated by thermal spray methods at highly nonequilibrium conditions), resulting in a capability for producing very thick coatings. So, nanocrystalline coatings were fabricated up to 0.65 cm thick and could probably be made with arbitrary thickness.[121] At the same time, in a conventional polycrystalline cermet coating, stress buildup limits coating thickness to typically 500–800 μm. This is naturally explained as caused by a stress relaxation mechanism (in the situation discussed, the formation of grain boundary misfit dislocations and disclinations) that comes into play in, namely, nanocrystalline films and coatings, and is different from and more effective than the standard mechanism—the formation of perfect misfit dislocations.

Grain boundary misfit dislocations and disclinations create long-range stress fields that compensate for, in part, internal stresses, in which case their formation effectively competes with failure and other relaxation processes induced by the internal stresses in nanocrystalline coatings. At the same time, these grain boundary defects create local stress inhomogeneities that can induce the formation of stable nanocracks in vicinities of grain boundary dislocations and especially disclinations.[25,73,104] In the context discussed, grain boundary defects play a double role. These defects, on the one hand, prevent failure processes induced by the internal stresses generated at interphase coating–substrate boundaries and, on the other hand, serve as preferable centers for nucleation of stable nanocracks in vicinities of the grain boundary defects.

Now let us turn to a brief discussion of relaxation mechanisms for internal stresses in nanoscale multilayer coatings (Fig. 3.1g). As noted previously, the internal stresses in nanoscale multilayer coatings relax mostly through the generation of misfit dislocations that form dislocation rows in interphase boundary planes. These misfit dislocations that create stress fields enhance the generation of nanoscale compositional inhomogeneities like nanowires[122] and influence plastic flow in nanoscale multilayer coatings.[123] At the same time, there are alternative mechanisms for effective relaxation of internal stresses in nanoscale multilayer coatings. In particular, following a theoretical analysis,[124] plastic deformation of

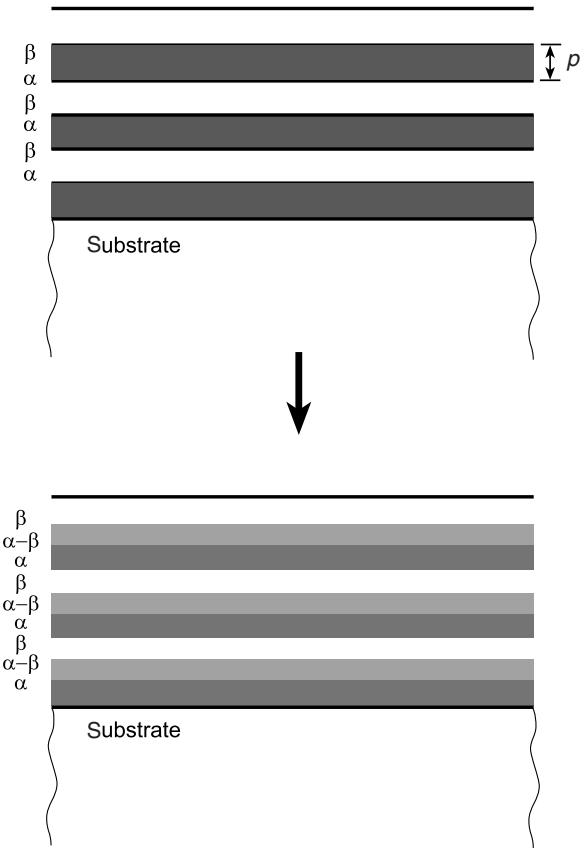

FIGURE 3.8. Solid-state amorphization in nanoscale multilayer coatings.

a substrate creates defects in the substrate, whose stresses are capable of causing relaxation of internal stresses and thereby preventing the formation of misfit dislocations in nanoscale multilayer coatings.

Another relaxation mechanism in nanoscale multilayer coatings is related to phase transformations at interphase boundaries. For instance, solid-state amorphizing transformations occur in multilayer coatings consisting of alternate layers, say, α and β.[125,126] In these circumstances, layers of the new amorphous alloyed phase α–β nucleate at α–β interfaces due to diffusional mixing of atoms α and β (Fig. 3.8). Recently, it has been experimentally revealed that the solid state amorphization does not occur in Ni–Ti multilayer coatings having the crystalline layer thickness in a composite below some critical thickness p (being several nanometers).[125] To account for these experimental data, solid-state amorphizing transformations have been theoretically described in Ref. 127 as phase transformations driven by a release of internal stresses. It has been found that there is a

minimal critical thickness p that characterizes the solid-state amorphization as an energetically favorable process in multilayer coatings. The stress-release-driven amorphization occurs, if the layer thickness is larger than p, and is forbidden, if the layer thickness is lower than p.

Finally, let us briefly discuss plastic deformation mechanisms that accommodate misfit stresses in semiconductor nanoisland films, that is, quantum dots. In general, self-assembled quantum dots exhibit unique functional properties exploited in electronic and optoelectronic devices.[128–132] Desired functional characteristics of quantum dots crucially depend on their structure and geometry. In particular, the formation of misfit dislocations releasing stresses in quantum dots leads to dramatic degradation of their functional properties.[128] In this context, knowledge of critical parameters of quantum dots, at which the formation of misfit dislocations that are energetically favorable, is of utmost importance for applications of such dots.

The standard deformation mechanism leading to a partial relaxation of misfit stresses in quantum dots is treated to be the generation of perfect misfit dislocations.[129,133–135] Recently, a new deformation mechanism in quantum dots has been suggested. It is the generation of partial and split misfit dislocations.[136,137] According to theoretical analysis,[136,137] the generation of partial misfit dislocations effectively competes with that of conventional perfect dislocations in germanium pyramid-like quantum dots on silicon substrate. In doing so, different partial dislocation structures are energetically preferred in different regions of the interface. Single partial dislocation is generated near lateral free surface of a nanoisland. Then, during its motion toward the nanoisland base center, the second partial dislocation is generated.

9. CONCLUDING REMARKS

Thus, defects and deformation mechanisms in nanostructured coating materials are characterized by the specific features associated with the interface and nanoscale effects in these coatings. In particular, owing to the interface and nanoscale effects, the set of deformation mechanisms in nanocrystalline coatings is richer than that in conventional coarse-grained polycrystalline coatings. Such grain-boundary-conducted deformation mechanisms as gain boundary sliding, rotational deformation mode, Coble creep, and triple junction diffusional creep are capable of effectively operating and causing plastic flow of nanocrystalline coatings with very small mean grain size $d < d_c = 30$ nm. The lattice dislocation slip is dominant in nanocrystalline coatings with mean grain size $d > 30$ nm. However, its action is strongly affected by grain and interphase boundaries which, on the one hand, obstruct movement of lattice dislocations and, on the other hand, emit perfect and partial lattice dislocations. Also, grain boundaries and their triple junctions contain defects whose stress fields induce the formation of nanocracks—elemental carriers of fracture processes—in nanocrystalline coatings.

Due to the existence of high-density ensembles of grain boundaries in nanocrystalline coatings, relaxation of internal stresses in these coatings effectively occurs via the formation of grain boundary dislocations and disclinations as misfit defects. Such grain boundary dislocations and disclinations induce stress fields that compensate for, in part, misfit stresses and are located at grain boundaries and their triple junctions (Fig. 3.7). The relaxation mechanism in question is capable of providing more effective release of residual stresses in nanocrystalline coatings, compared to their coarse-grained counterparts. This explains the experimentally documented capability for producing very thick nanocrystalline coatings, in contrast to conventional coarse-grained coatings where stress buildup essentially limits the coating thickness.

The specific features of defects and deformation mechanisms in nanostructured coating materials should definitely be taken into account in experimental research and theoretical description of the structure and behavior of these materials. Identification and systematic study of the specific defect structures and plastic flow mechanisms in nanostructures are important for both understanding the fundamentals of their unique mechanical and physical properties as well as development of current and novel technologies exploiting nanostructured coatings.

ACKNOWLEDGMENTS

This work was supported, in part, by the Office of US Naval Research (grants N00014-01-1-1020 and N00014-05-1-0217, INTAS (grant 03-51-3779), and Russian Science Support Foundation, Russian Academy of Sciences Program "Structural Mechanics of Materials and Construction Elements", and St. Petersburg Scientific Center. Author would like to thank S. V. Bobylev, M. Yu. Gutkin, A. L. Kolesnikova, A. B. Reizis, A. E. Romanov, A. G. Sheinerman, and N. V. Skiba for permanent collaboration, valuable contributions, fruitful discussions, and encouragements.

REFERENCES

1. H. S. Nalwa (ed.), *Handbook of Nanostructured Materials and Nanotechnology*, Vols. 1–5 (Academic Press, San Diego, CA, 1999).
2. G. M. Chow, I. A. Ovid'ko, and T. Tsakalakos (eds.), *Nanostructured Films and Coatings*, NATO Science Series (Kluwer, Dordrecht, 2000).
3. M. C. Roco, R. S. Williams, and P. Alivisatos (eds.), *Nanotechnology Research Directions* (Kluwer, Dordrecht, 2000).
4. T. Tsakalakos, I. A. Ovid'ko, and A. K. Vasudevan (eds.), *Synthesis, Functional Properties and Applications of Nanostructures*, NATO Science Series (Kluwer, Dordrecht, 2003).
5. C. C. Berndt, T. Fischer, I. A. Ovid'ko, G. Skandan, and T. Tsakalakos (eds.), *Nanomaterials for Structural Applications*, MRS Symposium Proceedings, Vol. 740 (Materials Research Society, Warrendale, PA, 2003).

6. S. A. Barnett, A. Madan, I. Kim, and K. Martin, Stability of nanometer-thick layers in hard coatings, *MRS Bull*. **28**, 169–172 (2003).
7. W. D. Munz, Large scale manufacturing of nanoscale multilayered hard coatings deposited by cathodic arc/unbalanced magnetron sputtering, *MRS Bull*. **28**, 173–179 (2003).
8. J. Patscheider, Nanocomposite hard coatings for wear protection, *MRS Bull*. **28**, 180–183 (2003).
9. S. Veprek and A. S. Argon, Toward the understanding of mechanical properties of super- and ultrahard nanocomposites, *J. Vac. Sci. Technol. B* **20**, 650–664 (2002).
10. A. Niederhofer, T. Bolom, P. Nesladek, K. Moto, Ch. Eggs, D. S. Patil, and S. Veprek, The role of percolation threshold for the control of the hardness and thermal stability of super- and ultrahard nanocomposites, *Surf. Coat. Technol*. **146–147**, 183–188 (2001).
11. I. A. Ovid'ko, C. S. Pande, R. Krishnamoorty, E. Lavernia, and G. Skandan (eds.), *Mechanical Properties of Nanostructured Materials and Nanocomposites*, MRS Symposium Proceedings, Vol. 791 (Materials Research Society, Warrendale, PA, 2004).
12. S. Veprek, Superhard and functional nanocomposites formed by self-organization in comparison with hardening of coatings by energetic ion bombardment during their deposition, *Rev. Adv. Mater. Sci*. **5**, 6 –17 (2003).
13. A. Misra, H. Kung, and J. D. Embury, Preface to the viewpoint set on: Deformation and stability of nanoscale metallic multilayers, *Scr. Mater.* **50**, 707–710 (2004).
14. F. Spaepen and D. Y. W. Yu, A comparison of the strength of multilayers, thin films and nanocrystalline compacts, *Scr. Mater.* **50**, 729–732 (2004).
15. N. Mara, A. Sergueeva, A. Misra, and A. K. Mukherjee, Structure and high-temperature mechanical behavior relationship in nano-scaled multilayered materials, *Scr. Mater.* **50**, 803–806 (2004).
16. L. H. Friedman, Towards a full analytic treatment of the Hall–Petch behavior in multilayers: Putting the pieces together, *Scr. Mater.* **50**, 763–767 (2004).
17. V. G. Gryaznov, I. A. Polonsky, A. E. Romanov, and L. I. Trusov, Size effects of dislocation stability in nanocrystals, *Phys. Rev. B* **44**, 42–46 (1991).
18. A. E. Romanov, Continuum theory of defects in nanoscaled materials, *Nanostruct. Mater*. **6**, 125–134 (1995).
19. R. A. Masumura, P. M. Hazzledine, and C. S. Pande, Yield stress of fine grained materials, *Acta Mater.* **46**, 4527–4534 (1998).
20. H. Van Swygenhoven, M. Spaczer, A. Caro, and D. Farkas, Competing plastic deformation mechanisms in nanophase metals, *Phys. Rev. B* **60**, 22–25 (1999).
21. H. Van Swygenhoven, M. Spacer, and A. Caro, Microscopic description of plasticity in computer generated metallic nanophase samples: A comparison between Cu and Ni, *Acta Mater.* **47**, 3117–3126 (1999).
22. H. S. Kim, Y. Estrin, and M. B. Bush, Plastic deformation behaviour of fine-grained materials, *Acta Mater.* **48**, 493–504 (2000).
23. A. A. Fedorov, M. Yu. Gutkin, and I. A. Ovid'ko, Triple junction diffusion and plastic flow in fine-grained materials, *Scr. Mater.* **47**, 51–55 (2002).
24. M. Y. Gutkin, I. A. Ovid'ko, and C. S. Pande, Theoretical models of plastic deformation processes in nanocrystalline materials, *Rev. Adv. Mater. Sci*. **2**, 80–102 (2001).
25. M. Y. Gutkin and I. A. Ovid'ko, *Plastic Deformation in Nanocrystalline Materials* (Springer, Berlin, Heidelberg, New York, 2004).
26. I. A. Ovid'ko, Materials science—Deformation of nanostructures, *Science* **295**, 2386 (2002).
27. M. Yu. Gutkin, I. A. Ovid'ko, and N. V. Skiba, Crossover from grain boundary sliding to rotational deformation in nanocrystalline materials, *Acta Mater.* **51**, 4059–4071 (2003).
28. I. A. Ovid'ko, Deformation and diffusion modes in nanocrystalline materials, *Int. Mater. Rev.* **50**, 65–82 (2005).
29. I. A. Ovid'ko, Superplasticity and ductility of superstrong nanomaterials, *Rev. Adv. Mater. Sci*. **10**, 89–104 (2005).

30. C. C. Koch, Optimization of strength and ductility in nanocrystallline and ultrafine-grained materials, *Scripta. Mater*. **49**, 657–662 (2003).
31. K. S. Kumar, H. Van Swygenhoven, and S. Suresh, Mechanical behavior of nanocrystalline metals and alloys, *Acta Mater.* **51**, 5743–5774 (2003).
32. S. Cheng, J. A. Spencer, and W. W. Milligan, Strength and tension/compression asymmetry in nanostructured and ultrafine-grain metals, *Acta Mater.* **51**, 4505–4518 (2003).
33. K. Sadananda and R. L. Holtz, in *Nanostructured Films and Coatings*, NATO Science Series, edited by G. M. Chow, I. A. Ovid'ko, and T. Tsakalakos (Kluwer, Dordrecht, 2000), p. 283.
34. J. D. Kunzt, G. D. Zhan, and A. K. Mukherjee, Nanocrystalline matrix ceramic composites for improved fracture toughness, *MRS Bull*. **29**, 22–27 (2004).
35. F. A. Mohamed and Y. Li, Creep and superplasticity in nanocrystallline materials: Current understanding and future prospects, *Mater. Sci. Eng. A* **298**, 1–15 (2001).
36. K. A. Padmanabhan, Mechanical properties of nanostructured materials, *Mater. Sci. Eng. A* **304**, 200–205 (2001).
37. A. Lasalmonie and J. L. Strudel, Influence of grain-size on the mechanical behavior of some high-strength materials, *J. Mater. Sci*. **21**, 1837–1852 (1986).
38. M. W. Chen, E. Ma, K. J. Hemker, H. W. Sheng, Y. M. Wang, and X. M. Cheng, Deformation twinning in nanocrystalline Al, *Science* **300**, 1275–1277 (2003).
39. X. Z. Liao, F. Zhou, E. Lavernia, S. G. Srinivasan, M. I. Baskes, D. W. He, and Y. T. Zhu, Deformation mechanisms in nanocrystalline Al: Partial dislocations slip, *Appl. Phys. Lett*. **83**, 632–634 (2003).
40. X. Z. Liao, F. Zhou, E. Lavernia, D. W. He, and Y. T. Zhu, Deformation twins in nanocrystallline Al, *Appl. Phys. Lett*. **83**, 5062–5064 (2003).
41. X. Z. Liao, F. Zhou, S. G. Srinivasan, Y. T. Zhu, R. Z. Valiev, and D. V. Gunderov, Deformation twinning in nanocrystalline copper at room temperature and low strain rate, *Appl. Phys. Lett*. **84**, 592–594 (2004).
42. J. C. M. Li and Y. T. Chou, Role of dislocations in flow stress grain size relationships, *Metall. Trans.* **1**, 1145 (1970).
43. R. W. Armstron and A. K. Head, Dislocations queueing and fracture in an elastically anisotropic material, *Acta Metall*. **13**, 759 (1965).
44. A. G. Evans and J. P. Hirth, Deformation of nanoscale cermets, *Scr. Metall*. **26**, 1675–1680 (1992).
45. C. S. Pande, R. A. Masumura, and R. W. Armstron, Pile-up based Hall–Petch relation for nanoscale materials, *Nanostruct. Mater.* **2**, 323–331 (1993).
46. C. S. Pande and R. A. Masumura, A model for flow stress dependence on grain size for nanocrystalline solids, in *Processing and Properties of Nanocrystalline Materials*, edited by C. Suryanarayana, J. Singh, and F. H. Froes (TMS, Warrendale, 1996), pp. 387–395.
47. A. A. Nazarov, A. F. Romanov, R. Z. Valiev, and B. Baudelet, The role of internal stresses in the deformation behavior of nanocrystals, in *Strength of Materials* (Japan Institute of Metals, Japan, 1994), pp. 877–879.
48. A. A. Nazarov, On the pile-up model of the grain size-yield stress relation for nanocrystals, *Scr. Mater.* **34**, 697–701 (1996).
49. J. Lian, B. Baudelet, and A. A. Nazarov, Model for the prediction of the mechanical-behavior of nanocrystalline materials, *Mater. Sci. Eng. A* **172**, 23–29 (1993).
50. G. A. Malygin, Self organization of dislocations and localizations of sliding in plastically deformed-crystals, *Phys. Solid State* **37**, 3–42 (1995).
51. J. C. M. Li, Petch relation and grain boundary sources, *Trans. TMS-AIME* **227**, 247–259 (1963).
52. A. G. Evans and J. P. Hirth, Deformation of nanoscale cermets, *Scr. Metall* **26**, 1675–1680 (1992).
53. K. Lu and M. L. Sui, An explanation to the abnormal Hall–Petch relation in nanocrystalline materials, *Scr. Metall. Mater.* **28**, 1465–1470 (1993).
54. R. O. Scattergood and C. C. Koch, A modified model for Hall–Petch behavior in nanocrystalline materials, *Scr. Metall. Mater.* **27**, 1195–1200 (1992).

55. R. W. Siegel, Nanophase materials, in *Encyclopedia of Applied Physics*, Vol. 11, edited by G. L. Trigg (VCH, Weinheim, Germany, 1994), pp. 173–200.
56. R. W. Siegel and G. E. Fougere, Mechanical properties of nanophase metals, *Nanostruct. Mater.* **6** (1–4), 205–216 (1995).
57. J. Pilling and N. Ridle, *Superplasticity in Crystalline Solids* (The Institute of Metals, London, 1989).
58. M. G. Zelin and A. K. Mukherjee, Geometrical aspects of superplastic flow, *Mater. Sci. Eng. A* **208**, 210–225 (1996).
59. A. P. Sutton and R. W. Balluffi, *Interfaces in Crystalline Materials* (Oxford Science Publications, Oxford, 1996).
60. H. Hahn, P. Mondal, and K. A. Padmanabhan, Plastic deformation of nanocrystalline materials, *Nanostruct. Mater.* **9**, 603–606 (1997).
61. H. Hahn and K.A. Padmanabhan, A model for the deformation of nanocrystalline materials, *Phil. Mag. B* **76**, 559–571 (1997).
62. I. A. Ovid'ko, Nanodefects in nanostructures, *Phil. Mag. Lett.* **83**, 611–620 (2003).
63. M. Yu. Gutkin, I. A. Ovid'ko, and N. V. Skiba, Strengthening mechanisms for high-strain-rate superplasticity in nanocrystalline materials, *J. Phys. D: Appl Phys.* **36**, L47–L50 (2003).
64. M. Yu. Gutkin, I. A. Ovid'ko, and N. V. Skiba, Strengthening and softening mechanisms in nanocrystalline materials under superplastic deformation, *Acta Mater.*, **52**, 1711–1720 (2004).
65. S. X. McFadden, R. S. Misra, R. Z. Valiev, A. P. Zhilyaev, and A. K. Mukherjee, Low temperature superplasticity in nanostructured nickel and metal alloys, *Nature* **398**, 684–686 (1999).
66. R. K. Islamgaliev, R. Z. Valiev, R. S. Mishra, and A. K. Mukherjee, Enhanced superplastic properties in bulk metastable nanostructured alloys, *Mater. Sci. Eng. A* **304**, 206–210 (2001).
67. R. S. Mishra, R. Z. Valiev, S. X. McFadden, R. K. Islamgaliev, and A. K. Mukherjee, High-strain-rate superplasticity from nanocrystalline Al alloy 1420 at low temperatures, *Phil. Mag. A* **81**, 37–48 (2001).
68. R. S. Mishra, V. V. Stolyarov, C. Echer, R. Z. Valiev, and A. K. Mukherjee, Mechanical behavior and superplasticity of a severe plastic deformation processed nanocrystalline Ti–6Al–4V alloy, *Mater. Sci. Eng. A* **298**, 44–50 (2001).
69. R. Z. Valiev, C. Song, S. X. McFadden, A. K. Mukherjee, and R. S. Mishra, TEM/HREM observations of nanostructured superplastic Ni_3Al, *Phil. Mag. A* **81**, 25–36 (2001).
70. R. Z. Valiev, I. V. Alexandrov, Y. T. Zhu, and T. C. Lowe, Paradox of strength and ductility in metals processed by severe plastic deformation, *J. Mater. Res.* **17**, 5–8 (2002).
71. A. K. Mukherjee, Elevated temperature crystalline plasticity at diminishing length scales, in *Creep Deformation: Fundamentals and Applications*, edited by R. S. Mishra, J. C. Earthman, and S. V. Raj (TMS, Warrendale, 2002), pp. 3–19.
72. A. K. Mukherjee, An examination of the constitutive equation for elevated temperature plasticity, *Mater. Sci. Eng. A* **322**, 1–22 (2002).
73. I. A. Ovid'ko and A. G. Sheinerman, Triple junction nanocracks in deformed nanocrystalline materials, *Acta Mater.* **52**, 1201–1209 (2004).
74. G. W. Nieman, J. R. Weertman, and R. W. Siegel, Mechanical behavior of nanocrystalline Cu and Pd, *J. Mater. Res.* **6**, 1012–1027 (1991).
75. A. B. Witney, P. G. Sanders, J. R. Weertman, and J. A. Eastman, Fatigue of nanocrystalline copper, *Scr. Metall. Mater.* **33**, 2025–2030 (1995).
76. J. E. Carsley, W. W. Milligan, S. A. Hackney, and E. C. Aifantis, Glasslike behavior in a nanostructured Fe/Cu alloy, *Metall. Mater. Trans. A* **26**, 2479–2481 (1995).
77. R. A. Andrievskii, G. V. Kalinnikov, N. P. Kobelev, Y. M. Soifer, and D. V. Shtansky, Structure and physicomechanical properties of nanocrystalline boride-nitride films, *Phys. Solid State* **39**, 1661–1666 (1997).
78. R. A. Andrievskii, The state-of-the-art of nanostructure high melting point compound-based materials, in *Nanostructured Materials: Science and Technology*, edited by G. M. Chow and N. I. Noskova (Kluwer, Dordrecht, 1998), pp. 263–282.

79. Q. Wei, D. Jia, K. T. Ramesh, and E. Ma, Evolution and microstructure of shear bands nanostructured Fe, *Appl. Phys. Lett.* **81**, 1240–1242 (2002).
80. D. Jia, K. T. Ramesh, and E. Ma, Effects of nanocrystalline and ultrafine grain sizes on constitutive behavior and shear bands in iron, *Acta Mater.* **51**, 3495–3509 (2003).
81. M. Murayama, J. M. Howe, H. Hidaka, and S. Takaki, Atomic level observation of disclination dipoles in mechanically milled nanocrystalline Fe, *Science* **295**, 2433–2435 (2002).
82. A. E. Romanov and V. I. Vladimirov, Disclinations in solids, in *Dislocations in Solids*, Vol. 9, edited by F. R. N. Nabarro (North-Holland, Amsterdam, Pub. Company, 1992), pp. 191–312.
83. M. Seefeldt, Disclinations in large-strain plastic deformation and work-hardening, *Rev. Adv. Mater. Sci.* **2**, 44–77 (2001).
84. M. Y. Gutkin, A. L. Kolesnikova, I. A. Ovid'ko, and N. V. Skiba, Disclinations and rotational deformation in fine-grained materials, *Phil. Mag. Lett.* **82**, 651–657 (2002).
85. M. Yu. Gutkin and I. A. Ovid'ko, Disclinations and rotational deformation in nanocrystalline materials, *Rev. Adv. Mater. Sci.* **4**, 79–114 (2003).
86. A. A. Fedorov, M. Yu. Gutkin, and I. A. Ovid'ko, Transformations of grain boundary dislocation pileups in nano- and polycrystalline materials, *Acta Mater.* **51**, 887–898 (2003).
87. A. H. King, The geometric and thermodynamic properties of grain boundary junctions, *Interface Sci.* **7**, 251–271 (1999).
88. V. B. Rabukhin, Triple junction diffusion and creep in polycrystallin 41, *Poverkhnost* **7**, 126 (1986).
89. B. Bokstein, V. Ivanov, O. Oreshina, A. Peteline, and S. Peteline, Direct experimental observations of accelerated Zn diffusion along triple junctions in copper, *Mater. Sci. Eng. A* **302**, 151–153 (2001).
90. K. M. Yin, A. H. King, Te. Hsieh, F. R. Chen, J. J. Kai, and L. Chang, Segregation of bismuth to triple junctions in copper, *Microsc. Microanal.* **3**, 417–422 (1997).
91. O. A. Kaibyshev, Nature of superplastic deformation, *Mater. Sci. Forum* **304-6**, 21–28 (1999).
92. K. Owusu-Boahen and A. H. King, The early stages of plastic yielding in polycrystalline gold thin films, *Acta Mater.* **49**, 237–247 (2001).
93. G. Gottstein, A. H. King, and L. S. Shvindlerman, The effect of triple-junction drag on grain growth, *Acta Mater.* **48**, 397–403 (2000).
94. M. Yu. Gutkin, I. A. Ovid'ko, and C. S. Pande, Yield stress of nanocrystalline materials: Role of grain boundary dislocations, triple junctions, *Phil. Mag.* **83**, 847–863 (2004).
95. V. Yamakov, D. Wolf, S. R. Phillpot, and H. Gleiter, Grain-boundary diffusion creep in nanocrystalline palladium by molecular-dynamics simulation, *Acta Mater.* **50**, 61–73 (2002).
96. C. J. Youngdahl, P. G. Sanders, J. A. Eastman, and J. Weertman, Compressive yield strengths of nanocrystalline Cu and Pd, *Scr. Mater.* **37**, 809–813 (1997).
97. R. Suryanarayanan, C. A. Frey, S. M. L. Sastry, B. E. Waller, S. E. Bates, and W. E. Buhro, Mechanical properties of nanocrystalline copper produced by solution-phase synthesis, *J. Mater. Res.* **11**, 439–448 (1996).
98. P. G. Sanders, J. A. Eastman, and J. R. Weertman, Elastic and tensile behavior of nanocrystalline copper and palladium, *Acta Mater.* **45**, 4019–4025 (1997).
99. P. G. Sanders, J. A. Eastman, amd J. R. Weertman, Mechanical behavior of nanocrystalline metal, in *Processing and Properties of NC Materials*, edited by C. Suryanarayana, J. Singh, and F. H. Froes (TMS, Warrendale, 1996), pp. 379–386.
100. R. Z. Valiev and I. V. Alexandrov, *Nanostructured Materials Processed by Severe Plastic Deformation* (Moscow, Logos, 2000) (In Russian).
101. K. S. Kumar, S. Suresh, M. F. Chisholm, J. A. Horton, and P. Wang, Deformation of electrodeposited nanocrystalline nickel, *Acta Mater.* **51**, 387–405 (2003).
102. R. Z. Valiev and T. G. Langdon, An investigation of the role of intergranular dislocation strain in the superplastic PB-62-percent Sn eutectic alloy, *Acta Metall. Mater.* **41**, 949–954 (1993).
103. M. Yu. Gutkin, I. A. Ovid'ko, and N. V. Skiba, Transformation of the grain boundaries due to disclination motion and emission of dislocation pairs, *Mater. Sci. Eng. A* **339**, 73–80 (2003).

104. M. Yu. Gutkin and I. A. Ovid'ko, Disclinations, amorphization and microcrack generation at grain boundary junctions in polycrystalline solids, *Phil. Mag. A* **70**, 561–575 (1994).
105. J. H. Van Der Merve, Misfit dislocations in heteroepitaxial films, *Crit. Rev. Solid State Mater. Sci.* **17**, 187–197 (1991).
106. S. C. Jain, A. H. Harker, and R. A. Cowley, Misfit strain and misfit dislocations in lattice mismatched epitaxial layers and other systems, *Phil. Mag. A* **75**, 1461–1515 (1997).
107. J. Th. M. De Hosson and B. J. Kooi, Structure and properties of heterophase interfaces, in *Handbook of Surfaces and Interfaces of Materials*, Vol. 1, edited by H. S. Nalwa (Academic Press, New York, 2001), pp. 1–114.
108. J. T. M. De Hosson and H. A. De Raedt, Effects of topography in nano-structured thin films: A Lorentz transmission electron microscopy and electron holography study, *Rev. Adv. Mater. Sci.* **5**, 403–412 (2003).
109. V. Ramaswamy, W. D. Nix, and B. M. Clemens, Coherency and surface stress effects in metal multilayers, *Scr. Mater.* **50**, 711–715 (2004).
110. S. V. Bobylev, M. Yu. Gutkin, and I. A. Ovid'ko, Nanograins with degrees grain boundaries in high transition temperature superconducting films, *J. Phys. Condens. Matter* **15**, 7925 (2003).
111. A. L. Kolesnikova and I. A. Ovid'ko, Orientation order in nanoparticles in composite films, *Phys. Rev. B* **69**, Art. No. 035412 (2004).
112. I. A. Ovid'ko and A. G. Sheinerman, Grain-boundary dislocations and enhanced diffusion in nanocrystalline bulk materials and films, *Phil. Mag.* **83**, 1551–1563 (2003).
113. I. A. Ovid'ko, Misfit dislocation walls in solid films, *J. Phys. Condens. Matter* **11**, 6521–6527 (1999).
114. I. A. Ovid'ko, Effects of misfit stresses on high T-c superconductivity in thin films cuprates, *J. Phys. Condens. Matter* **13**, L97–L103 (2001).
115. I. A. Ovid'ko and A. G. Sheinerman, Hyperdislocations in misfit dislocations networks in solid films, *J. Phys. Condens. Matter* **15**, 2127–2135 (2003).
116. I. A. Ovid'ko, A. G. Sheinerman, and N. V. Skiba, Competing relation mechanisms in strained semiconducting and superconducting films, *J. Phys. Condens. Matter* **15**, 1173–1181 (2003).
117. S. V. Bobylev, I. A. Ovid'ko, and A. G. Sheinerman, Effects of misfit stresses on the structure and transport properties of grain boundaries in high T-c superconducting films, *Phys. Rev. B* **64**, Art. No. 224507 (2001).
118. I. A. Ovid'ko, Interfaces and misfit defects in nanostructured and polycrystalline films, *Rev. Adv. Mater. Sci.* **1**, 61–67 (2000).
119. I. A. Ovid'ko and A. G. Sheinerman, Dislocation dipoles in nanocrystalline films, *J. Nanosci. Nanotechnol.* **1**, 215 (2001).
120. A. L. Kolesnikova, I. A. Ovid'ko, and A. E. Romanov, Misfit disclination structures in nanocrystalline and polycrystalline films, *Solid State Phenom.* **87**, 265–275 (2002).
121. L. T. Kabacoff, in *Nanostructured Films and Coatings*, NATO Science Series, edited by G. M. Chow, I. A. Ovid'ko, and T. Tsakalakos (Kluwer, Dordrecht, 2000), p. 373.
122. I. A. Ovid'ko and A. G. Sheinerman, Nano-wires associated with compositional inhomogeneities in multilayered films, *J. Phys. Condens. Matter* **13**, 9645–9653 (2001).
123. A. Misra, J. P. Hirth, and H. Kung, Single dislocation based strengthening mechanisms in nanoscale metallic multilayers, *Phil. Mag. A* **82**, 2935–2951 (2002).
124. I. A. Ovid'ko and A. G. Sheinerman, Misfit dislocations in multilayered films on disclinated substrate, *J. Phys. Condens. Matter* **13**, 7937–7951 (2001).
125. A. F. Jankovski, P. Sandoval, and J. P. Hayes, Superlattice effects on solid-state amorphization, *Nanostruct. Mater.* **5**, 497–503 (1995).
126. K. Samwer, Amorphization in solid metallic systems, *Phys. Rep.* **161**, 1–41 (1988).
127. M. Yu. Gutkin and I. A. Ovid'ko, Misfit strains and phase transformations in layered composite solids, *J. Phys. Cond. Matter* **11**, 8607–8616 (1999).

128. N. N. Ledentsov, V. M. Ustinov, V. A. Shchukin, P. S. Kop'ev, Zh. I. Alferov, and D. Bimberg, Quantum dot heterostructures: Fabrication, properties, lasers (Review), *Semiconductors* **32**, 343–365 (1998).
129. V. A. Shchukin and D. Bimberg, Spontaneous ordering of nanostructures on crystal surfaces, *Rev. Mod. Phys*. **71**, 1125–1171 (1999).
130. R. S. Williams and R. Medeiros Ribeiro, Size and shape of epitaxial nanostructures, in *Synthesis, Functional Properties and Applications of Nanostructures*, NATO Science Series, edited by T. Tsakalakos, I. A. Ovid'ko, and A. K. Vasudevan (Kluwer, Dordrecht, 2003), pp. 81–93.
131. V. V. Ustinov, Quantum dot semiconductor lasers, in *Synthesis, Functional Properties and Applications of Nanostructures*, NATO Science Series, edited by T. Tsakalakos, I. A. Ovid'ko, and A. K. Vasudevan (Kluwer, Dordrecht, 2003), pp. 543–559.
132. C. Teichert, Self organization of nanostructures in semiconductor heteroepitaxy, *Phys. Rep*. **365**, 335–432 (2002).
133. E. Pehlke, N. Moll, A. Kley, and M. Scheffler, Shape and stability of quantum dots, *Appl. Phys. A* **65**, 525–534 (1997).
134. H. T. Johnson and L. B. Freund, Mechanisms coherent and dislocated island morphologies in strained epitaxial material system, *J. Appl. Phys*. **81**, 6081–6090 (1997).
135. R. V. Kukta and L. B. Freund, Minimum energy configuration of epitaxial material clusters on a lattice-mismatched substrate, *J. Mech. Phys. Solids* **45**, 1835–1860 (1997).
136. I. A. Ovid'ko, Relaxation mechanisms in strained nanoislands, *Phys. Rev. Lett*. **88**, Art. No. 046103 (2002).
137. I. A. Ovid'ko and A. G. Sheinerman, Perfect, partial, and split dislocations in quantum dots, *Phys. Rev. B* **66**, Art. No. 245309 (2002).

4

Nanoindentation in Nanocrystalline Metallic Layers: A Molecular Dynamics Study on Size Effects

Helena Van Swygenhoven, Abdellatif Hasnaoui, and Peter M. Derlet

Paul Scherrer Institut, NUM/ASQ, Villigen, Switzerland

1. INTRODUCTION

The understanding of the mechanical properties of nanocrystalline (nc) materials (with grain sizes less than 100 nm) poses a fundamental challenge to materials science research.[1,2] For such nanometer scale grain sizes, the volume fraction of grain boundaries (GBs) becomes significant and the mechanical properties of nc materials exhibit unique properties when compared to their coarser grained counterparts. With decreasing grain sizes, a transition from dislocation-mediated plasticity within the grains, toward a plasticity that is primarily accommodated by the GB structure is to be expected. Many controversial results have been reported for these interface-dominated materials; however, despite the extensive efforts over the past decade, there is no fundamental understanding of the relation between the geometrical GB network, including details of GB structure, and the overall mechanical behavior.

Tensile deformation studies of nc systems show an increase in strength of up to six times the strength of their coarse-grained counterparts. The observed increase is dependent on the synthesis method and the different obtained microstructures.[1,3,4] The increase in strength is however accompanied by a dramatic loss in ductility, and several methods to improve ductility have been proposed.[5] In a recent study on nc Ni synthesized by electrodeposition and high-pressure torsion,[3,4] other typical features characterizing the deformation mechanism of nc metals were found, such as

- the increased strain-rate sensitivity, up to 10 times higher than the value of the coarse-grained material but still low compared to what is observed during superplastic deformation,
- a relatively low activation volume measured by strain rate jump tests, and
- a fast decrease in the work hardening, leading to limited uniform deformation and the onset of instabilities, resulting in shear bands at higher strain rates.

Moreover, it has been shown that the plastic deformation mechanism in electrodeposited Ni deforms with a mechanism that is characterized by a reversible X-ray diffraction peak broadening, which is generally not the case for coarse-grained face-centered cubic (fcc) metals.[6]

Atomistic simulations have provided a complimentary approach to the ongoing experimental effort. They have played an important role in the understanding of the discrete atomic processes that contribute to plastic deformation of nc materials under a uniaxial tensile load.[7–16] Using fully three-dimensional (3D) samples with mainly high-angle GBs and grain sizes up to 20 nm, two deformation mechanisms have been distinguished at room temperature: the first identified as grain boundary sliding (GBS) facilitated by atomic shuffling[17] and to a lesser extent stress-assisted free-volume migration; the second identified as a dislocation-mediated process, where the GBs act as source and sink for dislocations.[18,19] Moreover, cooperative GBS via the formation of shear planes that extend over a number of grains has been observed in simulations of nc Ni consisting of 125 grains, with an average grain size diameter of 6 nm.[20] Atomistic simulations have also provided an understanding of the experimentally observed dimple structures in the fracture surface of nc samples in terms of local shear planes formed around clustered grains that because of their particular misorientation cannot participate in the GB accommodation processes necessary to sustain plastic deformation.[21] With increasing grain size, all simulations indicate an increase in the level of dislocation activity. Careful examination of deformed samples has demonstrated that the dislocations are emitted from those areas in the GBs where misfit is accommodated, usually also identified by a high local value in tensile or compressive stress. The emission process always involves motion of free volume toward or away from the misfit area.

In spite of all experimental efforts and in spite of a maximum exploitation of the synergies between simulation and experiments, we are far from understanding the nc deformation mechanisms at the atomic level. One of the possible reasons might be that often measurement techniques are used that when applied to nc structures induce size effects, making quantitative interpretation of data uncertain.

Nanoindentation, a technique that offers to probe *in situ* high strain-rate plasticity and that is frequently used to measure hardness, is one of the techniques that might suffer from size effects when applied to nc structures. The development of the nanoindentation technique[22] and its combination with atomic force microscopy[23] and the interfacial force microscopy[24] have generated considerable interest in the detailed mechanisms of deformation during nanoindentation, particularly for experimental investigations of nanoscale structures.[25] It is now possible

to monitor, with high precision and accuracy, both the load and the displacement of an indenter down to the nanometer range,[26–28] revealing the presence of steps in the experimental load–indentation curves for conventional polycrystalline materials and single crystals.[28,29]

To provide a better insight into the atomic scale processes that occur under the indenter and to elucidate possible size effects, atomistic simulations can also here be called for help. For example, atomistic simulations could show that the steps in the load–indentation curves can be attributed to discrete dislocation bursts[30] and that surface inhomogeneities, such as surface steps, can greatly influence the onset of plasticity.[31] Most of these simulations have been performed on perfect single crystal structures.[30–35] To elucidate the role played by the GB in the process of dislocation nucleation, Christopher *et al*.[34] have indented on an Fe$\{100\}\{111\}$ GB under a bicrystal geometry and have observed a decrease in the maximum force by 40% in comparison to the case of a single crystal, and also observed material pileup on the $\{100\}$ grain surface. Lilleodden *et al*.[30] have studied the effect of the proximity of a GB, also in a bicrystal, to the indenter on an Au(111) surface, finding a lower critical stress for dislocation emission as the indenter approaches the GB. To investigate the role played by a more complex microstructure, nanoindentation simulations have been performed on nc metallic structures.[36,37]

In this chapter we discuss what atomistic simulations suggest on the deformation mechanism during nanoindentation in nc fcc gold structures. The interaction between dislocations nucleated under the indenter with the underlying GB structure and the possible GB accommodation processes are discussed. It is shown that these mechanisms contribute to an important relationship between grain size and indenter size, leading to size effects in nanoindentation measurements. The chapter begins with a brief discussion of the technique and its inherent limitations, an important issue that is too often neglected leading to incorrect evaluation of the simulated results.

2. ATOMISTIC MODELING

The atomistic simulation of nanoindentation on nc systems involves a number of techniques and procedures. First, there is the type of the atomistic simulation—for simulations at finite temperature, molecular dynamics (MD) is employed, whereas for zero-temperature simulations, the conjugate gradient (CG) technique is used to relax the structure with respect to the lowering of the indenter. Each of these methods contains inherent limitations and artifacts that must be understood when properly interpreting the results of the simulation. Both atomistic techniques require a model for the interaction between the atoms, where for the multimillion-atom simulations necessary to simulate an indentation simulation, a fast empirical atom–atom interaction is required to make the computational task tractable. To achieve this, such interatomic potentials approximate the true atom–atom interaction and are constructed to reproduce known bulk properties of ideal systems.

Thus, issues of transferability to atomic configurations far from the ideal systems must be taken into account when simulating atomic configurations that contain a certain degree of disorder such as in nc systems. Second, the nc system that is to be indented must be constructed in a way that it represents a true nc system as best as possible. This involves issues such as the number of grains simulated, their shape, their size, and the nature of the GB and triple junctions. It is important that former mentioned parameters are fully characterized for the simulated samples, since different preparation procedures can result in fundamentally different GB structures that are far from those expected for a metallic nc system. As an example, nc GB networks derived using an ultrafast cooling method from the melt, in the computer, resulted in a long-standing misconception that nc GBs were amorphous even in a pure metallic fcc system, and thus fundamentally different from those of the polycrystalline regime. Part of the misunderstanding in computer-generated GBs also arises from the definition used for the GB, leading to the importance of how atomic structures and processes can be visualized. Important differences in structural length scales are observed when using different definitions for GB atoms such as a definition based on energy, crystalline order, and positional disorder or stress.[19,38]

In what follows, fundamentals on the basic molecular dynamics and conjugant gradient techniques are given, and the model for the interatomic potential used for the nc simulations, the synthesis of computer-generated nc samples, and the visualization techniques are discussed. We conclude this section with a discussion on the inherent limitations of atomistic modeling when applied to nc systems.

2.1. Molecular Dynamics

MD involves the solution of Newton's equation of motion for an N-atom system:

$$m_i \ddot{\tilde{r}}_i(t) = F(\tilde{r}_1, \ldots, \tilde{r}_N) = -\tilde{\nabla}_i(\tilde{r}_1, \ldots, \tilde{r}_N) \tag{4.1}$$

where $\tilde{r}_i$ is the position of the ith atom. Since the precise atom dynamics is governed by N nonlinearly coupled differential equations, a numerical approach involving the discretisation of time is employed to evolve the system through time. For example, by approximating the acceleration via a simple finite difference representation, one obtains

$$m_i \frac{[r_i(t + 2\Delta t) - 2r_i(t + \Delta t) + r_i(t)]}{\Delta t^2} = -\tilde{\nabla}_i V\,(r_1(t), \ldots, r_N(t)) \tag{4.2}$$

from which a new configuration at time $t + 2\Delta t$ can be derived from the previous configurations at time $t + \Delta t$ and t. In practice this simple scheme is numerically unstable, and improved integration algorithms have been developed such as the Verlet[39] and Gear[40] predictor/corrector integrators, which are currently used. Such finite difference or integrator methods generally employ a time-step of the order of a femtosecond.

All thermodynamic variables can easily be measured and controlled within the framework of equilibrium MD. For example, the temperature T for a monoatomic system with mass m can be easily calculated using the principle of equipartition of energy:

$$\frac{3N}{2}k_{\mathrm{b}}T = \frac{1}{2}\sum_i m_i \dot{\tilde{r}}_i \cdot \dot{\tilde{r}}_i \tag{4.3}$$

Using this formula the temperature of the MD system can be controlled by rescaling the atomic velocities by the factor $\sqrt{T/T_{\mathrm{desired}}}$ every certain number of MD steps, eventually leading to an equilibrated system at the desired temperature. There exist more elaborate approaches to temperature through a fictitious damping term, the magnitude and sign of which is controlled by the difference between the desired temperature and the actual temperature of the system.[41] However, under equilibrium conditions, all such methods are expected to be equivalent.

The most widely used approach to apply a global stress to a simulation cell under full 3D periodicity is via the Parrinello–Rahman technique.[42] Within this framework, absolute atomic coordinates are represented via $\tilde{r}_i = \hat{B}\tilde{s}_i$, where $\hat{B}$ is a square matrix of rank 3, and $\tilde{s}_i$ are reduced dimensionless atomic coordinates ranging from -0.5 to 0.5. Thus, $\hat{B}$ has units of length and under orthorhombic geometry conditions, the diagonal components of $\hat{B}$ are simply the periodicity lengths. Higher derivatives of the atomic coordinates are represented in a similar fashion. The dynamical MD variables are now $\hat{B}$ and $\tilde{s}_i$, all of which follows differential equations, with the driving "force" of $\hat{B}$ being the difference between the applied global stress and the actual global stress of the simulation cell. Together, the temperature and stress control allow the simulation of equilibrium NPT systems.

2.2. Steepest Descent and Conjugate Gradient Methods

This approach entails finding the relaxed positions of a given unrelaxed atomic configuration—minimizing the total potential energy of the system with respect to the atomic coordinates. There exist a variety of quite general numerical procedures to minimize a function with respect to its degrees of freedom. The simplest method is the steepest descent algorithm, which minimizes the total potential energy by applying successive line minimizations along the $3N$ gradient vector:

1. Begin with an atomic configuration: $\tilde{r}_1, \ldots, \tilde{r}_N$ and potential energy $V(\tilde{r}_1, \ldots, \tilde{r}_N)$
2. (Line) minimize, with respect to λ, the potential energy $V(\lambda)$ where $V(\lambda) = V\left(\tilde{r}_1 + \lambda\tilde{h}_1, \ldots, \tilde{r}_N + \lambda\tilde{h}_N\right)$ and $\tilde{h}_1 = -\tilde{\nabla}_i V(r_i(t), \ldots, r_N(t))$
3. If $|V(\lambda_{\min}) - V(\tilde{r}_1, \ldots, \tilde{r}_N)|$ is less than some chosen tolerance energy then the system has relaxed to a local minima, else return to 1 with $\tilde{r}_i + \lambda_{\min}\tilde{h}_i \to \tilde{r}_i$.

Despite its simplicity, the steepest descent method exhibits slow convergence for large N systems, since each new gradient vector is not necessarily perpendicular to the previous one. As a result, minimizing along the next steepest descent direction may destroy, in part, the gains in reduction of potential energy, achieved in previous steepest descent steps. The CG approach minimizes this problem by calculating the new line minimization direction so that it is approximately orthogonal or conjugate to the previous line minimization. Rather than the new line minimization direction being simply the gradient at the minimum, the new conjugate direction is

$$\tilde{h}_i = -\tilde{\nabla}_i V\,(r_1(t), \ldots, r_N(t)) - \gamma_i \tilde{h}_{i-1} \tag{4.4}$$

where γ_i is the ratio of the magnitude of the forces at the current line minimum to the magnitude of the forces of the previous line minimum.

2.3. Interatomic Potentials

Although the condensed matter state remains fundamentally a quantum system, the difference in masses between the atoms and the electrons that contribute to the materials' bonding properties allows for a classical force to be defined between the atoms. This is, in essence, the adiabatic approximation where the atomic and electronic degrees of freedom can be decoupled from each other, allowing for the electronic degrees to be integrated out with respect to the atomic motion. Thus, the precise form of the classical interatomic potential is of quantum origin. For closed-shell systems, where there is not a strong electronic contribution to the bonding, a simple pair potential will suffice, which at short range will be repulsive and in the long range will be attractive. For metallic systems, the bonding originates from a combination of an ion—ion-type interaction described by a pair term and an electronic band energy term. For a general introduction to bonding in solids and the development of an empirical description of interatomic potentials, see Refs. 43 and 44.

To obtain an empirical description for metallic systems, the electronic band energy contribution as a function atomic position must capture the unsaturated nature of the metallic bond, in which, if one bond is broken, the remaining bonds are strengthened. A successful approach has been the embedded atom method,[45] which has its origins in density functional theory. In this model the total energy for an ideal metallic system is given by

$$E = \sum_i \left(F(\rho_i) + \frac{1}{2}\sum V(r_{ij})\right) \quad E = \sum_i \left(F(\rho_i) + \frac{1}{2}\sum V(r_{ij})\right) \tag{4.5}$$

where $F(\rho_i)$ is the so-called embedding function, $\rho_i = \sum_j \rho(r_{ij})$ is the local electronic density arising from nearby atoms, and $\frac{1}{2}\sum_j V(r_{ij})$ is the ion–ion-type pair interaction potential. Analogous forms of Eq. (4.5) can also be derived using effective medium theory.[46] For simple sp valent and transition metals with filled d

states, the electronic band term can be explicitly derived via the width of the band of electronic states, resulting in a term that is equal to the square root of the sum of bond overlap integrals between neighboring atoms [equivalent to the embedding energy term in Eq. (4.5)]. Such an approach is referred to as the second-moment tight-binding method.[43,47] For the nc Au nanoindentation simulations presented in this chapter, we employ the Cleri and Rosato second-moment tight-binding description for Au.[47]

The development of such empirical interatomic potentials for a given system generally involves searching for an optimal set of parameters for the chosen analytical interaction model, with respect to experimental and *ab initio*-calculated material properties. Such a database of properties is generally restricted to equilibrium atomic configurations of the system, such as lattice constants, cohesive energy, elastic constants, and local and extended defects such as vacancies, interstitials, and stacking faults for the fcc, body-centered cubic (bcc), and hexagonal close-packed (hcp) phases. The application of such empirical potentials to nc systems, which will always contain atomic configurations that are not explicitly included in the materials database used to construct the potential (such as GBs), assumes that the interatomic model is transferable. If the chosen analytical interatomic model captures the essential physics of the material's bonding, then it is not too unreasonable to make such an assumption, although one must always be aware of issues of accuracy in describing, for example, complex defect structures of low symmetry.

2.4. Creation of Nanocrystalline Atomistic Configurations

As in experiment, the structural and mechanical properties of computer-generated ncmaterials are strongly dependent on the method used for sample construction. For example, the issue of whether or not the metallic nc GB is amorphous depends on the sample preparation method, since the extent of how far the computer-generated nc state is from equilibrium depends strongly on the preparation method[12] and the relaxation times utilized, which are anyway orders of magnitude smaller compared to experiments. In turn, it is to be expected that the nc state will affect the nc mechanical properties.

The nc samples used in the present simulations are constructed by beginning with an empty simulation cell with fully 3D periodic boundary conditions (PBCs), and choosing randomly a number of positions. The number of positions is determined from the simulation cell size and the desired characteristic grain size. From each position, an fcc lattice of random orientation is constructed geometrically. When atoms from one-grain center are closer to the center of another grain, construction is halted. Eventually, construction will cease throughout the entire sample, resulting in a 3D granular structure according to the Voronoi construction.[48] At this stage atom pairs, each atom originating from a different crystallite, are inspected and when the nearest neighbor distance is less than 80% of the equilibrium fcc nearest neighbor distance, one atom is removed. Molecular statics is then

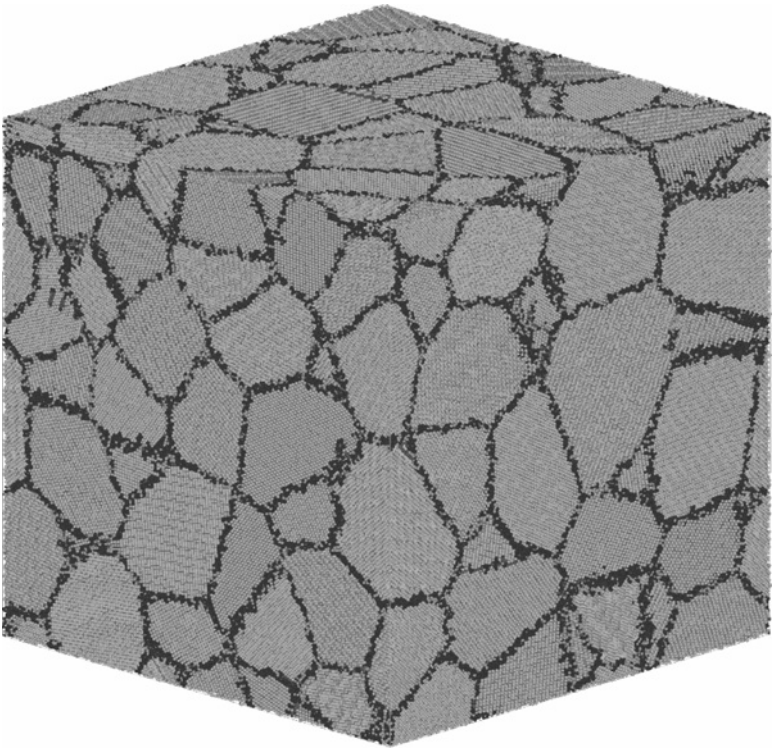

FIGURE 4.1. nc Au sample containing 100 grains with an average diameter of 10 nm. The sample contains 4.8 million atoms.

performed to relax any local high potential energy configuration that may exist, followed by NPT MD at room temperature to further relax and equilibrate the structure. The constant-pressure MD is performed using the Parrinello–Rahman Lagrangian with orthorhombic simulation cell geometry conditions.[42] For further details, see Refs. 8 and 38.

Figure 4.1 displays such an nc sample that is used in the atomistic simulations of nc systems. The coloring scheme used for the atoms is defined in Section 1.6.

2.5. Atomistic Nanoindentation Simulation Geometry

Figure 4.2 details a typical geometry used in the atomistic modeling of a nanoindentation simulation. The computer-generated nc layer is periodic in the two perpendicular (lateral) directions, while open boundary conditions (OBCs) exist for the third direction. Thus, in the third direction, two surfaces exist, one of which is the indentation surface and the other is attached to an infinitely hard substrate by fixing the position of the atoms on the lower surface. This is usually done by either

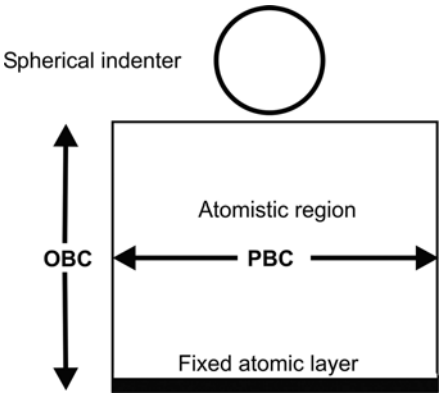

FIGURE 4.2. Geometry used for nanoindentation simulations. An ideal spherical indenter is lowered onto atomistic thin film sample, where there are periodic boundary conditions (PBCs) in the lateral direction and open boundary conditions (OBC) in the direction the indenter is lowered

fixing the 3D coordinates of the lower surface atoms or fixing only the coordinate in the direction normal to the surface (the so-called sliding surface boundary condition). For an nc system, the choice does not affect indentation simulation; however, for a perfect single crystal simulation, the choice can affect the nature of the dislocation activity. For example, using a fixed layer will repel dislocations (via strong image forces) from the bottom layer and keep them directly below the indenter region, whereas, for the sliding boundary conditions, the repulsion is not so strong and upon further lowering of the indenter the dislocations can propagate until the end of the atomistic region.

The nc samples in the present indentation work are the same as those used in the full 3D uniaxial tensile deformation simulations, where the thin film geometry is introduced by removing one of the periodic conditions and allowing the resulting surfaces to relax. For more details on this procedure, see Ref. 49. The grain directly below the indenter is generally chosen to have a 111 surface orientation. For a reference system, similar nanoindentation simulations are performed on perfect crystals with a 111 surface and of similar size to that of the nc system (see Ref. 36).

The indenter that is modeled is typically an ideal spherical indenter of radius R represented as the potential $V(r) = A\Theta(R - r)(R - r)^3$. Here r is the distance of the atom from the indenter center, A is a force constant, and $\Theta()$ a standard step function. Following Ref. 32, A is chosen as 5.3 nN/Å^2.

For MD simulations, such an indenter is lowered from above at a particular speed during which MD is performed on the atomistic region below. The indenter can be lowered by either a fixed velocity producing an indentation force versus indentation depth curve, or lowering the indenter via an applied force on the indenter corresponding to a load controlled experiment that produces an applied force

versus indentation depth curve. All of the work presented here employs a constant velocity nanoindentation simulation approach. For the CG method nanoindentation simulations, the atomic configuration is relaxed for every incremental lowering of the indenter.

2.6. Atomistic Visualization Methods for GB and GB Network Structure

To capture the essential properties of the nc system, a large number of grains must be included within the atomic configuration. This in turn involves a large number of atoms, often numbering in the millions. With such a large number of atoms, visualization at the atomic scale becomes difficult unless appropriate filters are applied to the atomic data. Motivation for such visualization is fundamentally important for nc simulations, since it allows for the characterization of the GB structure as well as the observation of atomic scale processes that lead to global plasticity. The former is particularly important, since the degree of plasticity is sensitive to the nc GB structure, which in turn depends on the sample synthesis procedure and its associated thermal history.

In addition to an atom's position, a number of physical and structural properties can be assigned to it, and via these quantities, a classification scheme can be developed to consider only those atoms that constitute the GB region. Of course, different classification schemes can lead to different GB region volumes. For example, if atoms that are locally non-fcc are classified as GB atoms, this will lead to an average GB thickness that is smaller than a GB defined via those atoms with a local stress higher than some critical value. Moreover, calculating then, for example, the resulting number density for the GB region will lead to different values. This demonstrates the importance of using a variety of schemes, alone or in conjunction, to investigate the GB structure resulting from computer synthesis methods, and to clearly state those used when quoting calculated GB properties.[12,19]

Atomic visualization of grains and GB structures has been facilitated greatly by a medium range order analysis of all atoms within the sample, which ascribes a local crystallinity class to each atom.[50] This is performed by selecting the common neighbors of a pair of atoms separated by no more than a second nearest neighbor distance, and introducing a classification scheme for the nearest neighbor bond pathways between the two atoms. Since each crystalline symmetry has a unique topological signature, when all second nearest neighbor bond permutations are enumerated, a local symmetry label can be assigned to each atom (see Table 4.1).

This local atomic classification scheme allows the GB network and structure to be easily identified. For examples of such atomic visualization of the GB, we refer to Refs. 8 and 9, in which both high-angle and low-angle general GBs are shown. A significant advantage of such a local crystallinity analysis is that (111) hcp planes represent twin planes, and two neighboring parallel (111) hcp planes represent

TABLE 4.1. Local Crystalline Symmetry Classification Used in the Atomic Visualization.

PFCC	fcc environment up to fourth nearest neighbor
GFCC	fcc environment up to first nearest neighbor
PBCC	bcc environment up to 4th nearest neighbor
GBCC	bcc environment up to first nearest neighbor
PHCP	hcp environment up to 4th nearest neighbor
GHCP	hcp environment up to first nearest neighbor
OT12	12-coordinated atom without the above symmetries
OT8	8-coordinated atom without the above symmetries

an intrinsic stacking fault. The visualization of the twin planes has allowed for the easy identification of GBs containing structural units of a $\Sigma = 3$ symmetric boundary.[9] In the case of stacking fault defects, this approach has given evidence for partial dislocation activity under uniaxial tensile loading conditions.

Another visualization technique used in the simulations of nanoindentation is based on the local stress. To calculate the global stress tensor within a computer simulation, the virial theorem[41] has been generally used, which in the thermodynamic limit of large V and N represents the true bulk homogeneous stress. To investigate the spatial dependence of the stress field within the nc sample, one generally applies the virial theorem directly to one or a number of atoms. It is however known that for such a volumetric partition, momentum is no longer conserved, leading to non-negligible artifacts such as oscillatory behavior in strongly inhomogeneous systems. A systematic approach has been developed[51] that can represent local stress more accurately via

$$\sigma^{\mu\nu} = \left\langle \frac{1}{\Omega} \left(\frac{1}{2} m v^{\mu} v^{\nu} \Lambda_i + \frac{1}{2} \sum_j F^{\mu} \left(r_{ij} \right) r_{ij}^{\nu} l_{ij} \right) \right\rangle \tag{4.6}$$

where Ω is the volume of some representative partition element, Λ_i is unity if atom i is within the volume element and zero otherwise, and l_{ij} is the fraction of the length of the bond between atoms i and j lying within the volume element. Equation (4.6) rigorously satisfies conservation of linear momentum. In the present work we choose the volume element to be a sphere centered on each atom, and define the resulting stress of that sphere as the local stress of the central atom. The radius of the sphere is taken as 4 Å and contains approximately 19 atoms. A thermal average is performed over 1 ps, which is typically several atomic vibrational periods. In what follows, we visualize the two scalar invariants of the stress tensor, the local hydrostatic pressure and local maximum resolved shear stress. In the present work, a positive value for the hydrostatic pressure represents compression and negative dilation.[12] On average, GBs are under a net tensile load although large variations between positive and negative hydrostatic pressure occur within the GB regions, whereas the grain interior is under compressive load.[52]

2.7. The Time- and Length-Scale Problem

The MD and CG methods carry with them many caveats that must be appreciated to interpret results in the context of experiment. For MD, the correct use of integrators [such as Eq. (4.2)] entails using a time step of a few femtoseconds, typically 1–2 fs. Thus, a simulation that runs for 1 million iterations corresponds to a physical time of only 1 ns. Even when using advanced parallel computing, large systems containing millions of atoms can only be realistically simulated for a few nanoseconds. For condensed matter atomistic systems, short- and long-range mass transport occurs primarily via discrete stochastic atomic activity such as migration via a diffusive hop, nucleation of a dislocation, and atomic shuffling within the GB region. Such processes have a longer timescale than the one associated with thermal vibration. Diffusion events can be therefore classified as rare events within the simulation timescale. To measure significant diffusion activity, simulations have to be performed over much longer time periods. There is a tendency to overcome this problem by performing simulations at temperatures close to the melting point[53] where diffusion is greatly enhanced, but this in turn introduces other worries, since experimentally it is known that nc metals are thermodynamically unstable at temperatures slightly above room temperatures. Time issues are a general problem of the MD technique: most of the computational time is spent with the atoms vibrating about their local minima, until a so-called "rare event" occurs, resulting in, for example, an atomic hop from one equilibrium position to another. Therefore, it has to be emphasized that MD techniques cannot catch the rate-limiting deformation process seen in experiment and can be used only to gather information on possible deformation mechanisms.

In the context of nanoindentation simulations, another timescale exists associated with the speed of the lowering indenter. To exploit the 1-ns timescale regime of MD simulations, the indenter must be lowered at a speed that is many magnitudes faster than that seen in experiment. In most published work, the indenter speed is typically 0.1 Å/0.5 ps corresponding to a speed of 40 m/s. Thus, in the context of experiment, such simulations actually correspond more closely to high-impact shot-pinning events.

In the case of CG methods, the atomic configuration is relaxed to a minimum energy for a given indentation depth. When this is found, the indenter is lowered (typically of the order of 0.1 Å) and the procedure repeated. Such a simulation might be seen as the zero kelvin infinitesimally slow indenter speed limit. However, one must be careful with this interpretation since the CG technique finds only a local minimum rather than the global minimum. A more accurate interpretation, but less useful definition, would be that the relaxed atomic configuration corresponds to a quasi-equilibrium structure obtained by lowering the indenter by small increments.[36]

Another possible artifact of the MD technique is the length-scale problem. In order to mimic an infinite sample, a replica technique is used, called periodic boundary conditions (PBCs). This however implies that the particular

microstructure considered in the sample is repeated in all directions. In terms of simulations of nanoindentation, the PBCs are used only in the in-plane directions (not in the indentation direction), resulting in a repetition of the indenter geometry on a scale that equals the simulation box. In order to avoid artifacts due to interaction of the indenters, it is important that the size of the indented region is considerably smaller than the box size.

In spite of all possible artifacts that accompany the simulation techniques, atomistic simulation can be considered as an excellent guidance in the interpretation of experimental results, as long as the caveats of the technique are properly recognized.

3. THE DEFORMATION MECHANISMS AT THE ATOMIC LEVEL IN NANO-SIZED GRAINS BENEATH THE INDENTER

Much simulation work has been undertaken for nc systems under uniaxial loading conditions, where a number of important deformation mechanisms have been identified. We briefly summarize these findings, and then proceed to the results of the nanoindentation simulations.

3.1. Deformation Mechanisms in nc fcc Metals Derived from Tensile Loading

In all samples with mean grain sizes up to 20 nm, GBS and dislocation activity have been observed as plastic deformation mechanisms, the latter being of increasingly importance with increasing grain size.

Careful analysis of the GB structure during sliding under constant tensile load shows that sliding includes a significant amount of discrete atomic activity, either through uncorrelated shuffling of individual atoms or, in some cases, through shuffling involving several atoms acting with a degree of correlation. In all cases, the excess free volume present in the disordered regions plays an important role. In addition to the shuffling, we have observed hopping sequences involving several GB atoms. This type of atomic activity may be regarded as stress-assisted free-volume migration. Together with the uncorrelated atomic shuffling, they constitute the rate-controlling process responsible for the GBS.[9]

In fully 3D Ni GB networks, which have been modeled now up to 20-nm grain sizes, only partial dislocations have been observed. MD simulations have shown that a GB dislocation emits a partial lattice dislocation meanwhile changing the GB structure and its dislocation distribution.[54,55] This mechanism is the reverse of what is often observed during absorption of a lattice dislocation, where the impinging dislocation is fully or partially absorbed in the GB, creating local changes in the structure and GB dislocation network. Extended partial dislocations have been observed in nc Cu up to grain sizes of 50 nm,[14] whereas in nc Al, partial and full

dislocation activity has been observed.[56] The origin of why partial dislocation or full dislocation activity occurs is under heavy discussion: on one hand, it has been recognized that the emission of the leading partial is accompanied by a local stress relief due to the structural relaxation, leading to a "delay" in the emission of the trailing partial, which might be of the order of the total simulation time.[12,19] On the other hand, the differences between Al and Cu have been tried to be explained in terms of the stacking fault energy of the empirical potential used.[56] However, the stacking fault only cannot explain the difference in behavior between Cu and Al, since simulations of nc Ni using a potential with a stacking fault energy much higher than the one in the Al potential demonstrate only the presence of extended partial dislocations. Recently, it has been shown that the dislocation activity in nc grains can be understood only when the entire generalized stacking fault energy curve (stable and unstable stacking fault energies) is considered.[57] Such an approach has also been used to understand the enhanced deformation properties of nc Al with grown-in twins.[58]

More recently, collective processes such as cooperative GBS via the formation of shear planes spanning several grains have been observed.[20,21] For simulation of such phenomena, a sample with 125 grains and a mean grain size of 5 nm was deformed. A large number of grains were necessary in order to minimize the effects imposed by the periodicity used to simulate bulk conditions. The small grain size is chosen to reduce the total number of atoms in the sample (up to 1.2 million) so that longer deformation times are possible at acceptable strain rates. In order to increase GB activity the deformation was done at 800 K. The underlying mechanisms that were observed for the formation of shear planes are (1) pure GBS-induced migration of parallel and perpendicular GBs to form a single shear interface, (2) coalescence of neighboring grains that form a low-angle GB facilitated by the propagation of Shockley partials, and (3) continuity of the shear plane by intragranular slip. A detailed description of the processes is given in Ref. 20.

3.2. Atomistic Mechanism under the Indenter

Figure 4.3 displays the force versus indentation depth curves obtained using CG (part a)and MD (part b) for nc Au systems with average grain sizes of 5 and 12 nm, with an indenter radius of 40 Å. Equivalent single crystal curves are also shown using the two methods. The CG runs exhibit a distinctive yield point, while the MD runs show significant noise due to temperature effects. The CG yield point for the single crystal is found at a load of 114 nN and an indentation depth of 4.7 Å, which is slightly higher than the ones found for the 12-nm nc sample at 107 nN/4.5 nm and for the 5-nm grain sample at 105 nN/5.4 Å. The indentation forces and indentation depths are many orders of magnitude smaller than those seen in typical nanoindentation experiments, and are an obvious result of the length and timescale restrictions of the atomistic technique.

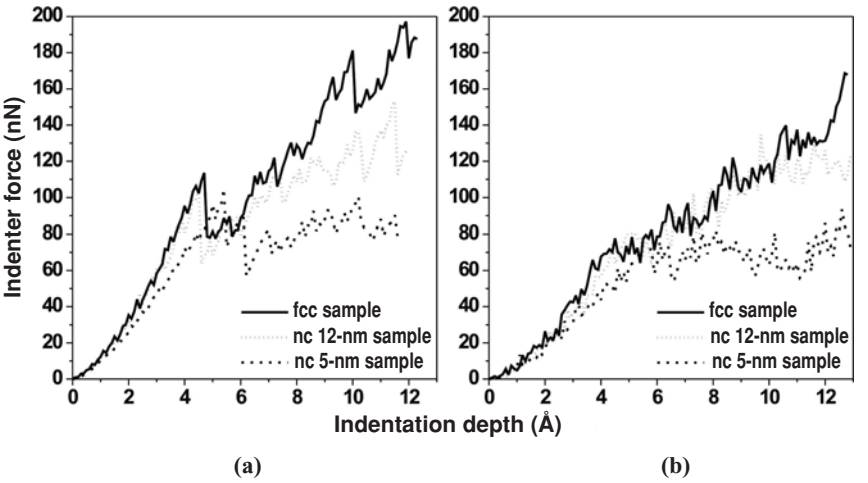

FIGURE 4.3. Load versus indentation depth plots for (a) CG and (b) MD simulation runs. (From Ref. 36).

The divergence of the CG runs during plastic deformation evidences the strong influence of the microstructure on indentation behavior. The load–indentation depth curve of the fcc sample shows multiple discrete reductions in load that can be directly related to discrete dislocation activity involving dislocation nucleation and/or reorganization of existing dislocation structures. Similar events also take place in the nc samples, but the effect on the load–displacement curve is less pronounced, especially in the 5-nm sample, where the active slip plane areas are reduced due to reduced grain size, and intergranular plastic activity becomes more significant.

The initial CG slip structure immediately after yield for the single crystal and the 12-nm grain samples consists of a stacking fault structure roughly of tetrahedral shape with its tip pointing into the sample, as seen by Li *et al*.[33] This nearly triaxial symmetry is immediately lost upon continuation of the indentation, where a complicated succession of partial dislocation reactions leads to a number of dislocation lock structures. All samples exhibit stacking fault planes parallel to the sample surface. For the MD technique the initial slip led to a wedge-shaped dislocation loop structure in both the single crystal and the 12-nm grain samples, similar to that seen in Refs. 31 and 32. In the 12-nm grain sample, for both the CG and the MD methods, the initial slip structure consists of partial dislocations that are immediately attracted to neighboring GBs.

Figure 4.4 shows the CG atomic structure under the indenter for the single crystal (part a) and the 12-nm grain sample at an indentation depth of 12 Å (part b). The blue plane of atoms indicates the upper indentation surface. At this indentation depth the dislocation structure remains confined to a compact zone beneath the indenter for the single crystal, whereas for the 12-nm grain sample, the initial

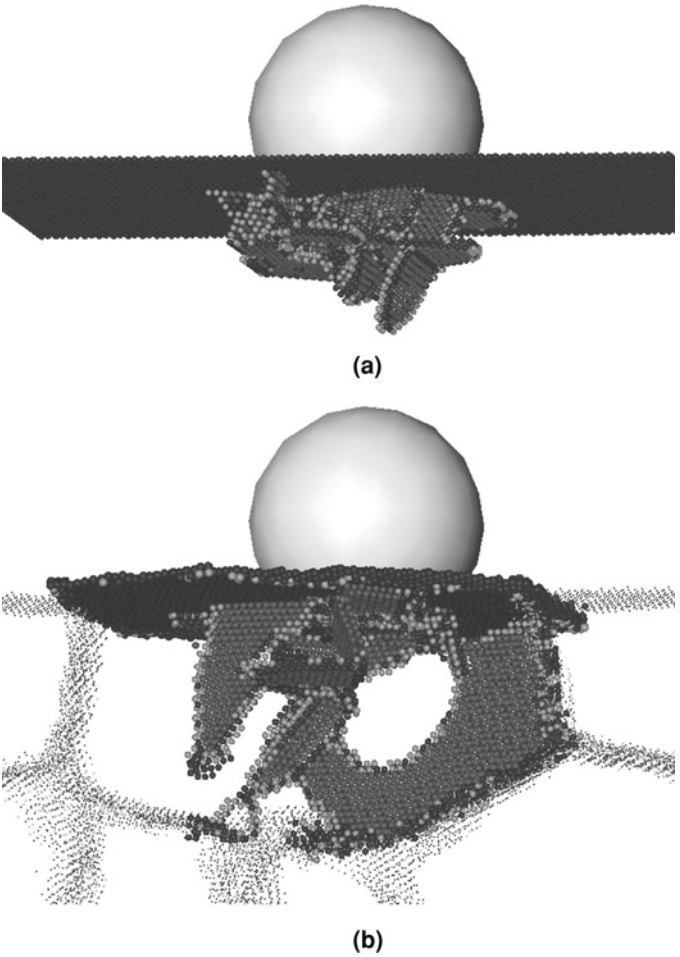

FIGURE 4.4. Zone beneath the indenter in CG for the (a) single crystal sample at a displacement of 12.3 Å and (b) ~12-nm grain sample at a displacement of 11.9 Å. Only non-fcc atoms are shown. (Taken from Ref. 36.)

dislocation loops are attracted to neighboring GBs identified by the green and blue atoms below the surface. Thus, the GBs act as dislocation sinks, accommodating the associated slip across the grain by structural changes within the GBs.

In the case of the 5-nm sample where the indenter diameter is larger than the average grain and therefore the indenter–substrate surface area is comparable to the size of the indented grain, the partial dislocation activity extends to neighboring grains and the onset of intergranular motion is observed in the MD run as a result of GBS. The 5-nm grain size nanoindentation simulation was continued to a depth

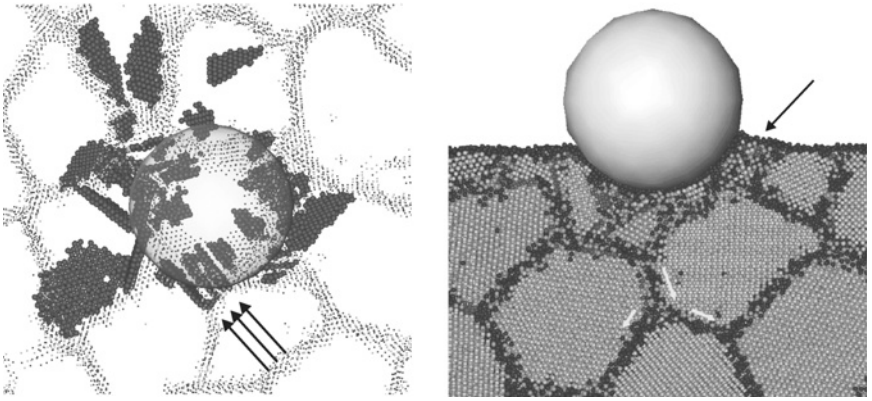

FIGURE 4.5. A view of the ~5-nm average grain size sample at an indentation depth of 20 Å. The yellow arrows signify relative motion of the grains relative to the center of mass of the yellow atoms. (From Ref. 36.)

of 20 Å. Figure 4.5 shows a schematic view of the relative motion of three grains under the indenter, where the largest relative displacement corresponds to a sliding of about 2 Å along the respective GB. The displacements are relative to those atoms shaded in yellow. Such activity is significantly less in the CG results, indicating that GBS is in general facilitated by GB atomic activity such as shuffling and stress-assisted free-volume migration—all of which are aided by temperature.[9] In this sample some atomic pileup around the indenter is seen (indicated by the black arrow in Fig. 4.5) with a maximum height of about three atomic layers.

An important observation in the present work is that the fcc sample appears "harder" than both the 5- and 12-nm grain size nc sample. In principle this contradicts experiment, which reveals the nc structure to be harder than the single or polycrystalline structures. Figure 4.4a shows that a compact plastic zone is created under the indenter for the fcc. Such a developing dislocation lock network below the indenter region will hinder further the dislocation-based processes. In the 12-nm grain size nc sample however, no such localized network exists, since dislocations are attracted to the GB network away from the indenter region. In the 5-nm nc sample (which appears "softer" than the 12-nm grain size sample) dislocations are also created in the neighboring grains and an increased intergranular activity (GB sliding) is observed. This contradiction has probably to be understood in terms of the short time and length scales of the simulation. Not only do the curves shown in Fig. 4.3 simulate very short timescales during which complicated dislocation networks cannot be formed, but also they result from a thin layer that is fixed to a rigid substrate. Such a hard substrate repels dislocations, keeping them near the indenter region, and this effect will be very much reduced in an nc structure due to the presence of the dense GB network. This suggests that simulating larger perfect crystal samples and/or using a sliding boundary condition at the

atomistic–substrate interface might lead to a reduction in the indentation force as a function of indentation depth for the fcc sample.

3.3. Interaction of Dislocations with the GB Network

In this section, the nature of the interaction between dislocations and the GB structure is studied, reflecting the importance of the GB network under the indenter.

Figure 4.6 is a series of snapshots, showing the atomic structure (parts a, b, and c) and the local hydrostatic pressure (parts d, e, and f) of a section of the sample

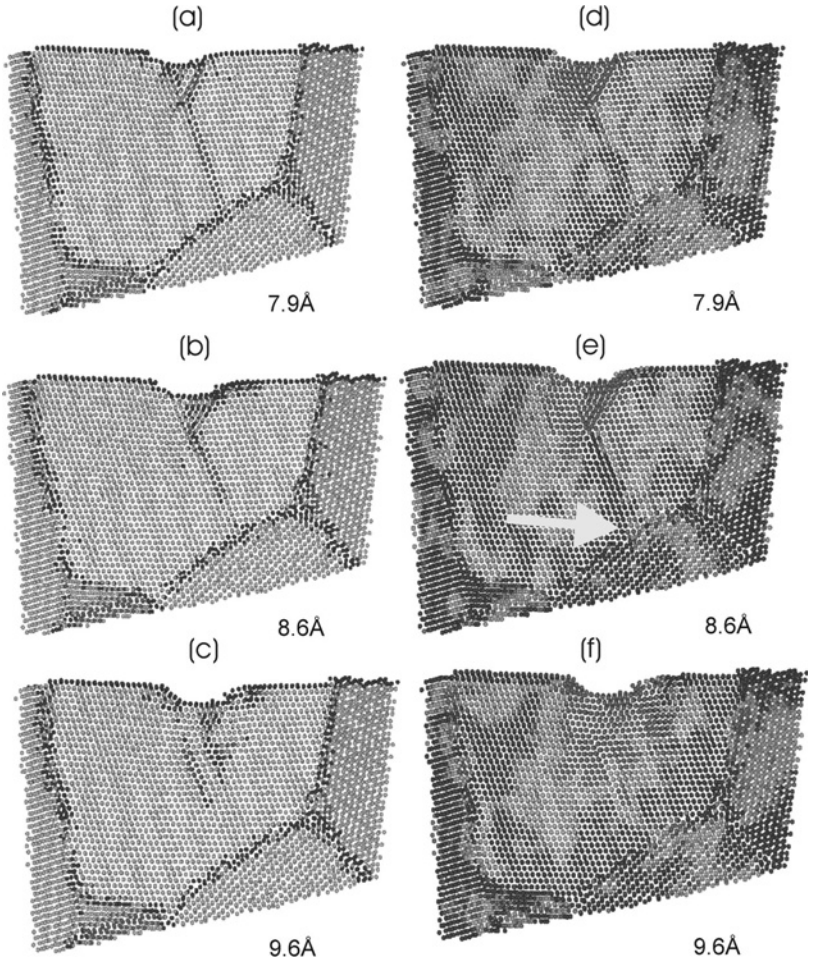

FIGURE 4.6. Dislocation repelled at high stress region of the GB. (From Ref. 37.) See also Color Plate 1 after p. 000.

involving a dislocation that approaches the GB on the lower right. Figure 4.6a shows the section at an indentation depth of 7.9 Å, where the dislocation, emitted from the plastic zone below the indenter, has propagated to GB1–6. The leading partial of this dislocation has reached the GB but the trailing did not follow, remaining at the plastic zone of the indenter. At a depth of 8.6 Å (Fig. 4.6b), the leading partial has returned to the plastic zone, and the full dislocation annihilates and a new dislocation nucleates three parallel 111 planes to the left (Fig.4.6c). To understand more about the possible reasons as to why the first dislocation was not absorbed by GB1–6, the hydrostatic pressure was inspected. In Fig. 4.6d–f, the atoms colored blue represent a hydrostatic pressure less than -0.5 GP and those colored red represent a hydrostatic pressure greater than 1.7 GPa (see color bar for intermediate values).

The yellow arrow in Fig. 4.6d shows the region of the GB1–6 where the first dislocation arrives. In past work it has been found that the GB region is on average under a tensile pressure, however containing strong load variations in hydrostatic pressure. In Fig. 4.6d we see that the local region to which the dislocation approaches is under a compressive pressure. Such strong variations in the GB pressure distribution are typical of what has been seen in the past. Since all dislocations carry with them a compressive stress field, the presence of the approaching dislocation adds temporarily to the local compressive pressure anomaly. After reflection of the dislocation to the plastic zone directly beneath the indenter, the stress anomaly is reduced (Fig. 4.6e). Inspection of the local GB structure to which the dislocation approaches revealed that the dislocation arrives in a coherent region where $\{111\}$ planes in grain 1 fit well with the $\{100\}$ planes in grain 6 (see Fig. 5 in Ref. 37). Moreover, during the entire life of this dislocation, no discrete atomic activity (shuffling and free-volume migration) within this area of the GB was observed.

In Fig. 4.7 we now follow the activity of the dislocation that is created upon the annihilation of the repelled dislocation in Fig. 4.6. At an indentation depth of 11.9 Å (Fig. 4.7a), this dislocation, emitted from the plastic zone just beneath the indenter, has propagated to GB1–6. At an indentation depth of 12.9 Å (Fig. 4.7b), the leading partial is completely absorbed by the GB, and at a depth of 13.9 Å the trailing partial is also absorbed. Thus the full dislocation has been absorbed by GB1–6. The Burgers vector of the two dislocations so far mentioned was found to be equal, demonstrating that in this case the orientation of the Burgers vector is not responsible for the manner in which each dislocation interacts with the GB. From the local hydrostatic pressure (Fig. 4.7d–f), this dislocation has propagated to a region of tensile pressure (Fig. 4.7d) in contrast to the previous dislocation that propagated to a region of compressive pressure (Fig. 4.6d). Note, however, that the absorption of this dislocation by GB1–6 increases the local stress in the region where it occurs (Fig. 4.7f). This could in part be due to the deposition of an extra $\{110\}$ plane associated with the full dislocation; however, it appears it arises primarily from the stress field associated with the lowering of the indenter. In this case the dislocation arrives and is absorbed in an incoherent region of GB1–6,

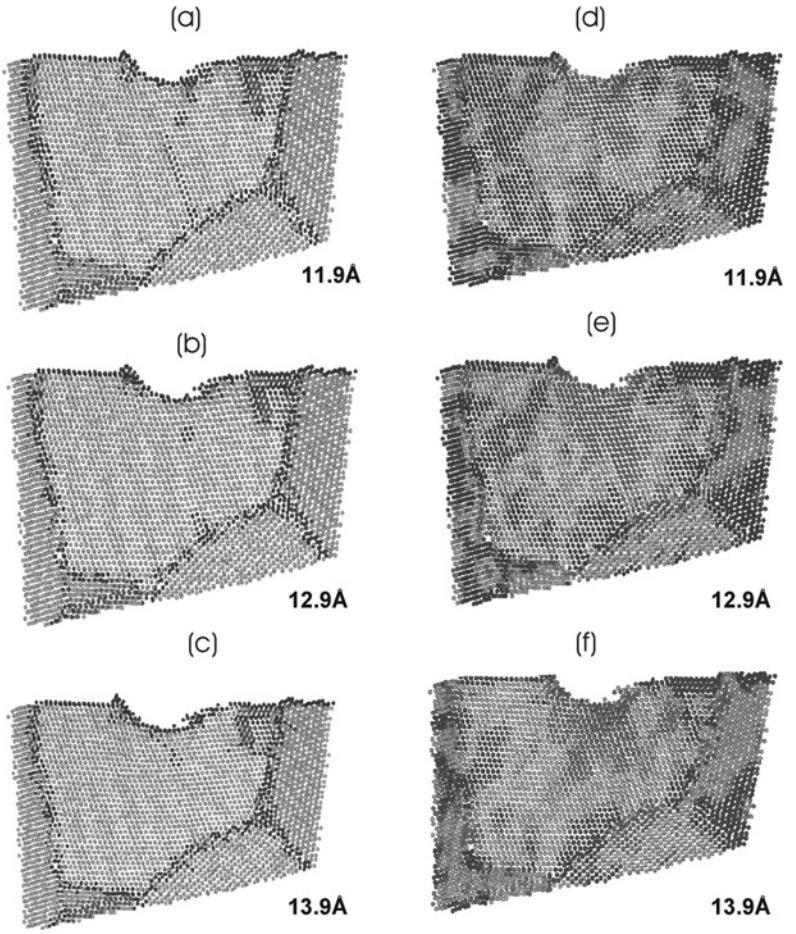

FIGURE 4.7. Dislocation absorbed at low stress region of the GB. (From Ref. 37.) See also Color Plate 2 after p. 000.

and associated with the absorption, significant discrete atomic activity was observed taking the form of atomic shuffling and also free-volume migration from neighboring incoherent regions toward the absorption site (see Fig. 5 in Ref. 37).

Figure 4.8 now displays the interaction of a third dislocation emitted from the plastic zone at an indentation depth of 21.7 Å in a slip plane parallel to those of the first two mentioned dislocations. As a full dislocation, this propagates toward GB1–6, during which time a new dislocation nucleates from GB1–6 and propagates into grain 1. The GB region to which the dislocation originating from the indenter region arrives is under compressive pressure (Fig. 4.8d) and its arrival leads to a further increase in compressive stress (Fig. 4.8e), which is relieved by the emission of the dislocation nucleated at the GB (Fig. 4.8f). This process of dislocation emission from the GB is accompanied by a decrease in the number of

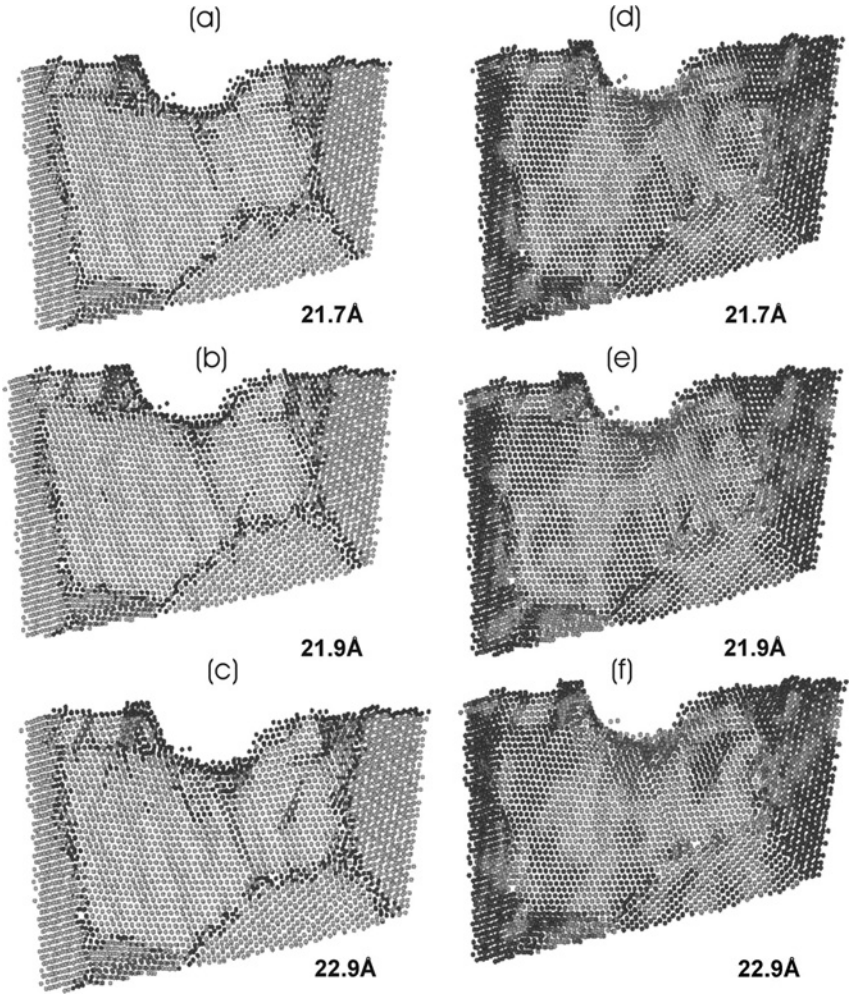

FIGURE 4.8. Dislocation emitted by high stress region of the GB. (From Ref. 37.) See also Color Plate 3 after p. 000.

GB dislocations and a rearrangement of the GB's dislocation network. We have also observed a free-volume migration along the GB toward the nucleation site that occurs after the emission of the full dislocation, i.e., the leading and the trailing partials, from the GB.

3.4. The Ratio between Indenter Size and Grain Size

The deformation processes that occur under the indenter reveal the importance of the GB network and, therefore, also the questions concerning the ratio between indenter and grain size.

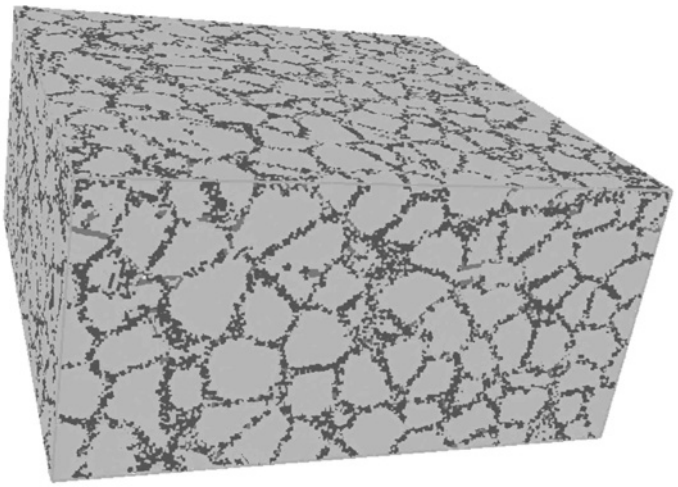

FIGURE 4.9. Computer-generated nc Au sample containing 750 fcc grains with an average diameter of 6 nm.

To investigate the role of indenter size with respect to grain size, simulations have been performed on a 6-nm mean grain size sample, using an indenter radius of 40 and 80 Å. For such a large indenter radius, large atomistic samples must be constructed in order to minimize the artifacts of the lateral PBCs (see Fig. 4.2), which include the strain field of the indenter interacting with its periodic image. Therefore, an nc sample containing 5 million atoms and consisting of 750 grains with an average grain diameter of 6 nm is created as shown in Fig. 4.9.

Figure 4.10 displays the force versus indentation depth curve (80 Å indenter) for this nc configuration during the loading phase, together with the unloading curves from approximately the yield point (point A), and from two other plastic points (points B and C). What becomes evident is that the load–indentation depth curve of the nc sample does not show any discrete reductions in load, and indeed there is no clear yield point as in the case of Fig. 4.4. We suggest that the absence of the so-called bursts in Fig. 4.10 is attributed, in addition to thermal noise, to two effects: (a) the high density of the GB network favors GB activity via GB sliding and GB migration; (b) dislocations are nucleated not only under the indenter, but also sequentially from several GBs in neighboring grains. With a smaller indenter size, the probed area (and the load) becomes smaller and some plastic events (like dislocation emission from GB) may become significant and thus more visible in the load–depth curve, as it has been seen for simulations using a 5-nm grain size sample indented with 4-nm tip radius[36] and also for experiment using 2.5-nm tip radius.[59]

The yield point in Fig. 4.10 is found at a load of 67.6 nN and an indentation depth of 4.8 Å. These values were estimated using the point where the

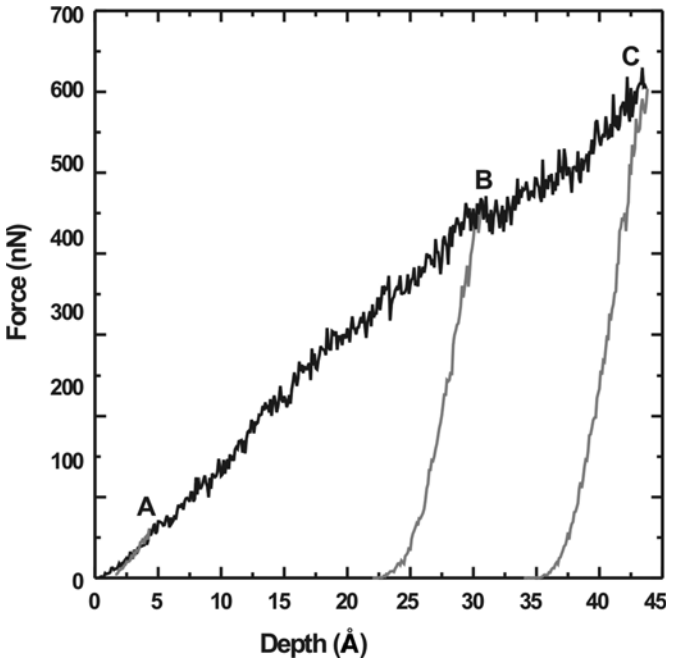

FIGURE 4.10. The force versus indentation depth curves, including the loading curve (green), the unloading form approximately the elastic point (red curve from point A), and the unloading curves from two plastic points (red curves from points B and C) corresponding to the unloading form 30.8 and 43.9 Å indentation depths, respectively.

elastic hertzian fitting curve deviates form the simulation curve. By the aid of a visualization of the crystalline order of the atoms, we observed a nucleation of partial dislocation from the GB just beneath the indenter at a depth of approximately 4 Å. Beyond the elastic regime, this partial dislocation extended into the whole grain eventually reaching the indentation surface. To investigate the anelastic nature of this event, the sample was unloaded at the depth of 4.2 Å (point A in Fig. 4.10), resulting in the unloading curve tracing back the original loading curve. The loading and unloading curves did not lie precisely over each other, indicating that despite being in the "elastic" regime, some GB relaxation does occur during this phase of the loading. The observation of plastic deformation before the apparent yield point of the load–indentation depth plot has also been noticed by Feichtinger *et al*.[36] during MD and CG simulations for the same grain size but with a different indenter radius and a smaller sample size (and different microstructure).

Using hertzian theory,[60] the Young's modulus can be calculated to investigate the effect of indenter size with respect to grain size in the elastic region. The loading curve in Fig. 4.10 up to the indentation depth of 4.8 Å was fitted to the isotropic

hertzian model[60]

$$P = \frac{4}{3} E^* \sqrt{R} h^{3/2} \tag{4.7}$$

where R is the radius of the indenter, h is the indenter depth, and E^* is the effective Young's modulus. The Young's modulus for the sample can be derived from the expression

$$E^* = \left(\frac{1 - v_s^2}{E_s} - \frac{1 - v_i^2}{E_i} \right)^{-1} \tag{4.8}$$

where $E_{i,s}$ and $\nu_{i,s}$ refer to the Young's modulus and the Poisson ratio of the indenter and the sample. The idealized indenter is simulated by a strong repulsive radial force that represents an infinitely hard indenter and thus $E_i = \infty$. The Poisson ratio equals 0.34, according to the Cleri and Rosato potential.

The above-mentioned procedure was applied for deriving Young's modulus for the 6-nm nc sample and for a single crystal of a comparable size [3.6 million atoms with a (111) surface] both using an indenter of 40 Å and of 80 Å. The strain fields at yield and the corresponding measured values for the Young's modulus are given in Fig. 4.11 for all samples and indenter radii considered. The elastic modulus derived for the single crystal does not depend on the indenter size and equals 86 GPa. This value is considerably lower than the value derived from the Cleri–Rosato potential (using elastic constants), which amounts 123.7 GPa for the (111) direction. The differences can be ascribed to temperature effects: indeed, the value derived from the potential is at 0 K, whereas the value derived from MD indentation curves is for 300 K. It was earlier shown[36] that Young's modulus derived from conjugant gradient methods, which do not include temperature, are of the same order as the values obtained directly from the elastic constants of the potential. For the nc Au structures, there is however a size effect in Young's modulus: a value of 51.6 GPa was derived from the indentation curve using an indenter of 40 Å and a value of 42.7 GPa using an indenter of 80 Å. The elastic modulus is, for both indentation curves, lower than its value for a single crystal, and additionally, the values seem to depend on the ratio between indenter- and grain size. The lower elastic modulus at a very small grain size compared to the single crystal, a trend that is also observed in some experiments,[22,61] might indicate a softening effect due the presence of the dense GB network where the GBs and triple junctions are assumed to have a lower Young's modulus.

The size effect related to the indenter size can be understood in terms of a shielding effect of GBs for the strain field under the indenter. Figure 4.11 shows that for the same type of indenter, the strain field extends deeper into the single crystal material than into an nc structure. These observations show that the obtained Young's modulus is not a value that represents the bulk material but a local average value representing the strained region below the indenter. The size of the probed region depends on the indenter size, and the specific nature of this region will depend on the grain size and GB network structure. The ratio between the

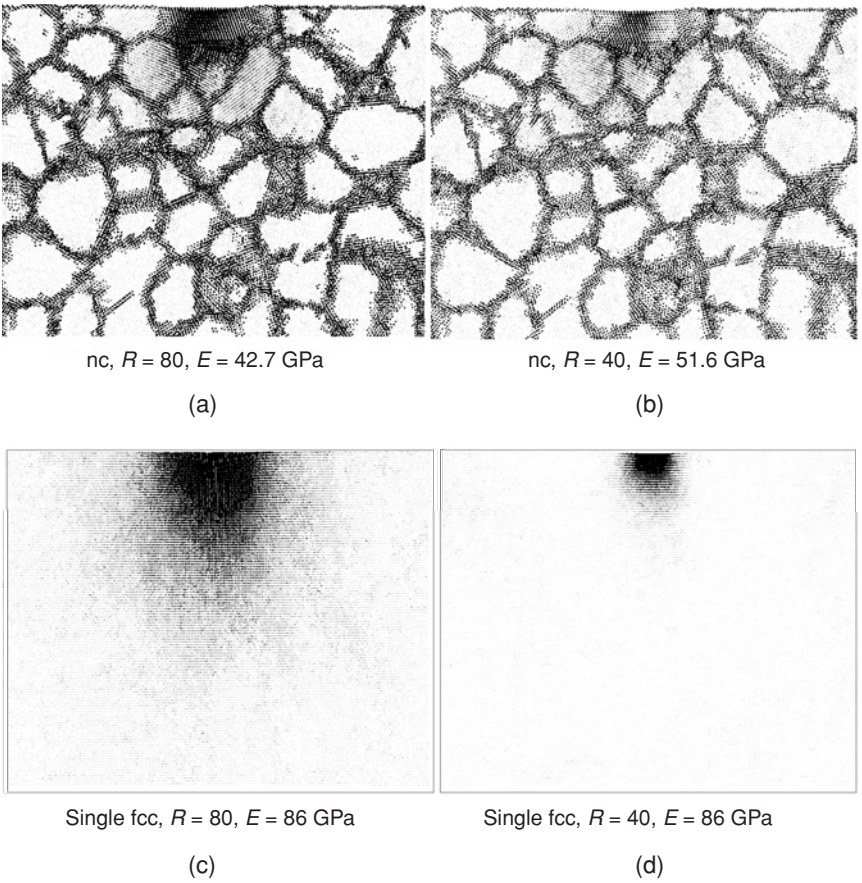

FIGURE 4.11. Strain field of a section of the sample during the elastic regime of the nanocrystalline sample (5-nm grain size, 750 grains) indented with (a) an indenter radius of 80 Å, (b) an indenter radius of 40 Å; and the single fcc crystal (3.6 millions of atoms) indented with (c) an indenter radius of 80 Å, (d) an indenter radius 40 Å. Vector displacements of 2 Å and more are in black and vector displacements of 0 Å are in white.

indenter size and the grain size influences the number of grains that are involved in the indentation, and this determines the deformation processes that are activated. Figure 4.12 shows the structure of the grains at the surface during two different indentation depths. The picture shows that deformation mechanisms are also induced in grains that are not directly involved in the indentation. Due to the spherical shape of the indenter and the nonsymmetric shape and position of the grains relative to the indenter, nonhomogeneous stress (strain) fields are generated around the indenter, inducing grain rotation, even in grains that are not in direct contact with the indenter. The rotation is often accommodated by dislocation activity.

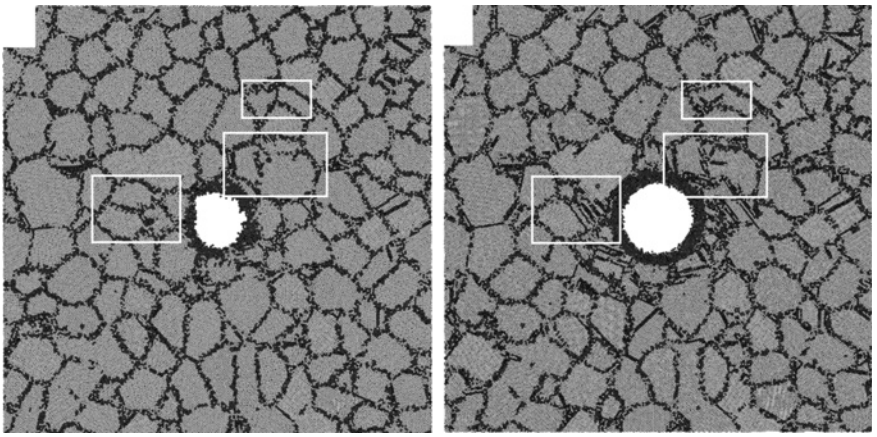

FIGURE 4.12. (a) and (b) are the atomic sections of the GB structure for two different indentation depths, where the squared regions indicate GB migration (with subsequent growth and shrinkage of associated grains) as well as extensive partial dislocation activity resulting, in some cases, in mechanical twinning to accommodate such grain coalescence and rotation.

3.5. Material Pileup

During the loading phase of the indentation simulation of the sample containing 750 grains with a mean grain size value of 5 nm and an indenter radius of 80 Å, a material pileup at the surface of the sample around the indenter is observed.

Figure 4.13 displays a section of atoms of the 5-nm grain size sample before and at loading to an indentation depth of 42.7 Å. We observe in this figure the formation of a material pileup on the left side at the edge of the contact area between the indenter and the sample (arrow in Fig. 4.13b). This material pileup began to form at a depth of about 20 Å and consists of predominantly an fcc structure containing a number of hcp-coordinated 111 planes. Such a phenomenon has also been observed by Christopher *et al*.[62] in fcc silver. The set of parallel stacking faults (two adjacent 111 red planes) observed in the grain on which the pileup occurred indicates that the material pileup occurred via a slip mechanism. Inspection of the entire rim of the indentation profile reveals that whether or not such a material pileup occurs is strongly dependent on the particular orientation of the grain at a given location. Figure 4.14 shows the surface contour map of the indented surface. The pileup is observed to occur preferentially on grains that are close to a (100) surface orientation. In particular, the grain where the material pileup is observed in Fig. 4.13a,b has a surface orientation close to (100), whereas on the right side of Fig. 4.13 the grain surface is close to (112) orientation. This result is in agreement with the results of Christopher *et al*.[62] who have noticed that the piling-up of material occurs preferentially via a slip along the close-packed planes. Indeed it

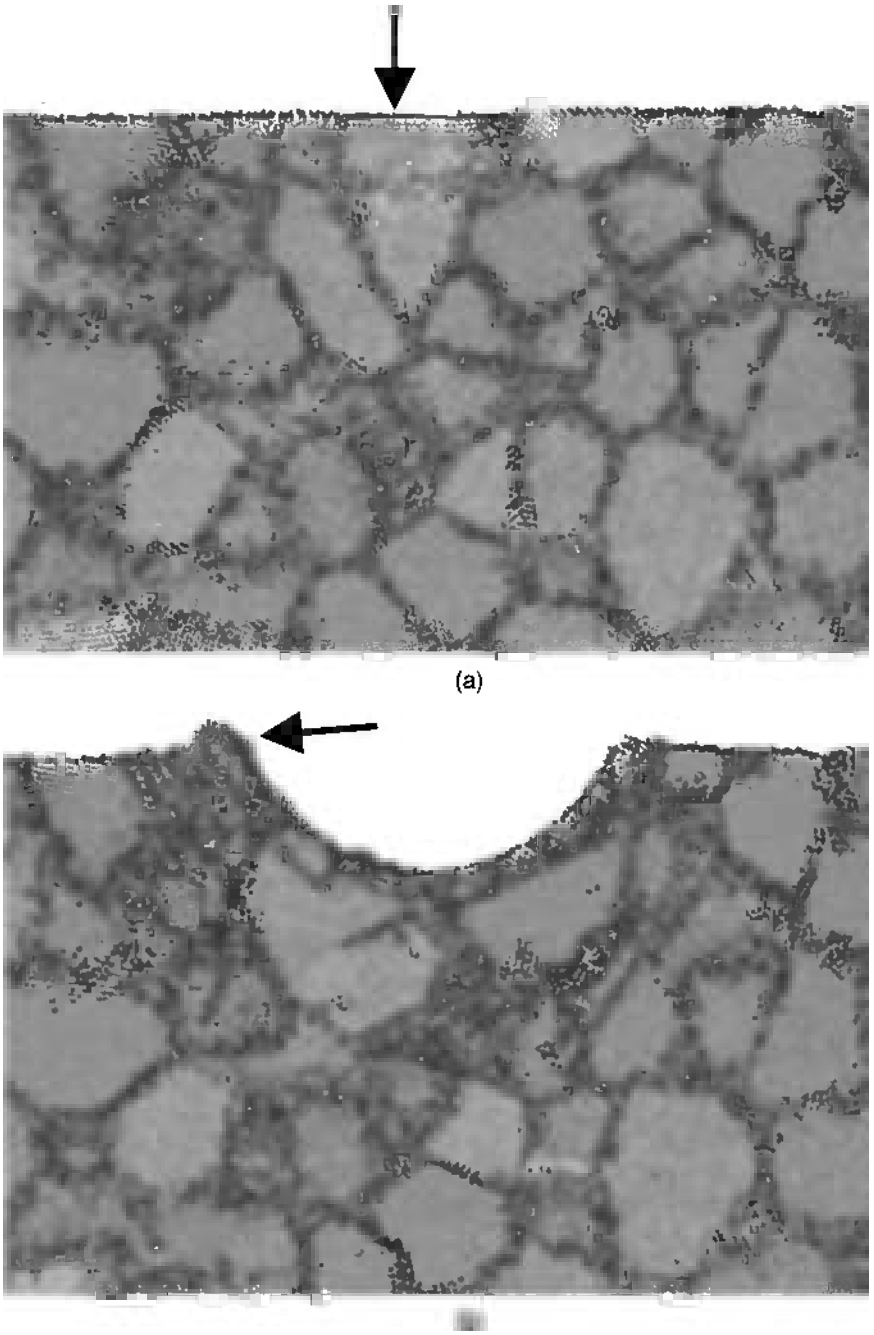

FIGURE 4.13. A section of atoms of the 6-nm grain size sample (a) before and (b) after loading at an indentation depth of 42.7 Å.

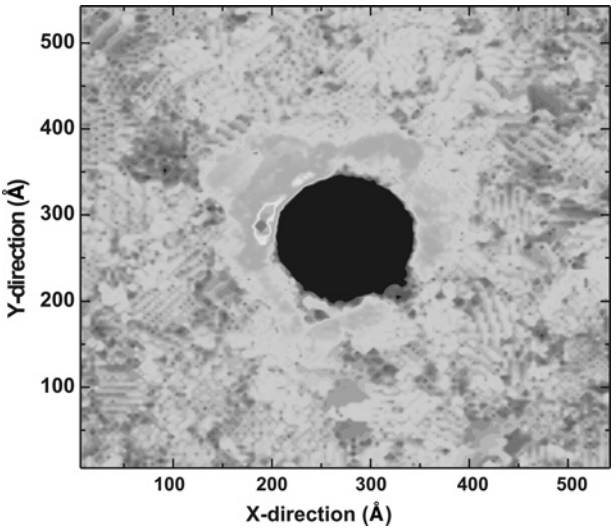

FIGURE 4.14. Surface contour map of indented region displaying irregular pileup around the rim of the indenter contact area. Here blue represents a surface height of 134 Å and red a height of 151 Å.

has been recently suggested, in Ref. 63, by using 2D simulation of nanoindentation of a single hexagonal Al crystal, that pileup requires cross-slip to take place during deformation. In contrast to single crystals,[64] the cross-slip is not necessary in a 3D nc material, since the GB network plays the role of dislocation source and then can allow the slip along plane directions that is favorable for the pileup. We note that in the experimental regime, the phenomenon of pileup is generally believed to arise from mass transport predominantly via (biased) diffusion mechanisms. The timescale restriction of atomistic simulations precludes such activity, allowing the possibility of observing pileup only via the much more rapid multiple slip activity on (111) planes, which we see, through Figs. 4.12 and 4.13, is a sensitive function of the grain orientation with respect to the indenter and the surface orientation.

3.6. Unloading Phase

During the indenter retraction (unloading phase begun at points B and C in Fig. 4.10), the contact area maintains its spherical indentation impression. Figure 4.15 displays the resulting profile upon unloading. During such unloading, significant plastic activity was observed. For example, the back propagation of leading partial dislocations (circled in Fig. 4.15a) to the GB region where it originally nucleated and also the nucleation of new partial dislocations (circled in Fig. 4.15c) and their propagation through entire grains was observed, resulting a mechanical twinning.

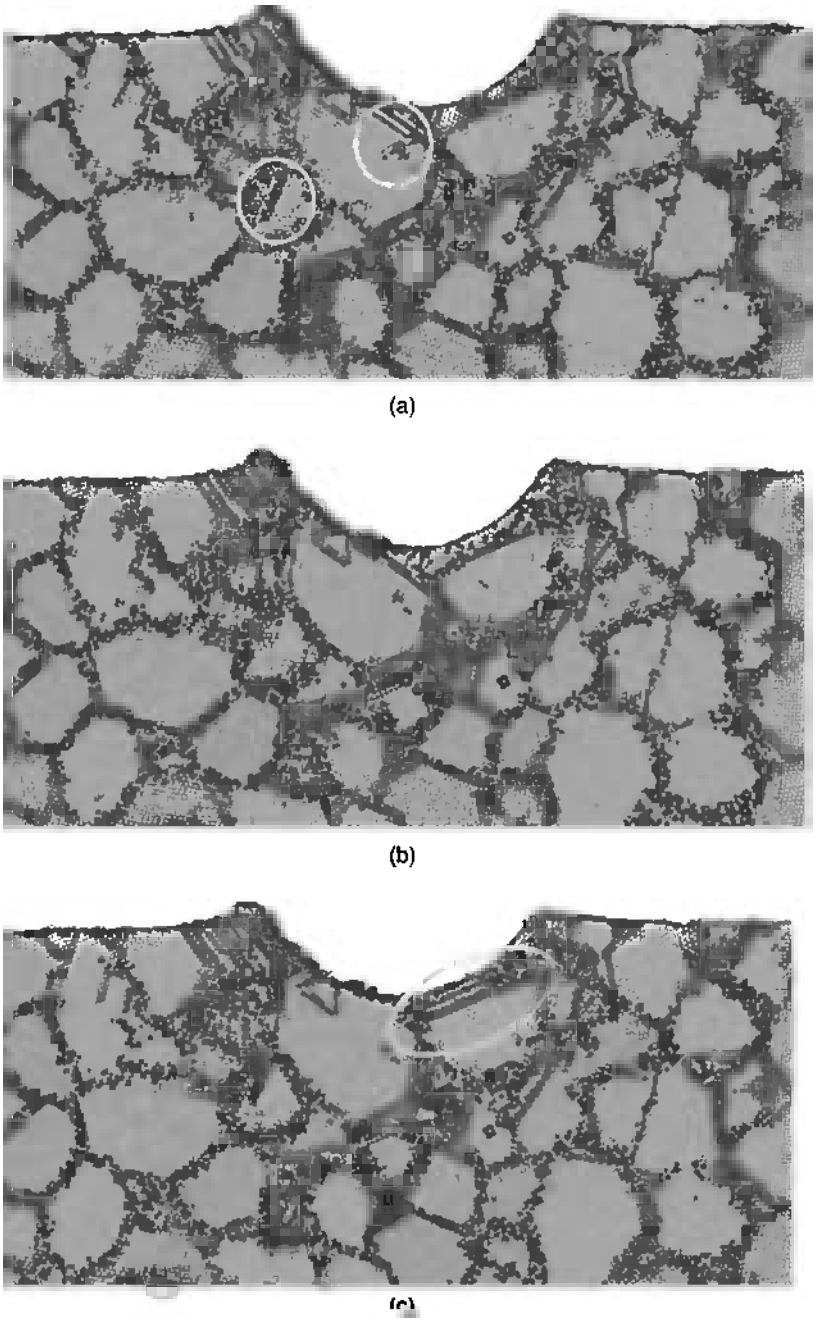

FIGURE 4.15. Snapshots of the same section of atoms involved in Fig. 4.13 during the unloading phase from point C indicated in Fig. 4.10. Depths (a) 45 Å, (b) 38.9 Å, and (c) 35.3 Å, which correspond to zero load. The circled regions in Fig. 4.15a,c show plastic deformation experienced by this section of atoms during the unloading phase.

In Fig. 4.10, two unloading curves are shown. The load recovery takes place over 6.8 and 6.4 Å for B and C unloading curves, respectively. This is about 15 and 22% of the total deformation. Despite the significant number of plastic events occurring during the unloading phase (Fig. 4.15), the unloading curves were used for the determination of the hardness H via $H = P_{\max}/A$ where $P_{\max}$ is the maximum load and A is the contact area determined by atomic visualization. The obtained values were 4.35 and 4.09 GPa for the B and C unloading curves, respectively, revealing a slight indentation size effect (hardening with increasing depth). This effect has also been observed experimentally by Saha and Nix[65] during the indentation of Al films where they have seen that the hardness decreases with increasing depth of indentation at extremely small depths. The values obtained here should not be taken as absolute values of the material because of the presence of plastic recovery during unloading phase. Nevertheless, we think that the observed indentation size effect is intrinsic to the nc material, which might be supported by the fact that load recovery takes place over similar depths, and so we can assume that the plastic recovery is similar for the two unloading curves.

4. DISCUSSION AND OUTLOOK

MD simulations have been very useful in detecting the possible deformation mechanisms in nc metals, under tensile load as well as under the load of an indenter. They have the advantage of capturing the atomic scale, which is missing in both experiments as well as continuum simulation techniques that mimic larger length scales. Therefore, these types of simulations have the power to reveal all possible deformation mechanisms, eventually relating them to the atomic scale structure of the GBs. However, MD simulations cannot quantitatively capture, at the present stage of development, any property that is controlled by a rate-limiting process. The high-stress/short-time restrictions inherent to MD make it impossible to determine the true rate-limiting processes, which involve long-range diffusion processes with mass transport as well as significant GB migration. When comparing the results of simulation with actual nanoindentation experiments, these issues must not be forgotten, with atomistic results being always considered as the early stage regime of a high-speed indentation simulated experiment.

At present there is no clear path for solving the timescale problem, although a number of attempts suitable for small systems containing limited disorder exist in the literature.[66,67] With modern parallel computing platforms containing increasingly larger numbers of processors the length-scale problem can be addressed by performing MD on atomic configurations involving much larger numbers of atoms. For example, 1 billion atoms will allow a nanoindentation simulation of an atomistic region with cubic volume of side length $\sim$250 nm. An alternative approach to the length-scale problem would be to employ the quasi-continuum method, which links disordered regions, requiring a complete atomistic description, with elastically deformed lattice regions that can be described using a

continuum approach.[68,69] This has been recently done to investigate the indenter radius size effect on an Au(100) surface, using indenter radii up to 700 Å for sample volumes in the micron range.[70] A disadvantage of this technique is that it is a 0-K method and thus the dynamical effects of temperature cannot be investigated. Moreover, there is at present no clear way to include an atomic scale representation of material microstructures such as that of an nc GB network.

The simulation work presented in this chapter uses an ideal spherical indenter with a radius of up to 80 Å. Such radii are small but comparable to typical diamond indenter tip dimensions, especially after continued operations. A clear improvement over such an ideal frictionless spherical indenter model would be to describe the indenter at the atomic scale, that is, to simulate the indenter as a MD atomic configuration. This has been performed and for this a hard diamond indenter has been constructed using simple model potentials such as a Lennard–Jones potential to capture the essential hardness of the diamond indenter.[34,71] This would naturally include the effect of friction in the indentation simulation and also lead to more complex atomic indenter–substrate interactions in which substrate atoms jump onto the indenter forming early necking between the tip and the substrate, and also localized melting.[71]

In summary, atomistic simulations of nanoindentation on nc substrates have revealed a highly complex class of atomic processes that are a sensitive function of the GB structure beneath the indenter. The principle finding is the ability of the nano-sized GB network to accommodate the lowering of the indenter by means of GBS and emission of partial and full dislocations, which interact strongly with the surrounding GB structure. Such an interaction involves structural changes in the network via atomic shuffling and stress-assisted free-volume migration, changing locally the structure in theGB, and allowing the redistribution of peak values of shear stress and compressive hydrostatic pressure in neighboring parts of the GB network. Furthermore, collective grain activity is observed via cooperative sliding, grain rotation, and coalescence. As already stated, these processes detail a list of possibilities of what can happen in an indented nc environment, complimenting experiment and providing a guide to the interpretation of experimental data. Alone, such simulations cannot provide the answer to the true rate-limiting processes that contribute to the experimentally derived hardness determined via nanoindentation; nevertheless, it is via the synergy between modeling and experiment that important advances can be made in our understanding of the mechanical properties of metallic nc systems.

REFERENCES

1. J. R. Weertman, Mechanical behaviour of nanocrystalline metals, in *Nanostructured Materials: Processing, Properties, and Potential Applications* (William Andrew Publishing, Norwich, 2002), Chap. 10.

2. K. S. Kumar, H. Van Swygenhoven, and S. Suresh, Mechanical behavior of nanocrystalline metals and alloys, *Acta Mater.* **51**, 5743–5774 (2003).
3. F. Dalla Torre, H. Van Swygenhoven, and M. Victoria, Nanocrystalline electrodeposited Ni: Microstructure and tensile properties, *Acta Mater.* **50**, 3957–3970 (2002).
4. F. Dalla Torre, *Microstructure and Mechanical Properties of Nanocrystalline Ni Produced by Three Different Synthesis Techniques*, Ph.D. Thesis entitled Microstructure and Mechanical Properties of Nanocrystalline Ni produced by Three Different Synthesis Techniques, Ecole Polytechnique Fédérale de Lausanne, Switzerland, 2003.
5. Y. M. Wang and E. Ma, Three strategies to achieve uniform tensile deformation in a nanostructured metal, *Acta Mater.*, in press.
6. Z. Budrovic, H. Van Swygenhoven, P. M. Derlet, S. Van Petegem, and B. Schmitt, Plastic deformation with reversible peak broadening in nanocrystalline Ni, *Science*, **304**, 273–276 (2004).
7. H. Van Swygenhoven, M. Spacer, and A. Caro, Microscopic description of plasticity in computer generated metallic nanophase samples: A comparison between Cu and Ni, *Acta Mater.* **47**, 3117–3126 (1999).
8. H. Van Swygenhoven, D. Farkas, and A. Caro, Grain boundary structures in nanocrystalline metals at the nanoscale, *Phys. Rev. B* **62**, 831–838 (2000).
9. H. Van Swygenhoven and P. M. Derlet, Grain-boundary sliding in nanocrystalline fcc metals, *Phys. Rev. B* **64**, 224105/1–9 (2001).
10. P. M. Derlet and H. Van Swygenhoven, On length scale effects in molecular dynamics simulations of the deformation properties of nano-crystalline metals, *Scr. Mater.* **47**, 719–724 (2002).
11. H. Van Swygenhoven, Grain boundaries and dislocations, *Science* **296**, 66–67 (2002).
12. H. Van Swygenhoven, P. M. Derlet, Z. Budrovic, and A. Hasnaoui, Unconventional deformation mechanism in nanocrystalline metals? *Z. Met. kd.* **10**, 1106–1110 (2003).
13. J. Schiøtz, F. D. Di Tolla, and K. W. Jacobsen, Softening of nanocrystalline metals at very small grain sizes, *Nature* **391**, 561–563 (1998).
14. J. Schiøtz and K. W. Jacobsen, A maximum in the strength of nanocrystalline copper, *Science* **301**, 1357–1359 (2003).
15. P. Keblenski, D. Wolf, S. R. Phillpot, and H. Gleiter, Structure of grain boundaries in nanocrystalline palladium by molecular dynamics simulation, *Scr. Mater.* **41**, 631–636 (1999).
16. V. Yamakov, D. Wolf, M. Salazar, S. R. Phillpot, and H. Gleiter, Length-scale effects in the nucleation of extended dislocations in nanocrystalline Al by molecular-dynamics simulation, *Acta Mater.* **49**, 2713–2722 (2001).
17. A. P. Sutton and R. W. Balluffi, *Interfaces in Crystalline Materials* (Clarendon, Oxford, 1995), Chap. 1.
18. H. Van Swygenhoven, P. M. Derlet, and A. Hasnaoui, Atomic mechanism for dislocation emission from nanosized grain boundaries, *Phys. Rev. B* **66**, 024101/1–8 (2002).
19. P. M. Derlet, A. Hasnaoui, and H. Van Swygenhoven, Atomistic simulations as guidance to experiments, *Scr. Mater.* **49**, 629–635 (2003).
20. A. Hasnaoui, H. Van Swygenhoven, and P. M. Derlet, Cooperative processes during plastic deformation in nanocrystalline FCC metals—A molecular dynamics simulation, *Phys. Rev. B* **66**, 184112/1–8 (2002).
21. A. Hasnaoui, H. Van Swygenhoven, and P. M. Derlet, Dimples on nanocrystalline fracture surfaces as evidence for shear plane formation, *Science* **300**, 1550–1552 (2003).
22. W. C. Oliver and G. M. Pharr, An improved technique for determining hardness and elastic modulus using load and displacement sensing indentation experiments, *J. Mater. Res.* **7**, 1564–1583 (1992).
23. W. W. Gerberich, J. C. Nelson, E. T. Lilleodden, P. Anderson, and J. T. Wyrobek, Indentation induced dislocation nucleation: The initial yield point, *Acta Mater.* **44**, 3585–3598 (1996).
24. S. A. Joyce and J. E. Houston, A new force sensor incorporating force-feedback control for interfacial force microscopy, *Rev. Sci. Instrum.* **62**, 710–715 (1991).
25. J. T.-M. De Hosson, G. Palasantzas, T. Vystavel, and S. Koch, Nanosized metal clusters: Challenges and opportunities, *J. Org. Met.* **56**, 40–46 (2004).

26. Y. Zhou, U. Erb, K. T. Aust, and G. Palumbo, The effects of triple junctions and grain boundaries on hardness and Young's modulus in nanostructured Ni–P, *Scr. Mater.* **48**, 825–830 (2003).
27. J. D. Kiely, R. Q. Hwang, and J. E. Houston, Effect of surface steps on the plastic threshold in nanoindentation, *Phys. Rev. Lett.* **81**, 4424–4427 (1998).
28. S. G. Corcoran and R. J. Colton, Anomalous plastic deformation at surfaces: Nanoindentation of gold single crystals, *Phys. Rev. B* **55**, R16057–R16060 (1997).
29. W. W. Gerberich, D. E. Kramer, N. I. Tymiak, A. A. Volinsky, D. F. Bahr, and M. D. Kriese, Nanoindentation-induced defect-interface interactions: Phenomena, methods and limitations, *Acta Mater.* **47**, 4115–4123 (1999).
30. E. T. Lilleodden, J. A. Zimmermann, S. M. Foiles, and W. D. Nix, Atomistic simulations of elastic deformation and dislocation nucleation during nanoindentation, *J. Mech. Phys. Solids* **51**, 901–920 (2003).
31. J. A. Zimmermann, C. L. Kelchner, P. A. Klein, J. C. Hamilton, and S. M. Foiles, Surface step effects on nanoindentation, *Phys. Rev. Lett.* **87**, 165507/1–4 (2001).
32. C. L. Kelchner, S. J. Plimpton, and J. C. Hamilton, Surface step effects on nanoindentation, *Phys. Rev. B* **58**, 11085–11088 (1998).
33. J. Li, K. J. Van Vliet, T. Zhu, S. Yip, and S. Suresh, Atomistic mechanisms governing elastic limit and incipient plasticity in crystals, *Nature* **418**, 307–310 (2002).
34. D. Christopher, R. Smith, and A. Richter, Atomistic modelling of nanoindentation in iron and silver, *Nanotechnology* **12**, 372–383 (2001).
35. K. J. Van Vliet, J. Li, T. Zhu, S. Yip, and S. Suresh, Quantifying the early stages of plasticity through nanoscale experiments and simulations, *Phys. Rev. B* **67**, 104105/1–15 (2003).
36. D. Feichtinger, P. M. Derlet, and H. Van Swygenhoven, Atomistic simulations of spherical indentations in nanocrystalline gold, *Phys. Rev. B* **67**, 024113/1–4 (2003).
37. A. Hasnaoui, P. M. Derlet, and H. Van Swygenhoven, Interaction between dislocations and grain boundaries during nanoindentation of nanocrystalline Au—Molecular dynamics simulations, *Acta Mater.* **52**, 2251 (2004).
38. P. M. Derlet and H. Van Swygenhoven, Atomic positional disorder in fcc metal nanocrystalline grain boundaries, *Phys. Rev. B* **67**, 014202/1–8 (2003).
39. L. Verlet, Computer "experiments" on classical fluids, I: Thermodynamical properties of lennard-jones molecules, *Phys. Rev.* **159**, 98–103 (1967).
40. C. W. Gear, *Numerical Initial Value Problems in Ordinary Differential Equations* (Prentice-Hall, Englewood Cliffs, NJ, 1971).
41. D. Frenkel and B. Smit, *Understanding Molecular Simulation: From Algorithms to Applications* (Academic Press, New York, 2002).
42. M. Parrinello and A. Rahman, Polymorphic transitions in single crystals: A new molecular dynamics method, *J. Appl. Phys.* **52**, 7182–7190 (1981).
43. D. Pettifor, *Bonding and Structure of Molecules and Solids* (Oxford University Press, Oxford, 1995).
44. M. Finnis, *Atomic Forces in Condensed Matter* (Oxford University Press, Oxford, 2003).
45. M. S. Daw and M. T. Baskes, Embedded-atom method: Derivation and application to impurities, surfaces, and other defects in metals, *Phys. Rev. B* **29,** 6443–6453 (1984).
46. K. W. Jacobsen, J. K. Nørskov, and M. J. Puska, Interatomic interaction in the effective-medium theory, *Phys. Rev. B* **35**, 7423–7442 (1987).
47. F. Cleri and V. Rosato, Tight-binding potentials for transition metals and alloys, *Phys. Rev. B* **48**, 22–33 (1993).
48. G. Z. Voronoi, Nouvelles applications des paramètres continus à la théorie des formes quadratiques. Deuxième mémoire: Recherches sur les parallélloèdres primitifs, *Reine Angew. Math* **134**, 199–287 (1908).
49. P. M. Derlet and H. Van Swygenhoven, The role played by two parallel free surfaces in the deformation mechanism of nanocrystalline metals: A molecular dynamics simulation, *Phil. Mag. A* **82**, 1–15 (2002).

50. D. J. Honeycutt and H. C. Andersen, Molecular dynamics study of melting and freezing of small lennard-jones cluster, *J. Phys. Chem.* **91**, 4950–4963 (1987).
51. J. Cormier, J. M. Rickman, and T. J. Delph, Stress calculation in atomistic simulations of perfect and imperfect solids, *J. Appl. Phys.* **89**, 99–104 (2001).
52. A. Hasnaoui, H. Van Swygenhoven, and P. M. Derlet, On non-equilibrium grain boundaries and their effect on thermal and mechanical behaviour: A molecular dynamics computer simulation, *Acta Mater.* **50**, 3927–3939 (2002).
53. V. Yamakov, D. Wolf, S. R. Phillpot, and H. Gleiter, Grain-boundary diffusion creep in nanocrystalline palladium by molecular-dynamics simulation, *Acta Mater.* **40**, 61–73 (2002).
54. H. Van Swygenhoven, P. M. Derlet, and A. Hasnaoui, An atomic mechanism for dislocation emission from nanosized grain boundaries, *Phys. Rev. B* **66**, 024101/1–8 (2002).
55. P. M. Derlet, H. Van Swygenhoven, and A. Hasnaoui, Atomistic simulation of dislocation emission in nanosized grain boundaries, *Phil. Mag.* **83**, 3569–3575 (2003).
56. V. Yamakov, D. Wolf, S. R. Phillpot, A. K. Mukherjee, and H. Gleiter, Deformation-mechanism map for nanocrystalline metals by molecular-dynamics simulation, *Nature Mat.* **3**, 43–47 (2004).
57. H. Van Swygenhoven, P. M. Derlet, and A. G. Frøseth. Nanocrystalline metals: stacking fault energies and slip, *Nature Mater.* **3**, 399 (2004).
58. A. G. Frøseth, P. M. Derlet, and H. Van Swygenhoven, The Influence of grown-in twin boundaries on the dislocation mechanisms in nc-Al, Ni, and Cu, *App. Phys. Lett.* **85**, 5863 (2004).
59. L. X. Ma and W. Yang, Molecular dynamics simulation on burst and arrest of stacking faults in nanocrystalline Cu under nanoindentation, *Nanotechnology* **14**, 1208–1215 (2003).
60. A. C. Fischer-Cripps, The hertzian contact surface, *J. Mat. Sci.* **34**, 129–136 (1999).
61. M. Liu, B. Shi, J. Guo, X. Cai, and H. Song, Lattice constant dependence of elastic modulus for ultrafine grained mild steel, *Scr. Mater.* **49**, 167–171 (2003).
62. D. Christopher, R. Smith, and A. Richter, Atomistic modelling of nanoindentation in iron and silver, *Nanotechnology* **12**, 372–383 (2001).
63. R. E. Miller, L. E. Shilkrot, and W. A. Curtin, A coupled atomistics and discrete dislocation plasticity simulation of nanoindentation into single crystal thin films, *Acta Mater.* **52**, 271–284 (2004).
64. R. Smith, D. Christopher, and S. D. Kenny, Defect generation and pileup of atoms during nanoindentation of Fe single crystals, *Phys. Rev. B* **67**, 245405/1–10 (2003).
65. R. Saha and W. D. Nix, Effects of the substrate on the determination of thin film mechanical properties by nanoindentation, *Acta Mater.* **50**, 23–38 (2002).
66. A. F. Voter, Hyperdynamics: Accelerated molecular dynamics of infrequent events, *Phys. Rev. Lett.* **78**, 3908–3911 (1997).
67. W. Cai, M. H. Kalos, M. de Koning, and V. V. Bulatov, Importance sampling of rare transition events in markov processes, *Phys. Rev. E* **66**, 046703/1–10 (2002).
68. E. Tadmor, M. Ortiz, and R. Phillips, Quasicontinuum analysis of defects in solids, *Phil. Mag. A* **73**, 1529–1563 (1996).
69. J. Knap and M. Ortiz, An analysis of the quasicontinuum method, *J. Mech. Phys. Solids* **49**, 1899–1923 (2001).
70. J. Knap and M. Ortiz, Effect of indenter-radius size on Au(001) nanoindentation, *Phys. Rev. Lett.* **90**, 226102/1–4 (2003).
71. Y. Hualiang, J. B. Adams, and L. G. Hector, Jr., Molecular dynamics simulation of high-speed nanoindentation, *Modelling Simul. Mater. Sci. Eng.* **10**, 319–329 (2002).
72. A. Gouldstone, H. J. Koh, K. Y. Zeng, A. E. Giannakopoulos, and S. Suresh, Discrete and continuous deformation during nanoindentation of thin films, *Acta Mater.* **48**, 2277–2295 (2000).

5

Electron Microscopy Characterization of Nanostructured Coatings

Jeff Th. M. De Hosson, Nuno J. M. Carvalho, Yutao Pei, and Damiano Galvan

Department of Applied Physics, Materials Science Center and Netherlands Institute for Metals Research, University of Groningen, Nijenborgh 4, 9747 AG Groningen, The Netherlands

1. INTRODUCTION

This chapter deals with fundamental and applied concepts in nanostructured coatings, in particular focusing on the characterization with high-resolution (transmission) electron microscopy. Generally speaking, microscopy in the field of materials science is devoted to link microstructural observations to properties and in fact the microstructure–property relationship is in itself a truism. In particular, mechanical properties of materials are structure sensitive. The microstructural features in turn are determined by chemical composition and processing, and consequently, advanced microstructural investigations require a microscope with a resolving power in the order of a nanometer or even better. However, the actual linkage between structural aspects of defects in a material studied by microscopy and its physical property is almost elusive. The reason is that various physical properties are actually determined by the collective behavior of defects rather than by the behavior of one singular defect itself. For instance, there exists a vast amount of electron microscopy analyses in the literature on *ex situ* deformed materials, which try to link observed patterns of defects to the mechanical behavior characterized by macroscopic deformation tests. However, in spite of the enormous effort that has been put in both theoretical and experimental work, a clear physical picture that could predict the stress–strain curve on the basis of these microscopy observations is still lacking.

There are at least two reasons that hamper a straightforward correlation between microscopic structural information and materials properties: one fundamental and one practical reason. Of course, it has been realized already for a long time

that in the field of dislocations, disclinations, and interfaces in materials, we are facing highly nonlinear and nonequilibrium effects. The defects determining many physical properties are in fact not in thermodynamic equilibrium and their behavior is very much nonlinear. This is a fundamental problem, since there does not exist an adequate physical and mathematical basis for a sound analysis of these highly nonlinear and nonequilibrium effects. Nevertheless, the situation is not hopeless, since there are two approaches to circumvent these problems, and microscopy contributes still quite a lot.

One has to do with numerical simulations of the evolution of defect structures, which incorporate the behavior of individual defects as known from both the classical theory and the microscopy observations of individual defects. It is often claimed that advanced microstructural investigations require a microscope with a resolving power in the order of a nanometer or even better. It has been shown that in some cases it is crucial to have information on an atomic level available, but surely it is not always necessary and sometimes rather more appropriate to image defects on a micrometer scale instead, to correlate the structural information to physical properties. Actually new measures have to be introduced at a different length scale. Therefore, it is argued that a more quantitative evaluation of the structure–property relationship of a coating requires sometimes a de-emphasis of analysis on an atomic scale, and an extra emphasis on *in situ* measurements. In addition, only recently ultrahigh-resolution microscopes, both in transmission and in scanning modes, make analyses of chemical composition at subnanometer scale and *in situ* measurements feasible.

Another more practical reason why a quantitative electron microscopy evaluation of the structure–property relationship of coatings is hampered has to do with statistics. As a matter of course this is not specific for a particular material system. Metrological considerations of quantitative electron microscopy from crystalline materials put some relevant questions to the statistical significance of the electron microscopy observations. In particular, in situations where there is only a small volume fraction of defects present or a very inhomogeneous distribution, statistical sampling may be a problem. In particular, for hard coatings the key challenge is to avoid grain boundary sliding, but as far as the toughness is concerned more compliant (amorphous) boundary layers might be more beneficial. Actually, boundary sliding may have a positive effect on wear-resistant coatings, by optimizing the ratio of hardness over the stiffness.[1,2] Not only grain boundary sliding seems to limit the further increase in hardness of superhard nanostructured coatings that are mainly used for dry machining tools, but also Coble creep at the higher temperature involved during dry machining may come into operation.[3] At first sight, dislocation motion becomes suppressed upon grain refinement but softening is expected if grain boundary diffusion predominates over bulk diffusion. As a rule of thumb, all the phases in a nanostructured hard coating must be made of strong material and the interfaces must be made sharp by optimizing the hardness–stiffness ratio. However, this is a too global view because knowledge of the deformation mechanisms in the nanostructured coatings is simply very rudimentary at the moment. For

instance, grain boundary ledges for the generation of dislocations may become increasingly important in the production of dislocations at smaller grain sizes. When the grain size drops below 20 nm or so in a homogeneous nanostructured material, the number of triple junctions per unit volume becomes appreciably large. Since the triple points possess disclination character, they may contribute substantially to the ductility of nanocomposites and softening is expected at the smallest grain sizes.[1,2] The misorientation across short grain boundaries in nanostructured materials may only be partly accomplished by grain boundary dislocations, and at small sizes the number of disclination dipoles will be increased. Further, crack deflection, crack branching, intergranular fracture, and transgranular fracture are probably very much different in these nanostructured materials compared to their micrometer-sized counterparts. In evaluating the performance of a nanostructured coating it is essential to examine the defect content as well as the microstructural features,[4] in particular the grain size dispersion, distribution of interface misorientation angles, and internal strains. Clearly, defects, such as microcracks, can completely mask the intrinsic strength of the nanostructured coatings. In the past, the low E-modulus of nanostructured materials has been often attributed to the unusual grain boundary structures present, but this phenomenon is actually determined by the defect structure, like porosity. Further, it can be anticipated that control of the grain size dispersion is extremely important in the experimental design of these nanostructured coatings. A nanostructured material with a broad grain size dispersion will exhibit a lower overall flow stress than a material with the same average grain size but with a much smaller grain size distribution. Consequently, experimental control over the grain size distribution is important to investigate concepts in materials design of nanostructured coatings. The situation of correlating the microstructural information obtained by microscopy of an interface to the macroscopic behavior of hard coatings is even more complex. The reasons are numerous, e.g., the limited knowledge of the interface structure (i.e., both topological and chemical) at an atomic level of only a small number of special cases, the complexity due to the eight degrees of freedom of an interface, and the lack of mathematical–physical models to transfer information learned from bicrystals to the actual polycrystalline form. The work presented in this chapter is focused on the characterization of promising wear-resistant physical vapor deposition (PVD) coatings that are available these days. We exemplify the use of high-resolution transmission electron microscopy (HRTEM) with two case studies. First, tungsten carbide–carbon (WC–C) multilayer coatings, by uniquely combining the properties of diamond-like carbon (DLC) and tungsten carbide, are evaluated for tribological low-friction applications. This uniqueness can be attributed to their high elasticity, chemical inertness, low static and dynamic friction coefficients coupling with metals and ceramics, and high wear resistance.[5] An important area of application lies in dry lubrication of sliding contacts with high contact stresses under conditions where fluid lubrication is beset with difficulties, e.g., at high and low pressures, high and low temperatures, and slow oscillations.[6] In these cases, the surfaces are coated with a thin low-friction and low-wear-rate solid lubricant. As a

second example we concentrate on nanostructured hard coatings. The application of hard TiN coatings to metal cutting tools has been hailed as one of the most significant technological advances in the development of modern tools. Although cutting tools have been the primary targets for the development of such coatings, TiN has also found other tribological applications, such as in bearings, seals, and as an erosion protection layer. Another important attraction of TiN is its potential application in microelectronics.[7] Finally, the golden color has also encouraged applications as decorative coatings. The TiN–(Ti,Al)N multilayer is part of an emerging class of new hard protective coatings based on the homogeneous TiN. The concept of coatings composed of a large number of thin layers of two or more different materials has shown to provide an improvement in the performance over comparable single layers.[8] In the present case, the multilayer combines, among others, the high-oxidation resistance of titanium aluminum nitride (Ti,Al)N at higher temperatures with the good adhesion of TiN to the substrate. Additionally, the introduction of a number of interfaces parallel to the substrate surface can act to deflect cracks or provide barriers to dislocation motion, thereby increasing the fracture resistance of the coating.[9] Consequently, the wear resistance of cutting tools, especially at high speed, is enhanced.

Regardless of the coating–substrate composites' undoubted success, they are often poorly characterized and badly understood. Clearly, if significant input is to be made in the design of improved coatings, a detailed knowledge of the relationship between the microstructure and mechanical properties is essential. Further, as multilayer coatings are materials engineered on the nanoscale, it is necessary to carry out a fundamental study of the interactions between each layer at this scale, in order to describe their wear mechanisms and tribological properties. Here, the focus is on a thorough characterization of the microstructure and mechanical properties. Additionally, a detailed study of the fracture mechanisms is performed by nanoindentation tests, allowing prediction of how the coated systems will perform in service.

The outline of this chapter is as follows: Section 2 provides the information regarding the characterization with transmission electron microscopy (TEM) of crystalline and noncrystalline coatings; Section 3 concentrates on the microstructure of WC–C multilayers; Section 4 describes a study of the microstructure of TiN and TiN–(Ti,Al)N multilayers; Section 5 concludes with an outlook.

2. EXPERIMENTAL METHODOLOGY AND MATERIALS

2.1. Materials

There are several ways in which a coating can be produced by PVD, but recent techniques all include the plasma-assisted PVD processes (PAPVD). The basic PAPVD is commonly entitled ion plating. PAPVD provides coatings that are very dense. The coatings contain only few macroscopic defects and possess a very

good adhesion to the substrate.[10,11] Currently, there are four main methods for evaporation: resistance heating, induction heating, and arc and electron beam gun (e-gun) sources.[12] The deposition process of WC–C consists of using dc magnetron sputtering of a pure WC target, with argon as a sputtering gas. The carbon phase was grown from plasma containing both hydrocarbon gas [acetylene (C_2H_2)] and argon. The process utilized six planar magnetrons arranged in a circle, with the substrate passing consecutively performing a planetary rotation (i.e., also rotating on its own axis). An interlayer of chromium was initially formed by DC-magnetron sputtering of a chromium target. Subsequently, the WC–C layer commenced to be deposited, i.e., DC-magnetron sputtering of the WC targets started—at the same argon pressure—and acetylene was introduced into the chamber. The substrate temperature was kept about 200–250°C during coating deposition. The TiN studied in this work was deposited using an electron beam gun source. Pure Ti was evaporated from a crucible with a high-voltage electron beam by means of a 270° electron gun. A plasma beam was operated between the hot filament and the crucible so as to ionize the metal vapor, the nitrogen, and the argon gas. The substrate was at a temperature of 480°C during the deposition process. The TiN–(Ti,Al)N multilayers were deposited using a hybrid process which combined reactive arc evaporation of pure Ti—from a crucible with a thermionic arc source to deposit TiN—and reactive magnetron sputtering of a titanium–aluminum alloy target for deposition of the (Ti,Al)N compound. The cathodic arc process uses glowing discharge plasma between the cathode and the crucible. The principal merit of arc evaporation is that no molten pool is formed, allowing the crucibles to be fitted in any orientation. Further, a major part of the emitted source material becomes highly ionized as it passes through the arc.[13] Nevertheless, a disadvantage of arc evaporation is that it also produces macroparticles in the coating matrix. Droplets of a metal, ejected from the source surface as the arc locally and rapidly melts the source material, create them.[14] The (Ti,Al)N layers were produced by magnetron sputtering of stoichiometric Ti–Al target materials, using a similar process as for the WC layers described above, in an argon and nitrogen atmosphere.

2.2. Characterization with Electron Microscopy Techniques

To understand the structure–property relationship of coated components and ultimately be able to predict their tribological behavior, it is imperative to gather as much information on morphology, elemental and phase composition, and microstructure as possible. The coating microstructure, e.g., grain size, phase, and lamella thickness, can be studied from plan-view and cross-sectional specimens by conventional and high-resolution TEM. In this work, the observations were carried out using the following microscopes: JEOL 4000 EX/II operating at 400 kV and JEOL 2010 FEG operating at 200 kV. Additional characterization was carried out with Philips-XL30(s)-FEG scanning electron microscopes and a JAMP-7800-FEG scanning Auger microscope. The electron-optical parameters of our microscopes

TABLE 5.1. Electron-Optical Properties of Various Transmission Electron Microscopes.

	JEOL 4000 EX/II	JEOL 2010F(UHR Pole piece)	JEOL ARM 1250(Side entry)
V (kV)	400	200	1250
C_s (mm)	0.97	1	2.7
Spread of defocus (nm)	7.8	4	11
Beam conv. (mrad)	0.8	0.1	0.9
Information limit (nm)	0.14	0.11	0.11
Point resolution (nm)	0.165	0.23	0.12
Scherzer defocus (nm)	47	58	51

are given in Table 5.1 and compared with the JEOL ARM 1250 at Max-Plank-Institute für Metallforschung in Stuttgart, Germany. In the following paragraphs some basic background of characterizations with HRTEM is presented.

In conventional TEM, diffraction contrast is employed where the contrast in the image is determined by the intensity of the imaging beams, i.e., the ones enclosed in the objective aperture; thus, a rather low-resolution information about the structure of the sample viewed along the direction of the incident beam can be obtained. In modern analytical transmission electron microscopes with reduced spherical aberration, a larger objective aperture can be used by which a large number of diffracted beams may interfere in the image, improving the image resolution. With the advent of (ultra) high-resolution TEM, it is nowadays even possible to derive from images the structural information at an atomic scale. However, the concept of resolution in HRTEM is still not without pitfalls and a thorough understanding of image formation is essential for a sound interpretation. The technique of HREM found its origin in the technique of phase contrast microscopy that was introduced in the field of optical microscopy by Frits Zernike[15]of the University of Groningen. In 1953 he received the Nobel Prize in physics for this invention that found applications, in particular, in biological and medical sciences. HRTEM imaging is based on the same principles used in phase contrast microscopy. Phase contrast imaging derives contrast from the phase differences among the different beams scattered by the specimen, causing addition and subtraction of amplitude from the forward-scattered beam. Components of the phase difference come from both the scattering process itself and the electron optics of the microscope. In a weak-phase object, the amplitude of the Bragg scattered beam is small compared with that of the forward-scattered beam. In reality, however, a HRTEM is not a perfect phase contrast microscope, as beams at different angles with the optical axis result in different phase shifts. In fact, the phase shift is a function of the spherical aberration coefficient C_s, and of the defocus value; this phase transfer function depends very sensitively on the defocus, and as will be explained later, it in general shows an oscillatory behavior as a function of the distance to the origin in the reciprocal space. The amplitude contribution of the different transmitted beams on

the image is therefore not constant and cannot be found in an intuitive way. Several textbooks and reviews have been written on the subject of (high-resolution) microscopy, sadly with different notation conventions. This text adopts the notation used in Ref. 16. Spence[17] has written a more in-depth description of imaging in HRTEM theory. Williams and Carter[18] have written a very clear and complete introductory textbook on general aspects of electron microscopy.

The conventional way to generate electrons is to use thermionic emission. Any material that is heated to a high enough temperature will emit electrons when they have enough energy to overcome the work function. In practice, this can be done only with high melting point materials (such as tungsten) or low work function materials like LaB_6. The Richardson–Dushman law describes thermionic emission as a function of the work function Φ and temperature T:

$$J_e = AT^2 e^{-\Phi/kT} \tag{5.1}$$

with J_e the electron flux density at the tip and A the so-called Richardson–Dushman constant. In electron microscopes, tungsten filaments were most commonly used until the introduction of LaB_6. These LaB_6 sources have the advantages of a lower operating temperature, which reduces the energy spread of the electrons and increases the brightness. Another way of extracting electrons from a material is to apply a high electric field to the emitter that enables the electrons to tunnel through the barrier. Sharpening the tip may enhance the electric field because the electric field at the apex of the tip is inversely proportional to the radius of the apex:

$$E = \frac{V}{\kappa R} \tag{5.2}$$

with κ a correction factor for the tip geometry (usually $\approx$2). The advantage of this cold field emitter gun (cold FEG) is that the emission process can be done at room temperature, reducing the energy spread of the electrons. The small size of the emitting area and the shape of the electric field result in a very small (virtual) source size in the order of nanometers with a brightness that is three orders of magnitude higher than for thermionic sources. It is thus possible to focus the beam to a very small probe for chemical analysis at an atomistic level or to fan the beam to produce a beam with high spatial coherence over a large area of the specimen. The disadvantages of this type of emitter are the need for (expensive) UHV equipment to keep the surface clean, the need for extra magnetic shielding around the emitter, and a limited lifetime.

Some of these disadvantages of cold FEG emitters can be circumvented by heating the emitter to moderate temperatures (1500°C) in the case of a thermally assisted FEG or by coating the tip with ZrO_2, which reduces the work function at elevated temperatures and keeps the emission stable (Schottky emitter). This causes a doubling in the energy spread of the electrons and some reduction in brightness. The Schottky emitter is most widely used in commercial FEG-TEMs because of its stability, lifetime, and high intensity (see Table 5.2).

TABLE 5.2. Properties of Different Electron Sources.[19]

	Tungsten	LaB_6	Cold FEG	Schottky	Heated FEG
Brightness (A/m^2 sr)	$(0.3–2) \times 10^9$	$(3–20) \times 10^9$	$10^{11}–10^{14}$	$10^{11}–10^{14}$	$10^{11}–10^{14}$
Temperature (K)	2500–3000	1400–2000	300	1800	1800
Work function (eV)	4.6	2.7	4.6	2.8	4.6
Source size (μm)	20–50	10–20	<0.01	<0.01	<0.01
Energy spread (eV)	3.0	1.5	0.3	0.8	0.5

After leaving the electron gun the electrons are accelerated toward the anode and enter the column. Because the velocity of the electrons approaches the speed of light, the wavelength of the electrons has to be corrected for relativistic effects:

$$\lambda = \left(\frac{2m_0\,\mathrm{eV}}{h^2} \left(1 + \frac{\mathrm{eV}}{2m_0c^2} \right) \right)^{-1/2} \tag{5.3}$$

For 400 kV electrons, $\lambda = 1.64$ pm, which is much smaller than the resolution of any electron microscope because the resolution is limited by aberrations of the objective lens and not by the wavelength of the electrons. The electron beam is now focused on the specimen with the condenser lenses and aligned using several alignment coils. The function of the condenser lens system is to provide a parallel beam of electrons at the specimen surface. In practice this is not possible and the beam always possesses a certain kind of convergence when imaging at high resolution, usually in the range of 1 mrad for LaB_6 emitters and 0.1 mrad for FEGs. After entering the specimen, most of the electrons are elastically scattered by the nuclei of the atoms in the specimen. Some electrons are inelastically scattered by the electrons in the specimen. Compared to X-ray or neutron diffraction, the interaction of electrons with the specimen is huge and multiple scattering events are common. For thick specimens at lower resolutions, an incoherent particle model can describe the interaction of the electrons with the specimen. However, with thin specimens at high resolution, this description fails because the wave character of the electrons is then predominant. The electrons passing the specimen near the nuclei are somewhat accelerated toward the nuclei, causing small, local, reductions in wavelength, and this, in turn, results in a small phase change of the electrons. Information about the specimen structure is therefore transferred to the phase of the electrons. Only elastically scattered electrons are of importance in formation of high-resolution images. The inelastic scattered electrons contribute mostly to the background of the image. These electrons can be removed by inserting an energy filter in the microscope between the specimen and recording device. Only the elastically scattered electrons are now used for the image formation. The energy loss spectrum of the inelastic scattered electrons contains valuable information about the chemical composition of the specimen. This information can be extracted by observing the electron energy loss spectrum or by filtering parts

of the loss spectrum. The inelastic scattered electrons also produce Kikuchi lines in the electron diffraction pattern, which are helpful for accurate crystallographic alignment of the crystals in the specimen.

To retrieve structural information on the specimen from the micrographs, it is necessary to calculate the trajectory of the electron wave through the specimen. In kinematic approximation, multiple scattering of the electrons in the sample is ignored and this results in an undisturbed central beam. This approach already fails at a small thickness or in case of a single atom. In dynamical calculations, all the scattered beams and their mutual exchange of intensity during the course of multiple scattering in the specimen are taken into account. It is possible to do full dynamical calculations but these are soon limited by the available computing power. Using the fact that the vast majority of the electrons are scattered in a forward direction with small diffraction angles, Cowley and Moodie[20] devised the multislice approximation. Here the three-dimensional (3D) crystal is divided into multiple thin slices perpendicular to the electron beam, and in between the electron wave propagates. The incident electron wavefront intensity is described by a plane wave with wave vector $\vec{k}$ propagating in vacuo:

$$\Psi_0(\vec{r}) = e^{2\pi i \vec{k}\cdot\vec{r}} \tag{5.4a}$$

$$k = |\vec{k}| = \frac{1}{\lambda} \tag{5.4b}$$

where λ is the wavelength of the electrons. The refractive index in every slice depends on the position in the slice because the electrons will be accelerated toward the nuclei, whereby their wavelength is reduced. This phase change can be expressed by multiplying $\Psi_0(\vec{r})$ with a transmission function $q(x,y)$, assuming that the specimen acts as a pure phase object:

$$q(x, y) = e^{-i\sigma\phi(x,y)} \tag{5.5}$$

where $\phi(x, y)$ is the projected potential distribution in the slice, averaged over the electron beam direction and $\sigma = \pi/\lambda V$ is the interaction constant. Absorption is neglected in this approach, the so-called phase–object approximation. A further simplification can be made by considering only the first-order approximation of Eq. (5.5):

$$q(x, y) = 1 - i\sigma\phi(x, y) \tag{5.6}$$

This is known as the weak-phase–object approximation in which the amplitude information is linearly related to the projected potential. The propagation between the slices, each of thickness δ, can be described by convoluting Eq. (5.5) with the Fresnel propagator:

$$p(x, y) = e^{-\pi i(x^2+y^2)/\lambda\delta} \tag{5.7}$$

and the emerging spherical wavefront is approximated by a paraboloidal wavefront.

The nth wave function can now be obtained by a convolution:

$$\Psi_n(x, y) = (\Psi_{n-1} \otimes p_{n-1}(x, y))\, q_n(x, y) \tag{5.8}$$

where p_{n-1} is the propagator from slice $n-1$ to slice n. In this way the exit wave computed can subsequently be used as input for the image formation calculations. Usually the convolution is done by a multiplication in Fourier space, which saves computing time. After the exit wave has left the specimen, the electron wavefront has to be converted into an image. Because the exit wave mainly contains phase information, these phase differences have to be converted to intensities, much like the phase contrast microscope invented by Frits Zernike. The exit wave can be described in reciprocal space by performing a Fourier transform. The effect of the spherical aberration of the objective lens is that the electrons entering the objective lens at different distances from the optical axis are focused at different planes and also travel different distances, causing a phase difference for the different scattered electrons. The phase factor $\chi(U)$ describes the phase difference introduced by the defocus and spherical aberration:

$$\chi(U) = \pi\lambda\Delta f U^2 + \frac{1}{2}\pi C_s\lambda^3 U^4 \tag{5.9}$$

where Δf is the defocus value of the objective lens, U the distance of the reciprocal lattice point from the optic axis, and C_s the spherical aberration. In reciprocal space, this phase factor can be accounted for by multiplying the exit wave with $B(U)$, which is equivalent to a convolution in real space:

$$B(U) = \exp(i\,\chi(U)) \tag{5.10}$$

If the specimen behaves as a weak phase object, only the imaginary part of $B(U)$ contributes to the intensity of the image $T(U)$:

$$T(U) = 2\,\sin(\chi(U)) = 2\,\sin\left(\pi\lambda\Delta f U^2 + \frac{1}{2}\pi C_s\lambda^3 U^4\right) \tag{5.11}$$

which is usually referred to as the objective lens transfer function if the specimen behaves like a weak phase object. Next, only the real part is considered because the phase information from the specimen is converted into intensity information by the phase shift of the objective lens. In the microscope an aperture is inserted in the back focal plane of the objective lens that transmits beams only to a certain angle. This can be represented by an aperture function $A(U)$, which is unity for $U < U_0$ and zero outside this radius. When $T(U)$ is negative, the atoms in the specimen would appear as dark spots against a bright background and vice versa. For $T(U) = 0$ no contrast results. An ideal behavior of $T(U)$ would be zero at $U = 0$ (very long distances in the specimen) and $U > U_0$ (frequencies beyond the aperture size) and large and negative for $0 < U < U_0$. The contrast of a high-resolution image depends strongly on the microscope settings and parameters. In practice, not all the information in $T(U)$ is visible in the image. This is caused by electrical instabilities in the microscope, creating a spread of focus because

of the chromatic aberration of the objective lens, which results in damped higher frequencies. Mechanical instabilities and energy loss due to inelastic scattering of the electrons by the specimen also contribute to the spread in defocus. The inelastic scattered electrons contributing to the image can be removed by inserting an energy filter in the microscope between the objective lens and the image recording media. Another factor that damps the higher frequencies is the beam convergence. Because the electron beam has to be focused on a small spot on the specimen, there is some convergence of the beam present. This also affects the resolution because the specimen is now illuminated from different angles at the same time. These effects that affect the resolution can be represented by multiplying $\sin(\chi)$ by the damping envelopes E_α and E_Δ, which represent the damping by the convergence and spread in defocus, respectively:

$$E_\Delta(U) = \exp\left[-\frac{1}{2}\pi^2\lambda^2\Delta^2U^4\right] \tag{5.12}$$
$$E_\alpha(U) = \exp[-\pi^2\alpha^2(\varepsilon + \lambda^2 C_s U^2)^2 U^2]$$

The resulting contrast transfer function (CTF) is plotted in Fig. 5.1 with the damping envelopes E_α and E_Δ. For higher frequencies the CTF is now damped and approaching zero. It becomes clear that defining a resolution for the HRTEM is not obvious. Several different resolutions can be defined as stated by O'Keefe[21]:

1. Fringe or lattice resolution: This is related to the highest spatial frequency present in the image. In thicker crystals, second-order or nonlinear interference may cause this. As the sign of $\sin(\chi)$ is not known, there is in general no correspondence between the structure and the image. This resolution is limited by beam convergence and spread in defocus.
2. Information limit resolution: This is related to the highest spatial frequency that is transferred linearly to the intensity spectrum. These frequencies may fall in a passband, with blocked lower frequencies. Usually this resolution is almost equal to the lattice resolution.
3. Scherzer resolution or point resolution: This is the highest possible resolution when no lower frequencies are blocked or passed with opposite sign. This is the most relevant resolution definition because it results in a projected image of the specimen structure. The exact definition for the Scherzer defocus varies slightly in literature. In general, for images taken at optimum defocus of $(\frac{4}{3}C_s\lambda)^{1/2}$, the highest transferred frequency is equal to $1.51\,C_s^{-1/4}\lambda^{-3/4}[\mathrm{m}^{-1}]$.

In Fig. 5.1 the CTFs of the JEOL 4000 EX/II and JEOL 2010F at Scherzer defocus are plotted with the damping envelopes. The CTF of the JEOL ARM 1250 at Max-Plank-Institute für Metallforschung in Stuttgart, Germany, is also given for comparison. The electron-optical parameters of the microscopes can be found in Table 5.1. The CTF of the JEOL 2010F shows the rapid oscillations of the FEG due to higher spatial coherence. In this case there is a big gap between point resolution and

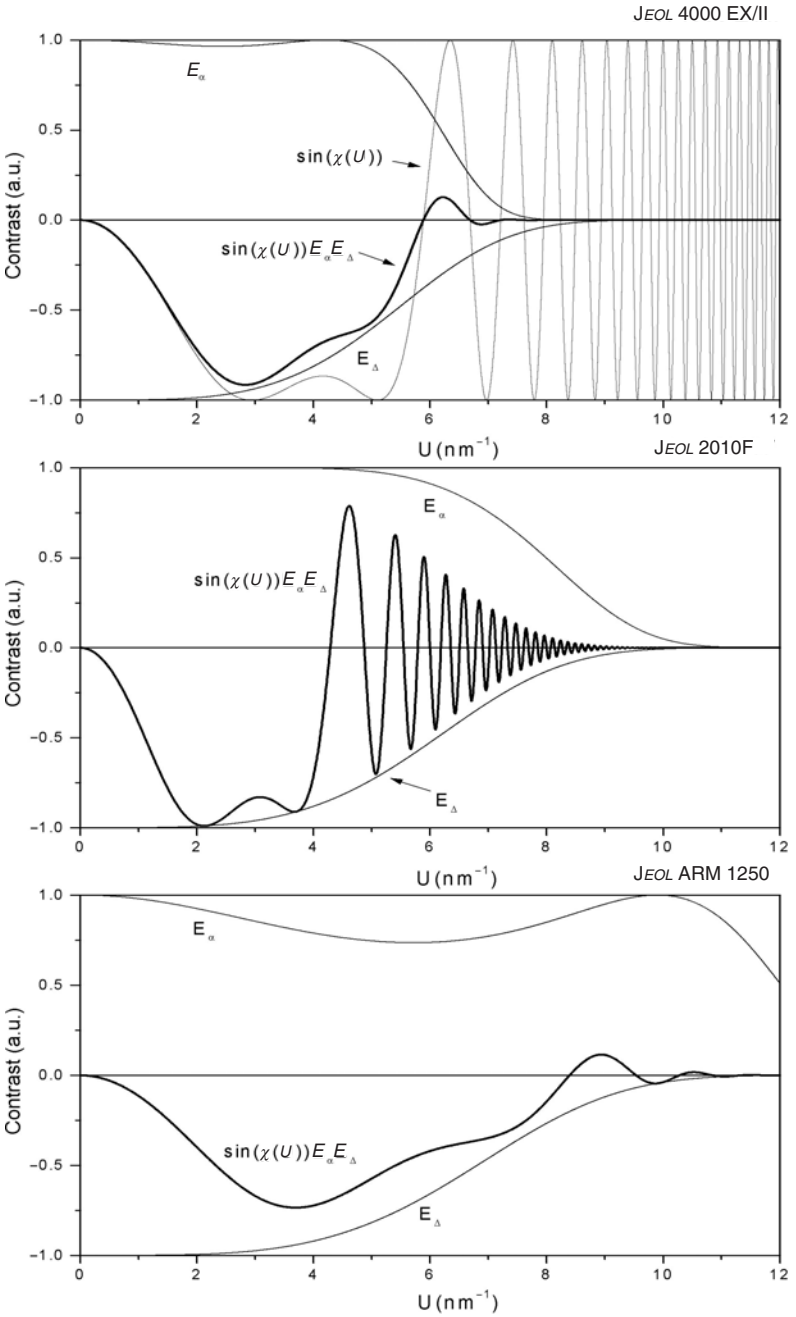

FIGURE 5.1. Contrast transfer functions (thick lines) and damping envelopes of the used microscopes at Scherzer defocus values of 47, 58, and 51 nm, respectively. Note the many oscillations in the CTF of the 2010F.

information limit. For the ARM 1250 microscope the damping envelope is limited by the spread of focus and the point resolution is almost equal to the information limit. Using a FEG will not substantially increase the resolution here. Generally speaking, using a FEG in lower voltage ($\leq$200 kV) instruments helps to increase the information limit because in these instruments beam convergence dominates the damping envelope. With higher voltage instruments the higher acceleration voltage increases the brightness of the source and the damping envelope is limited by the spread of defocus. The spherical aberration of the objective lens can be lowered but generally at the expense of a decrease in tilt capabilities of the specimen. It is possible to compensate C_s by a set of hexapole lenses as suggested by Scherzer[22] in 1947 but it became feasible only recently due to the complex technology involved. Haider demonstrated a C_s-corrected 200 kV FEG microscope[23] in which C_s was set at 0.05 mm to reach an optimum between contrast and resolution. The point resolution of this microscope was then equal to the information limit of 0.14 nm. Successful application of this technology would put the next limiting factors of the microscope at the chromatic aberration and mechanical vibrations that currently limit the resolution around 0.1 nm.

A point that has been overlooked quite frequently is the effect of the alignment on the structural observations. Correct alignment of the microscope is very important because misalignments affect the image. The electron beam may not be parallel to the optical axis of the objective lens, beam tilt, or the zone of the crystal may not be parallel to the incoming beam, crystal tilt. After the alignment procedure there will be some residual tilt. Beam tilt can be reduced to about 0.1 mrad, in principle, with the so-called coma-free alignment method, but it is rather difficult to perform. The voltage-center method that is routinely used is quick and easy but not correct. It leaves a beam tilt with a magnitude related to the mechanical tolerance with which the optical axis of the projecting system is aligned to the optical axis of the objective lens. Aligning the zone axis of the sample with the incoming beam is performed by tilting the specimen so as to obtain a diffraction pattern with equal intensities for spots related by symmetry. Apart from the difficulties this may present in itself, crystal tilt may differ on a length scale much smaller than the diameter of the electron beam, which inhibits alignment with a very high precision. This is a problem especially for thin metal foils. The effect of residual tilt on the image depends on the crystal structure of the sample. Many simple cubic structures will show minor changes in image contrast for tilts up to a few degrees, especially in thinner areas. Tilting does change the projected potential, leading to lower maxima, and a scattering situation that is closer to the weak phase approximation than the untilted case. Electrons entering the crystal with a small tilt will "feel" a thinner specimen. Because of the beam divergence, this will even be true at zero beam tilt. This effect is usually not taken into account in image simulate ion packages, and will contribute to an underestimation of specimen thickness.[21] The symmetry of the image will no longer correspond to that of the projection of the zone axis, but that may not be very apparent. In some cases the effects of beam- and crystal tilt on images may be profound, notably for structures containing glide

or screw axes. The considerations above referred to elastically scattered electrons only. At 400 keV, however, and for light elements, inelastic scattering can be of similar strength as elastic scattering. Electrons may be scattered to high angles by phonons, or to smaller angles by plasmons or single-electron excitations. Scattering by phonons is usually described as elastic scattering using scattering amplitudes that have been multiplied by a Debye–Waller factor. Some of the inelastically scattered electrons will pass through the objective aperture and contribute in one way or another to the image. As these electrons are not focused onto the same plane as the zero-loss electrons, due to the chromatic aberration of the objective lens, it has been assumed that they would produce only a slowly varying background to the high-resolution image. Such a contribution may be modeled by adding an imaginary component to the scattering factors. Finding correct values for the absorption parameters for use in HRTEM is a problem with this approach. However, it has been shown that electrons that undergo elastic and inelastic scattering may in fact produce high-resolution contrast.[24,25] From simulations it appears that the contribution is usually small, but may be appreciable for thick specimens (including the amorphous overlayer) of materials showing a sharp plasmon peak, and at relatively large underfocus values.

In comparing simulated images with measured images, specimen thickness is one of the major problems. The thickness of a sample is difficult to assess from independent measurements and is often treated as a free variable during fitting. In cases where estimations of thickness are available, fitting calculated and measured images usually leads to values for thickness that are far too low.[26] It has been suggested that this is because the multiple scattering effects are overestimated in the simulations and lead to a larger sensitivity on thickness in simulations than in reality. This overestimation stems from the fact that in the experiment, due to beam and crystal misalignments as well as beam divergence, the projected potential is lower than for the exact zone axis used in simulations. (As a side effect, the choice of a "realistic thickness"' may lead to a wrong value for the defocus because image contrast is equal for many combinations of thickness and defocus, at least for small period structures.) At low thickness, simulated images show few traces of dynamic effects. For a thick sample, high-frequency details due to dynamic scattering are damped by lateral vibrations of the sample. Fitting without allowing for vibrations may lead to erroneous interpretation of the absence of these high frequencies as being caused by low thickness. These vibrations are difficult to measure, but their effects can be used as a fitting parameter, and it seems to be possible to arrive at more realistic thickness, at least in some cases.[27] In order to image crystalline interfaces, in particular relevant in the field of hard coatings, in an HRTEM and derive the atomic structure, the interface must be observed edge-on, to view the atomic structure unobscured by moiré effects. Another necessity is the need to view the structure along a low-index zone axis to resolve separate atomic columns. In that way, small deviations in the atomic structure can be observed and measured. The interfaces have to be straight and without steps along the beam direction to be able to interpret the structure as formed by the interactions across the interface and

not by a projection of steps at the interface. The next difficulty in imaging interfaces is to judge exactly where the interface is located. For instance, inside an oxide the electrons are scattered to lower angles, causing the oxide to appear brighter. It is then tempting to locate the interface at the spot where the intensity changes from dark to light. However, at the interface a bright Fresnel fringe is often formed that leads to a misinterpretation of the location of the interface. First it has to be judged whether the atomic columns in the image correspond with dark or bright spots. When this is known, the interface can be located by looking at the disregistry at the interface. Due to delocalization,[28] that is, spreading of information over a larger area, the first layer is generally not considered further in image analysis.

To quantify the structural differences in the images it is necessary to quantify some of the features in the images. Due to the projective nature of TEM it is possible to observe only a projected image of the defects along the interface. When viewing the structure of crystalline materials along the interface, two effects can be observed: plane bending and column delocalization. Plane bending corresponds to a gradual increase of the lateral displacement of the average position of a column in a plane when approaching the interface, and column delocalization is the result of different lateral displacements of the atoms in a column, that is, corresponding to a "spread" of the column. The effect of this column bending on HRTEM images is not obvious. According to image simulation, column delocalization leads to brighter or darker spots where the atomic columns correspond to bright or dark spots, respectively. Plane bending can lead to small displacements of the spots in the image, which under suitable conditions can be measured in the image up to an accuracy of 0.01 nm. From the preceding discussion it has become clear that in general, a high-resolution image does not correspond to the structure of the specimen. Image simulations have to be performed to cross-check the proposed structure with simulations. At present two simulation programs are very popular in this field of research, MacTempas by Kilaas[29] and electron microscopy image simulation (EMS) by Stadelmann.[30] MacTempas calculates images using multislice approximation. The EMS is a set of command-line utilities that can calculate images using the multislice or Bloch waves method. Most relevant parameters of the microscope as well as the thickness of the specimen can be altered. The resulting simulations can be compared with the experimental image. The fact that there are many parameters that can be optimized poses a problem for the user because it is quite impossible to check all possible combinations manually. This cross-checking is usually done by eye and in a rather qualitative way and assumes prior knowledge of the structure under observation. A second approach to this problem is to do a "backward" calculation of the image to the exit wave. This is especially powerful to use with FEG-TEMs that have an information limit well beyond the Scherzer resolution. After multiple images with different defocus values are taken, it is possible to use the different passbands in the CTF to reconstruct the exit wave. The actual problem is then shifted to the question of how the exit wave is related to the structure. In LaB_6 TEMs the information limit is already close to point resolution, and thus this method does not reveal much more

information. Using a computer to calculate an image agreement factor between the experimental and simulated images and then change the imaging parameters automatically to optimize the image agreement can improve the image simulation process. This method has the advantage of an independent evaluation of the images and the possibility of checking many different parameters. A program that controls all these parameters is iterative digital image matching[31] developed by Möbus and coworkers. With this program it is possible to define a range of parameters that optimizes the correspondence with the experimental image. The parameters that can be varied include beam tilt, crystal tilt, and astigmatism. The correspondence is measured by using calculating image matching coefficients between simulation and experiment. To match the experimental and simulated images the contrast and brightness of the images have to be adjusted. To make a full comparison between experiment and simulation, the image intensity has to be normalized by stretching and shifting the histogram of the experimental image. Stretching both the experimental and the simulated images from minimum to maximum intensity or, in the case of noisy images, stretching the area in the histogram where almost all the intensity is located, which then serves to remove all noise specifications, can do this. Image matching is usually evaluated with the cross-correlation factor (xcf):

$$\mathrm{xcf} = \frac{\sum (E_{jk} - \bar{S})(S_{jk} - \bar{S})}{((E_{jk} - \bar{E})^2 (S_{jk} - \bar{S})^2)^{1/2}} \tag{5.13}$$

with the image intensities stored in arrays E and S for the experimental and simulated image, respectively. The xcf automatically matches the contrast and brightness without noise removal. Because of noise present in the image, totally black or white pixels might be present that influence the width of the histogram. This can be circumvented either by first smoothing the experimental image or by matching the brightness and contrast by fitting the histograms with a Gaussian distribution. The simulated images have periodic boundaries, which means that the selected experimental image also has to be selected as a periodic image. For interface simulation, skipping the borders in the calculation of the image agreement can circumvent this requirement. To optimize a simulated image the computer program first calculates an image, compares it with the experimental images, and then adjusts the imaging parameters accordingly. Three different optimization processes are available: 2D-grid scan; Powell's method[32]; and simulated evolution.[33,34] The 2D-grid scan is suitable to do a simple optimization and can find the optimum parameters from a 2D-grid of parameters, for example, thickness and defocus. It is not possible to scan over more than two parameters and this method requires all images to be calculated. This method is too time consuming for optimization of images when more parameters are included to be optimized. For these more complex optimizations, Powell's method is more suitable because more parameters can be optimized. This multidimensional optimization algorithm does not require a gradient of the function that is evaluated. With this method it is still possible to be trapped in a

local maximum in the parameter space and the computational effort is still quite substantial. Simulated evolution, based on the principles of biological evolution, can be used here because it uses random "mutations" of the parameters to obtain better images. One starts the simulation with a chosen set of parameters, and with a random number generator changing the set of parameters λ children are formed. From the children, a subset μ with the best agreement is selected, which consists of the parents of the next generation and which also acquires some parameters from the grandparents. This process is repeated until a fixed number of iterations have taken place or until the required fit of the image is reached. The parameter space has to be selected by hand.

In using HRTEM to study boundaries, in particular relevant in the field of hard coatings, one is seeking to find coordinates of atoms near the interface. In this case it is not just the point-to-point resolution that one is interested in, but also the precision with which small displacements perpendicular to the beam can be deduced from the images. In principle, lattice parameters and displacements in HRTEM can be determined with far greater precision than from point-to-point resolution. Rigid-body translations of grains near grain boundaries have been measured with an estimated error of 0.01 nm,[35] or less in cases that allowed for noise reduction by real space averaging.[36] Rigid-body translations at coherent (parts of) hetero-interfaces have also been measured, and errors of 0.02 nm,[37,38] and even 0.01 nm, have been reported. Determining the position of a single atomic column is less precise, but a general value cannot be given. First of all it should be kept in mind that maxima or minima do not have to correspond with the positions of columns, even for structures with spacings above the point-to-point resolution. The apparent positions of columns at aperiodic features, such as interfaces, may vary appreciably, by as much as 0.03 nm, in a defocus series.[39] Usually what one is really interested in is the smallest displacement that has a measurable effect on the image. The sensitivity of the image to changes depends on the local structure surrounding the defect. It also depends on the imaging parameters, such as thickness and accelerating voltage, and defocus. Furthermore, the precision with which the coordinates of an image characteristic can be determined depends on the possibilities for noise reduction. In the presence of noise, caused by amorphous overlayers, the position of a maximum on a perfect structure may be up to 0.02 nm away from the position where it should be. It is therefore crucial that noise be removed, either by preparation or by numerical filtering procedures. Spatial averaging is often impractical for metal–ceramic interfaces. They may, for example, be nonperiodic, or show a large period, across which imaging parameters may change. For periodic interfaces, clever Fourier filtering procedures are possible, but for aperiodic interfaces only a simple low-pass filter works. Although no single value of the smallest displacement detectable can be given, an order of magnitude may be derived from two recent publications.[40,41] Here, among many other free parameters, column positions were adjusted so as to achieve a best fit between calculated and measured intensities.

2.3. TEM Sample Preparation

There are several techniques described in literature for the preparation of plan-view and cross-sectional TEM specimens.[42,43] In this work,[44] specimen preparation for plan-view TEM consisted of cutting out a disk from the region of interest with 3-mm diameter using the Nd:YAG laser, followed by grinding and polishing from the substrate side to a thickness of 50 μm. The disk was further thinned to electron transparency by dual gun Ar^+ ion milling. The specimen was kept on rotation while the Ar^+ beam at 5 kV with an ion current of 0.5 mA was directed toward the substrate side with an incident angle of 8° from the specimen surface. Final etching was performed briefly from both sides, with the tilt angle reduced to 4° in order to clean the coating surface, to reduce ion induced artifacts, and to remove any amorphous redeposited surface layer.

For cross-sectional TEM specimen preparation of heterogeneous materials however, only a few methods exist in literature, which minimizes the differential thinning that occurs on either side of the interface of interest. The method used is a refinement of the one developed by Barna,[43] which is particularly advantageous when low-angle thinning is required. The basic tool is a titanium disk (diameter 3 mm, thickness 0.3 mm) containing three slots made by an Nd:YAG laser. The width of the central rectangular slot is 800 μm and should be chosen so as to be slightly larger than the thickness of the two pieces being embedded. The steps involved in preparation are illustrated in Fig. 5.2 and were as follows. After cutting, the two small pieces were placed film to film in the central slot (Fig. 5.2a). The walls of the slot were then bent using a small rounded screwdriver until the samples touched each other (Fig. 5.2b). The edges of the side slots were cut using a small chisel, causing a displacement at the ends of the walls of the central slot (Fig. 5.2c). The walls, acting like small springs, fixed the two pieces. The sample was then embedded in a two-component glue (Gatan glue). As a result of capillary force and gravity, the bonding material penetrated all the slots and filled them, appearing at the top of the Ti disk (Fig. 5.2d). The specimen was then placed in a temperature-controlled oven to solidify the glue. To avoid bonding between the hotplate and the specimen, a small piece of aluminum foil was placed underneath.

After solidification, the bonding material together with the aluminum foil was cut away from the titanium disk along its perimeter, which was followed by mechanical grinding and polishing (using a tripod polisher) on both sides to a thickness of 50 μm. This technique obviously has an advantage in the preparation of brittle materials due to the supporting titanium disk, without the disadvantage of the occurrence of shadowing during low-angle ion beam thinning. Ion beam milling was performed on the mechanically ground and polished specimen with two guns in mirror-image position on both sides, using a Gatan PIPS, model 691. The angle of incidence was 6° (ion energy 4 kV and ion current 40 μA) and the specimen was rotated. Final thinning to electron transparency was accomplished by rocking the specimen ±30° perpendicular to the coating–substrate interface with an incoming ion beam at 4°. This process continued until perforation took

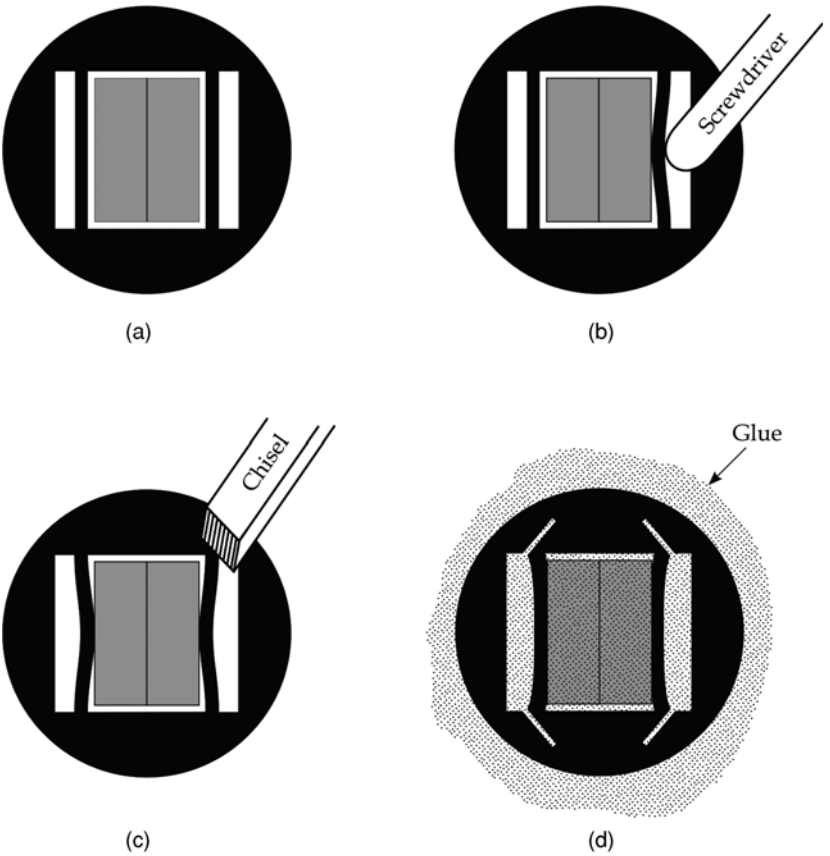

FIGURE 5.2. Steps involved in the preparation of a cross-sectional TEM specimen for low-angle ion milling. The 3-mm diameter titanium disk is shown in black. The two gray rectangles represent the sample: (a) Two slabs of coated material approximately 1300 × 350 × 300 mm are placed edge-on, film-to-film in the large rectangular slot of the titanium grid; (b) A small rounded tool is inserted into rectangular slots at each side and twisted to deform the thin band of titanium between the central and side slots. This holds the two pieces together with the coatings in the center of the sample; (c) A small chisel is pressed into the titanium grid, at the positions shown, to bend further the thin bands, and thus improve the grid support of the samples; (d) The grid containing the samples is immersed in a drop of Gatan glue, and placed in an oven to cure the glue.

place and the hole reached the region of interest. Finally, the surface contaminants (due to redeposited material) were reduced by using an ion energy of 2 kV and ion current of 4 μA while rotating the specimen.

In order to investigate the coated system response beneath the trigonal impression of a nanoindentation, cross-sectional TEM specimens from the contact sites were prepared. The novel method makes use of the titanium disk described

above. Two thin slabs (1300 × 50 × 350 μm) of coated material with the coating on the 1300 × 50 μm surface were fitted in the 100-μm central slot. Then three rows of indentations, distributed over the coated surface, were performed in each sample with a load ranging from 50 to 400 mN. After performing the indentations, the slabs were removed from the grid and fitted film to film in a 700-μm slot of other grid, followed by embedding in a two-component glue. When the glue was cured, which was accomplished by placing the specimen in a temperature-controlled oven, it was polished (using a tripod polisher) to remove 10 μm of material from each side. The following ion beam milling process was similar to the one employed for preparation of cross-sectional TEM specimens. However, to control the thinning process and to ensure that the electron transparent area was in the contact sites, the ion milling was periodically stopped and the specimen was examined with scanning electron microscopy (SEM).

3. MICROSTRUCTURE OF DIAMOND-LIKE CARBON MULTILAYERS

3.1. DLC Coatings

DLC coatings are amorphous and consist of a mixture of sp^3- and sp^2 carbon structures, where sp^2-bonded graphite-like clusters are embedded in an amorphous sp^3-bonded carbon matrix.[45] They have been subject to studies since the 1970s and several different types of DLC coatings have emerged. They can be roughly classified as hydrogenated (a-C:H) and hydrogen-free (a-C) amorphous carbon coatings.[46,47] Further, both can be metal doped (Me-DLC) or carbide doped (MeC-DLC). In the case hydrogen atoms are present in the random network as bound to C, they stabilize the sp^3 hybridization, which is responsible for high hardness and rigidity of the network. However, they decrease the interconnectivity of the sp^3-hybridized C sites, which has also a strong influence on the film's mechanical properties. From the mechanical point of view, the sp^3 fraction and H content in the films are very important, whereas the sp^2-C clustering has influence on the electronic properties of the films. DLC films with an sp^3 fraction higher than 70% are called tetragonally amorphous (ta-DLC); they have been synthesized in both hydrogenated and hydrogen-free forms, and in the latter they could yield hardness and Young's modulus values near to that of diamond.

Me-DLC and MeC-DLC have received considerable attention in recent years, owing to their low friction coefficient and high wear resistance in combination with substrate temperatures of some 200–400°C during deposition. Further, the fact that adhesion between the coating and the substrate has been improved by depositing an interlayer of chromium or molybdenum[48] has helped to promote the deposition of such coatings onto machine components subjected to a high shear stress component. Tungsten carbide–carbon (WC–C) is an example of a multilayer structure composed by carbide-doped hydrogen and hydrogenated DLC lamellae.

This coating has been reported to have successful engineering applications where low friction and high wear resistance are important requirements.[5,49] However, if the advantages are to be fully employed in improving the surface properties of engineering components, it is necessary to understand more thoroughly the detailed mechanisms by which surface properties are improved. Here we address the chemical composition, microstructure, and interfaces of several WC–C coatings. Moreover, the predominant features of and dissimilarities between the different films, which can be crucial for their performance, will be pointed out throughout the text. TEM—in conventional and high-resolution mode—was used as primary technique. All images were acquired close to the minimum contrast defocus. The difference observed between this defocus value and the optimum defocus consisted only on the granularity (noise) of the amorphous material. Since it was much coarser at the optimum defocus, the former value was adopted throughout. By combining direct imaging and electron diffraction, it was possible to obtain detailed information about phase composition, grain size and shape, and degree of preferred orientation of the crystalline phases. Nevertheless, complementary techniques such as analytical TEM, SEM, X-ray diffraction (XRD), and Auger electron spectroscopy (AES) were also used, providing additional invaluable information concerning the morphology, phase composition, and microchemistry of the coated systems.

3.2. Coated Systems

In this chapter three dissimilar WC–C coatings—denoted S1, S2, and T1—are investigated in detail.[50,51] Stainless steel (AISI 304) and tool steel (AISI D2) are used as substrate materials, having both circular (60-mm external diameter, 13-mm thickness) and rectangular ($90 \times 10 \times 1.5$ mm) geometries. The tool steel substrate has been heat treated and tempered at 520°C to obtain a hardness of 60 HRC (6.8 GPa). The substrate surfaces have been finished by polishing to an average roughness R_a of 0.03, 0.05, and 0.07 μm. The substrate properties of the coated systems are summarized in Table 5.3.

From XRD analysis, it was found that all coatings investigated consist of a cubic and an amorphous phase. In the case of coating systems S1 and T1, the chromium (110) lattice plane provided the most intense peak, while in system S2 both the (110) and (200) planes were most intense. Therefore, the chromium

TABLE 5.3. Substrate Properties of the Coated Systems

Sample ID	Substrate material	Substrate hardness H_v (GPa)	Substrate roughness R_a (μm)
S1	Stainless steel (AISI 304)	1.6	0.05
S2	Stainless steel (AISI 304)	1.6	0.03
T1	Tool steel (AISI D2)	6.8	0.07

TABLE 5.4. Total Coating Thickness and Surface Roughness

Sample ID	Coating thickness (μm)	Coating roughness R_a (μm)
S1	3	0.05
S2	2.8	0.05
T1	2.7	0.06

interlayer of systems S1 and T1 has a (110) preferred orientation parallel to the surface, whereas system S2 does show two possible orientations, (110) and (200). All systems displayed a broad peak characteristic of an amorphous phase, suggesting that both WC and carbon layers are amorphous. The only exception is in the system T1 where a single diffraction peak indicates the presence of a WC crystalline phase.

The morphology of the WC–C is disclosed by plan-view and cross-sectional scanning electron micrographs in Fig. 5.3. The coatings have a nodular surface morphology with growth defects—droplets—typical for PVD.[52] Their morphological difference is mainly based on the density of small droplets originating from the deposition process. It is thought that the increased droplets density observed in coating S2 was caused by slight decrease in either the bias sputtering (bias voltage applied during ion bombardment in planar sputtering apparatuses) or the working gas pressure. Both parameters are reported[53] to lower the ion energy of the atoms impinging upon the growing surface. Consequently, the effectiveness of the ions in suppressing the formation of droplets by sputter redistribution of coating material during growth was reduced.

The surface grooves in the coating are due to irregularities on the underlying substrate, as can be attested by the cross-sectional micrographs. The substrate irregularities, grooves, and ridges were still present after the pretreatment because the process was unidirectional. The polishing resulted in a smoother surface. However, it did not remove completely the deeper grooves or higher ridges. The coating thickness and surface roughness are presented in Table 5.4. The cross-sectional scanning electron micrographs were obtained with a backscattered electron (BSE) detector. Since the number of BSEs are known to increases with increasing atomic number, scanning electron micrographs in Fig. 5.3b, d, f revealed important insights regarding the coatings composition. Apparently, the concentration and distribution of tungsten, the element with higher atomic number, is different in the various coatings. Systems S1 and T1 are alike with respect to the thickness of the band with a higher tungsten concentration, whereas in system S2 the band is roughly twice as thick. As can be promptly perceived, this difference may have a direct influence on the elastic properties of the coating.

The tungsten enrichment of the brighter band observed in BSE micrographs was cross-checked by an AES line profile. This technique was utilized on a cross-sectional sample from system T1, prepared as described in Section 2. Figure 5.4 shows such AES line profile. It can be seen that both C and Cr Auger intensities

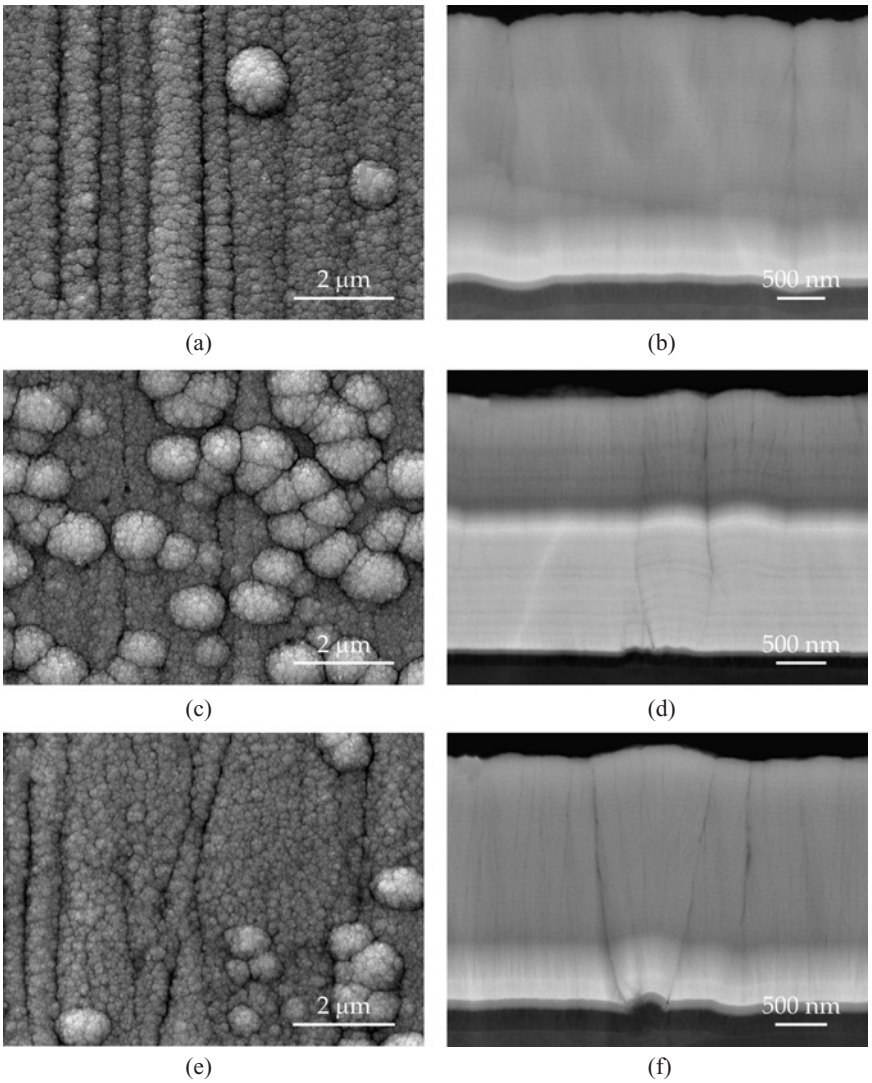

FIGURE 5.3. Scanning electron micrographs displaying the morphology of WC–C coatings. (a, b) Plan-view and cross section of coated system S1, respectively; (c, d) Micrographs of system S2; (e, f) Micrographs of system T1. The plan-view micrographs illustrate the coating nodular surface morphology, typical of PVD process, and grooves created by underlying substrate irregularities. The cross-sectional micrographs obtained with backscattered electron detector show differences in tungsten concentration.

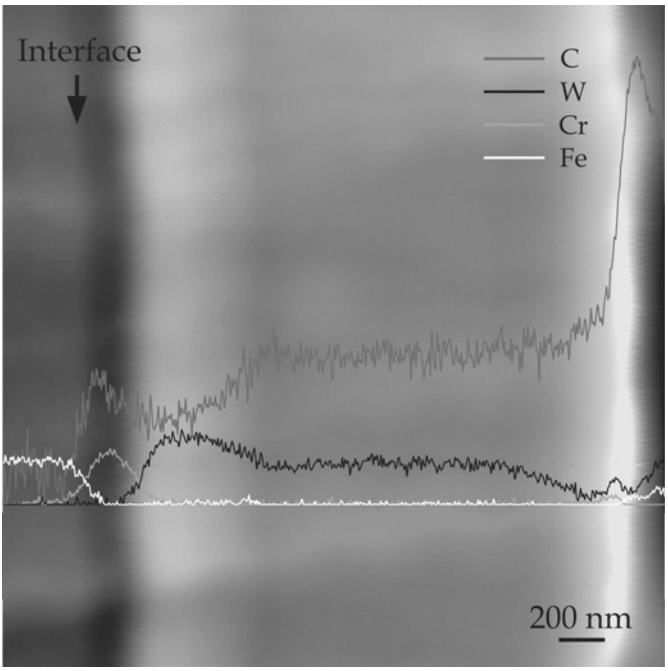

FIGURE 5.4. Line profile of C_{KLL}, W_{MNN}, Cr_{LMM}, and Fe_{KLL} Auger intensity plotted as function of film thickness. The data are superimposed on a scanning electron micrograph of the coated system T1. The zero intensity line corresponds to the position where the data were taken. The arrow indicates the coating–steel interface.

are enhanced at the Cr layer. After that, the W intensity increases reaching a maximum in the brighter band, while for C it is the opposite. The Cr drops to zero, indicating that the Cr deposition ceased. EDS analysis performed on cross-sectional TEM specimens, also confirm the W and C concentration gradient at the WC layer. However, beyond this region their intensities are uniform through the remaining multilayer until roughly half a micrometer from the top. From here on, the friction properties of the film are enhanced by an increase of C and decrease of W. The sharp C signal at the edge of the sample is related to a change in surface orientation of the sample (edge of the cross section) rather than a sudden increase in concentration.

The coating–substrate interface is shown by a HRTEM image in Fig. 5.5. There is an amorphous interfacial region (approximately 5 nm thick) between the crystalline steel substrate and the columnar chromium.

The interphase shows a relatively smooth top surface, whereas the interface to the underlying steel presents a slight roughness due to diffusion of chromium into steel. From a through-focal series of images it was learned that the interphase showed no contrast reversal, i.e., the contrast did not change from bright to dark as

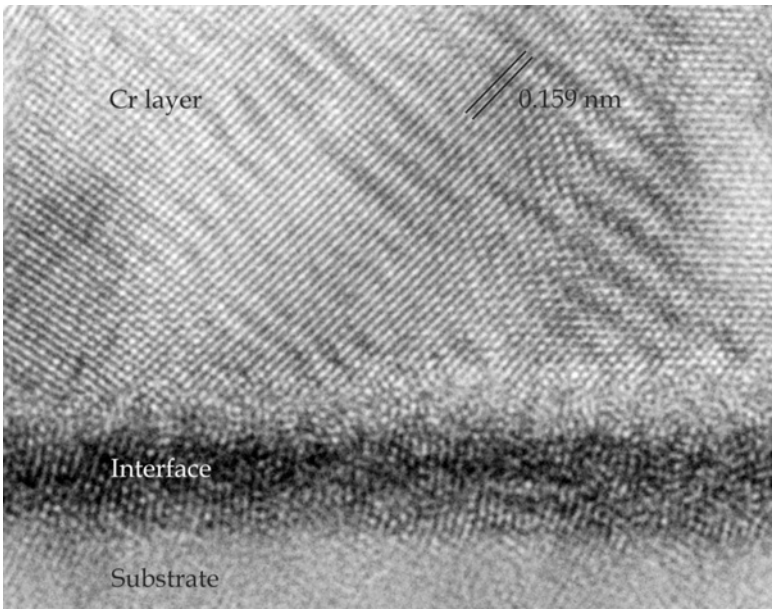

FIGURE 5.5. Cross-sectional HRTEM image of the coating–substrate interface region of coated system T1. The other systems' interphases are similar to this one.

the focus condition was changed from under- to overfocus. This indicates that the interfacial region is made up of a high-atomic-density phase.[54] It is believed that this high-density interfacial contact allows a robust adhesion of the chromium layer to the substrate. Further, the interphase initially has a higher contrast, suggesting that it is composed by a higher mass thickness. All these considerations allow assuming that first chromium had diffused into the steel, to an extent of $\sim$2.5 nm, and then an amorphous chromium region was formed. Within this amorphous layer the columnar structure must have been nucleated.

Figure 5.6 shows plan-view TEM images, with corresponding selected-area electron diffraction (SAED) patterns, from coatings S1, S2, and T1, respectively. The images clearly demonstrate that the coatings, at least the upper part from where the images were taken, are amorphous.

However, a medium-range order is present with an approximate average domain size of 3 nm in coatings S1 and S2, and 10 nm in T1. This type of microstructure has been described as a uniform 3D-network structure.[55] Accordingly, these coatings are composed of a mixture of sp^3- and sp^2-bonded carbon atoms. The sp^2 bonding, from energetic considerations and propensity to form planar ring and sheet structures, tend to segregate in small graphitic clusters containing fused six-fold rings, which are embedded within an sp^3-bonded random network. Further, it is reasoned that the granular structure seen in the images is related to strain, rather

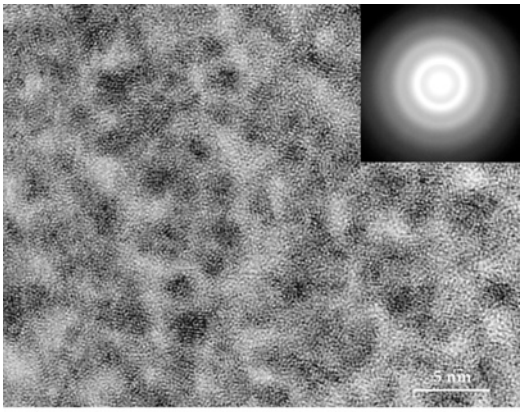

(a)

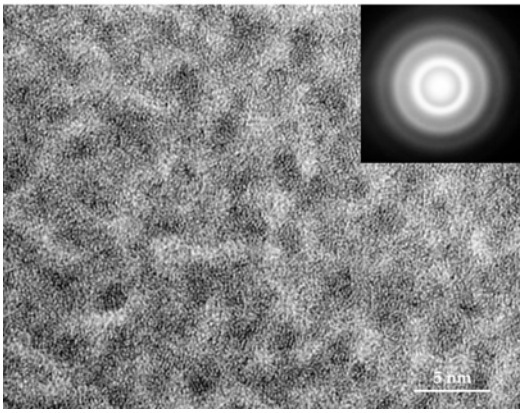

(b)

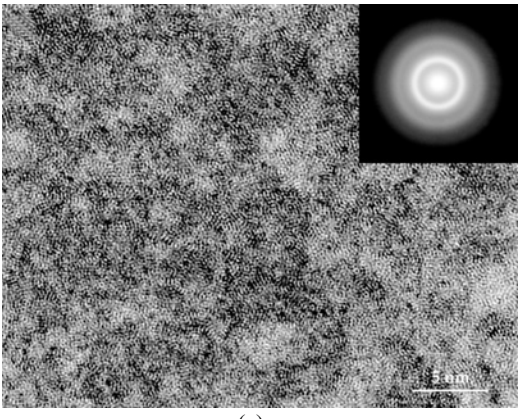

(c)

FIGURE 5.6. Plan-view TEM images exhibiting the planar microstructures of the coatings: (a) system S1; (b) system S2; (c) system T1. The SAED patterns are identical and indicative of an amorphous phase.

than to the percolating patterns of sp^2 and sp^3 bonds. The strain in the structure instead of being distributed randomly is relieved abruptly at the edges of the sp^2 islands, creating the difference in contrast.[56] Nevertheless, in coating T1 (Fig. 5.6), due to the larger cluster size, most likely caused by a lower hydrogen content, the strain relieve was more homogeneous.

The SAED patterns shown in the insets are identical and composed of diffuse diffraction rings typical of amorphous materials. The two most intense diffraction rings were observed to have an interplanar spacing of 0.245 and 0.140 nm, which is consistent with previous reports.[57] The measured interplanar spacing of these two rings reinforces the idea of a diamond-like structure, considering that for crystalline diamond the (111) and (220) strongest reflections correspond to $d = 0.206$ and 0.126 nm, respectively. The microstructure of the coating systems is presented by overview cross-sectional TEM images in Fig. 5.7. Their structure, when going from the interface with the substrate to the surface of the coating, is formed by a

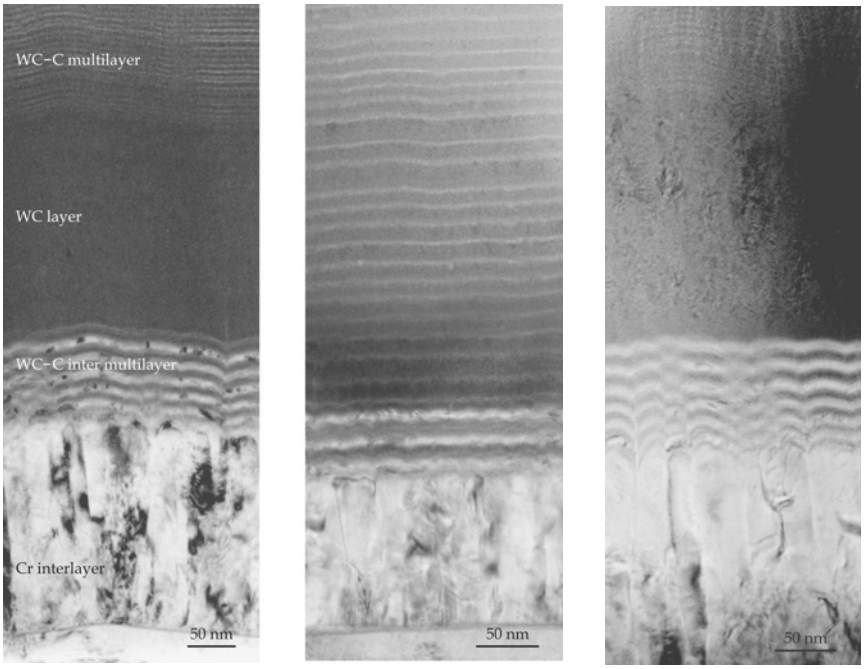

FIGURE 5.7. Cross-sectional overview TEM images showing the microstructure of the coatings: (a) system S1; (b) system S2; (c) system T1. The structure is constituted of a chromium interlayer, an inter-multilayer, a WC layer for systems S1 and T1, and the WC–C multilayers.

chromium interlayer, inter-multilayers of WC and carbon, a WC layer, and finally the WC–C multilayers.

The chromium interlayer has a dense columnar structure, typical of coatings grown under low energetic ion bombardment and limited adatom mobility conditions.[58] Its average thickness is ∼205 nm, except in system S2 where thickness is ∼120 nm. The average column diameter is 22, 18, and 24 nm for system S1, S2, and T1, respectively. This indicates that the columns broaden with increasing layer thickness. Therefore, the column diameter can be explained considering the three stages of development of textures in PVD films: nucleation, competitive growth, and steady growth. Once the (110) orientation achieved dominance in the competitive growth at the expenses of the (200) orientation, which is thought to occur after the first 100 nm, the interlayer grew steadily with this preferred orientation. The inter-multilayers are fashioned by WC and carbon amorphous layers, corresponding to darker and brighter bands, respectively. Their thickness in systems S1 and T1 is ∼93 nm with a periodic wavelength, Λ, of ∼15.5 nm. On the other hand, in system S2 they are ∼50 nm thick. Further, their structure is different, comprising three thicker carbon layers with thinner WC and carbon lamellae in between. The chromium columnar structure seems to have grown into all the inter-multilayers, distorting them by imposing a wavy structure with a period linked to the column diameter. As a result, nano-polycrystalline particles of chromium carbides were formed in the carbon layers. In between the inter-multilayer and the WC–C multilayers, there is an amorphous WC layer with a thickness of ∼200 nm in systems S1 and T1. In the former, the layer is truly amorphous while within the latter the polycrystalline columnar particles were grown. In addition, this layer is darker than the remaining coating, indicating that it has a higher mass thickness. Altogether, these interfacial bond layers between the WC–C multilayers and the substrate are employed to provide a good adherence in applications where a high shear stress component is present.[49]

The WC–C multilayers have an interlaminar structure with the darker lamellae being WC rich and the brighter lamellae carbon rich. Once again, the thicknesses of the interlaminants in systems S1 and T1 are roughly the same, ∼6 nm for WC and ∼2 nm for carbon. In the case of system S2, they were grown directly on the inter-multilayers with a Λ of ∼15.5 nm, and a WC lamella thickness of ∼13 nm. From HRTEM, it was found that the multilayers have a different interlaminar structure (see Fig. 5.8a,b). In systems S1 and T1, they consist of an amorphous phase, whereas in S2 they are constituted of an amorphous matrix with clusters of crystalline particles embedded in the WC lamellae. The carbon lamellae have approximately the same thickness in the three coatings. However, the C–WC interface in the former systems is rather diffuse, whereas in S2 the interface is sharper. As mentioned before, the possible lower bias sputtering employed during the deposition of coating S2 resulted in a weaker atomic mixing at the interface. This created a sharper interface with a reduced bonding between the lamellae. An overview of the constitution and dimensions of the coated systems is given in Table 5.5.

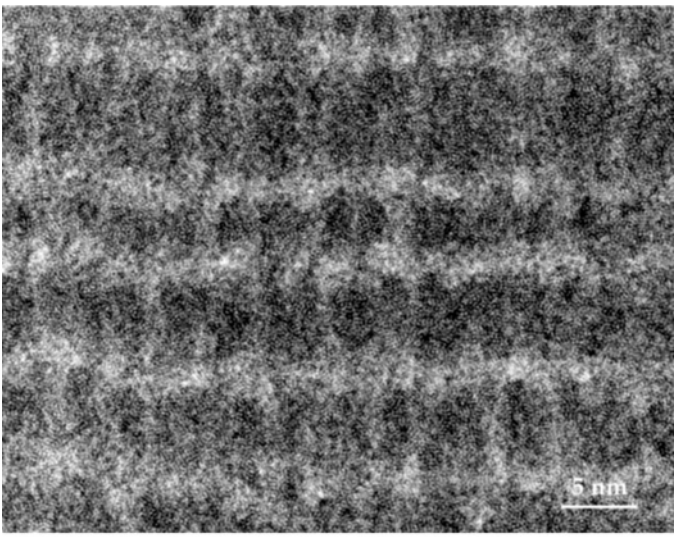

(a)

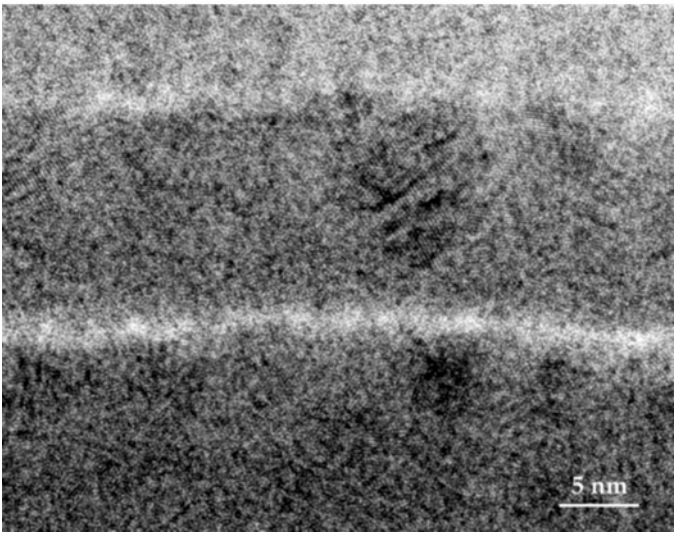

(b)

FIGURE 5.8. Cross-sectional HRTEM images of the interlaminar structures: (a) coated system S1 displaying the diffuse C–WC interface (the one from system T1 is similar); (b) coated system S2 with a sharp C–WC interface. In both images the brighter lamellae correspond to carbon.

TABLE 5.5. Structure and Dimensions of the Coated Systems.

Substrate material		System S1 Stainless steel	System S2 Stainless steel	System T1 Tool steel
Chromium layer (nm)		205	120	205
Intermultilayers (nm)	Thickness	93	50	93
	Periodicity	15.5	—	15.5
Amorphous WC layer (nm)		200	—	200
WC/C multilayers (nm)	Thickness	2750	2600	2360
	WC layer	6	13	6
	C layer	2	2.5	2

3.3. Particles Inside an Amorphous Structure

The structure of the inter-multilayers consists of WC and carbon layers, both being amorphous. However, in the latter, nano-polycrystalline particles were found. An example of such particles is shown in Fig. 5.9. As can be observed, the structure of the layers depends on the interface roughness originating from the individual chromium columnar structure. It is interesting to note that the shape of the polycrystalline particles follow the morphology of the carbon layers and are present only in these layers. The formation of these particles can be attributed to some residual chromium atoms that might still be present in the coating chamber after the interlayer growth, and due to their high affinity for carbon, chromium carbide nano-sized particles have been formed. This assumption is supported by electron-energy-filtered images of the inter-multilayers, where chromium was mapped in the carbon layers.

Another type of crystalline particles, embedded in the amorphous WC layer of system T1, is disclosed in Fig. 5.10a. These particles prevailed throughout the layer and have a structure similar to the ones formed by ballistic aggregation on a point seed.[59] However, the void streaks often observed in the columnar structure were replaced here by stacking faults. The growth direction of the particles was parallel to the $\langle 200 \rangle$ direction and normal to the coating–substrate interface.

From SAED pattern analysis, it was possible to identify the structure of these particles as face-centered cubic β-WC_{1-x}. This identification is also in agreement with the XRD pattern, where one diffraction peak corresponds to the (200) plane of the β-WC_{1-x} phase. As can be seen in the HRTEM image of Fig. 5.10b, the crystal has a high density of stacking faults in the $\{111\}$ planes. This fact is related to the cubic β-WC_{1-x} phase being stable only for a carbon concentration of $\sim$40 at%, while for higher carbon content the hexagonal structure is more favorable.[60] Nevertheless, microchemical analysis performed by EDS showed that the particles present in the amorphous layer have an atomic concentration of carbon related to their hexagonal structure. Therefore, the presence of intrinsic stacking faults in the close-packed $\{111\}$ planes allows local transformations of the cubic structure into

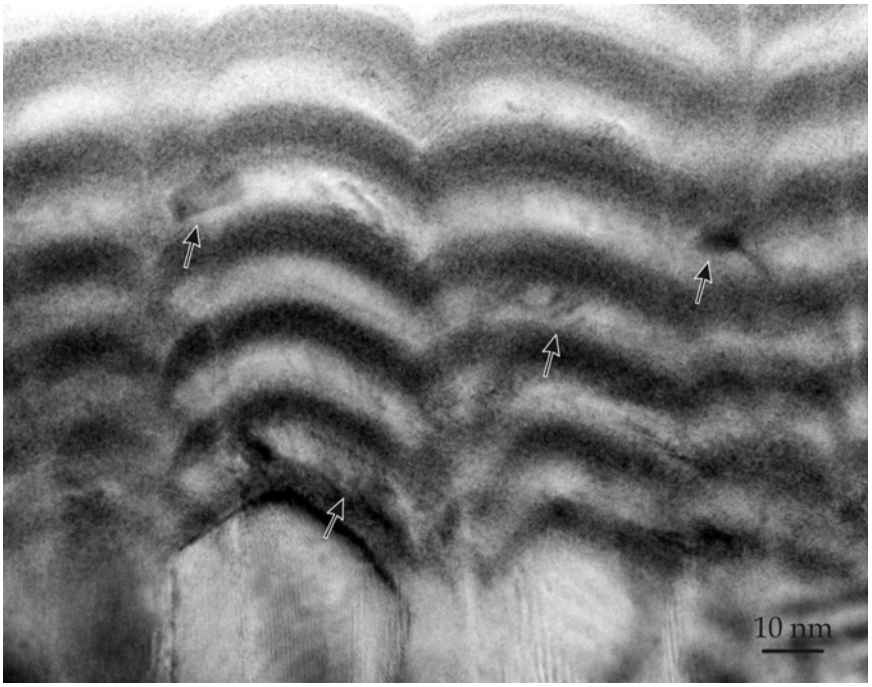

FIGURE 5.9. Cross-sectional TEM image of the inter-multilayers of coated system T1. The darker layers correspond to WC, whereas the brighter correspond to carbon. In the latter, nano-polycrystalline chromium carbide particles are present due to growth of chromium into the inter-multilayers (some are arrowed). Moreover, their morphology is related to the diameter and top morphology of the chromium columns. Planar defects were created at the interface of the columns whenever the columns presented a faceted top morphology.

hexagonal. The WC–C multilayers from coating system S2 are constituted by an amorphous interlaminar structure with clusters of crystalline particles in the WC lamellae. Figure 5.11 shows a HRTEM image of a WC lamella containing such nanocrystalline particles. They are equally distributed throughout the multilayers, having a relatively constant diameter of 4–10 nm. Their position in the lamella is always shifted slightly toward the upper part. This observation allows assuming that their nucleation did not occur at the first WC atomic layers, because the interface with the previous carbon lamella was not sharp, owing to interdiffusion of the latter. Therefore, as the particles' nucleation started roughly in the middle of the lamella and it was ceased by the growth of the next carbon lamella, they have obviously a smaller size than the lamellae thickness. Given their relatively small size, it was impossible to determine the crystal structure and hence the phase either with XRD analysis or with SAED. Thus, to calculate the structure of the clusters, Fourier transformation from the HRTEM images was applied to obtain the diffraction pattern. Subsequently, the diffraction pattern was rotated to get rings from the symmetrically distributed diffraction points, and the interplanar spaces

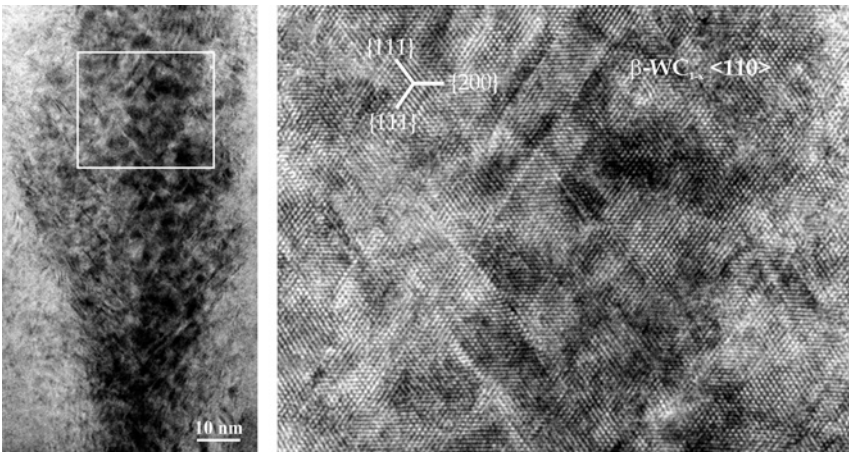

(a) (b)

FIGURE 5.10. Cross-sectional TEM image of (a) a crystalline columnar particle embedded in the amorphous WC layer from coated system T1. The particle is viewed along the <110> zone axis and was identified as having a cubic β-WC_{1-x} phase. (b) Detailed HRTEM image from indicated area in part (a) showing the intrinsic stacking faults in the {111} planes of the particle.

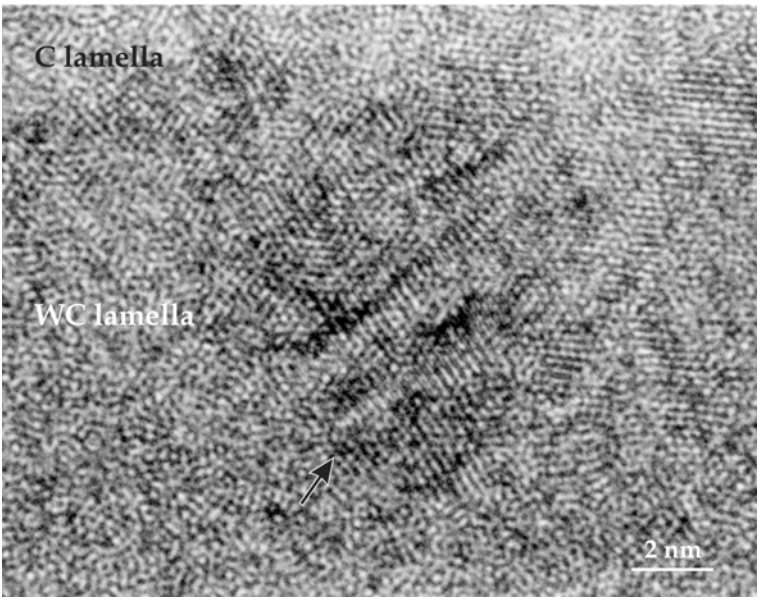

FIGURE 5.11. Cross-sectional HRTEM image of the interlaminar structure from coated system S2, exhibiting the nanocrystalline clusters embedded in the WC-rich lamella. The carbon-rich lamella is represented on top of the image by the brighter stripe. The arrow marks the position of a nanocrystalline cluster identified as having the cubic β-WC_{1-x} phase.

corresponding to the lattice points were measured. The same method was applied to the crystals present in the WC layer from system T1, and both were compared. The result allowed concluding that the clusters present in the WC lamellae of system S2 have the same phase—cubic β-WC_{1-x}—as the crystals present in the WC layer of system T1. In the other coating systems, the WC lamellae have no particles present, which is believed to be related to their reduced thickness of $\sim$6 nm, not enabling particle nucleation and growth.

3.4. Defect Structure

The coated systems exhibited two types of defects that are prone to jeopardize their mechanical properties. They were induced either by substrate surface irregularities or simply by the top morphology of the chromium columns. The defects produced by the substrate-ridged surface were transferred-through and magnified by the coating. Their growth structure was a direct consequence of the geometric shadowing because the high points on the growing surface received more coating flux than did the valleys.[61] Moreover, the application of low-energy ion bombardment with a small fraction of resputtering did not allow the production of planar surfaces. Thus, macroboundaries (defects) developed at the lower chromium surface within a groove, and at either side of a ridge (cf. Fig. 5.3b,f). The degree of openness is associated with the magnitude of the surface irregularity from where it was originated. Figure 5.12a displays a cross-sectional TEM image of two macroboundaries created by a substrate ridge. Although the macroboundaries in the image are due to the existence of a ridge, they were enhanced by the convex-shaped cusps formed by the two adjacent chromium columns at the rim of the ridge. These cusps have been reproduced by each individual layer because the coating did not loose the memory of the earlier steps in its growth (see Fig. 5.12b).

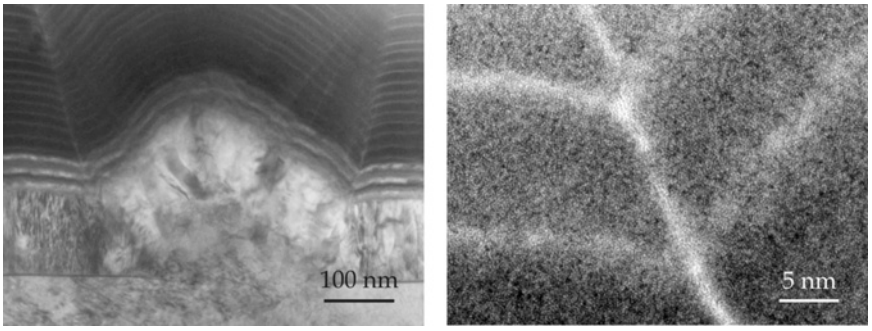

FIGURE 5.12. (a) Cross-sectional TEM image of the macroboundaries created by a substrate ridge. (b) HRTEM image revealing the defect morphology induced by the convex-shaped cusps produced by two adjacent chromium columns at the rim of the ridge.

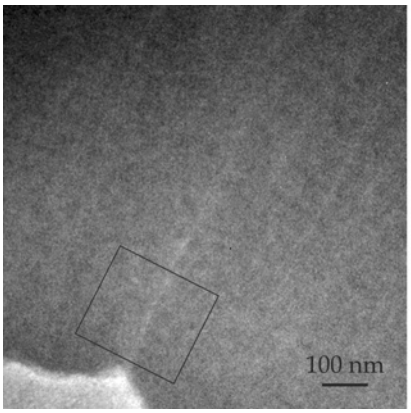

(a)

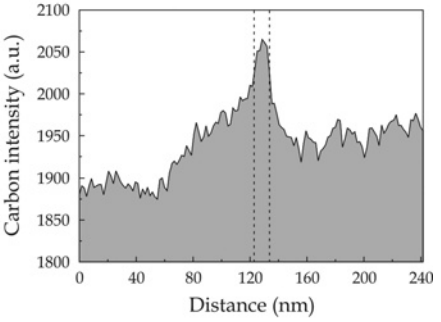

(b)

FIGURE 5.13. (a) Cross-sectional TEM carbon mapping image of a defect from coated system T1. (b) Compositional carbon profile across the defect for an integration width of 100 pixels (214.3 nm). The dash lines delimit the defect width measured from the zero-loss image.

Another type of defects, however, with a much smaller length scale, were formed whenever the chromium columns had a strongly faceted top morphology, resulting in deeper and sharper cusps between two adjacent columns. These planar defects propagated from the cusp minimum, but often only through the inter-multilayers. They were ceased by the growth of the WC layer. Others had a longer path but never reached the interface with the WC–C multilayers structure (cf. Fig. 5.9). Chemical information on the defects was extracted from transmitted electron-energy-filtering images recorded under high-resolution conditions. Figure 5.13a,b shows a carbon image mapping recorded using the C K-edge and the corresponding compositional profile taken perpendicular to the defect. The width of integration perpendicular to the resulting profile is a trade-off between resolution and noise. However, a good compromise was obtained by a 100-pixel width (100 pixel equals 214.5 nm). The carbon compositional profile demonstrates that there is enrichment along the defect, which must be caused by carbon segregation during the deposition process. Therefore, it is concluded that the lower mass thickness material present in the coating composes the macroboundaries and planar defects. The reduced path of the planar defects is related to the nonexistence of free carbon in the WC layer to stabilize their propagation.

3.5. Mechanisms of Crack Propagation

Contact-induced fracture in coated systems is complex and controlled by the coating material itself, the substrate upon which the coating is deposited, and the interface(s) that bond the system together. Ultralow load indentation (nanoindentation)

experiments have become increasingly widespread to gauge the mechanical properties of coated systems. The appeal of this technique is that very low loads and displacements are available, enabling characterization on a submicrometer scale. The nanoindentation response of the three-coated systems have been studied previously.[62,63] The loading curves of the systems with stainless steel as substrate—S1 and S2—displayed a discrete change in slope, related to annular through-thickness cracking around the indentation periphery. The response of coating system T1 did not show any change in the loading slope. Instead, the presence of nested cracks following the indentation profile was observed. The lower part of the unloading curve of system S2 was of considerable interest, since it was indicated that during the last stages of unloading the sample was relaxing elastically, and suddenly it tried to push the indenter out, as if the coating had popped-up by propagation of an interfacial crack. Confocal microscopy of the indentations revealed that the coating surface within the annular crack was displayed above the residual position. As coated systems S1 and S2 share the same substrate and chromium interlayer, the evidence of uplifting only on S2 suggested that the failure mechanism was decohesion within the coating rather than debonding from the substrate.

Cross-sectioning the nanoindentations was aimed at confirming that the failure mechanism was indeed decohesion within the coating. Figure 5.14 shows a

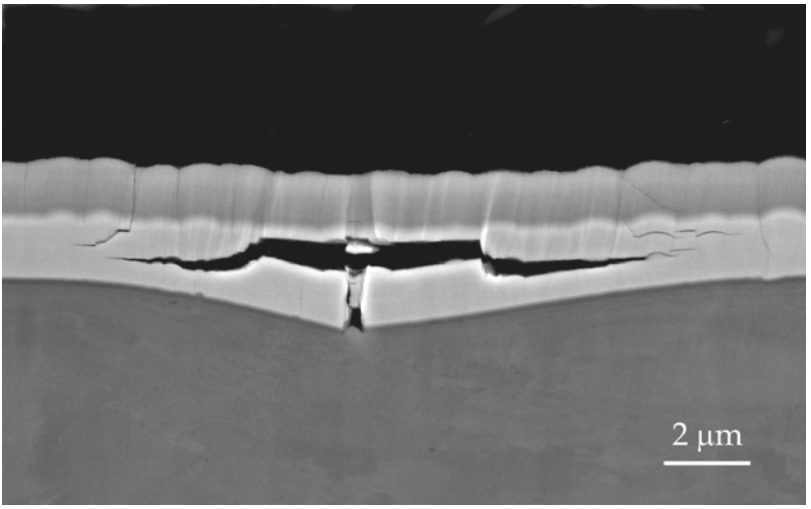

FIGURE 5.14. Scanning electron micrograph displaying a cross section of a 400-mN nanoindentation on system S2. The coating contrast is related to dissimilarity in tungsten concentration, where brighter band corresponds to a higher concentration. The right- and left-hand-side cracks normal to the surface are from the annular crack formed around the indentation periphery, while the central crack was created by the indenter apex. The micrograph clearly establishes that the crack propagation occurred inside the coating.

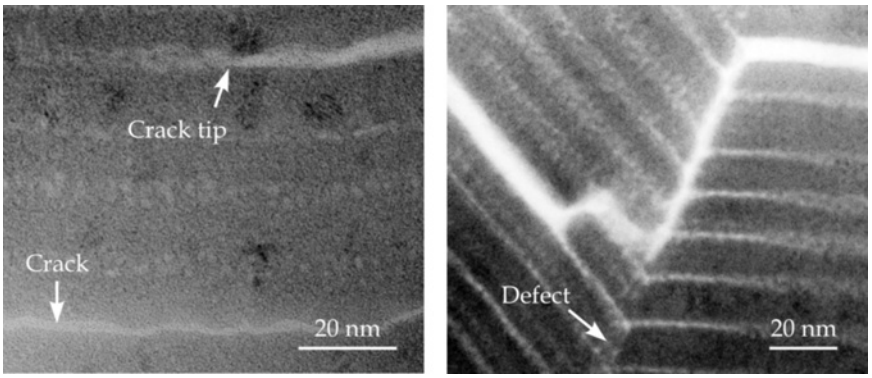

FIGURE 5.15. (a, b) Cross-sectional TEM images of the crack path. The images unequivocally confirm that crack propagates in the carbon lamellae of the multilayer and glides through carbon-enriched defects.

scanning electron micrograph of a cross-sectioned 400-mN nanoindentation. The area where the micrograph was taken can be precisely determined from the diameter of the annular crack and the orientation of the indenter tip. The presence of a brighter band in the coating is due to a higher tungsten concentration (cf. Fig. 5.4). The micrograph clearly establishes that the uplifting of the coating occurred not by interfacial fracture but by crack propagation inside the coating. Further, the cracks produced by tensile stresses, namely, the one related to the indentation apex and those through thickness are also observed. It is noteworthy that the elastic strain energy stored within the coating due to bending is not enough for, upon unloading, debonding the chromium interlayer from the steel substrate. Instead, as shown in Fig. 5.15, the energy was released by crack propagation in the carbon lamellae of the WC–C multilayers, where crack arrest occurred when the system reached equilibrium (see Fig. 5.15a). The crack propagated normal to the multilayers through carbon-enriched defects present in the coating, as seen in Fig. 5.15b. These defects were created either by substrate surface irregularities or simply by the top morphology of the chromium columns. The explanation for crack propagation in the carbon lamellae (ultimately leading to decohesion) of coated system S2, and not of system S1, is related to their multilayer microstructure. System S2 has a sharper interface between the lamellae (in contrast to the rather diffuse one of system S1). This difference in atomic mixing at the interface (cf. Fig. 5.8) is thought to be important for crack propagation. Moreover, the existence of an intermediate WC layer in the coating system S1 proves to be effective in supporting a fraction of the load and promoting the adhesion between the multilayers and the remaining coating. The sequence of deformation events occurring during indentation is illustrated schematically in Fig. 5.16. Initially, only the coating deforms elastic-plastically (as is confirmed by the initial linear portion of the $P - \delta^2$ curve). Hence, the coating is

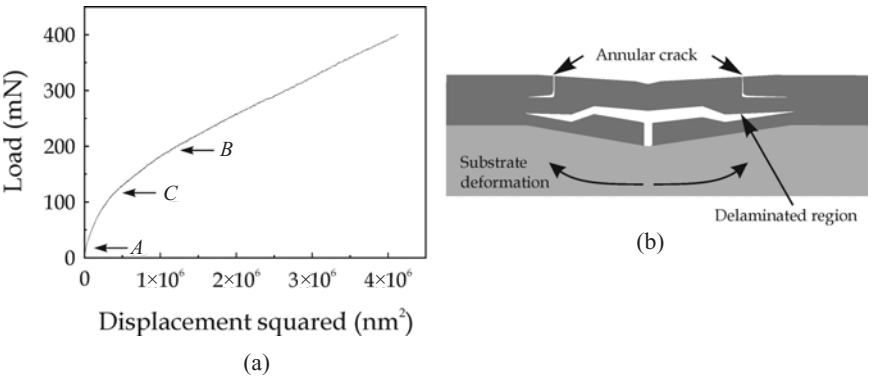

FIGURE 5.16. (a) Load–displacement data corresponding to the higher peak loads as load–displacement squared for system S2. A transition between the different regimes is observed. (b) Schematic diagram of the indentation-induced cracks in system S2.

deforming in response to the maximum hertz-like shear stress that lies well within the coating depth. As the shear stress will decrease with depth,[64] it is apparent that the maximum value experienced by the substrate at this load is not high enough to yield. Beyond A on the $P - \delta^2$ curve, the substrate commences to experience a sufficiently high shear stress for plastic yielding. This requires the coating to flex and bend to conform to the subsurface deformation. However, the shear stresses in the coating are only large enough to cause plastic flow in an area immediately around the axis of the contact and along the indenter edges. At the same time, as the coating is forced to bent to follow the substrate deformation and pileup, significant tensile stresses around the outer periphery of the contact zone in an approximately circular pattern are being generated. This corresponds to the region A–C on the $P - \delta^2$ curve. At a known but slightly variable load, corresponding to the change in $P - \delta$ loading slope (point C), the tensile stress reaches a maximum value, causing the coating to crack around the indentation periphery, resulting in an annular crack.

Presumably at this critical load, the tensile stresses beneath the indenter apex are sufficiently high to onset the crack propagation normal to the coating–substrate interface (this assumption was confirmed experimentally by cross-sectioning a 200-mN nanoindentation). Increasing the load, the coating still plays some role in the deformation mechanism until the third regime in the $P - \delta^2$ curve is reached. Beyond that (point B) the coating confined by the annular crack retains only a small portion of the membrane stresses and the substrate dominates the system response to deformation. Increased loading causes further annular cracks to occur as a larger proportion of the coating is bent into the substrate. When the load is released, the slope of the initially unloading curve is constant due to the elastic recovery within the indentation. However, during the last stages of unloading very significant levels of elastic recovery occur, followed by a sudden increase

of the load at the indenter apex, corresponding to crack propagation inside the carbon lamellae parallel to the interface. The crack propagation is driven by the elastic strain energy stored within the coating free from the annular crack, i.e., the portion of the layer thickness beneath the through-thickness annular crack tip. The annular crack tip is always deflected outwards from the indentation impression. The cracks propagate until the system reaches equilibrium, which occurs further than the position of the annular crack. The nonobservance of coating uplifting for peak loads above ∼500 mN is thought to be related to the elastic strain energy stored by bending of the small coating fraction beneath the annular crack tip. This energy is not enough to overcome the carbon cohesive energy and the energy necessary to push the coating volume (bounded by the annular crack) upwards.

Previous studies on the mechanical properties of these coated systems[65] permitted to conclude that the hardness of WC–C is ∼14 GPa and the effective Young's modulus is ∼220 GPa. The good performance of the WC–C multilayers is attributed to low friction and stress levels offered by their ductility properties. The carbon lamellae reduce the friction and most likely the surface temperature. On sliding wear tests the WC–C is eventually consumed, even under mild conditions and low wear rates, making it an unsuitable choice in tribological applications of long-term use. Nevertheless, it is beneficial under emergency situations, giving a low friction coefficient and a relative extensive lifetime.

In this section, the microstructure of WC–C coatings deposited on stainless steel and tool steel has been revealed. The main characteristics are the following:

- The interfacial region between the crystalline steel substrate and the columnar chromium consists of an amorphous high-atomic-density phase.
- The coating structure is constituted by a body-centered cubic chromium columnar interlayer, amorphous intermultilayer of WC and carbon, an amorphous WC layer, and finally the amorphous interlaminar WC–C structure.
- One of the differences between the coatings is the thickness of a ribbon with a higher tungsten concentration after the inter-multilayers. This ribbon is employed to improve the load capacity of the coating.
- Although the coatings are found to be primarily amorphous, crystalline particles are present, namely, nano-polycrystalline chromium carbides in the carbon layers of the inter-multilayers, cubic β-WC_{1-x} in the WC interlayer, and clusters of cubic β-WC_{1-x} phase in the WC lamellae of the interlaminar WC–C.
- Defect structures were generated by the presence of substrate surface irregularities and by the top morphology of the chromium columns. Both types of defects are mainly composed of carbon. There is evidence that the presence of a WC interlayer is beneficial for defect truncation because of the nonexistence of free carbon to stabilize the propagation of the defects.
- Whenever the load–displacement curve shows a discrete change in slope, annular cracks around the indentation periphery are present.

- The deformation mechanism of coated systems depends on the substrate plastic properties. For stainless steel substrates, annular cracks are formed, while for tool steel, nested cracks are created.
- The nanoindentation response gives accurate information whether or not the coating has popped-up during unloading.
- The WC–C system responds to the release of the elastic strain energy by crack propagation in the carbon layers, rather than by interfacial fracture.
- From the microstructural characterization and the mechanical performances studied in this section, it can be concluded that the system T1 (cf. Fig. 5.7c) appears to be the most promising for industrial applications.

4. CHARACTERIZATION OF TiN AND TiN–(Ti,Al)N MULTILAYERS

4.1. Transition Metal Nitrides

Transition metal nitrides have been studied intensively in the last decades due to their properties and are today widely used. Titanium nitride belongs to the group of so-called hard refractory metals. They are characterized as having a high melting point (1500–3400°C), hardness (20–30 GPa), brittleness, and metallic conductivity.[66] The bonding structure of these hard metals consists of a combination of localized metal-to-metal and metal-to-nonmetal interactions resembling both covalent and metallic bonding.[67] The metal-to-nonmetal bonding is favored by the octahedral grouping of the metal atoms around a central carbon or nitrogen atom; however, the presence of the nonmetal also tends to increase the strength of metal-to-metal bonds. There also exists an electronic charge transfer from the metal to the nonmetal atoms, being greater in the nitrides than in the carbides, i.e., with increasing electronegativity of the nonmetal atom.[68] Thus, the bonding arises from simultaneous contributions of covalent, metallic, and ionic bonding to the cohesive energy.[69] The Ti–N equilibrium phase diagram shows three stable solid phases. The cubic B1-NaCl crystal structure δ-TiN phase is stable over a wide composition range ($0.6 < \mathrm{N/Ti} < 1.2$) and the hexagonal α-Ti phase can dissolve up to 15 at% nitrogen. The ε-Ti_2N crystallizes in a tetragonal structure and exists only at a composition range of 33 at%.[66] However, it is the cubic δ-TiN phase that is mostly used in technological applications. Stoichiometric, as well as off-stoichiometric, polycrystalline films have been deposited by a variety of techniques including reactive dc-,[70] rf[71] magnetron sputtering,[72] activated reactive evaporation,[73] and triode ion plating (e-gun) with high plasma density.[74] However, the observed physical properties of these films are reported to vary over orders of magnitude, depending on both the growth technique and the particular deposition parameters.

During the last decade there has been an increasing interest in TiN because of the successful use in a variety of thin film applications. For example, its high

hardness gives a good resistance to abrasive wear, and the high chemical stability results in a high resistance to solution wear. Therefore, it is particularly useful for increasing the wear resistance of high-speed steel cutting tools, punches, and metal forming components.[75,76] In addition, due to the good corrosion and erosion resistance, relative inertness, high sublimation temperature, and optical and electronic properties, TiN coatings also have been considered for applications such as diffusion barriers in microelectronic devices,[77] cosmetic gold-colored surfaces,[78] and wavelength-selective transparent optical films.[79]

Even though titanium nitride coatings already have a dominant position, still considerable efforts are invested in the research and development of multilayer coatings to further enhance the wear resistance of coated components. By alternately depositing two (or more) chemically and/or mechanically different materials, the stress concentration and the conditions for crack propagation can be changed. The multilayer structure may act as a crack inhibitor, thereby increasing the coating fracture resistance. This effect is suggested to result from crack deflection due to weak interfaces,[80] crack tip shielding by plastic deformation in combination with strong interfaces,[81] a favorable residual stress distribution,[82] and crack deflection due to large differences in stiffness between the individual layer materials.[83] Moreover, the properties of the surface can be improved by the deposition of layers that separately have different kinds of effects on the surface, such as corrosion protection, wear protection, thermal isolation, electrical conductivity, diffusion barrier, and adhesion to the substrate. Coatings comprising many thin layers of TiN and (Ti,Al)N take advantage of the multilayer properties and the properties of each component. The primary advantage of (Ti,Al)N is its higher oxidation resistance at elevated temperatures. TiN oxidizes rapidly at temperatures above $\sim$600°C to form TiO_2. Because of the large difference in molar volumes between the TiO_2 and TiN, compressive stresses are developed in the oxide layer, resulting in its spallation.[84] On the other hand (Ti,Al)N forms a dense, highly adhesive Al_2O_3 layer on top of the coating, protecting it from further oxidation. The oxide layer has been demonstrated to be effective in decreasing the interdiffusion of oxygen and aluminum in the coating.[85] Accordingly, the diffusion wear, one of the major wear mechanisms on cutting tools, is reduced. Moreover, its lower thermal conductivity prompts more heat to be dissipated via chip removal, permitting higher cutting speeds due to lower thermal loading on the substrate.[86] Understanding the physical properties, such as the mechanical response, of such complex inhomogeneous materials requires a detailed knowledge of the microstructure. This section presents the results of an investigation on TiN and TiN–(Ti,Al)N multilayers deposited onto stainless steel and tool steel substrates.[87,88] Two different materials, one cold work tool steel (AISI D2) and the other stainless steel (AISI 304), with dimension $90 \times 10 \times 1.5$ mm were used as substrates for both coatings. The chemical compositions (other than iron) and hardness of the substrate materials are as follows. For AISI D2 (wt%): 1.55 C, 0.3 Si, 0.4 Mn, 5.8 Cr, 0.8 Mo, 0.8 V, hardness 6.8 GPa; for AISI 304 (wt%): max 0.08 C, 1.0 Si, 19.0 Cr, 2.0 Mn, 10.0 Ni, hardness 1.6 GPa. The tool steel was heat treated and tempered at 520°C to

obtain the above-mentioned hardness. All substrates were polished to mirror finish, corresponding to R_a values of approximately 0.05 μm. Total coating thickness determination was performed by direct measurements on polished or fractured cross sections, using SEM. The thickness of the individual layers was measured on cross-sectional (TEM) specimens. The coatings structure was determined by XRD measurements in Bragg–Brentano geometry. Microchemical analyses were performed by energy dispersive spectroscopy (EDS), using the focused electron probe of a transmission electron microscope. The focused electron probe—having a nominal probe diameter of 1.0 nm FWHM (full width at half maximum)—was scanned over the surface of a cross-sectional specimen to obtain the elemental line profile distribution. The microstructure of the as-deposited coatings was studied by plan-view and cross-sectional TEM.

Typical XRD diffraction patterns from TiN and TiN–(Ti,Al)N deposited onto stainless steel and bare substrate showed reflections of the substrate from the α-Fe and γ-Fe phases. TiN coatings are polycrystalline, exhibiting diffraction peaks related to cubic δ-TiN phase. However, apparently the peaks have shifted toward lower diffracting angles with respect to their nominal ASTM positions. In fact, the interplanar spacing d_{hkl} for the reflecting planes parallel to the surface determined from the XRD spectra shows, irrespective of the substrate material, higher values than those for a randomly oriented strain-free standard sample, where $d_{111} = 0.2449$ nm. The value obtained for the (111) planes of TiN onto stainless steel and TiN onto tool steel is 0.2464 and 0.2461 nm, respectively. This indicates that the coating is in a state of compressive stresses, which is in agreement with previous results on deposition of TiN. Textural analyses were performed with $I(hkl)$ values determined from the integrated intensity of each (hkl) reflection and $I_0(hkl)$ values obtained from the JCPDS data of TiN. The outcome revealed that the homogeneous coating displays a strong preferred (111) orientation parallel to the substrate surface. The presence of this texture is not surprising, since the (111) plane in the TiN is the one of lowest strain energy due to anisotropy in Young's modulus.[89] Therefore, its alignment normal to the growing direction will minimize the total energy under strain-energy-dominated growth.

The TiN and (Ti,Al)N layers from the multilayer coating also exhibited the B1-NaCl crystal structure. The (Ti,Al)N peaks are shifted to lower interplanar spacing values with respect to the TiN peaks. The smaller lattice parameter is due to the titanium atoms of the TiN lattice being replaced by aluminum atoms. Since the aluminum atomic radius is smaller than that of Ti, the TiN cell is increasingly reduced with higher aluminum content until the ratio of Al to Ti exceeds the limit of approximately 1.1.[90] The small difference in interplanar spacing between TiN and (Ti,Al)N layers makes it very difficult to perform accurate textural analyses using the same method as for homogeneous TiN. Nevertheless, previous XRD polar texture scan measurements have demonstrated that both layers are slightly textured with a (311) preferred orientation.[91] As the multilayers were deposited onto two substrates, the difference in residual stresses made it possible to calculate the Poisson's ratio, the stress-free lattice parameter, and consequently, the residual

TABLE 5.6. Poisson's Ratio and Lattice Parameter of TiN and (Ti,Al)N.

Coating	ν	A_0 (Å)
TiN	0.232 ± 0.002	4.243 ± 0.001
(Ti,Al)N	0.177 ± 0.003	4.170 ± 0.005

stresses of the individual layers. Tables 5.6 and 5.7 summarize the results on lattice strain and macrostresses measurements.

4.2. Microstructural Features

Figure 5.17 shows representative scanning electron micrographs of the surface of TiN and TiN–(Ti,Al)N multilayers. Their topography is typical of ion plating and sputtering deposition processes.[92] The former produces a smoother, shallow rippled surface, being to a certain extent, independent of the substrate roughness. The coating surface deposited from the latter process is flatter with fine grains. However, it memorized the surface topography of the underlying substrate. As can be seen in Fig. 5.17b the grooves and ridges are still present. Nevertheless, the surface also displays pronounced macroparticles and pinholes. The macroparticles are due to droplets that were incorporated during growth of the coating, and pinholes are caused by their debonding. Figure 5.18 displays the TiN–(Ti,Al)N multilayer tilted at approximately 20° to the plane of the surface to obtain information from both the surface and the cross section of the macroparticle and the pinhole. The macroparticles are uniformly distributed with an average diameter $\langle d \rangle$ ranging from tens of nanometer to a few micrometers. They are loosely bonded to the multilayer, as demonstrated by the crack at the rim and the morphology of the pinhole surface, which is similar to the coatings surface. Both coatings have a total thickness close to 5.0 μm, and no difference between the ones deposited on tool steel and stainless steel substrates could be discerned. Figure 5.19 shows a polished cross-sectional scanning electron micrograph of the multilayer obtained with a BSE detector, to emphasize the dissimilarity between TiN and (Ti,Al)N. TiN produces more BSEs and is therefore displayed as layers with brighter contrast. Although the multilayer had been defined as a stacking of TiN and (Ti,Al)N

TABLE 5.7. Residual Stresses (Gpa), with E = 450 GPa.

		Multilayer	
Substrate	TiN	TiN	(Ti,Al)N
Stainless steel	-5.6 ± 0.1	-10.1 ± 0.3	-4.2 ± 0.2
Tool steel	-4.2 ± 0.2	-8.0 ± 0.4	-2.7 ± 0.1

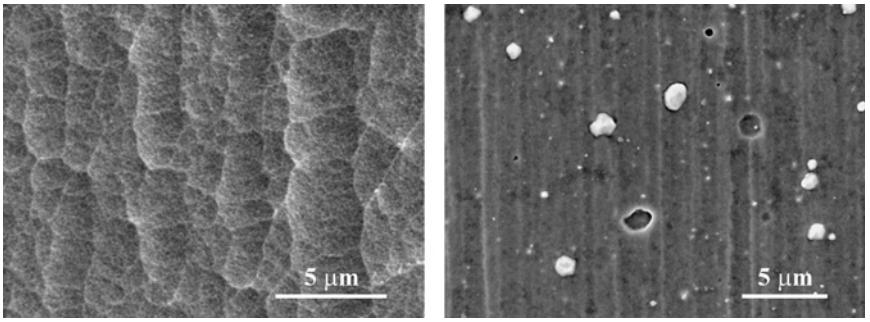

(a) (b)

FIGURE 5.17. Plan-view scanning electron micrographs displaying the surface morphology of (a) monolayer TiN and (b) multilayer TiN–(Ti,Al)N deposited onto tool steel substrate.

layers, the polished micrograph and TEM studies (see below) displayed their real structure, which consisted of a TiN interfacial layer and a periodical structure with the following sequence: (Ti,Al)N–(TiN–(Ti,Al)N), i.e., the multilayer was composed of (Ti,Al)N layers and a superlattice of TiN and (Ti,Al)N, and finally of a thick (Ti,Al)N top layer. This design takes advantage of the superior properties

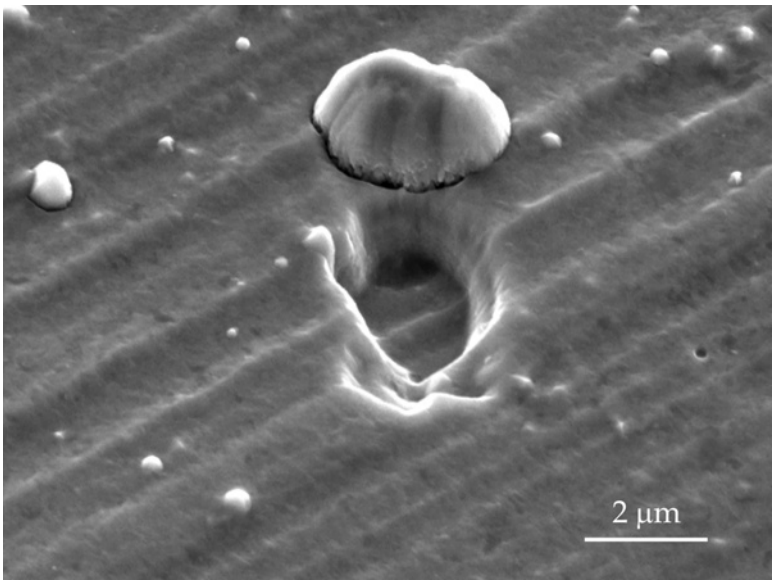

FIGURE 5.18. Scanning electron micrographs of the multilayer. Plan-view showing details from both the macroparticle and the pinhole. The sample is tilted at approximately 20°.

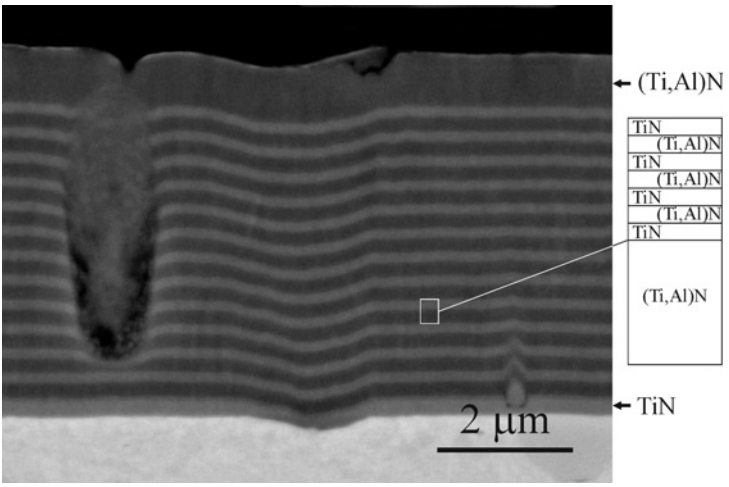

FIGURE 5.19. Cross-sectional backscattered scanning electron micrograph of the multilayers showing their structure and the distortion caused by droplets and substrate surface irregularities.

of each constituent. TiN provides the enhanced adhesion between the coating and the substrate, which can be jeopardized if aluminum is present, because of its high oxygen affinity. (Ti,Al)N protects the system from oxidation, because it has an improved resistance at a higher temperature than TiN.

The microstructure of the coatings was investigated using TEM. Figure 5.20a,b are plan-view TEM images taken near the coating surface, and Fig. 5.20c,d are the corresponding SAED patterns. Both samples are polycrystalline, with grain boundaries free of intergranular porosity and cracks. This feature sometimes made the grain boundaries difficult to observe. Therefore, one had to be careful in distinguishing large grains from clusters of extremely fine grains in close crystallographic orientation. Moreover, as one column might have consisted of several grains or subgrains, the grain size was often smaller than the column width. A high density of defects (dislocations) within the individual grains was also evident.

Moiré fringes from the monolayer TiN are clearly visible. Because they resulted from destructive interference of diffracted waves due to overlapping grains, it indicated that the TiN had a fibrous structure rather than columnar. The grain size distribution is homogeneous with an average size $\langle d \rangle$ of 50 nm. This small grain size is related to ion bombardment during film growth, which is known to create many radiation-induced defects in the growing film.[93] The defect density is sufficiently large to disrupt the columnar structure in such a way that new columns were nucleated periodically causing the suppression of large grains. The multilayer exhibited coarse moiré fringes. This effect is primarily due to the beam

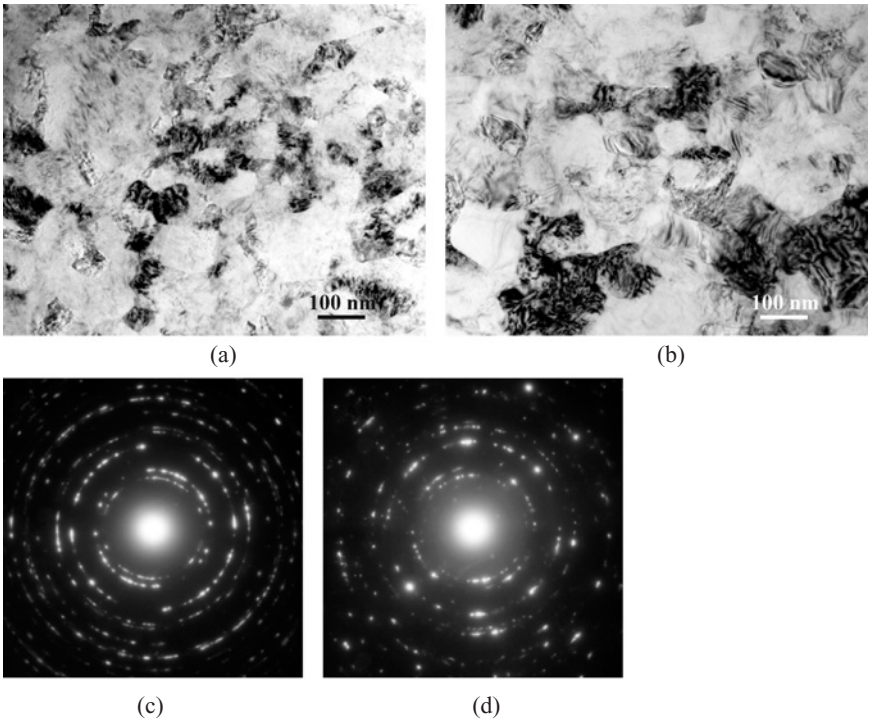

FIGURE 5.20. Plan-view TEM images near the coating surface. (a) and (b) are bright-field images of the monolayer and the multilayer, respectively. The electron diffraction patterns of the corresponding coatings are displayed in (c) and (d).

interference from the gratings of both layers—which have a lattice mismatch of 1.6%—when they are misoriented with respect to each other over a small angle. Nevertheless, although to a lesser extent than the monolayer, there are also moiré fringes produced from the overlap of columnar grains. In this case, the average grain size $\langle d \rangle$ is approximately 100 nm.

The SAED patterns in Fig. 5.20c,d correspond to the B1-NaCl structure. The diffraction rings from the multilayers are broader, resulting from the superposition of reflections from TiN and (Ti,Al)N, where the latter has a slightly reduced lattice parameter. Also, the more diffuse diffraction rings of the monolayer, in contrast to the dotted rings of the multilayers, confirms the relatively finer grain sizes and indicates a poorer crystalline perfection, i.e., the lattice distortion is retained.[94]

Cross-sectional TEM images provided a more detailed picture of the microstructure and evolution of the layers from the interface to the outer surface, as is shown in Fig. 5.21a,b. The monolayer has a dense fibrous structure typical of the zone T according to the zone classification proposed by Thornton.[95] This structure results from the ion-induced defects, such as point defect clusters

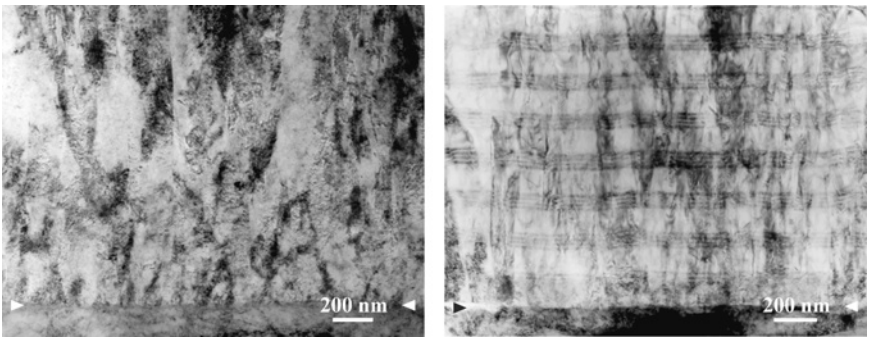

(a) (b)

FIGURE 5.21. Cross-sectional TEM images showing the near-interface microstructure of (a) monolayer and (b) multilayer deposited onto stainless steel substrates. The coating–substrate interface is indicated by the arrows.

and small dislocation loops being trapped in the film, hence leading to a continuous renucleation of new grains during growth that disrupts the columnar microstructure. Thus, only a very few columns (or grains) extend through the whole coating thickness. The average column diameter is rather difficult to calculate due to their twisted nature. However, it is estimated to be approximately 50 nm. The multilayer has a more pronounced columnar microstructure, with an average column diameter increasing with film thickness from ∼80 nm at the coating–substrate interface up to ∼150 nm at the top of the film. This indicates a continuous competition for growth among evolving columns.

From HRTEM it is observed that the monolayer–substrate interface is formed by an amorphous interfacial region of approximately 2 nm wherein the fibrous structure was nucleated. The columns formed in the nucleation and coalescence stages faced severe competition from the others for survival. However, above this region (∼140 nm) of tangled columns and, in some cases oversized grains, the fibrous microstructure became more uniform. This nucleation mode is commonly observed for TiN grown on stainless steel substrate, due to its lack of carbides and a large lattice mismatch between the TiN and steel substrate.[96] On the other hand, the multilayer has an abrupt interface between the TiN interlayer and the substrate. Their deposition process resulted in larger initial nuclei with a more homogeneous size, which led to the formation of wider, more uniformly sized columns that extended throughout the entire coating. The dark contrast observed on both samples below the film–substrate interface is due to strain fields. They are associated with defects within the matrix of the substrate grains induced by residual radiation damage as a result of intense ion irradiation during ion etching. The multilayer composition was determined by an EDS line profile, using the K_α lines for the measured intensity of titanium, aluminum, and nitrogen. The sensitivity factors were calculated using the theoretical cross-section method of *Zaluzec*, which gave the most reliable values. However, it should be emphasized

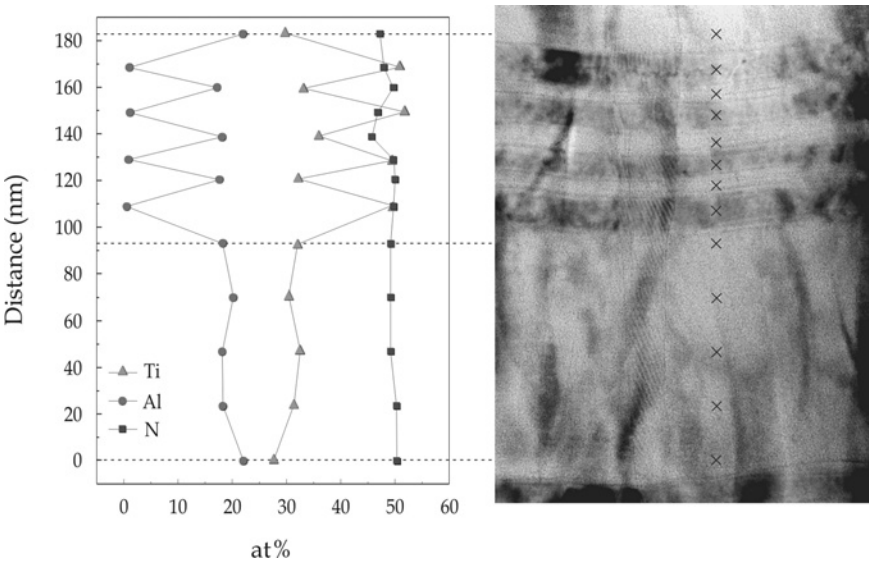

FIGURE 5.22. EDS line profile across the (Ti,Al)N layer and the superlattice. Positions where data are taken are indicated in the TEM image. The nominal probe diameter was 1 nm and the spot acquisition time 30 s.

that the concentrations presented in Fig. 5.22 are considered to be semiquantitative because no standards were used for calibration. The positions where the data were taken are indicated in the TEM image. The results of the analysis showed that the layers were near-stoichiometric with respect to nitrogen (i.e., Ti–N $\approx$ 1:1 and (Ti,Al)–N $\approx$ 1:1), and that the (Ti,Al)N layers of the superlattice have practically the same composition as the thicker layer. Moreover, it is also possible to confirm that when the Vegard's rule is applied to thin films deposited under nonequilibrium conditions, it might lead to inaccuracies in the estimation of the composition. In this particular case, the Al concentration found was too low. The undulation observed on the superlattice (cf. Fig. 5.21b) corresponds to the evolution of the columnar growth surfaces, which remarkably remained continuous across the grain boundaries. Their compositional modulation was measured to be $\Lambda = 21$ nm, and found to be constant throughout the film.

The ratio between the TiN layer thickness and the periodicity of the superlattice was found to be regular, with a value of approximately 0.46. Still, occasionally the first layer of the superlattice was thicker than expected, which can be related to instabilities in the activation of the superlattice deposition.

4.3. Formation and Microstructure of Macroparticles

The presence of macroparticles in the multilayer is considered as a drawback for the type of applications these coatings are designed for. Their incorporation alters

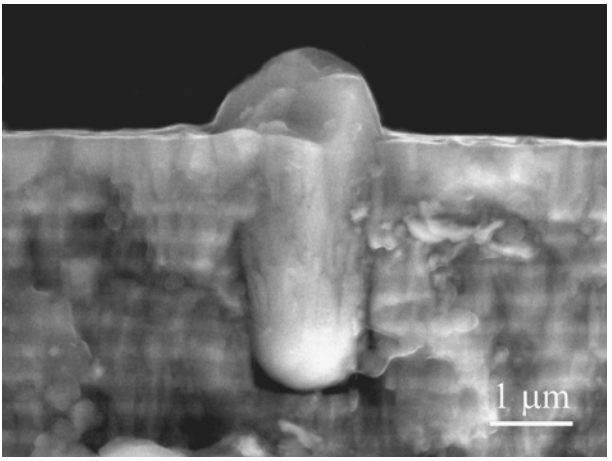

FIGURE 5.23. Cross-sectional scanning electron micrograph of the multilayers showing the morphology of a typical macroparticle.

significantly the surface morphology and roughness, changing the real contact area and thus the friction and wear. Additionally, the pinholes created by their debonding have a deleterious effect on the erosion and corrosion resistance of the coatings, by exposing the multilayer structure to the elements. Their morphology is revealed by a fractured cross-sectional scanning electron micrograph containing a typical macroparticle, shown in Fig. 5.23. The macroparticles originated from the incorporation of droplets with $\langle d \rangle \approx 1$ μm during the film growth. The height above the surrounding coating surface is similar to the droplet diameter, indicating that the net deposition on top of the droplet did not differ significantly from the flat surface. For droplets with a $\langle d \rangle$ smaller than 200 nm the subsequent coating deposition covers and buries them, leading to an undistorted surface. However, the columnar structure on top of the droplets is very pronounced with underdense boundaries to the bulk coating and often displaying a diameter as large as the droplet diameter.

All droplets analyzed are incorporated in the multilayer during the TiN growth and are never directly deposited on the steel substrate. Therefore, possible formation during the cleaning and heating stages before coating deposition, as it happens whenever cathodic-arc ion etching is used, was unlikely.[97]

From SAED patterns and EFTEM it is possible to identify the phase of the droplets and hence their nature. Figure 5.24a is a typical plan-view TEM image taken from a region inside of the coating showing a horizontal cross section of a droplet. The droplet has a lower defect density compared to the bulk coating, and consists of a core-shell structure with a few equiaxed grains and a rim with a microstructure different from the central area. Further, it is surrounded by a voided region attesting the weak bonding to the multilayer coating. The SAED patterns

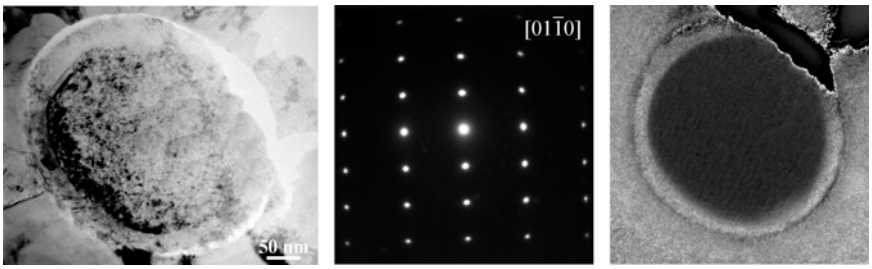

(a) (b) (c)

FIGURE 5.24. Plan-view TEM image of a droplet incorporated in the multilayer: (a) bright-field image; (b) SAED pattern of the droplet core showing the diffraction spots from α-Ti phase along the [01 $\bar{1}$0] zone axis; (c) energy-filtering transmission electron microscopy (EFTEM) image constructed from the ratio of nitrogen and titanium elemental maps.

from the central area of the droplet are taken along different zone axis, permitting the identification of the core as having the hcp structure of α-Ti. As an example, Fig. 5.24b shows the SAED taken along the [01$\bar{1}$0] zone axis of α-Ti. The electron energy loss spectroscopy (EELS) spectra of the core of the droplet displays only the Ti L_{23}-edge located at 456 eV, giving no indication on the presence of nitrogen, whose detection limit is about 3 at%. In contrast, the spectra of the rim of the droplet displays the Ti L_{23}-edge and also the N K-edge located at 401 eV. Figure 5.24c is a plan-view EFTEM image showing the droplet and the surrounding coating obtained by computing the ratio of nitrogen and titanium elemental distribution images and taking into account their partial ionization cross sections. The results show that the droplet is formed by a Ti core encircled by a TiN layer, in which the nitrogen had the same intensity as in the bulk coating.

To cross-check its nature, orientation imaging microscopy,[98] a technique that permits to obtain Kikuchi diffraction patterns from a sample, was utilized on droplets viewed in cross section. The outcome was a Kikuchi pattern that agreed with the SAED patterns obtained.

The near-spherical bottom shape and the voided boundary region formed beneath the droplets (cf. Fig. 5.23) suggested that even if they have left the target surface in the liquid state due to a local temperature higher than the melting point of Ti (1668°C),[14,99] they had solidified *en route* to the film surface. The formation of the thin TiN layer on the surface of the droplets occurred upon their emission from the target and migration to the film by reacting with the ionized titanium and nitrogen particles. Ljungcrantz *et al.*[100] estimated the mean diffusion distance of N into the α-Ti phase, and concluded that a diffusion of 30 nm at T_s for 1 h during growth could be achieved. The voids observed beneath the droplets were a result of the shadowing effect of the incoming atomic flux in combination with the limited adatom mobility. This reduced adhesion of the droplets combined with the developing compressive stresses of the multilayer during cooling from the deposition temperature triggered the removal of the ones close to the surface.

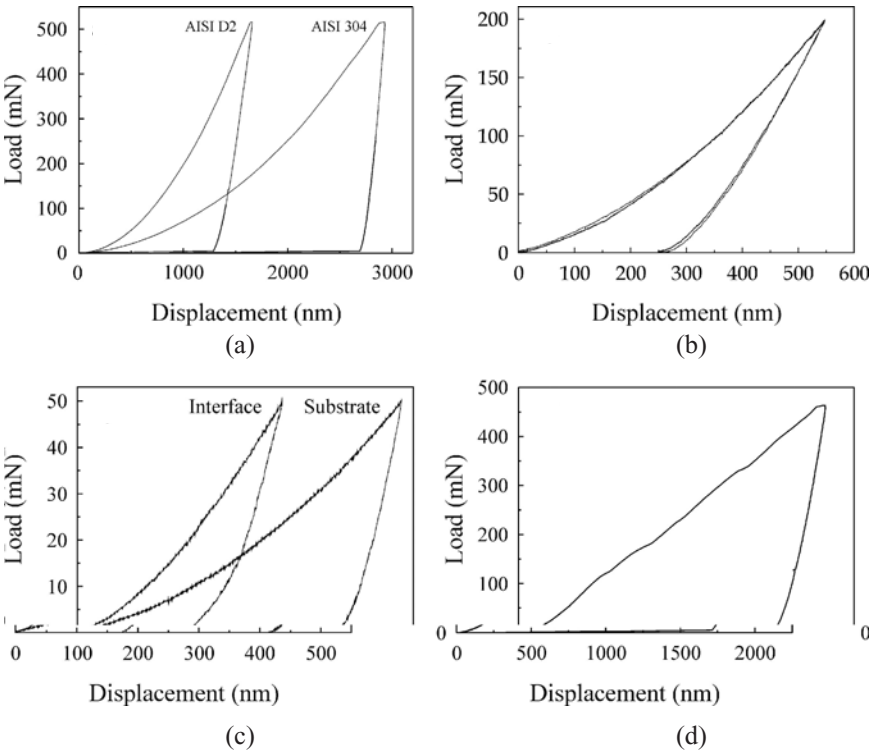

FIGURE 5.25. Nanoindentation load–displacement curves showing different characteristic features observed in the response of substrates, TiN-, and TiN–(Ti,Al)N-coated systems: (a) behavior of steel substrates for peak load of 500 mN; (b) overlapping curves of the TiN-coated systems with two different tool steel substrates (50 HRC and 60 HRC) at peak load of 200 mN; (c) load–displacement curves of the substrate and "interfacial" nanoindentations at 50 mN peak load; (d) load–displacement curve of TiN–(Ti,Al)N-coated system exhibiting a discrete displacement discontinuities produced by crack propagation in the coating.

4.4. Nanoindentation Response

The load–displacement curves of steel substrates are shown in Fig. 5.25a. The behavior is typical of a ductile, plastic material, i.e., like most metals. The loading curves are approximately parabolic and the unloading segments are very abrupt. This indicates that the elastic strains during indentation are small compared with the plastic strains, resulting in a little elastic recovery of the indentation depth. Plastic deformation is evident even at lower loads, being more pronounced on AISI 304 stainless steel due to its higher ductility.

Evaluating the response of coated systems with respect to the substrate enables one to highlight the properties of the coating itself. Figure 5.25b shows

typical load–displacements curves of TiN deposited onto tool steel substrates. In contrast to the substrates, the load–displacement curves of the coated systems exhibit increased amounts of elastic recovery on unloading, establishing that a higher proportion of the deformation is accommodated elastically. When these coated systems are compared at higher peak loads (note that the overall indenter displacement is still small compared with the coating thickness) the difference in percentage of elastic recovery is more pronounced. Also, the fact that the system with the softer substrate displays a smaller percentage of elastic recovery leads to the conclusion that the relative contribution of the coating to the system response is less. On the other hand, at low peak loads the influence of the substrate is very reduced, as can be seen by the similar maximum displacement of both curves. It indicates that at this contact load regime, the response of the system depends primarily on the ability of the coating to support the load.

The influence of the interfacial region, and hence an indication of the interfacial adhesion, is displayed in Fig. 5.25c. It shows the load–displacement curve of a nanoindentation at the interface by cross-sectioning the TiN coated system, and for comparison, the load–displacement curve of the substrate. The corresponding indentation impressions are presented by scanning electron micrographs in Fig. 5.26.

For the same peak load, the "interfacial" load–displacement curve exhibits a smaller indenter penetration than the substrate. Also, at the final stages of unloading, the interfacial curve becomes less steep, indicating a larger fraction of elastic recovery. Thus, even when nanoindentation is performed only with one side of the indenter penetrating the coating, it is possible to see the influence of the coating on the system. The load–displacement curve of TiN–(Ti,Al)N onto stainless steel is shown in Fig. 5.25d. The loading curve displays several steps or pop-in

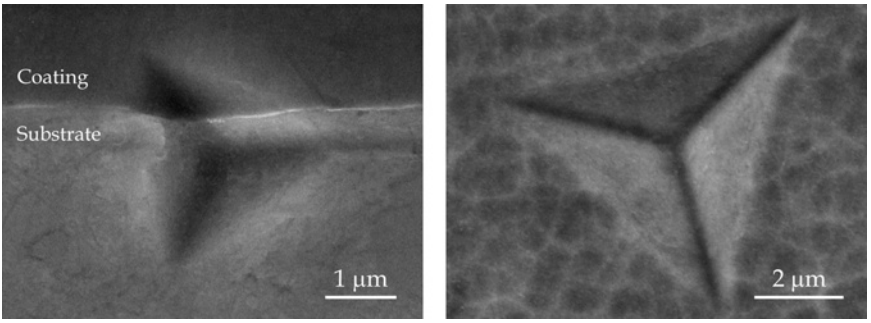

(a) (b)

FIGURE 5.26. Scanning electron micrographs showing the indentation impression on the TiN-coated system: (a) 50-mN nanoindentation performed on cross-sectional sample at the coating–substrate interface. Note that actually only one of the indenter vertices penetrates the coating. (b) 200-mN nanoindentation performed on plan-view sample.

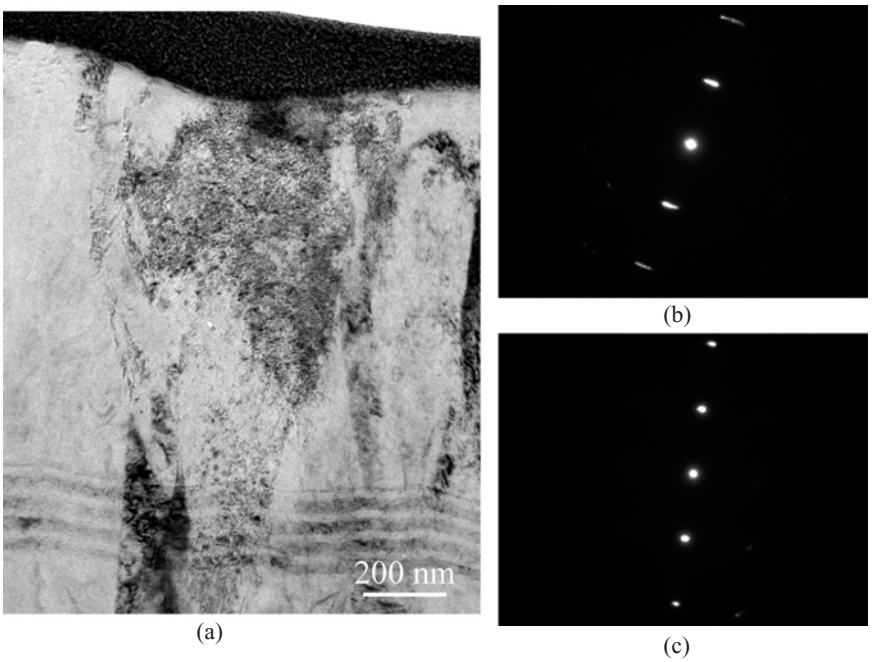

FIGURE 5.27. (a) TEM bright-field image of a cross section of a 50-mN indent on TiN–(Ti,Al)N deposited on tool steel; (b) Selected-area diffraction pattern showing the tilt of crystallographic planes under the indenter tip; (c) Selected-area diffraction pattern away from the indenter for comparison with (b).

events. Such sudden forward displacements without any increase in applied load are correlated with nested cracks in the indentation profile, relaxing locally any membrane or residual stresses.[101,102] Their occurrence indicates that the multilayer had stretched as the substrate yielded and plastically deformed to accommodate the indenter displacements.

The deformation mechanisms of the multilayers have been explored by cross-sectioning indents with different peak loads and observing the deformed regions by TEM. Figure 5.27a–c shows TEM bright field image and diffraction patterns of a 50-mN indent made on TiN–(Ti,Al)N multilayers grown on tool steel. From Fig. 5.27a, it can be seen that the columnar grains are bent at the edges of the indent, and cracking at their boundaries has occurred. Nevertheless, the multilayer stacking has not been disrupted, indicating that most of the deformation is accommodated by the TiAlN top layer in the region immediately under the indent. The layer has accommodated the surface displacement by rotation of the crystallographic planes under the indent tip. This is confirmed with the diffraction pattern in Fig. 5.27b, taken under the indent tip, which shows streaking of the diffraction spots due to tilting of the crystallographic planes (compare with the diffraction pattern taken

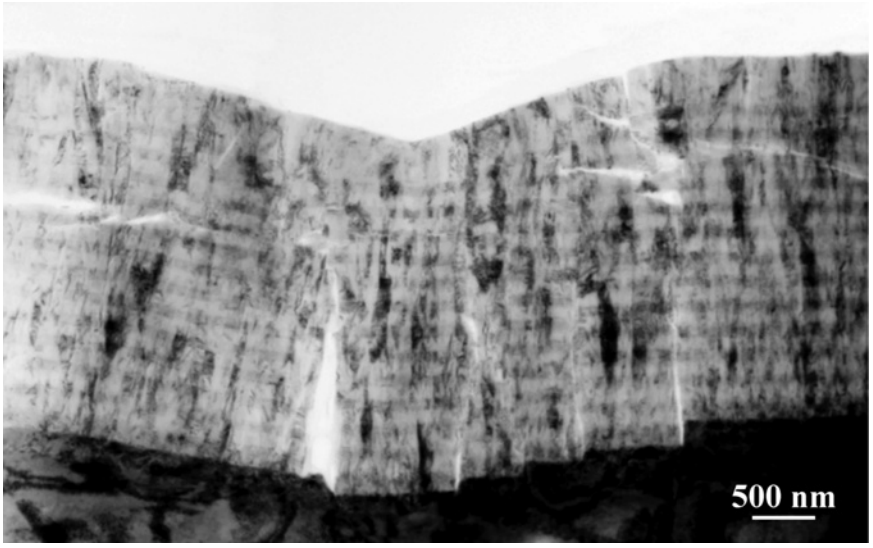

FIGURE 5.28. TEM bright-field image of a cross section of a 450-mN indent displaying the indentation fracture modes of the multilayers.

away from the indent in Fig. 5.27c). The phenomenon of rotation of the crystallographic planes can be interpreted as a means for plastic yield of the TiAlN layer. At higher loads the dominant mode of deformation of the coatings on steels substrate is by a membrane type of stretching induced by plastic deformation of the substrate.[103] Additional bending effects are also observed for the surface layer at the edges of the impression. Both mechanisms produce cracking: the former from the interface toward the free surface, and the latter on the free surface near the periphery of the impression through the coating thickness.

The observations permitted to conclude that the indentation fracture of the multilayers occurred by multiple cracking initiated at different sites and propagating in different directions, as seen in Fig. 5.28. Nevertheless, the cracking may be divided roughly into four categories: shear steps, edge cracks, cracks from interface, and lateral cracks.

The shear steps run parallel to the indenter edges. While they have the appearance of opening mode cracks from cross section, it is observed that there is a major component of shear. The tangential traction on the surface opens up the discontinuities as shear steps, where the scale of damage (i.e., crack spacing) is similar to that of the columnar spacing ($\sim$100 nm). The fact that these steps are in a zone of high compressive (radial and hydrostatic) stress rules out any mode I opening and extension below the surface. The edge cracks or circumferential cracks, depending on pileup or sink-in deformation mode, do not run completely through the coating thickness and have the tendency to deviate, when subsurface, away

from the thickness direction. Cracking from the interface is the most important fracture mode as far as crack length is concerned. They initiate at the interface during loading and move toward the surface due to stretching of the multilayer as the underlying substrate plastically deforms. The propagation occurs at the columnar grain boundaries by shear sliding deformation and ceases as it approaches the zone of compression, which exists near the top surface of the impression. This process might be particularly effective for strain energy dissipation, hence avoiding premature failure by tensile cracks. Their occurrence has been associated with the steps observed in the load–displacement curve (cf. Fig. 5.26d). Therefore, it appears that the first pop-in event is caused by the onset of plastic flow in the stainless steel substrate. This reasoning is in line with the commonly used rule of thumb, where the properties of the "film-only" are measured for indentation depths less than 10% of film thickness, since the first pop-in event is at a depth at which the substrate plays a considerable role in the system deformation behavior. The lateral cracks are located below the indentation impression. They are thought to originate on unloading of the indentation cycle, and tend to propagate approximately parallel to the layers releasing the elastic strain energy stored during bending. The inefficiency of the interfaces of the multilayer in obstructing or deflecting the cracking during unload of the indenter is suggested to be related to the reduced lattice mismatch between the layers and the small variation of the chemical composition across the interface. Thus, it is not surprising to observe transgranular cracking across several columnar grains, being deflected only when intersecting an existing columnar shear crack. The deleterious effect of the droplets incorporated in the multilayer could be observed when they were present underneath an indentation impression. The weak columnar boundaries of the macroparticle and the voided region beneath the droplet acted as preferential sites for crack nucleation and propagation during the unloading of the indent. Remarkably, interfacial delamination, a common mode of failure for many coating–substrate combinations, was not observed, attesting the strong bonding between the interfacial layer and the steel substrate.

The systems are plotted in Fig. 5.29 as a function of the displacement normalized to the coating thickness. The increase in hardness observed for shallow displacements is thought to result from uncertainties in the tip end-shape calibration, whereas the larger scatter is primarily due to the surface roughness of the as-deposited coatings. For penetration depths in the order of few hundred nanometers the influence of the substrate on the composite hardness values is much reduced. The hardness of the multilayers at low displacements is slightly higher than for the monolayer. This effect might be related to a hardening effect caused by the large number of interfaces parallel to the substrate surface. By assuming that at an indenter penetration of 200 nm the influence of both tip-shape irregularities (the tip radius is 40–50 nm) and substrate (penetration depth less than one tenth of coating thickness) are negligible, it is possible to estimate the coating hardness. Thus, the TiN and the TiN–(Ti,Al)N multilayers have a hardness of the order of 31 and 34 GPa, respectively.

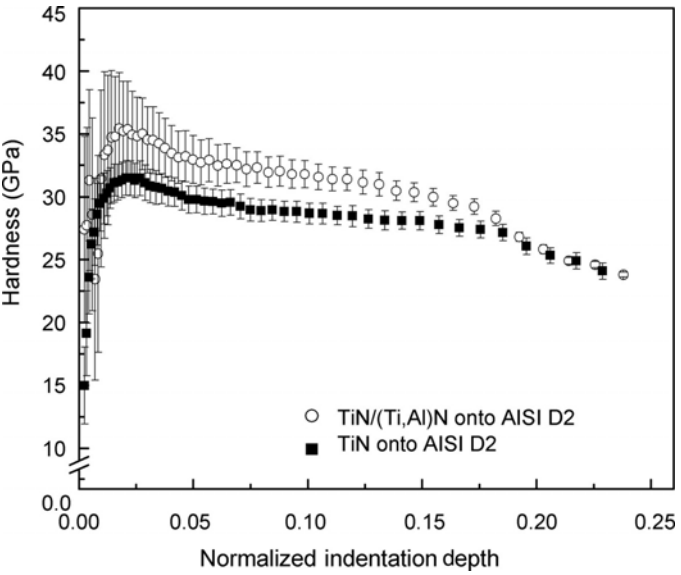

FIGURE 5.29. Mean hardness values as a function of the normalized indentation depth of the homogeneous TiN and the TiN–(Ti,Al)N multilayers onto steel substrates. The data were derived utilizing the continuous stiffness option.

When the hardness values obtained with the nanoindenter and Vickers[104] are correlated, it is possible to draw the following conclusions: At displacements corresponding to the coating thickness, the coating basically behaves as a cap on the tip of the indenter transmitting the applied load to the substrate; for lower displacements the coating properties commence to come into sight; and at displacements of the order of one tenth of the coating thickness the influence of substrate hardness is barely detectable. Figure 5.30 shows the mean effective Young's modulus as a function of normalized indenter displacement for TiN and TiN–(Ti,Al)N multilayer coated systems. The values were also derived from the continuous stiffness measurements. The effective modulus values decrease markedly with the increasing displacement into the coated system. The substrate influence is observed at smaller penetration depths because the long-range component of the elastic field starts extending rather earlier into the less compliant substrate.

Bare substrates were submitted to rolling contact fatigue tests under the same applied load as the coated ones, and no pitting or spalling of the bulk materials had occurred.[105] Therefore, this experimental method seems to be reliable for the determination of the cyclic bond strength of coated systems. Considerable disparity in fatigue durability is found among systems with different substrate surface finishing and roughness.[106] Therefore, the dependence of rolling contact fatigue on the pretreatment and surface roughness has been revealed. A finer polished surface is associated with longer lifetime. The major failure mode of coated systems under

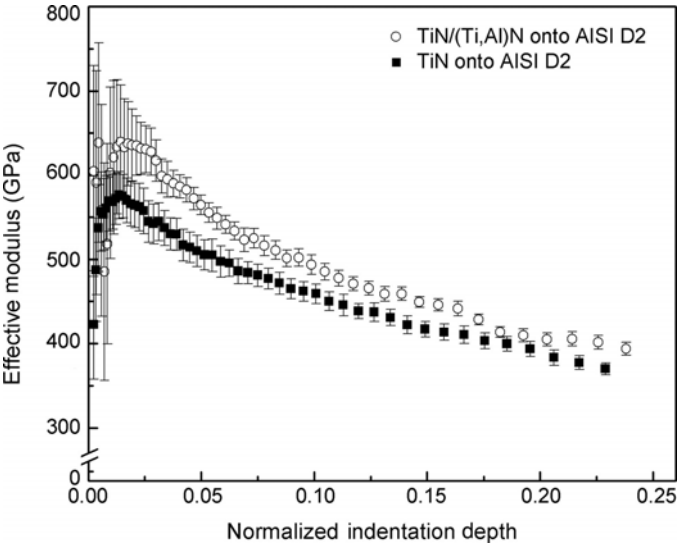

FIGURE 5.30. Mean effective Young's modulus values as a function of the normalized indentation depth of the homogeneous TiN and the TiN–(Ti,Al)N multilayers onto steel substrates. The data were derived utilizing the continuous stiffness option.

the present testing conditions is initiated at the interface region, indicating that the fatigue lifetime is very sensitive to the interfacial bonding strength. In the present study the lifetime of coated system with 60 HRC is longer than with the 50 HRC substrate. The coated system can improve the lifetime in rolling contact only if the substrate is hard enough to carry the load. Otherwise, plastic or elastic deformation will take place in the substrate under the contact and failure of the coated system occurs by fracture both in the coating and in the substrate. The failure mechanism of the TiN–(Ti,Al)N multilayers is similar to that of the homogeneous TiN.

In this section the mechanical properties of homogeneous TiN and TiN–(Ti,Al)N multilayers have been evaluated. The main conclusions are the following: The TiN and TiN–(Ti,Al)N multilayers investigated have a fibrous and columnar microstructure, respectively. The former is highly (111) textured with compressive stresses in the order of 4–5 GPa. The latter is slightly (311) textured each component having different compressive stresses, being 3–4 GPa for the (Ti,Al)N layer and 8–10 GPa for the TiN layer. There is also a compressive stress dependency on the type of substrate material, due to the thermal mismatch. The TiN–(Ti,Al)N multilayers are composed of (Ti,Al)N layers and a superlattice of TiN and (Ti,Al)N with a periodicity of 200 nm. The compositional modulation within the superlattice itself is 21 nm. Both materials have crystallized in a face-centered cubic B1-NaCl structure. The lattice parameter of (Ti,Al)N was slightly reduced with respect to

TiN due to the smaller atomic radius of aluminum atoms. The microstructure and composition of micrometer-sized droplets incorporated in the multilayers during deposition of TiN material were examined. It was demonstrated that they were incorporated in the solid state during deposition of the TiN material, and that they were weakly bonded to the bulk coating. The droplets were formed by a core structure with few equiaxed grains having the α-Ti phase and a rim of a thin TiN layer exhibiting a gradient in defect density. This could be explained as the effect of nitrogen diffusion into the core of the droplet both during the *route* to the film and at the growing film surface. Voided regions were always observed beneath the droplets as a consequence of shadowing of the atomic flux. Their reduced adhesion prompted the removal of the ones close to the surface, leaving craters behind with exposed multilayer. Two regimes of crack propagation were found in the microindentation experiments. The transition depends on the indentation depth rather than on the load applied. The hardness and Young's modulus of TiN and TiN–(Ti,Al)N multilayers are estimated using the continuous stiffness option provided with the nanoindenter. The hardness and Young's modulus of the former is 31 and 570 GPa, respectively, whereas for the latter is 34 and 640 GPa, respectively.

5. OUTLOOK

The main emphasis of microscopy lies in determining the structure–property relationship, so as to bridge the length-scale gap between atomic structures and macroscopic properties involved in the study of the stability of coatings. The basic philosophy should be that depending on the coating property one wishes to investigate, it is necessary to consider the appropriate length scale where the relevant processes take place. The challenging part of this rather mesoscopic approach is of course to define the physical basis at the various length scales and the corresponding transitions involved. Besides the fundamental reason mentioned in the introduction, one should realize that a quantitative electron microscopy evaluation of the structure–property relationship is also hampered by practical reasons, namely, because of statistics. This is not specific, of course, to coating systems. The metrological considerations of quantitative electron microscopy from crystalline materials have been summarized in Refs. 107–109, one of which is the statistical significance of the electron microscopy observations. In particular, in situations where there is only a small volume fraction of defects present, or a very inhomogeneous distribution, statistical sampling may be a problem. Hence, in the case of nano-sized particulates of the order of 10 nm and a volume fraction of the order of 1%, it is necessary to view a volume of 10^{-20} m^3. At smaller sizes and 50% volume fraction, a volume of 10^{-21} m^3 has to be investigated. In the case of interfaces, one should be aware of these aspects of quantitative metrology with electron microscopy. For example, to support or reject various models on

the structure–property relationship, for example, to determine the relationship between impurity segregation and interface structure, it is necessary to measure the boundary misorientation at very high precision, and they should be all aligned parallel to the electron beam for an effective quantitative analysis with electron microscopy. This is almost virtually impossible and only qualitative conclusions can be drawn. All these points are, in particular, relevant in the field of wear-resistant coatings. One recent breakthrough is superhard materials, where hardness is dramatically increased by using superlattice and amorphous/crystalline composite structures.[110–112] These structures were designed on a nanometer level to prevent operation of dislocation sources, restrain existing dislocations in adjusted nanolayers (or phases) with different elastic constants, and build-up material volume energy from grain boundary incoherence strains. While superhard coatings are very important for protection of cutting tools, most tribological applications require tough and low-friction coatings. A material is generally considered tough if it withstands high levels of loading (tensile, compressive, shear, etc.) and can dissipate strain energy without brittle fracture. A supertough coating must have high elastic modulus and high hardness, as well as permit strain relaxation and crack termination. For materials used to prevent wear, there are additional requirements due to the nature of loading. A wear-resistant coating must support high loads in sliding or rolling contact without failure by wear, cohesive fracture, or loss of adhesion at the substrate interface. Most frequently, a low friction coefficient is required, which helps to reduce friction losses and increases load-support capability. The later is clear from the fact that typical coating failures (deformations, cracks, delaminations, etc.) are caused by the tangential stress, which is proportional to the contact load through the friction coefficient. Finally, chemical and thermal stability are required to limit tribochemical reactions with the counterpart and the environment.

The development of tough wear-resistant coatings is quite a challenging task, requiring considerations of substrate materials, loading schemes, operational environment, tribochemical reactions, etc. Consequently, coatings must be tailored to more or less defined applications; so, currently there is no "universal" coating. Progress toward a "universal" coating can be made by developing materials that adapt their chemistry, mechanical characteristics, and tribological properties to the operating environment, temperature, and magnitude of loading. Recently, novel wear-resistant materials were developed, which combine nanocrystalline carbides (TiC, WC), dichalcogenides (MoS_2, WS_2), and amorphous DLC into nanocomposite structures. The surface chemistry, structure, and mechanical behavior of these nanocomposite materials can change reversibly in the tribological contact as a function of applied loads and operational environment, to maintain good friction and avoid wear. Such adaptive behavior has drawn an analogy to "chameleons" that change their color to match the environment. The following concepts were suggested for supertough nanocomposite structures[113] (see also discussion in Chapter 1):

(i) Combine crystalline carbide and amorphous DLC with high elastic modulus to achieve correspondingly high hardness.
(ii) Maintain nanocrystalline grain sizes at the 10–20-nm level to restrict initial crack size and create a large volume fraction of grain boundaries.
(iii) Separate the nanograins within an amorphous matrix of thickness above 2 nm to prevent interaction of atomic planes in the adjusted nanocrystalline grains and facilitate grain boundary sliding, but less than 10 nm to restrict the path of a straight crack.
(iv) Produce nanocrystalline grains with random orientation (high-angle grain boundaries) to minimize grain incoherence strain and facilitate grain boundary sliding.
(v) Release "overlimit" strain by grain boundary sliding at loads exceeding the composite elastic strength, providing hard or ductile behavior depending on the load.
(vi) Terminate nanocracks by deflection at grain boundaries and by energy loss within the amorphous matrix.

Such nanocomposite coatings with supertoughness, exceptional wear resistance, environmental stability, and low friction characteristics have been explored on the systems consisting of hard nanocrystalline carbide and amorphous DLC phases.[114] Hydrogen-free DLC is selected as a matrix material because it is amorphous, has very high hardness, high elastic modulus, low friction in humid ambient environments, and low wear.[115] Supertoughness is expected to be achieved by strain release via nanograined carbides sliding in the DLC matrix. Figure 5.31 shows an example of nc-TiC/a-C nanocomposite coatings where TiC nanocrystallites of 5-nm size are well separated by the matrix of amorphous carbon.

By changing deposition parameters, for instance using different levels of ion bombardment, it is possible to precisely control not only the chemistry but also the structure of both the amorphous DLC phase and the nanocrystalline TiC phase. Figure 5.32 demonstrates another nc-TiC/a-C coating where TiC nanoparticles and clusters of 10–20-nm size are embedded in an a-C matrix, with grain boundary separation of about 5 nm. Energy-filtered TEM observations, as seen in Fig. 5.33, more clearly reveal the distribution of the a-C matrix as well as the TiC nanoparticles.

Although direct structural observations in interface structures have become possible with the advent of HRTEM, the necessary chemical information at an atomic level is still missing. A field ion microscopy-imaging atom probe may be the answer to acquiring this information[116–118] but recent developments also point toward the exploration of an ultrahigh-resolution FEG transmission electron microscope with an EDS (energy-dispersive spectrometry; analysis probe of less than 0.5-nm diameter). In contrast to UHV-SAM (ultrahigh vacuum-scanning Auger microscopy), the FEG-HRTEM is capable of measuring segregation to boundaries without the necessity of the boundary first undergoing an intergranular fracture; therefore, segregation measurements can be made in samples that are

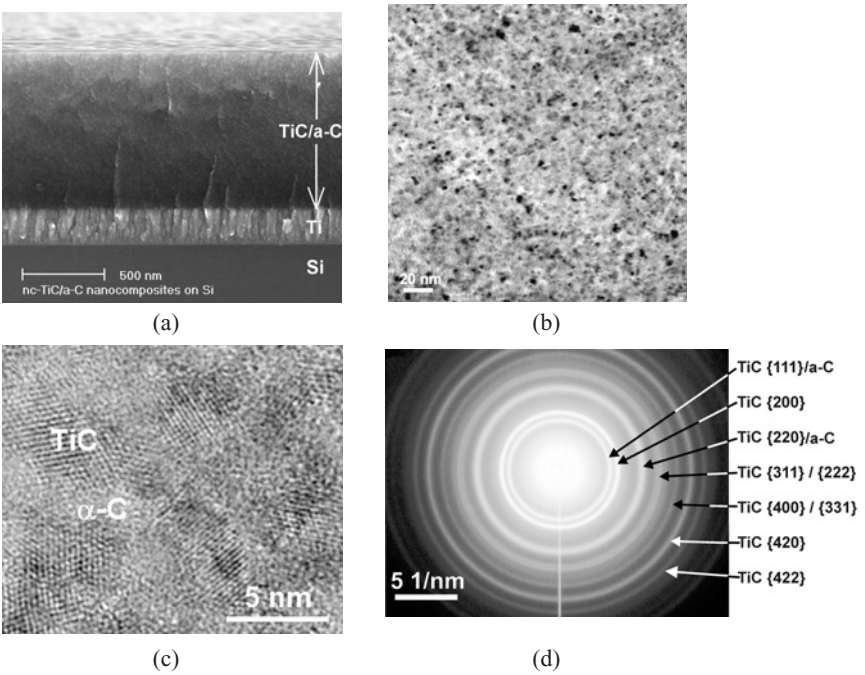

FIGURE 5.31. (a) Fractured cross section (SEM) of an nc-TiC/a-C nanocomposite coating (hardness = 28 GPa, E = 263 GPa) deposited on Si-wafer; (b) TEM image of the overall distribution of dark TiC nanocrystallites; (c) HRTEM image showing TiC nanocrystallites of 5-nm size embedded in a-C matrix; and (d) electron diffraction pattern of the coating—TiC crystals are detected.

not susceptible to such fracture. Furthermore, even if a sample is susceptible to intergranular fracture, the FEG-HRTEM can measure segregation to various boundaries, not just to those which fracture, which might not be representative of all boundaries in the metal. In particular for oxides, semiconductors, and metals on ceramic supports, high-resolution STEM is available with an annular detector allowing incoherent imaging at atomic resolution, the contrast of which strongly depends on the atomic number (Z-contrast).[119–121] As incoherent imaging has no phase problem, these Z-contrast images may be directly inverted to yield the projected atomic positions. As in transmission electron microscopes, the more recently commercially available scanning electron microscopes are also equipped with a field emission gun. Equally, the high brightness and spatial coherence make these sources excellent for use in high-resolution scanning electron microscopes. The penetration depth of the high-energy electrons will cause the electrons to be trapped in the material. When studying conducting materials, the electrons will be transported away from the point of incidence. However, if the specimen is a non-conducting material (ceramic coatings), the excess electrons will cause charging

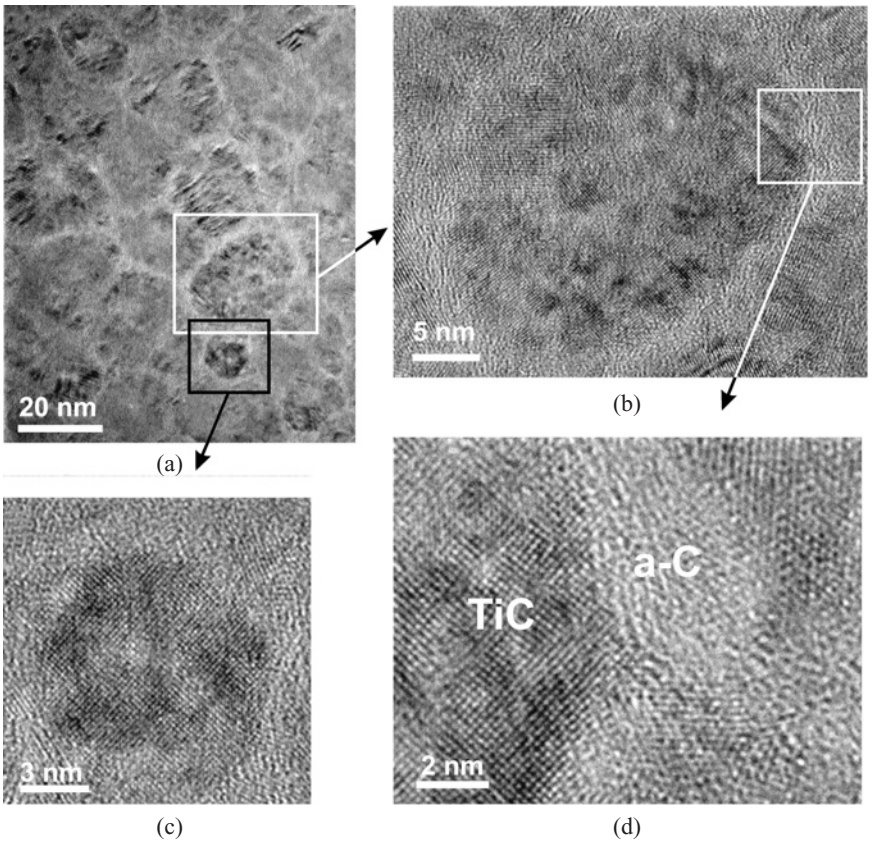

FIGURE 5.32. (a) HRTEM image of the nanostructure of another nc-TiC/a-C nanocomposite coating (hardness = 32.5 GPa, E = 301 GPa). TiC particles/clusters of size 10–20 nm are present. Magnified image to show a (b) large TiC particle and (c) cluster of TiC particles (d) surrounded by a-C.

of the surface. The electrostatic charge on the surface deflects the incoming electrons, giving rise to a distortion of the image. In order to reduce surface-charging effects, it is common practice to sputter a conducting layer of metal, with typical thickness of 10 nm, onto the surface. This layer will transport the excess electrons, reducing the negative charging effects. However, a negative effect of the sputtered layers is that it may diminish the resolving power of the microscope, because topographical information is no longer gained from the surface of the material, but from the sputtered layer. A more recent approach to minimize charging effects is to balance the incoming and emitted electron current, in which the energy of the primary beam is usually chosen to be 2–3 kV. A conducting layer is no longer required, and the balancing of the electron yield prevents the surface from charging.

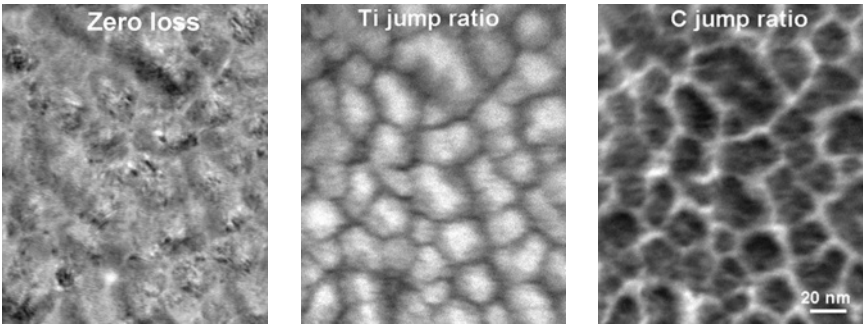

(a) (b) (c)

FIGURE 5.33. (a) Zero-loss image of the coating in Fig. 5.32; TiC particles are visible as dark spots for diffraction contrast. (b) Ti jump ratio image from the same area, showing that large TiC particles and clusters are formed. (c) C jump ratio image showing that α-C surrounds the TiC clusters.

However, charging of the surface is not the only factor determining the resolution of a scanning electron microscope. The width of the electron beam is also an important factor for the lateral resolution. A narrow electron beam results in a high resolution. The spot size, however, is a function of the accelerating voltage. The broadening of the spot size is the sum of broadening due to several processes. The first contributor is the beam itself, the brightness of the source, the beam current, and its divergence angle; the second is the contribution due to diffraction of the electrons of a particular wavelength by the size of the final aperture; and finally, broadening is caused by chromatic and spherical aberrations. In order to achieve the smallest spot size, all contributions should be as small as possible. Decreasing the accelerating voltage will not only cause the wavelength of the electrons to increase, but the chromatic aberration C_c also increases, resulting in an increase in the spot size and, as a consequence, a decrease in resolving power of the microscope. A field emission gun has a very high brightness, reducing the contribution in broadening due to the beam itself. The energy spread in the electron energies is also small. This, together with the fact that the coefficient of spherical aberration and C_c can be reduced by optimizing the lenses for low-energy electrons, provides the FEG low-voltage scanning electron microscope with very high resolving power. Recently, a resolution of 1.5 nm at l–3 kV can be attained in an FEG-SEM equipped with a backscattering Kikuchi diffraction detector.[122] Although conventional scanning electron microscopes (CSEMs) have superior resolution, depth of field, and microanalytic capabilities, they also possess a number of limitations because a high vacuum must be maintained in the sample chamber. The column requires a high vacuum in order to generate and focus the electron beam. The sample chamber also requires a high vacuum to permit the use of available secondary electron detectors. The latter, used in most conventional SEMs is known as the

Everhart–Thornley (ET) detector (named after its inventors). Like other secondary electron detectors, it uses a positive bias of a few hundred volts to attract the low-energy secondary electrons and to increase its collection efficiency. Because of its exposed high-voltage elements, an ET detector can only function in a high-vacuum environment. In a gas environment, it too will arc, often damaging or destroying itself in the process. There are two key technologies that differentiate the so-called environmental scanning electron microscope (ESEM) from all other SEMs.[123,124] The first is its multiple aperture, graduated vacuum system. This system maintains a very high vacuum in the electron column while permitting relatively high pressures in the sample chamber. The second key technology is the environmental/gaseous secondary electron detector, which uses gas ionization to detect and amplify the secondary electron signal. Gas ionization also suppresses charging artifacts on more insulating samples: the detectors are insensitive to light and heat. In the future, FEG-ESEMs may contribute considerably to *in situ* thermomechanical studies of metals and alloys, because both high-temperature and deformation stages are commercially available. It is anticipated that in the near future the emphasis in the field of advanced techniques of microscopy will lie rather on the combination of both structural and chemical information. In particular, EELS will be further integrated because it provides information about the density of (un)occupied states, which are relevant for the bonding behavior along boundaries and interfaces.[125,126] However, although EELS spectra can be obtained from very small regions, only subnanometers across these boundaries, these new methods may still be very disruptive. The electron beam focused on interfaces may cause beam-induced motion of the chemical constituents.[127] Electron beam-induced phenomena are apparent in TEM studies not only in small particles[128]but also in interfaces. In addition, from a theoretical point of view the precise nature of "charge transfer" at boundaries and interfaces is still rather controversial, although the common opinion is that the number of d-band electrons of transition metals will change if the atom is placed at the boundary. Therefore, the bonding behavior is altered, which may be estimated from the changed occupancy of the electronic states by EELS. It is quite clear that much more experimental and theoretical work is needed on the full characterization, that is, structural and chemical, of special (Z) and general boundaries, before firm conclusions can be drawn about the correlation between electronic charge transfer, bonding behavior, and properties.[129]

An interesting example of how quantitative analytical TEM may contribute to the chemical analysis of DLC-based nanocomposite coatings is that EELS is being performed with the final objective of estimating the sp^3–sp^2 hybridization ratio of the carbon atoms in the nanocomposite matrix. Several methodologies have been developed for the estimation of the sp^3–sp^2 parameter with the use of EELS that can be applied to hydrogen-free[130–132] and hydrogenated[133]pure a-C(:H) films, based on the analysis of the C K-edge structure. An example of a procedure valid for hydrogen-free a-C coatings is given below.

The carbon K-edge portion of the spectrum must be decomposed to compare the intensities of the σ^* and π^* features. The decomposition procedure is shown

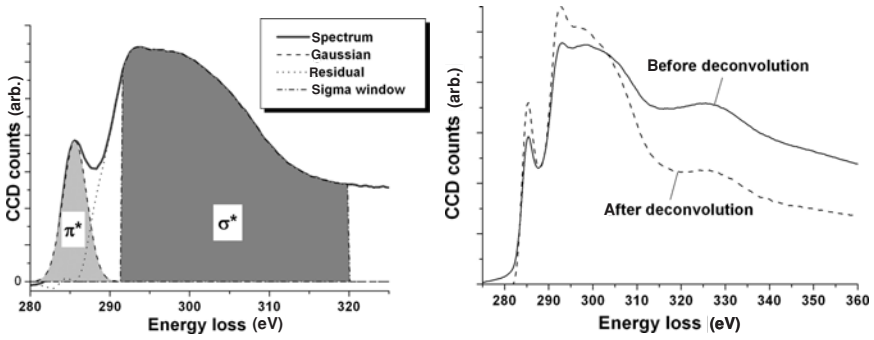

FIGURE 5.34. (a) Decomposition of the C K-edge spectrum into π^* and σ^* features. The areas used for peak and edge integration are indicated. (b) C K-edge prior and after deconvolution. The edge shape changes considerably after deconvolution.

in Fig. 5.34a. The π^* feature is fitted with a Gaussian peak. The procedure gives good fits with very low residuals (dotted line in Fig. 5.34a). The σ^* feature is integrated within an energy window that starts after the previously fitted Gaussian peak and terminates at a selectable value of the energy loss (320 eV in Fig. 5.34a). The fine-structure features of the EELS spectrum for the analyzed samples must be compared to the ones of a standard specimen that exhibits 100% sp^2 hybridization. The choice of a proper standard is crucial to obtain accurate results. The standard chosen here is a glassy carbon foil, which is known to exhibit 100% sp^2 hybridization, high purity, and lack of long-range crystallinity. Spectra should be acquired for the standard specimen and the coating of interest. By comparison of the values of the π^*/σ^* parameter, the sp^2 fraction in the coating (x) can be estimated using (from Refs. 130 and 131)

$$\frac{(\pi^*/\sigma^*)_{\mathrm{DLC}}}{(\pi^*/\sigma^*)_{\mathrm{std}}} = \frac{3x}{4-x} \tag{5.14}$$

It is crucial to perform a proper correction of the spectra for plural scattering and spectrometer point-spread function before using Eq. (5.14), as this effect can alter the intensities of the π^* and σ^* features and hinder the comparison between spectra collected at different foil thickness. EELS spectra have been recorded in spectrometer image mode and with a narrow microscope objective aperture to improve the signal to background ratio. The spectra analysis consists in the subtraction of the spectrum background, after which a deconvolution procedure is performed. The deconvolution consists in two steps: a Fourier-ratio deconvolution procedure is performed first, which removes plural scattering effects, estimated from the low loss portion of the spectrum; consequently, the spectra are sharpened to correct for the point-spread function of the spectrometer, estimated from the shape of the zero-loss peak. The appearance of a sample spectrum before and after

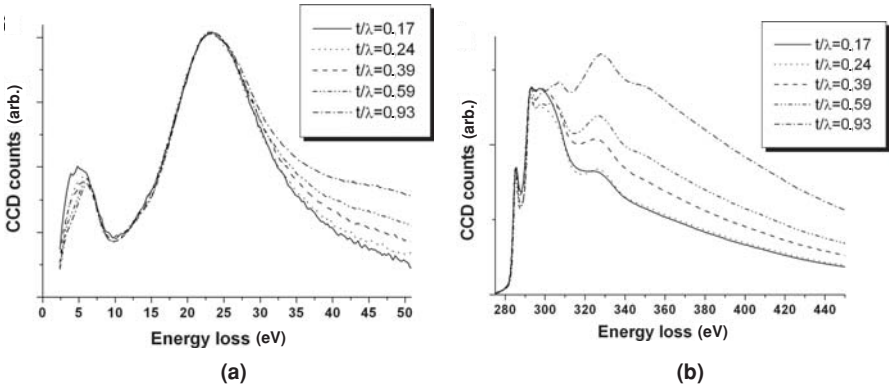

FIGURE 5.35. Portions of the EELS spectrum for the glassy carbon standard recorded on areas of varying thickness (indicated). (a) The plasmon peaks' position is constant for all the values of thickness investigated, but the intensity of the second plasmon peak tail varies as a function of sample thickness. (b) The C K-edge is reported for different sample thicknesses; its shape changes as a function of sample thickness.

deconvolution is shown in Fig. 5.34b. After deconvolution, the intensity of the spectrum on the edge tail is reduced whereas the edge peaks are enhanced. The extent of the intensity variation is a function of the thickness of the area investigated in terms of t/λ, a parameter determined from the analysis of the low-loss portion of the spectrum.

Spectra were recorded on different areas of the glassy carbon sample, which had different thickness, measured as t/λs as indicated in Fig. 5.35. The plasmon peaks are present at the same energy values for the areas investigated, and this indicates a constant density of the material. The intensity variation on the left of the second plasmon peak is proportional to the foil thickness. The carbon K-edge spectra differ in shape and intensity of the edge tail, which increases as the foils become thicker. After deconvolution, the spectra shapes become more uniform. The variation of the π^*/σ^* parameter after deconvolution, as a function of σ^* energy window width, is reported in Fig. 5.36a. The error in the determination of π^*/σ^* for different window sizes is estimated from the standard deviation and reported in Fig. 5.36b as percentage of the average value for each σ^* window width. Values are reported as calculated after background subtraction, Fourier-ratio deconvolution, and point-spread correction. The deconvolution procedure reduces the error to 2–4%, and allows the use of large window widths. The procedure described above can be readily implemented to the quantification of the sp^3–sp^2 parameter in pure hydrogen-free a-C films.

In the case of carbide-containing DLC-based nanocomposite coatings the problem is more complex, as the carbide C adds a contribution to the spectrum in correspondence to the π^* and σ^* features of the C K-edge, hindering

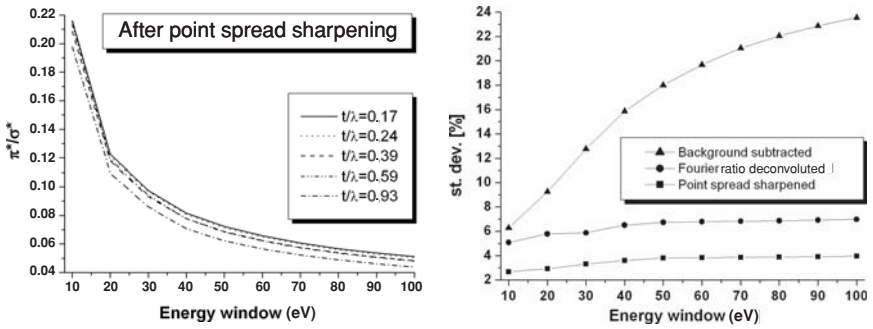

FIGURE 5.36. (a) Values of the π^*/σ^* parameter as a function of integration window width, after deconvolution, for the spectra shown above. The values are roughly constant for each σ^* integration window width. (b) Standard deviation of the π^*/σ^* values among the different thickness investigated, given as percentage of the average value for each σ^* integration window. The Fourier ratio deconvolution and point-spread sharpening procedures reduce the error considerably, as a result the final π^*/σ^* values are almost constant at each window width for different foil thickness.

quantification. In this case, a standard can be used to subtract the carbide contribution from the spectrum, but attention should be paid to the following complications:

- A considerable fraction of material in these coatings lies in the particles boundaries, and so the EELS spectrum from this portion of the material is not necessarily analogous to the one measured with the carbide standard, as electronic surface states are present here.
- If impurities or metal atoms are bound to a C site within the amorphous network, they will modify the EELS spectrum contribution from this C.
- The normal TEM sample preparation technique implies ion milling with high-energy (2–4 keV) Ar ions. Such energetic ion bombardment is known to cause C phase transformations.[134]

A sample EELS spectrum of an nc-TiC–a-C coating is shown in Fig. 5.37.

In particular for the mechanical properties of coatings the intricate interplay between mobile interface structures, crack propagation, and plasticity becomes an important aspect. For this reason, dynamic *in situ* studies are of crucial importance. Based on these fundamental and practical complexities of correlating quantitative microstructural electron microscopy information to coating properties, it is concluded that microscopy characterization, accompanied with complimentary techniques, may serve as a crucial input for a deeper understanding of the structure–property relationship. Nevertheless, the principal point of this outlook is that one should also refocus more on the generic features of defects, using a mesoscopic approach including various length-scale transitions, and on *in situ* rather than on postmortem observations of solely atomic structures.

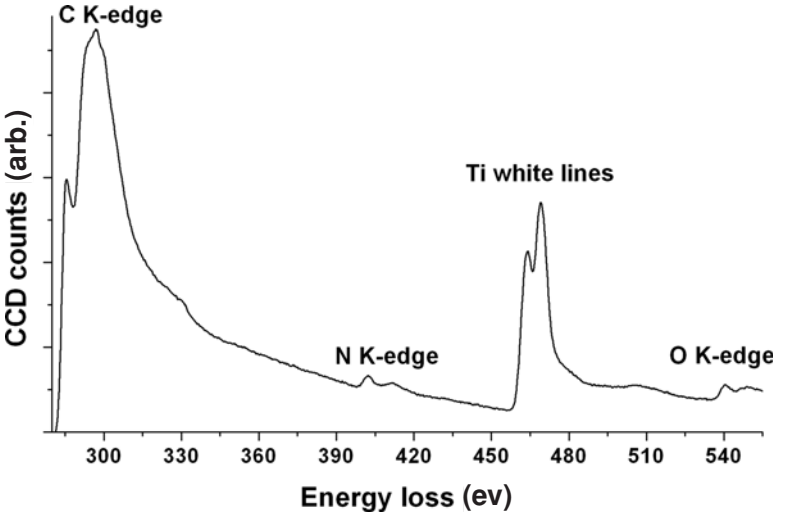

FIGURE 5.37. Typical EELS spectrum obtained from an nc-TiC–a-C nanocomposite coating.

For the progress in HREMs of nanocomposite coatings, references are made to our recent work.[135–138]

ACKNOWLEDGMENTS

Financial support over the years from the foundation for Fundamental Research on Matter (Physics Division, Netherlands Organization for Scientific Research, The Hague), TNO Institute of Industrial Technology, and the Netherlands Institute for Metals Research is gratefully acknowledged. Discussions with Bart Kooi, Patricia Carvalho, Bas Groen, and Stefan Mogck are gratefully acknowledged.

REFERENCES

1. I. A. Ovid'ko, Deformation of nanostructures, *Science* **295**, 2386 (2002).
2. M. Yu. Gutkin, I. A. Ovid'ko, and C. S. Pande, Physical mechanisms of plastic flow in nanocrystalline materials, in *Nanoclusters and nanocrystals*, edited by H. S. Nalwa (American Scientific Publishers, California, 2003), p. 255.
3. S. Veprek and A. S. Argon, Towards the understanding of mechanical properties of super- and ultrahard nanocomposites, *J. Vac. Sci. Technol. B* **20**, 650–664 (2002).
4. K. J. Van Vliet, J. Li, T. Zhu, S. Yip, and S. Suresh, Quantifying the early stages of plasticity through nanoscale experiments and simulations, *Phys. Rev. B* **67**, 104105 (2003); J. R. Weertman, D. Farkas, H. Kung, M. Mayo, R. Mitra, and H. Van Swygenhoven, Structure and mechanical behavior of bulk nanocrystalline materials, *MRS Bull.* **24**(2), 44–53 (1999).

5. J. Güttler and J. Reschke, Metal-carbon layers for industrial application in the automotive industry, *Surf. Coat. Technol.* **60**, 531–535 (1993).
6. D. Roth, B. Rau, S. Roth, J. Mai, and K. H. Dittrich, Large area and three-dimensional deposition of diamond-like carbon films for industrial applications, *Surf. Coat. Technol.* **74–75**, 637–641 (1995).
7. M. Wittmer, Properties and microelectronic applications of thin films of refractory metal nitrides, *J. Vac. Sci. Technol. A* **3**, 1797–1803 (1985).
8. J.-E. Sundgren, J. Birch, G. Hakansson, L. Hulman, and U. Helmersson, Growth, structural characterization and properties of hard and wear-protective layered materials, *Thin Solid Films* **193–194**, 818–831 (1990).
9. C. Subramaniam and K. N. Strafford, Review of multicomponent and multilayer coatings for tribological applications, *Wear* **165**, 85–95 (1993).
10. D. S. Rickerby and S. J. Bull, Engineering with surface coatings: The role of coating microstructure, *Surf. Coat. Technol.* **39–40**, 315–328 (1989).
11. O. Knotek, F. Löffler, and G. Krämer, Process and advantage of multicomponent and multilayer PVD coatings, *Surf. Coat. Technol.* **59**, 14–20 (1993).
12. K. Holmberg and A. Matthews, Coatings tribology, in *Tribology Series 28*, edited by D. Dowson (Elsevier, Amsterdam, 1994).
13. H. Randhawa and P. C. Johnson, Technical note: A review of cathodic arc plasma deposition processes and their applications, *Surf. Coat. Technol.* **31**, 303–318 (1987).
14. R. L. Boxman and S. Goldsmith, Macroparticle contamination in cathodic arc coatings: Generation, transport and control, *Surf. Coat. Technol.* **52**, 39–50 (1992).
15. F. Zernike, Das Phasekontrastverfahren bei der mikroskopischen Beobachtung, *Phys. Zschr.* 36, 848–851 (1935); Das Phasekontrastverfahren bei der mikroskopischen Beobachtung, *Zschr. Techn. Phys.* 16, 454–457 (1935); Beugungstheorie des Schneidenverfahrens und seiner verbesserten Form der Phasenkontrastmethode, *Physica* **1**, 689–704 (1934).
16. P. Buseck, J. Cowley, and L. Eyring, *High Resolution Transmission Electron Microscopy* (Oxford University Press, Oxford, 1992).
17. J. C. H. Spence, *Experimental High-Resolution Electron Microscopy*, 2nd edn (Oxford University Press, Oxford, 1988).
18. D. B. Williams and C. B. Carter, *Transmission Electron Microscopy, A Textbook for Materials Science* (Plenum, New York, 1996).
19. L. Reiner, *Image Formation in LVSEM*, 1st edn (SPIE Optical Engineering Press, Bellingham, WA, 1993).
20. J. M. Cowley and A. F. Moodie, The scattering of electrons by atoms and crystals, *Acta Crystallogr.* **10**, 609–619 (1957).
21. M. A. O'Keefe, "Resolution" in high-resolution electron microscopy, *Ultramicroscopy* **47**, 282–297 (1992).
22. O. Scherzer, The theoretical resolution limit of the electron microscope, *J. Appl. Phys.* **20**, 20–29 (1949).
23. M. Haider, H. Rose, S. Uhlemann, E. Schwan, B. Kabius, and K. Urban, A spherical-aberration-corrected 200 kV transmission electron microscope, *Ultramicroscopy* **75**, 53–60 (1998).
24. J. M. Cowley, Electron microscopy of crystals with time-dependent perturbations, *Acta Crystallogr. A* **44**, 847–853 (1988).
25. O. L. Krivanek, C. C. Ahn, and G. J. Wood, The inelastic contribution to high resolution images of defects, *Ultramicroscopy* **33**, 177–185 (1990).
26. M. J. Hÿtch and W. M. Stobbs, Quantitative comparison of high resolution TEM images with image simulations, *Ultramicroscopy* **53**, 191–203 (1994).
27. G. Möbus and M. Rühle, Structure determination of metal–ceramic interfaces by numerical contrast evaluation of HRTEM micrographs, *Ultramicroscopy* **56**, 54–70 (1994).
28. W. Coene and A. J. E. M. Jansen, Image delocalisation and HREM imaging with a FEG, *Scanning Microsc. Suppl.* **6**, 379–404 (1992).

29. R. Kilaas, *Proceedings 49th Annual EMSA Meeting*, (San Francisco Press, San Francisco, 1991), p. 528.
30. P. Stadelmann, EMS—A software package for electron diffraction analysis and HREM image simulation in materials science, *Ultramicroscopy* **21**, 131–145 (1987).
31. G. Möbus, R. Schweinfest, T. Gemming, T. Wagner, and M. Rühle, Iterative structure retrieval techniques in HREM: A comparative study and a modular program package, *J. Microsc.* **190**, 109–130 (1998).
32. W. H. Press, S. A. Tuekolsky, W. T. Vetterling, and B. P. Flannery, *Numerical Recipes in C* (Cambridge University Press, Cambridge, 1992).
33. G. Möbus, Retrieval of crystal defect structures from HREM images by simulated evolution, I: Basic technique, *Ultramicroscopy* **65**, 205–216 (1996).
34. G. Möbus and G. Behm, Retrieval of crystal defect structures from HREM images by simulated evolution, II: Experimental image evaluation, *Ultramicroscopy* **65**, 217–228 (1996).
35. K. L. Merkle, Quantification of atomic-scale grain boundary parameters by high-resolution electron microscopy, *Ultramicroscopy* **40**, 281–290 (1992).
36. G. J. Wood, W. M. Stobbs, and D. J. Smith, Methods for the measurement of rigid-body displacements at edge-on boundaries using high-resolution microscopy, *Phil. Mag. A* **50**, 375–391 (1984).
37. J. Mayer, G. Gutekunst, G. Möbus, J. Dura, C. P. Flynn, and M. Rühle, Structure and defects of MBE grown Nb–Al_2O_3 interfaces, *Acta Metall.* **40**(Suppl. 1), S217–S225 (1992).
38. A. Trampert, F. Ernst, C. P. Flynn, C. P. Fischmeister, and M. Rühle, High resolution transmission electron microscopy studies of the Ag/MgO interface, *Acta Metall.* **40**(Suppl. 1), S227–S236 (1992).
39. W. O. Saxton and D. J. Smith, The determination of atomic positions in high-resolution electron micrographs, *Ultramicroscopy* **18**, 39–47 (1985).
40. G. Möbus and M. Rühle, Structure determination of metal–ceramic interfaces by numerical contrast evaluation of HRTEM micrographs, *Ultramicroscopy* **56**, 54–70 (1994).
41. D. Hofmann and F. Ernst, Quantitative high-resolution transmission electron microscopy of the incoherent $\Sigma 3$ (211) boundary in Cu, *Ultramicroscopy* **53**, 205–221 (1994).
42. S. B. Newcomb, C. B. Boothroyd, and W. M. Stobbs, Specimen preparation methods for the examination of surfaces and interfaces in the transmission electron microscope, *J. Microsc.* **140**, 195–207 (1985).
43. G. Radnóczi and Á. Barna, Transmission electron microscopy characterization of hard coatings and films: Sample preparation aspects and results, *Surf. Coat. Technol.* **80**, 89–95 (1996).
44. N. J. M. Carvalho, *Low Friction and Wear Resistant Coatings—Microstructure and Mechanical Properties*, Ph.D. dissertation (University of Groningen, Groningen, The Netherlands, 2001).
45. E. G. Spencer, P. H. Schmidt, D. C. Joy, and F. J. Sansalone, Ion-beam-deposited polycrystalline diamondlike films, *Appl. Phys. Lett.* **29**, 118–120 (1976).
46. Y. Lifshitz, Diamond-like carbon—Present status, *Diamond Relat. Mater.* **8**, 1659–1676 (1999).
47. J. Robertson, Diamond-like amorphous carbon, *Mater. Sci. Eng. R* **37**, 129–281 (2002).
48. O. Wänstrand, M. Larsson, and P. Hedenqvist, Mechanical and tribological evaluation of PVD WC/C coatings, *Surf. Coat. Technol.* **111**, 247–254 (1999).
49. A. Matthews and S. S. Eskildesn, Engineering applications for diamond-like carbon, *Diamond Relat. Mater.* **3**, 902–911 (1994).
50. N. J. M. Carvalho, J. Th. M. De Hosson, Microstructure investigation of magnetron sputtered WC/C coatings deposited on steel substrates, *Thin Solid Films* **388**, 150–159 (2001).
51. N. J. M. Carvalho, A. Van der Borden, A. J. Huisin't Veld, and De Hosson, Microstructure and mechanical properties of PVD WC/C coatings, in *Surface and Modification Technologies XIII*, edited by T. S. Sudarshan, K. A. Khor, and M. Jeandin (ASM, Materials Park, OH, 1999), p. 235.
52. A. J. Thornton, The influence of bias sputter parameters on thick copper coatings deposited using a hollow cathode, *Thin Solid Films* **40**, 335–344 (1977).

53. A. Raveh, L. Martinu, S. C. Gujrathi, J. E. Klemberg-Sapieha, and M. R. Wertheimer, Structure–property relationships in dual-frequency plasma deposited hard a-C:H films, *Surf. Coat. Technol.* **53**, 275–282 (1992).
54. J. W. Edington, *Interpretation of Transmission Electron Micrographs* (MacMillan, London, 1975).
55. J. C. Angus and F. Jansen, Dense "diamondlike" hydrocarbons as random covalent networks, *J. Vac. Sci. Technol. A* **6**, 1778–1782 (1988).
56. J. Robertson, Amorphous carbon, *Adv. Phys.* **35**, 317–374 (1986).
57. D. A. Anderson, Electrical and optical-properties of amorphous-carbon prepared by glow-discharge technique, *Phil. Mag.* **35**, 17–26 (1977).
58. A. J. Thornton, The microstructure of sputter-deposited coatings, *J. Vac. Sci. Technol. A* **4**, 3059–3065 (1986).
59. P. Ramanlal and L. M. Sander, Theory of ballistic aggregation, *Phys. Rev. Lett.* **54**, 1828–1831 (1985).
60. L. E. Toth, *Transition Metal Carbides and Nitrides* (Academic Press, New York, 1971).
61. J. W. Patten, The influence of surface topography and angle of adatom incidence on growth structure in sputtered chromium, *Thin Solid Films* **63**, 121–129 (1979).
62. N. J. M. Carvalho and J. Th. M. De Hosson, Nanoindentation study of PVD WC–C coatings supported by cross-sectional electron microscopy observation, *Surf. Eng.* **17**, 105–111 (2001).
63. N. J. M. Carvalho and J. Th. M. De Hosson, Nano indentation studies of WC/C and TiN/(Ti,Al)N multilayer PVD coatings combined with cross-sectional electron microscopy observations, in *Advances in Surface Engineering—Fundamentals and Applications*, Materials Research Society Symposium Proceedings 697, edited by W. J. Meng, A. Kumar, G. L. Doll, Y.-T. Cheng, S. Veprek, and Y.-W. Chung (Materials Research Society, Warrendale, PA, 2001), p. P1.5.
64. K. L. Johnson, *Contact Mechanics* (Cambridge University Press, Cambridge, UK, 1985).
65. N. J. M. Carvalho and J. Th. M. De Hosson, Characterization of mechanical properties of tungsten carbide/carbon multilayers: Cross-sectional electron microscopy and nanoindentation observations, *J. Mater. Res.* **16**, 2213–2222 (2001).
66. L. E. Toth, *Transition Metal Carbides and Nitrides* (Academic Press, New York, 1971).
67. E. Vogelzang, J. Sjollema, H. J. Boer, and J. Th. M. De Hosson, Optical absorption in TiN_xO_y-compounds, *J. Appl. Phys.* **61**, 4606–4611 (1987).
68. V. Ern and A. C. Swittendick, Electronic band structure of TiC, TiN and TiO, *Phys. Rev.* **137**, A1927–A1936 (1965).
69. J.-E. Sundgren, B. O. Johansson, A. Rockett, S. A. Barnett, and J. E. Greene, in *Physics and Chemistry of Protective Coatings*, edited by W. D. Sproul, J. E. Greene, and J. A. Thornton (American Institute of Physics, Universal City, CA, 1985).
70. J. M. Poitevin, G. Lemperiere, and J. Tardy, Influence of substrate bias on the composition, structure and electrical properties of reactively d.c.-sputtered TiN films, *Thin Solid Films* **97**, 69–77 (1982).
71. J.-E. Sundgren, B. O. Johansson, and S.-E. Karlsson, Mechanisms of reactive sputtering of titanium nitride and titanium carbide: Influence of process parameters on film composition, *Thin Solid Films* **105**, 353–366 (1983).
72. M. K. Hibbs, B. O. Johansson, J.-E. Sundgren, and U. Helmersson, Effects of substrate temperature and substrate material on the structure of reactively sputtered TiN films, *Thin Solid Films* **122**, 115–129 (1984).
73. B. E. Jacobson, R. Nimmagadda, and R. F. Bunshah, Microstructures of TiN and Ti_2N deposits prepared by activated reactive evaporation, *Thin Solid Films* **63**, 333–339 (1979).
74. M. Bromark, M. Larsson, P. Hedenqvist, and S. Hogmark, Wear of PVD Ti/TiN multilayer coatings, *Surf. Coat. Technol.* **90**, 217–223 (1997).
75. R. Buhl, H. K. Pulker, and E. Moll, TiN coatings on steel, *Thin Solid Films* **80**, 265–270 (1981).
76. R. L. Hatschek, Am. Mach. Special Report 752, 1983, p. 129.
77. M. Wittmer, B. Studer, and H. Melchiar, Electrical characteristics of TiN contacts to N silicon, *J. Appl. Phys.* **52**, 5722–5726 (1981).

78. B. Zega, M. Kornmann, and J. Amiguet, Hard decorative TiN coatings by ion plating, *Thin Solid Films* **45**, 577–582 (1977).
79. E. Valkonen, T. Karlsson, B. Karlsson, and B. O. Johansson, Annual meeting of the society: SPIE stands for: Society of Photo-Optical Instrumentation Engineers. In 1981 the Society's name was defined as SPIE—The International Society for Optical Engineering, *Proc. SPIE—Int. Tech. Conf.* **401**, 41 (1983).
80. K. S. Chan, M. Y. He, and J. W. Hutchinsson, Cracking and stress redistribution in ceramic layered composites, *Mater. Sci. Eng. A* **167**, 576–574 (1993).
81. Y. Huang and H. W. Zhang, A correlation between stability of compounds and structure of hydrogen-induced amorphous alloys in GdM_2 (M = Fe, Co, Ni), *Acta Metall. Mater.* **41**, 1523–1530 (1993).
82. M. Y. He and A. G. Evens, Crack deflection at an interface between dissimilar elastic materials: Role of residual stresses, *Int. J. Solids Struct.* **31**, 3443–3455 (1994).
83. H. Holleck, Designing advanced coatings for wear protection, *Surf. Eng.* **7**, 137–144 (1991).
84. U. Wahlström, L. Hultman, J.-E. Sundgren, F. Adibi, I. Petrov, and J. E. Greene, Crystal growth and microstructure of polycrystalline $Ti_{1-x}Al_xN$ alloy films deposited by ultra-high-vacuum dual-target magnetron sputtering, *Thin Solid Films* **235**, 62–70 (1993).
85. L. A. Donohue, I. J. Smith, W.-D. Münz, I. Petrov, and J. E. Greene, Microstructure and oxidation-resistance of $Ti_{1-x-y-z}Al_xCr_yY_zN$ layers grown by combined steered-arc/unbalanced-magnetron-sputter deposition, *Surf. Coat. Technol.* **94–95**, 226–231 (1997).
86. J. H. Hsieh, C. Liang, C. H. Yu, and W. Wu, Deposition and characterization of TiAlN and multi-layered TiN/TiAlN coatings using unbalanced magnetron sputtering, *Surf. Coat. Technol.* **1081–1109**, 132–137 (1998).
87. N. J. M. Carvalho, E. Zoestbergen, B. J. Kooi, and J. Th. M. De Hosson, Stress analysis and microstructure of PVD monolayer TiN and multilayer TiN/(Ti,Al)N coatings, *Thin Solid Films* **429**, 178–189 (2003).
88. N. J. M. Carvalho, B. J. Kooi, and J. Th. M. De Hosson, Characterization of PVD multilayer coatings, in *1st International Surface Engineering Congress and 13th IFHTSE Congress*, edited by N. Dahotre (American Society for Metals, Columbus, OH, 2002), p. 273.
89. D. R. McKenzie, Y. Yin, W. D. McFall, and N. H. Hoang, The orientation dependence of elastic strain energy in cubic crystals and its application to the preferred orientation in titanium nitride thin films, *J. Phys. Condens. Mater.* **8**, 5883–5890 (1996).
90. W. D. Sproul, Multilayer, multicomponent and multiphase physical vapor deposition coatings for enhanced performance, *J. Vac. Sci. Technol. A* **12**, 1595–1601 (1994).
91. E. Zoestbergen, N. J. M. Carvalho, and J. Th. M. De Hosson, Stress state of TiN/TiAlN PVD multilayers, *Surf. Eng.* **17**, 29–34 (2001).
92. H. Randhawa, TiN-coated high speed steel cutting tools, *J. Vac. Sci. Technol. A* **4**, 2755–2758 (1986).
93. B. E. Jacobson, R. F. Bunshah, and R. Nimmagadda, Transmission electron microscopy studies of TiC and VC-TiC deposits prepared by activated reactive evaporation, *Thin Solid Films* **54**, 107–118 (1978).
94. D. T. Quinto, Mechanical properties and structure relationships in hard coatings for cutting tools, *J. Vac. Sci. Technol. A* **6**, 2149–2157 (1988).
95. J. A. Thornton, High rate thick film growth, *Annu. Rev. Mater. Sci.* **7**, 239–260 (1977).
96. M. K. Hibbs, B. O. Johansson, J.-E. Sundgren, and U. Helmersson, Effects of substrate temperature and substrate material on the structure of reactively sputtered TiN films, *Thin Solid Films* **122**, 115–129 (1984).
97. I. Petrov, P. Losbichler, D. Bergstrom, J. E. Greene, W.-D. Münz, T. Hurkmans, and T. Trinh, Ion-assisted growth of $Ti_{1-x}Al_xN/Ti_{1-y}Nb_yN$ multilayers by combined cathodic-arc/magnetron-sputter deposition, *Thin Solid Films* **302**, 179–192 (1997).
98. A. J. Schwartz, M. Kumar, and B. L. Adams, *Electron Backscatter Diffraction in Materials Science* (Kluwer Academic, New York, 2000).

99. G. Håkansson, L. Hultman, J.-E. Sundgren, J. E. Greene, and W.-D. Münz, Microstructures of thin films grown by various physical vapor-deposition techniques, *Surf. Coat. Technol.* **48**, 51 (1991).
100. H. Ljungcrantz, L. Hultman, J.-E. Sundgren, G. Håkansson, and L. Karlsson, Microstructural investigation of droplets in arc-evaporated films, *Surf. Coat. Technol.* **63**, 123–128 (1994).
101. T. F. Page and S. V. Hainsworth, Using nanoindentation techniques for the characterization of coated systems: A critique, *Surf. Coat. Technol.* **61**, 201–208 (1993).
102. A. J. Whitehead and T. F. Page, Nanoindentation studies of thin film coated systems, *Thin Solid Films* **220**, 277–283 (1992).
103. N. J. M. Carvalho, B. J. Kooi, and J. Th. M. De Hosson, On the microstructure and deformation mechanisms under indentations of TiN/(Ti,Al)N multilayer coatings, in *Surface Treatment VI: Computer Methods and Experimental Measurements for Surface Treatment Effects*, edited by C. A. Brebbia, J. Th. M. De Hosson, and S.-I. Nishida (WIT Press, Southampton, NY, 2002), p. 233.
104. N. J. M. Carvalho, A. J. Huis in't Veld, W. P. Vellinga, and J. Th. M. De Hosson, Micro and nano-indentation studies of PVD TiN coated tool steels, in *Surface and Modification Technologies XII*, edited by T. S. Sudarshan, K. A. Khor, and M. Jeandin (ASM, Materials Park, OH, 1998), p. 25.
105. A. J. Huis in't Veld, H. M. Slot, N. J. M. Carvalho, and J. Th. M. De Hosson, Surface fatigue resistance of tool steel coated with thin brittle PVD layers, in *Thinning Films and Tribological Interfaces*, *Tribology Series 38*, edited by D. Dowson (Elsevier, Amsterdam, 1999), p. 139.
106. N. J. M. Carvalho, A. J. Huis in't Veld, and J. Th. M. De Hosson, Interfacial fatigue stress in PVD TiN coated tool steels under rolling contact fatigue conditions, *Surf. Coat. Technol.* **105**, 109–116 (1998).
107. P. J. Goodhew, in , *Proceedings of the 70th European Congress on Electron Microscopy,* edited by A. Lopez-Galindo; M. L. Rodrigez-GarciB, *Electron Microsc.* **2**, 211–212 (1992).
108. J. Chone, in *Intemational Symposium on Quantitative Metallography*, Florence, Italy, 1978, edited by Association ltaliana di Metallurgica, p. 209.
109. J., Th., M. De Hosson, Transmission electron microscopy of metals and alloys, in *Handbook of Microscopy*, Vol. 3, edited by S. Amelinckx, D. van Dyck, J. van Landuyt, and G. van Tendeloo (VCH, New York, 1997), pp. 5–111.
110. M. Shin, L. Hultman, and S. A. Barnett, Growth, structure and microhardness of epitaxial TiN/NbN superlattices, *J. Mater. Res.* **7**, 901–910 (1992).
111. B. M. Clemens, H. Kung, and S. A. Barnett, Structure and strength of multilayers, *MRS Bull.* **24**, 20–26 (1999).
112. S. Veprek, New development in superhard coatings: The superhard nanocrystalline-amorphous composites, *Thin Solid Films* **317**, 449–454 (1998).
113. A. A. Voevodin and J. S. Zabinski, Supertough wear-resistant coatings with "chameleon" surface adaptation, *Thin Solid Films* **370**, 223–231 (2000).
114. Y. T. Pei, D. Galvan, J. Th. M. De Hosson, TiC/a-C nanocomposite coatings for low friction and wear resistance, *Mater. Sci. Forum* **475–479**, 3655–3660 (2005).
115. A. A. Voevodin, M. S. Donley, J. S. Zabinski, and J. E. Bultman, Mechanical and tribological properties of diamond-like carbon coatings prepared by pulsed laser deposition, *Surf. Coat. Technol.* **76–77**, 534–539 (1995).
116. H. Jang, D. N. Seidman, and K. L. Merkle, The chemical composition of a metal/ceramic interface on an atomic scale: The Cu/MgO {111} interface, *Interface Sci.* **1**, 61–65 (1993).
117. M. K. Miller, A. Cerezo, M. G. Hetherington, and G. D. W. Smith, *Atom Probe Field Ion Microscopy* (Oxford Science, Oxford, 1996), p. 377.
118. D. Blavette, D. Deconihout, A. Bostel, J. M. Sarrau, M. Bouet, and A. Menand, The tomographic atom probe: A quantitative three-dimensional nanoanalytical instrument on an atomic scale, *Rev. Sci. Instrum.* **64**, 2911–2919 (1993).
119. S. J. Pennycook and D. E. Jesson, High-resolution incoherent imaging of crystals, *Phys. Rev. Lett.* **64**, 938–941 (1990).

120. S. J. Pennycook and D. E. Jesson, High-resolution Z-contrast imaging of crystals, *Ultramicroscopy* **37**, 14–18 (1991).
121. S. J. Pennycook, P. D. Nellist, M. F. Chisholm, N. D. Browning, D. J. Wallis, and E. C. Dickey, Determination of atomic structure at surfaces and interfaces by high-resolution STEM, in *Atomic Resolution Microscopy of Surfaces and Interfaces*, Materials Research Society Symposium Proceedings 466, edited by D. J. Smith (Materials Research Society, Warrendale, PA, 1997), p. 3.
122. D. J. Randle and V. Randle, Microtextures determination by electron back scattering diffusion, *J. Mater. Sci.* **27**, 4545–4576 (1992).
123. G. D. Danilatos, Review and outline of environmental SEM at present, *J. Microsc.* **162**, 391–402 (1991).
124. R. Johnson, *Environmental Scanning Electron Microscopy* (Philips Electron Optics, Eindhoven, The Netherlands, 1996).
125. G. A. Botton and C. J. Humphreys, Analysis of EELS near edge structures to study the bonding character in intermetallic alloys, *Micron* **28**, 313–319 (1997).
126. G. A. Botton, G. Y. Guo, W. M. Temmerman, and C. J. Humphreys, Experimental and theoretical study of the electronic structure of Fe, Co, and Ni aluminides with the $B2$ structure, *Phys. Rev. B* **54**, 1682–1691 (1996).
127. L. M. Brown, G. Allen, P. Flewitt, Nanochemistry of grain boundaries, *Phys. World* May, 45 (1997).
128. L. D. Marks, Experimental studies of small particle structures, *Rep. Prog. Phys.* **57**, 603–649 (1994).
129. C. J. Humphreys, *EMAG 97* (Cambridge, UK, 1997); Inst. Phys. Conf. Ser. No. 153, p. 31.
130. S. D. Berger, D. R. McKenzie, and P. J. Martin, EELS analysis of vacuum arc-deposited diamond-like films, *Phil. Mag. Lett.* **57**(6), 285–290 (1988).
131. J. J. Cuomo, J. P. Doyle, J. Bruley, and J. C. Liu, Sputter deposition of dense diamond-like carbon films at low temperature, *Appl. Phys. Lett.* **58**(5), 466–468 (1990).
132. J. Bruley, D. B. Williams, J. J. Cuomo, and D. P. Pappas, Quantitative near-edge structure analysis of diamond-like carbon in the electron microscope using a two-window method, *J. Microsc.* **180**, 22–32 (1995).
133. C. Donnet, L. Ponsonnet, K. Varlot, J. M. Martin, A. Grill, and V. Patel, EELS analysis of hydrogenated diamond-like carbon films, *Thin Solid Films* **319**, 97–100 (1998).
134. S. Logothetidis, M. Gioti, and Ch. Lioutas, New forms of hydrogen-free amorphous carbon films, *Carbon* **36**(5–6), 539–543 (1998).
135. D. Galvan, Y. T. Pei, and J. Th. M. De Hosson, TEM characterization of a Cr/Ti/TiC graded interlayer for magnetron-sputtered TiC/a-C:H nanocomposite coatings, *Acta Mater.* **53**, 3925–3924 (2005).
136. Y. T. Pei, D. Galvan, and J. Th. M. De Hosson, Nanostructure and properties of TiC/a-C:H composite coatings, *Acta Mater.* **53**, 4505–4521 (2005).
137. D. Galvan, Y. T. Pei, and J. Th. M. De Hosson, Deformation and failure mechanism of nanocomposite coatings under nano-indentation. *Surf. Coat. Technol.* (2006), in press (available on-line Nov. 21, 2005).
138. D. Galvan, Y. T. Pei, and J. Th. M. De Hosson. Influence of deposition parameters on the structure and mechanical properties of nanocomposite Coatings, *Surf. Coat. Technol.* 135 (2006), in press (available on-line Jan. 18, 2006).

6

Measurement of Hardness and Young's Modulus by Nanoindentation

Thomas Chudoba

ASMEC Advanced Surface Mechanics GmbH, Rossendorf, Germany

1. INTRODUCTION

Hard nanostructured coatings make high demands on the measurement of their mechanical properties because they are mostly thin (in the thickness range below 5 μm) and very stiff. One of the most popular methods for the determination of their mechanical properties is nanoindentation. Modern instruments reach a depth resolution below 0.1 nm and a load resolution below 1 μN and allow, therefore, very accurate measurements of the penetration of diamond tips into the surface. Indentation modulus as well as indentation hardness can be derived from the load–displacement curve, in addition to some other mechanical properties. The indentation modulus can be slightly different from the Young's modulus because it is a weighted average of the elastic properties in a certain sample volume and the Young's modulus is directional. For isotropic materials, however, both values should be equal. In engineering sciences the Young's modulus is used as a measure of the elastic properties of larger samples, which contain mostly a lot of differently oriented grains. Therefore, it is also a weighted average of single crystalline elastic constants, which are valid in every single grain. This is the reason why both quantities are often not distinguished. In this chapter the term Young's modulus is used as long as isotropy is taken for granted, and indentation modulus is preferred if the direction dependency plays a role.

After a longer discussion in the scientific community, in 2002 the instrumented indentation test of hardness and materials parameters has been standardized in the international standard ISO 14577 part 1–3.[1] This standard is not particularly focused on the measurement of film properties. During the successful European project Indentation into Coatings (INDICOAT)[2] it became clear that accurate hardness and modulus measurements of coatings require particular care and additional

instructions. For this reason an extension of ISO 14577 for coatings is in preparation as part 4.[3]

In the following discussion, the theory of nanoindentation is explained in more detail in order to identify the critical issues for such measurements and to give an understanding of the present limits. Special care is given to the problem of comparability of results. Therefore, the consideration of instrument compliance and determination of the area function are discussed. The high demands on the measurements of thin films require specific necessary correction methods to reach the required accuracy. This also will be discussed. Finally, a method for the measurement of Young's modulus using spherical indenters is described.

2. THEORY OF INDENTATION MEASUREMENTS

Hardness is a very old measure familiar to engineers and geologists by whom it was first utilized to establish an order for the mechanical properties of minerals. According to the book of O'Neil[4] Barba produced a definition as early as 1640:

> . . . hardness is such a property of precious stones that those which file can scratch are not so classed.

This represents hardness as a measure of plastic properties that are responsible for the durability or failure of machines and tools. Consequently, the scratch hardness of Mohs[5] (1822) was the first hardness unit that allowed a ranking of minerals between 10 reference materials. Since that time, dozens of hardness definitions and units have been introduced. The most important change was the restriction from applying normal plus lateral forces in a scratch test to the purely normal loading in a hardness test. Such a limitation allowed a well-defined application of force and resulted in a better reproducibility and comparability. However, the diversity in hardness definitions continues to make it complicated to compare hardness values. The *ASM Metals Handbook, Vol. 8: Mechanical Testing* makes the following note:

> The definition of hardness varies depending on the experience or background of the person conducting the test or interpreting the test data. To the metallurgist, hardness is the resistance to indentation; to the design engineer, a measure of flow stress; to the lubrication engineer, the resistance to wear; to the mineralogist, the resistance to scratching; and to the machinist, the resistance to cutting.

A clear description of the conditions under which a hardness value was obtained is therefore absolutely necessary. The different hardness standards prescribe clear rules, which are not always communicated in publications.

The most important hardness definitions for engineers are by Vickers, Knoop, Brinell, and Rockwell. Apart from the last one, all of them define hardness as the quotient of applied load F and remaining area A of indentation, i.e., F/A. Vickers and Knoop use pyramids as indenter, Brinell a sphere, and Rockwell a sphere or a

cone with a spherical cap of 200-μm radius (with some exceptions). According to this definition, hardness cannot be measured if there is no remaining impression, i.e., when only elastic deformation took place. The area of the impression is normally measured by optical microscopy. In the case of Vickers hardness, the average length of both diagonals, d, is determined and the hardness is given by the formula

$$\mathrm{HV} = 0.1891 \frac{F}{d^2} \tag{6.1}$$

with F as force in kilogram-force and d in millimeters. While the force can be measured with good accuracy, the error in indentation area measurements can reach unsatisfactorily high values if the area is small and the end of the diagonals cannot be well resolved. By the early 1980s the desire to measure the mechanical properties of thin hard films and small depth ranges was rapidly increasing. Such measurements could be carried out only with smaller forces, and it became more and more difficult to get the accurate size of the indentation area.

This was the main reason for the development of a new measurement technique of hardness called depth sensing indentation or "instrumented indentation testing" . In this technique, depth and force are recorded simultaneously over the whole indentation cycle (loading and unloading). There is no need to measure the indentation area directly if it can be derived from the known shape of the indenter at any depth. The depth can be measured automatically with good accuracy and is independent of the operator. The first measurement technique with nanometer resolution can be dated back to about 1981.[6] When it became clear that depth changes of some nanometers could be resolved, it was not a big step to call this technique "nanoindentation." Four-sided Vickers pyramids were used as tips to enable a direct connection to the well-established Vickers hardness. However, Vickers diamonds have the common feature that the four faces do not meet each other in one point. The so-called "chisel edge" is often observed with a length between 300 nm and several micrometers. Therefore the nanoindenter community prefers three-sided Berkovich pyramids. They can be produced with sharper tips than Vickers pyramids and, therefore, allow a better depth resolution. Berkovich and Vickers pyramids have the same area to depth ratio, which enables, in principle, a direct comparison of the hardness results.

The advantage of not directly measuring the area soon turned out to generate new problems. The easiest way to determine the area is to assume that the tip has an ideal shape and to calculate the surface area from the maximum penetration depth, using the known (ideal) geometry. Again hardness is defined as force divided by area but, in this case, only a virtual area was used without knowledge about the true contact area or the area of the residual imprint. This simple approach was the basis for a new hardness definition, the Martens hardness (formerly "universal hardness"). The development of this hardness definition was closely connected with the development of a German hardness tester by the Helmut Fischer GmbH—the Fischerscope. For this reason it was first standardized in Germany as DIN 50359[7] and became later a part of the international standard ISO 14577. In the

course of the use of the Martens hardness definition, it became clear that it gave similar results to the conventional Vickers hardness for soft metals but the comparability failed for materials with high elasticity. The reason is that the measured depth is a result of both plastic and elastic surface deformations, which are not separated from each other. In contrast to previous hardness definitions, Martens hardness is a measure of elastic *and* plastic properties. As a second problem for small indentation depths below about 2 μm, it turned out that the tip does not have an ideal geometry and one gets increasing deviations from the real area with decreasing indentation depth.

Others worked to calculate the projected contact area from the measured depth and to retain the connection to the earlier hardness definitions. A solution for this problem was first derived by Doerner and Nix[8] and later improved by Oliver and Pharr.[9] The method, proposed by Oliver and Pharr, has been established as a *de facto* standard for nanoindentation since 1992 and was included in the new standard ISO 14577 in 2002. It is explained in the following paragraphs in more detail.

Figure 6.1 shows an indentation with a conical or pyramidal indenter at the time of maximum load and again after unloading. The maximum deformation of the sample surface, $h_{\max}$, can only be measured together with the deformation of the indenter itself, which is not considered here in the first part of the derivation. Let us first assume a rigid indenter for which only the displacement in the sample has to be considered. The absolute displacement consists of the elastic part h_e and plastic part h_p with

$$h_{\max} = h_e + h_p \tag{6.2}$$

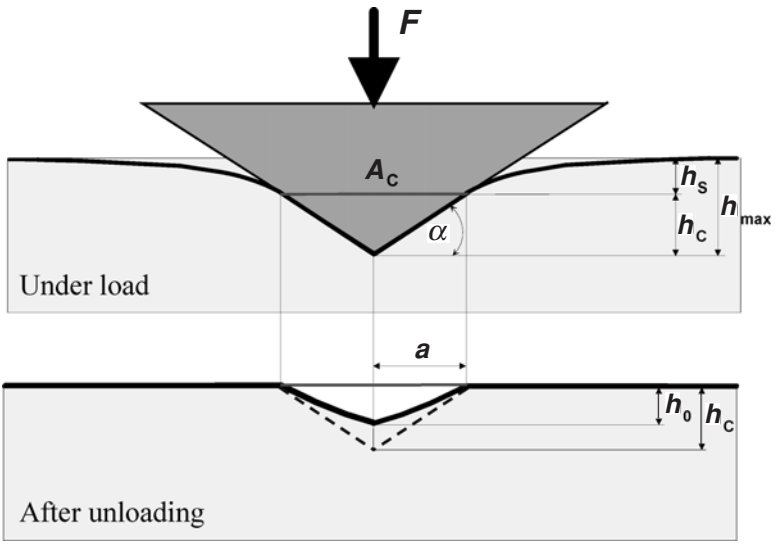

FIGURE 6.1. Geometry of an elastoplastic deformation with a conical indenter under load and after unloading.

We do not know the relation between them and actually we do not need to know it. What we want to know is the area of the impression after unloading, to reestablish the connection to the conventional hardness definition as a measure of plastic properties alone. This is the point where some assumptions and simplifications are required.

The main assumptions of the model are the following:

1. The projected contact area under load and the projected area of the impression after unloading are equal. In a first approximation there is no elastic recovery within the contact plane and the diameter of the indentation does not change when the load is removed (this approximation will be later corrected).
2. Plastic and elastic deformations do not influence each other. The Young's modulus of the plastically deformed material is the same as that for the undeformed material. The elastic deformation above the contact area is the same with and without plastic deformation, compared for equal contact areas.
3. Surface roughness as well as pileup and sink-in effects can be neglected.

None of these assumptions is absolutely true but they enable a great simplification of the contact problem.

If we know the true shape of the tip (as we will assume here), then the contact area and, with assumption (1), the remaining area of the impression can be derived from the contact depth h_c, provided we are able to determine the elastic deformation above the contact area, h_s. The elastic deformation below the contact $(h_c - h_0)$ (h_0 = final depth after unloading), which is responsible for the change of the impression shape during unloading, does not need to be known. The absolute elastic deformation is

$$h_e = h_s + (h_c - h_0) \tag{6.3}$$

and the real plastic deformation in the center of the contact is h_0. Often, the plastic deformation depth is set equal to the contact depth h_c but this is not correct.

The question now is how to get the elastic deformation above the contact area, h_s. Let us go back to wholly elastic deformations. In this case, we know from the theory of elasticity the force–displacement relationship for a cone:

$$F = \frac{2}{\pi} \frac{E}{\tan \alpha} h^2 \tag{6.4}$$

and for a sphere:

$$F = \frac{4}{3} E \sqrt{R}\, h^{3/2} \tag{6.5}$$

where $R$is the radius of the sphere and α the opening angle between surface and indenter side (see Fig. 6.1). The first derivative $\mathrm{d}F/\mathrm{d}h$ at h_{max} is called contact stiffness S. This can be determined from a fit to the unloading curve and is shown

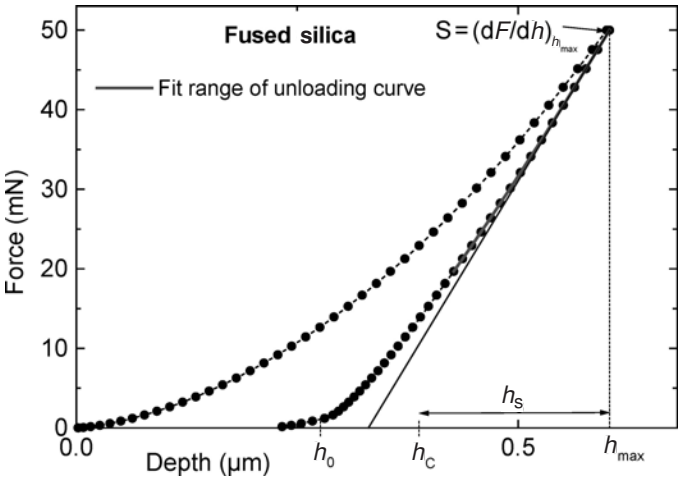

FIGURE 6.2. Force–displacement curve from a plastic indentation into fused silica with a maximum force of 50 mN.

in Fig. 6.2 as the tangent. If we divide force by contact stiffness, we get $h/2$ for the cone and $h/1.5$ for the sphere. The divisor is the exponent m of h in the force–displacement formulas (6.4) and (6.5). Now we need the ratio between the elastic deformation above the contact area and the absolute elastic deformation. This is also known from the theory of elastic solids. For a cone, for instance, the deformation at any position of the surface is given by Sneddon[10] as

$$w(r) = \left(\frac{\pi}{2} - \frac{r}{a}\right) a \tan\alpha \quad r \leq a \tag{6.6a}$$

$$w(x) = \frac{-2h}{\pi a}\left(a \sin^{-1}\left(\frac{a}{r}\right) - r + \sqrt{r^2 - a^2}\right) \quad r > a \tag{6.6b}$$

with r being the radial surface position and a the contact radius. Using $r = a$ at the contact edge and $r = 0$ in the center we get the ratio $h_s/h_{max} = 1 - 2/\pi$. The corresponding ratio for a spherical indenter is 1/2. The product of this ratio and the exponent m is the so-called epsilon factor ε. It is given in Table 6.1 for some indenter geometries. Finally we get the contact depth

$$h_c = h_{max} - \varepsilon \frac{F}{S} \tag{6.7}$$

with

$$\varepsilon = m \frac{h_s}{h_{max} - h_0} \tag{6.8}$$

and the contact area can be calculated.

TABLE 6.1. Comparison of Elastic Constants for Different Indenter Geometries

Indenter/pressure	h_s/h_{max}	m	
Flat punch	1	1	1
Sphere, paraboloid of revolution	0.5	3/2	0.75
Cone	$1-2/\pi = 0.3634$	2	0.7268
Constant pressure, circular boundary	$2/\pi = 0.6366$	1	0.6366

In a real measurement, the indenter itself is also elastically deformed. This can be easily considered in the formulas, by introducing instead of the sample modulus E a reduced modulus E_r, which is defined as

$$\frac{1}{E_r} = \frac{1-\nu_i^2}{E_i} + \frac{1-\nu_s^2}{E_s} \tag{6.9}$$

where ν is the Poisson's ratio and the subscripts i and s stand for indenter and sample, respectively. The consideration of the indenter displacement in this way is possible because there is a general relation for the displacement w in normal direction of the two bodies in contact

$$\frac{w_i}{w_s} = \frac{\left(1-\nu_i^2\right) E_s}{\left(1-\nu_s^2\right) E_i} \tag{6.10}$$

which is valid for any arbitrary-shaped body (see Ref. 11). The contact area increases for a deformable indenter in comparison to a rigid one and the contact stiffness decreases for equal load.

Up to now the derivation was done for wholly elastic deformation. The question arises whether this can also be applied when there is an additional plastic deformation. To give an answer, a look at the contact pressure for the different indenter geometries is useful (Fig. 6.3).

For a conical indenter the pressure becomes infinite in the center of the contact. The same is the case at the edge for a flat punch. No material can resist such a pressure and plastic flow immediately arises, which reduces the stresses significantly. The resulting pressure after plastic deformation is not known and can be estimated only by finite element (FE) calculations. However, an indication of the pressure profile can be obtained from an analysis of the unloading curve—the unloading exponent m. Oliver and Pharr[9] have shown that the unloading curve from elastoplastic deformations with a Berkovich indenter can be described by a power function

$$F = K(h-h_0)^m \tag{6.11}$$

and they got values for m between 1.2 and 1.6. They found that the best interpretation of experimental data was possible for an epsilon value of 0.75, which

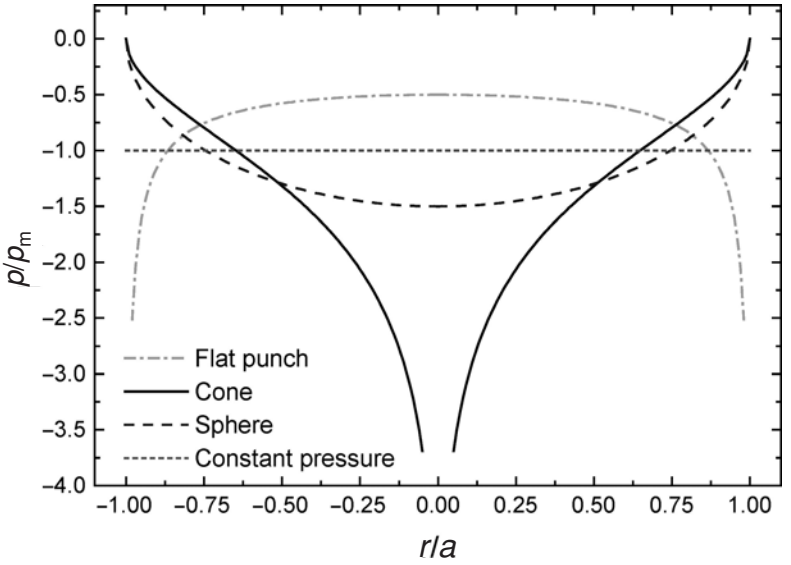

FIGURE 6.3. Comparison of pressure profiles below the contact area for different indenter geometries. The calculation was done for equal contact radius.

corresponds to an unloading exponent of 1.5 for a spherical indentation and not to that expected for a conical or pyramidal indenter of 2.

The reason is the change in the pressure profile due to plastic deformation. Although a pyramid was used as indenter, the profile is much closer to the hertzian pressure profile of a sphere. This has also been confirmed by FE calculations (see Ref. 12). Therefore, an epsilon value of 0.75 is required in the standard ISO 14577 for indentations with Vickers and Berkovich indenters. However, one should keep in mind that this is only an approximation and there may be materials with a bigger deviation from this value.

The final formula for the calculation of the indentation hardness H_{IT} is now

$$H = \frac{F}{C(h)\left(h - \varepsilon \frac{F}{S}\right)^2} \tag{6.12}$$

The geometrical factor $C(h)$ depends on the indenter shape and is 24.5 for ideal Vickers and Berkovich indenters. Real indenters deviate more or less from the ideal shape and practically in all cases an area function has to be determined instead (see Section 3).

In contrast to the Martens hardness, the indentation hardness is a measure of the resistance to permanent deformation or damage. For ideal conditions it should give the same hardness value as conventional Berkovich (or Vickers) hardness methods (which are based on the measurement of the permanent impression after

the indentation). However, a different name was chosen because the derivation of the contact area from the measured depth is still accompanied by some uncertainties and for most materials the results will be slightly different.

For comparison with Vickers hardness it has to be considered that the Vickers hardness is calculated with the surface area of an ideal pyramid (like Martens hardness) and not with the projected contact area. This results in a geometrical scaling factor of 0.927. Furthermore, Vickers numbers are quoted in the unit kgf/mm^2 instead of MPa for the indentation hardness, and so the final relation is

$$\mathrm{HV} = 0.094545 H_{\mathrm{IT}} \tag{6.13}$$

In scientific publications the unit GPa is used instead of MPa for a better comparison with the modulus, which has also GPa as the unit.

The indentation modulus (or Young's modulus for isotropic materials) is another parameter that can be measured by nanoindentation. If one compares the first derivative of Eqs. (6.4) and (6.5) and replaces the depth by the contact area, one can see that there is a shape-independent relation between contact stiffness and contact area:

$$S = \frac{2}{\sqrt{\pi}} E_{\mathrm{r}} \sqrt{A_{\mathrm{c}}} \tag{6.14a}$$

The reduced modulus E_{r} is the proportionality factor. Pharr *et al.*[13] have shown that this universal relation is valid for any axisymmetric indenter and can be used even for a predeformed surface with a plastic impression in it. However, Berkovich and Vickers indenters are not rotationally symmetric and the sharp edges should result in slight deviations from this formula. Therefore a β factor was introduced in Eq. (6.14):

$$S = \beta \frac{2}{\sqrt{\pi}} E_{\mathrm{r}} \sqrt{A_{\mathrm{c}}} \tag{6.14b}$$

Gao and Wu proved, by a perturbation method, that the contact stiffness of a layered medium is insensitive to the cross-section shape of a punch as long as the shape does not differ too much from a circle.[14] Several purely elastic calculations exist for the determination of β. The most known is that of King[15] for flat-ended punches of triangular and quadrilateral cross sections. Bilodeau has done a similar calculation with an approximate solution for pyramids.[16] Giannakopoulos *et al.*[17] used a very accurate FE calculation for the same pyramidal geometries and Hendrix[18] has done the calculation for a constant pressure profile with triangular or quadrilateral shape. Table 6.2 shows the results for β.

It is interesting to note that the constant pressure necessitates the smallest corrections. However, this is just the most probable pressure distribution after plastic deformation because the infinite stresses at any edges and the tip (punch and pyramid) will be reduced by the plastic displacement of material. Additionally, it is well known that the plastic zone of Vickers indentations is approximately rotationally symmetric (see, for instance, Ref. 19) because the high stresses at the

TABLE 6.2. Correction Factor for the Stiffness–Area Function with Respect to the Conical Indenter in Dependence on the Indenter Shape

Indenter/pressure	β (Triangular shape)	β (Quadrilateral shape)
Flat punch[15]	1.034	1.012
Pyramid[16]	1.141	1.051
Pyramid, FE calculation[17]	1.138	1.090
Constant pressure[18]	1.0226	1.0055

edges, which were predicted by purely elastic calculations, are especially reduced by plastic deformation. For these reasons, no value is given or recommended for β in the standard ISO 14577 and it is indeed better to use $\beta = 1$ for pyramidal tips. In fact there may be a slight deviation from 1 for highly elastic materials with a small plastic zone but one can expect that the error, introduced by the unknown value, is smaller than 5% in the worst case.

The indentation modulus according to ISO 14577 is calculated with the formula

$$E_{\mathrm{IT}} = \frac{1-\nu_{\mathrm{s}}^2}{\dfrac{1}{E_{\mathrm{r}}} - \dfrac{1-\nu_{\mathrm{i}}^2}{E_{\mathrm{i}}}} \quad \text{and} \quad E_{\mathrm{r}} = \frac{\sqrt{\pi}}{2}\frac{S}{\sqrt{A_{\mathrm{c}}}} \tag{6.15}$$

Only one elastic constant can be determined by one measurement. Therefore, an assumption has to be made for the Poisson's ratio of the sample if it is not known. The dependence of E_{IT} on Poisson's ratio is very small and a rough estimation is usually sufficient. Again the new name indentation modulus is used because there might be slight deviations from the Young's modulus determined by ultrasonic or other methods. For approximately isotropic materials there is no physical reason, however, for this differentiation, and both values should agree if the contact area can be correctly determined. Only for single crystals or composite materials canlarger deviations be expected.

A more detailed analysis of the conditions during an indentation shows that the main assumption (1) is a good approximation only for highly plastic materials such as most of the metals. All solutions for an elastic contact deliver not only a normal deformation but also a radial deformation u, which is zero in the center and reaches a maximum close to the contact edge. The radial deformation outside the contact radius a is given by

$$u_{\mathrm{r}} = \frac{-(1-2\nu)(1+\nu)}{2E} p_{\mathrm{m}} \frac{a^2}{r} \tag{6.16}$$

with ν being the Poisson's ratio, E the Young's modulus, p_{m} the mean contact pressure, and r the radius coordinate (see for instance Refs. 20 and 21). This formula is valid for all kinds of rotational symmetric indenters. The minus sign means that u_{r} is directed toward the center of the contact.

This formula has now to be applied to the conditions of a plastic deformation. In this case, the contact pressure can be replaced by the hardness H. We want to know the relative change of the contact radius under pressure due to elastic radial displacement at the contact edge, which leads us to the formula

$$\frac{u_\mathrm{r}}{a} = \frac{(1-2\nu)(1+\nu)}{2}\frac{H}{E} \tag{6.17}$$

As an additional correction we have to consider that the surface after plastic deformation is no longer flat and the elastic radial displacement has now to be estimated along the new deformed surface within the impression. This can be considered by the projection of u_r onto the original surface position. We get the correction term $\cos(\alpha_\mathrm{r})$—where α_r is the residual angle between the face of the impression and the surface—and slightly smaller than α in Fig. 6.1. α_r is given by

$$\alpha_\mathrm{r} \approx \tan\frac{h_0}{a} \tag{6.18}$$

with h_0 as residual depth. α_r is normally below 20° for Berkovich or Vickers indenters and the correction is smaller than 6%. The final formula is then

$$\frac{u_\mathrm{r}}{a} = \frac{(1-2\nu)(1+\nu)}{2}\frac{H}{E}\cos(\alpha_\mathrm{r}) \tag{6.19}$$

The radial displacement correction depends on the H/E ratio. It is therefore very small for most of the metals (<0.5%) and reaches larger values for highly elastic materials like fused silica. Since u_r is directed inwards under pressure, the contact radius increases by u_r during unloading. The size of the residual indent is therefore underestimated due to the calculation of A_c from the contact depth. The area increase for fused silica with $H/E = 0.13$ is about 9% and should be considered for a more accurate result. This is especially meaningful because fused silica is often used as reference material for the calibration of the indenter area function.

3. INFLUENCE AND DETERMINATION OF INSTRUMENT COMPLIANCE

Hard nanostructured coatings are often used for wear protection for cutting tools and these are often made of cemented carbide. Cemented carbide has the highest modulus of any material that is available in large amounts. Depending on the cobalt content, the Young's modulus is between 580 and 655 GPa. Among bulk materials, only diamond, cubic boron nitride, and pure tungsten carbide have a higher Young's modulus. Hard nanostructured coatings may also have a Young's modulus in this range. A high Young's modulus is accompanied by a high stiffness in indentation experiments. For high loads the contact stiffness is similar or even larger than the

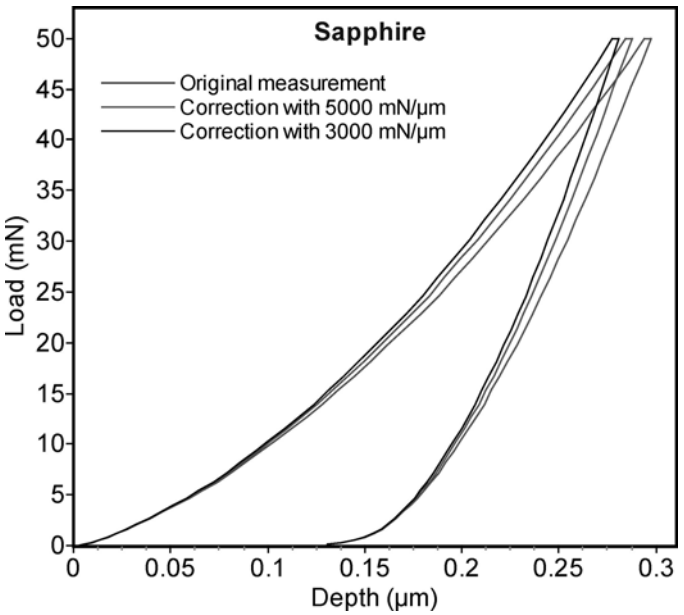

FIGURE 6.4. Influence of the assumed instrument stiffness on the shape of the load–displacement curve of sapphire.

instrument stiffness. The correct sample or film modulus can therefore be measured only if the instrument stiffness is well known and the measured displacements can be corrected.

Unfortunately, the determination of the instrument stiffness is one of the most difficult tasks in nanoindentation. Nearly all manufacturers of nanoindentation devices assume that their instrument stiffness is a constant, independent of the applied force. In reality this is not necessarily the case and a constant value is used as a first estimate only when no reliable method is available for the determination of a force-dependent stiffness.

The stiffness influence on load–displacement curves is shown in Figs. 6.4 and 6.5.

The contact stiffness of sapphire measured at 50 mN with a Berkovich tip was 540 mN/µm. At 500 mN it was already 1780 mN/µm. Remember that the measured contact stiffness depends on the bluntness of the tip; thus, slight differences may occur if one tries to repeat these measurements. In contrast to the contact stiffness, the instrument stiffness of the ultra-microindentation system (UMIS)-2000, which was used for the measurement, was about 5000 mN/µm. Typically, the instrument stiffness differs from instrument to instrument and is mostly in the range between 300 mN/µm and about 8000 mN/µm, depending on the instrument type. The stiffness correction reduces the measured indentation depth to a lower value. In

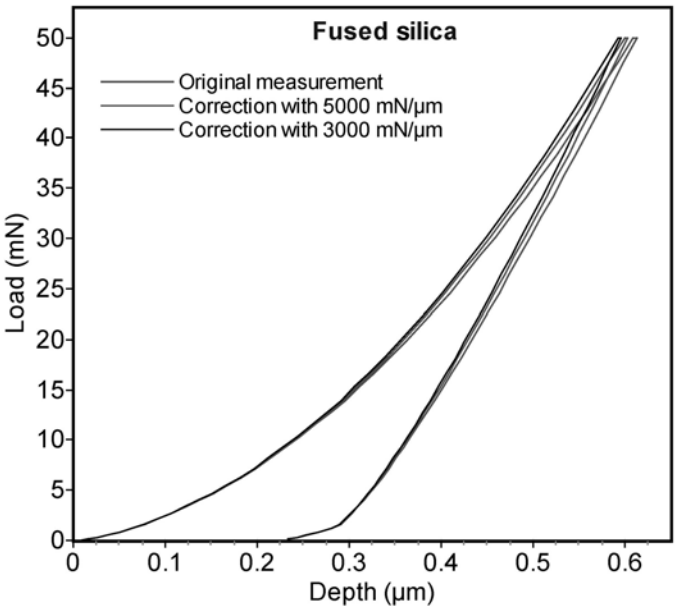

FIGURE 6.5. Influence of the assumed instrument stiffness on the shape of the load–displacement curve of fused silica.

the example of Figs. 6.4 and 6.5 the correct reduction is only 10 nm but it changes the curve shape, for the stiffer sapphire much more than for fused silica. The relative depth change is 3.5% for sapphire and only 1.7% for fused silica. The influence on the unloading stiffness and modulus, however, is larger depending on the unloading depth h_0. In the example of the 50-mN measurement on sapphire it is 10% and for fused silica 3.6%. In the case of the very steep unloading curve of an aluminum single crystal it is as much as 25%, although the maximum depth at 50 mN is 2.6 µm and therefore much bigger than for sapphire. These examples show that the measurement error may be considerable even at moderate loads if the instrument stiffness is not considered.

For the calculation of the instrument stiffness it is easier to work in terms of compliance C (being the inverse of stiffness) because sample compliance C_s and instrument or frame compliance C_f can be simply added. The total measured compliance C_t is then

$$C_t = C_s + C_f \quad \text{with} \, C_s = \frac{\sqrt{\pi}}{2E_r} \frac{1}{\sqrt{A_c}} \tag{6.20}$$

Thus

$$C_t = \frac{\sqrt{\pi}}{2\,E_r} \frac{1}{\sqrt{A_c}} + C_f \tag{6.21}$$

If the reduced modulus is constant and depth independent, a plot of C_t (uncorrected for frame stiffness) versus $1/\sqrt{A_c}$ is linear and intersects the stiffness axis at the frame compliance C_f. This method requires the knowledge of the contact area A_c, which is also not known *ab initio*. The determination of instrument compliance and of indenter area function depend upon each other and can be solved by iterative procedures only if there is no external measurement of the area function available. Doerner and Nix[8] proposed to make replicate indentations in elastically isotropic, homogeneous, and highly plastic materials and to measure the indents by independent means, for example, by atomic force microscopy or scanning electron microscopy. Such direct measurements are cumbersome and difficult, and in any case they do not have the required accuracy for small indents. A better method is the direct measurement of the diamond tip by an atomic force microscope (AFM)[2,22] and the derivation of the area function from the image (see below). Such measurements require a well-calibrated AFM and good expertise. Therefore, a method is preferred which is based on nanoindentation measurements alone.

Such a method was first proposed by Oliver and Pharr[9] in their early paper of 1992 and uses two different reference materials. Aluminum with low hardness and relatively good isotropy was used because it formed large indentations, where the area function of a perfect indenter can be used as first estimate. Fused silica was used as the second material to extend the area function into the small depth range. The contact areas for a series of indentations with different loads can be obtained by iteration according to the equation

$$A_c = \frac{\pi}{4}\frac{1}{E_r^2}\frac{1}{(C_t - C_f)^2} \tag{6.22}$$

and assuming that the instrument compliance is constant. The reduced modulus of the reference materials is known and can be used as an input parameter. This is not necessary but it results in quicker convergence. The contact area has to be calculated for at least five or six different loads. The result should give a straight line in the presentation of C_t as function of $A_c^{-1/2}$ which intersects the ordinate axis at C_f. The experience with this method shows that the resulting instrument compliance has quite a big uncertainty, and sometimes even a negative value is obtained, which has no physical meaning. A similar method with tungsten and fused silica as reference materials was proposed by Meneve *et al.*[23]

In a more recent work,[24] Oliver and Pharr proposed another method for the determination of instrument compliance. It works with only one reference material and the area function does not need to be known. With Eq. (6.14) and $H = F/A_c$ the ratio

$$\frac{F}{S^2} = \frac{\pi}{4}\frac{H}{E^2} \tag{6.23}$$

should be constant if hardness and modulus of the material are constant. This can be assumed for isotropic and homogeneous materials that do not pileup or sink-in

and that show a low tendency for cracking. In their work they preferred fused silica. The load over sample stiffness squared as function of depth should be a straight line parallel to the depth axis at larger depths where the tip rounding does not play a significant role. The instrument stiffness has to be varied in order to obtain this parallel position. However, this method has also a big disadvantage. Hardness is not a physical parameter and—in contrast to the case of the modulus—there exists no other method than indentation that could confirm a constant, depth-independent hardness.

A third method was proposed by Chudoba *et al.*,[25] which uses wholly elastic indentations with a spherical indenter and two or three reference materials with different moduli. Measurements with equal maximum force F and well-known elastic constants are required. The effective sphere radius R (which may be depth dependent for real indenters) and the instrument stiffness S_f can then be determined according to

$$R = \left(\frac{3}{4}\right)^2 \frac{F^2}{(h_1 - h_2)^3} \left(\frac{1}{E_{\mathrm{r}1}^{2/3}} - \frac{1}{E_{\mathrm{r}2}^{2/3}}\right)^3 \tag{6.24}$$

$$S_\mathrm{f} = \frac{F}{h_1 - \left(\frac{3}{4}\frac{F}{E_{\mathrm{r}1}}\right)^{2/3} \left(\frac{1}{R}\right)^{1/3}} \tag{6.25}$$

under the assumption that both values (R, S_f) are constant in the investigated depth and load range. Good results can therefore be obtained only if the sphere radius does not change much in the range between h_1 and h_2. This has to be confirmed by independent investigations. The accuracy of the method can be improved if three substrate materials are used in pairs. Equations (6.24) and (6.25) then deliver three independent results for R and S_f and their arithmetic average is the final value.

In the opinion of the author, the best method for the determination of instrument compliance is a direct comparison of indenter area functions, obtained with two different reference materials with large Young's modulus difference. The area function should not depend on the material. A possible difference can be caused by measurement uncertainty, inaccurate determination of the contact area from the contact stiffness due to pileup or sink-in effects, or by an incorrect value of the instrument compliance. Good experiences have been gained with single crystal sapphire ($E = 420$ GPa, $\nu = 0.234$) and fused silica ($E = 72$ GPa, $\nu = 0.17$). Both materials do not show pileup and only a very small sink-in (silica) and cracks occur only at somewhat higher forces (mostly >100 mN) or do not influence the results. The contact depth is calculated according to

$$h_\mathrm{c} = h_\mathrm{max} - F\,C_\mathrm{f} - \varepsilon\,F\,(C_\mathrm{t} - C_\mathrm{f}) \tag{6.26}$$

and the square root of the contact area A_c is

$$\sqrt{A_\mathrm{c}} = \frac{\sqrt{\pi}}{2}\,\frac{1}{E_\mathrm{r}}\,\frac{1}{C_\mathrm{t} - C_\mathrm{f}} \tag{6.27}$$

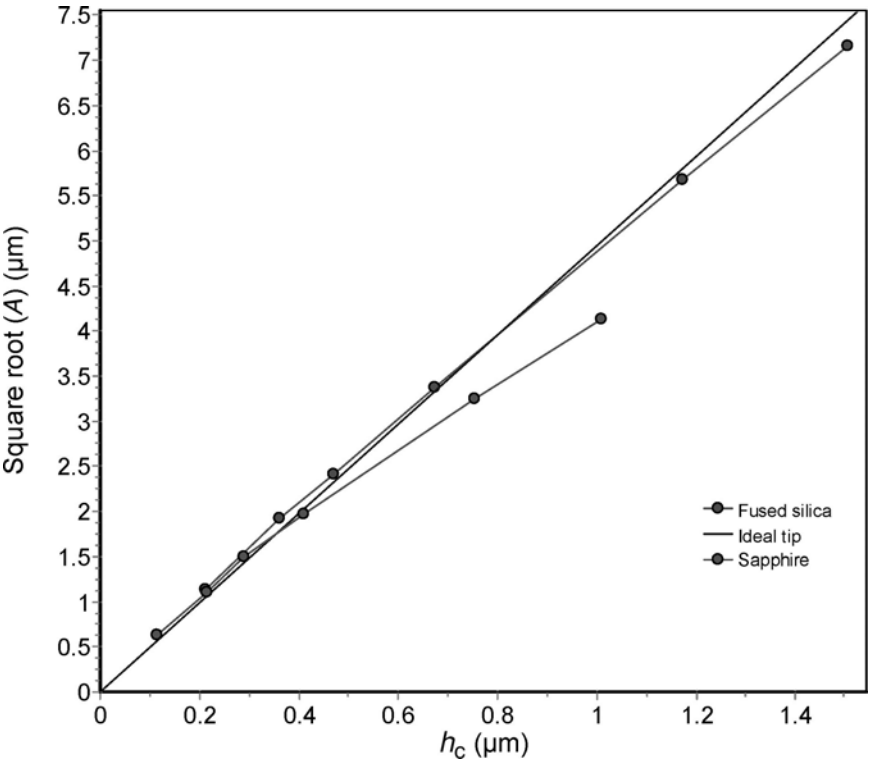

FIGURE 6.6. Calculated area functions obtained with fused silica (red points) and sapphire (green points), assuming zero instrument compliance. The straight line illustrates the ideal area for a Berkovich tip.

The reduced modulus E_r is given by Eq. (6.9). The ideal area function of a Berkovich tip in the presentation $\sqrt{A_c}(h_c)$ is a straight line with a slope of 4.95. In a first approach, C_f is set to zero. The result for fused silica and sapphire is shown in Fig. 6.6.

It can clearly be seen that the zero compliance results in too small a calculated area at higher depths, and this is worse for the stiffer sapphire. Now the instrument compliance value can be increased in Eqs. (6.26) and (6.27) for each data point of sapphire but keeping the fused silica area function unchanged. This increases the area for sapphire until the sapphire curve reaches the fused silica curve. In the next step, the new instrument compliance is used for both materials and this now increases the area for the fused silica curve. Both steps have to be repeated several times in an iterative procedure until convergence is achieved. The result is shown in Fig. 6.7.

The area functions of both materials agree very well over the whole overlapping depth range. The measurements in this example were carried out with a

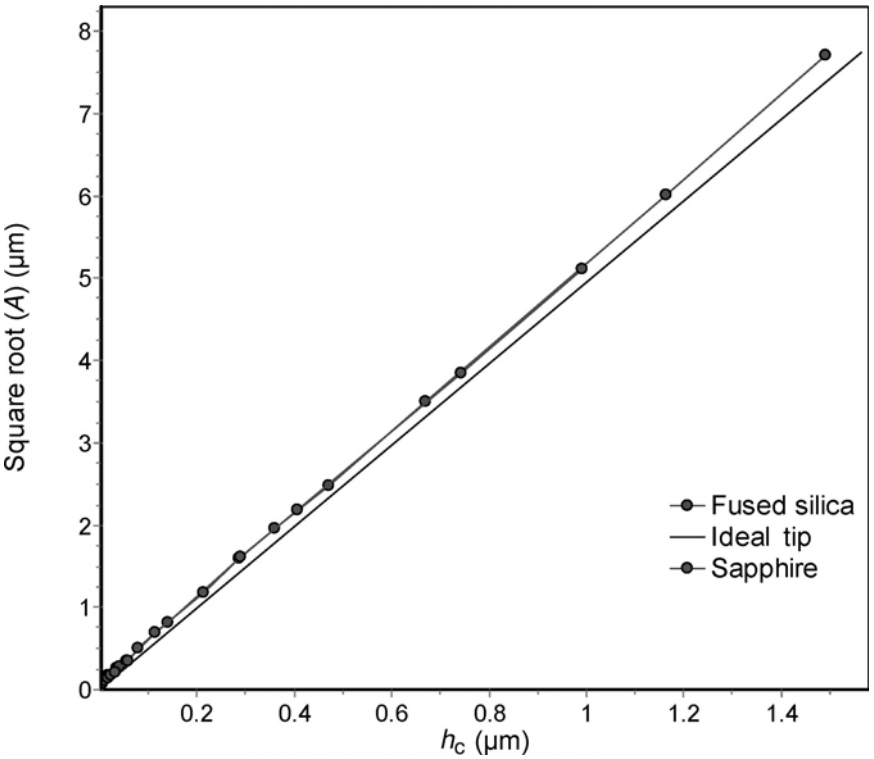

FIGURE 6.7. Area functions obtained with fused silica (red points) and sapphire (green points) after calculation of the correct instrument compliance. The straight line illustrates the ideal shape of a Berkovich tip.

Nanoindenter XP at about 10 different loads up to the maximum of 500 mN. The obtained stiffness function is given in Fig. 6.8. It shows an often-observed effect with this method: the stiffness is nearly constant at high loads but decreases at small loads. The effect is also visible for other instruments like the UMIS-2000. The reasons for this behavior are not completely clear. It is assumed that thin oil films in the positioning stages or the z-height gear as well as in the sample mount are responsible for this effect. Such a force dependence of the instrument compliance can be observed with this method only because all other methods deliver only a single constant as the compliance value.

The instrument stiffness in this example is high at more than 7000 mN/µm. The instrument compliance increases the measured depth at 100 mN by only 14 nm; however, this is still big enough for an adulteration of the modulus for stiffer materials. Other instruments show a bigger compliance and so require a good correction at lower forces. It should also be noted that there is no instrument with zero compliance, even if the depth measurement works with a reference tube

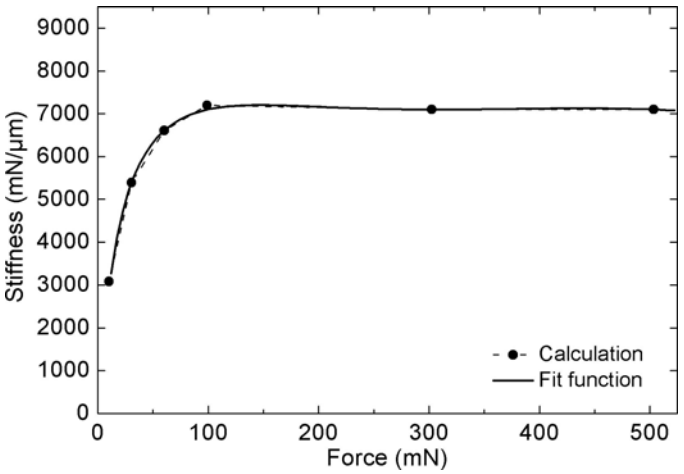

FIGURE 6.8. Instrument stiffness function obtained by a comparison of indenter area functions from two different reference materials.

or ring on the sample surface, e.g., the Fischerscope. This was discovered in the European projects INDICOAT[2] and DESIRED.[26] Inaccurate modulus results may be caused in particular for stiffer materials, if the instrument compliance is not appropriately considered in the analysis software of the instruments.

4. INFLUENCE AND DETERMINATION OF INDENTER AREA FUNCTION

No Berkovich or Vickers pyramid can be manufactured with an ideally sharp tip. Real tips have a tip rounding corresponding to a radius between about 50 nm and several hundred nanometers. The ISO 14577 part 2 standard prescribes a maximum tip radius of 200 nm for the nano range. Sharper tips than those with $R \approx 100$ nm can be prepared only by special methods and are available on the market as the so-called AccuTip^{TM}(MTS Systems Corporation, Nano Instruments Innovation Center). The tip rounding increases during the use of the diamond tips because even diamond wears.

The tip rounding becomes significant only if the indentation depth is small. The standard ISO 14577 recommends the use of an indenter area function if the indentation depth is less than 6 μm. For larger depth the ideal shape can be used with $A_c = 24.5\, h_c^2$. Significant hardness or modulus errors above 1% arise normally only in the depth range below about 2 μm. However, this is just the depth range that is used for measurements of hard nanostructured coatings. A correct area function has therefore to be determined and applied.

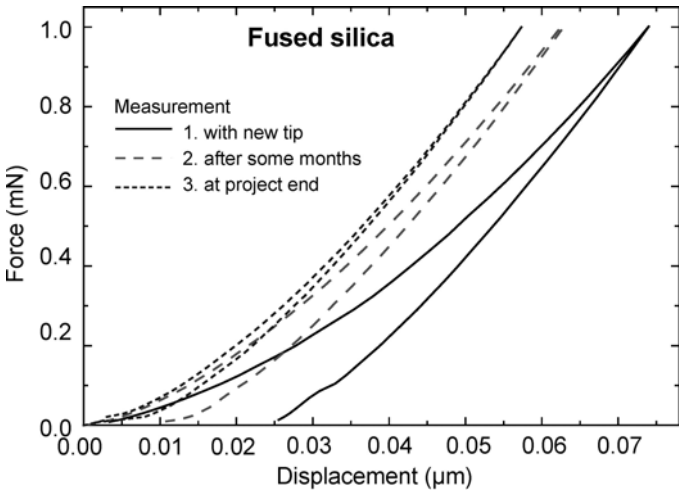

FIGURE 6.9. Comparison of force–displacement curves on the same sample and with the same Berkovich indenter at different times. Increasing tip rounding results in a decrease of the indentation depth.

An example for the effect of tip rounding is given in the following fused silica measurements. During the European INDICOAT project,[2] the area function of a new Berkovich indenter with a tip radius of 200 nm was determined with reference measurements on a fused silica sample. The validity of the area function was checked from time to time with the same reference sample. After several hundred measurements on different materials, a marked tip rounding was observed and the indentation depth at equal load had decreased (Fig. 6.9). More than 2 years later at the end of the project and after more than 10 000 measurements, the tip rounding had advanced further and was visible as a reduced displacement at equal load. The maximum indentation depth at 1 mN had reduced from 74 nm to only 57 nm. However, the change of the tip shape in the second half of the measurement period was smaller than in the first half. The experience shows that sharp tips wear faster than blunt tips and that the tip radius remains nearly constant over a long period of time if it has reached more than 500 nm. The final tip rounding in the given example amounts to 700 nm. A change in the tip shape can best be recognized at very small load where the relative depth change is the largest. A load between 500 μN and 3 mN is recommended, depending on the resolution of the instrument.

In ISO 14577 the area function can be determined by three methods:

- A direct measurement method using a traceable AFM.
- Indirectly by utilizing indentations into a homogeneous material of well-known Young's modulus.

- Indirectly by observing the departure from the indentation-depth-independent hardness.

The last method is difficult to apply because depth-independent hardness cannot be certified by another test method and hardness depends on definition, creep, loading, and unloading rate and other parameters (see Section 1). Therefore, it should be applied only in connection with Martens hardness, which is not addressed in this chapter (see Ref. 1 instead).

The first method requires another well-calibrated instrument (AFM). This is not always accessible and gives rise to higher costs. An example for the calibration by AFM is given in Ref. 27. A comparison between direct and indirect methods can be found in Ref. 22. It is shown that an agreement between both methods of more than 6% (2% for $h_c > 300$ nm) can be achieved if additional corrections like the radial displacement correction (see end of Section 1) are applied.

Mostly, the indirect method is favored using a sample of a well-known modulus. In this case the Eqs. (6.26) and (6.27) can be used for the calculation. Fused silica is very often used as reference material; however, other glasses or single crystals like sapphire are also well suited. As in the case of the determination of instrument compliance, care has to be taken in relation to pileup or sink-in effects or to cracking. Nearly all metals are unsuitable for the area function calibration in the nano range due to pileup, the influence of work hardening in a thin surface layer, caused by the preparation process, and the influence of oxide layers. Good results were obtained with tungsten for contact depths above 200 nm.[26] The search for applicable reference materials for the micro- and nano range is still in progress, for instance in the European project DESIRED: "Certified Reference Materials for Depth Sensing Indentation Instrumentation."[26]

The procedure for the indirect determination of the area function requires highly accurate measurements of the reference material of at least 8–10 different loads, preferably more. The load range should span between the smallest possible load of the instrument (typically 0.1–0.3 mN) and the maximum load. To improve the accuracy of the analysis, 10 or more measurements at each load should be carried out and averaged. The number can be reduced for the highest loads. Once corrected for thermal drift, the measurements deliver force, maximum depth, and contact stiffness, which are input in Eqs. (6.26) and (6.27), provided that the instrument compliance is known. Alternatively the "continuous stiffness" measurement method can be used for instruments with this option. In this case, measurements at only the maximum possible load are required. However, such measurements are not very accurate in the low load range due to problems with the zero point determination and point density. Therefore, some additional small load measurements are recommended.

If the area function determination is correct, the Young's modulus results for the reference materials should no longer depend on depth. This is shown in Fig. 6.10 (triangles). Every point belongs to measurements at different loads. However, if one omits to monitor the validity of the area function over time and applies it to

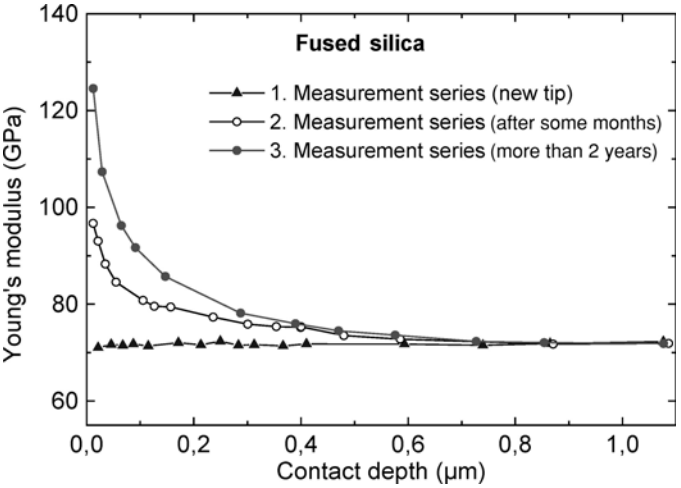

FIGURE 6.10. Modulus results as function of depth for fused silica after utilization of the area function of a new tip.

measurements at a later date, one can introduce considerable errors in the results if that tip has changed. In Fig. 6.10 the area function of the new tip was applied to the measurement series over time, given in Fig. 6.9. The apparent modulus of fused silica increases significantly for contact depths below 600 nm and the modulus error reaches more than 50% for contact depths below 100 nm.

This effect can also be observed for the indentation hardness (Fig. 6.11). The uniformity of the hardness when using the correct area function (triangles) is

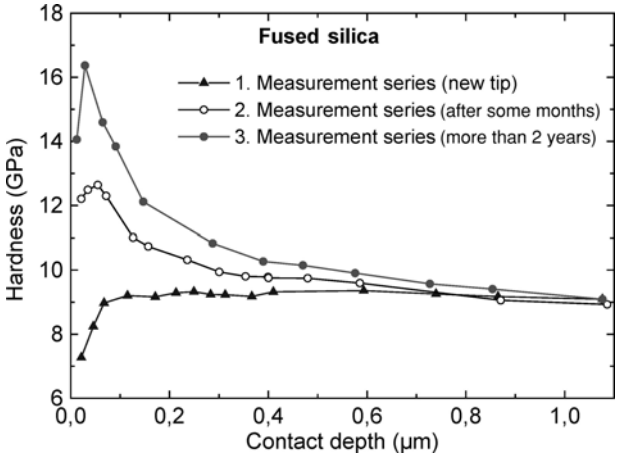

FIGURE 6.11. Hardness results as function of depth for fused silica after utilization of the area function of a new tip.

not as good as that of the Young's modulus. In particular, at low depth, a hardness decrease can be observed. This is due to the transition from wholly elastic deformation to a fully developed plastic zone and is explained in Section 6. In contrast to the hardness decrease for measurement series 1, the hardness increases markedly toward the surface due to the tip rounding if the correct area function is not applied.

The above example illustrates that an inaccurate or even incorrect area function not only prevents a comparison of results from different instruments, but also complicates the comparison of results from one and the same tip but measured at different times. The error increases with decreasing indentation depth and becomes significant for depths below 1 μm. Such a tip blunting does not necessitate a replacement of the tip—a recalibration of the area function enables an extension of the tip's working life. However, large tip rounding requires special care when interpreting hardness results in the elastic–plastic transition range.

The indenter area function is normally determined for 8–20 points (see in Fig. 6.7). ISO14577:2002 part 2 requires at least 10 points to be measured and that these points span the ranges of force and contact depth to be used. A description with a suitable function is therefore necessary. Oliver and Pharr[9] proposed the following fit function:

$$A(h_c) = C_0 h_c^2 + C_1 h_c + C_2 h_c^{1/2} + C_3 h_c^{1/4} + C_4 h_c^{1/8} + C_5 h_c^{1/16} + C_6 h_c^{1/32} + C_7 h_c^{1/64} + C_8 h_c^{1/128} \tag{6.28}$$

Such a function with nine coefficients allows an accurate description of the area function, even for small depth, if at least 10 different data points are available. Generally the number of data points for the fit has to be bigger than the number of coefficients. The coefficient C_0 is sometimes set to the constant value of 24.5 for an ideal Berkovich tip but it is better to include this term in the fit. In contrast to function (6.28), a fit with a polynom of third order or another function with only three terms is not accurate enough. This is shown in Fig. 6.12 for the first 300 nm of the area function of the blunt tip of measurement series 3 of our example. Some instruments provide a function with only three coefficients in their analysis software and therefore have problems to describe the tip shape in the low depth range where the biggest change takes place. It is mostly difficult to distinguish between a real hardness change in this depth range and an apparent hardness change introduced by an inappropriate fit function. Special care has to be taken for hard (nanostructured) coatings where an accurate area function in the low depth range is essential for correct results.

Another way to describe the indenter area by a function is to fit the square root of the area (as in Fig. 6.7). This has the advantage that in such a presentation the ideal indenter shape is given by a straight line and deviations in the low depth range can be better recognized.

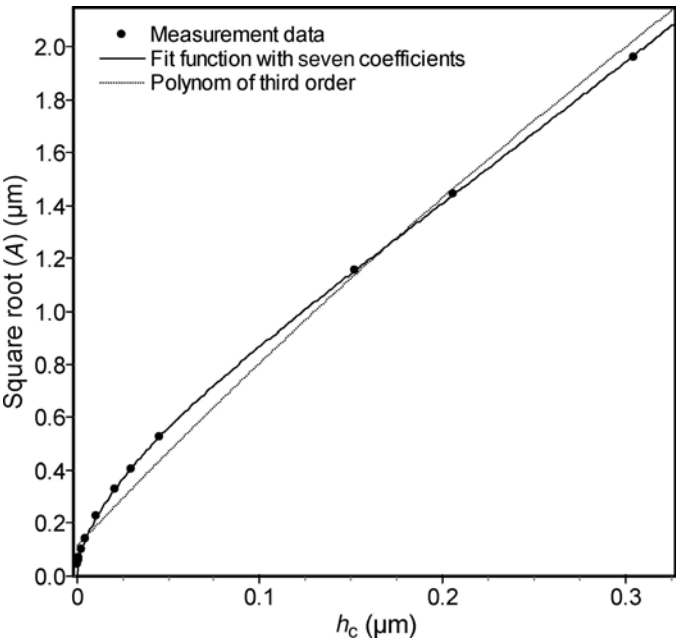

FIGURE 6.12. Low-depth detail of an area function for a depth range of 900 nm. A fit formula with seven coefficients describes the data much better than a polynom of third order.

Generally, an area function should be used only in the depth range over which it was measured; otherwise considerable errors can be produced, because the behavior of the function outside the fit range cannot be estimated. There are several possibilities to get an estimation of the indenter area outside the fit range if it is necessary to realize a big indentation depth. First, one can extrapolate the last part of the area function (the upper end of the depth range) and check if there is no strong deviation from the previous course. However, the extrapolation method should be used to extend the depth range only by 20–30%. For larger depth, one can assume the ideal tip shape and add an offset that is obtained from the difference between the ideal area and the area value obtained for the last valid depth value of the fit function. The best way would be to choose a softer reference material, which allows measurements at large-enough depths and to make a new area function valid for large depths.

Finally, it should be mentioned that the sum of the residuals of a least squares fit is the minimum achieved for only that particular fit function. It is also important how the function behaves between the measured data points, which were used for the calculation. The sum of the residuals (or their squares) can be used as a guide when comparing the relative suitability of different fit functions.

5. ADDITIONAL CORRECTIONS FOR HIGH-ACCURACY DATA ANALYSIS

For the measurement of hard coatings, the indentation depth rarely exceeds 1 μm and measurements with only 100-nm depth are not unusual. Therefore, all available correction procedures must be applied to achieve sufficient accuracy. Two of them shall be briefly explained.

5.1. Thermal Drift Correction

It is well known that length measurements are sensitive to thermal expansion of the measuring instrument and the sample during the measurement process. A thermal drift correction is therefore necessary. The typical measurement time of an indentation measurement with loading/unloading segment and holding time at maximum load is between 30 and 300 s. In this time the depth should not change more than 1 nm due to thermal effects. For the UMIS-2000 a thermal drift constant of 1.22 μm/K was determined.[2] A 1-nm accuracy of the depth measuring system would require a temperature stability of about 1 mK in the time interval of the measurement. This cannot be reached by an active environmental chamber or other temperature control systems. Therefore, the measuring unit itself is used to determine the thermal drift rate being experienced during each test. A second hold period of at least 40 s or preferably more is inserted, for example, in the unloading segment at a value between 5 and 30% of the maximum force. The complete measuring cycle is shown in Fig. 6.13 for a fused silica measurement with the UMIS-2000.

It is assumed that material influences can be neglected if the force and therefore the contact pressure are markedly reduced. This is a good assumption for most materials but it is definitely wrong for materials with viscoelastic properties, such as polymers. Fortunately, the indentation depth of polymers is so big that it is possible to neglect the thermal drift correction. For hard nanostructured coatings a thermal drift correction should always be applied. As a first approximation it can be assumed that the thermal drift is linear over short time periods. This can be tested, if necessary, by taking data over a longer hold period (for instance some minutes) and plotting the drift rate as a function of time. Such a longer hold period can also give valuable information about the influence of vibrations and the effect of active temperature control systems, if installed. A linear fit is applied to the depth–time data of the second hold period to deduce the drift rate. To further improve the accuracy, the first 15–20 s of the second hold period should not be included in the fit, because they may still be influenced by relaxation processes in the material. An example is given in Fig. 6.14 for fused silica.

The upper curve shows the nonlinear depth change during the first hold period at maximum force that is mainly determined by creep. The lower curve indicates

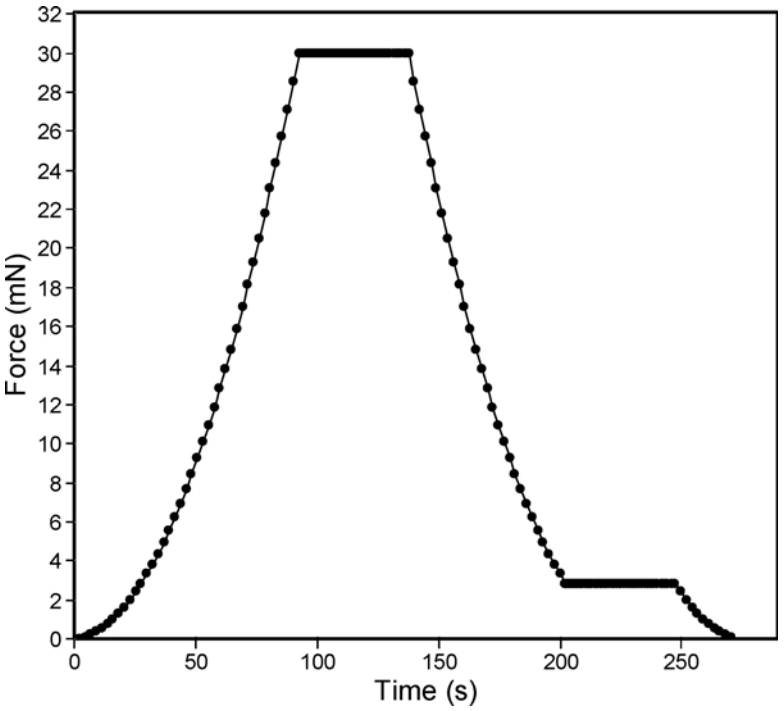

FIGURE 6.13. Typical measurement cycle of an indentation experiment with loading segment, hold period at maximum force, unloading segment, and second hold period at 10% of maximum force.

that the thermal drift is linear during the second hold period apart from the first 15 s which are still influenced by material effects. The start of the second curve was intentionally set to the depth value of the first one to enable a better comparison. Observe the high accuracy of the depth measurement. The depth change is only 0.8 nm in 45 s. Nevertheless, the drift rate is 0.0173 nm/s, which would result in a displacement error of 3.5 nm during a 200-s measurement time. This is less than a 1% error for this 30-mN measurement but it would reach 6% for a 1-mN measurement. The thermal drift correction can have a significant influence on the measurement uncertainty, especially if the data points, used for the fit, are disturbed by vibrations or other sources of scatter. A visual inspection of the fit accuracy is therefore recommended. The accuracy can be improved by increasing the data rate and the length of the hold period.

A thermal drift correction is still required even if the instrument measures the displacement against a ring or tube, sitting on the sample surface (for instance, in the case of the Fischerscope or the Nano-Hardness Tester (NHT) from CSM). An example is given in Fig. 6.15 for a 100-mN measurement of fused silica with a Fischerscope. The drift rate is –0.154 nm/s and therefore nine times higher than in

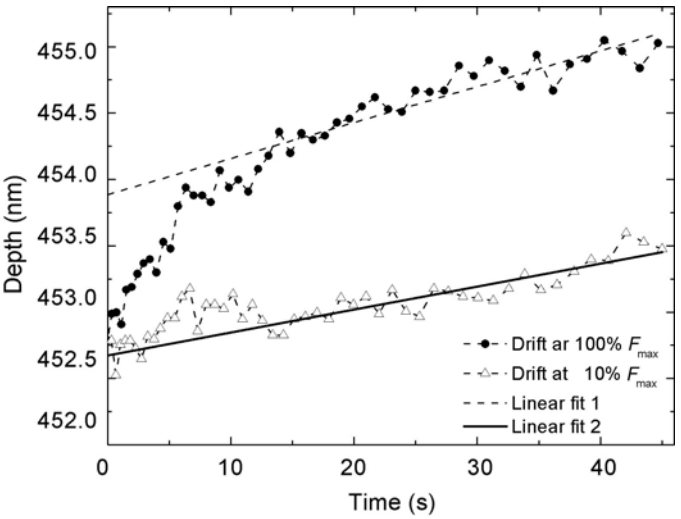

FIGURE 6.14. Depth change over time due to thermal drift (lower curve) and creep + thermal drift (upper curve). The straight lines represent a linear fit of the last 50% of the data (upper curve) and last 75% of the data (lower curve).

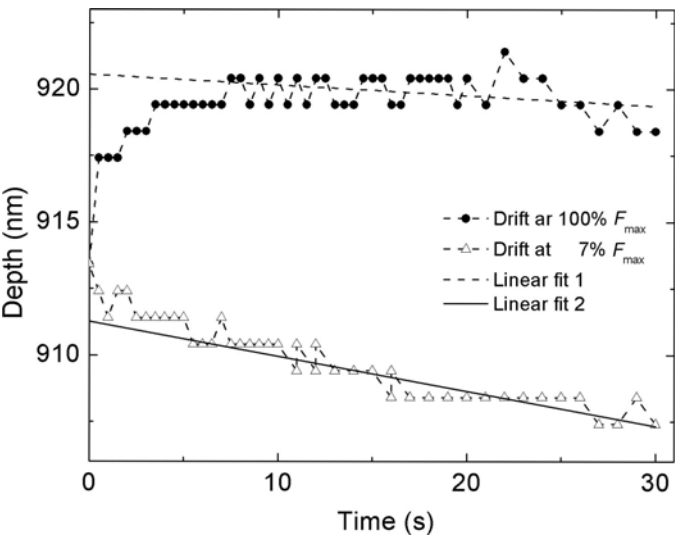

FIGURE 6.15. Depth change over time during the second hold period after unloading (lower curve) and at maximum force (upper curve) for a fused silica measurement with a Fischerscope. The straight lines represent a linear fit of the last 50% of the data (upper curve) and last 75% of the data (lower curve).

the example before. The measurement was done in standard laboratory conditions and is not an especially bad example. The somewhat coarser shape of the curve is due to the 1-nm digital resolution of this instrument. In contrast to the UMIS-2000, the Fischerscope is not positioned in an isolating chamber. Short thermal fluctuations have therefore a larger effect.

5.2. Zero Point Correction

Displacement measurements start from the point of first contact between indenter and sample. The determination of this point influences the whole load–displacement curve and should be carried out with care. The correct detection of the surface position is not an easy task, particularly in the nano range. Two different methods are generally used. For the first one, load and depth data are recorded already during the approach, and the touch point is determined by the first increase of test force or contact stiffness. The step size around this point shall be small enough so that the zero point uncertainty is less than the required limit. Otherwise a back-extrapolation method can be used as a correction method to improve the zero point accuracy.

The other method detects the surface at the depth at which the minimum possible contact force of the instrument is exceeded. Data before that point are not available. Typically this is in the range between 1 and 10 μN. The minimum contact force is an important parameter that distinguishes a nanoindentation instrument from a microindentation instrument. If the initial contact force is too large, then information about thin oxide or other layers is lost and the uncertainty of the zero point rises. However, no matter how small the contact force can be made, there is always already a small elastic penetration of the indenter beneath the surface. For instance, the elastic deformation of a fused silica surface by a sharp indenter with 200-nm radius is 2.4 nm at 5 μN and 1.3 nm at 2 μN. The first data points after contact are used for the back extrapolation to zero force with an appropriate fit function. The standard ISO 14577 proposes a polynomial of second degree. However, one can usually assume that the first contact at such small forces is purely elastic and the hertzian equations for the contact of spheres can be used. A good fit function is therefore given by the equation

$$F = C(h - h_0)^{3/2} \tag{6.29}$$

with h_0 as zero point correction. Even if the deformation is already in the plastic range, the deviation from the $F \sim h^{3/2}$ relation is small when the displacement is smaller than 20% of the tip radius. Figure 6.16 shows the first data points of a 3-mN measurement of fused silica with the UMIS-2000. The contact force was 4.5 μN. The best fit of the data (black points) with the hertzian equation (full line) was obtained for a zero shift of 1.55 nm. This is close to the theoretical value of 1.50 nm for elastic deformation obtained for a tip radius of 700 nm.

Sometimes, also a shift to the left is required for the best fit (h_0 is negative). Such behavior is observed when the surface is detected too early due to the influence

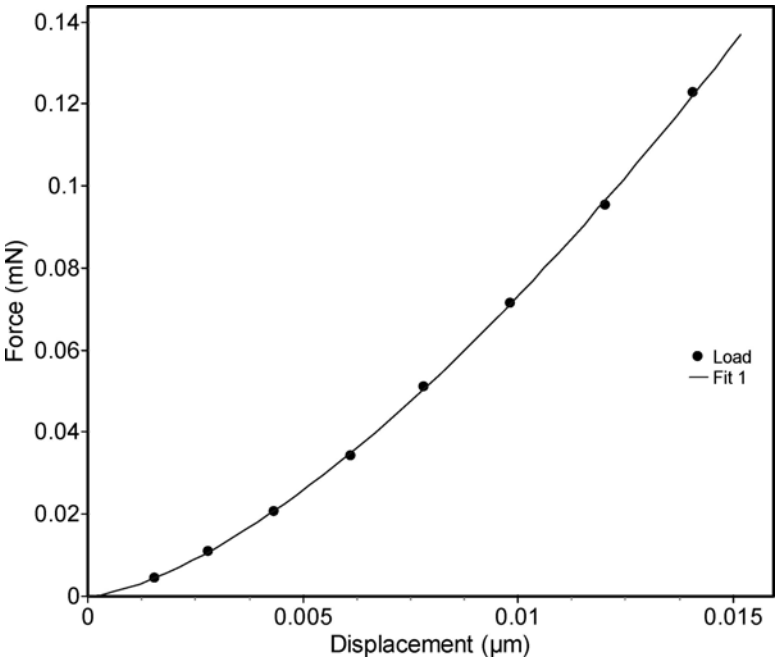

FIGURE 6.16. First data points (circles) of a fused silica measurement with 3 mN after zero point correction in comparison to the fit curve, obtained with Eq. (6.29).

of surface roughness and vibrations. The back-extrapolation method can therefore also, to a certain degree, reduce the disturbing influence of such factors. An example is given in Figs. 6.17 and 6.18 where 10 sapphire measurements at equal load were compared with and without zero point correction. The surface roughness of this sample was not as good as usual and the scatter of the curves could be markedly reduced by the back-extrapolation method of zero point correction.

6. SPECIFIC PROBLEMS WITH THE MEASUREMENT OF THIN HARD COATINGS

6.1. Consideration of Substrate Influence

Measurement of the mechanical properties of thin films is often not an easy task, especially if the film thickness is of the order of 1 μm or less. The situation becomes even more complicated if there is more than one layer, a multilayer system or a nanostructured coating. In the following, we assume that the indenter area function and instrument compliance are correctly determined and that the required corrections are applied.

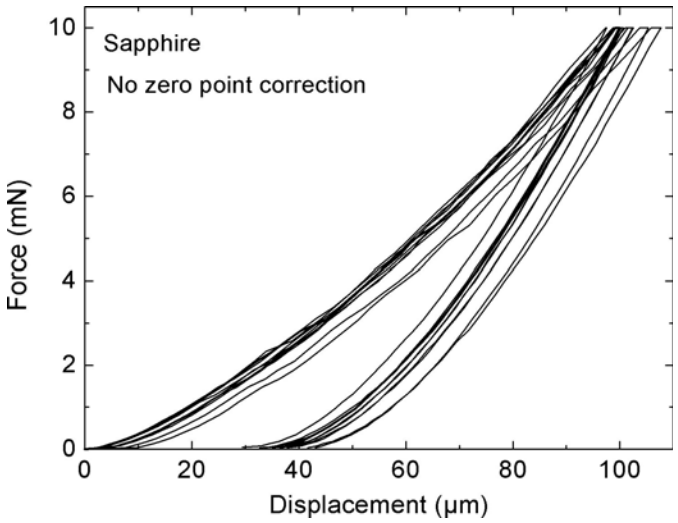

FIGURE 6.17. Comparison of 10 sapphire measurements without zero point correction.

It is often stated that the true hardness of coatings can be measured if the so-called 10% rule, or Bückle rule,[28,29] is kept. This rule requires the indentation depth to be less than 10% of the film thickness, otherwise the substrate influences the results. This rule is only a rule of thumb and is not derived from any physical laws;

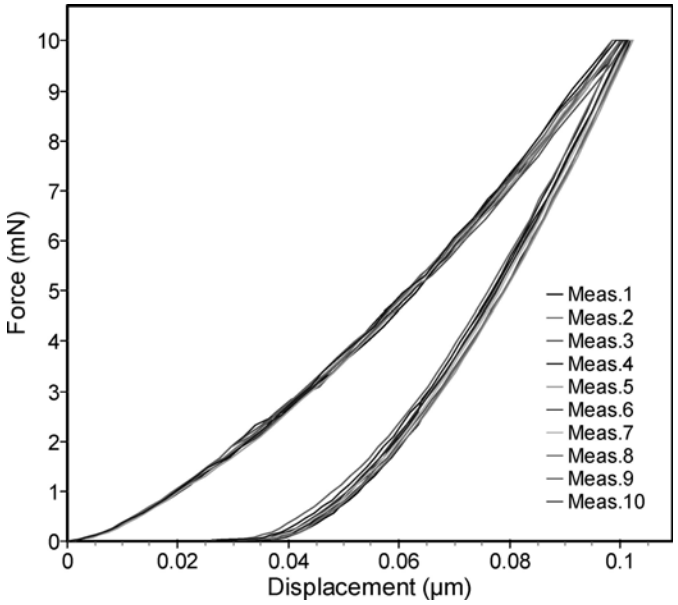

FIGURE 6.18. Comparison of 10 sapphire measurements after zero point correction.

however, the experience shows that it can be applied as upper limit to most of the film–substrate combinations with a hardness ratio lower than about 4:1. It should be used only if one has no possibility of proving the actual range of constant hardness in the films. If both the hardness and Young's modulus difference of coating and substrate are not too big, one will find that up to 20% is often allowable. The rule can generally be relaxed for the case of soft films on hard substrates.

It shall be pointed out here that even a very small depth to film thickness ratio is no guarantee for a correct film hardness measurement, because very shallow indentation depth results in another source of error (see below). Therefore, it is recommended to measure always at different loads and to check if there is a window in the depth range where a depth-independent film hardness can be observed.

The reason for the Bückle rule is that the plastic zone below the indenter (in plastically deforming materials) extends much deeper than the indentation depth (see for instance Weiler[19]) and that hard coatings may crack if the substrate undergoes plastic deformation.

Figure 6.19 shows the result of hardness measurements on a 477-nm-thin Si_3N_4 film on fused silica. The hardness increases at very small depth due to the transition from purely elastic to plastic deformation (the tip radius for these measurements was about 400 nm). It reaches a small plateau of 17.5 GPa and decreases for depths above about 70 nm due to the substrate influence. The substrate hardness is 9.3 GPa and approximately constant over depth. The depth to film thickness ratio for constant hardness here was 15% and therefore bigger than that given by the 10% rule. However, the general problem becomes clear. There is only a small depth range where the true film hardness can be measured if the film thickness is below about 500 nm and very small depths with blunt indenters may not initiate plastic flow.

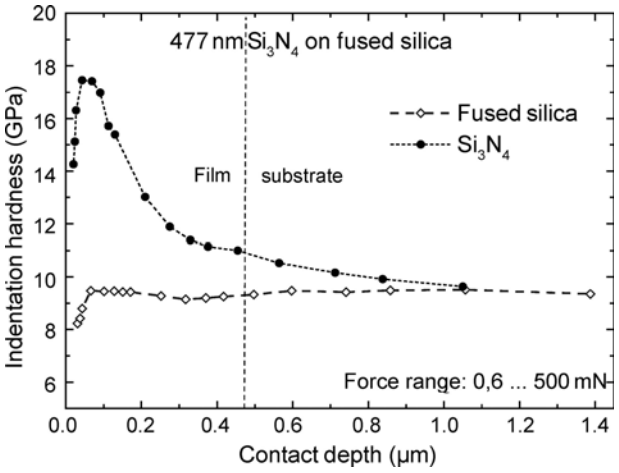

FIGURE 6.19. Indentation hardness versus contact depth for 477-nm Si_3N_4 on fused silica and an uncoated substrate. The interface position is indicated.

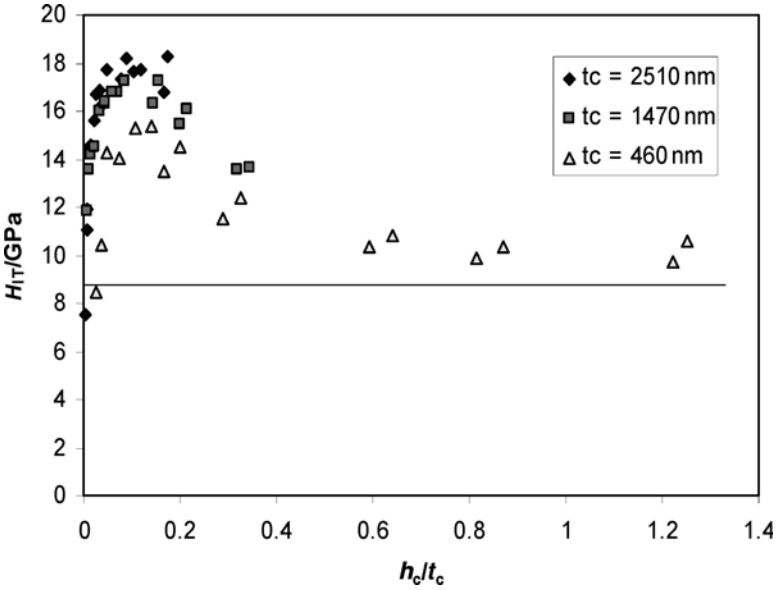

FIGURE 6.20. Indentation hardness versus normalized coating thickness DLC on steel; selected data showing the effect of substrate yield for the thinnest film. [Data are given from Berkovich and Vickers indenter geometries (from Ref. 1).]

Another example is given in Fig. 6.20. The results are taken form the INDICOAT project.[1] Three diamond-like carbon (DLC) films of different thickness but equal mechanical properties were measured with Berkovich and Vickers indenters. The indentation hardness is given as function of the contact depth, normalized by film thickness. The hardness of the thicker films agrees for depths between 5% and about 15% of the film thickness and decreases for larger depth. In contrast to that, the determined maximum hardness of the 460-nm-thin film is smaller. The only reason for this difference is that the true film hardness can no longer be measured at any depth due to the substrate influence and the radius of the tip being too large. The M2 steel substrate hardness is given in Fig. 6.20 as a straight line.

There are a lot of different models that are used for the calculation of the film hardness from the measured effective or composite hardness; however, none of them has been proven as generally applicable. They are valid only for special conditions like depth to film thickness ratio, failure mechanism (cracking or plastic deformation), hardness and/or modulus ratio, and so on. An overview of such models can be found in Refs. 30–32. Before a model is used for the calculation of the true film hardness it should be checked to ensure that it can be applied to the particular film–substrate combination to be tested. Otherwise a considerable error can arise.

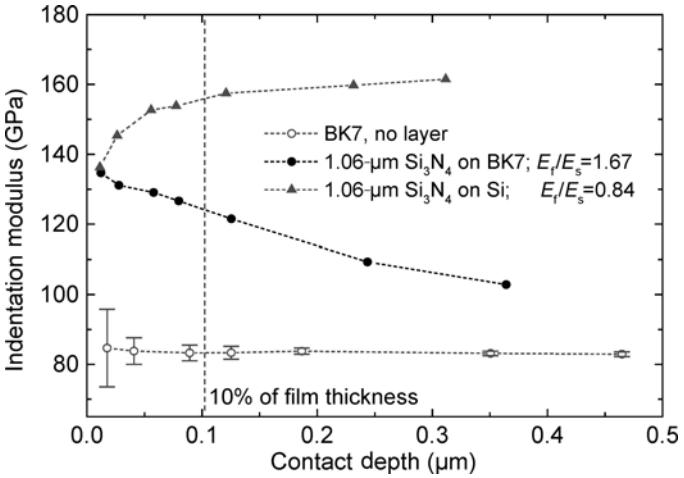

FIGURE 6.21. Depth-dependent effective modulus of 1.06-μm-thick Si_3N_4 coatings on BK7 glass and Si, measured with a Berkovich indenter.

A "10% rule" as in the case of indentation hardness *does not exist* for modulus measurements, because the extension of the elastic field is in principle infinite. This is demonstrated in Fig. 6.21. Si_3N_4 films 1060 nm thick were deposited with the same plasma-assisted chemical vapor deposition process both on silicon single crystal and on BK7 borosilicate glass substrates. For such conditions the film modulus should not depend on the substrate material. Details of the preparation process and the thickness measurement by means of spectroscopic ellipsometry can be found in Ref. 33. The modulus measurements were made with a Berkovich indenter and the UMIS-2000 instrument. Equal modulus for both samples could be observed only at very shallow contact depth of 12 nm. The maximum force corresponding to this measurement was 300 μN. Accurate measurements in this depth range require a very precise instrument and an excellent area function, which is difficult to obtain. The modulus result for Si_3N_4 was 137 GPa. The 10% film thickness depth is indicated in Fig. 6.21. The modulus change at this depth is already larger than 11% although the modulus ratio between film and substrate is relatively low (1.67 for BK7 and 0.84 for Si). For many film–substrate combinations the modulus ratio is larger than 2 and would give rise to a much steeper depth-dependent modulus change. The Young's modulus of BK7 glass is 82 GPa and was proven to be depth independent (see Fig. 6.21).

Another example is given in Fig. 6.22 for the same DLC coating on steel system as in Fig. 6.20.[2] Experimental results from spherical, Berkovich, and Vickers indenter geometries are compared with elastic–plastic finite element analysis (FEA) results. In contrast to Fig. 6.20 the reduced modulus is used as the ordinate. The modeled data are for a spherical indenter on DLC coatings with varying thickness and a reduced modulus of $E_r = 142.7$ GPa. The solid line is obtained

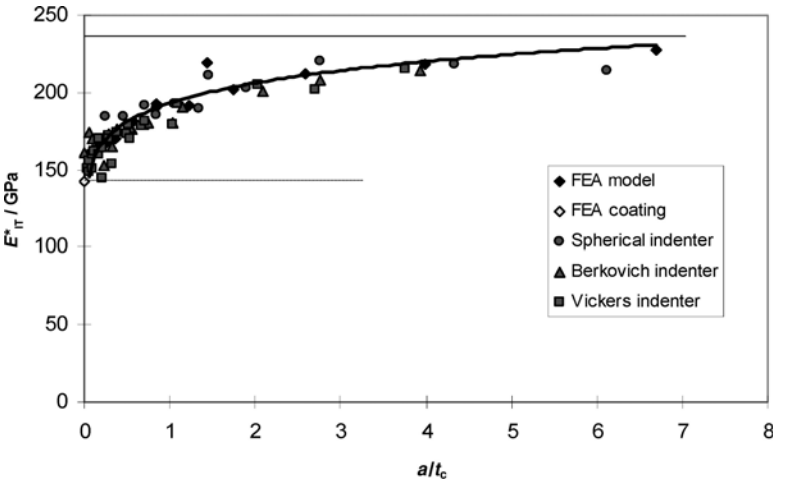

FIGURE 6.22. Indentation elastic plain strain modulus versus normalized coating thickness for DLC on steel; selected data plotted with values calculated from FEA simulation. The solid line is a nonlinear fit to the FEA data. (From Ref. 1.)

from a nonlinear fit to the FEA data. There is excellent agreement between the model and the experimental data, which confirms the nonlinear relation. However, the precise nature of the nonlinear relation cannot be derived from simple rules, since it depends on the combination of elastic constants in the system and their combined contributions as a function of relative coating thickness. The reduced moduli of steel substrate and film, which were used for modeling, are shown as straight lines. The results make it clear that the modulus change is the strongest in the low depth range and decreases with increasing depth. No limit can be given for the depth to film thickness ratio to derive the correct film modulus. The modulus error due to substrate influence is below 5% only when the contact depth is smaller than 2–3% of the film thickness and the modulus ratio between film and substrate is smaller than about 3. However, if the film is more than five times stiffer than the substrate, even 2% of the film thickness can be too much for an accurate modulus measurement. This can be shown for the case of a 1.8-μm-thick c-BN film on silicon. It was measured with a Berkovich indenter with a tip radius of 380 nm. The depth-dependent modulus results are given in Fig. 6.23. The Young's modulus is steadily increasing toward the surface with the largest measured value of 776 GPa at 3 mN. This is still below the true film modulus, which is between 800 and 850 GPa, although the contact depth was only 21 nm and the contact depth to film thickness ratio was 1%. The measurements on c-BN were purely elastic up to 5 mN and plastic effects could not influence the accuracy of the first two data points in Fig. 6.23.

There are three possibilities to derive the true film modulus from the measurement data. The easiest one is the extrapolation of the depth-dependent modulus

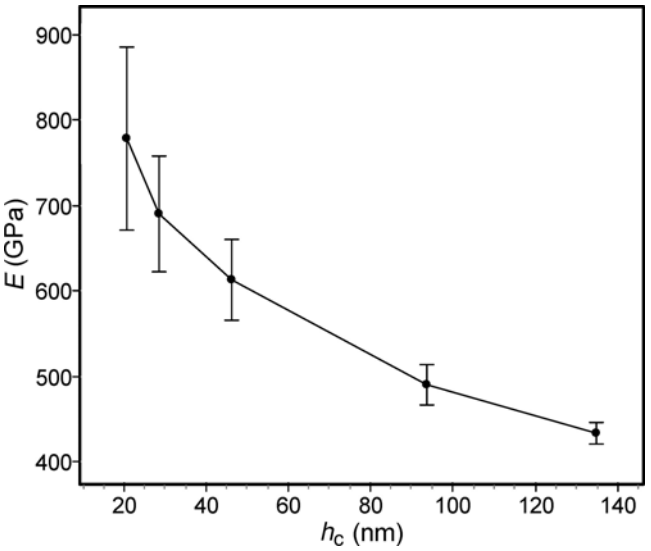

FIGURE 6.23. Modulus result as a function of contact depth for a 1800-nm-thick c-BN coating on silicon, measured with a Berkovich indenter with 380-nm tip radius. The true film modulus is 800–850 GPa.

data to zero depth. Data only from the smallest depth should be used with a linear fit. The second possibility is elastic measurements with an appropriate spherical indenter in combination with modeling of the elastic displacement (see Section 7). Finally, there is also the possibility to calculate the film modulus from the measured effective modulus and the known substrate modulus. Several authors have tried to derive formulas for the effective modulus or effective compliance of coated systems as a function of the elastic properties of both materials, and the ratio of contact radius or indentation depth to film thickness. Best known is the solution of King,[15] who used an integral equation technique to perform an elastic analysis of flat-ended punches of different shapes. Bhattacharya and Nix[34] compared King's results with their own FE results. King's calculations were seen to be in reasonable agreement with the FE results. However, for decreasing depth of indentation, it appears that the values predicted by King approach the modulus of the film too slowly. Gao *et al.*[35] adopted a perturbation method to construct a first-order-accurate solution for the contact compliance of a coated medium. Further, they have shown that interface cracks and debonding have a significant influence on the contact compliance in indentation experiments. Such effects reduce the reliability of Young's modulus determination in the presence of plastic deformation. Hence, wholly elastic measurements would be preferable. Menčik *et al.*[36] compared five different regression functions for the extraction of the film modulus from measurements with various indentation depths. They concluded that the Gao function[35] was the best of all and describes the indentation behavior of thin films reasonably

well. Sometimes, however, differences for the modulus results of the same coating material with various thicknesses on various substrates were larger despite the fits being relatively good. They recommended using the minimum possible load or indentation depth to obtain the best modulus results.

The method of choice should depend on the availability and accuracy of the data and on the possibility of carrying out purely elastic measurements.

6.2. Sink-In and Pileup Effects

"Pileup" is upward flow of material around the indentation that remains located above the original surface plane after unloading the indentation. The effect occurs mostly for work-hardened metallic materials and is often seen as causing convex (barrel-shaped) boundaries of the impression in plan view. The opposite sink-in effect results in concave (pincushion-shaped) boundaries and may occur with annealed metals or materials that densify. Both effects are intensified in coatings if the depth to film thickness ratio exceeds a certain limit. The disadvantage of the effects is that they cause an under- or overestimation of the contact area derived from the indentation depth. They violate the conditions for the analysis model given in Section 1. Bolshakov and Pharr[37] have shown for homogeneous materials that failure to account for pileup in the area determination can lead to a hardness overestimation of as much as 60%. At the moment, there is no method available (except for the direct measurement of the surface topography), which allows an area correction, unless the modulus of the material is known and is constant. For every film–substrate combination one should therefore try to analyze how much such effects could influence the results.

Figure 6.24 shows AFM images of 100-mN Berkovich indents in alumina films on nickel. A pronounced sink-in effect can be seen in the thicker 2-μm coating on the left. The depth here was 35% of the film thickness. The hard coating was pressed into the plastically deformed substrate but it is still intact. The right-hand image shows that the film breaks if the depth to film thickness ratio is greater. In this case there is no longer a sink-in observable as the line scan in the lower part of the image shows.

The pileup effect is shown in Fig. 6.25. A 1.1-μm thick aluminum film on BK7 glass was measured with 10 mN (left side) and 50 mN (right side) forces. The lower force results in a 0.4 μm deep impression with nearly no pileup. In contrast to this, the 0.9-μm-deep indent is accompanied by a 0.4-μm high wall in the middle of the side. This can be seen in the line scan along the line, indicated in the upper part of the image.

Hard nanostructured coatings in combination with softer substrates should show the sink-in effect only if the indentation depth is too big. The critical limit depends on the hardness ratio of both materials. Normally, a sink-in should not occur if the depth is below 10% of the film thickness. However, if the hardness ratio (film to substrate) is greater than about 10 this limit may no longer be sufficient for accurate measurements.

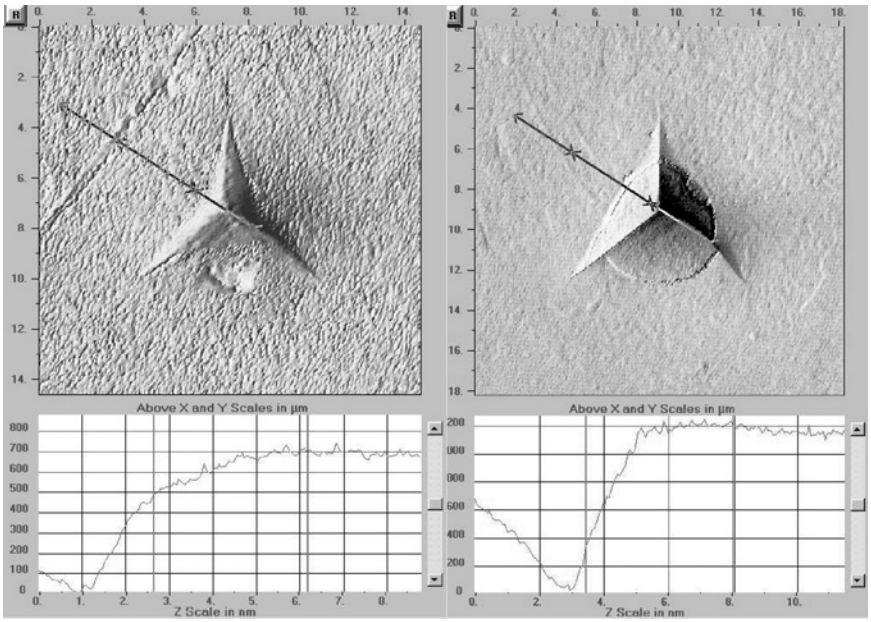

FIGURE 6.24. AFM images of Berkovich indents in alumina films on nickel. The left image shows a 0.7-µm-deep indent into a 2-µm coating and the right one a 1.2-µm-deep indent into a 0.7-µm coating. The maximum load was 100 mN in both cases.

7. LIMITS FOR COMPARABLE HARDNESS MEASUREMENTS

It was already mentioned in the last chapter that the hardness appears to decrease for very shallow indentation depths due to the tip rounding of the indenter. This can be observed most easily for hard materials because initially they behave purely elastically at very low loads, even if the tip is relatively sharp. In this case the calculated hardness value is just the contact pressure, which increases until plastic deformation starts. For fused silica for instance, the elastic–plastic transition is at 50 µN for a 200-nm radius tip and at 300 µN for a 500-nm radius. Plastic deformation starts at a depth of about half the contact radius below the indentation. This is 58 nm for fused silica and a 500-nm radius indenter. The plastic zone extends for higher loads until it eventually reaches the surface. For conical or pyramidal indenters with a spherical cap, it finally reaches a state where the shape no longer depends on force and indentation depth. The dimension of the plastic zone scales with the depth. It is growing but the width to depth ratio and the general form is kept constant. This is the condition of self-similarity, which is necessary for the measurement of a constant hardness for homogeneous materials.

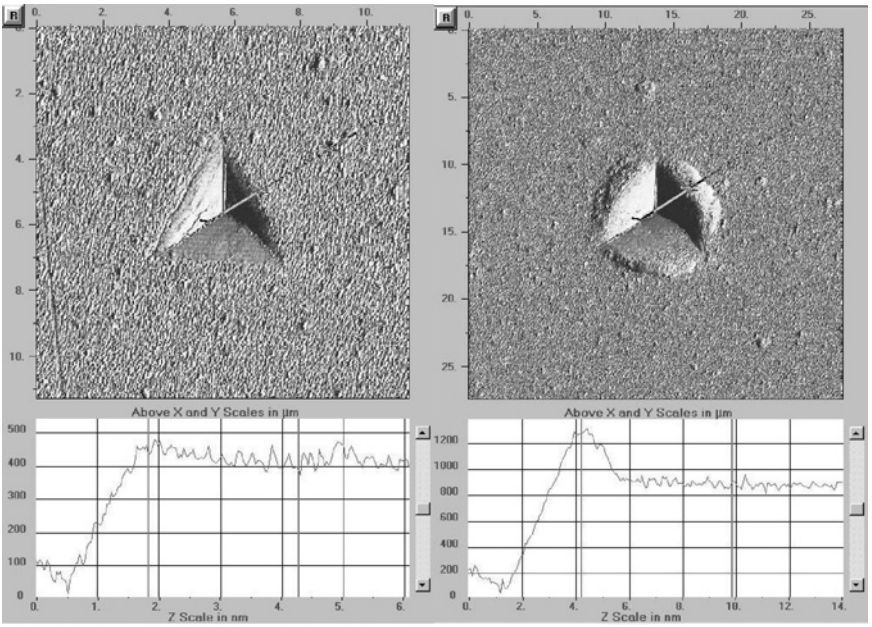

FIGURE 6.25. AFM images of Berkovich indents in aluminum films on BK7 glass. The left indent was made at 10 mN and the other at 50 mN. The lower part shows line scans along the lines, given in the upper images.

The question is now what is the minimum depth (in relation to the tip radius) where constant hardness can be expected. There are two limits that can be defined. Both are shown in Fig. 6.26 for a cone with a spherical cap.

The first limit (limit 1) is given by the point at which the spherical cap has the same slope as the ideal cone (19.7° is equivalent to a Vickers pyramid) and results in a smooth transition between both bodies. The corresponding depth is given in

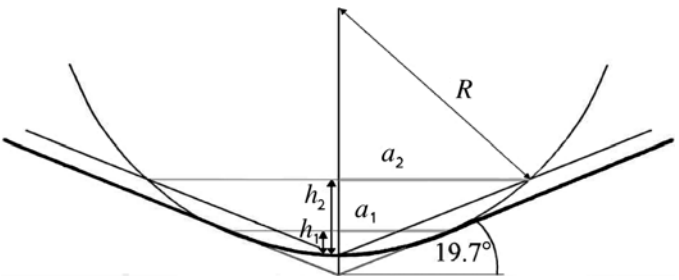

FIGURE 6.26. Representation of the two possible depth limits for comparable hardness measurements for a conical indenter with spherical cap. The local or the effective slope corresponds to that of an ideal cone with the same depth to area ratio as a Vickers indenter.

TABLE 6.3. Limits for Comparable Hardness Measurements

	Contact depth limit (nm)		Film thickness limit (nm)	
Tip radius(μm)	Limit 1	Limit 2	Limit 1	Limit 2
0,1	6	12	60	120
0,2	12	24	120	240
0,3	18	36	180	360
0,5	29	60	290	600
1,0	59	121	590	1210

Fig. 6.26 by h_1 and the segment radius by a_1. The other limit (limit 2) is at the point where a straight line, drawn from the outermost tip to the sphere surface, has the same angle as the side of the cone. This is depicted by a_2 and h_2 in Fig. 6.26. The depth to radius ratio of the first limit is $h_1/R = 1 - \cos(19.7^\circ) = 0.0585$ and that of the other is $h_2/R = 0.121$. Experience shows that the observable depth limit for constant hardness measurements is closer to limit 2 by about 10% of the radius and therefore closer to the larger number in the table. This corresponds to experiences with the comparison between Vickers and Brinell hardness. The minimum contact depth for comparable hardness measurements and the minimum film thickness that can be measured according to Bückles 10% rule are summarized for typical tip radii in Table 6.3. To get comparable hardness results the realized contact depth has to lie in between the contact depth limits of Table 6.3 or has to be larger. The thickness limits in Table 6.3 are the minimum film thicknesses where a substrate-independent film hardness can be measured if just a contact depth of limits 1 or 2 is realized. One will get inaccurate results due to the tip rounding if the depth is smaller, and one will also get inaccurate results due to the substrate influence if the depth is bigger. The contact depth range for comparable hardness measurements increases with increasing film thickness. The validity of the 10% rule has also to be considered (see discussion in Section 5.1).

It must be emphasized here again that exceeding the limits of Table 6.3 is no guarantee of a depth-independent hardness, because this also depends on the material itself.

The other limiting factor for comparable hardness measurements is the ratio between film and substrate hardness for coatings with a thickness smaller than the tip radius. To understand this we have to look at the von Mises comparison stress along the depth axis. The von Mises stress is defined by the equation

$$\sigma_{\mathrm{M}} = \sqrt{\frac{1}{2}\left((\sigma_{xx} - \sigma_{yy})^2 + (\sigma_{zz} - \sigma_{yy})^2 + (\sigma_{xx} - \sigma_{zz})^2 + 6\left(\tau_{xy}^2 + \tau_{xz}^2 + \tau_{zy}^2\right)\right)} \tag{6.30}$$

with σ_{ii} as normal stresses parallel to the Cartesian coordinate axis and τ_{ij} as the corresponding shear stresses. By means of the von Mises stress, a complicated multiaxial stress state can be related to the yield strength of a material. Yield starts

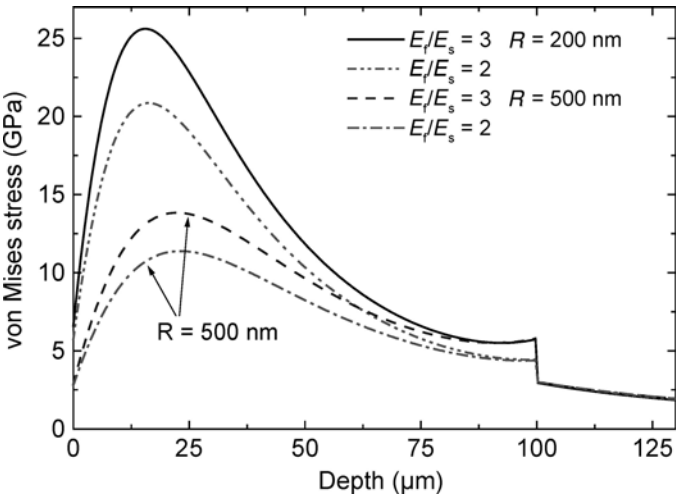

FIGURE 6.27. von Mises stress along the depth axis for different tip radii and film to substrate modulus ratio. The calculation was done for forces such that the maximum stress in the substrate is 3 GPa.

at the position of the maximum von Mises stress. An example is given in Fig. 6.27. Here, the case of 100-nm-thin coatings deposited on a hard steel substrate with a yield strength under compression of 3 GPa is considered. A Poisson's ratio of 0.3 is used for film and substrate. The Young's modulus of the steel is 200 GPa and the coatings have a two or three times higher modulus. A purely elastic calculation was performed for contacts with spherical tips of 200 nm (sharp Berkovich indenter) and 500 nm (blunt Berkovich indenter). The contact force was chosen so that the von Mises stress of the substrate just reaches the yield strength. Plastic deformation in the coating can be produced only if the yield strength of the film material is smaller than the calculated maximum of the von Mises stress. Otherwise, the plastic deformation starts in the substrate at the interface. This gives rise to high bending forces in the film, and cracks through the coating occur. The broken parts of the film will then be pressed into the substrate and increase the effective area of the indenter. A comparable hardness measurement of the coating is impossible under such circumstances. The critical stress limits for the 200-nm indenter were calculated to be 22.6 GPa for a modulus ratio of 3 and 18.1 GPa for a modulus ratio of 2. The critical limits for the 500-nm indenter are only 12.1 GPa for a modulus ratio of 3 and 9.9 GPa for a modulus ratio of 2. The yield strength of TiN with $E = 400$ GPa, for instance, is about 12 GPa and it will be impossible to measure the hardness of a 100-nm TiN film with a 500-nm radius indenter. The situation gets worse if the yield strength of the substrate is even smaller. A hard thin coating on a soft substrate like magnesium is therefore very difficult to measure. This

requires very sharp tips and thick-enough coatings. Hardness results for coatings below 500-nm thickness should therefore be critically examined, and it should be questioned whether the measurement conditions really allow a measurement of coating hardness. Beside that, the forces for the onset of yield in the substrate were very small in the given example of TiN on steel. The maximum force was between 50 and 64 μN. Hardness measurements of coatings below 200–300-nm thickness therefore require an instrument with resolution and noise floor in the μN range and very sharp tips.

8. YOUNG'S MODULUS MEASUREMENTS WITH SPHERICAL INDENTERS

Hard smooth coatings are ideally suited for measurements with spherical indenters in the purely elastic deformation regime. Depending on the indenter radius, the maximum force for purely elastic deformation is in the range of several mN, which can be easily resolved with modern instruments.

Nanoindentation experiments with spherical indenters were pioneered by Field and Swain.[38,39] They developed a method using multiple partial unloading experiments which allows the calculation of a depth-dependent modulus or contact pressure. However, this method is suited only for thicker coatings because it does not allow to exclude the substrate influence.

The situation can be improved by applying purely elastic measurements with spherical indenters. This was used in a new method, developed by Chudoba *et al.*[25] and Schwarzer *et al.*[40] It combines, for the first time, high accuracy indentation measurements with an analytical calculation of the elastic load–displacement curves for coated systems. The model of Schwarzer allows a quick calculation of the complete stress or deformation field for hertzian contact on a coated half-space. The theoretical load–displacement curve is fitted to the measurement data and the Young's modulus of thin coatings can be extracted with high precision. The substrate properties are considered in the calculation and therefore there is no limit for the indentation depth in relation to film thickness, which could prevent an accurate determination of the film modulus.

The required condition for elastic measurements is a sufficiently smooth surface, at least over a surface area with the dimension of the final indentation. A general roughness limit cannot be given but a mean roughness below 10 nm is desirable. Furthermore, accurate corrections of thermal drift, zero point, and instrument compliance are required as described in the preceding sections. In contrast to elastoplastic deformations, only one hold period at maximum force is required for the detection of the thermal drift, since there are no creep effects. More information can be found in Ref. 25. Under such conditions it is possible to reach

a displacement separation (between the loading and unloading segments) of less than 1 nm and both curves cannot be distinguished by eye in a graph.

In the following example, the 1.06-µm Si_3N_4 coating on BK7 glass (Fig. 6.21) is measured with a spherical indenter of about 50-µm radius. First, the modulus of the substrate has to be determined. This can also be done by elastic measurements if the substrate is hard and smooth enough. If the modulus and Poisson's ratio of the substrate are well known from the supplier or the literature, the substrate can be used for the calibration of the indenter radius. An effective radius can be calculated with Eq. (6.5) for every point of the force–displacement curve when depth h, force F, and reduced modulus E_r are known. The indenter radius is normally not depth independent due to unavoidable deviations from the ideal spherical shape. The determination and use of a radius function instead of using a constant radius value can therefore improve the accuracy of the modulus calculation. The word "effective" is used because the real shape is described by the radius of an ideal sphere which produces the same indentation depth at equal load.

Figure 6.28 compares the elastic measurements of the pure substrate and the coated sample to the modeled load–displacement curves. The modulus was calculated by a least squares fit between measurement data and theoretical load–displacement curve. This is done in an iterative procedure by varying the film modulus (or the bulk modulus for the substrate only). Although only one parameter is varied, the agreement between both curves is excellent over the whole depth range. The mean difference is less than 0.5 nm. This indicates that

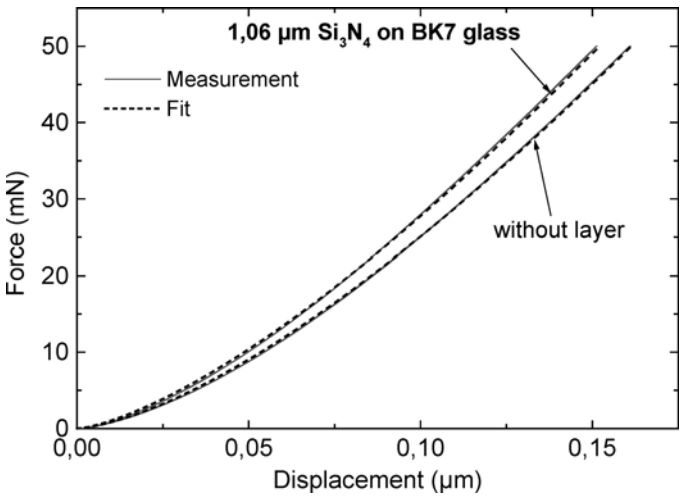

FIGURE 6.28. Comparison of measured and calculated force–displacement curves for a BK7 glass substrate and a 1.06-µm-thick Si_3N_4 coating on BK7. The difference is less than 1 nm.

the theoretical model used for the calculation is well suited for describing the contact conditions. The result for Si_3N_4 was a modulus of 137 GPa, exactly the value at which both curves in Fig. 6.21 meet each other and represent the film properties.

The mathematical model behind the calculation is quite complicated and described in more detail in Ref. 41. It uses recent results of potential theory[42,43] and a new theoretical method of image loads that gives a complete analytical three-dimensional solution for stress and strain fields caused by a hertzian pressure distribution on a substrate with several layers. This method is similar to the known method of image charges in electrostatics. Results are calculated completely in an analytical form; therefore, the calculation is much faster than FE treatments and small details of the elastic fields are usually better resolved. A software package ELASTICA (ASMEC GmbH, Germany) has been developed, which allows easy utilization of the results. Beside other things, the load–displacement curve can be calculated and fitted to experimental data to derive the Young's modulus of thin films independent of the substrate influence. This is a big advantage in relation to the conventional method because the indentation depth can be much bigger than 2–3% of the film thickness. In Ref. 44 a comparison with a surface acoustic wave method showed that the modulus of DLC coatings on silicon could be correctly measured with spherical indenters down to 4.3-nm-thick films. This was achieved with a 3-μm radius indenter and a maximum force of 7 mN. About 20 single measurements were carried out at different positions and averaged. The load–displacement curve of a 25-nm-thin DLC film is shown in Fig. 6.29. Differences

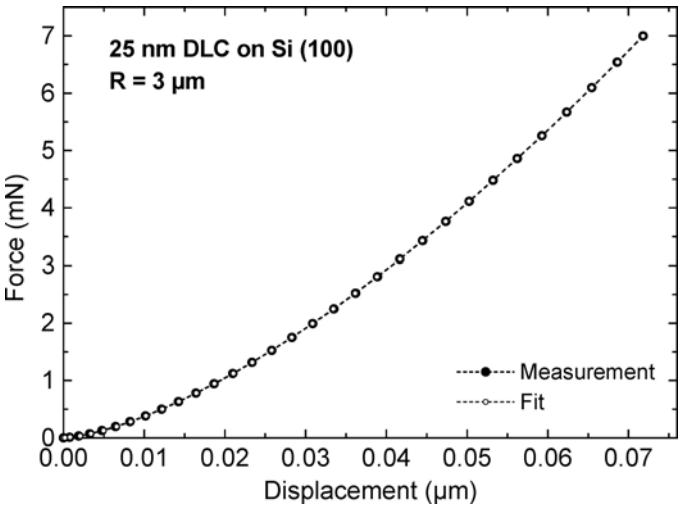

FIGURE 6.29. Comparison of measured and calculated elastic force–displacement curves for a 25-nm DLC coating on Si. Differences are smaller than 0.2 nm and cannot be resolved (see Ref. 44).

between measurement data and the fitted curve were only 0.2 nm at the most. The modulus result calculated for the DLC coating was 359 ± 28 GPa.

The optimum radius for elastic measurements has to be chosen to match the film thickness and material combination. The surface sensitivity is improved when a smaller radius is chosen. However this results in a smaller maximum load to stay in the elastic regime. This may result in unacceptably small forces for softer materials. A large radius enables the measurement of softer materials but it touches a larger area, and surface roughness has a greater influence. Our experience shows that the method cannot be applied with high accuracy to soft metals. For hard nanostructured coatings, however, it is an attractive alternative for the determination of the film modulus.

ACKNOWLEDGMENTS

The author would like to thank Frank Richter from the Technical University of Chemnitz, Germany, and Nigel Jennett from the National Physical Laboratory, United Kingdom, for fruitful discussions and helpful comments.

REFERENCES

1. ISO Central Secretariat, Metallic Materials—*Instrumented Indentation Test for Hardness and Materials Parameters*, ISO 14577 (ISO Central Secretariat, Geneva, Switzerland, 2002).
2. Determination of Hardness and Modulus of Thin Films and Coatings by Nanoindentation (INDICOAT), European project, Contract No. SMT4-CT98-2249, NPL Report MATC(A) 24, May 2001.
3. K. Herrmann, N. M. Jennett, S. R. J. Saunders, J. Meneve, and F. Pohlenz, Development of a standard on hardness and Young's modulus testing of thin coatings by nanoindentation, in *Proceedings of 2nd European Symposium on Nanomechanical Testing*, Hückelhofen, 25–27 September, 2001, Z. Met.kd. **93**(9), 879–885 (2002).
4. H. O'Neill, Hardness Measurement of Metals and Alloys (Chapman and Hall, London, 1967), p. 2.
5. F. Mohs, Grundriß der Mineralogie (Dresden, 1822).
6. J. B. Pethica, Microhardness test with penetration depth less than ion implanted layer thickness in ion implantation into metals, in Third International Conference on Modification of Surface Properties of Metals by Ion-Implantation, Manchester, England, 1981, June 23–26, edited by V. Ashworth, W. A. Grunt, und R. P. M. Procter (Pergamon Press, Oxford, 1982), pp. 147–157.
7. Universal Hardness Testing, DIN 50359 (DIN Deutsches Institut für Normung e.V., Berlin, 1997).
8. M. F. Doerner and W. D. Nix, A method for interpreting the data from depth sensing indentation instruments, J. Mater. Res. **1**, 601–609 (1986).
9. W. C. Oliver and G. M. Pharr, An improved technique for determining hardness and elastic modulus using load and displacement sensing indentation experiments, J. Mater. Res. **7**, 1564–1583 (1992).
10. I. N. Sneddon, Boussinesq's problem for a rigid cone, Proc. Camb. Phil. Soc. **44**, 492–507 (1948).
11. L. D. Landau and F. M. Lifschitz, Lehrbuch der Theoretischen Physik. Bd. 7:Elastizitätstheorie, (Verlag Harri Deutsch, Frankfurt am Main, 1991).
12. A. K. Bhattacharya and W. D. Nix, Finite element analysis of cone indentation, Int. J. Solids Struct. **27**, 1047–1058 (1991).

13. G. M. Pharr, W. C. Oliver, and F. R. Brotzen, On the generality of the relationship between contact stiffness, contact area, and elastic modulus during indentation, J. Mater. Res. **7**, 613–618 (1992).
14. H. Gao and T.-W. Wu, A note on the elastic contact stiffness of a layered medium, J. Mater. Res. **8**, 3229–3233 (1993).
15. R. B. King, Elastic analysis of some punch problems for a layered medium, Int. J. Solids Struct. **23**(12), 1657–1664 (1987).
16. G. G. Bilodeau, Regular pyramid punch problem, J. Appl. Mech. **59**, 519–523 (1992).
17. A. E. Giannakopoulos, P.-L. Larsson, and R. Vestergaard, Analysis of Vickers indentation, Int. J. Solids Struct. **31**, 2679–2708 (1994).
18. M. T. Hendrix, The use of shape correction factors for elastic indentation measurements, J. Mater. Res. **10**, 255–258 (1995).
19. W. Weiler, Zur definition einer neuen Härteskala bei der Ermittlung des Härtewertes unter Prüflast, Materialprüfung **28**, 217–220 (1986).
20. K. L. Johnson, Contact Mechanics (Cambridge University Press, Cambridge, 1985).
21. A. C. Fischer-Cripps, Introduction to contact mechanics, in Mechanical Engineering Series (Springer, Berlin, 2000).
22. T. Chudoba and K. Herrmann, Verfahren zur Ermittlung der realen Spitzenform von Vickers- und Berkovich-Eindringkörpern, HTM Härterei-Tech. Mitt. **56**, 258–264 (2001).
23. J. Meneve, J. F. Smith, N. M. Jennett, and S. R. J. Saunders, Surface mechanical property testing by depth sensing indentation, Appl. Surf. Sci. **100–101**, 64–68 (1996).
24. W. C. Oliver and G. M. Pharr, Measurement of hardness and elastic modulus by instrumented indentation: Advances in understanding and refinements to methodology, J. Mater. Res. **19**, 3–20 (2004).
25. T. Chudoba, N. Schwarzer, and F. Richter, Determination of elastic properties of thin films by indentation measurements with a spherical indenter, Surf. Coat. Technol. **127**, 9–17 (2000).
26. Certified Reference Materials for Depth Sensing Indentation Instrumentation (DESIRED), European Project, Contract no. G6RD-CT2000-00418, funded by the European Community under the "Competitive and Sustainable Growth" Program, finished March 2004.
27. K. Herrmann, N. M. Jennett, W. Wegener, J. Meneve, K. Hasche, and R. Seemann, Progress in determination of the area function of indenters used for nanoindentation, Thin Solid Films **377–378**, 394–400 (2000).
28. H. Bückle, Mikrohärteprüfung und Ihre Anwendung (Berliner Union Verlag, Stuttgart, 1965).
29. P. J. Burnett and D. S. Rickerby, Assessment of coating hardness, Surf. Eng. **3**(1), 69–75 (1987).
30. M. Wittling, A. Bendavid, P. J. Martin, and M. V. Swain, Influence of thickness and substrate on the hardness and deformation of TiN films, Thin Solid Films **270**, 283–288 (1995).
31. D. Chirac and J. Lesage, Absolute hardness of films and coatings, Thin Solid Films **254**, 123–130 (1995).
32. N. G. Chechenin, J. Bøttiger, and J. P. Krog, Nanoindentation of amorphous aluminum oxide films, I: The influence of the substrate on the plastic properties, Thin Solid Films **261**, 219–227 (1995).
33. T. Chudoba, N. Schwarzer, F. Richter, and U. Beck, Determination of mechanical film properties of a bilayer system due to elastic indentation measurements with a spherical indenter, Thin Solid Films **377–378**, 366–372 (2000).
34. A. K. Bhattacharya and W. D. Nix, Analysis of elastic and plastic deformation associated with indentation testing of thin film substrates, Int. J. Solids Struct. **24**, 1287–1298 (1988).
35. H. Gao, C.-H. Chiu, and J. Lee, Elastic contact versus indentation modeling of multi-layered materials, Int. J. Solids Struct. **29**, 2471–2492 (1992).
36. J. Menčik, D. Munz, E. Quandt, and E. R. Weppelmann, Determination of elastic modulus of thin layers using nanoindentation, J. Mater. Res. **12**, 2475–2484 (1997).
37. A. Bolshakov and G. Pharr, Influences on pileup on the measurement of mechanical properties by load and depth sensing indentation techniques, J. Mater. Res. **13**, 1049–1058 (1998).
38. T. J. Bell, J. S. Field, and M. V. Swain, Stress–strain behavior of thin films using a spherical tipped indenter, Mater. Res. Soc. Symp. Proc. **239**, 331–336 (1992).

39. J. S. Field and M. V. Swain, A simple predictive model for spherical indentation, J. Mater. Res. **8**(2), 297–307 (1993).
40. N. Schwarzer, F. Richter, and G. Hecht, The elastic field in a coated half-space under Hertzian pressure distribution, Surf. Coat. Technol. **114**, 292–304 (1999).
41. N. Schwarzer, Arbitrary load distribution on a layered half space, ASME J. Tribol. **122**, 672–681 (2000).
42. V. I. Fabrikant, Application of Potential Theory in Mechanics: A Selection of New Results (Kluwer Academic, Dordrecht, The Netherlands, 1989).
43. V. I. Fabrikant, Mixed Boundary Value Problems of Potential Theory and Their Applications in Engineering (Kluwer Academic, Dordrecht, The Netherlands, 1991).
44. T. Chudoba, M. Griepentrog, A. Dück, D. Schneider, and F. Richter, Young's modulus measurements on ultra-thin coatings, J. Mater. Res. **19**, 301–314 (2004).

7

The Influence of the Addition of a Third Element on the Structure and Mechanical Properties of Transition-Metal-Based Nanostructured Hard Films: Part I—Nitrides

Albano Cavaleiro, Bruno Trindade, and Maria Teresa Vieira

ICEMS, Mechanical Engineering Department, Faculty of Sciences and Technology, University of Coimbra, Coimbra, Portugal

1. INTRODUCTION

Transition metal (T_M) carbides and nitrides have been the most studied and investigated compounds since the beginning of the use of hard coatings to improve the performance of mechanical components. Since the pioneering study on the deposition and characterization of TiC and TiN, many different approaches have been followed in order to make these coatings perform better and better. In fact, the enthusiasm among researchers grew quite rapidly because the final results reached with coated components were so much better than with uncoated bulk materials. As a result, the application of hard coatings as a universal panacea for all the wear problems occurring in the mechanical industry was immediately installed. Nonetheless, it is obvious that whenever new situations were envisaged for the application of a hard coating, there were new demands that could not be satisfied with the existing Ti-based compounds.

In most of the studies performed to develop "new" hard coatings, the supporting ideas were naturally based on the acquired knowledge of researchers

on materials science and engineering. First, the study of other T_M carbides or nitrides deposition arose due to some of their specific advantages over TiC or TiN, such as higher oxidation resistance at high temperatures, higher fracture toughness, or better mechanical behavior at high temperatures. Second, the alloying of existing T_M nitrides or carbides with other elements is a common procedure used for the improvement in a particular property of a material, and a good example is the development of the steel through the course of time.

The original scope of the alloying of existing carbide and nitride thin films was based on the principle that supports the idea behind the existence of composite materials, i.e., the association of two dissimilar materials in order to build a "new" material that brings together the best properties of each individual material, thus avoiding their drawbacks. This was used with the Ti(C,N) system right from the very beginning. TiC was known as a very hard material but also very brittle, whereas, TiN, which was known to be softer, had superior fracture toughness and an improved adhesion to steel substrates. The motivation was the same for the first alloying studies on Ti nitride with Al and/or Zr.[1–12] TiN had a very low oxidation resistance, a drawback that made it less suitable for applications where the service temperature could reach several hundreds of degrees Celsius, as it is the case in the tip of cutting tools working at very high cutting speed. Both Al and Zr could increase the temperature for initiating oxidation of the coatings by more than 200°C, in comparison to TiN.

Nevertheless, researchers soon realized that the alloying procedure also had a beneficial effect on the coating's mechanical properties, with significant improvements in hardness, maintaining high values of fracture toughness and coating adhesion. Several explanations were given based on well-known hardening mechanisms such as those based on lattice distortion (solid solution, precipitation), decrease in grain size (grain boundaries), or electronic structure (valence electron concentration).

Since the beginning of the 1980s, when the first studies of coating modification with alloying were performed, thousands of papers were published on different systems and/or different deposition techniques used for film formation. The purpose of this chapter is not to conduct a complete and extended review of all these studies. This chapter will concentrate solely on the cases where the third element influenced the main phase of the binary system. The cases where nanocomposite structures were formed as a result of the alloying process will be dealt with separately in other chapters of this book. This chapter will review, for a large range of carbides and nitrides, the influence of the addition of a third element on the properties of the original materials deposited in the form of thin coatings. Many of the relationships presented, and more specifically the case concerning W-based systems deposited by sputtering technique, will be analyzed later, in more detail. There will be two parts to this contribution: the first one on T_M nitrides and the second one on T_M carbides.

2. THE ADDITION OF ALUMINUM TO T_M NITRIDES

The first system presented is the T_M-Al-N, and more specifically the Ti-Al-N case, because of its importance in the industry where it is extensively used. Figure 7.1a,b presents the hardness of Ti-Al-N and Cr-Al-N films, respectively, expressed as a

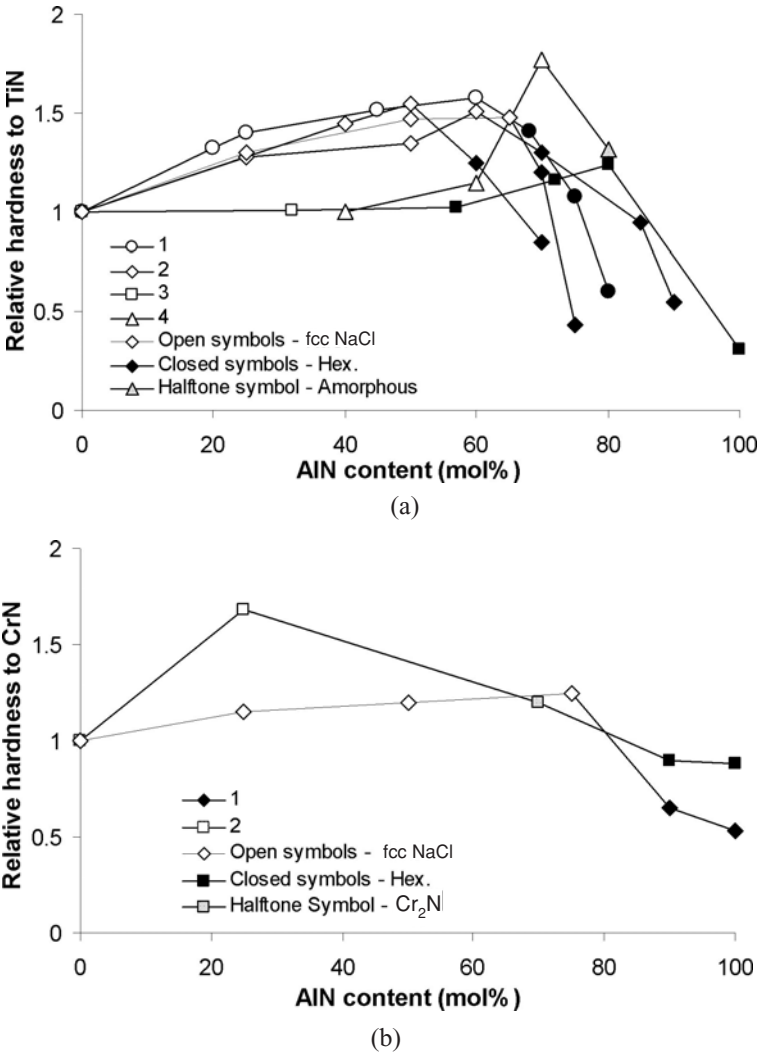

FIGURE 7.1. Hardness of T_M-Al-N films in relation to T_M nitrides as a function of the AlN content: (a) T_M = Ti (1 – Ref. 13; 2 – Ref. 14; 3 – Ref. 15; 4 –Ref. 16). (b) T_M = Cr. (1 – Ref. 14, 2 – Ref. 17)

function of the Al content.[13–17] Similar trends were found in most cases, i.e., the hardness increased up to a threshold value of the AlN molecular content and decreased thereafter. The decrease in the hardness coincided with the change in the phase composition of the coatings, forming the hexagonal wurtzite AlN to the detriment of the fcc NaCl-type phase characteristic of TiN. Makino and Miyake[14] concentrated their studies on the analysis of T_M-Al-N films deposited with different techniques. The specific deposition conditions used in the different techniques allowed for the achievement of cubic/hexagonal transformation at different Al contents. According to the authors' plotted results, the inflection on hardness did not depend on the AlN content, but the decrease always coincided with the rock salt cubic/wurtzite phase transformation.

A progressive decrease in the lattice parameter with the increase in the Al content was observed in the T_M-Al-N systems, suggesting the formation of a solid solution where the smaller Al atoms substitute the T_M positions (Fig. 7.2a,b).[15,17–25] However, as can be observed in the figure, the trend in the lattice parameter values, found by different authors, can diverge, showing a nonlinear behavior in some cases. To distinguish and exemplify these trends, two sets of points (the data points related to Refs. 19 and 21) in Fig. 7.2 are connected by straight lines, full and hatched, respectively. In the first case, a linear trend up to 70% AlN was observed, which suggested that only the fcc phase was being formed, with all the Al atoms replacing Ti in the TiN phase. In the second case, there was a clear change in the trend for AlN contents of ∼20%. This result demonstrates that the formation of the wurtzite phase could also occur during the film's deposition before the marked threshold value of AlN contents of ∼70% is reached. By using a partial structure map and the concept of two band parameters, Makino[26] predicted the maximum solubility of B4-type nitrides into B1-type T_M nitrides and found a value of 65.3% solubility for AlN into TiN. However, other experiments have also shown that this threshold depended on the deposition technique and the conditions used for the film formation.[14]

Matsui *et al.*[24] did not find variation in the lattice parameters of T_M-Al-N films deposited by reactive sputtering, for AlN contents of 20 and 40% (see Fig. 7.2). Taking into account the general trend shown in the figure for all the other results, these values were much higher than those expected. The authors justified this result by stating that there was insufficient mixing and substitution of the cations. The predicted values from the trend in Fig. 7.2 could be reached only after an annealing of the films at 700°C. These results were in accordance with the established description of the metastable $(Ti_{1-x}Al_x)N$ system where two solid solutions should be expected, one with the fcc phase of TiN for the low Al contents and the other with the AlN wurtzite-type phase for the highest Al contents. An immiscibility gap can exist between them, with the extension depending on the deposition conditions.[19,24,27,28]

Hirai *et al.*[17] performed a detailed characterization of T_M-Al-N coatings, including the measuring of residual stresses and grain sizes. They could not justify the hardness variations with the changes in these characteristics. In fact, there was

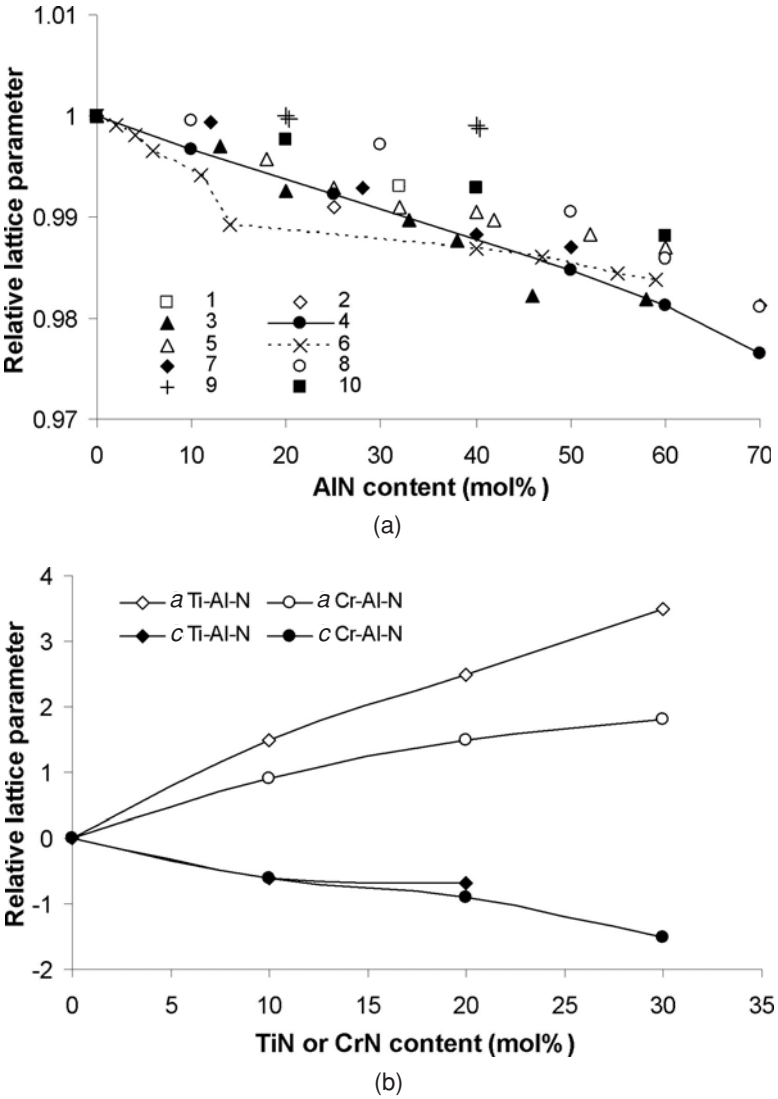

FIGURE 7.2. Lattice parameter of T_M-Al-N films in relation to (a) T_MN (fcc NaCl-type phase) as a function of the AlN content (1 – Ref. 15; 2 – Ref. 17; 3 – Ref. 18; 4 — Ref. 19; 5 — Ref. 20; 6 — Ref. 21; 7 — Ref. 22; 8 — Ref. 23; 9 — Ref. 24; 10 — Ref. 25) and (b) AlN (hexagonal phase) as a function of the T_MN content.[17]

no particular trend in the stress values as a function of the Al content and the stresses were quite low (the highest value was 0.5 GPa compressive stress) and insufficient to explain the hardness variation. With regards to the grain size they also found larger grains in the film doped with Al in comparison to single Cr-N

film (300 nm against 150 nm), results that contradict the well-known Hall–Petch relationship. According to this relationship, the lower the grain size, the higher the mechanical strength of a material should be. They attributed the hardening to the strain induced by the solid solution, similarly to what is common in metallic materials,[29] and they supported this conclusion with results in literature where similar hardening was detected in ceramic-based materials.[30,31]

Besides the influence of the lattice strain, Zhou *et al.*[32] suggested that the increase in the hardness could be due to an increase of the covalent energy of the bonding, since the decrease in the interatomic distance was related to the covalent band gap in an inversely proportional way.[33] The higher energy of the covalent bonding led to stronger interatomic forces and the improvement in film hardness.

When the situation is analyzed from the AlN perspective, it is also possible to state the hardening effect by solid solution. Figure 7.2b shows the evolution of *a* and *c* lattice parameters of the hexagonal AlN phase as a function of the TiN content. As can be observed, there was an expansion of *a* and a shrinkage of *c* parameters with the increase of the TiN content. This was due to the substitution of the Al atoms by the larger Ti atoms. The increase in the lattice strain originated by Ti alloying gave rise to an increase in the hardness of Ti-Al-N films in comparison to the pure AlN sample, as shown in Fig. 7.1.

Although the hardness values presented in Fig. 7.1 by Rauch *et al.*[15] followed the same trend as followed by values given by the other authors, the interpretation of their evolution with the AlN content could not be explained in the same way. In fact, the change in the structure from the fcc TiN to the hexagonal AlN phase did not give rise to a decrease in hardness. The authors justified the hardness values as the formation of a nanocomposite structure where, for low AlN contents, this phase was present in the amorphous state in the grain boundaries of TiN nanocrystallites, whereas, for the highest AlN contents, the opposite situation occurred, i.e., nanocrystalline grains of AlN were surrounded by an amorphous TiN layer. The presence of the amorphous phase in the grain boundaries prevented grain boundary sliding, leading to the hardening of the material, thus following the concept introduced by Veprek *et al.*[34] (this subject is addressed in Chapter 9 of this book).

It is not clear from the literature results that the addition of Al to Cr-N and to the Ti-N systems had a marked influence on the film grain size. Only a few authors[15,17,23,25] made reference to this structural parameter, and they did not mention any important changes in the grain size value for the fcc coating phase. However, they observed a strong decrease of approximately one order of magnitude in the grain size, when changing from the fcc nitride to the wurtzite phase. Generally, this trend was accompanied by an improvement in the density of the morphology with a marked transition from a columnar to a small fibrous morphology. Recently, Banakh *et al.*[35] found that the alloying of T_M nitride with Al could lead to a decrease in the grain size, a fact that they stated for the Cr-Al-N system.

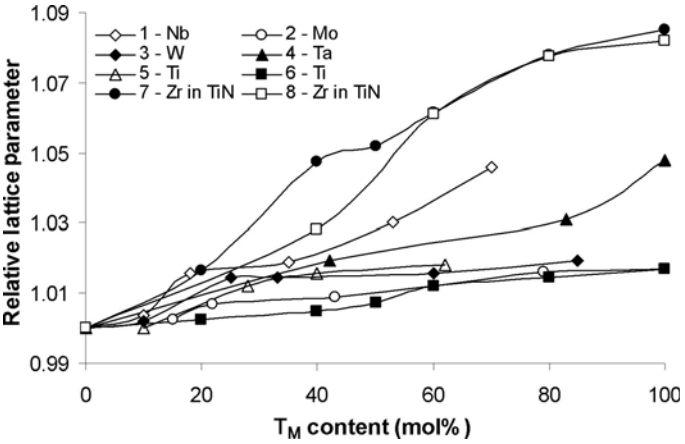

FIGURE 7.3. Lattice parameter of ternary T_M nitrides as a function of the increasing addition of the second T_M element. For the unspecified cases the T_M parent nitride is CrN. (1 – Ref. 36; 2 – Ref. 37; 3 – Ref. 36; 4 – Ref. 38; 5 – Ref. 36; 6 – Ref. 39; 7 – Ref. 39; 8 – Ref. 40)

3. TERNARY NITRIDES WITH T_M ELEMENTS FROM THE IV, V, AND VI GROUPS

In most cases, the mixing of T_M nitrides from the IV, V, and VI groups during the deposition of thin films gave rise to a close linear variation of the lattice parameter of the fcc nitride phase of the parent T_M element. Figure 7.3 exemplifies this trend for different elements added to CrN[36–39] and also for the influence of Zr in TiN.[39,40] This result indicated that a solid solution was expected, with the added atoms substituting the metal atoms in the nitride phase. Besides the experimental uncertainty in the lattice parameter calculation, the small changes to the linear trend that were detected could be due to either small variations in other coating characteristics, such as the residual stress values, or the N contents in the films. The deposition of these systems was carried out by reactive sputtering. Due to the different affinities of the T_M for nitrogen, the content of this element incorporated in the films can vary significantly, depending on the T_M element being added. Therefore, if a T_M with low N affinity is added to a nitride (e.g., W to TiN), a decrease in the N content of the film could be expected if adjustments are not made in the partial pressure ratio of N_2 during the deposition. For example, Moser *et al.*[41] found a decrease in the N content (N/(Ti + W) from 1.1 to 0.9) in Ti-W-N films when the W/Ti ratio increased in the films from 0 to 0.67. Moreover, these authors also found higher tensile stress values with the W increase, which was explained by an improvement in the coating density. The low adatom mobility conditions used by these authors for the film's deposition originated under dense structures. However, with the W addition, there was an improvement in density. The porous column

boundaries, which for low W contents could not sustain macrostress, improved the proximity and attractive forces among the columns, leading to an increase in tensile stress.

In conclusion, changes in both the stress state and the N content of the films, caused by the substitution of one metallic element by the other in the nitride phase, have effects on the lattice parameter and can therefore interfere in the trend, as can be observed in Fig. 7.3. Although the experimental values for the atomic radius are quite different, depending on the selected literature source, using the data for the atomic radius calculated according to Clementi *et al.*,[42] good congruity was obtained between the degree of the lattice dilatation shown in Fig. 7.3 and the atomic radius of the alloying element. The ascending series of the atomic radius of the elements shown in Fig. 7.3, beginning with Cr, is Cr, Ti, Mo, W, Nb, Ta, and Zr (0.166, 0.176, 0.190, 0.193, 0.198, 0.200, and 0.206 nm, respectively). As can be observed, the increase in the lattice dilatation with the content of the alloying element was as steep as the difference in the atomic radius values between the host T_M (Cr or Ti) element and the alloying element increased.

In the light of the effect introduced by solid solution hardening, the analysis of Fig. 7.4, where the influence of the addition of different T_Ms to TiN on the hardness is presented, allows for the conclusion that the lattice changes induced by the substitution of one element for another with a different radius could effectively lead to the improvement in hardness.[39,40,43,44] In fact, regardless of the side from which the analysis was performed, for the Ti-containing system, the ternary nitrides presented higher hardness than binary nitrides. This effect could not be attributed to grain size influence. Although there were no extensive references to the influence of the T_M addition on the grain size of TiN phase, for both Nb and Zr additions,

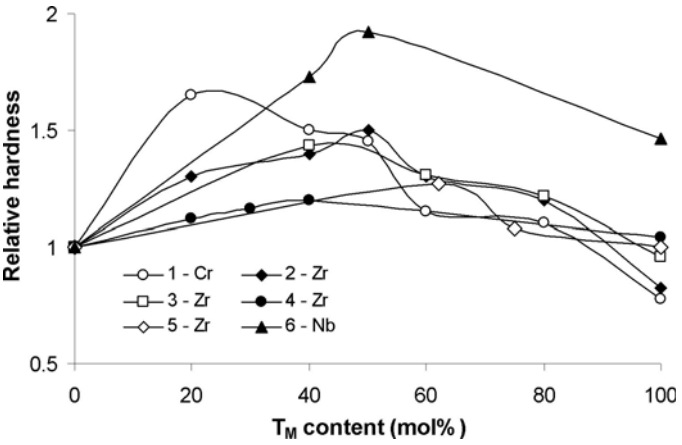

FIGURE 7.4. Hardness of Ti-T_M-N films in relation to TiN as a function of the T_M content. (1 – Ref. 39; 2 – Ref. 39; 3 – Ref. 40; 4 – Ref. 43; 5 – Ref. 44; 6 – Ref. 44)

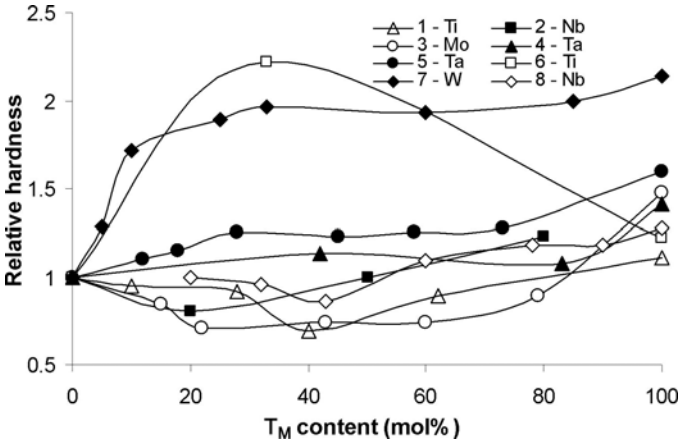

FIGURE 7.5. Hardness of Cr-T_M-N films in relation to CrN as a function of the T_M content. (1 – Ref. 36; 2 – Ref. 36; 3 – Ref. 37; 4 – Ref. 38; 5 – Ref. 45; 6 – Ref. 46; 7 – Ref. 47; 8 – Ref. 48).

Boxman *et al.*[44] did not find any significant variations in the grain size with the increasing alloy content.

In the case of Cr-T_M-N system, the trend in the hardness evolution with increasing T_M content changed from element to element, although the evolution of the lattice parameter was similar in all of them (see Fig. 7.3). Figure 7.5 shows that different trends were achieved[36–38,45–48]: (1) the hardness increased monotonously from single Cr-N up to single T_M-N (W, Ta); (2) there was an improvement in hardness when mixing occurred (Ti); (3) there was a decrease in the hardness values for ternary films in comparison to binary ones (Mo, Nb, Ti). For each case, the explanations suggested by the authors were quite diverse because it was not possible to use any particular set of hardening mechanisms to interpret all the results:

1. The addition of Ta to CrN led to broader X-ray diffraction (XRD) peaks, suggesting a decrease in the grain size that could have contributed to the small increase observed in the hardness for the ternary coatings.[38] In the case of Cr-W-N system,[47] several factors were considered to justify the increase in the hardness with the W content. The first factor that was considered was the structural parameters. When alloying the films with W, there was a decrease in the grain size, an increase in the compressive stress level, and an improvement in coating density from a columnar to a fine-grained morphology, all of which are factors known to contribute to the hardening of materials. Moreover, and more specifically for Cr-rich films, the authors suggested that the strong increase in hardness observed with the addition of a small percentage of W could be attributed to a change

in the bonding character. The presence of W species increased the covalent level of bonding with the consequent increase in hardness.

2. For the Cr-Ti-N system the interpretation is the reverse of the one previously suggested for the Ti-T_M-N systems.
3. For the other Cr-based systems, the previous suggestion based on the covalent bonding character seemed quite plausible for interpreting the trend in the hardness variation with the chemical composition in T_M element.[36,37] In the Cr-Mo-N, Cr-Ti-N, and Cr-Nb-N systems an excellent correlation between the hardness values and the difference in binding energy of the orbitals d of the metal and s of the nitrogen was found. This difference was also correlated to the charge transfer from the metal element to the nitrogen, which, in B1-type structures, led to a more important ionic character. Since the properties of nitrides are closely related to the strong covalent character of the bonding, the increase in the ionic contribution led to lower cohesive forces between the atoms and to a reduction of the mechanical strength of the material.[49] This fact explained the lower hardness of the ternary nitrides in comparison to the binary nitrides as shown in Fig. 7.5. It is important to note that in those studies other factors, such as, the residual stress, the morphology, the phase composition, and the grain size, which are usually taken into account as hardening mechanisms, were considered, but it was not possible to find significant changes between ternary and binary films that could explain the observed trend in the hardness.

4. THE SPECIFIC CASE OF THE ADDITION OF Si TO T_M NITRIDES

One of the most studied elements with which T_M nitrides have been alloyed is Si. There is still a great controversy concerning the interpretation of the mechanical property values of films deposited from the T_M-Si-N system. Therefore, these coatings will be analyzed in great detail in other chapters of this book. Only some general results will be presented in this chapter.

Si has a high affinity for nitrogen and has a much smaller atomic radius than the T_M. In the T_M-Si-N system the trend in the evolution of the hardness as a function of the Si content also included, for most cases, an improvement in the hardness in ternary films in comparison to binary T_M-N film (see Fig. 7.6).[50–62] There were many explanations given for this trend, but the most widely accepted was the one that refers to the formation of a nanocomposite structure (see Chapter 9). According to this theory, the maximum hardness occurred for a Si content that would be in the range of 6–10 at% (see, e.g., Refs. 63 and 64.) However, in many cases, empirical relationships were also established between the hardness values and structural parameters or residual stresses (Fig. 7.7).[53,56,59,60] Figure 7.7 shows that for two different T_M, the higher the compressive residual stress, the higher was

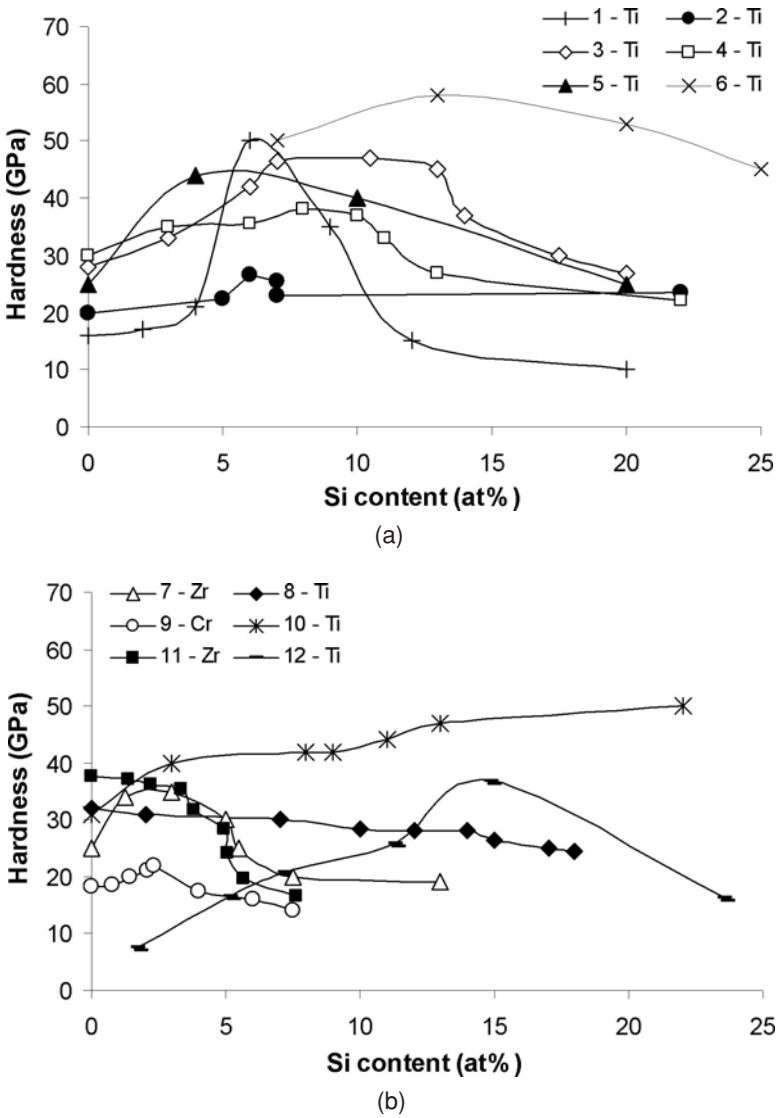

FIGURE 7.6. Hardness of T_M-Si-N films as a function of the Si content: (a) T_M = Ti, (b) T_M = Ti, Cr, Zr. (1 – Refs. 50 and 51; 2 – Ref. 52; 3 – Ref. 53; 4 – Ref. 56; 5 – Ref. 57; 6 – Ref. 60; 7 – Ref. 54; 8 – Ref. 55; 9 – Ref. 58; 10 – Ref. 59; 11 – Ref. 61; 12 – Ref. 62)

the hardness evaluated in the films. In the field of hard coatings, there are many references found in literature,[65–67] showing the importance of residual stress on the hardness of materials. In bulk materials, experimental and numerical research works allowed studying the influence of the residual stress on the mechanical

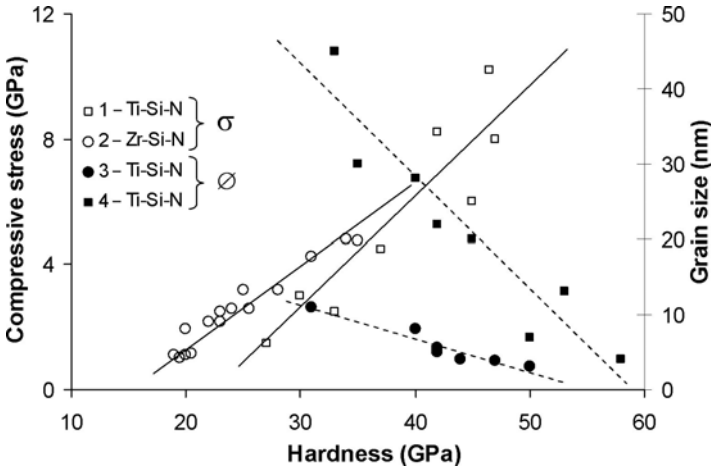

FIGURE 7.7. Empirical relationships between the hardness and residual stress and the grain size of T_M-Si-N films. (1 – Ref. 53; 2 – Ref. 56; 3 – Ref. 59; 4 – Ref. 60)

properties, using nanoindentation.[68,69] Experimental work carried out on a coated strip submitted to increasing deflections, so that different stress fields could be applied to the film, showed that they significantly changed the measured hardness values[70]: the higher the applied tensile stress value, the lower the measured hardness.

On the other hand, in Fig. 7.7, an example is also given showing good congruity between the decrease in grain size and the increase in hardness of Ti-Si-N films. Veprek and Reiprich[50] were the first researchers who found that the hardness of plasma-assisted chemical vapor deposition W-Si-N coatings followed the well-known Hall–Petch equation relating the hardness to the grain size, even for dimensions (<10 nm), which were known[71,72] to lead to the opposite trend. Such a behavior will be addressed in chapter 9 of this book. However, it is important to note that results from the same authors[50] showing the lattice strain for the same coatings also seemed to lead to a good empirical correlation between the hardness values and this structural parameter, as shown in Fig. 7.8.[50,51] Moreover, it was later demonstrated that superhardness could also be reached in Ti-Si-N films with much higher grain sizes (over 20 nm) in unstressed films—results that eliminated the direct importance of the grain size for the hardness values.[73,74]

Although the lattice strain could be justified by different factors (residual stresses, low grain size, etc.), the incorporation of a third element in a solid solution is obviously one of the factors that can induce significant lattice distortion in materials, as was presented before. In the case concerning the T_M-Si-N system, experimental evidence was found by extended X-ray absorption fine structure (EXAFS) and complemented by XRD analysis. This evidence suggested that Si

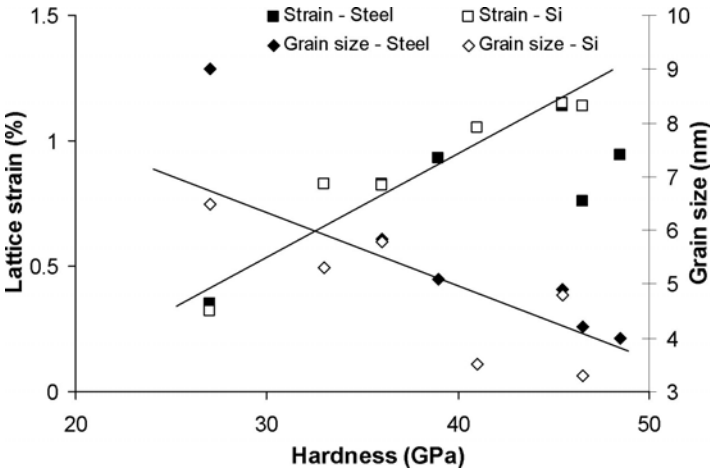

FIGURE 7.8. Empirical relationships between the hardness, the lattice distortion, and the grain size of T_M-Si-N films.[50,51]

atoms could also be incorporated in the lattice of the T_M nitride in substitutional positions.[75] Such a behavior was favored in deposition conditions of low adatom mobility. When studying the influence of the substrate bias on their Ti-Si-N films, these authors[75] observed the duplication of the main diffraction peaks of the fcc TiN phase with decreasing negative substrate bias. For very low values of this deposition parameter, only one peak that shifted to very high diffraction angles was detected. Thus, they proposed that two TiN-based phases could be deposited. For high adatom mobility, segregation of a Si-N phase occurred and the TiN phase presented a lattice parameter close to the standard value. For low adatom mobility, only partial or no segregation took place, in such a way that Si replaced Ti atoms in the TiN phase, giving rise to a decrease in the lattice parameter due to the lower atomic radius of Si in comparison to Ti. This suggestion was confirmed by EXAFS with which the authors confirmed the presence of Ti—Si bonds in the films.

Martinez *et al.*[58] also suggested that the improvement in hardness, at low Si contents, in Cr-Si-N films, could be due to the distortion introduced in the TiN lattice by the incorporation of Si atoms in interstitial positions. It is common knowledge[76] that T_M nitrides can admit a limited number of metal atoms in interstitial positions.

The distortion induced by the incorporation of Si atoms in the lattice of T_M nitride could also be probably related to the fact that T_M-Si-N films, with a Si content higher than a threshold value, became amorphous. The distortion induced by the presence of Si atoms could mechanically destabilize the lattice, leading to a progressive decrease in the degree of crystallinity and the formation of an amorphous structure. This fact was observed by several authors in T_M-Si-N films with different T_M elements (Ta, Ti, W, and Re).[54,59,62,77–84]

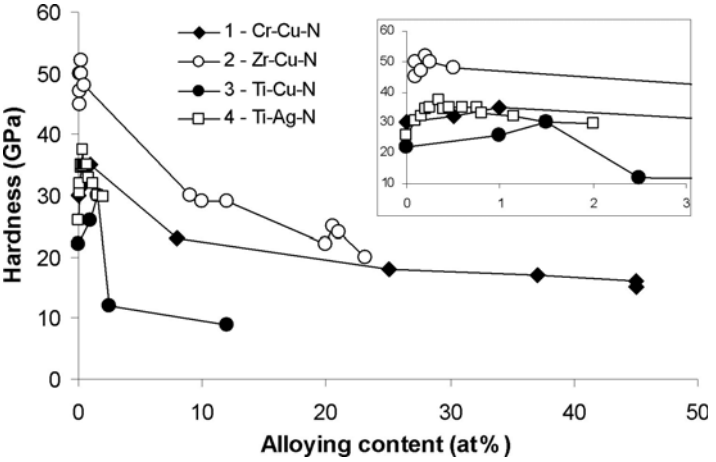

FIGURE 7.9. Evolution of the hardness with the alloying element content (Cu and Ag) in T_M-N films. (1 – Ref. 85; 2 – Ref. 86; 3 – Ref. 87; 4 – Ref. 89)

5. ADDITION OF LOW N-AFFINITY ELEMENTS TO T_M NITRIDES

There are few references in literature concerning the influence of increasing the addition of a third element, with very low affinity for nitrogen, to T_M nitrides.[85–89] Figure 7.9 presents the evolution of the hardness for these cases. The first conclusion from the analysis of this figure is that, similar to many other systems presented before, the hardness rose to a maximum and then significantly decreased thereafter, for the highest alloying contents. However, maximum hardness occurred for much lower alloying contents (<2 at%) in comparison to the cases analyzed before. The interpretation of the hardness increase was not consensual in all studies. He *et al.*[87] suggested that this could be due to the lattice distortion induced by the presence of Cu atoms in the T_M nitride phase. They supported their idea with the strong shift observed in the XRD peaks positions with small Cu additions, which was no more observed for higher Cu contents. The transition point on the lattice dilatation coincided with the change from an increase to a decrease in the hardness, with Cu addition. It should be noted that there were no changes in the grain size for low Cu contents, although a strong decrease in this parameter occurred thereafter. In other studies[85,86,89] the explanation for the hardness increase was based on the formation of a nanocomposite structure. In spite of the irrefutable evidence, particularly for contents higher than 2 at%, that showed the presence of individual Cu and Ag phases,[85,88] Han *et al.*[89] showed that there was a close relationship between the hardness and the shift in the XRD peaks position. They interpreted the shift as the presence of compressive residual stresses, but the distortion could also be due to the presence of Cu in solid solution form. Finally, contrary to what could be expected in view of the Hall–Petch relationship, Zeman *et al.*[86] found that the

highest hardness was reached for the highest grain size when the films showed a very strong (111) orientation for the ZrN phase.

6. W-BASED COATINGS

6.1. The Binary System W-X

6.1.1. Chemical Composition and Structural Features

The incorporation of a third element in W-based coatings can be better understood if the binary system without N is analyzed first. Single W films deposited by sputtering presented the bcc α-W phase preferentially oriented following the (110) planes. Figure 7.10 shows that generally, there was an increase in the lattice parameter of the bcc α-W phase with the increasing addition of the alloying element to W sputtered films.[90–93] Taking into account that all the films were deposited in similar conditions, it seemed reasonable that the addition of the element was done in solid solution form in the W lattice. Although the result was not surprising for the Ti element, i.e., since the atomic radius of Ti is higher than that of W and the substitution of W by Ti could increase the probability of dilatation of the lattice, the same could not be said for the other elements. In fact, both Ni and Si, particularly the latter, had an atomic radius significantly lower than tungsten, thus suggesting that a decrease in the lattice parameter could occur if W was replaced by Ni or Si atoms. Such a behavior was confirmed for the very low Si contents (see insert in Fig. 7.10) where a small decrease in the lattice parameter was observed in relation to the single W film. By taking the phase diagrams of W-Si and W-Ni[94] into account, it was concluded that the solid solubility of these elements in W was

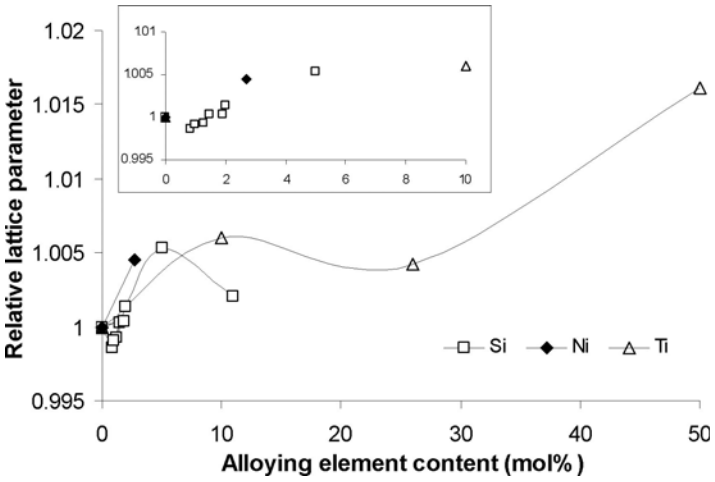

FIGURE 7.10. Relative lattice parameter of W-X films (X = Ti, Si, Ni) as a function of the X content.[90–93]

almost nil at room temperature. However, it is generally known that sputtering can significantly extend the solubility of an element in a given phase, creating metastable structures. Moreover, as suggested by several authors,[76,95] it was possible to place atoms of large dimensions in interstitial positions in the lattice of the main phase during the deposition of films by sputtering. Thus, the increase in the lattice parameter observed in Fig. 7.10 should be related to the incorporation of Si and Ni atoms in the interstitial positions of α-W phase. The trend observed for W-Si films suggested that after the first zone where the Si atoms were replacing the W atoms, for higher Si contents, their positioning in interstitial positions led to an increase in the lattice parameter.

With the increase in the alloying element content, there was an inversion in the above-described trend (Fig. 7.10). On the one hand, when the Ti content reached approximately 35 at%, the corresponding increase in the lattice parameter was not detected. In the W–Ti phase diagram,[94] a miscibility gap existed at high temperature in the domain of the total mutual solubility between both elements. The use of XRD showed that the hexagonal Ti phase was formed in this film.[93] Thus, the precipitation of this phase led to the depletion of Ti from the W lattice and the decrease in parameter in relation to the film with lower Ti content. However, for higher Ti contents, there was an increase in the lattice parameter once again, suggesting the incorporation of Ti in the W lattice.

On the other hand, for Si contents higher than 5 at%, a decrease in the lattice parameter was also observed (Fig. 7.10). In this case, the formation of the β-W form of tungsten occurred (Fig. 7.11). β-W was a metastable phase that could be stabilized with the presence of oxygen[96]; however, a long time ago, Goldschmidt[97] predicted the existence of a silicide (W_3Si) with this structure. Therefore, it is

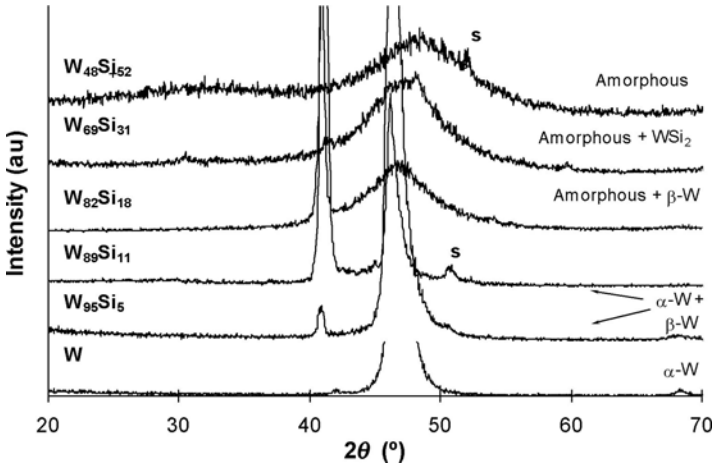

FIGURE 7.11. XRD patterns of W-Si sputtered films with increasing Si contents.[90,92]

possible that if a W phase rich in Si were formed, it would lead to lower Si content in the α-W phase with the consequent decrease in its lattice parameter.

The addition of Ti did not have significant influence on the grain size of the deposited films.[93] However, in the Ni and Si case, even for low contents, the grain size decreased to values lower than 10 nm.[91,92] For Si-containing films, an amorphous phase was detected for contents higher than 10 at% Si (see Fig. 7.11).[90,92] This phase acquired an increasing importance with the increase in the Si content; the film became completely amorphous for Si content higher than 50 at%. Many other authors[77,98–104] found amorphous coatings when depositing the W-Si system from either cosputtering individual W and Si targets or sputtering compound targets. The presence of Si in interstitial positions could destabilize mechanically the lattice cells, and/or the presence of another phase rich in Si could impede the growth of the α-W crystallites, factors that lead to a decrease in the crystallinity and that could give rise to amorphous phases.

6.1.2. Hardness

The evolution of the relative hardness of W-X films with increasing alloying content is shown in Fig. 7.12.[90–93] The absolute value for W films was about 20 GPa, which was a remarkably high value for a metallic coating. With the addition of Si, it was possible to reach values as high as 30 GPa.[90] In comparison to other W coatings referred to in the literature, these values were very high (3–15 GPa[105–108]) and the difference was also enhanced in relation to other single metallic films (e.g., Mo = 3–9 GPa,[109] Ti = 6.6–8 GPa[110]). The high hardness values in relation to the bulk material (~3 GPa) could be related to the synergetic action of several factors such

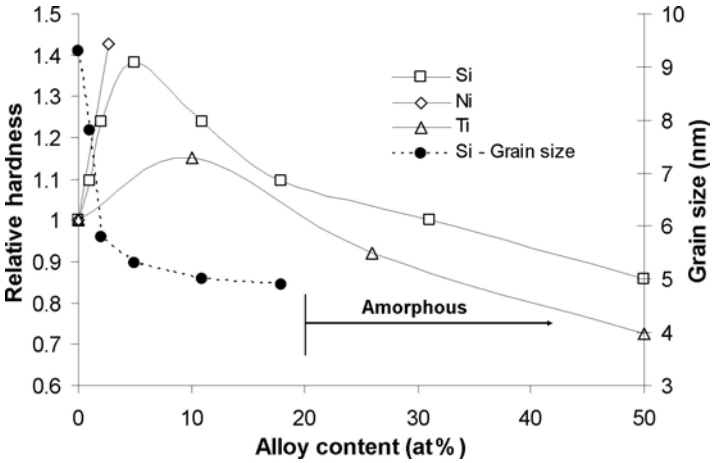

FIGURE 7.12. Evolution of the relative hardness (X = Ti, Si, Ni) and of the grain size (X = Si) of W-X films as a function of the X content.[90–93]

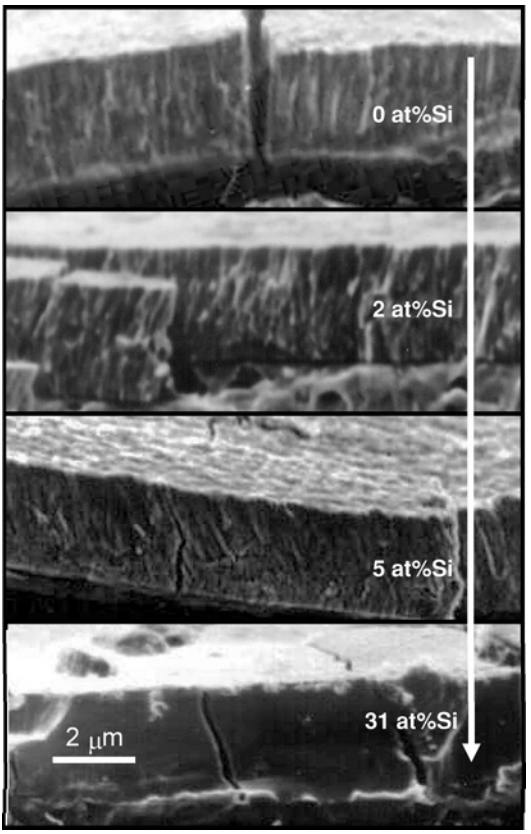

FIGURE 7.13. Cross-section scanning electron micrographs of W-Si films deposited with increasing Si contents.[111]

as the nanocrystalline dimension of the grains (∼20 nm), the high lattice distortion (0.5–1%, depending on the deposition conditions), and/or the compressive residual stresses (2–4 GPa, depending on the substrate used for the deposition).[90–93,111,112]

There was a close relationship between the hardness values and the distortion on the lattice parameter for W-Si films with low Si contents. In fact, the distortion of the lattice induced by the alloying in substitutional or interstitial positions led to an increase in the hardness for all cases.[90,111] However, other factors such as grain size could also contribute to the trend observed and shown in Fig. 7.12, which represents the case of Si as an alloying element. The decrease in the grain size was usually associated to an increase in hardness. Moreover, coating densification could also be invoked as a hardening effect. Figure 7.13 shows cross-section morphologies of W-Si films that became progressively denser with the increase in the Si content.[111]

The decrease in hardness after reaching a threshold alloying content could be interpreted after considering the formation of another phase. In the Ti case, as was

previously mentioned, the hexagonal Ti phase, which was much softer than the bcc W phase (single Ti sputtered films deposited in the same equipment had hardness of 7 GPa),[113] was formed.[93] The formation of an amorphous phase occurred for Si contents higher than 5 at%.[90,111] Although there were some references in the literature[114–116] in which amorphous materials were referred to as harder than crystalline ones of the same type, it was often observed that for W-based coatings the opposite occurred; this will be presented later on. Therefore, the growing importance of the amorphous phase with increasing Si content could justify the decrease in the hardness detected for Si contents higher than 5 at%, in spite of the beneficial effects arising from the decrease in the grain size of the crystalline phase and the improvement in the density of the cross-section morphology.

6.2. The Ternary System W–X–N

6.2.1. Coatings with the bcc α-W Phase

When the influence of the alloying element was considered on N-containing coatings, the hardness analysis was more complicated because both the N and the alloying element could influence the mechanical behavior. Generally, in coatings where only the bcc α-W phase was detected and analyzed, it seemed that the main factors needed to interpret the hardness variation were, once again, the distortion in the lattice parameter and the decrease in the grain size (Fig. 7.14a,b).[90–93,111] However, as shown in Fig. 7.14a, the evolution of the hardness for Ti- and Si-doped films followed different trends. In the first case, it was clear that the distortion degree depended on the Ti content in the film, whereas for Si-doped coatings the change in the distortion was dependent only on the nitrogen content (for each alloying element content, the plotted points correspond to different at% N). In fact, regardless of what the Si content was, all the points were very close to the same trend line that was plotted to represent the evolution, whereas, for Ti-doped films, a separate trend line was necessary for each Ti content. Such a result suggested that Ti could replace W in the α-W lattice, with a strong distortion being induced by the synergetic action of the higher atomic radius of Ti in substitutional solid solution and N in interstitial positions.[93] Besides, Si atoms could not be inserted in the lattice of N-containing films, especially when the N content was higher than Si content, and were, therefore, precipitated in the form of silicon nitride. Experimental results obtained by several techniques helped to support this suggestion, as follows:

- Figure 7.15 shows the evolution of the lattice parameter as a function of the increase of the alloying content.[111,117] Three cases are presented, two corresponding to the binary systems W-Si and W-N, and in the third case the plotted values are from coatings containing 2 at% of Si but with different N contents. If both elements were inserted in the bcc α-W phase, the value of the lattice parameter would be a function of the addition of the distortions caused by both elements. This was not the case as

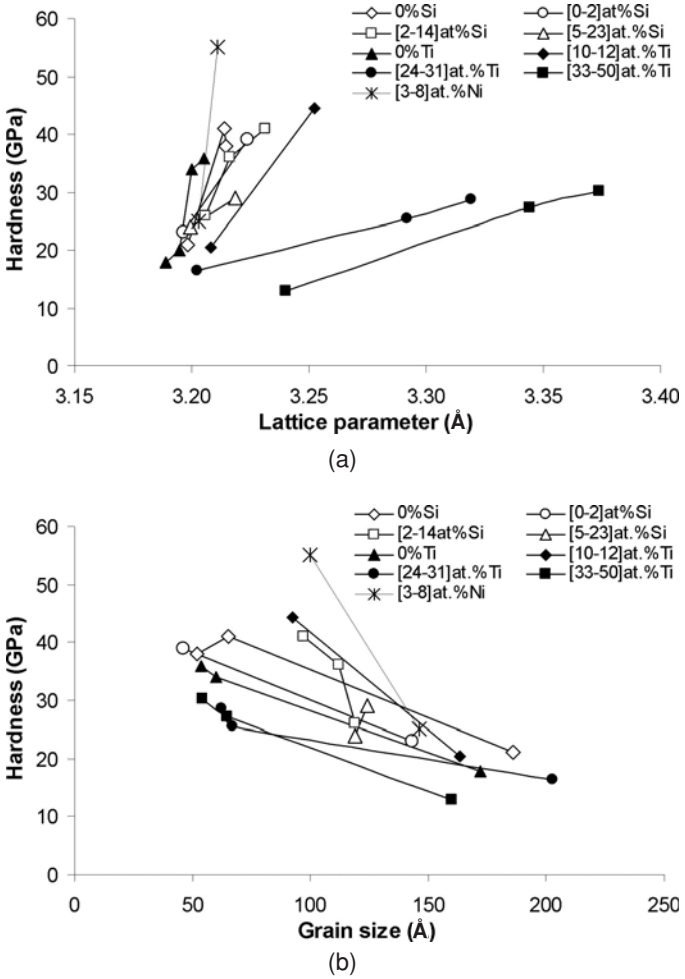

FIGURE 7.14. Evolution of the hardness of W-X-N sputtered films (X = Ti, Si, Ni)[90–93,111] as a function of (a) the lattice distortion and (b) the grain size, of the bcc α-W phase.

shown in Fig. 7.15; in spite of having 2 at% of Si, the films $W_{93}Si_2N_5$ and $W_{87}Si_2N_{11}$ had approximately the same lattice parameter as $W_{95}N_5$ and $W_{89}N_{11}$, respectively.

- X-ray photoelectron spectroscopy (XPS) analysis showed that in films of the ternary system W-Si-N,[111,117–119] it was possible to detect the Si—W bond only when the Si content was higher than three fourth of the N content; otherwise, only the Si—N bond was observed in the Si2p peak. On the other hand, the W—N bond in the W4f peak occurred only when the N

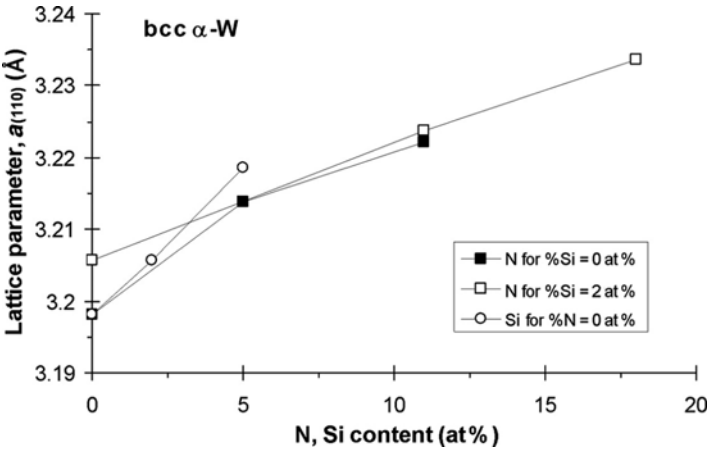

FIGURE 7.15. Evolution of the lattice parameter of the bcc α-W phase of W-Si-N sputtered films with increasing content of N and Si.[111,117]

content was high enough to completely consume the Si and form Si-N phases; the remaining N could then be bonded to W. Figure 7.16 shows the W4f and Si2p XPS spectra of $W_{54}Si_{24}N_{22}$ and $W_{34}Si_{12}N_{54}$ films and permits the exemplification of the type of bonding established between the elements of W-Si-N films.[111,117–119] As can be observed in Fig. 7.16b for the Si2p spectra of the two films, the Si—W bond was detected only when the at% Si/W ratio was higher than 0.75 ($W_{54}Si_{24}N_{22}$ sample). For lower values of this ratio ($W_{34}Si_{12}N_{54}$ film), besides the contribution attributed to the surface oxidation of the samples [Si-O, for E_b in the range (103.2–103.8 eV)], only the Si—N bond was detected. In the W4f peak, aside from the W-O contribution, the $W_{54}Si_{24}N_{22}$ sample showed only the W—W/S bond meaning that none of the nitrogen established bonds with the tungsten. The formation of W—N bonds was possible in this case only when the N content was high enough to completely consume the Si content available. For $W_{34}Si_{12}N_{54}$ film, W4f spectrum did not show any contribution to the W-W/Si; this was due to the fact that the N content was sufficiently high so as not to leave any free W in the film.

- Although no diffraction peaks corresponding to any known Si-based compounds were detected, in the XRD patterns it was possible to observe a broad feature superimposed on the crystalline peaks. This was attributed to the amorphous Si-N phase. Figure 7.17 shows the XRD patterns of two films having similar N contents, one without and the other with 9 at% of Si.[111] In this figure, it is possible to observe the difference in the background close to the crystalline diffraction peak. The film with Si showed a broader zone on the background, which corresponded with an amorphous phase.

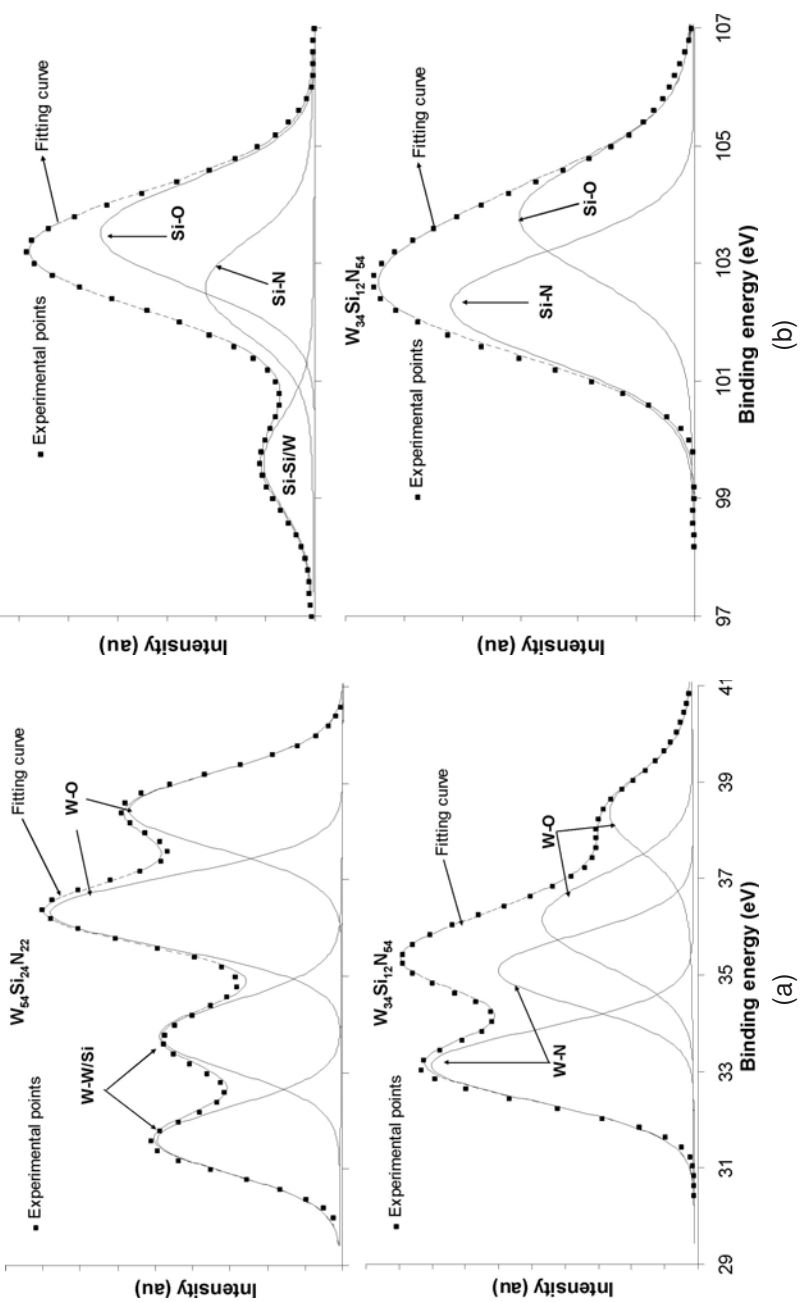

FIGURE 7.16. XPS spectra of $W_{54}Si_{24}N_{22}$ and $W_{34}Si_{12}N_{54}$ sputtered films:[111,117–119] (a) W4f; (b) Si2p.

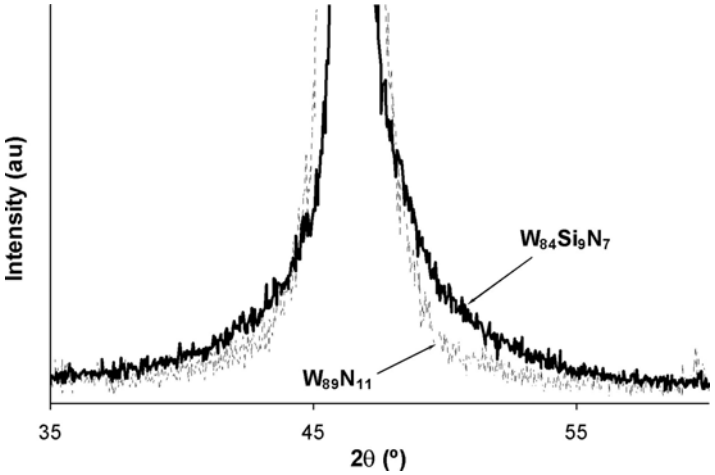

FIGURE 7.17. XRD diffraction pattern of two W-Si-N films (with and without Si) with similar N contents.[111]

> The presence of this noncrystalline Si-N phase was not surprising, since it was common knowledge that Si-N films deposited by sputtering were amorphous even after annealing at temperatures higher than 1000°C.[120–122]

The above considerations allow for the conclusion that in W-Si-N films, due to the much higher affinity of Si for N than for W ($\Delta H_f^{W_2N} = -17$ kcal/mol, $\Delta H_f^{Si_3N_4} = -178$ kcal/mol,[123] Si will bond preferentially to N, forming an amorphous phase; only the remaining Si that is not bonded will combine with W. With nitrogen, Si—N bonding is expected and W—N bonds will be formed, but only after the Si content is completely consumed.

6.2.2. Coatings with the fcc Nitride Phase

The W-nitride phase was detected for coatings with N contents higher than 20 at% (Fig. 7.18).[90,93,111] Regardless of the N content, the nitride could always be indexed as an fcc NaCl-type phase. In the case concerning the Si-containing coatings, this phase could be exclusively attributed to W_2N; Si formed an amorphous Si-N phase due to the preferential bonding of Si to N. Figure 7.18 clearly shows the simultaneous existence of the α-W and the W_2N phases in the range 20–36 at% N. For higher N values, only the W_2N phase was detected; this was true even for N contents as high as 55 at%.[90,111]

Figure 7.19a,b represents for different Si contents the evolution of the lattice parameter and the grain size (calculated by applying the Scherrer formula to the

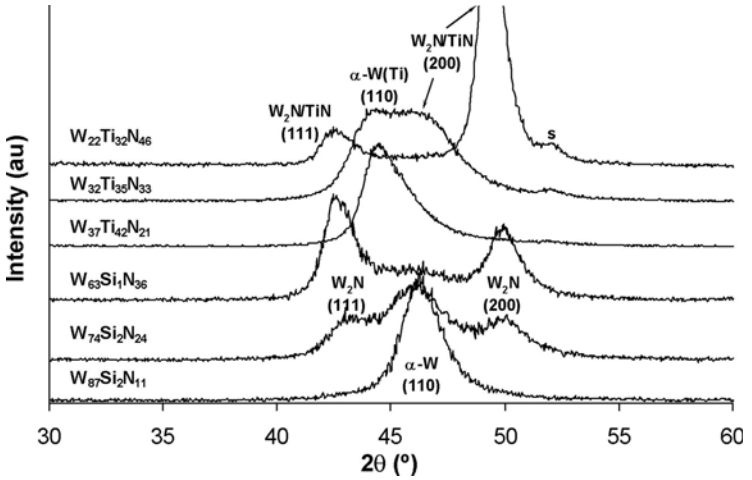

FIGURE 7.18. XRD diffraction patterns of W-X-N (X = Ti, Si) sputtered films deposited with increasing N content.[90,93,111]

integral width of the diffraction peaks)[124] of the W_2N phase detected in W-Si-N films that were deposited with increasing N contents[90,111] A strong heterogeneity was detected for both structural parameters, particularly for the highest N content films. This behavior has been observed by different researchers[65,109,125–128] on deposited films and has been attributed to the high residual stress level and the high number of crystalline defects. As can be seen in the figure, $a_{(200)}$ did not show significant changes with the increasing N content, suggesting that the incorporation of the increasing excess of nitrogen in relation to the stoichiometric W_2N occurred in the interstitial sites that favor distortion toward other directions (e.g., [111], [220]). For N contents up to 35 at% the presence of both W and W_2N phases allows the W_2N phase to always precipitate with approximately the same N content (the excess in W in relation to the W_2N stoichiometry forms the α-W phase); therefore, small changes in the interplanar distances of all the planes were expected. For N contents higher than 35 at%, the W phase disappeared and the exceeding N, in relation to stoichiometry, could be placed in the lattice of the W_2N nitride to promote distortion. However, the distribution of N atoms in the interstitial positions (in the fcc NaCl-type W_2N phase only half of the octahedral interstitial positions were occupied) was not homogeneous. Therefore, for low N contents the occupied octahedral positions induced a distortion toward [100] direction and, with increasing N contents, the filling in of the interstitial positions led to the increase of the other interplanar distances.[111] The analysis of the ICDD diffraction lines registered for the standard W_2N phase (International Center for Diffraction Data, Pennsylvania, Card 25–1257) allowed for the conclusion that even in this standard phase a strong heterogeneous distortion was detected [e.g., the a value

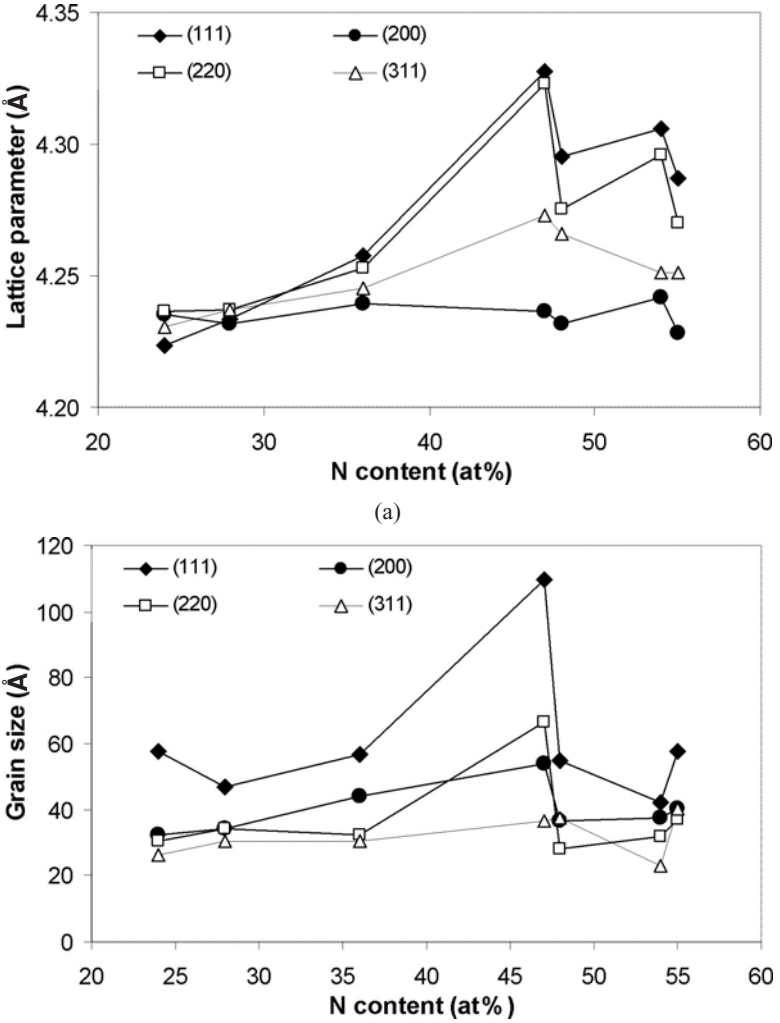

FIGURE 7.19. Evolution of (a) the lattice parameter and (b) the grain size of W-Si-N sputtered films deposited with increasing N contents, for Si contents lower than 12 at%.[90,111]

indicated is 0.4126 nm and the values calculated from the (111) and (200) planes are 0.412 and 0.41316 nm, respectively].

In regards to the grain size, there is also a clear anisotropy in the grain size when different diffraction peaks are used for its calculation.[90,111] The grains with (111) planes parallel to the substrate were larger than the other ones, according to the narrower peaks detected in the XRD patterns. It should be noted that no

relationship was found between the anisotropy in the grain size and the preferential orientation of the films. Even if the films showed a (200) or (311) preferential orientation, the size of the grains with (111) planes parallel to the substrate were always bigger than for the other orientations.[111]

For Ti-containing films the first detection and evolution of the fcc NaCl-type nitride in the XRD patterns was not so evident (e.g., three upper XRD patterns in Fig. 7.18). As for the other W-based coatings, the increase in N content between 0 and 20 at% gave rise only to a progressive shift of the diffraction peaks for lower angles.[93,112] Based on this experimental result, Cavaleiro *et al.*[93] suggested that this increasing distortion was due to N atoms progressively occupying the interstitial sites of the α-W(Ti) lattice. This statement did not agree with the suggestion made by Shaginyan *et al.*[129] about the possible precipitation of a nitride phase from the lowest N contents. A duplication of the (110) peak of the α-W phase with a second contribution placed at higher diffraction angles was clearly detected but only for N contents higher than 20 at%. With the increase of N content, this second peak assumed an increasing importance with a simultaneous progressive shift for higher angles until reaching the probable position of the (200) line of the nitride phase. This was observed only for ~50 at% N.[93,112] For higher N contents, an inversion in the preferential orientation occurred, with the strongest diffraction line now indexed as the (111) plane. The simultaneous detection of these two (200) and (111) diffraction lines allowed for the confirmation of the deposition of the fcc NaCl-type nitride. Taking into account the much higher affinity of Ti for N in comparison to W[49] it was quite probable that TiN would be the first phase to precipitate from the N-supersaturated α-W(Ti) solid solution. With the increasing N content, W would be integrated in the TiN phase in solid solution, as was demonstrated by the vanishing of the α-W signal. TiN and W_2N nitrides are isomorphous phases with similar lattice parameters, which could present extensive miscibility.[49,123]

Figure 7.20 shows the distortion of the Ti(W)N lattice parameter, calculated from (111) and (200) diffraction peak positions, as a function of the N content in the W-Ti-N films deposited from targets with different Ti contents.[93,112] A very strong heterogeneity was found in the specific case of the films deposited from the target with 20 wt% Ti with low N contents. Furthermore, contrary to what was observed for W-Si-N coatings, the highest value calculated for the lattice parameter was that corresponding to the (200) plane. This was always observed for Ti-containing films with low N contents, contrary to what was observed for single W-N films (see Fig. 7.20). However, for N contents >45 at%, the a value calculated for the (111) plane was higher than that for the (200) plane. For these high-N-content films, where the only phase observed was the nitride phase, the coatings deposited from the targets with increasing Ti contents had higher a values. This seemed to confirm the formation of a mixed nitride where the W atoms substituted the Ti atoms in the TiN lattice or vice versa, i.e., the Ti atoms substituted the W atoms in the W_2N lattice.

For W-based films where the nitride phase was detected, finding correlations between the structural parameters and the hardness was not as easy. In the case

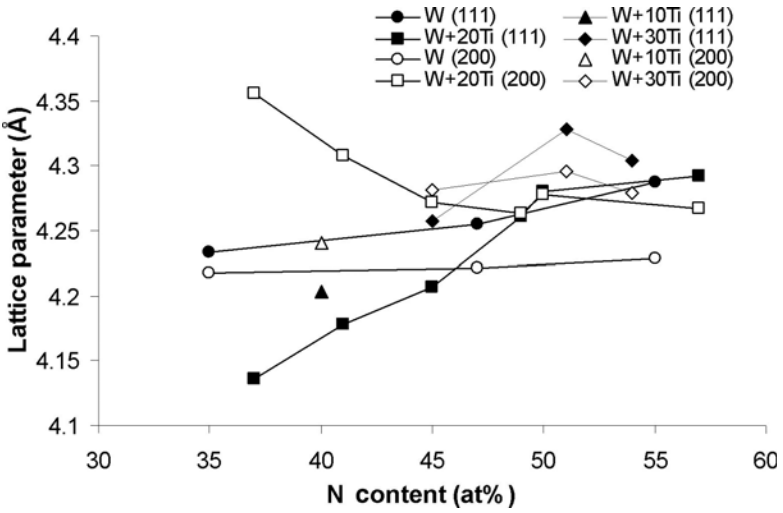

FIGURE 7.20. Evolution of the lattice parameter of W-Ti-N films sputtered from W targets with different Ti contents and deposited with increasing N contents.[93]

concerning Ti-containing films, with the exception of a few values, it seemed that the highest hardness values were measured in the films showing N contents close to the stoichiometric value.[93,112] Figure 7.21 shows the evolution of hardness as a function of a N parameter, which was calculated taking the stoichiometry of TiN

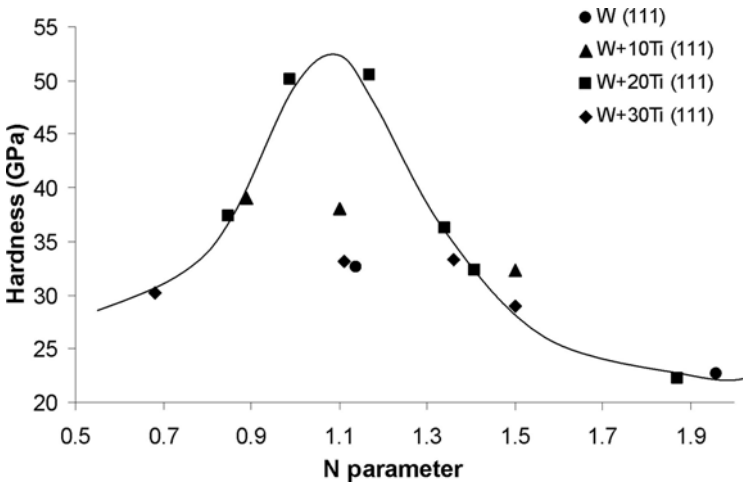

FIGURE 7.21. Evolution of the hardness of W-Ti-N films sputtered from W targets with different Ti contents as a function of a N parameter defined as $N = \text{at\% } N/[(\text{at\%W}/2) + \text{at\% } Ti]$.[93]

and W_2N compounds into account, i.e., N = at% N/[(at% W/2) + at% Ti].[93,112] When N was approaching unity, both phases were close to the equilibrium stoichiometric composition. The importance of the compositions close to the stoichiometry for the properties of PVD-deposited TiN films[127,130–132] has been known for quite some time. The presence of vacancies in both sublattices of the TiN phase (sub- or overstoichiometric films) was indicated as being responsible for the significant changes in the film properties, particularly for their hardness, when the chemical composition was deviated from the stoichiometry.

In the case concerning W-Si-N films there were insufficient results in the literature to come to any global correlation between the structural parameters and the hardness of the films. In some cases, it seemed there was an effect of decreasing grain size on the hardness increase, but this trend was not maintained in other films.[92] The films with [111] preferential orientation were also indicated in the same reference as being very hard; this was interpreted from the higher critical shear stresses needed for plastic deformation, as indicated by the calculation of the Schmid factors for the particular case of the fcc NaCl-type structure.[130,132] One of the main reasons why there were only scarce results available in the literature concerning T_M-Si-N films with the W_2N phase was that, in many cases, these films were deposited with an amorphous structure.

6.2.3. As-Deposited Amorphous Coatings

There is a huge amount of references in the literature about the deposition and structural characterization of amorphous T_M-Si-N films.[77,78,81,82,90,92,118,119,133–142] As previously mentioned, the incorporation of Si atoms in W could lead to the mechanical destabilization of the lattice and to the formation of an amorphous structure. When nitrogen was added to the system, it led to the formation of either two mutually insoluble nitrides or, in the low-affinity case of T_M for N (as for W), a metallic phase mixed with a Si-N amorphous phase. During the deposition, if the adatom mobility was very low, the formation of those phases in a separate mode was suppressed. Consequently, a network of dissimilar atoms that were randomly bonded in a nonperiodic way made the atomic diffusion and the consequent nucleation and grain growth processes difficult.[84] As a consequence, the amorphous phase could be obtained. However, there was experimental evidence that denoted the existence of a short-range structural order in the amorphous phase, as will be presented in the next paragraphs.

Figure 7.22 shows the XRD patterns of W-Si-N films deposited with increasing N contents, with a Si/W ratio close to 1.[111,143] A progressive shift of the X-ray amorphous diffraction peak for lower angles could be observed with increasing N. Similarly to well-crystallized structures, the position of this broad diffraction peak could be considered for the calculation of an interplanar distance value. By plotting the calculated $a$values as a function of the N content, it was also possible to find similar trends for films with different Si/W ratios (Fig. 7.23).[111,118,119,143]

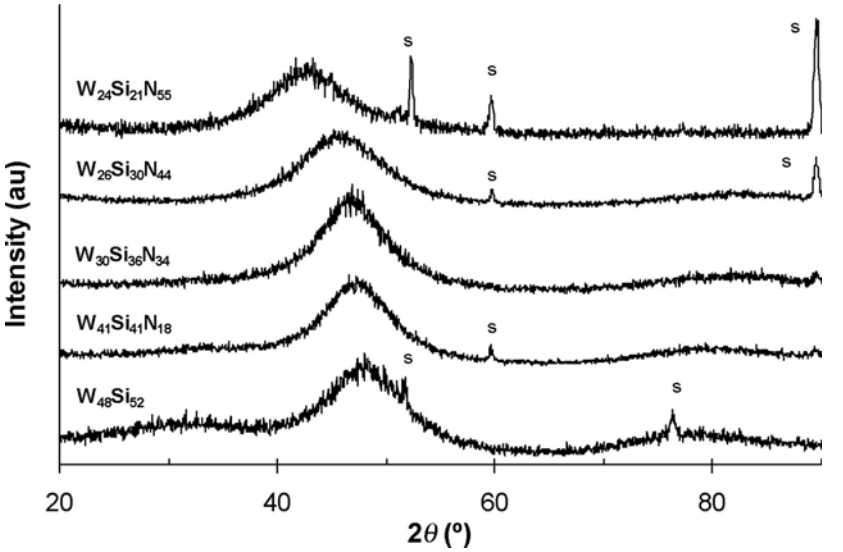

FIGURE 7.22. XRD patterns of sputtered W-Si-N films with similar Si/W ratio, deposited with increasing N contents.[111,143]

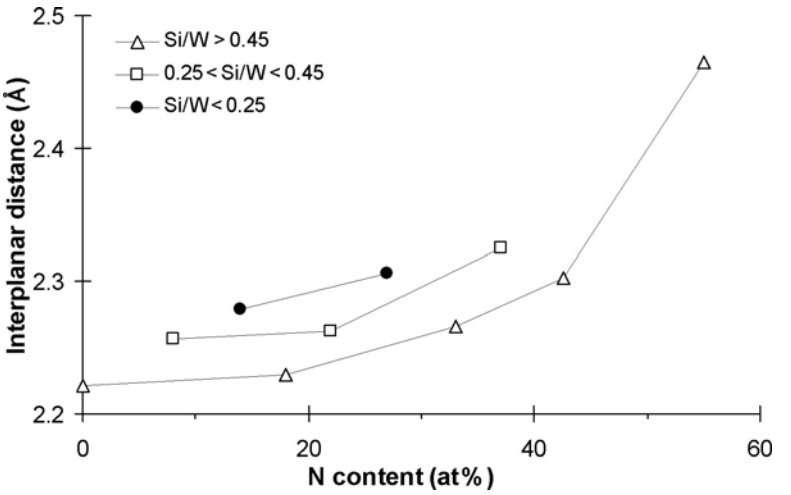

FIGURE 7.23. Evolution of the interplanar distance of amorphous sputtered W-Si-N films (different ranges of Si/W at% ratios), calculated from the position of the broad diffraction peak, as a function of the N content.[111,118,119,143]

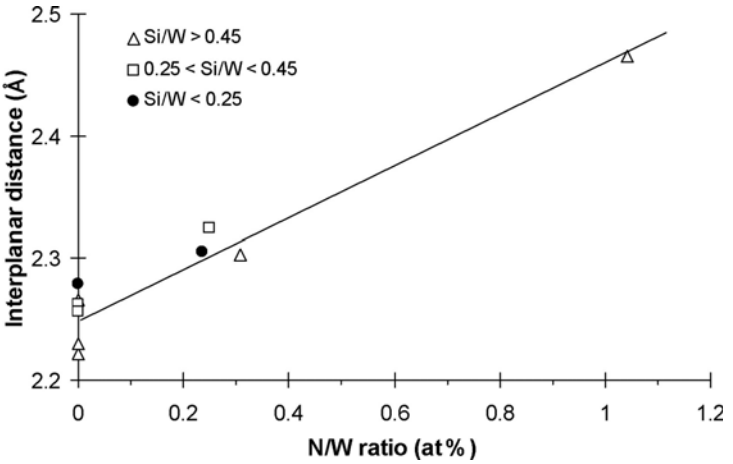

FIGURE 7.24. Re-plot of the data of Fig. 6.23 as a function of the N/W ratio, considering the N content as the one which was not bonded preferentially to Si (see text).[111,118,119,143]

Now, supposing that the assumption made before about the preferential bonding of Si with N atoms is true, the data in Fig. 7.23 can be re-plotted as a function of the N/W ratio, taking N as the remaining content of nitrogen not bonded to Si (Fig. 7.24). A remarkable linear correlation was found between these quantities, suggesting that a seed of a W-N phase was being formed in the so-called amorphous structure. Furthermore, the results of the calculated interplanar distances agreed with the values calculated from the position of crystalline peaks of W-N sputtered films.[92,93,111] For the Si contents 0, 20, and 55 at%, the values found in those studies/experiments for the interplanar distances were 2.25, 2.28, and 2.48 Å, respectively, which were very close to the values shown in Fig. 7.24 for similar N contents. These results allowed for the conclusion that in the amorphous films two different amorphous phases could exist, one with an atomic arrangement close to crystalline W-N-based films and the other of the Si-N type.

6.2.4. Achievement of Nanocrystalline Structures from the Crystallization of Amorphous Films of the T_M-Si-N System

The heat treatment of amorphous T_M-Si-N films induced the crystallization in the form of nanocrystalline structures. This was one of the procedures used recently for the development of magnetic materials with improved properties (see, e.g., Ref. 144), which claimed that both the precise control of the grain size of the crystalline phase being formed and the fraction of the crystallized material could be easily achieved. Figure 7.25 shows the crystallization temperature of several T_M-Si-N amorphous films.[70,77,81,84,111,118,133,134] From the analysis of this figure it is clear that the N-containing coatings have higher crystallization temperature

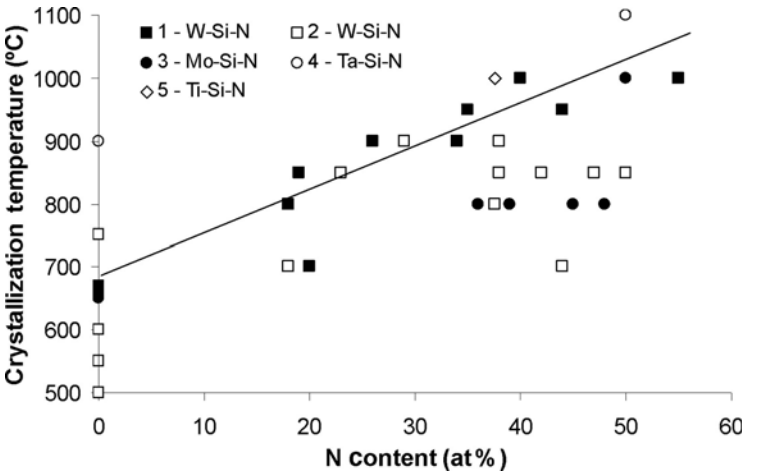

FIGURE 7.25. Crystallization temperature of amorphous T_M-Si-N sputtered films as a function of the N content. (1 – Ref. 70,111, and 118; 2 – Ref. 77, 81, 133, and 134; 3 – Ref. 77; 4 – Ref. 77; 5 – Ref. 84.)

than T_M-Si ones. Furthermore, in the case of a set of films with T_M = W studied by the same research group[70,111,118] the higher the N content, the higher was the crystallization temperature. It was also recently demonstrated that the effect of N in stabilizing the amorphous phase was enhanced for higher Si contents, i.e., for the same N content, the coatings with higher Si/W ratios had higher crystallization temperatures.[118] Nevertheless, it should be noted that for amorphous W-Si films (without N) the opposite happened.[81] The main factors indicated in literature that influence thermal stability of metal–metalloid amorphous compounds were[145] (1) the difference in the atomic radius of the elements; (2) the ability of the metalloid to form strong bonds with the metal; and (3) the ability of forming intermetallic compounds with different structures. A broad analysis of these factors allowed for the understanding of the different thermal stabilities of the amorphous T_M-Si-N films shown in Fig. 7.25. For W-Si films, the probability of forming silicides increased with Si content, which explained the observed decrease in their crystallization temperature. When N was added to this system, the formation of strong Si—N bonding in conjunction with the great difference between the atomic radius of W, Si, and N led to an increasing stability of the deposited amorphous phase. Nicolet and Giauque[84] gave another explanation for the high thermal stability of the T_M-Si-N films. They considered that the two nitrides (T_M and Si nitrides) differed in their crystallographic structure and had limited mutual stability. Since there were no stable intermediate ternary compounds in the fully nitrided alloy, the two nitrides formed a quasi-binary system. As a consequence, the T_M-Si-N amorphous phase could not crystallize polymorphically; it could only originate the primary nucleation of one or the other phase. For this, a long-range

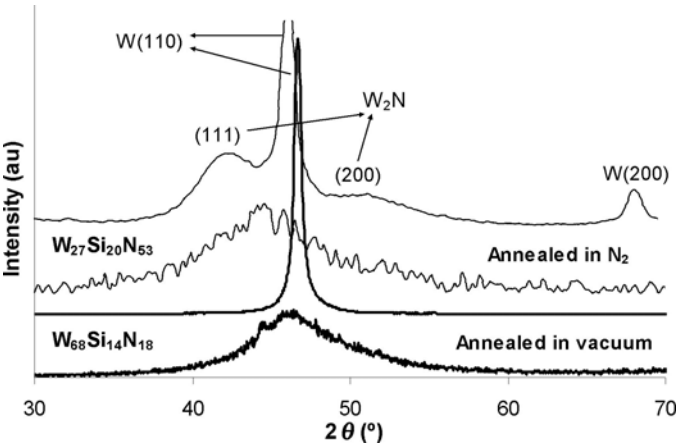

FIGURE 7.26. XRD patterns of W-Si-N films (a) and (c) before and (b) and (d) after annealing in vacuum and $N_2 + H_2$ atmospheres, respectively.[111,136]

diffusion process would be necessary, involving the transport of more than one species. Thus, the thermal stability of the amorphous phase would be enhanced in the ternary system.

The phases detected after crystallization generally depended on two factors: the Si/N ratio and the affinity of T_M for N. Thus, for T_M elements forming very stable nitrides, such as Ti or Ta,[49] the formation of Ti or Ta nitrides was detected after crystallization.[80,84,146] When dealing with elements such as W, which are characterized by their W—N bonds with very low affinity,[49] no T_M nitrides were detected after the annealing process.[70,77,111,118,144,147] For these T_M elements, the detection of a metallic phase of T_M element was achieved after crystallization. The example in Fig. 7.26 shows that the bcc α-W phase was the only crystalline phase presented in the XRD patterns immediately after crystallization and up to annealing temperatures of 1000°C.[111,136] The formation of tungsten nitride phases was possible only if the crystallization annealing was performed in an N-rich atmosphere[136]; this is confirmed in Fig. 7.26 for the case of $W_{27}Si_{20}N_{53}$ film after annealing at 1100°C.

The Si/N ratio determined the presence in the XRD patterns of other crystalline peaks besides those corresponding to T_M or T_M nitride. If the Si/N (at%) ratio was low (Si/N < 0.75), as was previously referred, stable T_M nitrides were formed simultaneously with a Si-N phase (e.g., Ti or Ta), or the Si-N phase was present with a crystallized phase of the metallic element (e.g., Mo and W).[70,77,80,84,111,118,144,146,147] The Si-N phase was present in the amorphous state, since no crystalline peaks were found in the XRD patterns. This was not an unexpected result, since either the deposition of Si-N by sputtering gave rise to amorphous films[122,148,149] or the crystallization of the amorphous Si-N phase occurred only for temperatures higher than 1000°C.[122,150,151]

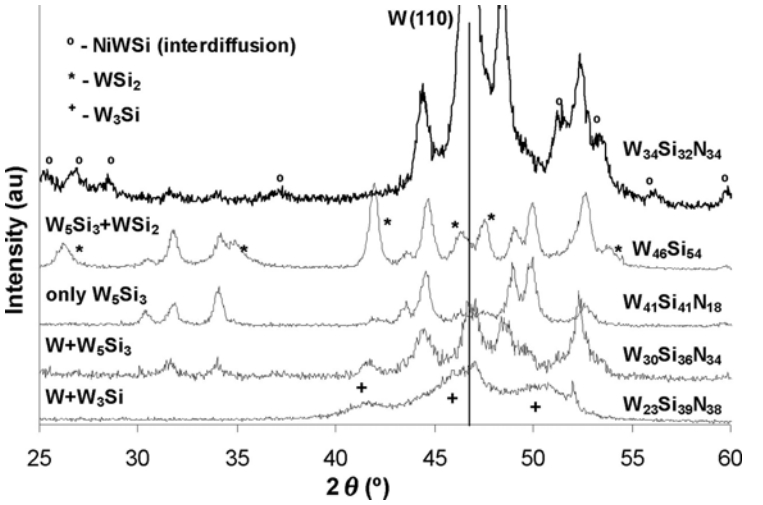

FIGURE 7.27. XRD patterns of W-Si-N films, having different atomic Si/W ratios (Si = Si content not bonded to N), after crystallization.[111,118,119]

If the Si/N atomic ratio was higher than 0.75 the probability of finding silicide phases increased, particularly for T_M elements with low affinity for N. For T_M = W, due to the preferential bonding between Si and N, a part of the Si content was available for bonding with W and formed W silicides.[111,118,119] Depending on the Si content available after bonding with N, different types of silicides could be detected. With the increasing available Si content (from 0 up to very high values) the phase formation sequence after crystallization was[119]

$$\alpha\text{-W} \rightarrow \alpha\text{-W} + \beta\text{-W}(W_3Si_{97}) \rightarrow \alpha\text{-W} + W_5Si_3 \rightarrow W_5Si_3 \rightarrow W_5Si_3 + WSi_2$$

Figure 7.27 shows typical XRD patterns of crystallized W-Si-N films deposited with different chemical compositions.[111,118,119] If Si and N contents were preferentially combined, for each film the remaining W and Si contents could be arranged in different phases as shown in the XRD patterns. For example, for the $W_{41}Si_{41}N_{18}$ film and the stoichiometry of Si_3N_4, the 18 at% N consumed approximately 14 at% of Si. The remaining Si content (~27 at%) was in proportion in relation to W (41 at%), which was very close to W_5Si_3; this was the only phase detected after the film crystallization (Fig. 7.27). When the available Si content was high enough to overcome the ratio Si/W > 3/5 (W_5Si_3 stoichiometry), other Si-richer silicides were indexed, such as the WSi_2 (film $W_{50}Si_{50}$). In both these cases, silicides were the unique phases present in the XRD pattern; the W-metallic phase was detected only when the atomic Si/W ratio (Si = remaining Si content not bonded to N) was lower than 3/5 ($W_{30}Si_{36}N_{34}$ and $W_{24}Si_{39}N_{37}$ films). In these cases, a mixture of α-W and W_3Si or W_5Si_3 phases were achieved.

Finally, in Fig. 7.27, the XRD pattern of the $W_{34}Si_{32}N_{34}$ film deposited on refractory steel (310 AISI) and annealed at 1000°C showed a set of diffraction peaks that could be indexed as a phase containing elements from the film and the substrate.[118,119] The peak positions matched well with different compounds such as NiWSi, NiW, and Fe_2W (International Center for Diffraction Data, Swarthmore, PA, Cards 15-0602, 47-1172, 03-0920). It was recently shown that for very high annealing temperatures (>800°C, depending on the chemical composition), particularly for Ni-containing Fe-based alloys with austenitic structure, interdiffusion between the film and the substrate occurred, giving rise to important changes in the chemical composition of the films and the possibility of formation of phases containing elements from the film and the substrate.[118]

6.2.5. Evolution of the Chemical Composition of T_M-Si-N Films During Thermal Annealing

In regards to the chemical composition of T_M-Si-N films (T_M elements with low affinity to N), after being annealed with increasing temperatures, these films showed no significant changes when Si/N > 0.75, whereas a loss of N, approximated to the excess in relation to the Si_3N_4 stoichiometry, was detected in films with the Si/N atomic ratio lower than 0.75 (see examples in Fig. 7.28).[118,119] As can be observed, the $W_{22}Si_{39}N_{39}$ film did not suffer any chemical composition change with annealing temperatures of up to 1000°C; this was due to its Si/N ratio being higher than 0.75. Due to the higher affinity of Si than W for N, all the N content was bonded to Si. At the beginning of crystallization, this bond was kept stable and, therefore, did not lead to any significant changes in the chemical composition.

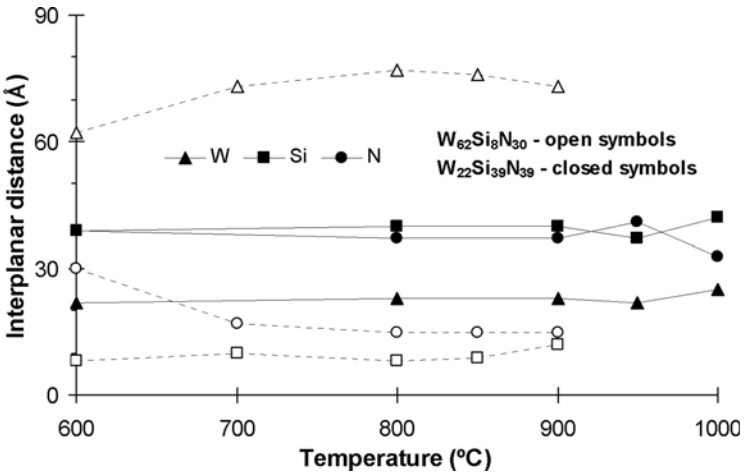

FIGURE 7.28. Evolution of the chemical composition of $W_{22}Si_{39}N_{39}$ and $W_{63}Si_8N_{29}$ films after annealing at increasing temperatures.[118,119]

On the other hand, when the Si/N content was lower than 0.75 ($W_{62}Si_8N_{30}$ film), and after the preferential bonding of N to Si, there was a remaining part of the N content available for forming W—N bonds. The low stability of this bond at high temperatures promoted the liberation of N and a consequent final overall decrease of its content during the thermal annealing process. The changes of the elemental composition shown in Fig. 7.28 at 950°C for the $W_{22}Si_{39}N_{39}$ film were attributed to the influence of the substrate during the annealing process.[118,119] In fact, as previously referred to, interdiffusion between the film and the substrate could take place, leading to different values of the chemical composition of the films. Figure 7.29 shows the element distribution across the thickness of the $W_{29}Si_{45}N_{26}$ film, after having been submitted to an annealing at 1000°C.[118,119] The measurements were performed in consecutive points, following a line in a crater made on the sample surface that went through the film thickness until reaching the substrate (Fig. 7.29a). The outwards diffusion of Fe, Ni, and Cr was clearly observed; Ni and Cr were preferentially accumulated in the interface zone, whereas, Fe diffused up to the surface. By their side, Si diffused inwards while N diffused both inwards and outwards. A depleted nitrogen zone was observed in the middle zone of the film thickness (Fig. 7.29c).

6.2.6. Mechanical Properties of T_M-Si-N Coatings after Thermal Annealing

6.2.6a. As-Deposited Amorphous Films. There are few references in the literature on the mechanical properties of amorphous Si-containing T_M-N films, before and after thermal annealing, with the exception of W-Si-N system.[70,90,92,111,118,137–139,152] As a general trend, the hardness of amorphous films was significantly lower than that of the crystalline as-deposited W-Si-N films. Figure 7.30 presents the hardness values measured in W-Si-N films after deposition.[70,90,92,111,118,137–139,152] With the exception of the films deposited without N, crystalline films had a higher hardness (in the range from 35 to 45 GPa) than amorphous ones (from 19 to 32 GPa). The white bar at the top of the columns shown in Fig. 7.30 was related to the values measured on the same film when deposited onto different types of Fe-based substrates. These substrates had thermal expansion coefficients (αs) between 4×10^{-6} and 18×10^{-6}/K. Since the films were deposited at temperatures close to 450°C, a cooling period was required to lower the temperature to room temperature. During this cooling process, compressive stresses were created with a magnitude as high as the difference between the thermal expansion coefficients of the film and those of the substrate. The highest hardness values were generally evaluated in the films deposited on the substrates with the highest αs values. Figure 7.31 presents the residual stresses of two as-deposited films: one crystalline and the other amorphous ($W_{85}Si_7N_8$ and $W_{51}Si_{22}N_{27}$, respectively).[152] In both cases the compressive residual stresses were lower when the films were deposited onto INVAR® substrates

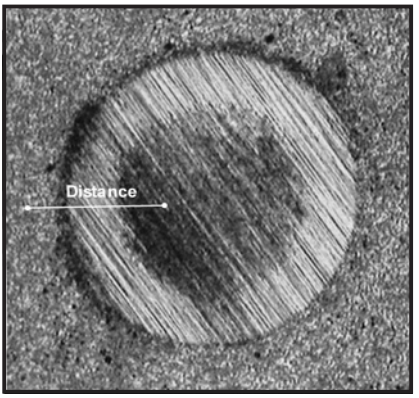

(a)

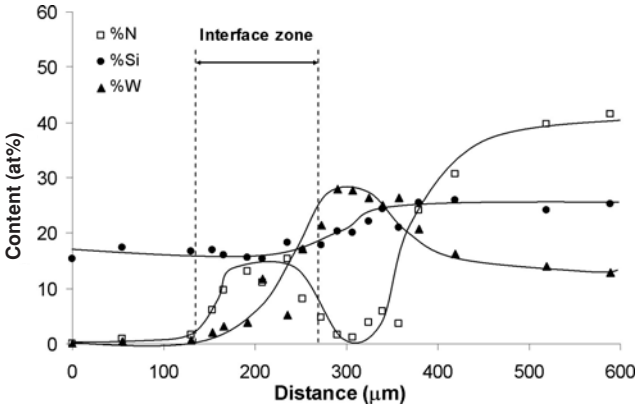

(b)

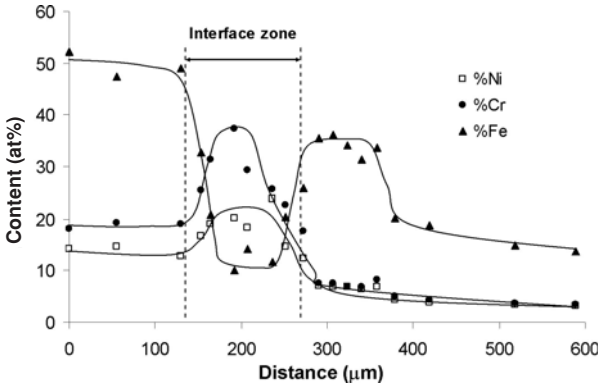

(c)

FIGURE 7.29. Evolution of the chemical composition across the thickness of $W_{29}Si_{45}N_{26}$ film deposited onto 310 (AISI) steel, after annealing at 1000°C. (a) micrograph of the crater where the EPMA measurements were performed; (b) elements from the film (W, Si, N); (c) elements from the substrate (Fe, Cr, Ni).[118,119]

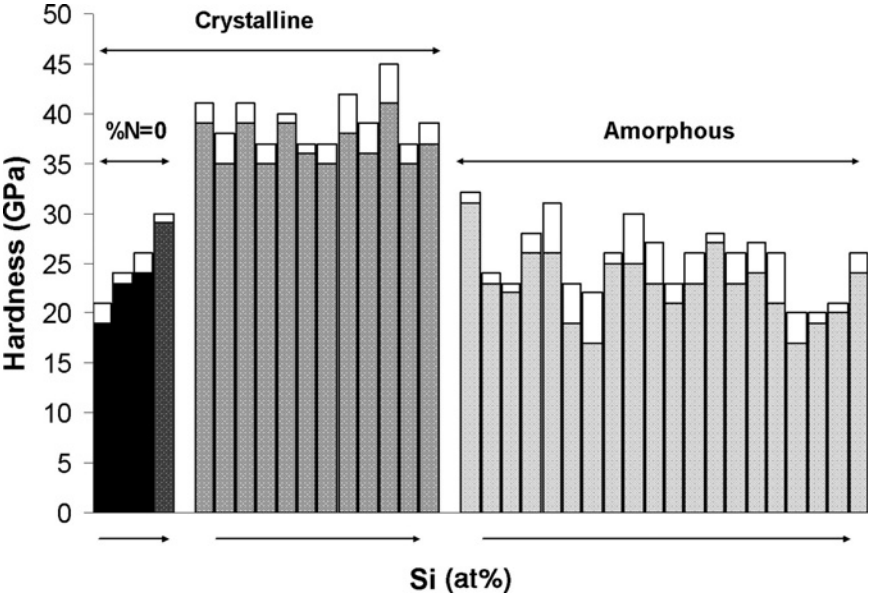

FIGURE 7.30. Comparison of the hardness of amorphous and crystalline W-Si-N sputtered films deposited onto different type of substrates.[70,90,92,111,118,137––139,152]

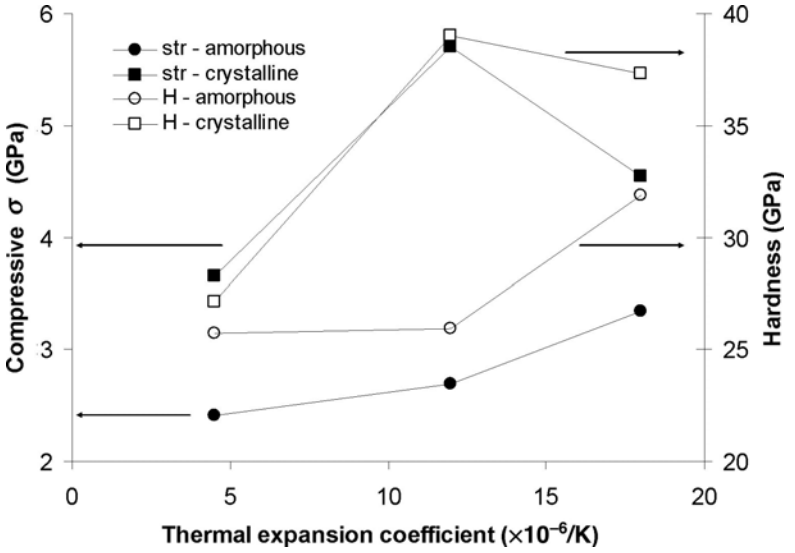

FIGURE 7.31. Hardness and residual stress of $W_{85}Si_7N_8$ and $W_{51}Si_{22}N_{27}$ films when deposited onto three Fe-based high-temperature alloys with different thermal expansion coefficients.[152]

($\alpha s = 4.5 \times 10^{-6}$/K, than when they were deposited onto other materials with higher αs values. Although the same tendency was observed for Fecralloy® and 310 (AISI) steel ($\alpha s = 12 \times 10^{-6}$/K and 18×10^{-6}/K, respectively) substrates coated with the amorphous film, the opposite trend occurred for the crystalline sample.[152] The analysis of Fig. 7.31 could also demonstrate good correlation between the hardness values and the residual stresses in these types of films and, simultaneously, gave an indication of one of the possible factors permitting the explanation of the lower hardness of the amorphous state in relation to crystalline films. In fact, on one hand, in all cases the variation of the hardness values was accompanied by a similar trend in the compressive residual stresses: the higher the stress, the higher is the hardness. On the other hand, it was clear that amorphous films, which presented lower hardness, had significantly lower compressive stresses than crystalline coatings, which, once again, confirmed the correlation between hardness and stress.

The hardness of amorphous films and their lower values in comparison to crystalline films was congruent with other systems deposited by sputtering. Amorphous Si-N coatings deposited by sputtering[116,148,153] had hardness values in the range 22–31 GPa, which were similar to those reached for the W-Si-N films. Moreover, in other W-based systems deposited by sputtering[154] the hardness of amorphous films was also in the range of 23–31 GPa, and globally these values were lower than those reached in crystalline films. Finally, in other T_M-Si-N films, researchers[54,62] have deposited amorphous coatings for highest Si content and have also found lower hardness values in relation to crystalline films.

6.2.6b. After Thermal Annealing. After crystallization, there was a significant increase in film hardness in comparison to the as-deposited amorphous state. Figure 7.32 shows the hardness values of W-Si-N as-deposited coatings and after thermal annealing. The plotted values are the highest found among all evaluated at the studied annealing temperatures.[70,111,118,119] There seemed to be congruity between the hardness and the type of phase resulting from the crystallization process. The only crystalline phase in the hardest films was the bcc α-W. It should be noted that in spite of being a metallic phase where no nitrogen was expected, the hardness values were very high (over 40 GPa) and similar to those reached in many T_M nitrides or carbides. The deposition by sputtering of W films with the bcc α-W phase gave rise to a hardness value close to 20 GPa, clearly below the previously mentioned value.[90–93,111] When only some nitrogen (5 at%) was added to as-deposited crystalline α-W films, the hardness improved up to 42 GPa.[92] Generally, the lattice parameter of bcc α-W phase in the annealed films was lower than that the one of as-deposited crystalline films (including W film),[118,119] in the ranges of 3.172–3.193 Å and 3.196–3.251 Å, respectively, values which were close to the standard ICDD value for this phase (3.168 Å [International Center for Diffraction Data, Swarthmore, PA, Cards 04-0806]). This result suggested that annealed films should contain very small contents of N and Si in the W lattice.

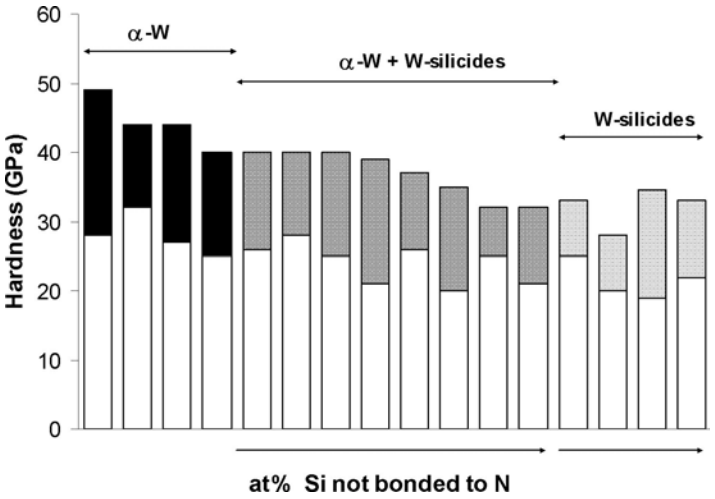

FIGURE 7.32. Hardness of amorphous W-Si-N sputtered films before and after crystallization during thermal annealing.[70,111,118,119]

When the Si content was high enough to consume the entire N available in the film, the formation of W silicide phases occurred. For low Si contents, W_3Si or W_5Si_3 were found with the bcc α-W, but, with increasing availability of Si, α-W progressively lost its importance until only silicides were detected: first only W_5Si_3, and finally, a mixture of this phase with WSi_2.[118,119] In this evolution, as can be observed in Fig. 7.32, the trend in the film hardness after crystallization shows decrease, with only a few exceptions as follows:

- First, the two cases of the α-W + silicide zone that have lower hardness than films of the silicides zone which correspond to either a film deposited without N or a film where interdiffusion between the film and the substrate took place.
- Second, the softer films in the silicides zone were deposited exclusively with the W_5Si_3 phase. This phase had lower hardness than WSi_2,[155] which explained the harder film with a structure of a mixture of silicides.

The trend in the evolution of the hardness of amorphous W-Si-N films with increasing temperatures was quite different among the studied films, depending on the chemical composition of the films and the substrates on which they were deposited (Fig. 7.33).[70,111,118,119] There were coatings that showed a steady increase in the hardness after annealing at increasing temperatures, even when the crystallization occurred ($W_{41}Si_{41}N_{18}$). Others presented a significant increase in the hardness either when crystallization took place ($W_{25}Si_{40}N_{35}$ and $W_{68}Si_{14}N_{18}$) or at the beginning of thermal annealing when the coating still had the amorphous structure ($W_{68}Si_{14}N_{18}$). Finally, there were coatings that after a smooth increase in

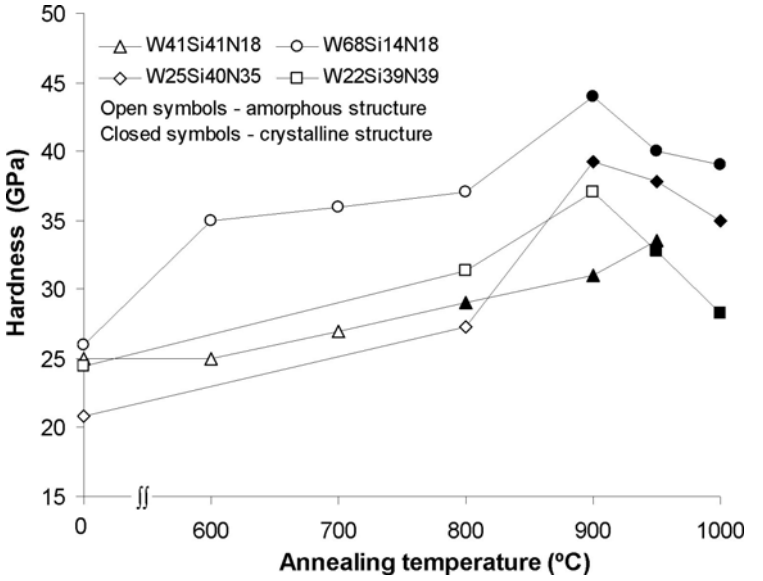

FIGURE 7.33. Evolution of the hardness of sputtered amorphous W-Si-N films as a function of the annealing temperature.[70,111,118,119]

the hardness with the thermal annealing showed a sudden decrease in this property after crystallization ($W_{22}Si_{39}N_{39}$). A decrease in the hardness was registered for the highest annealing temperatures for most coatings.

The steady increase in hardness with increasing annealing temperatures could be attributed either to small structural transformations in the amorphous state, which were not detected with the XRD technique, or to residual stresses, as follows:

- Quite some time ago, researchers[156,157] found an improvement in the mechanical strength of amorphous alloys, when these alloys were annealed. They attributed the hardness enhancement to structural relaxation including the precipitation of incipient crystallites of very low grain size.
- After the heating during the annealing process, stress relaxation occurred in the materials, leading to a decrease in stress the magnitude of which depended on the material characteristics.[118,152] Due to the difference in thermal expansion coefficients between the films (α_f) and the substrate (α_s), a "new" stress state can be created in the films while cooling from the annealing temperature. Generally, for W-based films and the utilized substrates, $\alpha_s > \alpha_f$; hence, compressive stresses were developed, which consequently led to hardness improvement.

In many cases, crystallization induced a further increase in the hardness values. As previously mentioned, crystalline films are harder than amorphous films with similar chemical compositions. In samples where a decrease in the hardness

was observed after crystallization, interdiffusion between the film and the substrate was detected after thermal annealing.[118,119,152] The formation of softer phases containing elements from the film and the substrate could explain the sudden inversion observed in hardness values after crystallization in Fig. 7.33.

For the highest annealing temperatures, almost all the coatings in Fig. 7.33 showed a decrease in the hardness, particularly when the films were already crystallized. Such a trend could be related to the recovery of the crystalline structure involving annihilation of dislocations, elimination of lattice defects, liberation of entrapped processing gases, and, finally, grain growth.[118,119,152] However, the fact that some coatings showed a remarkable thermal stability with no changes in the XRD patterns even at very high annealing temperatures (close to 1000°C) should be noted.[118] In other research studies[63] on T_M-Si-N crystalline coatings, the thermal stability was explained by the presence of the Si-N amorphous phase which inhibited the growth of the nanograins in the T_M-N phase, contributing to the low grain size presented by the films after having been annealed at temperatures as high as 1100°C.

6.2.6c. Hardening Mechanisms Involved in the Interpretation of Hardness Values. Regardless of the factors that could explain the increase in the hardness after thermal annealing, the residual stress influence could not be excluded. Figure 7.34 shows the evolution of both the residual stresses and the hardness of an amorphous and a crystalline W-Si-N film with the increase in the

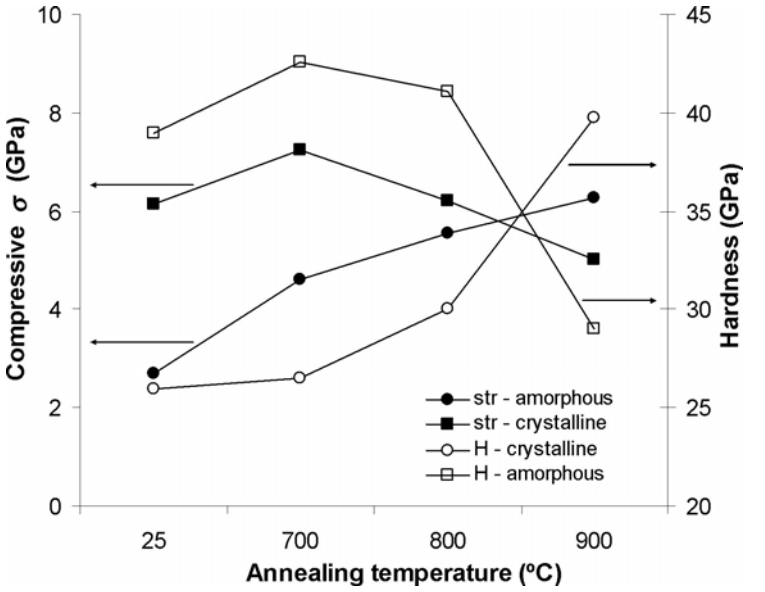

FIGURE 7.34. Evolution of the hardness and residual stress of $W_{85}Si_7N_8$ and $W_{51}Si_{22}N_{27}$ films after having been submitted to thermal annealing at increasing temperatures.[152]

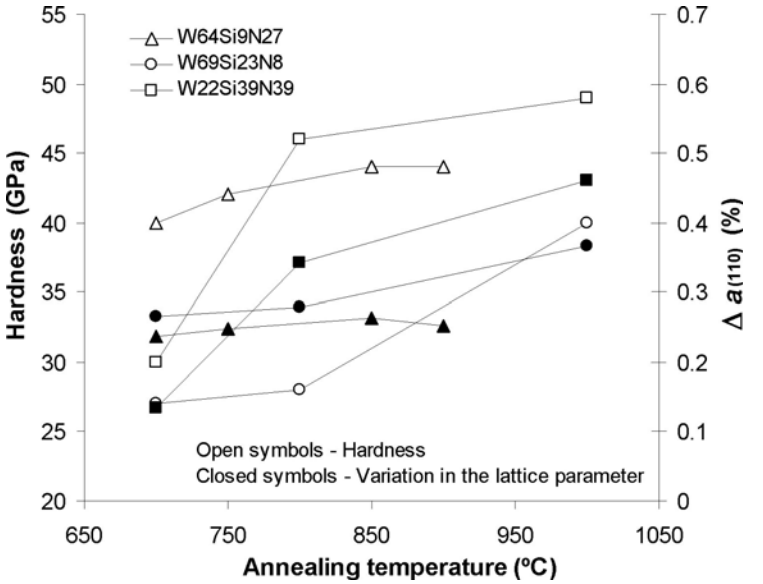

FIGURE 7.35. Evolution of the hardness and of the variation in the lattice parameter of the bcc α-W phase, calculated at the annealing temperature and at room temperature, as a function of the annealing temperature, after amorphous W-Si-N sputtered films crystallized.[111,118]

annealing temperature.[152] Congruity between the variations in the hardness and in the residual stress can be found in this figure. The residual stress could have been originated by different factors but, in the present case, a significant contribution came from the thermal component. For other W-Si-N coatings, XRD patterns were obtained *in situ* at the annealing temperature and after cooling down to room temperature.[111,118] Figure 7.35 presents the results comparing the hardness values and the differences in the lattice parameters[111,118] calculated from the peaks position on the XRD spectra obtained at both annealing temperature and room temperatures. The difference in lattice parameter values (Δa) must then be related exclusively to the thermal stresses created during the cooling down process. As can be observed, the correlation between the hardness and Δa was very good, indicating that the residual stress had an important contribution to the mechanical strength of the films.

Furthermore, the influence of the residual stress was also demonstrated by the hardness variation when the same film was deposited on substrates with different thermal expansion coefficients. During thermal annealing, if the structural evolution of amorphous films deposited on substrates with different thermal expansion coefficients (αs) was similar, the films deposited on the substrates with lower αs values were softer. This was attributed to their lower compressive stress

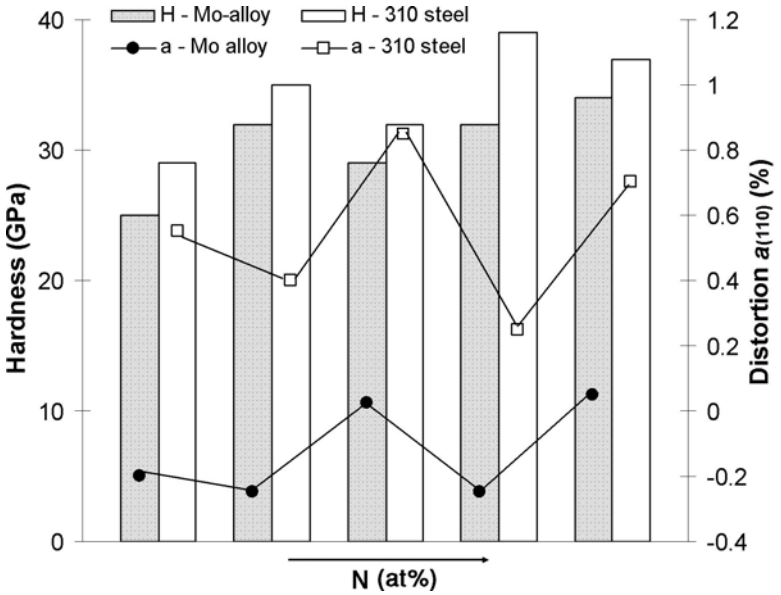

FIGURE 7.36. Hardness and lattice distortion, calculated in relation to the standard value of the bcc α-W phase, of sputtered W-Si-N coatings deposited onto 310 (AISI) steel and Mo alloy, after having been submitted to a 1000°C annealing.[119,158]

values.[119,158] Figure 7.36 shows the hardness of a series of amorphous W-Si-N sputtered films deposited with different N contents, which crystallized during annealing at 1000°C.[119,158] The films were deposited onto two substrates with significant differences in the αs values, 310 (AISI) refractory steel and Mo alloy with αs values of 18 and 5 $\times$ 10^{-6}/K, respectively. In all cases, the bcc α-W phase was the dominant phase after crystallization. In this figure, the lattice distortion calculated in relation to the standard value of the bcc α-W phase is also shown. As can be observed, the films deposited on the 310 steel were always harder than the same films deposited on the Mo alloy, and this was true for all cases. The films on the 310 steel always had positive distortions of the lattice, whereas, when deposited on the Mo alloy the distortion was much lower and, in some cases, it was negative. The positive distortion indicated an increase in the lattice parameter related to compressive residual stresses, whereas tensile stress was expected when the distortion was negative. Thus, as was expected, higher hardness values were reached in the films deposited onto the 310 steels.

Besides residual stresses, other structural parameters also influenced the coating hardness during thermal annealing. In some cases, the structural evolution showed that at the beginning of the crystallization a mixture of crystalline phases and the remaining amorphous material was observed. By deconvoluting the zone where the main diffraction peak occurred, it was possible to establish a relationship

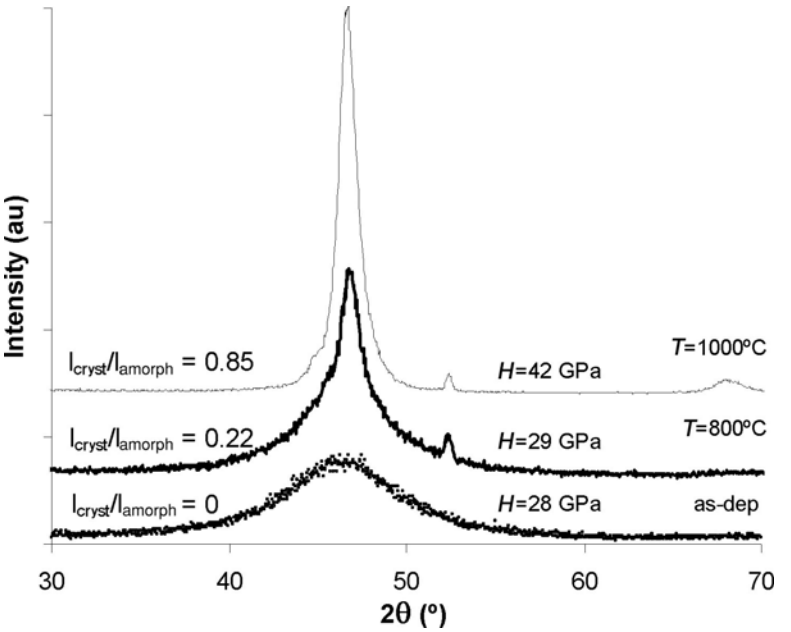

FIGURE 7.37. XRD patterns obtained on the sputtered amorphous $W_{52}Si_{23}N_{25}$ film before and after annealing at increasing temperatures. The ratio between amorphous and crystalline areas of the main diffraction peak as well as the measured hardness values are indicated in the figure.[111,138]

between the content in the crystalline phase and the film hardness.[111,138] Figure 7.37 shows the typical XRD spectra obtained after annealing at increasing temperatures, as well as the measured hardness values and the content in the crystalline phase for the $W_{52}Si_{23}N_{25}$ sample.[111,138] It was clear that the increase in the amount of the crystalline phase gave rise to an improvement in the coating hardness.

Another factor that has been indicated in the literature as a possibility for determining the hardness of thin films for a selected system is the degree of homogeneity in the lattice distortion.[108,159] For W compounds, the fact that the lattice distortion had a significant influence on hardness only if it occurred with the same value in all the crystalline directions was confirmed. If the values of the lattice distortion calculated from the position of different XRD peaks differed from each other, they did not promote the improvement in hardness that was expected from the magnitude of the distortion. For W–C system, it was shown that the introduction of C led to an increased distortion of the lattice parameter, a factor that resulted in an increase in hardness for the low C contents.[108,159] However, from a C threshold content, although the distortion continued to increase in some directions, in other directions the same trend was not observed, and this resulted in a decrease in hardness. Similar behavior was later observed by other researchers for W-N films.[92,111] Figure 7.38 shows the lattice distortion, calculated from the

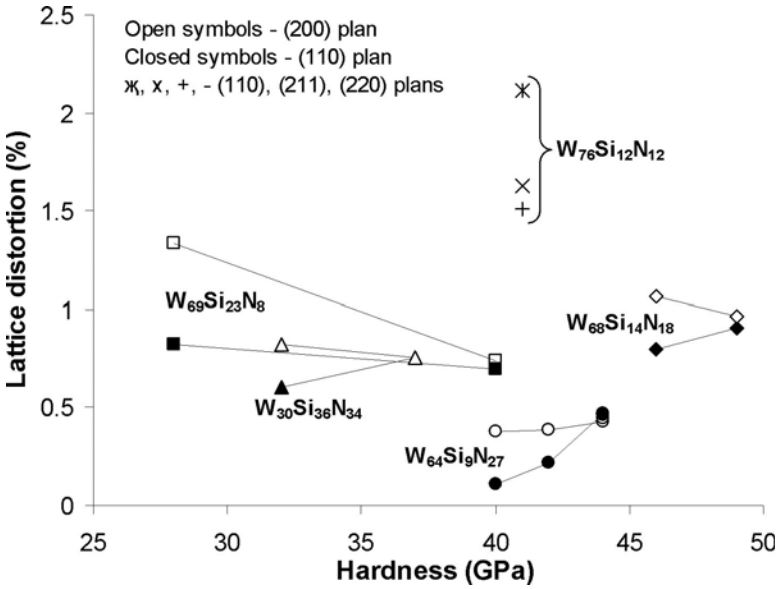

FIGURE 7.38. Influence of the degree of homogeneity of distortion of the lattice parameter, calculated in relation to the standard value of the bcc α-W phase, on the hardness of sputtered W-Si-N coatings after annealing at increasing temperatures.[111]

XRD peaks position, of different W-Si-N sputtered coatings crystallized with the bcc α-W phase.[92,111] As can be noted for each type of film, the highest hardness values coincided with the cases where the lattice distortion was similar for all the planes used in the calculation. It is also interesting to note that two coatings with approximated chemical composition ($W_{68}Si_{14}N_{18}$ and $W_{76}Si_{12}N_{12}$), presenting the same crystalline structure (bcc α-W phase), one of which originated from crystallization from the amorphous state and the other which originated in the as-deposited conditions, had different hardness values. In spite of the higher values of the lattice distortion in the as-deposited crystalline sample, it was less hard than the crystallized coating; the latter had a homogeneous distortion of the lattice whereas $W_{76}Si_{12}N_{12}$ showed a large range of values for the lattice parameter as a function of the diffraction line used for its calculation.

Finally, although the grains of the crystallized phases were, in all cases, of nanometric size (in the range from 3 to 20 nm) it was not possible to find any correlation between the grain size and the hardness of W-Si-N films after crystallization,[111,118,119,152] particularly for films presenting the bcc α-W phase. There were films with grain size lower than 5 nm (e.g., $W_{26}Si_{30}N_{44}$) showing hardness values over 40 GPa, a value clearly above those measured in the $W_{69}Si_{23}N_8$ film (in the range from 25 to 30 GPa) that presented grains with dimensions over 10 nm. Nevertheless, there were also films with "high" grain sizes (>15 nm) with hardness as high as 49 GPa (e.g., $W_{68}Si_{14}N_{18}$).

7. CONCLUSIONS

This chapter was dedicated to the role of the addition of a third element on the properties, in particularly on the hardness, of T_M nitrides.

The study, initially devoted to the addition of Al to T_M nitrides, included the most used ternary coatings in industrial applications, i.e., the Ti–Al–N system. With a few exceptions, the observed trend in the hardness was similar among the different studies presented in the literature. There is an improvement in the values of this parameter when both binary nitrides (T_M-N or AlN) are alloyed with increasing contents of the other nitride. The maximum hardness value is attained for an AlN content, depending on the deposition conditions, in the range from 50 to 70%. Within this composition range the structure changes from the fcc NaCl-type phase characteristic of T_M-N (T_M = Ti, Cr) to the wurtzite phase of AlN. None of the works presented clear evidence of a correlation between the hardness values, the grain size, and/or the residual stresses of the coatings. The evolution in the hardness values as a function of increasing addition of AlN to TiN or CrN was attributed to either the hardening by the strain induced by the solid solution or the increase of the covalent energy of the bonding due to the decrease in the interatomic distance with Ti substitution by smaller Al atoms.

In the second part of the chapter the mixing of T_M elements from IV, V, and VI groups when deposited as T_M nitrides was analyzed. It was concluded from the monotonous evolution of the lattice parameter that the alloying element was placed in solid solution substituting the T_M element in the nitride lattice. In many cases, the hardness presented a maximum for the ternary nitrides, suggesting that the hardening mechanism involved was again the strain induced by solid solution. However, the study of the Cr–T_M–N system showed a different behavior, where both a monotonous increase and an evolution that passes through a minimum value for a ternary composition could be found. The interpretation of these trends was based on a set of factors that include (1) the variation in the residual stresses; (2) the strain induced by solid solution; and (3) the change in the bonding character, with increasing T_M content.

For the T_M–Si–N system, the discussion was focused on the necessity of other hardening mechanisms, in addition to that based on the formation of a nanocomposite structure, which can complement the theory generally accepted for explaining the mechanical behavior of these coatings. For selected cases it was possible to establish a good correlation between the hardness measurements and other experimental parameters such as, the lattice strain, the grain size, and the residual stresses.

The addition of low contents (<2 at%) of low N-affinity elements (e.g., Cu and Ag) to T_M nitrides could lead to important hardness improvement. Even though some authors suggested that the increase observed in the hardness could be due to the formation of a nanocomposite structure, other researchers found a good correlation between the hardness and the lattice dilatation, which can be interpreted as either the increase in the compressive residual stresses or the incorporation of Cu/Ag atoms in solid solution in the T_M nitride lattice.

An important part of the chapter was dedicated to W-based coatings, since this subject falls in with the personal concerns of the authors on T_M nitrides and carbides. It was concluded that the much lower affinity of W for N in comparison to other T_M elements, such as Ti or Zr, makes this system very particular regarding the distribution of N between the alloying element and the tungsten. However, the final mechanical properties of the coatings are very similar, with the hardness reaching values as high as 50 GPa. Besides the hardening mechanisms already presented, such as the lattice strain, the residual stresses, and the grain size, which served for interpreting the observed variation in the hardness values, the degree of heterogeneity in the lattice distortion was presented as a determinant factor in the mechanical strength of the coatings. The highest hardness values were observed for films with similar strained lattice in all the crystallographic directions.

In this chapter the possibility of reaching nanocrystalline structures from the crystallization of amorphous coatings was also analyzed. Particular attention was given to the W-based system, where the addition of Si to the T_M nitrides is determinant for the amorphization. The crystallization temperature varied in the range from 600 to 1000°C, depending on the T_M element and the N content in the films. It was shown that the presence of N could stabilize the amorphous phase. In the case of $T_M = W$, important changes in the chemical composition were observed during the thermal annealing due to either the loss of nitrogen originally bonded to tungsten in the amorphous film or the interdiffusion between the film and the substrate.

One of the most important conclusions of the last part of the chapter was related to the excellent hardness shown by the nanocrystalline films obtained directly from the crystallization of amorphous structures. This fact opens a new direction for the production of nanocomposite structures, since the thermodynamic conditions at high temperatures makes easier the necessary segregation for the production of nanocomposite coatings.

ACKNOWLEDGMENTS

Financial support over the years from the EC through project BREU-Ct91-0403 and from FCT and FEDER through projects POCTI/1999/CTM/33933 and POCTI/1999/EME/33978 is gratefully acknowledged. Special thanks to C. Louro, P. Marques, and L. Ferreira, to whom the authors are particularly indebted, for many of the experimental results on W-based coatings.

REFERENCES

1. O. Knotek, M. Bohmer, and T. Leyendecker, On structure and properties of sputtered Ti and Al based hard compound films, *J. Vac. Sci. Technol. A* **4**, 2695–2700 (1986).
2. H. A. Jehn, S. Hofmann, V. E. Ruckborn, and W. D. Munz, Morphology and properties of sputtered (Ti,Al)N layers on high-speed steel substrates as a function of deposition temperature and sputtering atmosphere, *J. Vac. Sci. Technol. A* **4**, 2701–2705 (1986).

3. W. D. Munz, Titanium aluminium nitride films—A new alternative to TiN coatings, *J. Vac. Sci. Technol. A* **4**, 2717–2725 (1986).
4. O. Knotek, R. Elsing, M. Atzor, and H. G. Prengel, The influence of the composition and coating parameters of PVD Ti-Al-V(C,N) films on abrasive and adhesive wear of coated cemented carbides, *Wear* **133**, 189–198 (1989).
5. O. Knotek and T. Leyendecker, On the structure of (Ti,Al)N-PVD coatings, *J. Solid State Chem.* **70**, 318–322 (1987).
6. O. Knotek, W. D. Munz, and T. Leyendecker, Industrial deposition of binary, ternary and quaternary nitrides of titanium, zirconium and aluminium, *J. Vac. Sci. Technol. A* **5**, 2173–2179 (1987).
7. H. Jehn, S. Hofmann, and W. D. Munz, Surface and interface characterization of heat-treated (Ti,Al)N coatings on high-speed steel substrates, *Thin Solid Films* **153**, 45–53 (1987).
8. G. Hakansson, J. E. Sundgren, D. Mcintyre, J. E. Greene, and W. D. Munz, Microstructure and physical properties of polycrystalline metastable $Ti_{0.5}Al_{0.5}N$ alloys grown by dc magnetron sputter deposition, *Thin Solid Films* **153**, 55–65 (1987).
9. O. Knotek, M. Bohmer, T. Leyendecker, and F. Jungblut, The structure and composition of Ti-Zr-N, Ti-Al-Zr-N and Ti-Al-V-N coatings, *Mater. Sci. Eng. A* **106**, 481–488 (1988).
10. O. Knotek, M. Atzor, and H. G. Prengel, On reactively sputtered Ti-Al-V carbonitrides, *Surf. Coat. Technol.* **36**, 265–273 (1988).
11. H. Jehn, S. Hofmann, and W. D. Munz, (Ti,Al)N coatings—An example of ternary nitrides hard coatings, *Metall. Trans.* **42**, 658–669 (1988).
12. O. Knotek and A. Barinami, On spinoidal decomposition in magnetron sputtered (Ti,Zr) nitride and carbide thin films, *Thin Solid Films* **174**, 51–56 (1989).
13. T. Suzuki, D. Huang, and Y. Ikuhara, Microstructures and grain boundaries of (Ti,Al)N films, *Surf. Coat. Technol.* **107**, 41–47 (1998).
14. Y. Makino and S. Miyake, Structural change and properties of pseudobinary nitrides containing AlN, *Trans. JWRI* **30**, 39–43 (2001).
15. J. Y. Rauch, C. Rousselot, and N. Martin, Structure and composition of $Ti_xAl_{1-x}N$ thin films sputter deposited using a composite metallic target, *Surf. Coat. Technol.* **157**, 138–143 (2002).
16. S. H. Lee, J. W. Lim, D. K. Lee, Y. H. Han, and J. J. Lee, A study on the characteristics of $(Ti_{1-x}Al_x)N$ coatings deposited by plasma-enhanced chemical vapour deposition after heat treatment, *Surf. Coat. Technol.* **169**, 371–374 (2003).
17. M. Hirai, T. Suzuki, H. Suematsu, W. Jiang, and K. Yatsui, Mechanism of hardening in Cr-Al-N-O thin films prepared by pulsed laser deposition, *J. Vac. Sci. Technol. A* **21**, 947–954 (2003).
18. U. Wahlstrom, L. Hultman, J.-E. Sundgren, F. Adibi, I. Petrov, and J. E. Greene, Crystal growth and microstructure of polycrystalline $Ti_{1-x}Al_xN$ alloy films deposited by ultra-high-vacuum dual-target magnetron sputtering, *Thin Solid Films* **235**, 62–70 (1993).
19. S. Inamura, K. Nobugai, and F. Kanamaru, The preparation of NaCl-type $Ti_{1-x}Al_xN$ solid – solution, *J. Solid State Chem.* **68**, 124–127 (1987).
20. N. Yanase, K. Sano, K. Abe, and T. Kawakubo, Epitaxial growth of $Ti_{1-x}Al_xN$ buffer layer for a ferroelectric (Ba, Sr)TiO_3 capacitor on Si substrate, *Jpn. J. Appl. Phys. Part 2* **37**, L151–L153 (1998).
21. K. H. Kim and S. H. Lee, Comparative studies of TiN and $Ti_{1-x}Al_xN$ by plasma-assisted chemical vapor deposition using a $TiCl_4/AlCl_3/N_2/H_2$/Ar gas mixture, *Thin Solid Films* **283**, 165–170 (1996).
22. A. Kimura, H. Hasegawa, K. Yamada, and T. Susuki, Effects of Al content on hardness, lattice parameter and microstructure of $Ti_{1-x}Al_xN$ films, *Surf. Coat. Technol.* **120**, 438–441 (1999).
23. T. Ikeda and H. Satoh, Phase formation and characterization of hard coatings in the Ti-Al-N system prepared by the cathodic arc ion plating method, *Thin Solid Films* **195**, 99–110 (1991).
24. Y. Matsui, M. Hiratani, Y. Nakamura, I. Asano, and F. Yano, Formation and oxidation properties of $(Ti_{1-x}Al_x)N$ thin films prepared by dc reactive sputtering, *J. Vac. Sci. Technol. A* **20**, 605–611 (2002).

25. A. Kimura, M. Kawate, H. Hasegawa, and T. Suzuki, Anisotropic lattice expansion and shrinkage of hexagonal TiAlN and CrAlN films, *Surf. Coat. Technol.* **169**, 367–370 (2003).
26. Y. Makino, Application of band parameters to materials design, *ISIJ Int.* **38**, 925–934 (1998).
27. F. Adibi, I. Petrov, L. Hultman, U. Wahlstrom, T. Shimizu, D. McIntyre, J. E. Greene, and J. E. Sundgren, Defect structure and phase-transitions in epitaxial metastable cubic $Ti_{0.5}Al_{0.5}N$ alloys grown on MgO (001) by ultra-high-vacuum magnetron sputter deposition, *J. Appl. Phys.* **69**, 6437–6450 (1991).
28. A. Horling, L. Hultman, M. Oden, J. Sjolen, and L. Karlsson, Thermal stability of arc evaporated high aluminum-content $Ti_{1-x}Al_xN$ thin film, *J. Vac. Sci. Technol. A* **20**, 1815–1823 (2002).
29. Y. Yamabe-Mitarai and H. Aoki, Solid-solution hardening of Ir by Pt and Ni, *Mater. Lett.* **56**, 781–786 (2002).
30. H. Suematsu, K. Yatsui, and T. Yano, The relationship between the hardness and the point-defect-concentration in neutron-irradiated MgO center dot $3.0Al_2O_3$ single crystals, *Jpn. J. Appl. Phys., Part 1* **40**, 1097–1099 (2001).
31. T. Iseki, M. Tezuka, C. S. Kim, T. Suzuki, H. Suematsu, and T. Yano, Hardening by point-defects in neutron-irradiated AlN and SiC, *J. Nucl. Sci. Technol.* **30**, 68–77 (1993).
32. M. Zhou, Y. Makino, M. Nose, and K. Nogi, Phase transition and properties of Ti-Al-N thin films prepared by r.f.-plasma assisted magnetron sputtering, *Thin Solid Films* **339**, 203–208 (1999).
33. J. C. Phillips, Ionicity of chemical bond in crystals, *Rev. Mod. Phys.* **42**, 317–356 (1970).
34. S. Veprek, S. Reiprich, and S. H. Li, Superhard nanocrystalline composite-materials—The TiN/Si_3N_4 system, *Appl. Phys. Lett.* **66**, 2640–2642 (1995).
35. O. Banakh, P. E. Schmid, R. Sanjines, and F. Levy, High temperature oxidation resistance of $Cr_{1-x}Al_xN$ thin films deposited by reactive magnetron sputtering, *Surf. Coat. Technol.* **57**, 163–164 (2003).
36. P. Hones, R. Sanjines, and F. Levy, Sputter deposited chromium nitride based ternary compounds for hard coatings, *Thin Solid Films* **332**, 240–246 (1998).
37. P. Hones, R. Sanjines, F. Levy, and O. Shojaei, Electronic structure and mechanical properties of resistant coatings: The chromium molybdenum nitride system, *J. Vac. Sci. Technol. A* **17**, 1024–1030 (1999).
38. M. Cekada, P. Panjan, B. Navinsek, and F. Cvelbar, Characterization of (Cr,Ta)N hard coatings reactively sputtered at low temperature, *Vacuum* **52**, 461–467 (1999).
39. H. Hasegawa, A. Kimura, and T. Suzuki, $Ti_{1-x}Al_xN$, $Ti_{1-x}Zr_xN$ and $Ti_{1-x}Cr_xN$ films synthesized by the AIP method, *Surf. Coat. Technol.* **132**, 76–79 (2000).
40. L. A. Donohue, J. Cawley, and J. S. Brooks, Deposition and characterization of arc-bond sputter Ti_xZr_yN coatings from pure metallic and segmented targets, *Surf. Coat. Technol.* **72**, 128–138 (1995).
41. J. H. Moser, F. Tian, O. Haller, D. B. Bergstrom, I. Petrov, J. E. Greene, and C. Wiemer, Single-phase polycrystalline $Ti_{1-x}W_xN$ alloys ($0 \leq x \leq 0.7$) grown by UHV reactive magnetron sputtering: Microstructure and physical properties, *Thin Solid Films* **253**, 445–450 (1994).
42. E. Clementi and D. L. Raimondi, Atomic screening constants from scf functions, *J. Chem. Phys.* **38**, 2686–2689 (1963).
43. O. Knotek, F. Loffler, and G. Kramer, Arc-deposited Ti-Zr-N coatings on cemented carbides for use in interrupted cutting, *Surf. Coat. Technol.* **49**, 325–329 (1991).
44. R. L. Boxman, V. N. Zhitomirsky, I. Grimberg, L. Rapoport, S. Goldsmith, and B. Z. Weiss, Structure and hardness of vacuum arc deposited multi-component nitride coatings of Ti, Zr and Nb, *Surf. Coat. Technol.* **125**, 257–262 (2000).
45. S. R. Saha, R. B. Inturi, and J. A. Barnard, Structural and mechanical characterization of Cr-Ta-N hard coatings prepared by reactive magnetron sputtering, *Surf. Coat. Technol.* **82**, 42–47 (1996).
46. X. Zeng, S. Zhang, and J. Hsieh, Development of graded Cr-Ti-N coatings, *Surf. Coat. Technol.* **102**, 108–112 (1998).
47. P. Hones, R. Consiglio, N. Randall, and F. Levy, Mechanical properties of hard chromium tungsten nitride coatings, *Surf. Coat. Technol.* **125**, 179–184 (2000).

48. J. N. Tan and J. H. Hsieh, Deposition and characterization of (Nb,Cr) thin films by unbalanced magnetron sputtering, *Surf. Coat. Technol.* **167**, 154–160 (2003).
49. H. O. Pierson, *Handbook of Refractory Carbides and Nitrides—Properties, Characteristics, Processing and Applications* (Noyes Publications, Westwood, NJ, 1996), Chaps. 9–13.
50. S. Veprek and S. Reiprich, A concept for the design of novel superhard coatings, *Thin Solid Films* **268**, 64–71 (1995).
51. S. Veprek, M. Haussmann, S. Reiprich, S. Li, and J. Dian, Novel thermodynamically stable and oxidation resistant superhard coating materials, *Surf. Coat. Technol.* **394**, 86–87 (1996).
52. G. Llauro, R. Hillel, and F. Sibieude, Elaboration and properties of CVD Ti-N-Si coatings, *Chem. Vap. Depos.* **4**, 247–252 (1998).
53. F. Vaz, L. Rebouta, P. Goudeau, J. Pacaud, H. Garem, J. P. Riviere, A. Cavaleiro, and E. Alves, Characterization of $Ti_{1-x}Si_xN$ nanocomposite films, *Surf. Coat. Technol.* **133**, 307–313 (2000).
54. T. Mae, M. Nose, M. Zhou, T. Nagae, and K. Shimamura, The effect of Si addition on the structure and mechanical properties of ZrN thin films deposited by an r.f. reactive sputtering method, *Surf. Coat. Technol.* **142**, 954–958 (2001).
55. W. J. Meng, X. D. Zhang, B. Shi, R. C. Tittsworth, L. E. Rehn, and P. M. Baldo, Microstructure and mechanical properties of Ti-Si-N coatings, *J. Mater. Res.* **17**, 2628–2632 (2002).
56. M. Nose, Y. Deguchi, T. Mae, E. Honbo, T. Nagae, and K. Nogi, Influence of sputtering conditions on the structure and properties of Ti-Si-N thin films prepared by r.f. reactive sputtering, *Surf. Coat. Technol.* **174**, 261–265 (2003).
57. P. Jedrzejowski, J. E. Klemberg-Sapieha, and L. Martinu, Relationship between the mechanical properties and the microstructure of nanocomposite $TiN/SiN_{1.3}$ coatings prepared by low temperature plasma enhanced chemical vapor deposition, *Thin Solid Films* **426**, 150–159 (2003).
58. E. Martinez, R. Sanjines, O. Banakh, and F. Levy, Electrical, optical and mechanical properties of sputtered CrNy and $Cr_{1-x}Si_xN_{1.02}$ thin films, *Thin Solid Films* **447–448**, 332–336 (2003).
59. H. Watanabe, Y. Sato, C. Nie, A. Ando, S. Ohtani, and N. Iwamoto, The mechanical properties and microstructure of Ti-Si-N nanocomposite films by ion plating, *Surf. Coat. Technol.* **169**, 452–455 (2003).
60. D. Ma, S. Ma, and K. Xu, Influence of Si content on nano-structured Ti-Si-N films coated by pulsed-d.c. plasma enhanced CVD, *Surf. Coat. Technol.* **184**, 182–187 (2004).
61. D. Pilloud, J. F. Pierson, A. P. Marques, and A. Cavaleiro, Structural changes in Zr-Si-N films versus their silicon content, *Surf. Coat. Technol.* **180–181**, 352–356 (2004).
62. S. Zhang, D. Sun, Y. Fu, and H. Du, Effect of sputtering target power on microstructure and mechanical properties of nanocomposite nc-TiN/α-SiN_x thin films, *Thin Solid Films* **447–448**, 462–4670 (2004).
63. S. Veprek, The search for novel, superhard materials, *J. Vac. Sci. Technol. A* **17**, 2401–2420 (1999).
64. S. Veprek and A. S. Argon, Towards the understanding of mechanical properties of super- and ultrahard nanocomposites, *J. Vac. Sci. Technol. B* **20**, 650–664 (2002).
65. D. S. Rickerby, Internal-stress and adherence of titanium nitride coatings, *J. Vac. Sci. Technol. A* **4**, 2809–2814 (1986).
66. V. Valvoda, R. Kuzel, R. Cerny, and J. Musil, Structure of TiN coatings deposited at relatively high rates and low temperatures by magnetron sputtering, *Thin Solid Films* **156**, 53–64 (1988).
67. L. Karlsson, L. Hultman, and J.-E. Sundgren, Influence of residual stresses on the mechanical properties of TiC_xN_{1-x} ($x = 0, 0.15, 0.45$) thin films deposited by arc evaporation, *Thin Solid Films* **371**, 167–177 (2000).
68. T. Y. Tsui, W. C. Oliver, and G. M. Pharr, Influence of stress on the measurement of mechanical properties using nanoindentation, Part I: Experimental studies in an aluminium alloy, *J. Mater. Res.* **11**, 752–759 (1996).
69. A. Bolshakov, W. C. Oliver, and G. M. Pharr, Influence of stress on the measurement of mechanical properties using nanoindentation, Part II: Finite element simulations, *J. Mater. Res.* **11**, 760–768 (1996).

70. C. Louro and A. Cavaleiro, Mechanical behaviour of amorphous W-Si-N sputtered films after thermal annealing at increasing temperatures, *Surf. Coat. Technol.* **123**, 192–198 (2000).
71. R. W. Siegel and G. E. Fougere, Mechanical properties of nanophase metals, *Nanostruct. Mater.* **6**, 205–216 (1995).
72. H. Hahn, P. Mondal, and K. A. Padmanabhan, Plastic deformation of nanocrystalline materials, *Nanostruct. Mater.* **9**, 603–606 (1997).
73. S. Veprek, A. Niederhofer, K. Moto, P. Nesladek, H. Mannling, and T. Bolom, Nanocomposites nc-TiN/α-Si_3N_4/α- and nc-$TiSi_2$ with hardness exceeding 100 GPa and high fracture toughness, *Mater. Res. Soc. Symp. Proc.* **581**, 321–326 (2000).
74. A. Niederhofer, T. Bolom, P. Nesladek, K. Moto, C. Eggs, D. S. Patil, and S. Veprek, The role of percolation threshold for the control of the hardness and thermal stability of super- and ultrahard nanocomposites, *Surf. Coat. Technol.* **146**, 183–188 (2001).
75. F. Vaz, L. Rebouta, Ph. Goudeau, T. Girardeau, J. Pacaud, J. P. Riviére, and A. Traverse, Structural transitions in hard Si-based TiN coatings: The effect of bias voltage and temperature, *Surf. Coat. Technol.* **146**, 274–279 (2001).
76. I. Goldfarb, J. Pelleg, L. Zevin, and N. Croituru, Lattice distortion in thin-films of IVB metal (Ti, Zr, HF) nitrides, *Thin Solid Films* **200**, 117–127 (1991).
77. J. S. Reid, E. Kolawa, R. P. Ruiz, M.-A. Nicolet, Evaluation of amorphous (Mo, Ta, W)-Si-N diffusion barriers for Si/Cu metallizations, *Thin Solid Films* **236**, 319–324 (1993).
78. E. Blanquet, A. M. Dutron, V. Ghetta, C. Bernard, and R. Madar, Evaluation of LPCVD Me-Si-N (Me = Ta, Ti, W, Re) diffusion barriers for Cu metallizations, *Microelectron. Eng.* **37**, 189–195 (1997).
79. T. Kacsich, E. Kolawa, J. P. Fleurial, T. Caillat, and M.-A. Nicolet, Films of Ni-7 at% V, Pd, Pt and Ta-Si-N as diffusion barriers for copper on Bi_1Te_3, *J. Phys. D: Appl. Phys.* **31**, 2406–2411 (1998).
80. Y.-J. Lee, B.-S. Suh, S.-K. Rha, and C.-O. Park, Structural and chemical stability of Ta-Si-N thin films between Si and Cu, *Thin Solid Films* **320**, 141–146 (1998).
81. M. T. Wang, M. H. Chuang, L. J. Chen, and M. C. Chen, Effects of composition and N_2 plasma treatment on the barrier effectiveness of chemically vapor deposited WSi_x films, *J. Vac. Sci. Technol. B* **18**, 1929–1936 (2000).
82. M.-A. Nicolet, Reactively sputtered ternary films of the type TM-Si-N and their properties (TM = early transition metal), *Vacuum* **59**, 716–720 (2000).
83. J. W. Nah, W. S. Choi, S. K. Hwang, and C. M. Lee, Chemical state of (Ta, Si)N reactively sputtered coating on a high speed steel substrate, *Surf. Coat. Technol.* **123**, 1–7 (2000).
84. M.-A. Nicolet and P. H. Giauque, Highly metastable amorphous or near-amorphous ternary films (mictamict alloys), *Microelectron. Eng.* **55**, 357–367 (2001).
85. J. Musil, I. Leipner, and M. Kolega, Nanocrystalline and nanocomposite CrCu and CrCu-N films prepared by magnetron sputtering, *Surf. Coat. Technol.* **115**, 32–37 (1999).
86. P. Zeman, R. Cerstvy, P. H. Mayrhofer, C. Mitterer, and J. Musil, Structure and properties of hard and superhard Zr-Cu-N nanocomposite coatings, *Mat. Sci. Eng. A* **289**, 189–197 (2000).
87. J. L. He, Y. Setsuhara, I. Shimizu, and S. Miyake, Structure refinement and hardness enhancement of titanium nitride films by addition of copper, *Surf. Coat. Technol.* **137**, 38–42 (2001).
88. T. de los Arcos, P. Oelhafen, U. Aebi, A. Hefti, M. Duggelin, D. Mathys, and R. Guggenheim, Preparation and characterization of TiN-Ag nanocomposite films, *Vacuum* **67**, 463–470 (2002).
89. J. G. Han, H. S. Myung, H. M. Lee, and L. R. Shaginyan, Microstructure and mechanical properties of Ti-Ag-N and Ti-Cr-N superhard nanostructured coatings, *Surf. Coat. Technol.* **174**, 738–743 (2003).
90. C. Louro and A. Cavaleiro, Hardness versus structure in W-Si-N sputtered coatings, *Surf. Coat. Technol.* **119**, 74–80 (1999).
91. A. Cavaleiro, B. Trindade, and M. T. Vieira, Deposition and characterization of fine-grained W-Ni-C/N ternary films, *Surf. Coat. Technol.* **116**, 944–948 (1999).

92. A. Cavaleiro and C. Louro, Nanocrystalline structure and hardness of thin films, *Vacuum* **64**, 211–218 (2002).
93. A. Cavaleiro, B. Trindade, and M. T. Vieira, Influence of Ti addition on the properties of W-Ti-C/N sputtered films, *Surf. Coat. Technol.* **174**, 68–75 (2003).
94. T. B. Massalski, H. Okamoto, P. R. Subramanian, and L. Kacprzak, *Binary Alloy Phase Diagrams*, 2nd edn, Vol. 3 (ASM International, Materials Park, OH, 1992).
95. O. Knotek and A. Schrey, in *Handbook of Thin Film Process Technology*, edited by D. A. Glocker and S. I. Shah (Institute of Physics Publishing, Bristol, 1995), Part X (Materials), Chap. X, 1 (Hard and Protective Materials), sub. chap X1.0 (Introduction).
96. E. Hegedus, J. Neugebauer, and M. Meszaros, Apparent reversibility of the β-W, α-W transformation, *Int. J. Refract. Met. Hard Mater.* **16**, 31–35 (1998).
97. H. J. Goldschmidt, *Interstitial Alloys* (Butterworth, London, 1967), Chap. 7.
98. K. Akitmoto and K. Watanable, Formation of W_xSi_{1-x} by plasma chemical vapor-deposition, *Appl. Phys. Lett.* **39**, 445–447 (1981).
99. R. E. Thomas, J. H. Perepenzko, and J. D. Wiley, *Materials Research Society, Symposium Proceedings*, Vol. 54 (Materials Research Society, Pittsburgh, PA, 1986).
100. R. E. Thomas, J. H. Perepenzko, and J. D. Wiley, Crystallization of sputter deposited amorphous metal thin-films, *Appl. Surf. Sci.* **26**, 534–541 (1986).
101. S. Takatani, N. Matsuoka, J. Shigeta, N. Hashimoto, and H. Nakashima, Thermal-stability of WSi_x/GAAS interface, *J. Appl. Phys.* **61**, 220–224 (1987).
102. A. G. Lahav, C. S. Wu, and F. A. Baiocchi, WSi_x refractory metallization for GAAS metal–semiconductor field-effect transistors, *J. Vac. Sci. Technol. B* **6**, 1785–1795 (1988).
103. S. Gedevanishvili and Z. A. Munir, The influence of an electric-field on the mechanism of combustion synthesis of tungsten silicides, *J. Mater. Res.* **10**, 2642–2647 (1995).
104. J. S. Reid, R. Y. Liu, P. M. Smoth, R. P. Ruiz, and M.-A. Nicolet, W-B-N diffusion-barriers for Si/Cu metallizations, *Thin Solid Films* **262**, 218–223 (1995).
105. K. K. Shih and D. B. Dove, Ti/Ti-N HF/HF-N and W/W-N multilayer films with high mechanical hardness, *Appl. Phys. Lett.* **61**, 654–656 (1992).
106. P. Juliet, A. Rouzaud, K. Aabadi, P. Monge-Cadet, and Y. Pauleau, Mechanical properties of hard W-C physically vapor deposited coatings in monolayer and multilayer configuration, *Thin Solid Films* **290**, 232–237 (1996).
107. A. Madan, Yun-yu Wang, S. A. Barnett, C. Engstrom, H. Ljungcrantz, L. Hultman, and M. Grimsditch, Enhanced mechanical hardness in epitaxial nonisostructural Mo/NbN and W/NbN superlattices, *J. Appl. Phys.* **84**, 776–785 (1998).
108. E. Harry, A. Rouzaud, P. Juliet, and Y. Pauleau, Adhesion and failure mechanisms of tungsten–carbon containing multilayered and graded coatings subjected to scratch tests, *Thin Solid Films* **342**, 207–213 (1999).
109. P. J. Rudnik, M. E. Graham, and W. D. Sproul, High rate reactive sputtering of MoN_x coatings, *Surf. Coat. Technol.* **49**, 293–297 (1991).
110. W. Herr and E. Broszeit, Effect of an annealing process on the tribological properties of sputtered hard coatings, *Surf. Coat. Technol.* **97**, 669–674 (1997).
111. C. Louro, *Behavior of the W-Si-N System in Function of the Silicon Content*, Ph.D. Thesis (University of Coimbra, Coimbra, Portugal, 2000). (in Portuguese)
112. M. T. Vieira, A. Cavaleiro, and B. Trindade, The effects of a third element on structure and properties of W-C/N, *Surf. Coat. Technol.* **151–152**, 495–504 (2002).
113. S. Ramos, *Production and Characterization of Ceramic/Metal Multilayer Coatings*, M.Sc. Thesis (University of Coimbra, Coimbra, Portugal, 1997). (in Portuguese)
114. H. Kimura and T. Masumoto, *Amorphous Metallic Alloys*, edited by F. E. Luborsky (Butterworths, London, 1983), Chap. 12.
115. R. W. Cahn and A. L. Greer, *Physical Metallurgy*, Vol. 2, edited by R. W. Cahn and P. Haasen (North Holland, Amsterdam, 1996), Chap. 19.
116. H. Leiste, U. Dambacher, S. Ulrich, and H. Holleck, Microstructure and properties of multilayer coatings with covalent bonded hard materials, *Surf. Coat. Technol.* **116**, 313–320 (1999).

117. C. Louro, A. Cavaleiro, and F. Montemor, How is the chemical bonding of W-Si-N sputtered coatings? *Surf. Coat. Technol.* **142**, 964–970 (2001).
118. A. Cavaleiro and P. Marques, Structural and mechanical properties of amorphous W-Si-N sputtered films after thermal annealing, *Thin Solid Films* **441**, 150–160 (2003).
119. A. Cavaleiro and P. Marques, Achievement of nanocrystalline structures after thermal annealing amorphous W-Si-N sputtered films, in *Nanostructures: Synthesis, Functional Properties and Applications*, *Proceedings of NATO Science Series*, Vol. 128, edited by T. Tsakalakos, I. A. Ovid'ko, and A. K. Vasudevan (Kluwer Academic Publishers, Dordrecht, The Netherlands, 2003).
120. S. K. Ghosh and T. K. Hatvar, Preparation and characterization of reactively sputtered silicon nitride thin films, *Thin Solid Films* **166**, 359–366 (1988).
121. F. C. Stedile, I. J. R. Baumvol, W. H. Scheirener, and F. L. Freire, Jr., Study on radio-frequency reactive sputtering deposition of silicon-nitride thin films, *J. Vac. Sci. Technol. A.* **10**, 462–467 (1992).
122. H. Schmidt, W. Gruber, G. Borchardt, M. Bruns, M. Rudolphi, and H. Baumann, Thermal stability and crystallization kinetics of sputtered amorphous Si_3N_4 films, *Thin Solid Films* **450**, 346–351 (2004).
123. H. J. Goldschmidt, *Interstitial Alloys* (Butterworth, London, 1967), Chap. 5.
124. A. Niederhofer, P. Nesladek, H. D. Mannling, K. Moto, S. Veprek, and M. Jilek, Structural properties, internal stress and thermal stability of nc-TiN/α-Si_3N_4, nc-TiN/$TiSi_x$ and nc-$(Ti_{1-y}Al_ySi_x)$N superhard nanocomposite coatings reaching the hardness of diamond, *Surf. Coat. Technol.* **120**, 173–178 (1999).
125. J.-E. Sundgren, Structure and properties of TiN coatings, *Thin Solid Films* **128**, 21–44 (1985).
126. K. Kuzel, Jr., R. Cerny, V. Valvoda, M. Blomberg, M. Merisalo, and S. Kadlec, Complex XRD microstructural studies of hard coatings applied to PVD-deposited TiN films, Part II: Transition from porous to compact films and microstructural inhomogeneity of the layers, *Thin Solid Films* **268**, 72–82 (1995).
127. R. A. Andrievski, Films of interstitial phases: Synthesis and properties, *J. Mater. Sci.* **32**, 4463–4484 (1997).
128. P. Yashar, S. A. Barnett, J. Rechner, and W. D. Sproul, Structure and mechanical properties of polycrystalline CrN/TiN superlattices, *J. Vac. Sci. Technol. A* **16**, 2913–2918 (1998).
129. L. R. Shaginyan, M. Misina, J. Zemek, J. Musil, F. Regent, and V. F. Britun, Composition, structure, microhardness and residual stress of W–Ti–N films deposited by reactive magnetron sputtering, *Thin Solid Films* **408**, 136–147 (2002).
130. M. K. Hibbs, B. O. Johansson, J.-E. Sundgren, and U. Helmersson, Effects of substrate temperature and substrate material on the structure of reactively sputtered TiN films, *Thin Solid Films* **122**, 115–129 (1984).
131. M. K. Hibbs, J.-E. Sundgren, B. O. Johansson, and B. E. Jacobson, The microstructure of reactively sputtered Ti-N films containing the Ti_2N phase, *Acta Metall.* **33**, 797–803 (1985).
132. H. Ljungcrantz, M. Odén, L. Hultman, J. E. Greene, and J.-E. Sundgren, Nanoidentation studies of single-crystal (001)-, (011)- and (111)-oriented TiN layers on MgO, *J. Appl. Phys.* **80**, 6725–6733 (1996).
133. J. G. Fleming, E. Roherty-Osmun, P. M. Smith, J. S. Custer, Y.-D. Kim, T. Kacsch, M.-A. Nicolet, and C. J. Galewski, Growth and properties of W-Si-N diffusion barriers deposited by chemical vapour deposition, *Thin Solid Films* **320**, 10–14 (1998).
134. O. H. Gokce, S. Amin, N. M. Ravindra, D. J. Szostak, R. J. Paff, J. G. Fleming, C. J. Galewski, J. Shallenberger, and R. Eby, Effects of annealing on X-ray amorphous CVD W-Si-N barrier layer materials, *Thin Solid Films* **353**, 149–156 (1999).
135. C. U. Pinnow, M. Bicker, U. Geyer, S. Schneider, and G. Goerigk, Decomposition and nanocrystallization in reactively sputtered amorphous Ta-Si-N thin films, *J. Appl. Phys.* **90**, 1986–1991 (2001).
136. L. Ferreira, C. Louro, A. Cavaleiro, and B. Trindade, The influence of heat treatment on the structure of (W, Si)N sputtered films, *Key Eng. Mater.* **230**, 640–643 (2002).

137. C. Louro, F. Teixeira-Dias, L. F. Menezes, and A. Cavaleiro, Effect of the substrate thermal expansion coefficient on the thermal residual stresses in W-Si-N sputtered films, *Key Eng. Mater.* **230**, 513–516 (2002).
138. C. Louro, A. Cavaleiro, S. Dub, P. Smid, J. Musil, and J. Vlcek, The depth profile analysis of W-Si-N coatings after thermal annealing, *Surf. Coat. Technol.* **161**, 111–119 (2002).
139. M. C. Gaspar, A. Ramalho, and A. Cavaleiro, Effect of the counterface material on the fretting behaviour of sputtered W-Si-N coatings, *Wear* **255**, 276–286 (2003).
140. M. Zhou, M. Nose, Y. Deguchi, T. Mae, and K. Nogi, Influence of sputtering conditions on microstructure and mechanical properties of Zr-Si-N films prepared by radio-frequency-reactive sputtering, *J. Vac. Sci. Technol. A* **21**, 1791–1795 (2003).
141. H. Zeman, J. Musil, and P. Zeman, Physical and mechanical properties of sputtered Ta-Si-N films with a high ($\geq$40 at %) content of Si, *J. Vac. Sci. Technol. A* **22**, 646–649 (2004).
142. C. Louro, Hardness evaluation of W-Si-N sputtered coatings after thermal degradation, *Surf. Coat. Technol.* **180**, 544–550 (2004).
143. C. Louro and A. Cavaleiro, Thermal behaviour of hard nanocomposite coatings of W-Si-N system in oxidant and protective atmospheres, *Surf. Coat. Technol.* accepted for publication.
144. J. Rivas and M. A. Lopez-Quintela, *Nanocrystalline and Nanoscale Materials* (World Scientific, Singapore, 1998).
145. M. G. Scott, Crystallization, in *Amorphous Metallic Alloys*, edited by F. E. Luborsky (Butterworths Monographs Materials, London, 1983), Chap. 10.
146. X. Sun, J. S. Reid, E. Kolawa, and M.-A. Nicolet, Reactively sputtered Ti-Si-N films, Part I: Physical properties, *J. Appl. Phys.* **81**, 656–663 (1997).
147. A.-M. Dutron, E. Blanquet, V. Ghetta, R. Madar, and C. Bernard, Morphology and thermal stability of Me-Si-N (Me = Re, W, Ta) for microelectronics, *J. Phys. IV* **5**, 1141–1148 (1995).
148. A. Bendeddouche, R. Berjoan, E. Bêche, and R. Hillel, Hardness and stiffness of amorphous SiC_xN_y chemical vapor deposited coatings, *Surf. Coat. Technol.* **111**, 184–190 (1999).
149. A. Oliveira, A. Cavaleiro, and M. T. Vieira, Production and characterization of Si-N films obtained by r.f. magnetron sputtering, *Surf. Coat. Technol.* **60**, 463–467 (1993).
150. Y. Hirohata, N. Shimamoto, T. Hino, T. Yamashima, and K. Yabe, Properties of silicon nitride films prepared by magnetron sputtering, *Thin Solid Films* **253**, 425–429 (1991).
151. R. Riedel and M. Seher, Crystallization behaviour of amorphous silicon nitride, *J. Eur. Ceram. Soc.* **7**, 21–25 (1991).
152. A. Cavaleiro, A. P. Marques, V. Fernandes, N. J. M. Carvalho, and J. Th. De Hosson, Evolution of the structure, residual stresses and mechanical properties of W-Si-N coatings after thermal annealing, *J. Mater. Res.* **20**, 1356–1368 (2005).
153. A. Oliveira, *Sputtering as Deposition Technique for the Production of Silicon Nitride Coatings*, M.Sc. Thesis (University of Coimbra, Coimbra, Portugal, 1995). (in Portuguese)
154. A. Cavaleiro and M. T. Vieira, Evaluation of the hardness of sputtered W-C-Co thin films, *Surf. Eng.* **10**, 147–151 (1994).
155. M. Ostling and C. Zaring, Mechanical properties of TM silicides, in *Properties of Metal Silicides*, edited by K. Maex and M. van Rossum (Leuven, Belgium, 1995), Chap. 1.2.
156. T. Masumoto and R. Maddin, Mechanical properties of palladium 20 a/o silicon alloy quenched from the liquid state, *Acta Metall.* **19**, 725–741 (1971).
157. H. S. Chen and C. C. Lo, Structure relaxations and hardness of metallic glasses, in *Rapidly Quenched Metals II*, Vol. 1, edited by N. J. Grant and B. C. Giessen (Massachusetts Institute of Technology Press, Boston, 1976).
158. A. Cavaleiro, C. Louro, and A. P. Marques, The effect of the substrate on the annealing behaviour of W-Si-N sputtered films, *Presentation B3-1-3 at ICMCTF 2002*, 22–26 April 2002, San Diego, CA, 2002.
159. E. Quesnel, Y. Pauleau, P. Monge-Cadet, and M. Brun, Tungsten and tungsten-carbon PVD multilayered structures as erosion-resistant coatings, *Surf. Coat. Technol.* **62**, 474–479 (1993).

8

The Influence of the Addition of a Third Element on the Structure and Mechanical Properties of Transition-Metal-Based Nanostructured Hard Films: Part II—Carbides

Bruno Trindade, Albano Cavaleiro, and Maria Teresa Vieira

ICEMS, Mechanical Engineering Department, Faculty of Sciences and Technology, University of Coimbra, Coimbra, Portugal

1. INTRODUCTION

In the last few decades, the research undertaken in the area of materials engineering has always aimed at conceptualizing and developing "new materials" with properties required for specific technologies. The technological evolution in the area of thin film deposition allowed obtaining materials with metastable structures (nanocrystalline or amorphous) with unique physical–chemical properties suitable for industrial applications in high-speed machining, tooling, and wear applications. An example of this is the development of transition metal–metalloid-based materials for applications requiring high hardness and good wear resistance.

The designing of advanced hard coatings, such as nanostructured or amorphous coatings, nanocomposite coatings, or nanoscale multilayer coatings, must take into account several factors, depending on the chemical composition of the coating, the substrate material, the deposition technique, and the processing parameters. In terms of chemical composition, three main approaches have been adopted for the synthesis of hard coatings for mechanical applications: (i) deposition of metastable transition metal carbide or nitride (hereafter T_M-C or T_M-N, respectively) coatings, with or without substitutional or interstitial alloying elements;

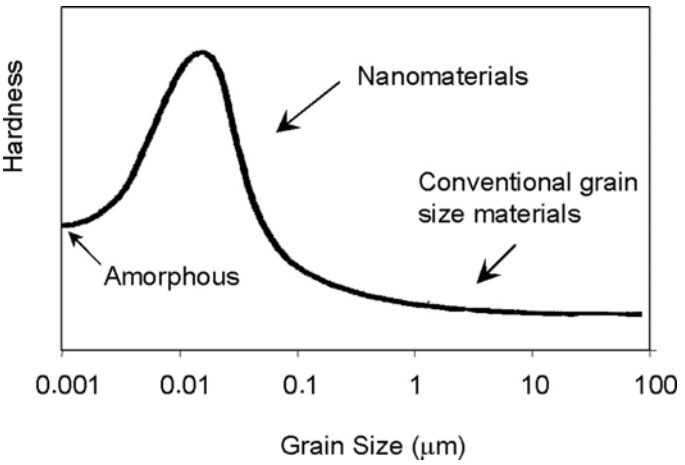

FIGURE 8.1. Hardness of a material as a function of the grain size.[1]

(ii) production of multilayer coatings based on the same materials with layers of nanometric size; and (iii) nanocomposite coatings formed by nanocrystalline and amorphous phases in which the nanocrystalline phase (usually a transition metal carbide or nitride) is embedded in an amorphous phase as diamond-like carbon (DLC), carbon nitride, or other material with high hardness and Young's modulus. Depending on their hardness, these coatings are classified as hard materials (20–40 GPa), superhard materials (40–80 GPa), and ultrahard materials (>80 GPa).

The addition of a transition metal to a metal–carbon binary system can play an important role in modifying its degree of structural order and consequently its mechanical properties, e.g., hardness (Fig. 8.1). With a decrease in grain size down to ≈10 nm, the multiplication and mobility of the dislocations are hindered and the hardness of materials increases according to the "Hall–Petch" relationship. For lower values, a reduction in grain size implies a decrease in strength due to the existence of a huge amount of defects in the grain boundaries, which allow the fast diffusion of atoms and vacancies under stress (grain boundary sliding).[2,3] Therefore, in order to obtain superhard materials, these phenomena must be avoided, i.e., dislocation movement and grain boundary sliding, as well as plastic deformation, must not occur. This is the case of recently obtained nitride-based films by Veprek *et al*.[4,5] in which the authors claimed the production of superhard nanocomposites (H = 50–80 GPa) formed by nanograins of titanium nitride involved with amorphous Si-N and Ti-N phases in grain boundaries.

To obtain enhanced hardness, the nanocrystalline phase must be below 10 nm, while the amorphous phase involving the nanocrystals must be maintained at only a few atomic bond lengths.[6] Apparently, the more complex the system is, in terms of number of different phases, the higher is the hardness of the system. Veprek *et al*. claimed the production of an ultrahard nanocomposite formed mainly by nc-TiN/a-Si_3N_4, with hardness of 105 GPa.[7] Other nanocomposite hard coatings include

TiN–TiB_2,[8] (Ti,Si,Al)N,[9] WC–TiAlN,[10] nc-TiC/a-C (with or without hydrogen),[11] as well as other metal nitride and carbide/boride systems. These last two papers concern the production of nanocomposites based on hard transition metal carbides. Voevodin *et al.*[11] embedded a TiC nanocrystalline phase in a DLC matrix and obtained a nanocomposite material with hardness of 32 GPa. The same matrix was used by Zhang *et al.*[12] to synthesize superhard nanocomposites ($H = 40$ GPa), with 8–15 nm TiCrCN crystals as main phase.

The segregation of a hard phase to grain boundaries gives rise to a strengthening effect and stops grain growth, which means a significant increase of hardness and other mechanical properties such as tensile strength or elastic modulus. However, the same is not true for toughness, and most of the researchers realized that the increase of hardness of these superhard materials occurred to the detriment of their toughness. In fact, it is necessary to have a certain degree of dislocation movement and grain boundary sliding to obtain relatively tough materials. One of the possibilities for overcoming this problem is to design a nanocomposite material that has multiphase structures with interfaces with high cohesive strength, i.e., the combination of two or more nanocrystalline/amorphous phases with complex boundaries to accommodate coherent strain. This can be achieved by the codeposition of a high-strength amorphous phase as matrix and a hard transition metal nitride/carbide (see, e.g., Refs. 7, 11, and 13), or by the codeposition process of two metals and a metalloid element (N or C) in which one of the metals is converted in nitride/carbide (superhard phase) and the other forms a ductile phase,[14] thus improving toughness. Transition metal carbides such as Ti-C, W-C, and Zr-C are probably the most extensively studied with high hardness values, making them attractive materials for wear-resistant coatings. TiC has the highest hardness of the transition metal carbides at room temperature (28–30 GPa),[15] although this is not true at elevated temperatures, where WC maintains a higher hardness.[15,16] These carbides have been obtained by sputter deposition doped with a third element, with two objectives in mind: (i) to increase toughness—in this case a group VIII metal, such as cobalt,[14,16–21] iron,[14,22,23] both iron and cobalt,[14,24,25] or nickel,[14,26,27] has been used as the addition element; and (ii) to increase hardness and structural stability with temperature—systems W-Ti-C[28–32] and Ti-Mo-C[28] have been obtained by either multilayer deposition of the constituent carbides or codeposition with two targets in a reactive or nonreactive atmosphere. In a recent paper on the influence of titanium on the properties of W-Ti-C/N sputtered films, Cavaleiro *et al.*[29] deposited various thin films by dc reactive magnetron sputtering from W-Ti targets with 0, 10, 20, and 30 wt% Ti. The results showed different compositional dependencies of the structure and grain size of the films. The binary W-Ti and the ternary W-Ti-C/N films with low and medium C/N contents were formed by a metastable solid solution of Ti in the α-W phase. W-Ti-C films with high carbon contents were formed by a metastable fcc $(Ti,W)C_{1-x}$ phase. No amorphous phases were detected in this ternary system. The phase formation in sputter-deposited TiMo-C and Ti-W-C thin films obtained by dual carbide targets (TiC/Mo_2C and TiC/WC) was studied by Koutzaki *et al.*[28] The authors concluded that the ternary Ti-Mo-C films with their compositions having 20.4–80.8% Mo were formed by a solid

solution of Mo in TiC with a B1 crystal structure and a (111) preferred orientation. Films with 86 and 91 at% Mo had multiphase structures of (Ti,Mo)C, Mo_3C_2, and Mo_2C. In relation to the Ti-W-C system, a single phase was obtained for all the films consisting of a (Ti,W)C solid solution. No amorphous phases were detected in these systems.

2. AMORPHOUS CARBIDE THIN FILMS DEPOSITED BY SPUTTERING

During sputtering, the atoms condensing in an intermixed state try to find a stable configuration with a low free energy of formation. Structural order in a thin film results largely from the mobility of the adatoms. The very high cooling rates attained during sputtering ($\approx 10^8$°C/s)[33] do not give the adatoms time to organize themselves in stable structures, giving rise to structures with a reduced structural order (nanocrystalline or amorphous) and with higher solubility domains than those indicated in the literature. They also have chemical compositions and physical, chemical, and mechanical properties that are impossible to reach by conventional techniques.

The first authors to claim the formation of amorphous structures in sputtered carbide-based thin films were Wickersham *et al.*[34] in 1981. These authors synthesized some W-Co-C coatings by reactive sputtering for satellite thermoelectric generator walls and found that their structure was dependent on the partial pressure of the C_2H_2 reactive gas, and became amorphous at high pressures. Since that work, a considerable number of scientific papers have been published concerning the production of amorphous T_M-C-based hard coatings (see, e.g., Refs. 16, 20–27, and 35–39) by means of different sputtering routes (e.g., reactive/nonreactive atmosphere, balance/unbalance, rf/dc, diode/magnetron, etc.) and deposition parameters (e.g., substrate bias, deposition pressure, specific power target, etc.). These carbides are of great scientific and technological interest and have been used in applications requiring high hardness and good wear resistance. There are mainly three ways to improve the performance of a hard material: (i) to vary the concentration of the nonmetallic element in the carbide (e.g., MC_{1-x}); (ii) to introduce a second substitutional element in the metal lattice of the compound phase; and (iii) to add another metal with great affinity for carbon. This may introduce variations in the structure of the thin films, with the formation of amorphous or nanocrystalline phases.

3. STRUCTURAL MODELS FOR PREDICTION OF AMORPHOUS PHASE FORMATION

Distinguishing the transition between the amorphous and nanocrystalline structural states is complex, because there is some kind of structural range order in

the amorphous materials, which extends over a maximum length scale of 2 nm, intermediate between the short-range order of liquids and the long-range order of crystals. The determination of intermediate-range order in amorphous materials remains fundamental, yet is still an unresolved issue.[40] Most of the researchers that deal with these kinds of materials consider that the structural range order of an amorphous material is lower than 2 nm. Below this value the material may be present in low-range order (LRO) or medium-range order (MRO). The value of 0.5 nm has been claimed as the frontier for these two states. More recently, different definitions can be found in literature. Inoue[41] claims that a material formed by particles/grains with sizes ranging from 1 to 100 nm, with common boundaries or embedded in an amorphous matrix-forming nanocomposite, is nanocrystalline. This means that there is some controversy surrounding the definition range order between 1 and 2 nm. In this chapter, a material formed by crystallites of about 2 nm will be called amorphous.

Various models have been proposed to predict the range of composition of amorphous transition metal alloys, based on information extracted from phase diagrams, thermodynamic information for equilibrium states, differences in sizes of the constituent elements, or the enthalpy of mixing. In 1979, Gaskell[42] proposed the first model for amorphous transition metal–metalloid systems in which groups of atoms—coordination polyhedra with defined local geometry—are packed randomly in a dense, three-dimensional array. Diffraction results showed that the average coordination number of the metalloid element was lower than that of the metal, with no interstitial–interstitial first neighbors. Based on these results, Gaskell suggested that the local order around the metalloid element could be described by trigonal prismatic polyhedra. The validity of this model was checked with the data available for the Pd-Si alloys and according to the author provides a good description of the structural properties of the amorphous alloys. Three years later, Giessen[43] proposed an amorphization criterion based on the heat of formation and atomic size ratio, where two elements will form an amorphous structure if they have small size ratios (i.e., large size differences) and high negative heat of formation. At about the same time, Massalski[44] and Whang[45,46] proposed other models derived from information extracted from phase diagrams, where the approach was based on thermodynamic information for equilibrium states. Between 1984 and 1987, some authors (see, e.g., Refs. 47 and 48) claimed that amorphization is related to the differences in size of the constituent elements. Egami and Waseda[47] proposed a correlation between the glass formability and the extent of the atomic size mismatch of the constituent atoms in several binary alloys given by

$$C_{\min} = 0.1/|(R_B/R_A)^3 - 1| \tag{8.1}$$

where $C_{\min}$ is the minimum concentration of a solute element needed to amorphize the matrix, and R_A and R_B are the radii of a host atom A and a solute atom B, respectively. This equation was derived on the assumption that the alloying elements substitute for the matrix atoms at a regular lattice site. In this case, the

concentration of the solute required to destabilize the crystal lattice decreased as the difference in atomic size between the two elements increased. This is because a larger strain is introduced per atom for smaller substitutional atoms. In 1988, Van der Kolk *et al.*[49] reviewed the various methods for prediction of amorphous-forming ability and concluded that the effect of atomic size alone was not sufficient to describe the formation of amorphous structures and that the crystal structure of the constituent elements should also be taken into account. Moreover, they referred to the existence of several examples of amorphous phases constituted by elements with either positive heat of formation or atomic ratios close to unity. According to these authors,[49] the range of relatively stable amorphous phases is determined by three factors. One is the elastic mismatch energy, whose contribution in the case of systems with large size mismatches is important; another factor, which may favor the formation of an amorphous phase, is the structural contribution. A large positive structural contribution to the enthalpy is expected for systems that consist of two elements, one with a number of valence electrons per atom $Z = 5$ or 6 and the other with $Z = 8$ or 9. For alloys in which one of the constituents has five or six valence electrons and the other has eight or nine, the structural term tends to raise the enthalpy of the solid solution relative to the enthalpy of the amorphous phase. Consequently, a wide composition range is observed where amorphous phases are found, even when the size mismatch is insignificant. The third factor defines the difference in enthalpy between solid solution and the amorphous phase, i.e., the enthalpy of fusion minus the decrease in enthalpy caused by structural relaxation of the amorphous phase. Structural relaxation strongly favors the formation of amorphous phases. At the same time, Loeff *et al.*[50] developed a method for amorphous alloys, and their approach was based on the difference of atomic size and the average number of valence electrons. In 1990, Clements and Sinclair[51] introduced a classification of the metal–carbon systems according to the thermodynamic driving force for solid-state amorphization reactions, which was corrected for alloying effects. According to this criterion, various transition metal–carbon systems lie in a region associated with solid-state amorphization. In the 1990s, Zhang and Yu[52] proposed the rhomb unit structural model for amorphous structures. Recently, Inoue[41] proposed three empirical rules for achieving glass-forming ability (GFA) for metallic alloys, based on the multicomponents of the amorphous alloys with high GFA: (i) multicomponent systems containing more than three elements, (ii) significant difference in atomic ratios above about 12% among the main constituent elements, and (iii) negative heats of mixing among their elements. These authors summarized the reasons for achieving a high GFA for ternary systems in a schema (Fig. 8.2).

According to Inoue[41] the combination of these two factors (large atomic ratios and negative heats of mixing) leads to a high liquid–solid interfacial energy as well as the difficulty of atomic rearrangements giving rise to low atomic diffusivity and high viscosity.

All the referred models have some limitations and in some systems do not agree with the experimental observations. Besides this, there is a difference

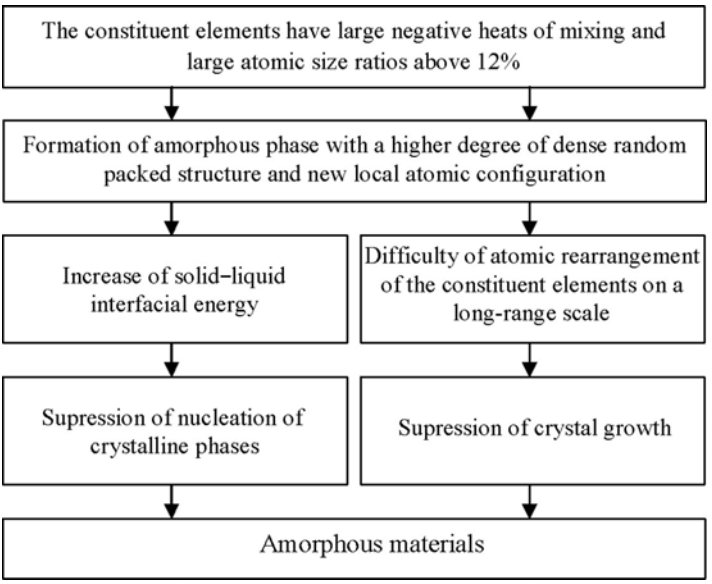

FIGURE 8.2. Reasons for achieving a high GFA in ternary alloy systems.[41]

between the predicted results and the experimental ones: they are smaller in the case of systems obtained by rapid quenching than in the case of systems obtained by vapor deposition (i.e., sputtering). One reason for this might be the different cooling rates induced by the various far-from-equilibrium processes (Table 8.1).

Recently, Senkov and Miracle[58] developed a topological approach based on analysis of atomic size distributions and applied it to multicomponent amorphous alloys with different GFAs. In this model, each alloying element in a specific alloy provides a data point where the atomic size is plotted versus elemental concentration. The curve obtained for all the elements of an alloy is called the atomic size distribution. According to the authors, the shapes of the curves distinguish between ordinary amorphous alloys with marginal GFA, i.e., alloys with a critical

TABLE 8.1. Departure from Equilibrium Achieved in Different Nonequilibrium Processing Techniques[53]

	Quenching rate (°C/s)	Departure from equilibrium (kJ/mol)	
	Ref. 54	Ref. 55	Refs. 56 and 57
Quenching	10^3	—	16
Rapid solidification	10^5–10^8	2–3	24
Mechanical alloying	—	30	30
Ion implantation	10^{12}	—	30
Vapor condensation	10^{12}	—	160

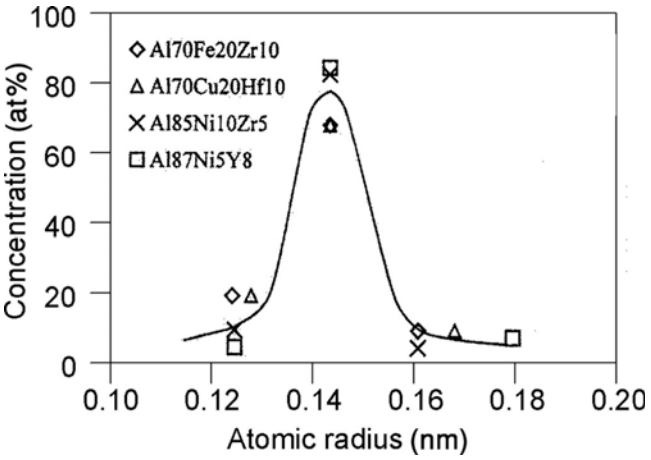

FIGURE 8.3. Atomic size distributions in Al-based ordinary amorphous alloys.[58] Critical cooling rates of 10^4–10^6°C/s.

cooling rate greater than 10^3°C/s, and bulk metallic glasses, i.e., materials with critical cooling rates lower than 10^3°C/s. Amorphous materials of the former case are typically ternary or high-order alloys with 60–90% of the base metal and a concentration of each alloying element higher than 5%. According to the author, at least one element is smaller and at least one is larger than the base element. This gives rise to atomic size distribution curves concaving downward (Fig. 8.3), which is the case of the Fe-, Ni-, and Al-based systems.

However, according to the same author, atomic size distributions of many bulk metallic glasses have completely different shape (concave upward) with a minimum at the intermediate atomic size (Fig. 8.4). In this case, the base element has the largest atomic size and the smallest atom often has the next-highest concentration (Pd-, La-, Nd-, Y-, and Sm-based systems).

Senkov and Miracle proposed a model to explain the concave upward shape of the atomic size distributions of these systems.[58] This model takes into account that all alloying elements in bulk amorphous are smaller than the matrix element, and that some of them are located in interstitial sites while others substitute for matrix atoms in a reference crystalline solid solution.

The interstitial and substitutional atoms attract each other and produce short-range-ordered atomic configurations that stabilize the amorphous state. If the alloying atom is much smaller than the base atom it tends to occupy interstitial positions in the lattice. Otherwise, it occupies substitutional positions. A critical feature is expected for alloy elements with a radius between about $0.6R_A$ and $0.85R_A$. It is likely that atoms in this size range partition between interstitial and substitutional sites. The distortions decrease if the size difference between the matrix and interstitial atoms increases, which is opposite to the case of substitutional atoms. The

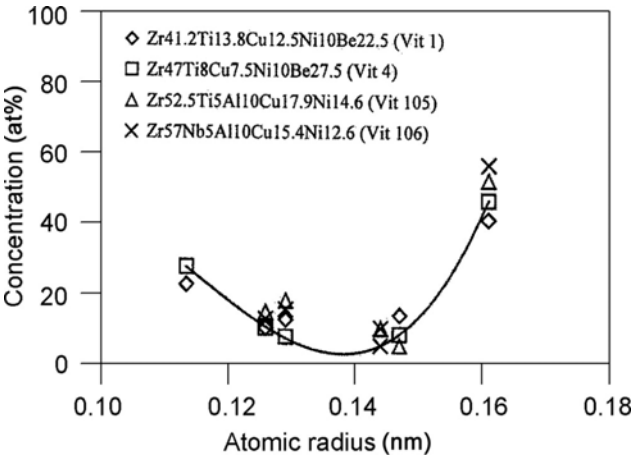

FIGURE 8.4. Atomic size distributions in Zr-based bulk amorphous alloys.[58] Critical cooling rates of ≈1–500°C/s.

authors concluded that a higher concentration of an interstitial atom is required in order to reach a critical internal stress for destabilization of the crystal lattice when the atomic size of the atom decreases relative to the size of the matrix atom, which is the opposite for the situation with substitutional atoms. Moreover, the interstitial atoms produce tensile strains, attract the substitutional atoms smaller than the matrix atoms, and repulse the substitutional atoms larger than those of the matrix. In the former case, dense and stable short-range-order atomic configurations may be produced, and these may stabilize the amorphous state. This can also explain why bulk metallic glasses containing large amount of interstitial elements do not generally contain solute elements with atomic sizes larger than the atomic size of the base element. This is the case with transition metal carbides, such as the well-known W-C, doped with group VIII metals, e.g., Co, Fe, or Ni in the form of bulk materials or as thin films for tribological applications.

4. AMORPHOUS PHASE FORMATION IN T_M-T_{M1}-C (T_M AND T_{M1} = TRANSITION METALS) SPUTTERED FILMS

4.1. T_M-Fe-C (T_M = Ti, V, W, Mo, Cr) Thin Films

Trindade and Vieira[59] have synthesized carbides of different groups of the periodic table (Ti-C, V-C, W-C, Mo-C, and Cr-C) by nonreactive sputtering from sintered targets with and without other T_M alloying elements (Fig. 8.5) in order to determine a general amorphization criterion for these very interesting technological materials.

The structure of the thin films was evaluated mainly by means of X-ray diffraction (XRD), scanning electron microscopy (SEM), transmission electron

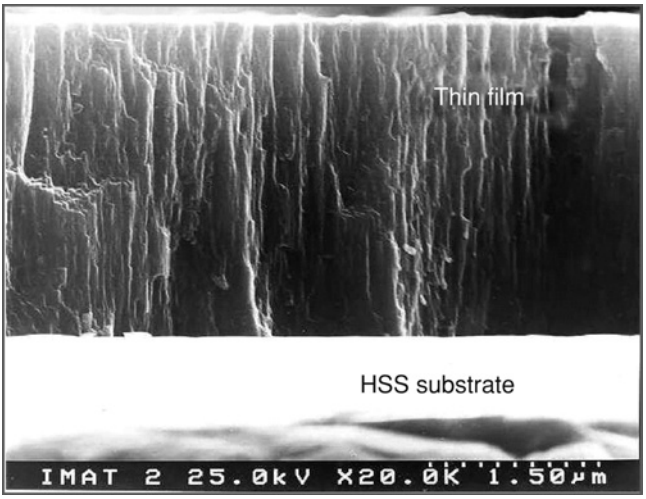

FIGURE 8.5. Cross-section morphology of a sputtered Mo-Fe-C thin film with 5 at% Fe, as a typical example of all the other T_M-T_{M1}-C films.

microscopy (TEM), extended X-ray absorption fine structure (EXAFS) and Mossbauer spectroscopy. The results were discussed as a function of the chemical composition of the films, atomic radii of the constituent elements, and the affinity of the T_M for carbon. The results showed that all but the Cr-C binary thin films are nanocrystalline (grain size <50 nm), formed by a NaCl-type face-centered cubic (fcc) structure (Figs. 8.6 and 8.7). The amorphous thin films are characterized by an XRD pattern with two very wide peaks (a stronger broad peak and a weaker

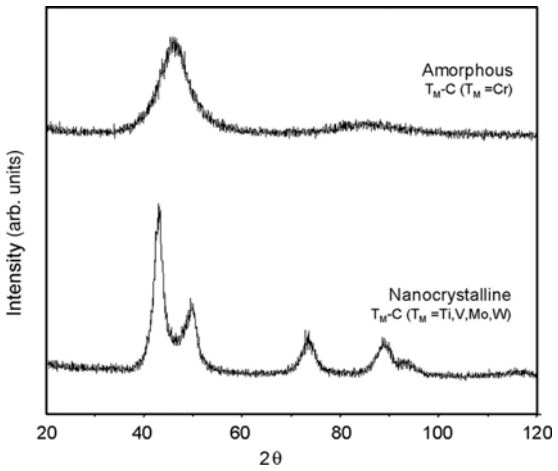

FIGURE 8.6. Typical XRD patterns of the binary sputtered T_M-C thin films.

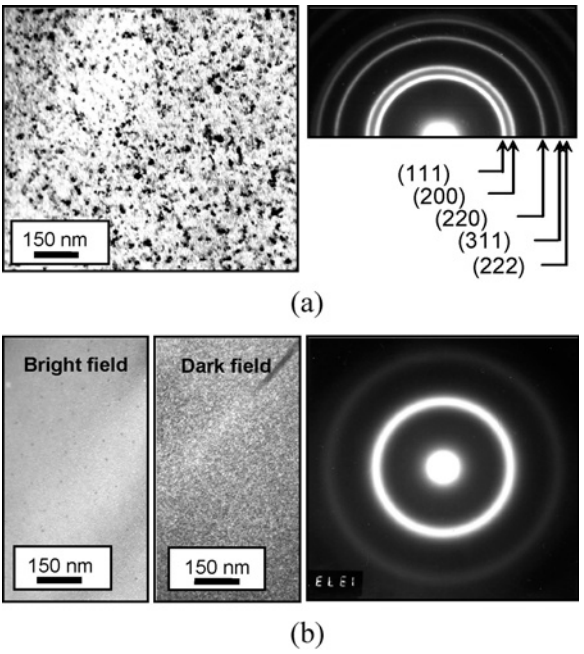

FIGURE 8.7. Typical TEM and SADP images of W-C-Co (a) nanocrystalline and (b) amorphous thin films.

subpeak) and low-contrast TEM images associated with diffuse and large electron diffraction rings. According to Sherrer's equation, the values of the full width at half-maximum intensity of the main XRD peak of the amorphous samples correspond to crystallites of about 2 nm. With a codeposition process of two metals and a metalloid element (carbon), the authors concluded that it was possible to significantly decrease the structural range order of these carbide base thin films with the introduction of a third element from group VIII, such as iron, cobalt, nickel, or even palladium. In their work concerning the modification of the structural order of transition metal–carbon systems by addition of a group VIII element, they demonstrated that iron influences the range of structural order of the thin films and forms amorphous structures as the iron content increases (Fig. 8.8). The iron content required for occurrence of this structure depends on the transition metal forming the carbide, and the percentage of iron increases as the affinity of the transition metal for carbon increases. The authors discussed the formation of amorphous structures in sputtered W-M1-C thin films in terms of the three parameters: (i) distortion of the MC_{1-x} (M = W, metal M1) lattice due to the difference between the atomic radii of the two metals; (ii) stability of the metal–carbon systems, which decreases from group IVA to group VIA of the periodic table; and (iii) the tendency of the systems to crystallize or not, in structures of the NaCl type. This structure has a high compactness, a high number of interstitial positions (which permits

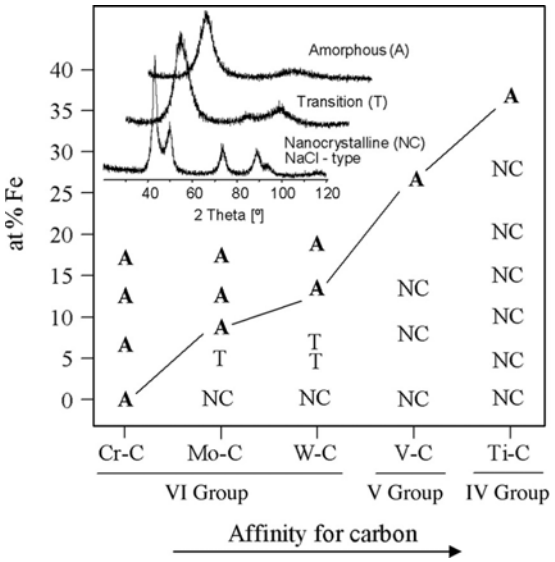

FIGURE 8.8. Influence of iron on the structure of the thin T M-Fe-C films.

structurally identical films, with very different chemical compositions, i.e., with extensive solubility domains), and strong cohesion of the metal–carbon covalent bonds. According to Cottrell,[60] the strong cohesion of the NaCl-type carbides of groups IVA–VIA is essentially due to strong covalent bonds between the p electrons of nonmetal atom and the d electrons of the transition metal (one in the s band, two in pdσ bonding orbitals, and one in pdπ bonding orbitals). Metals from groups IVA and VA have a strong affinity for carbon; i.e., in presence of this element they form carbides MC_{1-x}, with $x \rightarrow 1$. These include the face-centered cubic- and hexagonal close-packed (hcp) metal sublattices, each of which provides one octahedral site per M atom. These two structures have similar cohesive energies, same octahedral sites for C, and same M–M nearest neighbor coordination. However, for the M–M nearest neighbor spacing R, the distance between some C–C nearest neighbors is smaller in the hcp structure, which gives rises to an enhanced C–C repulsion in this structure and is disadvantageous relative to fcc-based one for higher carbon contents.

In the binary stoichiometric WC fcc carbide (metal of group VIA), not all the six valence electrons of tungsten ([Xe] $4f^{14}5d^{4}6s^{2}$) are used in the W–C bonds. In other words, there is a certain degree of W–W bonding in WC, and its contribution toward the cohesion of the carbide is minor when compared to the W–C bonding. For nonstoichiometric WC_{1-x}, there is more W–W bonding amongst the nearest neighbors and the density of states is reduced in proportion to the smaller fraction of carbon atoms. Moreover, the existence of vacant carbon sites gives rise to

weak bonds, with the second nearest W–W neighbors across the vacancies. This might be the reason why the fcc structure is the predominant structure of sputtered M-C thin films with carbon contents close to 50 at %. Thus, it is natural that the systems that have this type of structure have better conditions for becoming crystalline, even in a metastable state. With the exception of Cr-C system, the fcc NaCl-type phase exists in all the phase diagrams of the M-C systems studied by Trindade and Vieira,[59] at room temperature (TiC, V_4C_3, and Mo_2C). This could be the reason why the Cr-C system is amorphous while the others are crystalline. This hypothesis is consistent with other results on the sputter deposition of carbides from groups VIIA and VIII. This is the case of Mn-C[61] and Fe-C[62] systems, which are claimed to be amorphous when obtained by sputtering.

The carbon content in the thin films might be an additional factor favoring amorphization due to the formation of metastable structures with a lower range of structural order. On comparing the results obtained for the Ti-Fe-C systems deposited with different sputtering targets, with and without constant Ti/C atomic ratios, the authors claimed that the higher the carbon content, the lower the iron percentage required for amorphization. This observation has been reported in other studies.[12,63] Moreover, the higher values of d(111) obtained from the Ti-Fe-C thin films with Ti/C ratios function of the iron content (Ti/C < 1) can be explained by the presence of higher percentage of carbon in interstitial positions.

4.2. W-T_M-C (T_M = Ti, Cr, Fe, Co, Ni , Pd, and Au) Thin Films

The possibility to significantly decrease the degree of structural order of tungsten carbide by introducing a group VIII element of the periodic table, like Ni, Fe, Co, or Pd, is well known; however, the same cannot be said for the addition of transition metal elements of other groups of the periodic table. Trindade *et al.*[23] studied the amorphous-phase-forming ability in W-T_M-C (T_M = Ti, Cr, Fe, Ni, Pd, and Au) sputtered films and found that those with Ti, Cr, or Au were crystalline (Fig. 8.9) with a metastable fcc β-$(W,T_M)C_{1-x}$ structure, with $1-x$ extending from near unity down to about 0.6. In opposition to these, films with T_M = group VIII transition metal show crystalline to amorphous state transitions for T_M percentages in the range of 5–10 at%. Based on these results, the authors claimed that the amorphous-phase-forming ability in tungsten–carbon sputtered thin films is exclusive to group VIII metals, such as iron or palladium. The explanation for this was related to a set of factors connected to the electronic configuration of these elements, and was related not only to the atomic size of the element added, but also to the crystalline structure and its affinity for carbon. This is in agreement with the Van der Kolk *et al.* criteria.[49] However, it should be noted that in contrast to Van der Kolk's study, Trindade *et al.*'s study concerned carbides with a mixture of covalent/metallic bonding between the metallic element and carbon. The addition of iron decreased the covalent character of the chemical bonding and induced distortion of the crystallographic lattice, leaning toward amorphization. Finally

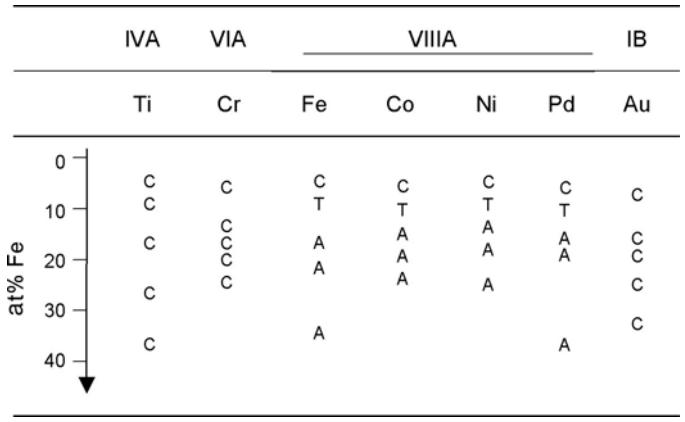

FIGURE 8.9. Compilation of XRD and TEM structural results of W-T_M-C (T_M = transition metal) thin films. (C, crystalline; T, transition; A, amorphous)[29]

the authors stated that it was possible to amorphize all the carbides studied, by adding iron, and the percentage of this element required for the amorphization of the various systems depended on the specific transition metal forming the carbide. Among these systems, the W-Fe-C system was one of the most extensively study by Trindade *et al.*[22–25] On the basis of EXAFS (Fig. 8.10 and Table 8.2), Mossbauer spectroscopy (Fig. 8.11 and Table 8.3), and XRD results obtained for W-Fe-C coatings with different iron contents, the authors assumed that the structure of these films consisted of small β-(W,Fe)C_{1-x} crystallites with a size of a few unity cells, surrounded by a disordered phase rich in Fe. Therefore, the atomic arrangement of these materials was not completely random, but maintained a degree of structural order (less than 2 nm).

Figure 8.10 shows the radial distribution functions (RDFs) of the EXAFS spectra (Fig. 8.10) recorded from samples $W_{56}C_{44}$, $W_{52}Fe_4C_{44}$, and $W_{42}Fe_{20}C_{38}$ at tungsten L- and iron K-edges (W L and Fe K, respectively). Note that data are not corrected for phase shift, and thus radial distances R (Å) do not reflect true bond lengths. The $W_{56}C_{44}$ thin film had a typically crystalline tungsten L-edge spectrum with some well-defined shells of neighbors. The oscillations in the lower side of the first peak were due to determination errors of the Fourier transform and were not of structural origin. The differences between the W L spectra of films with and without iron essentially concerned the second coordination shell, the RDF intensity of which was lower for the films with iron. Both W-Fe-C films had W L EXAFS spectra typical of ordered materials with well-defined RDF peaks. However, the Fe K spectra of the W-Fe-C films were quite different. The Fourier transform of the film with 4 at% Fe shows well shells of neighbors with an overlapping of the first two RDF peaks. On the other hand, the Fourier transform pattern of the film with 20 at% Fe was characteristic of disordered structures, i.e., amorphous.

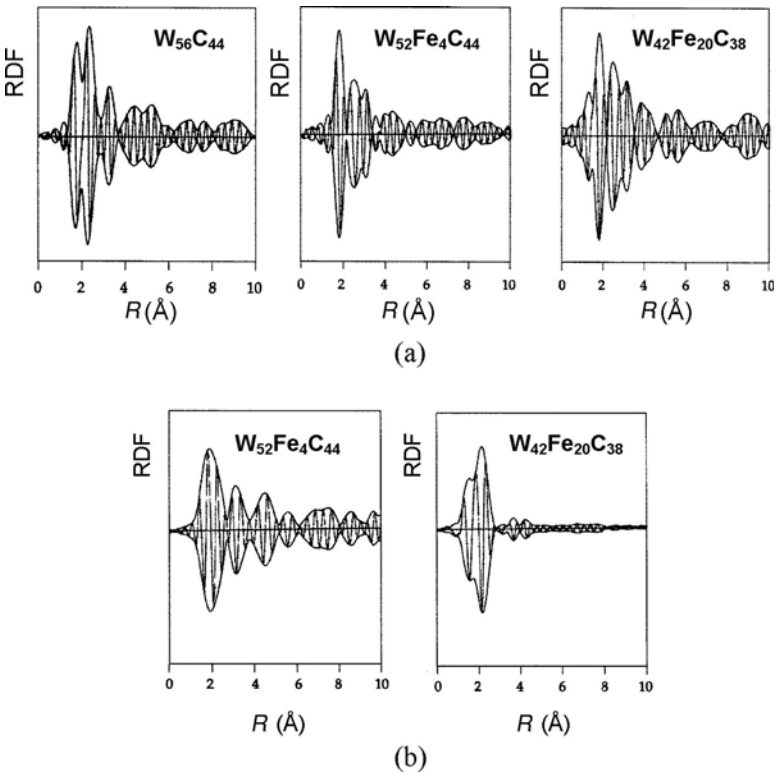

FIGURE 8.10. Fourier transforms of the EXAFS spectra recorded at (a) W L- and (b) Fe K-edges for films $W_{56}C_{44}$, $W_{52}Fe_4C_{44}$ and $W_{42}Fe_{20}C_{38}$.[23]

Table 8.2 presents the W—C, W—W, and W—Fe bond lengths obtained from the least squares fittings of the normalized W L EXAFS spectra. Due to the peak amplitude reduction and broadening, analysis was performed only for the first three shells of neighbors. These distances are consistent to an fcc structure with a lattice parameter of 4.34 Å. This value is slightly higher than the one given by the ICCD card for the β-MC_{1-x} carbide (4.25 Å). The addition of 4 at% Fe to W-C

TABLE 8.2. Structural Results of W-C-Fe Films (W L EXAFS) for the First Three Shells of Neighbors[23]

	$W_{56}C_{44}$	$W_{56}Fe_4C_{40}$	$W_{42}Fe_{20}C_{38}$
W–C bond length (1st neighbors)	2.17	2.17	2.13
W–W bond length (1st neighbors)	2.92	2.92	2.97
W–Fe bond length (1st neighbors)	—	2.92	2.67
W–C bond length (2nd neighbors)	3.62	3.62	3.67

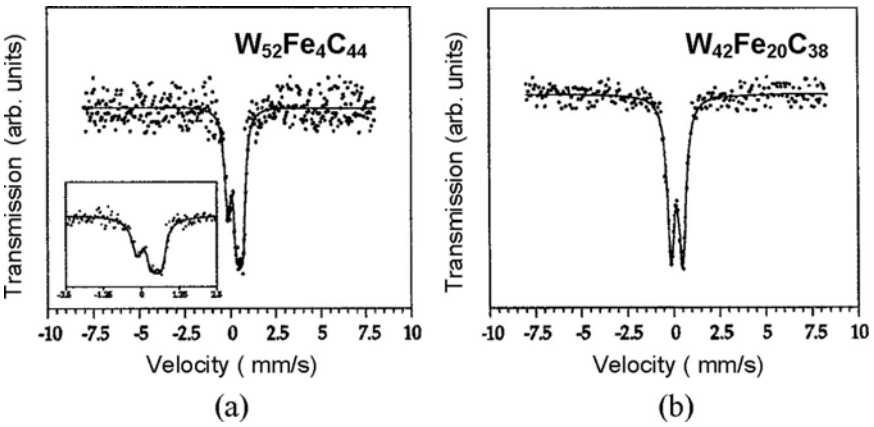

FIGURE 8.11. Mossbauer spectra of film (a) $W_{52}Fe_4C_{44}$ and (b) $W_{42}Fe_{20}C_{38}$.[23]

films did not alter these distances considerably. Moreover the W–W distance is similar to the W–Fe distance. The W L and Fe K EXAFS curves recorded from the iron richer W-Fe-C film ($W_{42}Fe_{20}C_{38}$) allowed for the conclusion of the structural order of the amorphous state. The W L curve of this film did not differ from those of W-C and $W_{52}Fe_4C_{44}$ films. However, the Fe K curve significantly decreases in intensity even for low interatomic distances. This is a clear indication that iron atoms form a short-range-ordered structure probably involving the W-C base crystallites.

The experimental Mossbauer spectra of several W-Fe-C thin films (Fig. 8.11) were fitted by a least squares method developed by LeCaer[64] in order to examine the local environmental effect. Taking the X-ray results obtained for these thin films into account, the spectra of samples with iron contents up to 6 at% (with an fcc structure) were fitted by two symmetric doublets, while spectra from samples richer in iron were fitted by two independent Lorentzian line shapes. The results show that the linewidths of the peaks depended on the iron content. For samples with an fcc structure the linewidth of the doublet I increased with the increasing iron content

TABLE 8.3. Mossbauer Hyperfine Parameters of the W-Fe-C Thin Films[23]

Sample (at%Fe)	IS (mm/s)	QS (mm/s)
4.0	0.29 (0.42[a]/0.16[b]	0.53 (0.40[a]/0.65[b]
5.8	0.28 (0.40[a]/0.16[b]	0.52 (0.39[a]/0.63[b]
12.7	0.11	0.65
20.0	0.10	0.61
33.3	0.08	0.58

[a]Site I.
[b]Site II.

while the corresponding value of doublet II remained constant. The samples richer in iron (with a decreased structure order) showed no significant differences in the linewidths of the quadrupole doublet. The value of 0.5 mm/s obtained for these samples was larger than the one expected for a single-site absorption line, implying a distribution of both the isomer shift (IS) and the quadrupole spitting. The values of the average hyperfine parameters of the W-Fe-C films are listed in Table 8.3. As can been seen, there was a systematic decrease in the IS with the increasing iron content in the films, meaning that there was an increase in charge density in the iron nucleus. This indication reveals that a certain amount of iron must be bonded to W and/or C.

In agreement with the XRD results, the values of the quadrupole splitting obtained for the W-Fe-C sputtered films pointed toward the existence of a structural transition from a crystalline to an amorphous state, for an iron content close to 6 at%. This conclusion was also supported by quadrupole splitting probability curves, P(QS), extracted from Mossbauer experimental data with the LeCaer's method.[64] In fact, very broad P(QS) curves were obtained for amorphous samples, in contrast to the samples with lower iron contents, which presented sharp distributions. On the basis of these Mossbauer results the authors stated that the hyperfine parameters obtained from samples with low iron contents correspond to an fcc structure, which was consistent with presence of the metastable MC_{1-x} (M = W, Fe) phase, indexed by XRD analysis.

The results obtained from the T_M-T_{M1}-C (T_M = Ti, V, Cr, Mo, W and T_{M1} = Ti, Cr, Fe, Co, Ni, Pd, and Au)[23,58] are not consistent with Senkov and Miracle's model.[58] Figures 8.12 and 8.13 show the atomic size distributions for the sputtered

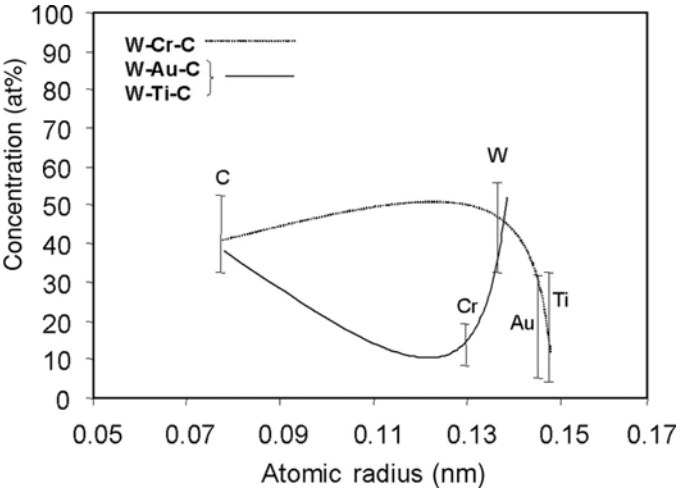

FIGURE 8.12. Atomic size distributions of W-T_M-C crystalline thin films, calculated on the basis of the work of Trindade *et al.*[23]

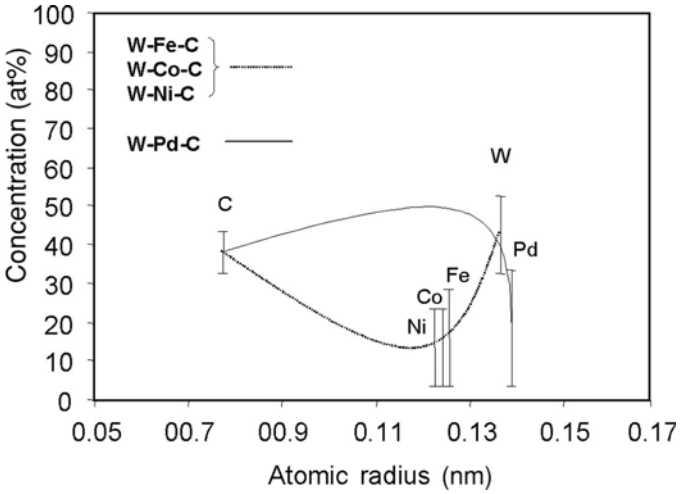

FIGURE 8.13. Atomic size distributions of W-T_M-C amorphous thin films, calculated on the basis of the work of Trindade *et al.*[23]

W-T_M-C thin films synthesized by Trindade *et al.*[23,59] Figure 8.12 corresponds to the crystalline films (T_M = Cr, Au, Ti) and Fig. 8.13 to amorphous films (T_M = Cr, Fe, Co, Ni, Pd). Two different atomic distribution curves can be observed in these systems. W-T_M-C with T_M = Cr, Fe, Co, and Ni have a concave upward distribution, which according to Senkov and Miracle[58] should lead to a considerable decrease in atomic diffusion, nucleation, and growth of crystalline phases and consequently to bulk glass formation. If this is true for group VIII alloying elements, the same cannot be said for the W-Cr-C system, probably because of the small difference in the tungsten and chromium atomic radii, which might not introduce important strain of the lattice. It is likely that higher concentrations of Cr would lead to amorphous materials. For the W-T_M-C systems with T_M = Pd, Au, and Ti, atomic size distributions with asymmetric concave downward shape, which resulted from the higher atomic radii of Ti, Au, and Pd compared to W, were obtained; nevertheless no amorphous structures were formed in the W-Ti-C and W-Au-C systems.

5. HARDNESS AND YOUNG'S MODULUS OF SPUTTERED T_M-T_{M1}-C THIN FILMS

5.1. Ternary T_M-C/T_{M1}-C Systems (T_M = Group VA Metal; T_{M1} = Group VIA Metal)

In the last two decades, ternary transition metal carbide films have been deposited on, e.g., cemented carbides or high-speed steels for wear applications. Most of

these carbides, especially those presenting an fcc structure, exhibit large solubility domains, i.e., large variations in composition. This is the case for the group IVA metal carbides (e.g., TiC/HfC) or group IV and VA metal carbides, such as TiC–NbC, ZrC–TaC, or TiC–VC just to mention a few. As an example, Krzanowski *et al.*[65] deposited single fcc phase TiC-50% HfC thin films with different grain sizes (from 35 to 11 nm) and hardness values (7.5–35 GPa, respectively). Contrarily, association of carbides of different groups located some distance from each other (e.g., IVA and VIA) in the periodic table may have a limited mutual solubility and may give rise to multiphase structures for some chemical compositions. This is the case of the ternary W-Ti-C and Ti-Mo-C systems.[66] Many studies have been done on the development of coatings based on the W-Ti system. Originally, the driving force for these studies was the good thermal behavior of this system, which made it suitable as a diffusion barrier in integrated circuits. Nowadays, ternary W-Ti-C sputtered thin films are used for wear applications.[67–69] The TiC and W_2C carbides are isomorphous and they have a similar lattice parameter, which means that they are extensively miscible.[70] In this case, the substitution of one of the metals by the other shall induce lattice distortion with consequent increase in hardness. Another possibility is the formation of heterogeneous multiphase carbides coatings being formed by other phases of the W-Ti-C system. This is the case of the TiC–WC and TiC–W_2C phases which can be formed, depending on the carbon stoichiometry. Yoon *et al.*[67] synthesized WC–TiN superhard multilayered coatings formed by a superlattice of TiN and β-WC_{1-x} phases. The microhardness of the film on cemented carbide was found to be 40 GPa. Koutzaki *et al.*[68] synthesized Ti-Mo-C and Ti-W-C films by cosputtering from carbide targets in order to examine the phase formation, the microstructure, and the mechanical properties. The results showed that multiphase Ti-Mo-C films, containing the (Ti,Mo)C, Mo_2C, and Mo_3C_2 phases, were obtained only in highly Mo-rich films. The other Ti-Mo-C films were formed by solid solutions of Mo in the TiC structure. The hardness of most Ti-Mo-C films was in the range of 8–10 GPa. The multiphase films had even lower hardness values.

Concerning the Ti-W-C films, they were observed to be formed by a (Ti,W)C solid solution with hardness values in the range of 15–17 GPa; however, a sample with 40 at% W had a hardness of 29 GPa. The high hardness of this specimen was attributed to Hall–Petch strengthening on the basis of TEM observations, which revealed an extremely small grain size and a higher film density. In a recent work, Cavaleiro *et al.*[69] presented results on the structure and mechanical properties of sputtered W-Ti-C/N thin films with different titanium and carbon contents. These films were deposited by dc reactive magnetron sputtering from targets of W-xTi alloys with $x = 0$, 10, 20, and 30 wt% in a mixed Ar + CH_4 atmosphere with a CH_4/Ar partial pressure ratio in the range 0–1. The results were compared to those available in the literature for these systems. The influence of the carbon content on the hardness, Young's modulus, and grain size of W-Ti-C films is illustrated in Fig. 8.14a–d. The increase in C content gave rise to increasing hardness values in all but the W-C films. The hardness of the binary W-C system reached a maximum for

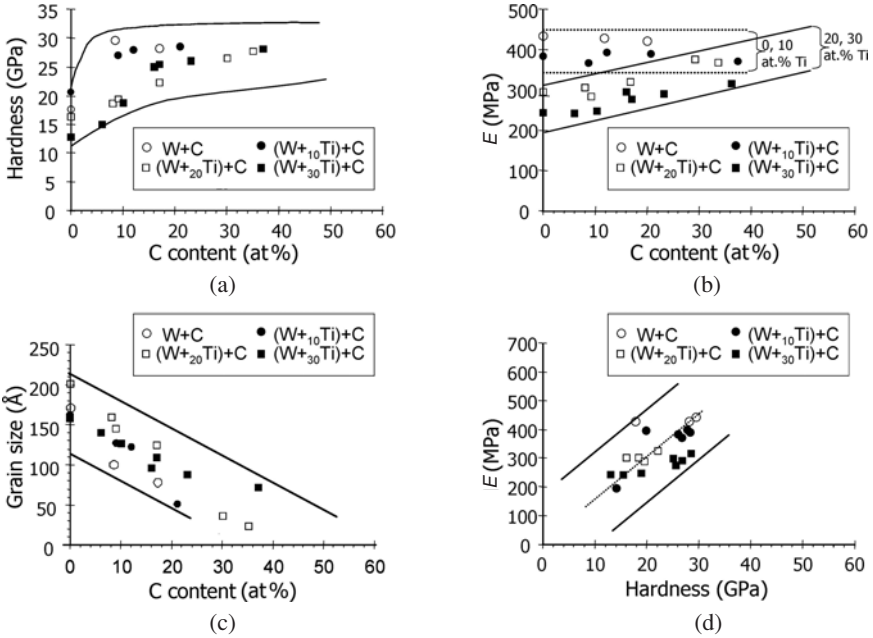

FIGURE 8.14. The effect of carbon content on the hardness, Young's modulus, and grain size of W-Ti-C films.

≈10 at% C and decreased thereafter. This result is in accordance with other studies on this system.[71–77] The highest value of hardness referred to in the literature for carbon-poor W-C coatings was obtained by Pauleau and Gouy-Pailler[73] and is slightly higher than the value obtained by Cavaleiro *et al.*[69] (35 GPa against 30 GPa, respectively). The lattice distortion induced by the presence of increasing amounts of C in the interstitial positions of the bcc α-W phase is responsible for the reduction of the structural range order in the films and for their hardness decrease. However, it should be pointed out that hardness values of 40 GPa are reported in the literature[72–76] for carbon-richer coatings in which the carbide phase is formed. The Young's modulus of the W-C films remained almost constant with carbon content increasing.

For the W-Ti-C coatings the hardness increased for low carbon contents and then stayed almost invariable for high carbon contents (Fig. 8.14a). The thin films were formed by an interstitial bcc W solid solution with a progressive shift of their diffraction peaks to lower angles with the increase in carbon content. The hardness values measured by Cavaleiro *et al.*[69] in these films were higher than the majority of the values (≈15 GPa) reported in the literature by Koutzaki *et al.*[68] These authors explained that the relatively low values of hardness obtained were due to the extremely small grain size of the (W,Ti)-C solid solution. Figure 8.14b shows

that like the binary W-C system, the Young's modulus of the (W-10wt% Ti)-C thin films remained approximately constant with the increase in carbon content. On the other hand, the grain size of the coatings decreased with the increase in carbon content, i.e., there was a decrease in their structural range order. In regards to the (W-20wt% Ti)-C and (W-30wt% Ti)-C thin films both the hardness and the Young's modulus increased with increasing carbon content. There was good congruity between the increase in hardness and the decrease in grain size, as can be confirmed by the simultaneous analysis of Fig. 8.14a,c. In light of the influence of structural parameters on the hardness of hard coatings, both the grain size and the lattice distortion have been the most utilized parameters to establish empirical correlations. The referred to lattice distortion induced by the presence of the increasing amounts of C in the interstitial positions of the bcc α-W phase is, according to Cavaleiro *et al.*,[69] responsible for the reduction of the structural range order of the films and for the increase in hardness. Figure 8.14d shows the relationship between E and H. As can be seen, the higher the hardness, the higher is the Young's modulus.

5.2. Other Ternary T_M-T_{M1}-C Systems

The (W-C)-based system has been extensively studied mainly due to its importance for cemented carbide applications. It was shown in Section 5.2 that the structural range order of coatings from this system can be altered by the addition of a group VIII metal. This section deals with the relationship between the chemical composition, the structure, and the hardness of W-T_M-C sputtered coatings. The results concern W-C thin films with and without alloying elements from groups IVA (Ti) and VIII (Co and Ni). As previously mentioned, these elements have a different influence on the structural range order of the W-C base coatings. In contrast to Ti, elements Co and Ni reduce the range of structural order of the fcc structure of the binary WC_{1-x} coatings, thus giving rise to amorphous structures for contents close to 6 at%. It should be noted that the hardness values of the W-Ti-C presented in this section are the same as those shown in Fig. 8.14a. Figure 8.15a,b illustrates the relationship between hardness and structure of W-T_M-C (T_M = Ti, Co, Ni) thin films. The hardness values were splitted into three groups: <25 GPa, 25–35 Gpa, and >35 GPa, which define three different domains: (i), (ii), and (iii) in Fig. 8.15. As can be seen, the higher hardness values of the ternary coatings are obtained for low T_M contents and carbon contents up to 50 at%. These films are formed by a single nanocrystalline solid solution of bcc W, for low carbon contents, or β-WC_{1-x} carbide, for carbon contents close to 50 at% ($x = 0$). The high hardness values were the result of a lattice distortion provoked by interstitial and substitutional elements, which lead to compressive or tensile stresses, depending on their size. In contrast, the softer coatings were located in two different zones of the W-T_M-C ternary diagram; one starting from the W-C axis and the other from the T_M-W axis. The first domain includes thin films with

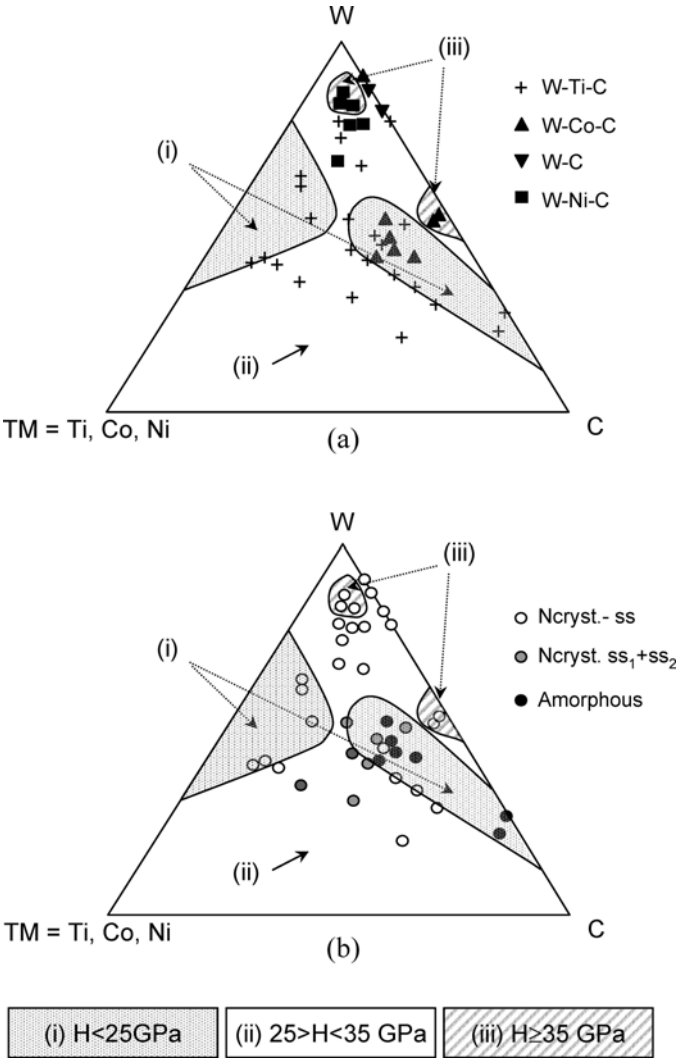

FIGURE 8.15. (a) Hardness and (b) structure of W-T_M-C (T_M = Ti, Co, Ni) thin films. (Ncryst.-ss, nanocrystalline solid solution)

low range order, i.e., amorphous (Fig. 8.15b), with chemical compositions characterized by T_M contents higher than 5 at% or carbon contents higher than 50 at%. The second domain includes nanocrystalline single-phase W-Ti-C coatings (Fig. 8.15b) with W/Ti atomic ratios close to 1 and with low carbon contents. Finally, the films with intermediate hardness values are formed either by a W base nanocrystalline single phase (on the center top of the Fig. 8.15b) or by a mixture

of two nanocrystalline phases (films with equiatomic chemical compositions in the center of the diagram). These results show that, as expected, the formation of amorphous structures in sputtered M1-M2-C thin films does not give rise to materials with improved hardness. In these ternary carbides the higher hardness values correspond to single-phase materials alloyed with interstitial (carbon) and substitutional (transition metal) elements in a relatively low percentage, in order to avoid the formation of a second phase. Nevertheless, according to the literature, a material with equiaxed or isotropic crystallites with a grain size <10 nm separated from each other by a second phase should suppress the dislocation movement, and, therefore increase hardness. This is not the case of the so-called amorphous T_M-T_{M1}-C thin films, which present the lowest hardness values. As referred to in Section 5.2, these amorphous materials are formed by small crystallites with a size of a few unity cells, surrounded by a disordered phase rich in element M2 (element from group VIII). The occurrence of these disordered phases, of relatively ductile elements, with a huge amount of defects that allow fast diffusion of atoms and vacancies under stress (grain boundary sliding) must be responsible for the decline in hardness. Moreover, the higher the content of element M2 in the thin film the lower is the hardness. This is also true for the elastic properties, e.g., Young's modulus.

Figure 8.16 shows the hardness and Young's modulus of sputtered T_M-Fe-C (T_M = W, Mo, Cr) thin films.[78] In this figure the hardness (H) and Young's modulus (E) were normalized to the W-C system. As can be seen, both hardness and Young's modulus of the binary films decreased from the first to the third long period, i.e., toward a greater metal–carbon bonding stability. This was also true

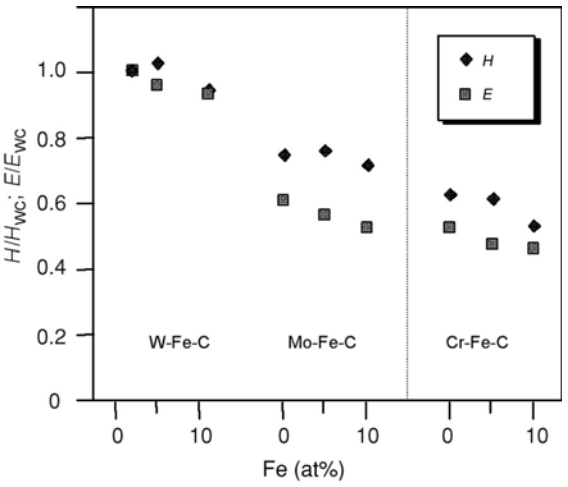

FIGURE 8.16. Hardness and Young's modulus of sputtered T_M-Fe-C (T_M = W, Mo, Cr) thin films.[78]

for bulk carbides. The increasing iron content leads to a progressive decrease in the elastic modulus of the films and an increase in their hardness for iron contents of about 5 at%, followed by a decline for higher percentages. According to the authors,[78] this can be explained by the type of chemical bonding between the different elements within the carbide and by the range of structural range order of the films. Iron reduces the number of covalent bonds, leading to a reduction in Young's modulus. However, in opposition, there was an increase in hardness in W-Fe-C and Mo-Fe-C films for medium iron contents, which is attributed to a distortion of the nanocrystalline fcc phase with a consequent decrease in grain size. For higher iron contents, these films became amorphous and the hardness dropped. Cavaleiro *et al.*[24] observed the same trend on reactive deposition of W-Ni-C ternary films with increasing partial pressures of methane and substrate bias. In conclusion, the authors stated that the structural range order of the films decreased with increasing nickel and carbon contents. The higher hardness and Young's modulus values were obtained for nanocrystalline single-phase films (α-W) with carbon and nickel contents of 8 and 7 at%, respectively. For higher contents of these elements the films became amorphous with decreased mechanical properties.

In many mechanical applications the use of protective coatings must take into account not only hardness, oxidation resistance, and wear behavior but also fracture toughness. Usually, a significant increase in hardness and other mechanical properties such as tensile strength or elastic modulus occurs to the detriment of toughness. These T_M-T_{M1}-C coatings, with T_{M1} = metal from group VIII, present a certain degree of dislocation movement and grain boundary sliding, which is responsible for their relatively high fracture toughness. Consequently, the design of a hard coating for mechanical applications depends on the required properties.

The new generation of nanocomposite hard coatings for wear protection (e.g., nc-TiN/a-Si_3N_4), formed by nanocrystalline crystals lower than 10 nm surrounded by an amorphous layer with a few atomic bond lengths, presents very high hardness and low friction coefficients. However, it is not yet known if these materials can support high contact pressures without cracking. M1-M2-C sputtered coatings, however, are reported to be less hard than the nanocomposite nc-/a-coatings, and their structure can be altered by thermal annealing at adequate temperatures. This is the case for the as-deposited amorphous M1-M2-C films whose mechanical properties could be improved by controlling the crystallization process and grain growth. The phases formed during annealing at increasing temperatures should have a grain size of a few nanometers, in order to improve hardness; otherwise, a decrease in hardness will occur for the nc-TiN/a-7 at% Si_3N_4 system during annealing.[6] This author mentioned that for temperatures higher than 500°C, there was a grain growth of the nanocrystalline TiN phase with a consequent hardness loss upon annealing (33 to 27 GPa for a grain size of 12 to 25 nm, respectively).

6. THERMAL STABILITY OF SPUTTERED AMORPHOUS M1-M2-C THIN FILMS

The structural stability of the amorphous W-T_M-C (T_M = Fe, Co, Ni) thin films at elevated temperatures was studied by Trindade *et al.*[25,26,79,80] by means of *in situ* TEM and thermal analysis during continuous heating up to 1000°C. XRD was used as complementary technique for phase identification after each differential scanning calorimetry (DSC) run, at room temperature. The knowledge of the crystallization temperatures of these systems is crucial for two main reasons. On one hand it may extend experimental information to the mechanism of crystal nucleation and growth from the amorphous phase, thus contributing toward obtaining nanocrystalline phases with phase distribution suitable for mechanical applications. On the other hand it is crucial for an adequate technological application, since the operating temperature range will be determined by the structural changes (crystallization) occurring with increasing temperature.

Figure 8.17 shows the crystallization temperatures of amorphous W-T_M-C thin films as a function of the T_M atomic content. These temperatures were determined on the basis of DSC curves (see Fig. 8.18) recorded from the amorphous as-deposited films at temperatures up to 1150°C.[80]

As can be observed in Fig. 8.17, the thermal behavior of the as-deposited amorphous phase is strongly dependent on the chemical composition. The higher the T_M content the lower the structural stability of the amorphous phase is. This is particularly true for low T_M atomic contents. Moreover, films with Ni are less stable than films with iron or cobalt, which agrees with the results available in the literature for bulk materials. Figures 8.19 and 8.20 show some TEM bright-field

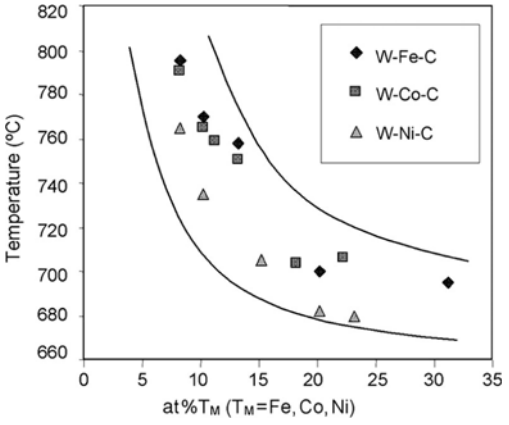

FIGURE 8.17. Crystallization temperatures of amorphous W-T_M-C (T_M = Fe, Co, Ni) thin films.

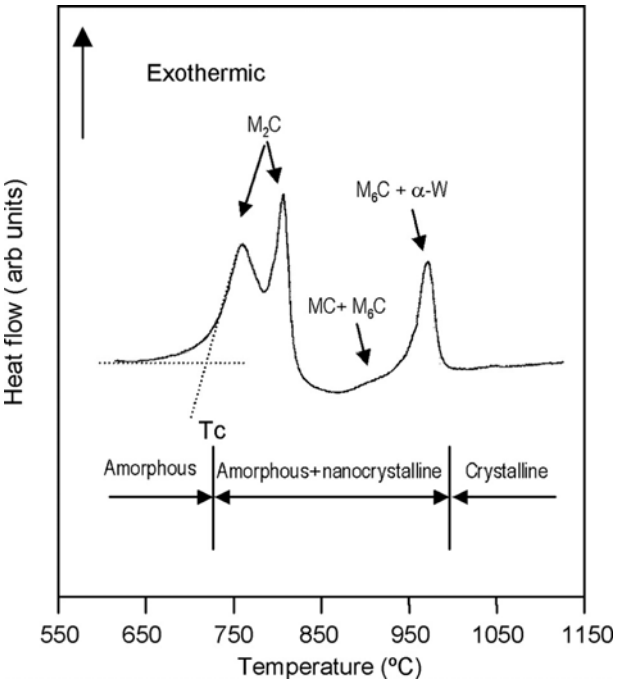

FIGURE 8.18. DSC curves recorded from an amorphous W-Co-C thin film, as a typical example of all the other amorphous systems. Phase transformations were determined by XRD analysis after various DSC runs up to different maximal temperatures.

micrographs and selected area electron diffraction patterns (SAEDPs) of W-T_M-C, corresponding to the crystallization of amorphous as-deposited films obtained by Trindade *et al*. Figure 8.19a–c corresponds to a $W_{53}Ni_{10}C_{37}$ thin film and Fig. 8.19d concerns a $W_{46}Fe_{13}C_{41}$ thin film. Figure 8.20 shows TEM bright-field micrograph and corresponding SAEDP of a crystallized $W_{45}Ni_{15}C_{40}$ thin film at 750 and 800°C. The crystallization of the W-Ni-C coatings occurred with the formation of M_2C for films with at% Ni < 10 (Fig. 8.19a–c) and α-Ni + MC for films with at% Ni ≥ 10 (Fig. 8.20a,b). Once the crystallization products were formed from the amorphous phase, they tend to grow rapidly with further increase in temperature.

The crystallization of the W-TM-C (T_M = Fe, Co) thin films leads to the formation of M_2C, MC, M_6C, and α-W. The authors explained that the two different crystallization processes observed in the W-Ni-C and W-(Fe,Co)-C coatings were due to the higher solubility of tungsten in nickel than in iron or cobalt.

Overall, the massive crystallization of the films occurred for temperatures between 680 and 800°C. The first crystals formed from the amorphous phase were more or less globular (Fig. 8.19a). The corresponding SAEDP showed some rather well-defined rings ascribed to the M_2C carbide (for Ni-rich films, the α-Ni + MC phases are formed instead of M_2C), as well as large electron diffraction (ED) rings

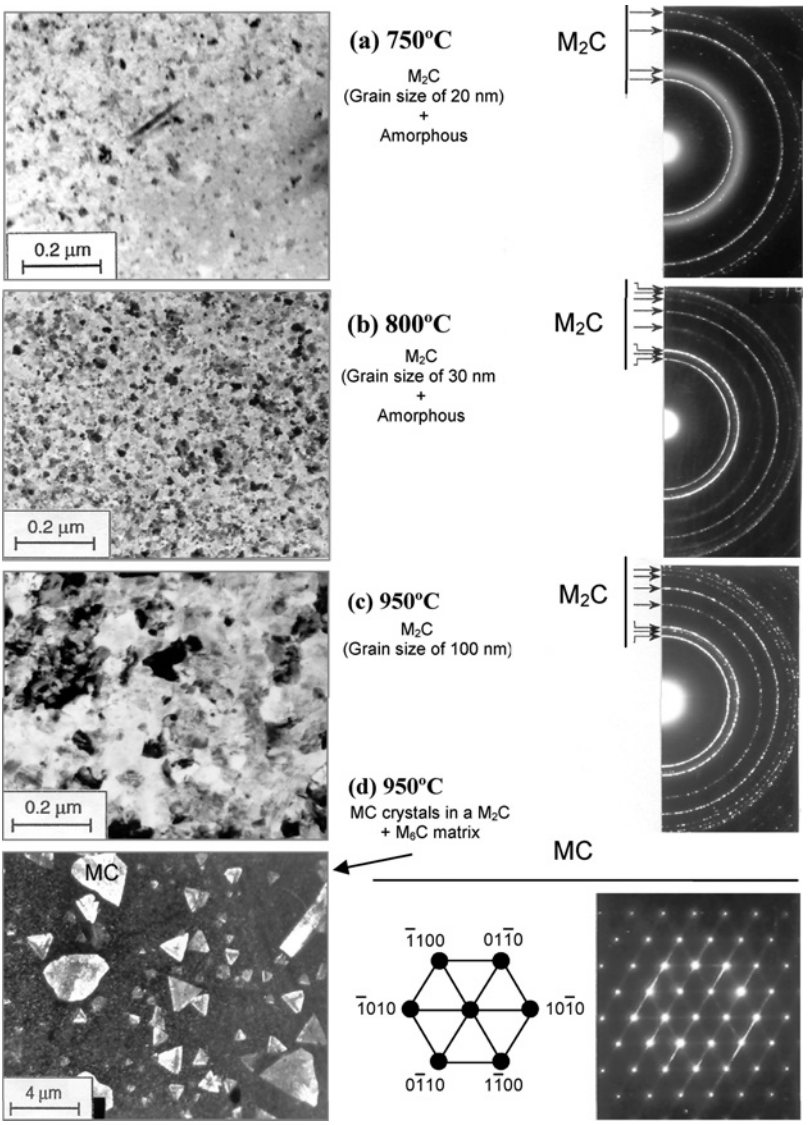

FIGURE 8.19. TEM bright-field micrographs and corresponding SAEDP showing the crystallization of W-T_M-C amorphous as-deposited films. (a), (b), and (c) correspond to a $W_{53}Ni_{10}C_{37}$ thin film and (d) concerns a $W_{46}Fe_{13}C_{41}$ thin film.

from the amorphous phase. This transformation was classified as a primary-type crystallization in which one phase precipitates, resulting in an enrichment of the remaining elements in the amorphous phase. Taking into account that M_2C is a tungsten-rich carbide and that it may dissolve only small amounts of a group

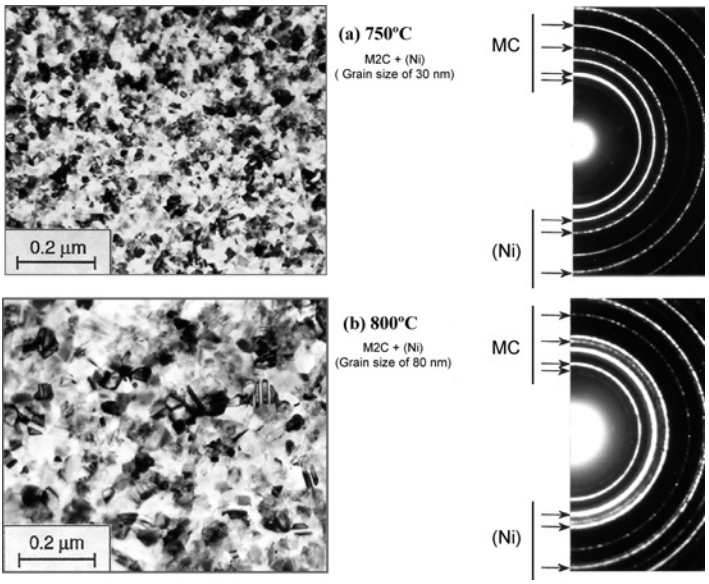

FIGURE 8.20. TEM bright-field micrograph and corresponding SAEDP of a crystallized $W_{45}Ni_{15}C_{40}$ thin film at (a) 750°C and (b) 800°C.

VIII element, a gradual enrichment of the matrix in iron during crystallization is conceivable. Continued heating resulted in an intensive crystallization with formation of further M_2C (Fig. 8.19b) and subsequently grain growth of this phase (Fig. 8.19c). Isothermal *in situ* annealing of W-(Fe,Co)-C films at temperatures close to 900°C led to the appearance of big crystals, indexed as MC, with essentially two morphology types: prismatic shape and rod shape (Fig. 19d).

7. CONCLUSIONS

This chapter reviewed the present status of the research on the design of hard coatings based on transition metal carbides for mechanical applications. As stated, these coatings consist of metastable transition metal carbides, as monolithic or multilayer coatings, or nanocomposite materials of a nanocrystalline phase(s) embedded in an amorphous phase.

The addition of a transition metal to a metal–carbon binary system modifies its range of structural order and consequently its mechanical properties, e.g., hardness. The amorphous-phase-forming ability in sputtered thin films of transition metal carbides is characteristic of elements with no great affinity for carbon, e.g., elements of group VIII of the periodic table. In binary T_M-C systems, it is easy to synthesize amorphous carbides from groups VIA to VIII with chemical compositions similar to those of the equilibrium crystalline phases. The atomic

size of the elements does not seem to play a vital role in the amorphization of the T_M-C carbides. The systems in which the NaCl-type structure MC_{1-x} is an equilibrium structure, be it at room temperature or at elevated temperature, have a propensity to give rise to crystalline thin films. This is the case of groups IVA and VA metals, which form a single fcc MC_{1-x} carbide with the lowest enthalpy of formation when bounded to carbon. For the VIA group, the situation is somewhat different: contrarily to tungsten and molybdenum, chromium (the element from group VI with the lowest affinity for carbon) forms an amorphous structure with carbon. The same is true for Mn (group VIIA) and for iron (group VIII). Nevertheless, it is possible to significantly decrease the structural range order for carbides of IVA–VIA metals with the addition of a group VIII element, such as Fe, Co, Ni, or Pd. The percentage of these elements required for the appearance of amorphous structures is a function of the constituent transition metal of the carbide, and is higher for stronger carbide formers. This knowledge can be of great importance in the development of carbide base thin films with enhanced properties so they can be used in extreme conditions. Moreover, by subsequent annealing, it is possible to modify the microstructure of the as-deposited coatings and to control their grain size by choosing adequate thermal cycles function of the chemical composition and structure of the sputter-deposited coatings.

REFERENCES

1. S. Zhang, D. Sun, Y. Fu, and H. Du, Recent advances of superhard nanocomposite coatings: A review, *Surf. Coat. Technol.* **167**, 113–119 (2003).
2. J. Schiotz, Simulation of nanocrystalline metals at the atomic scale, what can we do? What can we trust? in *Proceedings of the 22th Riso lnternational Symposium on Materiais Science*, Vol. 127, edited by A.R. Dinesen *et al*. (Rokilde, Denmark, 2001).
3. J. Schiotz, T. Vegge, F. D. Di Tolla, and K. W. Jacobsen, Atomic scale simulations of the mechanical deformation of nanocrystalline metals, *Phys. Rev. B* **60**, 11971–11983 (1999).
4. S. Veprek, The search for novel, superhard materials, *J. Vac. Sci. Technol. A* **17**, 2401–2420 (1999).
5. S. Christiansen, M. Albrecht, H. P. Strunk, and S. Veprek, Microstructure of novel superhard nanocrystalline amorphous composites as analyzed by high resolution transmission electron microscopy, *J. Vac. Sci. Technol. B* **16**, 19–22 (1998).
6. J. Patscheider, Nanocomposite hard coating for wear protection, *MRS Bull.* **28**, 180–183 (2003).
7. S. Veprek, A. Niederhofer, K. Moto, T. Bolom, H. D. Mannling, P. Nesladek, G. Dollinger, and A. Bergmaier, Composition, nanostructure and origin of the ultrahardness in nc-TiN/a-Si_3N_4/a and nc-$TiSi_2$ nanocomposites with Hv = 80 to $\leq$ 105 GPa, *Surf. Coat. Technol*. **113**, 152–159 (2000).
8. S. Carvalho, L. Rebouta, A. Cavaleiro, L. A. Rocha, J. Gomes, E. Alves, Microstructure and mechanical properties of nanocomposite (Ti,Si,AI)N coatings, *Thin Solid Films* **398**, 391–396 (2001).
9. C. Mitterer, P. H. Mayrhofer, M. Beschliesser, P. Losbichler, P. Warbichler, F. Hofer, P. N. Gibson, W. Gissler, H. Hruby, J. Musil, and J. Vlcek, Microstructure and properties of nanocomposite Ti-B-N and Ti-B-C coatings, *Surf. Coat. Technol*. **121**, 405–411 (1999).
10. J. S. Yoon, H. Y. Lee, J. G. Han, S. H. Yang, and J. Musil, The effect of Al composition on the microstructure and mechanical properties of WC-TiAlN superhard composite coating, *Surf. Coat. Technol.* **142**, 596–602 (2001).
11. A. A. Voevodin, J. P. O'Neill, and J. S. Zabinski, Nanocomposite tribological coatings for aerospace applications, *Surf. Coat. Technol*. **116**, 36–45 (1999).

12. S. Zhang, Y. Q. Fu, H. J. Du, X. T. Zeng, and Y. C. Liu, Magnetron sputtering of nanocomposite (Ti,Cr)CN/DLC coatings, *Surf. Coat. Technol*. **162**, 42–48 (2003).
13. T. Zehnder, J. Mattey, P. Schwaller, A. Klein, P.-A. Steinmann, and J. Patsheider, Wear protective coatings consisting of TiC SiC-a-C:H deposited by magnetron sputtering, *Surf. Coat. Technol*. **163**, 238–244 (2003).
14. B. Trindade, M. T. Vieira, and E. Bauer-Grosse, Amorphous phase forming ability in (W-C)-based sputtered films, *Acta Mater.* **46**, 1731–1739 (1998).
15. L. E. Toth, *Transition Metal Carbides and Nitrides* (Nova Science, New York, 1971).
16. A. Cavaleiro, M. T. Vieira, and G. Lemperiere, The structure of thin films deposited from a sintered tungsten carbide with a high cobalt content (15 wt%), *Thin Solid Films* **185**, 199–217 (1990).
17. A. Cavaleiro, M. T. Vieira, and G. Lemperiere, Structure and chemica1 composition of W-C-(Co) sputtered films, *Thin Solid Films* **197**, 237–255 (1991).
18. A. Cavaleiro and M. T. Vieira, Evaluation of the hardness of sputtered W-C-Co thin films, *Surf. Eng*. **10**, 147–151 (1994).
19. A. Cavaleiro, M. T. Vieira, and G. Lemperiere, Influence of deposition conditions on the morphology of sputtered W-C-(Co) films, *Thin Solid Films* **213**, 6–12 (1992).
20. K. Jia, T. E. Fisher, and B. Gallois, Microstructure, hardness and toughness of nanostructured and conventional WC-Co composites, *Nanostruct. Mater*. **10**, 875–891 (1998).
21. Y. C. Zhu, C. X. Ding, K. Yukimura, T. D. Xiao, and P. R. Strutt, Deposition and characterization of nanostructured WC-Co coating, *Ceram. Int.* **27**, 669–674 (2001).
22. B. Trindade and M. T. Vieira, Structural characterization of cosputtered W-C-Fe films, *Thin Solid Films* **206**, 318–322 (1991).
23. B. Trindade, M. T. Vieira, and E. Bauer-Grosse, In situ high temperature crystallization study of sputter deposited arnorphous W-Fe-C films, *Acta Metall. Mater*. **43**, 93–99 (1995).
24. A. Cavaleiro, B. Trindade, and M. T. Vieira, Structural analysis of sputtered $(W\text{-}C)_{1-x}M_x$ (M = Fe, Co) films with $0 \leq x \leq 0.20$, *Surf. Coat. Technol.* **60**, 411–415 (1993).
25. B. Trindade, M. T. Vieira, and E. Bauer-Grosse, Characterization of W-Me-C (Me = Fe, Co) films and their structural behaviour with temperature, *Mater. Sci. Eng. A* **174**, 165–171 (1994).
26. B. Trindade, M. T. Vieira, and E. Bauer-Grosse, Structural stability and crystallization studies of metastable sputtered W-Ni-C films, *Thin Solid Films* **252**, 82–88 (1994).
27. A. Cavaleiro, B. Trindade, and M. T. Vieira, Deposition and characterization of fine-grained W-Ni-C/N temary films, *Surf. Coat. Technol.* **116**, 944–948 (1999).
28. S. H. Koutzaki, J. E. Krzanowski, and J. J. Nainaparampil, Phase formation and microstructure in sputter-deposited Ti-Mo-C and Ti-W-C thin films, *Metal. Mater. Trans. A* **33**, 1579–1588 (2002).
29. A. Cavaleiro, B. Trindade, and M. T. Vieira, Influence of Ti addition on the properties of W-Ti-C/N sputtered films, *Surf. Coat. Technol.* **174**, 68–75 (2003).
30. A. Cavaleiro, M. T. Vieira, F. Ramos, and J. P. Dias, The ultimate vacuum pressure and the characteristics of sputtered coatings, *Thin Solid Films* **290**, 238–242 (2002).
31. K. Abourayak, S. Feyeulle, L. Vincent, C. Ribeiro, A. Cavaleiro, and M. T. Vieira, Tribological behaviour at elevated temperatures of thin physical vapour deposited coatings, *Surf Coat. Technol*. **80**, 171–175 (1996).
32. M. T. Vieira, A. Cavaleiro, and B. Trindade, The effects of a third element on structure and properties of W-C/N, *Surf. Coat. Technol*. **151**, 495–504 (2002).
33. H. A. Davies, Butterworths monographs in materials, in *Amorphous Metallie Alloys*, edited by F. E. Luborsky (Butterworths, London, 1983).
34. C. E. Wickersham, E. Foster, and G. Stickford, Reactively sputter-deposited high-emissivity tungsten carbide-carbon coatings, *J. Vac. Sci. Technol*. **18**, 223–225 (1981).
35. K. Fuchs, P. Rodhammer, E. Bertel, F. P. Netzer, and E. Gomik, Reactive and non-reactive high rate sputter deposition of tungsten carbide, *Thin Solid Films* **151**, 383–395 (1987).
36. K. Machida, M. Enyo, and I. Toyoshima, Preparation of W-C thin-films by reactive r.f. sputtering and auger-electron spectroscopy surface characterization, *Thin Solid Films* **161**, L91–L95 (1988).

37. F. Kustas, B. Mishra, and J. Zhou, Metal/carbide co-sputtered wear coatings, *Surf Coat. Technol*. **121**, 489–494 (1999).
38. S. Groudeva-Zotova, R. G. Vitchev, and B. Blanpain, Phase composition of Cr-C thin films deposited by a double magnetron sputtering system, *Surf. Interface Anal*. **30**, 544–548 (2000).
39. G. Tomé, B. Trindade, and M. T. Vieira, Synthesis and characterisation of new sputtered metastable carbides, *Vacuum* **64**, 205–210 (2002).
40. J. D. Martin, S. J. Goettler, N. Fossé, and L. Iton, Designing intermediate range order in amorphous materiaIs, *Nature* **419**, 381–384 (2002).
41. A. Inoue, Bulk amorphous alloys, in *Amorphous and Nanocrystalline Materiais Advances in Materiais Research*, edited by A. Iooue and K. Hashimoto (Springer, Berlin, 2001).
42. P. H. Gaskell, A new structural model for amorphous transition metal silicides, borides, phosphides and carbides, *J. Non-Cryst. Solids* **32**, 207–224 (1979).
43. B. C. Giessen, in *Proceedings of the 4th International Conference on Rapidly Quenched Metals*, edited by T. Matsumoto and K. Suzuki (Japan Institute of Metals, Sendai, 1982), p. 213.
44. T. B. Massalski, in *Proceedings of the 4th International Conference on Rapidly Quenched Metais*, edited by T. Matsumoto and K. Suzuki (Japan Institute of Metals, Sendai, 1982), p. 203.
45. S. H. Whang, Glass forming ability for binary alloys systems by modified T-C map in relation to phase diagram, *J. Non-Cryst. Solids* **61**, 841–846 (1984).
46. S. H. Whang, New prediction of glass-forming ability in binary alloys using a temperature-composition map, *Mater. Sci. Eng*. **57**, 87–95 (1983).
47. T. Egami and Y. Waseda, Atomic size effect on the formability of metallic glasses, *J. Non-Cryst. Solids* **64**, 113–134 (1984).
48. S. H. Liou and C. L. Chen, Composition range of binary amorphous-alloys, *Phys. Rev. B* **35**, 2443–2446 (1987).
49. G. J. Van der Kolk, A. R. Miedema, and A. K. Niessen, On the composition range of amorphous binary transition metal alloys, *J. Less-Common Met.* **145**, 1–17 (1988).
50. P. I. Loeff, A. W. Weeber, and A. R. Miedema, Diagrams of formation enthalpies of amorphous-alloys in comparison with the crystalline solid-solution, *J. Less-Common Met.* **140**, 299–305 (1988).
51. B. M. Clements and R. Sinclair, Metastable phase formation in thin films and multilayers, *MRS Bull.* **15**, 19–28 (1990).
52. S.-G. Zhang and Y. Yu, Structure and density of transition metal–metalloid amorphous alloys, *Mater. Sci. Eng. A* **134**, 1008–1011 (1991).
53. C. Suryanarayana, Mechanical alloying and milling, *Prog. Mater. Sci.* **46**, 1–184 (2001).
54. D. Turnbull, Metastable structures in metallurgy, *Metall. Trans. A* **12**, 695–708 (1981).
55. P. H. Shingu, in *Processing Materials for Properties*, edited by H. Henein and T. Oki (TMS, Warrendale, PA, 1993).
56. F. H. Froes, C. Suryanarayana, K. Russell, and C. M. Ward-Close, Far from equilibrium processing of light metals, in *Novel Techniques in Synthesis and Processing of Advance Materiais*, edited by J. Singh and S. M. Copley (TMS, Warrendale PA, 1994).
57. F. H. Froes, C. Suryanarayana, K. Russell, and C.-G. Li, Synthesis of intermetallics by mechanical alloying, *Mater. Sci. Eng. A* **192**, 612–623 (1995).
58. O. N. Senkov and D. B. Miracle, Effect of the atomic size distribution on glass forming ability of amorphous metallic alloys, *Mater. Res. Bull*. **36**, 2183–2198 (2001).
59. B. Trindade and M. T. Vieira, Modification of the structural order of transition metal–carbon systems by the addition of a group VIII element, *Mater. Sci. Eng. A* **52**, 195–201 (2003).
60. A. Cottrell, The affinity of transition metals for carbon, in *Chemical Bonding in Transition Metal Carbides*, edited by Institute of Materials (Institute of Materials, London, 1995).
61. A. Aouni and E. Bauer-Grosse, New periodic and aperiodic triangular prismatic sheet carbides obtained by crystallization of $Mn_{1-x}C_x$ amorphous films and described by the chemical twinning model, *J. Alloys Compd.* **335**, 157–164 (2002).

62. G. Lecaer and E. Bauer-Grosse, Aperiodic carbides formed by crystallization of amorphous Fe-C alloys, *Hyperfine Interact.* **47**, 55–67 (1987).
63. A. V. Granato, Interstitially model for condensed matter states of face-centered-cubic metals, *Phys. Rev. Lett*. **68**, 974–977 (1992).
64. G. Lecaer and J. M. Dubois, Evaluation of hyperfine parameter distributions from overlapped mossbauer-spectra of amorphous alloys, *J. Phys. E Sci. Instrum*. **12**, 1083–1090 (1979).
65. J. E. Krzanowski, J. L. Endrino, and S. H. Koutzaki, Determining the limit of hardness in ternary carbide thin films, *Mater. Res. Soc. Symp. Proc.* **697**, P1.4.1–P1.4.6 (2002).
66. *ASM Handbook of Ternary Alloy Phase Diagrams* (ASM Intemational, MateriaIs Park, OH, 1995).
67. J. S. Yoon, H. S. Myung, J. G. Han, and J. Musil, A study on the synthesis and microstructure of WC-TiN superlattice coating, *Surf. Coat. Technol.* **131**, 372–377 (2000).
68. S. H. Koutzaki, J. E. Krzanowski, and J. J. Nainaparampil, Phase formation and microstructure in sputter-deposited Ti-Mo-C and Ti-W-C thin films, *Metall. Mater. Trans. A* **33**, 1579–1588 (2002).
69. A. Cavaleiro, B. Trindade, and M. T. Vieira, Influence of Ti addition on the properties of W-Ti-C/N sputtered films, *Surf. Coat. Technol.* **174**, 68–75 (2003).
70. H. O. Pierson, *Handbook of Refractory Carbides and Nitrides* (Noyes Publications, New Jersey, 1996).
71. J. M. Castanho and M. T. Vieira, The influence of the interstitial element on tribological behaviour of tungsten coatings, *Surf. Coat. Technol.* **102**, 50–62 (1998).
72. G. Keller, I. Barzen, R. Erz, W. Dotter, S. Ulrich, K. Jung, and H. Ehrhardt, Crystal-structure, morphology and composition of magnetron sputtered tungsten carbide films, *Fresenius J. Anal. Chem.* **341**, 349–352 (1991).
73. Y. Pauleau and Ph. Gouy-Pailler, Very hard solid-solution-type tungsten-carbon coatings deposited by reactive magnetron sputtering, *Mater. Lett*. **13**, 157–160 (1992).
74. D. Garg, P. N. Dyer, D. B. Dirnos, S. Sunder, H. E. Hintermann, and M. Maillat, Low-temperature chemical vapor-deposition tungsten carbide coatings for wear erosion resistance, *J. Am. Ceram. Soc*. **75**, 1008–1011 (1992).
75. E. Quesnel, Y. Pauleau, P. Monge-Cadet, and M. Brun, Tungsten and tungsten-carbon PVD multilayered structures as erosion-resistant coatings, *Surf. Coat. Technol*. **62**, 474–479 (1993).
76. A. Cavaleiro and M. T. Vieira, Evaluation of the hardness of sputtered W-C-Co thin films, *Surf. Eng*. **10**, 147–151 (1994).
77. I. N. Mihailescu, E. Gyorgy, G. Marin, M. Popescu, V. S. Teodorescu, J. Van Landuyt, C. Grivas, and A. Hatziapostolou, Crystalline structure of very hard tungsten carbide thin films obtained by reactive pulsed laser deposition, *J. Vac. Sci. Technol. A* **17**, 249–255 (1999).
78. *Fundamentals of Nanoindentation and Nanotribology*, Vol. 522 (Materials Research Society, Warrendale, PA, 1998).
79. B. Trindade, M. T. Vieira, and E. Bauer-Grosse, In situ high temperatme crystallization study of sputter deposited amorphous W-Fe-C films, *Acta Metal. Mater*. **43**, 93–99 (1995).
80. B. Trindade and M. T. Vieira, Crystallisation kinetics of amorphous W-Co-C sputtered films, *Thin Solid Films* **322**, 68–73 (1998).

9

Concept for the Design of Superhard Nanocomposites with High Thermal Stability: Their Preparation, Properties, and Industrial Applications

Stan Veprek and Maritza G. J. Veprek-Heijman

Institute for Chemistry of Inorganic Materials, Technical University Munich, Lichtenbergstr. 4, D-85747 Garching b. Munich

1. INTRODUCTION

This chapter will focus on superhard nanocomposites prepared according to our generic design principle.[1] These coatings, when correctly prepared, possess an unusual combination of mechanical properties, such as a high hardness of 40–100 GPa, high elastic recovery of 80–94%, elastic strain limit of $>10\%$, and high tensile strength of 10 to $\geq$40 GPa which is approaching the ideal strength of flaw-free materials.[2,3] Moreover, the nanostructure and the concomitant superhardness (measured at room temperature after each annealing step) remain stable up to $\geq 1100^{\circ}$C.[4]

Because these nanocomposites were in the past often confused with ordinary hard coatings in which the superhardness is achieved by energetic ion bombardment during their deposition, we shall briefly summarize the advantages and drawbacks of these different techniques for the preparation of superhard coatings. The emphasis will be on their thermal stability and oxidation resistance. It will be shown that the hardening by energetic ion bombardment yields coatings with a too low thermal stability. Therefore we expect that such superhard coatings will be only of a limited industrial use.

Recently, some researchers doubted our published data on the high hardness and suggested that our hardness measurements were incorrect (see, e.g., Ref. 5and reply in Ref. 6). Therefore, we shall also briefly summarize the recent results on

the possible artifacts during the hardness measurements on superhard coatings and how to avoid them in order to obtain correct data.

In Section 2 we shall outline our design concept[1] and describe the properties of selected classes of the nanocomposite coatings. It will be also shown that, as outlined in our earlier review,[7] several researchers had already prepared such nanocomposites earlier, without having realized their very special nature and generality of the preparation principle. Afterwards, we shall analyze examples of the published papers with respect to the deposition conditions and impurity content as far as available in these papers. It will be shown that the lack of success of some researchers to reproduce our results is due to either an incorrect choice of the deposition conditions (too low nitrogen pressure and/or deposition temperature), or impurities, or a combination of these.

The recent progress in the development of the coating technology and industrialization of the nc-$(Al_{1-x}Ti_x)N$/a-Si_3N_4 coatings is briefly summarized in the last section. The new lateral rotating arc cathode, LARC®, that uses Virtual Shutter® for precleaning of the cathodes is presented, together with an example of the excellent cutting performance of these new coatings.

1.1. Possible Artifacts During Hardness Measurement on Superhard Coatings

Static indentation hardness is the pressure under the indenter which causes the material to flow, i.e., deform plastically.[8,9] Thus, upon indentation at a low load the response is purely elastic, and only when the pressure L/A_C reaches the yield stress σ_Y, plastic deformation commences (L is the applied load and A_C is the contact area between the indenter and the material being tested). Considering, for simplicity, an ideal elastic–plastic behavior of the material, it becomes clear that when the pressure under the indenter reaches the yield stress, the static indentation hardness $H = L/A_C$ is independent of the applied load (for more details see Refs. 7–9). This is an important criterion of the correctness of the measured values.

With the modern automated load-depth sensing techniques, very often the "size indentation effect" (SIE) is observed. SIE means that the measured value of the hardness of a materials decreases (or, in the case of soft thin film on hard substrates increases) with applied load. The SIE may have a number of different reasons, such as finite radius of the indenter tip that has not been fully corrected for (see Refs. 10 and 11 and references therein), finite distance between the deformation bands,[12] dislocation pinning within a surface layer of an oxide, carbide, etc., strain hardening, and others (see e.g., Refs. 2 and 13, p. 74, and references therein). In the case of a very small load in the range of tens of micronewtons, the SIE may also be due to the low probability of the appearance of the critical flaw in the small volume being tested by the nanoindentation. This phenomenon is well known in the fracture physics and mechanics since the pioneering work of Leonardo da Vinci 500 years ago (e.g., Ref. 14, p. 241), and it has been recently convincingly illustrated by the excellent work of the Suresh's group. These researchers have shown

that with a load and indentation depth of 10–20 μN and 10–20 nm, respectively, soft single crystals of Al, Au, Cu, etc., show an ideal behavior.[15,16] With indentation depth of about ≤10 nm, it was impossible to initiate plastic deformation in these soft metals because such deformation requires a finite activation volume.[17] When measuring the hardness of soft materials with such a low load, one can easily obtain values that are factor of 5–20 higher than the correct bulk hardness, because the flow limit is not fully achieved due to the low pressure under the indenter. Also the frequently quoted use of "sharp diamond indenter" has its limitation because of the difficulties to fabricate very sharp tips of a regular shape (e.g., Ref. 13, p. 77). Even the sharpest tip becomes dull (radius of about 0.5 μm) when used for measurements on superhard materials. For these reasons the only reliable way of determining the hardness of superhard coatings is to measure it as a function of the maximum applied load, and to take the load-independent value, which is achieved typically for loads between 50 and 150 mN. This has been emphasized already in our first paper[1] and used consequently through the whole subsequent work.

Moreover, it is advisable to check the value of the hardness obtained from the indentometer with that calculated from the contact area that is measured by means of calibrated scanning electron microscope (SEM; of course, the projected area that is measured by SEM has to be converted into the contact one, according to the geometry of the indenter used). These problems together with other possible artifacts that may occur and the possibilities how to solve them were discussed in our recent papers to which we refer for further details.[2,18,19] Here we limit ourselves to two illustrative examples.

Figure 9.1 shows an example of SIE that occurs in the superhard nanocomposites (Fig. 9.1a) even when the tip correction was done very carefully (Fig. 9.1b). Because the indentation depth at the low load where the SIE appears is <0.3 μm (Fig. 9.1a, right-hand-side scale), one might believe that it is due to the tip rounding, as discussed by others.[10,11,20,21] However, the load independence of the hardness of silicon and sapphire as shown in Fig. 9.1b makes this explanation unlikely, and the fact that the SIE as shown in Fig. 9.1a is not observed on all superhard coatings (particularly on the nc-TiN/a-Si_3N_4, see Refs. 1 and 22) excludes such possible explanation. The SIE shown in Fig. 9.1a may be due to elastic deformation of the diamond indenter (see Fig. 3 in Ref. 2), or it can be associated with a particular mechanism of plastic deformation of the material of that coating. Although this question needs further studies to be unambiguously answered, the example in Fig. 9.1 shows clearly that hardness values reported from indentation at low load are likely to be subjected to SIE and, therefore, cannot be considered as reliable. This fact has to be kept in mind when considering the relevance of published data on hardness that were measured with a very low load of a few tens of micronewtons (e.g., Ref. 23).

Figure 9.2 shows a comparison of the load-independent values of hardness measured by the indentometer at maximum applied load between about 30 and 150 mN with those calculated from the contact area determined by means of calibrated

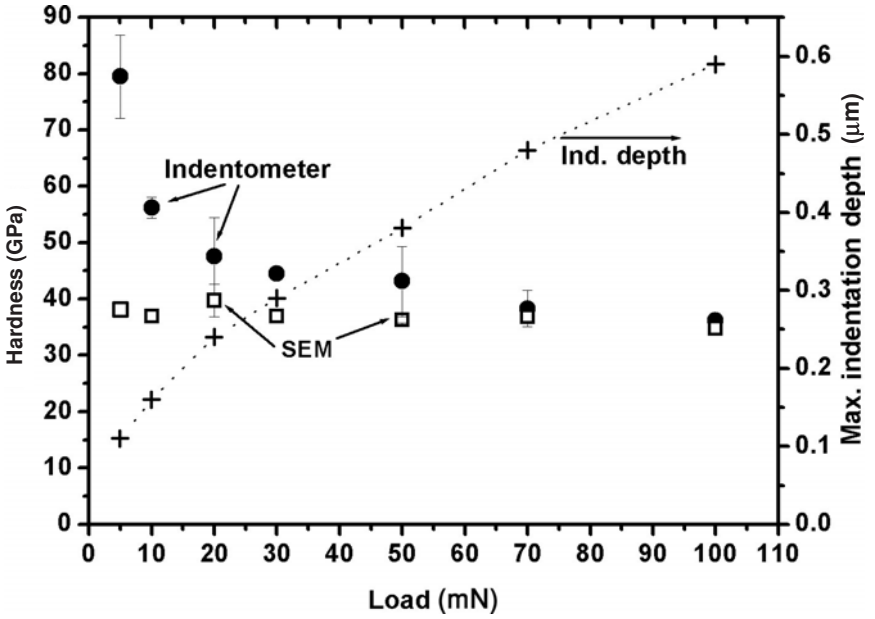

(a)

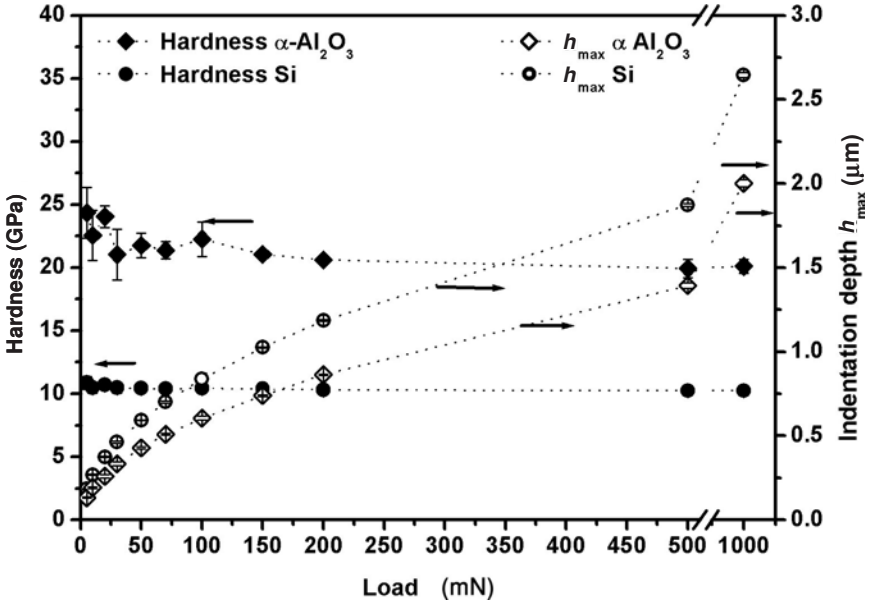

(b)

FIGURE 9.1. (a) Hardness of 6-μm-thick superhard nc-TiN/a-BN coating deposited on stainless steel substrate versus the maximum applied load as obtained from the indentometer with careful correction for the tip rounding (full symbols) and calculated from the contact area of the remaining plastic deformation measured by calibrated SEM (the projected area as recalculated to the contact one). (b) Hardness and maximum indentation depth of Si and sapphire versus maximum applied load. (From Ref. 2.)

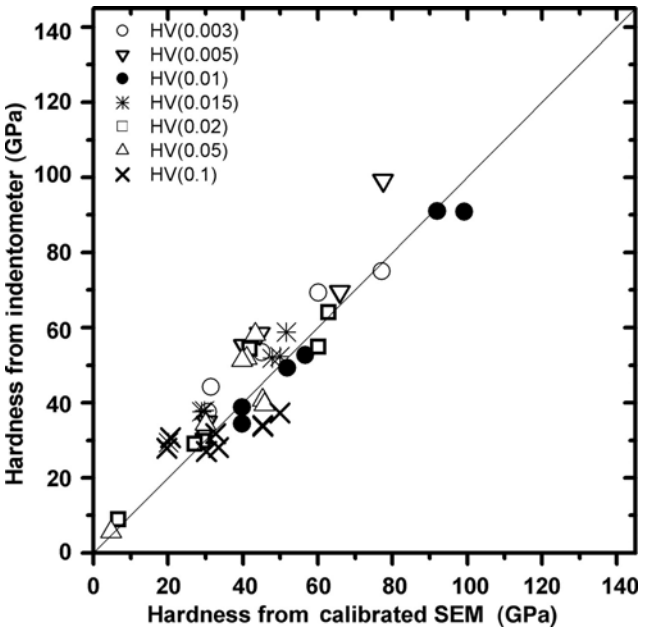

FIGURE 9.2. Load-independent hardness from the indentometer Fischerscope 100 in comparison with that calculated from the contact area of the remaining indentation, using calibrated SEM. (See text and Ref. 2.)

SEM. There is no doubt that such data are correct even for the highest values of 100 GPa, i.e., in the range of diamond.

1.2. Requirements on the Thickness of the Coatings

It has been noticed by several researchers in the past that in order to measure the hardness of hard coatings on softer substrate correctly, the maximum indentation depth must not exceed 10% of the thickness of the coating, because above this value plastic deformation occurs in the softer substrate, such as steel. For example, Lichinchi *et al.*,[24] who carried out modeling by means of finite element method (FEM), have shown that the indentation into TiN on high strength steel (HSS) causes plastic deformation in the substrate when the indentation depth reaches 15%. Similar results were reported by other researchers as well. Our FEM simulation of the indentation into the superhard coatings revealed that because of the higher strength of these materials, the maximum indentation depth should not exceed about 5% of the coating's thickness in order to avoid the plastic deformation in the substrate.[25]

In summary, the maximum indentation depth should be larger than about 0.3 μm in order to avoid SIE and simultaneously not exceed 5% of the thickness of the superhard coatings to avoid the effect of the substrate; reliable measurements are

possible only when the thickness of the coatings is ≥6–8 μm. This rule was met in the majority of our reported measurements with exception of only some of the earlier ones, where we used about 4-μm-thick coatings before realizing that the "rule of 10%" is not sufficient for superhard coatings. The limited space available here does not allow us to analyze all the published values of hardness in the range of ≥40 GPa that were measured on much thinner coatings (e.g., less than 0.5 μm)[23] using small loads in the range of tens of μN. Therefore we leave this question to the judgment of the reader.

2. THE EARLIER WORK

Nowadays, there are many superhard nanocomposites of different chemical composition reported in the literature. However, because "Ti-Si-N" is the most frequently studied system so far, we shall first focus on this as a model one. Many researchers studied the thermodynamic phase diagrams of the Ti-Si-N system (for a summary see Ref. 26) and the deposition of such films by means of thermal chemical vapor deposition (CVD) (e.g., Ref. 27). Because of thermodynamic and kinetic reasons, high temperatures are needed for the thermal CVD in this system. Therefore no hardness enhancement was reported.(For lack of space we cannot include a more detailed discussion and all references here.)

Li *et al*. were the first authors who reported on the deposition of superhard "Ti-Si-N" coatings by means of plasma chemical vapor deposition (PCVD) using chlorides as a source for Ti and Si.[28] Li *et al*. attributed the hardness enhancement to the precipitation of small Si_3N_4 particles within TiN nanocrystals. A hardness of 60 GPa reported by Li *et al*. was probably due to the ternary nc-TiN/a-Si_3N_4/a-$TiSi_2$ nature of these coatings, as found in subsequent joint work.[29–33] (Notice that in the binary systems nc-Me_nN/a-Si_3N_4, a maximum hardness of only 50–60 GPa has been achieved; see below.) Together with Li we also found that, after a period of few months, the hardness of these coatings decreased, and we attributed this degradation to the relatively large chlorine content in these coatings.[33] Recent studies revealed that this degradation is an intrinsic property of these systems due to chemical degradation of the $TiSi_2$ phase by water from air in a similar way as it is known for silica fibers.[34] Furthermore, when we found later that the crystallite size is only 3–4 nm it became clear that the original explanation based on a dispersion hardening[28] could not be correct. This led us to the development of the generic design concept.[1,3]

Many researchers (Knotek *et al*., Andrievski *et al*., Gissler *et al*., Hammer *et al*., Mitterer *et al*., etc.) have published papers on the deposition and properties of "Ti-B-N" coatings (for a review of the earlier work, see Ref. 7). In the recent review[7] it was pointed out that based on the immiscibility of the stoichiometric TiN and TiB_2 phases and on the development of the morphology of these coatings as a function of their composition and hardness, these were also nanocomposites. This is seen on the development of the morphology of the Ti-B-N coatings as

a function of their composition and hardness reported by Andrievski (Fig. 1 of Ref. 35). The columnar structure of the coatings deposited by magnetron reactive sputtering almost vanished at the composition where the maximum hardness of $\geq$50 GPa was found.

In the majority of coatings deposited by physical vapor deposition (PVD) techniques at low pressure of the order of $<10^{-3}$ mbar and negative substrate bias, there is a large biaxial compressive stress of 5–8 GPa due to the energetic ion bombardment during their deposition. Therefore, one has to carefully check if the measured hardness is not enhanced by that bombardment, as it will be discussed below.

Figure 9.3 shows an example from the works of Hammer *et al*.[36] and more recent results of Mitterer *et al*.[37] We discussed these combined results[38] in order to emphasize the difference between these two mechanisms of hardness enhancement, i.e., by energetic ion bombardment and by the formation of stable nanocomposite structure due to self-organization upon the spinodal phase segregation. When the coatings deposited by Hammer *et al*. at room temperature were annealed to 600–800°C, the hardness increased to about 40 GPa (see Fig. 9.3a) and the originally amorphous films showed nanocrystalline X-ray diffraction (XRD) pattern. Thus, although the $TiB_{2.2}$ and TiN coatings deposited by Mitterer *et al*. have a high hardness enhanced by energetic ion bombardment during their deposition (see Fig. 9.3b), the hardness of the "Ti-B-N" coatings from the middle of the nitrogen range in Fig. 9.3b is due predominantly to the formation of the nanocomposite structure as obvious by comparison of the values from Fig. 9.3b with those in Fig. 9.3a. The hardness maximum at about 27% of nitrogen is less pronounced than that usually found in our nanocomposites deposited by PCVD (see below), probably because of some additional enhancement due to the energetic ion bombardment. Would this enhancement be absent, the maximum were probably much more pronounced as indicated by the broken lines which are approaching the bulk hardness of TiB_2 on the left and TiN on the right-hand side of Fig. 9.3b. We shall see later that this is a typical behavior of systems that forms stable nanocomposites according to our design principle. Mayrhofer *et al*.[39,40] presented recently a detailed, convincing evidence for the nanocomposite nature of these coatings, as suggested in our earlier review[7] and discussed here.

To the best of our knowledge, Knotek was also the first author who reported the hardness enhancement in the "superstoichiometric TiC_{1+x}" or "TiC/a-C"[41,42] similar to that found in our nc-TiN/a-Si_3N_4, when the excess carbon content reached about 20 at%. This and many similar systems were studied later by other authors (e.g., Refs. 43 and 44). Further systems having some analogy with the TiC/a-C were reported by Sproul*et al*. These researchers deposited multilayers consisting of TiN and CN_x[45–47] (or ZrN and CN_x)[48] at a relative low temperature of $\leq$200°C. When the thickness of the double layers ("the period") decreased to about 4 nm the hardness increased to about 40 GPa as well known from the "heterostructures." However, when the period was further decreased to about 2 nm, a nanocomposite structure was formed spontaneously and the layered structure vanished, as shown

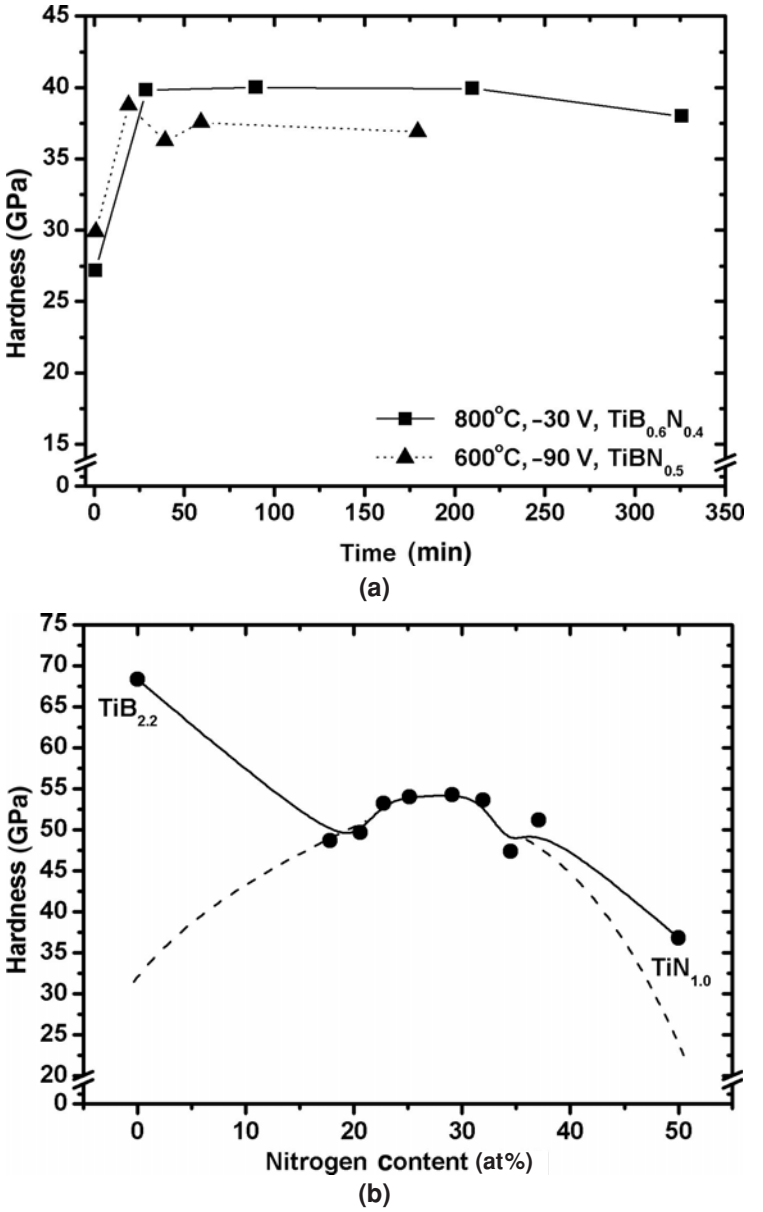

FIGURE 9.3. (a) Increase of hardness of Ti-B-N coatings upon annealing when a nanocomposite structure is formed by self-organization.[38] (b) Dependence of the hardness of Ti-B-N coatings deposited by magnetron sputtering and energetic ion bombardment during the deposition.[36,37]

by XRD and high-resolution transmission electron microscopy (HRTEM) in these papers. There are many further, more recent examples in the literature. Because the "Ti-B-N," "TiC_{1+x}," and other related systems are discussed in other chapters of this book, we shall concentrate mainly on the "Ti-Si-N" and related ones that consist of a hard, nanocrystalline transition metal nitride and an amorphous, covalent nitride, such as Si_3N_4 or BN.

3. SUPERHARD NANOCOMPOSITES IN COMPARISON WITH HARDENING BY ION BOMBARDMENT

The easiest way to prepare superhard coatings is to apply energetic ion bombardment during the deposition of hard materials, such as stoichiometric TiN, (TiAlV)N, HfB_2, as well as so-called "nanocomposites" consisting of a hard transition metal nitride and a soft metal which does not form a stable nitride (ZrN/Ni, ZrN/Cu, Cr_2N/Ni, etc.).[49] Because the latter coatings are frequently confused with superhard nanocomposites prepared according to our generic principle (see below), we shall briefly discuss, in this section, how to experimentally distinguish these two mechanisms of hardness enhancement.

One possibility is to study the behavior of the hardness (measured after each annealing step at room temperature) upon annealing to high temperatures, as shown in Fig. 9.4. The hardness that has been enhanced by energetic ion bombardment strongly decreases with annealing temperature to the ordinary bulk value upon

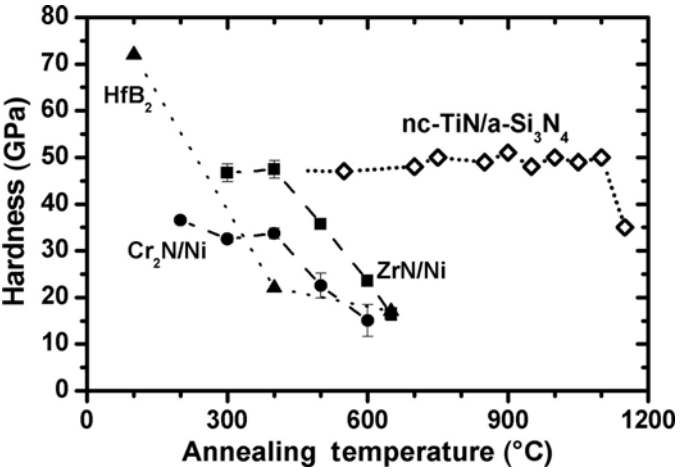

FIGURE 9.4. Dependence of the hardness of HfB_2,[50] Cr_2N/Ni, and ZrN/Ni[51] coatings hardened by energetic ion bombardment and the stable superhard nc-TiN/a-Si_3N_4 nanocomposites on the temperature of isochronal annealing in pure nitrogen.[4,7] (The hardness was measured at room temperature after each annealing step.)

annealing to 400–600°C whereas that of the superhard nanocomposites remains unchanged upon annealing up to 1100°C (see Fig. 9.4; for further examples, see Refs. 4, 51, and 52). This softening upon annealing of superhard coatings hardened by energetic ion bombardment is a general phenomenon associated with the relaxation of ion-induced defects in the films.[53] The hardness of these coatings decreases also with increasing deposition temperature in a similar manner as shown in Fig. 9.4 for the annealing (see Fig. 2 in Ref. 54.) The reason for that is the thermal relaxation of the ion-induced defects within the growing film in a depth larger than the projected range of the ions.

Another possibility how to distinguish between the stable, superhard nanocomposites, and the ordinary coatings is the dependence of hardness on their composition, shown in Fig. 9.5. It is important to notice that superhard nanocomposites prepared according to our design principle[1–3,7] show a maximum hardness at a composition corresponding to the percolation threshold when the surface of the polar transition metal nitrides is covered with about one monolayer of Si_3N_4[30] or BN.[52]

Figure 9.5 illustrates the excellent reproducibility of the hardness enhancement obtained in our laboratory when the superhard nanocomposites are deposited under conditions of high activity (partial pressure) of nitrogen and high temperature of $\geq$500°C, as explained in our earlier papers.[1,3,55] The $TiN_{1-x}C_x$ system displays solubility within the whole composition range and, therefore, the hardness follows

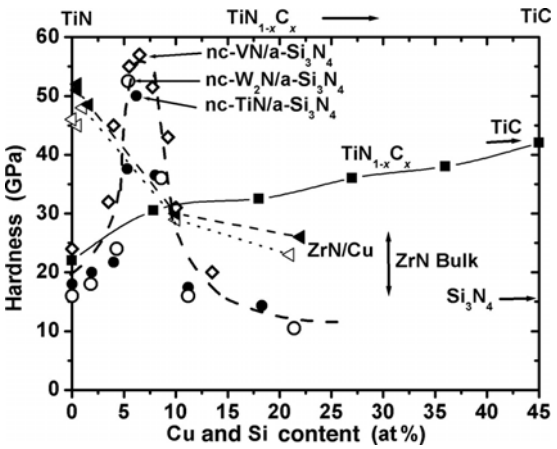

FIGURE 9.5. Dependence of hardness of various coatings on their composition. $TiN_{1-x}C_x$ forms a solid solution and therefore the hardness follows the rule of mixtures.[55] In the case of the so-called "nanocomposites" consisting of a hard transition metal nitride and ductile metal, the maximum hardness is achieved with the pure nitride without that metal. (Adapted from Ref. 54.) The superhard nanocomposites prepared according to our design principle show a maximum hardness at a percolation threshold.[1,7,30]

the rule of mixtures (Ref. 14, p. 391) increasing, with increasing carbon content, monotonously from the value of pure TiN to that of TiC.[55] The so-called "superhard nanocomposites" Me(1)N/Me(2) consisting of hard transition metal nitride and a ductile metal[49] reach the highest hardness enhancement (caused by the energetic ion bombardment during their deposition) for a very low content of the ductile metal or when this is absent, as seen in Fig. 9.5. This behavior was found for many other Me(1)N/Me(2) systems as well.(J. Musil, private communication, 2003.) It resembles the behavior of cemented carbide in which the hardness also decreases with increasing content of cobalt.

The effect of energetic ion bombardment applied during the deposition of thin films (also called "ion plating" and "activated reactive evaporation") as pioneered by D. Mattox and R. F. Bunshah, respectively,[56] on their microstructure, porosity, surface roughness, and hardness was investigated in many papers. Hoffman and Gaerttner were probably the first researchers who reported on the decrease of surface roughness and change of the biaxial stress from tensile, which is typical for thermally evaporated films, to compressive one.[57] Veprek *et al*. have reported the complex, synergistic effect of energetic ion bombardment on the properties of nanocrystalline silicon[58,59] and compared the measured data with theoretical Transport of ions in matter (TRIM) calculations.[60] They have shown that besides the smoother surface and the built-up of biaxial compressive stress, the ion bombardment also results in a decrease of the average crystallite size, build-up of displacement damage (i.e., the formation of Frenkel pairs), and, above a certain threshold, to the amorphization of the deposited film.

It is the complex, synergistic effect of all these processes that results in the high hardness enhancement frequently found in hard coatings deposited at relatively low temperature of $\leq 300^{\circ}$C (e.g., Refs. 50 and 61–64). The highest hardness enhancement of 100 GPa due to this effect was reported by Musil *et al*. for (TiAlV)N and 80 GPa for TiN coatings.[62] The compressive stress of 5–8 GPa (at a higher stress, delamination of the coatings occurs) alone cannot explain the observed hardness enhancement shown in Fig. 9.4 for these coatings. The reason is only that the biaxial compressive stress σ_c acts against the shear stress under the indenter in direction parallel to the substrate, and, therefore, the resulting hardness enhancement is only equal to the value of that compressive stress $H(\sigma_c) = H_0 - \sigma_c$ (notice that compressive stress $\sigma_c < 0$). This has been studied and confirmed in many papers and recently summarized by Pharr *et al*.[65–67] Nevertheless, because the stress is relatively easy to measure, one finds and reports often a correlation between the hardness and the compressive biaxial coatings as shown in Fig. 9.6.

The TiN_x (see Fig. 9.6a) coatings deposited by magnetron sputtering at low temperature[63] in a similar way as the (TiAlV)N with hardness of 100 Gpa,[62] as well as the "Ti-Si-N" nanocomposites of Vaz[68] show a clear correlation between the hardness and compressive biaxial stress. Thus, one may ask the question as to what extent is the hardness in the coatings of Vaz due to the energetic ion bombardment and/or to the formation of nanocomposite structure. Again, the answer is provided

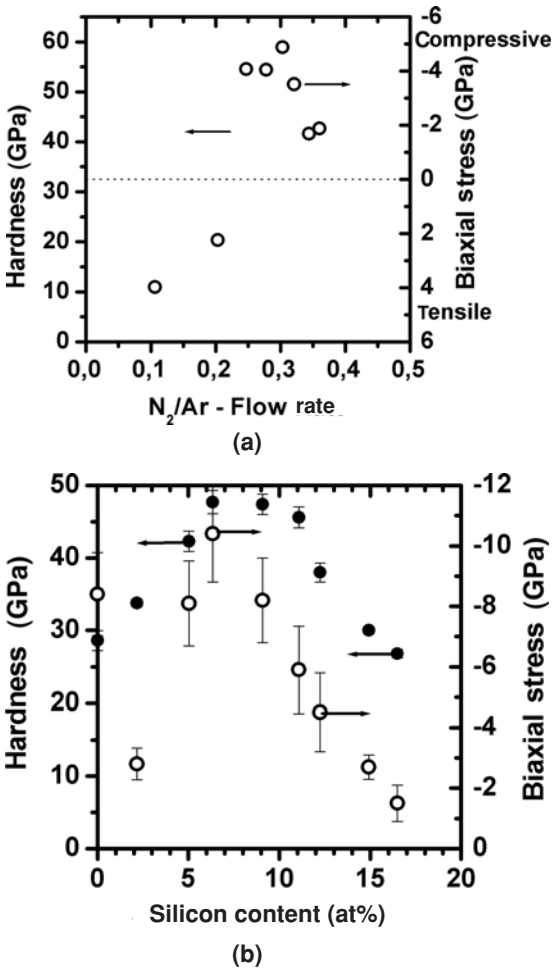

FIGURE 9.6. (a) Hardness and compressive stress of TiN_x coatings deposited by magnetron sputtering.[62,63] (b) Hardness and compressive stress of Ti-Si-N coatings deposited by magnetron sputtering at $\leq 300^{\circ}C$.[68]

by the annealing experiment: Whereas the hardness of the TiN coatings decreases upon annealing in a similar way as shown in Fig. 9.4, the hardness of the Ti-Si-N coatings of Vaz remains nearly constant as shown in Fig. 9.7.[69] This is not necessarily valid for all coatings deposited by magnetron sputtering. Very often, these coatings show self-hardening upon annealing (e.g., Ref. 70), which is a clear evidence that they were deposited under inappropriate conditions that do not assure the formation of stable nanostructure during the deposition (see below). Interestingly, only one coating reported in the recent review[70] showed some self-

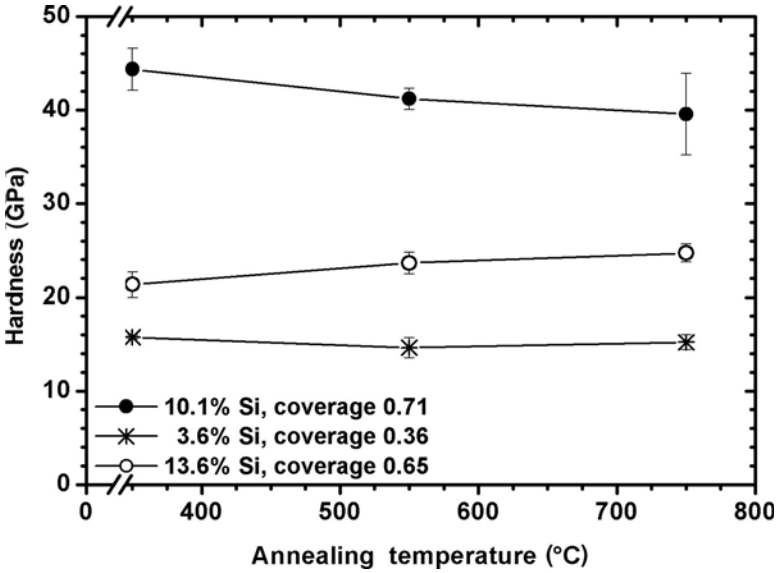

FIGURE 9.7. Annealing behavior of the "Ti-Si-N" coatings deposited by Vaz at higher temperatures than those shown in Fig. 9.6b. (From Ref. 69.)

hardening, whereas the other softened upon annealing already to $\geq$500°C. This leaves the question regarding the origin of the hardness enhancement in the coatings of Patscheideropen.

4. SUPERHARD NANOCOMPOSITES WITH HIGH THERMAL STABILITY

4.1. The Design Concept for the Deposition of Stable Superhard Nanocomposites

As already mentioned, the original explanation of Li *et al*. for the strong hardness enhancement found in their coatings was based on the assumed precipitation of small Si_3N_4 particles dispersed within the TiN crystals.[28] However, when we later analyzed our coatings in more details and determined the crystallite size, we realized that this explanation could not be correct because such precipitates cannot be formed within a few nanometers of small crystallites. [This is not any criticism of Li *et al*. In fact, because the XRD measurements of their coatings was done at our laboratory (see acknowledgment in Ref. 28), we should have realized this already in 1992.] This led us to the development of a design concept for the superhard nanocomposites[1] that has proven to be of generic nature.[3]

This concept is based on a strong, thermodynamically driven and diffusion rate controlled (spinodal) phase segregation that leads to the formation of a stable nanostructure by self-organization.[1,3,7] In our first paper on this subject[1] we originally included the concept of the spinodal decomposition following the inspiring paper of Cahn in which he described the hardening upon formation of long-range coherent composition fluctuations by spinodal phase separation,[71] and because it was suggested to be responsible for the self-hardening of (TiZr)N coatings upon annealing, as observed by Knotek[72] and later repeated by Andrievski *et al.*[73] However, when checking carefully the latter two papers we realized that the very small increase of the hardness was found only for one coating with the composition $(Ti_{0.3}Zr_{0.7})N$ but not for $(Ti_xZr_{1-x})N$ with $x = 0.5$ and 0.7 in the paper of Knotek and Barimani. In the paper of Andrievski *et al.*, the composition was unknown.[73](R. A. Andrievski, private communication, 2003.) Because the hardening was not observed for any other composition and there was no evidence for it in the references quoted in Ref. 72, we dropped the term "spinodal" at that time but kept the term "thermodynamically driven compositional modulation" (see Ref. 1, p. 66, line 13) in order to bring this concept into discussion. In course of the more recent work there is growing experimental evidence that the stable nanostructure is indeed formed by spinodal decomposition (see below). However, the final evidence in terms of the dependence of the Gibbs free energy of the formation of the mixed phase on the composition, which has to show negative second derivative, is still lacking. With this limitation in mind we shall describe how the formation of the nanostructure by self-organization upon spinodal phase segregation operates.

In the nc-TiN/a-Si_3N_4 and analogous systems, such as nc-W_2N/a-Si_3N_4,[74] nc-VN/a-Si_3N_4,[55] and others, the spinodal phase segregation is thermodynamically driven by a high activity (partial pressure) of nitrogen, and rate controlled by the diffusion that requires a sufficiently high temperature. (For further details about the spinodal decomposition see Refs. 75 and 76.) Under these conditions, the spinodal phase segregation occurs when the second derivative of the Gibbs free energy is negative, because the mixed system is inherently unstable against any infinitesimally small, local fluctuation.[3,75,76] This is illustrated in Fig. 9.8a for the lower curve within the whole range of the composition and for the upper one for the range between the compositions x_1 and x_2. The latter curve corresponds to the case of a lower activity (partial pressure) of nitrogen of less than about 10^{-3} mbar for T_{dep} of about 500–700°C, and/or a too high temperature where the decomposition of the stoichiometric nitrides commences (for TiN and Si_3N_4) above about 1000°C in vacuum.

For illustration, we show in Fig. 9.8b, a simplified phase diagram of the Ti-S-N system at about 900–1100°C.[77] One can see that at a sufficiently high activity of nitrogen (partial pressure of $>10^{-5}$ bar $= 10^{-2}$ mbar) the fully segregated, stoichiometric TiN and Si_3N_4 phases are formed. Under such conditions, the spinodal decomposition occurs during the deposition, resulting in the formation

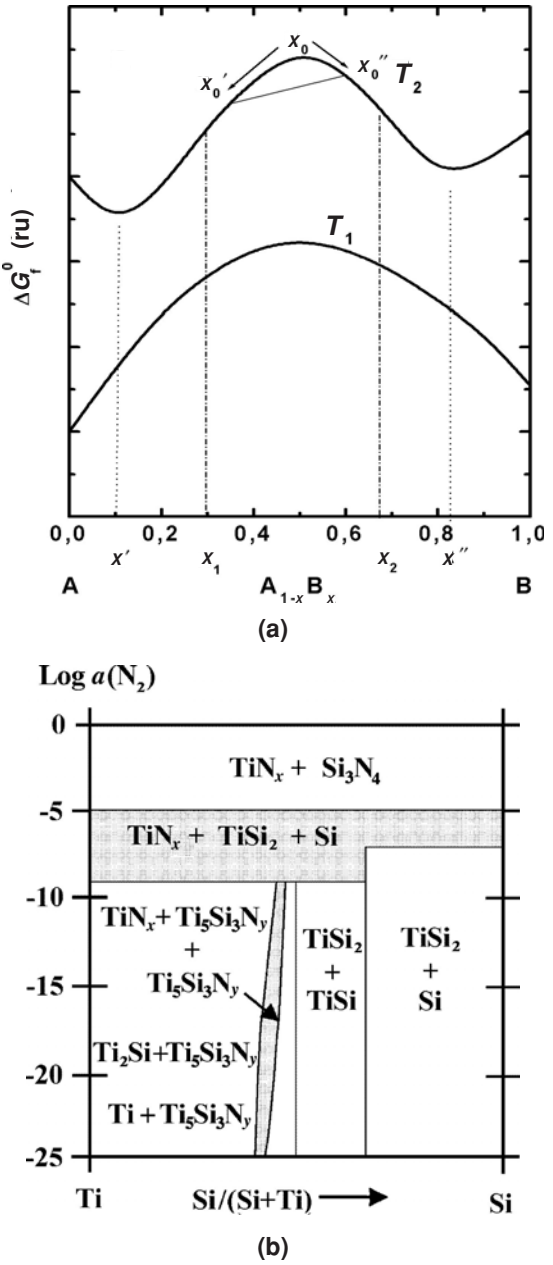

FIGURE 9.8. (a) Schematic dependence of the free energy of formation of a binary solution $A_{1-x}B_x$ on the composition, which shows immiscibility between the composition x' and x'' for a low pressure of nitrogen and a too high temperature T_2 and within the whole range at a sufficiently high pressure of nitrogen and a lower temperature T_1 of about 550°C. (b) A simplified phase diagram of the Ti-Si-N system at a temperature of about 900–1100°C.

of an nc-TiN/a-Si_3N_4 nanocomposite ("thermodynamically driven compositional modulation")[1] with a small and regular crystallite size, as confirmed by HRTEM, in Fig. 9.9.[78] The medium-resolution transmission electron micrographs show a regular nanostructure that is typical of spinodally segregated binary system. Would the segregation and nanostructure formation have occurred by nucleation and growth, one would have to see a much larger size distribution of the compositional modulation, i.e., of the crystallite sizes. (For an example of such micrographs, the reader should consult Fig. 6.14 on p. 166 in Ref. 79.) Fig. 9.9b shows a high-resolution micrograph with a few nanocrystals where resolved crystal lattice planes are seen. Because the random orientation of the crystallites is reached at the silicon content of about $\geq$8 at%, only few crystallites whose lattice plains are oriented parallel to the electron beam appear in the lattice resolution. A small tilting of the sample in the microscope results in vanishing of these lattice images and appearance of others in areas where the micrograph in Fig. 9.9b appears structure-less. For each sample under study several tens of micrographs were taken and evaluated.[78]

The size of these nanocrystals of 3–4 nm agrees very well with that determined from XRD using Warren–Averbach Fourrier transform method (see Fig. 4 in Ref. 78). The selected area electron diffraction pattern shown in Fig. 9.9c confirms, in agreement with XRD studies on a large number of our films, that TiN is the only crystalline phase. Because the Si 2p line in X-ray photoelectron spectra shows a chemical shift typical of Si fourfold coordinated to nitrogen, as in Si_3N_4 (see Fig. 4 in Ref. 1), there is no doubt left regarding the nanostructure of the nc-TiN/a-Si_3N_4 nanocomposites. Let us emphasize that in course of these studies[78] we investigated 10 coatings with different composition and found the same results regarding the TiN and Si_3N_4 segregation (of course, the crystalline size changed as shown in Fig. 9.10a and in Fig. 4 in Ref. 78).

When, however, the nitrogen activity is too low (partial pressure of $<10^6$ atm) the stoichiometric and fully segregated TiN and Si_3N_4 phases are not stable. Instead, mixed phases and $TiSi_2$ are formed (see the phase diagram in Fig. 9.8b), and the interfaces are not sharp, which results in a decrease of the hardness due to an easier grain boundary sliding. These conditions have been already emphasized in our first paper together with a simple thermodynamic calculation (see Fig. 1 in Ref. 1) in order to illustrate the necessity of using a sufficiently high nitrogen pressure.

As pointed out already, a sufficiently high nitrogen pressure assures only the thermodynamically driven force for the segregation. Because the rate of that segregation is diffusion controlled, a sufficiently high temperature is needed. We reported[1] that a temperature of 500–550°C is sufficient and still low enough to be compatible with the majority of substrates used, e.g., for cutting tools [notice that even high speed steel (HSS) is stable up to about 540°C]. Let us also emphasize that if significantly higher temperatures are used during the deposition or annealing, the nitrogen activity has to be increased correspondingly in order to bring the system into the fully segregated stoichiometric TiN and Si_3N_4.

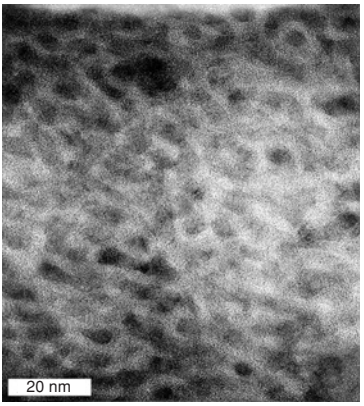

(a)

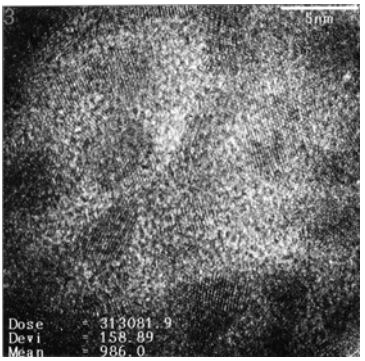

(b)

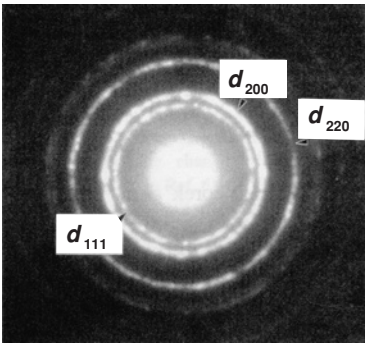

(c)

FIGURE 9.9. (a) Medium- and (b) high-resolution transmission electron micrograph of nc-TiN/a-Si_3N_4 nanocmposites. (c) Selected area (ca. 50×50 nm^2) electron diffraction pattern. (From Ref. 78.)

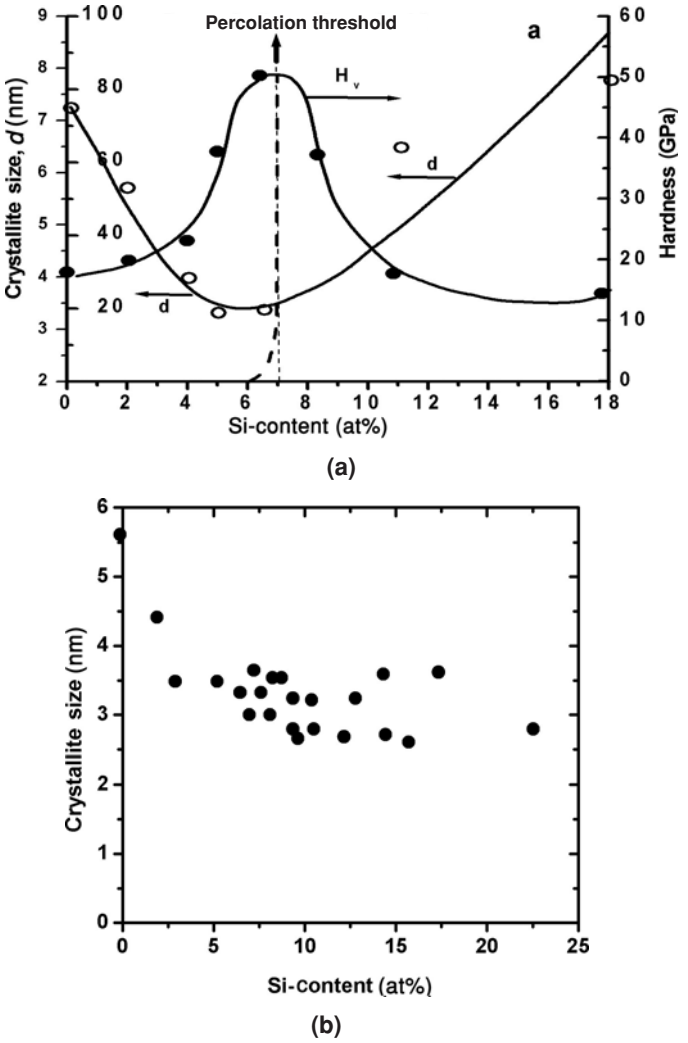

FIGURE 9.10. (a) Dependence of the crystallite size and hardness on the total silicon content (bonded as Si_3N_4) in nc-TiN/a-Si_3N_4 for coatings deposited by PCVD upon low-energy ion bombardment.[1] The hardness reaches maximum and the crystallite size minimum at the percolation threshold of the Si_3N_4 phase. (b) Dependence of the crystallite size on Si content for nc-TiN/a-Si_3N_4 nanocomposites deposited under energetic ion bombardment at the cathode of an abnormal glow discharge at current density of 2.5 mA/cm^2.[30] (c) The maximum hardness is achieved when the TiN nanocrystals are covered by about one monolayer of Si_3N_4.[30] (d) Also in the systems nc-TiN/a-BN and nc-TiN/a-BN/a-TiB_2 the maximum hardness corresponds to the situation when the TiN nanocrystals are covered with about one monolayer of the nonpolar, covalent BN.[52]

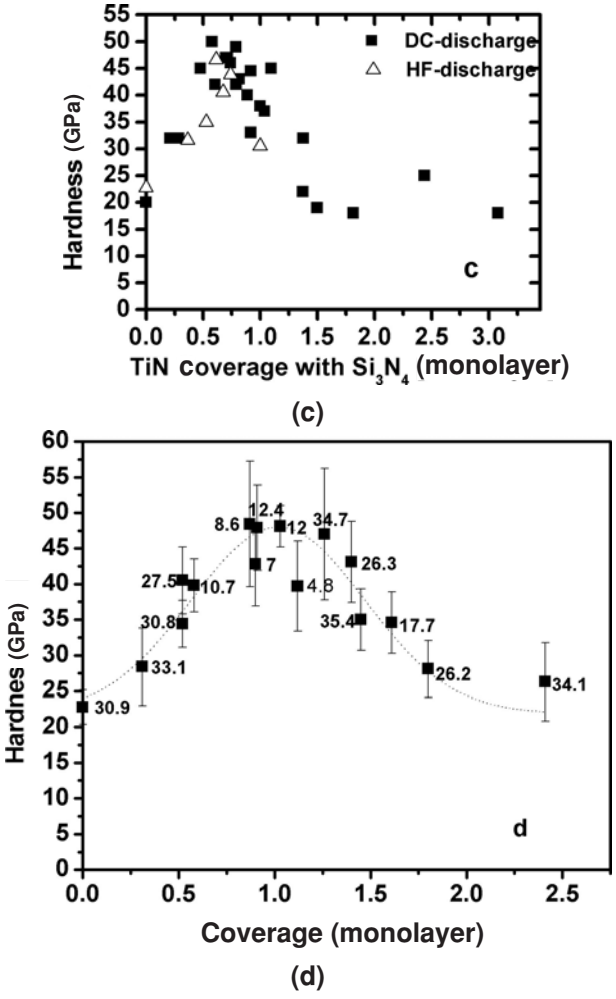

FIGURE 9.10. (*Continued*)

Although these conditions were described and explained in Ref. 1 and subsequent papers from our group (see, e.g., Refs. 3, 55, and 74), there are still many papers being published at the present time where the authors use a too low nitrogen pressure and/or low temperature and, consequently, are unable to reproduce our results. This issue will be discussed in more detail in Section 5.

When the deposition conditions are properly chosen as to provide the high thermodynamic driving force and sufficiently high deposition temperature, and the energy of ions reaching the surface of the growing film is low as in a high-frequency (HF)discharge at high pressure,[1,74] the hardness reaches a maximum of 50–60 GPa at a silicon content of about 8–10 at% as shown in Fig. 9.10a when the

nanocrystals of the transition metal nitrides (or carbides) are covered with about one monolayer of silicon[1,30] (Fig. 9.10c), or of boron nitride in the case of the nc-TiN/a-BN system (see Fig. 9.10d.)[52]

When, however, the surface of the growing film is bombarded by energetic ions as on the cathode of an intense (2.5 mA/cm^2) abnormal direct current glow discharge, the crystallite size is largely controlled by that ion bombardment[58,59] and shows only a slight decrease from TiN to nc-TiN/a-Si_3N_4 as shown in Fig. 9.10b. However, as seen in Fig. 9.10c, in both cases, i.e., low and high energetic ion bombardment, the maximum hardness is achieved when there is about one monolayer of Si_3N_4 between the TiN nanocrystals.

Thus, it is not the volume content of the Si_3N_4 or BN tissue alone that corresponds to the maximum hardness but its ratio to the specific interface area of the nanocrystalline phase, which depends on the crystallite size and shape.[30,52] When prepared under conditions that enable the formation of the stable nanostructure during the deposition, the crystallite size and the hardness behaved in the same way as shown in Fig. 9.10a for nc-TiN/a-Si_3N_4. When the maximum hardness was achieved, the crystallites were of regular shape with a size of about 3–4 nm for all the nc-Me_nN/a-Si_3N_4 [Me = Ti, W, V, ($Al_{1-x}Ti_x$)] systems that were studied so far.[30,55,74] We have further shown that under the conditions where the crystallite size reaches minimum and the hardness maximum (Fig. 9.10), the thickness of the amorphous tissue is about 0.3–0.5 nm, i.e., about one monolayer of Si_3N_4 (see last line on p. 70 in Ref. 1). This was later confirmed by a more detailed analyses for all systems studied in detail so far.[30,55,74]

As predicted[1,74] the universality of our design principle was verified by a successful preparation of a variety of superhard nanocomposites based on transition metal nitrides in a combination with covalent, nonmetallic silicon or boron nitride, such as nc-W_2N/a-Si_3N_4, nc-VN/a-Si_3N_4, nc-TiN/a-Si_3N_4/a- & nc-$TiSi_2$, nc-TiN/a-BN, and nc-TiN/a-BN/a-TiB_2 (see Refs. 1, 30, 74, 80, and references therein). Based on the generality of the thermodynamical design principle, we also predicted that it should work in a variety of systems including carbides, borides, and others that meet the conditions specified in our earlier papers.[1,7,74]

As already mentioned,[7] several researchers indeed prepared such nanocomposites earlier without having realized the generality of the design concept.

Interestingly, the crystallite size of the nc-TiN/a-BN nanocomposites with the optimum composition and maximum hardness is larger than in the case of nc-TiN/a-Si_3N_4. The numbers in Fig. 9.10d indicate the respective crystallite size for a given sample. For nc-TiN/a-BN with a negligible fraction of a-$TiSi_2$ the crystallite size is larger than about 12 nm and it decreases when a larger fraction of TiB_2 is present (points with numbers $\leq$10 nm in Fig. 9.10d). As one can see, the optimum coverage of the TiN nanocrystals is decisive in achieving the maximum hardness in both these systems.

The higher value of the crystallite size in the binary nc-TiN/a-BN system as compared with the nc-TiN/a-Si_3N_4 can be understood in terms of the theory of the spinodal segregation.[75,76] The "period" of the spinodally segregated system

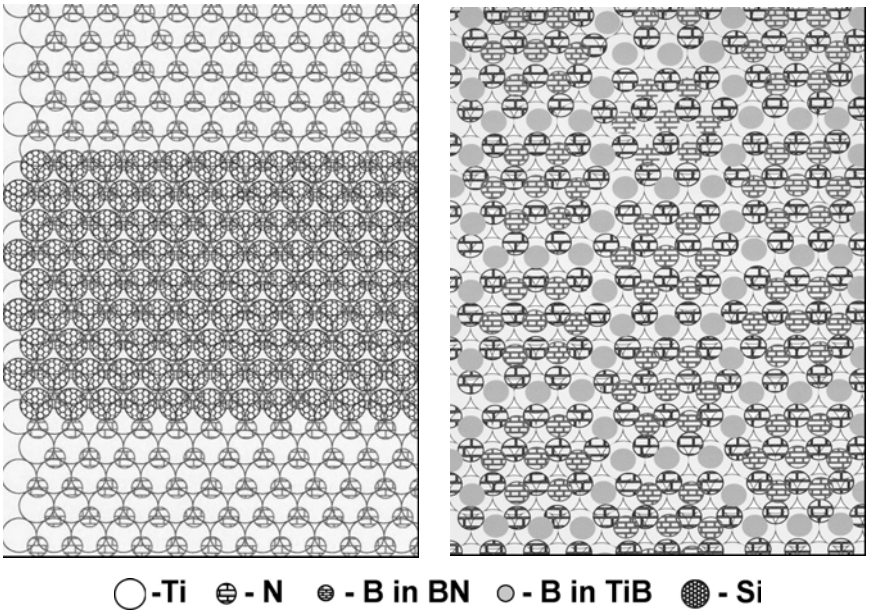

FIGURE 9.11. Left: Nitrogen-terminated [111] surface of TiN with Si atoms on top of the N ones shown in the middle part of that figure. Right: Nitrogen-terminated [111] surface of TiN covered with B atoms (see text). (From Ref. 80.)

is determined by a balance between the decrease of the Gibbs free energy of the mixed system when the segregation is completed and the opposing, destabilizing effect of structural mismatch between the phases. With increasing mismatch the period increases.[75,76] As shown in Fig. 9.11, the Si atoms are matching fairly well with the nitrogen-terminated [111] TiN surface (lowest energy one) whereas the B atoms are too small. When the B atoms are coordinated to the terminal nitrogen on that surface (further called "BN"), the nitrogen atoms must slightly move, thus opening a space for other B atoms that are coordinated to Ti (further called "Ti-B-N"; see Fig. 9.11, right-hand side). Although this model may appear to be too simplified, it provides a surprisingly good agreement with the experiment. From a variety of such models one can estimate the ratio of the "BN" to "Ti-B-N" atoms to be about 2:1, which agrees very well with the intensity ratio shown in the X-ray photoelectron spectroscopy (XPS) signal of the B 1s region in Fig. 9.12b. When the TiB_2 fraction increases but the coverage is still close to the maximum in Fig. 9.10c, this ratio remains nearly constant. In the case of nc-TiN/a-Si_3N_4 where the Si atoms are matching the TiN surface much better, only the Si 2p signal corresponding to Si fourfold coordinated to nitrogen is seen (see Fig. 12a and Fig. 4 in Ref. 1). Because of the larger mismatch in the nc-TiN/a-BN system, one has to expect a larger crystallite size in agreement with the theory of the spinodal segregation. This result further supports the concept

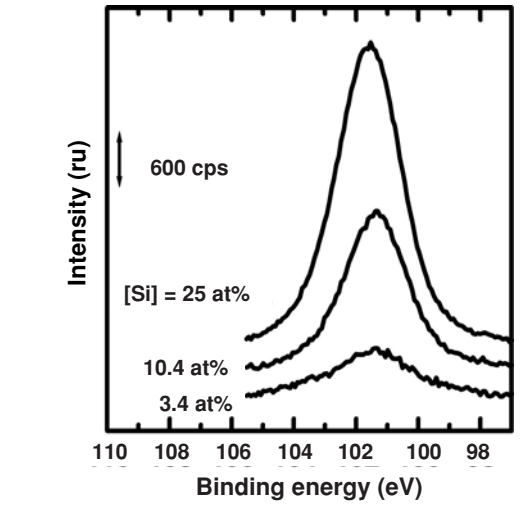

(a)

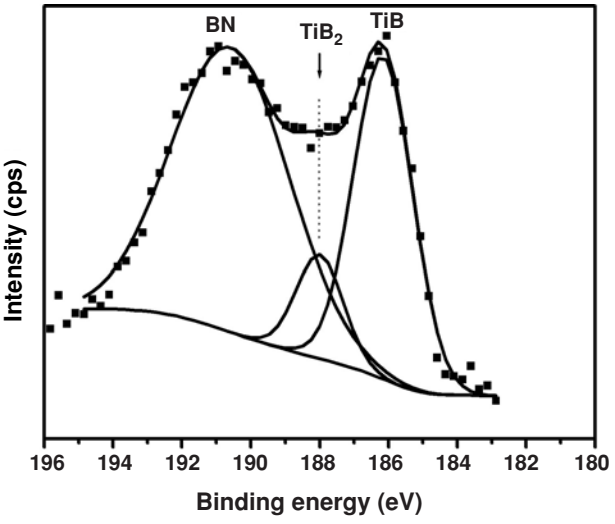

(b)

FIGURE 9.12. (a) Si 2p XPS signal from nc-TiN/a-Si_3N_4 nanocomposites deposited by PCVD in an intense discharge at nitrogen pressure of $\geq$0.3 mbar. (b) B 1s XPS signal from nc-TiN/a-BN coatings corresponding to the maximum of the hardness in Fig. 9.10c. (From Ref. 52.)

of spinodal phase segregation, in these systems in agreement with our generic concept.

A critical reader would surely wish to see a direct experimental evidence that would show that indeed Si_3N_4 and BN are covering the surface of the TiN nanocrystals. Unfortunately, the spatial resolution of HRTEM with electron energy

loss spectrometry of $\geq$0.8 nm is not sufficient. Therefore we have tried, in collaboration with another laboratory, to use the pulsed field desorption time-of-flight mass spectrometry (also called "three-dimensional-atom-probe," e.g., Ref. 81). However, in spite of a large effort and invested time, we could not obtain sufficient signals because of mechanical instability of the specimen that has to be fabricated in the form of a very sharp tip in order to obtain a controllable field desorption of the ions. Thus, the direct experimental verification remains a challenge. Nevertheless, all the data presented so far strongly support the concept because Si or B atoms dissolved within a substoichiometric TiN_{1-x} would have to show different chemical shift than experimentally observed (notice that Si and B atoms are not soluble within stoichiometric TiN). Furthermore, the correlation of the hardness maximum with the calculated surface coverage close to 1 in all the systems that we investigated can hardly be a coincidence with no functional relationship.

This statement does not mean that workers who reported Si dissolved in, e.g., "Al-Ti-Si-N" were wrong (e.g., Ref. 82). When the conditions for the spinodal phase segregation are not met (low nitrogen pressure and temperature and low plasma density) the mixed phases may form. However, in such a case the hardness enhancement of these coatings of $\leq$35 GPa (see Fig. 6 in Ref. 82) does not reach the high values as reported for the fully segregated stoichiometric TiN [or $(Al_{1-x}Ti_x)N$] and Si_3N_4 phases.

4.2. Properties of the Fully Segregated Superhard Nanocomposites

4.2.1. Thermal Stability, "Self-Hardening," and Stabilization of $(Al_{1-x}Ti_x)N$

High thermal stability and oxidation resistance of coatings is important for a variety of applications including fast, dry machining of difficult-to-cut materials, such as hard steels, titanium and nickel alloys, and others. The thermal stability of nitride thin films (mainly deposited by PVD) was recently discussed in an excellent review by Hultman.[53] Here we focus on the thermal stability of the nanocomposites because fine grain polycrystalline materials recrystallize when annealed to about $\geq 0.4 \cdot T_m$ (T_m, melting point; this recrystallization is called "Ostwald ripening").[75,76] Thus, one may be surprised by observing such a high thermal stability, as shown for nc-TiN/a-Si_3N_4 nanocomposites in Fig. 9.4, because the Ostwald ripening is thermodynamically driven by the excess (destabilizing) contribution of the surface (or grain boundary) energy to the total Gibbs free energy of the formation, i.e., the larger crystallites are growing on the expense of the smaller ones. The large thermal stability and oxidation resistance was reported already in our first paper[1] and studied in more detail later. Selected examples from the published papers are shown in Fig. 9.13 for different coatings. Figure 9.13a shows one of many nc-TiN/a-Si_3N_4 coatings deposited by PCVD in intense discharge at high nitrogen pressure of $\geq$0.3 mbar and temperature of 550°C[1,4,83] (notice that the coating shown here was annealed in 10 mbar of "forming gas," 90% N_2 + 10% H_2,

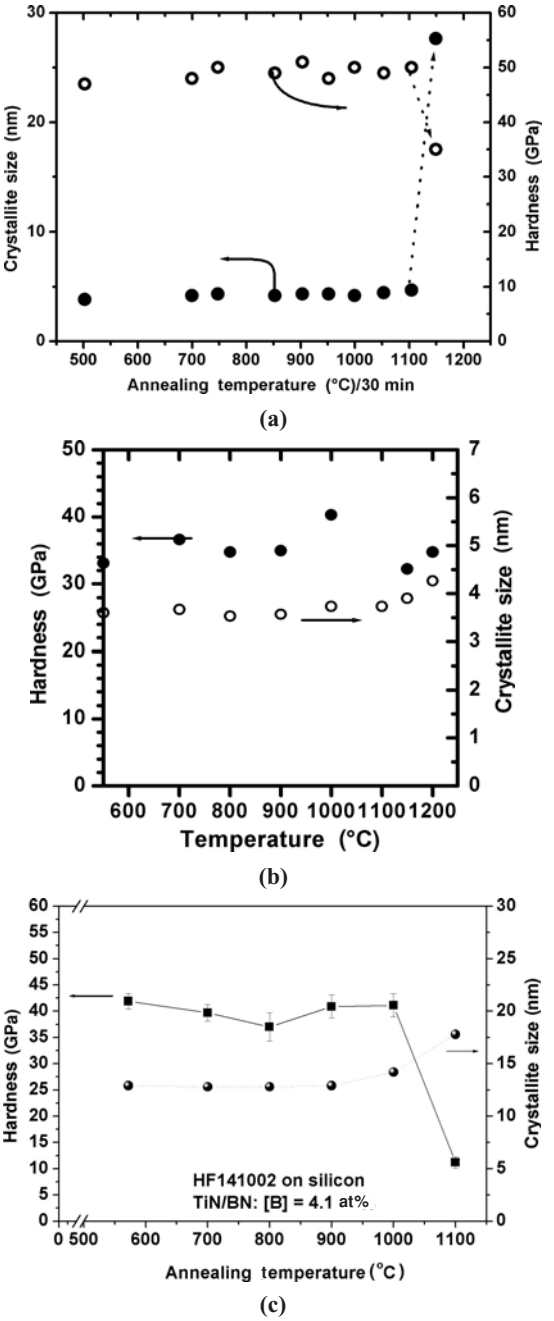

FIGURE 9.13. Thermal stability (isochronal annealing in pure N_2 for 30 min at each temperature) of (a) nc-TiN/a-Si_3N_4 deposited by PCVD on Si substrate with a TiN interfacial layer[1,4,83]; (b) nc-TiN/a-Si_3N_4 deposited by magnetron sputtering close to the optimum deposition conditions[77]; and (c) nc-TiN/a-BN coatings deposited by PCVD.[52,80] All coatings were deposited on Si substrates.

whereas all the others in 1 atm N_2). Figure 9.13b shows nc-TiN/a-Si_3N_4 deposited by reactive magnetron sputtering under conditions close but still not exactly in the optimum [$P(N_2)/P(A_r) = 1$, $P(\text{total}) = 2 \times 10^{-3}$ mbar, $T_{\text{substr}} = 550°C$, deposition rate $r_{\text{dep}} = 1.8$ nm/s[80]] (notice that under the optimum conditions the hardness of our PVD coatings exceed 50 GPa; see below). Figure 9.13c shows nc-TiN/a-BN deposited by PCVD under similar condition as those for the nc-TiN/a-Si_3N_4 coatings in Fig. 9.13a using BCl_3 instead of SiH_4.[80] All these coatings were deposited on silicon substrates in order to avoid the diffusion of metals from steel, Mo, and other metallic substrates, which commences above about 800°C, enhances the recrystallization, and, therefore, decreases the apparent thermal stability of the coatings[84–86]; somewhat lower stability of the nc-TiN/a-BN coatings is due to partial oxidation of the BN by residual oxygen in the N_2 used (purity 99.999%) and loss of boron by the sublimation of BO_x as shown in our recent publications.[84,87] Considering the stability limit of 1100°C for the nc-TiN/a-Si_3N_4 coatings, one realizes that this is 63% of the decomposition temperature of Si_3N_4 (defined as that where the saturation pressure of nitrogen reaches 1 atm),[88] i.e., significantly higher than the temperature of about $0.4T_m$ where the Ostwald ripening usually occurs.

The absence of Ostwald ripening can be due either to the absence of diffusion or to the absence of a reaction at the interface, i.e., immiscibility of the two phases.[75] In our earlier paper we estimated the lower limit of the diffusion coefficient, which would be needed if the absence of the Ostwald ripening observed at 1000°C were due to a too slow diffusion, to be of $D \leq 10^{-20}$ cm^2/s (see p. 145 in Ref. 83.) In that paper we have also shown by comparison with published data that this is orders of magnitude lower than any reasonably expected value (see for comparison also Ref. 53). Therefore, the high thermal stability of these nanocomposites cannot be due to slow diffusion. Obviously, it is due to the "absence of reaction at the interface,"[75] i.e., due to the strong immiscibility of stoichiometric TiN and Si_3N_4 phases. The strong immiscibility is a consequence of the spinodal nature of the phase segregation as seen from Fig. 9.8.

"*Self-hardening*," i.e., an increase of the hardness upon annealing was reported by Holubar *et al*. for nc-$(Al_{1-x}Ti_x)$N/a-Si_3N_4 coatings deposited in an industrial production unit by vacuum arc evaporation under nitrogen pressure of 2×10^{-3} mbar and deposition temperature of 550°C (see Table II in Ref. 89). Figure 9.14 shows an example of such behavior from our collaborative work with Holubar *et al*. of nc-$(Al_{1-x}Ti_x)$N/a-Si_3N_4 nanocomposites deposited in their industrial unit under different temperature and substrate bias.[90,91] One notices that, regardless of the initial crystallite size after the deposition, it approaches the "optimum" value of about 3–4 nm as we found for all the nc-Me_nN/a-Si_3N_4 coatings deposited by PCVD in an intense discharge under conditions that enabled the formation of the stable nanostructure to be completed during the deposition.

Therefore, the self-hardening is typical of an incomplete phase segregation upon the deposition, and it results from the completion of the spinodal phase segregation upon annealing as outlined by Cahn already some time ago.[71] Recently, Mayrhofer *et al*.[92] have reported a similar but only temporary self-hardening upon

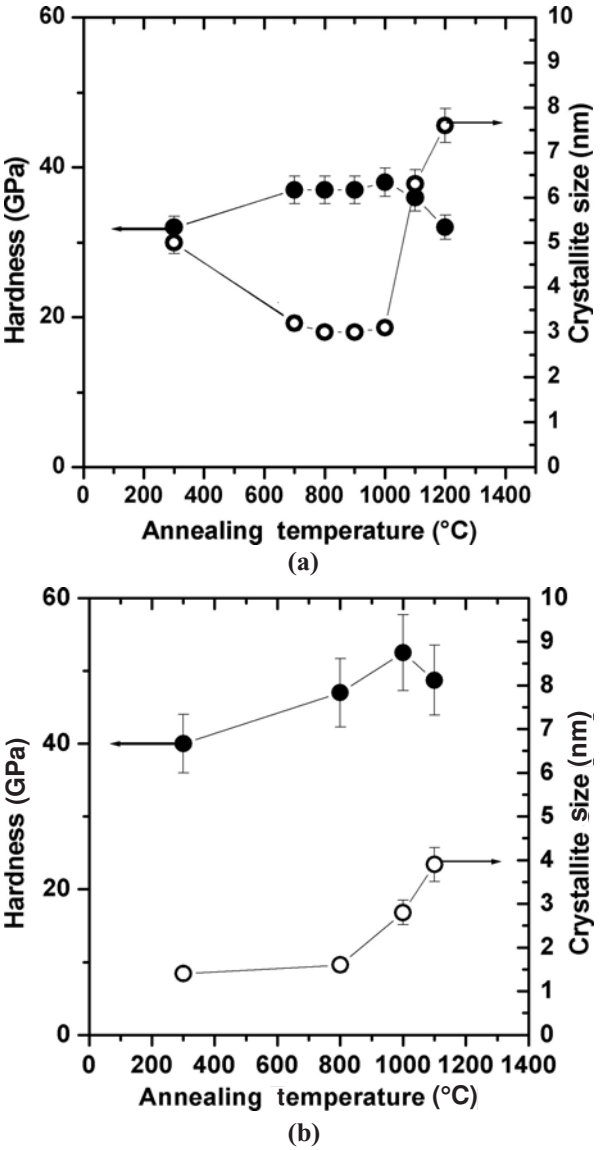

FIGURE 9.14. Self-hardening and the concomitant change of the crystallite size to about 3–4 nm upon annealing of nc-$(Al_{1-x}Ti_x)N$/a-Si_3N_4 nanocomposites that were deposited under conditions remote from the optimum, resulting in (a) a too large crystallite size (high temperature and low ion bombardment) or (b) a too small crystallite size (low temperature and energetic ion bombardment).[90,91]

the initial stage of the decomposition of $(Ti_{1-x}Al_x)N$, which proceeds via the formation of an intermediate, metastable cubic c-AlN phase, at a temperature of about 800–900°C. This c-AlN phase is formed by spinodal decomposition of the supersaturated $(Ti_{1-x}Al_x)N$ solid solution and, upon further annealing to >900°C, it decomposes to h-AlN and the coating softens. Our nanocomposites possess such a high thermal stability because the final, fully segregated nc-TiN/a-Si_3N_4 nanostructure corresponds to the final stage of the spinodal segregation of the stoichiometric phases. A simple thermodynamic consideration (see, e.g., Refs. 26, 74, and 88) shows that the same conclusion is valid for a number of nc-Me_nN/a-Si_3N_4 and nc-Me_nN/a-BN and other systems. Therefore, our design concept is of a general validity.

4.2.1a. Avoiding Decomposition and Softening of $(Al_{1-x}Ti_x)N$. As seen in Fig. 9.11, the Si_3N_4 grows almost hetero-epitaxially on the [111] TiN surface. Thus, this configuration is expected to possess high stability, and this makes it more difficult for the c-AlN phase, which is an intermediate of the final stage of the decomposition and softening c-$(Al_{1-x}Ti)N \rightarrow$ c-TiN + h-AlN, to nucleate on the surface of the $(Al_{1-x}Ti_x)N$ crystals (for further details see Ref. 92 and references therein). This is the most probable reason of the extremely high thermal stability of the nc-$(Al_{1-x}Ti_x)N$/a-Si_3N_4 coatings shown in Fig. 9.15.[91] The temperature of

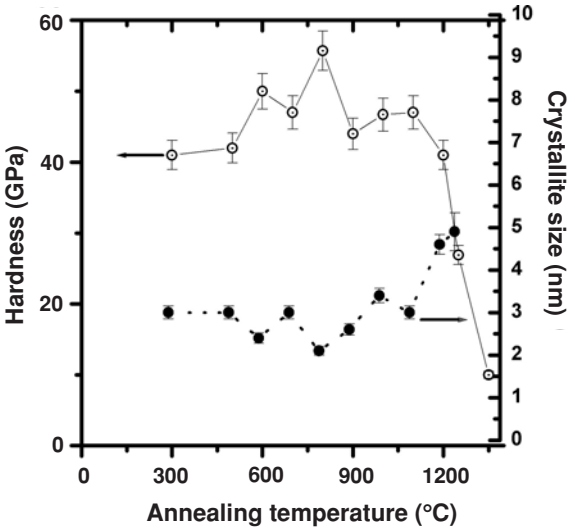

FIGURE 9.15. The complex behavior of the nc-$(Al_{1-x}Ti_x)N$/a-Si_3N_4 nanocomposites upon isochronal annealing (30 min in 1 atm N_2) with a self-hardening up to 50 GPa shows that these coatings prepared in an industrial prototype unit were still not in the state of a stable, fully segregated nanostructure. In spite of that, the decomposition and softening due to the reaction c-$(Al_{1-x}Ti_x)N \rightarrow$ c-TiN + h-AlN is absent (for XRD and further detail see Ref. 91).

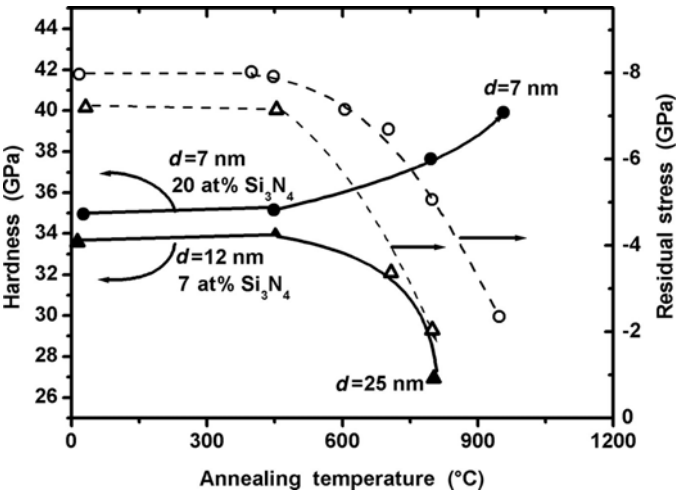

FIGURE 9.16. Annealing behavior of the "Ti-Si-N" coatings deposited by Patscheider by means of reactive sputtering. The crystallite size and Si content are indicated by the corresponding lines denoting the hardness (From Ref. 70.). The terminology "at%" of Si_3N_4 was taken from that review; probably it should read "mol%").

1200°C, where the recrystallization and softening commences, is not necessarily the stability limit of the nanocomposites because a strong diffusion of cobalt from the substrate made of cemented carbide was found after annealing at that temperature (see Fig. 3 in Ref. 91). Thus, the thermal stability of tools coated with these coatings is limited by the thermal stability of the cemented carbide.

The investigation into the thermal stability of the nanocomposites was published later, by several groups. Regarding the "Ti-B-N" system we refer to Fig. 9.3a and to a recent work of Mayrhofer *et al.*[39,40] and references therein. As a typical example for the "Ti-S-N" coatings that were deposited under inappropriate conditions we reproduce in Fig. 9.16 the results of Patscheider from his recent review.[70] As one can see, the coating with "7 at% of Si_3N_4" (should probably read "mol% of Si_3N_4" or "at% of Si") shows a strong decrease of the hardness and of the compressive stress already upon annealing to $\geq$500°C. The simultaneous decrease of the hardness and of the compressive stress (from ≥ -7 Gpa to about -2 GPa) and a comparison with the behavior of coatings hardened by ion bombardment (see Figs. 9.4 and 9.6) suggest that the modest hardness enhancement of 34 GPa in the coatings shown in Fig. 9.16 is due predominantly to the energetic ion bombardment. Let us mention that we have never observed such a low thermal stability in any of our nc-TiN/a-Si_3N_4 nanocomposites deposited under the conditions that assured the formation of stable nanostructure during the deposition (see above).

The deposition conditions of the "Ti-Si-N" coatings are not specified in Ref. 70 and the Ph.D. Thesis of M. Diserens to which reference is made (see Ref. 29 in the review in Ref. 70) is difficult to access. Thus, we can only assume that the conditions were similar as specified in an earlier paper of these workers, i.e., the temperature "never exceeded 350°C," the surface bias was between −100 and −125 V, and the "variation of silicon content (in the coatings) was achieved by using different nitrogen partial pressures, which were varied between 8×10^{-2} and 1.2×10^{-1} Pa" (0.0008–0.0012 mbar) with a "base pressure in the reactor lower than 2×10^{-4} Pa" (2×10^{-6} mbar; see Ref. 93). Similar information regarding the deposition conditions in the work of Patscheider *et al*. can also be found in other papers of this group.[44,94–96]

When comparing the deposition conditions in many papers where the hardness enhancement due to ion bombardment was found (see, e.g., references quoted in Figs. 9.4 and 9.6), one finds that the conditions used by Patscheider *et al*. are typical for the hardening by energetic ion bombardment. In such a way, one can understand why the "Ti-Si-N" coatings of these researchers behave completely differently than ours although they have the same Si content. The small self-hardening observed for the coating with a high content of "20 at% of Si_3N_4" (see Fig. 9.16) might be due to the phase segregation as described above. This content of Si_3N_4 is close to that where the maximum hardness was found in all the nc-Me_nN/a-Si_3N_4 coatings reported by us (see Fig. 9.5) and that remain stable upon annealing up to 1100°C (see Fig. 9.13a,b). This comparison shows again that the deposition conditions and the resulting nanostructure of the "Ti-Si-N" coatings reported by these workers were far from the optimum (see also below). Unfortunately, we cannot discuss the possible reasons in more details because of incomplete data regarding the deposition conditions, impurity content, etc., in the papers of Patscheider, who does not refer, even in his reviews,[44,70] to similar and more precise studies reported by us and others much earlier.

4.2.2. Oxidation Resistance

Already in 1995 we reported that the oxidation resistance of the nc-TiN/a-Si_3N_4 coatings with the optimum composition and hardness of about 50 GPa is comparable to the best state-of-the-art ($Ti_{1-x}Al_x$)N coatings (see Fig. 7 in Ref. 1). Figure 9.17a from Ref. 55 compares the thermal stability of our nc-TiN/a-Si_3N_4 nanocomposites deposited by PCVD[1] with a variety of hard industrial coatings as reported by Münz already in 1986[97] and later extended to the ($Ti_{1-x}Al_x$)N coatings stabilized with yttrium.[98–100] Figure 9.17b shows the oxidation stability of nc-TiN/a-BN superhard nanocomposites deposited by PCVD[84,87] and nc-TiN/a-Si_3N_4 superhard nanocomposites deposited by magnetron sputtering under conditions that assured the formation of stable nanostructure during the deposition (cf. Fig. 9.15b).[77,85]

As one can see, the oxidation resistance of the stable and superhard nc-TiN/a-Si_3N_4 nanocomposite (with the highest hardness 50 GPa)[1] compares with

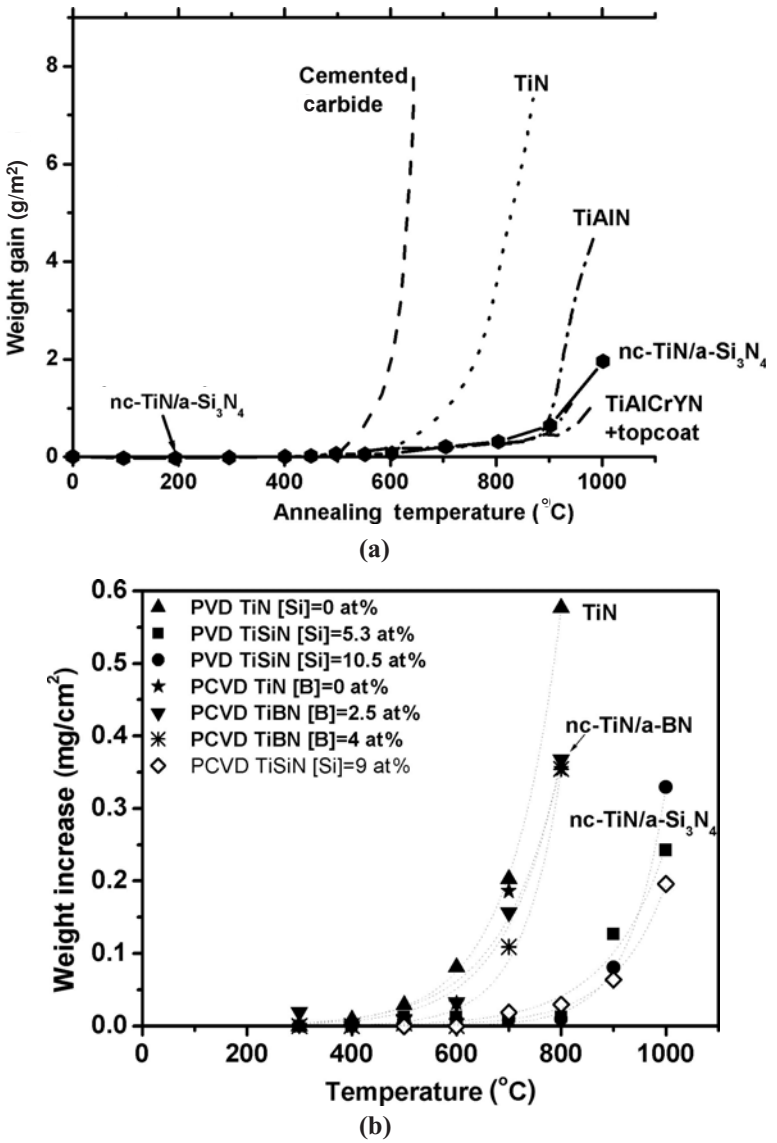

FIGURE 9.17. (a) Oxidation resistance of nc-TiN/a-Si_3N_4 nanocomposites deposited by PCVD[1] in comparison with other industrial hard coatings (From Ref. 55.) The oxidation resistance of TiC, TiN, and $(Ti_{1-x}Al_x)N$ coatings was taken from Ref. 97 and that of "TiAlCrYN" from Refs. 98–100. (b) Oxidation resistance of nc-TiN/a-BN superhard nanocomposites deposited by PCVD[84,97] and of nc-TiN/a-Si_3N_4 superhard nanocomposites deposited by magnetron sputtering under conditions that assured the formation of stable nanostructure (cf. Fig. 9.15b) during the deposition.[77,85]

that of the yttrium-stabilized $(Al_{1-x-y}Ti_xY_y)N$ ones. The oxidation stability of the nc-TiN/a-BN superhard nanocomposites is slightly better than that of TiN but much lower than that of nc-TiN/a-Si_3N_4. The high oxidation resistance of the latter coatings is due to the strong and dense Si_3N_4 interface that hinders the oxygen diffusion along the grain boundaries. (Notice that the role of yttrium in the $(Al_{1-x-y}Ti_xY_y)N$ coatings is also the hindrance of the oxygen diffusion along the grain boundaries.) The lower stability of the nc-TiN/a-BN nanocomposites is due to a lower oxidation resistance of the BN phase. This was shown in our recent paper where, upon the oxidation, boron was lost due to the oxidation and sublimation of BO_x suboxides.[80,87]

In our earlier papers[1,55] as well as here, we limited these studies to the nanocomposites with the optimum composition and maximum hardness of about 50 GPa because the lower oxidation resistance of TiN was known from the work of Münz and the much higher oxidation resistance of Si_3N_4 is well documented in the textbooks. Like SiC, Si_3N_4 forms, upon oxidation, a dense SiO_2 layer that hinders diffusion of oxygen up to high temperatures below the glass transition of SiO_2 of close to 1600°C. On the other hand, because of the low melting point of B_2O_3 of 450°C,[88] the oxidation stability of the BN phase is lower. Therefore, the oxidation resistance of the nc-TiN/a-Si_3N_4 coatings increases with increasing content of Si_3N_4 (but notice that above about 20 vol% of Si_3N_4 the hardness decreases),[1,55] whereas in the case of the nc-TiN/a-BN only the coatings with the optimum composition [about one monolayer of BN covering the TiN nanocrystals (see Fig. 9.10d)] and maximum hardness have the maximum oxidation resistance. With BN content either decreasing or increasing from this optimum, the oxidation resistance decreases (for details see Ref. 80).

The improved oxidation resistance of "Ti-Si-N" coatings as compared with the TiN ones was later reported by several research groups (e.g., Ref. 93, and in the recent review of Patscheider),[70] however without any new, more advanced results and/or comparison and without any reference to the earlier results summarized here. Therefore it makes little sense to discuss these papers here.

The formation of the nc-$(Al_{1-x}Ti_x)N$/a-Si_3N_4 nanocomposites also improves their oxidation resistance as compared with $(Al_{1-x}Ti_x)$[139] This is not surprising because when the Si_3N_4 phase stabilizes the $(Al_{1-x}Ti_x)N$ against the decomposition and softening (see Fig. 9.15), the Si_3N_4 interfacial phase remains still stable and dense.

Interesting is the result of Tanaka *et al.*[82] who have reported a significantly improved oxidation resistance of "Ti-Al-Si-N" coatings as compared with the "(AlTi)N" ones, although, according to their analysis, their coatings were not nanocomposites as discussed here but rather a solid solution of Si in the (AlTi)N phase (see Ref. 82 for further details). As mentioned above, these coatings also have a lower hardness than the superhard nanocomposites. In spite of that their oxidation resistance was significantly improved as compared with $(Al_{1-x}Ti_x)N$ alone.[82]

4.2.3. Morphology and Microstructure

It is well known that hard (and many other) coatings deposited by plasma PVD and CVD at relatively low temperatures of 300–600°C have a columnar morphology. There are many papers dealing with this problem experimentally, theoretically, and by computer simulations (see, e.g., Ref. 55). The development of the morphology in PVD coatings as a function of the deposition temperature and ion bombardment is described by the Thornton structure-zone diagram (e.g., Ref. 55, p. 712), which is an extended structure-zone diagram originally introduced by Movchan and Demchisin for thermally evaporated films (see Ref. 55, p. 711). By an appropriate combination of the "homologous temperature" $T_h = T/T_m$ (T is the deposition temperature and T_m is the melting point of the given material) and the energy deposited into the surface of the growing film by ions per deposited atom, one can prepare coatings within the so-called "zone T," which correspond to a still columnar but fairly dense microstructure.

Already in 1992, Li *et al*. have shown that the columnar morphology of their "Ti-Si-N" films deposited by PCVD (as mentioned above, these were the ternary nc-TiN/a-Si_3N_4/a-$TiSi_2$ coatings) vanished when about 10 at% of Si was added (see Fig. 3 in Ref. 28). With a further increase of the Si content the morphology remained isotropic but the hardness decreased as in our coatings (Fig. 9.10). We do not show their scanning electron micrographs here because of their poor quality when we tried to scan them from the original paper, but we emphasize that Li *et al*. were the first authors who reported these very encouraging results.

As reported in 1996, the columnar morphology of the transition metal nitrides (TiN, W_2N, and others) completely vanishes when the stable nc-Me_n/a-Si_3N_4 nanocomposites are deposited by means of PCVD in an intense discharge.[74] Figure 9.18 reproduces an example of the development of the morphology upon the addition of the Si_3N_4 [notice that in all these coatings, silicon is bonded as in Si_3N_4 only without any noticeable contribution of $TiSi_2$ phase (see Fig. 9.12a)]. With increasing content of Si_3N_4 the columnar structure of TiN (see Fig. 9.18a) vanishes (Fig. 9.18b) and a perfectly isotropic morphology is found for the optimal composition and maximum hardness (Fig. 9.18c). (Notice that the coatings deposited on Si substrates were broken and the micrographs were taken without any polishing of the surfaces.) Upon a further increase of the Si_3N_4 content, the isotropic morphology remains but the hardness decreases again (Fig. 9.18d). The same behavior was reported by us for nc-W_2N/a-Si_3N_4 nanocomposites (see Fig. 5 in Ref. 74) and all others (nc-VN/a-Si_3N_4, nc-TiN/a-Si_3N_4/a- & nc-$TiSi_2$, as well as nc-$(Al_{1-x}Ti_x)$/a-Si_3N_4) that we have investigated but not published because of lack of novelty.

This is an important result because the columnar morphology, even if within the dense "T-zone," still suffers in terms of mechanical properties due to weaker bonding between the columns. Therefore, the complete vanishing of the columnar morphology is important for the excellent mechanical properties of the stable superhard nanocomposites. In order to underline the universality of this dependence

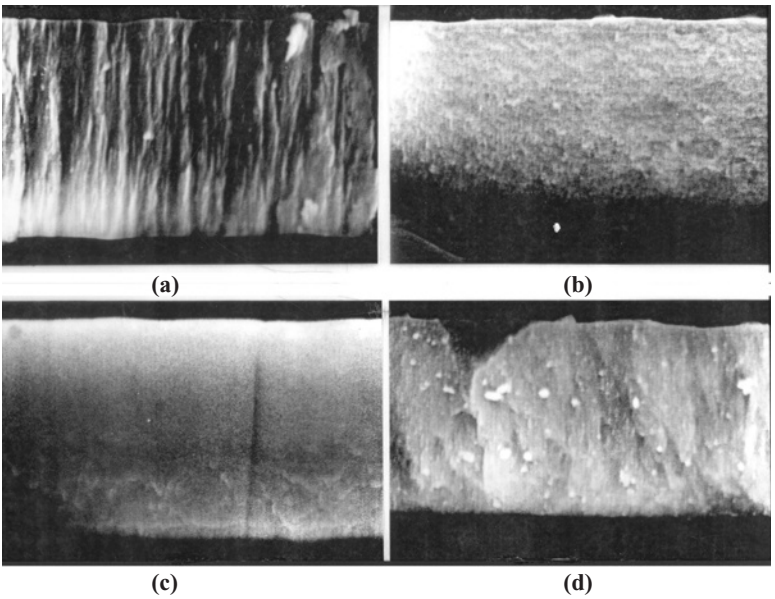

FIGURE 9.18. (a) Cross-sectional view of the columnar morphology of TiN coatings deposited by means of PCVD from $TiCl_4$, SiH_4, and large excess of N_2 and H_2 at 550°C; (b) nc-TiN/a-Si_3N_4 nanocomposites with about 5 at% of Si and hardness of about 35 GPa (cf. Fig. 9.10a); (c) nc-TiN/a-Si_3N_4 nanocomposites with the optimum composition of about 7–8 at% of Si and stable nanostructure with hardness of about 50 GPa; (d) nc-TiN/a-Si_3N_4 nanocomposites with a too high Si content of about 9 at% of Si and hardness of about 30 GPa. (From Ref. 74.)

of the morphology upon the formation of stable superhard nanocomposites, let us mention that recently we found the same isotropic structure also in the nc-TiN/a-BN coatings. Owing to space limitation we do not show the scanning electron micrographs here, but the reader may refer to Fig. 8 in Ref. 80 for this convincing evidence.

Several groups repeated these results and confirmed them to some extent (e.g., H.-D. Männling, M. Jilek, P. Holubar, and S. Veprek, 2004, manuscript in preparation and Ref. 101). However, in the majority of these papers (e.g., Refs. 72 and 103–105) the morphology still remains columnar upon addition of Si, although less pronounced than in the pure nitride coating, and there is an ongoing discussion about the mechanism that governs these morphology changes, completely ignoring the concept of the spinodal phase segregation formulated years ago.[1,74] For example, in his recent review Patscheider suggests some kind of an unspecified "renucleation" of TiN grains due to a "partial covering of the TiN by Si_3N_4," again with references to his papers only. The meaning of the uncommon term "renucleation" is not explained in that paper. The scanning electron micrographs published

in the papers of this group show however that their coating with 12 at% of Si, where maximum hardness of about 40 GPa was achieved,[44,70,93–95] still has a pronounced columnar morphology (see Fig. 3b in Ref. 94). Also Hu *et al*.[104] found a similar trend when the Si content increased from 0 at% (pure TiN) to about 5 at%, but the morphology still remained columnar and, upon a further increase of the Si content, the crystallite size did not decrease as in our earlier work[1,74] for nc-Me_nN/a-Si_3N_4 coatings deposited in intense HF discharge under conditions of low energy ion bombardment. Hu *et al*. suggest a speculative explanation[104] of their results, fully ignoring the thermodynamics and kinetics explained much earlier elsewhere.[1,74]

As reported earlier, the increase of the crystallite size with Si content increasing above the optimum (where the maximum hardness is achieved) is observed only when energetic ion bombardment is absent. Even in coatings deposited by means of PCVD but under energetic ion bombardment, as, e.g., at the cathode of an abnormal direct current discharge, the crystallite size decreases to about 3–4 nm when the Si content increases from 0 at% to about 7 at% and remains almost constant upon a further increase of the Si content (see Fig. 10b and Ref. 30).

The different findings of Hu *et al*. can be easily understood by considering their values of hardness (see Fig. 6 in Ref. 104). The maximum hardness of about 36 GPa was obtained at Si content of about 4 at% only for coatings deposited at room temperature, whereas at T_{dep} of 400°C the maximum hardness decreased to 28 GPa. From these results it is clear that the hardness enhancement in coatings deposited at room temperature is largely due to energetic ion bombardment that is always present in magnetron sputtering at a low gas pressure because of the primary ions reflected from the target. Notice that the base pressure in the system of Hu *et al*. was 10^{-6} mbar and the partial pressure of nitrogen 2×10^{-4} mbar only. Therefore, as stated by the workers, silicon was present not only as Si_3N_4 but also as Si. (However, a critical reader will notice that the Si 2p XPS signal attributed by these workers to elemental Si might also be due to $TiSi_2$.) From these results it is obvious that the coatings of Hu *et al*. and of Patscheider *et al*. were deposited under inappropriate conditions that did not allow the formation of a stable, fully segregated nanostructure during the film growth and, therefore, the columnar morphology persisted although somewhat less pronounced.

There are many other papers where the researchers report somewhat different behavior of the hardness, morphology, etc., and suggest different explanations. Because of lack of complete characterization of the deposition conditions and/or of the samples, it is difficult to review all these papers in a rational and analytical manner and to exclude detrimental effects of impurities (see below). For example, Jiang *et al*.[105] deposited a series of "Ti-Si-N" coatings at room temperature using unbalanced magnetron reactive sputtering at a total Ar + N_2 pressure of 2.6×10^{-3} mbar but unspecified partial pressure of nitrogen. Thus, it is not surprising that at a higher total Si content, only a part of Si incorporated in the coatings was bonded as in Si_3N_4, the rest remaining "unreacted," and the morphology remained columnar (see Fig. 5 in Ref. 105). Because of the small thickness of about 1 μm (see Table I in Ref. 105) the hardness measurements were done at low load and

maximum indentation depth of $\leq$80 nm where the obtained values should have been carefully checked for the possible presence of SIE that may falsify them (see Sections 1.1. and 1.2.). The authors report a hardness enhancement up to about 35 GPa for Si content of about 8–10 at%. However, the presence of 5–8 at% of oxygen impurities in their coatings (see p. 169, right-hand-side column, Ref. 105) makes such paper of little interest for improving our understanding of these systems. The same applies to many other papers where, the deposition was done

> . . . without bias application or substrate heating in order to examine only the effect of silicon addition. . . [106]

and, later, the deposition temperature was increased to 300°C and substrate bias of -100 V applied during the deposition,[103] where the hardness enhancement due to energetic ion bombardment is still found as obvious from the correlation of the hardness and compressive stress (see Figs. 2 and 3 in Ref. 103.)

In order to show that our generic design principle applies also to the deposition of the nanocomposites by reactive magnetron sputtering, we reproduce in Fig. 9.18b the development of the morphology and in Fig. 9.19 the dependence of the hardness on Si content (all Si bonded as in Si_3N_4 as verified by XPS) for nc-TiN/a-Si_3N_4 superhard nanocomposite deposited by reactive magnetron sputtering in ultrahigh vacuum compatible apparatus and high deposition rates of 1.6–1.8 nm/s.[77,85] As one can see, both the morphology and the hardness show the same dependence on the Si content as found for nc-Me_nN/a-Si_3N_4 (Me = Ti. W, V) deposited by PCVD. A more detailed observation, in particular HRTEM investigations (work in progress), reveal that even the hardest coatings deposited by magnetron sputtering still have a slightly columnar morphology, which is due to the fact that the nitrogen pressure of 2×10^{-3} mbar used here is still relatively low (notice that only nitrogen was used as both the sputtering and reactive gas in our work) and, therefore, the thermodynamic driving force for the spinodal phase segregation is not quite sufficient. The maximum hardness of about 45 GPa that was measured with maximum applied load between 30 and 100 mN on $\geq$ 8-μm-thick coatings is limited by about 0.2 at% of oxygen impurities present in these coatings[77,85] (see below). The detrimental effect of oxygen impurities will be discussed in the next section.

5. REPRODUCIBILITY OF THE PREPARATION OF SUPERHARD, STABLE NANOCOMPOSITES

5.1. The Role of Impurities

Already some time ago we reported on the detrimental role of impurities that when incorporated into the coatings during the growth made it impossible to achieve the superhardness.[83,107] Recent studies[108] confirmed these finding in a more quantitative manner. In the earlier papers it was shown that the hardness decreases when

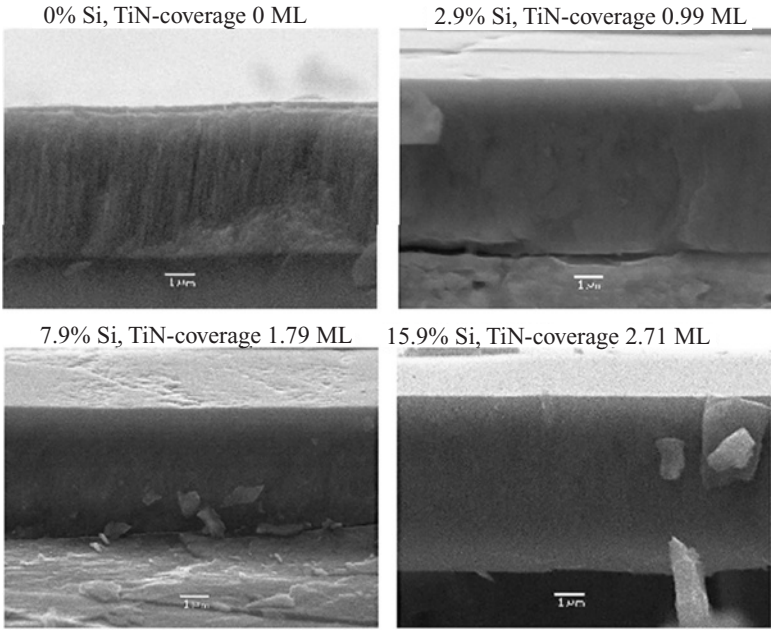

(a)

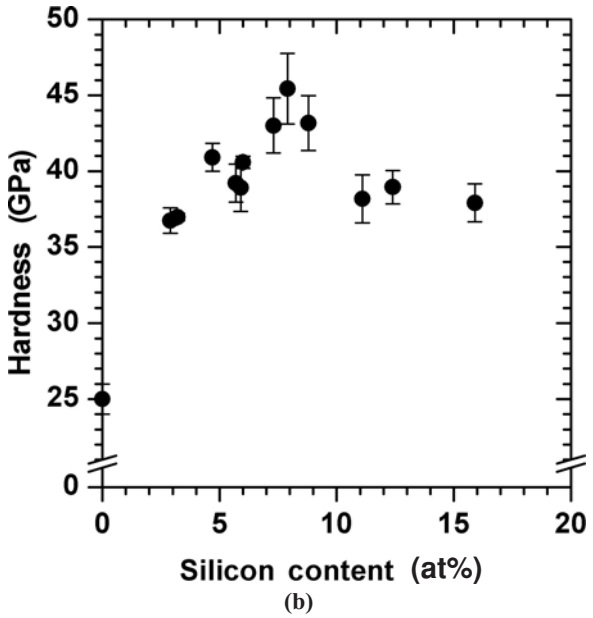

(b)

FIGURE 9.19. Development of (a) the morphology and (b) the hardness of nc-TiN/a-Si_3N_4 nanocomposites, deposited by reactive magnetron sputtering in pure N_2 at a total pressure of 0.002 mbar, substrate temperature of 630°C, and high deposition rate of 1.6–1.8 nm/s, with increasing Si content.[77,85]

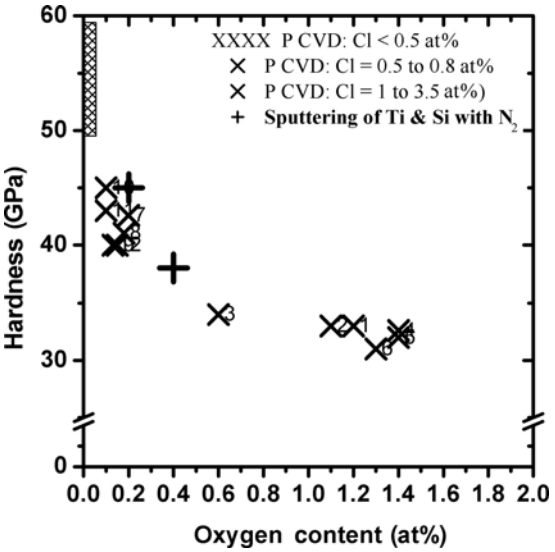

FIGURE 9.20. Dependence of the maximum achievable hardness (i.e., for an optimum composition as in Fig. 9.10) on the oxygen impurity content for nc-TiN/a-Si_3N_4 coatings deposited by PCVD using $TiCl_4$ and SiH_4 and by reactive sputtering (symbols +).[77,85] Hardness of ≥40 GPa can be achieved only when the oxygen impurity content is ≤0.2 at%. When the oxygen content is above 0.6 at%, the hardness remains below 35 GPa.

few atomic percent of chlorine and other impurities were incorporated. The most dramatic effect is provided by oxygen, as illustrated in Fig. 9.20. Interesting is the finding that the data available so far from three different PCVD deposition and two different sputtering units agree very well. Obviously, oxygen impurity content of less than 0.2 at% is required if a load-independent hardness of thermally stable nanocomposites of ≥40 GPa should be achieved. The effect of chlorine on the hardness is somewhat less dramatic, but chlorine impurity of more than about 0.5 at% causes degradation of the coatings when they are stored in air for a longer period of time.[108]

The reason for the strong effect of minor oxygen impurities on the hardness is presently under investigation. Because the maximum hardness is achieved when there is about one monolayer of Si_3N_4 acting as a "glue" tissue between the TiN nanocrystals, it is easily understandable why a polar Ti—O and Si—O bonds within this tissue may have such a strong effect.

Figure 9.21 shows that when the impurity content is further decreased by a more extensive and prolonged outgassing of the apparatus so that the background gas pressure prior to the deposition with the substrate at 660°C decreases to less than 1×10^{-6} mbar, the high, load-independent hardness (measured on ≥8 μm thick coatings) of more than 50 GPa is obtained by reactive sputtering at a similar Si content as in the nc-TiN/a-Si_3N_4 nanocomposites deposited by PCVD.[77] This

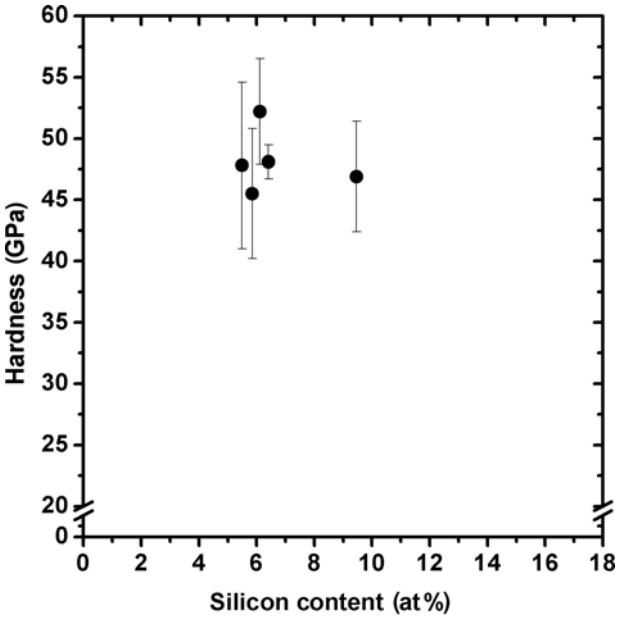

FIGURE 9.21. Examples of nc-TiN/a-Si_3N_4 coatings with hardness approaching or even exceeding 50 GPa deposited by reactive sputtering with nitrogen only at high deposition rates of 1.6–1.8 nm/s and with a prolonged outgassing of the apparatus as compared with the results in Fig. 9.19.[77]

work is presently in progress in our laboratory and the results shown in Fig. 9.21 are reproducible.

As already mentioned, reactive sputtering that operates at a relatively low pressure and low deposition rates as seen from the small thickness of the coatings has been used in the majority of papers (e.g., Refs. 23, 70, 93, 94, 109, and 110). Let us consider, as an example, a deposition rate of about one monolayer (ca. 0.25–0.3 nm) per second that yields about 1-μm-thick coating deposited within about 1 h. The background pressure reported by the workers is typically between 2×10^{-6} and 7×10^{-6} mbar[94,109,111,112] (but it is not clearly stated in these papers if that pressure was measured with the substrate at room temperature or at the deposition temperature). The number of impurity atoms adsorbed at 1 cm^2 of the surface of the growing film per second is

$$\Phi = 0.25\, s n v_{\text{th}}, \tag{9.1}$$

where s is the sticking coefficient, n the number density of the given residual gas, and v_{th} the mean thermal velocity. Assuming that the background gas composition corresponds to that of air (usually in this pressure range the background pressure of a tight chamber is dominated by the more reactive water), i.e., the partial pressure of O_2 is $(0.4–1.4) \times 10^{-6}$ mbar, which corresponds to a density of $n \approx (1.1–3.8) \times 10^{10}$ cm^3. With $v_{\text{th}} \approx 3 \times 10^4$ cm/s and sticking coefficient of oxygen on clean

Ti surface of $s > 0.1$ the adsorbed flux of oxygen is $\Phi_O \approx (3.3–11) \times 10^{13}$ O atoms/(cm^2s). For comparison, a deposition rate of one monolayer per second corresponds to about $(0.7–2) \times 10^{15}$ atoms/(cm^2s). This simple estimate shows that oxygen impurity content in the range of several atomic percent is expected in such coatings.

This is in agreement with the data reported, e.g., by Jiang *et al.*,[105] Shtansky *et al.*,[113] and Zhang *et al.*[114] Only much higher deposition rates and long-term outgassing of the apparatus with the substrate at the high temperature allowed us to decrease the oxygen impurity down to 0.2 at% and reach the load-independent, stable hardness of ≈52 GPa for several coatings prepared by reactive magnetron sputtering at high deposition rates of 1.6–1.8 nm/s.[77] Let us emphasize that the standard nc-TiN/a-Si_3N_4 nanocomposites deposited in our laboratory by means of PCVD have oxygen impurity content between about 0.01 and 0.05 at% (see the hatched field in Fig. 9.20).

In order to be able to determine quantitatively such a small oxygen impurity level, one has to use an appropriate analytical technique. The frequently used X-ray photoelectron spectroscopy and Rutherford back scattering have a too low dynamic range for this purpose. The most appropriate technique is the elastic recoil detection (ERD) spectroscopy where the sample is bombarded with high-energy (10–30 MeV) heavy ions (e.g., Cl^+) and the secondary ions ejected from the sample are analyzed with respect to their mass and kinetic energy. ERD spectroscopy provides both a high sensitivity and dynamic range (see Ref. 32 and references quoted there).

5.2. Conditions Needed to Obtain Complete Phase Segregation During the Deposition

The decisive fact that should to be kept in mind is that the formation of a nanostructure with a high thermal stability (see Fig. 9.13) requires a sufficiently high chemical activity of the system to provide a thermodynamic driving force for phase segregation, and a sufficiently high temperature of 500–600°C to provide the fast diffusion that is necessary to complete the segregation during the growth (see above). When these conditions are not met, the high hardness of 50–60 GPa is difficult to reach in the binary systems, the morphology remains columnar, the coatings may show self-hardening upon subsequent annealing, and the maximum hardness appears at different total content of silicon because of a different crystallite size and shape in different papers of different groups. Furthermore, impurities, such as oxygen and chlorine strongly degrade the hardness as reported by us already in 1997/1998[83,107] and discussed in more detail in the foregoing section.

Unfortunately, the majority of published papers on the "Ti-Si-N" and similar coatings do not report these decisive parameters and conditions. Therefore, it is difficult to find out what could be the possible reasons for the lack of reproducibility of our data in all these works. (In course of preparation of this review we have accumulated and studied more than 50 recent papers on the "Ti-Si-N" and similar

coatings. But because of the lack of the relevant data regarding the deposition conditions we cannot discuss why the hardness that the authors reported was low, the morphology columnar, etc.) In order to provide at least some guidelines for the reader where the possible reasons should be searched for, we shall limit our discussion to a few typical examples. Figure 9.22 shows the hardness versus the Si content for "Ti-Si-N" coatings deposited by PCVD (Fig. 9.22a) and by reactive sputtering (Fig. 9.22b) as reported in the quoted papers. As it was shown in our later work,[33] the coatings of Li *et al.*[28] were the ternary nc-TiN/a-Si_3N_4/a-$TiSi_2$ nanocomposites, in which hardness of 80 to $\geq$100 GPa was achieved.[31,32] As one can see from Fig. 9.22, the hardness of other coatings just approaches 40 GPa and its maximum appears at different Si content. Moreover, there is no hardness enhancement found in coatings reported by Meng *et al.*[110] Instead, the hardness of their coatings decreases from about 32 GPa for pure TiN (correct value for TiN is about 21 Gpa)[116] to about 21 GPa for Si_3N_4 (correct value is about 17 Gpa).[116] On the other hand, the reproducibility of our nc-MeN/a-Si_3N_4 (Me = Ti, W, V) coatings is very good (see Figs. 9.5, 9.19, and 9.22a).

The limited space available here does not allow us to discuss the possible reasons of these discrepancies between different papers in more details. We just emphasize that our coatings prepared by means of PCVD were deposited in an intense glow discharge with a sufficiently high pressure of nitrogen of $\geq$0.5 mbar and high deposition temperature of 550°C, which are the conditions required for the reproducible deposition of superhard and stable nanocomposites as explained in Ref. 1 but ignored in the majority of the papers from different groups. Furthermore, the impurity content was below 0.5 at% for chlorine and hydrogen and less than 0.05 at% for oxygen. The coatings of Li *et al.* were deposited in a much weaker discharge and, therefore, the $TiSi_2$ phase was formed. Lee *et al.* used an "inductively coupled" discharge that according to the specification in their paper and our experience with glow discharges provided probably the weakest plasma of the three examples in Fig. 9.22a.

The poor reproducibility found in many papers, where either reactive sputtering or vacuum arc evaporation or a combination of them were used (only few examples are shown in Fig. 9.22b) is due to a choice of either a too low nitrogen pressure, or too low temperature, or impurities or a combination of these effects. For example, Meng *et al.*[110] used a very low partial pressure of nitrogen of 0.198 mTorr (0.00015 mbar = 1.5×10^{-7} atm) and a too low deposition temperature of about 250°C. After we have turned their attention to the necessity of using a higher temperature and nitrogen pressure, they recently succeeded to somewhat improve the nanohardness of their coatings up to about 38 Gpa.[23] The main results of the last paper is the finding that

> ... increasing the deposition temperature from 250°C to ~700°C decreases the Ti dissolution ... within the a-Si:N matrix.[23]

Thus, these workers discovered 8 years after the first publication on that subject what has been reported there[1] and in many papers later. There are still

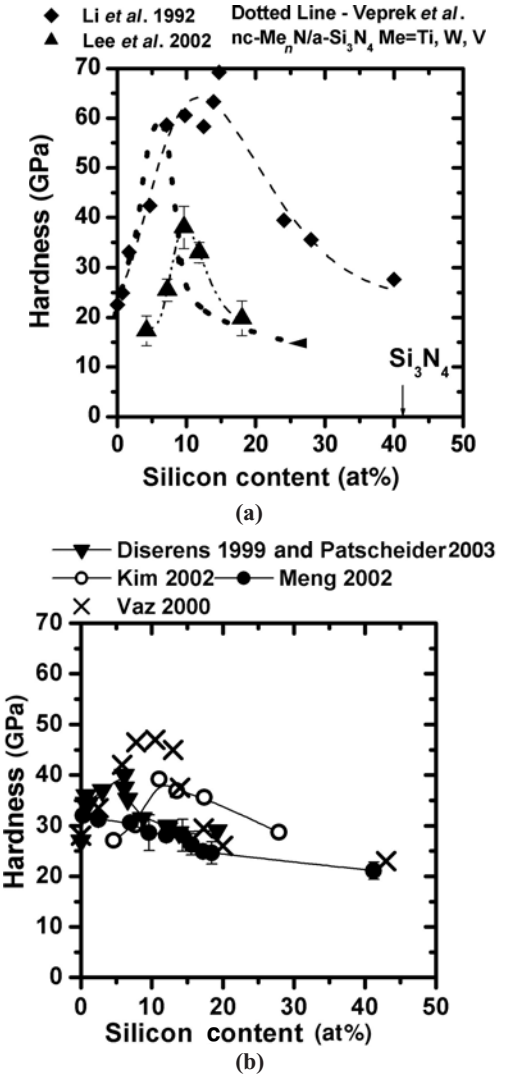

FIGURE 9.22. Hardness of (a) nc-TiN/a-Si_3N_4 nanocomposites deposited by PCVD (From Refs. 28 and 115. For our data see Fig. 9.5.) (b) Hardness of "Ti-Si-N" coatings deposited by reactive sputtering references.[70,93,109,110,112]

many open questions left in the paper of Meng *et al.*: How does the hardness change with Si content between TiN (Si content 0) and about 10 %? which is not reported in Fig. 6b of Ref. 23? Why do these workers need such a high temperature of 700°C when we and others (see e.g., Fig. 9.3 in Ref. 115 and Fig. 5a in Ref. 112) found an optimum temperature to be about of 500–600°C? How reliable are the

hardness measurements when the maximum indentation depth is $\leq$65 nm, i.e., in the range where serious indentation size effects are expected?[12,15,20,21] Why was the thickness of the coatings only "...in the range of 160–410 nm?" How large was the impurity content, mainly of oxygen, particularly if one considers the very small thickness of $\leq$0.41 μm,[23] which is a strong indication of a low deposition rate?

The values of the hardness reported by Vaz *et al*. are comparable with our nc-Me_nN/a-Si_3N_4 nanocomposites deposited by PCVD (Figs. 9.5 and 9.22a) and by reactive sputtering (Figs. 9.19 and 9.22b). The somewhat broader maximum and a slightly lower hardness are due probably to the relatively low deposition temperature of 300°C used in this series. The hardness clearly showed dependence on the substrate bias (the data reproduced in Fig. 9.10b are for the optimum bias of −50 V, see Fig. 4b in Ref. 112) and on the deposition temperature. The researchers found the maximum hardness for a deposition temperature of about 500°C in agreement with our earlier data.[1] Because of the relatively low pressure of nitrogen, the coatings were probably not quite in the stable state as indicated also by the appearance of a new "phase 2" in the XRD pattern[111] that, however, vanished upon annealing. Because the thickness of the coatings was up to 3.3 μm the reported values of the hardness can be considered as more reliable than those of Meng *et al*.

In the majority of papers, oxygen impurities are not reported but they may likely be the reason for the low hardness. As outlined in the foregoing section, at typical deposition rates of 0.1–0.5 nm/s and a residual gas pressure of $(1–7) \times 10^{-6}$ mbar reported in these papers (or estimated by us when these data are lacking), the oxygen impurity in the range of up to several atomic percent are incorporated into the coatings during their growth, as shown in Section 5.1.

5.3. Conditions Needed to Achieve Hardness of 80 to $\geq$ 100 GPa

As outlined in our earlier paper,[30] the ultrahardness was achieved so far only in ternary and quaternary nanocomposites nc-TiN/a-Si_3N_4/a- & nc-$TiSi_2$ when the surface of all nanocrystals was covered with about one monolayer of Si_3N_4 (see Fig. 9.23a) and the oxygen impurity content was 0.01–0.05 at%. There is a very narrow compositional range for the coexistence of all three phases, i.e., TiN, Si_3N_4, and $TiSi_2$, and it is not an easy task to *meet all* these requirements simultaneously. Therefore, the reproducibility of obtaining the high hardness was somewhat lower than in the case of the binary nc-TiN/a-Si_3N_4 nanocomposites. The process variable during this deposition was the discharge current density (see Refs. 31 and 32). Nevertheless, we succeeded to deposit more than 15 ultrahard (i.e., $H \geq 80$ GPa) coatings. From these, six reached a hardness of $\geq$100 GPa (Musil1 reply). In order to avoid possible artifacts that could falsify the hardness measurements we always reported a load-independent hardness, typically in the range of maximum applied load of 30–100 mN.[1] Moreover, we verified these

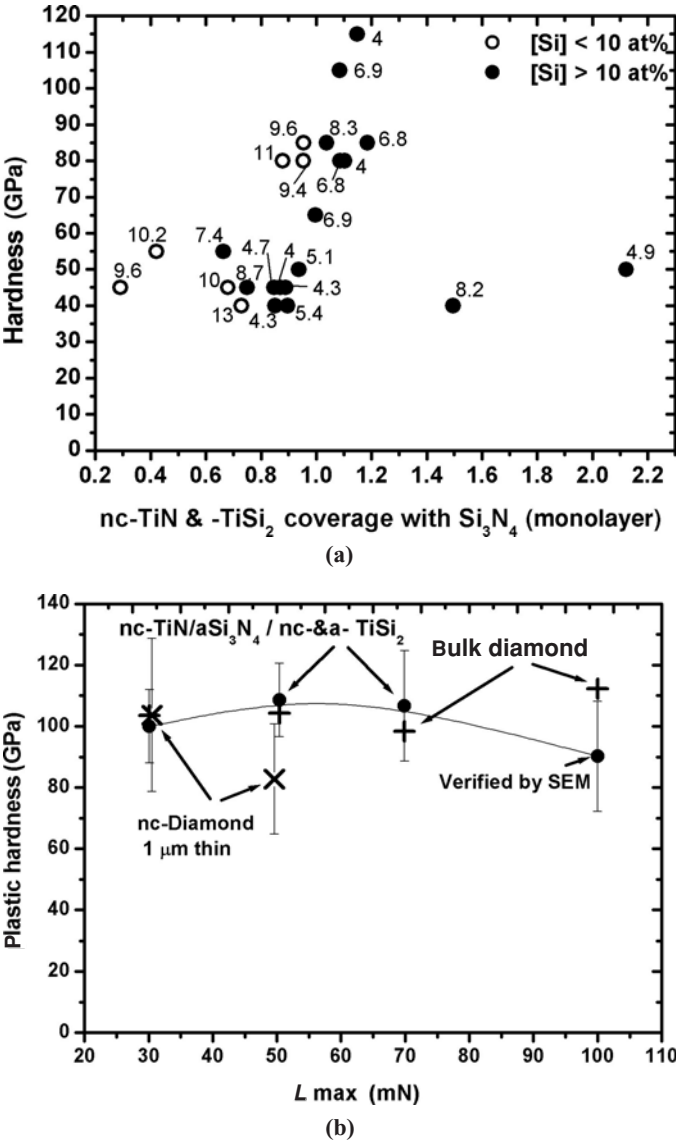

FIGURE 9.23. (a) Hardness of the ternary and quaternary nc-TiN/a-Si_3N_4/a- & nc-$TiSi_2$ nanocomposites versus the coverage of the surface of the nc-TiN and—whenever present—nc-$TiSi_2$ nanocrystals with Si_3N_4. The numbers indicate the crystallite size (see text); (b) Example of the measurements of the load-independent hardness of the second hardest coating from Fig. 9.23a in comparison with bulk diamond and single-phase nc-diamond coating. At the load of 100 mN the hardness decreases because the indentation depth exceeded 10% of the thickness of 3.5 μm. The value of the hardness was also verified by calibrated SEM.[31]

values by a calibrated SEM and with measurement on single crystal diamond, as shown in Fig. 9.23b and outlined above. Let us emphasize that the thinnest coating that was prepared and characterized in this series was 3.5 μm thick, but the thickness of the majority of these coatings was ≥6 μm.

These coatings are of interest because they demonstrated the possibility of the preparation of materials with the hardness in the upper range of the hardness of diamond. From the practical point of view, the coatings containing the $TiSi_2$ phase suffer an instability of this phase upon a long-term exposure to air. As mentioned above, the decrease of the hardness observed in the coatings of Li *et al.*,[28] after several months, was attributed to the relatively high chlorine impurity content. However, we found a similar decrease in our nc-TiN/a-Si_3N_4/a & nc-$TiSi_2$ ultrahard coatings after a period of 6–8 months, although their chlorine content was low (typically <0.5 at%). This instability is related to the instability of the titanium silicide, which forms several phases of different stoichiometry Ti_5Si_3, TiSi, and $TiSi_2$ of which the latter should be the most stable one.[117,118] However, when prepared at a relatively low temperatures of 500–600°C it forms the metastable C49-$TiSi_2$, which transforms to the stable C54-$TiSi_2$ only at high temperatures. Because this phase transition is kinetically hindered in a small volume, the nanocomposites containing $TiSi_2$ are susceptible to chemical attack by the polar water.[117,118] The situation is similar to silica fibers, which, when freshly drawn, can reach the ideal tensile strength of 24 GPa. However, when exposed to moist air, their hardness decreases quickly and, after 24 h, hardly reaches 0.3 GPa because of the formation of surface microcracks (see Ref. 34, p. 172 ff).

6. MECHANICAL PROPERTIES OF SUPERHARD NANOCOMPOSITES

6.1. Recent Progress in the Understanding of the Extraordinary Mechanical Properties

In this section we shall briefly summarize the recent progress in the understanding of the mechanical properties of the superhard, stable nanocomposites. Because of the limited space, we refer the reader to the quoted references. Our original concept was based on the absence of dislocation activity in a few nanometer small crystallites, a very small stress concentration factor for ≤1 nm small nanocracks, and, therefore, a large stress needed to initiate and propagate a crack in such systems where the grain boundary sliding is absent.[1,7,30,32,55,74,83] The grain boundary sliding limits the strength of nanocrystalline metals prepared by consolidation (see, e.g., Refs. 119–122).

More recently, a significant, much deeper understanding was achieved due to the important contribution of Professor Argon.[3,123] It will be shown that the mechanical properties of these nanocomposites can be easily understood in terms of

the conventional fracture physics scaled down to a crystallite size of few nanometers and about one monolayer thick amorphous tissue when these materials are free of flaws. The latter property, which is the consequence of the formation of the stable nanostructure by self-organization upon the spinodal phase segregation, makes them significantly different from the nanocrystalline materials prepared by consolidation, sintering, and other techniques. In the latter materials, the hardness monotonously decreases when the crystallite size decreases below about 8–10 nm due to an increasing fraction of the material within the grain boundaries that is responsible for the increasing tendency to grain boundary sliding.[124] As shown above, in the stable nanocomposites, the hardness reaches a maximum when the nanocrystals are covered with about one monolayer of Si_3N_4 or BN (Figs. 9.9 and 9.23) although the crystallite size may be significantly different [cf. nc-TiN/a-Si_3N_4 with nc-TiN/a-BN in Fig. 9.9, and the ternary and quaternary nc-TiN/a-Si_3N_4/a- & nc-$TiSi_2$ (Fig. 9.23) with the binary nc-TiN/a-Si_3N_4 in Fig. 9.9].

Conventional, hard materials have a low elastic recovery limit of the strain of $\leq$0.1% above which brittle fracture occurs. The elastic limit of strong metals, such as steels, reaches about 0.3–0.5%. The maximum elastic recovery limit of 2% was achieved in metallic glasses. Plastic deformation in ductile materials, such as metals, occurs via dislocation activity or a shear transformation such as deformation twins or martensitic transformations.[14,17] In glassy solids, such as amorphous metals, plastic flow occurs by recurring shear transformations in fertile volume elements where the shear transformations are of ca. 3–4-nm size.[125] Plastic deformation by either of these mechanisms requires a finite activation volume.[15–17,126] This is a similar situation as found for pressure-induced structural phase transition in nano-sized single crystals, where the pressure of the transition increases with decreasing size of the crystals, and the reverse transition upon unloading shows a hysteresis that also increases with decreasing crystallite size (see, e.g., Ref. 127). If the size of the specimen of a material is too small, none of these mechanisms of plastic deformation can occur and the strength of such material approaches the *ideal strength*. This is well known for crystal plasticity where the dislocation activity vanishes when the crystallite size decreases to $\leq$10–20 nm. Plastic deformation of such small nanocrystals can occur only by sliding of crystal lattice planes. The shear stress needed for such process to occur is about 10% of the shear modulus.[128,129]

The effect of decreasing size of a specimen on the mechanical properties is less understood in the case of glasses, particularly for the covalently bonded ones, such as Si_3N_4 and BN that are acting as a "glue" between the nanocrystals in the stable nanocomposites. Usually, the increasing strength with decreasing size of the specimen or the volume being tested is attributed to the decreasing size and probability of the appearance of a critical flaw, such as microcrack.[1,34]

In their recent molecular dynamic modeling of Si glass, Demkowicz and Argon have shown that localized plastic deformation events in covalently bonded amorphous solids are triggered by a simultaneous, collective movement of five to

six atoms and the rearranging clusters, where the plastic transformation occurs, contain 100–500 atoms.[126] Obviously, it is essentially impossible to trigger the plastic deformation within one monolayer of the Si_3N_4 or BN tissue in the stable superhard nanocomposites whose strength should then also approach the ideal strength.

The ideal strength of a perfect glass is given by the ideal decohesion strength $\sigma_C \approx (E_Y \gamma_S / a_0)^{0.5}$ [E_Y is the Young's modulus, γ_S is surface energy, and a_0 is interatomic bond distance (see, e.g., Ref. 14, pp. 239–240)]. From these relations one can easily estimate that the ideal strength of strong solids should reach up to 20–50 GPa, as indeed observed for whiskers and freshly drawn glass fibers. For example, the tensile strength of freshly drawn SiO_2 glass fibers reaches 24 GPa, which corresponds to about 25% of Young's modulus (see Ref. 14, p. 240). Furthermore, the elastic recovery strain of an ideal glass approaches 20% (see Ref. 14, pp. 239 and 240; and Refs. 2 and 3 and references therein).

Based on the universal binding energy relations (UBER),[130,131] Argon estimated the ideal cohesive strength of our nanocomposites to be about 46 GPa and compared it with the tensile stress of about 33 GPa occurring at the periphery of the contact between the indenter and the coatings upon the maximum applied load of 70 mN.[123] The application of the hertzian analysis for the measurement of the tensile strength of glasses was demonstrated by Argon *et al*. earlier.[132] Therefore we used this procedure to determine the tensile ("radial") stress for crack-free indentation into a number of different super- and ultrahard nanocomposites.[2] Figure 9.24 shows that the tensile radial stress of such indentation, which represents the lower limit of the tensile strength of the nanocomposites, indeed approaches the ideal strength calculated for these materials. A detailed hertzian analysis of a number of experimental indentation curves into the nanocomposites and into diamond confirmed the self-consistency of the measurements and of the high values of hardness found for these materials.[2,18,123] Also the results of the numerical modeling by means of FEM confirm the experimental data (see Fig. 9.24). We refer to these papers for further details.

As already mentioned, the unusual combination of the mechanical properties of the nanocomposites, such as a high hardness combined with a high elastic recovery of $\leq$95% and high elastic recovery limit of $\leq$20% can be easily understood on the basis of the behavior of materials that are free of flaws. This has been discussed in some detail in our recent papers.[2,3,18,123] Here we shall only very briefly discuss some concepts that are misinterpreted or confused in some recent papers.

6.2. The Resistance Against Brittle Fracture

Very often one refers to a high "*fracture toughness*" in these materials because with a large load of, e.g., 1000 mN into a 6–10-μm thin coating on a soft steel substrate, where the strain reached 20%, the indentation did not cause any fracture (see Fig. 9.25b, and also Figs. 8 and 9 in Ref. 2 in order to underline the reproducibility of these results). In the case of a thinner coating (see Fig. 9.25a), only the circular

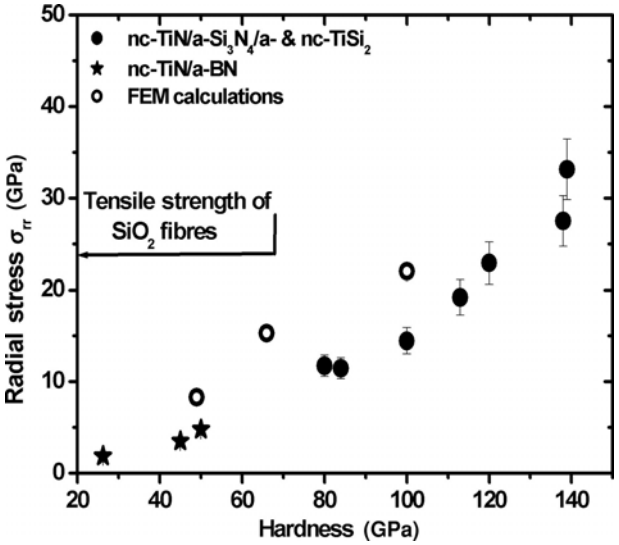

FIGURE 9.24. Radial stress, calculated from Eq. (6) from Ref. 105, which the superhard coatings sustain without any cracks formation, versus hardness. For all the indentations in various coatings used here, both the $\log(h)$ vs. $\log(L)$ [Eq. (5) from Ref. 105] was linear and the tip radius estimated from Eq. (9.7) from Ref. 105 was close to 0.5 μm. Open symbols are the results of FEM calculation.[2]

"hertzian" cracks are seen but no radial ones which should be starting from the corners of the indented area. These examples show that these materials are indeed very resistant against the brittle fracture, but the scanning electron micrographs alone do not reveal the reason of this strength.

Fracture toughness is the resistance of a material against the propagation of a prefabricated crack. It is quantitatively described by the stress intensity factor K_I or energy release rate. For a simple case of a planar crack of the size $2a$, the stress intensity factor $K_I = \sigma(\pi a)^{0.5}$ where σ is the stress needed to cause the propagation of a crack of the size $2a$. K_I can be measured, e.g., by the indentation technique when radial cracks are formed at the corners of the indentations, provided that the thickness of the specimen is much larger than the length of the cracks, which is difficult to meet in the coatings. Nevertheless, the absence of any radial cracks in many of the indentation experiments that we reported in combination with the high tensile strength is characteristic of a material in which there is a large threshold for the initiation of a crack and not necessarily of a high stress intensity factor.[3]

6.3. High Elastic Recovery

In addition to this high resistance against brittle fracture, the nanocomposites display a high elastic recovery of up to 94% upon a load of 70 mN where the load-

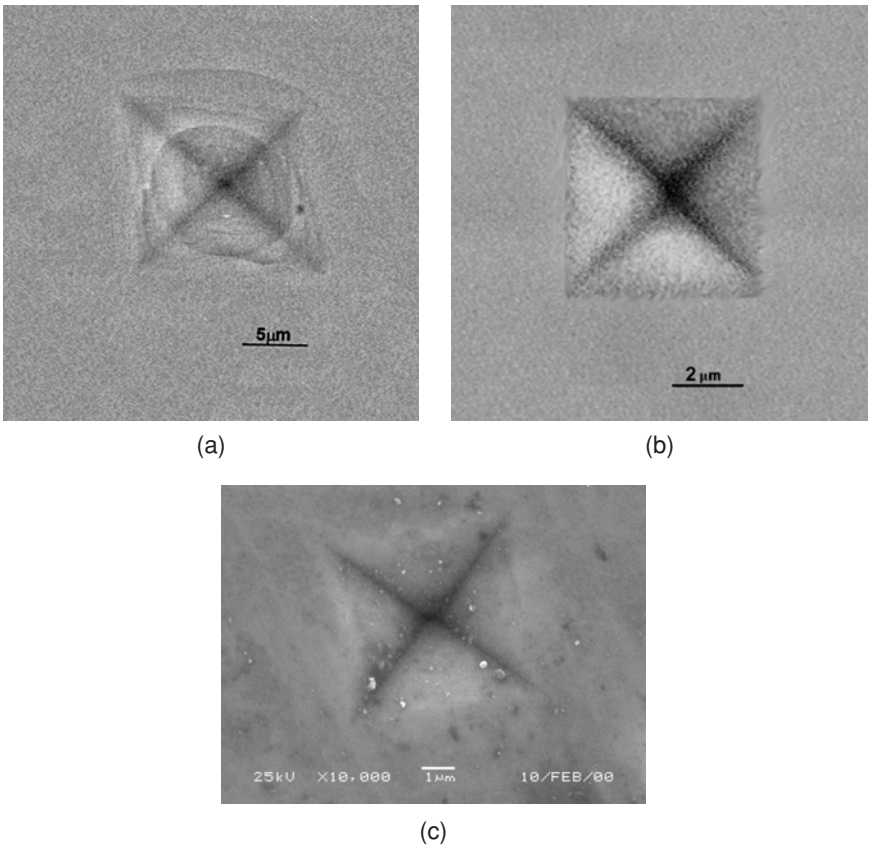

FIGURE 9.25. Scanning electron micrographs of the indentation into a (a) 3.5-μm-thick ultrahard coating (load-independent hardness of about 105 GPa, see Fig. 9.23) after applied load of 1000 mN where the coating was pressed deep into the soft steel substrate; (b) 10.7-μm-thick coating ($H_V \approx 38$ GPa) after indentation with a load of 1000 mN. (c) 6.1 μm thick ultrahard coating ($H_{0.005} \approx 100$ GPa) after applied load of 1000 mN. Notice the absence of radial cracks in the diagonal direction in both cases.

independent hardness of more than 100 GPa is found (see Fig. 1a in Ref. 3) and elastic limit of $\geq$10% upon a load of 1000 mN. For example, when about a 6-μm-thin coating is pressed with a load of 1000 mN about 2 μm deep into the soft steel substrate ($H_V \approx 1.8$ GPa), it does not show any cracks, the composite hardness of the coating and substrate is still about 40 GPa, and, upon unloading, the coatings recovers almost 10% in spite of the fact that it is hold by the severely plastically deformed substrate (see Fig. 25c from Ref. 3). The absence of any cracks, even under the surface of the coatings, was carefully checked by means of hertzian analysis and by observation of the loading curves (see, e.g., Figs. 8 and 9 in Ref. 2).

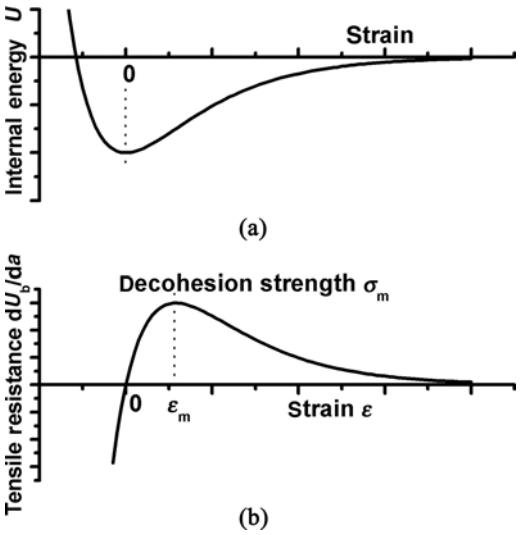

FIGURE 9.26. (a) Internal energy versus strain of an ideal material; (b) Universal decohesion curve, i.e., the first derivative of the curve in Fig. 9.26a with strain that corresponds to the recovery force.[2] Notice that the first derivative of the tensile resistance with strain at the equilibrium (= 0) is the Young's modulus.

6.4. Ideal Decohesion Strength

The mechanical properties discussed in section 6.3 are consistent with the nearly defect-free nature of the material as illustrated in Fig. 9.26. Imagine a perfect glass without any defect. The change of the internal energy due to strain (Fig. 9.26a) corresponds roughly to the change of the interatomic binding energy integrated over the whole specimen. The tensile resistance is the restoring force that acts so as to bring the energy of the system to its minimum (i.e., the interatomic distances and bond angles to their equilibrium values), as shown in Fig. 9.26b. Notice that the restoring force is the first derivative of the internal energy with the strain. Upon tension, the first derivative of the tensile resistance with the strain at the equilibrium (the tangent to the curve) is the Young's modulus, i.e., $E_Y = (d^2U/d\varepsilon^2)_0$. It is noticed that the value of the elastic modulus increases upon compression ($\varepsilon < 0$) and decreases upon tension ($\varepsilon > 0$). The maximum of the tensile resistance corresponds to the decohesion strength σ_m that is reached at the maximum recovery strain (elastic limit) $\varepsilon_m \approx 15$–20%, which is approximately the limit where upon tension an interatomic covalent bond breaks (see Fig. 9.26b). The whole range of $0 < \varepsilon < \varepsilon_m$ corresponds to purely reversible, elastic deformation that, however, is nonlinear because of the dependence of the elastic modulus on the strain.

These considerations show that a material that is free of any defects should sustain a reversible strain of 15–20% without fracture and its strength should

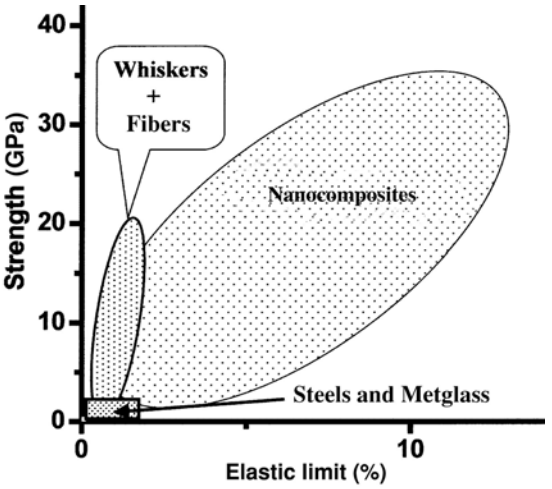

FIGURE 9.27. Tensile strength and elastic limit of strong materials in comparison with the superhard nanocomposites (see text).

reach the ideal decohesion strength. This is illustrated by Fig. 9.27 that shows a comparison of the strength and elastic limit of the nanocomposites with those of conventional materials and with whiskers and freshly drawn silica fibers.[2] Notice that the ideal strength is proportional to root square of Young's modulus that is significantly larger for the nanocomposites (about 450 GPa) than for SiO_2 (about 90 GPa).

The comparison shown in Fig. 9.27 illustrates why the extraordinary mechanical properties of the superhard, stable nanocomposites can be simply understood in terms of the conventional fracture physics of flow-free materials. Freshly drawn silica fibers and whiskers (a few micrometer thin single crystals) are essentially free of any flaws. Therefore, their strength approaches the ideal strength of flaw-free, strong materials. There is no need to evoke any new terminology or models as suggested in several recent papers.

6.5. The Future Research Work

The real challenge for the future research is a deeper understanding of the nonlinear elastic response and of the mechanism of plastic deformation in these materials. For example, in the case of a 50–60-GPa hard coating, the bulk modulus under the indenter is pressure enhanced to $B(P) \approx B(0) + 5P$ (here $B(0)$ is the zero pressure bulk modulus and $B(P)$ the bulk modulus at pressure P). The proportionality factor of 5 was measured by means of high pressure XRD[19] and it is in agreement with the values predicted by the UBER.[130,131] Considering this dependence, the bulk modulus of our coatings of $B(0) = 295 \pm 15$ GPa determined by high-pressure

XRD[19] is during the hardness measurement enhanced to 545–595 GPa (notice that the pressure under the indenter corresponds approximately to the hardness $H = L/A_C$, see above). For these reasons conventional FEM codes cannot handle this strongly nonlinear elastic problem. Although most of the elastic response upon unloading comes from distant areas where the pressure enhancement is smaller, the magnitude of the strain that has to be included into the calculations is large. A similar situation arises with the mechanism of the plastic deformation that is most probably occurring within the amorphous tissue.[123,133]

7. INDUSTRIAL APPLICATIONS

The industrialization of the nc-$(Al_{1-x}Ti_x)N$/a-Si_3N_4 nanocomposites was pioneered by the SHM company in Czech Republic.[89,134] Tanaka *et al*. developed the "Al-Ti-Si-N" coatings in which, according to their analysis, the silicon was dissolved within the (Al,Ti)N phase.[82] Also these coatings showed and improved cutting performance, although their hardness was lower than that of the nc-$(Al_{1-x}Ti_x)N$/a-Si_3N_4 nanocomposites. Later, SHM and a larger Swiss company PLATIT developed a new coating technology dedicated to the large-scale industrial production. The limited space available here does not allow us to extend on this topic. Therefore, we summarize briefly the achievements and refer to the recent papers[134–147] for further details.

The new coating technology uses a special design of vacuum arc that is localized to a narrow track by a strong magnetic field that provides a very high velocity of the movement of the cathodic spot. This reduces strongly the emission of the droplets, which improves the surface roughness to less than 0.1 μm. Furthermore, the special arrangement of the magnetic field allows one to preclean the surface of the cathodes prior to the deposition, by depositing the surface material that was contaminated during the exposure to air (loading of the tools to be coated). This "Virtual Shutter®" allows one to turn the magnets of the cathode backward and deposit the contaminated material from the surface of the cathode on the back wall. When the tools were cleaned, the magnets are turned back and pure material is deposited. This "Virtual Shutter®" improves significantly the adhesion and the cutting performance of the coatings. The rotation of the cylindrical cathodes assures their uniform erosion that results in an increase of the lifetime by about a factor of 6 to 7 as compared with the planar ones. An asymmetric arrangement of the tools being coated with respect to the cathodes yields compositionally modulated nanolayers of the nanocomposites, which further improves their resistance against crack propagation.

The cutting performance of the nc-$(Al_{1-x}Ti_x)N$/a-Si_3N_4 nanocomposites in dry or minimum lubricant machining is typically a factor of 2–4 better than that of the state-of-the-art $(Al_{1-x}Ti_x)N$ coatings. For example, in dry drilling of a tough steel, the lifetime of the coated drill made of cemented carbide and coated with

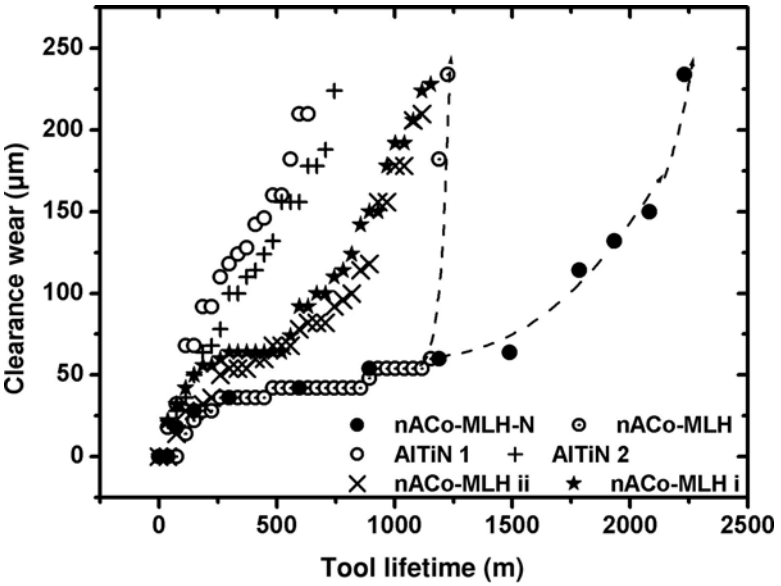

FIGURE 9.28. Example of the excellent cutting performance of the nc-$(Al_{1-x}Ti_x)$7a-Si_3N_4 nanocomposites coatings. Hard milling of 57 HRC steel. Tool: Ball-nosed solid carbide end mills, $d = 10$ mm $\times$ 57, hydrochuck, rpm = 18500, feed (fz) = 0.18 mm, depth per tooth (ap) = 0.25 mm, depth of cut (ae) = 0.6 mm, external minimum jet lubrication.[138]

the nanolayered nanocomposites is a factor of 4 longer than that coated with the best state-of-the-art $(Al_{1-x}Ti_x)N$.[135–137] Very often, the better cutting performance becomes evident upon a faster machining (e.g., in taping). Figure 9.28 shows a more recent example of the hard, minimum lubricant (essentially dry) milling of the very hard 57 HRC (Rockwell hardness C) steel . As one can see from the different curves for different layered structure of the nc-$(Al_{1-x}Ti_x)$M/a-Si_3N_4 nancocomposite coatings, the lifetime of the tool could be significantly increased.

8. CONCLUSIONS

The easiest way to prepare superhard coatings is the application of energetic ion bombardment during the deposition as pioneered by Musil.[49,61,62] However, these coatings, sometimes also incorrectly called "nanocomposites,"[49] suffer from a too low thermal stability.[3,51]

The generic concept for the design of superhard and thermally very stable nanocomposites[1] is based on a thermodynamically driven, strong spinodal phase segregation that results in the formation of a stable nanostructure by self-organization. In order to achieve this formation of the nanostructure during the deposition, sufficiently high nitrogen activity (partial pressure $\geq 1 \times 10^{-3}$ mbar)

and temperature (500–600°C) are needed because the nitrogen has to provide the high thermodynamic driving force and the temperature has to assure the diffusion rate-controlled phase segregation to proceed sufficiently fast during the deposition.

The maximum hardness is achieved when about one monolayer of the covalent nitride, such as Si_3N_4 or BN (or AlN, etc.), is covering the surfaces of the polar, hard transition metal nitride nanocrystals. This design concept was verified in a large number of different systems. Therefore, it is expected to work also in any other nc-Me_nN/a-Si_3N_4, nc-MeN_nN/a-BN (Al, etc., instead of BN), and nc-Me_nC/C, and in many other systems that meet the conditions outlined in Refs. 1 and 74, and in subsequent papers. When these conditions are not fulfilled, low hardness enhancement or no enhancement[23] is found. When the coatings are deposited under conditions that are close but not fully in the optimum, self-hardening is found upon annealing to 600–800°C due to the completion of the phase segregation.[3] However, when the coatings are deposited at a sufficiently high nitrogen pressure and temperature as outlined in our first paper,[1] they show an excellent thermal stability upon annealing in nitrogen up to 1100–1200°C[4] and high oxidation resistance to $\geq$800°C.[1,77]

Small amounts of impurities in the nanocomposite coatings degrade their mechanical properties. Most critical is oxygen because if the oxygen impurity content in the coatings is larger than about 0.2 at% the hardness of $\geq$40 GPa cannot be reached. Much lower oxygen content is needed if a hardness of $\geq$50 GPa should be reached. In the majority of papers reporting on the preparation of the nanocomposite coatings by means of PCVD and PVD the oxygen impurities are not reported and in those where they are, it lies in the range of several atomic percent. These facts explain in a simple way why so many workers have difficulties to reproduce the high values of the hardness. Other, speculative explanations[5] are obviously not needed.[6]

Reliable measurements of the hardness of superhard coatings are possible only when $\geq$6–8 μm thick coatings are prepared and the load-independent value of the hardness is found, typically for maximum applied load of 50–150 mN. Using low loads of <30 mN and indentation depth of <0.2–0.3 μm is likely to yield erroneous values of the hardness due to the indentation size effect, which may occur due to a variety of reasons.[2,12,18–21]

The extraordinary mechanical properties of the stable nanocomposites prepared according to the generic principle can be understood on the basis of conventional fracture physics. Because these nanocomposites are free of defects, their strength approaches the ideal strength of flow-free materials in a similar way as it is known for whiskers and freshly drawn silica fibers.

The nc-$(Al_{1-x}Ti_x)$N/a-Si_3N_4 nanocomposite coatings deposited in large-scale industrial coating equipment show an excellent thermal and oxidation stability. The thin Si_3N_4 tissue stabilizes the Al-rich $(Al_{1-x}Ti_x)$N metastable solid solution against the decomposition into c-TiN and h-AlN and concomitant softening. In hard, dry (or minimum lubricant) machining, these coatings show

excellent cutting performance, which is superior to the state-of-the-art $(Al_{1-x}Ti_x)N$ coatings.

ACKNOWLEDGMENTS

We thank all the coworkers and colleagues whose names are on the joint publications for their collaboration and excellent work. Our particular thanks are due to Prof. Li Shizhi for friendly sharing his ideas with us, to Dres. M. Jilek, Holubar, and Cselle for many interesting discussions, and to Prof. A. S. Argon for his substantial contribution to the understanding of the mechanical properties of the superhard nanocomposites. The work has been supported by the NATO Science for Peace Programme Project No. 972379 "Protection Coatings," by the European Commission within the 6th framework program under Contract No. AST 3-CT-2003-502741 – "MACHERENA" and Contract No. CA 505549-1 – "DESHNAF."

REFERENCES

1. S. Veprek and S. Reiprich, A concept for the design of novel superhard coatings, *Thin Solid Films* **268**, 64–71 (1995).
2. S. Veprek and A. S. Argon, Towards the understanding of mechanical properties of super- and ultrahard nanocomposites, *J. Vac. Sci. Technol. B* **20**, 650–664 (2002).
3. S. Veprek, S. Mukherjee, P. Karvankova, H.-D. Männling, J. L. He, K. Moto, J. Prochazka, and A. S. Argon, Limits to the strength of super- and ultrahard nanocomposite coatings, *J. Vac. Sci. Technol. A* **21**, 532–544 (2003).
4. H.-D. Männling, D. S. Patil, K. Moto, M. Jilek, and S. Veprek, Thermal stability of superhard nanocomposite coatings consisting of immiscible nitrides, *Surf. Coat. Technol.* **146–147**, 263–267 (2001).
5. J. Musil, H. Zeman, F. Kunz, and J. Vlcek, Measurement of hardness of superhard films by microindentation, *Mater. Sci. Eng. A* **340,** 281–285 (2003).
6. S. Veprek, S. Mukherjee, H.-D. Männling, and J. L. He, On the reliability of the measurements of mechanical properties of superhard coatings, *Mater. Sci. Eng. A* **340,** 292–297 (2003).
7. S. Veprek, The search for superhard materials, *J. Vac. Sci. Technol. A* **17,** 2401–2420 (1999).
8. E. Meyer, Untersuchungen über Härteüprüfung und Härte, *Zt. Vereines Deutsch. Ing.* **52**, 645–654 (1908).
9. D. Tabor, *The Hardness of Metals* (Clarendon Press, Oxford, 1951).
10. M. F. Doener and W. D. Nix, A method for interpreting the data from depth-sensing indentation instrument, *J. Mater. Res.* **1**, 601–609 (1986).
11. G. M. Pharr, Measurements of mechanical properties by ultra-low load indentation, *Mater. Sci. Eng. A* **253**, 151–159 (1998).
12. S. J. Bull, T. F. Page, and E. H. Yoffe, An explanation of the indentation size effect in ceramics, *Philos. Mag. Lett*. **59,** 281–288 (1989).
13. A. C. Fischer-Cripps, *Nanoindentation* (Springer-Verlag, New York, 2002).
14. R. W. Hertzberg, *Deformation and Fracture Mechanics of Engineering Materials*, 3rd edn (Wiley, New York, 1989).
15. A. Gouldstone, K. J. Van Vliet, and S. Suresh, Nanoindentation simulation of defect nucleation in crystal, *Nature* **411,** 856–865 (2001).

16. K. Van Vliet, J. Li, T. Zhu, S. Yip, and S. Suresh, Quantifying the early stages of plasticity through nanoscale experiment and simulation, *Phys. Rev.B* **67**, 104105 (2003).
17. A. S. Argon, Mechanical properties of single-phase crystalline media: Deformation at low temperatures, in *Physical Metallurgy*, 4th edn, Vol. III, edited by R. W. Cahn and P. Haasen (North-Holland, Amsterdam, 1996), pp. 1878–1955.
18. S. Veprek, S. Mukherjee, P. Karvankova, H.-D. Männling, J. L. He, K. Moto, J. Prochazka, and A. S. Argon, Hertzian analysis of the self-consistency and reliability of the indentation hardness measurements on superhard nanocomposite coatings, *Thin Solid Films* **436,** 220–231 (2003).
19. S. Veprek, S. Mukherjee, P. Karvankova, H.-D. Männling, J. L. He, J. Xu, J. Prochazka, Q. F. Fang, S. Z. Li, M. Manghani, S. Tkachev, and P. Zinin, Possible artefacts in measurements of hardness and elastic modulus on superhard coatings and the verification of the correctness of the data, in *Surface Engineering 2002-Synthesis*, *Characterization and Applications*, edited by A. Kumar, W. J. Meng, Y. T. Cheng, J. S. Zabinski, G. L. Dolls, and S. Veprekand, *Mater. Res. Soc. Symp. Proc.* **750,** 9–14 (2003).
20. S. J. Bull, Interface engineering and graded films: Structure and characterization, *J. Vac. Sci. Technol. A* **19,** 1404–1414 (2001).
21. S. J. Bull, Modelling the hardness response of bulk materials, single and multilayer coatings, *Thin Solid Films* **398–399,** 288–291 (2001).
22. S. Veprek, Nanostructured superhard materials, in *Handbook of Ceramic Hard Materials*, edited by R. Riedel (Wiley-VCH, Weinheim, Germany, 2000), pp. 104–139.
23. M. Lichinchi, C. Lenardi, J. Haupt, and R. Vitali, Simulation of Berkovich nanoindentation experiments on thin films using finite element method, *Thin Solid Films* **312**, 240–248 (1998).
24. J. L. He and S. Veprek, Finite element modeling of indentation into superhard coatings, *Surf. Coat. Technol.* **163–164,** 374–379 (2003).
25. X. D. Zhang, W. J. Meng, W. Wang, L. E. Rehn, P. M. Baldo, and R. D. Evans, Temperature dependence of structure and mechanical properties of Ti-Si-N coatings, *Surf. Coat. Technol.* **177–178**, 325–333 (2003).
26. P. Rogl and J. C. Schuster, *Phase Diagrams of Ternary Boron Nitride and Silicon Nitride Systems* (ASM The Materials Society, Materials Park, OH, 1992).
27. E. Blanquet, A. M. Dutron, C. Bernard, G. Llauro, and R. Hillel, Different applications of the CVD thermodynamic simulations in the Ti-Si-N system: Oxidation and microelectronic materials, in *Chemical Vapor Deposition*, *Proceedings of the 14th International Conference and EUROCVD-11*, Paris, September 5–9, 1997, edited by M. D. Allendorf and C. Bernard; *Electrochem. Soc.* Vol. **97–25**, 23–30 (1997).
28. S. Z. Li, Y. Shi, and H. Peng, Ti-Si-N films prepared by plasma-enhanced chemical vapor deposition, *Plasma Chem. Plasma Process.* **12,** 287–297 (1992).
29. S. Veprek, S. Reiprich, and S. Z. Li, Superhard nanocrystalline composite materials: The SiN/Si_3N_4 system, *Appl. Phys. Lett.* **66,** 2640–2642 (1995).
30. A. Niederhofer, T. Bolom, P. Nesladek, K. Moto, C. Eggs, D. S. Patil, and S. Veprek, The role of percolation threshold for the control of the hardness and thermal stability of super- and ultrahard nanocomposites, *Surf. Coat. Technol.* **146–147**, 183–188 (2001).
31. S. Veprek, A. Niederhofer, K. Moto, P. Nesladek, H.-D. Männling, and T. Bolom, Nanocomposites nc-TiN/a-Si_3N_4/a- & nc-$TiSi_2$ with hardness exceeding 100 GPa and high fracture toughness, *Mater. Res. Soc. Symp. Proc.* 5**81**, 321–326 (2000).
32. S. Veprek, A. Niederhofer, A. Moto, A. Bolom, H.-D. Männling, P. Nesladek, G. Dollinger, and A. Bergmaier, Composition, nanostructure and origin of the ultrahardness in nc-TiN/a-Si_3N_4/a- and nc-$TiSi_2$ nanocomposites with $H_V = 80$ to ≥ 100 Gpa, *Surf. Coat. Technol.* **133–134**, 152–159 (2000).
33. S. Li, S. Veprek, *et al*., unpublished.
34. B. Lawn, *Fracture of Brittle Solids*, 2nd edn (Cambridge University Press, Cambridge, 1993), p. 173.

35. R. A. Andrievski, Nanocrystalline borides and related compounds, *J. Solid State Chem.* **133**, 249–253 (1997).
36. P. Hammer, A. Steiner, R. Villa, M. Baker, P. N. Gibson, and J. Haupt, Titanium boron-nitride coatings of very high hardness, *Surf. Coat. Technol.* **68–69,** 194–198 (1994).
37. C. Mitterer, P. H. Mayhofer, M. Beschliesser, P. Losbichler, P. Warbichler, F. Hofer, P. N. Gibson, W. Gissler, H. Hruby, J. Musil, and J. Vlcek, Microstructure and properties of nanocomposite Ti-B-N and Ti-B-C coatings, *Surf. Coat. Technol.* **120–121,** 405–411 (1999).
38. S. Veprek, P. Karvankova, J. Prochazka, and H.-D. Männling, Different mechanisms leading to superhard coatings: Stable nanocomposites and high biaxial compressive stress, *Mater. Res. Soc. Symp. Proc.* **697**, 27–32 (2002).
39. P. H. Mayrhofer, C. Mitterer, J. Wen, I. Petrov, and J. E. Greene, Self-arranged nanocolumnar structure of sputtered TiB_2 coatings, *Appl. Phys. Lett.* **86**(13), 131909 (2005).
40. P. H. Mayrhofer, Thermal stability and self-arrangement of nanocrystalline hard coatings, in *Proceedings of NATO-RussiaAdvanced Research Workshop (RARW), Nanostructured Thin Films and Nanodispersion Strengthened Coatings*, Moscow State Institute of Steel and Alloys, Technological University, December 8–10, 2003, in NATO Science Series II. Mathematics, Physics and Chemistry, edited by A. A. Voevodin, D. V. Shtansky, E. A. Levashov, and J. J. Moore, Kluwer Academic Publisher, Dordrecht, Vol. 155, 2004.
41. O. Knotek, in: *Mater. Res. Soc. Fall Meeting*, Boston, Deccember 2–5, 1996 (1996).
42. O. Knotek, E. Lugscheider, F. Löffler, B. Bosserhoff, and S. Schmitz, Superstoichiometric PVD carbide coatings, *Mater. Sci. Eng. A* **209**, 394–398 (1996).
43. A. Voevodin and J. S. Zabinski, Supertough wear-resistant coatings with "chameleon" surface adaptation, *Thin Solid Films* **370**, 223–231 (2000).
44. R. Hauert and J. Patscheider, From alloying to nanocomposites—Improved performance of hard coatings, *Adv. Eng. Mater.* **2**, 247–259 (2000).
45. D. Li, X. Chu, S. C. Cheng, X. W. Lin, V. P. Dravid, Y. W. Chung, M. S. Wong, and W. D. Sproul, Synthesis of superhard carbon nitride composite coatings, *Appl. Phys. Lett.* **67**, 203–205 (1995).
46. D. Li, W. W. Lin, S. C. Cheng, V. P. Dravid, M. S. Wong, and W. D. Sproul, Structure and hardness studies of CN*x*/TiN nanocomposite coatings, *Appl. Phys. Lett.* **68**, 1211–1213 (1996).
47. Y. W. Chung, Synthesis and mechanical properties of crystalline carbon nitride superhard coatings, *Surf. Rev. Lett.* **3**, 1597–1602 (1996).
48. M. L. Wu, X. W. Lin, V. P. Dravid, Y. W. Chung, M. S. Wong, and D. Sproul, Preparation and characterization of superhard CN*x*/ZrN multilayers, *J. Vac. Sci. Technol. A* **15**, 946–950 (1997).
49. J. Musil, Hard and superhard nanocomposite coatings, *Surf. Coat. Technol.* **125**, 322–330 (2000).
50. W. Herr and E. Broszeit, The influence of a heat treatment on the microstructure and mechanical properties of sputtered coatings, *Surf. Coat. Technol.* **97**, 335–340 (1997).
51. P. Karvankova, H.-D. Männling, C. Eggs, and S. Veprek, Thermal stability of ZrN-Ni and CrN-Ni superhard nanocomposite coatings, *Surf. Coat. Technol.* **146–147**, 280–285 (2001).
52. P. Karvankova, M. G. J. Veprek-Heijman, O. Zindulka, and S. Veprek, Superhard nc-TiN/a-BN and nc-TiN/a-BN/a-TiB_2 coatings prepared by plasma CVD and PVD: A comparative study of their properties, *Surf. Coat. Technol.* **163–164**, 149–156 (2002).
53. L. Hultman, Thermal stability of nitride thin films, *Vacuum* **57**, 1–30 (2000).
54. P. Zeman, R. Cerstvy, P. H. Mayrhofer, C. Mitterer, and J. Musil, Structure and properties of hard and superhard Zr-Cu-N nanocomposite coatings, *Mater. Sci. Eng. A* **289**, 189–197 (2000).
55. S. Veprek, M. Haussmann, S. Reiprich, S. Z. Li, and J. Dian, Novel thermodynamically stable and oxidation resistant superhard coating materials, *Surf. Coat. Technol.* **86–87**, 394–401 (1996).
56. R. F. Bunshah, *Handbook of Deposition Technologies for Films and Coatings*, 2nd edn (Noyes Publications, Park Ridge, NJ, 1994).
57. D. W. Hoffman and M. R. Gaerttner, Modification of evaporated chromium by ion bombardment, *J. Vac. Sci. Technol.* **17**, 425–428 (1979).

58. S. Veprek, Effect of substrate bias on the structural, optical and electrical properties of microcrystalline silicon, in *Proceedings of the Material Research Society of Europe*, edited by P. Pinard and S. Kalbitzer (Les éditions de physique, Les Ulis, France, 1983), pp. 425–444.
59. S. Veprek, F.-A. Sarott, and Z. Iqbal, Effect of grain boundaries on the Raman spectra, optical absorption and elastic light scattering in nanometer-sized crystalline silicon, *Phys. Rev. B* **36,** 3344–3350 (1987).
60. S. Veprek, F.-A. Sarott, S. Lambert, and E. Taglauer, Surface hydrogen content and passivation of silicon deposited by plasma induced chemical vapor deposition from silane and the implications for the reaction mechanism, *J. Vac. Sci. Technol. A* **7**, 2614–2624 (1989).
61. J.-E. Sundgren, Structure and properties of TiN coatings, *Thin Solid Films* **128**, 21–44 (1985).
62. J. Musil, S. Kadlec, J. Vyskocil, and V. Valvoda, New results in d. c. reactive magnetron deposition of TiN_x films, *Thin Solid Films* **167**, 107–119 (1988).
63. V. Valvoda, R. Kuzel, and R. Cerny, Structure of TiN coatings deposited at relatively high rates and low temperatures by magnetron sputtering, *Thin Solid Films* **156**, 53–63 (1988).
64. H. Ljungcrantz, L. Hultman, and J.-E. Sundgren, Ion induced stress generation in arc-evaporated TiN films, *J. Appl. Phys.* **78**, 832–837 (1995).
65. T. Y. Tsui, W. C. Oliver, and G. M. Pharr, Influence of stress on the measurement of mechanical properties using nanoindentation, Part I: Experimental studies in an aluminium alloy, *J. Mater. Res.* **11**, 752–759 (1996).
66. A. Bolshakov, W. C. Oliver, and G. M. Pharr, Influence of stress on the measurement of mechanical properties using nanoindentation, Part II: Finite element simulations, *J. Mater. Res.* **11**, 760–768 (1996).
67. J. G. Swadener, B. Taljat, and G. M. Pharr, Measurements of residual stress by load depth sensing indentation with spherical indenters, *J. Mater. Res.* **16**, 1–12 (2001).
68. F. Vaz Titel, Ph.D. Thesis, University of Mino, Portugal, 2000. (in Portuguese; we could not find this figure in any of the publications of Vaz *et al.*)
69. J. Prochazka, F. Vaz, L. Rebouta, S. Carvalho, M. G. J. Veprek-Heijman, and S. Veprek, Comparative study of thermal stability of superhard coatings and nanocomposites, *Surf. Coat. Technol.*, in press.
70. J. Patscheider, Nanocomposite hard coatings for wear protection, *MRS Bull.* **28**(3), 180–183 (2003).
71. J. W. Cahn, Hardening by spinodal decomposition, *Acta Metall.* **11**, 1275–1282 (1963).
72. O. Knotek and A. Barimani, On spinodal decomposition in magnetron-sputtered (Ti,Zr) nitride and carbide thin films, *Thin Solid Films* **174**, 51–56 (1989).
73. R. A. Andrievski, I. A. Anisimova, and V. P. Anisimov, Structure and microhardness of TiN compositional alloyed films, *Thin Solid Films* **205**, 171–175 (1991).
74. S. Veprek, M. Haussmann, and S. Reiprich, Superhard nanocrystalline W_2N/amorphous Si_3N_4 composite materials, *J. Vac. Sci. Technol. A* **14**, 46–51 (1996).
75. H. Schmalzried, *Chemical Kinetics of Solids* (VCH Verlag, Weinheim, Germany, 1995).
76. D. A. Porter and K. E. Easterling, *Phase Transformations in Metals and Alloys*, 2nd edn (Stanley Thornes, Cheltenham, UK, 2001).
77. J. Procházka, P. Karvánková, M. G. J. Veprek-Heijman, and S. Veprek, Conditions required for achieving superhardness of $\geq$45 GPa in nc-TiN/a-Si_3N_4 nanocomposites, *Mater. Sci. Eng. A* **384**, 102–116 (2004).
78. S. Christiansen, M. Albrecht, H. P. Strunk, and S. Veprek, Microstructure of novel superhard nanocrystalline-amorphous composites as analysed by high resolution transmission electron microscopy, *J. Vac. Sci. Technol. B* **16**, 19–22 (1998).
79. J. Zarzycki, *Glasses and the Vitreous State* (Cambridge University Press, Cambridge, 1991).
80. P. Karvankova, M. G. J. Veprek-Heijman, D. Azinovic, and S. Veprek, Properties of superhard nc-TiN/a-BN and nc-TiN/a-BN/a-TiB_2 nanocomposite coatings prepared by plasma induced chemical vapor deposition, *Surf. Coat. Technol.*, **200**, 2978–2989 (2006).

81. M. Leisch, Three-dimensional nanoscale analysis in physical metallurgy, *Vacuum* **67**, 435–442 (2002).
82. Y. Tanaka, N. Ichimiya, Y. Onischi, and Y. Yamada, Structure and properties of Al-Ti-SiN coatings prepared by the cathodic arc ion plating method for high speed cutting applications, *Surf. Coat. Technol.* **146–147**, 215–221 (2001).
83. S. Veprek, P. Nesladek, A. Niederhofer, F. Glatz, M. Jilek, and M. Sima, Recent progress in the superhard nanocrystalline composites: Towards their industrialization and understanding of the origin of the hardness, *Surf. Coat. Technol.* **108–109**, 138–147 (1998).
84. P. Karvankova, *Superhard nc-TiN/a-BN/a-TiB$_2$ and nc-M$_n$N/a-Metal Nanocrystalline Composite Coatings*, Ph.D. Thesis (Technical University Munich, Munich, Germany, 2003).
85. J. Prochazka, *Superharte TiN/Si$_3$N$_4$ nanokomposite durch reaktive magnetronzerstäubung kombiniert mit chemischer gasphaseabscheidung*, Ph.D. Thesis (Technical University Munich, 2003).
86. H.-D. Männling, *vergleichende untersuchungen der darstellung und eigenschaften von superharten nanokompositen dargestellt durch plasma CVD und reaktive zerstaubung*, Ph.D. Thesis (Technical University Munich, Munich, Germany, 2003).
87. P. Karvankova, M. G. J. Veprek-Heijman, M. F. Zawrah, and S. Veprek, Thermal stability of nc-TiN/a-BN/a-TiB$_2$ nanocomposite coatings deposited by plasma CVD, *Thin Solid Films* **467**, 133–139 (2004).
88. M. W. Chase, C. A. Davies, J. R. Downey, D. J. Frurip, R. A. McDonald, and A. N. Syverud, *JANAF Thermochemical Tables*, 3rd edn, *J. Phys. Chem. Data*, **14**(1), (1985).
89. P. Holubar, M. Jilek, and M. Sima, Present and possible future applications of superhard nanocomposite coatings, *Surf. Coat. Technol.* **133–134**, 145–151 (2000).
90. H.-D. Männling, *mechanische und strukturelle eigenschaften sowie thermische stabilität superharter nanokomposite nc-TiN/a-Si$_3$N$_4$and nc-(TiAlSi)N*, Diploma Work (Technical University of Munich, Munich, Germany, 1999).
91. S. Veprek, H.-D. Männling, M. Jilek, and P. Holubar, Avoiding the high-temperature decomposition and softening of (Al$_{1-x}$Ti$_x$)N coatings by the formation of stable superhard nc-(Al$_{1-x}$Ti$_x$)N/a-Si$_3$N$_4$ nanocomposite, *Mater. Sci. Eng. A* **366**, 202–205 (2004).
92. P. H. Mayrhofer, A. Hörling, L. Karlssson, J. Sjölén, T. Larsson, C. Mitterer, and L. Hultman, Self-organized nanostructures in the Ti-Al-N system, *Appl. Phys. Lett.* **83**, 2049–2051 (2003).
93. M. Diserens, J. Patscheider, and F. Lévy, Mechanical properties and oxidation resistance of nanocomposite TiN-SiN$_x$ physical-vapor-deposited thin films, *Surf. Coat. Technol.* **120–121,** 158–165 (1999).
94. M. Diserens, J. Patscheider, and F. Lévy, Improving the properties of titanium nitride by incorporation of silicon, *Surf. Coat. Technol.* **108–109**, 241–246 (1998).
95. J. Patscheider, T. Zehnder, and M. Dieserens, Structure–performance relations in nanocomposite coatings, *Surf. Coat. Technol.* **146–147**, 201–208 (2001).
96. R. Hauert, J. Patscheider, L. Knoblauch, and M. Diserens, New coatings by nanostructuring, *Adv. Mater.* **11**, 175–177 (1999).
97. W.-D. Münz, Titanium aluminum nitride films: A new alternative to TiN coatings, *J. Vac. Sci. Technol. A* **4**, 2717–2725 (1986).
98. W.-D. Münz, Oxidation resistance of hard wear resistant Ti$_{0.5}$Al$_{.5}$N coatings grown by magnetron sputter deposition, *Werkst. Korros.* **41**, 753–754 (1990).
99. L. A. Donohue, I. J. Smith, W.-D. Münz, I. Petrov, and J. E. Greene, Microstructure and oxidation resistance of Ti$_{1-x-y-z}$Al$_x$Cr$_y$Y$_z$N layers by combined steered-arc/unbalanced-magnetron-sputter deposition, *Surf. Coat. Technol.* **94–95**, 226–231 (1997).
100. W.-D. Münz, M. I. Lembke, D. B. Lewis, and I. J. Smith, The role of yttrium incorporation into TiAlN coatings deposited on cemented carbide tools during dry high speed cutting, in *Ind. Tooling 2001*, September 5–6, 2001, Proc. Ed. by the Southampton Institute Conference Centre, Southampton (2001) p. 1–11.

101. Z. Li, S. Miyake, M. Kumagai, H. Saito, and Y. Muramatsu, Structure and properties of Ti-Si-N films deposited by dc-magnetron cosputtering on positively biased substrates, *Jpn. J. Appl. Phys.* **42**, 7510–7515 (2003).
102. H. Watanabe, Y. Sato, C. Nie, A. Ando, S. Ohtani, and N. Iwamoto, The mechanical properties and microstructure of Ti-Si-N nanocomposite films by ion plating, *Surf. Coat. Technol.* **169–170**, 452–455 (2003).
103. M. Nose, Y. Deguchi, T. Mae, E. Honbo, T. Nagae, and K. Nogi, Influence of sputtering conditions on the structure and properties of Ti-S-N thin films prepared by r.f.-reactive sputtering, *Surf. Coat. Technol.* **174**, 261–265 (2003).
104. X. Hu, Z. Han, G. Li, and M. Gu, Microstructure and properties of Ti-Si-N nanocomposite films, *J. Vac. Sci. Technol. A* **20**, 1921–1926 (2002).
105. N. Jiang, Y. G. Shen, Y.-W. Mai, T. Chan, and S. C. Tung, Nanocomposite Ti-Si-N films deposited by reactive unbalanced magnetron sputtering at room temperature, *Mater. Sci. Eng. B* **106**, 163–171 (2004).
106. N. Nose, M. Zhou, T. Mae, and M. Meshii, Microstructure and mechanical properties of Zr-Si-N films prepared by reactive sputtering, *J. Vac. Sci. Technol. A* **20**, 823–828 (2002).
107. S. Veprek, A. Niederhofer, P. Nesladek, and F. Glatz, Superhard nanocrystalline transition metal–amorphous Si_3N_4 composites: A comparison of HF with DC plasma CVD and the stability of the nanostructure, *Electrochem. Soc. Proc.* **97–25**, 317–324 (1997).
108. S. Veprek, H.-D. Männling, A. Niederhofer, D. Ma, and S. Mukherjee, Degradation of superhard nanocomposites by built-in impurities, *J. Vac. Sci. Technol. B* **22**, L5–L9 (2004).
109. S. H. Kim, J. K. Kim, and K. H. Kim, Influence of deposition conditions on the microstructure and mechanical properties of Ti-Si-N films by DC reactive magnetron sputtering, *Thin Solid Films* **420–421**, 360–365 (2002).
110. W. J. Meng, X. D. Zhang, B. Shi, R. C. Tittsworth, L. E. Rehn, and P. M. Baldo, Microstructure and mechanical properties of Ti-Si-N coatings, *J. Mater. Res.* **17**, 2628–2632 (2002).
111. F. Vaz, L. Rebouta, P. Godeau, T. Girardeau, J. Pacaud, J. P. Riviere, and A. Traverse, Structural transition in hard Si-based TiN coatings: The effect of bias voltage and temperature, *Surf. Coat. Technol.* **146–147**, 274–279 (2001).
112. F. Vaz, L. Rebouta, P. Godeau, J. Pacaud, H. Garem, J. P. Riviere, A. Cavaleiro, and E. Alves, Characterization of $Ti_{1-x}Si_xN_y$ nanocomposite films, *Surf. Coat. Technol.* **133–134,** 307–313 (2000).
113. D. V. Shtansky, I. V. Lyasotsky, N. B. D'yakonova, F. V. Kiryukhantsev-Korneev, S. A. Kulinich, E. A. Ievashov and J. J. Moore, Comparative investigation of Ti-Si-N films magnetron sputtered using Ti_5Si_3 + Ti and Ti_5Si_3 + TiN targets, *Surf. Coat. Technol.* **182**(2–3), 204–214 (2004).
114. C. H. Zhang, Z.-J. Liu, K. Y. Li, Y. G. Shen, and J. B. Luo, Microstructure, surface morphology, and mechanical properties of nanocrystalline TiN/amorphous Si_3N_4 composite films synthesized by ion beam assisted deposition, *J. Appl. Phys.* **95**, 1460–1467 (2004).
115. E.-A. Lee and K. H. Kim, Deposition and mechanical properties of Ti-Si-N coated layer on WC-Co by RF inductively coupled plasma-enhanced chemical vapor deposition, *Thin Solid Films* **420–421**, 371–376 (2002).
116. H. Holleck, Materials selection for hard coatings, *J. Vac. Sci. Technol. A* **4,** 2661–2669 (1986).
117. K. Maex, Silicides for integrated circuits: $TiSi_2$ and $CoSi_2$, *Metr. Sci. Eng. R* **11,** 53–153 (1993).
118. S. P. Muraka, Refractory silicides for integrated circuits, *J. Vac. Sci. Technol.* **17,** 775–792 (1980).
119. H. Gleiter, Nanocrystalline materials, *Prog. Mater. Sci.* **33**, 223–315 (1989).
120. H. Gleiter, Nanostructured materials: State of the art and perspectives, *Nanostruct. Mater.* **6**, 3–14 (1995).
121. R. W. Siegel and G. E. Fougere, Mechanical properties of nanophase metals, *Nanostruct. Mater.* **6**, 205–216 (1995).
122. S. Yip, Nanocrystals—The strongest size, *Nature* (*London*) **391,** 532–533 (1998).

123. A. S. Argon and S. Veprek, A consistent rationale for the superior strength and ultra-hardness of ceramic nano-composite coatings, in *Surface Engineering 2001—Fundamentals and Applications* edited by Meng A. Kumar, G. L. Doll, Y. T. Cheng, S. Veprek, and Y. W. Chung, Boston, November 2001, *Mater. Res. Soc. Symp. Proc.* **697,** 3–8 (2001).
124. J. E. Carsley, J. Ning, W. W. Miligan, S. A. Hackney, and E. C. Aifanitis, A simple, mixtures-based model for the grain-size dependence of strength in nanophase metals, *Nanostruct. Mater.* **5**, 441–448 (1995).
125. A. S. Argon, Inelastic deformation and fracture of glassy solids, in *Materials Science and Technology. A Comprehensive Treatment*, edited by R. W. Cahn, P. Haasen, and E. J. Kramer (CVH-Verlag, Weinheim, Germany, 1993), pp. 461–508.
126. M. J. Demkowicz and A. S. Argon, High-density liquid-like component facilitates plastic flow in amorphous silicon, *Phys. Rev Lett.* **93**(2), Art. No. 025505 (2004).
127. K. Jacobs, D. Zaziski, E. C. Scher, A. B. Herhold, and A. P. Alivisatos, Activation volumes for solid–solid transformations in nanocrystals, *Science* **293**, 1803–1806 (2001).
128. C. Kittel, *Introduction to Solid State Physics*, 4th edn (Wiley, New York, 1971), p. 671 ff.
129. A. Kelly and N. H. Macmillan, *Strong Solids*, 3rd edn, (Clarendon Press, Oxford, 1986), p. 1 ff.
130. J. H. Rose, J. R. Smith, F. Guinea, and J. Ferrante, Universal features of the equation of state of metals, *Phys. Rev. B* **29**, 2963–2969 (1084).
131. J. R. Smith, J. Ferrante, P. Vinet, J. G. Gay, R. Richter, and J. H. Rose, Universal properties of bonding at metal interfaces, in *Chemistry and Physics of Fracture*, edited by R. M. Latanision and R. H. Jones (Martinus Nijhoff, Dordrecht, 1987), pp. 329–362.
132. A. S. Argon, Y. Hori, and E. Orowan, Indentation strength of glass, *J. Am. Ceram. Soc.* **43**, 86–96 (1960).
133. A. S. Argon, M. J. Demkowicz, and S. Veprek, Role of plastic resistance of amorphous covalent compounds in the superior performance of superhard nano-structured ceramic composite coatings for cutting tools, in *Materials Processing and Design: Modeling, Simulation and Applications* (*NUMIFORM 2004*), Vol. 1, edited by S. Gosh *et al.* (American Institute of Physics, New York, 2004), pp. 3–13.
134. M. Jilek, P. Holubar, M. G. J. Veprek-Heijman, and S. Veprek, Towards the industrialization of superhard nanocrystalline composites for high speed and dry machining, in *Surface Engineering 2002—Synthesis*, *Characterization and Applications*, edited by A. Kumar, W. J. Meng, Y. T. Cheng, J. S. Zabinski, G. L. Doll, and S. Veprek, *Mater. Res. Soc. Symp. Proc.* **750,** 393–398 (2003).
135. M. Jilek, T. Cselle, P. Holubar, M. Morstein, M. G. J. Veprek-Heijman, and S. Veprek, Development of superhard nanocomposite coatings for dry, hard machining and of the coating technology for industrial production, in *Proceedings of the 16th International Symposium on Plasma Chemistry*, Taormina, Italy, June 22–27, 2003, edited by R. d'Agostino (Department of Chemistry, University of Bari, Italy) (2003).
136. T. Cselle, Nanostructured coatings for high performance tools, *Werkzeug Technik* No. 77, March 2–7, 2003.
137. M. Jilek, T. Cselle, P. Holubar, M. Morstein, M. G. J. Veprek-Heijman, and S. Veprek, Development of novel coating technology by vacuum arc with rotating cathodes for industrial production of nc-$(Al_{1-x}Ti_x)N$/a-Si_3N_4 superhard nanocomposite coatings for dry, hard machining, *Plasma Chem. Plasma Process.* **24**(4), 493–510 (2004).
138. T. Cselle, Driving forces of today's manufacturing technology, in Keynote Lecture presented at "*Industrial Tooling 2003*", Southampton, Sept. 11, 2003. M. Morstein and T. Cselle, 2004.
139. S. Veprek, H.-D. Männling, M. Jilek, and P. Holubar, Avoiding the high-temperature decomposition and softening of $(Al_{1-X}Ti_XN)$ coatings by the formation of stable superhard nc-$(Al_{1-X}Ti_X)N$/a-Si_3N_4 nanocomposite, *Mater. Sci. Eng. A* **366**, 202–205 (2004).

10

Physical and Mechanical Properties of Hard Nanocomposite Films Prepared by Reactive Magnetron Sputtering

J. Musil[1,2]

[1]Department of Physics, University of West Bohemia, Plzeň, Czech Republic

[2]Institute of Physics, Academy of Sciences of the Czech Republic, Praha, Czech Republic

1. INTRODUCTION

Nanocomposite coatings represent a new generation of materials. They are composed of at least two separated phases with a nanocrystalline and/or amorphous structure. Nanocomposite materials, due to very small ($\leq$10 nm) grains, from which they are composed, and a more significant role of boundary regions surrounding individual grains, behave in a different manner compared to the conventional materials with grain size greater than 100 nm and exhibit completely new properties. New unique physical and functional properties of the nanocomposite coatings are a main driving force stimulating the development of these materials; see for instance, recent review papers.[1–28]

At present, the nanocomposite coatings are prepared using different methods, particularly by plasma-assisted chemical vapor deposition (PACVD) from a gas phase,[14] magnetron or ion beam sputtering from a solid target, i.e., by the physical vapor deposition (PVD) process (see for instance Ref. 16 and references therein), and combined PVD and PACVD processes, e.g., by cathodic arc evaporation and PACVD[29] or magnetron sputtering and laser ablation, i.e., by the hybrid process called as magnetron sputtering and pulsed-laser deposition (MSPLD).[30] For industrial production of the nanocomposite coatings the most suitable method is the magnetron sputtering.

Main advantages of the magnetron sputtering are the following: (1) the sputtering is a *nonequilibrium process* at an atomic level, in which condensing atoms have a high energy (several eV compared with approximately 0.1 eV in the evaporation

process); (2) the simplicity to sputter *alloys* and their compounds, such as nitrides and carbides; (3) the formation of *high-temperature phases* on unheated substrates[31]; (4) the *selective reactive sputtering* of nitride of alloys, which allows to form a nanocomposite of the type nc-MeN/metal, due to a difference in the nitride decomposition temperatures for the element A and B of the AB alloy—here nc denotes the nanocrystalline phase and Me = Ti, Zr, Cr, W, Mo, etc.; (5) the high-rate reactive magnetron sputtering (RMS) of oxides in the transition mode of sputtering[32]; and (6) the possibility *to simply scale up the magnetron* into big industrial machines.

For sputtering of nanocomposite coatings, three basic sputtering systems can be used: (1) one magnetron with an alloyed target; (2) two magnetrons equipped with the targets made of different elements (e.g., Ti, Si), alloys (e.g., TiAl, CrNi), compounds (e.g., TiB_2, $TaSi_2$), or their combinations; or (3) pulse-operated dual magnetron, which can easily control individual elements in the alloy film or makes it possible to deposit nonconductive materials at high deposition rates. Hard nanocomposite films are usually prepared by the RMS, i.e., the magnetron cathode (target) is sputtered in a mixture of Ar and the reactive gas (RG) (nitrogen, oxygen, etc.). In the case when only one element is converted into a nitride, this process is called *selective magnetron sputtering*. According to the number of elements in the sputtered alloy, two- or several-phase films can be prepared.

2. FORMATION OF NANOCRYSTALLINE AND NANOCOMPOSITE COATINGS

A main task in the development of the nanocomposites is to master the preparation of films with nanocrystalline structure. At present, two basic processes are usually used to control the size and crystallographic orientation of grains in the growing film: (1) low-energy ion bombardment and (2) mixing process based on an incorporation of the additional elements (AE) into a base material.

2.1. Low-Energy Ion Bombardment

The ion bombardment is a strongly nonequilibrium process, in which ions transfer their kinetic energy to the growing film and heat it at an atomic level. Therefore, this process is called the atomic scale heating (ASH). The ion bombardment significantly differs from conventional heating because the kinetic energy of bombarding ions is transferred into very small areas of atomic dimensions and is accompanied by an extremely fast (about 10^{14} K/s) cooling. Moreover, it is necessary to note that the energy delivered to the growing film by the conventional heating (T_s/T_m) and the particle bombardment (E_{bi}) is *not physically equivalent*; here, T_s is the substrate temperature and T_m is the melting point of the film material.[33] In spite of this fact the ASH makes it possible to produce dense films with extraordinary properties, corresponding to a zone T in the Thornton structural zone model (SZM),[34]

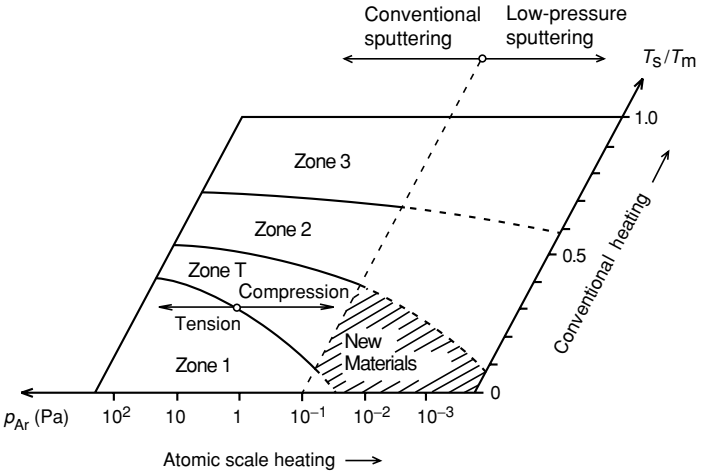

FIGURE 10.1. Thornton SZM extended into the region of low-pressure sputtering—a way to produce new advanced materials at low deposition temperatures T_s.[35] (Reprinted from Ref. 35. Copyright (1998) with permission from Elsevier.)

if sputtering is carried out at low pressures of about 0.1 Pa and lower (see Fig. 10.1). The low-pressure sputtering shifts the transition zone T into a region of low values of the ratio T_s/T_m, and so it allows to create dense films, corresponding to the zone T, at low deposition temperatures T_s (for more details, see Ref. 35).

The ion bombardment of the growing film can restrict the grain growth. The size and crystallographic orientation of grains can be controlled by (i) the energy and flux of bombarding ions and condensing atoms and (ii) the deposition rate a_D of the sputtered film. This control of the film structure is, however, accompanied by the *film heating* and it is not convenient for every application.

2.2. Mixing Process

The mixing process consists in the addition of one or several elements to a base one-element material. Since at least two elements are always present in the film, the *alloy films* are formed by this process. This process is an efficient method convenient for the production of nanocrystalline and amorphous films. Comparing with the ion bombardment, *no substrate bias and heating* are necessary to form films with nanocrystalline structure.

2.3. Structure of Films

Main parameters, which can be used to control the film structure, are the substrate temperature T_s, energy E_{bi} delivered to the growing film by bombarding ions and fast neutrals, and the amount and type of added elements. The following factors,

however, also play the substantial role in the formation of nanocrystalline films: (i) the mutual miscibility or immiscibility of the film elements, (ii) the ability of elements to form solid solutions or intermetallic compounds, and (iii) the enthalpy of the alloy formation ΔH_f (negative or positive). Which structure of the alloy film is created strongly depends on factors given above and their mutual combination (see for instance Refs. 12 and 36).

Experiments show that there are two groups of binary alloy films: (1) the films that are characterized by relatively narrow X-ray reflection lines (FWHM $\leq$ 1 deg.), for instance $Ni_{80}Cr_{20}$ alloy film,[12,36] and (2) the films composed of very fine nanocrystalline grains characterized by very broad low-intensity reflections (FWHM > 1 deg.), for instance $Zr_{55}Cu_{45}$ alloy film[12,36] or an X-ray amorphous structure characterized by no X-ray reflections, for instance Al–Ti alloy film with 35–60 at% Ti.[37] This means that not all combinations of different elements can automatically form alloys films with a nanocrystalline structure. In reality, there are at least four possible ways to how to form nanocrystalline or X-ray amorphous films: (1) rapid cooling of the alloy from a liquid state; (2) addition of a metalloid, such as Si, Pb, B, N, C etc., to a base one-element material, for instance Ti-Si,[37,38] Ti-B,[39] and Ti-C[39–41]; (3) selection of a correct amount of both elements in the alloy, for instance Ag-Ni,[42] Ag-Y,[42] and Al-Ti[37,39]; and (4) addition of a certain amount of nitrogen to the alloy, i.e., to form a nitride of the alloy, for instance Ni-Cr-N[43] and Ti-Al-N.[44–48]

The formation of nanocrystalline and/or X-ray amorphous films using last two processes is schematically shown in Fig. 10.2. From this figure it is seen that for the $A_{1-x}B_x$ alloy or the nitride of alloy $A_{1-x}B_xN$, at a certain stoichiometry x there is a transition from A(B) to B(A) or A(B)N to B(A)N solid solutions,

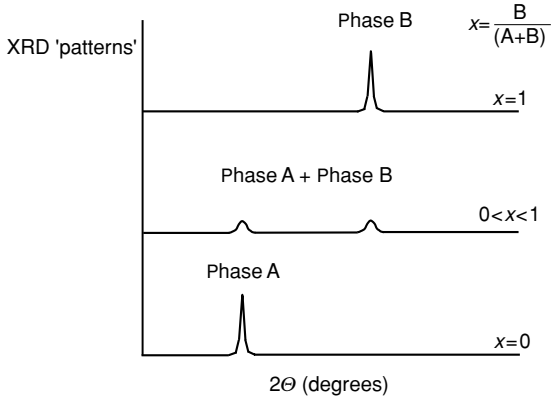

FIGURE 10.2. Schematic illustration of the development of X-ray diffraction patterns from two-phase $A_{1-x}B_x$ alloy or $A_{1-x}B_xN$ alloy nitride with increasing ratio $x = B/(A + B)$, from $x = 0$ (pure element A or binary nitride AN) to $x = 1$ (pure element B or binary nitride BN).

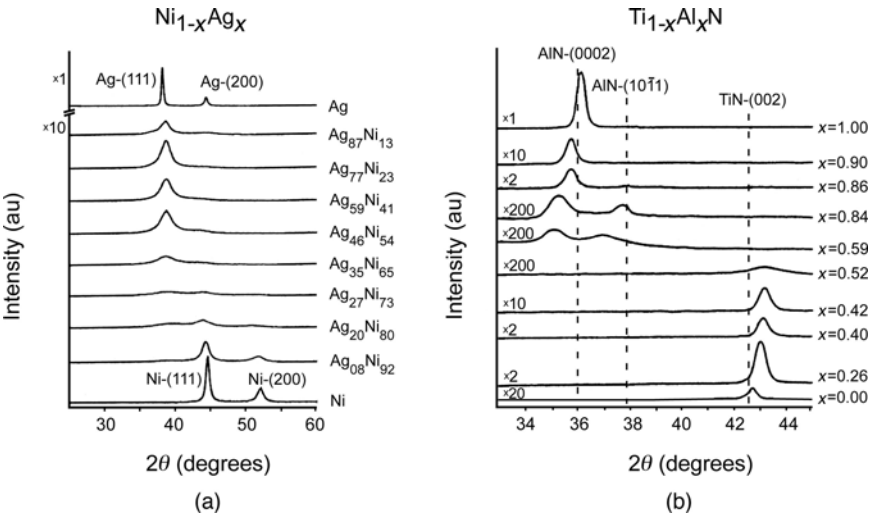

FIGURE 10.3. A development of X-ray diffraction (XRD) patterns from (a) $Ni_{1-x}Ag_x$ alloy film co-condensed using electron beam evaporation of Ni and Ag onto single crystal sapphire substrates at RT and (b) $Ti_{1-x}Al_xN$ films co-sputtered from Ti and Al targets of 75-mm diameter and 99.999 % purity. (Adapted from Refs. 42 and 45, respectively.)

respectively. In the interval x corresponding to these transitions, nanocrystalline and/or X-ray amorphous single-phase or two-phase films may be created. This fact is documented by a development of the structure of the $Ni_{1-x}Ag_x$ alloy film[42] and the $Ti_{1-x}Al_xN$ nitride alloy film[45] with increasing stoichiometry from $x = 0$ to $x = 1$ (see Fig. 10.3).

In both cases there is a "window," i.e., an interval x, in which the films exhibit X-ray amorphous structure. The width of this window (transition) depends on the elemental composition of the film and the deposition conditions under which the film is formed. For $Ni_{1-x}Ag_x$ films, a continuous transition from one-phase Ni(111) film through two-phase Ni(111) + Ag(111) films again to one-phase Ag(111) film is clearly seen in the concentration range between approximately 60 and 80 at% Ni. A similar situation takes place also for $Ti_{1-x}Al_xN$ films (see Fig. 10.3b). Compared to the preceeding case, in the transition region of $Ti_{1-x}Al_xN$ films, located in the interval between approximately 0.5 and 0.85, two kinds of nanocomposites can however be formed: (1) nanocomposite films composed of a mixture of grains with NaCl TiN structure and wurtzite AlN structure at x approximately between 0.5 and 0.6, i.e., two-phase films composed of grains of different chemical composition and (2) nanocomposite films, characterized by broad low-intensity reflections and composed of a mixture of wurtzite grains of different (0002) and (1011) orientations at x approximately between 0.6 and 0.85, i.e., single-phase films composed of grains of the same material but different crystallographic

orientation (for details see Refs. 44–49). Recent experiments clearly show that just Al-rich $Ti_{1-x}Al_xN$ films with $x \geq 0.6$ exhibit an enhanced hardness.[48] In addition, the facts given above simply explain why hard wear-resistant $Ti_{1-x}Al_xN$ films with $x \approx 0.5$, prepared in different laboaratories,[50–53] do not exhibit the enhanced hardness. Simultaneously, we see that a correct choice of x is of a key importance when we want to prepare films with enhanced properties.

At present, it is not fully clear what mixture of grains—with (i) different phases or (ii) different orientations—is responsible for the enhanced hardness of binary nitrides. A further study is necessary to separate both these effects. Also, it is worthwhile to note that the enhanced hardness observed in the single-phase materials can be caused just by the coexistence of small single-phase grains of different crystallographic orientations. Therefore, a special attention must be devoted also to the preparation of films with a controlled orientation of grains and particularly to the determination of deposition conditions under which a jump in the crystallographic orientation of grains takes place. Also, in this case there is a transition region in which nanocrystalline and/or X-ray amorphous films are created, similarly as in the case when the relative amount of elements A and B in the alloy $A_{1-x}B_x$ is varied.

A strong change in the crystallographic orientation of grains can be easily realized in *the RMS* of nitrides of alloys; see for instance, a development of X-ray diffraction (XRD) patterns from the Ti-Al-V-N films with increasing partial pressure of nitrogen p_{N_2} displayed in Fig. 10.4.[54] From this figure it is seen that the transition region is located in the interval p_{N_2}/p_T between 0.1 and 0.3. While the lower edge of this interval is dominated by the films with a strong TiN(111) reflection, its upper edge is dominated by the films with a strong TiN(200) reflection. Films created in the center of the transition region are (i) characterized by three broad, low-intensity TiN(111), TiN(200), and TiN(220) reflections and (ii) exhibit enhanced hardness of approximately 36 GPa. This means that the films with enhanced hardness are composed of a mixture of nanocrystalline grains of different crystallographic orientation. Below, we will give further evidence that also other nanocrystalline films composed of *a mixture of grains of the same material but different crystallographic orientations* exhibit the enhanced hardness.

In summary, we can conclude that there is quite a lot of possibilities how to prepare nanocrystalline and/or X-ray amorphous films. A further systematic investigation is, however, needed to find (i) new nanocrystalline and/or amorphous materials and (ii) new conditions under which noncrystalline states are favored thermodynamically and/or maybe chemically, in comparison with crystalline ones. Such an investigation is now underway. For instance, recently, maximum solubilities of B4-type nitrides into B1-type transition metal nitrides predicted on band parameters were reported[55–58] (see Table 10.1). The largest solubility of AlN into TiN fits very well with the transition region of Ti-Al-N films (Fig. 10.3b) and correlates well with the enhanced hardness (≈47 GPa) of the $Ti_{0.44}Al_{0.56}N$ film reactively sputtered just in the transition region between two phases[48] as well. These data could be used in the design of new hard nanocomposite coatings.

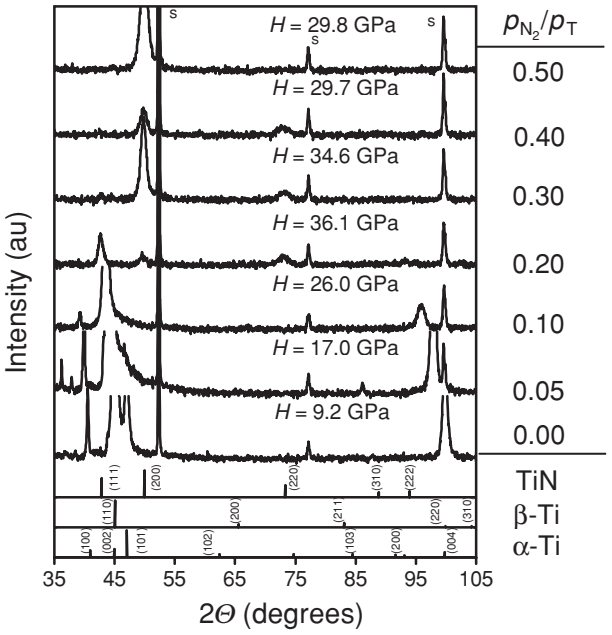

FIGURE 10.4. A development of XRD patterns from 3-μm-thick Ti-Al-V-N films, magnetron sputtered from an alloyed TiAlV (Al 7 at%, V 7 at%) target in a mixture Ar + N_2, with increasing ratio P_{N_2}/p_T at $p_T = 2$ Pa = const. Deposition parameters: $I_d = 2$ A, $U_s = -100$ V, $i_s = 1.5$ mA/cm^2, $T_s = 300^\circ$C, $d_{s-t} = 70$ mm. The microhardness H was measured at a load $L = 20$ mN of the Vicker's diamond indenter.[54] (Reprinted from Ref. 54. Copyright (2003) with permission from Elsevier.)

TABLE 10.1. The maximum solubilities of B4-type nitrides into B1-type transition metal nitrides, i.e., in the system Al-M-N, predicted by the partial structure map and two band parameters, where M = Ti, V, Cr, Zr, Nb, Hf and W.[56]

	TiN	VN	CrN	ZrN	NbN	HfN	WN
AlN (%)	65.3	72.4	77.2	33.4	52.9	21.2	53.9

3. MICROSTRUCTURE OF NANOCOMPOSITE COATINGS

The microstructure of single-phase films is qualitatively well described by SZMs developed by Movchan and Demchishin[59] and Thornton.[34] These models, however, strongly change if impurities or selective additives are incorporated in the film. Impurities or additives stop the grain growth and stimulate the renucleation of grains. This phenomenon results in the formation of a globular structure, which expands in the SZM's from low to high values of T_s/T_m with increasing content of

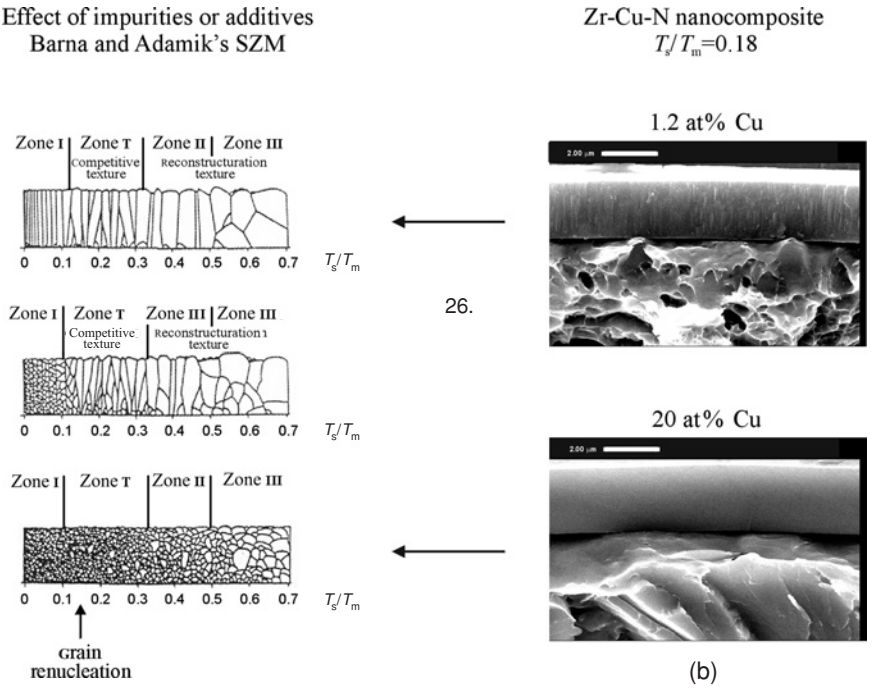

FIGURE 10.5. Comparison of the Barna and Adamik SZM with experiment. (a) SZM for two-phase films and (b) the cross-section Scanning Electron Microscopy (SEM) photos of the Zr-Cu-N films with a low (1.2 at%) and high (20 at%) content of copper, respectively, prepared at $T_s/T_m = 0.18$.[19] (Reprinted from Ref. 19. Copyright (2001) with permission from Elsevier.)

impurities or additives in the film; here T_s is the substrate deposition temperature and T_m is the melting temperature of the coating material (see Fig. 10.5).

For medium and high content of impurities or additives the columnar microstructure, which is typical mainly for the zone I of the SZMs of single-phase films, fully disappears. This fact describes a model that was developed by Barna and Adamik.[60] The two-phase nanocomposite coatings exhibit the microstructure that is identical with that predicted by the Barna and Adamik model (see Fig. 10.5). Here, the microstructure of the Zr-Cu-N nanocomposite films with low (1.2 at%) and high (20 at%) content of Cu is compared with this model. It should be mentioned that already about 7 at. % Cu is sufficient to form the dense fine-grained Zr-Cu-N films without a columnar microstructure.[19,61]

Recently, a similar conversion of the columnar microstructure to a dense fine-grained one was also found for the sputtered TiN films into which Si atoms were incorporated, i.e., for the Ti-Si-N films.[62–68] It was shown that while the Ti-Si-N films with a low ($\leq$5 at%) content of Si exhibit the columnar microstructure, those with 11 at% Si[64] and 14.9 at% Si[65] already exhibit no columnar microstructure

and are composed of nanocrystalline equiaxial TiN grains. Moreover, it is worthwhile to note that (i) the transition from columnar to nanocrystalline equiaxial microstructure corresponds well to the transition from the crystalline to the X-ray amorphous phase in the binary Ti–Si alloy[39] and (ii) the Ti–Si alloy film with approximately 12 at% Si already exhibits several diffuse diffraction peaks.[38] This means that this film is composed of a mixture of grains of different crystallographic orientations. The Ti-Si binary alloy films with 12 at% Si content greater-than are amorphous.[39] A similar behaviour is also exhibited by sputtered Zr-Si-N films.[69] The columnar microstructure appears to vanish if the amount of Si added to the base Zr-N material overpasses approximately 5 at%.

These experiments indicate that the conversion of the columnar microstructure to a dense fine-grained one could take place also in the case when the one-phase material changes into two-phase one, for instance, by a variation of its chemical composition. This phenomenon was demonstrated for the WC-$Ti_{1-x}Al_xN$ superlattice films.[70] While these films with $x = 0.3$ exhibited a clear columnar microstructure, those with $x = 0.57$ were very homogeneous and exhibited no columnar microstructure. The stoichiometry $x = 0.57$ fits well into the concentration range between 50 and 60 at% Al, in which the two-phase films composed of the mixture of the NaCl TiN grains and the wurtzite AlN grains can be formed. This change in the film stoichiometry corresponds quite well also to the transition from the crystalline to amorphous phase in the binary Ti-Al alloy. Namely, it was found that the Ti–Al alloy films, containing 35–59 at% Al, are X-ray amorphous.[39]

The experiments given above indicate that the films with the dense fine-grained microstructure can be produced not only by the incorporation of impurities and/or additives, but also by the selection of such deposition conditions, which allow to form films composed of (1) *a mixture of nanocrystalline grains of different materials, different crystallographic orientations, and/or different lattice structures or* (2) *grains with a strong preferred crystallographic orientation*. For more details, see Ref. 71. Below, it will be shown that a key role in the formation of nanostructured films is played by the energy delivered to the film during its growth.

4. ROLE OF ENERGY IN THE FORMATION OF NANOSTRUCTURED FILMS

At present, it is well known that a correlation *between properties of solids and their structure* is of fundamental importance not only for materials science but also for thin film physics. However, what structure will be formed depends on process parameters used in the formation of the film and its chemical composition. A problem is the fact that in every deposition process there are many deposition parameters, which are mutually coupled. In magnetron sputtering these parameters are magnetron discharge current I_d and voltage U_d; substrate bias U_s; substrate ion current density i_s; substrate temperature T_s; substrate-to-target distance d_{s-t}; deposition rate a_D; flow rate of sputtering gas ϕ; partial pressure of RG p_{RG};

total pressure of sputtering gas $p_T = p_{RG} + p_{Ar}$ and also a pumping speed of the pumping system; base pressure in the deposition chamber p_0; location of inlets of sputtering gases; mutual orientation of the magnetron target and the substrate surface (perpendicular or tilted deposition); stationary, rotating, or linearly moving substrates; plasma enhancement by additional rf, microwave, or hollow cathode discharges or improvement of plasma confinement using an external magnetic field, usually produced by Helmholtz electromagnetic coils; and geometry of the deposition chamber.

The most important deposition parameters for every sputtering machine are I_d, U_s, i_s, T_s, d_{s-t}, a_D, p_{RG}, and p_T. Every combination of these parameters gives, however, one discrete structure only. Therefore, it is practically impossible, by changing one process parameter in this combination, to change continuously the structure of deposited film. This is the main reason why the formation of a film with a prescribed structure, i.e., with the prescribed properties, is very difficult and a so far not solved problem. In our opinion, a key to the solution of this problem is a control of the energy E delivered to the film during its growth. This energy can be delivered by three ways: (1) substrate heating T_s; (2) particle bombardment by (i) ions, E_{bi}, (ion bombardment controlled by the ion energy E_i, the flux of ions ϕ_i, and the deposition rate a_D), and (ii) fast neutrals E_{fn} (atom-assisted deposition controlled by p_T, energy E_{ffp}, and ϕ_{ffp} of the film-forming particles); and (3) chemical reactions ΔH_f (in exothermic reactions, when $\Delta H_f < 0$, the heat is released and the total energy is increased and, on the contrary, in endothermic reactions, when $\Delta H_f > 0$, the heat is consumed and the total energy decreases); here, ΔH_f is the formation energy of compounds. All three components of the total energy influence the film growth simultaneously, but the effect of individual components can be very different. For instance, in deposition of pure metals, contribution of energy from the chemical reactions is zero. On the contrary, in deposition of the film using the ion-plating process, when the growing film is bombarded by low-energy ions, the energy E_{bi} delivered to it by bombarding ions has a decisive effect on its growth. Therefore, the ion bombardment is very often used to control properties of deposited films (see for instance Refs. 72–86).

The energy E_{bi} delivered to the growing film by bombarding ions has a crucial effect on its structure and so on its physical and functional properties. In a *collisionless discharge* this energy can be determined from three easily measured quantities, i.e., the substrate bias U_s, the substrate ion current density i_s, and the deposition rate a_D of the film, according to the following formula[87]

$$E_{bi} = E_i \, \nu_i/\nu_m = e(U_p - U_s) \, \nu_i/\nu_m \propto eU_s i_s/a_D \quad \text{at } T_s = \text{const} \tag{10.1}$$

Here E_i is the energy of ions, ν_i and ν_m are the fluxes of ions bombarding the growing film and coating atoms, respectively, and U_p is the plasma potential. Typical values of U_s range from a floating potential U_{fl} to approximately -200 V. For the effective control of the film microstructure, the values of $i_s \geq 1$ mA/cm^2 are necessary.

Every material can be characterized by a certain critical value of energy E_c. The films produced at $E_{bi} < E_c$ are porous, soft, have a matt appearance, and

are in tension. On the contrary, films produced at $E_{bi} > E_c$ are compact, dense, have a smooth surface, exhibit a high reflection, and are in compression. The films produced at $E_{bi} = E_c$ exhibit zero macrostress σ. The same value of E_{bi}, however, need not correspond to the same microstructure of the film. According to Eq. (10.1) the same value of E_{bi} can be achieved at different combinations of the ion energy E_i and the ratio ν_i/ν_m, i.e., under conditions, when different physical processes can dominate. This means that the parameters E_i and ν_i/ν_m *are not physically equivalent*. For more details see, for instance, Ref. 88.

In a *collision discharge* the energy E_{bi}, delivered per unit volume of the deposited film can be expressed in the following form[54]

$$E_{bi}(J/cm^3) = U_s(i_s/a_D)N_{imax} \quad \text{at } T_s = \text{const} \tag{10.2}$$

where $N_{i\,max} = \exp(-L/\lambda_i)$ is the amount of ions arriving at the substrate with a maximum energy eU_s, e is the elementary charge, L is the sheet thickness, and λ_i is the ion mean free path for collisions leading to losses of the ion energy in the sheet. The ion mean free path can be calculated from the Dalton law as $\lambda_i \approx 0.4/p$ (cm, Pa).[89] The high-voltage ($U_s >> U_{fl}$) sheath thickness L can be calculated from the Child–Langmuir equation for the dc sheath, where U_{fl} is the floating potential. The sheet thickness L can be expressed in the following form[90]:

(a) The collisionless dc sheet near the substrate ($L/\lambda_i < 1$)

$$L = (0.44\varepsilon_0)^{1/2}(2e/m_i)^{1/4}U_s^{3/4}i_s^{-1/2} \tag{10.3}$$

where ε_0 is the free-space permittivity and m_i is the ion mass.

(b) The collision dc sheet near the substrate ($L/\lambda_i > 1$)

$$L = (0.81\varepsilon_0)^{2/5}(2e/m_i)^{1/5}\lambda_i^{1/5}U_s^{3/5}i_s^{-2/5} \tag{10.4}$$

This simple analysis shows that the energy delivered to the growing film by ion bombardment strongly depends on conditions under which sputtering of the films is carried out. The energy E_T transported by ions to the negative electrode (substrate) and the amount of ions $N_{i\,max}$ arriving at the negative electrode with the maximum energy eU_s as a function L/λ_i is shown in Fig. 10.6. The energy E_T decreases with the increasing ratio L/λ_i, i.e., with increasing sputtering gas pressure p_T because $\lambda_i = 0.4/p_T$ and so $L/\lambda_i \sim p_T$. A decrease in the energy of bombarding ions with increasing p_T significantly influences the mechanism of the growth and the structure of deposited films. This fact explains well why properties of the films sputtered at the same values of U_s and i_s differ if they are deposited at different values of p_T. For more details see Ref. 54.

4.1. Ion Bombardment in Reactive Sputtering of Films

Equation (10.1) has been used by many researchers to characterize the effect of low-energy ion bombardment on the microstructure of sputtered films and their

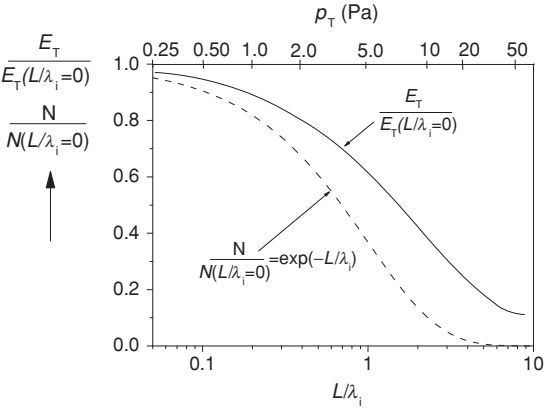

FIGURE 10.6. The amount of ions $N_{i\,max}$ arriving at the substrate with a maximum energy eU_s and the total energy E_T transported to the growing film, normalized with corresponding values for $L/\lambda_i = 0$. The axis p_T was calculated for films sputtered at $U_s = -100$ V and $i_s = 1.5$ mA/cm^2.[91] (Reprinted from Ref. 91. Copyright (2003) with permission from Elsevier.)

properties. For instance, the effect on (i) grain size, lattice distortion, dislocation density in Ag, Cu, Pd films is investigated in Ref. 75; (ii) microstructure in Refs. 76–79 and 82; (iii) microhardness H, macrostress σ, and microstrain e in the TiN_x films in Refs. 76, 77, 80, and 81; (iv) formation of ε-Ti_2N phase in the TiN_x films in Refs. 74 and 78; (v) preferred orientation of the TiN films in Refs. 83–86, etc. In spite of a relatively large utilization of the ion-plating process, there is a little knowledge on the correlation between the energy E_{bi} and the properties of reactively sputtered films.

Despite the fact that it is well known that the reactive sputtering of films is accompanied by a target (cathode) poisoning, which results in a dramatic decrease of the film deposition rate a_D, only few people realize that changes in a_D, caused by a change in the partial pressure of RG p_{RG} (RG = N_2, O_2, CH_4, etc.) under constant deposition conditions, induce huge changes in the energy E_{bi} delivered to the film during its growth (see Fig. 10.7). For instance, for nitrides $a_D(Me) \approx 4\ a_D(MeN_x)$ and for oxides even $a_D(Me) \approx (10–15)\ a_D(MeO_x)$, where Me is the metal, and MeN_x and MeO_x are the metal nitride and metal oxide, respectively (see e.g., Refs. 32 and 93–107). Therefore, it is necessary to expect that changes in the properties of reactively sputtered films will be created in consequence of a combined action of two parameters: (1) the elemental and chemical composition of the film, particularly the amount of RG atoms incorporated in the film and (2) the energy E_{bi}, i.e., the parameters that both depend on the partial pressure of RG, p_{RG}. In the reactive mode of sputtering the effect of increased E_{bi}, due to the decrease in a_D with increasing p_{N_2}, can be very strong (see Fig. 10.7).

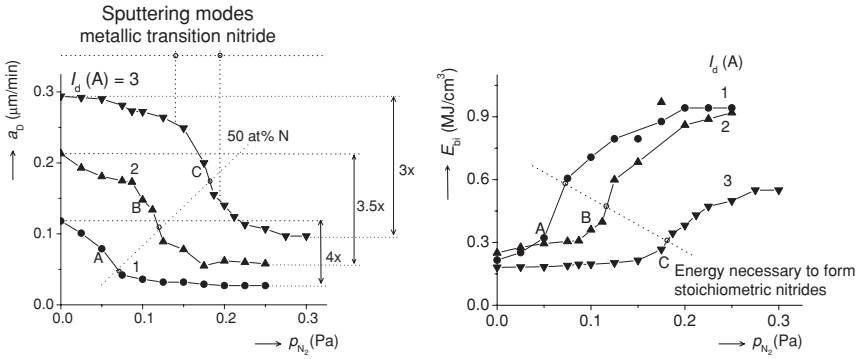

FIGURE 10.7. Deposition rate a_D of Ti(Fe)N_x films, sputtered at $U_s = -100$ V, $T_s = 300°C$, $p_T = 0.5$ Pa, and the energy E_{b_i} delivered to these films during their growth as a function of nitrogen partial pressure p_{N_2}.[108] (Reprinted from Ref. 108. Copyright (2004) with permission from Elsevier.)

We believe that just the decrease in a_D with increasing p_{RG} is responsible for a dramatic change in crystallographic orientation of the single-phase films based on solid solutions, such as Ti(Fe)N_x films. Details are given further in the Section 5.6.

The energy E_{bi} strongly influences not only the structure of the film and its elemental and chemical composition, for instance, due to desorption of the atoms of RG from the surface of sputtered film, but also the macrostress σ induced in the film by ion bombardment.

4.2. Effect of Ion Bombardment on Elemental Composition of Sputtered Films

It is well known that an elemental composition of the sputtered alloy film may differ from that of the alloyed or composed target from which it is sputtered. This is mainly due to a preferential resputtering of some atoms from the growing film by bombarding ions if the films are prepared using the so-called sputter ion-plating process (see, for instance, a preferential resputtering of the copper from Ti-Cu films).[61] In a dc RMS, when the alloyed target is sputtered in a mixture of Ar and the RG, e.g., N_2, O_2, CH_4, etc., RG atoms are also incorporated into the growing film. Also, in the case of dc RMS, performed at a constant partial pressure of RG p_{RG}, the amount of atoms of RG incorporated into the film is not always constant because their amount in the film is controlled by the energy delivered to the growing film by (1) bombarding ions (U_s, i_s, a_D) and condensing particles (p_T, a_D), and (2) substrate heating (T_s), i.e., by resputtering and desorption of the RG atoms from the film surface. This means that the elemental composition of sputtered films strongly depends on the deposition parameters, particularly

on I_d, U_d, U_s, i_s, a_D, T_s, p_{RG}, p_T, ϕ_{RG}, used in their sputtering; here, ϕ_{RG} is the flow rate of RG into the deposition chamber. On the other hand, a correct selection of the deposition parameters is an efficient tool for control of the elemental composition of sputtered films. Below, three examples illustrating the effect of ion bombardment on the elemental composition and structure of sputtered film are given.

4.2.1. Resputtering of Cu from Zr-Cu-N Films

A resputtering of atoms from an alloyed or compound film depends particularly on (i) sputtering yield γ of atoms from which the film is composed; (ii) energy ($E_i \sim U_s$), flux (i_s) and mass (m_i) of ions bombarding the growing film, and time of bombardment; and (iii) bounds between atoms in the alloy or compound. As an example, we present the deposition of the Zr-Cu-N films using the magnetron sputter ion-plating process at $U_s = -200$ V and different values of i_s ranging from 0.5 to 1.25 mA/cm^2 (see Table 10.2).

It is known that the sputtering yield of Cu is greater than that of Zr; $\gamma_{Cu} \approx 1.1$ atom/ion and $\gamma_{Zr} \approx 0.2$ atom/ion for Ar^+ ion with energy $E_i = 200$ eV.[109] This means that the content of Cu in the film should decrease with increasing i_s used in its formation. This expectation is really in an excellent agreement with the experiment (see Table 10.2).

TABLE 10.2. Development of the Elemental Composition of Zr-Cu-N Films with Increasing i_s of Bombarding Ar^+ Ions.

i_s (mA/cm^2)	0.5	0.75	1.0	1.25
Cu (at%)	22.5	12.3	0.9	0.9
Zr (at%)	39.0	41.4	48.1	47.4
N (at%)	38.5	46.3	51.0	51.7

From Ref. 61; Deposition conditions: $I_d = 1$ A, $U_s = -200$ V, $T_s = 400$°C, $d_{s-t} = 60$ mm, $p_{N_2} = 0.05$ Pa, $p_T = 0.7$ Pa.

4.2.2. Desorption of Nitrogen from Sputtered Nitride Films

The energy E_{bi} delivered to the growing MeN_x film can result in a preferential desorption of nitrogen and thus in the decrease of its stoichiometry $x = N/Me$. Starting with a threshold value of E_{bi}, the N desorption from the surface of the growing film increases with increasing E_{bi}. In the RMS E_{bi} increases, in a full agreement with Eq. (10.1), with increasing p_{N_2} due to decreasing a_D (see Fig. 10.7). Therefore, N desorption from the surface of growing film also increases with increasing p_{N_2}, and under a strong ion bombardment the film stoichiometry x can paradoxically decrease with increasing p_{N_2}. This process was really found in the magnetron sputtering of the Zr-Ti-Cu-N films[110] (see Table 10.3).

TABLE 10.3. Development of the Stoichiometry x in the Zr(Ti, Cu)Nx Films with a Low ($\leq$ 15 at %) Ti and ($\leq$ 2 at %) Cu, Reactively Sputtered at $I_d = 1$ A, $U_s = -100$ V, $i_s = 1$ mA/cm^2, $T_s = 500^\circ$C, $P_T = 0.7$ Pa with increasing p_{N_2}.[110]

Film	p_{N_2}(Pa)	N (at%)	x = N/(Zr + Ti)	a_D (μm/min)	E_{bi} (MJ/cm^3)
A	0.03	49.6	0.994	0.057	1.05
B	0.05	49.1	0.999	0.031	1.93
C	0.10	46.9	0.897	0.029	2.07
D	0.15	45.7	0.852	0.021	2.85

At first sight, the paradox result, i.e., the decrease of x with increasing p_{N_2}, can be easily explained by increasing N desorption from the film caused by increasing E_{bi} due to decreasing a_D with increasing p_{N_2} in RMS. The same phenomenon can be expected to appear also in sputtering of other nitrides.

4.3. Effect of Ion Bombardment on Physical Properties of the Film

Ions bombarding the growing film can very effectively modify the mechanism of the film growth. The ion bombardment strongly influences the film crystallinity, microstrain e, and size of grains d. This effect is illustrated on the properties of sputtered Ti(Al,V)N$_x$ films.[54] From Fig. 10.8 and Table 10.4 it can be seen that a higher energy E_{bi} results in (1) better crystallinity of the film and (2) lower value of the microstrain e. However, both films (1 and 2) have almost the same average grain size d. This is probably the reason why the films sputtered at different values of p_{N_2} with different deposition rates a_D exhibit the same values of the microhardness H and effective Young's modulus $E^* = E/(1 - \nu^2)$; here ν is the Poisson's ratio.

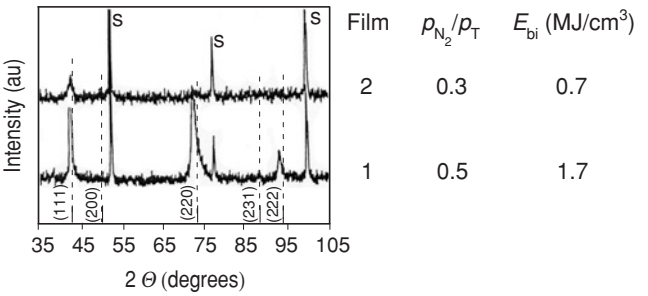

FIGURE 10.8. XRD patterns from Ti(Al,V)N$_x$ films reactively sputtered at two values of the energy of bombarding ions E_{bi}. Constant deposition parameters: $I_d = 2$ A, $U_s = -100$ V, $i_s = 1.5$ mA/cm^2, $T_s = 300^\circ$C, $p_T = 0.5$ Pa, and Ti (6 at% Al, 4 at% V) target.

TABLE 10.4. Physical and Mechanical Properties of Ti(Al,V)N_x Films with the same Hardness H Sputtered at Low (<1 MJ/cm^3) and High (>1 MJ/cm^3) values of E_{bi}.[a]

Film	p_T	p_{N_2}/p_T	a_D (μm/min)	E_{bi} (MJ/cm^3)	d (nm)	e (10^{-3})	H (GPa)	E^* (GPa)	x
1	0.5	0.5	0.053	1.7	70	3.3	42	387	n.m.
2	0.3	0.5	0.122	0.7	77	13.6	42	383	n.m.
3	0.25	0.2	0.253	0.4	6	7.5	38	250	0.5
4	2.0	0.2	0.058	1.5	23	9.1	36	399	1.3

n.m. = Not measured.
[a]Ref. 54; Constant deposition parameters: $I_d = 2$ A, $U_s = -100$ V, $i_s = 1.5$ mA/cm^2, $T_s = 300$°C.

The film with the same hardness H can exhibit either almost the same Young's modulus E^* (film 1 and 2) or different values of E^* (film 3 and 4) (see Table 10.4). The film with a lower value of E^* is produced when a lower E_{bi} is delivered to the growing film. All obtained results cannot be, however, explained using only the energy E_{bi} delivered to the growing film by bombarding ions. Also important is *the structure of the film and its elemental and phase composition*. Therefore, the properties of film are determined by *a combined action of physical and chemical processes* controlled by the energy E_{bi} and the film stoichiometry x.

The experiment described above shows that, in principle, it is possible to prepare films with different combinations of physical properties (d, e, structure and elemental composition defining their stoichiometry and phase composition) and thus with different functional properties, e.g., mechanical ones. This indicates a possibility to tailor sputtered films with prescribed properties for a given application. To achieve this goal a systematic investigation of correlations between the process parameters, chemical and phase composition of the film, its structure, and physical and functional properties has to be carried out because in the formation of sputtered films many processes, such as resputtering, desorption, transfer of kinetic energy of fast neutrals (Ar atoms and condensing sputtered atoms) at low pressures, release or consumption of the energy during formation of chemical compounds, segregation of atoms from solid solutions, recombination of ions if the films are formed from ionized sputtered atoms, etc., influence the mechanism of the film growth. The aim of these investigations should be to determine which processes are dominant under a given combination of process parameters. This is a very complex and very urgent task.

Relations between the hardness H, size d of grains, and microstrain e in the film are of great importance in development and design of new materials and so they are intensively studied (see for instance Refs. 24, 54, 62, 63, 111, and 112, and references therein). As an example, the correlation between H, d, and e in sputtered Ti(Al,V)N_x films reactively sputtered from an alloyed Ti(Al,V) target under different combinations of deposition parameters is given in Fig. 10.9. From this figure it is seen that (1) almost all Ti(Al,V)$N_{x\approx1}$ films with $H \geq 37$ GPa, sputtered at low pressures $p_T \leq 0.5$ Pa, and those with H ranging from approximately 25 to 37 GPa, sputtered at a high pressure $p_T = 2$ Pa, are composed of small

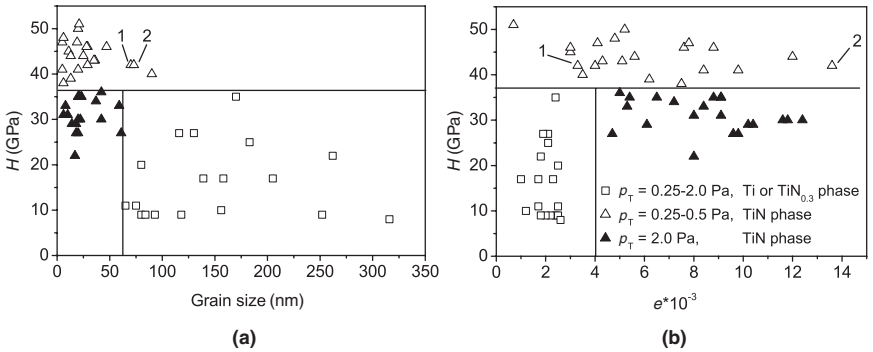

FIGURE 10.9. Microhardnesses of Ti(Al,V)N_x films sputtered under different combinations of deposition parameters as a function of (a) size d of grains and (b) microstrain. e were evaluated from a broadening of the X-ray reflection line with maximum intensity using the Voigt function.[54] (Reprinted from Ref. 54. Copyright (2003) with permission from Elsevier.)

(<50 nm) grains and exhibit relatively high values of the microstrain $e(\geq 3 \times 10^{-3}$ and 4×10^{-3}, respectively); (2) strongly substoichiometric $TiN_{x<1}$ and/or alloy Ti(Al,V) films are composed of large (>70 nm) grains and exhibit a low (<3×10^{-3}) microstrain e; and (3) hardest films are (i) formed only at low pressures $p_T \leq 0.5$ Pa and (ii) are nearly stoichiometric and exhibit an optimum structure, which is created only in the case if sufficient energy $E_{bi} \geq E_{bimin} = 0.5$ MJ/cm^3 is delivered to the growing film. The optimum structure is characterized by at least two broad, low-intensity X-ray reflections. For more details, see Ref. 54. These dependencies seem to have a general validity.

Some selected dependencies of the mechanical properties (H, E^*) of hard nanocomposite films on the energy E_{bi} are given in the Section 5.6.2. More details are given in the Ref. 54.

4.4. Ion Bombardment of Growing Films in Pulsed Sputtering

A further progress in the development of new nanocomposite films require not only to understand fully the relations between process parameters, structure of the film, and its physical and functional properties but also to develop new sputtering systems, which will be operated under new physical conditions. Very perspective are (1) pulsed dual magnetrons, which enable to perform the reactive sputtering of oxide films with a high deposition rate $a_{D\,oxide}$, achieving up to approximately 80% of that of the pure metal, $a_{\mathrm{D\,Me}}$,[32,98,107,113–116] and (2) high-rate, high-power pulse magnetrons generating ionized sputtered metal ions Me^+ and producing films without macroparticles.[117–124] Both sputtering systems open new possibilities in formation of new advanced materials.

A pulsed sputtering process exhibits two important properties: (1) time-dependent difference $V_p - V_{fl}$, where V_p is the plasma potential and V_{fl} is the floating potential of the substrate and (2) generation of ions of the sputtered metal. Both properties can be used for the ion bombardment of the growing film. This process very effectively densifies the film during its growth and also can stimulate crystallization of the films sputtered at low deposition temperatures T_s. The formation of films from ionized metal atoms is expected to be, in a very near future, a new advanced deposition process, which undoubtedly enables to prepare new advanced films with unique properties. At present, the investigation of these films is, however, at its beginning and so further the ion bombardment process is described only briefly.

Any object immersed inside a discharge is negatively biased to the floating potential V_{fl} with respect to the plasma potential V_p. Because $V_{fl} < 0$, positive ions are extracted from the plasma to the floating substrate and the difference $V_p - V_{fl}$ determines an energy E_i of the ion acquired in a collisionless voltage sheath in front of the substrate. Under the assumption of a Maxwellian electron energy distribution with an electron temperature T_e and a collisionless sheath, the energy E_i of singly charged ions can be expressed using the formula for the difference $V_p - V_{fl}$[109] as follows:

$$E_i = e(V_p - V_{fl}) = (kT_e/2)\ \ln(m_i/2.3m_e) \tag{10.5}$$

where k is the Boltzmann constant and e is the elementary charge. The total energy E delivered to the growing film by all bombarding ions is a product of the energy E_i and the total flux of bombarding ions ν_i. It can be expressed either as an energy delivered to the surface of the growing film

$$E(\mathrm{J/scm^2}) = E_i\nu_i = E_iN_e\nu_B = E_iN_e(kT_e/m_i)^{1/2} \propto T_e^{3/2}N_e \tag{10.6}$$

or an energy delivered to the volume of the growing film under the assumption of its constant density

$$E\ (\mathrm{J/cm^3}) = E_i\nu_i/a_D = E\ (\mathrm{J/scm^2})/a_D\ (\mathrm{cm/s}) \tag{10.7}$$

Here, N_e is the electron density near the plasma–sheath interface, ν_B is the Bohm velocity, and a_D is the deposition rate of film.

From Eq. (10.6) it is clearly seen that the energy delivered to the growing film is proportional to the product $T_e^{3/2}N_e$. Just these two quantities, the electron temperature T_e and the electron density N_e, strongly vary during the pulse in pulsed plasmas. At the beginning of the pulse, when the plasma builds up, its electron density N_e is very low and increases from zero with increasing time; the electron temperature T_e is, on the contrary, very high and decreases with increasing time to a stationary value. Because, no measured data of T_e and N_e in a pulsed high-power magnetron (HPM) plasma were published till now,[124] the time development of $T_e(t)$ and $N_e(t)$ in the pulsed microwave plasma is given in Fig. 10.10[88] as an example. From this figure it is seen that T_e at the pulse beginning achieves high values up

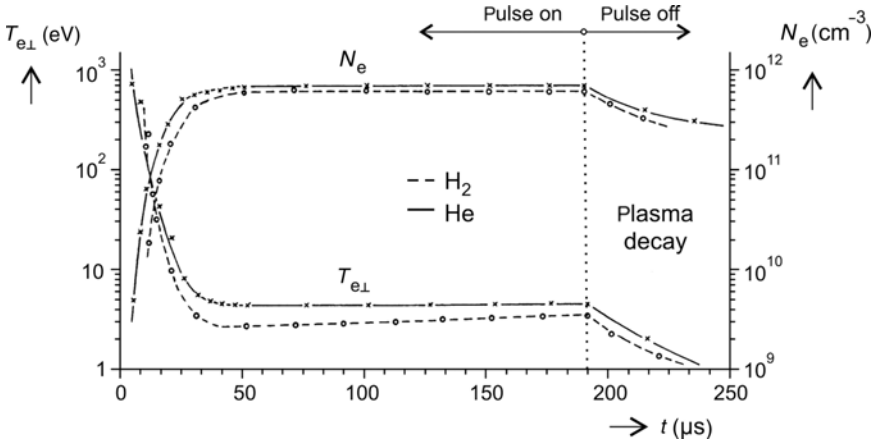

FIGURE 10.10. Time dependence of the electron density N_e and the transverse electron temperature $T_{e\perp}$ in hydrogen and helium microwave magnetoactive plasma generated by the power 2 kW CW at frequency 2.45 GHz and pressure 0.1 Pa. (Adapted from Ref. 88.)

to approximately 1 keV. This value of T_e depends on the energy delivered to the discharge. The high-energy ion bombardment with $E_i \geq 100$ eV at the beginning of every pulse is followed by a low-energy ion bombardment with $E_i \leq 5$ eV during a stationary state of the pulse. A similar ion bombardment occurs in dc-pulsed HPM discharges and it makes possible to produce dense films on unbiased substrates (for instance, see Ref. 125). In conclusion, it is worthwhile to note that efficiency of the ion bombardment during pulsed magnetron sputtering will strongly depend on operating pressure $p_T = p_{Ar} + p_{RG}$.

Very important feature of pulsed magnetron discharges is the production of ionized sputtered ions Me^+. However, to produce Me^+ ions the magnetron must be operated at high values of the target power loading, which results in intensive sputtering of the target and the rarefaction of argon gas, i.e., a HPM must be used. The rarefaction of argon gas is caused by its heating caused by a transfer of energy from the copper atoms leaving the target with a kinetic energy of several electron volts to argon atoms.

In this process the temperature T of Ar gas increases and this increase in T is compensated by a decrease of the density n of Ar atoms approximately according to the equation $p = nkT$, where p is the pressure. Under these conditions an efficient ionization of Cu atoms in the bulk plasma takes place due to its low ionization energy (7.72 eV) and Cu^+ ions prevail over Ar^+ ions in the plasma (see Fig. 10.11a,b.) Here, the effect of the target power density and Ar gas rarefaction, respectively, is illustrated. This experiment clearly shows that in the HPM sputtering discharges, the flux of Me^+ ions can be more than 10 times higher than that of Ar^+ ions and progressively increases with increasing time from the pulse

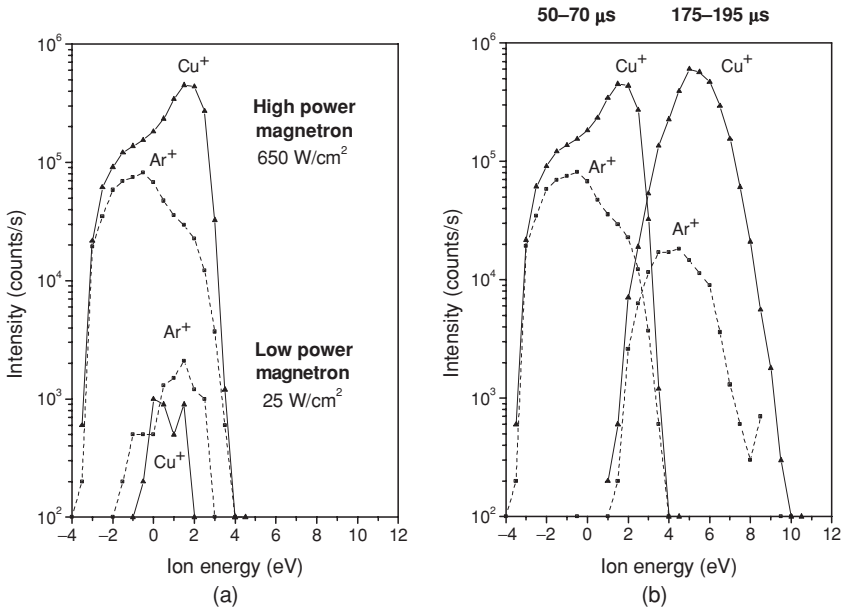

FIGURE 10.11. Energy distribution of Cu^+ and Ar^+ ions measured in front of the substrate ($d_{s-t} = 100$ mm) in a pulsed magnetron discharge, operated with a Cu target at a repetition frequency $f_r = 1$ kHz, length of voltage pulse 200 μs, $p_{Ar} = 1$ Pa, at (a) interval 50–70 μs after the pulse beginning at average pulse current $I_{da} = 50$ A (∼450 W/cm^2) and (b) two time intervals 50–70 μs and 175–195 μs (∼650 W/cm^2) after the pulse beginning and at $I_{da} = 50$ A. (Adapted from Ref. 123.)

beginning. At the average pulse current $I_{da} = 50$ A the predominance of the Cu^+ ions in the total ion flux is approximately 82 and 96% in the interval 50–70 μs and at the end of the pulses, respectively (see Fig. 10.11b). More detailed analysis is given in Refs. 119, 123, and 124.

5. ENHANCED HARDNESS

Many experiments clearly demonstrate that the nanocrystalline and nanophase materials, which are composed of small (≤10 nm) grains, exhibit enhanced properties such as mechanical (hardness), tribological (friction), physical (field emission in ultrananocrystalline diamond,[126–129] elements solubility,[25] thermal conductivity, and photocatalytic effect[130–132]), optical, magnetic,[133] and electrochemical[134]. These enhanced properties occur in the case when the size of grains is approximately 10 nm or less and/or the grain boundary regions start to play a comparable or even dominant role over that of the grains. Qualitatively new processes, such as grain boundary interaction and grain boundary enhancement or sliding, result in new unique physical and functional properties.

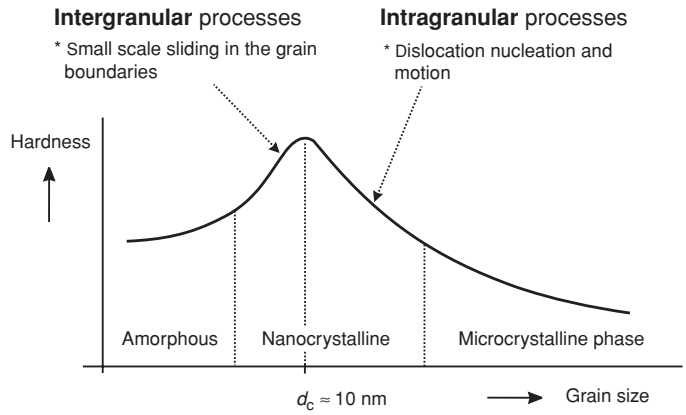

FIGURE 10.12. Schematic illustration of development of the hardness in materials with decreasing grain size *d*. (Adapted from Refs. 13 and 22.)

Enhanced properties of the nanophase materials do not meet the rule of mixture.[135] For example, the hardness of two-phase nanocomposite coating H_n is given by the following inequality:

$$H_n > (1/V_n)(H_1V_1 + H_2V_2) \tag{10.8}$$

where H_1, H_2 and V_1, V_2 are the hardness and the volume of the first and second phase, respectively, and V_n is the total volume of the nanocomposite coating. A maximum value of the enhanced hardness $H_{n\,max}$ can be more than two times greater than that of the hardest component of the nanocomposite. Main mechanisms, which are responsible for the hardness enhancement, are (1) dislocation-dominated plastic deformation, (2) cohesive forces between atoms, and (3) nanostructure of materials. The magnitude of enhancement depends on processes operating in the material at a given range of the size d of grains (see Fig. 10.12). There is critical value of the grain size $d_c \approx 10$ nm at which a maximum value of H is achieved. A region around the maximum hardness H_{max} at $d = d_c$ corresponds to a continuous transition from the operation of *intragranular processes* at $d > d_c$, dominated by the dislocation activity and described by the Hall–Petch law (HPL) ($H \sim d^{-1/2}$),[136,137] to that of *intergranular processes* at $d < d_c$, dominated by a small-scale sliding in grain boundaries.

In materials composed of small ($d \leq 10$ nm) grains (1) the grain boundary regions play a dominant role in deformation processes and (2) dislocations already do not generate. Therefore, besides chemical bonding between atoms, namely, the nanostructure of the materials determines their mechanical behavior. The properties of these materials strongly depend on the size and shape of grains, their chemical composition, crystallographic orientation, and lattice structure. Therefore, the hardness enhancement can be explained by a co-existence *of at least two kinds of nanophase domains*. At present, there is only a little knowledge about

these materials. It is due mainly to the fact that (i) it is very difficult, and in some cases even almost impossible, to form the materials with grains continuously varying in the range between 1 and 10 nm, and (ii) the relations between the material properties and the size of grains and/or nanophase domains are unknown.

5.1. Open Problems in Formation of Nanocomposite Films with Enhanced Hardness

In spite of a great progress in the development of hard and superhard films, there is still a little knowledge for making it possible to form the nanocomposite films with prescribed properties. This is due to the fact that the films are formed in a medium generated as a consequence of the action of many process parameters (factors), which are mutually and very tightly coupled. In such systems, it is very difficult to control the films properties by changing one process parameter, for instance, the flux of ions bombarding the growing film, while keeping the other parameters constant. This may result in jump changes in the structure of the film and its final properties, and/or the incorrect explanation of the origin of its enhanced properties. Therefore, a further systematic investigation of the nanocomposite films is highly needed. At present, considerable attention is concentrated, particularly on the following problems.

1. Macrostress σ generated in sputtered nanocomposite films.
2. Origin of enhanced hardness in single-phase films.
3. Thermal stability of nanocomposite films.
4. Nanocrystallization from the amorphous phase.
5. Interrelationships between the energy delivered to the growing film, its chemical and phase composition, structure, size of grains, and the film properties.
6. Grain and/or domain size-dependent phenomena.

In this chapter, only the problems 1, 2, and 3 will be discussed in more details.

5.2. Macrostress in Sputtered Films

At present, there is a strong discussion if the microhardness H of the superhard sputtered films is due to a high compressive macrostress σ, generated during their growth by the ion bombardment, or if it is possible to sputter low-stress (≤ -0.5 GPa), thick ($\sim$4 μm), superhard (>40 GPa) films also. Recent experiments demonstrate that low-stress superhard films can be really sputtered. This means that the superhardness of the sputtered film can be due not only to its macrostress σ, but also to its nanostructure and/or to the strong interatomic bonds, e.g., shortened covalent bonds. Therefore, this section is devoted to a generation of the macrostress σ in sputtered films and to ways of its reduction or full elimination.

The main aim of this section is (i) to show that several-μm-thick hard sputtered films can exhibit a low (< -1 GPa) compressive macrostress σ, if deposition conditions are correctly selected, and (ii) to demonstrate that the enhanced hardness

of the sputtered, superhard films is not always caused by high values of σ only. At first, we briefly summarize general features of the macrostress σ, which can be generated in the film during its growth.

It is well known that the films produced by plasma-assisted vapor deposition processes exhibit, in the as-deposited state, a macrostress σ, which strongly influences their physical and functional properties.[138–149] The excessive amount of σ can result in severe failure problems, e.g., the film and substrate cracking in the case of the tensile stress ($\sigma > 0$) or the film decohesion by buckling caused by the compressive stress ($\sigma < 0$)[150] if σ overpasses a threshold value. Therefore, it is vitally important to reveal the origin of σ and to find a way that enables to control the level of σ generated in the film. Besides, it is known that (i) mechanical and tribological properties of coated components are strongly influenced by the magnitude and the in-depth distribution of the residual stresses,[150,151] and (ii) residual stresses can be relaxed if the films are operated at temperatures T higher than those used in their deposition, i.e., at $T > T_s$.[144] Therefore, it is not surprising that many research groups[138–179] deal with a systematic investigation of stresses generated in the films during their formation, look for methods that make possible to reduce σ in as-deposited films,[167–169] and investigate their thermal stability.[159–165] A comprehensive understanding of the relationships between the stresses and the mechanical properties of thin films is one of major goals of the materials science.

The macrostress σ consists of two components: (1) *intrinsic* (*growth*) *stress* σ_i and (2) *thermal stress* σ_{th}, i.e., the total stress $\sigma = \sigma_i + \sigma_{th}$. The intrinsic stress σ_i occurs as a consequence of an accumulation of crystallographic defects that are built into the film during its deposition and is connected with the energy delivered to the growing film by bombarding ions and condensing particles. The thermal stress σ_{th} is due to the difference in thermal expansion coefficients of the film α_f and the substrate α_s and can be calculated from the following formula[175]

$$\sigma_{th} = [E_f/(1 - \nu_f)](\alpha_s - \alpha_f)(T - T_s) \tag{10.9}$$

Here, $E_c/(1 - \nu_f)$ is the biaxial elastic modulus of the film, T_s, and T are the substrate temperature during the film deposition and the temperature at which the macrostress σ is measured, respectively, and υ_f is the Poisson's ratio of the film.

The macrostress σ in sputtered films can be controlled by (1) the substrate heating, i.e., by the ratio T_s/T_m, and (2) the energy $E = E_{bi} + E_{ca}$ delivered to the growing film by condensing and bombarding particles; here T_s is the substrate temperature, T_m is the melting temperature of the material of the sputtered film, and E_{ca} is the energy of fast condensing atoms. This is clearly shown in Fig. 10.13, where σ as a function of T_s/T_m is given.

The intrinsic stress σ_i dominates over the thermal stress σ_{th} at low values of the ratio T_s/T_m (≤ 0.3).[145] On the contrary, the thermal stress σ_{th} dominates at high values of the ratio T_s/T_m (≥ 0.3), i.e., at high deposition temperatures T_s and low melting temperatures T_m of the film material, see Fig. 10.13.[144] The most important finding is the fact that the intrinsic stress σ_i does not generate or its value is very low at $T_s \geq 0.3\ T_m$.[144] The last inequality can be shifted to lower values of

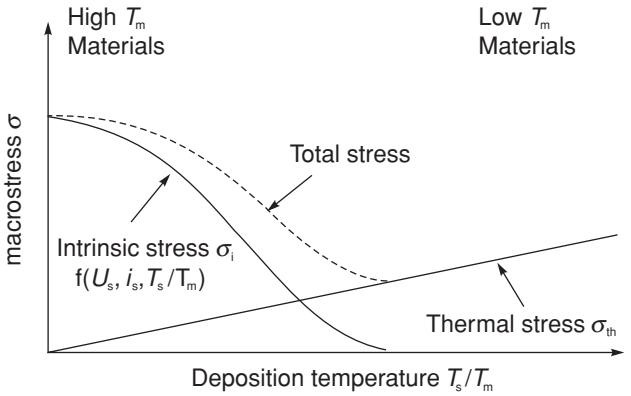

FIGURE 10.13. Schematic diagram of the macrostress σ versus T_s/T_m. (Adapted from Ref. 144.)

T_s/T_m if compound films, such as TiN and TiO_2, are reactively sputtered and an additional energy, released in the exothermic reaction, also contributes to relax σ_i. Because σ_{th} is generally considerably lower than σ_i there are no principal reasons that prevent to sputter the films with low σ.

This analysis shows that σ depends on the total amount of energy delivered to the film during its formation, i.e., on (1) deposition temperature T_s, (2) ion bombardment (U_s, i_s, a_D, p_T), and (3) thickness of the film h[170,171] and also on the difference between α_f and α_s [see Eq. (10.9)]; here i_s is the substrate ion current density and a_D is the film deposition rate. This statement is fully confirmed by experiments the results whose are displayed in Figs. 10.14[80] and 10.17 (see Section 5.2.1).

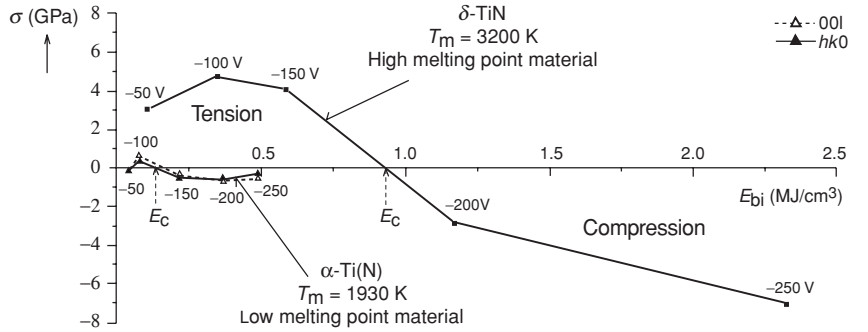

FIGURE 10.14. Macrostress σ in sputtered α-Ti(N) and δ-$TiN_{x\approx1}$ films as a function of the energy $E_{bi} = U_s i_s / a_D$ delivered to them during their formation by bombarding ions at $p_T = 5$ Pa and $T_s = 350°C$, i.e., at $T_s/T_m = 0.32$ and 0.19 for α-Ti(N) and δ-$TiN_{x\approx1}$, respectively. (Adapted from Ref. 80.)

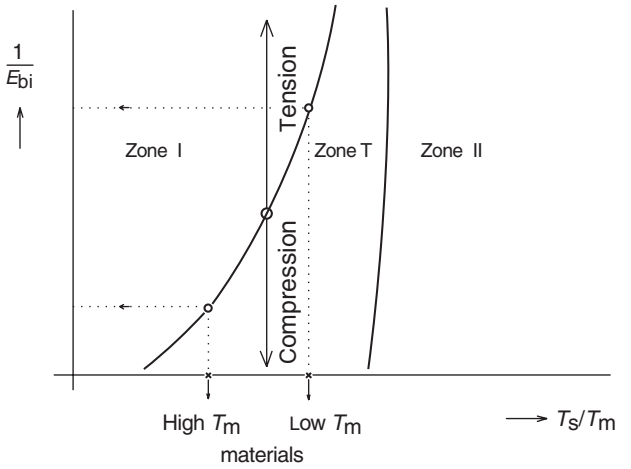

FIGURE 10.15. Schematic illustration of low-temperature part of Thornton's SZM for sputtered films using new system of coordinates (T_s/T_m, $1/E_{bi}$).[80] (Reprinted from Ref. 80. Copyright (1993) with permission from Elsevier.)

From Fig. 10.14 it is clearly seen that (1) the films created at $E_{bi} = E_c$ exhibit a zero macrostress $\sigma = 0$; (2) the value E_c decreases from about 0.9 to 0.15 MJ/cm^3 with increasing ratio T_s/T_m from 0.19 (δ-TiN$_x$ films) to 0.32 [α-Ti(N) films]; (3) the films deposited at $E_{bi} < E_c$ are in tension ($\sigma > 0$) and those sputtered at $E_{bi} > E_c$ are in compression ($\sigma < 0$); and (4) the compressive macrostress σ *decreases with increasing ratio* T_s/T_m, and for $T_s/T_m = 0.32$, i.e., α-Ti(N) films, its value is already very low ($\sigma \leq -0.5$ GPa). The energy E_c approximately corresponds to a transition between the zone T and the zone I in the Thornton SZM[144] (see Fig. 10.15). This conclusion also confirms the change in the surface morphology of these films. For details, see Ref. 80.

The possibility to control the macrostress σ by the energy of bombarding ions E_{bi} is a very important finding. Results displayed in Fig. 10.14 show that it is possible to sputter films not only with a low (≤ -1 GPa) macrostress σ but also with stress-free ($\sigma \approx 0$) films by a proper selection of the optimum energy delivered to the film during its formation. This optimum energy must be equal to E_c. However, it is necessary to expect that the value of E_c will vary with the material of the coating. This fact is clearly shown in Fig. 10.14; $E_c = 0.15$ and 0.9 MJ/cm^3 for the α-Ti(N) and δ-TiN$_x$ films, respectively. Besides, it is necessary to note that fims produced at $E_{bi} = E_c$ do not exhibit a maximum hardness H_{max} (see for instance Refs. 172–174). As an example, Fig. 10.16 shows a development of H, σ, e, and intensities of X-ray reflection lines from approximately 4-μm-thick TiN$_x$ films, sputtered at $I_d = 4$ A, $U_s = 0$, T_s = 150°C, and $p_T = 0.3$ Pa, as a function of the ratio ϕ_{N_2}/ϕ_{Ar}. The maximum hardness $H_{max} \approx 60$ GPa correlates with the maximum of compressive macrostress $\sigma_{max} \approx -4$ GPa. However, this value of σ_{max} alone cannot explain the measured H_{max}, because the hardness is

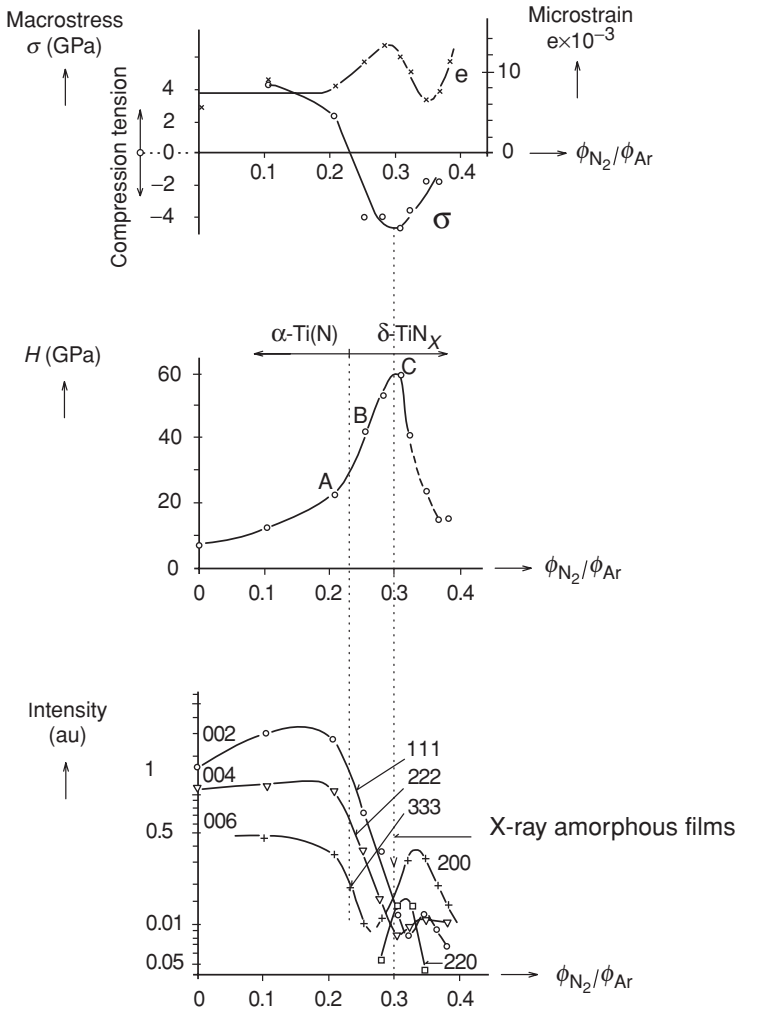

FIGURE 10.16. Microhardness H, macrostress σ, microstrain e, phase composition, and integrated intensities of X-ray reflections from reactively sputtered TiN_x films as a function of the ratio ϕ_{N_2}/ϕ_{Ar}.[172] (Reprinted from Ref. 172. Copyright (1988) with permission from Elsevier.)

defined as $H \approx 3\sigma$.[176] This means that H_{max} cannot be caused only by σ, but for the enhanced hardness some other phenomena are responsible. The TiN_x film with the highest H (i) is substoichiometric $TiN_{x\approx0.6}$ film[172]; (ii) has a structure close to X-ray amorphous (see a strong decrease in preferred orientation of crystallites in Fig. 10.16); (iii) exhibit very dense microstructure[172]; and (iv) is composed

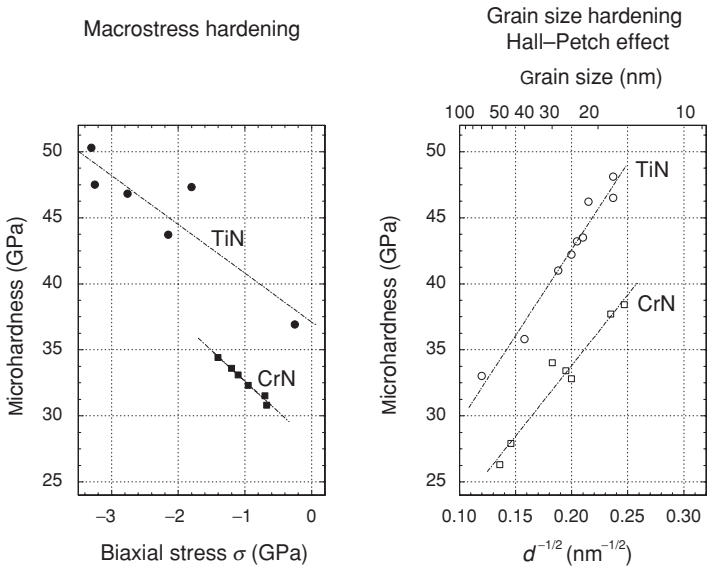

FIGURE 10.17. Hardness of TiN films dominated by (a) biaxial compressive stress σ and (b) grain size d (films with stresses close to zero, $\sigma \leq -0.5$ GPa; TiN,[165] CrN.[164]) (Adapted from Ref. 166.)

of a mixture of small grains of two crystallographic orientations δ-TiN(111) and δ-TiN(200) (see Fig. 5 in Ref. 172). Mainly the last fact, i.e., the mixture of small grains of different crystallographic orientations, is responsible for a rise of the enhanced hardness.

5.3. High-Stress Sputtered Films

Under a strong ion bombardment (high U_s, i_s, and low a_D) and fast atoms bombardment (low sputtering gas pressure p_T) high compressive stresses are generated in the film during its formation. The hardness H in such films is mainly determined by high values of σ, and H increases with increasing σ (see Fig. 10.17a). Similar results are also reported, for instance, in Refs. 77, 172, 173, and 179. For a comparison, Fig. 10.17b displays the hardness H in the films, which exhibit a low macrostress σ and their H values depend on the average size d of grains from which they are composed. More details are given below.

However, the macrostress σ is not the only parameter which determines H. The hardness H can also be increased in the film with a strong chemical bonding between atoms, and/or in the film in which the average size d of grains is decreased (Fig. 10.17b), as predicts the HPL, defined by the Eq. (10.10).[136,137]

$$\sigma = \sigma_0 + k(d)^{-1/2} \tag{10.10}$$

where σ is the yield stress, d is the average size of grain, σ_0 is the lattice frictional stress required to move individual dislocations, and k is the positive constant called the Hall–Petch (H–P) slope.

In many cases, all phenomena discussed above can operate simultaneously. Therefore, often it is very difficult to determine which process dominates and is responsible for the enhanced hardness. Below we will show that under different conditions different processes can be dominant.

5.4. Low-Stress Sputtered Films

Recently, the following low (< -1 GPa) stress, superhard ($\geq$40 GPa) several micrometers (typically 4 μm) thick sputtered films were prepared: Al-Cu-N films with $H = 47$ GPa and $\sigma = -0.2$ GPa[180]; Al-Si-Cu-N films with $H = 39.5$ GPa and $\sigma = -0.8$ GPa[181]; $TiB_{x=2.4}$ films with $H = 73$ GPa and $\sigma = -0.1$ GPa[182]; and (Ti,Al,V)N_x films with $H = 50.7$ GPa and $\sigma = -0.5$ GPa.[54] In all cases, the energy delivered to the growing film was optimized by decreasing U_s and increasing the ratio T_s/T_m.

Very often, when the film is deposited at an elevated temperature T_s and cooled down to RT, it is discussed what is a value of the thermal macrostress σ_{th} due to the thermal expansion mismatch between the film and the substrate. To answer this question, it is necessary to separate σ_{th} from the measured value of the total macrostress $\sigma = \sigma_i + \sigma_{th}$. It can be performed in two cases: (1) if the film is deposited on the substrates with different thermal expansion coefficients α_s or (2) under the assumption that α_f of the film is known[182] (see Fig. 10.18). Here, it is worthwhile to note that the value of α_f strongly depends on its microstructure and so α_f must be measured (α of the corresponding bulk material can be very different from the real value α_f of film; more details are given in Ref. 183).

5.4.1. Effect of Chemical Bonding

Thick (up to 8 μm) Ti-B alloy films, magnetron sputtered from a sintered TiB_2 target under a low ion bombardment and at a sufficiently high ratio $T_s/T_m \geq 0.24$, can serve as a good example of a superhard material, which exhibits a very low (<-0.3 GPa) compressive macrostress σ. The macrostress σ in Ti-B films can be controlled by the energy E_p delivered to the growing film by (i) ion bombardment (U_s, i_s, a_D, p_T) and (ii) substrate heating T_s, i.e., the ratio T_s/T_m (see Fig. 10.18).[182]

Figure 10.18 displays a lattice distortion $\Delta c/c_0$ of 3-μm-thick $TiB_{x=2.4}$ films, magnetron sputtered under a low ion bombardment ($U_s = -50$ V, $i_s = 1$ mA/cm^2), as a function of the linear thermal expansion coefficient of the substrate α_s; here $\Delta c = c - c_0$, c is the lattice constant of the film, and $c_0 = 0.32295$ nm is the lattice constant reported for TiB_2 powder standard.[184] This experiment makes it possible to separate σ_i and σ_{th}, because we know that (1) $\alpha_{TiB_2} = (5.5–6) \times 10^{-6}/K^{-1}$ and (2) $\sigma_{th} = 0$ for $\alpha_f = \alpha_s$ [see Eq. (10.9)]. The intrinsic stress σ_i is determined

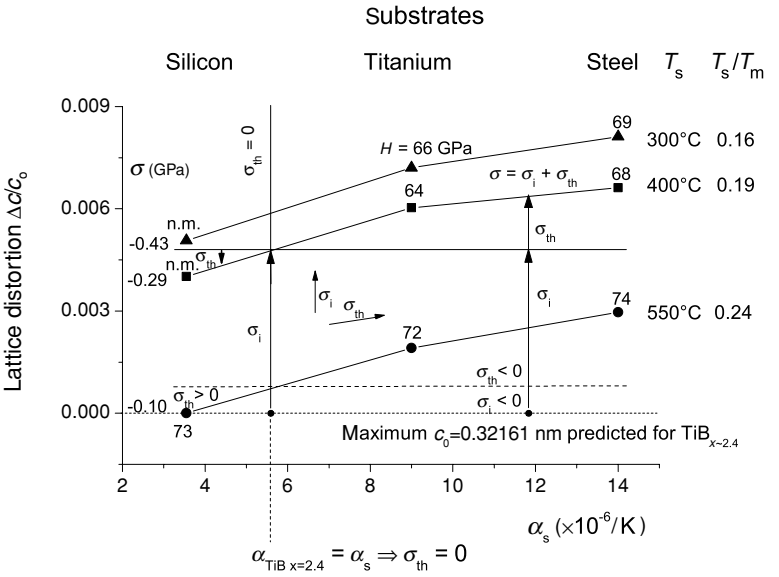

FIGURE 10.18. Lattice distortion $\Delta c/c_0$ of 3-μm-thick $TiB_{x\approx2.4}$ films, sputtered on Si(100), Ti, and steel substrates at $I_d = 1$ A, $U_s = -50$ V, $i_s = 1$ mA/cm^2, $d_{s-t} = 60$ mm, $p_{Ar} = 0.6$ Pa and three substrate temperatures $T_s = 300$, 400, and 500°C, as a function of the linear thermal expansion coefficient α_s of substrate. Values of σ (GPa), given in the figure, were measured from a bending of the Si(100) substrate.[185] (Reprinted from Ref. 182. Copyright (2003) with permission from Elsevier.)

by the cross section of the function $\Delta c/c_0 = f(\alpha_s)$ with the line $\alpha_f = \alpha_s$ and strongly decreases with increasing T_s/T_m. The value of σ_i is very small (approaches to zero) for $T_s/T_m = 0.24$ and can be even lower than σ_{th} if the misfit in the thermal expansion coefficients of the film and the substrate is large, as it is in the case when the $TiB_{x=2.4}$ film is deposited on a steel substrate. This means that the deposition temperature T_s, satisfying *the ratio* $T_s/T_m = 0.24$*, is already sufficient to relax the growth macrostress* σ_i. Then, the total macrostress $\sigma = \sigma_i + \sigma_{th}$, generated in the film, is mainly due to the difference $\Delta\alpha = \alpha_s - \alpha_f$ in the thermal expansion coefficients of the substrate and the film, i.e., $\sigma = \sigma_i + \sigma_{th} \approx \sigma_{th}$. The production of almost stress-free $TiB_{x\approx2.4}$ film is in an excellent agreement with the prediction of d'Heurle and Harper[145] and the dependence $\sigma = f(T_s/T_m)$ given in Fig. 10.13.

In agreement with Eq. (10.9), the thermal macrostress σ_{th} in the Ti-B film increases with increasing value of α_s. However, more than twofold increase in $\Delta\alpha = \alpha_s - \alpha_f$ for the Ti-B film deposited on the steel substrate compared to that deposited on Ti substrate results only in a very small ($\sim 1.06\times$) increase of the film hardness H from 64 to 68 GPa. This result indicates that the thermal component of the macrostress σ_{th} cannot explain the hardness of the Ti-B film, sputtered under conditions given above. This means that the macrostress σ, generated in the film

during its formation, cannot be responsible for a very high hardness of $TiB_{x\approx 2.4}$ films, similarly as it is in the case, for instance, of TiN[170,186,187] or HfB_2[188] films. The *enhanced hardness* of the *stress-free thick* $TiB_{x=2.4}$ *film* is very probably caused by *a strong chemical bonding* between Ti and B atoms and/or its nanostructure. The superhard stress-free thick $TiB_{x=2.4}$ films exhibit a good thermal stability of physical and mechanical properties up to 700°C. More details are given in Ref. 182.

5.4.2. Effect of Grain Size

The concept of a strong chemical bonding cannot explain the enhanced hardness H in all sputtered, low-stressed superhard films. A great role in the hardness enhancement can also be played by the size of grains, d. According to the HPL, defined by Eq. (10.10), the film hardness H should increase with decreasing d. However, this fact is very difficult to demonstrate, because (1) the sputtered films mostly exhibit a high compressive macrostress σ, due to an ion and/or fast neutrals (atoms) bombardment, and (2) the melting temperature of nitrides, which form the nanocomposite films, is high and so the ratio $T_s/T_m < 0.2$ is too low to recover the growth macrostress σ_i; for instance, for TiN the ratio $T_s/T_m = 0.18$ at $T_s = 300°C$ because $T_{m\,TiN} = 2950°C$.[189] Under such conditions, the hardness enhancement is a result of a combined action of the growth macrostress σ_i and the effect of grain size hardening according to the HPL. Therefore, if we want to demonstrate only the effect of grain size d on the film hardness we must to suppress the growth macrostress σ_i. This can be achieved in the case if either (i) the films are deposited at low ion energies E_i or (ii) the melting temperature T_m of the film material is low and the ratio $T_s/T_m > 0.3$.[145] The second requirement is automatically fulfilled, for instance, as the CrN films sputtered already at $T_s = 300°C$, because $T_{mCrN} = 1050°C$ and the ratio $T_s/T_m = 0.43$.

The dependence $H = f(d^{-1/2})$ for TiN and CrN films sputtered under a low ion bombardment at $T_s = 300°C$ is shown in Fig. 10.17b. These films exhibit a very low (< -0.5 GPa) compressive macrostress σ and their hardness H increases with decreasing d in an excellent agreement with the HPL, according to Eq. (10.10). On the contrary, Fig. 10.7a shows that the hardness H of films deposited under a strong ion bombardment (i) is dominated by a high (>-1 GPa) compressive macrostress σ and (ii) linear increase of H with increasing σ. This experiment shows that a proper selection of U_s, i_s, and T_s enables almost completely the suppression of the growth macrostress σ_i and that the total macrostress $\sigma \approx \sigma_{th}$. Here, it is necessary to note that a key role in generation of σ in the film during its growth is also played by the deposition rate a_D of the film [see Eq. (10.1)].

5.4.3. Effect of Deposition Rate a_D on Macrostress σ

For an industrial production of films, their deposition rate a_D is very important, because it decides about the price of the coatings. However, not everybody fully

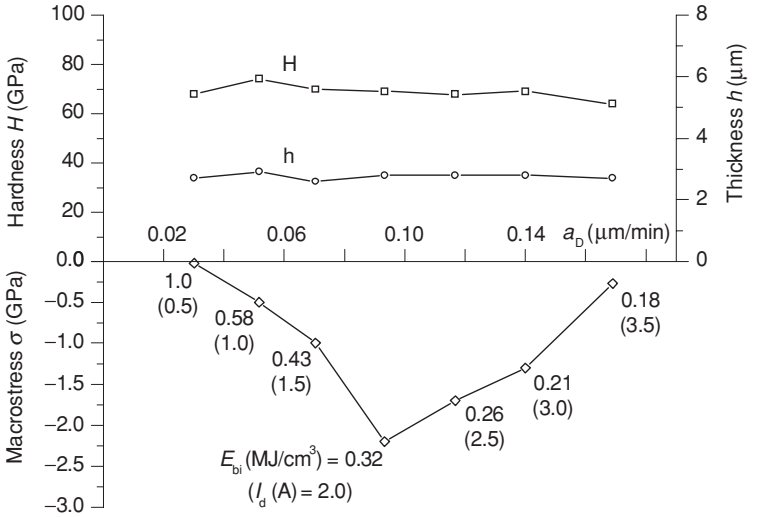

FIGURE 10.19. Effect of deposition rate a_D on the hardness H and macrostress σ in $TiB_{x\approx2.4}$ films of the same thickness $h = 2.7$ μm sputtered from TiB_2 target. Deposition conditions: $I_d = 0.5$, 1, 1.5, 2, 2.5, 3, and 3.5 A; $U_s = -50$ V; $i_s = 1$ mA/cm^2; $T_s = 550^\circ$C; $d_{s-t} = 60$ mm; $p_{Ar} = 0.6$ Pa. Hardness was measured at the Vickers diamond load $L = 50$ mN.

realizes that properties of the films strongly change with increasing a_D. These changes are due to the fact that the energy E_{bi} delivered to the growing film is inversely proportional to a_D and decreases with increasing a_D [see Eq. (10.1)]. Also important is the fact that the time during which the kinetic energy of bombarding ions is delivered to the top monolayer and neighboring subsurface layers decreases with increasing a_D. This process strongly influences the mechanism of growth and particularly σ generated in the film. Recent experiments clearly confirm this fact, including changes in σ, which take place in both the sputtered metal films,[74,190–192] and the sputtered nitride films,[77,82,173,174] at high sputtering rates (high magnetron currents I_d), i.e., at high deposition rates a_D of the film.

As an example, the effect of a_D on σ in sputtered $TiB_{x\approx2.4}$ is illustrated in Fig. 10.19. All $TiB_{x\approx2.4}$ films were sputtered under the same deposition conditions with the exception of magnetron discharge current I_d, which was the only variable parameter. Also, the thickness of all films was the same, $h \approx 2.7$ μm, to exclude an eventual dependence of σ on h. The films were sputter deposited on the Si substrates and σ was evaluated from their bending. From Fig. 10.19 it is seen that (i) all $TiB_{x\approx2.4}$ films exhibit the compressive macrostress ($\sigma < 0$); (ii) the macrostress σ at first increases with increasing a_D up to -2.2 GPa at $a_D = 0.095$ μm/min and for $a_D \geq 0.1$ μm/min decreases to a low value of $\sigma \approx -0.5$ GPa at $a_D = 0.17$ μm/min; (iii) $TiB_{x\approx2.4}$ films with low values of $\sigma \leq -0.5$ GPa can be produced at both high (1 MJ/cm^3) and low (0.18 MJ/cm^3) energies E_{bi} delivered

to the film during its growth; and (iv) the hardness H of the $TiB_{x\approx 2.4}$ films is very high (approximately 70 GPa) and mainly independent of a_D, i.e., independent of the energy E_{bi}. The increase in σ with decreasing E_{bi}, i.e., with increasing a_D from 0.03 to approximately 0.1 μm/min, can be explained by a reduction of σ relaxation with decreasing E_{bi} and the subsequent decrease in σ for $a_D > 0.1$ μm/min by decreasing of the growth stress σ_i due to a further decrease of E_{bi} with increasing a_D.

From this experiment two important issues can be drawn: (1) the hardness H of the $TiB_{x\approx 2.4}$ films, sputtered under conditions given above, is not caused by the growth macrostress σ but very probably by a strong chemical bonding between Ti and B atoms, and (2) the $TiB_{x\approx 2.4}$ films with a high hardness ($H \approx 70$ GPa) can exhibit a very low (< -0.5 GPa) macrostress σ if deposition conditions, i.e., U_s, i_s, a_D, p_T, and the ratio T_s/T_m, are correctly chosen. These results are very important for an industrial production of the low-stress, hard and superhard coatings.

5.4.4. Macrostress σ in X-ray Amorphous Films

Recent experiments show that the incorporation of Si into hard films results in a reduction of their macrostress σ with almost no effect upon their hardness. This finding is very important from the point of view of technological applications. A strong reduction of σ was found, for instance, for Si-DLC (a-C:H) films,[193,194] Ti-Si-N,[159] Zr-Si-N films,[195] and Ta-Si-N films.[196] Figure 10.20 illustrates the development of H and σ with increasing (i) negative substrate bias U_s and (ii) substrate temperature T_s for reactively sputtered 5.7- and 3-μm-thick Ta-Si-N,

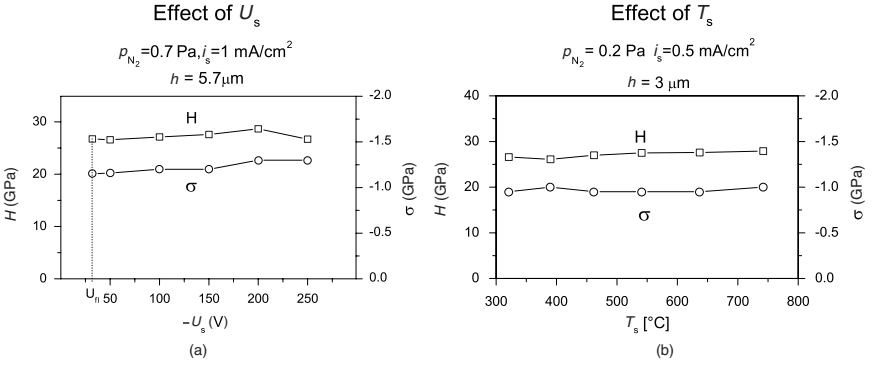

FIGURE 10.20. Hardness H and macrosress σ in Ta-Si-N films with a high (≥40 at%) Si content, sputtered from $TaSi_2$ alloyed target on Si(100) substrate at $I_d = 1$ A, $d_{s-t} = 60$ mm, $p_T = 0.7$ Pa, as a function of (a) substrate bias U_s at $T_s = 500°C$ and (b) substrate temperature T_s at $U_s = -50$ V.

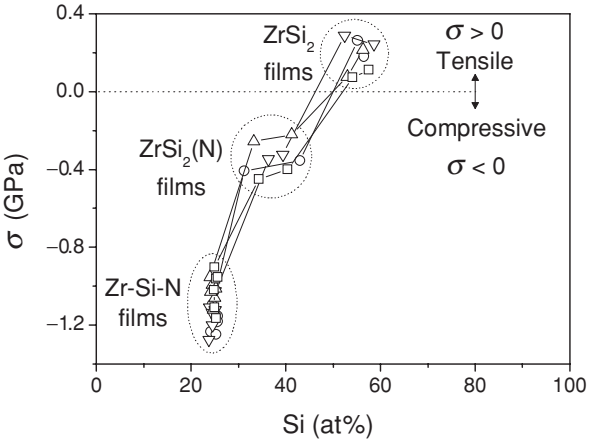

FIGURE 10.21. Macrostress σ in 4-μm-thick Zr-Si-N films, sputtered from $ZrSi_2$ alloyed target on Si(100) substrate at $I_d = 1$ A, $T_s = 500°C$, $d_{s-t} = 50$ mm, $p_T = 0.7$ Pa, dc bias ($U_s = -100$ V, $i_s = 1$ mA/cm^2) and dc pulsed bias ($U_s = -100$ V, $f_r = 1$, 20, and 50 kHz), as a function of Si content in the film.

films using an unbalanced magnetron. From this figure it is seen that (1) both H and σ do not depend either on U_s or on T_s; (2) macrostress σ is low (≈ -1 GPa) and compressive; and (3) the hardness of the Ta-Si-N films is higher than that of a bulk Si_3N_4 ($H_{Si_3N_4} = 17.2$ GPa)[189] but comparable to that of TaN and Ta_2N ($H_{TaN} = 32.4$ GPa and $H_{Ta_2N} = 30$ GPa.[197] The nondependence of σ on U_s indicates that the macrostress σ_i, induced by ion bombardment, is automatically recovered due to a high ratio $T_s/T_m = 0.35$ ($T_s = 500°C$ and $T_{m\,Si_3N_4} = 1900°C$),[189] which moreover increases with T_s increasing above 500°C. This indicates that the macrostress σ is an inherent property of the Ta-Si-N material, which does not depend on the film thickness h. Moreover, all these films are *X-ray amorphous* up to 750°C (maximum T_s used in our experiments). It demonstrates a good thermal stability of the amorphous Ta-Si-N films.

Similar properties as to the macrostress σ are also exhibited by Zr-Si-N films.[195] The macrostress σ as a function of the content of Si in the film is displayed in Fig. 10.21. From this figure it is seen that the compressive stress $\sigma < 0$ decreases with increasing Si content and even changes to the tensile stress $\sigma > 0$ for Si content greater than approximately 50 at%. The tensile stress is exhibited by $ZrSi_2$ films with a high hardness $H \approx 20$ GPa sputtered at $p_{N_2} = 0$ Pa. More details are given in Ref. 195.

At present, it is not clear what is the primary cause of low values of σ—the incorporation of Si into the film or simply very fine grains from which the film with X-ray amorphous structure is composed, as indicated by some recent experiments (for instance, see Fig. 10.22).[198] This is due to the fact that Si belongs to metalloids,

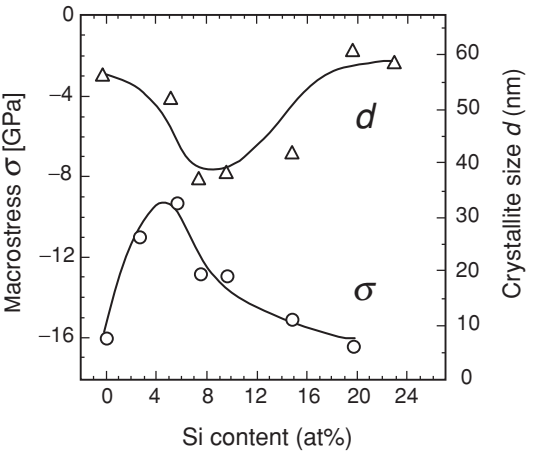

FIGURE 10.22. Internal stress σ and crystallite size d in the Ti-Si-N films sputtered in a facing targets rf sputtering system on unheated and unbiased ceramic (Al_2O_3–TiC) substrate ($50 \times 4 \times 0.4$ mm^3).[198] (Courtesy of M. Nose, Y. Deguchi, T. Mae, E. Honbo, T. Nagae and K. Nogi.) (Reprinted from Ref. 66. Copyright (2003) with permission from Elsevier.)

such as B and N, which very effectively stabilize the amorphous structure, i.e., form very-fine-grained materials, and simultaneously can form Si−H bonds, which are suggested to play a role in reducing the compressive stress $\sigma < 0$.[194] Unfortunately, it is impossible to separate these two roles of Si. Therefore, next investigation should be concentrated on the investigation of (1) the correlation between σ and molar content of the Si_3N_4 phase in hard films with the aim to find if the magnitude of σ in the hard films containing Si can be controlled by the content of the Si_3N_4 phase in the film and (2) the correlation between σ and size of grains in the hard films, which contain no Si.

To answer these two questions is very important not only from scientific but also from practical point of view. Simply, we need to reduce σ not only in films containing Si but also in the hard films without Si. Some recent experiments show that (1) the incorporation of other elements, for instance, Ti and Al in Ta-C film,[199] Cu into AlN,[180] and (2) the reduction of size d of grains in two-phase nanocomposites and in the films with X-ray amorphous structure, for instance, Ti-Si-N,[200] TiB_xN_y and TiB_xC_y,[163] Zr-Ni-N,[201] Al-Si-Cu-N,[202] Zr-Ti-Cu-N,[203]and Ti(Al,V)N,[54] result in generation of a low (<−1 GPa) macrostress σ in the film. These results indicate that the size d of grains could play a dominant role in σ reduction and starting at some critical size ($d \leq 10$ nm) of grains the macrostress σ, generated in individual grains, could be automatically compensated. However, the confirmation of this hypothesis requires further experiments to be done.

5.5. Concluding Remarks on Reduction of Macrostress σ in Superhard Films

In principle, there are at least three ways to eliminate or to decrease the macrostress σ which is generated in a film during its formation: (1) to use a *low-energy bombardment*, which ensures that the energy delivered to the growing film by bombarding ions and/or incident particles is insufficient to generate macrostress σ; (2) to increase the substrate deposition temperature T_s to a value, which ensures that *the ratio* $T_s/T_m \geq 0.25$ and generated macrostress σ is automatically relaxed by relaxed by thermal annealing of the growing film and (3) to form the films, which are composed of a *mixture of small* ($\leq$10 nm) *grains* of different chemical composition and/or different crystallographic orientation. The last method is closely connected with formation of the films with nanocrystalline and/or X-ray amorphous structure.

Using procedures given above, it is possible to sputter low-stress (<–1 GPa) hard nanocomposite films. This means that the hardness H of the hard sputtered films is not always caused by a high (>–1 GPa) macrostress σ only. This result is of fundamental importance for an industrial production of the hard films by sputtering.

6. ORIGIN OF ENHANCED HARDNESS IN SINGLE-PHASE FILMS

Similarly as in the case of two- or several-phase materials (nanocomposites), *the enhanced hardness of single-phase materials* can be also explained by the existence of *a mixture of at least two different kinds of grains* in the nanocomposite.[28,71] Contrary to the two-phase nanocomposites, which are composed of grains created of materials of different chemical composition (Fig. 10.23a), e.g., Ti-Al-N and Ti-Zr-N,[204] the single-phase films are composed of a mixture of grains of the same material but with different crystallographic orientations and/or different lattice structures (see Fig. 10.23b).

This means that there are two groups of nanocomposites: (1) *heterogeneous*, which are composed of grains of different material with different chemical composition; and (2) *homogenous*, which are composed of grains of the same material but different crystallographic orientation and/or different lattice structure.

The single-phase films can be easily produced.[54,108] As an example, single-phase Ti(Fe)N_x nanocomposite films are given.[108] The Ti(Fe)N_x films with a low (<15 at%) Fe content is a typical example of the single-phase material. A development of the structure of these films, characterized by the XRD patterns, with increasing p_{N_2}, is given in Fig. 10.24. From this figure it is clearly seen that in the interval $x = N/(Ti + Fe)$ from 0.86 to 1.20 there is a transition region. The transition region lies in the transition mode of sputtering and separates Ti(Fe)N_x films with a strong (200) preferred crystallographic orientation on side of lower p_{N_2}

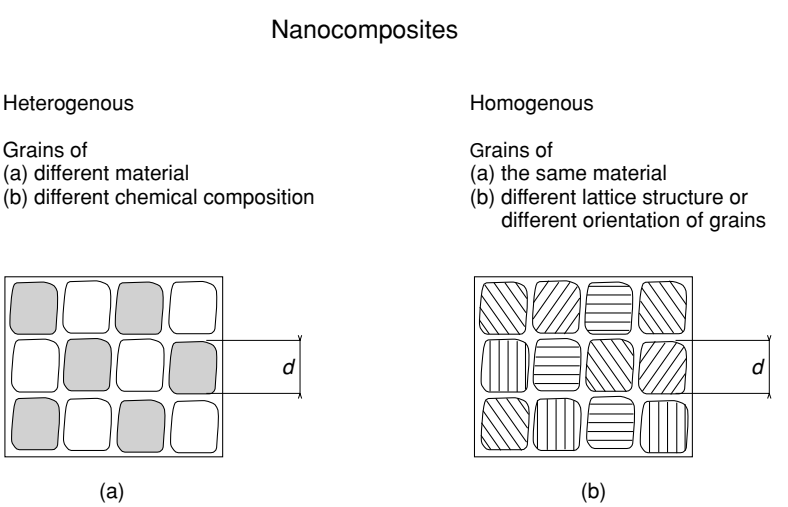

FIGURE 10.23. Schematic illustration of (a) heterogeneous and (b) homogeneous nanocomposite materials.

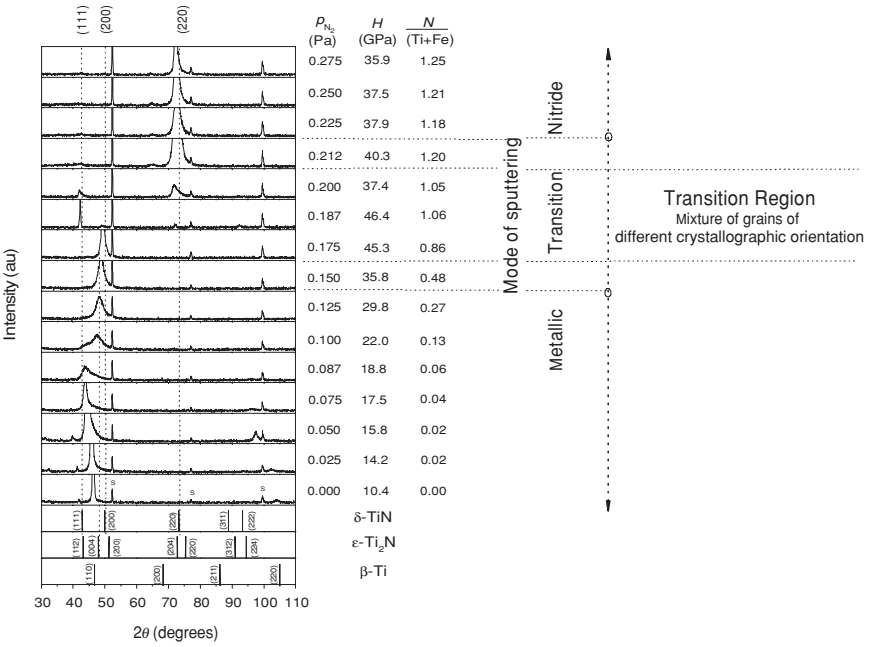

FIGURE 10.24. Development of XRD patterns from reactively sputtered Ti(Fe)N_x films with increasing p_{N_2}.[108] (Reprinted from Ref. 108. Copyright (2004) with permission from Elsevier.)

from those with a strong (220) preferred orientation on side of higher p_{N_2}. Films produced inside the transition region are characterized by several low-intensity X-ray reflections. This fact is of key importance for explanation of enhanced hardness in single-phase materials.

The Ti(Fe)N_x films produced in the transition region are (i) composed of *a mixture of fine grains of different crystallographic orientations* and (ii) nearly stoichiometric $x \approx 1$, and exhibit *the enhanced hardness* $H \geq 40$ GPa. The rise of the transition region is connected with a jump change in the preferred crystallographic orientation of the film from δ-TiN(200) to δ-TiN(220) with increasing p_{N_2}. In addition, it is necessary to note that films produced at the edges of this transition region also exhibit enhanced hardness (see Fig. 10.24). This means that single-phase nanocomposite films can exhibit enhanced hardness in two cases: (1) if they are composed of a mixture of small grains of different crystallographic orientations or (2) if they exhibit a very strong preferred crystallographic orientation. These two materials strongly differ in their microstructure. The films of the first group exhibit a dense, very fine-grained microstructure. On the contrary, the films of second group exhibit a columnar microstructure.[71]

Besides, it is worthwhile to note that during a continuous increase of the partial pressure of nitrogen p_{N_2} with all other parameters constant, the jump change in preferred orientation from (200) to (220) takes place. A continuous increase in p_{N_2} cannot explain this jump. However, it can be explained by an increase of the energy E_{bi}, which increases with increasing p_{N_2} due to decrease in the film deposition rate a_D. We believe that just in this transition region, the energy E_{bi} delivered to the growing film by bombarding ions surpasses a threshold value $E_{bi\,thr}$, which is necessary to create films with a (220) preferred orientation. This means that extraordinary properties of reactively sputtered films, e.g., the highest hardness or maximum resistance to plastic deformation, are the result of a combined action of physical and chemical processes controlled by the energy E_{bi} and the film stoichiometry x, respectively.

The jump change in the preferred orientation of grains in sputtered Ti(Fe)N_x films is also a typical feature for other sputtered nitrides, containing a small ($\leq$15%) amount of the added element (e.g., Y, Ni) forming a solid solution with the base element (see for instance Zr-Y-N,[205] Zr-Ni-N,[201] and Cr-Ni-N).[43] Also, these materials show the enhanced hardness when they are produced in the transition region or on its edges where films with very strong preferred orientation are formed. Therefore, based on experiments given above, we can formulate a complete concept of nanocomposite coatings with enhanced hardness.

7. CLASSIFICATION OF NANOCOMPOSITES ACCORDING TO THEIR STRUCTURE AND MICROSTRUCTURE

The films with enhanced hardness are always closely connected with the existence of transition regions, in which the structure of the film strongly changes. There

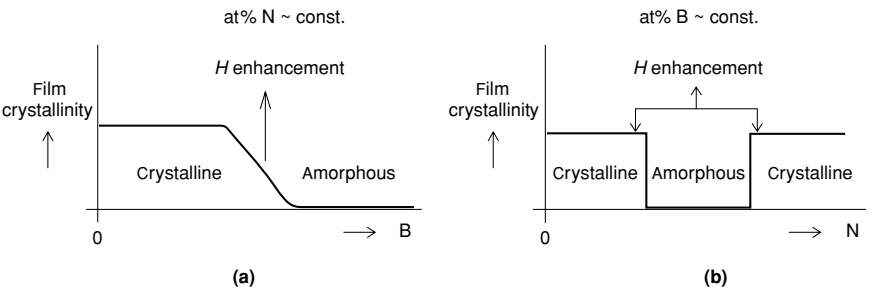

FIGURE 10.25. Schematic illustration of two possibilities of the hardness enhancement in nanocomposite films. (a) Transition between the crystalline and amorphous phase; (b) "window" between materials with two kinds of nanograins of different phases or different crystallographic orientations.

are three groups of these transitions: (1) smooth transition from the crystalline to amorphous phase (Fig. 10.25a), (2) sharp transition between two phases of different material (Figs. 10.2 or 10.25b), and (3) sharp transition between two preferred orientations of grains of the same material (Fig. 10.25b).

It is worthwhile to note that the nanocomposites with enhanced hardness can exhibit a very different microstructure. The nanocomposites of the first group are composed of nc grains surrounded by a thin (1–2 monolayers) tissue phase and exhibit columnar microstructure.[71,206] This columnar microstructure, in which columns are perpendicular to the substrate–film interface, should also exhibit the nanocomposites of second and third group produced at edges of the sharp transition. A demonstration of the validity of last statement is now under investigation in our laboratories. On the contrary, the nanocomposites of second and third group produced inside the "window" are composed of small nanograins and exhibit dense globular microstructure.

According to the film microstructure, the nanocomposites with enhanced hardness can be classified into three groups:

1. Nanocomposites with columnar microstructure composed of grains assembled in nanocolumns; there is insufficient amount of the second (tissue) phase to cover the whole surface of all grains (see Fig. 10.26a).
2. Nanocomposites with a dense microstructure composed of grains fully embedded in a tissue phase (see Fig. 10.26b).
3. Nanocomposites with a dense globular microstructure composed of a mixture of grains of different materials or different crystallographic orientations and/or lattice structures (see Fig. 10.26c).

This classification clearly shows that the origin of enhanced hardness is closely connected with the shape of building blocks from which nanocomposites

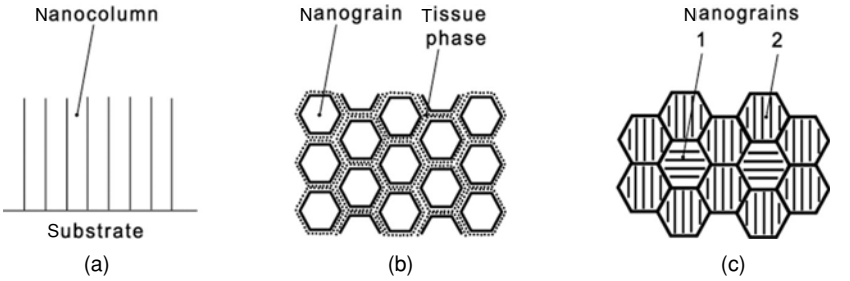

FIGURE 10.26. Schematic illustration of microstructure of nanocomposites with enhanced hardness: (a) columnar; (b) nanograins embedded in tissue phase; and (c) mixture of nanograins.

are composed. Therefore, the classification of nanocomposites with enhanced hardness according to the shape of building blocks–nanocolumns, mixture of grains—seems to be the most correct.

8. MECHANICAL PROPERTIES OF HARD NANOCOMPOSITE COATINGS

Mechanical properties of nanocomposite coatings are well characterized by their hardness, H, effective Young's modulus, $E^* = E/(1 - \nu^2)$, and elastic recovery, W_e; here E is the Young's modulus and ν is the Poisson's ratio. These quantities can be evaluated from loading/unloading curves measured by a dynamic microhardness tester such as Fischerscope H 100. Measured values of H and E^* permit to calculate the ratio H^3/E^{*2}, which gives an information on resistance of the material to plastic deformation.[207] The likelihood of plastic deformation is reduced in materials with high hardness H and low modulus E^*. In general, a low modulus is desirable, as it allows the given load to be distributed over a wider area. All data given in this chapter were measured in our laboratories using a Fischerscope H 100 manufactured in 1996.

Mechanical properties of the nanocomposite coatings strongly depend on (i) the elements, which form individual phases (see Fig. 10.27) and (ii) the relative content of individual phases in the nanocomposite.[18] To simplify the explanation, experimental data given in Fig. 10.27 are approximated by straight lines in spite of the fact that a spread of these data around them can be large. This scatter of experimental data is due to an existence of many possible combinations of process parameters, which can result in different structure and phase compositions of deposited films.

From Fig. 10.27 it can be seen that (1) the film wih a given H can have different values of E^*, (2) the value of E^* can be controlled by the elemental

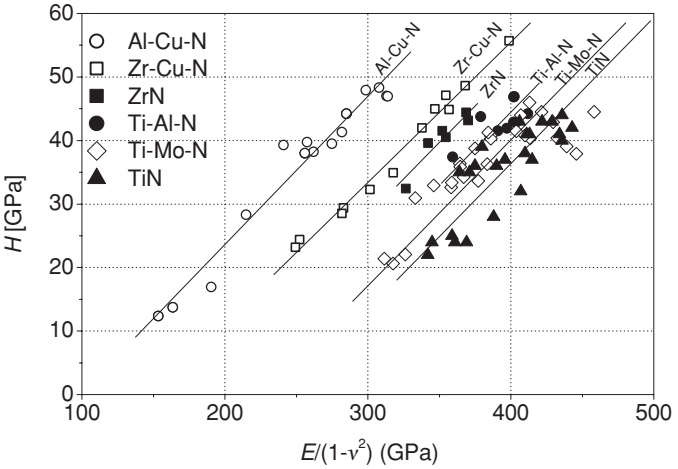

FIGURE 10.27. Microhardness of selected hard nanocomposite and binary nitride films, magnetron sputtered under different deposition conditions.[19,24] (Reprinted from Ref. 19. Copyright (2001) with permission from Elsevier.)

composition of the nanocomposite, and (3) the nanocomposite films composed of two hard phases (Ti-Al-N and Ti-Mo-N) and single-phase nanostructured hard nitrides of transition metals (e.g., TiN and ZrN) exhibit higher E^* compared to that of the two-phase nanocomposites composed of one hard and one soft (metal) phase (e.g., Al-Cu-N and Zr-Cu-N films). The Young's modulus can be changed not only by the selection of elements forming the nanocomposite but also by the selection of deposition conditions, and mainly by the energy delivered to the growing film by condensing and bombarding particles. This makes it possible to control the resistance of the film to plastic deformation, which is proportional to the ratio H^3/E^{*2}, and to tailor mechanical properties of the nanocomposite for a given application. As an example, the relationships between H, E^*, W_e, and H^3/E^{*2} for several selected nanocomposite coatings are given in Fig. 10.28. This figure shows clear trends in interrelationships between the mechanical properties of the nanocomposite film.

Hard films with $H < 40$ GPa are characterized by low (≤ 300 GPa) values of E^* and exhibit (i) a low elastic recovery W_e increasing with increasing H, up to about 70% for $H \approx 30$ GPa and (ii) a *high plastic deformation* increasing with decreasing H, up to 70% for $H \approx 10$ GPa. On the contrary, *superhard films* with $H \geq 40$ GPa are characterized by high (> 300 GPa) values of E^* and exhibit (i) a *high elastic recovery* W_e increasing up to approximately 85% with increasing H and (ii) a low plastic deformation increasing with decreasing H only to about 25% for $H \approx 40$ GPa. These conclusions seem to have a general validity. For details, see Refs. 16, 24, and 211.

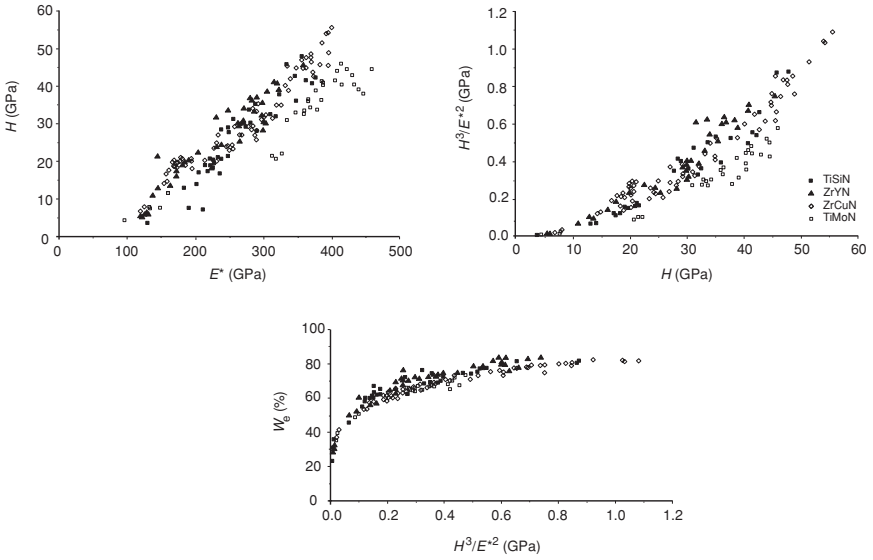

FIGURE 10.28. Dependencies $H = f(E^*)$, $H^3/E^{*2} = f(H)$, and $W_e = f(H^3/E^{*2})$ for Ti-Si-N,[208] Zr-Y-N,[205] Zr-Cu-N,[209] and Ti-Mo-N[210] nanocomposite films sputtered at different deposition conditions, i.e., T_s, U_s, i_s, and p_{N_2}. H was measured at the diamond indentor load $L = 20$ mN. (Adapted from Ref. 211.)

8.1. Interrelationships between Mechanical Properties of Reactively Sputtered Ti(Fe)N$_x$ Films and Modes of Sputtering

Interrelationships between the mechanical properties of sputtered Ti(Fe)N$_x$ films, i.e., the dependencies $H = f(E^*)$, $W_e = f(H)$ and $H^3/E^{*2} = f(H)$, are given in Fig. 10.29a–c, respectively. Here, the films sputtered in metallic, transition, and nitride modes of sputtering are denoted; some are enclosed by dotted lines. This representation shows a clear difference in the mechnical properties of the films sputtered in different modes of the reactive sputtering.

From Fig. 10.29 it can be seen that (i) H increases with increasing E^*; (ii) W_e and H^3/E^{*2} increase with increasing H for the films sputtered in the metallic mode; (iii) the films sputtered in the transition mode exhibit the highest values of H, W_e, and H^3/E^{*2}; and (iv) the films sputtered in the nitride mode exhibit a lower H compared to that of the hardest film produced in the transition mode, and the films with the same H as those produced in the transition mode exhibit higher values of E^*. This fact results in lower values of W_e and H^3/E^{*2} of the films sputtered in the nitride mode compared to those of the films produced in the transition mode. The films produced in the nitride mode are more plastic. The last fact correlates well with the amount of N incorporated in the sputtered film. The

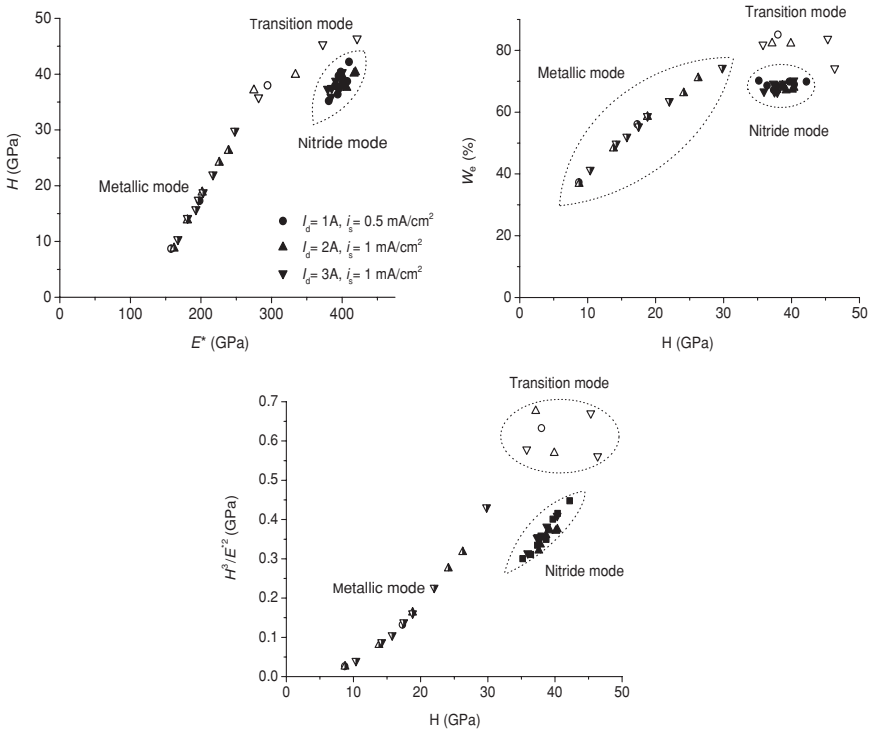

FIGURE 10.29. Interrelationships between mechanical properties of reactively sputtered Ti(Fe)N_x films.[108] (Reprinted from Ref. 108. Copyright (2004) with permission from Elsevier.)

films produced in the nitride mode contain more N compared to those produced in the transition mode and are overstoichiometric Ti(Fe)$N_{x>1}$ nitrides.

8.2. Effect of Stoichiometry x and Energy E_{bi} on Resistance to Plastic Deformation and Hardness of Reactively Sputtered Ti(Fe)N_x Films

The effect of the film stoichiometry $x = N/(Ti + Fe)$ on a resistance of the Ti(Fe)N_x films to plastic deformation, characterized by the ratio H^3/E^{*2}, is displayed in Fig. 10.30. From this figure it is seen that the ratio H^3/E^{*2} (i) increases with increasing x for the films sputtered in the metallic mode, (ii) is approximately constant and reach the highest (0.57–0.67) values for the films with x ranging from approximately 0.5 to 1, i.e., for the films sputtered in the transition mode, and (iii) is considerably lower (0.3–0.4) for overstoichiometric films with $x > 1$ sputtered in the nitride mode. Besides, it was found that the films sputtered in the nitride mode exhibit (a) a lower H compared to the film with the highest H produced in the transition mode and (b) the highest values of E^*. Therefore, these films exhibit a lower

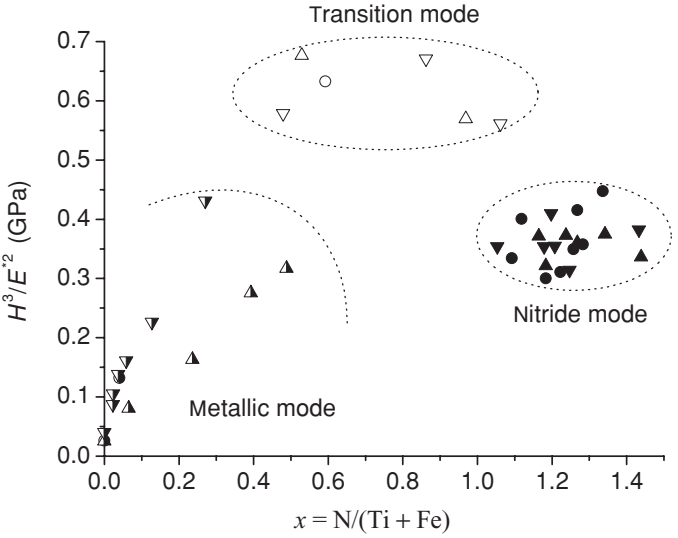

FIGURE 10.30. The ratio H^3/E^{*2} of reactively sputtered Ti(Fe)N$_x$ films as a function of their stoichiometry $x = \mathrm{N}/(\mathrm{Ti} + \mathrm{Fe})$.[108] (Reprinted from Ref. 108. Copyright (2004) with permission from Elsevier.)

(i) elastic recovery W_e and (ii) resistance to plastic deformation, i.e., a lower ratio H^3/E^{*2}, compared to the Ti(Fe)N$_x$ films produced in the transition mode of sputtering.

The effect of the energy E_{bi} delivered to the growing Ti(Fe)N$_x$ film by bombarding ions on its hardness H is displayed in Fig. 10.31. From this figure it is seen that the superhard Ti(Fe)N$_x$ films with $H \geq 40$ GPa are produced in the transition and nitride modes of sputtering and only in the case if the energy $E_{\mathrm{bi}} > E_{\mathrm{bi\,min}}$. The value of $E_{\mathrm{bi\,min}}$ slightly decreases with increasing I_{d} and $E_{\mathrm{bi\,min}} \approx 0.3$ MJ/cm^3 for $I_{\mathrm{d}} = 3$ A. This experiment clearly shows that the energy E_{bi} plays an important role in the formation of the hard films with $H > 35$ GPa. To form hard films with $H \geq 35$ GPa, the energy $E_{\mathrm{bi}} > E_{\mathrm{bi\,min}}$ must be used. A similar result was already found in the formation of superhard Ti(Al,V)N$_x$ films.[54,212] Besides, it was found that the films sputtered in the nitride mode, i.e., at the energy $E_{\mathrm{bi}} > E_{\mathrm{bi\,min}}$, have the highest values of E^* and so exhibit (i) considerably lower values of H^3/E^{*2}, i.e., lower resistance to plastic deformation, and (ii) lower elastic recovery W_{e}, compared to the films sputtered in the transition mode of sputtering.

The transition mode of sputtering is very important for the production of films with extraordinary properties. To produce such films a transition region has to be created (see Fig. 10.24). The width of the transition region is, however, usually very narrow; it is almost zero in weak ($I_{\mathrm{d}} \leq 1$ A, $\emptyset_{target} = 100$ mm, i.e., $i_{\mathrm{s}} \leq 13$ mA/cm^2) magnetron discharges and increases with increasing I_{d}. This is a main reason why in weak magnetron discharges it is very difficult to form superhard films composed

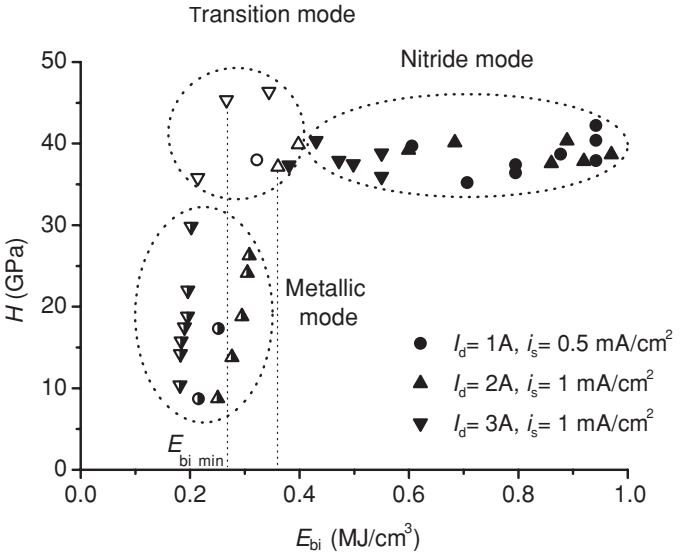

FIGURE 10.31. Dependence of the hardness H of reactively sputtered Ti(Fe)N_x films on the energy E_{bi} delivered to them by ion bombardment during their growth.[108] (Reprinted from Ref. 108. Copyright (2004) with permission from Elsevier.)

of small grains of different crystallographic orientations; to state simply, it is almost impossible to select deposition conditions to fit the transition region. Therefore, denser magnetron discharges are more suitable to realize reactive sputtering and to produce films with extraordinary properties. It was clearly demonstrated in reactive sputtering of superhard Ti(Fe)N_x films with $H > 40$ GPa (see Figs. 10.24, 10.29, and 10.30). This statement seems to be of general validity.

9. TRENDS OF FUTURE DEVELOPMENT

Recent investigations clearly show that there is a strong correlation between the total energy E_T delivered to the growing film during its growth, the film structure, and physical and functional properties of the film. However, the energy E_T is only a necessary, but not sufficient, condition, which controls the formation of nanocomposite films with prescribed properties. The nanocomposite films can be formed only under *a combined action of physical and chemical processes*, controlled by the energy E_T and the chemical composition of the film, respectively. This was clearly shown in the case when the hard films with maximum hardness H_{max} were investigated.[54,108] In addition, it was found that two conditions are necessary to be fulfilled to form films with H_{max}: (1) $E_T \geq E_{min}$ and (2) the film must have an optimum structure; here E_{min} is the minimum energy needed to form the optimum structure.[54] The optimum structure of the films with H_{max} is either

a very fine grained crystalline structure, close to X-ray amorphous characterized by at least two broad, low-intensity X-ray reflections lines, or crystalline structure characterized by a strong preferred crystallographic orientation. In the first case the nanocomposite films with H_{max} are composed of a mixture of small (< 10 nm) grains either of different chemical composition (heterogeneous nanocomposites) or of the same chemical composition but different crystallographic orientations or different lattice structures (homogeneous nanocomposites). In the second case the nanocomposites are composed of nanocolumns. These findings are of a key importance and seem to have a general validity. Therefore, it can be expected that new nanocomposites with enhanced properties, for instance, optical, electrical, magnetic, electronic, and photocatalytic, will be also composed of either a mixture of small grains or nanocolumns. To discover these enhanced properties of new nanocomposites, at first it is necessary to master a method that makes it possible to produce the nanostructured film composed of grains with controlled size, shape, crystallographic orientation, and lattice structure.

At present, there is no technological process that can produce nanocrystalline films composed of precisely defined grains in a controlled way. Therefore, at present, one of the basic tasks is to develop a new deposition process which enables to produce the films composed of small ($\leq$10 nm) grains whose size will be continuously varied from approximately 1 to 10 nm. Such a process can be based, for instance, on a nanocrystallization of material from the amorphous phase (see Fig. 10.32). This process is, compared to the RMS currently used, a two-step process, which consists of (1) the formation of metallic glasses and (2) the

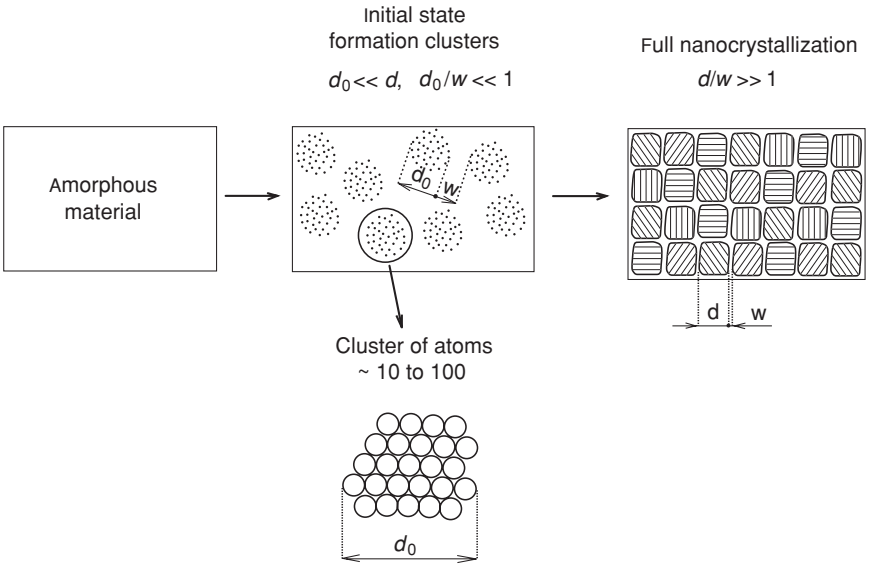

FIGURE 10.32. Schematic illustration of nanocrystallization from amorphous phase.

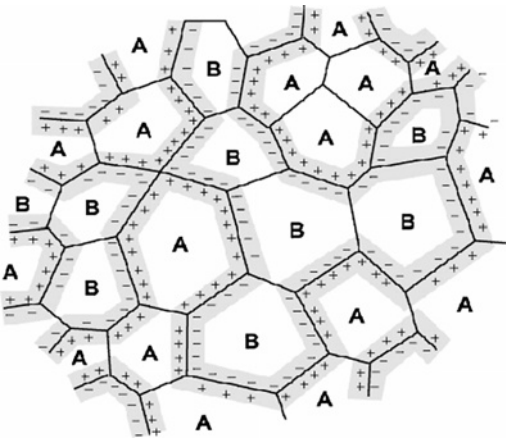

FIGURE 10.33. Schematic illustration of space charge regions in metallic nanocomposites composed of element A (e.g., Mo) and element B (e.g., V). Grey areas are electronically modified regions due to space charge effect. (Adapted from Ref. 25.)

nanocrystallization from the amorphous phase. In principle, two types of materials can be created: (i) materials composed of an amorphous matrix in which cluster of atoms will be embedded (in an initial state of nanocrystallization) and (ii) materials composed of a mixture of small grains in the case if the nanocrystallization is fully developed. In addition, this process avoids the presence of impurities or porosity typical for other processes used for production of the nanostructured films.

As soon as such a process will be developed, a systematic investigation of size-dependent phenomena, i.e., dependences of the film properties on the size and shape of grains from which the film is composed, will start. Obtained results make it possible to develop new nanostructured materials with new unique properties and to investigate new phenomena existing in these materials. For instance, in the nanostructured materials composed of small ($d \leq 10$ nm) grains, very important role will play so called an electronic effect, i.e., an electronic charge transfer, which occurs at any interface between two metallic grains with different chemical compositions and different Fermi energies (see Fig. 10.33).[20,25] One can expect that the utilization of this effect enables to develop materials with new functional properties. Considerable attention will be concentrated, for instance, on the development of TiO_2-based films with photocatalytic, self-cleaning, antifogging and antibactericidal properties.[213–224] At present, there are many open problems such as an urgent need to shift the photocatalytic and antibactericidal activation of TiO_2 films from the ultraviolet light in visible light region. This task requires to dope the base TiO_2 material with an element, i.e., to form an oxide nanocomposite. Similarly, a prolongation of the lifetime of these materials will require to add some additional material (as a built-in reservoir) to ensure a self-healing functionality. Also, it is expected that a doping of oxides by metal is a good way to produce new nanocomposites, which will simultaneously exhibit high strength and ductility. Therefore, it is reasonable to expect that the doped oxides will very soon

represent a new generation of nanocomposites based on oxides. Their production will require, however, to master fully a dc pulsed high-rate magnetron sputtering of oxides. It is also a huge challenge to develop new advanced high-density sputtering and plasma sources.

ACKNOWLEDGMENTS

This work was supported in part by the Ministry of Education of the Czech Republic under Project No. MSM 235200002. The author would like to thank Prof. RNDr. Jaroslav Vlček, CSc., Head of the Department of Physics, University of West Bohemia in Plzň, Czech Republic, for many valuable and stimulating discussions, and his Ph.D. students for their enthusiastic work on this project.

REFERENCES

1. H. Gleiter, Nanocrystalline materials, *Prog. Mater. Sci.***33**, 223–315 (1989).
2. R. Birringer, Nanocrystalline materials, *Mater. Sci. Eng. A***117**, 33–43 (1989).
3. R. W. Siegel, Cluster-assembled nanophase materials, *Annu. Rev. Mater. Sci.* **21**, 559–579 (1991).
4. S. A. Barnett, Deposition and mechanical properties of superlattice thin films, in *Physics of Thin Films*, edited by M. H. Fracombe and J. A. Vossen (Academic Press, New York, 1993), Chap. 1, pp. 1–73.
5. R. W. Siegel, What do we really know about the atomic-scale structures of nanophase materials? *J. Phys. Chem. Solids* **55**(10), 1097–1106 (1994).
6. R. W. Siegel and G. E. Fougere, Grain size dependent mechanical properties in nanophase materials, in *Materials Research Society Symposium Proceedings*, Vol. 362, edited by N. J. Grant, R. W. Armstrong, M. A. Otooni, and K. Ishizaki (Materials Research Society, Warrendale, PA, 1995), pp. 219–229.
7. S. Vepřek and S. Reiprich, A concept for the design of novel superhard coatings, *Thin Solid Films* **265**, 64–71 (1995).
8. H. Gleiter, Nanostructured materials: State of the art and perspectives, *Nanostruct. Mater.* **6**, 3–14 (1996).
9. K. Lu, Nanocrystalline metals crystallized from amorphous solids: Nanocrystallization, structure, and properties, *Mater. Sci. Eng. R***16**, 161–221 (1996).
10. B. X. Liu and O. Jin, Formation and theoretical modelling of non-equilibrium alloy phases by ion mixing, *Phys. Stat. Sol. A* **161**, 3–33 (1997).
11. F. Vaz, L. Rebouta, M. F. da Silva, and J. C. Soares, Thermal oxidation of ternary and quaternary nitrides of titanium, aluminium and silicon, in *Protective Coatings and Thin Films*, edited by Y. Pauleau and P. B. Barna (Kluwer Academic, Dordrecht, The Netherlands, 1997), pp. 501–510.
12. J. Musil and J. Vlček, (1998). Magnetron sputtering of films with controlled texture and grain size, *Mater. Chem. Phys.* **54**, 116–122 (1998).
13. S. Yip, The strongest size, *Nature* **391**, 532–533 (1998).
14. S. Vepřek, The search for novel, superhard materials, *J. Vac. Sci. Technol. A* **17**, 2401–2420 (1999).
15. A. Niederhofer, K. Moto, P. Nesládek, and S. Vepřek, Diamond is not the hardest material anymore: Ultrahard nanocomposite nc-TiN/a- & nc-$TiSi_2$ prepared by plasma CVD, in *Proceedings of the 14th International Symposium on Plasma Chemistry*, Vol. III, Prague, Czech Republic, August 2–6, 1999, edited by M. Hrabovský, M. Konrád, and V. Kopecký (Institute of Plasma Physics AS CR, Prague, Czech Republic, 1995), pp. 1521–1525.

16. J. Musil, Hard and superhard nanocomposite coatings, *Surf. Coat. Technol.* **125**, 322–330 (2000).
17. A. A. Voevodin and J. S. Zabinski, Supertough wear-resistant coatings with "chameleon" surface adaptation, *Thin Solid Films* **370**, 223–231 (2000).
18. H. Gleiter, Nanostructured materials: Basic concepts and microstructure, *Acta Mater.* **48**, 1–29 (2000).
19. J. Musil and J. Vlček, Magnetron sputtering of hard nanocomposite coatings and their properties, *Surf. Coat. Technol.* **142–144**, 557–566 (2001).
20. H. Gleiter, Tuning the electronic structure of solids by means of nanometer-sized microstructures, *Scr. Mater.* **44**, 1161–1168 (2001).
21. S. Vepřek and A. S. Argon, Mechanical properties of superhard nanocomposites, *Surf. Coat. Technol.* **146–147**, 175–182 (2001).
22. V. V. Brazhkin, A. G. Lyapin, and R. J. Hemley, Harder than diamond: Dreams and reality, *Philos. Mag. A* **82**(2), 231–253 (2002).
23. S. Veřek and A. S. Argon, Towards the understanding of mechanical properties of super- and ultrahard nanocomposites, *J. Vac. Sci. Technol. B* **20**(2), 650–664 (2002).
24. J. Musil, J. Vlček, F. Regent, F. Kunc, and H. Zeman, Hard nanocomposite coatings prepared by magnetron sputtering, *Key Eng. Mater.* **230–232**, 613–622 (2002).
25. H. Gleiter and M. Fichtner, Is enhanced solubility in nanocomposites an electronic effect? *Scr. Mater.* **46**, 497–500 (2002).
26. G. M. Demyashev, A. L. Taube, and E. Siores, Superhard nanocomposite coatings, in *Handbook of Organic-Inorganic Hybrid Materials and Nanocomposites*, *Vol. 1: Hybrid Materials*, edited by H. S. Nalwa (American Scientific Publishers/Stevenson Ranch, CA, USA, 2003), Chap. 1, pp. 1–82.
27. G. M. Demyashev, A. L. Taube, and E. Siores, Superhard nanocomposites, in *Encyclopedia of Nanoscience and Nanotechnology*, Vol. X, edited by H. S. Nalwa (American Scientific Publishers/ Stevenson Ranch, CA, USA, 2003), pp. 1–46.
28. J. Musil, Hard nanocomposite films prepared by magnetron sputtering, in *Nanostructured Thin Films and Nanodispersion Strengthened Coatings*, *Invited Lecture at the NATO-Russia Advanced Research Workshop,* December 8–10, 2003, Moscow, Russia, NATO Science Series Volume, edited by A. A. Voevodin, E. Levashov, D. Shtansky, and J. Moore (Kluwer Academic, Dordrecht, The Netherlands, 2004), pp. 43–56.
29. S. Vepřek, P. Nesládek, A. Niederhofer, F. Glatz, M. Jílek, and M. Šíma, Recent progress in the superhard nanocrystalline composites: Towards their industrialization and understanding of the origin of the superhardness, *Surf. Coat. Technol.* **108–109**, 138–147 (1998).
30. A. A. Voevodin and J. S. Zabinski, Superhard, functionally gradient, nanolayered and nanocomposite diamond-like carbon coatings for wear protection, *Diamond Relat. Mater.***7**, 463–467 (1998).
31. J. Musil, A. J. Bell, J. Vlček, and T. Hurkmans, Formation of high temperature phases in sputter deposited Ti-based films below 100°C, *J. Vac. Sci. Technol. A* **14**(4), 2247–2250 (1996).
32. J. Musil, P. Baroch, J. Vlček, K. H. Nam, and J. G. Han, Reactive magnetron sputtering of thin films. Present status and trends, in *Invited Lecture at the 4th Asian-European International Conference on Plasma Surface Engineering (AEPSE 2003)*, JeJu City, Korea, September 28-October 3, 2003; *Thin Solid Films*, **475**, 208–218 (2005).
33. J. Musil, Recent advances in magnetron sputtering technology, *Surf. Coat. Technol.* **100–101**, 280–286 (1998).
34. J. A. Thornton, High rate thick films growth, *Annu. Rev. Mater. Sci.* **7**, 239–260 (1977).
35. J. Musil, Low-pressure magnetron sputtering, *Vacuum* **50**(3–4), 363–372 (1998).
36. J. Musil and J. Vlček, Magnetron sputtering of alloy-based films and its specificity, *Czech. J. Phys.* **48**(10), 1209–1224 (1998).
37. M. Naka, T. Shibayanagi, M. Maeda, S. Zhao, and H. Mori, Formation and physical properties of Al base alloys by sputtering, *Vacuum* **59**, 252–259 (2000).
38. M. Naka, T. Matsui, M. Maeda, and H. Mori, Formation and thermal stability of amorphous Ti-Si alloys, *Mater. Trans., JIM* **36**(7), 797–801 (1995).

39. M. Naka, T. Shibayanagi, M. Maeda, H. Mori, and Y. Ogata, Formation and physical properties of non-equilibrium titanium base alloys by plasma PVD process, in *Proceedings of the International Symposium on Environmental-Conscious Innovative Materials Processing with Advanced Energy Sources*, Kyoto, Japan, November 24–27, 1998, edited by N. Inoue and K. Inoue (High Temperature Society of Japan, Osaka, 1998), pp. 341–346.
40. A. Kaloyeros, M. Hoffman, and W. S. Williams, Amorphous transition metal carbides, *Thin Solid Films* **141**, 237–250 (1986).
41. A. A. Voevodin and J. S. Zabinski, Load-adaptive crystalline-amorphous nanocomposites, *J. Mater. Sci*. **33**, 319–327 (1998).
42. G. Weigang, H. Hecht, and G. von Minnigerode, Further investigations of cocondensation as a preparation method for amorphous states in transition metal alloys, *Z. Phys. B* **96**, 349–355 (1995).
43. J. Musil and F. Regent, Formation of nanocrystalline NiCr-N films by reactive dc magnetron sputtering, *J. Vac. Sci. Technol. A* **16**, 3301–3304 (1998).
44. Y. Tanaka, T. M. Gür, M. Kelly, S. B. Hagstrom, and T. Ikeda, Structure and properties of $(Ti_{1-x}Al_x)N$ films prepared by reactive sputtering, *Thin Solid Films* **228**, 238–241 (1993).
45. U. Wahlström, L. Hultman, J.-E. Sundgren, F. Abidi, I. Petrov, and J. E. Greene, Crystal growth and microstructure of polycrystalline $Ti_{1-x}Al_xN$ alloy films deposited by ultra-high vacuum dual-target magnetron sputtering, *Thin Solid Films* **235**, 62–70 (1993).
46. F. Vaz, L. Rebouta, M. Andritschky, F. M. da Silva, and J. C. Soares, Oxidation resistance of (Ti,Al,Si)N coatings in air, *Surf. Coat. Technol.* **98**, 912–917 (1998).
47. Y. Min, Y. Makino, N. Nose, and K. Nogi, Phase transformation and properties of Ti-Al-N films by rf-plasma assisted magnetron sputtering method, *Thin Solid Films* **339**, 203–208 (1999).
48. J. Musil and H. Hrubý, Superhard nanocomposite $Ti_{1-x}Al_xN$ films prepared by magnetron sputtering, *Thin Solid Films* **365**, 104–109 (2000).
49. H. Hasegawa, A. Kimura, and T. Suzuki, $Ti_{1-x}Al_xN$, $T_{1-x}Zr_xN$ and $Ti_{1-x}Cr_xN$ films synthesized by the AIP method, *Surf. Coat. Technol.* **132**, 76–79 (2000).
50. W. D. Münz, Titanium aluminium nitride films: A new alternative to TiN coatings, *J. Vac. Sci. Technol. A* **4**(6), 2717–2725 (1986).
51. F. Abidi, I. Petrov, J. E. Greene, L. Hultman, and J.-E. Sundgren, Effects of high-flux low-energy (20–100 eV) ion irradiation during deposition on microstructure and preferred orientation of $Ti_{0.5}Al_{0.5}N$ alloys grown by ultra-high vacuum reactive magnetron sputtering, *J. Appl. Phys.* **73**(12), 8580–8589 (1993).
52. T. Suzuki, D. Huang, and Y. Ikuhara, Microstructures and grain boundaries of (Ti,Al)N films, *Surf. Coat. Technol.* **107**, 41–47 (1998).
53. A. Kimura, T. Murakami, K. Yamada, and T. Suzuki, Hot-pressed Ti-Al targets for synthesizing $Ti_{1-x}Al_xN$ films by arc ion plating method, *Thin Solid Films* **382**, 101–105 (2001).
54. H. Poláková, J. Musil, J. Vlček, J. Allaart, and C. Mitterer, Structure–hardness relations in sputtered Ti-Al-V-N films, *Thin Solid Films* **444**, 189–198 (2003).
55. Y. Makino, Y. Setsuhara, and S. Miyake, Prediction of single phase formation of non-equilibrium pseudobinary nitrides assisted by energetic particle bombardment, in *Ion Beam Modification of Materials, Proceedings of the 9th International Conference on Ion Beam Modification of Materials*, Canberra, Australia, February 5–10, 1995, edited by J. S. Williams, R. G. Elliman, and M. C. Ridgway (Elsevier Science, Amsterdam, 1996), pp. 736–739.
56. Y. Makino, Application of band parameters to materials design, *ISIJ Int.* **38**(9), 925–934 (1998).
57. Y. Makino, Structural design of intermetallics: Structural mapping, site preference of third alloying element and planar defects, *Intermetallics* **4**, S11–S16 (1996).
58. Y. Makino and S. Miyake, Estimation of bulk moduli of compound by empirical relations between bulk modulus and interatomic distance, *J. Alloys Compounds* **313**, 235–241 (2000).
59. B. A. Movchan and A. V. Demchishin, Study of the structure and properties of thick vacuum condensates of nickel, titanium, tungsten, aluminum oxide and zirconium oxide, *Phys. Metal. Metall.* **28**, 83–90 (1969).

60. P. B. Barna and M. Adamik, Formation and characterization of the structure of surface coatings, in *Protective Coatings and Thin Films*, edited by Y. Paleau and P. B. Barna (Kluwer Academic, Dordrecht, The Netherlands, 1997), pp. 279–297.
61. P. Zeman, C. Mitterer, P. H. Mayrhofer, R. Čerstvý, and J. Musil, The structure and properties of hard and superhard Zr-Cu-N nanocomposite coatings, *Mater. Sci. Eng. A* **289**, 189–197 (2000).
62. F. Vaz, L. Rebouta, B. Almeida, P. Goudeau, J. Pacaud, J. P. Riviere, and J. Bessa e Sousa, Structural analysis of $Ti_{1-x}Si_xN_y$ nanocomposite films prepared by reactive magnetron sputtering, *Surf. Coat. Technol.* **120–121**, 166–172 (1999).
63. F. Vaz, L. Rebouta, Ph. Goudeau, T. Girardeau, J. Pacaud, J. P. Riviere, and A. Traverse, Structural transitions in hard Si-based TiN coatings: The effect of bias voltage and temperature, *Surf. Coat. Technol.* **146–147**, 274–279 (2001).
64. P. Kaufmann, G. Dehm, E. Arzt, V. Schier, S. Henke, A. Schattke, and T. Beck, Microstructure of physical vapour deposited Ti-Si-N coatings, in *Materials Research Society Symposium Proceedings*, Vol. 704, edited by R. K. Singh, H. Hofmann, and M. Senna (Materials Research Society, Warrendale, PA, USA, 2002), W 7.3.1–W 7.3.6.
65. Z. Li, S. Miyake, M. Kumagai, H. Saito, and Y. Muramatsu, Structure and properties of Ti-Si-N films deposited by dc magnetron cosputtering on positively biased substrates, *Jpn. J. Phys. Pt. 1* **42**(12), 7510–7515 (2003).
66. M. Nose, Y. Deguchi, T. Mae, E. Honbo, T. Nagae, and K. Nogi, Influence of sputtering conditions on the structure and properties of Ti-Si-N thin films prepared by reactive sputtering, *Surf. Coat. Technol.* **174–175**, 261–265 (2003).
67. X. D. Zhang, W. J. Meng, W. Wang, L. E. Rehn, P. M. Baldo, and R. D. Evans, Temperature dependence of structure and mechanical properties of Ti-Si-N coatings, *Surf. Coat. Technol.* **177–178**, 325–333 (2004).
68. N. Jiang, Y. G. Shen, Y.-W. Mai, T. Chan, and S. C. Tung, Nanocomposite Ti-Si-N films deposited by reactive unbalanced magnetron sputtering at room temperature, *Mater. Sci. Eng. B* **106**, 163–171 (2004).
69. M. Nose, W. A. Chiou, M. Zhou, and T. Mae, M. Meshii, Microstructure and mechanical properties of Zr-Si-N films prepared by rf reactive sputtering, *J. Vac. Sci. Technol. A* **20**(3), 823–828 (2002).
70. J. S. Yoon, H. Y. Lee, J. G. Han, S. H. Yang, and J. Musil, The effect of Al composition on the microstructure and mechanical properties of WC-TiAlN superhard composite coating, *Surf. Coat. Technol.* **142–144**, 596–602 (2001).
71. J. Musil, Nanocomposite coatings with enhanced hardness, *Acta Metall. Sin.*, **18** (3) 433–442 (2005).
72. S. M. Rossnagel and J. J. Cuomo, Ion beam bombardment effects during film deposition, *Vacuum* **38**(2), 73–81 (1988).
73. R. A. Roy and D. S. Lee, Control of film properties by ion-assisted deposition using broad beam sources, in *Handbook of Ion Beam Technology*, edited by S. M. Rossnagel and H. R. Kaufman (Noyes Publications, Park Ridge, IL, 1989), pp.194–218.
74. V. Poulek, J. Musil, R. Černý, and R. Kužel, Jr., ε-Ti_2N phase growth in titanium nitride films, *Thin Solid Films* **170**, L55–L58 (1989).
75. S. M. Rossanagel and J. J. Cuomo, Film modification by low energy ion bombardment during deposition, *Thin Solid Films* **171**, 143–156 (1989).
76. J. Musil and S. Kadlec, Reactive sputtering of TiN films at large substrate to target distances, *Vacuum* **40**(5), 435–444 (1990).
77. J. Musil, S. Kadlec, V. Valvoda, R. Kužel, Jr., and R. Černý, Ion-assisted sputtering of TiN films, *Surf. Coat. Technol.* **43–44**, 259–269 (1990).
78. V. Poulek, J. Musil, V. Valvoda, and L. Dobiášová, TiN films created in close vicinity of transition from α-Ti(N) to δ-TiN_x phase, *Mater. Sci. Eng. A* **140**, 660–665 (1991).
79. L. Hultman, W. D. Münz, J. Musil, S. Kadlec, I. Petrov, and J. E. Greene, Low-energy ($\sim$100 eV) ion irradiation during growth of TiN deposited by reactive magnetron sputtering: Effects of ion flux on film microstructure, *J. Vac. Sci. Technol. A* **9**, 434–438 (1991).

80. J. Musil, V. Poulek, V. Valvoda, R. Kužel, Jr., H. A. Jehn, and M. E. Baumgätner, Relation of deposition conditions of Ti-N films prepared by dc magnetron sputtering to their microstructure and macrostress, *Surf. Coat. Technol.* **60**, 484–488 (1993).
81. J. Musil, J. Vyskočil, and S. Kadlec, Hard coatings prepared by sputtering and arc evaporation, in *Physics of Thin Films*, Vol. 17, edited by M. H, Fracombe and J. Vossen (Academic Press Inc. Sond Diego, CA, USA, 1993), Chap. 3, pp. 79–143.
82. R. Černý, R. Kužel, Jr., V. Valvoda, S. Kadlec, and J. Musil, Microstructure of titanium nitride thin films controlled by ion bombardment in a magnetron-sputtering device, *Surf. Coat. Technol.* **64**, 111–117 (1994).
83. I. Petrov, F. Abidi, J. E. Greene, L. Hultman, and J.-E. Sundgren, Average energy deposited per atom: A universal parameter for describing ion-assisted film growth? *Appl. Phys. Lett.* **63**, 36–38 (1993).
84. L. Hultman, J.-E. Sundgren, J. E. Greene, D. B. Bergstrom, and I. Petrov, High-flux low-energy ($\approx$20 eV) N_2^+ ion irradiation during TiN deposition by reactive magnetron sputtering: Effects on microstructure and preferred orientation, *J. Appl. Phys.* **78**(9), 5395–5403 (1995).
85. J.-S. Chun, I. Petrov, and J. E. Greene, Dense fully 111-textured TiN diffusion barriers: Enhanced lifetime through microstructure control during layer growth, *J. Appl. Phys.* **86**(7), 3633–3641 (1999).
86. B. Rauchenbach and J. W. Gerlach, Texture development in titanium nitride films grown by low-energy ion assisted deposition, *Cryst. Res. Technol.* **35**, 675–688 (2000).
87. J. Musil, Sputtering systems with enhanced ionization for ion plating of hard wear resistant coatings, in *Proceedings of the 1st Meeting on Ion Engineering Society Japan*, IESJ-92, Tokyo, edited by T. Takagi (Ionics Publishing Corporation, Tokyo, Japan, 1992), pp. 295–304.
88. J. Musil, Basic properties of low temperature plasma, in *The Physics of Diamond*, *Proceedings of the International School of Physics "Enrico Fermi" Course CXXXV*, edited by A. Paoletti and A. Tucciarone, (IOS Press, Amsterdam, 1997), pp. 145–177.
89. J. Vlček, K. Rusňák, V. Hájek, and L. Martinů, Reactive magnetron sputtering of CN_x films: Ion bombardment effects and process characterization using optical emission spectroscopy, *J. Appl. Phys.* **86**, 3646–3654 (1999).
90. M. A. Lieberman and A. J. Lichtenberg, *Principles of Plasma Discharges and Materials Processing* (Wiley Interscience, New York, 1994).
91. A. Leyland, K. S. Fancey, and A. Matthews, Plasma nitriding in a low pressure triode discharge to provide improvements in adhesion and load support for wear resistant coatings, *Surf. Eng.* **7**(3), 207–215 (1991).
92. S. Schiller, U. Heisig, Chr. Korndörfer, G. Beister, J. Reschke, K. Steinfelder, and J. Strümpfel, Reactive dc high-rate sputtering as production technology, *Surf. Coat. Technol.* **33**, 405–423 (1987).
93. A. Belkind, W. Gerristead, Z. Orban, D. Dow, J. Felts, and R. Laird, Reactive co-sputtering of oxides and nitrides using a C-MAG^{TM} rotable cylindrical cathode, *Surf. Coat. Technol.* **49**, 155–160 (1991).
94. A. Belkind, R. Laird, Z. Orban, and P. W. Rafalko, Serial co-sputtering of mixed Al/Zr and Al_2O_3/ZrO_2 films, *Thin Solid Films* **219**, 46–51 (1992).
95. R. Laird and A. Belkind, Cosputtered films of mixed TiO_2/SiO_2, *J. Vac. Sci. Technol. A* **10**(4), 1908–1912 (1992).
96. A. Belkind, Sputtering and serial cosputtering using cylindrical rotable magnetrons, *J. Vac. Sci. Technol. A* **11**(4), 1501–1509 (1993).
97. A. Belkind and J. Wolfe, Enhancement of reactive sputtering rate of TiO_2 using a planar and dual rotable cylindrical magnetrons, *Thin Solid Films* **248**, 163–165 (1994).
98. W. D. Sproul, New routes in the preparation of mechanically hard films, *Science* **273**, 889–892 (1996).
99. J. M. Schneider and W. D. Sproul, Reactive pulsed dc magnetron sputtering and control, *Handbook of Thin Film Process Technology* (IOP Publishing, Bristol, 1998), pp. A5.1:1–A5.1:12.

100. I. Safi, Recent aspects concerning dc reactive magnetron sputtering of thin films: A review, *Surf. Coat. Technol.* **127**, 203–219 (2000).
101. S. J. Nadel and P. G. Greene, Strategies for high rate reactive sputtering, *Thin Solid Films* **392**, 174–183 (2001).
102. W. Graf, F. Brucker, M. Köhl, T. Tröscher, V. Witter, and L. Herlitze, Development of large area sputtered solar absorber coatings, *J. Non-Cryst. Solids* **218**, 380–387 (1997).
103. G. Bräuer, J. Szczyrbowski, and G. Techner, New approaches for reactive sputtering of dielectric material on large scale substrates, *J. Non-Cryst. Solids* **218**, 19–24 (1997).
104. R. J. Hill and F. Jansen, The use of ac power on cylindrical magnetrons, *J. Non-Cryst. Solids* **218**, 35–37 (1997).
105. R. J. Hill, Reactive sputtering and the use of anodes for optical coatings, *J. Non-Cryst. Solids* **218**, 54–57 (1997).
106. V. Kirchoff and T. Kopte, High-power pulsed magnetron sputter technology, in *Proceedings of the 39th Annual Technical Conference* (Society of Vacuum Coaters, Albuquerque, NM, USA, 1996), pp.117–122.
107. J. M. Schneider, W. D. Sproul, R. W. J. Chia, M. S. Wong, and A. Matthews, Very-high-rate reactive sputtering of alumina hard coatings, *Surf. Coat. Technol.* **96**, 262–266 (1997).
108. J. Musil, H. Poláková, J. Šůna, and J. Vlček, Effect of ion bombardment on properties of hard reactively sputtered Ti(Fe)N_x films, *Surf. Coat. Technol.* **177–178**, 289–298 (2003).
109. B. Chapman, *Glow Discharge Processes* (Wiley, New York, 1980), pp. 376 and 380.
110. J. Musil and R. Daniel, Structure and mechanical properties of magnetron sputtered Zr-Ti-Cu-N films, *Surf. Coat. Technol.* **166**, 243–253 (2003).
111. S. Vepřek, A. Niederhofer, K. Moto, T. Bolom, H.-D. Männling, P. Nesládek, G. Dollinger, and A. Bergmaier, Composition, nanostructure and origin of the ultrahardness in nc-TiN/a-Si_3N_4/a- and nc-$TiSi_2$ nanocomposites with $H_v = 80$ to ≥ 105 GPa, *Surf. Coat. Technol.* **133–134**, 152–159 (2000).
112. A. Niederhofer, P. Nesládek, H.-D. Männling, K. Moto, and S. Vepřek, Structural properties, internal stress and thermal stability of nc-TiN/a-Si_3N_4, nc-TiN/$TiSi_x$ and nc-$(Ti_{1-y}Al_ySi_x)N$ superhard nanocomposite coatings reaching the hardness of diamond, *Surf. Coat. Technol.* **120–121**, 173–178 (1999).
113. W. M. Posadowski, Pulsed magnetron sputtering of reactive compounds, *Thin Solid Films* **343–344**, 85–89 (1999).
114. P. Yashar, J. Rechner, M. S. Wong, W. D. Sproul, and S. A. Barnett, High-rate reactive sputtering of yttria-stabilized zirconia using pulsed dc power, *Surf. Coat. Technol.* **94–95**, 333–338 (1997).
115. W. D. Sproul, High-rate reactive dc magnetron sputtering of oxide and nitride superlattice coatings, *Vacuum* **51**(4), 641–646 (1998).
116. S. J. Nadel, P. Greene, J. Rietzel, and J. Strümpfel, Equipment, materials and processes: A review of high rate sputtering technology for glass coating, in *Proceedings of the 4th International Conference on Coatings on Glass* (*4th ICCG*), Braunschweig, Germany, November 3–7, 2002, pp. 53–58.
117. K. Macák, V. Kouznetsov, J. Schneider, and U. Helmersson, Ionized sputter deposition using an extremely high plasma density pulsed magnetron discharge, *J. Vac. Sci. Technol. A***18**(4), 1533–1538 (2000).
118. J. T. Gudmunsson, J. Alami, and U. Helmersson, Evolution of the electron energy distribution and plasma parameters in a pulsed magnetron discharge, *Appl. Phys. Lett.* **78**, 3427–3429 (2001).
119. J. Vlček, P. Bělský, A. D. Pajdarová, M. Kormunda, J. Leština, and J. Musil, Optical emission spectroscopy and energy—Resolved mass spectrometry in pulsed dc magnetron discharges for ionized high-rate sputtering, in *Proceedings of the 14th International Conference on Gas Discharges and their Applications* (*GD 2002*), September 2–6, 2002, Liverpool, UK, (University of Liverpool, 2002), Vol. 2, pp. 92–95.
120. J. W. Bradley, H. Bäcker, Y. Aranda-Conzalvo, P. J. Kelly, and R. D. Arnell, The distribution of ion energies at the substrate in an asymmetric bi-polar pulsed dc magnetron, *Plasma Sources Sci. Technol.* **11**, 165–174 (2002).

121. J. T. Gudmunsson, J. Alami, and U. Helmersson, Spatial and temporal behavior of the plasma parameters in a pulsed magnetron discharge, *Surf. Coat. Technol.* **161**, 249–256 (2002).
122. A. P. Ehiasarian, R. New, W.-D. Munz, L. Hultman, U. Helmersson, and V. Kuznetsov, Influence of high power densities on the composition of pulsed magnetron plasmas, *Vacuum* **65**, 147–154 (2002).
123. J. Vlček, A. D. Pajdarová, and J. Musil, Pulsed dc magnetron discharges and their utilization in plasma surface engineering, *Contrib. Plasma Phys.* **44**(5–6), 426–436 (2003).
124. A. D. Pajdarová, J. Vlček, P. Kudláček, and J. Lukáš, Electron energy distribution and plasma parameters in high-power pulsed dc magnetron sputtering discharges, *J. Appl. Phys.* submitted.
125. P. J. Kelly, C. F. Beevers, P. S. Henderson, R. D. Arnell, J. W. Bradley, and H. Bäcker, A comparison of the properties of titanium-based films produced by pulsed and continuous dc magnetron sputtering, *Surf. Coat. Technol.* **174–175**, 795–800 (2003).
126. D. Zhou, T. G. McCauley, L. C. Qin, A. R. Krauss, and D. M. Gruen, Synthesis of nanocrystalline diamond films from an Ar-CH_4 microwave plasma, *J. Appl. Phys.* **83**, 540–543 (1998).
127. A. R. Krauss, D. M. Gruen, D. Zhou, T. G. McCauley, L. C. Qin, T. Corrigan, O. Auciello, and R. P. H. Chang, Morphology and electron emission of nanocrystalline CVD diamond thin films, in *Materials Research Society Symposium Proceedings*, Vol. 495 (Materials Research Society, Warrendale, PA, USA, 1998), pp. 299–311.
128. A. R. Krauss, O. Auciello, M. C. Ding, D. M. Gruen, Y. Huang, V. V. Zhirnov, E. I. Givargizov, A. Breskin, R. Chenchen, E. Shefer, V. Konov, S. Pimenov, A. Karabutov, A. Rakhimov, and N. Suetin, Electron field emission for ultrananocrystalline diamond films, *J. Appl. Phys.* **89**, 2958–2967 (2001).
129. S. Bhattacharyya, O. Auciello, J. Birrell, J. A. Carlisle, L. A. Curtiss, A. N. Goyette, D. M. Gruen, A. R. Krauss, J. Schlueter, A. Sumant, and P. Zapol, Synthesis and characterization of highly-conducting nitrogen-doped ultrananocrystalline diamond films, *Appl. Phys. Lett.* **79**(10), 1441–1443 (2001).
130. A. Fujiyama and K. Honda, Electrochemical photolysis of water at a semiconductor electrode, *Nature* **238**, 37–38 (1972).
131. A. Fujiyama, K. Hashimoto, and T. Watanabe, *TiO_2Photocatalysis—Fundamentals and Applications*, 1st edn (BKC Inc., Tokyo, Japan, 1999).
132. A. Fujiyama, T. N. Rao, and D. A. Tryk, Titanium dioxide photocatalysis, *J. Photochem. Photobiol. C Photochem. Rev.* **1**, 1–21 (2000).
133. D. Vollath, D. V. Szabó, R. D. Taylor, and J. O. Willis, Synthesis and magnetic properties of nanostructured maghemite, *J. Mater. Res.* **12**(8), 2175–2182 (1997).
134. Q. Chen, D. M. Gruen, A. R. Krauss, T. D. Corrigan, M. Witek, and G. M. Swain, The structure and electrochemical behavior of nitrogen-containing nanocrystalline films deposited from CH_4/N_2/Ar mixtures, *J. Electrochem. Soc.* **148**, E44–E51 (2001).
135. H. S. Kim, A composite model for mechanical properties of nanocrystalline materials, *Scr. Mater.* **39**(8), 1057–1061 (1998).
136. E. O. Hall, The deformation and ageing of mild steel, III: Discussion and results, *Proc. Phys. Soc. B* **64**, 747–753 (1951).
137. N. J. Petch, The cleavage strength of polycrystals, *J. Iron Steel Inst.* **174**, 25–28 (1953).
138. J. A. Thornton, J. Tabock, and D. W. Hoffman, Internal stresses in metallic films deposited by cylindrical magnetron sputtering, *Thin Solid Films* **64**, 111–119 (1979).
139. D. W. Hoffman and J. A. Thornton, Internal stresses in Cr, Mo, Ta, and Pt films deposited by sputtering from a planar magnetron source, *J. Vac. Sci. Technol.* **20**(3), 355–358 (1982).
140. D. W. Hoffman, Stress and property control in sputtered metal films without substrate bias, *Thin Solid Films* **107**, 353–358 (1983).
141. D. S. Rickerby, Internal stress and adherence of titanium nitride coatings, *J. Vac. Sci. Technol. A* **4**(6), 2809–2814 (1986).
142. D. S. Rickerby, B. A. Bellamy, and A. M. Jones, Internal stress and microstructure of titanium nitride coatings, *Surf. Eng.* **3**(2), 138–146 (1987).

143. D. S. Rickerby, G. Eckold, K. T. Scott, and I. Buckley-Golder, The interrelationship between internal stress, process parameters and microstructure of physically vapour deposited and thermally sprayed coatings, *Thin Solid Films* **154**, 125–141 (1987).
144. J. A. Thornton and D. W. Hoffman, Stress-related effects in thin films, *Thin Solid Films* **171**, 5–31 (1989).
145. F. M. d′Heurle and J. M. E. Harper, Note on the origin of intrinsic stresses in films deposited via evaporation and sputtering, *Thin Solid Films* **171**, 81–92 (1989).
146. A. M. Haghiri-Gosnet, F. R. Ladan, C. Mayeux, H. Launois, and M. C. Joncour, Stress and microstructure in tungsten sputtered thin films, *J. Vac. Sci. Technol. A* **7**(4), 2663–2669 (1989).
147. R. A. Roy and D. S. Yee, Control of film properties by ion-assisted deposition using broad beam sources, in *Handbook of Ion Beam Technology*, edited by J. J. Cuomo, S. M. Rossnagel, and H. R. Kaufman (Noyes Publications, Park Ridge, NJ, 1989), pp. 194–218.
148. D. W. Hoffman and R. C. McCune, Microstructural control of plasma-sputtered refractory coatings, in *Handbook of Plasma Processing Technology*, edited by S. M. Rossnagel, J. J. Cuomo, and W. D. Westwood (Noyes Publications, Park Ridge, NJ, 1990), pp. 483–517.
149. B. Window, G. L. Harding, C. Horrigan, and T. Bell, Stress and microhardness in sputter deposited molybdenum and chromium films, *J. Vac. Sci. Technol. A* **10**(5), 3278–3282 (1992).
150. M. Bromark, M. Larsson, P. Hedenqvist, M. Olsson, S. Hogmark, and E. Bergmann, PVD coatings for tool applications: Tribological evaluation, *Surf. Eng.* **10**, 205–214 (1994).
151. G. Kleer, R. Kassner, E.-M. Meyer, M. G. Schinker, and W. Döll, Effect of process parameters on the residual stresses and the wear behavior of aluminium nitride physical vapor deposition coatings, *Surf. Coat. Technol.* **54–55**, 167–172 (1992).
152. E. Broitman, W. T. Zheng, H. Sjörström, I. Ivanov, J. E. Greene, and J.-E. Sundgren, Stress development during deposition of CN_x thin films, *Appl. Phys. Lett.* **72**(20), 2532–2534 (1998).
153. V. Teixeira, M. Andritschky, W. Fischer, H. P. Buchkremer, and D. Stöver, Effects of deposition temperature and thermal cycling on residual stress state in zirconia-based thermal barriers coatings, *Surf. Coat. Technol.* **120–121**, 103–111 (1999).
154. J. Michler, M. Mermoux, Y. von Kaenel, A. Haouni, G. Lucazeau, E. Blank, *Thin Solid Films* **357**, 189–201 (1999).
155. L. Karlsson, L. Hultman, and J.-E. Sundgren, Influence of residual stresses on the mechanical properties of TiC_xN_{1-x} (x = 0, 0.15, 0.45) thin films deposited by arc evaporation, *Thin Solid Films* **371**, 167–177 (2000).
156. L. P. Kendig, Z. U. Rek, S. M. Yalisove, and J. C. Bilello, The role of impurities and microstructure on residual stress in nanoscale Mo films, *Surf. Coat. Technol.* **132**, 124–129 (2000).
157. Y. G. Shen and Y. W. Mai, Effect of deposition conditions on internal stresses and microstructure of reactively sputtered tungsten nitride films, *Surf. Coat. Technol.* **127**, 239–246 (2000).
158. Th. Göbel, S. Menzel, M. Hecker, W. Brückner, K. Weitzig, and Ch. Genzel, Stress measurements in thermal loaded (Ti,Al)N hard coatings, *Surf. Coat. Technol.* **142–144**, 861–867 (2001).
159. F. Vaz, L. Rebouta, Ph. Goudeau, J. P. Riviere, E. Schäffer, G. Kleer, and M. Bodmann, Residual stress states in sputtered $Ti_{1-x}Si_xN_y$ films, *Thin Solid Films* **402**, 195–202 (2002).
160. A. Niederhofer, P. Nesládek, H.-D. Männling, K. Moto, S. Vepřek, and M. Jílek, Structural properties, internal stress and thermal stability of nc-TiN/a-Si_3N_4, nc-TiN/$TiSi_x$ and nc-$(Ti_{1-y}Al_ySi_x)N$ superhard nanocomposite coatings reaching the hardness of diamond, *Surf. Coat. Technol.* **120–121**, 173–178 (1999).
161. H.-D. Männling, D. S. Patil, K. Moto, M. Jílek, and S. Vepřek, Thermal stability of superhard nanocomposite coatings consisting of immiscible nitrides, *Surf. Coat. Technol.* **146–147**, 263–267 (2001).
162. P. Karvánková, H.-D. Männling, C. Egg, and S. Vepřek, Thermal stability of ZrN-Ni and CrN-Ni superhard nanocomposite coatings, *Surf. Coat. Technol.* **146–147**, 280–285 (2001).
163. P. H. Mayrhofer and C. Mitterer, High-temperature properties of nanocomposite TiB_xN_y and TiB_xC_y coatings, *Surf. Coat. Technol.* **133–134**, 131–137 (2000).

164. P. H. Mayrhofer, G. Tischler, and C. Mitterer, Microstructure and mechanical/thermal properties of Cr-N coatings by reactive unbalanced magnetron sputtering, *Surf. Coat. Technol.* **142–144**, 78–84 (2001).
165. P. H. Mayrhofer, F. Kunc, J. Musil, and C. Mitterer, A comparative study on reactive and non-reactive unbalanced magnetron sputter deposition of TiN coatings, *Thin Solid Films* **415**, 151–159 (2001).
166. C. Mitterer, P. H. Mayrhofer, and J. Musil, Thermal stability of PVD hard coatings, *Vacuum* **71**, 279–284 (2003).
167. M. Shiraishi, W. Ischizama, T. Oshino, and K. Murakami, Low-stress molybdenum/silicon multilayer coatings for extreme ultraviolet lithography, *Jpn. J. Appl. Phys. Pt 1, No. 12B*, **39**, 6810–6814 (2000).
168. M. Berger, L. Karlsson, M. Larsson, and S. Hogmark, Low stress TiB_2 coatings with improved tribological properties, *Thin Solid Films* **401**, 179–186 (2001).
169. D. Sheeja, B. K. Tay, L. Yu, and S. P. Lau, Low stress thick diamond-like carbon films prepared by filtered arc deposition for tribological applications, *Surf. Coat. Technol.* **154**, 289–293 (2002).
170. V. Valvoda, R. Černý, R. Kužel, Jr., J. Musil, and V. Poulek, Dependence of microstructure of TiN coatings on their thickness, *Thin Solid Films* **158**, 225–232 (1988).
171. M. K. Puchert, P. Z. Timbrell, and R. N. Lamb, Thickness-dependent stress in sputtered carbon films, *J. Vac. Sci. Technol. A* 12(3), 727–732 (1994).
172. J. Musil, S. Kadlec, J. Vyskočil, and V. Valvoda, New results in dc reactive magnetron deposition of TiN_x films, *Thin Solid Films* **167**, 107–119 (1988).
173. V. Valvoda, R. Kužel, Jr., R. Černý, and J. Musil, Structure of TiN coatings deposited at relatively high rates and low temperatures by magnetron sputtering, *Thin Solid Films* **156**, 53–63 (1988).
174. J. Musil, V. Poulek, J. Vyskočil, R. Kužel, Jr., and R. Černý, Influence of deposition rate on properties of reactively sputtered TiN_x films, *Vacuum* **38**(6), 459–461 (1988).
175. B. M. Kramer, Requirements for wear-resistant coatings, *Thin Solid Films* **108**, 117–125 (1983).
176. G. Tabor, *The Hardness of Metals* (Clarendon Press, Oxford, 1951).
177. J. Musil, L. Bárdoš, A. Rajský, J. Vyskočil, J. Doležal, G. Lončar, K. Dad'ourek, and V. Kubíček, TiN_x films prepared by dc reactive magnetron sputtering, *Thin Solid Films* **136**, 229–239 (1986).
178. C. J. Tavares, L. Rebouta, K. Pischow, and Z. Wang, Nanometer-scale multilayered $Mo/Ti_{0.4}Al_{0.6}N$ hard coatings, in *Advanced Materials Forum I: 1st International Materials Symposium, Materiais'2001,* Coimbra, Portugal, April 9–11, 2001, *Key Engineering Materials*, edited by T. Vieira, (Trans Tech Publications, Switzerland, 2002) Vols. 230–232, pp. 623–626.
179. V. Kulikovsky, P. Bohač, F. Franc, A. Deineka, V. Vorlíček, and L. Jastrabík, Hardness, intrinsic stress, and structure of the a-C and a-C:H films prepared by magnetron sputtering, *Diamond Relat. Mater.* **10**, 1076–1081 (2001).
180. J. Musil, H. Hrubý, P. Zeman, H. Zeman, R. Čerstvý, P. H. Mayrhofer, and C. Mitterer, Hard and superhard nanocomposite Al-Cu-N films prepared by magnetron sputtering, *Surf. Coat. Technol.* **142–144**, 603–609 (2001).
181. J. Musil, H. Zeman, and J. Kasl, Relationship between structure and mechanical properties in hard Al-Si-Cu-N films prepared by magnetron sputtering, *Thin Solid Films* **41**, 121–130 (2002).
182. F. Kunc, J. Musil, P. H. Mayrhofer, and C. Mitterer, Low-stress superhard Ti-B films prepared by magnetron sputtering, *Surf. Coat. Technol.* **174–175**, 744–753 (2003).
183. H. Zeman, J. Musil, J. Vlček, P. H. Mayrhofer, and C. Mitterer, Thermal annealing of sputtered Al-Si-Cu-N films, *Vacuum* **72**, 21–28 (2003).
184. Joint Committee on Powder Diffraction Standards, *Powder Diffraction File* (International Center for Diffraction Data, Swarthmore, PA, 2002), Card 35-0741.
185. J. D. Wilcock and D. S. Campbell, A sensitive bending beam apparatus for measuring the stress in evaporated thin films, *Thin Solid Films* **3**, 3–12 (1969).
186. V. Valvoda, R. Kužel, Jr., R. Černý, and J. Musil, Structure of TiN coatings deposited at relatively high rates and low temperatures by magnetron sputtering, *Thin Solid Films* **156**, 53–63 (1988).

187. J. Musil and J. Vyskočil, *Titanium Nitride Thin Films* (Studie ČSAV, Academia Praha, 1989). (in Czech)
188. W. Herr and E. Broszeit, The influence of a heat treatment on the microstructure and mechanical properties of sputtered coatings, *Surf. Coat. Technol.* **97**, 335–340 (1997).
189. H. Holleck, Material relation for hard coatings, *J. Vac. Sci. Technol. A* **4**(6), 2661–2669 (1986).
190. D. W. Hoffman, Film stress in the sputter deposition of metals, in *Proceedings of the 7th International Conference on Vacuum Metallurgy*, Tokyo, Japan, November 26–30, 1982, pp. 145–156.
191. D. W. Hoffman and C. Peters, Control of stress and properties in sputtered metal films on nonconductive and heat-sensitive substrates, in *Proceedings of the 9th Intentional Vacuum Congress and 5th International Conference on Solid Surfaces*, Madrid, Spain, September 26–30, 1983, pp. 415–424.
192. D. W. Hoffman, Stress and property control in sputtered metal films without substrate bias, *Thin Solid Films* **107**, 353–358 (1983).
193. J. C. Damasceno, S. S. Camargo, Jr., F. L. Freire, Jr., and R. Carius, Deposition of Si-DLC films with high hardness, low stress and high deposition rates, *Surf. Coat. Technol.* **133–134**, 247–252 (2000).
194. M. Ban and T. Hasegawa, Internal stress reduction by incorporation of silicon in diamond-like carbon films, *Surf. Coat. Technol.* **162**, 1–5 (2002).
195. J. Musil, R. Daniel, and O. Takai, Structure and mechanical properties of magnetron sputtered Zr-Si-N films with a high ($\geq$25 at%) Si content, *Thin Solid Films* **478**(1–2), 238–247 (2005).
196. H. Zeman, J. Musil, and P. Zeman, Physical and mechanical properties of sputtered Ta-Si-N films with a high ($\geq$40 at%) content of Si, in *Proceedings of International Workshop on Designing of Interfacial Structures in Advanced Materials and their Joints* (DIS'03), Vienna, Austria, July 13–16, 2003, pp. 51—57; *J. Vac. Sci. Technol. A* **22**(3), 646–649 (2004).
197. G. Berg, C. Friedrich, E. Broszeit, and C. Berger, Data collection of properties of hard materials, in *Handbook of Ceramic Materials*, edited by R. Riedel (Wiley-VCH Verlag GmbH, Weinheim, Germany, 2000), Table 1, p. 968.
198. M. Nose, Z. Deguchi, T. Mae, E. Honbo, T. Nagae, and K. Nogi, Influence of sputtering conditions on structure and properties of Ti-Si-N films prepared by rf-reactive magnetron sputtering, *Surf. Coat. Technol.* **174–175**, 261–265 (2003).
199. B.-K. Tay, Y. H. Cheng, X. Z. Ding, S. P. Lau, X. Shi, G. F. Yon, and D. Sheeja, Hard carbon nanocomposite films with low stress, *Diamond Relat. Mater.* **10**, 1082–1087 (2001).
200. S. Vepřek, P. Nesládek, A. Niederhofer, H.-D. Männling, and M. Jí, Superhard nanocrystalline composites: Present status of the research, in *Surface Engineering: Science and Technology I*, edited by A. Kumar, Y.-W. Chung, J. J. Moore, and J. E. Smugeresky (The Minerals, Metals & Materials Society, Warrendale, PA, 1999), pp. 219–231.
201. J. Musil, P. Karvánková, and J. Kasl, Hard and superhard Zr-Ni-N nanocomposite films, *Surf. Coat. Technol.* **139**, 101–109 (2001).
202. J. Musil, H. Zeman, and J. Kasl, Relationship between structure and properties in hard Al-Si-Cu-N films prepared by magnetron sputtering, *Thin Solid Films* **413**, 121–130 (2002).
203. J. Musil and R. Daniel, Structure and mechanical properties of magnetron sputtered Zr-Ti-Cu-N films, *Surf. Coat. Technol.* **166**, 243–253 (2003).
204. H. Hasegawa, A. M. Kimura, and T. Suzuki, $Ti_{1-x}Al_xN$, $Ti_{1-x}Zr_xN$ and $Ti_{1-x}Cr_xN$ films synthesized by the AIP method, *Surf. Coat. Technol.* **132**, 76–79 (2000).
205. J. Musil and H. Poláková, Hard nanocomposite Zr-Y-N coatings. Correlation between hardness and structure, *Surf. Coat. Technol.* **127**, 99–106 (2000).
206. J. Musil and S. Miayke, Nanocomposite coatings with enhanced hardness, in *Novel Materials Processing by Advanced Electromagnetic Energy Sources (MAPEE'04)*, edited by S. Miayke (Elsevier, Oxford Tokyo, 2004), pp. 345–356.
207. T. Y. Tsui, G. M. Pharr, W. C. Oliver, C. S. Bhatia, R. L. White, S. Anders, A. Anders, and I. G. Brown, Nanoindentation and nanoscratching of hard carbon coatings for magnetic disks, *Mater. Res. Soc. Symp. Proc.* **383**, 447–452 (1995).

208. J. Musil, H. Jankovcová, and V. Cibulka, Formation of $Ti_{1-x}Si_x$ and $Ti_{1-x}Si_xN$ films by magnetron co-sputtering, *Czech. J. Phys.* **49**, 359–372 (1999).
209. J. Musil, P. Zeman, H. Hrubý, and P. H. Mayrhofer, ZrN/Cu nanocomposite film—A novel superhard material, *Surf. Coat. Technol.* **120–121**, 179–183 (1999).
210. F. Regent and J. Musil, Magnetron sputtered Cr-Ni-N and Ti-Mo-N films. Comparison of mechanical properties, *Surf. Coat. Technol.* **142–144**, 146–151 (2001).
211. J. Musil, F. Kunc, H. Zeman, and H. Poláková, Relationships between hardness, Young's modulus and elastic recovery in hard nanocomposite coatings, *Surf. Coat. Technol.* **154**, 304–308 (2002).
212. J. Musil and H. Poláková, Structure–properties relations in hard sputtered nanostructured films, in *Proceedings of the International Conference on Designing of Interfacial Structures in Advanced Materials and their Joints* (DIS'02), November 25–28, 2002 (Joining and Welding Research Institute, Osaka Universty, Osaka, 2002), pp. 149–156.
213. K. Tanaka, T. Hisanaga, and A. P. Rivera, Effect of crystal forms of TiO_2 on the photocatalytic degradation of pollutants, in *Photocatalytic Purification and Treatment of Water and Air*, edited by D. F. Ollisand and H. Ai-Ekabi (Elsevier Science, Amsterdam, 1993), pp. 169–178.
214. K.-I. Ishikashi, A. Fujiyama, T. Watanabe, and K. Hashimoto, Quantum yield of active oxidative species formed on TiO_2 photocatalyst, *J. Photochem. Photobio. A Chem.* **134**, 139–142 (2000).
215. H. Yamashita, Y. Ichihashi, M. Takeuchi, S. Kishiguchi, and M. Anpo, Characterization of metal ion-implanted titanium oxide photocatalysts operating under visible light irradiation, *J. Synchrotron Radiat.* **6**, 451–452 (1999).
216. J. M. Herman, J. Disdier, and P. Pichat, Effect of chromium doping on the electrical and catalytic properties of powder titania under UV and visible illumination, *Chem. Phys. Lett.* **108**, 618–622 (1984).
217. E. Borgarello, J. Kiwi, M. Grantzel, E. Pelizzetti, and M. Visca, Visible-light induced water cleavage in colloidal solutions of chromium-doped titanium-dioxide particles, *J. Am. Chem. Soc.* **104**, 2996–3002 (1982).
218. T. Umebayashi, T. Yamaki, H. Itoh, and K. Asai, Band gap narrowing of titanium dioxide by sulfur doping, *Appl. Phys. Lett.* **81**(3), 454–456 (2002).
219. R. Asahi, T. Morikawa, T. Ohwaki, K. Aoki, and Y. Taga, Visible-light photocalysis in nitrogen-doped titanium oxides, *Science* **293**, 269–271 (2001).
220. T. Morikawa, R. Asahi, T. Ohwaki, K. Aoki, and Y. Taga, Band-gap narrowing of titanium dioxide by nitrogen doping, *J. Appl. Phys.* **40**, L561–L563 (2001).
221. S. Komuro, T. Katsumata, H. Kokai, T. Morikawa, and X. Zhao, Change in photoluminescence from Er-doped TiO_2 thin films induced by optically assisted reduction, *Appl. Phys. Lett.* **81**, 4733–4735 (2002).
222. A. Vomiero, G. D. Mea, M. Ferroni, G. Martinelli, G. Roncarati, V. Guidi, E. Comini, and G. Sberveglieri, Preparation and microstructural characterization of nanosized Mo-TiO_2 and Mo-W-O thin films by sputtering: Tailoring of composition and porosity by thermal treatment, *Mater. Sci. Eng. B* **101**, 216–221 (2003).
223. L. Miao, S. Tanemura, H. Watanabe, Y. Mori, K. Keneko, and S. Toh, The improvement of optical reactivity for TiO_2 thin fims by N_2-H_2 plasma treatment, *J. Cryst. Growth* **260**, 118–124 (2004).
224. Y. Xie and C. Yuan, Photocatalysis of neodymium modified TiO_2 sol under visible light irradiation, *Appl. Surf. Sci.* **221**, 17–24 (2004).

11

Thermal Stability of Advanced Nanostructured Wear-Resistant Coatings

Lars Hultman[1] and Christian Mitterer[2]

[1]Department of Physics and Measurement Technology (IFM), Linköping University, S-581 83 Linköping, Sweden

[2]Department of Physical Metallurgy and Materials Testing, University of Leoben, Franz-Josef-Strasse 18, A-8700 Leoben, Austria

1. INTRODUCTION

Hard nanostructured coatings prepared by various deposition techniques and conditions exhibit the widest variety of structures among materials in terms of grain size and crystallographic orientation, lattice defects, texture, and surface morphology as well as phase composition. Gradients or inhomogeneities over the film thickness are typically present by design or process determination. Such coating synthesis is also driven by the industrial demand for low-temperature deposition, often done by plasma-assisted growth methods like physical vapor deposition[1] (PVD) or plasma-assisted chemical vapor deposition[2] (PACVD). Obviously, thermodynamic equilibrium is not obtained during this kind of deposition. In fact, it is the kinetic limitation induced by low-temperature deposition that allows for controlled synthesis of metastable phases and artificial structures such as nanolaminate and nanocomposite materials. The *as-deposited* coatings can in turn be subject to annealing and consequential recovery (stress relaxation), interdiffusion, recrystallization, or phase transformation. These phenomena are technologically relevant, since the resulting microstructure has a large impact on the film properties. This enables application of strengthening methods known from bulk materials science, i.e., strain hardening by high defect densities, grain size refinement down to the nanometer range, solid solution hardening including the formation of supersaturated phases, and nanocomposite phase arrangements.[3,4] Most noteworthy, age hardening has recently been demonstrated in coating materials.[5]

In the last few years, advanced surface engineering design approaches have led to the development of coating materials with unique properties or property combinations, e.g., superhardness combined with high toughness,[6] or chameleon-like frictional self-adaptation,[7] both of which have a functional nanostructure. It should be appreciated that the number of coating material systems explored is rapidly growing. For this book, nitride-based materials serve as good model systems from which characteristic behavior for thermal stability of the materials can be demonstrated.

Starting from single-phase TiN,[8] which is still a standard coating for many tooling applications, microstructurally designed hard coatings enable new machining applications, e.g., high-speed cutting or even dry cutting.[9] In these applications, extreme loads are imposed on the coating, e.g., severe friction and wear, corrosion and oxidation, and mechanical and thermal fatigue. Typically, when applied onto cemented carbide cutting tools, the temperature at the cutting edge may exceed 1000°C,[10–12] giving rise to microstructural changes affecting application-oriented properties. Thus, the thermal stability, in particular of advanced microstructurally engineered coatings, is of vital importance. This condition has impact for the choice of constituent elements for the coating. It is significant that present research and development work is in a stage of rapid expansion for testing and investigating a growing number of new combinations.

This chapter is focused on the microstructural and compositional changes of advanced wear-resistant coatings occurring at elevated temperatures. The first section describes important measurement techniques available for characterization of the thermal stability of coatings. In the main part of the chapter, we deal with recovery, recrystallization and grain growth, phase separation, interdiffusion, and oxidation phenomena. Finally, we present an outlook for the research on the thermal stability of nanostructured coatings with some unsolved problems.

2. MEASUREMENT TECHNIQUES

In addition to annealing treatments of coated specimens, there are several *in situ* methods for characterization of the thermal stability of hard coatings. Among them are high-temperature X-ray diffraction (HT-XRD), which is used to study microstructural changes of the coating in inert and also in aggressive environments, and electrical resistivity measurements at elevated temperatures. The latter has additional complexities, since electron mobility arises not only from scattering at point defects and grain boundaries, which are related to the thermal stability of hard coatings, but also from phonon, surface and interface scattering.[13] In the following sections, we briefly describe some of the methods relevant for the investigation of the resistance of nanostructured hard coatings against softening at elevated temperatures and discuss their advantages and limits.

2.1. Biaxial Stress–Temperature Measurements

Coatings with hardnesses well above the values of the respective bulk materials may be synthesized using high ion energies, making use of strain hardening by high defect densities where the defects responsible for the residual stresses also act as obstacles for dislocation movement. In fact, an apparent linear relationship between residual stress and hardness has been reported for several single-phase coatings, e.g., TiN,[14] Ti(C,N),[15,16] or CrN,[17] deposited by different PVD methods. Crystallites with grain sizes of a few nanometers often give broad X-ray diffraction (XRD) peaks of low intensity, preventing stress measurements by X-ray techniques. Thus, the cantilever beam method may beneficially be applied to evaluate the thermal resistance of a coating against softening by stress relaxation. The biaxial coating stress σ can be calculated from the substrate-curvature radius r (e.g., measured by the deflection of two parallel laser beams) using the modified Stoney equation:[18]

$$\sigma = \frac{E_s}{1-\nu_s}\frac{t_s^2}{6\,t_c}\frac{1}{r} \tag{11.1}$$

Here, E_s and ν_s are Young's modulus and Poisson's ratio of the substrate, t_s and t_c are the thickness of substrate and coating, respectively. It should be mentioned here that both intrinsic σ_{int} (i.e., growth induced) and thermal stresses σ_{th} (i.e., due to the mismatch of thermal expansion coefficients of substrate and coating) contribute to σ calculated via Eq. (11.1).

Figure 11.1 shows an example of biaxial stress–temperature measurement (BSTM) cycles for a sputtered nanocomposite $TiB_{0.6}N_{0.7}$ coating deposited onto Si

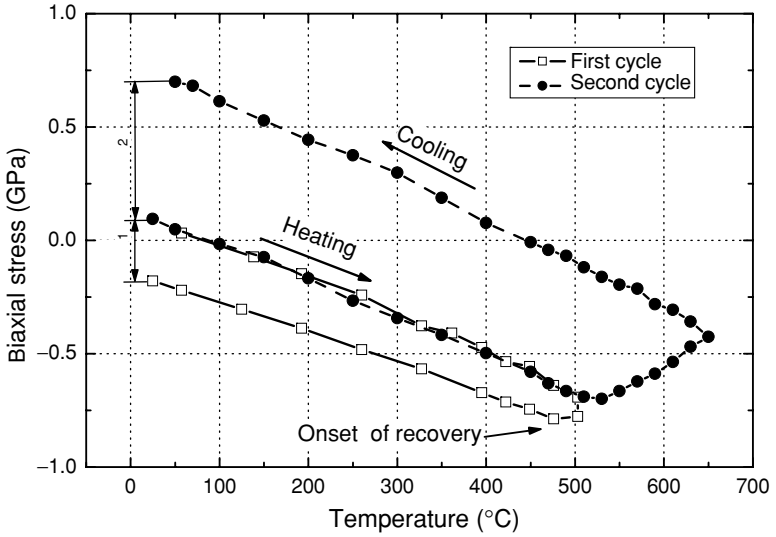

FIGURE 11.1. BSTM cycles of a $TiB_{0.6}N_{0.7}$ coating for two different maximum temperatures (heating rate 5 K/min). (From Ref. 19.)

substrate. During heating of the film–substrate composite, the compressive stresses increase because of the higher thermal expansion coefficient of the coating with respect to the Si substrate. In coatings having tensile stresses at room temperature, the heating first relaxes these tensile stresses and then eventually causes the film to go into a state of compression (cf. Fig. 11.1). This thermoelastic behavior as a result of different thermal expansion coefficients of substrate ($\alpha_{Si} = 3.55 \times 10^{-6}/K$) and coating ($\alpha_{TiBN} = (6-7) \times 10^{6}/K$)[20] is valid only until recovery occurs. During the cooling segment, the stress–temperature curve again shows linear thermoelasticity. A second annealing treatment immediately after the first one does not show any significant deviation of the heating segment from the cooling segment of the previous run, provided that no tensile cracks have been formed after cooling down from the first cycle.[21] A deviation of the straight line during the heating portion of the second run appears if the annealing temperature exceeds the maximum of the first run. For coatings without tensile cracks formed in the cooling phase, plastic deformations in the coating or substrate during this heat treatment can be excluded, enabling elucidation of information on recovery from these BSTM curves.

From the BSTM cycles, essentially two types of informations on the thermal stability of coatings may be obtained. The first one is the onset temperature for recovery, T_{rec}, representing a measure for the thermal stability of the coating itself. The second one is the amount of stress relaxation, $\Delta\sigma$, for a given maximum temperature and heating and cooling rate, respectively, which is related to the hardness loss after the annealing treatment.

The apparent activation energy, E_a, for the recovery processes can be determined depending on the type of measurement performed for the relaxation of stress. Using the method of Damask and Dienes,[22] E_a can be calculated from XRD peak broadening data. Assuming that defect annealing occurs by a single, thermally driven process with an activation energy E_a and rate constant K_0, the defect density n is described by

$$\frac{dn}{dt} = F(n)K_0 \exp\left(\frac{E_a}{k_B T}\right) \tag{11.2}$$

where $F(n)$ is a continuous function of n and k_B is the Boltzmann constant. Using isochronal annealing curves, the two times t_1 and t_2 necessary to reach a given value of n at temperatures T_1 and T_2, respectively, are related by

$$\ln\left(\frac{t_1}{t_2}\right) = \frac{E_a}{k_B}\left(\frac{1}{T_1} - \frac{1}{T_2}\right) \tag{11.3}$$

In the case where the defect annealing occurs via a single process, which has a constant activation energy for all defect concentrations, performing this calculation at different values of n should yield a constant activation energy. If either or both of these assumptions are not valid, however, a variable activation energy will be obtained by this method. In this example,[22] the X-ray structural broadening is due to inhomogeneous strains, which in turn are associated with defects in the crystal

lattice. Assuming this broadening to be proportional to the defect density, Eq. (11.3) can be used along with data for the variation of X-ray structural broadening, β, for a given peak with tempering temperature to determine the apparent activation energy for defect relaxation in a coating. Values for E_a are determined at various defect concentrations (values of β) by defining the fractional amount of defects remaining in the coating, ρ, as

$$\rho = \frac{\beta - \beta_f}{\beta_0 - \beta_f} \tag{11.4}$$

where β_0 and β_f represent the structural broadening in the *as-deposited* and *tempered* coatings, respectively. This approach was used by Almer *et al.*[23] for determining E_a in Cr-N coatings made by arc deposition.

In the method of Mittemeijer *et al.*,[24] E_a is determined from the rate of recovery of the stress. The model does not depend on any specific kinetic mechanism, but assumes that the fraction transformed, f, is fully determined by a state variable β, i.e., $f = F(\beta)$. For isothermal annealing, $\beta = k \cdot t$ where k is $k_0 \exp(-E_a/R \cdot T)$. The final expression is

$$\ln(t_{f2} - t_{f1}) = \frac{E_a}{kT} - \ln k_0 + \ln(\beta_{f2} - \beta_{f1}) \tag{11.5}$$

where $t_{f2} - t_{f1}$ is the time for the recovery to proceed from fraction f_1 to f_2 at temperature T, and k_B is the Boltzmann constant. E_a for the process can be obtained by measuring the slope of the $\ln(t_{f2} - t_{f1})$ versus $1/kT$ plot. This method was applied by Karlsson *et al.*[16] and will be discussed in Section 3.1.

2.2. Differential Scanning Calorimetry and Thermogravimetric Analysis

Differential scanning calorimetry (DSC) is a method where the (exothermic or endothermic) energy released from or consumed by the sample is measured as a function of temperature.[25] If applied to coatings, the substrate material has to be removed to avoid superposition of microstructural changes of substrate and coating. This may be done by chemical dissolution of the substrate, e.g., thin low-alloyed steel substrates may be dissolved in nitric acid. To achieve a suitable heat flow, a minimum mass of coating material is required (e.g., 30 mg). DSC measurements may be performed in inert or aggressive environments; however, for investigating the thermal stability against microstructural changes, an inert atmosphere such as argon has to be used. Figure 11.2 shows an example of a dynamical DSC measurement performed on a nanocomposite $TiB_{1.0}N_{0.7}$ coating demonstrating the evaluation procedure to calculate the heat flow released by grain growth from the area under the exothermic peak.[26] For this purpose, each measurement has to be immediately followed by a second run (rerun), which serves as a baseline (i.e., where no microstructural changes occur) for the first one. In this way, the deviation between the first measurement and the rerun shows all exothermic and

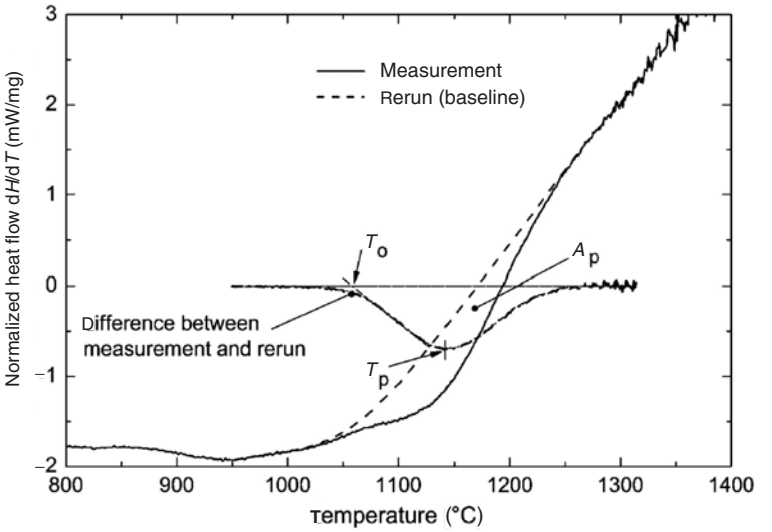

FIGURE 11.2. Experimental DSC curve for a nanocomposite $TiB_{1.0}N_{0.7}$ coating obtained during a thermal treatment in argon atmosphere up to 1400°C using a heating rate of 27 K/min. T_o indicates the onset temperature, T_p the peak temperature, and A_p the area of the exothermic peak. (From Ref. 26.)

endothermic reactions of the coating. The reaction itself is quantified by the onset and peak temperature T_o and T_p, and the peak area A_p, respectively (see Fig. 11.2). The enthalpy change ΔH of the coating can be calculated by dividing A_p with the used heating rate B.

To determine the activation energy E_a for a microstructural reaction by means of the Kissinger equation[27] [Eq. (11.6)], different heating rates B during the DSC experiment are necessary.

$$\ln\left(\frac{B}{T^2}\right) = -\frac{E_a}{RT} + \text{constant} \tag{11.6}$$

Here, R is the gas constant and T a specific temperature such as the onset temperature T_o or the peak temperature T_p of the reaction peak. By using T_o or T_p values for the different heating rates, plots of $\ln(BT^{-2})$ versus T^{-1} yield straight lines showing the same slope allowing the determination of E_a.[28] This method was applied by Mayrhofer *et al.*[26] and will be discussed in Section 3.1.

Oxidation reactions may also be studied using DSC, which can be combined with thermogravimetric analysis (TGA) to obtain not only the enthalpy change due to oxidation, but also the mass gain as a function of temperature (dynamical) or time (isothermal). Dynamical TGA is used to determine the onset temperature for oxidation, whereas the rate constants for linear (usually observed for porous oxide scales) and parabolic growth (for dense oxide layers hindering the

diffusion of metal and oxygen) of the oxide scale can be obtained from isothermal investigations.[29] The temperature dependence of the linear and parabolic rate constants is generally written as an Arrhenius relationship

$$k = k_0 \exp\left(-\frac{E_a}{RT}\right) \tag{11.7}$$

where k is the rate constant, k_0 is the pre-exponential constant, E_a is the activation energy for the oxidation process, and R and T are the gas constant and absolute temperature, respectively.

3. RECOVERY

Recovery involves all annealing phenomena that occur before the appearance of new strain-free grains, i.e., migration and combination of point defects, rearrangement and annihilation of dislocations, and growth and coalescence of subgrains.[3] It is a relatively homogeneous process, where the whole volume of the material is involved, if the defect density does not vary significantly. Thus, investigation of recovery effects can be done by the measurement of intrinsic coating stresses.

3.1. Single-Phase Coatings

3.1.1. Compound and Miscible Systems

Before dealing with recovery, we first consider shortly the origin of stress-generating defects in hard coatings. Stresses are generally induced via energetic particle bombardment during film growth. In magnetron sputtering, these particles are generated from the sputtering gas and consist of back-scattered inert gas neutrals or ions of Ar or the reactive gas (i.e., Ar^+ and N_2^+) accelerated by a negative substrate bias potential toward the growing film.[30] For the case of arc evaporation or high-power pulsed sputtering, there are metal ions of multiple ionization states. For making predictions on thermal stability of *as-deposited* coatings, it is important to know the lattice defect arrangements responsible for the stress and how they depend on the energetic species. We now consider examples from arc-deposited coatings of TiN and TiC_xN_{1-x} films where compressive residual stress builds up for increasing negative substrate bias up to $V_s = 50 - 100$ V. For the larger biases (up to 800 eV studied), however, stress *decreases* and levels out at 2–3 GPa.[15] A maximum stress of -7 GPa is obtained, limited by interior cracking of the films. It is suggested that the apparent relaxation of the stress with increasing energy of the incident metal ions is determined by the defect annihilation processes occurring in the collision cascade in the growing film surface,[31] and that the effective stability of defect complexes increases with increasing carbon content in TiC_xN_{1-x}. In comparison, for magnetron-sputtered coatings with inert gas discharge, the intrinsic stress continuously increases by an apparent square-root

dependency of the bombarding particle energy, following the forward sputtering models.[32]

While different residual defects can be responsible for a given stress state depending on material and deposition parameters, the thermal stability of the respective defects should be different as would the resulting physical properties of the material. Although the stress relaxation by migration, redistribution, or annihilation of stress-active lattice defects as thermally activated processes are relatively straightforward to study for obtaining apparent activation energies, the very nature of point defects or defect clusters remains to be understood. From this perspective, even Si and TiN in their pure components constitute quite complex systems, notwithstanding ternary or multinary compounds.

Generally, recovery of coatings deposited by plasma-assisted deposition techniques occurs during annealing above the given deposition temperature. For example, magnetron-sputtered TiN[14] and CrN[17] exhibit an annihilation of the point defects created by ion irradiation during deposition that starts more or less immediately above that temperature. The intention here is to discuss the stability of homogeneous single-phase coatings like TiN, CrN, and TiC_xN_{1-x} with respect to composition and compressive intrinsic (growth-induced) residual stress. Oettel *et al*. observed a decrease in compressive residual stresses in arc-evaporated TiN and $Ti_{1-x}Al_xN$ films after annealing.[33] Herr and Broszeit[34] reported a decrease of the apparent hardness of TiN films from 36 to 27 GPa when the compressive stress decreased from -6.7 to -2.1 GPa upon annealing for 1 h at 650°C. Perry studied the change in XRD peak widths of e-beam-evaporated TiN films deposited between 400 and 500°C.[35] He annealed the films up to 900°C and obtained an activation energy of 2.1 eV, which was attributed to diffusion of self-interstitials into excess vacancies.

Figure 11.3 shows an apparent linear relation between the onset temperature for recovery and the biaxial stress in the *as-deposited* state of magnetron-sputtered TiN coatings. Using high ion/atom flux ratios at moderate ion energies, the onset temperature may be shifted slightly toward higher values. This may be explained by the promoted relaxation of stress-active defects due to a more intense low-energy ion bombardment during growth. However, it is also obvious from Fig. 11.3 that higher ion energies, causing a higher defect density, lower the thermal stability of the coating. This shows that for a stronger driving force (i.e., higher biaxial stress) a lower thermal activation is needed to start recovery. However, it should be mentioned that this is valid only for coatings showing dense crystalline structures. Coatings with a pronounced columnar growth deviate from this linear dependence because of the possibility of stress relaxation at open-voided column boundaries.

The effects of annealing up to 900°C on the intrinsic stress, σ_{int}, and hardness of arc-evaporated TiC_xN_{1-x} films have been addressed recently by Karlsson *et al*.[16] Figure 11.4 shows the residual stress measured in TiC_xN_{1-x} films as a function of annealing time and temperature, respectively.

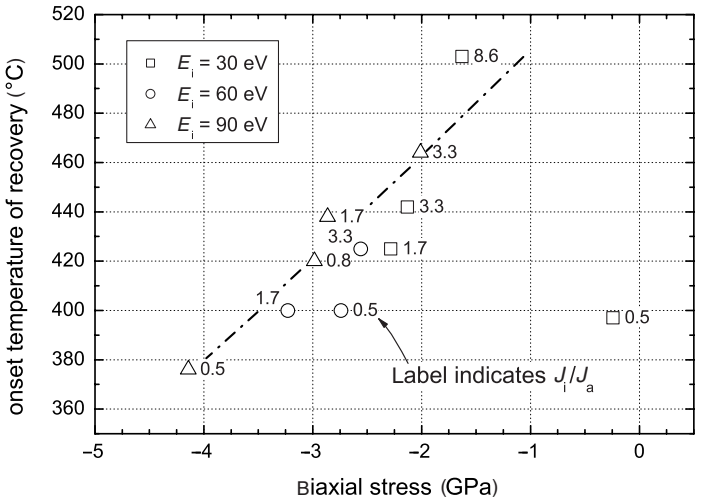

FIGURE 11.3. The onset temperature for recovery for sputtered TiN coatings as a function of the biaxial stress in the *as-deposited* state. The coating deposited at an ion energy of 30 eV and an ion/atom flux ratio of 0.5 is characterized by open-voided column boundaries allowing easy stress relaxation. The deposition temperature was 300°C. (From Ref. 14.)

Films with $x = 0, 0.15$, and 0.45, each having an initial compressive intrinsic stress $\sigma_{int} = -5.4$ GPa, were deposited by varying the substrate bias V_s and the gas composition.[15] Annealing above the deposition temperature leads to a steep decrease in the magnitude of σ_{int} to a saturation stress value, which is a function of the annealing temperature. For temperatures above the deposition temperature T_{dep}, σ_{int} steeply decreases in the first 10–20 min, after which the stress relaxation process essentially saturates. The magnitude of the saturation stress level progressively decreases with increasing T_a. For instance, annealing $TiC_{0.45}N_{0.55}$ at 500°C for nearly 32 h decreased σ_{int} by only 0.5 GPa (see Fig. 11.4a). The intrinsic stress decreases in a roughly linear fashion with increasing annealing temperature, T_a, and deviates from linearity with increased stress relaxation (see Fig. 11.4b). For comparison, the σ_{int} values of *as-deposited* films grown at different T_{dep} obtained from Ref. 15 are also shown. For $TiC_{0.45}N_{0.55}$ films with different initial stress values, the final stress values approach each other with increasing T_a and are indistinguishable at $T_a \geq 800$°C. Note that a film deposited at a low $T_{dep} = T_1$ and annealed at $T_a = T_2 (T_2 \geq T_1)$ has a higher stress level than an *as-deposited* film of the same composition deposited at $T_{dep} = T_2$. This observation indicates that stress relaxation during deposition is more efficient, i.e., causes a larger stress recovery, than a post-thermal annealing treatment at the same temperature.

The corresponding apparent activation energies for stress relaxation are $E_a = 2.4$, 2.9, and 3.1 eV, for $x = 0$, 0.15, and 0.45, respectively, as shown in Fig. 11.5, which is an Arrhenius plot for the stress relaxation versus inverse

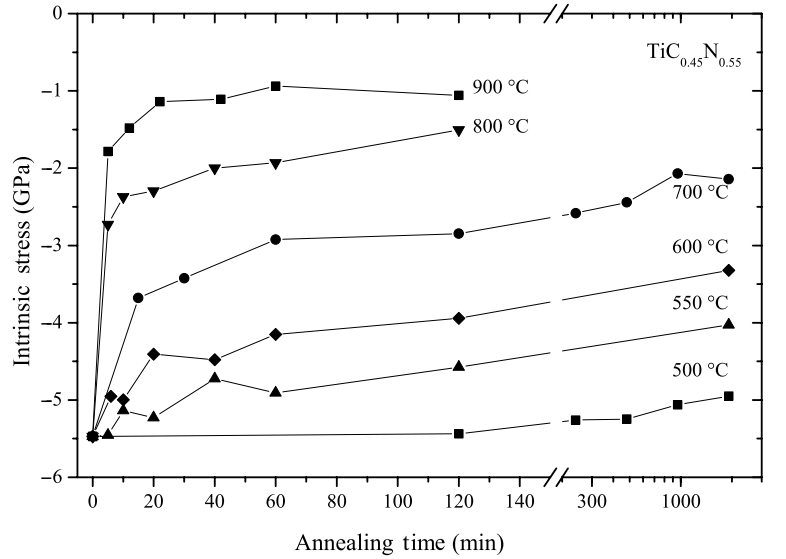

(a)

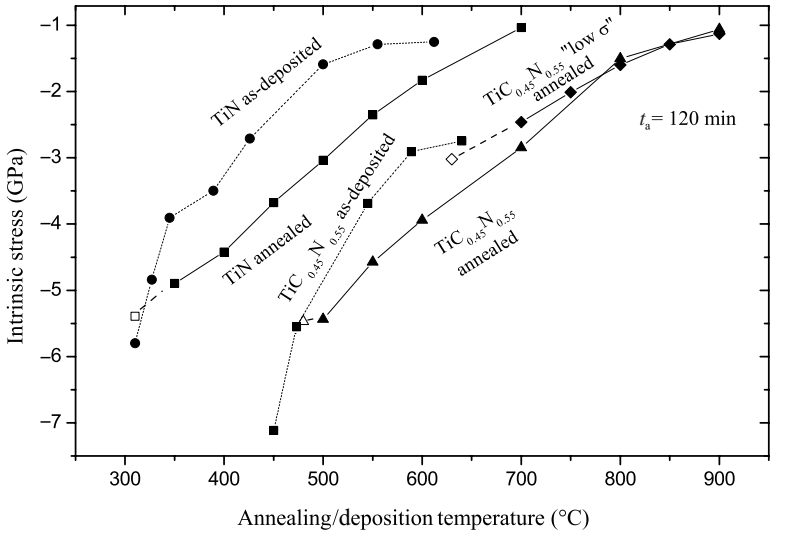

(b)

FIGURE 11.4. (a) Intrinsic stress versus annealing time plots obtained at various annealing temperatures for $TiC_{0.45}N_{0.55}$ coatings. Note the time axis changes from a linear scale to a logarithmic scale at $t_a = 140$ min. Annealing was done in a hot-wall quartz-tube furnace in flowing Ar at 1 atm. (From Ref. 16.) (b) Intrinsic stress plotted as a function of annealing temperature (solid lines) after 120 min isochronal anneals. Open symbols represent the intrinsic stress of *as-deposited* films at the corresponding deposition temperature. Intrinsic stress versus deposition temperature data from Ref. 15 (dotted lines) are also shown for comparison. (From Ref. 16.)

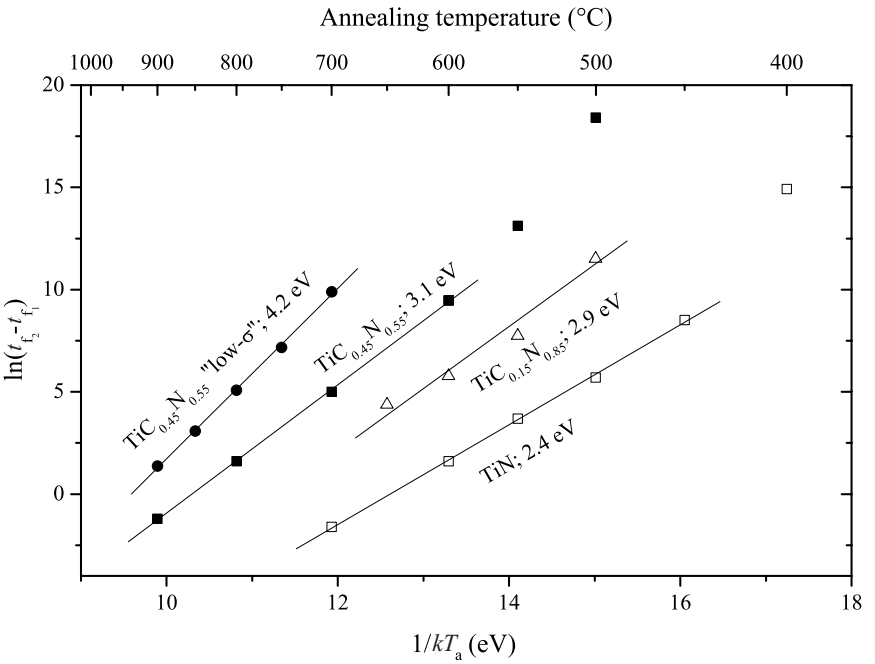

FIGURE 11.5. Plot of ln $t_{50\%}$ versus $1/k_B Ta$. The activation energy Ea is determined by measuring the slope. (From Ref. 16.)

temperature.[16] $TiC_{0.45}N_{0.55}$ films with a lower initial stress $\sigma_{int} = -3$ GPa, obtained using a high substrate bias, show a higher activation energy $E_a = 4.2$ eV. In all the films, stress relaxation is accompanied by a decrease in defect density indicated by the decreased width of XRD peaks and decreased strain contrast in transmission electron microscopy (TEM). Correlation of these results with film hardness and microstructure measurements indicates that the stress relaxation is a result of point-defect annihilation taking place both during short-lived metal-ion surface collision cascades during deposition and during postdeposition annealing by thermally activated processes. The difference in E_a for the films of the same composition deposited at different V_s proves the existence of different types of point-defect configurations and recombination mechanisms.

Recovery was found to be activated for arc-evaporated Cr-N coatings with energies in the range of 2.1–3.1 eV, depending on the initial stress state σ, which in turn was a function of the deposition conditions.[23] It was also concluded that for the Cr-N coating system, possessing a relatively low melting temperature, defect diffusion during growth at 400°C was active. The values are similar to those observed for bulk diffusion of nitrogen in CrN.

The amount of the recovery occurring during thermal annealing strongly depends on the amount of defects in the coating, i.e., on the biaxial stress in the

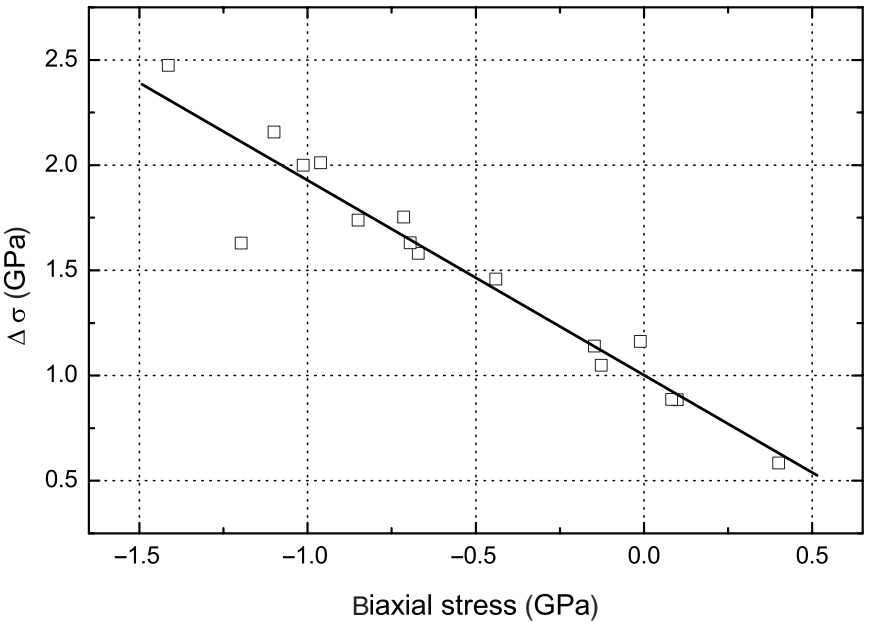

FIGURE 11.6. Influence of the biaxial stress in the *as-deposited* state on stress relaxation during annealing up to 700°C for sputtered CrN coatings deposited at different ion bombardment conditions. (From Ref. 36.)

as-deposited state, providing the driving force for recovery. This is illustrated in Fig. 11.6 for sputtered stoichiometric CrN coatings where a linear relation between the amount of recovery and the biaxial stress in the *as-deposited* condition was found.[36] If a coating shows compressive stresses in the *as-deposited* state (substitution and displacements of atoms on interstitial lattice sites, Frenkel pairs, and Anti-Schottky defects), recovery effects cause stress reduction. However, intrinsic tensile stresses as a result of voids or vacancies (Schottky defects), which are promoted by an insufficient ion bombardment especially if the total working gas pressure is high, may even increase during annealing. The thermal activation causes these defects to anneal out or move to grain boundaries, which are favored places for lattice imperfections, determining the total amount of stress relaxation due to annealing. Recovery effects contain, in addition to a better arrangement of point defects, also annihilation and rearrangement of dislocations into lower energy configurations. Especially if the coating retains a high dislocation density, subgrain formation is promoted. On annealing, excess dislocations will arrange into lower energy configurations in the form of regular arrays or low-angle grain boundaries (polygonization). The stored energy in a substructure is still large and can be further lowered by coarsening of the subgrains. This leads to a reduction of the total area of low-angle grain boundaries and again to stress relaxation.

Almer *et al.*[23] studied the thermal stability of Cr-N coatings prepared by arc evaporation. The *as-deposited* coatings consisted of slightly nitrogen-deficient cubic-structure CrN and were under compressive residual stress. Significant reductions in the defect density accompanied by the formation of equiaxial grains of equilibrium phase fractions of β-Cr_2N and stoichiometric CrN were found to take place after furnace tempering between 400 and 550°C for 270 min in an Ar atmosphere. Correspondingly, Herr and Broszeit[34] have shown that significant stress relaxation occurs in sputter-deposited CrN coatings after annealing between 400 and 650°C.

For the studies of stress recovery in a range of other nitrides, Perry has reported on the effects of tempering for TiN, ZrN, and HfN films under compressive stress.[35] He found that the expanded lattice parameter in the *as-deposited* state contracts above 400°C, where the contraction is completed after 1 h annealing at 800°C. However, the lattice parameters found were still above the equilibrium values indicating defects, which are still resistant to thermal treatment at this temperature. For sputtered low-stress (i.e., −0.4 GPa) VN coatings deposited at a substrate temperature of 300°C, an extremely low onset temperature of 330–350°C for recovery has been reported.[37]

Residual stress engineering can be used for improving film performance by application of strain hardening, but the temperature stability becomes correspondingly more important. The gradual decrease of the contribution of strain hardening results in a hardness loss at temperatures above the deposition temperature, thus limiting the application of highly stressed coatings in high-temperature applications. Although a hardness loss at elevated temperatures due to vanishing strain hardening is unavoidable, recently a constant high hardness well above the bulk hardness up to 700°C has been reported for sputtered overstoichiometric TiB_2 coatings.[38] There, the excess boron results in a compositional modulation with a boron-rich tissue phase surrounding TiB_2 nanocolumns during growth. This modulation contributes to the hardness enhancement and is not affected up to 700°C (although stress recovery during the same annealing treatment occurs), thus explaining both the extremely high hardness of overstoichiometric TiB_2 coatings and their high thermal stability.

3.1.2. Pseudo-Binary Immiscible Systems

The best known example for single-phase coatings consisting of immiscible phases within pseudo-binary systems can be found in the system TiN-AlN,[39] where Al has been added to TiN, originally primarily to enhance the oxidation resistance due to the formation of a protective Al-rich oxide layer at the film surface.[40] Low-temperature ion-assisted (20–50 eV) PVD growth processes are useful to stabilize single-phase coating alloys with compositions *within* the miscibility gap in a metastable state.[41–43] This function relies on the fact that the processes operate at kinetically limited conditions and with ion-bombardment-induced recoil mixing of surface atoms and thus work against thermodynamically driven segregation.

PVD phase field arguments for a range of pseudo-binary nitride systems including TiN-AlN were presented early by Holleck.[44] A stability regime in terms of temperature and AlN content for a face-centered cubic (fcc) phase solid solution in the $Ti_{1-x}Al_xN$ system at temperatures normal for PVD processes (300–700°C) was thus predicted. Recently, modified metastable and still single-phase fcc-$Ti_{1-x}Al_xN$ coatings with small Cr and Y additions have been suggested to improve oxidation and corrosion resistance further.[45]

Compared to TiN, the incorporation of Al (and, likewise, Cr and Y) into the TiN lattice causes an increase of compressive stress due to hindered annihilation of point defects, thus increasing lattice distortion.[20,45] Donohue *et al*.[45] reported on a reduction of compressive stress from −6.8 GPa for $Ti_{0.43}Al_{0.52}Cr_{0.03}Y_{0.02}N$ in the *as-deposited* condition to −2.3 GPa upon annealing at 900°C, and attributed this to either thermally activated plastic deformation or recovery resulting from annihilation of stress-active defects produced during the coating process. Suh *et al*. found a gradual reduction of compressive stress in $Ti_{1-x}Al_xN$ after annealing up to 600°C.[46] BSTM measurements of $Ti_{1-x}Al_xN$ coatings with low Al contents (up to 8 at%) deposited by PACVD at 500°C yielded an onset temperature for recovery of about 620°C (which is slightly lower compared to PACVD TiN coatings grown at the same substrate temperature).[20] Likewise, the amount of stress relaxation after a BSTM cycle up to 700°C was significantly higher compared to TiN. Both effects are related to the higher driving force for recovery in the case of the higher defect density of $Ti_{1-x}Al_xN$ coatings in the *as-deposited* condition with respect to TiN. The activation energy E_a for recovery for an arc-evaporated $Ti_{0.34}Al_{0.66}N$ coating was given to be 3.4 eV, in Ref. 5.

3.2. Multiphase Coatings

3.2.1. Nanocomposite Coatings

Nanocomposite coatings are materials consisting of at least two phases where phase separation typically occurs already during synthesis. According to Holleck,[47] the diffusion length of a condensed adatom via surface diffusion (which is assumed to dominate in low-temperature deposition) is estimated to a few nanometers, making formation of large columns without coalescence of several growing crystals[48] impossible. Nanostructured coatings may thus be grown in the miscibility gap of quasi-binary compound systems. There, continuous nucleation, segregation of insoluble elements, formation of thin segregated layers of the second phase on top of the growing nuclei preventing coalescence, and repeated nucleation take place, thus limiting grain size. In the last decade, several systems have been studied extensively, e.g., combinations of two hard compounds like TiN–Si_3N_4[6,49] and TiN–TiB_2[50] or one hard and one soft phase like ZrN–Cu,[51] all of them representing two-phase materials in the *as-deposited* state.

A motivating factor for the research on nanocomposite coatings has been to achieve a superhard material (see other chapters of this book). Design concepts

for nanocomposites were postulated by Vepřek and Reiprich.[49] Thus, the constituting phases should be selected for strong segregation (immiscibility), strong interface bonding, and high shear moduli. It is a known condition that nanometer-sized grains exhibit no dislocation activity. Alternative means for plasticity can be through grain boundary sliding/rotation.[52] Most coatings made be PVD processing are prone to residual (compressive) stress formation. Strain hardening is, however, often assumed as not to contribute significantly to the extremely high hardness values of nanocomposites because of easy migration of defects to phase boundaries during growth,[6] and, consequently, often relatively low stress values (e.g., below 1 GPa of compressive stress) have been reported.[53] Thus, only relatively limited stress relaxation effects at elevated temperatures have been found for low-stress nanocomposite coatings, for example, in the TiN–Si_3N_4 system.[54] There, not only stress relaxation is an effect of recovery mechanisms (i.e., annihilation of point defects and dislocations), but also grain boundary sliding/rotation events[52] are assumed to contribute. In agreement with the less pronounced stress relaxation, only limited hardness losses after annealing below the recrystallization temperature have been reported for several nanocomposite coatings. For example, Männling *et al*.[55] found no hardness decrease for TiN–Si_3N_4 nanocomposite coatings up to an annealing temperature of 800°C. For the systems TiN–TiB_2 and TiC–TiB_2, the formation of nanocomposite films with stresses below 1 GPa by magnetron sputtering has been reported.[19] The onset of stress recovery was found to vary between 400 and 480°C, which is again only slightly above the deposition temperature of 300°C. The maximum onset temperature was found for comparable amounts of TiN (or TiC) and TiB_2 and well-defined phase boundaries obtained by low-energy ion irradiation during growth. Again, no hardness loss was reported for an annealing cycle up to 700°C.[21]

Up to now, only very limited information is available for the thermal stability of nanocomposite coatings consisting of a hard and a soft phase. Karvánková *et al*.[56] reported softening of sputtered highly stressed (compressive stress up to several GPa) ZrN–Ni and CrN–Ni films upon annealing up to 400–600°C. They attribute this hardness loss to stress recovery, evidenced by the decreasing lattice parameter of the nitride phase, and found no significant effect of the annealing temperature on the grain size up to 700°C. Although the lower thermal stability against stress relaxation compared to low-stress nanocomposite coatings can be explained by the high compressive stress and consequently high defect density representing a higher driving force, the origin for the high stress levels in these coatings is still unclear. Zeman *et al*. reported recently on the stress recovery of complex Al-Si-Cu-N films,[57] which were distinguished in nanocomposite (consisting of Al, Al_2Cu, and AlN phases in the *as-deposited* condition) and amorphous coatings. BSTM cycles up to 700°C showed that low-nitrogen-containing crystalline films (i.e., coatings with Al and Al_2Cu phases) showed stress relaxation due to recovery and recrystallization at temperatures above 300°C. Here, stress relaxation is related to changes in the phase structure and texture of the films. Amorphous low-stress high-nitrogen-containing films showed no apparent stress

relaxation and no hardness loss after thermal cycling. However, these coatings show small deviations from thermoelasticity during the BSTM heating and cooling cycles, indicating that small sliding events accommodate the thermal stresses introduced due to the mismatch of the thermal expansion coefficients.

3.2.2. Superlattices

Besides the three-dimensional arrangement of two phases in a nanocomposite structure, dual-phase materials may also be arranged in a multilayer or, when the periodicity is in the nanometer range, in the superlattice form. The superlattice approach, originally presented in the late 1980s,[58] provides a challenging method for the synthesis of materials with superhardness and has been transferred to production in the last years.[59]

It should be noted that the deposition conditions for superlattices with sequential fluxes offer additional conditions for the formation process of residual stress via the energetic particle–surface interactions during nucleation and growth. There are examples in literature of both stress increase and decrease in a given layered system depending on the periodicity. For example, for residual stresses in TiN/NbN nitride superlattices, a decreased compressive stress state was found compared to the homogeneous nitride films.[60] The exact mechanisms of the decreased stress generation in superlattice films are unknown. It is proposed that the strain level built up by point defects created in the collision cascades can be partly relaxed, together with the coherency-strain relaxation of the nitride overlayers, during misfit dislocation formation. Surface tension effects at the interfaces, however, may also be present in the superlattice.[61] Furthermore, for different mass number of the elements in the constituent layers, the ion–surface interactions—in terms of recoil, forward sputtering, and Frenkel pair production—will be different, depending on what layer is growing. We suggest that the degree of freedom for defect annihilation increases with decreasing superlattice periodicity. Thus, the residual stress should decrease correspondingly.

Although superlattice coatings with different stress levels (up to -9 GPa have been reported in Ref. 62) have been studied extensively, there is only limited information available on their stress recovery behavior. It is significant that initial annealing of *as-deposited* superlattice structures or multilayers can exhibit apparent interface sharpening. This phenomenon is little studied while it may be quickly transient during annealing experiments. It can be due to phase separation of constituent layers that are in a chemically intermixed state from the synthesis or arise from interface sharpening due to a surface energy minimization of structurally rough interfaces. It is termed differently in literature including "chemical cleaning" or "reverse diffusion" as studied in the Ni-Nb/C system,[63] "negative interdiffusion" for the CoMoN/CN system,[64] and "preannealing stabilization" for the W/C system.[65] A typical gauge for the effect is XRD peak sharpening and intensity increase for reflectivity or diffraction measurements of the film structures during initial annealing. Eventual interdiffusion or layer coarsening takes place

for extended annealing, depending on the miscibility of the system. For example, Setoyama *et al*. reported[66] on a slight increase of the intensity of the superlattice peak in HT-XRD at 300°C for TiN/AlN superlattices with a periodicity of 2.9 nm, which indicates sharpening of the interfaces due to faster interfacial diffusion.

4. RECRYSTALLIZATION AND GRAIN GROWTH

Recrystallization involves the formation of new strain-free grains in certain parts of the specimen and the subsequent growth of these to consume the microstructure having defects.[3] The microstructure at any time is divided into recrystallized or non-recrystallized regions, and the fraction recrystallized increases from 0 to 1 as the transformation proceeds. The kinetics of primary recrystallization is similar to those of a phase transformation, which occurs by nucleation and growth. During recrystallization, nucleation corresponds to the first appearance of new grains in the microstructure, and growth describes the consumption of the original grains by new ones and by already existing larger grains at the expense of smaller ones (Ostwald ripening). Recrystallization occurs if the thermal activation and driving force are sufficient. In nanostructured materials, an extremely high interfacial energy is stored due to the high amount of grain and phase boundaries,[67] which can reach 70–80 vol% for grain sizes of 2–3 nm.[68] The high interfacial energy represents an extremely high driving force for recrystallization and grain growth, and consequently, rapid coarsening has been reported for nanocrystalline metal films for relatively low recrystallization temperatures.[69]

4.1. Single-Phase Coatings

4.1.1. Compound and Miscible Systems

The phenomenon of recrystallization has different relevance depending on the melting temperature of the thin film material. While ultrapure In, Pb, and Sn film materials exhibit grain recrystallization with grain growth even below room temperature, Al films are sensitive at above 80°C; mostly refractory carbides and nitrides are usually not considered in this context due to the large difference between melting temperature of the material and the deposition temperature or the temperature of application for the film.[70] However, as this section will show, the small grain size and large levels of compressive intrinsic stress typical for PVD films offer significant driving forces for recrystallization also of the ceramics at relatively low temperatures. The relaxation of compressively stressed films may also occur not only through effective point-defect annihilation, but also by creep or recrystallization. Below will follow a comparison of the different technologically relevant nitride systems Cr-N, TiC_xN_{1-x}, and $Ti_{1-x}Al_xN$, which exhibit a large variation in thermal stability with respect to recrystallization. The lowest apparent stability is observed for Cr-N films as indicated in the previous section, and the

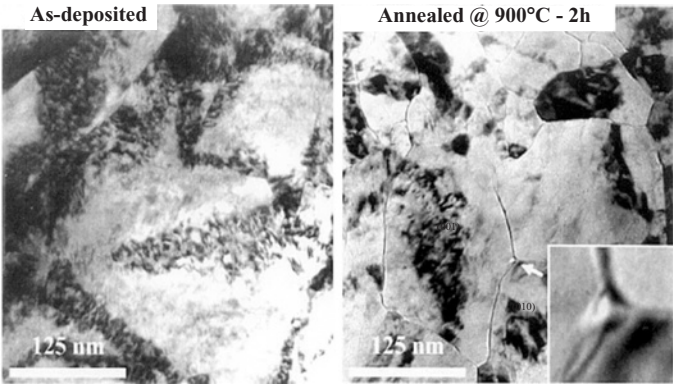

FIGURE 11.7. Representative plan-view TEM micrographs from $TiC_{0.45}N_{0.55}$ films (a) in the *as-deposited* state, and (b) after annealing at 900°C for 2 h. Insert is a high-magnification micrograph showing metallurgical grain boundary formation (120° angles) and void formation at the triple points. (From Ref. 16.)

other follow in the order of appearance. Significant reductions in the defect density accompanied by the formation of equiaxial grains of equilibrium phase fractions of β-Cr_2N and stoichiometric CrN were found to take place after tempering at 400–550°C for 270 min.[23] In fact, precipitation of β-Cr_2N took place inside CrN columnar grains. Héau *et al*. reported on the decomposition of Cr_2N and CrN films prepared by magnetron sputtering.[71] For both coating types an increase of the grain size obtained by HT-XRD was found above 400–450°C. The onset temperature for formation of β-Cr_2N phase was in the same temperature range. It should be mentioned here that O incorporation in the CrN lattice up to 25 at% yielded a comparable onset for grain coarsening; however, a dramatic slowdown of the crystallite size increase was found.[72]

For the case of TiC_xN_{1-x} system, Fig. 11.7 shows plan-view TEM micrographs from an arc-evaporated $TiC_{0.45}N_{0.55}$ film in (a) *as-deposited* state and (b) after *annealing* at 900°C for 2 h.[16] The *as-deposited* film exhibited a dense microstructure with no porosity and a residual stress of −5.5 GPa. Due to the presence of strong strain contrast (a high lattice defect density), grain boundaries could not be imaged easily. However, from following the shift of bending contours (seen as bright and dark areas in Fig. 11.7a) over the sample during tilting, it was possible to obtain a measure for the cell size in the film. During coating growth, dislocations have aligned themselves within the emerging grains, resulting in the formation of subgrain boundaries to partly relax intrinsic stresses (polygonization).[3] This is similar to dynamical recovery occurring during hot rolling of metal sheets. Characteristic cell sizes were 100–300 nm similar to those obtained from cross-section images of samples grown under the same condition.

The annealed sample, however, exhibited a granular structure with grain sizes in the range of 25–100 nm (see Fig. 11.7b). This is lower than the cell size of the *as-deposited* coating, which is a result of the high nucleation density for recrystallization, where the cell boundaries with high dislocation density may act as nuclei *within* the original grains. There was an apparent reduction in defect density; however, isolated dislocations do not appear. Annealing also resulted in the formation of voids between grains and at grain boundary triple points. A larger magnification of such an area is shown in the inset of Fig. 11.7b. In effect, the investigation by TEM showed that annealing changed the film microstructure from what resembles a "cold-worked" material formed by cell boundaries of extreme dislocation density to a recrystallized material with well-defined grain boundaries (c.f. Fig. 11.7). The presence of grain boundary voids shows that vacancies (or any excess nitrogen (N)) have segregated during the course of the annealing.

4.1.2. Pseudo-Binary Immiscible Systems

Recrystallization of single-phase coatings grown within the miscibility gap of a pseudo-binary immiscible system like $Ti_{1-x}Al_xN$ is following decomposition of the metastable phase (for details of the decomposition process, see Section 5). Although the thermodynamically driven decomposition of a metastable phase is unavoidable, these coatings may be characterized by high thermal stability against softening at practical operation conditions. The highest apparent stability with respect to stress relaxation and recrystallization observed to date for a transition metal nitride is that of metastable fcc-$Ti_{1-x}Al_xN$[73] and Ti-B-N;[19,26] the latter represents a nanocomposite coating, which will be treated in Section 4.2.1. Initial results for $Ti_{0.33}Al_{0.67}N$ films grown by arc evaporation show that annealing at 900°C for 1 h (hot-wall quartz-tube furnace in Ar atmosphere) yields no observable recrystallization in TEM. Using DSC, recrystallization of the decomposed fcc-TiN + fcc-AlN structure (see Section 5.1) of arc-evaporated $Ti_{0.5}Al_{0.5}N$ and $Ti_{0.33}Al_{0.67}N$ films was found to take place at temperatures above 1000°C, with a slightly higher thermal stability for the $x = 0.5$ composition.[5] For the decomposed material, recrystallization is accompanied by the transformation of fcc-AlN into the stable hexagonal wurtzite-structure w-AlN phase.[5,73] Both mechanisms are accompanied by significant softening of the coating. Very recently, it has been reported that the softening due to recrystallization and fcc → hcp transformation can be shifted up to 1100°C, if the metastable fcc-$Ti_{1-x}Al_xN$ phase is separated by an amorphous Si_3N_4 tissue phase of approximately 1-nm thickness.[74]

The incorporation of B up to 19 at% into single-phase TiN coatings was found to improve the thermal stability considerably. For TiN without B addition, the diffracted intensity in HT-XRD was found to increase above 600°C, which is attributed to recrystallization.[71] For TiN with 19 at% B, TiB_2 formation and thus decomposition of the initially single-phase coating took place at about 600°C; however, no recrystallization and grain growth were yielded up to 900°C.

4.2. Multiphase Coatings

4.2.1. Nanocomposite Coatings

Grain sizes of a few nanometers and a high amount of interfaces provide a high driving force for recrystallization and grain growth. Although this is an important aspect determining applicability of nanocomposite coatings with superhardness, only limited information on their resistance against softening by recrystallization and grain growth is available. Literature data focus on the systems TiN–Si_3N_4 and TiN–TiB_2, and the main results obtained will be summarized in the following discussion.

For the case of nanocrystalline TiN–Si_3N_4 composite films (consisting of crystalline TiN separated by an amorphous Si_3N_4 tissue phase), recrystallization of the TiN phase takes place at temperatures between 800 and 1200°C, with an increasing onset temperature for grain sizes decreasing from about 10 to 2 nm.[6,53,55] The crystallization of the amorphous Si_3N_4 phase in thin films made by reactive rf magnetron sputtering takes place during annealing at temperatures between 1300 and 1700°C with the formation of α-Si_3N_4 and β-Si_3N_4.[75] The crystallization process of silicon nitride was also described as three-dimensional, interface-controlled growth from preexisting nuclei. The determined rate constants followed a thermal activated behavior with a single activation energy of 5.5 eV.

Recently, recrystallization and grain growth in nanocrystalline dual-phase TiN–TiB_2 films (consisting of crystalline TiN and TiB_2 phases) have been studied by a combination of XRD and DSC measurements using the approach described in Section 2.2.[19,26] The onset temperature for recrystallization increases from 1030°C for TiN-rich coatings with a grain size of 6 nm to 1070°C for TiB_2-rich coatings with a grain size of 2 nm (see Fig. 11.8a).[26] A slightly higher thermal stability has been found for dual-phase TiC–TiB_2 coatings.[19] For nanocomposite coatings consisting of crystalline TiN and amorphous BN, coarsening of the TiN phase has also been found to occur above 1000°C.[76] Contrarily, amorphous TiN films prepared by magnetron sputtering crystallize from 400°C with diffusion as the rate-limiting step.[77]

The huge difference of onset temperatures for recrystallization and grain growth for TiN-based coatings in pure single-phase form and dual-phase coatings with Si_3N_4, TiB_2, or BN phases added points toward a stabilizing mechanism of grain and phase boundaries. Pure single-phase nanocrystalline coatings are thermodynamically unstable, where a lower grain size corresponds to a higher driving force and, consequently, to a reduced thermal stability against grain growth by the well-known Gibbs–Thomson effect. Gleiter[67] applied classical concepts of physical metallurgy for nanocrystalline materials. Thereby, grain growth may be prevented on the one hand by the fine-dispersed inclusion of a second phase acting as pinning sites for the grain boundaries and on the other hand by slowing down the growth kinetics by reducing the driving force (i.e., the grain boundary energy) or the grain boundary mobility. This can be achieved by segregation of insoluble elements to the interfacial area between nanocrystals, either already during growth as in nanocomposite coatings or during postdeposition annealing. As an example

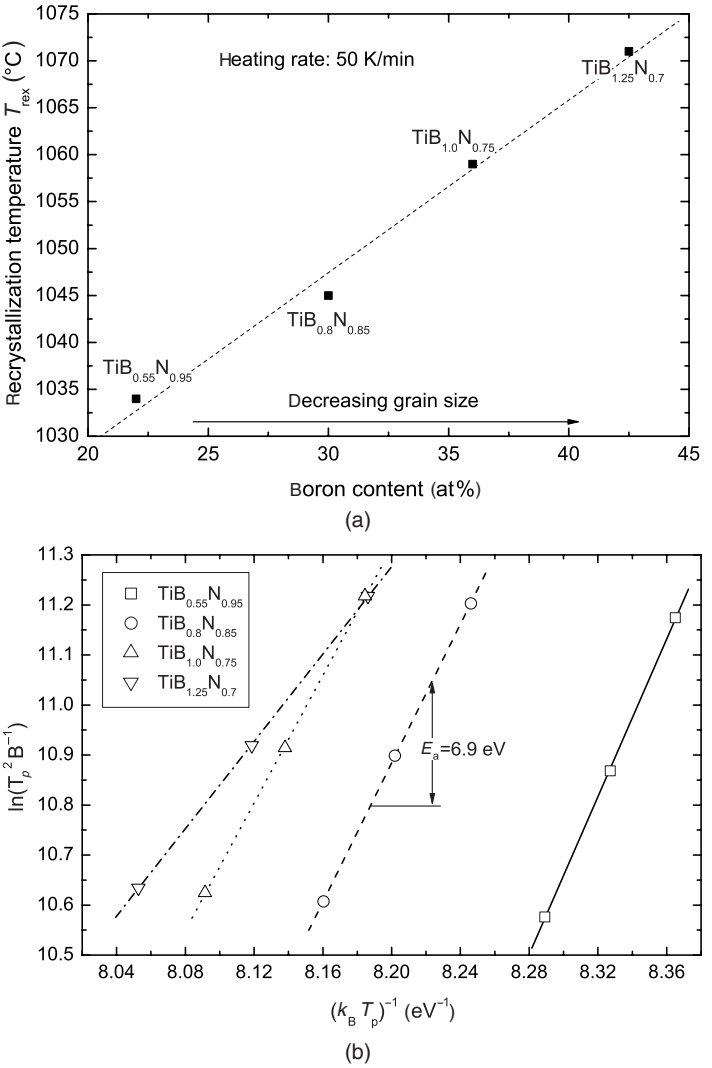

FIGURE 11.8. (a) Recrystallization temperature of dual-phase TiN–TiB_2 coatings as a function of their boron content, determined by DSC using a heating rate of 50 K/min. (From Ref. 26.) (b) Kissinger's analysis of the apparent activation energy for grain growth of four different chemical compositions of dual-phase TiN–TiB_2 coatings, calculated from the change in DSC peak temperature with heating rate. (From Ref. 26.)

for the latter, in the Fe-P system, the grain boundary energy decreases linearly with the logarithm of P content and should approach zero, where the kinetics of P segregation determines the kinetics of grain coarsening.[78] We conclude that the particle coarsening rate in nanostructured coatings as well as in bulk alloys can be

minimized by selecting phases with small diffusion coefficient D, small interface energy γ, and a small mutual solubility X_e.

Figure 11.8b shows Kissinger plots for four different chemical compositions of nanocrystalline dual-phase TiN–TiB_2 coatings obtained using different heating rates during DSC experiments.[26] The apparent activation energies E_a for grain growth were obtained from the slopes of these lines, as described in Section 2.2, yielding values of 7.9, 6.9, 6.4, and 4.4 eV for the compositions $TiB_{0.55}N_{0.95}$, $TiB_{0.8}N_{0.85}$, $TiB_{1.0}N_{0.75}$, and $TiB_{1.25}N_{0.7}$, respectively. For comparison, E_a for vacancy diffusion in TiN films is 2.09 eV,[79] whereas E_a for self-diffusion of N in TiN is 2.1 eV.[35] E_a for diffusion of metal atoms in the nitride phase is in general higher than that of N atoms.[70] However, only for pure metals there exists consistency between self-diffusion and the activation energy for the movement of grain boundaries.[3] For TiN–TiB_2 coatings, it is reasonable that grain size, grain and phase boundary structure, and the different bulk and interface diffusion of Ti, B, and N atoms in TiN, TiB_2, and their grain and phase boundaries, respectively, play major roles in determining the activation energy for grain growth. E_a decreases with increasing TiB_2 content, which is related to the decreasing grain size (see Fig. 11.8a) due to the higher amount of stored interfacial energy. Likewise, the heat released during grain growth increases.[26,36] However, E_a shows significantly different values only for coatings having a predominant TiN or TiB_2 phase, respectively, which is assumed to be related to the competing influence of interfacial energy and phase structure and chemistry on the driving force for grain coarsening.

The evolution of the dual-phase structure of nanocomposite TiN–TiB_2 coatings has recently been studied using high-resolution TEM (HR-TEM) investigations after annealing at temperatures between 700 and 1400°C for 1 h.[80,81] Figure 11.9 shows schematically that in the *as-deposited* state the coating consists

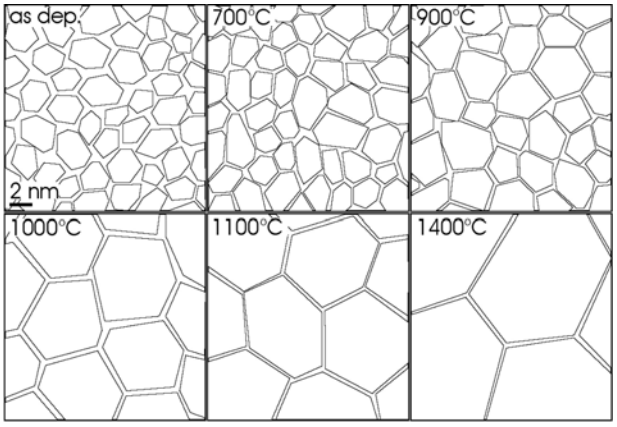

FIGURE 11.9. Scheme of the nanostructural evolution of a dual-phase TiN–TiB_2 coating of composition $TiB_{1.0}N_{0.75}$ with annealing temperature. (From Ref. 80.)

of TiN and TiB_2 nanocrystals with a grain size of 2–4 nm. After annealing, an increase in grain size and a reduction of the amorphous phase surrounding the nanocrystals can be observed, where atoms from the boundary region crystallize onto the surrounded TiN and TiB_2 grains. Upon annealing up to 1000°C, a hardness increase from 41 GPa in the *as-deposited* state up to 51 GPa occurred, where the hardness maximum corresponds to nanocrystals with a diameter of about 5 nm fully percolated by an amorphous phase separating them by approximately 0.5 nm. The same mechanism could explain the hardness increase by 40–50% for Ti-B-N coatings after annealing at 400°C up to 6 h, as reported by Mollart *et al.*[82] The recrystallized and coarsened structure shown in Fig. 11.9 for annealing temperatures exceeding 900°C with grain sizes above 7 nm results in a loss of hardness.

4.2.2. Superlattices

The high density of interfaces makes artificial superlattices or nanolaminates susceptible to thermodynamically driven microstructural changes upon annealing,[83] out of which four different types can be distinguished: (*i*) interdiffusion; (*ii*) coarsening of the layering; (*iii*) reactions between the layers to produce a new phase; and (*iv*) transformation within one or both layer types. Below will be given examples from the first two effects.

Interdiffusion of thin film layers results in a modification of the composition profile. As an effect, this can remove the precondition for mechanical hardness enhancement in nitride superlattices or loss of reflectivity in optical mirrors based on nanolayered coatings, both of which show a reciprocal dependence upon the interface width.[83–88] The use of superlattice or nanolaminate thin films as hard protective coatings on cutting tools, however, exposes the structure to elevated temperatures during the cutting process which may subject the tool to temperatures as high as 1000–1200°C.[12] TiN/NbN superlattices show constant mechanical behavior during annealing up to 700°C [89] similar to the $Ti_{1-x}Al_xN$/CrN system that exhibits stability up to 750°C.[90]

Recently, the metal interdiffusion in TiN/NbN superlattices[91,92] was investigated by annealing samples in a high-vacuum chamber in a purified He atmosphere at 1 atm. The TiN/NbN system exhibits solid solubility.[93,94] Using the decay of X-ray superlattice satellite intensities in both low-angle regime (reflection measurement) and high-angle (diffraction) as shown in Fig. 11.10a,b, a range of apparent activation energies were found; $E_a = 1.2$ eV for annealing temperatures $T_a \leq 830$°C,[91] $E_a = 2.6$ eV for T_a up to 875°C,[91] and $E_a = 4.5$ eV for T_a up to 930°C[92] (see Fig. 11.11). While the lower energy should correspond to defect-mediated diffusion (as will be discussed below), the 2.6 and 4.5 eV value may correspond to grain boundary or even bulk diffusion. During interdiffusion in this system, Ti diffuses at a faster rate into NbN than vice versa while a compositionally abrupt interface was retained.

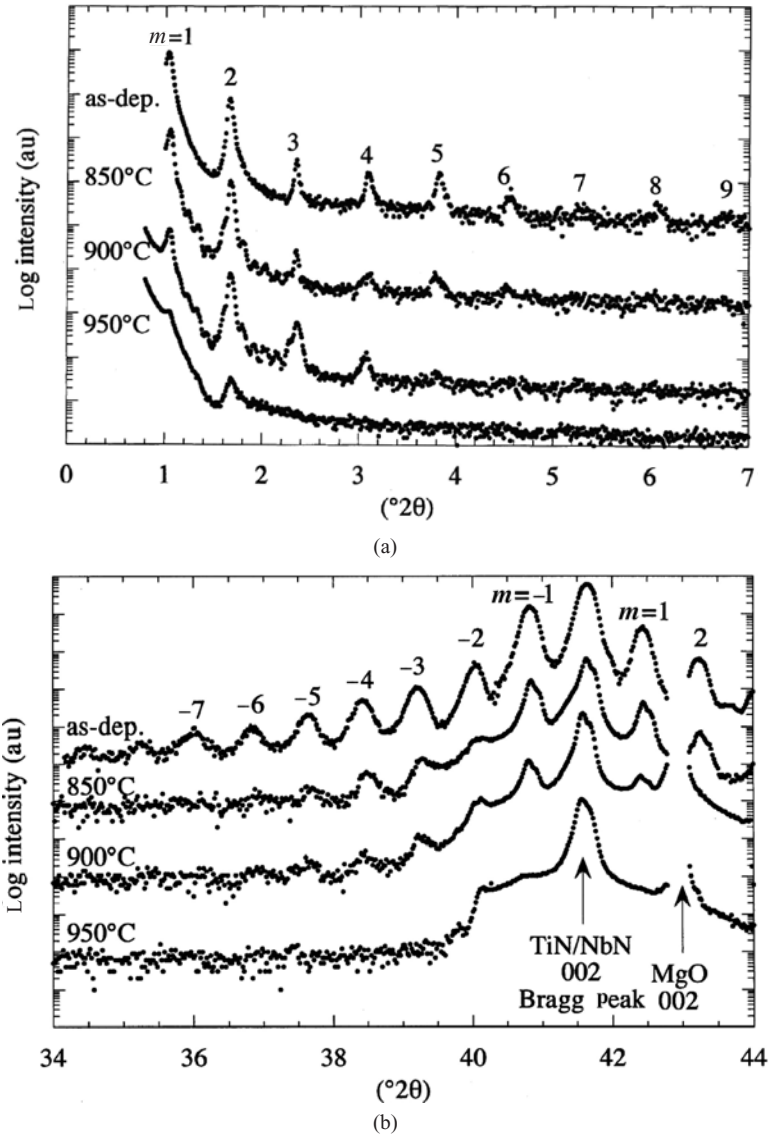

FIGURE 11.10. (a) X-ray reflectivity curves from 11.7-nm period TiN/NbN superlattice films in the *as-deposited* state, and after annealing for 1 h at 850, 900, and 950°C. Superlattice peaks are indicated by their order *m*. (From Ref. 92.) (b) XRD patterns around the (002)TiN/NbN average Bragg reflections from 11.7-nm period TiN/NbN superlattice films in the *as-deposited* state, and after annealing for 1 h at 850, 900, and 950°C. Superlattice peaks are indicated by their order *m*. (From Ref. 92.)

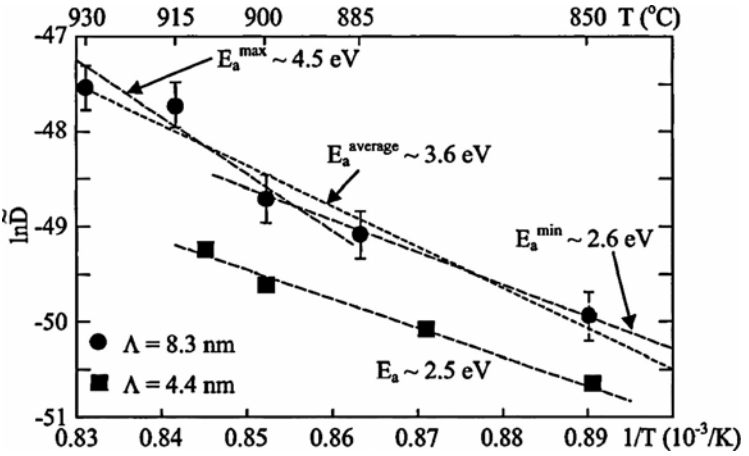

FIGURE 11.11. Temperature-dependent diffusivities for TiN/NbN superlattice interdiffusion, plotted in a semilogarithmic Arrhenius plot. The figure shows the variation of the diffusivity with temperature for an 8.3-nm period TiN/NbN superlattice, as well as a reference from previous measurements on a 4.4-nm TiN/NbN film by Hultman et al.[92] A linear fit to the data points yields the activation energy E_a, as is discussed in the text. (From Ref. 92.)

Engström *et al.*[95] studied the high-temperature stability (up to 1100°C) of epitaxial Mo/NbN nanolaminates which represent a nonisostructural system (body-centered cubic metal and face-centered cubic nitride). After 3 h at 1000°C, an interfacial reaction resulted in the formation of a tetragonal MoNbN phase. The superlattice satellite peaks were correspondingly reduced in intensity and interpreted as a gradual coarsening of the Mo, NbN, and MoNbN phases.

Other superlattice systems produced by PVD methods have also been investigated with respect to thermal stability, including $Ti_{1-x}Al_xN$/CrN,[90] TiN/CN_x,[96,97] and ZrN/CN_x.[98] For $Ti_{1-x}Al_xN$/CrN superlattices with compositional modulation period of 3.6 nm, annealing at 750°C resulted in effectively interdiffused layers after 16 h.[90] The Ti(Zr)N/CN_x couples are thermodynamically unstable with respect to the formation of TiN–TiC and ZrN–ZrC solid solutions.

The lifetime for 8-nm period TiN/NbN superlattices at 850°C was calculated to be 1 h.[95] During annealing the superlattice hardness was reduced from >30 to 27 GPa. Further annealing to 950°C resulted in a drop to 23 GPa. Such values are a useful input for selecting cutting data in application.

For crystalline/amorphous superlattice structures, the group of Barnett studied TiN/TiB_2 and ZrN/ZrB_2 systems.[99] High-angle XRD on *as-deposited* polycrystalline superlattices showed amorphous boride peaks and crystalline nitride peaks. On the other hand, monolithic boride films generally showed both (001) and (002) X-ray reflections, indicating that a crystalline structure was present, with the hexagonal basal planes oriented out of plane. Thus, boride crystallization was inhibited

for nanometer-thick layers. After annealing at 1000°C for 1 h, XRD results showed clear boride (001) peaks, indicating that these layers had crystallized. Superlattice reflections were observed in the low-angle reflectivity scans and were retained after annealing, indicating that the nanolayers were stable. TiN/TiB_2 and ZrN/ZrB_2 are thus good examples of nanolayers that can exhibit good high-temperature stability, which is in good agreement with the $TiN–TiB_2$ nanocomposites discussed in Section 4.2.1. In these superlattice structures, the rock-salt nitride (111) planes match well with the hexagonal boride basal planes.

5. PHASE SEPARATION IN METASTABLE PSEUDO-BINARY NITRIDES

5.1. Spinodal Decomposition

It is imperative that many alloys exhibit miscibility gaps from a limited solid solubility. Spinodal decomposition[100] (requiring negative second derivative of the Gibbs free energy and thermal activation for diffusion) is known from studies of the bulk. A relevant example is the decomposition in TiMoCN.[101] However, little is known for thin films. Here, both *surface* and *in-depth* decomposition can take place during synthetic growth by deposition processes that give effectively quenched alloys. The shape and properties of the so-formed components might also be controlled by anisotropic conditions. For example, *surface-initiated* spinodal decomposition of $Ti_{1-x}Al_xN$ takes place *during growth*, to form a rod-like nanostructure of fcc-TiN- and fcc-AlN-rich domains with a period of 2–3 nm (see Fig. 11.12).[41,102]

Other thin film systems exhibiting spinodal decomposition include the group III–V systems and quaternary InGaAsSb epitaxial layers deposited deep into the miscibility gap.[42]

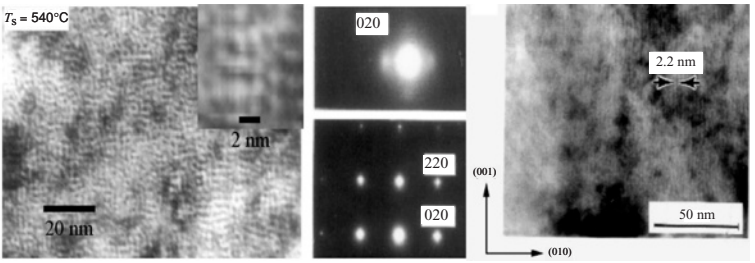

FIGURE 11.12. Plan-view (left) and cross-sectional (right) TEM images with selected area electron diffraction patterns revealing surface-initiated spinodal decomposition during growth of a $Ti_{0.5}Al_{0.5}N$ (001) film at substrate temperature $T_s = 540°C$ by dual target reactive magnetron sputtering. High-magnification of the (020) reflection shows satellite peaks along [010] direction in a cross-sectional view and along both [010] and [100] in plan-view. (From Ref. 41.)

The occurrence of spinodal decomposition during annealing of *as-deposited* ternary ceramic coating materials, in particular the Ti-Zr-N system, has been proposed by Knotek and Barimani[103] and Andrievski and colleagues[104–106] and later by others.[55,107–109] However, a critical review reveals that there has been no direct evidence presented in these cases. As shown in Fig. 11.12, the $Ti_{1-x}Al_xN$ solid solution of NaCl-structure is metastable and tends to decompose into fcc-TiN and fcc-AlN. The equilibrium phases are fcc-TiN and hexagonal wurtzite-structure w-AlN. The solid solubility of fcc-TiN and w-AlN is extremely limited with less than 2 at% Al in TiN at 1000°C.[110]

To investigate the decomposition path of supersaturated fcc-$Ti_{1-x}Al_xN$ films, TiN, $Ti_{0.5}Al_{0.5}N$, and $Ti_{0.34}Al_{0.66}N$ were deposited onto cemented carbide substrates in a high-vacuum arc-evaporation system and subjected to furnace annealing.[73] The depositions were made using $Ti_{1-x}Al_x$ cathodes in a 99.995% pure N_2 atmosphere. The substrates were negatively biased and kept at a temperature of 500°C throughout the deposition. A constant cathode evaporation-current power supply was employed to give a deposition rate of 3 μm/h. The films were grown to a thickness of $\sim$3 μm. Isothermal annealing of all samples was carried out in a hot-wall quartz-tube furnace with a 0.40-m-long constant temperature ($\pm$5°C) zone. The annealing experiments were performed in flowing Ar at atmospheric pressure for a duration of 120 min.

XRD and TEM studies showed that *as-deposited* $Ti_{1-x}Al_xN$ films were NaCl-structure solid solutions for $x \leq 0.67$ and mixed phase NaCl/wurtzite for $x = 0.75$. For magnetron sputtering, the composition limit for single-phase fcc-$Ti_{1-x}Al_xN$ films seems to be similar; however, there is a tendency for higher aluminum concentrations in the films compared to the respective target.[111] Cross-sectional TEM micrographs of the *as-deposited* $Ti_{0.34}Al_{0.66}N$ film in Fig. 11.13 revealed a dense and columnar microstructure with a high defect density and overlapping strain fields from ion-bombardment-induced lattice defects corresponding to a compressive residual stress of 2–3 GPa. With respect to the initialized spinodal decomposition at 900°C observed by XRD, the micrographs of the annealed sample revealed a structure similar to the *as-deposited* condition, except for column boundaries appearing more clearly defined and a reduced contrast from lattice-defect-induced strain fields. Annealing at 1100°C resulted in phase separation of the metastable fcc-$Ti_{1-x}Al_xN$ structure into w-AlN precipitates in an fcc-$Ti_{1-x}Al_xN$ matrix. Original column boundaries were also dissolved at this temperature, and a fine-textured structure consisting of subgrains of diameter 50–100 nm evolved, in which the spinodal decomposition progressed. After annealing at 1250°C, grains of both hexagonal and cubic phase were found to coarsen.

XRD analysis showed that initially the $Ti_{0.50}Al_{0.50}N$ and $Ti_{0.33}Al_{0.67}N$ films were of single-phase NaCl-structure. For annealing at 600, 700, and 800°C, the film peak broadening remained constant at 0.50° 2Θ up to 600°C, and decreased to 0.45° 2Θ after annealing at 700°C. Above 700°C, the broadening increased symmetrically. Annealing at 900°C resulted in additional broadening of the film (200) peaks, but also loss of peak symmetry,[73] as seen in Fig. 11.14.

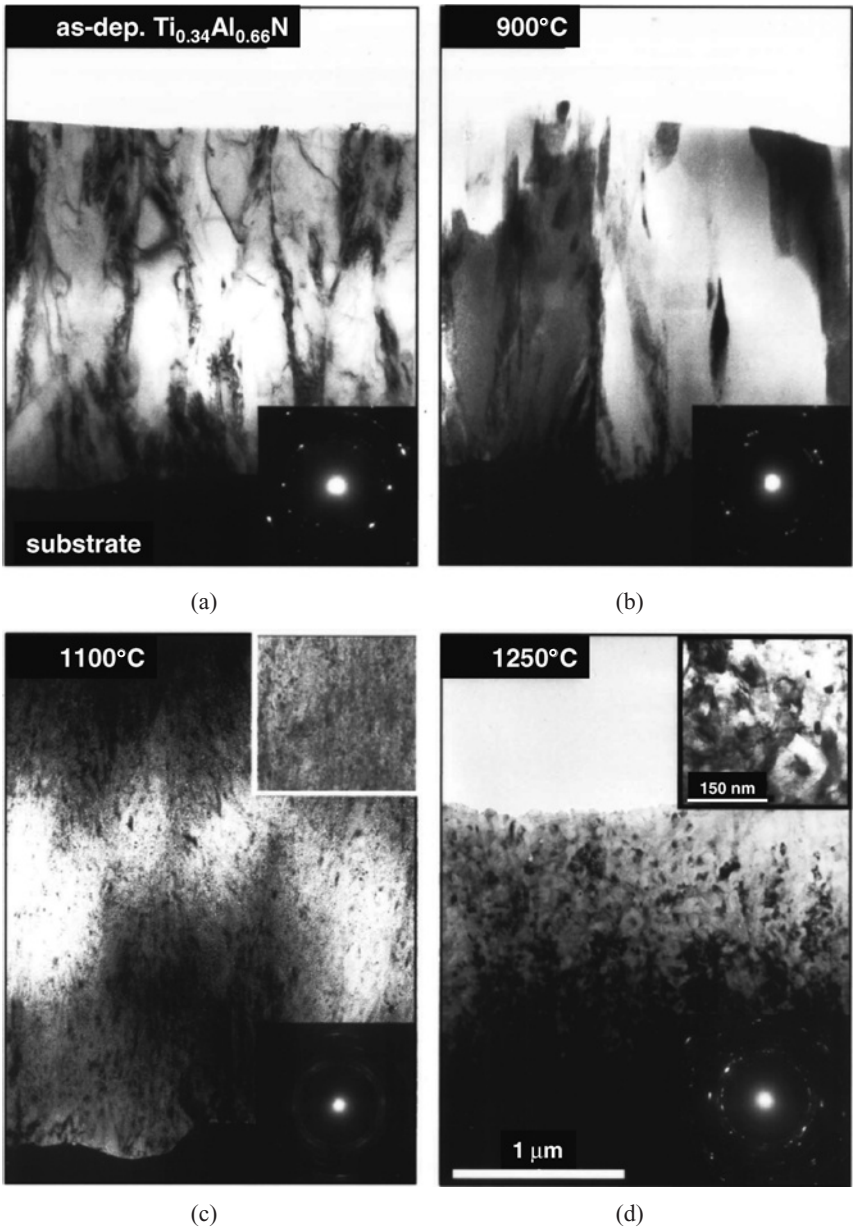

FIGURE 11.13. Cross-sectional TEM micrographs of arc-deposited $Ti_{0.33}Al_{0.67}N$ films in (a) *as-deposited* and (b–d) 120 min annealed conditions. (From Ref. 73.)

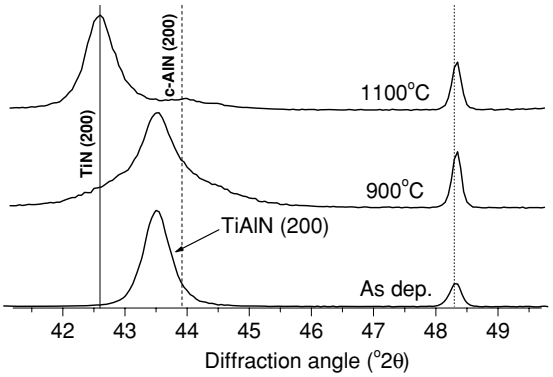

FIGURE 11.14. XRD patterns obtained from $Ti_{0.33}Al_{0.67}N$ films in *as-deposited* and annealed conditions revealing spinodal decomposition. (From Ref. 73.)

During annealing, exothermic reactions are seen in DSC (see Fig. 11.15)[5] including the sequential thermal activation of the processes given as follows: (1) recovery including lattice defect annihilation with residual stress relaxation; (2) Al-N segregation from the matrix; (3) Ti-N segregation; and (4) w-AlN precipitation,

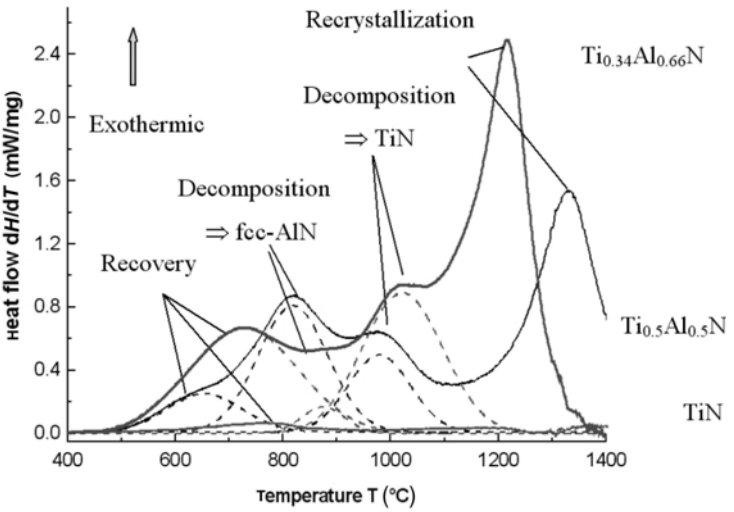

FIGURE 11.15. DSC traces from reactive arc-deposited TiN, $Ti_{0.5}Al_{0.5}N$, and $Ti_{0.34}Al_{0.66}N$ films showing heat flow dH/dT as a function of annealing temperature. The coatings were heated at 50 K/min in a flow of Ar at atmospheric pressure. Four exothermic peaks are indicated for the $Ti_{1-x}Al_xN$ films, whereas only one (recovery) was observed for pure TiN. The dashed lines elucidate the first three exothermic reactions in the films. (From Ref. 5.)

recovery, and grain growth. Initial results using small-angle neutron scattering on a $Ti_{0.50}Al_{0.50}N$ film after annealing at 860°C (i.e., above the temperature of the DSC peak for Al-N segregation shown in Fig. 11.15) indicate an average size of the domains formed of about 1.2 nm. The activation energies for recovery and the formation of TiN domains were determined to be 3.4 eV. Recovery and spinodal decomposition are diffusion controlled within one phase, thus explaining the similar values. For the NaCl to wurtzite structure transformation of AlN and subsequent recrystallization, additional nucleation is needed resulting in $E_a = 3.6$ eV. Considering the similarity of these values with that reported for surface diffusion of Ti on TiN of 3.5 eV,[112] we infer that spinodal decomposition can be a defect-assisted process.

The observations made by XRD, TEM, and DSC provide evidence for spinodal decomposition operating in the bulk of $Ti_{1-x}Al_xN$ thin films or coatings at temperatures starting at 800–900°C. For comparison, the *surface-initiated* spinodal decomposition in the Ti-Al-N system discussed above (cf Fig. 11.12) took place *during growth* at $T_s \geq 540$°C. The much lower T_a for that process is explained by the difference in activation energy for surface and bulk diffusion.

5.2. Age Hardening

Age hardening in metallurgy is studied since 100 years. It has been speculated that the hardness increase for some ternary ceramic coating materials at elevated temperatures is caused by phase separation and spinodal decomposition.[55,103−−109] However, a critical review reveals that there is a lack in explaining the responsible microstructural changes and providing supporting observation. We confirmed spinodal decomposition with a connected increase in film hardness in metastable $Ti_{0.34}Al_{0.66}N$ *thin films* between 700 and 1000°C.[5,73] The corresponding age hardening effect can be seen in Fig. 11.16. Hardening does not occur for TiN,[5,16,73] which instead softens at $T_a \geq 400$°C, due to stress recovery by annihilation of deposition-process-induced defects, and recrystallization.[14,16,70] For comparison, the compressive stress in the $Ti_{1-x}Al_xN$ films decreased from 2–3 GPa only to ∼1 GPa during annealing.[113]

Effectively, the $Ti_{1-x}Al_xN$ coatings harden as a nanocomposite in which dislocation activity ceases for a given small grain size.[6,17,49,114−118] The material adapts in strength to the annealing temperature conditions and can thus be considered to be functional or "smart" for its application. The reasons for this behavior lie in the coherence strain from the 2.8% lattice mismatch between such volumes ($a_{\text{fcc-TiN}} = 4.24$ Å, $a_{\text{fcc-AlN}} = 4.12$ Å) and also hardening from a difference in shear modulus, which hinder dislocation movements for the larger domains.[119]

We submit that the commercial success of $Ti_{1-x}Al_xN$ coatings is not only based on its superior oxidation resistance,[40,120−126] but also on the ability for self-adaptation to the thermal load in tribological testing or cutting operations. In fact, such coated cutting tools exhibit a lower wear rate in ball-on-disk testing at 700°C compared to room temperature[111] and in milling operations compared

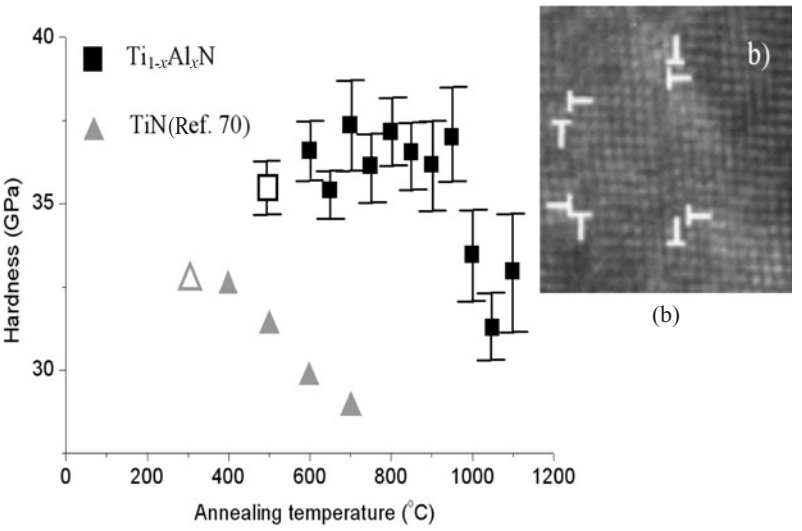

FIGURE 11.16. (a) Influence of isothermal (2 h) annealing on hardness of arc-deposited $Ti_{0.34}Al_{0.66}N$ coatings.[5] Results for a TiN coating is shown for comparison. Open symbols refer to as-deposited samples. (b) HR-TEM image of a $Ti_{0.34}Al_{0.66}N$ coating annealed at 1100°C for 2 h, showing the [001] projection of $Ti_{1-x}Al_xN$ lattice with dissociated 110 ⟨110⟩ misfit dislocations due to relaxation of coherency strains between fcc-AlN and fcc-TiN.

to TiN in machining of cast iron where the rake face heats up to above 900°C. Initial results also show that during the process of spinodal decomposition, there is a concomitant increase in cutting tool life.[113] (Note: Face milling tests of low-C steel (42CrMo4) workpieces with a width of 80 mm were performed using $12 \times 12 \times 3$ mm^3 pressed and sintered WC—13 wt% Co milling inserts (SEKN 1203 AFTN-M14), 125-mm diameter of milling cutter, 300 m/min cutting speed, 0.2 mm/rev feed, 2.5-mm cutting depth, and 4-min time of engagement for the cutting edges.) For face milling tests of low-C steel, the tool life increases by ∼50% (compared to pure TiN) with increasing Al contents up to approximately $x = 0.66$, after which the tool life is drastically reduced to half of that for the TiN reference. This performance decrease is related to the formation of a dual-phase structure consisting of fcc-$Ti_{1-x}Al_xN$ and w-AlN phases during coating growth.[39]

A note for consideration is that the phase transformation of w-AlN from metastable fcc-$Ti_{1-x}Al_xN$ during tools service at elevated temperatures can be detrimental to the coating cohesion and adhesion.[113] This is due to the 20% expansion in molar volume associated with the fcc- to hexagonal-structure transformation of AlN. We also propose that this mechanism provides an explanation for the observed drop in hardness for TiN/AlN multilayer films with longer periodicities, e.g., 16 nm, containing a mixture of cubic and hexagonal-

structure AlN phase during annealing between 800 and 1100°C.[127] The cubic AlN-based nanolayers, however, generally exhibit higher hardness values than coatings with w-AlN structures[83,128,129] and are stable during high-temperature (1000°C) annealing.[83,127]

6. INTERDIFFUSION

As indicated above, most of the presently applied wear-resistant coatings are ceramics with a high melting temperature. Thus, for a preferred dense coating, interdiffusion phenomena are seldom encountered except at very high service temperatures approaching 50% of the melting temperature. There are, however, some types of coating materials that are more sensitive than others. The high interface density of nanostructured hard coatings provides numerous paths for interdiffusion between coating and substrate or workpiece in contact, respectively, which results in composition gradients and probably modifications of coating structure. In the examples given below, indiffusion refers to atoms from the environment diffusing into the coating; outdiffusion is the diffusion of substrate atoms toward the surface of the coating.[129] Aspects of interdiffusion in nanolaminate structures have already been treated in Section 4.2.2.

Strategies to combat interdiffusion are usually based on application of dense diffusion barriers, where oxide-forming elements are added to single-phase or nanocomposite coatings. Indiffusion of workpiece atoms during machining results in diffusional wear or crater wear, especially on the rake face of cutting tools.[39] Indiffusion can be effectively hindered by the *in situ* formation of dense oxide layers on top of the coating, for example, Al-rich layers on top of $Ti_{1-x}Al_xN$-based coatings.[40,120–126] The addition of Y to $Ti_{1-x}Al_xN$ coatings further reduces not only the oxidation rate,[130] but also the indiffusion and outdiffusion of substrate and workpiece materials. Specifically, Y is said to hinder pipe diffusion of substrate elements (Fe or Ti) *due to the segregation of Y and* YO_x *to grain boundaries*.[131–133] Si additions to $Ti_{1-x}Al_xN$-based coatings were also found to reduce diffusional wear.[134] In contrast, the resistance of nanocomposite coatings in the Ti-B-N system against diffusional wear seems to be lower compared to Si-alloyed $Ti_{1-x}Al_xN$,[134,135] which can be attributed to their lower oxidation resistance.[20]

Outdiffusion of Fe in TiN coatings occurs via grain boundary diffusion with a low activation energy $E_a = 0.48$ eV and a diffusion coefficient $D_0 = 1.4 \times 10^{-11}$ cm^2/s for the temperature range from 200 to 600°C.[136] Al, Cr, Si, and Y are known to reduce both in- and outdiffusion;[131,132,134] however, high Cr contents in $Ti_{1-x}Cr_xN$ coatings ($x = 0.79$) have been reported to promote outdiffusion of Fe substrate atoms.[137] Outdiffusion of substrate atoms may be further enhanced by low-density films providing diffusion paths via intergranular voids or oxidized grain boundaries,[70] high interface densities, and coating defects, e.g., macroparticles or droplets. For example, outdiffusion of Co through $Ti_{1-x}Al_xN$ coatings on

WC-Co cemented carbide substrates has been observed to take place at temperatures above 1200°C, where Co diffusion occurs via open-voided grain boundaries above these defects.[73] After annealing at 1250°C for 2 h, Co-rich islands were found evenly distributed on $Ti_{0.34}Al_{0.66}N$ and $Ti_{0.26}Al_{0.74}N$ films covering approximately one third of their surface. Compound formation has been reported in amorphous W-Si-N films sputtered onto Fe-based superalloys due to outdiffusion of Fe, Ni, Cr, Al, and C after annealing at 1000°C.[138,139] For sputtered nanocomposite coatings consisting of TiN and TiB_2 grown on molybdenum substrates, outdiffusion of Mo and formation of the compounds MoB and Mo_2B have been found following annealing at 1200°C.[140] Fe outdiffusion has also been reported for nanocomposite TiB_2–TiC–TiN films deposited onto austenitic stainless steel substrates after annealing in air at 900°C for 2 h.[141]

Another aspect of outdiffusion is the loss of coating atoms via the coating surface. Here, we exemplify this with carbon nitride, which is a resilient coating[142] and an emerging material for wear-resistant applications of mechanical components. The fullerene-like CN_x compounds generally exhibit a low work of indentation usually connected to high-hardness materials. Yet, CN_x shows a low-to-moderate resistance to penetration depending on deposition conditions. Since the deformation energy is predominantly stored elastically, the material possesses an extremely resilient character. This new class of materials consists of sp^2-coordinated basal planes that are buckled from the incorporation of pentagons and cross-linked at sp^3-hybridized C sites, both of which arise due to structural incorporation of nitrogen. CN_x thus deforms elastically due to a bending of the structural units. The orientation, radius of curvature of the basal planes, and the degree of cross-linking in between them have been shown to define the structure and properties of the material. It exhibits in addition to diffusion also a reaction with a concomitant loss of N. The thermal stability of carbon nitride thin films was studied for post-deposition annealing.[143,144] Films were grown at temperatures of 100 (amorphous structure), 350, and 550°C (fullerene-like structure). For $T_A > 300$°C, N is lost and graphitization takes place. At $T_A = 500$°C this process takes up to 48 h while at 900°C it takes less than 2 min. By comparing the evolution of X-ray photoelectron spectroscopy, electron energy-loss spectroscopy, and Raman spectra during annealing, pyridine-like and graphite-like N as well as nitriles can be distinguished. For $T_A > 800$°C, preferentially pyridine-like N and –C≡N are lost from the films, mainly in the form of molecular N_2 and C_2N_2, while graphite-like N is preserved for the longest period. Due to graphitization, the hardness of the material decreases upon annealing; however, the elastic recovery actually increases slightly. This shows that the high elastic response of fullerene-like CN_x films can be largely attributed to the graphitic basal plane structure. However, the annealing does not promote the formation of cross-links between the planes, and therefore the overall deformation resistance degrades if annealed at too high temperatures.

The trends discussed here were the same for all carbon nitride films, regardless of the deposition temperature. However, film properties appeared to be stable to at least that temperature. This means that a film grown at 500°C can be operated at

that temperature without having the material properties degraded. Films grown at 100°C, however, cannot be operated at temperatures exceeding ~300°C. Caution should, however, be taken if the film is being operated in the presence of oxygen or hydrogen, since these elements can react with the film and promote decomposition. Fernández-Ramos *et al*. defined the temperature limit for practical use of CN_x films in air to be 300°C.[145] This temperature is largely sufficient for many important applications, such as wear-protective coatings on components for light load application, e.g., hard disks and recorder heads. As soon as higher loads are applied, their contact pressure equivalent to temperature must be considered.

7. OXIDATION

7.1. Alloying of Hard Coatings to Improve Oxidation Resistance

Hard coatings should also be designed for chemical stability and oxidation resistance for a given application. Since these processes are thermally activated, we should consider them in the context of this chapter. The oxidation resistance has up to now been considered as the key factor for the improvement in mechanical properties and cutting performance of TiN-based coatings. Compared to TiN, TiC, Ti(C,N), and CrN, $Ti_{1-x}Al_xN$ coatings have better oxidation resistance, higher hardness, and remain stable at higher temperatures.[120–124,146–148] This alloying approach is reflected in hard coating technology, where the general trend during recent years in improving the properties of $Ti_{1-x}Al_xN$ has been to increase the Al content of the coating so as to promote the formation of an alleged protective outer Al_2O_3 layer during tool operation, while avoiding phase separation into a two-phase equilibrium structure (fcc-TiN and hcp-AlN) with TiO_2 formation during deposition. While the high-temperature oxidation of TiN to rutile TiO_2 is pseudolinear with spallation of oxide layer due to the increased molar volume of TiO_2 compared to TiN,[40,149] $Ti_{1-x}Al_xN$, however, has a parabolic oxidation rate constant that gives the passive double layer. Oxidation of $Ti_{0.5}Al_{0.5}N$ proceeds by outward diffusion of Al to form Al-rich oxide at the topmost surface and inward diffusion of O to form Ti-rich oxide at the interface to $Ti_{1-x}Al_xN$.[40] The oxidation mechanisms behind the formation of an outer Al_2O_3 and inner TiO_2 layer were worked out in the 1980s.[49,125,150] It has, however, not been made clear whether the contact zone between cutting insert and workpiece in continuous cutting is actually exposed to atmospheric oxygen.

Also, thermal stresses during usage of the coated objects can affect the coating integrity. For example, McIntyre *et al*.[40] have shown that the failure during high-temperature oxidation of $Ti_{0.5}Al_{0.5}N$ coatings deposited on stainless steel substrates occurs through crack formation in the films. The tensile stress caused by the larger thermal expansion coefficient of the substrate compared to the film was found to be high enough to initiate crack formation in the films when heated

to temperatures above 800°C after deposition. However, it was also demonstrated that in this case, the cracking resistance of the films and thus their oxidation protective properties were considerably increased. This happened because of a built-in compressive stress level in the *as-deposited* films, obtained by applying a negative substrate bias during growth. However, if the coating is subjected to thermal cycling during application, e.g., in interrupted cutting or die casting, the compressive stresses should be limited to moderate values. Otherwise the tensile stress introduced during the cooling phase in the near-surface zone below the coating is increased by the tensile component balancing the compressive stress of a well-adherent coating, giving rise to early failure of the near-surface zone.[151]

Coating stresses have also been shown to affect the oxidation resistance via the mobility of diffusing species in, e.g., sputtered CrN coatings. Tensile stresses caused by the formation of voids or vacancies during coating growth favor diffusion, thus yielding lower values for the apparent activation energy for oxidation compared to coatings under compressive stress.[152]

Münz and coworkers have shown that additions of alloying elements Cr and Y can further reduce the oxidation rate of $Ti_{1-x}Al_xN$ coatings and make them stable up to above 950°C.[129,153] The incorporation of Y reduces the oxide layer thickness from ~3000 nm for $Ti_{0.43}Al_{0.53}Cr_{0.03}N$ to ~300 nm for $Ti_{0.43}Al_{0.52}Cr_{0.03}Y_{0.02}N$ after 1-h exposure at 950°C,[131] where the path along column boundaries for indiffusion of oxygen and outdiffusion of substrate elements is blocked by segregation of Y and YO_x (see Section 6).[153]

The addition of Si to TiN-based hard coatings results in an increased oxidation resistance due to SiO_2 formation; however, the mass gain during oxidation is considerably higher compared to $Ti_{1-x}Al_xN$.[154] A comparison of the oxide layer thickness of nanocomposite TiN–Si_3N_4 coatings with different amounts of Si_3N_4 at temperatures between 600 and 1000°C in air showed that coatings with high Si contents oxidize with high apparent activation energies up to a certain temperature, above which accelerated oxidation with an activation energy typical for TiN takes place. This transition temperature is a function of the Si content of the coating, i.e., the thicker the amorphous Si_3N_4 layer is, the longer it takes the oxygen to reach the encapsulated TiN nanocrystals. Once oxidation of TiN commences, cracking of the Si-rich oxide occurs, giving rise to further access of oxygen and acceleration of oxidation.[108,155] From coating application aspects, the as-formed SiO_2 layer is apt to evaporate due to a relatively high vapor pressure at temperatures above 850°C.

Similar to Si, B incorporation into TiN coatings causes an improvement of the oxidation resistance, but is less effective compared to Al.[20] For nanocomposite TiC–TiB_2 coatings, catastrophic failure during TGA occurred at 650–760°C. These coatings deposited onto stainless steel have been shown to be completely oxidized after air exposure at 900°C for 2 h, with rutile TiO_2, B_2O_3, and Fe_2O_3 phases formed. The TiB_2 and TiC components oxidize in sequence, with apparent activation energies of 1.33 and 1.53 eV, respectively.[141]

7.2. Self-Adaptation by Oxidation

Recently, several approaches have been suggested to improve the tribological properties of hard coatings by tailoring their oxidation behavior. Examples for these developments, which could be used to add functional self-adaptive features to the structural properties of hard coatings, are summarized below. All of these attempts are based on the assumption that the contact zone between cutting tool and workpiece is exposed to oxygen, which is true for, e.g., interrupted cutting, but not verified yet in other cases.

The unavoidable Cl impurities in TiN coatings deposited by PACVD using $TiCl_4$ as precursor cause a significant decrease of the oxidation resistance compared to PVD coatings (i.e., without Cl).[20] However, it has recently been shown that these Cl impurities have some concurrent beneficial effects on the coating constitution. They exhibit, on the one hand, grain refinement by continuous renucleation during growth.[156] On the other hand, in humid air, the formation of a thin rutile layer is stimulated at the topmost surface.[157] These rutile layers provide easy-shearing crystallographic lattice planes and thus a lubrication effect in ball-on-disk testing, reducing the friction coefficient against steel from 0.7 without Cl impurities to 0.15 for Cl contents above 3 at%.[158] The low-friction effect is obtained by self-adaptation after a certain running-in distance in ball-on-disk testing, where Cl segregated to the grain boundaries is released from the coating by abrasion and then is accommodated at the contact zone. The length of the running-in distance is either determined by the Cl content itself,[159] by the hardness of the counterpart determining coating abrasion and thus Cl release,[159] and by the sliding contact conditions.[157,158] This Cl-induced low-friction effect has been demonstrated for several coating systems, e.g., TiN,[156–158,160–162] TiC_xN_{1-x},[163] and nanocomposite Ti-B-N,[164] where the Cl addition was provided by the PACVD process or by Cl ion implantation, respectively. Since one of the preconditions for this effect is the adsorbed water film on top of the coating,[157] low friction is provided for temperatures below 60°C.[158] However, the effect might be beneficial for cold working applications like deep drawing or metal forming.[165]

Rutile TiO_2 has crystallographic similarities to the Magnéli-phase oxides based on V, W, Mo, and Ti, which provide easy shear planes and low melting temperatures, making them interesting candidates for high-temperature lubrication. Recently, it has been proposed to employ the V_2O_5 Magnéli-phase by thermo- and tribo-oxidation of sputtered VN coatings, which start to oxidize at 520°C. The formed V_2O_5 phase melts at 660°C providing a liquid oxide film in the contact zone in ball-on-disk testing.[37] The liquid oxide lubrication effect reduces the friction coefficient obtained at 700°C against steel and alumina to below 0.2. The low-friction concept based on the oxidation $VN \rightarrow V_2O_5$ has been applied to improve the tribological properties of $Ti_{1-x}Al_xN$ coatings, either in the form of $Ti_{1-x}Al_xN$/VN superlattices[166–169] or $Ti_{1-x}Al_xN$ coatings alloyed with V.[170] V_2O_5 formation and the lubrication effect have been confirmed; however, due to the reduction of V_2O_5

to higher melting oxide phases like VO_2 during exposure,[171] the low-friction effect is limited with time.[169] Nevertheless, the concept may be advantageous for lubrication at high temperatures, e.g., during dry cutting, where other solid lubricants begin to fail in their effectiveness due to environmental degradation,[172] providing functional behavior of hard coatings.

8. CONCLUSIONS AND OUTLOOK

There is a growing interest in the studies of thermal stability of nanostructured wear-resistant coatings, in particular for the transition metal nitrides due to their widespread application in wear protection. Research in these directions is also motivated by other applications such as nuclear fuel material, diffusion barriers, laser diodes, or electrical contacts where elevated temperatures are implicit. It is further an incentive to design materials with retained thermal stability by means of self-organization during operation of a coated component or tool. This structural modification can be controlled by studying the secondary phase transformations and reactions that take place on the nanometer scale in coatings grown in a metastable state.

Softening and loss of performance of wear-resistant nanostructured coatings when exposed to elevated temperatures occur via diffusion-controlled mechanisms like stress relaxation by recovery, recrystallization and grain coarsening, interdiffusion of the individual layers or phases in nanolaminate or nanocomposite coatings, or oxidization. Diffusion measurements in ceramic materials with their very high melting points are, however, difficult to perform. Furthermore, many of these materials are largely nonstoichiometric and contain impurities or growth-induced defects depending on the synthesis processes. To follow and predict the resulting phase transformations becomes a correspondingly demanding task, due to a common lack of characterization of the composition, bonding, and structure at the nanometer level. From this perspective, even TiN constitutes a quite complex system, notwithstanding carbonitrides or metal alloy nitrides, e.g., Ti(C,N) and $Ti_{1-x}Al_xN$—as the simplest examples—that are now part of the coating market. It is reassuring that the analysis instrumentation, e.g., analytical electron microscopy, is under rapid development such that it will offer unsurpassed capability to address the above problems in the next few years.

The stress relaxation rate in coatings during thermal annealing (recovery) is a strong function of the *as-deposited* material stress level, which is influenced by the deposition temperature and bias voltage in PVD or PACVD processing. The final stress state of the film is due to both short-range momentum transfer processes in the ion collision cascade during deposition and thermally activated point-defect transport and agglomeration. Essentially nothing is known about the nature of point defects or defect clusters that form in the coatings synthesized by

ion-assisted deposition techniques. This is potentially limiting the full exploitation of nanostructured coatings, since residual stress engineering, phase selectivity, or grain size design is of concern. Stress recovery during deposition is generally greater than during postdeposition anneals at the same temperature, due to the larger degrees of freedom for adatom diffusion and defect annihilation near a free surface. The kinetics of stress recovery has been described in just a few cases and materials. Typically, there is a range of defects with different activation energies for effective recovery. In fact, defect annihilation takes place in the order of their stability during annealing. For the compressive stress relaxation in nitrides, a range of apparent activation energy values are found below that for self-diffusion. We submit that residual stress engineering with a retained thermal stability is an important field for future research in coating technology.

Recrystallization and grain coarsening leading to the loss of the precondition for mechanical hardness enhancement in nanolaminates or nanocomposites is driven by their high interfacial energy stored. Again, more detailed studies on the influence of the interface on the thermal stability are needed to exploit the full potential of nanostructured coatings.

The revelation that *thin films* can be age hardened through spinodal decomposition or by nucleation and growth (precipitation) in secondary phase transformation has vast technological importance for the design of next generations of wear-resistant coatings by advanced surface engineering. These sorts of transformations are expected to occur in several of the ternary, quaternary, and multinary transition metal nitride based systems, as they exhibit miscibility gaps and can be processed by state-of-the-art vapor deposition processes in such metastable states.

Application of hard coatings exposes them not only to high temperatures, but also to oxygen-containing environments. Oxidation has been studied for a huge variety of coating materials where onset temperatures and the weight gain have been determined. However, detailed studies on the oxidation mechanisms and their apparent activation energies are rare, although these data will allow designing coatings with a tailored response to the thermal load applied, e.g., where dense oxide scales formed prevent indiffusion of workpiece atoms or provide lubricious properties. Also dynamic experiments need to be performed in addition to static ones, in order to establish the access and relevance of oxygen to the contact zone in, e.g., cutting operation.

From industrial interest in increased cutting speed and feeding rate, as well as for dry cutting, there is consequently a demand for coatings that can withstand high temperatures. To enable further developments in this area, diffusion-related phenomena controlling recovery, recrystallization, segregation, grain growth, interdiffusion, and oxidation have to be studied in much more detail, in particular for the exploitation of nonequilibrium-state wear-resistant coatings. Such data will be an important input to calculate the lifetime of a coating and to select cutting data for a given application. This is nanoscience and nanotechnology at work.

ACKNOWLEDGMENTS

LH acknowledges support from the Swedish Research Council (VR) and the Swedish Foundation for Strategic Research (SSF) Material Research Program on *Low-Temperature Thin Film Synthesis*. Part of the work done at the University of Leoben was financially supported by the Technologie Impulse GmbH in the frame of the *K-plus Competence Center* program.

REFERENCES

1. J. M. Schneider, S. L. Rhode, W. D. Sproul, and A. Matthews, Recent envelopments in plasma assisted physical vapour deposition, *J. Phys. D Appl. Phys.* 33, R173–R186 (2000).
2. S. S. Eskildsen, C. Mathiasen, and M. Foss, Plasma CVD: Process capabilities and economic aspects, *Surf. Coat. Technol.* 116–119, 18–23 (1999).
3. J. D. Verhoeven, *Fundamentals of Physical Metallurgy* (Wiley, New York, 1975).
4. E. Arzt, Size effects in materials due to microstructural and dimensional constraints: A comparative review, *Acta Mater.* 46, 5611–5626 (1998).
5. P. H. Mayrhofer, A. Hörling, L. Karlsson, J. Sjölén, T. Larsson, C. Mitterer, and L. Hultman, Self-organized nanostructures in the Ti–Al–N system, *Appl. Phys. Lett.* 83, 2049–2051 (2003).
6. S. Vepřek, The search for novel, superhard materials, *J. Vac. Sci. Technol. A* 17, 2401–2420 (1999).
7. A. A. Voevodin and J. S. Zabinski, Supertough wear-resistant coatings with "chameleon" surface adaptation, *Thin Solid Films* 370, 223–231 (2000).
8. J.-E. Sundgren, Structure and properties of TiN coatings, *Thin Solid Films* 128, 21–44 (1985).
9. V. Derflinger, H. Brändle, and H. Zimmermann, New hard/lubricant coating for dry machining, *Surf. Coat. Technol.* 113, 286–292 (1999).
10. J. Kopac, M. Sokovic, and S. Dolinsek, Tribology of coated tools in conventional and HSC machining, *J. Mater. Process. Technol.* 118, 377–384 (2001).
11. H. O. Gekonde and S. V. Subramanian, Tribology of tool–chip interface and tool wear mechanisms, *Surf. Coat. Technol.* 149, 151–160 (2002).
12. P. A. Dearnley and E. M. Trent, Wear mechanisms of coated carbide tools, *Met. Technol.* 9, 60–75 (1982).
13. H.-D. Liu, Y.-P. Zhao, G. Ramanath, S. P. Murarka, and G.-C. Wang, Thickness dependent electrical resistivity of ultrathin (<40 nm) Cu films, *Thin Solid Films* 384, 151–156 (2001).
14. P. H. Mayrhofer, F. Kunc, J. Musil, and C. Mitterer, A comparative study on reactive and non-reactive unbalanced magnetron sputter deposition of TiN coatings, *Thin Solid Films* 415, 151–159 (2002).
15. L. Karlsson, L. Hultman, and J.-E. Sundgren, Influence of residual stresses on the mechanical properties of TiC_xN_{1-x} ($x = 0$, 0.15, 0.45) thin films deposited by arc evaporation, *Thin Solid Films* 371, 167–177 (2000).
16. L. Karlsson, A. Hörling, M. P. Johansson, L. Hultman, and G. Ramanath, The influence of thermal annealing on residual stresses and mechanical properties of arc-evaporated TiC_xN_{1-x} ($x = 0$, 0.15 and 0.45) thin films, *Acta Mater.* 50, 5103–5114 (2002).
17. P. H. Mayrhofer, G. Tischler, and C. Mitterer, Microstructure and mechanical/thermal properties of Cr-N coatings deposited by reactive unbalanced magnetron sputtering, *Surf. Coat. Technol.* 142–144, 78–84 (2001).
18. J. D. Wilcock and D. S. Campbell, A sensitive bending beam apparatus for measuring the stress in evaporated thin films, *Thin Solid Films* 3, 3–12 (1969).

19. P. H. Mayrhofer and C. Mitterer, Structure/property relations in PVD hard coatings, in *Recent Research Developments in Vacuum Science & Technology*, Vol. 4, edited by S. G. Pandalai (Transworld Research Network, Trivandrum, 2003), pp. 71–97.
20. P. H. Mayrhofer and C. Mitterer, High-temperature properties of nanocomposite TiB_xN_y and TiB_xC_y coatings, *Surf. Coat. Technol.* 133–134, 131–137 (2000).
21. C. Mitterer, F. Holler, F. Üstel, and D. Heim, Application of hard coatings in aluminium die casting—soldering, erosion and thermal fatigue behaviour, *Surf. Coat. Technol.* 125, 233–239 (2000).
22. A. C. Damask and G. J. Dienes, *Point Defects in Metals* (Gordon and Breach, New York, 1963).
23. J. Almer, M. Odén, L. Hultman, and G. Håkansson, Microstructural evolution during tempering of arc-evaporated Cr–N coatings, *J. Vac. Sci. Technol. A* 18, 121–130 (2000).
24. E. J. Mittemeijer, L. Cheng, P. J. van der Schaaf, C. M. Brakman, and B. M. Korevaar, Analysis of nonisothermal transformation kinetics; tempering of iron–carbon and iron–nitrogen martensites, *Met. Trans. A* 19, 925–932 (1988).
25. M. E. Brown, Principles and practice, in *Handbook of Thermal Analysis and Calorimetry*, Vol. 1 (Elsevier, Amsterdam, 1998).
26. P. H. Mayrhofer, H. Willmann, and C. Mitterer, Recrystallization and grain growth of nanocomposite Ti-B-N coatings, *Thin Solid Films* 440, 174–179 (2003).
27. H. E. Kissinger, Reaction kinetics in differential thermal analysis, *Anal. Chem.* 29, 1702–1706 (1957).
28. K. Lu, Z. F. Dong, I. Bakonyi, and A. Cziraki, Thermal stability and grain growth of a melt-spun $HfNi_5$ nanophase alloy, *Acta Met. Mater.* 43, 2641–2647 (1995).
29. K. Hauffe, *Oxidation of Metals*, (Plenum, New York, 1965).
30. S. M. Rossnagel, Energetic particle bombardment of films during magnetron sputtering, *J. Vac. Sci. Technol. A* 7, 1025–1029 (1989).
31. C. A. Davis, A simple model for the formation of compressive stress in thin films by ion bombardment, *Thin Solid Films* 226, 30–34 (1993).
32. H. Windischmann, An intrinsic stress scaling law for polycrystalline thin films prepared by ion beam sputtering, *J. Appl. Phys.* 62, 1800–1807 (1987).
33. H. Oettel, R. Wiedemann, and S. Preissler, Residual stresses in nitride hard coatings prepared by magnetron sputtering and arc evaporation, *Surf. Coat. Technol.* 74, 273–278 (1995).
34. W. Herr and E. Broszeit, The influence of a heat treatment on the microstructure and mechanical properties of sputtered coatings, *Surf. Coat. Technol.* 97, 335–340 (1997).
35. A. J. Perry, On the existence of point defects in physical vapor deposited films of TiN, ZrN, and HfN, *J. Vac. Sci. Technol. A* 6, 2140–2148 (1988).
36. C. Mitterer, P. H. Mayrhofer, and J. Musil, Thermal stability of PVD hard coatings, *Vacuum* 71, 279–284 (2003).
37. G. Gassner, P. H. Mayrhofer, K. Kutschej, C. Mitterer, and M. Kathrein, A new low friction concept for high temperatures: Liquid oxide formation on sputtered VN coatings, *Tribol. Lett.* 17, 751–756 (2004).
38. P. H. Mayrhofer, C. Mitterer, J. Wen, J. E. Greene, and I. Petrov, Self-organized nanocolumnar structure in superhard TiB_2 thin films, *Appl. Phys. Lett.* 86, 131909–131911 (2005).
39. S. S. PalDey and C. Deevi, Single layer and multilayer wear resistant coatings of (Ti,Al)N: A review, *Mater. Sci. Eng. A* 341, 58–79 (2003).
40. D. McIntyre, J. E. Greene, G. Håkansson, J.-E. Sundgren, and W.-D. Münz, Oxidation of metastable single-phase polycrystalline $Ti_{0.5}Al_{0.5}N$ films: Kinetics and mechanisms, *J. Appl. Phys.* 67, 1542–1553 (1990).
41. F. Adibi, I. Petrov, L. Hultman, U. Wahlström, T. Shimizu, D. McIntyre, J. E. Greene, and J.-E. Sundgren, Defect structure and phase transitions in epitaxial metastable cubic $Ti_{0.5}Al_{0.5}N$ alloys grown on MgO(001) by ultra-high-vacuum magnetron sputter deposition, *J. Appl. Phys.* 69, 6437–6450 (1991).

42. R. Kaspi, L. Hultman, and S. A. Barnett, Growth of InGaAsSb layers in the miscibility gap: Use of very-low-energy ion irradiation to reduce alloy decomposition, *J. Vac. Sci. Technol. B* 13, 978–987 (1995).
43. T. Seppänen, G. Z. Radnoczi, S. Tungasmita, L. Hultman, and J. Birch, Growth and characterization of epitaxial wurtzite $Al_{1-x}In_xN$ thin films deposited by UHV reactive dual DC magnetron sputtering, *Mater. Sci. Forum* 433–436, 987–990 (2003).
44. H. Holleck, Metastable coatings—Prediction of composition and structure, *Surf. Coat. Technol.* 36, 151–159 (1988).
45. L. A. Donohue, D. B. Lewis, W.-D. Münz, M. M. Stack, S. B. Lyon, H.-W. Wang, and D. Rafaja, The influence of low concentrations of chromium and yttrium on the oxidation behaviour, residual stress and corrosion performance of TiAlN hard coatings on steel substrates, *Vacuum* 55, 109–114 (1999).
46. C.-M. Suh, B.-W. Hwang, and R.-I. Murakami, Behaviors of residual stress and high-temperature fatigue life in ceramic coatings produced by PVD, *Mater. Sci. Eng. A* 343, 1–7 (2003).
47. H. Holleck, Neue Entwicklungen bei PVD-Hartstoffschichten, *Metall* 7, 614–624 (1989).
48. P. B. Barna, Crystal growth and recrystallization during structure evolution of thin films, in *Diagnostics and Applications of Thin Films*, edited by L. Eckertová and T. Ruzicka (Institute of Physics Publishing, Bristol, 1992), pp. 295–310.
49. S. Vepek and S. Reiprich, A concept for the design of novel superhard coatings, *Thin Solid Films* 268, 64–71 (1995).
50. C. Mitterer, P. H. Mayrhofer, M. Beschliesser, P. Losbichler, P. Warbichler, F. Hofer, P. N. Gibson, W. Gissler, H. Hruby, J. Musil, and J. Vlček, Microstructure and properties of nanocomposite Ti-B-N and Ti-B-C coatings, *Surf. Coat. Technol.* 120–121, 405–411 (1999).
51. J. Musil, J. Vlček, P. Zeman, Y. Setsuhara, S. Miyake, S. Konuma, M. Kumagai, and C. Mitterer, Morphology and microstructure of hard and superhard Zr-Cu-N nanocomposite coatings, *Jpn. J. Appl. Phys.* 41, 6529–6533 (2002).
52. J. Schiøtz, T. Vegge, F. D. DiTolla, and K. W. Jacobson, Atomic-scale simulations of the mechanical deformation of nanocrystalline metals, *Phys. Rev. B Condens. Matter* 60, 11971–11983 (1999).
53. A. Niederhofer, P. Nesládek, H.-D. Männling, K. Moto, S. Vepřek, and M. Jílek, Structural properties, internal stress and thermal stability of nc-TiN/a-Si_3N_4, nc-TiN/$TiSi_x$ and nc-$(Ti_{1-y}Al_ySi_x)N$ superhard nanocomposite coatings reaching the hardness of diamond, *Surf. Coat. Technol.* 120–121, 173–178 (1999).
54. F. Kauffmann, *Mikrostruktur und Eigenschaften von Titannitrid/Siliciumnitrid-Schichten*, Ph.D. Dissertation (University of Stuttgart, Stuttgart, Germany, 2003).
55. H.-D. Männling, D. S. Patil, K. Moto, M. Jílek, and S. Vepřek, Thermal stability of superhard nanocomposite coatings consisting of immiscible nitrides, *Surf. Coat. Technol.* 146–147, 263–267 (2001).
56. P. Karvánková, H.-D. Männling, C. Eggs, and S. Vepek, Thermal stability of ZrN–Ni and CrN–Ni superhard nanocomposite coatings, *Surf. Coat. Technol.* 146–147, 280–285 (2001).
57. H. Zeman, J. Musil, J. Vlček, P. H. Mayrhofer, and C. Mitterer, Thermal annealing of sputtered Al-Si-Cu-N films, *Vacuum* 72, 21–28 (2004).
58. U. Helmersson, S. Todorova, S. A. Barnett, J.-E. Sundgren, L. C. Markert, and J. E. Greene, Growth of single-crystal TiN/VN strained-layer superlattices with extremely high mechanical hardness, *J. Appl. Phys.* 62, 481–484 (1987).
59. P. Eh. Hovsepian and W.-D. Münz, Recent progress in large-scale production of nanoscale multilayer/superlattice hard coatings, *Vacuum* 69, 27–36 (2002).
60. H. Ljungcrantz, C. Engström, L. Hultman, M. Olsson, X. Chu, M. S. Wong, and W. D. Sproul, Nanoindentation hardness, abrasive wear, and microstructure of TiN/NbN polycrystalline nanostructured multilayer films grown by reactive magnetron sputtering, *J. Vac. Sci. Technol. A* 16, 3104–3113 (1998).

61. H. Holleck, M. Lahres, and P. Woll, Multilayer coatings—Influence of fabrication parameters on constitution and properties, *Surf. Coat. Technol.* 41, 179–190 (1990).
62. P. Eh. Hovsepian, D. B. Lewis, and W.-D. Münz, Recent progress in large scale manufacturing of multilayer/superlattice hard coatings, *Surf. Coat. Technol.* 133–134, 166–175 (2000).
63. S. Vitta and P. Yang, Thermal stability of 2.4 nm period Ni–Nb/C multilayer x-ray mirror, *Appl. Phys. Lett.* 77, 3654–3656 (2000).
64. H. L. Bai, Q. H. Guo, Z. J. He, W. B. Mi, P. Wu, Z. D. Li, and E. Y. Jiang, Interdiffusion in low-temperature annealed amorphous CoMoN/CN compound soft-X-ray optical multilayer mirrors, *J. Phys. Condens. Matter* 15, 1235–1246 (2003).
65. J. B. Kortright, St. Joksch, and E. Ziegler, Stability of tungsten/carbon and tungsten/silicon multilayer x-ray mirrors under thermal annealing and x-radiation exposure, *J. Appl. Phys.* 69, 168–174 (1991).
66. M. Setoyama, M. Irie, H. Ohara, M. Tsujioka, Y. Takeda, T. Nomura, and N. Kitagawa, Thermal stability of TiN/AlN superlattices, *Thin Solid Films* 341, 126–131 (1999).
67. A. Gleiter, Nanostructured materials: Basic concepts and microstructure, *Acta Mater.* 48, 1–29 (2000).
68. H. S. Kim and M. B. Bush, The effects of grain size and porosity on the elastic modulus of nanocrystalline materials, *Nanostruct. Mater.* 11, 361–367 (1999).
69. R. Dannenberg, E. A. Stach, J. R. Groza, and B. J. Dresser, In-situ TEM observations of abnormal grain growth, coarsening, and substrate de-wetting in nanocrystalline Ag thin films, *Thin Solid Films* 370, 54–62 (2000).
70. L. Hultman, Thermal stability of nitride thin films, *Vacuum* 57, 1–30 (2000).
71. C. Héau, R. Y. Fillit, F. Vaux, and F. Pascaretti, Study of thermal stability of some hard nitride coatings deposited by reactive magnetron sputtering, *Surf. Coat. Technol.* 120–121, 200–205 (1999).
72. P. Wilhartitz, S. Dreer, and P. Ramminger, Can oxygen stabilize chromium nitride?—Characterization of high temperature cycled chromium oxynitride, *Thin Solid Films* 447–448, 289–295 (2004).
73. A. Hörling, L. Hultman, M. Odén, J. Sjölén, and T. Karlsson, Thermal stability of arc evaporated high aluminum-content $Ti_{1-x}Al_xN$ thin films, *J. Vac. Sci. Technol. A* 20, 1815–1823 (2002).
74. S. Vepřek, H. D. Männling, M. Jílek, and P. Holubar, Avoiding the high-temperature decomposition and softening of $(Al_{1-x}Ti_x)N$ coatings by the formation of stable superhard nc-$(Al_{1-x}Ti_x)N$/a-Si_3N_4 nanocomposite, *Mater. Sci. Eng. A* 366, 202–205 (2004).
75. H. Schmidt, W. Gruber, G. Borchardt, M. Bruns, M. Rudolphi, and H. Baumann, Thermal stability and crystallization kinetics of sputtered amorphous Si_3N_4 films, *Thin Solid Films* 450, 346–351 (2004).
76. P. Karvánková, M. G. J. Vepek-Heijman, O. Zindulka, A. Bergmaier, and S. Vepřek, Superhard nc-TiN/a-BN and nc-TiN/a-TiB_x/a-BN coatings prepared by plasma CVD and PVD: A comparative study of their properties, *Surf. Coat. Technol.* 163–164, 149–156 (2003).
77. A. Tarniowy, R. Mania, and M. Rekas, The effect of thermal treatment on the structure, optical and electrical properties of amorphous titanium nitride thin films, *Thin Solid Films* 311, 93–100 (1997).
78. R. Kirchheim, Grain coarsening inhibited by solute segregation, *Acta Mater.* 50, 413–419 (2002).
79. F. Elstner, H. Kupfer, and F. Richter, Activation energy of point defect diffusion in low-temperature deposited TiN, *Phys. Status Solidi A* 147, 373–377 (1995).
80. P. H. Mayrhofer, Thermal stability and self arrangement of nanocrystalline hard coatings, in *Nanostructured Thin Films and Nanodispersion Strengthened Coatings*, *NATO Science Series II: Mathematics, Physics and Chemistry*, edited by A. A. Voevodin, D. V. Shtansky, E. A. Levashov, and J. J. Moore (Kluwer, Amsterdam, 2004), pp. 57–68.
81. P. H. Mayrhofer, C. Mitterer, J. G. Wen, I. Petrov, and J. E. Greene, Thermally-induced self-hardening of nanocrystalline Ti-B-N thin films, *J. Appl. Phys.*, accepted.

82. T. P. Mollart, M. Baker, J. Haupt, A. Steiner, P. Hammer, and W. Gissler, Nanostructured titanium boron nitride coatings of very high hardness, *Surf. Coat. Technol.* 74–75, 491–496 (1995).
83. S. A. Barnett, A. Madan, I. Kim, and K. Martin, Stability of nanometer-thick layers in hard coatings, *MRS Bull.* 28, 169–172 (2003).
84. P. B. Mirkarimi, L. Hultman, and S. A. Barnett, Enhanced hardness in lattice-matched single-crystal $TiN/V_{0.6}Nb_{0.4}N$ superlattices, *Appl. Phys. Lett.* 57, 2654–2656 (1990).
85. X. Chu and S. A. Barnett, Model of superlattice yield stress and hardness enhancements, *J. Appl. Phys.* 77, 4403–4411 (1995).
86. A. Madan, Y. Y. Wang, S. A. Barnett, C. Engström, H. Ljungcrantz, L. Hultman, and M. Grimsditch, Enhanced mechanical hardness in epitaxial nonisostructural Mo/NbN and W/NbN superlattices, *J. Appl. Phys.* 84, 776–785 (1998).
87. X. Chu, M.-S. Wong, W. D. Sproul, and S. A. Barnett, Deposition, structure, and hardness of polycrystalline transition-metal nitride superlattice films, *J. Mater. Res.* 14, 2500–2507 (1999).
88. V. Rigato, A. Patelli, G. Maggioni, G. Salmaso, V. Mattarello, M. G. Pelizzo, P. Nicolosi, L. Depero, E. Bontempi, and P. Mazzoldi, Effects of ion bombardment and gas incorporation on the properties of Mo/a-Si:H multilayers for EUV applications, *Surf. Coat. Technol.* 174–175, 40–48 (2003).
89. S. Lopez, M.-S. Wong, and W. D. Sproul, Thermal behavior of carbon nitride and TiN/NbN superlattice films, *J. Vac. Sci. Technol. A* 13, 1644–1648 (1995).
90. I. Wadsworth, I. J. Smith, L. A. Donohue, and W.-D. Münz, Thermal stability and oxidation resistance of TiAlN/CrN multilayer coatings, *Surf. Coat. Technol.* 94–**95**, 315–321 (1997).
91. C. Engström, J. Birch, L. Hultman, C. Lavoie, C. Cabral, and J. Jordan-Sweet, Interdiffusion studies of single crystal TiN/NbN superlattice thin films, *J. Vac. Sci. Technol. A* **17**, 2920–2927 (1999).
92. L. Hultman, C. Engström, and M. Odén, Mechanical and thermal stability of TiN/NbN superlattice thin films, *Surf. Coat. Technol.* 133–134, 227–233 (2000).
93. T. Yamamoto, S. Kikkawa, M. Takahashi, Y. Miyamoto, and F. Kanamaru, High pressure synthesis of B1-type solid solutions $Nb_{1-x}M_xN$ (M = Ga, Ti), *Physica C* 185–189, 2719–2720 (1991).
94. H. Holleck, *Binäre and Ternäre Carbid- und Nitridsysteme der Übergangsmetalle* (Gebrüder Borntraeger, Berlin, 1994).
95. C. Engström, A. Madan, J. Birch, M. Nastasi, L. Hultman, and S. A. Barnett, High-temperature stability of epitaxial, non-isostructural Mo/NbN superlattices, *J. Mater. Res.* 15, 554–559 (2000).
96. D. Li, X. Chu, C. Cheng, W. Lin, V. P. Dravid, Y. W. Chung, M. S. Wong, and W. D. Sproul, Synthesis of superhard carbon nitride composite coatings, *Appl. Phys. Lett.* 67, 203–205 (1995).
97. D. Li, W. Lin, C. Cheng, V. P. Dravid, Y. W. Chung, M. S. Wong, and W. D. Sproul, Structure and hardness studies of CN_x/TiN nanocomposite coatings, *Appl. Phys. Lett.* 68, 1211–1213 (1996).
98. M. L. Wu, W. W. Lin, V. P. Dravid, Y. W. Chung, M. S. Wong, and W. D. Sproul, Preparation and characterization of superhard CN_x/ZrN multilayers, *J. Vac. Sci. Technol. A* 15, 946–950 (1997).
99. K. Martin, Structure, mechanical properties, and high temperature stability of nanolayered titanium nitride/titanium diboride and zirconium nitride/zirconium diboride thin films, Ph.D. Dissertation (Northwestern University, Evanston, IL, 2001).
100. J. W. Cahn, On spinodal decomposition, *Acta Metall.* 9, 795–801 (1961).
101. E. Rudy, Boundary phase stability and critical phenomena in higher order solid solution systems, *J. Less-Common Met.* 33, 43–70 (1973).
102. L. Hultman, Transmission electron microscopy of metastable materials, *Key Eng. Mater.* 103, 181–195 (1995).
103. O. Knotek and A. Barimani, On spinodal decomposition in magnetron-sputtered (Ti,Zr) nitride and carbide thin films, *Thin Solid Films* 174, 51–56 (1989).
104. R. A. Andrievski, I. A. Anisimova, and V. P. Anisimov, Structure and microhardness of TiN compositional and alloyed films, *Thin Solid Films* 205, 171–175 (1991).

105. R. A. Andrievski, Films of interstitial phases: Synthesis and properties, *J. Mater. Sci*. 32, 4463–4484 (1997).
106. R. A. Andrievski, Review: Stability of nanostructured materials, *J. Mater. Sci*. 38, 1367–1375 (2003).
107. R. Prange, R. Cremer, and D. Neuschütz, Plasma-enhanced CVD of (Ti,Al)N films from chloridic precursors in a DC glow discharge, *Surf. Coat. Technol*. 133, 208–214 (2000).
108. J. Patscheider, T. Zehnder, and M. Diserens, Structure–performance relations in nanocomposite coatings, *Surf. Coat. Technol*. 146, 201–208 (2001).
109. P. Holubar, M. Jílek, and M. Sima, Present and possible future applications of superhard nanocomposite coatings, *Surf. Coat. Technol*. 133–134, 145–151 (2000).
110. J. S. Schuster and J. Bauer, The ternary system titanium–aluminum–nitrogen, *J. Solid State Chem*. 53, 260–265 (1984).
111. K. Kutschej, P. H. Mayrhofer, M. Kathrein, P. Polcik, R. Tessadri, and C. Mitterer, Structure, mechanical and tribological properties for sputtered $Ti_{1-x}Al_xN$ coatings with $0.5 \leq x \leq 0.75$, *Surf. Coat. Technol*., **200**, 2358–2365 (2005).
112. S. Kodambaka, V. Petrova, A. Vailionis, P. Desjardins, D. G. Cahill, I. Petrov, and J. E. Greene, TiN(001) and TiN(111) island coarsening kinetics: In-situ scanning tunneling microscopy studies, *Thin Solid Films* 392, 164–168 (2001).
113. A. Hörling, L. Hultman, M. Odén, J. Sjölén, and L. Karlsson, Mechanical properties and machining performance of $Ti_{1-x}Al_xN$-coated cutting tools, *Surf. Coat. Technol*. 191, 384–392 (2005).
114. M. Jílek and S. Vepřek, Super- and ultrahard nanacomposite coatings: Generic concept for their preparation, properties and industrial applications, *Vacuum* 67, 443–449 (2002).
115. K. S. Kumar, H. van Swygenhoven, and S. Suresh, Mechanical behavior of nanocrystalline metals and alloys, *Acta Mater.* 51, 5743–5774 (2003).
116. K. L. Merkle and L. Thompson, Atomic-scale observation of grain boundary motion, *J. Mater. Lett*. 48, 188–193 (2001).
117. J. Schiøtz and K. W. Jacobsen, A maximum in the strength of nanocrystalline copper, *Science* 301, 1357–1359 (2003).
118. H. van Swygenhoven, Grain boundaries and dislocations, *Science* 296, 66–67 (2002).
119. J. S. Koehler, Attempt to design a strong solid, *Phys. Rev. B* 2, 547–551 (1970).
120. O. Knotek, W. Bosch, T. Leyendecker, W.-D. Münz, and R. Falkenstein, Reactive sputter properties of ion plated TiAl-nitride films, in *Special Melting/Refining and Metallurgical Coating Under Vacuum or Controlled Atmosphere*, *Proceedings of the 8th International Vacuum Metallurgy Conference*, Linz, Austria, September 30–October 4, 1985, p. 339.
121. O. Knotek, W. Bosch, and T. Leyendecker, Wear resistant Ti-Al-C-N-O films produced by sputtering, in *Special Melting/Refining and Metallurgical Coating Under Vacuum or Controlled Atmosphere*, *Proceedings of the 8th International Vacuum Metallurgy Conference*, Linz, Austria, September 30–October 4, 1985, pp. 340–352.
122. O. Knotek, M. Böhmer, and T. Leyendecker, On structure and properties of sputtered Ti and Al based hard compound films, *J. Vac. Sci. Technol. A* 4, 2695–2700 (1986).
123. H. Jehn, S. Hoffmann, V.-E. Rückborn, and W.-D. Münz, Morphology and properties of sputtered (Ti,Al)N layers on high speed steel substrates as a function of deposition temperature and sputtering atmosphere, *J. Vac. Sci. Technol. A* 4, 2701–2705 (1986).
124. W.-D. Münz, Titanium aluminum nitride films: A new alternative to TiN coatings, *J. Vac. Sci. Technol. A* 4, 2717–2725 (1986).
125. W.-D. Münz and J. Göbel, Properties of CrN and (Ti, Al)N coatings produced by high rate sputter deposition, *Surf. Eng*. 3, 47–51 (1987).
126. S. Hofmann and H. Jehn, Selective oxidation and chemical state of Al and Ti in (Ti,Al)N coatings, *Surf. Interface Anal*. 12, 329–333 (1988).
127. D.-G. Kim, T.-Y. Seong, and Y.-J. Baik, Effects of annealing on the microstructures and mechanical properties of TiN/AlN nano-multilayer films prepared by ion-beam assisted deposition, *Surf. Coat. Technol*. 153, 79–83 (2002).

128. M. Setoyama, A. Nakayama, M. Tanaka, N. Kitagawa, and T. Nomura, Formation of cubic-AlN in TiN/A1N superlattice, *Surf. Coat. Technol.* 86–87, 225–230 (1996).
129. W.-D. Münz, Large-scale manufacturing of nanoscale multilayered hard coatings deposited by cathodic arc/unbalanced magnetron sputtering, *MRS Bull.* 28, 173–179 (2003).
130. D. B. Lewis, L. A. Donohue, M. Lembke, W.-D. Münz, R. Kuzel, Jr., V. Valvoda, and C. J. Blomfield, The influence of the yttrium content on the structure and properties of $Ti_{1-x-y-z}Al_xCr_yY_zN$ PVD hard coatings, *Surf. Coat. Technol.* 114, 187–199 (1999).
131. I. Petrov, J. E. Greene, L. A. Donohue, I. J. Smith, and W.-D. Münz, Microstructure and oxidation-resistance of $Ti_{1-x-y-z}Al_xCr_yY_zN$ layers grown by combined steered-arc/unbalanced-magnetron-sputter deposition, *Surf. Coat. Technol.* 94–95, 226–231 (1997).
132. I. J. Smith, W.-D. Münz, L. A. Donohue, I. Petrov, and J. E. Greene, Improved $Ti_{1-x}Al_xN$ PVD coatings for dry high speed cutting operations, *Surf. Eng.* 14, 37–41 (1998).
133. C. Leyens, M. Peters, P. Eh. Hovsepian, D. B. Lewis, Q. Luo, and W.-D. Münz, Novel coating systems produced by the combined cathodic arc/unbalanced magnetron sputtering for environmental protection of titanium alloys, *Surf. Coat. Technol.* 155, 103–111 (2002).
134. P. Holubar, M. Jilek, and M. Sima, Nanocomposite nc-TiAlSiN and nc-TiN–BN coatings: Their applications on substrates made of cemented carbide and results of cutting tests, *Surf. Coat. Technol.* 120–121, 184–188 (1999).
135. P. Holubar, M. Jilek, and M. Sima, Present and possible future applications of superhard nanocomposite coatings, *Surf. Coat. Technol.* 133–134, 145–151 (2000).
136. G. I. Grigorov, K. G. Grigorov, M. Stojanova, J. L. Vignes, J. P. Langeron, P. Denjean, and L. Ranno, Iron diffusion from pure Fe substrate into TiN buffer layers, *Physica C* 251, 397–400 (1995).
137. D. B. Lee, M. H. Kim, Y. C. Lee, and S. C. Kwon, High temperature oxidation of TiCrN coatings deposited on a steel substrate by ion plating, *Surf. Coat. Technol.* 141, 232–239 (2001).
138. A. P. Marques and A. Cavaleiro, Structural and mechanical properties of amorphous W–Si–N sputtered films after thermal annealing, *Thin Solid Films* 441, 150–160 (2003).
139. C. Louro, A. Cavaleiro, S. Dub, P. Smid, J. Musil, and J. Vlcek, The depth profile analysis of W-Si-N coatings after thermal annealing, *Surf. Coat. Technol.* 161, 111–119 (2002).
140. C. Mitterer, M. Rauter, and P. Rödhammer, Sputter deposition of ultrahard coatings within the system Ti-B-C-N, *Surf. Coat. Technol.* 41, 351–364 (1990).
141. D. Zhong, J. J. Moore, B. M. Mishra, T. Ohno, E. A. Levashov, and J. Disam, Composition and oxidation resistance of Ti-B-C and Ti-B-C-N coatings deposited by magnetron sputtering, *Surf. Coat. Technol.* 163–164, 50–56 (2003).
142. L. Hultman, J. Neidhardt, N. Hellgren, H. Sjöström, and J.-E. Sundgren, Fullerene-like carbon nitride: A resilient coating material, *MRS Bull.* 28, 194–202 (2003).
143. N. Hellgren, N. Lin, E. Broitman, V. Serin, S. E. Grillo, R. Twesten, I. Petrov, C. Colliex, L. Hultman, and J.-E. Sundgren, Thermal stability of carbon nitride thin films, *J. Mater. Res.* 16, 3188–3201 (2001).
144. S. E. Grillo, N. Hellgren, V. Serin, E. Broitman, C. Colliex, L. Hultman, and Y. Kihn, Monitoring the structural and chemical properties of CN_x thin films during in situ annealing in a TEM, *Eur. Phys. J. Appl. Phys.* 13, 97–105 (2001).
145. C. Fernández-Ramos, M. J. Sayagués, T. C. Rojas, M. D. Alcalá, C. Real, and A. Fernández, Study of the thermal stability of carbon nitride thin films prepared by reactive magnetron sputtering, *Diamond Relat. Mater.* 9, 212–218 (2000).
146. B. F. Coll, P. Sathrum, R. Fontana, J. P. Peyre, D. Duchateau, and M. Benmalek, Optimization of arc evaporated (Ti,Al)N film composition for cutting tool applications, *Surf. Coat. Technol.* 52, 57–64 (1992).
147. W.-D. Münz, T. Hurkmans, G. Keiren, and T. Trinh, Comparison of TiAlN coatings grown by unbalanced magnetron and arc bond sputtering techniques, *J. Vac. Sci. Technol. A* 11, 2583–2589 (1993).

148. G. Beenoh-Marchwicka, L. Kröl-Stepniewska, and P. Posadowski, Structure of thin films prepared by the cosputtering of titanium and aluminium or titanium and silicon, *Thin Solid Films* 82, 313–320 (1981).
149. J. Desmaison, P. Lefort, and M. Billy, Oxidation of titanium nitride in oxygen: Behavior of $TiN_{0.83}$ and $TiN_{0.79}$ plates, *Oxid. Met.* 13, 203–222 (1979).
150. B.-J. Kim, Y.-C. Kim, J.-W. Nah, and J.-J. Lee, High temperature oxidation of $(Ti_{1-x}Al_x)N$ coatings made by plasma enhanced chemical vapor deposition, *J. Vac. Sci. Technol. A* 17, 133–137 (1999).
151. C. Mitterer, F. Holler, C. Lugmair, R. Nöbauer, R. Kullmer, and C. Teichert, Optimization of PACVD hard coatings for their application in aluminium die casting, *Surf. Coat. Technol.* 142–144, 1005–1011 (2001).
152. P. H. Mayrhofer, H. Willmann, and C. Mitterer, Oxidation kinetics of sputtered Cr-N coatings, *Surf. Coat. Technol.* 146–147, 222–228 (2001).
153. M. I. Lembke, D. B. Lewis, W.-D. Münz, and J. M. Titchmarsh, Significance of Y and Cr in TiAlN hard coatings for dry high speed cutting, *Surf. Eng.* 17, 153–158 (2001).
154. F. Vaz, L. Rebouta, P. Goudeau, J. Pacaud, H. Garem, J. P. Rivière, A. Cavaleiro, and E. Alves, Characterisation of $Ti_{1-x}Si_xN_y$ nanocomposite films, *Surf. Coat. Technol.* 133–134, 307–313 (2000).
155. M. Diserens, J. Patscheider, and F. Lévy, Mechanical properties and oxidation resistance of nanocomposite TiN–SiN_x physical-vapor-deposited thin films, *Surf. Coat. Technol.* 120–121, 158–165 (1999).
156. M. Stoiber, E. Badisch, C. Lugmair, and C. Mitterer, Low-friction TiN coatings deposited by PACVD, *Surf. Coat. Technol.* 163–164, 451–456 (2003).
157. E. Badisch, C. Mitterer, P. H. Mayrhofer, G. Mori, R. J. Bakker, J. Brenner, and H. Störi, Characterization of tribo-layers on self-lubricating PACVD TiN coatings, *Thin Solid Films* 460, 125–132 (2004).
158. E. Badisch, M. Stoiber, G. A. Fontalvo, and C. Mitterer, Low-friction PACVD TiN coatings: Influence of Cl-content and testing conditions on the tribological behavior, *Surf. Coat. Technol.* 174–175, 450–454 (2003).
159. E. Badisch, G. A. Fontalvo, and C. Mitterer, The response of PACVD TiN coatings to tribological tests with different counterparts, *Wear* 256, 95–99 (2004).
160. A. Mitsuo and T. Aizawa, Effect of chlorine distribution profiles on tribological properties for chlorine-implanted titanium nitride films, *Surf. Coat. Technol.* 158–159, 694–698 (2002).
161. T. Akhadejdamrong, T. Aizawa, M. Yoshitake, A. Mitsuo, T. Yamamoto, and Y. Ikuhara, Self-lubrication mechanism of chlorine implanted TiN coatings, *Wear* 254, 668–679 (2003).
162. T. Aizawa, T. Akhadejdamrong, and A. Mitsuo, Self-lubrication of nitride ceramic coating by the chlorine ion implantation, *Surf. Coat. Technol.* 177–178, 573–581 (2004).
163. E. Badisch, M. Stoiber, G. Fontalvo, and C. Mitterer, Adhesion and wear properties of hard coatings on tool steels, in *Tribology 2001*, *Proceedings of the World Tribology Congress*, edited by F. Franek, W. J. Bartz, and A. Pauschitz (Austrian Tribology Society, Vienna, CD-Rom, 2001).
164. M. Stoiber, C. Mitterer, T. Schoeberl, E. Badisch, G. Fontalvo, and R. Kullmer, Nanocomposite coatings within the system Ti-B-N deposited by plasma assisted chemical vapor deposition, *J. Vac. Sci. Technol. B* 21, 1084–1091 (2003).
165. C. Mitterer, F. Holler, D. Reitberger, E. Badisch, M. Stoiber, C. Lugmair, R. Nöbauer, Th. Müller, and R. Kullmer, Industrial applications of PACVD hard coatings, *Surf. Coat. Technol.* 163–164, 716–722 (2003).
166. H. Meidia, A. G. Cullis, C. Schönjahn, W.-D. Münz, and J. M. Rodenburg, Investigation of intermixing in TiAlN/VN nanoscale multilayer coatings by energy-filtered TEM, *Surf. Coat. Technol.* 151–152, 209–213 (2002).
167. Z. Zhou, W. M. Rainforth, B. Rother, A. P. Ehiasarian, P. Eh. Hovespian, and W.-D. Münz, Elemental distributions and substrate rotation in industrial TiAlN/VN superlattice hard PVD coatings, *Surf. Coat. Technol.* 183, 275–282 (2004).

168. D. B. Lewis, S. Creasey, Z. Zhou, J. J. Forsyth, A. P. Ehiasarian, P. Eh. Hovsepian, Q. Luo, W. M. Rainforth, and W.-D. Münz, The effect of (Ti + Al):V ratio on the structure and oxidation behaviour of TiAlN/VN nano-scale multilayer coatings, *Surf. Coat. Technol.* 177–178, 252–259 (2004).
169. P. H. Mayrhofer, P. Eh. Hovsepian, C. Mitterer, and W.-D. Münz, Calorimetric evidence for frictional self-adaptation of TiAlN/VN superlattice coatings, *Surf. Coat. Technol.* 177–178, 341–347 (2004).
170. K. Kutschej, P. H. Mayrhofer, M. Kathrein, P. Polcik, and C. Mitterer, A new low-friction concept for $Ti_{1-x}Al_xN$ based coatings in high temperature applications, *Surf. Coat. Technol.*, 188–189, 358–363 (2004).
171. Y. Ningyi, L. Jinuha, and L. Chenglu, Valence reduction process from sol–gel V_2O_5 to VO_2 thin films, *Appl. Surf. Sci.* 191, 176–180 (2002).
172. A. Erdemir, M. Halter, and G. R. Fenske, Preparation of ultralow-friction surface films on vanadium diboride, *Wear* 205, 236–239 (1997).

12

Optimization of Nanostructured Tribological Coatings

Adrian Leyland and Allan Matthews

Department of Engineering Materials, The University of Sheffield, Sheffield, UK

1. INTRODUCTION

One of the main attributes which nanostructured coatings may possess is extreme hardness; indeed, that aspect of such coatings is emphasized throughout this book. Based on classical theories of tribology,[1] one might assume that this attribute would make nanostructured coatings ideal for tribological applications. However research has shown that in many wear contacts, obtaining appropriate levels of elasticity and strain tolerance can be just as important as the achievement of high hardness, in ensuring that wear-resistant coatings function effectively. This leads to the concept of optimizing both hardness (H) to a (sufficiently) high value *and* elastic modulus (E) to an appropriate (relatively low) level, when designing tribological coatings. These requirements translate to the need for a high "H/E ratio" and—as we shall describe—nanostructured coatings hold considerable promise in attaining this goal. By harnessing the benefits of nanocrystallinity, and by careful selection of the "matrix-phase" and "reinforcement-phase" coating constituents (with appropriate mechanical and tribochemical properties), it is now possible to produce wear-resistant coatings exhibiting novel combinations of hardness, "resilience" (determined primarily by the elastic properties of the coating material) and "engineering toughness" (determined primarily by coating ductility), which can be optimized to suit a wider range of substrate materials and tribology applications.

Holmberg and coworkers have written extensively on developments in the understanding of tribological contacts and the implications for coating design.[2–5] In particular, they have discussed how the mechanisms occurring in a contact should be considered at five main levels in order to achieve a systematic, holistic understanding (and optimization) of the complete tribological processes. These mechanisms are (a) macromechanical, (b) micromechanical, (c) material transfer,

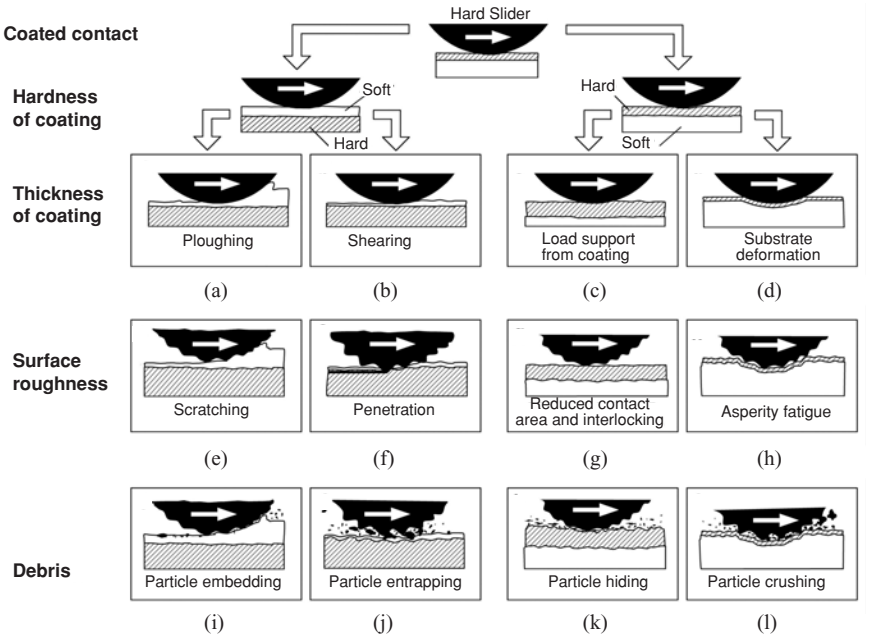

FIGURE 12.1. Tribological phenomena observed in sliding contacts, resulting from changes in coating parameters.[2,5]

(d) tribochemical, and (e) nanomechanical. Macromechanical mechanisms relate to the macroscopic deformations that occur under load, i.e., the near-surface stresses and strains and the total elastic and plastic deformations. For coated surfaces, the relative coating and substrate hardnesses, the coating thickness, the roughness, and the size and hardness of any debris all play a part in these stresses and the consequent tribological behavior, as illustrated in Fig. 12.1.

The origins of the wear and frictional effects observed at the macro-level can be found in the mechanisms that occur at the micro-level, i.e., the stresses and strains occurring between contacting asperities, and the crack generation and propagation, leading to material liberation and formation of debris. Effective coating design must prevent such damaging effects—and the concern to ensure adequate elasticity and toughness is thus particularly appropriate. In effect the coating must interpose between the surfaces to accommodate the stresses and strains present and to prevent cracking (as well as to limit tribochemical effects such as corrosion). Berthier *et al.*[6,7] identified four mechanisms by which velocity differences between two contacting surfaces can be accommodated: elastic deformation, fracture, shear, and rolling. If we assume that the second of these mechanisms must be avoided, and that the third and fourth may be feasible only in specially designed systems, then it follows that adequate elasticity is a requirement in most systems if micromechanical failure mechanisms are to be avoided.

The material transfer and tribochemical responses of a surface are material- and phase-dependent properties, which can be optimized to suit a particular operating environment and counterface type. In fact, ideally they should be controlled in a way that makes the coating adapt to the operating environment and contact conditions, so that the friction and wear behavior are continuously optimized. Coatings exhibiting such adaptive behavior have been termed "chameleon-like." Nanomechanical mechanisms are increasingly being recognized as highly influential on the frictional properties of a material pairing. Scientific understanding in this area of tribology is, at present, still in its infancy, although rapid progress can be expected with the increasing availability of equipment such as the atomic force microscope, and associated devices, designed to measure atomic-scale contact mechanisms and friction forces. This is beginning to allow an understanding of the reasons why certain hard materials sometimes exhibit low friction by, for example, the creation of an ultrathin low shear strength surface layer.

Overall, the recent developments in understanding of the tribological phenomena referred to above confirm many of the observations of an early study by Oberle,[8] which showed that tribological surfaces must possess a suitable combination of hardness and elasticity to be able to deform without yielding plastically, under load. Also, historically, bearing designers have utilized the H/E ratio in a parameter called the "plasticity index," which defines the mechanical property (and surface roughness) requirements for bearing surfaces.[9] For a coated surface the H/E ratio becomes even more important, since the coating needs to be able to deflect in sympathy with the substrate (as the system deforms under load). To achieve this, the coating and substrate elastic moduli should ideally be as closely matched as is practically possible; this is beneficial in minimizing both peak surface contact pressures in hard-coated contacts[10] and strain mismatch—reducing the risk of high interfacial stresses between substrate and coating.[11] When it is not possible to utilize a low-modulus (compliant) coating, and an ultrahard (brittle) one is necessary, it becomes particularly important to provide adequate load support to the coating—for example, by hardening the substrate surface prior to coating. In the next section we describe some theoretical considerations, which have been developed in order to meet the tribological contact requirements we have described.

2. THE SIGNIFICANCE OF *H/E* IN DETERMINING COATING PERFORMANCE

In spite of the evidence of a need for wear-resistant coatings that are also resilient and tough, the imperative for coating developers over many years has been to strive for harder (and stiffer) coatings (e.g., thin-film diamond, cubic boron nitride, and, more recently, carbon nitride—C_3N_4). However, as mentioned above, it is now recognized increasingly that coating resilience and toughness can be equally (if not more) important factors in reducing wear—particularly under conditions of

impact, abrasion, or erosion. In terms of elastic "resilience" (i.e., an ability to absorb deformation energy), it has been shown that the ratio H^2/E provides a suitable ranking parameter between different materials. Also, the ratio H/E provides an indicator of the "elastic strain-to-failure."[9,12,13] Furthermore, Ramalingam and Zheng[11,14] have emphasized a need to match the coating elastic modulus to that of the intended substrate. However, investigations by Tsui and coworkers,[15–17] (using nanoindentation techniques to examine the behavior of both coatings and bulk materials) illustrate that other important near-surface material properties for tribological applications, such as the contact yield pressure and the fracture toughness, can (if the contact geometry is known) also be described in terms of the measured hardness (H) and elastic modulus (E). For example, the yield pressure P_y—a parameter that defines resistance to plastic deformation in a "rigid-ball on elastic/plastic plate" contact—can be determined by the following equation:

$$P_y = 0.78r^2(H^3/E^2) \tag{12.1}$$

where r is the contacting sphere radius; thus H^3/E^2 should be a strong indicator of coating resistance to plastic deformation in such types of loaded contact. This equation relates to the earlier analysis of Johnson[9] and to the observations of Tabor,[18] and others, that the hardness of a conventional polycrystalline (metallic) approximately material is, typically, three times its yield strength.

Furthermore, as Lawn *et al.*[19] and more recently Pharr[16] have suggested that an indication of fracture toughness (i.e., resistance to crack propagation, leading to failure) can be obtained by examining the surface radial cracks created during indentation, and described by the equation

$$K_c = \alpha_1(E/H)^{1/2}(P/c^{3/2}) \tag{12.2}$$

where P is the peak indentation load, c is the radial crack length, and α_1 is an empirical constant related to the indenter geometry. K_c describes the "critical stress intensity" factor for crack propagation; however, it is not an intrinsic parameter that can be used to measure directly fracture toughness. Based on Griffith's crack propagation theory (and making the general assumption of a material that exhibits brittle behavior, but with some local plastic deformation), the "critical strain energy release rate" (per crack tip) G_c is arguably a more useful measure of the 'global' fracture toughness,[20] and can be related to K_c by the following equation:

$$K_c = (EG_c)^{1/2} \quad \text{(for plane stress)} \tag{12.3}$$

$$K_c = [EG_c/(1-\upsilon^2)]^{1/2} \quad \text{(for plane strain)} \tag{12.4}$$

where υ is Poisson's ratio ($\upsilon \approx 0.3$ for most metals). Substituting Eq. (12.3) into Eq. (12.2) and rearranging gives a measurable indicator of fracture toughness, i.e.,

$$G_c = \alpha_2(P^2/Hc^3) \tag{12.5}$$

Thus, if P is known and H and c can be measured, a numerical ranking of relative coating fracture toughness should be obtainable by low-load indentation;

it should also be possible to relate P (and therefore G_c) back to P_y in Eq. (12.1). Of more practical and commercial relevance, however, would be the correlation of such measurements to actual durability in dynamic tribological applications, as typified by tests such as pin-on-disk (or reciprocating-sliding) wear, rubber-wheel/sand abrasion, and ball-on-plate impact.

For ductile materials, the Irwin–Orowan modification to the Griffith (linear-elastic fracture-based) equation gives the critical stress σ_c for fast fracture as

$$\sigma_c = [(2\gamma_s + \gamma_p)E/(\pi a)]^{1/2} \tag{12.6}$$

where a is the critical crack size. The $(2\gamma_s + \gamma_p)$ function, in which γ_p is the plastic contribution (associated with crack tip blunting) to the energy required for fracture, describes the fracture toughness $G_{c.}^{20}$ For ductile materials γ_p may be many times larger than the γ_s term, which describes the free energy of the crack surfaces formed. Inserting G_c in Eq. (12.6) and rearranging yields

$$G_c = \sigma_c^2 \pi a/E \tag{12.7}$$

Thus fracture toughness would appear to be improved by both a high critical stress for fast fracture (which implies a high hardness) and a *low* elastic modulus. With particular regard to fracture toughness, however, Veprek[21] argues that the deformation of ceramic–ceramic or ceramic–amorphous nanocomposite materials (particularly where an amorphous matrix is generated as the minority phase) is likely to occur through nanocracking in the matrix (and possible associated rotation of the "defect-free" nanograins), with a maximum crack length determined by the grain size. Furthermore, it can be inferred that the effective (global) fracture toughness may increase, due to the higher energy input required to link these nanocracks together, particularly if there is strong interfacial bonding (i.e., coherency) between the matrix and the nanograins. One might consider that such arguments are contradictory, based on Eq. (12.7), since a small "a" should not be conducive to high values of G_c. However, the empirical relationships that underpin simple elastic fracture mechanics theory are not necessarily valid in this case, and the maximum crack length considered by Veprek is probably not the same as the "a" parameter in Eq. (12.7); i.e., it is only after a large number of nanocracks have linked-up that the critical flaw size for fast fracture is reached. Thus, as Eq. (12.7) suggests, a large critical crack size for fast fracture is commensurate with a high G_c value and in our opinion Veprek's suppositions are, within certain theoretical constraints, valid. Importantly, they may also hold true for softer, lower modulus "metal–metal" nanocomposites where the essentially dislocation-free nanograins (if dislocations are indeed present it will be difficult for them to multiply) will resist plastic flow, although there may be partial slip in the matrix, allowing conformal deformation to occur under high loads (which may ultimately lead to nanocrack formation). This should, in principle, create a coating that is hard and tough, but also exhibits elastic properties closely matched to those of typical commercial substrate materials—an important consideration for "real-life" coating durability that is often overlooked. We would expect the toughening effects of a combination of

moderately high hardness and low elastic modulus (with associated resistance to yielding, or fracture, under application of a high local strain) to be detectable in, for example, nanoindentation measurements where a smaller "c" value in Eq. (12.5) may result—allowing coating fracture toughness improvements to be quantified.

In regard to microstructural effects, it is well known from classical deformation theory that hardness and grain size are, in conventional polycrystalline materials, interdependent. This is as described by the Hall–Petch equation whereby, for a given grain size d

$$H_d = H_0 + k_1 d^{-1/2} \tag{12.8}$$

where H_0 is an intrinsic material parameter and k_1 a constant, related both to the shear modulus (and thus, indirectly, to E) and to the critical shear stress for dislocation movement in the material. Similarly, the yield stress will be grain size dependent (i.e., $\sigma_y = \sigma_0 + k_2 d^{-1/2}$), and will tend to increase linearly as a function of $d^{-1/2}$. Furthermore, it is well known that the corresponding fracture stress σ_f also tends to increase (initially sublinearly) as a function of $d^{-1/2}$ such that, at large grain sizes (and particularly at higher strain rates), brittle fracture tends to occur before the expected elastic limit is reached. More importantly for our considerations, as the grain size decreases below the point at which $\sigma_y = \sigma_f$, increasing ductility (at least in compression) and, in many practical cases, associated higher maximum stress accommodation (through local conformal yielding) may be obtained.[22]

From the above arguments it becomes apparent that a higher coating hardness will be beneficial in terms of increased resistance to plastic deformation. It is however also apparent that for a given coating hardness, a lower elastic modulus may often be particularly beneficial if E can be adjusted to match closely that of the underlying substrate material, minimizing coating–substrate interfacial stress discontinuities under load and allowing the coating to deflect without fracture or yielding. This is generally not possible with traditional hard ceramic coatings, where E is typically at least three to four times higher than that of a desired substrate material (e.g., steel or some other metal alloy). Revisiting Eq. (12.5), it becomes clear that (as one might intuitively predict) high hardness is unlikely to be beneficial for coating fracture toughness. Here the microstructural characteristics of the coating material will be important as, in practice, it is factors such as grain size and phase distribution that are likely to control crack propagation mechanisms in the coating, i.e., factors relating to "a" in Eq. (12.7) and (in attempting to measure such effects) "c" in Eq. (12.5).

Much of the classical bulk fracture mechanics theory is based on the assumption of a pre-existing crack or flaw, which necessarily imposes a high material stiffness requirement (i.e., a high E value) to prevent flaw growth to some critical dimension at which catastrophic failure occurs. The empirical models that describe such effects may indeed provide a very accurate representation of the behavior of certain materials (e.g., bulk ceramics) but, for a tribological coating on a metallic industrial component, conformal cracking—or indeed limited plastic

deformation—of the coating is not necessarily undesirable. It may be beneficial in improving strain tolerance, or perhaps in providing other consequential benefits; for instance, a lubricant reservoir (as in the case of crack networks in electroplated hard chrome). What will be beneficial in practical applications, we believe, is closely matched strain behavior between coating and substrate, up to (and even beyond) the elastic limit of the substrate. By generating a large H/E value—i.e., a sufficiently high hardness (to resist plastic deformation)—but with a low elastic modulus[23] (similar to or ideally slightly below that of the substrate material), we believe the most durable coatings will be obtained for many applications. Nevertheless, in tribological contacts where high stiffness (and tribochemical inertness) at or near the surface is a fundamental requirement (e.g., for many cutting tools), ceramic nanocomposite coating systems of the Ti-B-N/Ti-B-C type[24–30] offer a diverse range of possibilities in functional grading of properties between (i) the coating–substrate interface, (ii) the body of the coating, and (iii) the coating surface. In each case, very different characteristics in terms of the balance between elasticity/stiffness, ductility/hardness, and frictional/tribochemical behavior may be required simultaneously. Work by the authors has explored, in some detail, the use of both sputter- and electron-beam physical vapor deposition (EB-PVD) to produce coatings based on a Ti-Al-B-N quaternary system, where a wide range of mechanical, structural, and tribological properties may be available concurrently from carefully chosen source materials.[23,31–34] Such developments are now being extended to other ternary and quaternary systems based on (for example) the substitution of chromium for titanium/aluminum and/or silicon for aluminum/boron, with a number of commercial applications for such nanostructured films (particularly for CrAlN, TiSiN, TiCrAlN, and TiAlSiN—as well as the now widely used TiAlN) now emerging.

3. PRACTICAL CONSIDERATIONS FOR VAPOR DEPOSITION OF NANOSTRUCTURED COATINGS

Following on from the work on Ti-Al-B-N (and other, similar ceramic nanocomposite systems such as those mentioned above), the authors have proposed an approach to tribological coatings development based on predominantly metallic (rather than ceramic) coatings. The advantages of vapor deposition techniques (particularly low-temperature plasma-assisted PVD methods) can be harnessed to provide the required structure, adhesion, and high hardness—together with improved toughness and/or resilience, compared to ceramic films. The inherent ability of such techniques to provide a high quench rate in the depositing film and generate unusual levels of supersaturation of both interstitial and low-miscibility substitutional alloying elements is a key factor in promoting nanocrystalline (or even glassy) phase formation in vapor-deposited coatings. Furthermore, it is widely known that thin ceramic films, despite their (tribo)chemical inertness, do not usually provide adequate corrosion resistance—since they tend to suffer defects and

porosity through which the coating–substrate interface can be attacked, leading to spallation. Such effects are exacerbated when (as is often the case) a thin metallic interlayer is deposited between coating and substrate (the latter of which is already highly activated by the sputter precleaning process), to improve interfacial adhesion and accommodate strain mismatch. For example, the titanium interlayer deposited between a (typically steel) substrate and a PVD TiN coating is known to be susceptible to galvanic attack.[35] Metallic films can generally be vapor deposited with lower residual compressive stress than their ceramic counterparts, allowing thicker films to be deployed with reduced risk of spallation. Also, the maximum rate at which a metallic film of the required stoichiometry and structural integrity can (for a chosen substrate temperature) be deposited is usually many times higher than for ceramic compounds. With current commercial vapor deposition technology, growth rates of only a few micrometers per hour are realistically attainable for dense ceramic films at 200–400°C deposition temperatures suitable for many metallic substrate materials. However, there is realistic scope to deposit nanostructured metallic films at rates of 10 μm/h or higher at these temperatures (with low porosity and high abrasion/erosion resistance), creating prospects to compete (on thickness and cost) with, for example, electroplated hard chromium or electroless nickel–phosphorus coatings. There are also strong arguments in the literature that nanograined or amorphous metals might provide more uniform and predictable sacrificial corrosion protection, primarily due to their small and uniformly distributed features;[36] such arguments might reasonably be expected to translate directly to the behavior of nanostructured metallic films. We address some of these issues in the following sections of this chapter, indicating where possible what the likely design and materials selection criteria might be, to achieve the desired combinations of mechanical, tribological, and other (e.g., corrosion-resistant) properties in such films.

4. DESIGN AND MATERIALS CONSIDERATIONS FOR METALLIC-NANOCOMPOSITE AND GLASSY-METAL FILMS

4.1. Background to Metal Nanocomposite Films

As we see above, recent developments in plasma-assisted PVD and chemical vapor deposition (CVD) thin film technology—particularly in production of nanostructured films—reveal possibilities to adjust the hardness and elastic modulus of a tribological coating with some degree of independence, introducing exciting possibilities to produce wear-resistant surfaces with combinations of previously unobtainable properties. Scientific interest in, particularly, sputter PVD processes (but also in plasma-assisted CVD) to produce nanocomposite coatings is so far directed primarily toward the development of "superhard" i.e., $H \geq 40$ GPa) coatings for dry sliding wear resistance and high thermal stability, based on the premise of

creating composites of a nanocrystalline ceramic reinforcement phase embedded in an amorphous ceramic[21,37,38] (i.e., *ceramic–ceramic* nanocomposite) or low-miscibility metallic[39,40] (i.e., *ceramic–metal* nanocomposite) matrix phase. As we suggested earlier, many such films also tend to exhibit a high elastic modulus—which may be beneficial for coated tooling, but perhaps not in other applications. This led us to propose that *metal–metal* nanocomposite coatings might be an equally rewarding subject of investigation,[12,41] since they promise considerable scope to provide (and adjust) a low coating elastic modulus—in a range similar to that of many candidate substrate materials—while, with selection of appropriate materials and processing routes, allowing "ceramic" values of hardness (i.e., of the order of 15–20 GPa, or higher) to be achieved. This approach stemmed mainly from our earlier work with metallic coatings based on Cr,[42] W,[43] TiAl,[23] or stainless steel,[44,45] each "doped" (i.e., interstitially supersaturated) with nitrogen, carbon, and/or boron, where we found frequently that the coating that performed best in a wear application was not necessarily that which was hardest but, more often, that which exhibited a high H/E ratio.

Taking for instance the example of "nitrogen-doped" chromium,[42] we found that moderately hard (i.e., 12–15 GPa) metallic films with, correspondingly, around 12–15 at% N in supersaturated solid solution (the "equilibrium" solubility of nitrogen in chromium is expected to reach a maximum of ∼4.3 at% between 1650 and 1700°C and be negligible below 1000°C)[46] gave results superior to those of significantly harder (i.e., 20–25 GPa) ceramic nitride films, when subjected to severe impact wear. Experiments were performed using a "ball-on-plate" configuration, whereby a 10-mm-diameter ball of either chromium steel or WC-Co was repeatedly driven against a coated plate at a load of several hundred newtons, sufficient to cause considerable plastic deformation of the underlying substrate material. For both ball materials, the impact crater wear volume after 50 000 cycles was high for low-nitrogen (i.e., low hardness) chromium films, but similarly low for both high-nitrogen chromium and ceramic nitride films; i.e., increased hardness beyond 15 GPa had little further effect in reducing the impact crater volume. However, the overall performance of the high-nitrogen metallic films was superior in that (despite substantial substrate plastic deformation) little or no cracking or debonding of tough, lower modulus metallic films occurred, whereas brittle, higher modulus ceramic films exhibited extensive circumferential cracking around the crater rim, with substantial fracture and debonding in the central zone of the crater itself. Analogous observations can be made regarding the superior abrasion and erosion behavior of Ti/TiN multilayer films[47] or CrN/electroless-nickel duplex coatings,[48] where the relatively ductile metallic constituents facilitate plastic strain accommodation (and thicker coating deposits), to the benefit of both wear and corrosion behavior.

Returning momentarily to nitrogen-doped chromium metal PVD coatings, in the light of the above (and of the likely benefits of nanostructured metal films), one next logical step might be to modify a nitrogen-doped chromium film by the introduction of a secondary, ideally low-modulus, "immiscible-metal" constituent

which would either be captured substitutionally in the chromium (increasing lattice friction) or, with suitable choice of deposition parameters (and/or postcoat annealing), form a thin intergranular phase and promote a nanograined composite structure, with similarly increased resistance to plastic deformation (not least through Hall–Petch effects—although other, anomalous, effects may also occur).[12] In either case, the expected result would be a further substantial increase in yield strength (and, by implication, hardness), with E remaining similar or, with appropriate alloying, substantially reduced. Thus a significant increase in the H/E ratio would occur, to the benefit of coating resilience (and probably also toughness). This generates prospects to tailor both composition and structure to engineer coating resilience, toughness, and modulus to match closely the mechanical properties of almost any (but particularly any metallic) substrate material that might be chosen. Our preliminary work in this area was directed toward addition of copper to the Cr(N) metallic film system, since copper exhibits almost complete immiscibility with chromium under most near-equilibrium conditions, has (in bulk, microcrystalline form) roughly half the elastic modulus (130 GPa, cf. 280 GPa) and, from a practical perspective, is relatively inexpensive and widely available at suitably high purity. Our work on this coating system, with additions of both nitrogen and boron, has demonstrated a number of encouraging results.[49–51] There are many other candidate coating systems that might be considered for the synthesis of wear-resistant metallic films (based on the above-mentioned requirements and on other materials-related design considerations),[41] as outlined in the following section.

4.2. Design Considerations

In attempting to design effective metal–metal nanocomposite coatings, one consideration to be made is that of an appropriate choice of alloy composition—and grain size issues related to this. As the authors have discussed previously,[12] one claimed advantage of a nanograined structure is anomalously high hardness in (typically) the 10–100-nm grain size range. Additional to the Hall–Petch relationship between increasing hardness (or yield strength) and decreasing grain size (where essentially the stress required to propagate a dislocation from one grain to another increases as the size of the latter is reduced), there is theoretically a dimension of several tens to one or two hundreds of nanometers (depending on the chosen element or alloy) below which a Frank–Read dislocation loop source (widely believed to be the main means of dislocation multiplication and therefore grain boundary pile-up that tends to drive the deformation process from grain to grain) cannot operate. Thus, high hardness, and also reduced tensile ductility, may result from a nanograined structure. On the other hand, it has been observed that, as the grain size approaches the order of a typical grain boundary dimension (i.e., the grain diameter reduces below 5–10 nm), grain rotation within the "matrix" (i.e., the intergranular regions) can occur, leading to an "inverse Hall–Petch" softening effect. Furthermore, in an idealized metallic nanocomposite, one might envisage a

TABLE 12.1. Example Estimations of the Cu Content Required to Create (Amorphous) Intergranular Layers of Different Widths for a Range of Cr Grain Sizes in an Idealized Cr-Cu Metal Nanocomposite.

Intergranular Cu layer width, atoms (nm)	Required Cu content (atom%)				
1 (0.28)	13.1	5.86	2.45	1.53	0.63
2 (0.56)	22.3	10.9	4.74	3.00	1.25
3 (0.84)	29.1	15.2	6.90	4.43	1.86
5 (1.4)	38.5	22.3	10.9	7.09	3.05
10 (2.8)	50.9	34.4	18.9	13.0	5.86
15 (4.2)	57.0	42.0	25.2	17.9	8.46
Cr grain size (nm)	4	10	25	40	100
Cr grain width (number of atoms)	∼16	∼40	∼100	∼160	∼400

majority of hard transition-metal nanocrystals (e.g., chromium, interstitially supersaturated with nitrogen) surrounded by a minority, disordered intergranular phase of a low-modulus, immiscible metal phase (e.g., copper), as being the type of structure likely to provide desirable combinations of hardness, resilience, and ductility. The amount of (for example) copper that would need to be added to chromium to achieve such a structure (assuming that a processing route could be found to deposit a coating with these properties) would be interdependent with the chromium grain size produced.[41,50] Table 12.1 explores such a scenario, by examining the amount of copper theoretically required to produce a continuous grain boundary layer (of anywhere between 1 and 15 atoms thick), for different sizes of Cr nanograins in the range of interest. Although many assumptions have to be made in such a simplistic treatment, it is nevertheless illuminating to examine the general trends that emerge. For example, if it were possible to choose conditions whereby a coating with relatively large ($\geq$100 nm) Cr nanograins was produced, the amount of Cu required to generate a continuous ("fully percolated") intergranular region of, say, 5–10 atoms wide would be only 3–5 at% (Table 12.1). On the other hand, at grain sizes $\leq$10 nm, up to 50 at% Cu might be needed to generate the same effect, based on identical criteria. Such a high content of (soft and ductile) intergranular material might not be expected to benefit coating mechanical and tribological properties. Particularly at such small grain sizes, the grain radius is approaching the dimensions of the intergranular region, such that small fluctuations in grain boundary phase content could encourage grain rotation, making it difficult to accurately (and repeatably) control coating behavior in a "real" deposition process. Conversely, substantial fluctuations of local intergranular phase content could be better accommodated at larger grain sizes, since the grain width would always remain an order of magnitude higher than the intergranular phase dimension, suppressing grain rotation. In practice, one might ideally choose an intermediate grain size (i.e., 25–40 nm Cr) and composition (i.e., 10–15 at% Cu). Certainly, this range of

grain sizes—and a 90/10 to 85/15 ratio between nanocrystalline and amorphous-intergranular phase content—appears to work well in TiAlBN nanocrystalline–amorphous (i.e., pseudo-binary nc-TiAlN/a-BN) ceramic–ceramic nanocomposite coatings for cutting tool applications.[33,52] It remains to be seen whether there is an optimum grain size and structure for metal–metal nanocomposite films (and, if so, what this might be).[41,50] Other authors have however achieved considerable success with ceramic–ceramic nanocrystalline–amorphous films (e.g., nc-TiN/a-SiN_x)[37,38] at similar phase ratios and very small grain sizes (less than 5 nm). The key to good performance in this case appears to be the avoidance of a fully percolated structure (i.e., nanograins completely separated from each other by the matrix),[53] since interpenetrating networks of crystalline and amorphous regions may control the grain boundary rotation issues referred to above. This argument is supported by the trends revealed in Table 12.1; it is obvious that (although the elements/phases involved are very different) a >5 nm TiN grain size, combined with an amorphous SiN_x content of less than 15%, is unlikely to generate structures where complete coverage of the nanocrystallites by the intergranular phase can occur. Spontaneous unmixing of (inherently immiscible) binary metal alloy elements at the limit of metastability (so-called "spinodal decomposition") has historically been shown often to create such interpenetrating networks, with the "uphill" diffusion processes and timescales involved tending naturally to produce a periodic spacing of ~5–10 nm (see Ref. 54). One of the main challenges in developing metallic nanocomposite coatings will be to determine which possible structural features outlined above can give the most appropriate tribological behavior in individual applications; it seems unlikely that one particular approach will provide a universal solution.

4.3. Materials Selection for Nanostructured and Glassy Films

For reasons stated above, the chromium–copper–nitrogen system appeared to the authors to be an obvious materials choice for further investigation of the potential benefits of metallic nanocomposite films—over and above the (to some extent proven) benefits of, for example, PVD "nitrogen-doped" hard chromium metal films. However, it became apparent that a number of other candidate systems should exist,[41] with the potential to develop a diverse spectrum of unusual and extreme mechanical/tribological properties, which might not be attainable through many of the conventional materials processing (or vapor deposition) approaches currently favored for scientific investigation. First, consider the "nitride-forming" elements that are generally selected for the production of refractory ceramic nitride, carbide, boride, or oxide materials used in tribology: namely, the group IVb–VIb elements (Ti/Zr/Hf; V/Nb/Ta; Cr/Mo/W) and the group IIIa/IVa elements Al and Si. Whether bulk materials or coatings, these are the 11 elements which, in various combinations, tend (almost exclusively) to be used—together with B, C, N, and/or O—to produce wear-resistant "engineering ceramics," although other light and rare-earth elements (e.g., Be, Mg, Sc, and Y) might arguably also qualify. Excepting Al, the remaining 10 elements all have melting temperatures (T_m)

TABLE 12.2. Candidate "Nitride-Forming" and "Non-nitride-Forming" Low-Miscibility Elements That Might Be Considered for Alloying to Produce Metallic Nanocomposite or Glassy Metal Films.

Element	Structure	Modulus E (GPa)	Atomic radius (pm)	T_m [°C (K)]	$T/T_m = 1/3$[°C (K)]
Nitride forming					
Ti	cph	115	140	1675 (1948)	376 (649)
Zr	cph	68	160	1852 (2125)	435 (708)
Hf	cph	78	155	2150 (2423)	535 (808)
V	bcc	128	135	1895 (2168)	450 (723)
Nb	bcc	105	145	2470 (2743)	641 (914)
Ta	bcc	186	145	2996 (3269)	817 (1090)
Cr	bcc	280	140	1890 (2163)	448 (721)
Mo	bcc	330	145	2610 (2883)	688 (961)
W	bcc	410	135	3415 (3688)	956 (1229)
Al	bcc	70	125	660 (933)	38 (311)
Si	Cubic	47	112	1410 (1683)	288 (561)
Non-nitride forming					
Mg	cph	44	150	651 (924)	35 (308)
Ca	Cubic	20	180	845 (1118)	100 (373)
Sc	cph	74	160	1539 (1812)	331 (604)
Ni	fcc	200	135	1455 (1728)	303 (576)
Cu	fcc	124	135	1083 (1356)	179 (452)
Y	cph	64	180	1497 (1770)	317 (590)
Ag	fcc	76	160	961 (1234)	138 (411)
In	fct	11	155	157 (430)	−130 (143)
Sn	bct	40	145	232 (505)	−105 (168)
La	cph	37	195	920 (1193)	125 (398)
Au	fcc	78	135	1063 (1336)	172 (445)
Pb	fcc	16	180	328 (601)	−73 (200)

cph, close-packed hexagonal; bcc, body-centered cubic; fcc, face-centered cubic; fct, face-centered tetragonal; bct, body-centered tetragonal.

of ∼1700 K or above (up to ∼3700 K, in the case of W) and are therefore inherently quite refractory (see Table 12.2). Let us now also consider (somewhat arbitrarily) a homologous temperature (T/T_{m}) of 1/3 as a point at which, one might argue, diffusion mechanisms could start to significantly alter the microstructure of a bulk material over a fairly short time frame (i.e., of the order of a few hours to a few tens of hours). One might infer that the 10 elementary materials in question would tend to exhibit some inherent thermal stability up to a few hundred degrees Celsius or more, and could therefore be considered quite suitable as candidate tribological materials in their own right—assuming, for instance, that a (nonequilibrium) nanocrystalline microstructure could be generated, to maximize their hardness and load-bearing capability.[41] For the purposes of creating such a small grain size, the addition of a second, low-miscibility element has been shown to be very effective—particularly in vapor deposition of metallic thin films (e.g., Al-Y,[55] or Cr-Cu[49,50]). There are (perhaps surprisingly) a large number of (metallic) elements that, when

introduced to create a binary alloy with the candidate elements identified above, exhibit a wide miscibility gap in the solid state. Examples of elements for which there is evidence of such behavior when mixed with some or all of the group IIIa, IVa, IVb, Vb, and VIb "nitride-forming" elements identified are, in order of atomic number, Mg, Ca, Sc, Ni, Cu, Y, Ag, In, Sn, La, Au, Pb—although this list is by no means exhaustive. Of these 12, only five (Sc, Ni, Y—and perhaps also Cu and Au) might be considered sufficiently "refractory" (i.e., $T_m > 1000^\circ C$) that they could be expected to demonstrate some inherent thermal stability above ambient. Such considerations may be relevant in selecting material combinations in applications such as (for example) dry or marginally lubricated sliding, where local "flash" temperatures may reach several hundred degrees Celsius. On the other hand, low-melting-point metals such as In, Sn, and Pb (with, it can be argued, little inherent thermal stability) also exhibit very low elastic moduli (11, 40, and 16 GPa, respectively), which may be attractive in adjusting the overall modulus of a tribological film to meet a specific substrate requirement (e.g., protective coatings for magnesium alloys, where the substrate elastic modulus is only ~45 GPa). Conversely, the more refractory, group IVb transition metal elements (e.g., Zr, Hf) and their low-miscibility rare-earth neighbors (Sc, Y) have surprisingly low elastic moduli in the 60–80 GPa range, making them potentially very suitable candidates for coating aluminum alloys with similar elastic properties. Furthermore, refractory combinations such as Ta-Ni ($T_m = 2996$ and $1455^\circ C$, $E = 186$ and 200 GPa, respectively) might be considered for protection of steel substrates with similar moduli. By way of comparison, the elastic moduli of most refractory ceramics are in the 400–700 GPa range, i.e., an order of magnitude higher than those of a typical magnesium or aluminum light alloy. Intuitively, one would not expect a coating of such a ceramic to provide any long-term wear protection to these kinds of substrate materials, whereas (as proposed above) considerable promise is shown by the concept of a relatively hard metallic coating with similar elastic properties to the chosen substrate. As one final point on this topic, the candidate "nitride-forming" elements above (and the PVD coating process) lend themselves to the production of functionally graded films, whereby the substrate–coating interface can be "elastically matched," but the nitrogen (or indeed carbon, boron, or oxygen) content can be adjusted as a function of coating deposition time, to generate an increasing high-modulus (and tribochemically stable) ceramic phase content near the surface of the film, should the intended application necessitate such a requirement.

Having considered firstly simple binary metal alloy systems (disregarding the introduction of a supersaturated interstitial component), we now turn our attention to the implications for coating properties of combining three or more elements. In the alloying of different (metallic) elements, Hume-Rothery and Coles[56] proposed a "14% rule," whereby it can be considered that atoms of two elements whose atomic radii differ by more than 14% will most likely be quite restricted in their mutual solubility, with considerable lattice strain occurring (and implied "lattice friction" increases) if one element is substituted for the other in a crystalline

structure; one expected result of such an effect would be substantially increased yield strength (and hardness). Thus, very large (e.g., with diameters of 0.18 nm or above) or small (e.g., with diameters of 0.12 nm or below) substitutional atoms would tend not to be highly miscible with an "average" (0.15 ± 0.01 nm diameter) metal atom. Even notionally very similar atoms, such as the group IVb metals Ti ($\sim$0.14 nm) and Zr ($\sim$0.16 nm), can be quite different in size, and one might expect substantial lattice strain to occur when they are mixed. Superimposed with this effect, many of the elements identified in, respectively, the upper and lower portions of Table 12.2 exhibit very different crystallographic structure, due in part to their contrasting valence electron configurations. Thus, many of these elements, despite being of similar atomic size, show electronic incompatibilities that often restrict their mutual solubility (again, the bcc-Cr/fcc-Cu system provides a typical example of this). When attempts are made to mix several elements with different atom sizes and preferred crystallographic structures, it is often the case that the driving force for crystallization during solidification from the melt, or vapor (in the case of PVD or CVD), is suppressed to the extent that creation of an amorphous structure is equally (or more) favorable energetically. In other words, the formation of a regular, crystalline lattice is "frustrated" by the existence of many incompatible atom sizes and electron configurations, such that long-range order is thermodynamically difficult to establish—even at very mild quench rates of the order of $\sim$1 K/s. Such a phenomenon was predicted over 50 years ago by Turnbull and Fisher,[57] who first described the concept of a "reduced" glass transition temperature (i.e., T_g/T_m) that, when rising from around 1/2 to 2/3, would (due to the alloying effects mentioned above) increasingly cause homogeneous nucleation from an (undercooled) alloy melt to proceed more slowly. Subsequent work by Duwez *et al.*,[58] Chen and Turnbull,[59,60] and more recently by others such as Davies,[61] Tanner and Ray,[62] Johnson and Peker,[63,64] and Inoue *et al.*,[65–67] has led to the development of a range of bulk metallic glass-forming alloys, which can be characterized broadly into "ferrous" and "nonferrous" systems.[65] Many of these systems (particularly the ferrous ones) are of interest for "soft" magnetic applications where, for example, the lack of grain boundaries can be of considerable benefit, but several authors have commented on the high yield strengths and low moduli obtainable (i.e., providing high H/E ratios—although this is not explicitly said), which suggests suitability for certain mechanical and tribological applications. So far, however, very few attempts have been made to exploit the bulk mechanical,or surface tribological, properties of these materials.[68,69] A particular issue observed with bulk metallic glasses is the tendency toward "brittle" behavior in tension. In reality this observation appears to relate more to shear band localization, leading to unstable yield behavior and early fracture. A lack of grain boundaries and dislocations (and thus also of work hardening mechanisms) is believed to be the main cause of such behavior.[66] Some current work in this area is being directed toward procedures to introduce crystalline phases (e.g., by partial devitrification[65] or production of amorphous-matrix/crystalline-fiber composite materials[66]) to "delocalize" shear band formation. On the other hand, it is claimed that impact tests

generally indicate fairly high fracture toughness values for metallic glasses (although still somewhat lower than for most polycrystalline metals);[66] furthermore, many metallic glasses can be successfully cold rolled to very thin sections without annealing (e.g., see Ref. 64) and might be said to exhibit superplastic deformation behavior in this respect. In fact, numerous other physical benefits have also been observed for metallic glasses (again due largely to the absence of grain boundaries), such as better corrosion resistance[70]—with more uniform sacrificial behavior and reduced pitting (and improved fatigue behavior) claimed. The potential benefits of glassy phase formation in vapor-deposited thin films are enormous, but are as yet under-researched, with only a few authors (e.g., Sanchette and coworkers)[71–73] having explored the topic in any systematic way. The (unusual) capability to "post-coat amorphize" a nanocrystalline film through plasma-diffusion treatment[44,45] or, conversely, to post-coat anneal a glassy film—promoting partial devitrification and a controlled nanocomposite structure[51,65,66]—are two examples of topics in the vapor-deposited thin-film field which appear to merit further investigation for applications in tribology. Furthermore, low-temperature (i.e., $\leq 350^{\circ}C$) plasma-assisted PVD techniques, in particular, raise the exciting prospect of investigating new metallic glass compositions that may currently be difficult to synthesize via conventional bulk casting methods, but might yield novel physical behavior (particularly when devitrified)—whether that be mechanical, tribological, chemical, magnetic, or other functional properties.[41]

5. EXAMPLES OF PVD METALLIC NANOSTRUCTURED AND GLASSY FILMS

Having observed that several of the recently developed bulk metallic glass systems are based substantially on mixtures of low-miscibility "nitride-forming" and "non-nitride-forming" transition metals such as those detailed in Table 12.2 above, the authors began to look more closely at the metallic nanocomposite coatings under development in their laboratory, many of which exhibit strongly X-ray amorphous structures over surprisingly wide ranges of composition. Having carried out preliminary studies on, for example, Cr-Cu and Mo-Cu binary metal PVD coatings, and then adding-in nitrogen at increasing levels of "doping" (primarily to assess limits of interstitial supersaturation beyond which nitride phases would start to appear), we began to add further elements, such as Ti and B, to the Cr-Cu-N system, with a view to widening the range of coating compositions (and deposition conditions) over which a glassy metal coating would result. Examples of some of the results we obtained are summarized below.

5.1. CrCu(N) and MoCu(N) Nanostructured Films

We investigated a range of binary (metal–metal) and pseudo-binary (nitrogen-doped metal–metal) coatings based on low-miscibility mixtures of the

"nitride-forming" transition metals chromium[49,50] and molybdenum[74] with copper. In the case of Cr, a range of Cu contents from 2 to 20 at%[49] and 2 to 50 at%[50] were investigated at fixed nitrogen gas flow rates in the "reactive" deposition process; the varying Cu contents were produced within individual deposition cycles by placing up to six different substrate coupons at various positions between (and at an angle of 45° to) Cr and Cu magnetron sputter targets mounted at 90° to each other. In the case of Mo, a fixed (low) Cu content of ∼1 at% was chosen and coatings produced at a particular position were compared in a series of coating runs performed at different nitrogen flow rates.[74] In the former case, coating hardnesses of up to 20 GPa were observed; in the latter, hardnesses of 30 GPa or above were achieved. In both, however, it was generally not the case that the hardest coatings were those that performed best in a variety of tribological tests (e.g., abrasion, impact, and sliding wear). A stronger correlation was found between wear performance and H/E ratio, whereby coatings that were slightly less hard, but had a substantially lower elastic modulus often gave the most promising results—as appeared to be the case in previous work on metallic films.[23,42–45] The main advantage of the nanocomposite structure of these copper-containing films appears to be the capability to raise the hardness to 20 GPa and above while retaining the (low) modulus of the metal; for example, the CrNx ($x < 0.16$) metallic films produced previously[42] exhibited hardnesses no greater than 15 GPa unless ceramic phases were also present.

A typical plan-view transmission electron microscopy (TEM) image is shown in Fig. 12.2, where the structural features across an individual CrCu(N) coating column can be seen. Although the information presented in the figure is structural,

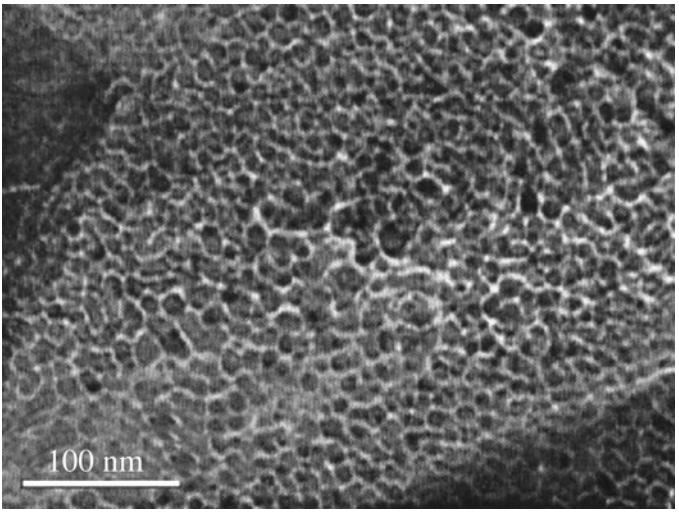

FIGURE 12.2. TEM plan view of nanostructure in a Cr(N)-Cu PVD nanocomposite coating.

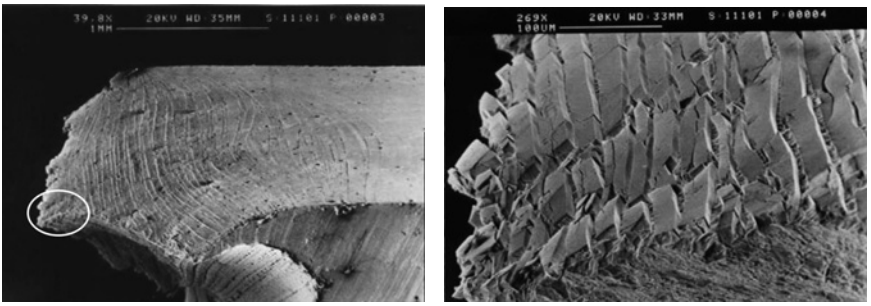

(a) (b)

FIGURE 12.3. Scanning electron micrographs of a ~10 μm thick Mo(N)-Cu metallic nanocomposite coating deposited on an AISI 316 stainless steel coupon which was subsequently strained to fracture, showing (a) fracture edge and (b) enlarged image of the leading fracture edge, illustrating excellent coating adhesion and toughness, despite the extreme substrate deformation incurred.

rather than compositional (resolving short-range compositional changes in such nan ostructures is in any case challenging), corresponding X-ray diffraction (XRD) and X-ray photoelectron spectroscopy (XPS) data (not shown here) suggest mainly Cr nanograins of (from the micrograph in Fig. 12.2) typically 5–20 nm diameter, dispersed in a 1–2 nm wide, Cu-rich (we believe) intergranular phase. The Cr nanograins will have an interstitial supersaturation of nitrogen—and probably some Cu—in solid solution; there is also a suggestion from the data that a minority of the (smaller) nanograins are, in fact, Cr_2N (i.e., the film is not entirely metallic in this case). Figure 12.3 presents scanning electron micrographs of a relatively thick (approaching 10 μm) MoCu(N) coating deposited on an AISI 316 austenitic stainless steel substrate. The substrate has been strained to fracture in tension at room temperature; yet the coating, despite cracking, remains remarkably well adhered up to the fracture edge (Fig. 12.3b), demonstrating—in a crude, but effective manner—the excellent adhesion and interfacial toughness of such metallic films, even under extreme substrate plastic deformation. The elastic modulus of the film in this case remained somewhat higher than that of the substrate ($E_{Mo} \sim 330$ GPa), and yet was still substantially lower than that of most ceramic nitride films, which would in any event be difficult to deposit at such a thickness—particularly under the combination of high deposition rate (7–8 μm/h) and low substrate temperature (~320°C) conditions employed here.

5.2. CrTiCu(B,N) Glassy Metal Films

We found a tendency toward amorphization in some of the CrCu(N) coatings with higher copper (i.e., 30 at% and above) and nitrogen contents; however, such coatings were generally quite soft, with hardness below 15 GPa. This led us to

consider what other alloying additions could be incorporated into the CrCu(N) film to extend the composition range over which a glassy film would result, and/or increase coating hardness to 20 GPa or above. Referring to the bulk glassy metal work of Inoue *et al*. (e.g., Refs. 65 and 66) and others, the approach of adding an cph transition metal component (e.g., Ti, Zr, Hf)—and another "small" atom (e.g., Al, Si, B)—to the bcc-Cr/fcc-Cu mixture appeared most promising, particularly from the aspect of maximizing structural and electronic disorder, thus creating highly favorable conditions energetically for crystallization to be avoided on condensation. The middle portion of a three-piece, rectangular Cr sputter target was replaced with a TiB_2 segment, to allow CrTiCu(B,N) films to be deposited[51,75] (as with the coatings described in the previous section, the 75-mm diameter Cu target was mounted at 90° to the Cr/TiB_2/Cr "composite" target). Boron was also of particular interest due to its known grain boundary segregation and grain refinement properties[23,34,51,75,76] that we expected to assist in producing very small grain sizes in the composition ranges where a crystalline coating might result (or on annealing from the as-deposited glassy state). XRD data (standard $\theta/2\theta$ coupled scans; monochromated Cu-K_α radiation) are shown in Fig. 12.4 for 2.5–4.0-μm-thick coatings produced at 10 sccm nitrogen flow rate and sputter target powers of 2.5 kW (Cr/TiB_2/Cr) and 0.5 kW (Cu), with a substrate temperature of ~320°C. Corresponding coating compositions determined from XPS data are also shown in Table 12.3. The slightly lower nitrogen content in positions 5 and 6 (near the Cu target) probably relates to the reduced nitrogen "gettering" capability of the Cu-rich films in these positions. The content of the other elements (Cr, Ti, B) generally decreases from positions 1 to 6, as might be expected. Figure 12.4a shows "as-deposited" information for each of the six sampling positions between the two targets. As can be seen, all positions gave films that are almost completely X-ray amorphous, in a wide range of composition from essentially >55 at% Cr (with low Cu content) to ~55 at% Cu (with moderate Cr content). Film Knoop hardness (HK 25 g) however ranged from 40 GPa (position 1) to only 7 GPa (position 6). The coatings were also vacuum annealed for up to 1 h after deposition, at a range of temperatures up to 600°C.[51] Figure 12.4b shows XRD data for position 2 after a 1-h anneal at four temperatures from 450 to 600°C. The coatings appear to remain almost completely X-ray amorphous, which is surprising. However, despite the apparent stability of the films, significant changes in hardness were seen in certain positions. Again surprisingly, a hardness *increase* was generally the result; for example, position 2 (Fig. 12.4b) increased in hardness from 24 GPa (as-deposited) to a maximum of 40 GPa at 550°C (reducing slightly to 38 GPa at 600°C). It may be that partial devitrification of the coatings is occurring during annealing (electron diffraction studies carried out by the authors and their co-workers suggest this), but the crystallites are too small and few in number to be detected by conventional methods (e.g., by XRD). There would thus appear to be considerable promise in developing techniques to deposit glassy PVD metallic films, which can subsequently be devitrified by a postcoat heat treatment stage, to develop the exact nanostructure required for tribological coatings (this route has already

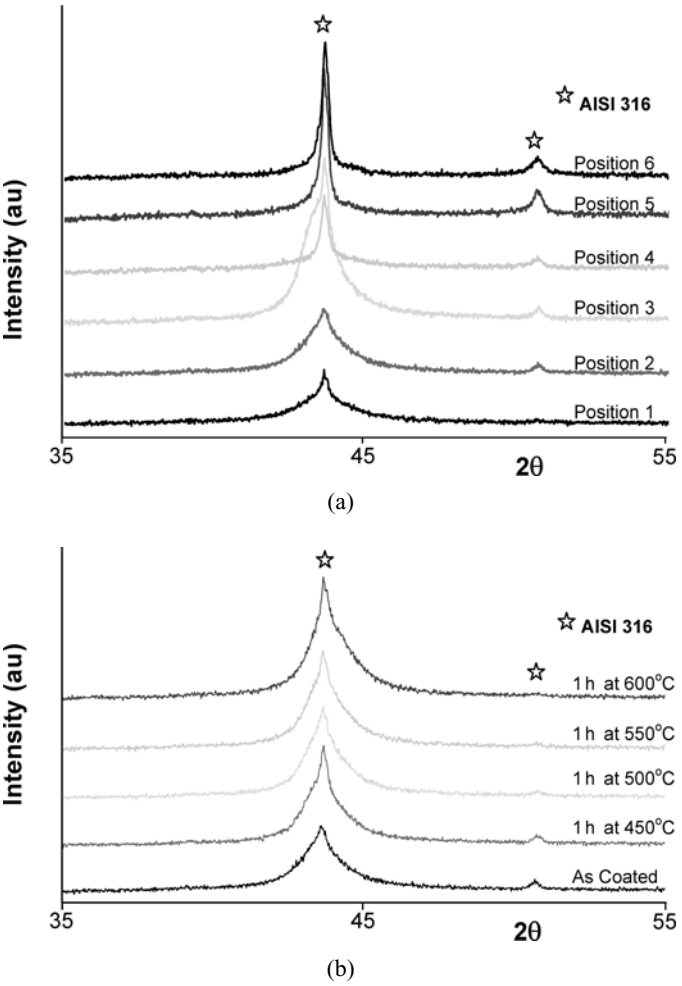

FIGURE 12.4. XRD data for CrTiCu(B,N) coatings deposited with 10 sccm nitrogen flow rate at ~320°C substrate temperature: (a) as deposited, (b) sample from position 2 annealed for 1 hour at temperatures up to 600°C (see Table 12.3 for composition).

been taken with, for example, electroless nickel coatings and sputtered magnetic thin films). Based on the preliminary results outlined above, such an approach could perhaps be considered as analogous to an "age-hardening" process (as used for aluminum–copper and other bulk alloys), whereby thermally induced clustering and aggregation of low-miscibility components in the film can be tailored to optimize both hardness and (tensile) ductility. As Wang and coworkers recently discussed,[77] a predominantly nanograined structure, interdispersed with larger microcrystallites, can be shown to be beneficial in this respect for bulk metals. It may

be possible to replicate such effects in the processing of glassy and/or partially nanocrystalline metallic-alloy tribological films—whether deposited by autocatalytic, electrochemical, thermal spray, or PVD methods—or indeed by some other means.

TABLE 12.3. XPS Composition Data (atom%) for CrTiCu(B,N) Coatings Produced at 10 sccm Nitrogen Flow Rate and a Substrate Temperature of ~320°C.

Sample	Cr	Ti	Cu	B	N
1	58.7	4.3	1.7	10.9	24.4
2	57.6	3.6	2.9	12.9	23.0
3	56.3	3.4	4.5	13.1	22.7
4	47.6	3.0	13.8	6.5	29.1
5	37.7	2.7	31.1	5.3	23.2
6	22.2	2.4	53.5	5.1	16.8

6. ADAPTIVE COATINGS

The general concept of "intelligent" or "smart" materials is one that is gaining increasing attention in the research community, not least amongst those who develop coatings. An intelligent (or "adaptive") coating can be defined as one that alters its properties to suit the operating conditions encountered. While this may appear at first sight to be a rather "blue-skies" concept, such adaptability is in fact a property that has existed in many coatings for decades. One example is coatings designed to resist high-temperature corrosion in gas turbine engines; here the coating forms a protective oxide scale (of varying composition, depending on the environment) on its surface during operation.

Similar observations can be made for some of the most recently developed cutting tool coatings, based on (for example) TiAlN, which produces a stable oxide during high-temperature cutting operations. This effect has been further enhanced in TiAlN coatings that contain additions of yttrium and/or chromium to help to extend oxide film stability over a wider range of temperatures.[78–80] In some ways, diamond and diamond-like carbon (DLC) films can also be regarded as adaptive, in the sense that the formation of a temperature-induced low shear strength layer in the contact is thought to be the source of the low friction demonstrated by many such coatings.

Another issue that is perhaps worthy of mention in the context of adaptive coatings is the recently renewed (and increasing) interest in the use of Ni-Ti, and other (e.g., copper-based[81]), shape memory alloys as wear-resistant coatings—proposed as being suitable for MEMS devices and microactuators,[81–84] due to their perceived desirable mechanical, tribological, and corrosion-resistant properties.[85–91] Such materials are known, perhaps somewhat incorrectly (since the "elastic" strain

behavior is essentially nonlinear, hysteretic, and strain-path/temperature dependent), as "superelastic" materials. A more correct term might, in general, be "pseudoelastic." These materials (in bulk form or as coatings) can exhibit desirable wear-resistant characteristics with (it is claimed) very low sliding friction coefficients. These properties are usually represented as being due to a reduced "ploughing" term during sliding contacts (i.e., the unrecoverable plastic deformation, which also absorbs "frictional" energy during sliding). In essence, this equates to a similar argument to that presented earlier for the need to maximize the H/E ratio (and therefore the "elastic strain-to-failure"). Notwithstanding the applicability (or otherwise) of that hypothesis for these particular materials (bearing in mind the time- and temperature-dependency of their properties), it is nonetheless clear that a family of "martensitic" materials can be produced which exhibit thermally recoverable (if not necessarily fully temperature-reversible) high-strain characteristics that can provide enhanced tribological properties in certain types of contacts and environments. Some of the most promising of the these alloys, produced as coatings[81–84] or surface-modified bulk materials,[85,87] comprise Ni-Ti-based compounds with additions of other elements—either substitutional,[81,82,91] or interstitial[86,87,91]—which harness the "recoverability" of the shape memory alloy, and also provide enhanced hardness, with the latter, in some cases, being provided by "Hall–Petch" hardening (i.e., a nanocomposite, high H/E coating approach[12,31–34,41,42,49–52,74,75,89–91]). However, it does appear that to gain the most effective control of friction and wear behavior, it can still be beneficial to deposit a coating with the desired tribochemical (and hardness) characteristics on top of the Ni-Ti-based alloy.[89,90]

Zabinski and coworkers have developed solid lubricant coatings that are capable of adapting to temperatures from ambient up to 500°C and beyond—even up to 800°C. At such temperatures conventional oils and greases cannot be used, and graphite and metal dichalcogenides such as MoS_2 and WS_2 have historically been employed as alternatives. Their lubricous nature is generally attributed to weak interplanar bonding and low shear strength; favorable conditions may however not prevail at higher temperatures, where such materials oxidize. Zabinski *et al.*[92,93] have reported that this oxidation may become a problem at temperatures as low as 350°C, and have carried out research into the deposition of coatings with additives such as graphite fluoride (CF_x) in order to extend the permissible operating temperature up to 450°C. They utilized a pulsed laser deposition method, showing that WS_2/CF nanocomposite films were less sensitive to moisture than WS_2 alone, achieving friction coefficients of 0.01–0.04 against a stainless steel counterface in dry air. Although not fully adaptive, such coatings nevertheless point the way forwards toward coating materials that can be effective over a wider operating range.

To provide lubricity in the higher 500–800°C temperature range, other materials must be considered. Oxides such as ZnO, along with fluorides such as CaF_2 and BaF_2, are lubricious in this regime, due to their low shear strength and high ductility. The oxides and, to a lesser extent, the fluorides are also chemically stable in air at high temperatures. At ambient temperatures, however, these materials are brittle and subject to cracking and high wear rates. Thus an answer to producing

a lubricant coating that can operate over a broad temperature range is to combine low- and high-temperature lubricant materials uniformly dispersed throughout the coating in either a nanolayered or a nanocomposite structure. Zabinski *et al*.[93] examined both layered and composite structures of CaF_2 and WS_2 grown by pulsed laser deposition. Subsequent work on steel and TiN-coated steel substrates illustrated that these films were lubricious up to 500°C. The CaF_2 and WS_2 materials interacted to form $CaSO_4$, among other compounds. Thus, the coatings in effect adapted to their environment by forming a low-friction outer layer. Voevodin and coworkers applied the "adaptive" or "chameleon" coating concept to a range of DLC-based coatings, and demonstrated that nanocomposite coatings can be produced, which are adaptive to load, environment, and temperature.[94–96]

The concept of combining coating materials to extend the operating range has been applied using several other compounds, for example MoS_2 with PbO and WS_2 with ZnO, to provide lubrication over a wide temperature range.[97–102] In these cases, the metal dichalcogenides reacted with the oxides to form $PbMoO_2$ and $ZnWO_4$, which were found to be lubricous at high temperatures. The problem with these coatings was that they were adaptive only on heating; that is, the low-temperature lubricant materials reacted to form a high-temperature lubricant—but the reaction was irreversible. After returning to room temperature, the lubricous properties had disappeared. Work is proceeding to control the reactions using diffusion barrier coatings with layered structures, to develop fully "chameleon-like" coatings—which will function reversibly through multiple temperature cycles.

Ultimately, the ideal structure for such adaptive coatings may well be a nanodispersion of non-percolated (or perhaps partially percolated) active constituents. One key issue is controlling the extent of interpenetration of the constituent phase networks (and thus the rates of supply and reaction of the species); our current work confirms that this is best achieved by coatings exhibiting nanocomposite structures. Such structures have two significant benefits for adaptive coatings (beyond those already mentioned). They allow control of the ingress of environmental species (e.g., humidity, oxygen, etc.) and also provide a degree of control of the availability of active constituents. In other words the "release-rate" of ingradients can be adapted *in situ*, to suit the operating life requirements.

7. SUMMARY

This chapter has illustrated the importance of optimizing the ratio between hardness and elastic modulus (H/E) when developing coatings for wear resistance applications. It has been shown that nanocomposite coatings offer specific attractions in this regard. Metal–metal nanocomposites in particular are promising, because of not only their mechanical and tribological behavior, but also their corrosion properties and potential to compete cost-effectively with traditional coatings in terms of achievable thicknesses and deposition rates. Finally, we have discussed how nanocomposite tribological coatings lend themselves to the goal of incorporating

"adaptive" and "chameleon-like" attributes to permit self-optimization of performance during operation, particularly for extreme high-temperature applications—and in other severe environments.

REFERENCES

1. J. F. Archard, Contact and rubbing of flat surfaces, *J. Appl. Phys.* **24**, 981 (1953).
2. K. Holmberg and A. Matthews, Coatings tribology: Properties, techniques and applications in surface engineering, in *Elsevier Tribology Series*, Vol. 28 (Elsevier, Amsterdam, 1994).
3. K. Holmberg and A. Matthews, Coatings tribology: A concept, critical aspects and future directions, *Thin Solid Films* **253**, 173–178 (1994).
4. K. Holmberg, A. Matthews, and H. Ronkainen, Coatings tribology—Contact mechanisms and surface design, *Tribol. Int*. **31**, 107–120 (1998).
5. A. Matthews, A. Leyland, K. Holmberg, and H. Ronkainen, Design aspects for advanced tribological coatings, *Surf. Coat. Technol*. **100–101**, 1–6 (1998).
6. Y. Berthier, M. Godet, and M. Brendle, Velocity accommodation in friction, *Tribol. Trans.* **32**, 460–496 (1989).
7. Y. Berthier, L. Vincent, and M. Godet, Velocity accommodation in fretting, *Wear* **125**, 25–38 (1988).
8. T. L. Oberle, Properties influencing wear of metals, *J. Met*. **3**, 438–439 (1951).
9. K. L. Johnson, *Contact Mechanics* (Cambridge University Press, Cambridge, UK, 1985). (ISBN No: 0-521-34796-3)
10. M. Godet, Y. Berthier, L. Vincent, and L. Flamand, Hard coatings for tribological applications: A pluridisciplinary approach, *Surf. Coat. Technol*. **45**, 1–8 (1991).
11. S. Ramalingam and L. Zheng, Film–substrate interface stresses and their role in the tribological performance of surface coatings, *Tribol. Int*. **28**(3), 145–161 (1995).
12. A. Leyland and A. Matthews, On the significance of the H/E ratio in wear control: A nanocomposite approach to optimised tribological behaviour, *Wear* **246**, 1–11 (2000).
13. A. Matthews, The value of deposition processes for industrial tools, in *Proceedings of the 1st Conference on Materials Engineering,* The University of Leeds, UK, July (Institution of Metallurgist, London, 1984), p. 175. (ISBN No: 0-901-46224-1)
14. S. Ramalingam and L. S. Zheng, Multi-layer and composite structures for advanced coatings, *Surf. Coat. Technol*. **81**, 52–71 (1996).
15. T. Y. Tsui, G. M. Pharr, W. C. Oliver, C. S. Bhatia, R. L. White, S. Anders, A. Anders, and I. G. Brown, Nanoindentation and nanoscratching of hard carbon coatings for magnetic disks, *Mater. Res. Soc. Symp. Proc*. **383**, 447–452 (1995).
16. G. M. Pharr, Measurement of mechanical properties by ultra-low load indentation, *Mater. Sci. Eng. A* **253**(1–2), 151–159 (1998).
17. T. Y. Tsui and G. M. Pharr, Substrate effects on nanoindentation mechanical property measurement of soft films on hard substrates, *J. Mater. Res*. **14**(1), 292–301 (1999).
18. D. Tabor, *The Hardness of Metals* (Oxford University Press, Oxford, UK, 1951). (ISBN No: 0-521-29183-6)
19. B. R. Lawn, A. G. Evans, and D. B. Marshall, Elastic/plastic indentation damage in ceramics: The median/radial crack system, *J. Am. Ceram. Soc*. **63**, 574–581 (1980).
20. J. C. Anderson, K. D. Leaver, R. D. Rawlings, and J. M. Alexander, *Materials Science* (Van Nostrand Reinhold, Wokingham, UK, UK, 1985). (ISBN No: 0-442-30626-1)
21. S. Veprek, New development in superhard coatings: The superhard nanocrystalline–amorphous composites, *Thin Solid Films* **317**, 449–454 (1998).
22. P. Haasen, *Physical Metallurgy* (Cambridge University Press, Cambridge, UK, 1978). (ISBN No: 0-521-29183-6)

23. C. Rebholz, A. Leyland, J. M. Schneider, A. A. Voevodin, and A. Matthews, Structure, hardness and mechanical properties of magnetron-sputtered titanium-aluminium boride films, *Surf. Coat. Technol*. **120–121**, 412–417 (1999).
24. H. Holleck, Material selection for hard coatings, *J. Vac. Sci. Technol*. *A* **4**(6), 2611–2669 (1986).
25. H. Holleck and H. Schulz, Preparation and behaviour of wear-resistant TiC/TiB_2, TiN/TiB_2 and TiC/TiN coatings with high amounts of phase boundaries, *Surf. Coat. Technol*. **36**, 707–714 (1988).
26. C. Mitterer, M. Rauter, and P. Rödhammer, Sputter deposition of ultrahard coatings within the system Ti-B-C-N, *Surf. Coat. Technol*. **41**, 351–363 (1990).
27. H. Ronkainen, I. Nieminen, K. Holmberg, A. Leyland, K. S. Fancey, A. Matthews, B. Matthes, and E. Broszeit, Evaluation of some new titanium-based ceramic coatings in tribological model wear and metal cutting tests, *Mater. Sci. Eng*. *A* **140**, 602–608 (1991).
28. H. Ronkainen, I. Nieminen, K. Holmberg, A. Leyland, A. Matthews, B. Matthes, and E. Broszeit, Evaluation of some titanium-based ceramic coatings on high speed steel cutting tools, *Surf. Coat. Technol*. **49**, 468–473 (1992).
29. W. Gissler, Structure and properties of Ti-B-N coatings, *Surf. Coat. Technol*. **68–69**, 556–563 (1994).
30. C. Mitterer, P. Losbichler, F. Hofer, P. Warbichler, P. N. Gibson, and W. Gissler, Nanocrystalline hard coatings within the quasi-binary system TiN-TiB_2, *Vacuum* **50**(3–4), 313–318 (1998).
31. C. Rebholz, H. Ziegele, A. Leyland, and A. Matthews, Structure, mechanical and tribological properties of Ti-B-N and Ti-Al-B-N thin films produced by electron beam evaporation, *J. Vac. Sci. Technol*. *A* **16**(5), 2851–2857 (1998).
32. C. Rebholz, J. M. Schneider, A. A. Voevodin, J. Steinebrunner, C. Charitidis, S. Logothetidis, A. Leyland, and A. Matthews, Structure, mechanical and tribological properties of sputtered TiAlBN thin films, *Surf. Coat. Technol*. **113**, 126–133 (1999).
33. C. Rebholz, A. Leyland, and A. Matthews, Deposition and characterisation of TiAlBN coatings produced by direct electron-beam evaporation of Ti and Ti-Al-B-N material from a twin crucible source, *Thin Solid Films* **343–344**, 242–245 (1999).
34. C. Rebholz, A. Leyland, P. Larour, C. Charitidis, S. Logothetidis, and A. Matthews, The effect of boron additions on the tribological behaviour of TiN coatings produced by electron-beam evaporative PVD, *Surf. Coat. Technol*. **116–119**, 648–653 (1999).
35. C. Liu, A. Leyland, Q. Bi, and A. Matthews, Corrosion resistance of multi-layered PAPVD TiN and CrN coatings, *Surf. Coat. Technol*. **141**(2–3), 164–173 (2001).
36. C. Suryanarayana and C. C. Koch, Nanocrystalline materials—Current research and future directions, *Hyperfine Interact.* **130**, 5–44 (2000).
37. S. Veprek, The search for novel superhard materials, *J. Vac. Sci. Technol. A* **17**(5), 2401–2420 (1999).
38. S. Veprek and A. S. Argon, Towards the understanding of mechanical properties of super and ultra-hard nanocomposites, *J. Vac. Sci. Technol*. *B* **20**(2), 650–664 (2002).
39. J. Musil, I. Leipner, and M. Kolega, Nanocrystalline and nanocomposite CrCu and CrCu-N films prepared by magnetron sputtering, *Surf. Coat. Technol*. **115**, 32–37 (1999).
40. J. Musil and R. Daniel, Structure and mechanical properties of magnetron sputtered Zr-Ti-Cu-N films, *Surf. Coat. Technol*. **166**(2–3), 243–253 (2003).
41. A. Leyland and A. Matthews, Design criteria for wear-resistant nanostructured and glassy-metal coatings, *Surf. Coat. Technol*. **177–178**, 317–324 (2004).
42. C. Rebholz, H. Ziegele, A. Leyland, and A. Matthews, Structure, mechanical and tribological properties of nitrogen-containing chromium coatings prepared by reactive magnetron sputtering, *Surf. Coat. Technol*. **115**, 222–229 (1999).
43. C. Rebholz, J. M. Schneider, A. Leyland, and A. Matthews, Wear behaviour of carbon-containing tungsten coatings prepared by reactive magnetron sputtering, *Surf. Coat. Technol*. **112**, 85–90 (1999).

44. A. Matthews, A. Leyland, B. Dorn, P. R. Stevenson, M. Bin-Sudi, C. Rebholz, A. A. Voevodin, and J. M. Schneider, Plasma-based surface engineering processes for wear and corrosion protection, *J. Vac. Sci. Technol. A* **13**(3), 1202–1207 (1995).
45. B. Rähle, *Thick Nitrogen-Doped Stainless Steel Coatings for Wear and Corrosion Protection, Produced by High-rate UBM Sputtering*, M.Sc. Thesis (University of Hull, Hull, UK, 1999).
46. A. E. McHale (ed.), *Phase Equilibria Diagrams: Volume X—Borides, Carbides and Nitrides* (American Ceramic Society, Westerville, OH), p. 415. (ISBN No: 0-944904-74-2)
47. A. Leyland and A. Matthews, Thick Ti/TiN multilayered coatings for abrasive and erosive wear resistance, *Surf. Coat. Technol*. **70**, 19–25 (1994).
48. M. Bin-Sudin, A. Leyland, A. S. James, A. Matthews, J. Housden, and B. L. Garside, Substrate surface finish effects in duplex coatings of PAPVD TiN and CrN with electroless nickel–phosphorus interlayers, *Surf. Coat. Technol*. **81**, 215–224 (1996).
49. M. A. Baker, P. J. Kench, M. C. Joseph, C. Tsotsos, A. Leyland, and A. Matthews, The nanostructure and mechanical properties of PVD CrCu(N) coatings, *Surf. Coat. Technol*. **162**, 222–227 (2003).
50. M. A. Baker, P. J. Kench, C. Tsotsos, P. N. Gibson, A. Leyland, and A. Matthews, Evaluating the nanostructure of PVD CrCu(N) coatings, *J. Vac. Sci. Technol. A* **23**(3), 423–433 (2005).
51. C. Tsotsos, K. Kanakis, A. Davison, M. A. Baker, A. Matthews, and A. Leyland, Mechanical and tribological properties of CrTiCu(B,N) glassy-metal coatings deposited by reactive magnetron sputtering, *Surf. Coat. Technol*., **200**(14–15), 4601–4611 (2006).
52. M. A. Baker, S. Klose, C. Rebholz, A. Leyland, and A. Matthews, Evaluating the microstructure and performance of nanocomposite PVD TiAlBN coatings, *Surf. Coat. Technol*. **151–152**, 338–343 (2002).
53. J. Patscheider, T. Zehnder, and M. Diserens, Structure–performance relations in nanocomposite coatings, *Surf. Coat. Technol*. **146–147**, 201–208 (2001).
54. K. Binder and P. Fratzl, in *Phase Transformations in Materials*, edited by G. Kostorz (Wiley-VCH Verlag GmbH, Weinheim, Germany, 2001), p. 411. (ISBN No: 3-527-30256-2)
55. Y. Liu, R. Singh, K. Poole, R. J. Diefendorf, J. Harriss, and K. Cannon, Characterization of Al-Y alloy thin films deposited by direct current magnetron sputtering, *J. Vac. Sci. Technol. B* **15**(6), 1990–1994 (1997).
56. W. Hume-Rothery and B. R. Coles, *Atomic Theory for Students of Metallurgy*, 6th edn. (Maney Publishing, London, 1988). (ISBN No: 0-901462-39-X) (1st edn. published 1946).
57. D. Turnbull and J. C. Fisher, Rate of nucleation in condensed systems, *J. Chem. Phys*. **17**(1), 71–73 (1949).
58. P. Duwez, R. H. Willens, and W. Klement, Continuous series of metastable solid solutions in silver-copper alloys, *J. Appl. Phys*. **31**(6), 1136–1137 (1960).
59. H. S. Chen and D. Turnbull, Evidence of a glass–liquid transition in a gold–germanium–silicon alloy, *J. Chem. Phys*. **48**(6), 2560–2571 (1968).
60. H. S. Chen and D. Turnbull, Formation, stability and structure of palladium–silicon based alloy glasses, *Acta Metall*. **17**(8), 1021–1031 (1969).
61. H. A. Davies, The formation of metallic glasses, *Phys. Chem. Glasses* **17**(5), 159–173 (1976).
62. L. E. Tanner and R. Ray, Metallic glass formation and properties in Zr and Ti alloyed with Be, *Acta Metall*. **27**(11), 1727–1747 (1979).
63. W. L. Johnson, Thermodynamic and kinetic aspects of the crystal to glass transformation in metallic materials, *Prog. Mater. Sci*. **30**(2), 81–134 (1986).
64. A. Peker and W. L. Johnson, A highly processable metallic glass: $Zr_{41.2}Ti_{13.8}Cu_{12.5}Ni_{10.0}Be_{22.5}$, *Appl. Phys. Lett*. **63**(17), 2342–2344 (1993).
65. A. Inoue, Bulk amorphous and nanocrystalline alloys with high functional properties, *Mater. Sci. Eng. A* **304–306**, 1–10 (2001).
66. D. V. Louzguine and A. Inoue, Comparisons of the long-term thermal stability of various metallic glasses under continuous heating, *Scr. Mater*. **47**, 887–891 (2002).

67. A. Inoue, W. Zhang, T. Zhang, and K. Kurosaka, Cu-based bulk glassy alloys with high tensile strength of over 2000 MPa, *J. Non-Cryst. Solids* **304**(1–3), 200–209 (2002).
68. W. L. Johnson, Bulk glass-forming metallic alloys: Science and technology, *MRS Bull*. **24**(10), 42–56 (1999).
69. D. J. Branagan, W. D. Swank, D. C. Haggard, and R. J. Fincke, Wear-resistant amorphous and nanocomposite steel coatings, *Metall. Mater. Trans*. *A* **32**, 2615–2621 (2001).
70. S. Pang, T. Zhang, K. Asami, and A. Inoue, Formation of bulk glassy $Fe_{75-x-y}Cr_xMo_yC_{15}B_{10}$ alloys and their corrosion behaviour, *J. Mater. Res*. **17**, 701–704 (2002).
71. F. Sanchette, T. H. Loi, A. Billard, and C. Frantz, Structure–properties relationship of metastable Al-Cr andAl-Ti alloys deposited by r.f. magnetron sputtering: Role of nitrogen, *Surf. Coat. Technol*. **74–75**, 903–909 (1995).
72. F. Sanchette, A. Billard, and C. Frantz, Mechanically reinforced and corrosion-resistant sputtered amorphous aluminium alloy coatings, *Surf. Coat. Technol*. **98**, 1162–1168 (1998).
73. F. Sanchette and A. Billard, Main features of magnetron sputtered aluminium-transition metal alloy coatings, *Surf. Coat. Technol*. **142–144**, 218–224 (2001).
74. M. C. Joseph, C. Tsotsos, M. A. Baker, P. J. Kench, C. Rebholz, A. Matthews, and A. Leyland, Characterisation and tribological evaluation of nitrogen-doped molybdenum–copper PVD metallic nanocomposite films, *Surf. Coat. Technol*. **190**, 345–356 (2005).
75. M. Monclus, M. A. Baker, C. Tsotsos, A. Davison, A. Leyland, and A. Matthews, Investigation of the nanostructure and post-coat thermal treatment of wear resistant PVD CrTiCuBN coatings, *Surf. Coat. Technol*. **200**(1–4), 310–314 (2005).
76. B. Rother and H. Kappl, Results on the thermal stability of cathodic arc-deposited (Cr,B)N coatings, *Surf. Coat. Technol*. **73**, 14–17 (1995).
77. Y. Wang, M. Chen, F. Zhou, and E. Ma, High tensile ductility in a nanostructured metal, *Nature* **419**, 912–915 (2002).
78. W. D. Munz, I. J. Smith, L. A. Donohue, A. P. Deeming, and R. Goodwin, TiAlN based PVD coatings tailored for dry cutting operations, in *Proceedings of the 40th Annual Technical Conference of the Society of Vacuum Coaters SVC*, SVC Albuquerque, New Mexico, USA, 1997, pp. 89–93.
79. E. Pfluger, A. Schroer, P. Voumard, L. Donohoue, and W. D. Munz, Influence of incorporation of Cr and Y on the wear performance of TiAlN coatings at elevated temperatures, *Surf. Coat. Technol*. **115**, 17–23 (1999).
80. A. Savan, E. Pfluger, R. Goller, and W. Gissler, Use of nanoscaled multilayer and compound films to realise a soft lubrication phase within a hard wear resistance matrix, *Surf. Coat. Technol*. **126**, 159–165 (1999).
81. A. C. Kneissl, K. Kutschej, and X. Wu, Production and characterisation of Cu-Al-Ni shape memory thin films, *J. Physique IV* **112**, 571–574 (2003).
82. K. Bhattacharya and R. D. James, A theory of thin films of martensitic materials with applications to microactuators, *J. Mech. Phys. Solids* **47**, 531–576 (1999).
83. Y. Fu, H. Du, and S. Zhang, Sputtering deposited TiNi films: Relationship among processing, stress evolution and phase transformation behaviours, *Surf. Coat. Technol*. **167**, 120–128 (2003).
84. W. Ni, Y.-T. Cheng, and D. S. Grummon, Microscopic shape memory and superelastic effects under complex loading conditions, *Surf. Coat. Technol*. **177–178**, 512–517 (2004).
85. G. L. Sheldon, R. Wang, and R. A. Clark, Characteristics of Ni-Ti surface alloys formed by electrospark deposition, *Surf. Coat. Technol*. **36**, 445–454 (1988).
86. K. Bouslykhane, P. Moine, J.-P. Villain, and J. Grilhé, Mechanical properties and wear resistance of ion-beam-assisted sputter-deposited NiTi(N) coatings, *Surf. Coat. Technol*. **49**, 457–461 (1991).
87. H. C. Lin, H. M. Liao, J. L. He, K. M. Lin, and K. C. Chen, Wear characteristics of ion-nitrided $Ti_{50}Ni_{50}$ shape memory alloys, *Surf. Coat. Technol*. **92**, 178–189 (1997).
88. J. Koskinen, E. Haimi, A. Mahiout, V. K. Lindroos, and S.-P. Hannula, Superelastic NiTi coatings with good corrosive wear resistance, *J. Physique IV* **112**, 1137–1140 (2003).

89. W. Ni, Y.-T. Cheng, M. J. Lukitsch, A. M. Weiner, L. C. Lev, and D. S. Grummon, Effects of the ratio of hardness to Young's modulus on the friction and wear behavior of bilayer coatings, *Appl. Phys. Lett.* **85**(18), 4028–4030 (2004).
90. W. Ni, Y.-T. Cheng, M. J. Lukitsch, A. M. Weiner, L. C. Lev, and D. S. Grummon, Novel layered tribological coatings using a superelastic NiTi interlayer, *Wear* **259**, 842–848 (2004).
91. S. Zhang, D. Sun, Y. Fu, Y.-T. Pei, and J. Th. M. De Hosson, Ni-toughened nc-TiN/a-SiN_X nanocomposite thin films. *Surf. Coat. Technol*., **200**(5–6), 1530–1534 (2005).
92. J. S. Zabinski, M. S. Donley, S. D. Walck, T. R. Schneider, and N. T. McDevitt, The effects of dopants on the chemistry and tribology of sputter-deposited MoS_2 films, *Tribol. Trans.* **36**, 894–904 (1995).
93. J. S. Zabinski, J. E. Florkey, S. D. Walck, J. E. Bultman, and N. T. McDevitt, Friction properties of WS_2/graphite fluoride thin films grown by pulsed layer deposition, *Surf. Coat. Technol*. **76–77**, 400–406 (1995).
94. A. A. Voevodin and J. S. Zabinski, Load-adaptive crystalline–amorphous nanocomposites, *J. Mater. Sci*. **33**, 319–327 (1998).
95. A. A. Voevodin, J. P. O'Neill, and J. S. Zabinski, WC/DLC/WS_2 nanocomposite coatings for aerospace tribology, *Tribol. Lett*. **6**, 75–78 (1995).
96. A. A. Voevodin, T. A. Fitz, J. J. Hu, and J. S. Zabinski, Nanocomposite tribological coatings with "chameleon surface adaption," *J. Vac. Sci. Technol. A* **20**(4), 1434–1444 (2002).
97. M. S. Donley and J. S. Zabinski, *Tribological Coatings in Pulsed Laser Deposition of Thin Films*, (Wiley, New York, 1994).
98. J. S. Zabinski, S. V. Prasad, and N. T. McDevitt, Advanced solid lubricant coatings for aerospace systems in tribology for aerospace systems, in *Proceedings of NATO AGARD SMP Conference*, Sesimbra, Portugal, May 6–7, 1996, AGARD-CP-589.
99. J. S. Zabinski, M. S. Donley, V. J. Dyhouse, and N. T. McDevitt, Chemical and tribological characterisation of PbO-MoS_2 films grown by pulsed laser deposition, *Thin Solid Films* **214**, 156–163 (1992).
100. S. D. Walck, M. S. Donley, J. S. Zabinski, and V. J. Dyhouse, Characterisation of pulsed laser deposited PbO/MoS_2 by transmission electron microscopy, *J. Mater. Sci*. **9**, 236–245 (1994).
101. S. D. Walck, J. S. Zabinski, N. T. McDevitt, and J. E. Bultman, Characterisation of air-annealed pulse laser deposited ZnO-WS_2 solid film lubricants by transmission electron microscopy, *Thin Solid Films* **305**, 130–143 (1997).
102. J. S. Zabinski and M. S. Donley, Lubricant coatings, *US Patent* 5,282,985 (1994).

13

Synthesis, Structure, and Properties of Superhard Superlattice Coatings

Lars Hultman

Thin Film Group, Department of Physics, IFM, Linköping University, 581 83 Linköping, Sweden

1. INTRODUCTION

Nanolaminated coating structures such as ceramic superlattices (SLs) are attractive in that the materials can be designed for high strength, stiffness, and hardness.[1,2] Superhard materials can be made by limiting dislocation glide and any crack propagation in SLs.[2,3] Theory thus presumes plasticity with dislocation hindering at interfaces between phases with different shear modulus.

Model systems for the nanolaminates reviewed here are artificial nitride SLs. It is reassuring that such coatings as a type of nanostructure-engineered material are offered commercially.[4] Discovered in the 1980s —and thus predating the so called nanoscience and nanotechnology era—such nanolaminates of transition metal nitrides made by physical vapor deposition (PVD) processes are an emerging class of wear-protective coatings. Increased hardness (to >50 GPa) as compared to single layers is reported for both as-deposited single crystal SL[1,5–8] and polycrystalline nanolayered thin films,[4,9] e.g., the material systems TiN/NbN, TiN/VN, TiN/AlN, and their alloyed derivates. Hardness enhancement is explained by dislocation hindering at the interfaces due to differences in shear moduli, and by coherency strain in the lattice-mismatched materials.[2,3,10,11]

Plastic deformation and interdiffusion (thermal stability) mechanisms are poorly understood for these materials, in particular, interactions of dislocations between and within the constituent phases.[12,13] Recent studies for the dislocation activity in nitride SL systems during both lattice misfit strain relaxation at layer interfaces and in response to mechanical load will be reviewed in this chapter. The thermal stability of SLs is presented elsewhere in this book.

2. GROWTH OF SUPERLATTICE FILMS

Layers with defined compositional modulation and interface smoothness are preferably grown by PVD methods where interdiffusion and roughening during deposition is limited due to kinetic constraints. In order to control composition modulation, care has to be taken for the deposition flux. Layers with virtually atomically abrupt interfaces can be obtained by sequential magnetron sputtering deposition. For more industrially applied processes, where substrate rotation is between fixed sources, however, graded interfaces are expected. Even second or higher order modulation is reported in case of threefold rotational geometry.[14]

We employed transmission electron microscopy (TEM) to study the growth modes of (001)-oriented transition metal nitride bilayer and SL films.[11] In particular, the conditions for coherently strained growth of successive layers and eventual relaxation by misfit dislocation formation were studied in epitaxial bilayer films of TiN, NbN, VN, and TiNbN as a function of overlayer film thickness and degree of lattice mismatch. The deposition process was dual-cathode ultrahigh vacuum magnetron sputtering onto MgO(001) substrates.

During initial deposition after nucleation and during coalescence, partially relaxed overlayers were found to exhibit edge misfit dislocations with Burgers vectors out of the interface plane and lines along $\langle 100 \rangle$ directions, as well as dislocations with Burgers vectors in the interface plane and lines along $\langle 110 \rangle$ directions.[11] This can be seen in Fig. 13.1a,b for a 2-nm-thick epitaxial NbN layer on TiN(001). With increasing overlayer thickness or mismatch, however, the continuous layers were found to be more fully relaxed and the predominant dislocations were of the latter type, see Fig. 13.2a,b for the case of 10-nm NbN(001) layer thickness.

In addition, threading dislocation segments were often observed at the ends of the misfits. This is exemplified in Fig. 13.3 for a 4.5-nm-thick epitaxial VN layer on TiN(001). The results can be explained by the following model. Relaxation is initiated by the nucleation of half-loops and their glide to the interface to form misfit dislocations and trailing threading dislocations. This is the same mechanism proposed for relaxation of lattice-mismatched semiconductor films by Matthews and Blakeslee.[15]

The dislocations glide to the (001) interface on inclined $\{011\}$ planes, resulting in the observation of $b = 1/2\langle 0\bar{1}1 \rangle$ dislocations with $s = \langle 100 \rangle$ early in the relaxation process. For more complete relaxation, dislocations only with $b = 1/2\langle 110 \rangle$ and $s = \langle 1\bar{1}0 \rangle$ were observed, presumably due to dislocation reactions of the type $1/2[0\bar{1}1] + 1/2[10\bar{1}] \rightarrow 1/2[1\bar{1}0]$. The primary misfit dislocation system was thus of edge type with line direction [110] and Burgers vectors $1/2[1\bar{1}0]$ within the (001) plane of the interface. That represents the shortest lattice vector in these NaCl-structure nitrides.[1,16]

Dislocations were also investigated using high-resolution cross-sectional TEM (HRTEM) of multilayered films. The edge dislocations discussed above

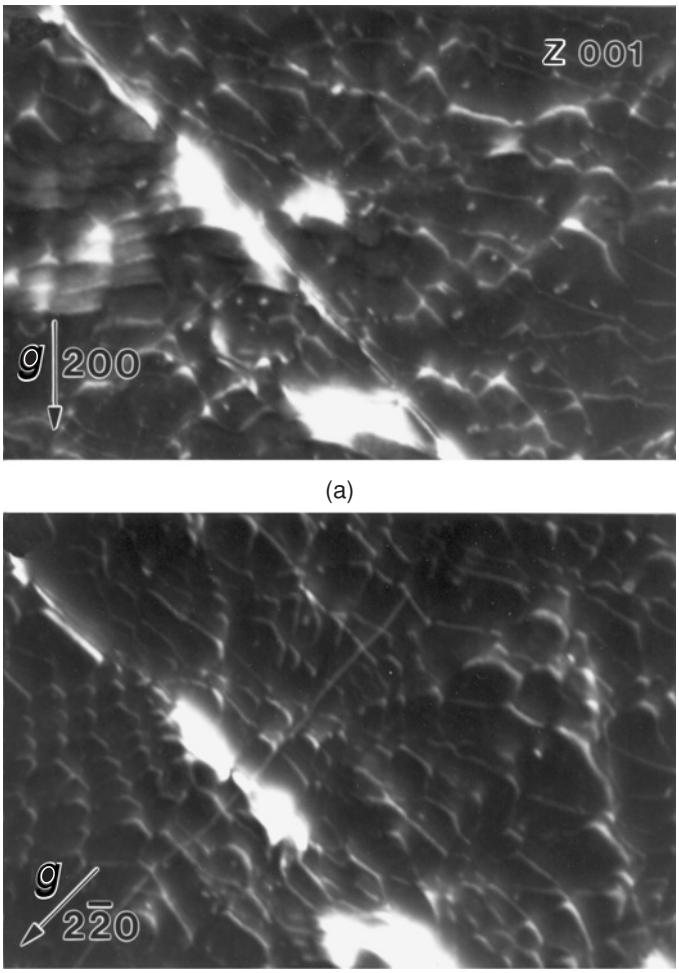

FIGURE 13.1. Dark-field plan-view transmission electron images of a 2-nm-thick epitaxial NbN film deposited on TiN(001). The same area is imaged using different diffracting vectors $\boldsymbol{g}$: (a) [200] and (b) [2 $\bar{2}$ 0]. (From Ref. 11.)

with $b = 1/2\langle 110\rangle$ could now be imaged in lattice resolution. Figure 13.4a is a HRTEM image from a TiN/NbN SL film with a period $\Lambda = 9.4$ nm that was partially relaxed.[11] The locations of two edge dislocations with $b = 1/2[101]$ and $1/2[10\bar{1}]$, respectively (out of the interface plane), are shown together with a simplified schematic drawing of the atomic structure of the dislocation (see Fig. 13.4b).[11] Dislocations with $b = 1/2[110]$ in the interface plane could not be imaged with the [010] zone axis used.

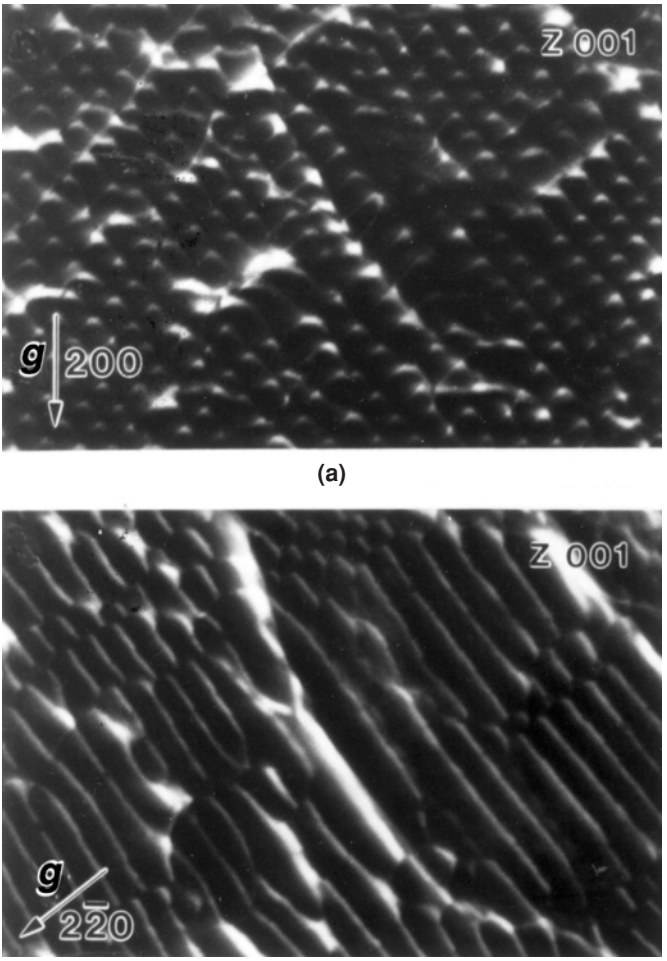

FIGURE 13.2. Dark-field plan-view transmission electron images of a 10-nm-thick epitaxial NbN film deposited on TiN(001). The same area is imaged using diffracting vectors ***g***: (a) [200] and (b) [2 $\bar{2}$ 0]. (From Ref. 11.)

Since $\{001\}$ is not a preferred glide plane for these nitrides, the misfit dislocations are considered to be nonglissile. The critical thickness for the onset of strain relaxation in bilayer nitride systems increased with decreasing mismatch εgrom <2 nm for NbN/TiN (εg 3.6%) to 2–3 nm for VN/TiN and TiN/$Ti_{0.3}Nb_{0.7}N$ ($\varepsilon = 2.4\%$) and to 3–5 nm for NbN/$Ti_{0.3}Nb_{0.7}N$ ($\varepsilon = 1\%$). The strain relaxation onset follows that predicted by Matthews–Blakeslee theory.[15,17] For SLs with equal layer thicknesses, TiN/VN (2.4% mismatch) and TiN/NbN (3.6% mismatch) SLs begin to relax at layer thicknesses of $\approx$20 and 12 nm, respectively.[11]

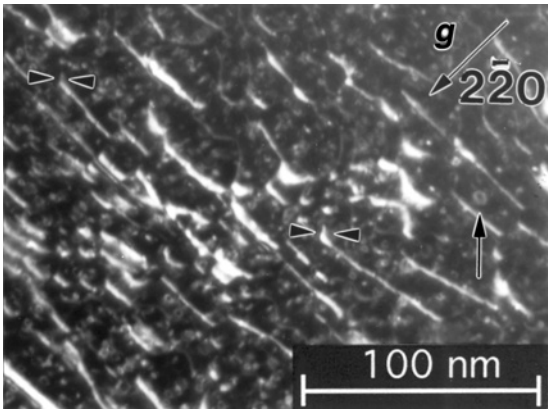

FIGURE 13.3. Dark-field plan-view transmission electron micrograph of a 4.5-nm-thick VN film deposited on a 100-nm TiN(001) layer under imaging condition $\boldsymbol{g} = [2\ \bar{2}\ 0]$ showing misfit dislocations along [110], relatively short (∼5 nm) threading dislocation segments (marked by arrows) at the ends of misfit dislocations, and small (2–5 nm) dislocation loops many of which are in the TiN layer. (From Ref. 11.)

3. ORIGIN OF SUPERHARDENING

Enhanced hardness of up to 300% compared to single-layered material is observed for nitrides with a periodicity of 5–10 nm, for both single- and polycrystalline

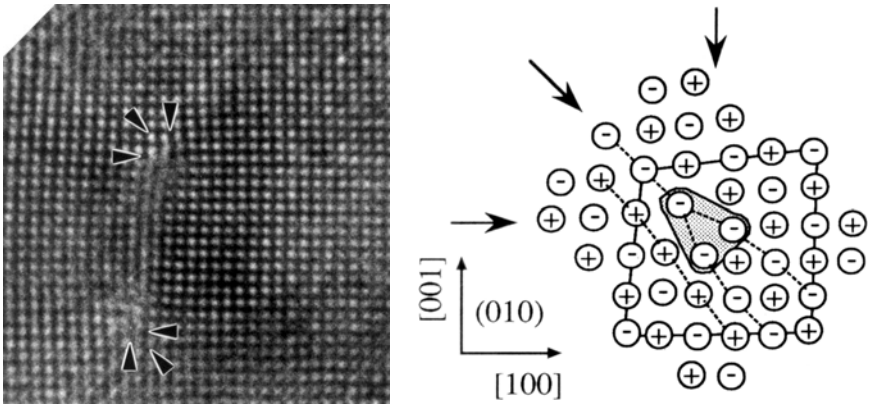

FIGURE 13.4. (a) Cross-sectional high-resolution lattice fringe image from the [010] zone axis of a TiN/NbN(001) SL film with period $\Lambda = 9.4$ nm. Edge dislocations with Burgers vector corresponding to [101] are indicated by arrows. (b) Schematic drawing of the atomic structure of the (110) edge dislocation in the sodium chloride structure similar to TiN and NbN. (From Ref. 11.)

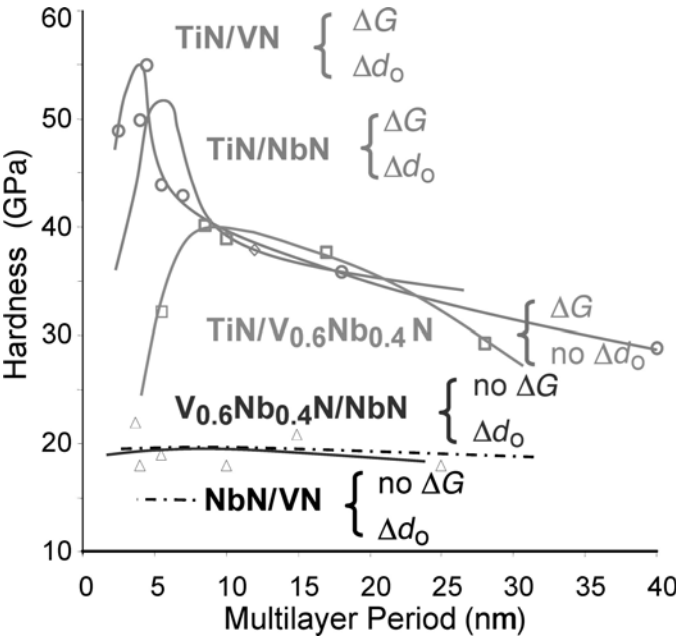

FIGURE 13.5. Hardness of different combinations of nitride SLs representing different conditions of shear modulus difference (ΔG) and lattice parameter difference ($\Delta d0$). (From Refs. 6 and 10.)

SLs.[1,18] Figure 13.5 shows results from different combinations of nitride SL with a difference in shear modulus (ΔG) or lattice parameter (Δd_0).

Many of the issues regarding elastic properties are unsolved; however, a few explanations of the strengthening effects were put forward. Those were reviewed by Barnett.[2] Elastic-moduli differences of the constituting layer materials are considered to be a critical factor as confirmed by the data in Fig. 13.5. Elastic anomalies, however, are either nonexistent or too small to explain the strength/hardness enhancements. For small-period SLs, yield stress enhancements are determined by calculating the stress required to move dislocations across the layers, as proposed by Koehler[3] and developed by Lehoczky.[19,20] For large periods—larger than that giving the hardness maximum—the yield stress would be limited by operation of dislocation sources[19] and dislocation glide[21,22] within layers. Thus, it is necessary to know the operating dislocation glide systems as well as values for the shear moduli (dislocation line energies).

Coherency strain between crystalline layers with epitaxial orientationships or low-angle grain boundaries is shown to contribute to hardening, but to a much lesser extent than the shear modulus difference effect[2] (cf. Fig. 13.5). The misfit dislocation arrays discussed above (see Figs. 13.1–13.4) will of course also play a role in plastic deformation.

4. MECHANICAL DEFORMATION AND WEAR MECHANISMS

For Cu/Nb and Cu/Ni nanolayer composites after deformation, Lu *et al*.[23] and Anderson *et al*.[24] used cross-sectional transmission electron microscopy (XTEM) to see dislocation bowing in opposite directions in the alternating layers and dislocation glide limited to single layers. Layer thickness was, however, larger than the most interesting scale at 5–10 nm for accessing the maximum in hardness. In that case, as for the nitride SL systems discussed below, the resolution limit in electron microscopy for imaging dislocations in strain contrast becomes comparable to the individual layer thickness.

The deformation and stability of nanolaminates and artificial SLs has become an important field of research in the last few years.[12] Figure 13.6 first shows HRTEM images of a TiN/NbN SL .[25] Layers with defined compositional modulation and interface smoothness were grown by reactive magnetron sputter deposition process with dual targets. It is also seen that the layers are coherently strained for the 3.5% lattice-mismatched system with epitaxial growth of TiN and NbN.[5]

Studies of slip in mechanically deformed zones of single-crystal TiN/NbN and TiN/VN SL were conducted using nanoindentation in combination with transmission electron microscopy and atomic force microscopy.[26,27] The mechanical deformation in these SL during indentation experiments is elastoplastic. The focused ion beam cross-section sample-preparation technique for the electron microscope

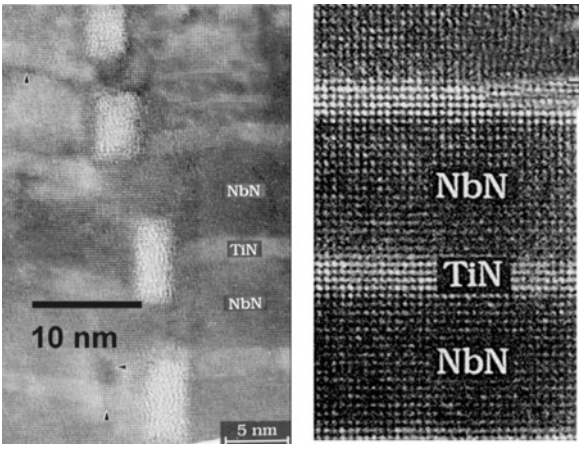

(a) (b)

FIGURE 13.6. Cross-sectional TEM images of single-crystal TiN/NbN SLs with (a) self-organized nanovoids at layer cusps and (b) dense coherently strained layers. (From Ref. 25.)

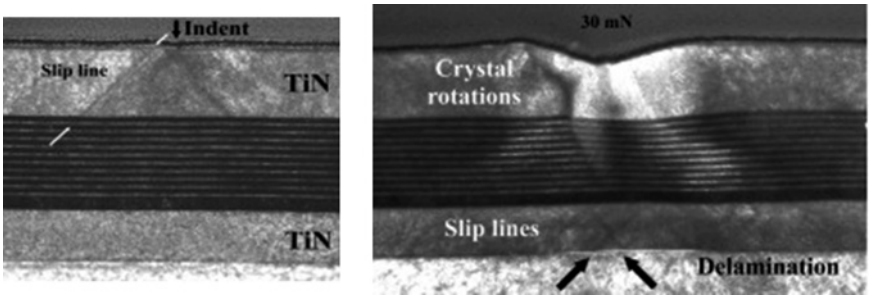

FIGURE 13.7. XTEM images of the mechanically deformed zone under Berkowich nanoindents with load of 10 mN (left image) and 30 mN (right image) into an epitaxial heterostructure of a TiN(001)/TiN/NbN(001) SL stack and TiN(001) buffer layer on MgO(001), respectively. From Ref. 28.

studies has proven further useful to demonstrate how slip is arrested at the SL interface.[25] Berkovich indents made into a model stack of TiN/NbN(001) SL are depicted in Fig. 13.7. For a 10-mN load, it is evident that slip lines propagate through top TiN layer, but stop at the SL. For 30-mN load, however, slip lines nucleate at bottom TiN layer, but not within the SL; there are crystal rotations in top TiN layer and SL; the layered structure is preserved; and there has been material flow within the SL layers.

Figure 13.8 shows an XTEM image of a TiN/NbN SL after nanoscratching.[13] The induced deformation zone exhibits pileup at the scratch rim and contains the following features: (1) retained SL domains rotated with respect to each other; (2) deformation along column boundaries; and (3) deformation-induced differences in SL period between regions. Deformation is localized to apparent column boundaries that were present in the as-deposited case, but aligned perpendicular to the film surface sample. Such boundaries can be the site for nano-sized voids (see Fig. 13.6a)[25] formed by a self-organized process under kinetically limited growth conditions (low temperature in combination with shadowing of the deposition flux by surface protrusions).

The change in SL period induced by the mechanical deformation suggests transportation of material. HRTEM imaging revealed bending of the lattice by ordering of glide dislocations. The deformed lattice stays straight within layers, but forms knees at layer interfaces, indicating that low-angle grain boundaries have been formed by these dislocations.

The deformation zone in TiN/NbN SL is obviously smaller and more complex compared to that in monolithic TiN. Layers stay relatively intact with no large slip bands, whereas for TiN, extensive slip bands were observed on $\{110\}$ planes, in agreement with the $\{110\}\langle 1\bar{1}0\rangle$ slip system for TiN[1,16] (cf., Fig. 13.7). Glide within layers of the SL is the dominating deformation mechanism in support of the prevailing models for SL hardening.[2,3]

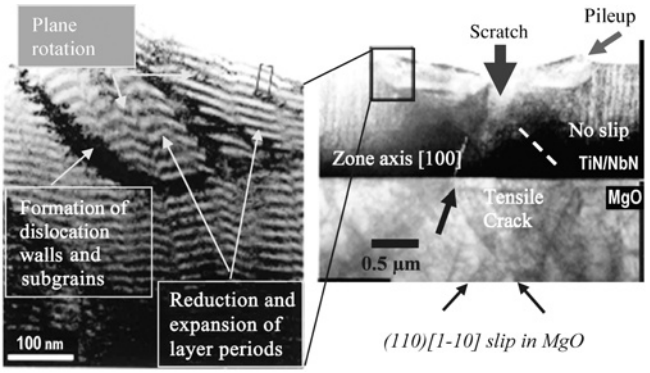

FIGURE 13.8. XTEM image of a 12-nm-period (001)-oriented single-crystal TiN/NbN SL [deposited on MgO(001) substrate] after nanoscratching with 35-mN Berkovitch diamond tip. (From Ref. 13.)

Results from the deformed zone in the TiN/NbN(001) SL films from nanoindents are similar to that of nanoscratches.[29] Previously, dislocation confinement to individual layers was reported for metallic multilayers (cf., Cu/Ni).[24]

Considering the high hardness enhancement aimed for compared to the monolithic films, the SL definition becomes correspondingly important. Thus, the films must be free of flaws, like grain boundary porosity (common to magnetron sputtered films at low ion energetic conditions) or macroparticle inclusions (common to cathodic arc deposition). Such flaws would act as weak points for microcracking or dislocation sources. Molina *et al.*[29] thus showed for TiN/NbN SL films that deformation occurred preferentially along voided column boundaries with an accompanying hardness limitation.

An example of this condition can be seen in Fig. 13.9 for a magnetron-sputtered polycrystalline TiN/TiAlN multilayer after a 450-mN indentation.[30] Here, the material exhibits a bimodal cracking at column boundaries and through layers. The crack pattern in Fig. 13.9, however, also shows that nanolaminates can serve to enhance fracture toughness of a coating. This is by virtue of the crack deflection and its effective elongation.

In partial conclusion, one should avoid these weak points by increasing the ion flux during deposition. The ion energy tuning, however, becomes a sensitive factor, since too high momentum transfer to the growing film induces lattice defects and compressive residual stress. The consequences of that will be discussed below.

For nonisostructural SLs of, e.g., the bcc-W/fcc-NbN system,[31] there are no common slip systems. This implies that deformation mechanisms should be different to the isostructural materials discussed above. Recently XTEM observations of W–NbN epitaxial SL films with periodicity $\Lambda = 20$ nm were made after wedge indentation[31] by a technique developed by Kramer *et al.*[32] While the films exhibit

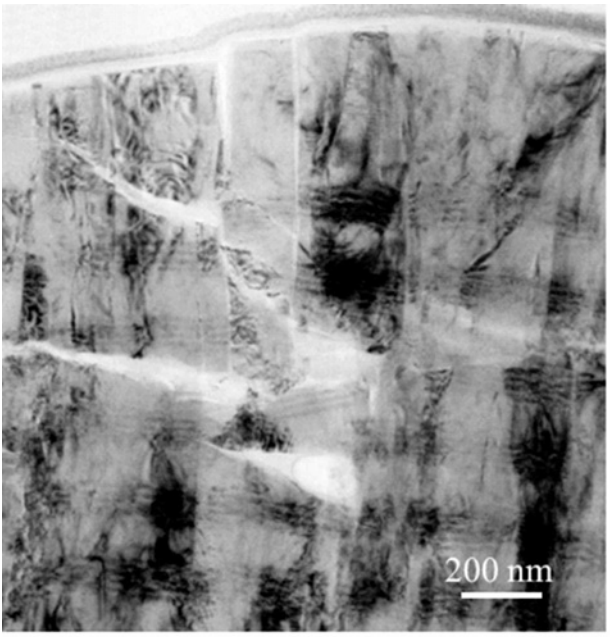

FIGURE 13.9. XTEM image of a polycrystalline TiN/TiAlN multilayer after indenting at 450 mN. (From Ref. 30.)

significant SL hardening, it was shown that the W layers appear to deform by dislocation loop motion, in agreement with a dislocation loop mechanism. On the other hand, the nitride layers exhibited linear twin-like features. Other possibilities are that a secondary slip system is activated at high stress levels, allowing glide across layers, or that the stress concentrations at dislocation pileups in one layer would lead to dislocations in the next layer, i.e., the basis for the Hall–Petch equation. Similar to our results, Xu *et al.*[33] subsequently reported enhanced hardness for cubic-NbN/hexagonal-TaN because of difference in slip system.

The first study of mechanical properties of well-defined *oxide* SLs Y_2O_3/ZrO_2, however, revealed *no* significant hardness enhancement with layer periodicity.[34] It was postulated that the lack of hardening for this class of materials is due to dislocation pileup and microcracking in the nanoindentation experiment.

Hardness enhancement by a factor of two compared to the constituent phases from nanolayering has also been observed in TiN/Si_3N_4 SLs.[35,36] For this system that represents a case of crystalline/amorphous layering, the term *superlattice* is, however, not commonly accepted, due to the presence of an amorphous layer phase. The material structure nevertheless exhibits well-defined and many-order apparent SL peaks at low-angle reflection corresponding to the strong compositional modulation. Figure 13.10 shows a schematic and XTEM image of a TiN/Si_3N_4 SL made by reactive dual magnetron sputtering.[36] Here, the TiN grain size becomes limited

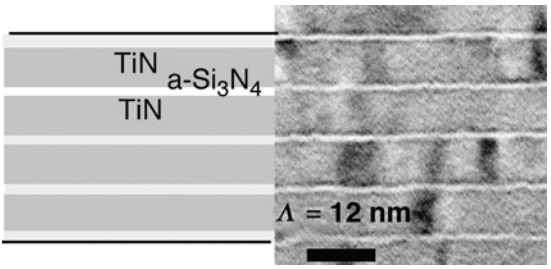

FIGURE 13.10. Schematic and XTEM image of a TiN/Si_3N_4 SL made by dual magnetron sputtering process. (From Ref. 36.)

to layer thickness and the hardness has its maximum around a few monolayers of Si_3N_4. Initial results from a study of the deformed region under a nanoindent in the SL show that the material exhibits pileup and thus plasticity.[37]

The obtained interfacial structure and mechanical properties are in many aspects similar between SLs and nanocomposites in this Ti-Si-N system. Nanocomposites with microstructures comprising nanocrystalline grains in an amorphous matrix are thus found to produce super- to ultrahard materials.[35,36] In a conceptual design of tough nanocomposites the requirements are for the crystallites and amorphous matrix to consist of high-elastic-modulus materials, and that the grain–matrix interfaces are strongly bonded. A strength-determining factor is grain rotation.[37] Recent computer simulations reveal that grain boundary sliding occurs even at room temperature.[37] Direct atomic-scale observation of grain boundary migration in Au revealed a step mechanism and the cooperative transformation of groups of atoms into the lattice of the growing grain.[38] Hardening results from the condition that dislocation loops do not form for crystal sizes $\leq$10 nm. While requiring a higher energy, however, block slip is perceivable, but has not been observed. For TiC-a-C nanocomposite,[39] a development of nanocracks along phase boundaries has been shown to result in pseudoplasticity. Fracture toughening is obtained from restriction of initial crack size for small and densely packed crystallites, with a large volume of grain boundary. Multiple deflection of cracks at the crystallites may dissipate energy during fracture.

Cutting tests of nitride SL made by unbalanced magnetron sputtering for dense grain boundaries were reviewed by Münz.[4] For wear tests of TiAlN/CrN SL, Luo *et al.*[40,41] found plastic deformation with the dissolution of the layered structure in the $\sim$50-nm near surface region (see Fig. 13.11). A distorted SL structure by possible grain rotation was obtained 50–100 nm deeper. Micro- and nanocracking occurs at column boundaries. It is interesting that these boundaries, however dense, constituted the weakest link.

It should not be expected that SL hardening in nitrides can be completely added to defect hardening. In fact, defect hardening from a PVD process operated with ion bombardment may lead to intrinsic compressive stress of

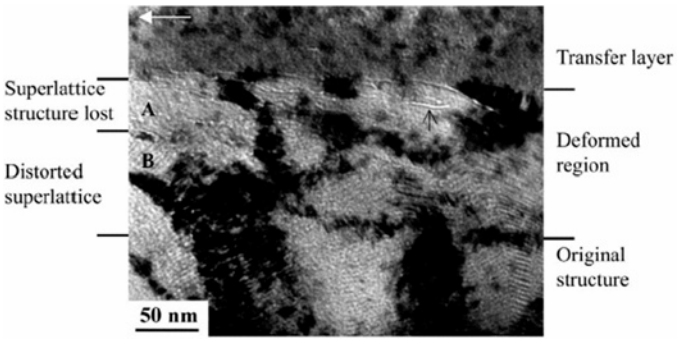

FIGURE 13.11. XTEM image of a polycrystalline TiAlN/CrN SL coating made by unbalanced magnetron sputtering dry wear testing (Region A corresponds to the region where the superlatice structure is lost by the work of defermation and Region B to the region where the superlattice is disterted.). (From Ref. 41.)

several gigapascals with some 50% hardness increase compared to the monolithic material.[42] This is because SL hardening requires dislocation activity and the lattice (point) defects hinder that process or the mode of deformation changes. Typically, commercially produced polycrystalline SL coatings, such as the TiAlN/CrN case above, contain substantial residual compressive stress of the order of one to several GPa (see Fig. 13.5.)[31]

While nitride SLs can exhibit better wear resistance compared to pure nitride films,[4,43] the fracture behavior in the latter is anisotropic with fracture primarily on $\{110\}$ planes in radial directions from the indent. When indenting nitride SL films, concentric cracks occur around the indentation, implying that no predefined

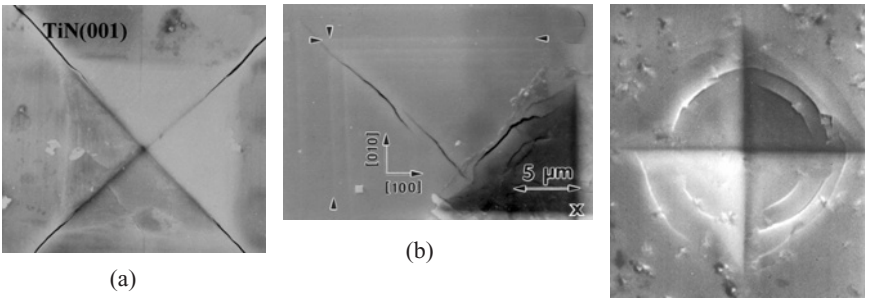

(a) (b) (c)

FIGURE 13.12. Scanning electron microscopy images of the mechanically deformed zone around Vickers diamond imprints with 60-g load into 2-μm-thick films on MgO(001) (a, b) TiN(001) film and (c) TiN/NbVN(001) SL film with a 7-nm periodicity. For (a), flow lines in the <100> directions [marked by arrowheads in (b)] from plastic deformation at a Vickers diamond imprint (marked by a cross). Cracks run in <110> directions. For (c), concentric cracks are predominant. The label "X" in (b) indicates the center of the indent.

fracture planes exist. This is illustrated in Fig. 13.12 for single-crystal model systems. The figure thus demonstrates the additional fracture toughness expected for the SL design compared to monolithic nitride films.

For TiN/Cu multilayers, hardness was limited by fracture in the relatively brittle TiN layers because of stress concentrations resulting from the compliant Cu layers.[44] We infer that the dislocation pileup together with the observed formation of domains in TiN/NbN SL (see Fig. 13.8) will cause stress concentration, which dictates the fracture behavior and eventually suppresses the material toughness.

5. CONCLUSIONS

Several nanolaminate and SL systems exhibit so-called superhardening compared to the monolithic phases. The nitride SLs have been the subject of most studies to date and also found application. With them, theoretical models for the hardening have become validated. The hardening is based on dislocation activity and thus requires that the constituent layers have a difference in shear modulus. To a lesser extent, coherency strains at layer interfaces from a difference in lattice parameter also play a role. It is significant that observations indicate that dislocation glide during mechanical deformation is more or less confined within layers. It remains, however, a challenge to make direct observation of such effect in layers only a few nanometers thick. For more massive deformation, the dislocation activity can form subgrains by dislocation wall formation and corresponding crystal rotation. Nanocracking as a mechanism for limiting SL strength is observed to operate in cases of coatings containing porosity or voids (as is the case for low-energetic deposition conditions and limited adatom mobility), compressive stresses (as is the case for high-energetic conditions with residual lattice defects), or in brittle materials systems. We submit that SL hardening and defect hardening (residual stress case) are not nonadditive or even mutually excluding, since the former requires dislocation activity that the latter impedes.

Obviously the SLs should have defined layers. That requires heteroepitaxial growth for each layer in a given grain or column as has been demonstrated in polycrystalline multilayers deposited on, e.g., steel substrates. The requirement of layer definition also places demands on the deposition process or application employed, whereby intermixing of atoms across interfaces must be avoided for the material to be defined and functional in service. These conditions place demands on the deposition process that should be operated at a substrate temperature sufficiently high to maintain dense film growth. Also, substrate rotation or shutter operation with respect to the deposition sources as a means for producing the layering must be designed to avoid cross talk. Interdiffusion is then perhaps the most encountered problem for retaining a SL structure. This is hard to avoid for most nitrides above $\sim$900°C unless immiscible components are selected. In the latter case, there will be a longer service time expected due to lack of interdiffusion, however, thermodynamics will eventually drive layers to coarsen.

It can further be noted that however complex the SLs are in their fabrication in terms of process control, they have been a pilot system in developing PVD methods to some perfection for the homogeneous coating of three-dimensional components and tools. Also, they have promoted the theoretical understanding and nanostructural characterization of materials years before the age of nanotechnology. Finally, the SLs should prove useful as model systems of reduced dimensionality to enable studies of the mechanical deformation in the complex nanocomposites.

While the slip systems are worked out for common nitrides at ambient temperature, hot deformation—like in a tool operation case—can be expected to activate additional dislocation glide.

REFERENCES

1. H. Helmersson, S. Todorova, S. A. Barnett, J. E. Sundgren, L. C. Markert, and J. E. Greene, Growth of single-crystal TiN/VN strained-layer superlattices with extremely high mechanical hardness, *J. Appl. Phys*. **62**(2), 481–484 (1987).
2. S. A. Barnett, in *Physics of Thin Films*, Vol. 17, edited by M. H. Francombe and J. L. Vossen (Academic Press, San Diego, CA, 1993), p. 1.
3. J. S. Koehler, Attempts to design a strong solid, *Phys. Rev.B* **2**, 547 (1970) .
4. W. D. Münz, Large-scale manufacturing of nanoscale multilayered hard coatings deposited by cathodic arc/unbalanced magnetron sputtering, *MRS Bull.* **28**(3), 173–179 (2003).
5. P. B. Mirkarimi, S. A. Barnett, K. M. Hubbard, T. R. Jervis, and L. Hultman, Structure and mechanical properties of epitaxial $TiN/V_{0.3}Nb_{0.7}N(110)$ superlattices, *J. Mater. Res*. **9**(6), 1456–1467 (1994).
6. M. Shinn, L. Hultman, and S. A. Barnett, Growth, structure, and microhardness of epitaxial TiN/NbN superlattices, *J. Mater. Res*. **7**(4), 901–911 (1992).
7. P. B. Mirkarimi, L. Hultman, and S. A. Barnett, Enhanced hardness in lattice-matched single-crystal $TiN/V_{0.6}Nb_{0.4}N$ superlattices, *Appl. Phys. Lett*. **57**(25), 2654–2656 (1990).
8. Q. Li, I. W. Kim, S. A. Barnett, and L. D. Marks, Structures of AlN/VN superlattices with different AlN layer thicknesses, *J. Mater. Res*. **17**(5), 1224–1231 (2002).
9. H. Ljungcrantz, C. Engström, L. Hultman, M. Olsson, X. Chu, M. S. Wong, and W. D. Sproul, Nanoindentation hardness, abrasive wear, and microstructure of TiN/NbN polycrystalline nanostructured multilayer films grown by reactive magnetron sputtering, *J. Vac. Sci. Technol. A***16**(5), 3104–3113 (1998).
10. X. Chu and S. A. Barnett, Model of superlattice yield stress and hardness enhancements, *J. Appl. Phys*. **77**(9), 4403–4411 (1995).
11. L. Hultman, M. Shinn, P. B. Mirkarimi, and S. A. Barnett, Characterization of misfit dislocations in epitaxial (001)-oriented TiN; NbN, VN, and (Ti,Nb)N film heterostructures by transmission electron microscopy, *J. Cryst. Growth* **135**(1–2), 309–317 (1994).
12. Preface to the viewpoint set on: Deformation and stability of nanoscale metallic multilayers, *Scr. Mater.* **50**(6), 707–812 (2004).
13. L. Hultman, C. Engström, and M. Odén, Mechanical and thermal stability of TiN/NbN superlattice thin films, *Surf. Coat. Technol*., **133**, 227–233 (2000).
14. Z. Zhou, W. M. Rainforth, B. Rother, A. P. Ehiasarian, P. Eh. Hovespian, and W. D. Münz, Elemental distributions and substrate rotation in industrial TiAlN/VN superlattice hard PVD coatings, *Surf. Coat. Technol.* **183**(2–3), 275–282 (2004).
15. J. W. Matthews and A. E. Blakeslee, Defects in epitaxial multilayers, Part 1: Misfit dislocations, *J. Cryst. Growth* **27**, 118–127 (1974).

16. Z. Wokulski, Mechanical properties of TiN wiskers, *Phys. Stat. Sol. A* **120**(1), 175–184 (1990).
17. Matthews, J.W. (eds.), *Epitaxial Growth, Part B* (Academic Press, London, 1975) p. 437.
18. X. Chu, M. S. Wong, W. D. Sproul, S. L. Rohde, and S. A. Barnett, Deposition and properties of polycrystalline TiN/NBN superlattice coatings, *J. Vac. Sci. Technol. A* **10**(4, Pt 2), 1604–1609 (1992).
19. S. L. Lehoczky, Retardation of dislocation generation and motion in thin layered metal laminates, *Phys. Rev. Lett*. **41**(26), 1814–1818 (1978).
20. S. L. Lehoczky, Strength enhancement in thin-layered Al-Cu laminates, *J. Appl. Phys*. **49**(11), 5479–5485 (1978).
21. J. D. Verhoeven, L. S. Chumbley, F. C. Labbs, and W. A. Spitzig, Measurement of filament spacing in deformation processed Cu-Nb alloys, *Acta Metall. Mater*. **39**(11), 2825–2834 (1991).
22. J. G. Sevillano, in *Strength of Metals and Alloys. Proceedings ICSMA 5*, edited by P. Haasen *et al*. (Pergamon, Oxford, 1980), p. 819.
23. Y. C. Lu, H. Kung, A. J. Griffin *et al*., Observations of dislocations in Cu/Nb nanolayer composites after deformation, *J. Mater. Res*. **12**(8), 1939–1941 (1997).
24. P. M. Anderson, T. Foecke, and P. M. Hazzeldine, Dislocation-based deformation mechanisms in metallic nanolaminates, *MRS Bull.* **24**(2), 27–33 (1999).
25. L. Hultman, L. R. Wallenberg, M. Shinn, and S. A. Barnett, Formation of polyhedral voids at surface cusps during growth of epitaxial TiN/NbN superlattice and alloy films, *J. Vac. Sci. Technol. A* **10**(4, Pt 2), 1618–1824 (1992) .
26. M. Odén, H. Ljungcrantz, and L. Hultman, Characterization of the induced plastic zone in a single crystal TiN (001) film by nanoindentation and transmission electron microscopy, *J. Mater. Res*. **12**(8), 2134–2142 (1997).
27. L. Hultman, C. Engström, J. Birch, M. P. Johansson, M. Odén, L. Karlsson, and H. Ljungcrantz, Review of the thermal and mechanical stability of TiN-based thin films, *Z. Met.kd.* **90**(10), 803–813 (1999).
28. J. M. Molina-Aldareguia, L. Hultman, T. Joelsson, W. J. Clegg, and M. Odén, unpublished.
29. J. M. Molina-Aldareguia, S. J. Lloyd, W. J. Clegg, M. Odén, and L. Hultman, Deformation structures under indentations in TiN/NbN single-crystal multilayers deposited by magnetron sputtering at different bombarding ion energies, *Phil. Mag. A* **82**(10), 1983–1992 (2002).
30. N. J. M. Carvalho and J. Th. M. De Hosson, Nano indentation studies of WC/C and TiN/(Ti,Al)N multilayer PVD coatings combined with cross-sectional electron microscopy observations, in *Materials Research Society Symposium Proceedings*, Vol. 697, edited by W. J. Meng, A. Kumar, G. L. Doll, Y.-T. Cheng, S. Veprek, and Y.-W. Chung (2002), Materials Research Society, Pittsburgh, Pennsylvania, pp. 1.5 .
31. S. A. Barnett and A. Madan, Hardness and stability of metal-nitride nanoscale multilayers, *Scr. Mater.* **50**(6), 739–744 (2004).
32. D. E. Kramer, M. F. Savage, A. Lin, and T. Foecke, Novel method for TEM characterization of deformation under nanoindents in nanolayered materials, *Scr. Mater.* **50**(6), 745–749 (2004).
33. J. Xu, M. Kamiko, Y. Zhou, R. Yamamoto, G. Y. Li, and M. Y. Gu, Superhardness effects of heterostructure Nb/N/TaN nanostructured multilayers, *J. Appl. Phys.* **89**(7), 3674–3678 (2001).
34. P. Yashar, S. A. Barnett, L. Hultman, and W. D. Sproul, Deposition and mechanical properties of polycrystalline Y_2O_3/ZrO_2 superlattices, *J. Mater. Res*. **14**(9), 3614–3622 (1999).
35. S. Veprek M. Haussmann, and S. Reiprich, Superhard nanocrystalline W_2N/amorphous Si_3N_4 composite materials, *J. Vac. Sci. Technol. A* **14**(1), 46–51 (1996).
36. H. Söderberg, J. M. Molina-Aldareguia, L. Hultman, and M. Odén, Nanostructure formation during deposition of TiN/SiNx nanomultilayer films by reactive dual magnetron sputtering, *J. Appl. Phys.* **97**, 114327 (2005) .
37. J. Schiotz, F. D. DiTolla, and K. W. Jacobsen, Softening of nanocrystalline metals at very small grain sizes, *Nature* **391**(6667), 561–563 (1998).
38. K. L. Merkle and L. J. Thompson, Atomic-scale observation of grain boundary motion, *Mater. Lett*. **48**(3–4), 188–193 (2001).

39. A. A. Voevodin and J. S. Zabinski, Load-adaptive crystalline-amorphous nanocomposites, *J. Mater. Sci*. **33**(2), 319–327 (1998).
40. Q. Luo, W. M. Rainforth, and W. D. Münz, TEM observations of wear mechanisms of TiAlCrN and TiAlN/CrN coatings by combine steered arc/unbalanced magnetron deposition, *Wear* **229**(Pt 1), 74–82 (1999) .
41. Q. Luo, W. M. Rainforth, and W.-D. Münz, TEM studies of the wear of TiAlN/CrN superlattice coatings, *Scr. Mater.* **45**(4), 399–404 (2001).
42. L. Karlsson, L. Hultman, and J.-E. Sundgren, Influence of residual stresses on the mechanical properties of $TiC_xN_{1-x}(x = 0, 0.15, 0.45)$ thin films deposited by arc evaporation, *Thin Solid Films* **371**, 167–177 (2000) .
43. M. Nordin, Ph.D. Dissertation, No 509 (Faculty of Science and Technology, Uppsala University, Uppsala, Sweden, 2000) .
44. H. Ljungcrantz, *Growth, Microstructure, and Mechanical Properties of Ti and TiN Thin Films, and TiN-Based Superlattices*, Ph.D. Dissertation. No. 408 (Linköping University, Linköping, Sweden, 1995).

14

Synthesis, Structure, and Applications of Nanoscale Multilayer/Superlattice Structured PVD Coatings

P. Eh. Hovsepian and W.-D. Münz

Nanotechnology Center for PVD Research, Materials and Engineering Research Institute, Sheffield Hallam University, Sheffield S1 1WB, UK

1. ASPECTS OF INDUSTRIAL DEPOSITION OF NANOSCALE MULTILAYER/SUPERLATTICE HARD COATINGS

1.1. Introduction

Superlattice structured physical vapor deposition (PVD) hard coatings have been reported to exhibit hardness values up to Vickers hardness (HV) 5000.[1,2] Figure 14.1 represents the first published set of results achieved with single crystal TiN/VN {100} superlattices. These amazing hardness properties gave rise to a series of further investigations revealing comparable results for various material combinations based on TiN or TiAlN. The nature of these high hardness values has been discussed in terms of special layer thickness relationships, on the related diffusibilty of crystalline defects, and on the shear modulus of the materials involved.[3] In the meantime, the superlattice approach has been discussed in connection with industrial applications with material combinations such as TiN/NbN,[4] TiN/WN,[5] TiAlN/CrN,[6,7] TiN/AlN,[8] TiAlCrYN,[9,10] W/ZrN, and ZrN/ZrB_2.[11] In all cases, remarkable progress has been achieved in comparison to monolithically grown multicomponent coatings depending on the special demands of the application.

Another interesting property of the superlattice structured hard coating besides the high hardness values has been discovered recently by transmission electron microscopy (TEM) investigations on the wear mechanisms of TiAlN/CrN superlattice coatings in comparison with monolithically grown multicomponent coatings.[12] Figure 14.2 schematically outlines the results of this study. The

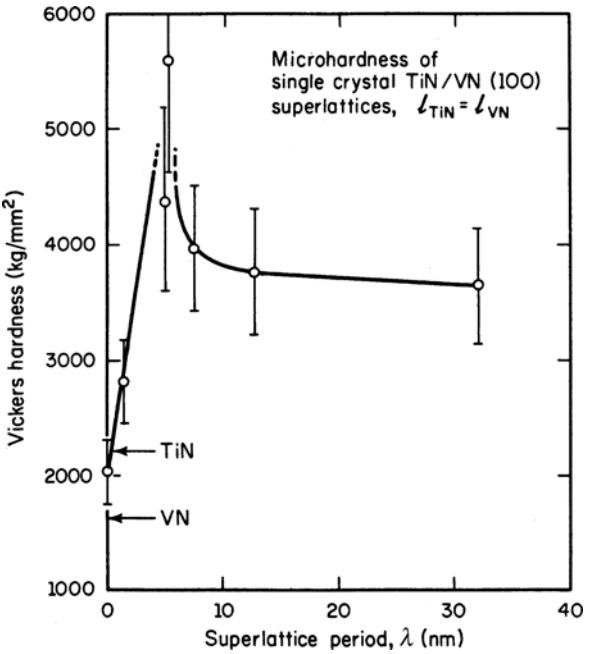

FIGURE 14.1. First published results on superlattice hardness.[1]

mechanical failure appears quite different when the two types of coating are exposed to severe shear forces as occur in the case of abrasive wear. The individual grains of columnar and monolithically grown coatings experience severe plastic deformation, which turns out to be the source of mechanical breakage. The observed depth of these failures reaches typically 50–75 nm. In contrast to these structure-related defects, a chipping or micro-delamination mechanism was observed in the case of the superlattice structured coating with a typical chipping

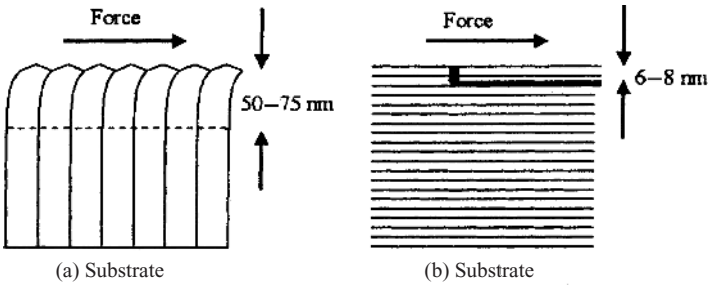

FIGURE 14.2. Mechanical failure in (a) monolithically grown and superlattice (b) grown coatings.

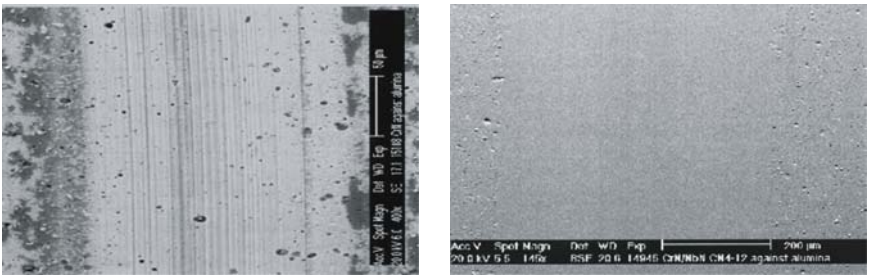

(a) (b)

FIGURE 14.3. Scanning electron microscopy (SEM) image of pin-on-disk wear tracks on (a) CrN and (b) CrN/NbN after 3.14 km of travel (counterpart Al_2O_3).

depth of 6–8 nm only. This result deserves particular interest, as the superlattice coating also exhibits a columnar growth structure. However, its growth is obviously interrupted, and so the superlattice structure leads obviously to similar results as postulated for multilayers in general,[13] namely that the penetration depth of the cracks is substantially reduced in layered structures.

The superlattice structure reveals the additional chance to minimize the penetration depth. Simple pin-on-disk tests further underline these conclusions. Figure 14.3 shows the morphology of the wear track in a monolithically grown columnar CrN coating in comparison with that of a CrN/NbN superlattice coating with an Al_2O_3 ball used as the counterpart. Whereas the wear track in the CrN coating shows deep fissures, which probably resulted from the coarse wear debris generated through the test, a smooth wear track is observed in the case of the superlattice coating, confirming the fact that the wear debris might have been much finer grained. In the following production criteria, reproducibility and further new results on superlattice coatings are discussed.

1.2. Production Aspects

It is a requirement of the modern age that improvements in performance should not necessarily lead to a proportionate increase in cost. It is therefore imperative for the coating process that the deposition technique itself does not enhance the cost; however, the influence of the material costs cannot be avoided. Substantial effort has been employed in the development of PVD deposition processes, which allow the manufacturing of coatings on the same price level as for conventional binary nitrides such as TiN. Magnetron sputtering has been found to be the most appropriate deposition technology,[14–17] although some attempts have also been made to deposit such coatings by cathodic arc evaporation.[8] To achieve reasonably economical process, complicated installations, including shielding and shuttering, that reduce the deposition rate need to be avoided. In addition, reactive gas control should not be too complicated, in order to avoid high equipment costs. On the other

hand, the distribution of the deposition rate has to be very well defined so that the relatively narrow-thickness tolerances in the vicinity of the hardness maximum peak (Fig. 14.1, H-delta) can be satisfied. Consequently, linear cathodes in combination with up to threefold substrate rotation must be used in order to achieve homogeneous rate distribution over the whole height of the vacuum chamber.

To satisfy these demanding requirements, a deposition process has been developed and industrially implemented, using a four-target PVD coater HTC-1000 ABS (arc bond sputtering), manufactured by Hauzer Techno Coating Europe, Venlo, The Netherlands.[18] The cathodes furnishing this equipment allow steered cathodic arc evaporation, magnetron sputtering, or unbalanced magnetron (UBM) sputtering. These processes can be carried out either sequentially or simultaneously. The steered arc process is used mainly to generate a highly ionized discharge to supply multi-ionized metal ions,[19] which are implanted into the substrate surface to allow optimized adhesion values.[20,21] The coating process is carried out by using the cathodes in the UBM mode. However, if coating materials are used with substantially different poisoning characteristics, the less poisoning material is deposited by UBM, while the more sensitive material is deposited in the steered arc mode.[15] Both modes can be operated simultaneously and fully independent from each other.

Figure 14.4 shows a schematic cross section of the coating plant. The distance between opposing cathodes is 1 m. Substrates are mounted on a threefold rotating planetary turntable to provide homogeneous coating in the growth direction. Six-hundred-mm-long vertically mounted rectangular (linear) dual-purpose cathodes are used to guarantee uniform coatings over a large portion of the height of the coating chamber. Circular point sources are not suitable to deposit superlattice coatings with precise enough thickness or period tolerances. The cathodes are laid out as balanced magnetrons by using a SmCo magnet array. Concentric electromagnetic coils produce a controlled unbalancing effect. The cathodes can be operated either in magnetron sputtering mode or in steered cathodic arc evaporation mode. In the

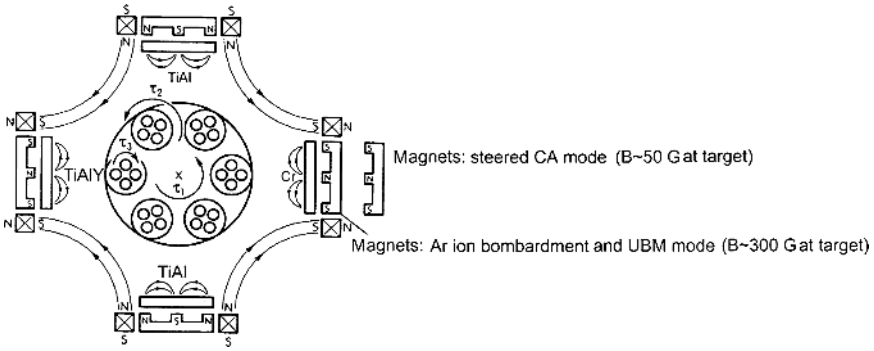

FIGURE 14.4. Schematic diagram of the HTC-1000 ABS coater. (CA, cathodic arc)[15]

steered cathodic arc mode, the SmCo permanent magnets are withdrawn pneumatically to reduce the magnetron parallel magnetic field strength from 300 G to typically 50 G. The magnets and the polarization of the electromagnetic coils are arranged in a closed magnetic field configuration to achieve high plasma density [typically 4×10^9ions/(cm^3 kW)] and, therefore, high ion-to-neutral species (maximum 6) in the vicinity of the substrates. The nature of the electromagnetic coils also allows easy control of the resultant substrate temperature. Low-temperature processes (~200°C) are operated with typical coil currents of 3 A, and high-temperature processes (450°C) are operated with coil currents of 6 A, depending on the number of windings in the coil.

Uncontrolled target poisoning is a major concern when all cathodes are operated in a common reactive atmosphere. As a first step to prevent target poisoning, two 2250 l/s turbomolecular pumps were installed to provide a high pumping speed. Increasing the pumping speed automatically leads to less target poisoning and, therefore, flatter hysteresis curves. Figure 14.5 schematically shows hysteresis curves for three pumping speed conditions.

Various superlattice structured coatings such as TiAlN/CrN, CrN/NbN, TiAlCrN/TiAlYN, TiAlN/VN, and TiAlN/ZrN have been successfully deposited with

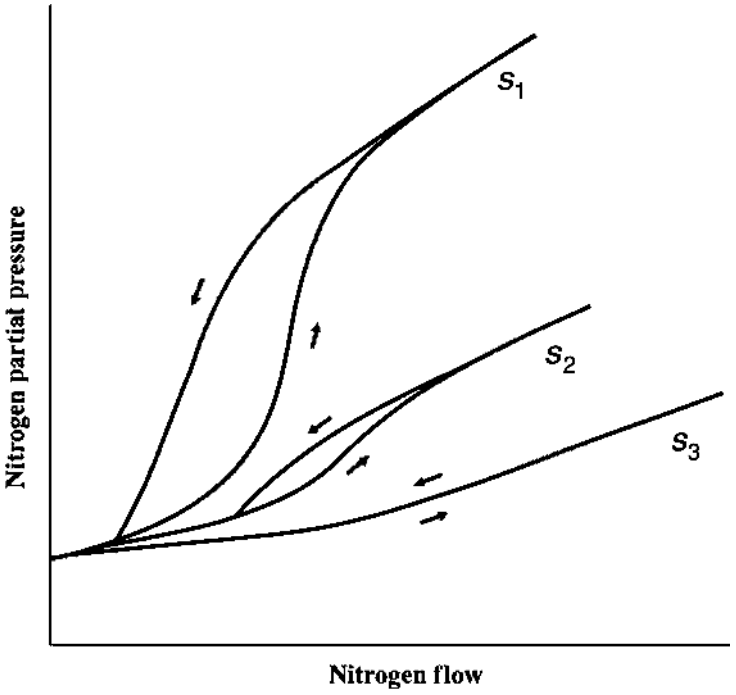

FIGURE 14.5. Schematic drawing of the effect of system pumping speed S on the hysteresis loop for $S_1 < S_2 < S_3$.[22]

TABLE 14.1. Target and Power Selection for Various Superlattice Coatings.

System	Target no.	Power per target
TiAlN/CrN	3TiAl/1 Cr	3 × 8 kW/1 × 8 kW (UBM)
TiAlN/VN	2TiAl/2 V	2 × 8 kW/2 × 8 kW (UBM)
TiAlN/ZrN	3TiAl/1 Zr	3 × 8 kW (UBM)/1 × 100 A (ARC)
CrN/NbN	2 Cr/2 Nb	2 × 5 kW/2 × 10 kW (UBM)

the described system, utilizing the high pumping speed approach.[23] Only in the case of TiAlN/ZrN was the pumping speed insufficient to operate the Zr targets. In this case, the Zr targets were operated in a steered cathodic arc mode. Reactive gas control was carried out in a simple manner: assuming that the pumping speed of turbomolecular pumps is independent of the gas pressure in the pressure range of (1–8) $\times$ 10^{-3}mbar, the Ar partial pressure was controlled by flow meters only. The reactive gas partial pressure was controlled by keeping the total pressure—the sum of ΔP_{Ar} and $\Delta P_{N^{2-}}\Delta$—constant using accurate manometers such as the Leybold Viscovac or MKS Baratron. Of course, more sophisticated approach is also available by utilizing mass spectrometer monitoring.[22]

The number of targets used and the power dissipated on each simultaneously operating cathode depends on the individual sputter yield typical for each material. Table 14.1 gives a brief survey of the typical deposition conditions.

The deposition takes place at a total pressure of 3×10^{-3} mbar. No mechanical shielding or gas flow guide plates were used whatsoever. This means that the risk of some intermixing of materials was accepted intentionally. It will be shown later that superlattice coatings are exhibiting rather high internal stress values up to 10 GPa. Under such conditions, the demands on the coating adhesion are extraordinarily high. Experience has shown that all reproducibility-determining demands on the adhesion could be satisfied, using appropriate metal ion bombardment prior to the coating process and starting the deposition process with a low stressed monolithically grown base layer. Figure 14.6a,b outlines the process sequence and the layer architecture schematically. Further details are given in Refs. 15, 16, and 23.

When using industrially sized coating system without any shutters or plasma guiding systems as described above, which can be classified as an "open" system, a fundamental question can be asked about the accuracy of the nanoscale multilayer structure when the coating is deposited on three-dimensional (3D) real parts. Within a research program on development of superhard coatings on sharp blades, a cross section from textile blade coated with 3-μm-thick CrN/NbN superlattice coating has been imaged in the TEM for microstructure investigation.[24] Micrographs of dark- and bright-field (BF) images are shown in Fig. 14.7a,b.

The lower magnification micrograph in Fig. 14.7a reveals that a uniform 3-μm-thick coating was deposited on the cutting edge from both sides of the blade. The base layer was clearly imaged as a fine-structured brighter band adjacent to

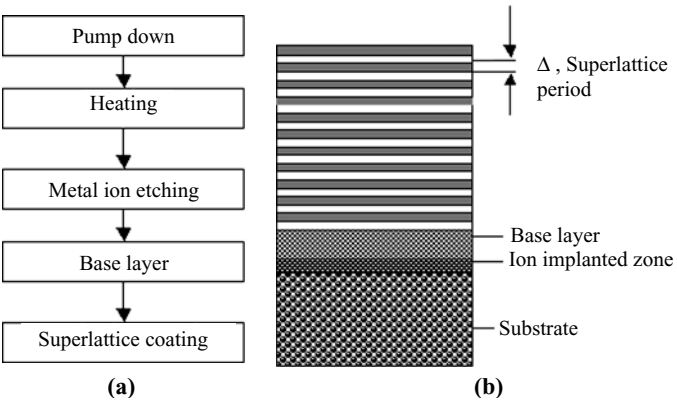

FIGURE 14.6. a) Major processing steps and b) Schematic cross section through a superlattice hard coating.

the blade surface. The CrN/NbN coating showed a general columnar structure. The perfect nanoscale multilayer structure of the coating however can be seen in Fig. 14.7b (the edge is in vertical position). The image in Fig. 14.7b reveals that the superlattice structure of the CrN/NbN coating has been maintained with high

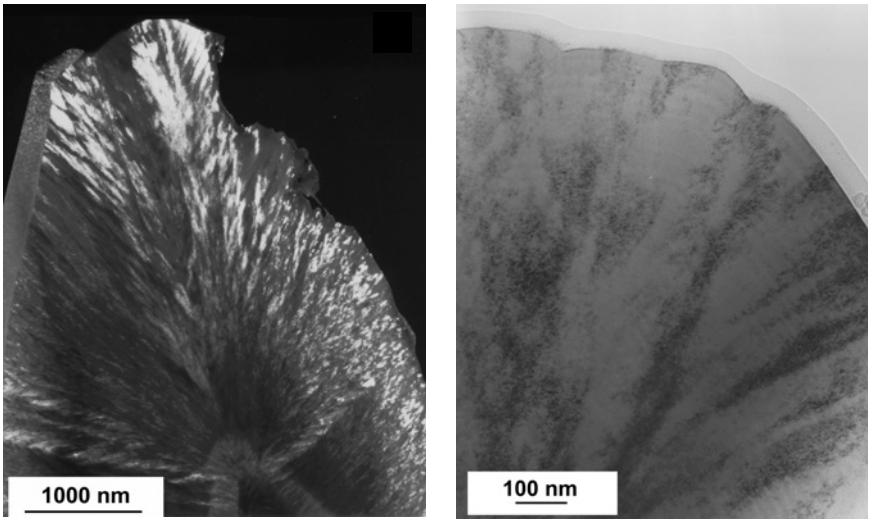

FIGURE 14.7. Cross-sectional transmission electron microscopy (XTEM) micrographs of CrN/NbN superlattice coating deposited on the cutting edge of a textile blade: (a) dark-field (DF) image; (b) bright-field (BF) image.[18]

accuracy over more than 2000 bilayers, thus demonstrating that utilizing the ABS technology in a multitarget industrial coating system has great potential to produce nanoscale structured PVD coatings on real 3D parts with extremely high precision.

1.3. Arc Bond Sputtering Interface

As pointed out above, the ABS technology utilizes two types of plasma modes. The plasma generated by a steered cathodic arc discharge is mainly used to provide intensive metal ion etching prior to the coating process, which takes place in glow discharge plasma generated by the UBM discharge.[18] Figure 14.8 summarizes the ionization phenomena as measured by optical emission spectroscopy (OES).[17]

In case of the steered arc plasma, Nb has been evaporated in the presence of Ar. Accordingly, the spectrum shows peaks of Ar^+, Nb^+, and Nb^{2+} but also a series of lines stemming from the excited atoms Ar^*. As reported in Ref. 19, Nb can undergo fivefold ionization in the arc discharge, resulting in an average ionization state of $Nb^{3.0+}$. The used OES equipment allows the detection of wavelengths corresponding only to twofold ionization. Conversely to the arc plasma, the UBM spectrum is dominated by signals stemming from Ar atoms as well as exited Nb atoms. Only a weak Nb^+ line is present in comparison to the arc discharge. Substantial differences have been observed with respect to the ion densities in the arc and the glow discharge plasma. Using one cathode of the HTC-1000-4 ABS

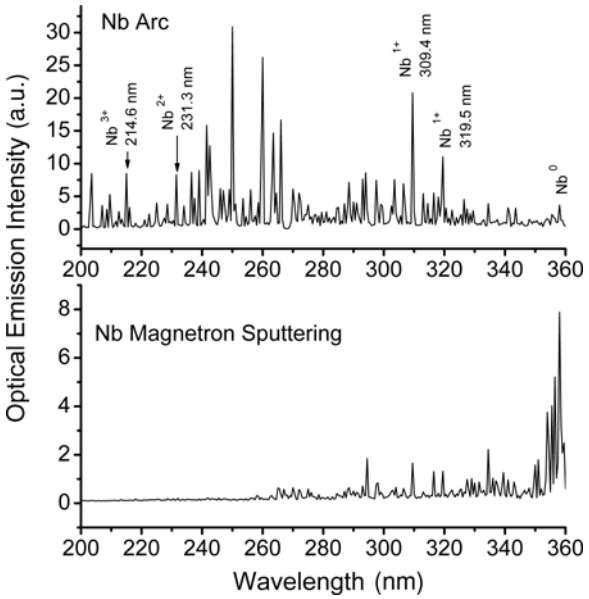

FIGURE 14.8. Optical emission spectra of Nb arc or glow discharge respectively.[17]

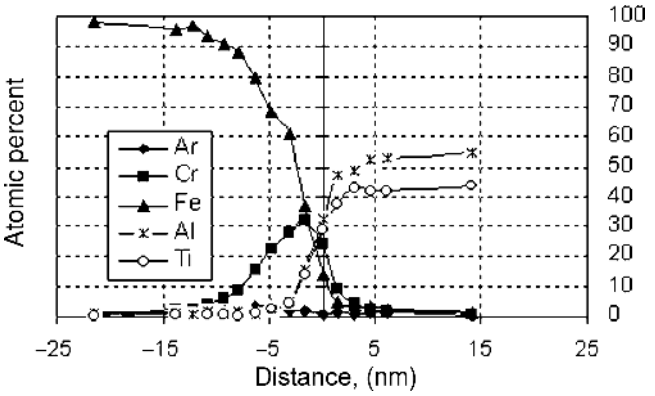

FIGURE 14.9. Profile from low carbon steel–TiAlN interface showing Cr ion implantation.

system as the steered arc source, a typical ion density was measured up to $2.5 \times 10^{10}/\text{cm}^3$ (distance probe–cathode: 25 cm) whereas the ion density in the UBM mode reaches $3.5 \times 10^{10}/\text{cm}^3$. These two values are related to the power dissipation of 4 kW for the arc and 10 kW for the magnetron discharge. If one relates the ion density values to the power dissipation, substantial differences are found: $0.6 \times 10^{10}/(\text{cm}^3\,\text{kW})$ for the arc and $0.35 \times 10^{10}/(\text{cm}^3\,\text{kW})$ for the magnetron. Figure 14.4 schematically outlines the position of the permanent magnet array when switching from steered arc to UBM mode of operation. As a result of continuing research and development on the ABS, Nb turned out to be the preferred ion when PVD is used to deposit corrosion-resistant coatings,[16,25] whereas Cr ions are used prior to deposition of wear-resistant coatings. In case of a Cr steered arc discharge, the diameter of droplets, typically found in the arc discharge, are clearly smaller and less in number compared, e.g., to Ti as cathode material, which leads to smoother surfaces.[26,27] Furthermore appropriate bombardment of steel and cemented carbide (CC) substrates leads to ion implantation of Cr in the subsurface, thus providing condensation conditions so that the sputter deposited film shows local epitaxial growth.[28,29] Figure 14.9 shows an implantation profile of Cr ($U_B = -1200$ V) in mild steel, subsequently covered with a UBM-deposited TiAlN coating.[21]

Figure 14.10 represents a selected area electron diffraction (SAED) pattern of the CC substrate surface, which was exposed to a Cr ion pretreatment ($U_B = -1200$ V) and then covered with a TiAlN coating.[30] Superimposition of the two diffraction patterns reveals a perfect match of the TiAlN–fcc lattice on the hexagonal lattice of WC.

In general, local epitaxy is seen to be highly beneficial for adhesion.[31] The typical exposure time to ion bombardment during the ion-etching step is 20 min.[21,30] This long exposure time is used to ensure a clean surface. However, particularly for small tools and parts this long etching time may lead to local substrate overheating, depending on the tool geometry, causing detrimental softening effects. In addition,

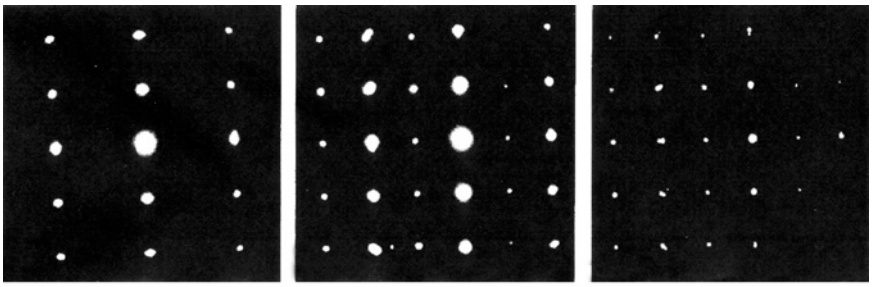

FIGURE 14.10. Local epitaxial growth of TiAlN on tungsten carbide after Cr ion bombardment at $U_B = -1200$V (a) Selected area diffraction pattern (SADP) of TiAlN grain (b) superimposition of the TiAlN pattern and tungsten carbide pattern (c) SADP of tungsten carbide grain.

the number of droplets deposited on the substrate during ion bombardment increases with the etching time, thus leading to growth of nodular defects when, e.g., $Ti_xAl_{(1-x)}N$ is deposited on top of the droplet by magnetron sputtering.[28] The microstructure of the nodule near the lower part of the droplet is severely underdense, while the portion of the film grown on the top of the droplet is composed of dense columnar grains extending outward in a feather-like pattern. This difference in the structure is attributed to the atomic shadowing effect and to the ion-induced microstructure changes during film growth.[32] Growth defects reduce locally the oxidation and the corrosion resistance of the coated substrate[33,34] and also increase the surface roughness of the coating.[35] Therefore, a minimization of the exposure time is desirable. Finally, a reduction of the overall process time and prolongation of target life leads to further reduction of production costs.

To address these issues, an improved sputter-cleaning process with reduced exposure times has been developed.[36] The modified etching procedure consists of two steps: first, the steered arc discharge is carried out over a period of 8 min in the environment of a relatively high partial pressure of Ar (approximately 0.1 Pa) allowing a high substrate etching rate. Second, the Ar pressure is reduced to base pressure level (0.06 Pa) promoting enhanced ion implantation (2 min) resulting in a total etching time of 10 min. Previous experiments with Ti ions have shown that the etching procedure is indeed more aggressive when taking place at low gas pressure levels,[37] leading also to a deeper penetration depth of the incorporated Ti atoms.[38] A 3.2-μm-thick TiAlCrYN coating was deposited by UBM sputtering on three different substrate materials: low carbon steel for TEM analysis, austenitic stainless steel for X-ray diffraction (XRD), and high-speed steel for critical load measurements. Figure 14.11 schematically outlines the main differences between the one- and two-step etching procedures.

Although due to the reduced etching time in the two-step etching, the total removal of carbon steel substrate material was reduced to approximately 80 nm

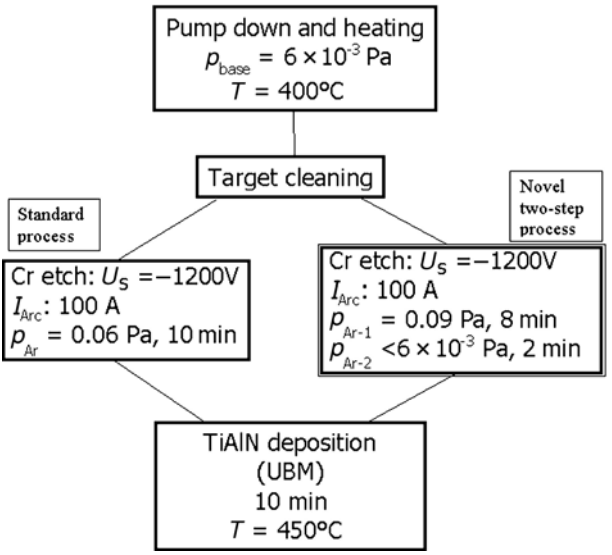

FIGURE 14.11. Process sequence of the one-step and two-step, (the right hand side box, surrounded with a double line) etching procedures.

compared to140 nm achieved with the one-step process, the substrate surface was found to be clean enough to provide conditions for local epitaxial growth of $Ti_xAl_{(1-x)}N$ on α-Fe. A definite indication of local epitaxial growth of the $Ti_xAl_{(1-x)}N$ coating on the ferritic low carbon steel substrate was observed from plan-view TEM imaging. This can be concluded from dark-field (DF) images, as given in Fig. 14.12a. Regions of identical crystallographic orientation extend over several micrometers, exhibiting sharp grain boundaries between adjacent grains. These boundaries are correlated to grain boundaries of the underlying steel substrate as was previously shown by cross-sectional TEM (XTEM) for the case of 20-min Cr ion bombardment at $p_{Ar} = 6\times 10^{-2}$Pa,indicating typical grain sizes of several micrometers. In the absence of local epitaxial growth on substrate grains, typical column sizes revealed by TEM are two to three orders of magnitude smaller (see, e.g., Ref. 21).

These results are confirmed, as exemplified by the DF image in Fig. 14.12b, in the present experiments of sample treatment with mixed Cr + Ar ion bombardment at $p_{Ar} = 6 \times 10^{-2}$Pa, despite the fact that the etching time has been reduced to 10 min.

Despite the similarities in the microstructure of the $Ti_xAl_{(1-x)}N$ coatings grown subsequently after etching, significant differences in the interface chemistry are observed when the one-step etching process ($p_{Ar} = 6 \times 10^{-2}$Pa) is compared to the modified two-step etching case starting with a mixed $Cr^+ + Ar^+$ ion bombardment at $p_{Ar} = 9 \times 10^{-2}$ Pa followed by "pure" Cr ion bombardment at residual

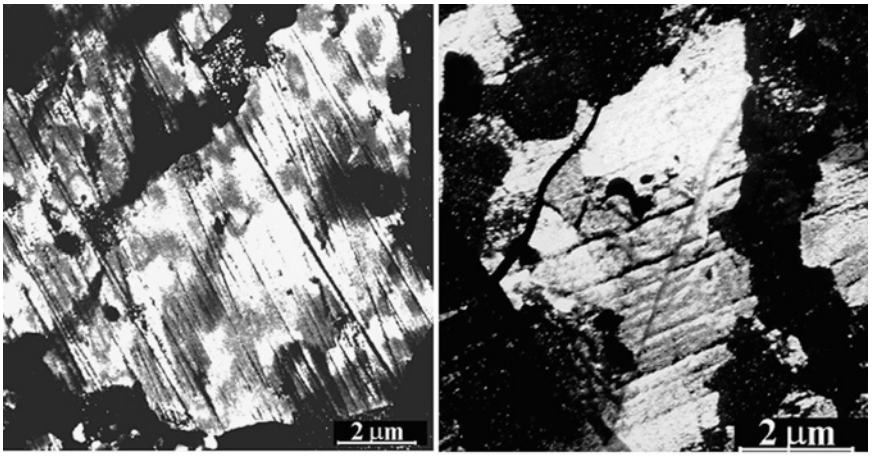

FIGURE 14.12. Plan view DF images of $Ti_xAl_{(1-x)}N$ coating grown on low carbon steel after (a) 10-min two-step sputter cleaning procedure and (b) 10-min one-step sputter-cleaning procedure.

gas pressure. Scanning transmission electron microscopy energy-dispersive X-ray (STEM-EDX) profiles of the resulting two interfaces are shown in Fig. 14.13.

An apparently identical maximum concentration of Cr of about 37 at% is observed for both the one-step and the modified two-step etching cases (Fig. 14.13). It has to be acknowledged that these values of maximum concentration at the interface involve the uncertainty caused by the limited lateral resolution of ± 2.7 nm. However, the shape of the implantation profiles exhibits significant differences. A comparably sharp interface profile for the 10-min process with mixed $Cr^+ + Ar^+$ bombardment (Fig. 14.13a) is observed. In contrast, the corresponding profile of Cr in the two-stage process, which is completed with the "pure" Cr bombardment, exhibits close to the interface a narrow plateau extending 4.5 nm into the steel (Fig. 14.13b). In addition, a deeper Cr penetration is observed in the latter case. Here a significant Cr peak (not shown) was detected in the EDX spectrum even as deep as 20 nm, whereas in the case of the one-step etching procedure, significant levels of Cr could be found only to a depth of 13 nm (Fig. 14.13a). These results indicate clearly a more efficient implantation when a "pure" Cr ion bombardment of only 2-min duration completes the etching process. This conclusion is further confirmed by the determination of the integrated peak areas of 368 ± 27 at% nm representing Cr incorporated in the two-step etching procedure, compared to 216 $\pm$ 34 at% nm for Cr incorporation in the one-step etching mode.

Further differences between the two etching processes were found with respect to the stress distribution across the interfaces as measured by glancing angle XRD. The stress levels measured directly at the interface of the etched, but

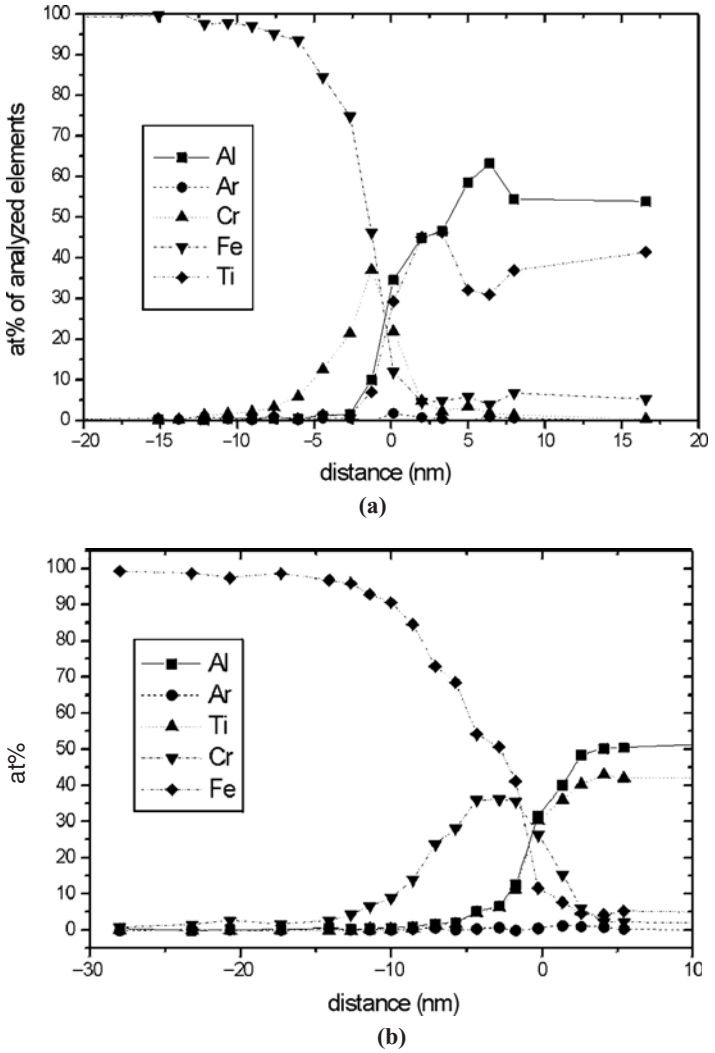

FIGURE 14.13. STEM-EDX profiles across low carbon steel–TiAlN interfaces obtained by (a) mixed Cr/Ar bombardment at $p_{Ar} = 6 \times 10^{-2}$ Pa for 10 min and (b) mixed Cr/Ar ion bombardment at $p_{Ar} = 9 \times 10^{-2}$ Pa, followed by pure Cr ion bombardment.

uncoated austenitic stainless steel substrates are too low to be quantified. However, high compressive stresses were found in the 100-nm-thin coatings grown after both sputter-cleaning processes. The interface with the lower Cr incorporation (one-step etching procedure, mixed Cr/Ar bombardment) exhibited a higher compressive residual stress in the coating of −8.3 GPa. In comparison, when pure Cr ion bombardment was involved (two-step etching procedure) lower values of

compressive stress of −6.8 GPa were measured. It is interesting to note that the average residual stress in a 3.5-μm-thick $Ti_xAl_{(1-x)}N$ coating was 3 GPa, independent of the two etching procedures applied.

The lower stress gradient found in the two-stage etching process might explain the significant differences in the critical load values L_C obtained for both interfaces. Indeed, the critical load values for samples processed in the two-step etching mode showing the enhanced Cr incorporation ranged at $L_C = 85\pm 5$ N as compared to samples prepared after the one-step etching procedure ($L_C = 63\pm 3$ N). Although the high stress values found in the 100-nm-thin $Ti_xAl_{(1-x)}N$ coating adjacent to the interface could be attributed to grain size effects when competitive growth is involved (Hall–Petch), it is believed that epitaxial stresses are more likely to explain the observed effects. The higher Cr content found at the steel surface resulting from the two-stage sputter-cleaning procedure could therefore be responsible for an increase of the lattice parameter of the substrate, which should reduce the mismatch between steel and $Ti_xAl_{(1-x)}N$ coating, thus leading to a lower epitaxial stress component and a flatter stress gradient at the interface. Similar observations were made for plasma nitriding the surfaces.[39]

1.4. Main Criteria Defining Superlattice Structure

The hardness-determining superlattice period, frequency, λ, is mainly controlled by the prime rotation speed of the substrate turntable, the power dissipated at the cathodes, and the degree of target poisoning. The turntable frequency specifies the deposition time per target and material pass, whereas the latter two parameters determine the deposition rate. Figure 14.14 demonstrates the critical influence of the substrate rotation speed. Depositing TiAlN/ZrN superlattice coatings in the described coating machine at low rotation speed leads to the formation of a layered structure where TiAlN and ZrN crystallize in their individual lattices. Choosing the appropriate rotation frequency of the turntable, a single-phase coating was found, with a preferred orientation in the ⟨100⟩ direction. This was the case with the prime rotation frequencies beyond 6 rpm, which is a frequency technically easy to handle, with the selected power range for the magnetron sputtering.

The second and third rotation controls mainly the uniformity of the composition in growth direction and the homogeneous distribution of the superlattice coating around 3D parts, such as complicated cutting tools.

Figure 14.15 shows an XTEM taken from a TiAlN/ZrN coating deposited by combined UBM (unballanced magnetron sputtering) and steered arc deposition.

The image shows the exact parallelity and linearity of the single layers. This geometrically perfect appearance has been regularly observed, when the combined UBM–ARC deposition process was used or when a pure UBM process was carried out involving heavy atoms, particularly when using W in TiN/WN superlattice coatings. In fact, it is possible to specify a peak-to-peak roughness, X, of deposited superlattices[28] describing the waviness of the various superlattice coatings. It has been also found that the peak-to-peak roughness increases with

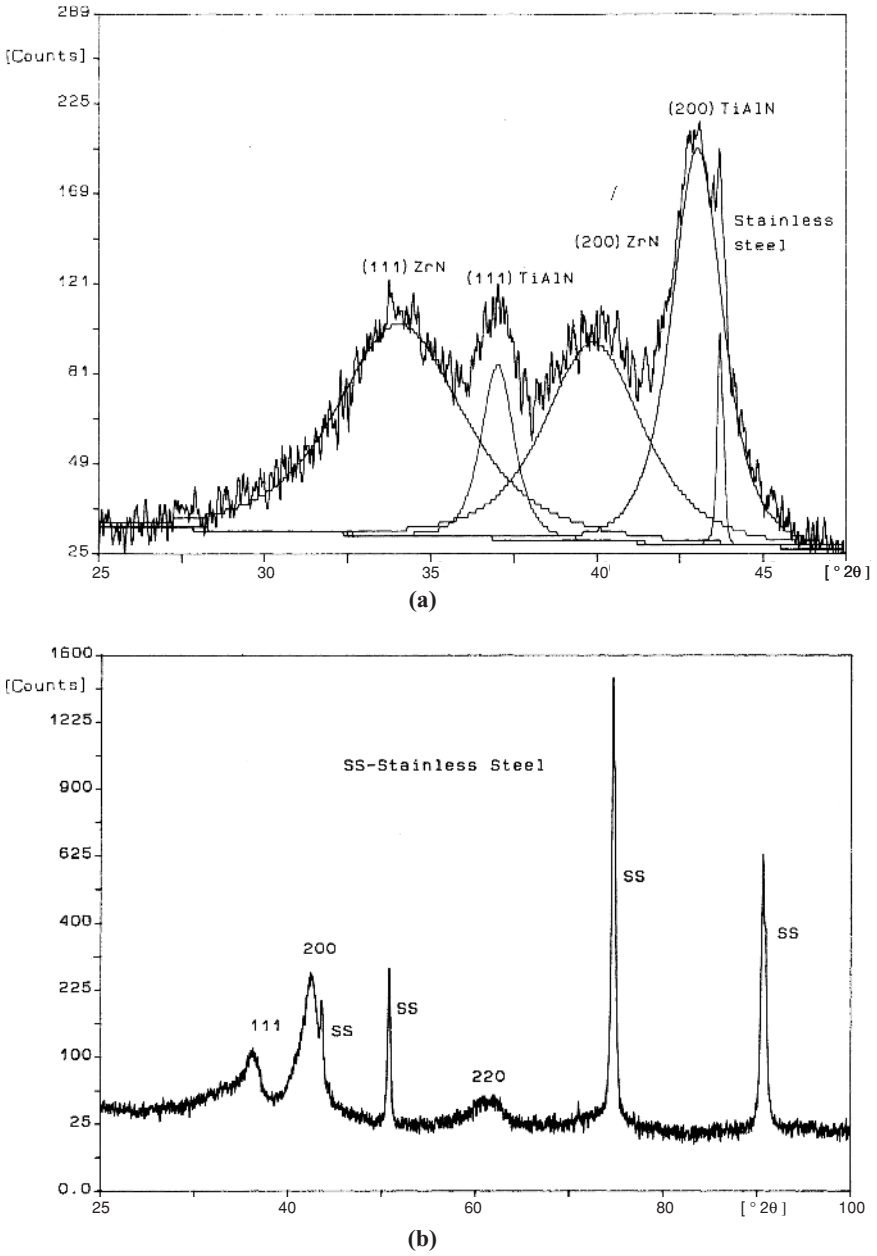

FIGURE 14.14. XRD analysis explaining the influence of substrate rotation speed on the structure of TiAlN/ZrN: (a) slow rotation; (b) fast rotation.

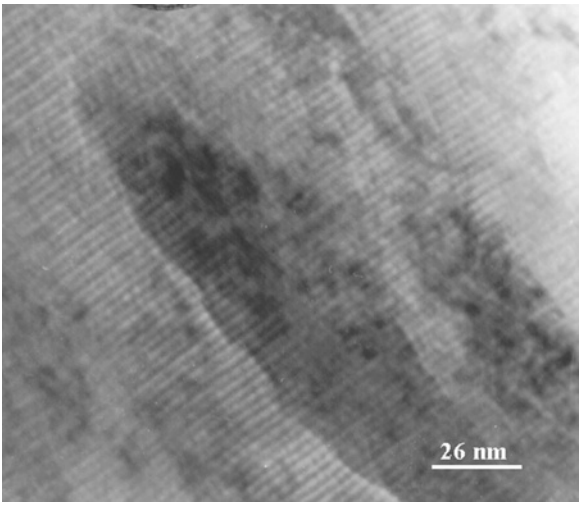

FIGURE 14.15. XTEM image of a TiAlN/ZrN superlattice coating with a period λ of 2.6 nm.

increasing coating thickness and that the waviness is reduced when the bias voltage is increased. Although the available results are not yet fully complete, Table 14.2 gives a vivid impression of the wide spray of X and its controllability. In the case of the TiAlN/TiNbN,[28] a very rough surface of the coating was observed when UBM is used as the deposition method. Increasing the ionization of the plasma by using the combined UBM–ARC (bias current density increases in the described case by a factor 2.5) leads to considerable smoothening of the surface.

The observed X value at half the film thickness was even lower than 5 nm. Similar plane superlattice structures were found in the combined UBM–ARC process for TiAlN/ZrN, as has been demonstrated also by the XTEM image (Fig. 14.15). In the case of the rather light V as a partner in the TiAlYN/VN superlattice, a

TABLE 14.2. Dependence of Peak-to-Peak Roughness X on Coating Material, Deposition Method, Bias Voltage and Position in Coating.

Coating	Deposition mode	Bias voltage (V)	Period, λ (nm)	X (nm)	Position in coating
TiAlN/TiNbN	UBM	−75	2.1	25	Top
	UBM/ARC	−75	2.2	5	Top
TiAlN/ZrN	UBM/ARC	−75	2.6	3.6	Middle
TiAlYN/VN	UBM	−75	3.5	8	Middle
		−95	4.0	5	Top
CrN/NbN	UBM	−75	3.5	8	Middle
		−120	3.0	3	Middle
CrN/NbN	ARC	−100	2.2	2	Middle

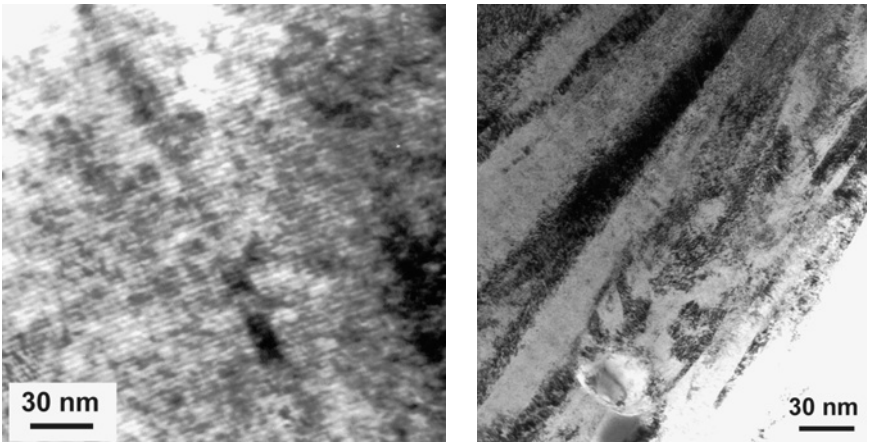

FIGURE 14.16. XTEM micrographs of arc-deposited CrN/NbN superlattice coating showing (a) low superlattice roughness and (b) "self-healing" of a structural defect originating from a "droplet" buried in the bulk of the coating.

rather large peak-to-peak value at half thickness of the coating (8 nm) was found. An increase in the bias voltage from $U_B = -75$ V to $U_B = -95$ V reduces the peak-to-peak roughness X already to 5 nm, although the value was taken at the surface of the coating. Using the CrN/NbN superlattice system, the influence of the bias voltage in the UBM deposition process has been confirmed.[16] Measured at half the coating thickness, the peak-to-peak roughness decreased from 8 to 3 nm when the bias voltage was increased from $U_B = -75$ V to $U_B = -120$ V. The lowest peak-to-peak roughness values have been found for fully ARC-deposited CrN/NbN superlattice coatings (Fig. 14.16a). The structure of these coatings was characterized by extremely flat layers due to the high mobility of the ad-atoms of the condensing species. The higher ad-atom mobility is a direct consequence of using arc evaporation, a method known for generating highly ionized metal plasma and enhanced ion bombardment due to the applied bias voltage during deposition. The main disadvantage of the arc evaporation, the ejection of macroparticles or "droplets," which generally deteriorate the density and the roughness of the coatings, seems not to be as critical in coatings with superlattice structure. A quick "self-healing" of growth defects originating from droplets was observed to occur in the arc-deposited CrN/NbN coatings. It can be seen in Fig. 14.6b that the growth defect generated from a "droplet" annihilates after deposition of approximately 70-nm (200 bilayers) thick superlattice coating on the top. Thus, the growth defect remains buried within the coating and does not reach the surface, which contributes to enhanced coating density. The observed "self-healing" effect could be attributed to the higher compressive stress in the arc-deposited coatings.

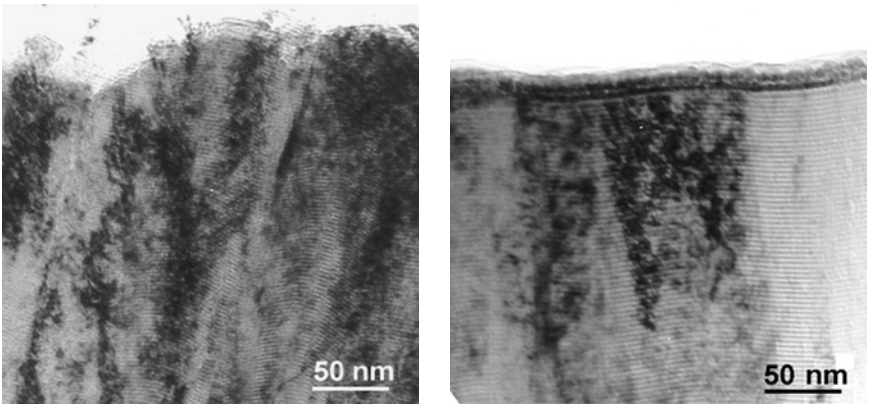

FIGURE 14.17. XTEM image of a TiAlYN/VN superlattice coating deposited at (a) $U_B = -75$ V and (b) $U_B = -95$ V.

The influence of the bias voltage on the peak-to-peak roughness of the UBM-deposited TiAlYN/VN superlattice coating is demonstrated in Fig. 14.17a,b.

At a bias voltage of $U_B = -75$ V, we observe grains with superlattices of rather high waviness; other grains are permeated by rather curved superlattice layers. No electron diffraction analysis is available yet, giving information as to whether these irregularities may be correlated with the crystallographic structure of the individual grains. In the case of $U_B = -95$ V, the peak-to-peak roughness is significantly reduced. The reduction in the peak-to-peak roughness with increasing bias voltage is also reflected by the XRD analysis (Fig. 14.18a,b). On investigating the CrN/NbN superlattices, it was found that both the low-angle as well as the high-angle XRD patterns give evidence of a more pronounced superlattice structure, if the bias voltage is increased.[16,40] In the case of the low-angle results, an increase in the peak intensity with increasing bias voltage was observed. Even the first signals of a second-order peak become visible at $U_B = -150$ V compared with the $U_B = -75$ V XRD pattern. In the case of the high-angle XRD analysis for the coatings deposited at higher bias voltages, again, the sharpening of peaks accompanied by the appearance of satellite peaks around the $\{111\}$ and $\{200\}$ reflections can be observed.

Superlattices fabricated under laboratory conditions with precise shuttering to prevent intermixing of the two material streams show very pronounced high-order peak development and intense satellite reflections in the high-angle XRD pattern.[41] Both the high ionization (combined UBM–ARC deposition) as well as the enhanced bias voltage might reduce the deposition of loosely bound and scattered material by resputtering, which initially leads to intermixing and therefore a reduction in the sharpness of peaks in the XRD pattern and to reduced material contrast in the XTEM images.

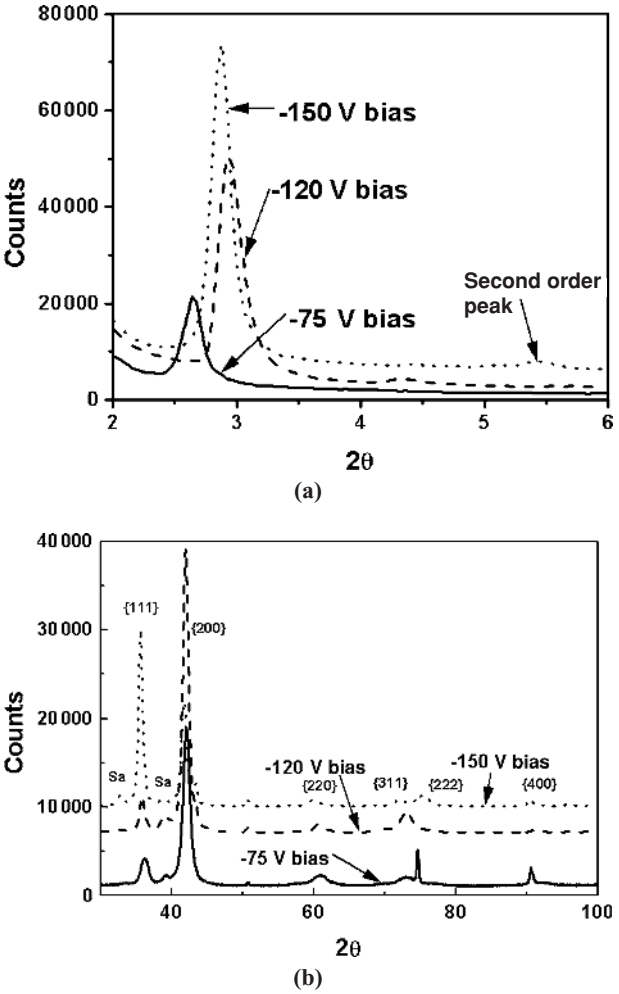

FIGURE 14.18. Influence of bias voltage on the (a) low-angle and (b) high-angle XRD patterns of CrN/NbN superlattce coating.

Although the effect of the ion bombardment is clearly understood and exploited as an effective tool for production of superlattice structured coatings with flatter individual layers, the interface sharpness is still largely influenced by the relatively open geometry in the industrial systems such as HTC-1000-4 shown in Fig. 14.4. This open geometry promotes certain degree of intermixing of the coating elements, which is even more pronounced for isostructural and mutually miscible nitride multilayers such as TiAlN/VN. The degree of mixing between the layers in TiAlN/VN, ($\lambda = 3.0 \pm 0.1$ nm), produced in HTC-1000-4 system under

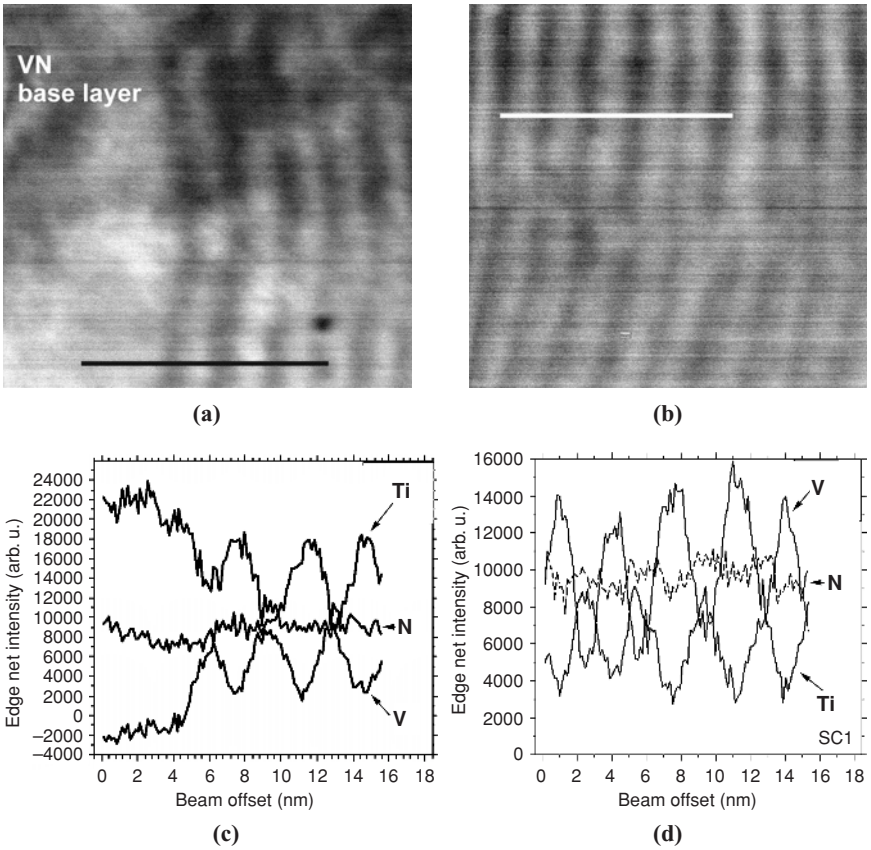

FIGURE 14.19. High-angle annular dark-field (HAADF) image (a) adjacent to the base layer; (b) from the multilayer close to the outer region of the coating; (c, d) line scans from regions marked on (a, b) showing the N, Ti, and V distributions.

the conditions of threefold rotation has been studied by using a spherical aberration corrected STEM, utilizing a 0.1-nm beam, by chemical-specific high-angle annular dark-field (HAADF) imaging and electron energy loss spectroscopy (EELS).[42] Figure 14.19a,b shows HAADF images close to the base layer (including the base layer) and close to the outer region of the coating, using a 0.1-nm probe, which is sufficiently small to reveal the position of the atomic columns. Figure 14.19c,d shows corresponding EELS-integrated intensity along the line scans from the respective lines marked on Fig. 14.19a,b. The EELS spectra demonstrate that there is mixing between layers, i.e., there is Ti present throughout the VN layer, while V is present throughout the TiAlN layer. The interface between layers is approximately 1 nm wide, while each VN layer contains a region of broadly constant V concentration for around ∼1 nm (much of the finer oscillations correspond to

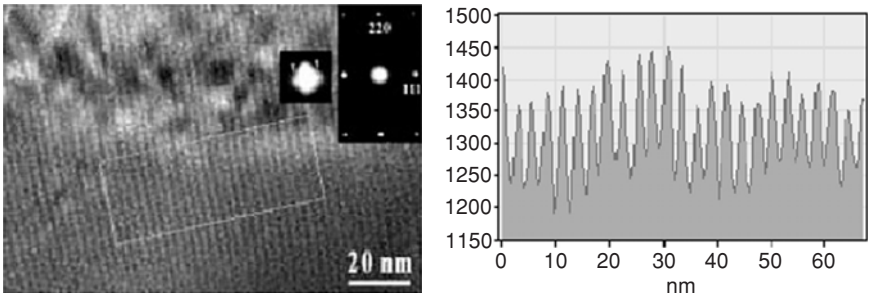

FIGURE 14.20. (a) BF-TEM image (zero-loss filtered) of a cross section in the middle of a TiAlN/VN superlattice coating. Inset is the SADP with the left diffraction spot enlarged. (b) Line-scan profile of the intensity variation of the selected area in (a) showing the alternating TiAlN and VN layers.[47]

small intensity differences between individual atomic layers). The layers contained regions at their center of around 1-nm width of roughly constant composition.

In addition to the interface broadening resulting from the cross contamination due to the open geometry of the HTC-1000-4 system, additional compositional modulation within each of the individual layers has been also observed. This additional oscillation in the chemical composition of the central part of the layers was related to the threefold rotation of the substrate during coating deposition.

The effect of threefold rotation on the film growth rate has been modeled and found to give rise to characteristic oscillations.[43,44] The growth oscillations can be influenced by rotation radii, frequencies and frequency ratios of the basic rotations, as well as the number and position of particle sources. Validation of the oscillation structure has been performed for elemental concentrations in (Cr,Ti)N coatings by glow discharge optical emission spectroscopy (GDOES) and auger electron spectroscopy (AES) depth profiling.[43] However, both methods failed to reveal the details of high-frequency oscillations due to resolution limitations. The extremely fine structures of the industrial superlattice coatings require state-of-the-art electron microscopy techniques to reveal local physical and chemical structure as a function of position within the coating.[45,46] To study the distributions of Ti and V in a TiAlN/VN superlattice, field emission gun transmission electron microscopy (FEG-TEM) coupled with energy-filtered TEM (EF-TEM) and Z contrast imaging were used to determine the microstructure and composition distributions on the nanometer scale.[47] Figure 14.20a gives a zero-loss EF-TEM BF image of the multilayer from the middle of a TiAlN/VN superlattice coating. Inset is the selected area diffraction pattern (SADP) from this area. The superlattice diffraction spots are symmetrically located at both sides of the transmitted spot, which indicates that the bilayers were growing parallel to the (111) planes in this grain. Figure 14.20b gives a line scan showing the image intensity variations in the selected area of a region where the individual layers were as close as possible to parallel.

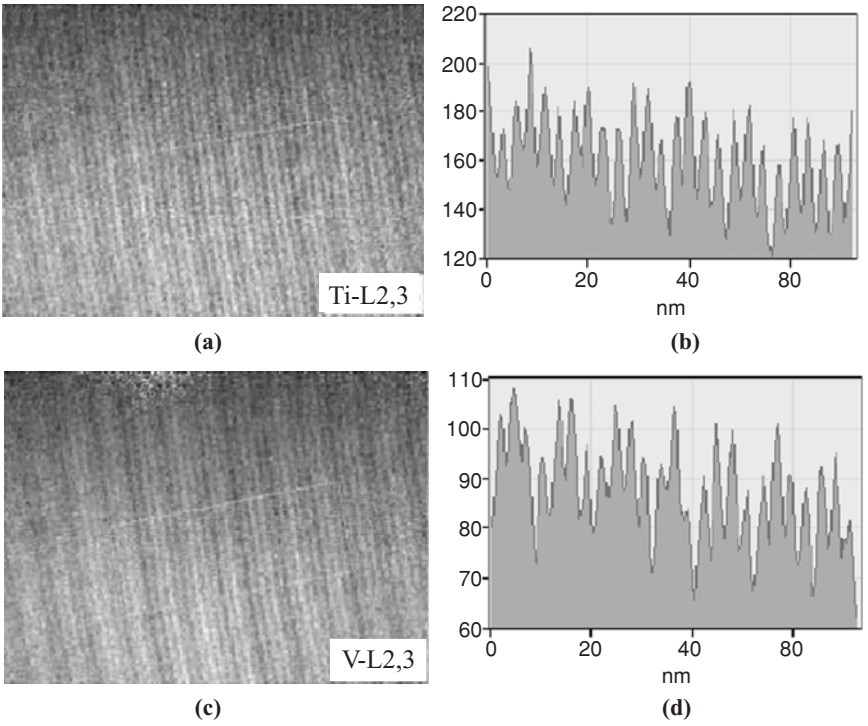

FIGURE 14.21. (a, c) Ti and V elemental maps. (b, d) Line-scan profiles of Ti and V elemental distribution in the selected area indicated in corresponding elemental maps revealing the additional modulation.[47]

The BF-TEM micrograph in conjunction with the intensity profile demonstrated the presence of alternating TiAlN and VN layers with an average periodicity of 3 nm. The bilayer thickness was calculated from the peak-to-peak positions of such intensity profiles.

Figure 14.21a,b shows electron spectroscopic images (ESIs) from the Ti-$L_{2,3}$ and V-$L_{2,3}$ edges, which confirmed the complimentary distribution of Ti and V concentration. The integrated intensities of Ti and V signals as a function of distance were derived from the elemental maps using digital micrograph software and are presented in Fig. 14.21b,d. The ESIs, in conjunction with concentration profiles, demonstrate an additional modulation superimposed on the basic period of coatings due to the threefold rotation of the sample. The influence of the processing parameters (the type of the rotation) on the microstructure of coatings, in particular, intermixing between layers, was further studied by theoretical modeling of the process.[47] Numerical calculation was conducted based on a mathematical model calculating normalized flux distributions and growth rates at a rotating sample surface. The calculations also identified an additional modulation, which resulted from the substrate rotation, consistent with the experimental observations.

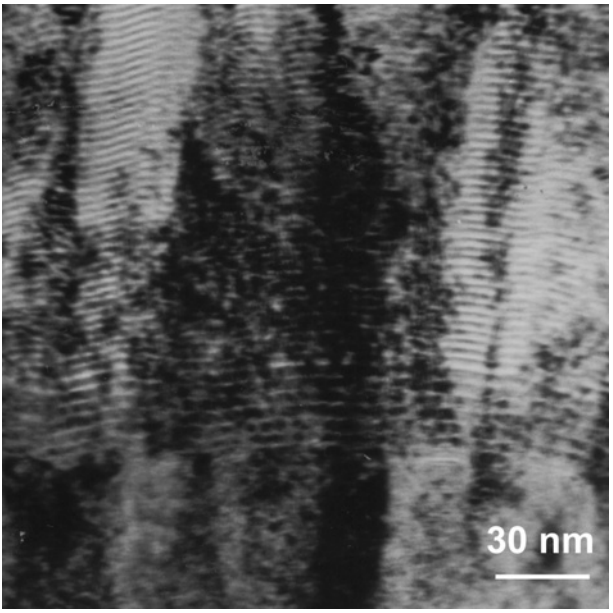

FIGURE 14.22. Influence of target poisoning on the superlattice period.

Figure 14.22 outlines clearly how sensitive but also how exact the resulting TiAlN/VN superlattice architecture relies on the deposition conditions. Film deposition starts with the formation of a columnar grown base layer of VN sputtered from two adjacently mounted V targets. During this period, the two TiAl targets are operated at a very low power level to avoid cross contamination with V. After switching the TiAl to full power, a layered structure immediately appears. After approximately 20 rotations, the targets reach equilibrium of poisoning. The deposition rate is reduced and remains constant, resulting in a precisely consistent periodicity of the superlattice coating, with a period, as measured by low-angle XRD analysis, of $\lambda = 3.4$ nm.

The influence of the target power dissipation and therefore the influence of the deposition rate on the period, λ, of a superlattice system is demonstrated using the example of TiAlN/CrN. Figure 14.23 shows the low-angle XRD patterns attained from coatings deposited by varying the power dissipation at the Cr target from 2 to 12 kW. The result shown in Fig. 14.23 reflects clearly the steady and practically predictable shift in the positions of the XRD reflections from low to high Cr power levels. At a power level of 8 kW, an equal film thickness of TiAlN and CrN is reached.

1.5. Texture and Residual Stress

A matrix of binary and ternary nitrides containing lighter elements (Al, Ti, V, and Cr) with atomic mass <52 and heavier elements (Nb and W) with atomic mass

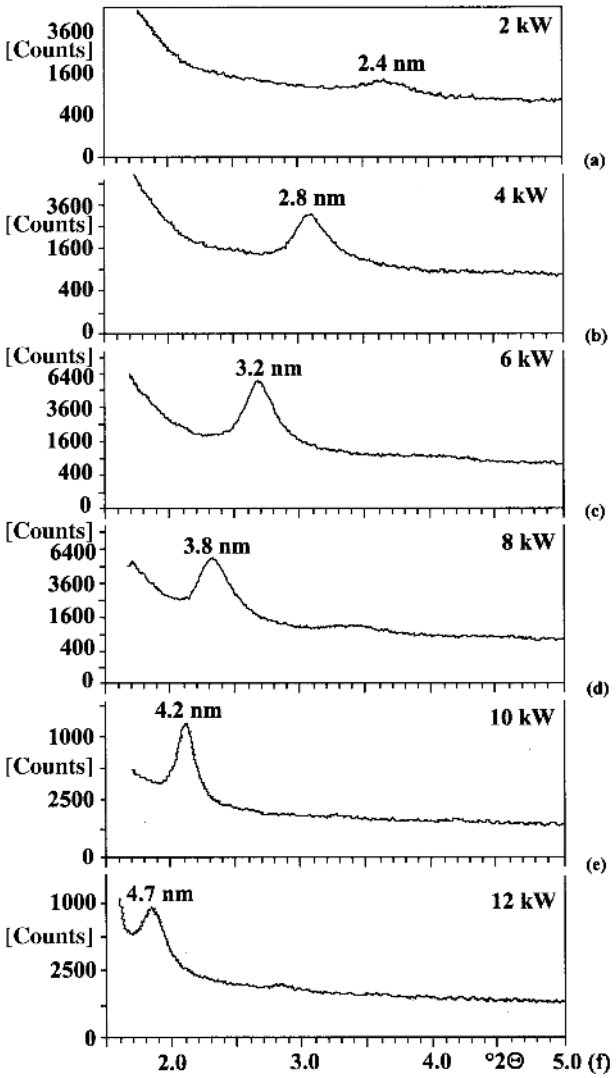

FIGURE 14.23. Influence of continuous stepwise increase in Cr target power dissipation on the position of the low-angle XRD peak in a TiAlN/CrN superlattice.

>89 has been produced and the texture and residual stress of these nitrides have been studied as a function of bias voltage during superlattice coating deposition step.[48] Texture, T^*, was determined in accordance with the Harris inverse pole figure technique.[49] Figure 14.24a–d shows the effect of bias voltage U_B on the texture development in TiAlN/VN, TiAlN/CrN, CrN/NbN, and TiN/WN nanoscale multilayer coatings.

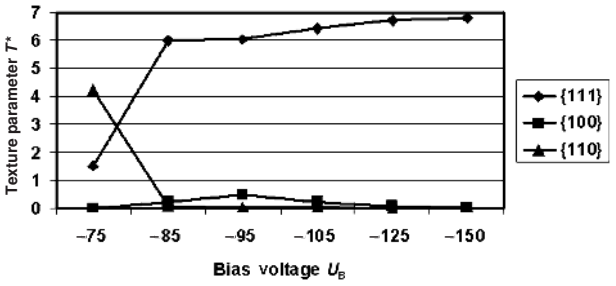

(a)

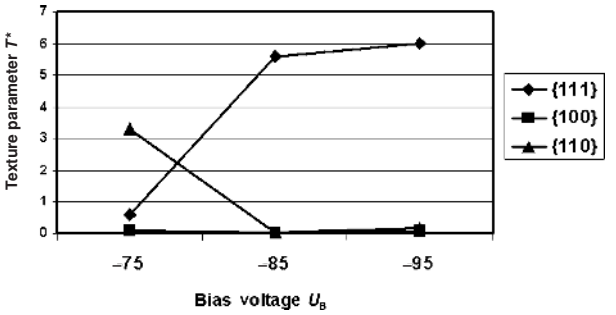

(b)

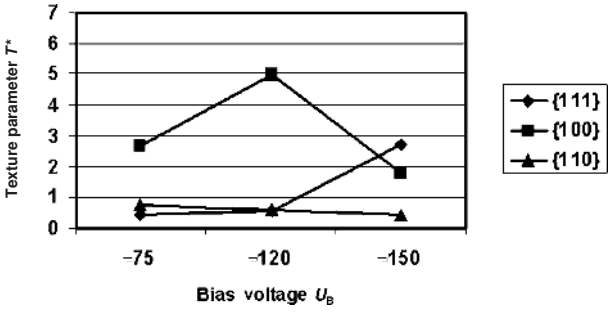

(c)

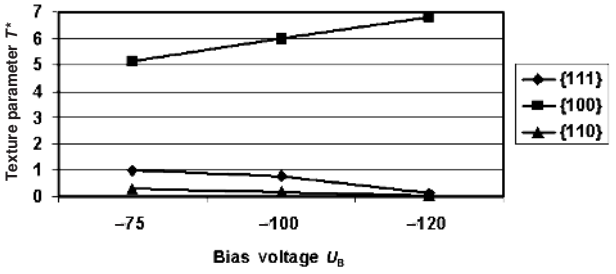

(d)

FIGURE 14.24. Effect of bias voltage U_B on texture development in (a) TiAlN/VN, (b) TiAlN/CrN, (c) CrN/NbN, and (d) TiN/WN superlattice coatings.[48]

From Fig. 14.24a–d, it is clear that significant differences in texture were observed between films containing lighter elements (atomic mass >52) e.g., TiAlN/VN and TiAlN/CrN, compared with those containing heavier elements, e.g., CrN/NbN and TiN/WN, when deposited at a bias voltage $U_B = -75$ V. The TiAlN/VN and TiAlN/CrN films exhibited a pronounced {110} texture, while the CrN/NbN and TiN/WN films exhibited a {100} texture (see Fig. 14.24a–d). The presence of a {110} texture is common in high CrN containing TiAlN films[50] where a process of competitive growth predominates. In fact, strong {110} textures are present in magnetron-sputtered monolithically grown CrN[51] and VN[52] films grown under similar bias voltage conditions. This would indicate that at $U_B = -75$ V the CrN- or VN-rich components were responsible for the development of {110} textures in TiAlN/CrN and TiAlN/VN coatings. In contrast, the {100} texture develops when the surface energy becomes dominant[53] and the film evolves by a process of continuous renucleation. The latter effect is commonly observed in the CrN/NbN and TiN/WN films as well as in TiAlN systems where heavier atoms such as Nb[28] and Zr[54] are involved in the growth process.

For the TiAlN/VN and TiAlN/CrN films, increasing the substrate bias voltage to -85 V results in a pronounced change in texture from {110} at −75 V to strong {111} textures at -85 V (i.e., $T^* = 6.02$ and 5.6 respectively). In the TiAlN/CrN and TiAlN/VN films, further increases in bias voltages $U_B = -95$ V and $U_B = -150$ V, respectively lead to further increases in the intensity of the {111} texture (see Fig. 14.24a,b). In contrast, increasing the bias voltage of the CrN/NbN and TiN/WN films to $U_B = -120$ V did not favor the development of a {111} but in fact increased the intensity of the {100} texture. At a bias voltage of $U_B = -150$ V at least for the CrN/NbN film, however, the {111} texture predominates.

The texture evolution in the CrN/NbN and TiAlN/VN was further studied by XTEM and selected area XRD analysis. Figure 14.25a–c shows BF/DF typical transmission electron micrographs from a CrN/NbN coating deposited at $U_B = -120$ V with the DF images showing adjacent {100} and {111} oriented grains (bright regions). In Fig. 14.25b, there is some evidence of continuous renucleation of new {100} oriented grains that are growing at the expense of the {111} oriented grain shown in Fig. 14.25c, thus resulting in the formation of the {100} observed by XRD.

In contrast, the TiAlN/VN film in Fig. 14.25d evolved by a process of competitive columnar growth and SADPs showed that the predominant growth direction was ⟨111⟩ which is in agreement with the strong {111} texture ($T^* = 6.05$) measured by XRD.

Texture evolution[53] can be discussed on the basis of both surface and strain energies. Thus, for TiN and other fcc nitrides, because the {100} plane has the highest packing density (4.0 at/a^2, compared with {220} having a packing density of 2.83 at/$a^2$and {111} of 2.31 at/a^2) and hence the lowest surface free energy,[55,56] the {100} texture would develop when the surface energy is the dominant parameter.[53] Conversely, when the strain energy is dominant, the texture tends toward the {111}

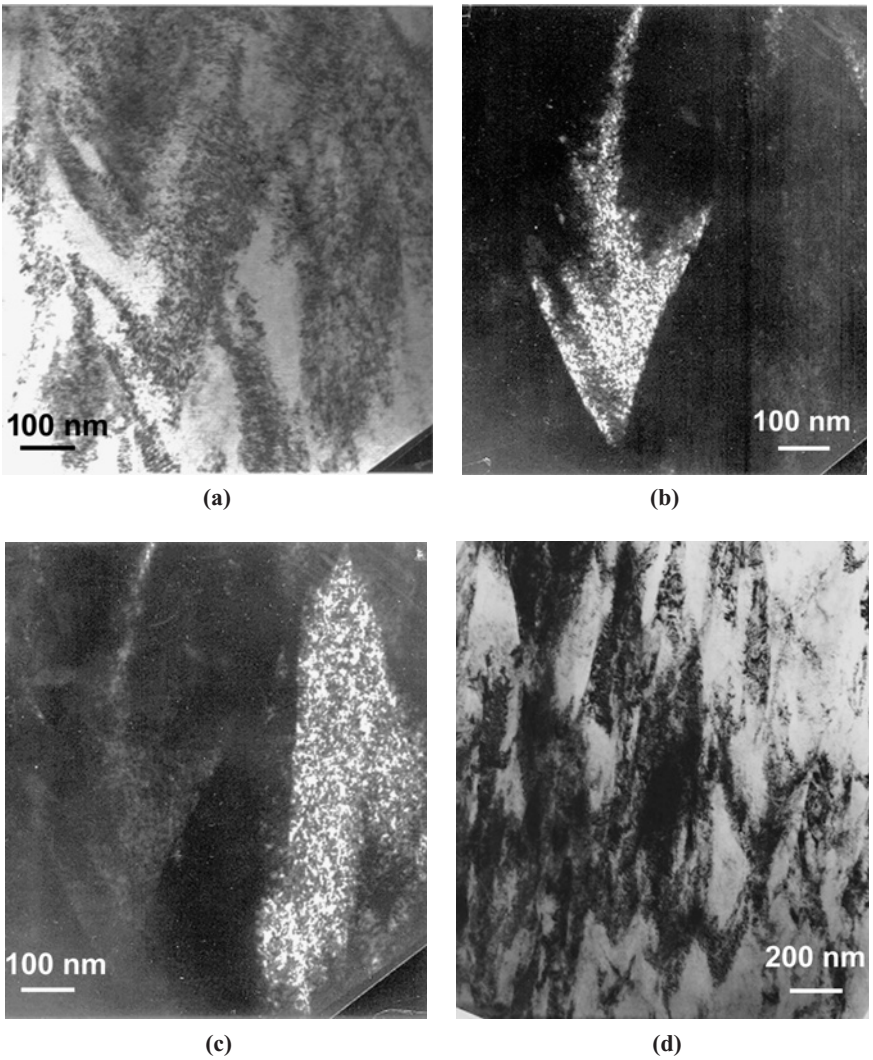

FIGURE 14.25. (a–c) Transmission electron micrographs of CrN/NbN deposited at $U_B = -120$ V: (a) BF image; (b) DF image from $\{200\}$ diffraction ring segment; (c) DF image from $\{111\}$ diffraction ring segment; (d) transmission electron micrographs of TiAlN/VN deposited at $U_B = -95$ V, BF image.[48]

plane, which has the lowest strain energy. In very thin films, the surface energy controls the growth and so a $\{100\}$ texture would be expected, whereas in thicker films the strain energy predominates and hence a $\{111\}$ texture would be expected. In the TiAlN/VN nanoscale multilayer films, the coatings are evolved by a competitive columnar growth process, which after sufficient growth favors the

development of a {111} texture.[56] In the competitive growth process, as the layer thickness increases, the {111} texture develops because the {111} oriented grains with the lowest strain energy grow and increase in diameter at the expense of other less favorable orientations with a higher strain energy, e.g., {100}. In the micrographs (Fig. 14.25d), there is clear evidence of coarsening of the structure by competitive growth. In contrast, in the CrN/NbN films deposited at bias voltages up to −120 V the coating is evolved by a continuous renucleation of new grains rather than by competitive growth of existing grains resulting in the development of a {100} texture (see Fig. 14.25b).

Currently it is not clear whether the interfaces between the individual component layers in the superlattice coatings are coherent or incoherent. The significant differences in texture observed between the different superlattice coatings seem to indicate that different growth mechanisms predominate in the different films. During competitive growth (TiAlN/VN), development of the superlattice film in the growth direction will be relatively unhindered and the individual component layers may develop coherent interfaces. In contrast, in coatings exhibiting a {100} preferred orientation (CrN/NbN), textures have been observed to evolve by a process of continuous renucleation and therefore interrupted growth, which possibly results in the formation of an incoherent interface.

Residual stress values for TiAlN/CrN, TiAlN/VN, CrN/NbN, and TiN/WN films as a function of bias voltage U_B are shown in Fig. 14.26. All the coatings investigated exhibited residual compressive stress states. However, at $U_B = -75$ V,

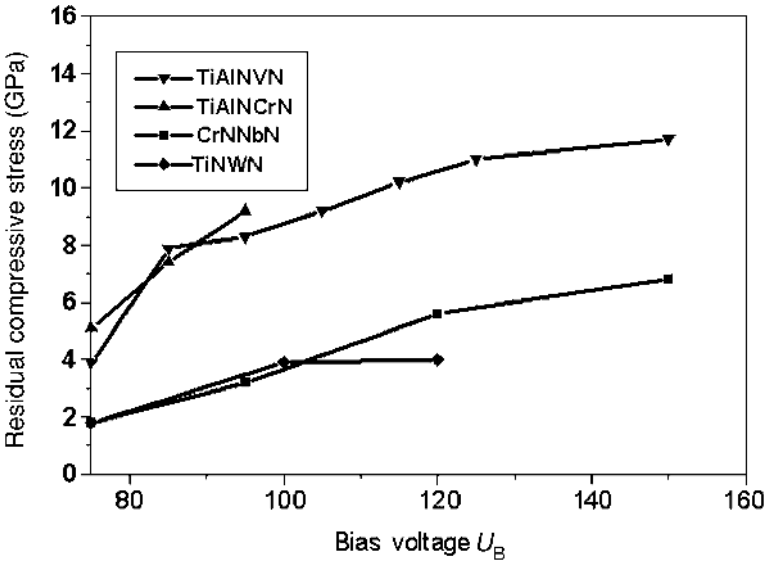

FIGURE 14.26. Effect of bias voltage on the residual stress of various ABS-deposited nanoscale coatings.[48]

the TiAlN-based nanoscaled multilayer coatings containing VN and CrN had considerably higher residual stresses of −3.9 and −5.0 GPa, respectively, when compared with CrN/NbN and TiN/WN nanoscaled multilayer coatings, which had a comparably low residual stress values of −1.8 GPa. This clearly indicates that where one of the components of the bilayer is dominated by a heavy element a lower residual stress is observed. It is generally accepted that higher residual stresses are associated with higher defect densities induced during ion bombardment.[28] In UBM-deposited coatings, the dominant bombarding specie is Ar^+ ion. Two of the many processes occurring simultaneously during ion bombardment are energy transfer to the condensing atoms and defect formation during coating growth. One possible explanation for the systematically lower residual stress observed in CrN/NbN and TiN/WN coatings is that higher activation energies are required for surface diffusion of less mobile heavier atoms (Nb and W, atomic mass >52) than for more mobile lighter atoms (Al, Ti, V, and Cr, atomic mass <52).

For coatings involving heavy atoms, considering the energy conservation issue during deposition, at the same bias voltage, less energy is available for defect formation because a larger part of the energy is spent in moving atoms to their equilibrium position. In this case, a smaller portion of the total energy will be available for defect formation and therefore a lower residual stress in the coating will be produced. An example of this effect can be demonstrated in CrN/NbN and TiN/WN coating systems where the maximum stress measured at $U_B = -75$ V is only −1.8 GPa. Further increases in bias voltage up to $U_B = -150$ V for the CrN/NbN nanoscale multilayer led to a systematic increase in the residual stress to a value of -6.8 GPa. In contrast, the residual stress for the TiN/WN nanoscale multilayer containing the heavier element W increased to only 4 GPa when the bias voltage, U_B, was increased to −120 V.

In the case of the TiAlN/VN coatings, involving only light elements (atomic mass <52) increases in the bias voltage, U_B, to −125 V and −150 V lead to residual stresses of −11.0 and −11.7 GPa, respectively. These are almost greater by a factor 2 and 3 respectively, than the CrN/NbN and TiN/WN coatings deposited at similar bias voltages. These increases in residual stress can obviously be associated with increases in defect densities resulting from increases in the energy portion available for defect formation with increasing bias voltage.

1.6. Mechanical and Tribological Properties

The mechanical and tribological properties of a series of hard coatings are summarized in Table 14.3 as a function of the bias voltage U_B.

The results on HP (plastic hardness) demonstrate impressively that practically all coatings belong to the "superhard" category of hard coatings. As pointed out earlier, the achieved HP values correspond to the observed stress values, as higher the hardness higher is the stress. The results for the coefficient of friction depend very much on the method of measurement. If the generated debris is not

TABLE 14.3. Mechanical and Tribological Characteristics of Various Superlattice Coatings.[16]

	Bias (V)	H (GPa)	Stress (GPa)	Coefficient of friction, μ (with debris)	Coefficient of friction, μ (without debris)	Wear coefficient ($m^3/N\,m$)	Scratch adh. L_c (N)	R_a (μm)
TiAlN/VN	−75	39	−3.3	0.4	0.18	1.3×10^{-17}	70	0.066
TiAlYN/VN	−75	42	−4.0	0.6	0.2	2.5×10^{-16}	30	0.073
TiAlYN/VN	−95	78	−8.5	0.65	0.22	4.5×10^{-16}	39	0.053
TiAlN/CrN	−75	55	−5.1	0.7	0.2	2.4×10^{-16}	50	0.075
TiAlN/CrN	−95	60	−9.2	0.92	0.2	3.1×10^{-15}	52	0.062
TiAlN/ZrN	−75	55	−10	0.6	—	—	55	0.060
CrN/NbN	−75	42	−1.8	0.69	0.2	2.1×10^{-15}	50	0.072
CrN/NbN	−120	56	−6.5	0.9	0.23	5.0×10^{-15}	62	0.033

removed from the wear track, the observed friction values measured against an Al_2O_3 counterpart can be rather high with values up to 0.92. In this case, the debris acts as a third body. However, if the debris is removed gently and continuously by soft brushes, the coefficient of friction drops down to 0.18. The highest values have been measured for the CrN/NbN coating, whereas the TiAlN/VN coating exhibits the lowest value probably due to the formation of a vanadium oxide, which acts as a dry lubricant. The values for the sliding wear coefficient correlate to the values for the coefficient of friction measured against the Al_2O_3counterpart. The best performance has been observed for TiAlN/VN with a sliding wear coefficient of 1.3×10^{-17} $m^3/(N\,m)$, whereas the stoichiometric CrN/NbN coating shows a value of 5.0×10^{-15} $m^3/(N\,m)$, which is approximately 300 times higher than that of a TiAlN/VN coating. It is also interesting to observe that with increasing bias voltage, plastic hardness, and residual stress, the sliding wear coefficient increases correspondingly. This behavior is not yet understood and is subject to ongoing investigations. All scratch critical load values derived from scratch test experiments reach sufficiently high values. Although the stress increases with increasing bias voltage, no corresponding decrease of critical load is observed. Conversely, a slight increase of critical load L_C is observed. Table 14.3 also shows that the roughness of the coating surface decreases with increasing bias voltage and internal stress. The enhanced internal stress contributes obviously to the expulsion or closing ("self-healing") of growth defects, which leads to a smoother coating.

Figure 14.1 shows a very sharp maximum in the resultant hardness as a function of the superlattice period. Such a steep dependence is consequently accompanied with large tolerances in hardness values and would undoubtedly aggravate an industrial realization of superlattice technology, particularly, if one has to coat

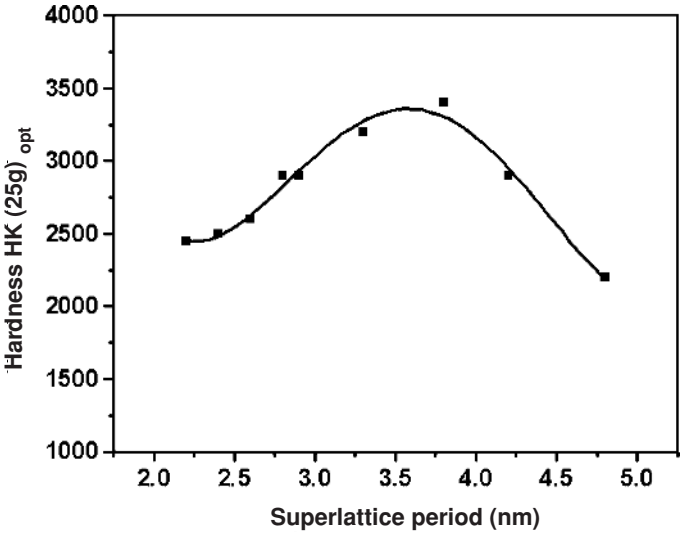

FIGURE 14.27. Influence of the superlattice period λ on the hardness of a TiAlN/CrN superlattice coating. (Note: Opt stands for optical evaluation of the length of the Indent produced by the knoop diamond, sometimes with small indents SEM is used.)

complex shaped 3D parts. It is therefore not surprising that in an industrially sized coating system with its simplified deposition conditions with expected intermixing of the coating materials, under the described parameters, a much less pronounced hardness maximum has been evaluated. Figure 14.27 illustrates the situation for TiAlN/CrN.[7] The maximum hardness $HK_{0.025}$ (Knoop hardness) corresponds to a plastic hardness HP of 55 GPa. Similar dependencies have been found for TiAlN/VN, TiAlYN/VN, TiAlN/ZrN, and CrN/NbN. Effectively, we can reproduce the HP peak hardness of the various coatings by ±2 GPa.

The hardness of all the above-mentioned superlattice coatings strongly depends on the applied bias voltage during coating deposition. Increasing of the bias voltage significantly increases the hardness, which can be related to the increased residual stress, dislocation density, and defect density produced by the intensive ion bombardment during coating growth. Plastic hardness values for TiAlN/VN and CrN/NbN films as a function of bias voltage U_B are shown in Fig. 14.28. The trends in the plastic hardness almost exactly mirror those of the respective residual stress in the coatings, with clear relation to the atomic weight of the coating elements as discussed in Section 1.5. As it is demonstrated in Fig. 14.28, plastic hardness values as high as 80 GPa can be easily achieved with coatings based on lightweight elements (TiAlN/VN); however, the question of how much hardness can be tolerated in the PVD coatings dedicated for real-life applications needs to be carefully considered.

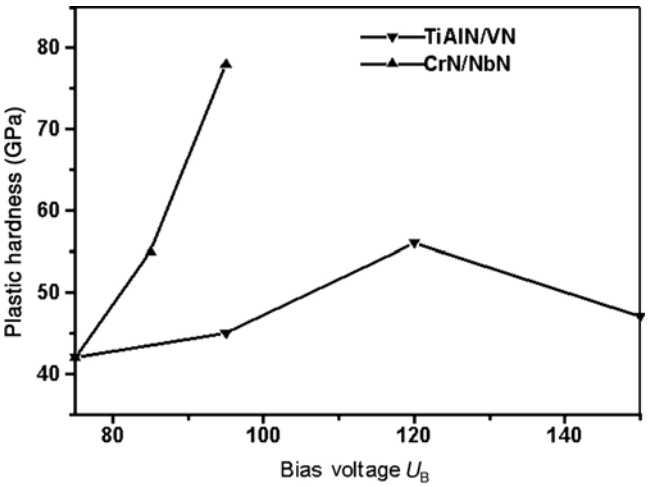

FIGURE 14.28. Effect of bias voltage on the plastic hardness of ABS-deposited nanoscale coatings.[48]

2. INDUSTRIAL APPLICATIONS OF VARIOUS NANOSCALE MULTILAYER/SUPERLATTICE STRUCTURED PVD COATINGS

2.1. Application-Tailored Superlattice Coating Family

Figure 14.29 describes the family of superlattice coatings developed at Sheffield Hallam University (SHU) in England. A nanoscale multilayer coating consisting of $TiAlCr_{0.03}$ N and TiAlYN with a bilayer thickness of 1.7 nm has been developed to satisfy high-temperature (950°C) applications such as dry high-speed cutting of die steel[29]; TiAlN/VN is also designed for cutting operations and for protection of wear parts. However, the incorporation of VN in the coating introduces a component that acts as a dry lubricant. During sliding, VN is converted into V_2O_5, thus reducing the friction coefficient. TiAlN/VN is a universal coating for high-speed steel cutting tools or for cutting operations using dry or cooled CC tools. CrN/NbN is a nanoscale multilayered coating for applications where corrosion and wear play a major role.[58] Nb belongs to the group of metals with the highest chemical stability, whereas CrN is a hard coating that can be applied with excellent adhesion at 200°C. The combination of these coatings satisfies requirements for low-temperature applications such as carbon steels. Another low-friction coating has been introduced and evaluated by combining nanoscale layers of Cr and C.[59,60] These coatings are relatively soft ($HK_{0.025} = 2500$), but due to the low friction coefficient ($\mu = 0.2$), sliding-wear coefficients of the order of 10^{-17} $m^3/(N\,m)$ can be achieved.

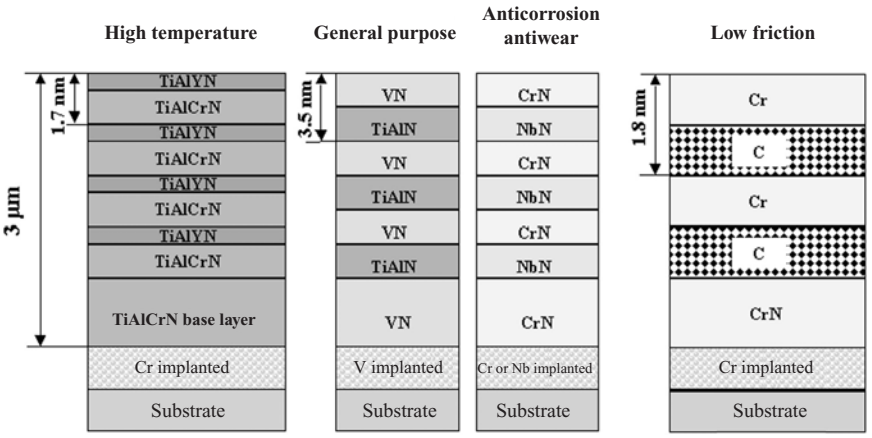

FIGURE 14.29. The superlattice coatings family developed at Sheffield Hallam University (SHU) in England.[57]

2.2. Superlattice Coatings Dedicated to Serve High-Temperature Applications

2.2.1. Structure and High-Temperature Behavior of TiAlCrN/TiAlYN and TiAlN/CrN Nanoscale Multilayer Coatings

TiAlN coatings are well known for their high oxidation resistance up to 800°C[61,63]; therefore, they are preferred partners in superlattice structures for high-temperature applications. Currently, two combinations of TiAlN-based superlattice coatings are available, in which TiAlYN or CrN were selected as a second partner material to produce TiAlCrN/TiAlYN or TiAlN/CrN. Table 14.4 summarizes the mechanical and tribological properties of these coatings.

The coatings are deposited by the combined steered cathodic arc/UBM sputtering method in industrially sized Hauzer HTC-1000-4 system (Fig. 14.4). For

TABLE 14.4. Mechanical and Tribological Characteristics of Various Superlattice Coatings.

Coating	Bias (V)	HP (GPa)	Stress (GPa)	Coefficient of friction, μ (Al_2O_3)	Sl. Wear coefficient ($m^3/(N\,m)$	Scratch Adh. L_c (N)	R_a (μm)
TiAlCrN/ TiAlYN	−75	28	−7.0	0.9	2.5×10^{-16}	50	0.08
TiAlN/ CrN	−75	55	−5.1	0.7	2.4×10^{-16}	50	0.08

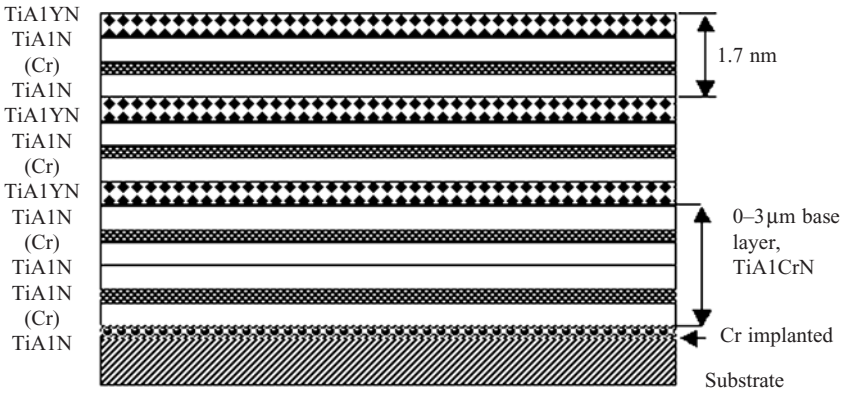

FIGURE 14.30. "Superlattice"-like layer sequence deposited by four magnetrons comprising one Cr target, two TiAl targets and one TiAlY target.

the deposition of TiAlCrN/TiAlYN, two targets with 50:50 at% Ti–Al, one target 48:48:4 at% Ti–Al–Y and one 99.8% Cr are utilized. Detailed technological parameters of the deposition process are given in Ref. 29. Production of TiAlN/CrN requires three targets with 50:50 at% Ti: Al and one target 99.8% Cr.[6] Both coatings utilize Cr^+ metal ion etching and stress reducing $\sim$ 0.3-μm-thick base layer of TiAlCrN or CrN for TiAlCrN/TiAlYN and TiAlN/CrN respectively. Due to the special target arrangement for deposition of the TiAlCrN/ TiAlYN, yttrium is incorporated consequently in a layered manner. Figure 14.30 illustrates the layer sequence.

The incorporation of Y in the TiAlN coatings gives rise to severe changes of the microstructure, the texture, and the internal stress of the films. It has been shown[29] that addition of 2% Y results in formation of less pronounced columnar nearly equi-axed microstructure (Fig. 14.31). It is important to mention that

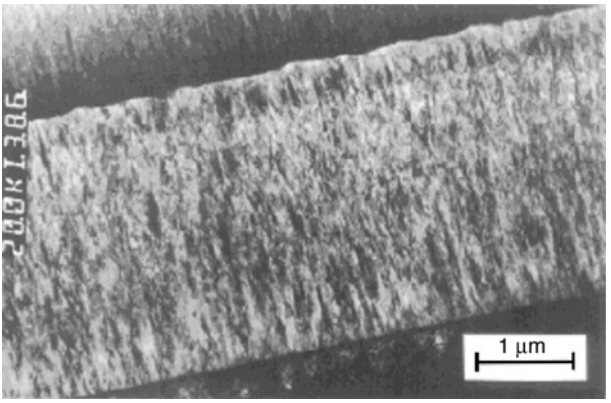

FIGURE 14.31. XTEM micrograph of an as-deposited TiAlCrN/ TiAlYN coating[9]

this fine structure is observed only when deposition occurs in multitarget coating equipment; e.g., two targets consist of Y-free TiAl and a third contains the total amount of the yttrium used in the deposition process. In case of a uniform distribution of the amount of yttrium over all three targets, only minor changes in the microstructure, texture, and compressive stress are reported.[10] It has been shown further that the incorporation of 2% Y leads to an enhanced compressive stress level. TiAlN and low concentration of Cr containing 3-μm-thick TiAlCrN coatings exhibit internal stress of around 3 GPa, very similar to TiN and other hard coatings. In contrast, TiAlCrN/ TiAlYN shows a compressive stress as high as 7 GPa. However, utilization of Cr^+ metal ion etching as a substrate pretreatment together with deposition of Y-free TiAlCrN base (transition) layer provide excellent adhesion of these highly stressed coatings.

Recently, in an attempt to further enhance the oxidation and more importantly the tribo-oxidation performance of TiAlCrN/ TiAlYN, a 400-nm-thick special top layer has been developed. This approach allowed reduction of the friction coefficient of the wear-resistant ceramic hard coating against steel as workpiece material from 0.9 to 0.65. The top layer consists of a TiAlYN/CrN nanoscaled multilayer, which is embedded in a TiAlCrY–oxy-nitride. The oxygen content is continuously increased during the deposition of the outermost 200 nm of the coating by continuously replacing nitrogen in the reactive sputter deposition process with medical dry air.[62] Figure 14.32 shows a schematic diagram (a) and a TEM cross section (b) of the coating. This coating has been made commercially available as Supercote 11 (SC 11) by Bodycote SHU Coatings Ltd, Sheffield, UK.

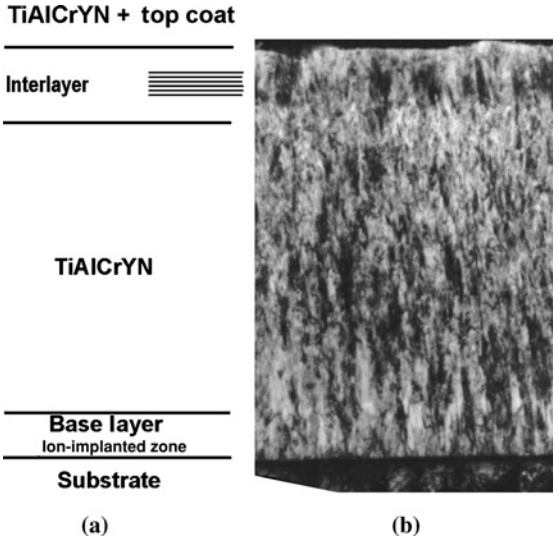

FIGURE 14.32. TiAlCrN/ TiAlYN with top coat as (a) schematic and (b) cross-sectional BF-TEM image.

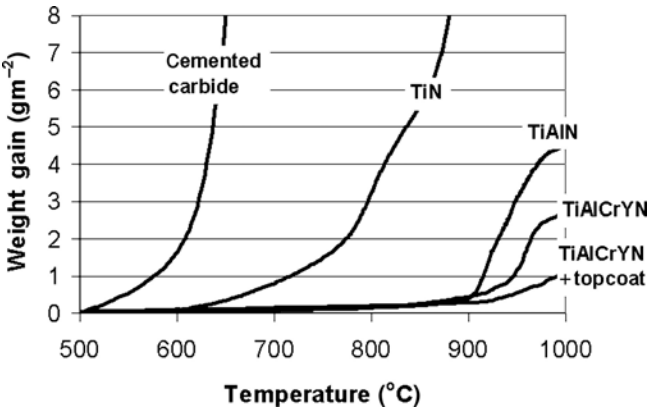

FIGURE 14.33. Continuous thermogravimetric measurement. Heating rate: with 50 °C/min to 400 °C and with 1 °C/min to 1000 °C.

One of the biggest advantages of the Y-stabilized TiAlN-based pseudo-superlattice coatings is their unique high-temperature oxidation behavior. Thermogravimetric experiments have shown that the onset of severe oxidation of TiAlN occurs at temperatures above 750°C.[61] A detailed analysis of the oxidation process reveals that a sandwich structured oxide is formed with an amorphous Al-rich top oxide and a crystalline Ti-rich oxide between the top oxide and the TiAlN base film. It has been further discussed that the Al-rich top oxide controls the diffusion of oxygen toward the interface of the Ti-rich oxide and the nitride, thus reducing substantially the formation rate of Ti-rich scales as compared to TiN. The addition of 2 at% Y to TiAlN-based coatings allows peak temperatures up to 950°C.[29]

Thermogravimetric data shown in Fig. 14.33 confirm the dramatic difference in the oxidation behavior of tungsten carbide when compared with TiAlCrYN.[29,33] The results from Fig. 14.33 also clearly demonstrate the progress in improvement of the oxidation resistance of the TiAlN achieved due to a logical and systematic approach in the coating development, based on sequentially adding special purpose elements such as Cr and Y as well as utilization of tailor-made top layers of dense and glassy oxy-nitrides.

The incorporation of Y during deposition led to a fine-grained interrupted columnar growth structure, which increases the diffusion path for in- and outward diffusion of substrate elements. Furthermore, it has been found that at high temperatures above 800°C, Y diffuses preferentially to the column boundaries, thus further blocking the potential diffusion paths in the coating.[29] In case of CC as substrate material, extensive investigations using STEM and EDX mapping on cross-sectional samples have been carried out to localize the influence of Y. Distribution maps of the coating and substrate elements taken after heat treatment for 1 h at 900°C are shown in Fig. 14.34. Whereas all elements such as Al, Ti, and Cr are uniformly distributed in the coating, there is clear evidence of out-diffusion of Co

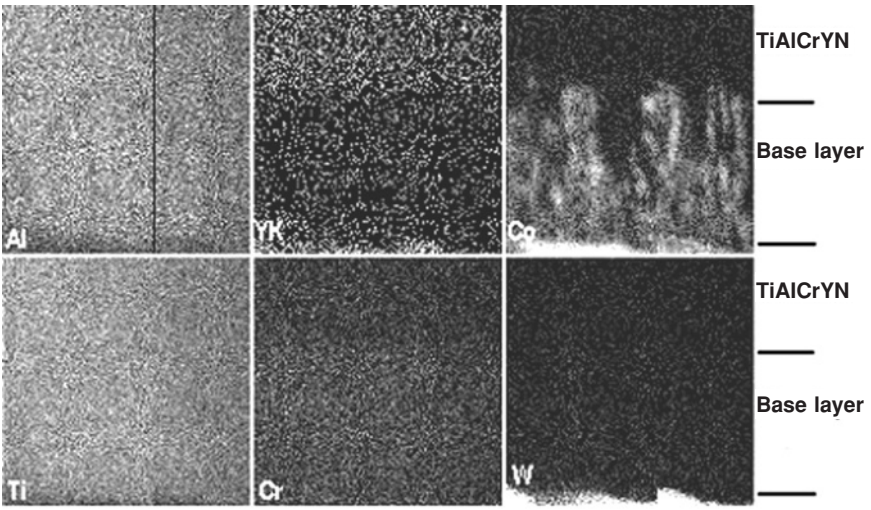

FIGURE 14.34. Elemental distribution maps of TiAlCrN/TiAlYN with top coat deposited onto CC after 1h at 900 °C.

from the CC substrate into the base layer. In parallel, a very uniform distribution of Y in the TiAlCrYN coating has been observed. Figure 14.34 is a clear indication that Co diffuses mainly along column boundaries in the base layer and is blocked in the Y-containing layer section. At the higher magnification (Fig. 14.35) the above-mentioned Y segregation taking place in the Y-containing part of the coating also becomes evident.

The beneficial effect of the Y segregation mechanism can also be seen in the effective hindering of in- and outward diffusion of oxygen or substrate material

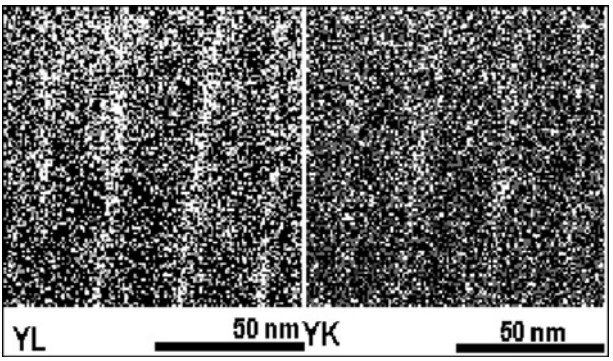

FIGURE 14.35. YL and YK maps of TiAlCrN/TiAlYN with top coat.

elements, which is expected to take place at high temperatures. Secondary neutral mass spectroscopy (SNMS) and EDX depth profiling of TiAlCrN/TiAlYN and TiAlCrN/TiAlYN + oxy-nitride top coat exposed for 1 h to air at 950°C have undoubtedly confirmed that the accumulation of Y at the grain boundaries inhibits effectively the diffusion of migrating oxygen and substrate species through the film.[64,65]

The Y segregation discussed above influences very strongly the high-temperature wear properties of TiAlCrN/TiAlYN. To investigate this effect, high-temperature wear test was conducted on the TiAlCrN/TiAlYN and TiAlCrN coatings using a reciprocating sliding ball-on-disk configuration using a 10-mm-diameter hard metal ball at conditions of normal load 15 N (initial hertzian contact pressure 2.1 GPa), reciprocating stroke 2 mm, and frequency 15 Hz, and temperatures of 400, 600, 800, and 900°C in air.[66] In this test, the two coatings showed very different wear behavior. For TiAlCrN, increasing the test temperature from 400 to 900°C led to consistent increase of the depth of the wear crater from 0.076 to 0.97 μm, whereas the Y-stabilized coating after an initial increase in the wear depth to 1.82 μm at 600°C showed consistent decrease of the wear depth at higher temperatures, reaching the lowest value of 0.82 μm at 900°C. Further more the friction coefficient showed similar behavior, reducing its values from 0.9 at 600°C to 0.65 at temperatures in the range of 850–950°C. This peculiar behavior can be related to the progressive coating densification ("self-healing") with the temperature increase due to the operation of the Y segregation mechanism.

2.2.2. Application of TiAlCrN/TiAlYN in Dry High-Speed Cutting Operations

Dry high-speed machining (DHSM) is gaining increasing importance in modern production technology. Dry high-speed milling of dies and moulds represents the current state of the art. Cutting speeds between 15 and 25 krpm have been reported to machine steels in the hardness range of 55–62 HRC. In this application, CC cutting tools must be protected with hard oxidation-resistant coatings, as localized temperatures are typically up to a 1000°C. Table 14.5 summarizes temperature measurement results during milling various steels with two-flute ball-nosed 8-mm-diameter solid carbide end mills. As it can be seen in this application, indeed temperatures greater than 900°C can be reached. In this temperature range, tungsten carbide and also PVD–TiN and PVD–TiCN coating material suffer severe oxidation. Therefore, coatings with enhanced oxidation resistance, which can show reasonably long lifetime, are in high demand. Furthermore, in dry high-speed milling, the tools are subjected to enormous interrupted reciprocating mechanical impacts and under these conditions adhesion is of paramount importance. Previous work has shown that the adhesion measured by scratch testing (critical load, L_c) can be directly related to the microchemistry of the interface resulting in localized epitaxial growth of the deposited TiAlN hard coating.[21] The absolute value of the critical load L_C can be controlled by a dedicated low-energy ion implantation

TABLE 14.5. Overview of Temperatures at the Cutting Edge of Coated Cemented Carbide Ball-Nosed End Mills During Machining of Various Steels.

Workpiece material	DIN	Hardness (HRC)	Cutting conditions	Temperature (after 5 min)
EN24 C0.40, Mn0.60, Ni1.5, Cr1.1, Mo0.3	1.6582	38	v_c = 385 m/min, Ax = 3.8 mm, radial feed = 1 mm, feed = 0.1 mm/rev, spindle = 16 000 rpm	<700°C
P20 C0.32, Mn0.80, Cr1.60, Mo, 0.40	1.2311	48	v_c = 385 m/min, Ax = 3.8 mm, radial feed = 0.4 mm, feed = 0.1 mm/rev, spindle = 16 000 rpm	<700°C
P20 C0.32, Mn0.80, Cr1.60, Mo0.40	1.2311	48	v_c = 510 m/min, Ax = 3.8 mm, radial feed = 0.4 mm, feed = 0.1 mm/rev, spindle = 20 000 rpm	~ 810°C
H13 C0.35, Si1.0, Cr5.25, Mo1.5, W1.25, V0.30	1.2344	53	v_c = 385 m/min, Ax = 3.8 mm, radial feed = 0.4 mm, feed = 0.1 mm/rev, spindle = 16 000 rpm	~ 810°C
A2 C1.0, Mn0.65, Cr5.0, Mo1.0, V0.3	1.2363	58	v_c = 385 m/min, Ax = 3.8 mm, radial feed = 0.4 mm, feed = 0.1 mm/rev, spindle = 16 000 rpm	~ 880°C
A2 C1.0, Mn0.65, Cr5.0, Mo1.0, V0.3	1.2363	58	v_c = 510 m/min, Ax = 3.8, radial feed = 0.4 mm, feed = 0.1 mm/rev, spindle = 20 000 rpm	~ 910°C

(Note: DIN is a European Standard for steels.)

process, carried out in a steered arc discharge, as a process step of the ABS technology, during the metal-ion-etching procedure of the substrate surface (20-min duration) prior to coating as discussed in Section 1.2. The implantation of 1.2 keV Cr^+ ions prior to deposition of a TiAlN coating leads to the highest scratch test values (L_c = 135 N), when compared with a pretreatment of 1.2 keV Ar^+ (L_c = 35 N), Nb^+ (L_c = 90 N), and V^+ (L_c = 115 N) ions. Additionally, a decrease of adhesion was observed, when the accelerating voltage during ion implantation was only 0.6 keV (Cr; L_C = 60 N). Figure 14.36 reflects the lifetime of TiAlCrN/TiAlYN-coated CC end mills machining HRC 58 A2 die steel (rotation speed 15 krpm). In these experiments, two-flute end mills fabricated from identical CC material were pretreated with various ion species and then coated with 3 μm TiAlCrN/TiAlYN using identical deposition parameters. The results clearly demonstrate the importance of the technology utilized to engineer the coating substrate interface to meet the application demands.

The first substantial breakthrough in the application of TiAlCrN/TiAlYN coating was achieved by coating solid carbide end mills. Particularly in dry cutting

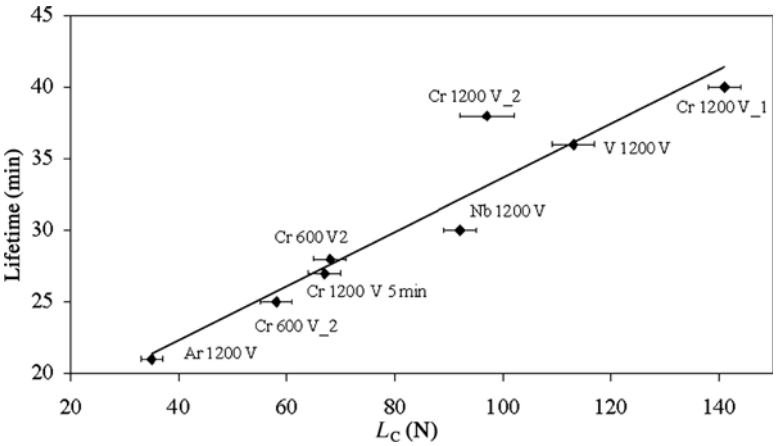

FIGURE 14.36. Lifetime in dry high-speed machining (DHSM) versus critical load values in scratch adhesion testing.

of die steel, remarkable improvement compared to current commercially available state-of-the-art quality has been accomplished. The results of conventional TiN-coated tools have been exceeded by a factor 4.5, when the HRC 58 steel (X 100 Cr Mo V 51) was cut with 6-mm two-fluted ball-nosed CC end mills (fabricated by Hydra Tools International Plc, Sheffield, Great Britain) with spindle rotation speed of 30 000 rpm and a linear feed rate 6 m/min. Figure 14.37 compares the results gained with commercially available TiN, TiCN, and TiAlN with the TiAlCrN/TiAlYN without oxy-nitride top coat. The coating has been made available on a routine basis by Bodycote SHU Coatings Ltd, Sheffield, and has been commercialized by Bodycote Int.

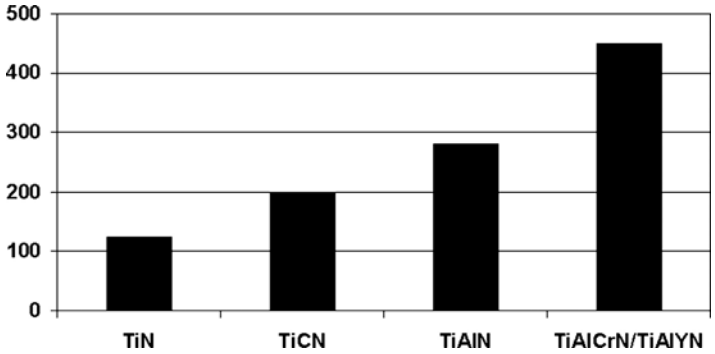

FIGURE 14.37. The average cutting performance of ball-ended 2-flute CC end mills coated with commercially available TiN, TiCN, TiAlN, and TiAlCrN/TiAlYN.

FIGURE 14.38. PVD-coated end mills in a dry high-speed cutting operation.

Figure 14.38 shows a typical example of coated end mills in action.

The performance of the latest version of TiAlCrN/TiAlYN with Cr-containing top coat (Supercote 11) has been compared to commercially available Y-free TiAlN coatings deposited by cathodic arc evaporation (suppliers I and II) and an increasingly popular sandwich coating TiN/TiAlN (∼30 layers), also deposited by cathodic arc.[67] All tools were manufactured by the same tool supplier using CC material stemming from an i.dentical production lot. In the tests, 8-mm two-flute ball-nosed end mills were used to mill A2 (HRC 58) die steel. Figure 14.39 summarizes the results of the end-of-life tests for two different cutting speeds, namely $v_c = 385$ m/min (16 krpm) and $v_c = 500$ m/min (20 krpm). The tests at 16 krpm illustrate the superiority of TiAlCrYN against arc-deposited TiAlN and

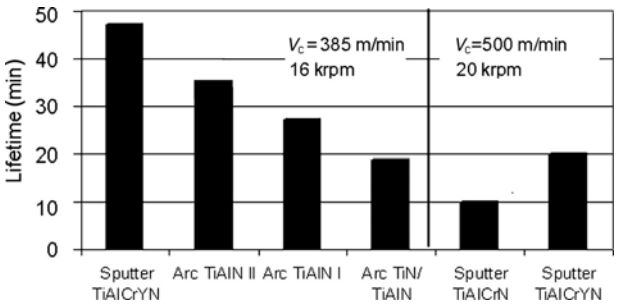

FIGURE 14.39. Milling test results from various coatings grown on CC ball-nosed end mills.

the multilayer system TiN/TiAlN. In the 20-krpm test TiAlCrYN is compared with TiAlCrN. At these high cutting temperatures (∼800°C; see Table 14.1) the influence of Y becomes again clearly evident. One at% Y doubles the lifetime of TiAlN.

2.2.3. Application of TiAlCrN/TiAlYN in Forming and Forging Operations

Another very lucrative-appearing utilization of the nanoscale multilayer TiAlCrN/TiAlYN is represented by the coating of moulds for the glass-producing industry. In this particular case, the enormous thermal stability of the interface between the coating and the mould (cast iron) comes into force, combined with the excellent adhesion properties typical for the ABS coating technology. Additionally, the coating was enriched with carbon graded toward the coating surface, thus forming there a $TiAlCrYC_{0.3}N_{0.7}$carbonitride. The graded incorporation of carbon was distributed across the outer third of the coating. Despite thermal shock events taking place with high frequencies (approximately 30 cycles/min) and covering temperature differences up to 950°C, lifetime values of up to 7 days have been achieved when operating the moulds in an unlubricated blow–blow process. Figure 14.40 displays a set of coated components for glass-bottle-forming operation. TiAlCrN/TiAlYN have shown excellent performance in hot forging operations. Figure 14.41 shows an extrusion die and an as-produced forged product. This forging process involves a forming temperature of typically 1100°C whereby the workpiece material is extruded through the die under an applied load of 300 ton. The coating of the die appears to delay the "drag-through" of the die material from the bell of the die to the final area, thereby prolonging the usability of the die from 2800 components to more than 4000 components before retirement. In addition to

FIGURE 14.40. Coated components for glass-bottle-forming operation.[9]

FIGURE 14.41. Extrusion die and as-produced component.[9]

an enhancement of the productivity of the die, the geometrical tolerances of the produced components are also improved.

Figure 14.42 illustrates a die manufactured from H13 material used for precision hot forging of turbine blades for aeroengines. These dies under a load of 500 ton are used to "stampout" components from billets of Inconel 718 material preheated to ∼1100°C. In an as-machined and uncoated condition this die produced 700 components before critical areas on the blade went out of tolerance due to wear and plastic flow of the die material. After subsequent remachining and with the addition of the TiAlCrN/TiAlYN coating, this die went on to produce an additional 1600 components, thereby completing the production requirement and giving a lifetime of at least 2.3 times that of the uncoated die. On examination, it was concluded that the coated die, which exhibited only minor wear, was still serviceable and could be used for further production.

Another only very recently discovered new application of TiAlCrN/TiAlYN superlattice coatings is the protection of steel moulds used in aluminum injection

FIGURE 14.42. Precision forging die for the production of turbine blades for aeroengines.[9]

FIGURE 14.43. Moulds for aluminium dye casting.

processing. Here, a typical increase of lifetime by a factor of 2 was found. Figure 14.43 shows moulds used in the automotive industry. The positive result may be explained by the reduction of inward/outward diffusion of substrate and workpiece elements due to the presence of Y, which diffuses at elevated temperatures to the grain bounderies and acts there as a diffusion blocker.

2.2.4. Application of TiAlCrN/TiAlYN, and TiAlN/CrN in Protection of Gamma Titanium Aluminides

For high-temperature applications in aeroengines, there exists an increasing interest in advanced titanium alloys as well as titanium aluminides. Due to their low density and their well-balanced mechanical properties, near-α and $\alpha + \beta$ titanium alloys are presently used for compressor components such as disks and airfoils. Service temperatures are limited to about 500°C,[68] mainly due to the insufficient environmental resistance of the structural material. The degradation mechanisms are characterized by formation of rapidly growing nonprotective oxide scales containing predominantly rutile (TiO2) and embrittlement of the subsurface zone by dissolution of interstitials (mainly oxygen and nitrogen).[69,70] From a mechanical standpoint, advanced near-α alloys such as TIMETAL 834 offer the potential of useful service temperature up to 600°C,[71] provided that oxidation resistance is improved significantly. Surface treatments, first and foremost various types of coatings, aiming at improved environmental resistance of titanium alloys have been investigated for more than three decades.[72] One major problem of coating development for titanium alloys has been that although reasonable short-term oxidation resistance was achieved in many cases, most of these coatings tended to be inherently brittle, or formed brittle phases with the substrate material, thus degrading its mechanical properties, especially fatigue behavior. Since the embrittlement problem has never acceptably been solved, none of the coatings proposed for improved oxidation resistance has been brought into service. Promising avenues for coating development have been demonstrated with sputter-deposited TiAl-based coatings.[73]

In addition to enhanced oxidation resistance, these coating systems demonstrated reasonable mechanical properties such as creep[74] and fatigue behavior.[75]

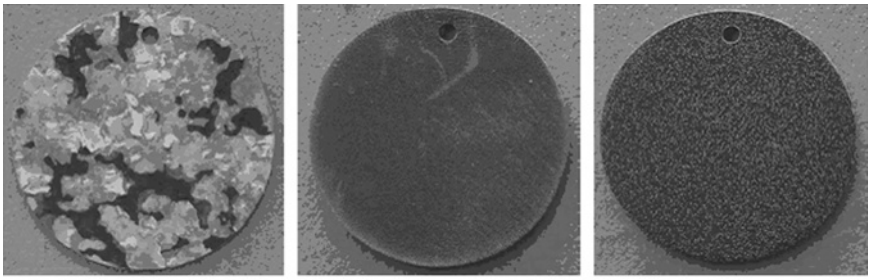

FIGURE 14.44. Micrograph of bare (a) TIMETAL 834; (b) TIMETAL 834 coated with TiAlCrYN/CrN; (c) TiAlCrN/TiAlYN.

Cr additions to TiAl-based coating demonstrated significantly improved environmental resistance.[76] Recently, a new approach has been undertaken to improve the environmental resistance of titanium alloys utilizing nitride overlay coatings produced by the combined cathodic arc/UBM sputtering.[77,78] Two types of nanostructured PVD coatings namely TiAlCrN/TiAlYN and TiAlYN/CrN have been investigated to protect TIMETAL 843 alloy as well as commercial γ-TiAl alloy Ti–48Al–2Cr–2Nb over a long period of time between 1000 and 3000 h. Macrographs of the specimens after oxidation testing at 750°C isothermal exposure for 1000 h confirmed significant differences in oxidation behavior of the samples (Fig. 14.44). While the reference uncoated samples suffered from severe oxide scale spallation (Fig. 14.44a), both the superlattice TiAlYN/CrN (Fig. 14.44b) and the pseudo-superlattice TiAlCrN/TiAlYN (Fig. 14.44c) coating demonstrated formation of reasonably protective oxide scales.

This observation was further confirmed by the thermogravimetric oxidation test results. Cyclic oxidation tests were carried out at the German Aerospace Center, DLR, in Cologne, Germany, in automated rigs in air at 750°C up to 2000 cycles. One cycle consisted of 1 h at high temperature and 10 min cooling down to 70°C. Figure 14.45 compares the oxidation resistance of uncoated Ti–45Al–8Nb included as reference material to that of the same material coated with TiAlCrYN/CrN and TiAlCrN/TiAlYN nanoscale multilayer PVD coatings. Both coatings clearly provide significant protection to the gamma Ti alloys, with TiAlCrN/TiAlYN performing slightly better in this test. Detailed cross-section TEM analysis of the TiAlYN/CrN after high temperature (750°C) exposure indicated a layered substructure consisting of an ~0.8-μm protective outer scale of alumina, a 95-nm transition layer between the oxide and the nitride layer, 3.8-μm retained nitride layer with an unchanged structure, and a 275-nm transition layer between the titanium alloy and the nitride coating. Underneath the transition zone, the titanium alloy was recrystallized with fine grains in a 460-nm layer. EDS analysis across the coating–substrate interface revealed that neither oxygen nor nitrogen or chromium was present in this layer, indicating both excellent protection of the nitride layer against

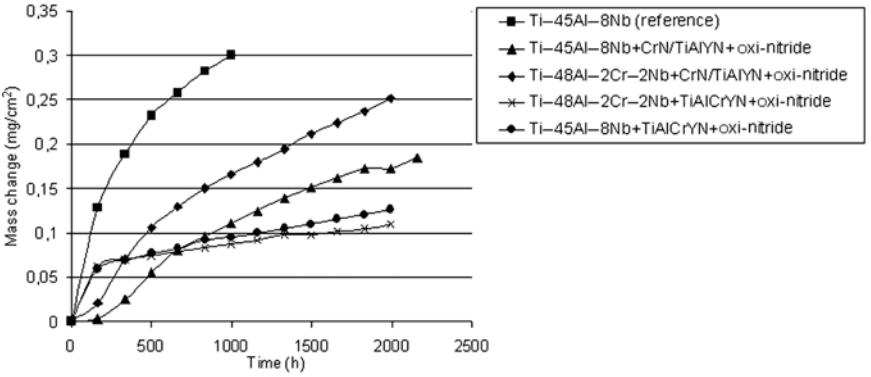

FIGURE 14.45. Mass change versus number of 1-h cycles plot for various substrate alloys coated with superlattice nitride/oxy-nitride duplex coatings.

diffusion of nitrogen and oxygen from the gas atmosphere during exposure as well as very little interdiffusion between the nitride coating and the substrate alloy. The TiAlCrN/TiAlYN showed similar behavior; however, a much thicker top oxide layer of 1.1 μm was formed after the test, thus supporting the results from the thermogravimetric analysis. Figure 14.46 shows an XTEM overview image of the nanostructured TiAlCrN/TiAlYN coating isothermally oxidized for 1000 h at 750°C in air. Both coating systems are promising candidates for environmental protection of titanium alloys due to their high-temperature stability and the absence of cross diffusion of substrate and coating elements. If reliably protected, Ti alloys will find broad application for aircraft engine parts, for example, as compressor components such as disks, vanes, and blades or in automotive engines for valves and turbocharger components.

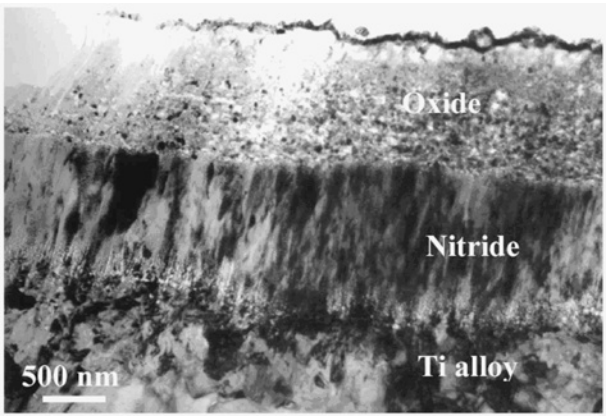

FIGURE 14.46. TEM overview image of TiAlCrN/TiAlYN coating isothermally oxidised for 1000 h at 750 °C in air.

2.3. Superhard Low-Friction Superlattice Coatings and Their Applications

2.3.1. Structure and Tribological Properties of TiAlN/VN Superlattice Coating

TiAlN/VN has been designed as a wear-resistant coating for broad-scale tribological applications, to protect cutting tools and machine wear parts. The superlattice concept was utilized as a tool to achieve enhanced material properties and combine the highly abrasion-resistant TiAlN with VN selected as friction-reducing material. The lower friction coefficient was expected to result from the formation of V_2O_5, a lubricious oxide owing to its low melting point, at the asperity contacts during sliding wear.[79]

The coating was grown by sputtering from two pairs of TiAl (50:50 at%) and pure V targets in mixed N_2 and Ar atmosphere, using V^+ ion etching/implantation to pretreat the substrate surface, followed by the deposition of 0.25-μm-thick VN base layer. Superlattice structured coatings with bilayer thickness typically in the range of 3.2 nm have been deposited by proper selection of the substrate rotation speed, the power dissipated on the magnetrons, the bias voltage, and the pressure of the reactive atmosphere. Detailed description of the technological process for TiAlN/VN superlattice coating deposition can be found elsewhere.[16,23] The microstructure of the coating is illustrated in Fig. 14.47a,b. The low-magnification

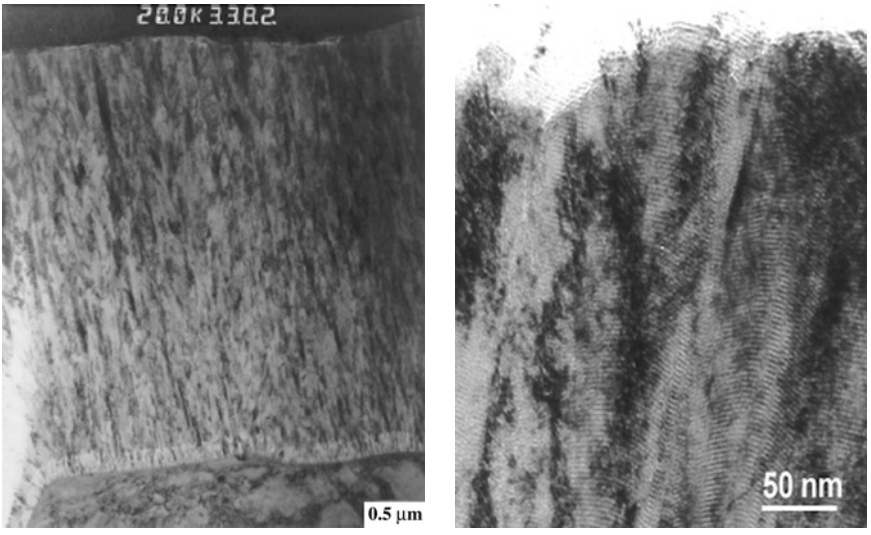

FIGURE 14.47. (a) Low-magnification and (b) high-magnification BF-XTEM images of TiAlN/VN superlattice coating.

TABLE 14.6. Mechanical and Tribological Properties TiAlN/VN Superlattice Coating.

Coating	Bias (V)	HP (GPa)	Stress (GPa)	Coefficient of friction, μ	Sl. wear coeffcient ($m^3/(N\,m)$	Scratch adh. L_c (N)	R_a (μm)
TiAlN/VN	−75	42	−4.0	0.45	1.26×10^{-17}	70	0.06

XTEM image (Fig. 14.47a) shows the typical competitive columnar grain growth associated with {111} oriented TiAlN/VN. The micrograph also clearly depicts the dense 0.25-μm-thick TiAlN base layer. The higher magnification image on the other hand reveals the fine nanoscale multilayer structure of the TiAlN/VN superlattice coating, in which the individual layers of sequentially deposited TiAlN and VN are clearly resolved.

Table 14.6 summarizes the mechanical and tribological properties of the TiAlN/VN deposited on HSS material.

The excellent wear behavior of TiAlN/VN in dry sliding conditions has been widely reported elsewhere.[16,23,80] However, the exceptionally low wear rate of $1.26 \times 10^{-17} m^3/(N\,m)$ is difficult to be explained by the superhardness (42 GPa) alone or by the distinctive wear mechanism of the superlattice structured coatings, which suggests material removal in 6–8-nm-thick nanolayers as opposed to monolithically grown coatings, where due to severe plastic deformation, bending, and cracking of the columns, release of large 50–75-nm particles is observed.[12] In the special case, when V is incorporated in the coating constitution, the effect of tribo-oxidation wear mechanism in dry sliding has to be carefully considered. Vanadium is known to form Magnéli phases with oxygen, with "easy" crystallographic shear planes[81] that can under certain conditions act as solid lubricants. Additionally, the low melting point of the V_2O_5 (T_m = 685°C), which lies in the range of the flash temperatures achieved at the asperity contacts during sliding, implies friction reduction due to sliding over a molten phase. XTEM analysis of TiAlN/VN coatings of the wear track in pin-on-disk indeed showed formation of 10–20-nm-thick tribo-film (Fig. 14.48). EDS analysis and Raman spectroscopy of the wear debris revealed the presence of V_2O_5 as well as mixed Ti–V–Al oxides.[82,83] Scanning electron microscopy (SEM) observations of the wear track after 1 million laps in room temperature pin-on-disk test showed extremely smooth surface and almost no transfer of material from the alumina ball used as a counter part.[23] Examples of the wear track morphology produced during sliding of two coatings, CrN and TiAlN/VN, with similar coefficient of friction in the range of 0.5 are shown in Fig. 14.49a,b. With the monolithically grown CrN (Fig. 14.49a) deep grooving along the wear direction occurred after a relatively short sliding distance of 3 km. In contrast, the TiAlN/VN superlattice coating after nearly 70 km of wear shows a rather smooth and very shallow (less than 1 μm deep) wear track (Fig. 14.49b).

The low friction coefficient of 0.5 measured in this test can be related to the behavior of the tribo-oxide film containing V_2O_5. It is believed that the small

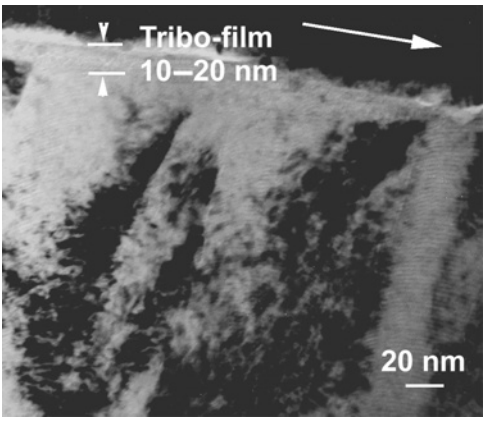

FIGURE 14.48. XTEM micrograph of TiAlN/VN superlattice coating from the wear track region after pin-on-disk test showing the tribo-film formation.

amount of V_2O_5, which forms predominantly at the asperity contacts, reduces the coefficient of friction due to melting. The sliding wear mechanism in such conditions very much resembles boundary lubrication, where the surfaces are separated and the junction formation mechanism is suppressed by adsorbed molecular films (in this case molten phase) although appreciable asperity contact may still occur. Thus, the synergy between the fine delamination wear mechanism characteristic of superlattice structures and the low melting point of the tribo-film controls the low friction coefficient at room temperature. In the view of potential high-temperature applications, the oxidation and the tribological behavior of TiAlN/VN at elevated temperatures have been studied extensively.[84–86] A combination of differential scanning calorimetry (DSC) investigations and high-temperature (up to 700°C) tribometry revealed a unique self-adapting behavior of TiAlN/VN to combined

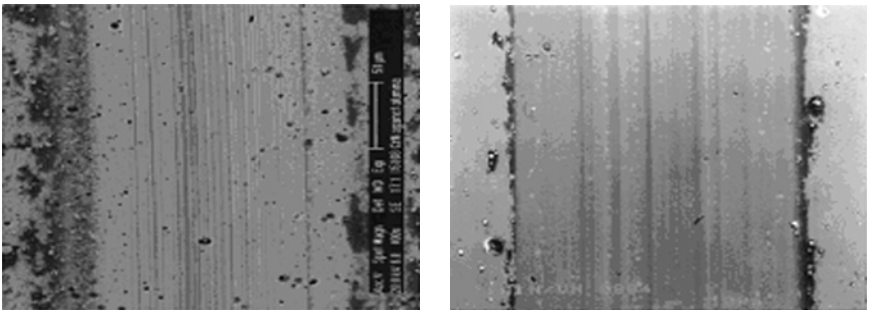

(a) **(b)**

FIGURE 14.49. SEM images of pin-on-disk wear tracks: (a) CrN film worn over 50 000 cycles (3.14 km); (b) TiAlN/VN film worn over 1.1×10^6 cycles (69 km).

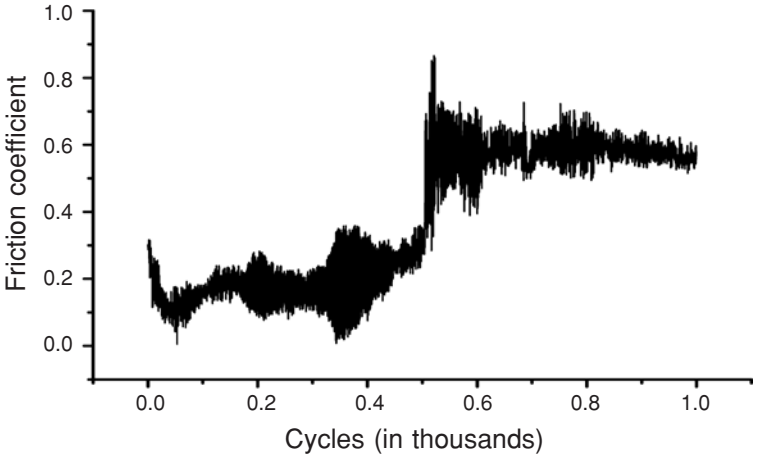

FIGURE 14.50. Friction coefficient curve of TiAlN/VN superlattice coating tested at high temperature of 700 °C in air atmosphere.

thermal, mechanical, and chemical wear.[84] It has been shown that at 700°C in steady state conditions, low friction coefficient in the range of 0.55 was achieved (Fig. 14.50), which in effect is similar to the friction coefficient measured at room temperature. To explain this effect, an operation of a specific controlling mechanism has been suggested that involves sliding against liquefied oxide scale and conversion of V_2O_5 to lower oxidized Magnéli phases.[84]

The very low value for the coefficient of friction of 0.18 (Fig. 14.50) measured for the initial stages of the sliding process was related to a sliding-over liquefied V_2O_5 phase. A SEM cross section (Fig. 14.51a) produced through the wear track in

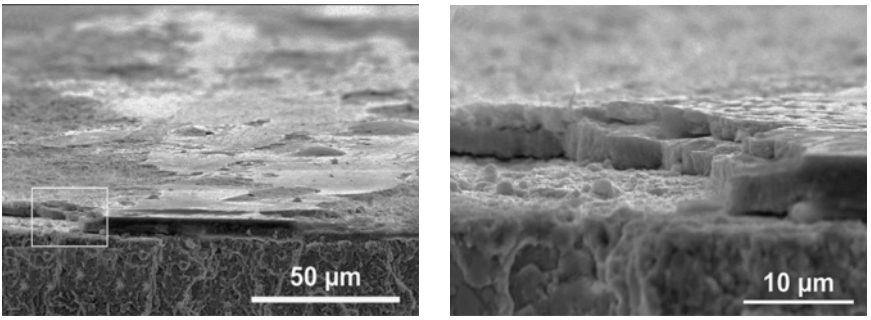

(a) **(b)**

FIGURE 14.51. (a) Cross-sectional SEM overview of the wear track on a TiAlN/VN superlattice coating after a tribo-test at 700 °C; (b) detailed image of the oxidized coating surface from the indicated area in Fig. 14.51a of the wear track.

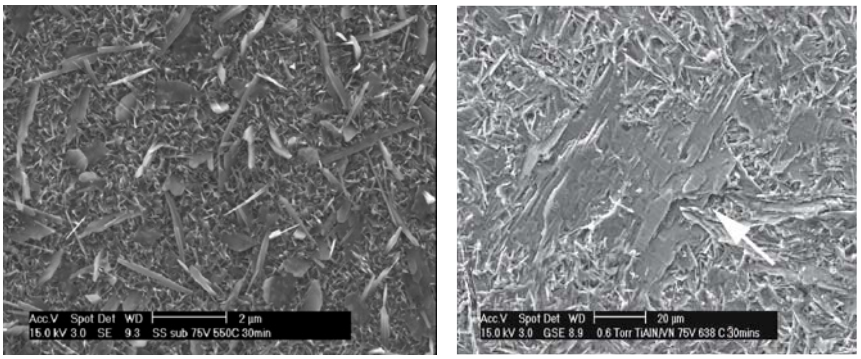

(a) **(b)**

FIGURE 14.52. (a) SEM image from the surface of TiAlN/VN superlattice coating isothermally treated at T = 550 °C, for 30 min; (b) after oxidation in air at 638 °C for 30 min.

TiAlN/VN evidences conclusively the existence of a molten phase during sliding at 700°C. A smooth surface, with typical features for a solidified layer, can be observed. The more detailed view shown in Fig. 14.51b, indicates that the melting occurs just for the near surface region, which also implies that the bulk of the TiAlN/VN coating remains intact at these temperatures.

The second part of the friction curve in Fig. 14.50 represents the friction behavior in steady state conditions. The exceptionally low friction coefficient of 0.55 for hard coatings at this temperature range is believed to result from sliding against low shear strength Magnéli phases of $V_6O_{13}$and VO_2 produced by a reduction process of V_2O_5.[87] The operation of the above-described mechanism, however, requires availability of significant amount of V_2O_5 phase, the largest portion of which at 700°C is produced by thermal oxidation process. Thermogravimetric oxidation experiments and isothermal oxidation tests at 550°C for 30 min showed that the surface of the TiAlN/VN was almost free of V_2O_5.[85,86] Figure 14.52a shows an SEM image of the surface after isothermal oxidation at 550°C. After 30-min exposure, only very thin oxide layer with a needle-like morphology has been formed, which did not produce signal intensive enough to be detected by XRD. In the temperature range of 500°C, indeed, significant increase of the friction coefficient was recorded,[84] which implies for the existence of a transition regime in the control mechanisms operating at room and elevated temperatures. At higher temperatures (above 600°C) however, formation of V_2O_5 mixed predominantly with $AlVO_4$ is detected in sufficient amount to trigger the control mechanism for low friction in steady state conditions. An SEM image of the surface after exposure for 30 min to 638°C shows that the coating surface was uniformly oxidized (Fig. 14.52b). A large area of the surface was covered by fine needles/plates, which form with a certain preferred orientation (arrowed). EDX selected area analysis showed

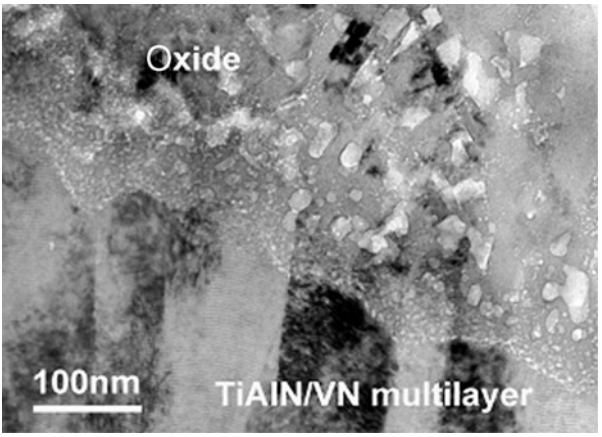

FIGURE 14.53. BF-XTEM image of oxide–coating interface region of TiAlN/VN superlattice coating oxidised in air at 600 °C for 30 min.

that these fine needles/plates were highly V rich. Further XRD analysis confirmed the presence of the V_2O_5 phase.

Figure 14.53 shows a BF-XTEM image of oxide–coating interface region from a sample isothermally oxidized at 600°C for 30 min. The cross section clearly demonstrates that the high temperature did not affect the superlattice structure of the TiAlN/VN below the top oxide layer. The Fresnel contrast from the nanoscale multilayer structure extended right up to the oxide–coating interface, suggesting that no interdiffusion between the individual layers has taken place. This observation demonstrates that the bulk of the coating retains the enhanced mechanical properties of the superlattice coatings and the material responds to the environment by altering its surface properties only.

2.3.2. Application of TiAlN/VN Superlattice Coatings in Dry High-Speed Machining of Medium-Hardness Low-Alloyed and Ni-Based Steels

The consistently low and almost identical coefficient of friction recorded for room and elevated temperatures determine the major application fields of TiAlN/VN, such as protection of wear parts and cutting tools used for machining of softer but much "stickier" materials, e.g., Ni-based or Al alloys.

A modified version of the TiAlN/VN superlattice coating with added 2% Y showed excellent performance in milling tests. Solid carbide two-flute ball-nosed end mills, 8 mm in diameter, were coated with a TiAlYN/VN superlattice coating (Fig. 14.54) and compared with a monolithically grown TiCN coating when dry cutting EN24 steel, HRC 38. The cutting conditions were as follows: cutting speed 385 m/min, feed/rev. 0.2 mm, and axial depth 3.8 mm.

FIGURE 14.54. TiAlYN/VN-coated two-flute ball-nosed cutters (Whisper Mill, Hydra Tools, Sheffield, UK).

The results from the milling test are outlined in Fig. 14.55. Whereas the uncoated tool showed a lifetime of only 7 min, the commercially available TiCN coating increased the lifetime to 53 min. The TiAlYN/VN superlattice tripled the lifetime of TiCN-coated tools, thus demonstrating the advantages of the superlattice structured PVD coatings.

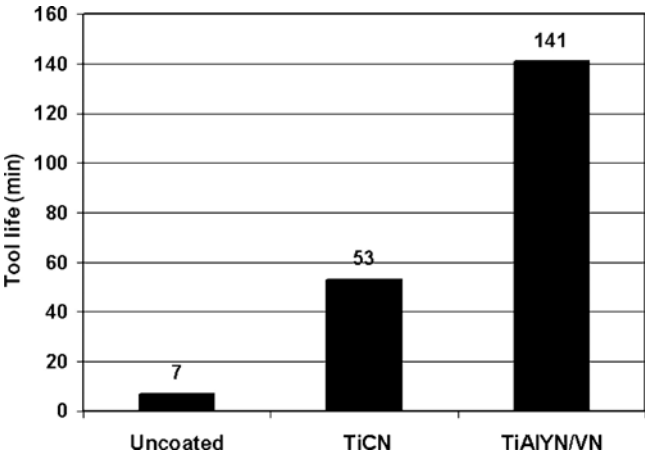

FIGURE 14.55. Lifetime of solid carbide end mills coated with various PVD coatings.

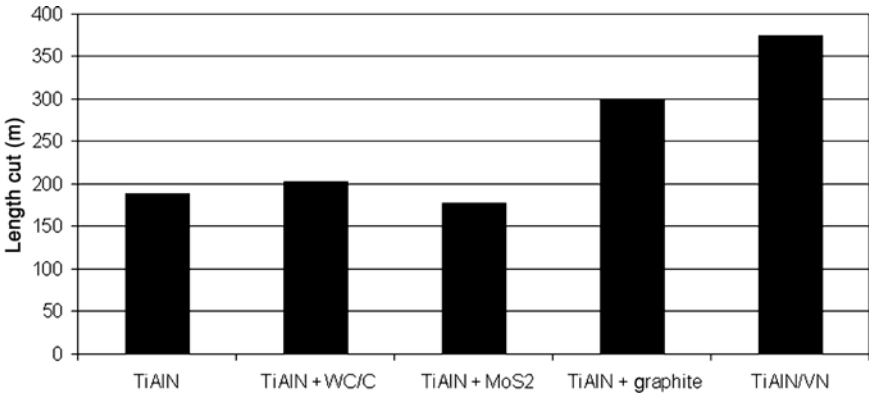

FIGURE 14.56. Cutting performance of TiAlN-coated and TiAlN/VN-coated two-flute ball-nosed cutters under dry milling conditions. (Source: D. K. Aspinwall, R. C. Dewes, E.-G. Ng, C. Sage, S. L. Soo, University of Birmingham, Rolls-Royce plc, Filton.)

Another demanding application where TiAlN/VN superlattice coatings have great potential is in the machining of tough materials such as Inconel and stainless steel. TiAlN/VN coated 8-mm two-flute ball-nosed end mills were tested in dry cutting of Inconel 718, HRC 43, with cutting conditions a follows: cutting speed 90 m/min, axial depth of cut 0.5 mm, feed 0.2 mm. The superlattice-coated tools showed the longest length of cut of 380 m, outperforming various PVD coatings: TiAlN, TiAlN + WC/C, TiAlN + MoS_2, TiAlN + graphite, thus demonstrating the importance of maintaining the low coefficient of friction at elevated temperatures. This result is demonstrated in Fig. 14.56, which shows the lifetime of various coatings in machining Inconel 718 alloy.

2.3.3. Application of TiAlN/VN Superlattice Coatings in Dry High-Speed Machining of Al Alloys

DHSM of aerospace aluminum alloys used in the manufacture of precision engine support components, such as engine infrastructure parts, is now one of the main drivers for enabling component manufacturers to reduce cost per part and environmental waste impact in the industry. To achieve such cost reductions, the machine cost per part index must be kept as low as practically possible. The machining cost index is governed by series of direct factors of which tool life, machining efficiency, and cutting fluid usage/waste disposal costs play a fundamental part in the equation. It is now an accepted opinion that the major influencing factors are increased tool life, sustainable increase in metal removal rates, reduced machining costs index, and lower environmental impact. These factors are determined by the type and efficiency of the tool coating for protecting tools. As new generation CNC machines are now being designed to facilitate ultrahigh speed and feed rates

(spindle speeds up to 100 krpm), aerospace manufacturing components will need tool coatings to enable tools to perform well by giving consistent performance under such regimes in order to have cost- and quality-effective manufacturing. The key to DHSM is the use of high-speed metal cutting techniques: research has shown that a combination of high feed rate with very high spindle speed in excess of 20 krpm reduces rather than increases the cutting forces on the tool. This technique concentrates intense heat and prompts local melting of the chip, as most of the heat energy (formed by friction with the face and forming energy in the shear plane) is generated immediately in front of the tool surface. The occurrence of liquified Al brings the problem of intensive cutting tool–workpiece material interaction, resulting in dissolution wear as an additional wear mechanism to the microabrasive wear. A simple strategy therefore would be utilization of low-friction highly inert coatings to protect the cutting edge.

Two types of dedicated PVD coatings for tool applications, TiAlCrN/TiAlYN and TiAlN/VN, have been deposited on 25-mm diameter end mills supplied by Hydra Clarkson Tools Ltd, Sheffield, using the combined steered cathodic arc/unbalance magnetron deposition technique. The coated tools have been tested to machine aerospace-grade aluminum alloy Al-7010-T7651. This is a high-strength (tensile strength as certified 509 MPa) $Zn_{6.1}$–$Mg_{2.25}$–$Cu_{1.63}$–Al alloy widely used for production of aircraft components, such as wingbox ribs. A Mazak-FJV25 CNC machine was used for dry machining under the following cutting conditions: spindle speed 24 krpm, cutting speed 31.3 m/s, axial depth of cut 4 mm, feed rate 0.33 mm/rev. Each cutter was programmed to cut in a traverse straight-line mode until the cutter flank wear reached 0.23 mm, which has been used as a lifetime criteria of wear. The time/number of traverse passes was logged to calculate the "end life curves" and mean tool-cutting forces.

SEM examination of tools uncoated and coated with TiAlCrN/TiAlYN and TiAlN/VN superlattice coatings after DHSM of Al-7010 alloy showed clear differences in the wear behavior of these surfaces (Fig. 14.57a–c). The unprotected tools

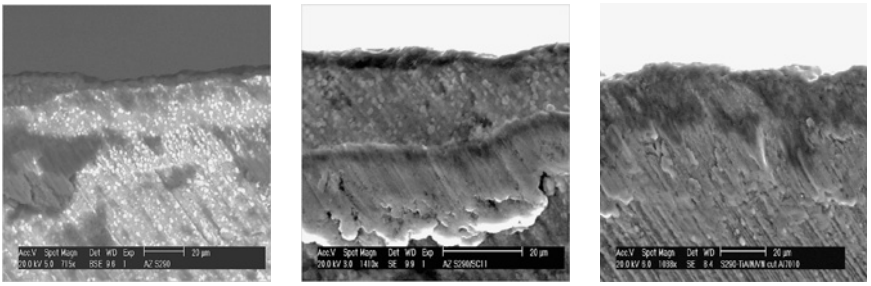

(a) **(b)** **(c)**

FIGURE 14.57. SEM images of the flank surface of (a) uncoated; (b) TiAlCrN/TiAlYN-coated; (c) TiAlN/VN-coated end mills after machining of Al-7010 alloy.

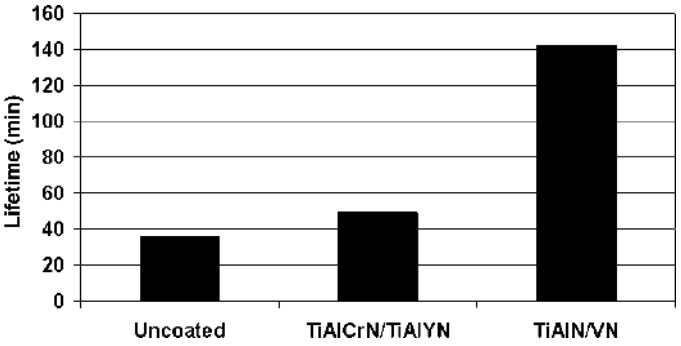

FIGURE 14.58. Lifetime of 25-mm diameter end mills uncoated and coated with various nanoscale multilayer PVD coatings, achieved in DHSM of Al-7010 alloy.

(Fig. 14.57a) suffer severe microabrasive wear evident from the exposure of the Me-carbide particles in the steel, imaged as white spots on the surface. The cutting edge is fully covered with Al, evidencing formation of build-up edge (BUE), as well as a significant Al pickup (the grey areas) on the flank surface can be observed. Both PVD-coated surfaces show less abrasive wear and almost no BUE formation. However, due to the higher surface roughness introduced by the growth defects in the coating, the Al pickup is more developed with significantly higher amount for TiAlCrN/TiAlYN-coated surface (Fig. 14.57b) compared to the TiAlN/VN-coated one (Fig. 14.57c). This effect is also clearly influenced by the significant differences in the coefficient of friction of the two coatings. The positive effect from the almost factor of two lower coefficient of friction of TiAlN/VN can be further seen in cutting forces measurements. Significantly lower cutting forces of 180 N were measured for the TiAlN/VN-superlattice-coated tools compared to 310 N force for TiAlCrN/TiAlYN and 450 N for uncoated tools. These values gave excellent correlation to tools lifetime values (Fig. 14.58). Both coatings demonstrated the protection capabilities of the PVD coatings in DHSM of Al-7010 alloy. However, the combination of superhardness and low coefficient of friction achieved with TiAlN/VN superlattice coating proved to be the most beneficial in this demanding application.

Typical aircraft structures produced by high-speed milling are shown in Fig. 14.59. The combination of complicated 3D shape and very thin and tall rib-sections introduces the difficulty of high level of vibrations during milling. Therefore, employment of friction (cutting force)-reducing PVD coatings becomes of a paramount importance in this application. It is also important to mention that in the highly competitive market of the aerospace industry, cutting the costs by reducing machining and downtimes is the only way to sustainable growth. Cutting tool surface modifications by properly selected PVD coatings, therefore, are seen as a viable alternative to satisfy the demands of the aerospace sector.

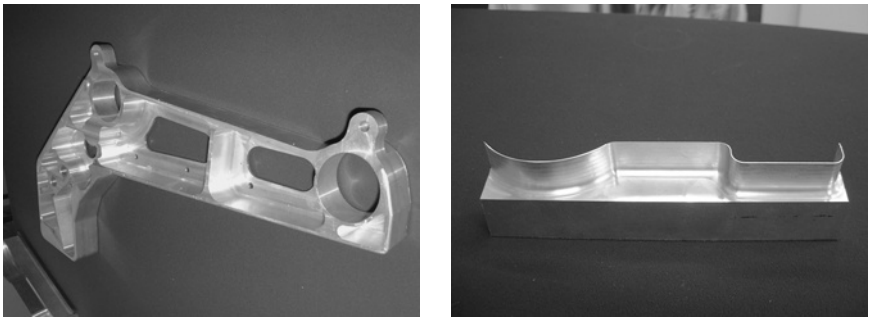

(a) (b)

FIGURE 14.59. Typical aircraft structures produced by high-speed milling. (Courtesy of Hydra Clarkson International Ltd, Sheffield, UK.)

2.4. Nanoscale Multilayer Coatings Designed For Very Low Friction and Their Applications

2.4.1. Structure and Tribological Properties of C/Cr Nanoscale Multilayer Coatings

Carbon-based coatings have attracted great interest in a wide range of industries due to their excellent properties, such as low friction coefficients and good wear resistance. However, diamond-like carbon (DLC) and pure carbon coatings often suffer from poor toughness and brittleness due to high compressive residual stress. These deficient properties can be improved by doping the carbon coating with a small amount of more ductile metals, e.g., Cr,[59,88] Ta, W, or Ti.[89] Further improvement can be achieved by multilayering of coatings, which allows the selection and combination of materials according to the desired properties. Multilayer C/Cr coatings, registered as Graphit-iC^{TM}, have been produced by UBM sputtering[90] and recently nanoscale multilayer C/Cr coatings have been developed, by utilizing the combined steered cathodic arc/UBM sputtering (ABS) technology.[60] The main difference between these two techniques is that the ABS technology utilizes metal ion pretreatment to further improve the adhesion between the substrate and the coating. The technological process of nanoscale multilayer C/Cr deposition comprises three distinct steps: Cr^+ ion etching, CrN base layer deposition, and multilayer coating deposition. The metal ion etching was performed in steered cathodic arc mode by applying an arc current of 100 A on Cr target and a bias voltage of -1200 V on the substrates. The 0.25-μm-thick CrN base layer was deposited by reactive sputtering of Cr in Ar + N_2 atmosphere and at a substrate bias of -75 V. The C/Cr nanoscale multilayer coatings were deposited by nonreactive UBM sputtering using three graphite and one Cr targets. Table 14.7 summarizes the mechanical and tribological properties of the C/Cr coatings.

TABLE 14.7. Mechanical and Tribological Properties of C/Cr Nanoscale Multilayer Coating.

Coating	Bias (V)	HP (GPa)	Stress (GPa)	Coefficient of friction, μ	Sl. wear coefficient ($m^3/(N\,m)$)	Scratch adh. L_c (N)	R_a (μm)
C/Cr	−75	25	−2.0	0.17	1.0×10^{-17}	>70	0.04

A considerable interest in the research of thin carbon films arises from the possibility of changing the film properties, by tailoring the microstructure, i.e., from graphite like to diamond like with an amorphous or crystalline structure, and the variation in sp^2/sp^3 ratio depending on the deposition techniques and conditions.[91–93] The energy of ion bombardment and the ion-to-neutral ratio during the film growth is well known to strongly affect the growth, structure, and thus the properties of the coatings. Appropriate control of the ion energies during coating deposition has been shown to influence the density and nucleation rates of the growing film,[94,95] leading to better performance coatings. For carbon nitride (CN) thin films, for example, it has been shown that an increase in bias voltage from −25 to −40 V leads to smoother films and changes in the degree of curvature of the graphitic sheets, extent and alignment of the microstructure as well as results in improvement in strength, toughness, and elasticity of the coatings.[96] It is anticipated that due to the very low elemental sputtering yield of C (sputtering yield for 500 eV Ar^+ ions of C = 0.12, Cr = 1.18)[97] the films will grow under conditions of intensive ion bombardment (high ion to neutral ratios). Indeed, for the deposition conditions used, an average ion flux to the substrate of $J_i = 5.6 \times 10^{15}$ ions/(cm^2 s) and neutral deposition flux of $J_n = 1.07 \times 10^{15}$ atoms/(cm^2 s) have been measured, showing that the condensation of the film takes place at a very high J_i/J_n ratio of 5.2.[98] The conditions of intensive ion bombardment combined with the higher mobility of the C atoms explain the observed differences in the structure of the sputtered C/Cr films as a function of the applied bias voltage.[98,99]

Figure 14.60a,b shows low-magnification BF-XTEM images of C/Cr coatings deposited at bias voltages $U_B = -75$ V and −95 V respectively, showing an overview of the coating architecture composed of an Cr-ion irradiated substrate, 0.25-μm CrN base layer, and the 1.6-μm-thick C/Cr coating. In the BF-XTEM view (Fig. 14.60a) the coating appears overall brighter than the substrate and the base layer due to its lower average atomic number. The coating does not exhibit diffraction contrast, indicating an amorphous structure. The SAED pattern from the C/Cr layer [Fig. 14.60b (inset)] is composed of broad halo-like rings with uniform intensity, confirming the amorphous structure of the coating. The analysis of the diffraction pattern revealed that the coating contains graphitic carbon and chromium. The SAED pattern of the CrN base layer (Fig. 14.60b, inset C) reveals a B1-NaCl structure with a weak 002 texture in the growth direction.

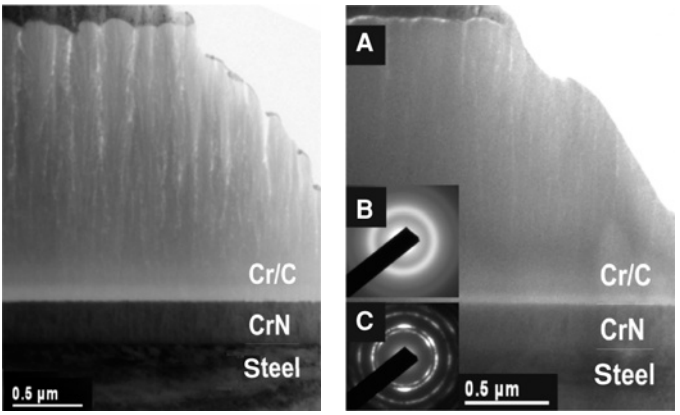

FIGURE 14.60. BF-XTEM micrographs of C/Cr deposited at (a) $U_B = -75$ V, (b) $U_B = -95$ V.[98]

A distinct feature of the structure of the C/Cr coatings is the accumulated carbon at the grain boundaries, which is imaged as a brighter phase (weak phase). HAADF and lattice resolution imaging techniques have confirmed the segregation mechanism and justified the coating density.[98]

Although the overall C/Cr microstructure appears similar for the coatings deposited at -75 and -95 V, some important differences can also be observed. The width of the column boundaries in the sample deposited at -75 V is markedly larger compared to that of the sample deposited at $U_B = -95$ V; also, the top surface is considerably rougher. The surface roughness estimated from XTEM decreased from 140 to 95 nm, to 45 nm as the bias voltage is increased from -65 to -75, to -95 V due to the smoothening effect of ion irradiation. In agreement with the general observations in the literature, the effect of the increased ion energy during the deposition of the C/Cr layer is to produce smoother coating surface and denser coating.

Figure 14.61a,b shows BF-XTEM images of C/Cr coating microstructure near the surface for the samples deposited with $U_B = -75$ V and $U_B = -95$ V. Investigation of the micrographs with higher magnifications further confirms that the weak-phase column boundaries are not completely open voids. The amorphous matrix is continuous between columns, although the overall atom density(especially the local Cr concentration) appears to be lower as compared with the interior of the column. The multilayer nanostructure of the C/Cr coating is not readily apparent. It is revealed by careful investigation, as exemplified in the inset in Fig. 14.61b, of areas of the sample with appropriate sample thickness. The multilayers have an average periodicity of $\sim$2 nm, which is consistent with the one calculated on the basis of the total deposition thickness and the period of sample rotation.

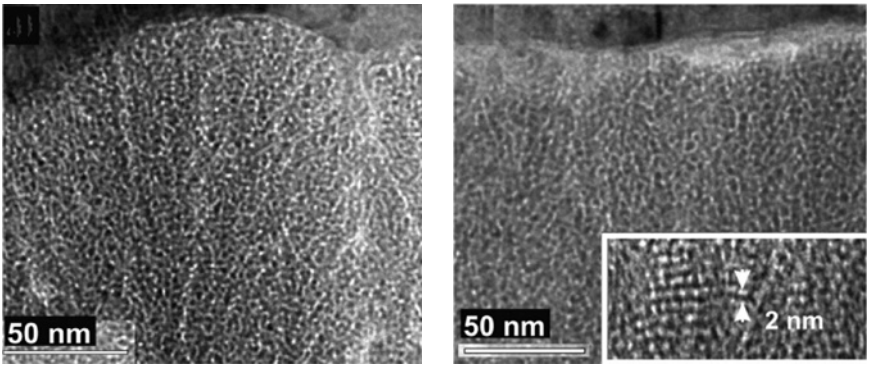

FIGURE 14.61. BF-XTEM micrographs of C/Cr coating near-surface region for (a) $U_B = -75$ V, (b) $U_B = -95$ V.[98]

Investigations carried out at high magnifications by lattice resolution imaging technique revealed further interesting details in the structure of C/Cr coatings deposited at higher bias voltage of $U_B = -95$ V. Small Cr-rich regions with a curved structure, often described in the literature as onion-like structures, have been observed (Fig. 14.62). These regions, which in this imaging mode appear with slightly darker contrast, exhibit higher concentration of curved graphite planes, indicating that Cr may act to cross-link and bend the graphite planes.

Nanoscale multilayer C/Cr coatings produced by the ABS technology has demonstrated excellent adhesion ($L_c = 70$ N) and good tribological properties (low wear rate of $\sim 10^{-17}$ m^3/(N m) and coefficient of friction ~ 0.17).[98] It has been shown, however, that both the friction and the wear behavior are strongly influenced by the coatings microstructure and the testing environment. The lowest values for the coefficient of friction of 0.21–0.23 have been measured when sliding against both the C/Cr coated and uncoated 440C balls used as a counterpart in open air. When tested in dry nitrogen, however, the friction coefficient becomes significantly higher, i.e., 0.7–0.8, and the lifetimes of coatings are shorter. The high wear resistance of C/Cr films in open air can be attributed to their high adhesion, mechanical strength, and hardness, whereas their low friction behavior may have been largely due to the presence of adsorbed water and/or oxygen molecules on their sliding surfaces. These adsorbed species can reduce the amount of adhesive interactions between sliding carbon film surfaces and hence result in lower friction. When such species are essentially absent and cannot be replenished (as in dry nitrogen) in a continuous manner, the friction coefficients of such sliding interfaces becomes very high, mainly because of the presence of high levels of adhesive interactions between rubbing surfaces. Such interactions may in turn give rise to rapid wear of carbon films from the coated surfaces. It can be speculated that under high ambient temperature and velocities the coating would

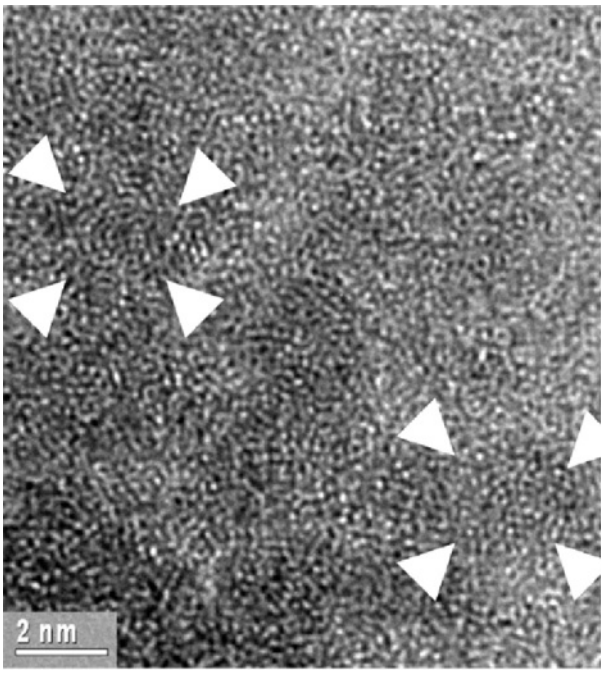

FIGURE 14.62. High–resolution XTEM of C/Cr coating deposited at $U_B = -95$ V, showing regions with curved, onion-like structure (arrowed).[98]

form a protective chrome oxide layer that could prevent thermal degradation of the coatings.

The effect of the bias voltage on the friction behavior of the C/Cr coatings has been studied by testing on C/Cr-coated HSS samples sliding against 100Cr6 ball in air. It has been found that the coefficient of friction of C/Cr coatings decreases from 0.22 to 0.2 to 0.16 with increase in substrate bias voltage from -65 to -75 V, to -95 V (Fig. 14.63). This result can well be correlated with the findings of XTEM, which show decreasing surface roughness and significant densification of the coating as the bias voltage is increased from -65 to -95 V, due to the ion-irradiation effect. At lower bias voltage, the coating has a rougher surface, larger grain size, bigger columns, and weak phase accumulated at the grain boundaries that tend to open and crack, thus generating large particles, which accumulate in the wear track and promote third-body sliding and higher friction coefficient. In contrast, at higher bias voltage, due to the smoothening and densification of the multilayer coating, the sliding wear occurs layer by layer and exhibits a lower friction coefficient with smoother curve (Fig. 14.63, the curve for $U_B = -95$ V). Additionally, the excellent wear behavior of the C/Cr film, especially the reported low wear coefficient [$\sim 10^{-17}$ m^3/(N m)] and high load-bearing capacity, can be

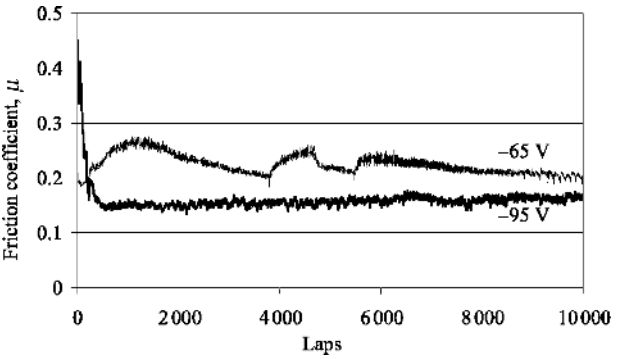

FIGURE 14.63. Coefficient of friction of C/Cr coatings as a function of bias voltage (pin-on-disk test, 5-N load, 100Cr6 ball, 0.1 m/s speed, in air.)[98]

attributed to the observed curved onion-like structure of the coating (Fig. 14.62). As it has been described,[96] this type of structure tends to show high material integrity and toughness due to the unique slip-hindering mechanism resulting from the cross-linking and the geometrical interlocking of the graphite planes.

The C/Cr coating can be used as a single coating or in combination with other hard PVD coatings serving as underlayers. Table 14.8 summarizes the tribological properties of the C/Cr system in such combinations.[57] In addition, data for reference materials are given. Consistently, low friction coefficients in the range of 0.16–0.2 were measured, depending on the type of the underlayer material. Although being harder, the underlying TiAlCrYN and TiN increase the wear rate. This result has to be related to the existence of growth defects generated by the use of the cathodic arc technology during the substrate-etching step. Consequently, the arc TiN underlayer

TABLE 14.8. Pin-on-Disc Dry Sliding Wear Test of Various Coatings.[a]

Material	Coefficient of friction	Wear coefficient of the disk, Kc (m^3/(N m)	Wear coefficient of the ball, Kc (m^3/N m)
Arc TiN	0.73	5.3×10^{-16}	2.1×10^{-16}
Arc TiN + C/Cr	0.22	1.5×10^{-16}	2.4×10^{-17}
TiAlCrYN	0.65	2.5×10^{-16}	1.4×10^{-16}
TiAlCrYN + C/Cr	0.19	8.0×10^{-17}	1.8×10^{-17}
Polished M2 + C/Cr	0.16	1.5×10^{-17}	8.0×10^{-19}
Arc CrN	0.5	9.0×10^{-15}	na
CrN/NbN	0.65	2.1×10^{-15}	na
TiAlN/VN	0.45	1.3×10^{-17}	na
Hard Cr	0.72	5.8×10^{-14}	na

[a] Sliding speed: 10 cm/s, normal load: 5 N, sliding distance: 22.6 km, counterpart: 6 mm 100Cr6 ball. The sliding distance for the reference coatings was 4.5 km, using Al_2O_3 counterpart.

shows the highest friction and wear coefficients. In contrast, the ABS-deposited TiAlCrYN coating exhibits already reduced friction and wear data. The lowest coefficient of friction of 0.16 was measured when the coating was deposited on mirror-polished HSS sample, and this result has been retained during sliding in dry air, oil, and in water environment. The combination of hard PVD coating with C/Cr over-coat reduces the friction and wear coefficients of the carbon-free hard coatings by almost a factor of 4. Furthermore, the wear of the counterpart, e.g., an uncoated 100Cr6 ball, is also reduced substantially, especially when the sliding partner is a hard coating. This type of wear behavior becomes of extreme importance when protection of engineering components is required.

2.4.2. Application of Nanoscale Multilayer C/Cr Coating in Machining of Ni-Based Alloys

The combined hard nitrides with friction-reducing C/Cr top coat have been tested in side milling of highly abrasive high-Co-containing Ni-based alloys, (20-mm diameter CC end mills, cutting speed 25 m/min, depth of cut 0.5 mm, and axial depth 25 mm). Figure 14.64a–c compares the uncoated, TiAlCrYN-coated, and TiAlCrYN/C/Cr-coated cutting edge of solid carbide end mills after wear. It can be seen that the presence of the lubricious and nonsticking C/Cr top coat better preserves the cutting edge geometry (width of flank wear) and reduces the material transfer effect. The SEM images show the superior behavior of the combined coating, even when the cutting duration is increased.

In the conditions of this test, the introduction of the low-friction C/Cr top coat has led to reduction of both rake and flank wear by factors of 7 and 3.5, respectively, when compared to the uncoated end mills (Fig. 14.65).

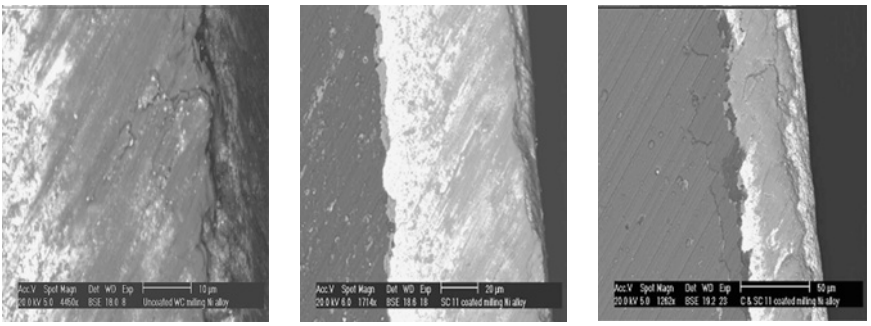

(a) **(b)** **(c)**

FIGURE 14.64. SEM micrograph showing the flank wear of solid carbide end mills: (a) uncoated after 22-min. cutting, (b) coated with TiAlCrYN after 45-min. cutting and (c) coated with TiAlCrYN/C/Cr after 60 min.

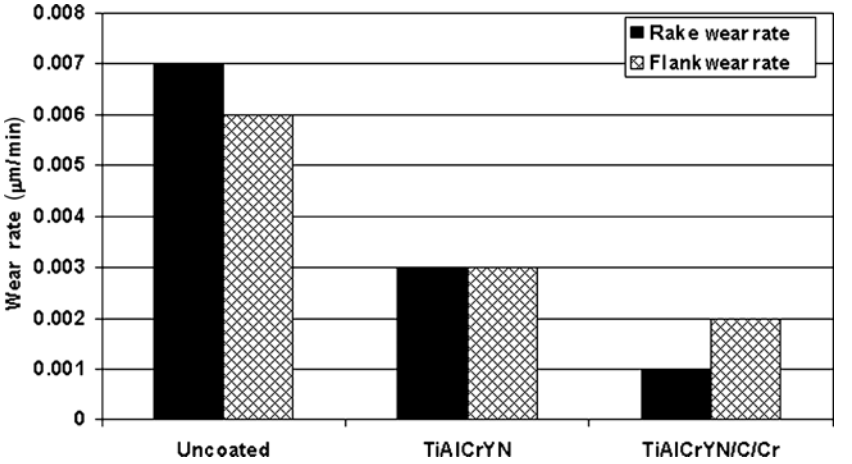

FIGURE 14.65. Rake and Flank wear rates of 20-mm diameter solid carbide end mills after side cutting in Co-containing Nimonic alloy: $V_{cut} = 25$ m/min, depth of cut = 0.5 mm, axial depth = 25 mm.

2.5. CrN/NbN Superlattice Coating Designed for High Corrosion and Wear Applications

2.5.1. Microstructure and Corrosion Resistance of CrN/NbN Superlattice Coatings

The main purpose of combining Nb and Cr in a superlattice coating of CrN/NbN was to develop an environment-friendly replacement for hard chromium. The rationale behind selecting NbN was to utilize the excellent corrosion resistance of the electrochemically inert Nb,[100] whereas CrN and has been chosen to allow low deposition temperatures (∼200°C). It was assumed that the combined enhanced corrosion resistance and superhardness (HP 40 GPa) would lead to a new 4–5-μm-thick PVD product with a wear performance equivalent to that of a 20-μm-thick electroplated Cr coating.[16,51,101]

CrN/NbN superlattice coatings have been deposited by sputtering of two adjacent pairs of Cr and Nb targets, 99.8% pure, in a common $Ar + N_2$ atmosphere, using the ABS technique. Depending on the application, either Cr^+- or Nb^+ ion etching has been employed, followed by deposition of 0.3-μm CrN base layer and of the 4–5-μm CrN/NbN superlattice coating with a superlattice period λ = 3 to 4 nm. Depending on the substrate material and the application, two types of processes have been developed: utilizing low deposition temperatures of 250°C and high deposition temperatures of 450°C. XTEM micrographs illustrating the structure of CrN/NbN deposited at bias voltages of $U_B = -75$ V and $U_B = -120$ V are shown in Fig. 14.66a,b.

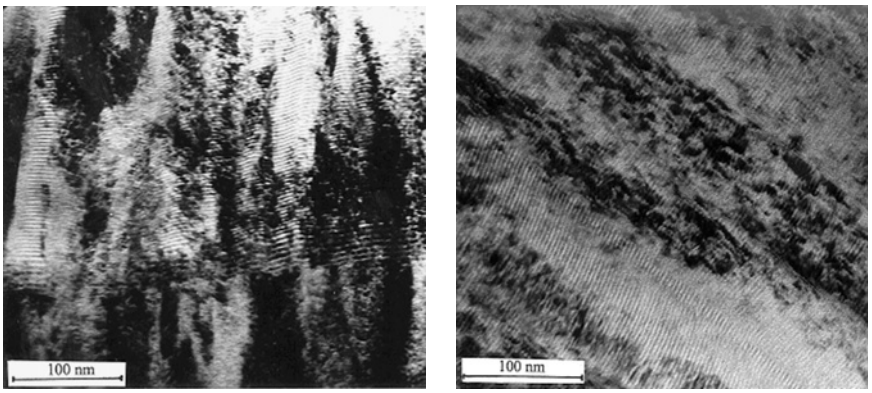

FIGURE 14.66. XTEM micrographs of CrN/NbN superlattice coating deposited at various bias voltages: (a) $U_B = -75$ V, in the region of base layer and superlattice coating, (b) $U_B = -120$ V, superlattice coating.[16]

As discussed in Section 1.4, increasing the bias voltage suppresses the superlattice roughening effect and leads to sharpening of the interfaces between the individual layers in the superlattice stack. Additionally, the coating surface morphology changes significantly. Smoother surfaces with less growth defects are observed for CrN/NbN coatings deposited at higher bias voltages (Fig. 14.67a–c). This effect is related to the increased compressive stress in the higher bias

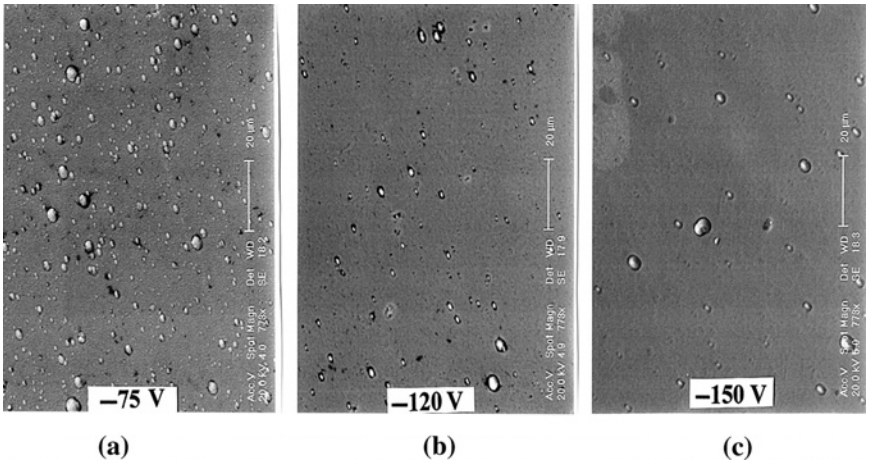

FIGURE 14.67. SEM micrographs illustrating the effect of the bias voltage on the surface morphology of CrN/NbN superlattice coating: (a) $U_B = -75$ V; (b) $U_B = -120$ V; c) $U_B = -150$ V.[101]

TABLE 14.9. Mechanical and Tribological Properties of Various CrN/NbN Superlattice Coatings and Hard Chrome.

Coating	Bias (V)	HP (GPa)	Stress (GPa)	Coefficient of friction, μ	Sl. wear coefficient ($m^3/(N\,m)$	Scratch adh., L_c (N)	R_a (μm)
CrN/NbN, deposited at 450°C	−75	42	−1.8	0.69	2.1×10^{-15}	50	0.07
CrN/NbN, deposited at 250°C	−75	36	−2.7	0.7	3.6×10^{-15}	45	0.04
Hard Cr	—	14	—	0.72	5.8×10^{-14}	15	0.05

voltage samples, which leads to self—healing of the growth defects originating from droplets deposited at the coating–substrate interface during the ion-etching step, as discussed in Section 1.4.

Table 14.9 summarizes the main mechanical and tribological properties of both versions of CrN/NbN superlattice coatings deposited at high and low temperatures. Data for electroplated hard chrome are also included as reference.

The potentiodynamic polarization tests showed that the CrN/NbN superlattice structured coatings provide substantially improved protection against corrosion and pitting, in comparison to that provided by the monolithically grown PVD coatings, due to fewer interconnecting pores and defects penetrating through the coating.[102] However, further extended investigations revealed the importance of parameters such as composition, N/Me ratio, residual stress levels, and the consistency of the CrN base layer in the corrosion performance of CrN/NbN coatings.[103] Substoichiometric (N/Me = 0.5) highly stressed CrN/NbN coatings generally showed lower corrosion current densities, but pitting occurred at lower potentials when compared with stoichiometric coatings (N/Me = 1) apparently due to the higher residual stress.[103,104] The corrosion resistance of both types of coatings, substoichiometric and stoichiometric, improved when deposited on a single-phase CrN base layer. The mixed-phase (Cr_2N + CrN) base layer induced a higher residual stress in the superlattice coatings and showed a rather voided, porous structure when examined by TEM. It has also been found that the corrosion resistance is strongly affected and even dominated by the growth defects caused by the generation of droplets at the substrate–coating interface during the cathodic arc-etching step. Very often, channels are formed allowing direct access of the corrosive media to the substrate material.[105] Increasing the bias voltage from −75 to −120 V led to a smoother surface, as shown by SEM observations (Fig. 14.67) and surface profilometry. Figure 14.68 shows representative polarization data for 304L steel: one Cr-plated and two Cr^+-ion-etched stoichiometric CrN/NbN superlattice coatings deposited at various bias voltages on a single-phase CrN base layer. The electroplated chromium did not show a good performance in polarization tests, with no significant passivity evident. Low bias voltage (−75 V) superlattice coatings exhibited pitting potentials in the range of +370 mV and, more significantly,

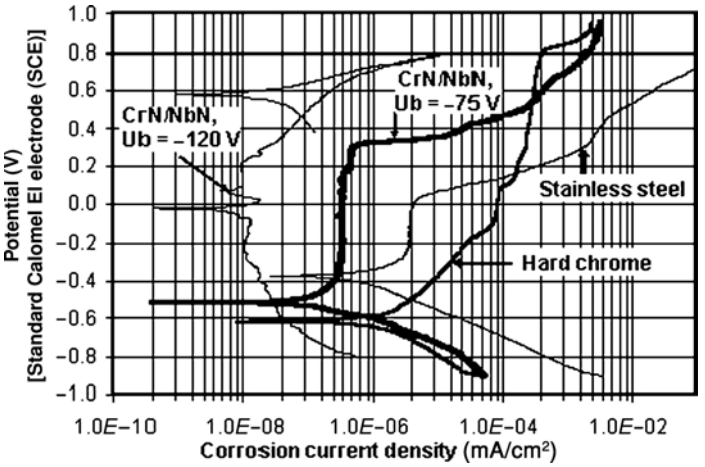

FIGURE 14.68. Representative polarisation curves for Cr^+-etched CrN/NbN coatings, hard Cr and 304L stainless steel.[16]

the passive current density was two orders of magnitude lower [(3 to 5)$\times$ 10^{-7} mA/cm^2] than that of electroplated Cr and stainless steel. However, recent experiments with high bias voltage (-120 V) CrN/NbN superlattice coatings showed even improved corrosion resistance with corrosion current densities in the range of 1.0 $\times$ 10^{-8} mA/cm^2, and practically no evidence of pitting was observed up to $+800$ mV. The reverse part of the polarization curve showed a constant corrosion current of 1.0 $\times$ 10^{-7} mA/cm^2 within the polarization potential range from $+800$ to -500 mV, thus demonstrating the advantages of the less defected coating surface.

To further improve the corrosion resistance of the substrate–coating interface, a Nb^+ etch ($U_B = -1200$ V) was used for the surface pretreatment of stainless steel. According to the equilibrium diagram, Nb forms only limited solid solutions with Fe [γFe (Nb)], ε(Fe,Nb), and [αFe (Nb)] , which cannot explain the high adhesion obtained in these coatings. However, the higher charge state of the Nb^+ ions (average = 3) allows low energy implantation, thus providing excellent adhesion with a critical load for CrN/NbN coatings of up to 70 N on a high-speed steel substrate. XTEM observations showed the existence of a dense "amorphized" Nb layer at the interface (Fig. 14.69) which appears to have a tremendous effect on the corrosion performance of the PVD coatings. It has been demonstrated that if the "amorphized" layer is applied in an appropriate manner, a 1-μm-thick PVD Nb coating can compete with 20-μm hard chromium and electroless-deposited Ni coatings.[106]

The polarization behavior of specially optimized CrN/NbN coatings is characterized by potentiodynamic corrosion curves with a broad passivation shoulder stretched up to pitting potentials of $+750$ mV (Fig. 14.70). Absolutely outstanding

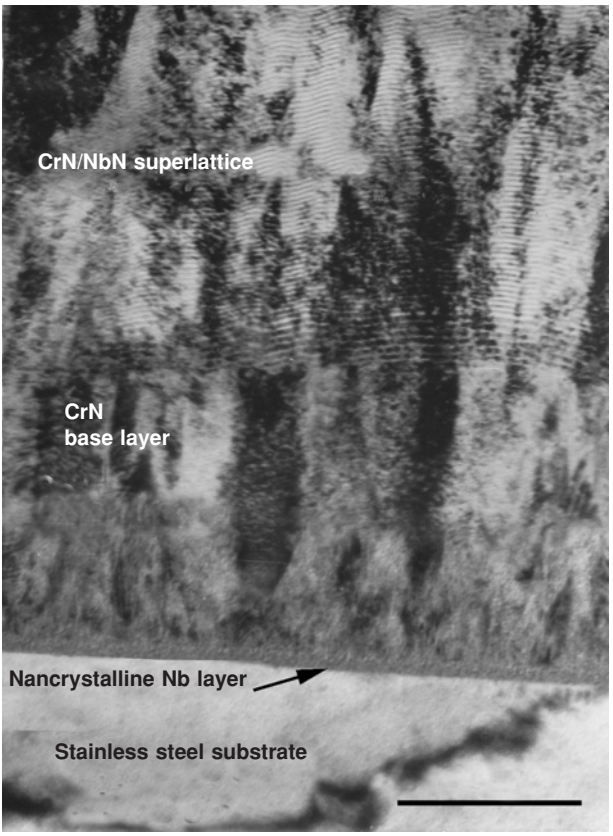

FIGURE 14.69. XTEM micrograph of Nb^+-etched CrN/NbN superlattice coating.[16]

low-corrosion current densities in the range of 2×10^{-9}mA/cm^2 and no pitting up to potentials of +800 mV were achieved when N^+ etching was combined with the smooth CrN/NbN coating surface obtained by using higher bias voltage (−120 V) during the deposition process.

The ultimate corrosion test, however, which is accepted by the electroplating industry, is the test carried out in a salt-spray environment. Typical conditions of the test are environment temperature 35°C, humidity 95–98%, solution concentration NaCl 50 g/l, pH = 6.5–7.2. The lifetime of 25-μm-thick electroplated hard chrome on 100-μm-thick bronze underlayer in these conditions is expected to be over 1000 h to red-rust appearance. Similar performance of 1575 h has been achieved with Nb^+-etched, 4.5-μm stoichiometric CrN/NbN superlattice coatings when deposited on 304L steel. Only isolated small pits on the surface of the superlattice coating have been observed to develop after this long exposure to the aggressive salt-containing environment (Fig. 14.71).

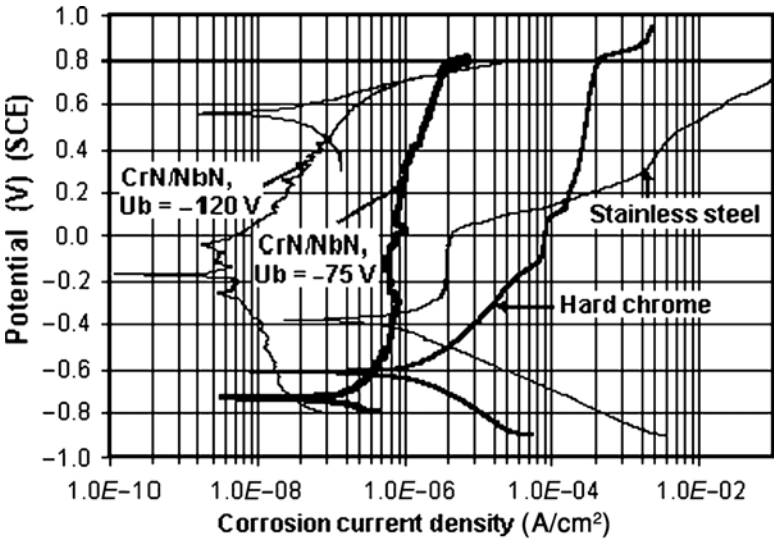

FIGURE 14.70. Representative polarization curves for Nb^{+}-etched CrN/NbN coatings, hard Cr and 304L stainless steel.[16]

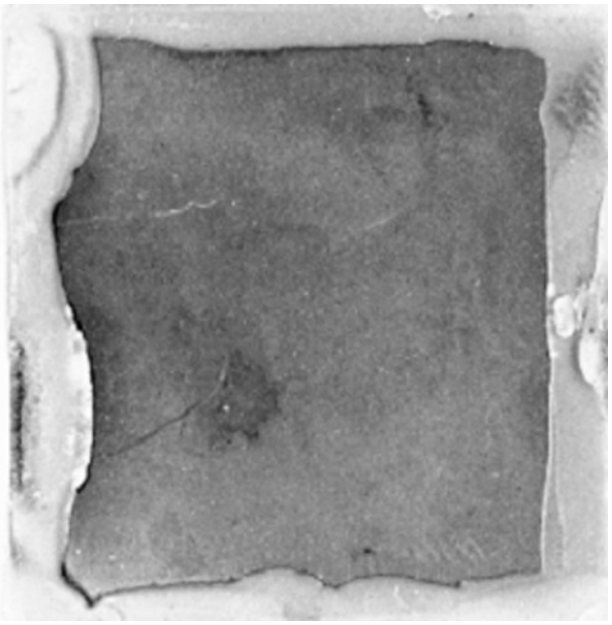

FIGURE 14.71. Optical micrograph of stoichiometric CrN/NbN superlattice coating after 1575-h test in salt-spray environment.[101]

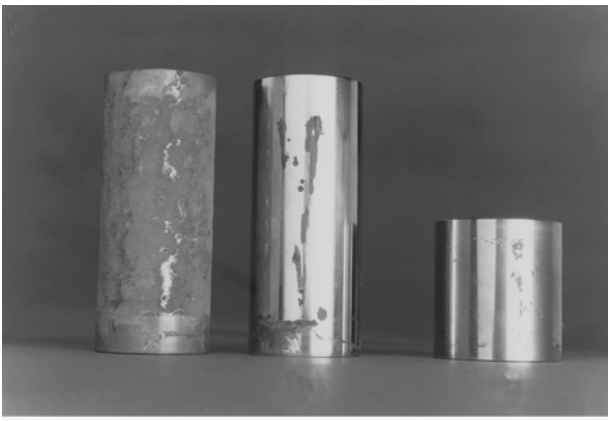

FIGURE 14.72. Surface of mild steel samples protected by various coatings after salt spray test: (a) CrN/NbN deposited directly on mild steel, after 24 h; (b) Chromium electroplated mild steel, after 200 h; (c) mild steel coated with CrN/NbN superlattice coating containing Nb barrier layer, after 300 h.[108]

Further success was achieved in the case of protecting mild steel, a less noble material, from a corrosion point of view. In this application, a special UBM-deposited pure Nb layer was introduced at the coating–substrate interface to serve as a further barrier to corrosion.[107] Along with the clear passivation behavior and low (1×10^{-6}A cm^2) corrosion current densities, in salt-spray tests, CrN/NbN coatings containing a Nb barrier layer showed remarkably high lifetime compared to that of hard Cr (Fig. 14.72). In the conditions of the salt-spray test (solution concentration NaCl 50 g/l, pH = 6.5–7.2, humidity 98%, and $T = 35^{\circ}$C), first corrosion damage for 20-μm hard Cr was observed after 200 h (Fig. 14.72b). Mild steel coated directly with CrN/NbN showed only a short lifetime of 24 h (Fig. 14.72a), whereas the introduction of the UBM-deposited Nb barrier layer increased the lifetime to 300 h (Fig. 14.72c).[108]

The results from this development clearly demonstrate the superiority of the PVD superlattice structured CrN/NbN coatings when compared with hard chrome, which opens prospects for various applications where corrosion attack is involved.

2.5.2. Tribological Performance of CrN/NbN Superlattice Coatings

The tribological behavior of CrN/NbN superlattice coatings has been studied extensively by various test methods such as dry sliding, microabrasive and erosion wear tests, as well as combined corrosion–erosion tests.[16,58,109]

Under dry sliding conditions, distinct differences in the wear behavior of substoichiometric and stoichiometric, high-temperature CrN/NbN have been

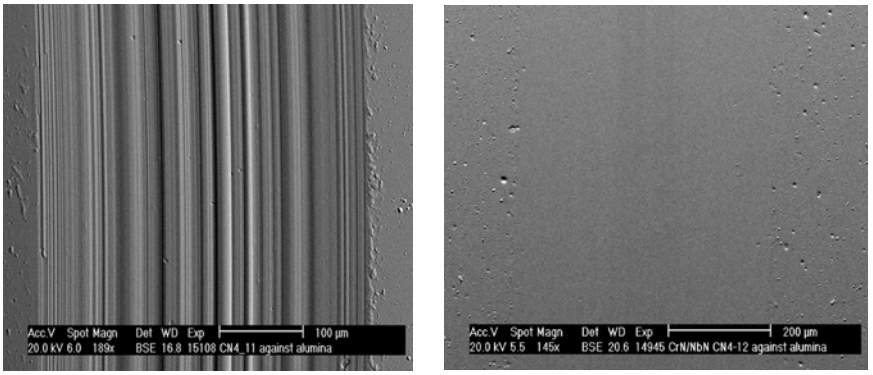

(a) **(b)**

FIGURE 14.73. SEM micrographs of the wear surface of (a) substoihiometric and (b) stoihiometric CrN/NbN superlattice coating.

observed. SEM observations of the wear track of the substoichiometric coatings revealed that the wear surface is rough, with many groves parallel to the sliding direction (Fig. 14.73a). The wear marks are produced by small abrasive particles detached from the coating via brittle failure mechanism, which play the role of a third body in the tribological system. X-ray photoelectron spectroscopy (XPS) and Raman spectroscopy indeed showed that the wear debris released during dry sliding comprise a mixture of abrasive oxides, such as Cr_2O_3, $CrNbO_4$, and Nb_2O_5, corresponding to the CrN/NbN coating constitution.[83] This behavior is typical for the highly stressed and, therefore, brittle materials. Indeed, compressive stress values as high as -7.5 GPa have been measured for the substoichiometric CrN/NbN, compared to only -1.8 GPa measured for the coatings with stoichiometric composition. The increased compressive stress in the coatings usually results

TABLE 14.10. Tribological Properties of Sub- and Near-Stoichiometric, High Temperature CrN/NbN and Electroplated Hard Chrome.[58]

		CrN/NbN	
Tribological properties	Hard Cr	Substoichiometric	Near-stoichiometric
Coating thickness (μm)	20	6.6	5.2
Hardness ($HK_{0.25}$)	1450	3580	3500
Surface roughness, R_a (μm)	0.053	0.058	0.051
Adhesion, L_C (N)	15	25	50
Coefficient of friction	0.72	0.92	0.69
Wear depth (dry sliding) (μm)	13.5	4.65	0.93
Microabrasive wear coefficient $[m^3/N\ m]$	8.8×10^{-14}	6.6×10^{-14}	6.1×10^{-14}

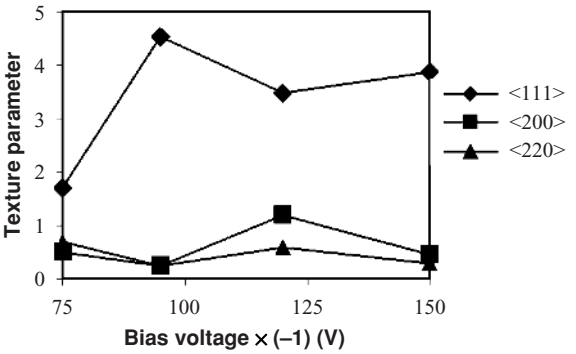

FIGURE 14.74. Texture parameter of low-temperature CrN/NbN coatings, as a function of bias voltage.

in increased friction and wear coefficients (Table 14.10; see also Table 14.3). In contrast, for the stoichiometric CrN/NbN the wear track appears very smooth, suggesting fine layer-by-layer wear mechanism, releasing only very fine wear debris, which would be typically expected from nanoscale multilayer structured coatings (Fig. 14.73b).

The results summarized in Table 14.10 clearly show that the stoichiometric CrN/NbN superlattice coatings are superior to electroplated hard chromium. In dry sliding conditions, CrN/NbN outperforms hard chrome by a factor of almost 13 (compare the wear depth measurements), thus demonstrating the success of the PVD approach.

Very interesting tribological behavior was observed with CrN/NbN superlattice coatings deposited at low temperatures of 250°C[110]. It has been found that the coating texture can be controlled by the bias voltage. Figure 14.74 shows that strongly $\{111\}$ textured coating can be produced at higher bias voltages. Pin-on-disk dry sliding tests revealed that there is a strong correlation between the degree of order in the coating structure and the friction and wear behavior of the material. It appears that with highly textured films lower friction coefficient and higher wear resistance can be achieved. Figure 14.75 illustrates this finding, showing that the coefficient of friction decreases from 0.7 for less strongly textured CrN/NbN coatings deposited at bias voltage of $U_B = -75$ V to 0.5 for the highly textured films deposited at $U_B = -150$ V.

Similarly, the wear rate of the coatings, i.e., coefficient of sliding wear, decreases from 1.31×10^{-14} m^3/(N m) at $U_B = -75$ V to 2.8×10^{-15} m^3/(N m) at $U_B = -150$ V. It can be speculated that the strongly textured coating material provides larger number of atomic planes oriented parallel to the sliding direction, which provides better conditions for interplanar gliding, and therefore better friction behavior.

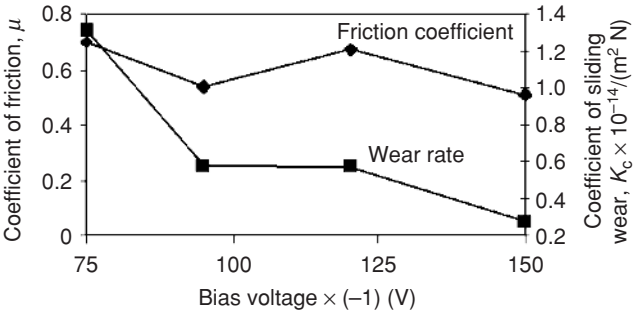

FIGURE 14.75. Coefficient of friction and coefficient of sliding wear of low-temperature CrN/NbN coating as a function of bias voltage.

2.5.3. High-Temperature Performance of CrN/NbN Superlattice Coatings

In many applications such as gas and steam turbine as well as automotive engines, in addition to the high wear and corrosion resistance, high resistance against oxidation is often required. In all these applications, the work temperature is between 550 and 750°C, which can be regarded as medium- to high temperature range. Being CrN based, CrN/NbN is a good candidate to serve under conditions of severe environmental attack. Stoichiometric CrN/NbN superlattice coatings (Me/N = 1), 4.5 μm thick, were deposited on Ti–6Al–4V alloy substrate to investigate the applicability of the coating for protection of automotive engine valves.[111] The oxidation resistance of CrN/NbN superlattice coatings has been studied by thermogravimetric analyses and compared to that of monolithically grown CrN and NbN used as reference coatings. For NbN coating, accelerated rapid oxidation occurred in a relatively low temperature range in between 500 and 550°C. The oxidation of both CrN and CrN/NbN was hardly measurable up to 700°C. However, above this temperature the weight gain of CrN increased almost linearly. In case of the CrN/NbN coatings, the resistance against oxidation was retained up to 820–850°C; thereafter, an accelerated rapid oxidation occurred. GDOES depth profile analysis revealed that after 168-h exposure at 700°C in air, a thin, approximately 0.8-μm-thick, oxide layer was formed on top of the CrN/NbN coating. The duration of the high-temperature exposure was informed by a relevant industrial standard. Within the oxidized layer, two compositionally different regions were distinguished. Correspondingly, Nb-rich surface layer, followed by Cr -ich zone, was formed on top of the CrN/NbN superlattice coating. In contrast, complete oxidation of the CrN/NbN coating was observed for the samples exposed to air at 800°C for 168 h. The presence of a two-layered oxide structure on top of the superlattice was further confirmed by glancing incidence XRD. X-ray diffraction patterns taken at 1° and 5° revealed that the top oxide layer comprises a tetragonal $CrNbO_4$, followed by a rhombohedral Cr_2O_3. The structure of the double-layer oxide formed after

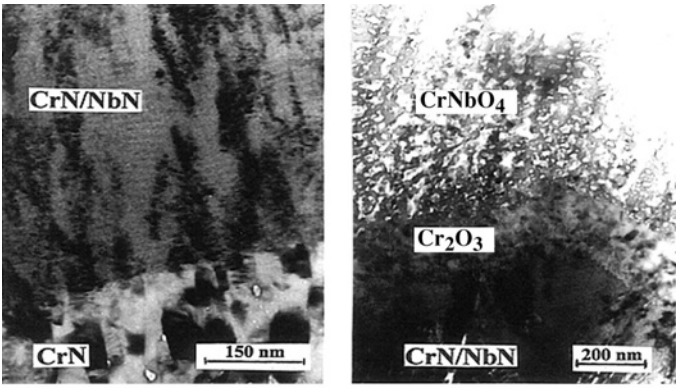

FIGURE 14.76. XTEM micrographs of CrN/NbN coatings oxidized at 700 °C for 168 h: (a) the coating structure below the oxide layer; (b) the structure of the double oxide layer.[111]

exposure to air at 700°C for 168 h was observed by TEM (Fig. 14.76a,b). Very importantly, the TEM observations revealed that the remaining CrN/NbN coating below the oxide layer has preserved its original nanoscale multilayer structure. It can also be stated that the oxidation resistance is controlled by the formation of higher density Cr_2O_3, which can provide more reliable barrier to the oxygen diffusion compared to the rather porous top $CrNbO_4$ layer. The results clearly defined 700–750°C as the temperature range where CrN/NbN can provide sufficient environmental protection while retaining their structure and properties.

2.5.4. Application of CrN/NbN Superlattice Coatings in Textile Industry

Textile machines, due to their specific design based on a multiplicity of production positions, represent a unique niche where the demand for protective coatings reaches its highest extent. The fiber- and yarn-contacting machine parts, usually a few hundreds in a single machine, are subject to severe wear and corrosion resulting from both the aggressiveness of the fiber material and the working environment.

Man-made fibers used for conventional clothing or high-performance engineering textile, such as polyester, polypropylene, polyamide (nylon), often contain TiO_2 used as a delustring agent. Together with dust particles, mainly SiO_2, these abrasive materials turn the yarn into a million metres long saw blade, which is able to cut even the hardest ceramic components used in textile machines. Corrosion on the other hand occurs mainly due to the high level of humidity in the textile production mills often required by the technological process. Friction and corrosion are not the only sources of surface damage. Fast rotating parts (up to 200 000 rpm and more), experience high dynamic stress at the contact area with

the yarn, leading to a fatigue failure of the material at the processing surface or severe adhesion problems if coating is involved.[112] Apart from the mechanical strength and chemical stability of the surface, the productivity and the quality achieved by the textile machines are strongly influenced by the topography of the contacting surfaces. Rough surfaces may cause yarn damage and increase airborne fiber concentration, which could lead to hazards and risks to humans exposed to man-made fibers.[113] Smoother surfaces in principle allow for higher process speed; however, very smooth surfaces have implications on the quality of the yarn and cause fiber transport problems. Coatings have shown great potential to modify the surface characteristics of textile machine components to provide fiber-friendly surfaces and match the demanding conditions at the tribological contact. A range of coatings, such as chromium steel, nickel diamond dispersion, aluminum oxide coating with low- and high titanium oxide content, and chromium oxide coatings deposited by atmospheric plasma spray or high-velocity oxy-fuel technologies, are currently available on the market, to meet a wide variety of textile industry applications, where high hardness and wear resistance are needed. Corrosion resistance is improved by a galvanically applied intermediate nickel layer, special sealing, or impregnation. However, due to the increased surface roughness, all the aforementioned coatings cause a substantial degree of damage to the thread. A significant improvement of the surface topography and therefore less damage to the yarn has been achieved by a monolithically grown PVD TiAlN coating (hardness of 25 GPa).[114] For false-twist texturing operations, PVD-coated Al disks have outperformed disks made of Al_2O_3 sintered ceramic and showed performance similar to disks made of polyurethane, which are gentle on the thread material, although having a short lifetime. The progress in the development of multilayer, superlattice coatings has now made PVD coatings available with plastic hardness value in the range of 40–60 GPa, with extremely smooth surface and enhanced adhesion. Among them, CrN/NbN is one of the best candidates to meet the requirements for high corrosion and wear resistance and deliver smooth yarn-friendly surfaces.[115]

2.5.4a. Combing Rollers for Rotor Spinning. The yarn quality in spinning is strongly influenced by the combing roller tooth geometry (shape and pitch) and surface characteristics. Combing roller rings of S 21 type (tooth shape and pitch suitable for spinning man-made fibers) coated with electroless Ni, PVD TiAlN and smooth superhard CrN/NbN were tested in field trials.

The trials used an Autocoro rotor-spinning machine with 216 spindles running in a spinning mill under normal production and environmental conditions (22–25°C temperature and about 60% relative humidity). The yarn produced was 100% PES (polyester), from either Tergal 118 (Rhone-Poulenc) or Grisuten 11 (Märkische Faser) types and a fineness from 1.3 dtex/38 mm up to 1.5 dtex/38 mm, bright and semi-dull. The production parameters were as follows: yarn count: Nm 20–Nm 34 (Ne 12–Ne 20); sliver count, Nm 0.25 (Ne 0.15); rotor speed up to 88 000 rpm; combing roller speed: 9200 rpm.

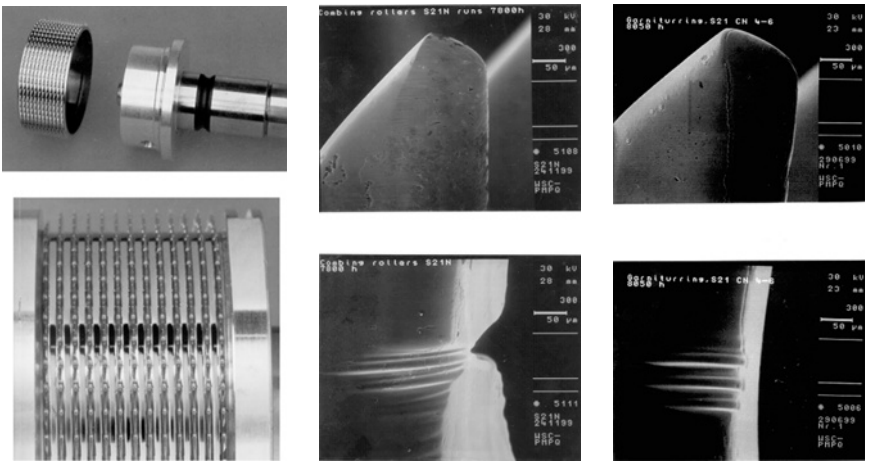

(a) (b) (c)

FIGURE 14.77. Wear marks on the breast and the tip of the teeth of the combing rollers coated with various coatings after several hours of operation. (a) Combing rollers, overview; (b) standard electroplated Ni coating, 7800 h; (c) CrN/NbN superlattice coating, 8050 h.[115]

During the test at 3-monthly intervals the following parameters were monitored:

- yarn data (strength, elongation, evenness, hairiness, and abrasion) – six packages of each type
- wearing of the teeth (SEM) – random samples of each type
- dust deposition in the combing roller housing (visually)

Figure 14.77a–c shows the overview of the components as well as the extent of wear at the breast and tip of the teeth on the combing rollers coated with Ni and CrN/NbN superlattice coatings, respectively (∼8000 running hours). Deep wear marks (cuts) were observed on the breasts while the tips were worn flat on Ni-coated rollers, which led to unacceptable yarn quality and need of replacement. The CrN/NbN coating showed only a little wear, and continued to provide high-quality yarn for up to 10 000–12 000 h. No fiber dust, indicating damaging of the PES fibers, was observed in the combing rollers housing, and the yarn parameters such as strength, elongation, evenness, and hairiness were well within the required standard values. The yarn abrasion rate by use of the superlattice-coated combing rollers was estimated to be as low as 1 mg/10 g yarn, which demonstrates the excellent wear behavior of the CrN/NbN in the conditions of this study.

2.5.4b. Textile Scissors. Textile scissors for cutting various types of textile yarn coated with low-temperature (250°C) CrN/NbN superlattice coating were

FIGURE 14.78. Textile scissors for cutting various types of textile yarn, coated with low-temperature (250 °C) CrN/NbN superlattice coating.[101]

tested at Schlafhorst, Germany .The blades have to withstand relatively high air humidity and are in contact with different fiber-finishing agents. The scissors (Fig. 14.78) cut yarn cleanly on AUTOCONER winding machines and the life expectancy is several years. A specialized testing rig was used, allowing parallel evaluation of wear and corrosion of scissors. After more than 2.5 million cuts, the cutting edge performance was still acceptable. Pre-series of CrN/NbN superlattice-coated scissors blades have been installed in different mills, where the blades have shown excellent performance in real working environments.

2.5.4c. Textile Blades for Chopped Fiber Production. In order to chop polymeric fiber, specialized textile blades are used, mounted on a carousel approximately 600–700 mm in diameter with the sharp edges of the blades facing outwards (Fig. 14.79). Incoming continuous polypropylene fiber "belt" is fed around the rotating carousel under a light load, resulting in chopped fibers with lengths equal to the blade spacing. The textile blades are made from 1% carbon, 2% tungsten steel strip that is hardened in a continuous process, followed by a 280°C temper. The tungsten-graded steel is used to achieve the necessary hardness (700 HV 10) while retaining a high level of toughness. A brittle blade could have a potentially catastrophic effect on the production line if failure occurs.

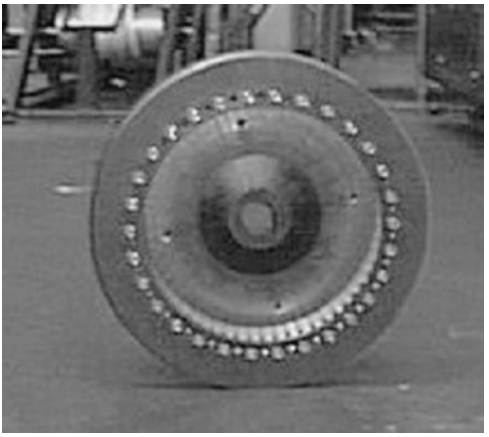

FIGURE 14.79. A carousel with blades coated with CrN/NbN for chopped fiber production.

The nominal blade thickness is 0.64 mm and the edge is ground to an included primary angle of 21° with a secondary angle of 42°. The textile blades were coated with the low-temperature (250°C) CrN/NbN superlattice coating. The performance of the new CrN/NbN superlattice coating was compared to an uncoated blade and chromium oxide coating, which is currently available on the market. Trials for initial sharpness and wear properties were carried out at CATRA (Cutlery & Allied Trades Research Association, UK), using sharp edge testing equipment. The testing is carried out as per BS EN ISO 8442:5:1999—Test for Blade Cutting Performance. The principle of the test is relatively simple in that the blade is mounted with the edge vertical and cuts into a pack of specially developed synthetic paper, containing 5% quartz as an abrasive media, that is automatically lowered on it. By plotting the depth of card cut against the number of cycles, it is possible to obtain a measure of the initial sharpness and subsequent wear rate, generally quoted as ICP and TCC. ICP (initial cutting performance) represents the cutting ability (sharpness) as supplied and is the culmination of the amount of card cut in the first three cycles. TCC (total card cut) represents the life of the blade by giving a measure of its total cutting ability. The ICP and TCC values as evaluated by the edge test for uncoated and coated textile blades are shown in Fig. 14.80. The estimated lifetime of the blades under the conditions of this test is presented in Fig. 14.81. The results revealed that little benefit was being achieved with the chromium oxide coating, whereas the PVD coating gave significant increases in blade performance.

On the basis of these tests, factory trials were carried out using the PVD-coated blades. These blades were installed in carousels on various production runs while processing a product line known to have aggressive wear properties. In these conditions, estimates were that CrN/NbN-coated blades achieved a fourfold increase in life compared to uncoated blades.

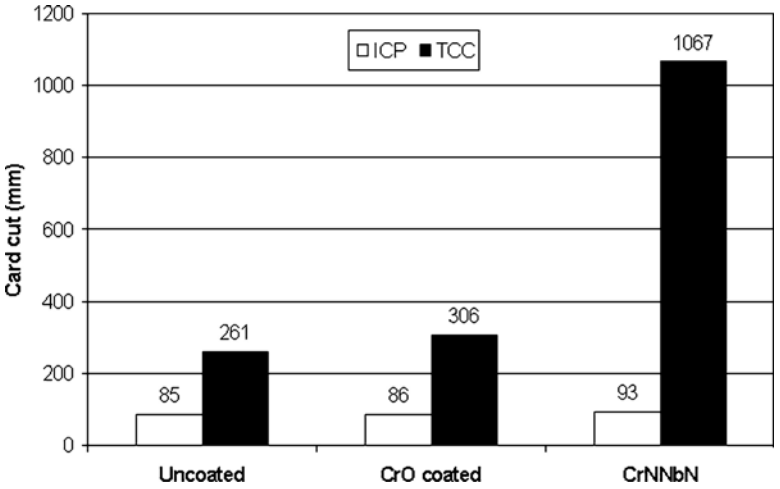

FIGURE 14.80. Edge test results of uncoated and coated textile blades. Initial cutting power (ICP) and total card cut (TCC) values.

2.5.5. Application of CrN/NbN Superlattice Coatings in Cutlery Industry

Another promising field of application is the cutlery industry.[24,116] Examples are CrN/NbN-coated knife blades (Fig. 14.82a). As can be seen from the XTEM image in Fig. 14.82b the superlattice structure is well developed at the sharp knife edge.

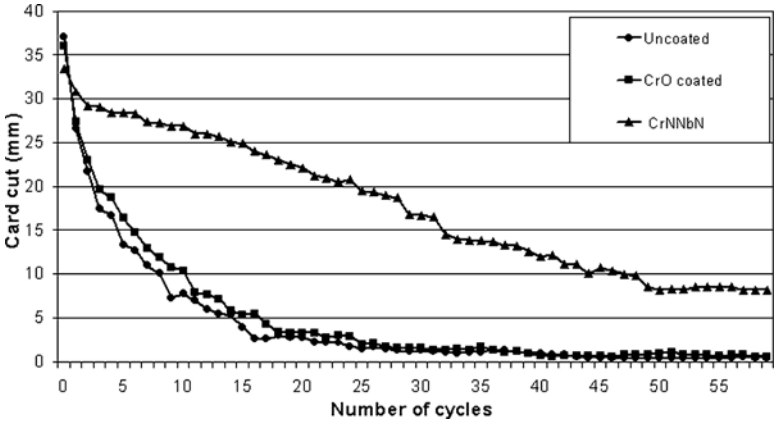

FIGURE 14.81. Edge test results of uncoated and coated textile blades. Lifetime of coated and uncoated blades.

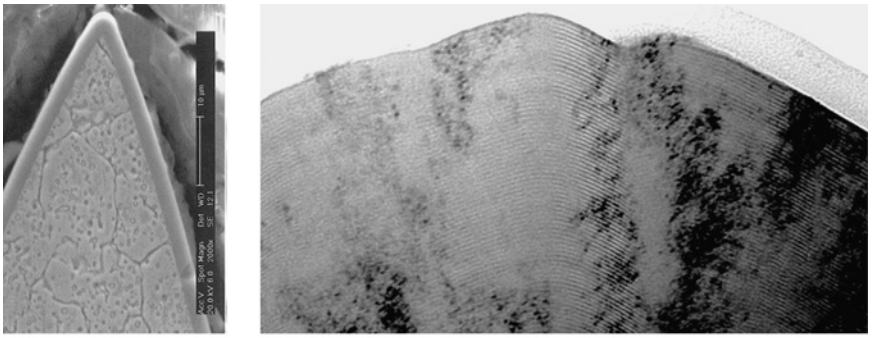

FIGURE 14.82. (a) SEM cross section of CrN/NbN-coated knife blade; (b) XTEM showing the superlattice structure on a knife edge.[24]

Such CrN/NbN superlattice coating outperforms PVD CrN (ARC) and amorphous carbon or amorphous metal carbon films, as shown in Fig. 14.83. To evaluate the cutting power of the coated sharp edges, a standard testing procedure used in cutlery was applied, employing cutting into specially designed abrasive paper media as explained in Section 2.5.4. The numbers of TCC, which represent the wear resistance of the cutting edge in this test, for various coating materials, are shown in Fig. 14.84.

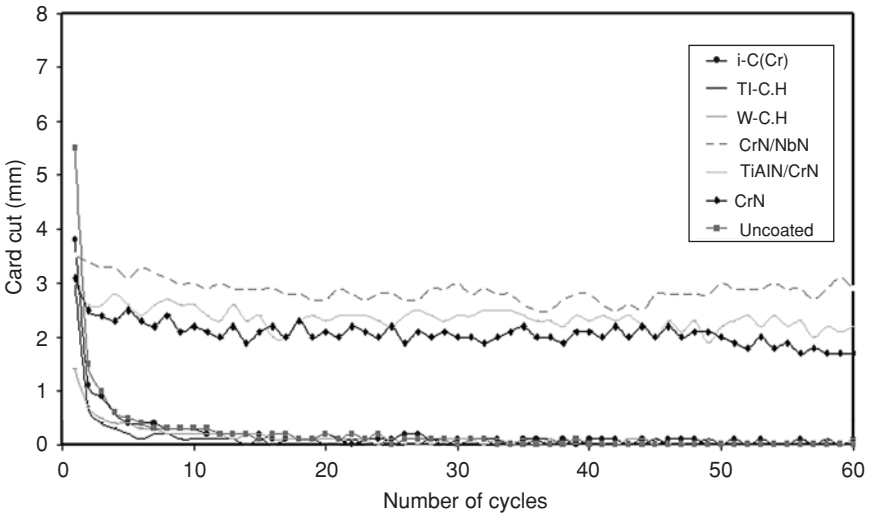

FIGURE 14.83. Superior performance of CrN/NbN-coated blades in TCC test.

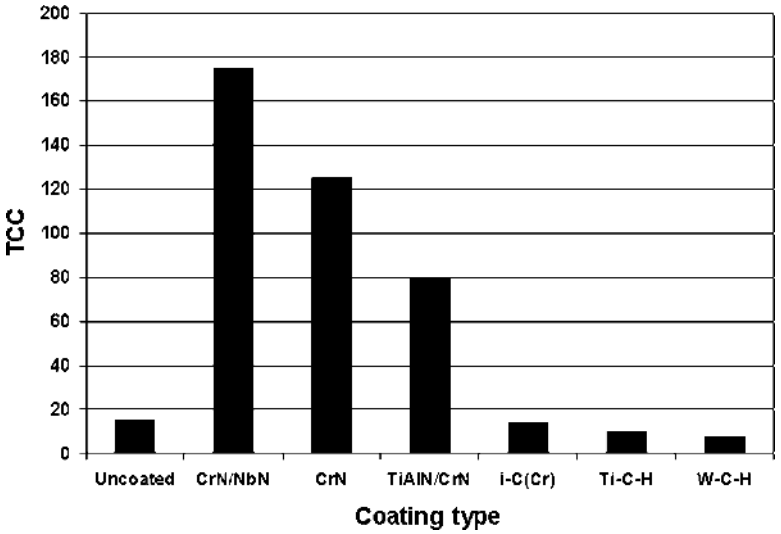

FIGURE 14.84. Comparison of mean TCC values obtained from various PVD coatings.[116]

2.5.6. Application of CrN/NbN Superlattice Coatings in Printing Industry

Successful protection of fine sharp edges by CrN/NbN superlattice coating was demonstrated in printing industry. Very thin (0.5 mm) flexible knives used for cutting of labels were coated with low-temperature (250°C) CrN/NbN superlattice coating Fig. (14.85). The labels are cut from extremely abrasive Al-based alloy strip material and the tiny cutting edge of the flexible blade suffers severe wear.

FIGURE 14.85. Label cutting flexible knives coated with low-temperature CrN/NbN superlattice coating.

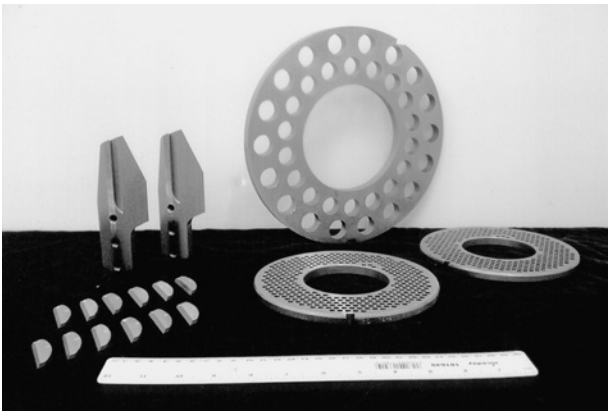

FIGURE 14.86. Heavy-duty shredding knives and front grid for meat processing, coated with low-temperature CrN/NbN superlattice coating.

The lifetime in this particular application was increased from 2 to 90 days. A number of various parts used in printing machines can be serviced effectively by the low-temperature CrN/NbN superlattice coating.

2.5.7. Application of CrN/NbN Superlattice Coatings in Leather Industry

Heavy-duty shredding knives and front grid used to process meat scrap in the leather industry were coated with low-temperature CrN/NbN superlattice coating (Fig. 14.86). In this application, the lifetime of the PVD-coated cutting set has been improved by a factor of 7, compared to that of the uncoated set. Due to their biocompatibility, and high reistance to corrosion and wear, the Nb-based CrN/NbN superlattice coatings are seen as coatings that will find successful applications in food industry as well. Typical applications in this sector include meat of vegetable-slicing blades, food-processing machines, and juice-producing equipment.

2.5.8. Application of CrN/NbN Superlattice Coatings for Protection of Surgical Blades

Very often, due to their fine geometry (small included angles typically 12° and 14°), sharp objects such as surgical blades face strength problems under mechanical loads and fail to provide the necessary support to the superhard PVD coatings. It is anticipated that including plasma nitriding as a pretreatment prior to the superlattice coating deposition would provide solution to this problem. A combined process of low-pressure plasma nitriding and PVD coating integrated in one unit has been developed, dedicated to the surgical blade application.[117] The plasma nitriding process was carried out, utilizing the plasma generated by the magnetrons in a

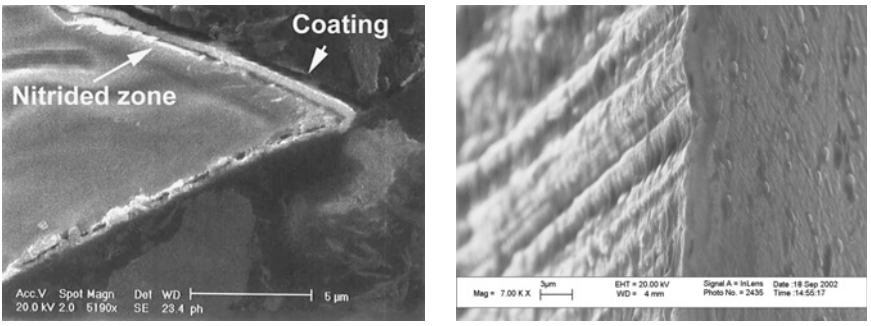

(a) **(b)**

FIGURE 14.87. (a) SEM cross section of the blade tip showing the nitrided zone and the CrN/NbN coating; (b) SEM front view of the cutting edge showing excellent coverage.[117]

PVD system, operated at low power and an auxiliary discharge ignited at the substrates due to the high substrate bias, U_B, in the range of -1000 V. The process was carried out in pure nitrogen atmosphere in the pressure range of $\sim 10^{-3}$ mbar.

CrN/NbN nanoscale multilayer PVD coatings have been deposited on surgical blades that were plasma nitrided at optimized conditions, and their cutting performance evaluated.

Because of the fine cutting edge geometry, it is very important that a uniform edge coverage is achieved and edge rounding is avoided. The structure of the nitrided zone and the uniformity of the PVD coating over the tip of the blades have been investigated by cross-section SEM (Fig. 14.87a). The image shows that the coating uniformly covers the cutting edge very much retaining the sharpness of the profile. Front viewing of the cutting edge of the CrN/NbN-coated blades, using higher magnifications, demonstrated even better the excellent quality of the coating (Fig. 14.87b). The cutting tests have been carried out using specialized equipment and procedures. The cutting efficiency of the blades was defined by the number of cutting strokes needed to cut through an elastic synthetic material with defined thickness under constant normal load. Two parameters characterize the cutting performance of the blades, namely, the initial cutting efficiency of the blade and its lifetime. The initial cutting efficiency is defined as the number of strokes required for cutting through the test piece during the first test cycle. Whereas the number of repeat cycles in this type of test is indicative of the long-term performance ("lifetime") of the cutting edge.

Figure 14.88 demonstrates the effect of the bias voltage during plasma nitriding and the effect of the combined treatment, nitriding and PVD coating, on the initial cutting efficiency of the cutting blades.

The best performance has been achieved for blades nitrided at bias voltage of $U_B = -1000$ V. Deposition of CrN/NbN nanoscale multilayer PVD coatings on blades that were plasma nitrided at optimized conditions reduced the number of

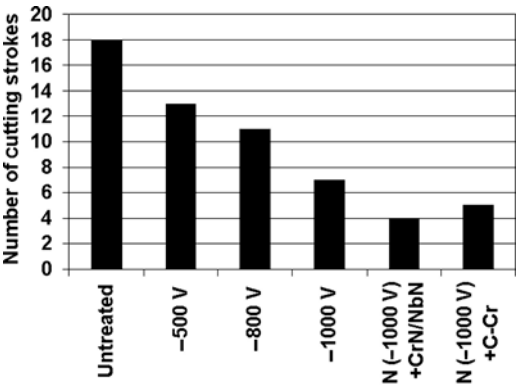

FIGURE 14.88. Cutting efficiency of surgical blades low-pressure plasma nitrided and coated with CrN/NbN; C/Cr is included for reference.[117]

cuttings strokes from 18 for the untreated blades to the range of 5–6. The cutting ability of the blades treated by the combined technology has been retained for more than 28 test cycles, outperforming the nitrided-only blades by a factor of 3 and showed almost 10 times longer lifetime when compared to untreated blades.

REFERENCES

1. U. Helmersson, S. Todorova, S. A. Barnett, J.-E. Sundgren, L. C. Markert, and J. E. Greene, Growth of single-crystal TiN/VN strained-layer superlattices with extremely high mechanical hardness, *J. Appl. Phys.* **62**, 481–484 (1987).
2. X Chu, M. S. Wong, W. D. Sproul, S. L. Rohde, and S. A. Barnett, Deposition and properties of polycrystalline TiN/NbN superlattice coatings, *J. Vac. Sci. Technol. A***10**, 1604–1614 (1992).
3. S. A. Barnett, Mechanics and dielectric properties, in *Physics of Thin Films*, Vol. 17, edited by M. H. Francombe and J. L. Vossen (Academic Press, Boston, 1993).
4. M. Shinn, L. Hultman, and S. A. Barnett, Growth, structure, and microhardness of epitaxial TiN/NbN superlattices, *J. Mater. Res.* **7**, 901–911 (1992).
5. T. Hurkmans, T. Trinh, D. B. Lewis, J. S. Brooks, and W.-D. Münz, Multilayered titanium tungsten nitride coatings with a superlattice structure grown by unbalanced magnetron sputtering, *Surf. Coat. Technol.* **76**, 159–166 (1995).
6. I. Wadsworth, I. J. Smith, L. A. Donohue, and W.-D. Münz, Thermal stability and oxidation resistance of TiAlN/CrN multilayer coatings, *Surf. Coat. Technol.* **94–95**, 315–321 (1997).
7. I. J. Smith, *Improvement of TiAlN by the Incorporation of Cr and Y*, Ph.D Thesis (Sheffield Hallam University, Sheffield, UK, 1998).
8. M. Setoyama, A. Nakayama, M. Tanaka, N. Katagawa, and T. Nomura, Formation of cubic-A1N in TiN/A1N superlattice, *Surf. Coat. Technol.* **86**, 225–230 (1996).
9. W.-D. Münz and I. J. Smith, Wear resistant PVD coatings for high temperature (950°C) applications, in *Proceedings of 42nd Annual Conference of Soc. of Vacuum Coaters SVC*, Chicago, April 1999, pp. 350–356.

10. D. B. Lewis, L. A. Donohue, M. Lembke, W.-D. Münz, R. Kuzel, V. Valvoda, and C. Blomfield, The influence of the yttrium content on the structure and properties of $Ti_{1-x-y-z}Al_xCr_yY_zN$ PVD hard coatings, *Surf. Coat. Technol.* **114**, 187–199 (1999).
11. S. A. Barnet, K. Martin, A. Madan, J. Ji, I. Kim, and A. Inspekton, Nanolayered hard coatings for high-temperature applications, in *Proceedings of 45th Annual Technical Conference of Soc. of Vacuum Coaters SVC*, Lake Buena Vista, Florida USA, April 2002, pp. 59–63.
12. Q. Luo, W. M. Rainforth, and W.-D. Münz, TEM observations of wear mechanisms of TiAlCrN and TiAlN/CrN coatings grown by combined steered-arc/unbalanced magnetron deposition, *Wear* **229**, 74–82 (1999).
13. H. Holleck and V. Schier, Multilayer PVD coatings for wear protection, *Surf. Coat. Technol.* **76**, 328–336 (1995).
14. P. Yashar, S. A. Barnett, J. Rechner, and W. D. Sproul, Structure and mechanical properties of polycrystalline CrN/TiN superlattices, *J. Vac. Sci. Technol. A* **16**(5), 2913–2918 (1998).
15. L. A. Donohue, W.-D. Münz, D. B. Lewis, J. Cawley, T. Hurkmans, T. Trinh, I. Petrov, and J. E. Greene, Large scale fabrication of hard superlattice thin films by combined steered arc evaporation and unbalanced magnetron sputtering, *Surf. Coat. Technol.* **93**, 69–87 (1997).
16. P. Eh. Hovsepian, D. B. Lewis, and W.-D. Münz, Recent progress in large scale manufacturing of multilayer/superlattice hard coatings, *Surf. Coat. Technol.* **133**, 166–175 (2000).
17. W.-D. Münz, D. B. Lewis, P. Eh. Hovsepian, C. Schönjahn, A. P. Ehiasarian, and I. Smith, Industrial scale manufactured superlattice hard PVD coatings, *Surf. Eng.* **17**(1), 15–27 (2001).
18. W.-D. Münz, D. Schulze, and F. J. M. Hauzer, A new method for hard coatings: ABS^{TM} (arc bond sputtering), *Surf. Coat. Technol.* **50**, 169–178 (1992).
19. A. Anders, Ion charge state distributions of vacuum arc plasmas: The origin of species, *Phys. Rev. E* **55**, 969–981 (1997).
20. P. Eh. Hovsepian, Influence of the parameters of the metal ion etching on the structure and the adhesion of TiN coatings deposited by the cathodic arc evaporation in vacuum, *Arch. Metall. Polish Acad. Sci.* **33**(4), 577–582 (1988).
21. C. Schönjahn, L. A. Donohue, D. B. Lewis, W.-D. Münz, R. D. Twesten, and I. Petrov, Enhanced adhesion through local epitaxy of transition-metal nitride coatings on ferritic steel promoted by metal ion etching in a combined cathodic arc/unbalanced magnetron deposition system, *J. Vac. Sci. Technol. A* **18**(4), 1718–1723 (2000).
22. W. D. Sproul, High rate reactive sputtering process control, *Surf. Coat. Technol.* **33**, 73–81 (1987).
23. W.-D. Münz, L. A. Donohue, and P. Eh. Hovsepian, Properties of various large-scale fabricated TiAlN- and CrN-based superlattice coatings grown by combined cathodic arc–unbalanced magnetron sputter deposition, *Surf. Coat. Technol.* **125**, 269–277 (2000).
24. P. Eh. Hovsepian, W.-D. Münz, A. Medlock, and G. Gregory, Combined cathodic arc/unbalanced magnetron grown CrN/NbN superlattice coatings for applications in the cutlery industry, *Surf. Coat. Technol.* **133**, 508–516 (2000).
25. H. Paritong, I. Wadsworth, L. A. Donohue, and W.-D. Münz, Corrosion resistant Nb coatings grown by combined steered arc unbalanced magnetron deposition, *Trans. IMF* **76**(4), 144–148 (1998).
26. W.-D. Münz, I. J. Smith, D. B. Lewis, and S. Creasey, Droplet formation on steel substrates during cathodic steered arc metal ion etching, *Vacuum* **48**, 473–481 (1997).
27. S. Creasey, D. B. Lewis, I. J. Smith, I.J., and W.-D. Münz, SEM image analysis of droplet formation during metal ion etching by a steered arc discharge, *Surf. Coat. Technol.* **97**, 163–175 (1997).
28. I. Petrov, P. Losbichler, D. Bergstrom, J. E. Greene, W.-D. Münz, T. Hurkmans, and T. Trinh, Ion-assisted growth of $Ti_{1-x}Al_xN/Ti_{1-y}Nb_yN$ multilayers by combined cathodic-arc/magnetron-sputter deposition, *Thin Solid Films* **302**, 179–192 (1997).
29. L. A. Donohue, I. J. Smith, W.-D. Münz, I. Petrov, and J. E. Greene, Microstructure and oxidation-resistance of $Ti_{1-x-y-z}Al_xCr_yY_zN$ layers grown by combined steered-arc/unbalanced-magnetron-sputter deposition, *Surf. Coat. Technol.* **94–95**, 226–231 (1997).

30. C. Schönjahn, D. B. Lewis, W.-D. Münz, and I. Petrov, Substrate ion etching in combined steered cathodic arc–UBM deposition system: Effects on interface architecture, adhesion, and tool performance, S*urf. Eng*. **16**, 176–180 (2000).
31. D. A. Porter and K. E. Easterling, Crystal interfaces and microstructure, in *Phase Transformations in Metals and Alloys* (Chapman & Hall, London, 1992), Chap. 3, pp.142–147.
32. J. E. Greene, Fundamentals, in *Handbook of Crystal Growth,* Vol. I, edited by D. T. J. Hurle (Elsevier, Amsterdam, 1993), pp. 639.
33. M. I. Lembke, D. B. Lewis, and W.-D. Münz, Localised oxidation defects in TiAlN/CrN superlattice structured hard coatings grown by cathodic arc/unbalanced magnetron deposition on various substrate materials, *Surf. Coat. Technol*. **125**, 263–268 (2000).
34. H. W. Wang, M. M. Stack, S. B. Lyon, P. Eh. Hovsepian, and W.-D. Münz, Wear associated with growth defects in combined cathodic arc/unbalanced magnetron sputtered CrN/NbN superlattice coatings during erosion in alkaline slurry, *Surf. Coat. Technol*. **135**, 82–90 (2000).
35. W.-D. Münz, D. B. Lewis, S. Creasey, T. Hurkmans, T. Trinh, and W. Ijzendorm, Defects in TiN and TiAIN coatings grown by combined cathodic arc/unbalanced magnetron technology, *Vacuum* **46**(4), 323–330 (1995).
36. C. Schönjahn, A. P. A. Ehiasarian, D. B. Lewis, R. New, W.-D. Münz, R. D. Twesten, and I. Petrov, Influence of the interface composition on the corrosion behavior of unbalanced magnetron grown niobium coatings on steel, *J. Vac. Sci. Technol. A***19**(4), 1392–1398 (2001).
37. J. S. Brooks, J. L. Davidson, S. D. Forder, W.-D. Münz, and M. Larsson, A Mössbauer spectroscopy study of Ti–Fe interfaces produced by the PVD process, *Thin Solid Films* **308**, 351–357 (1997).
38. G. Håkansson, L. Hultman, J.-E. Sundgren, J. E. Greene, and W.-D. Münz, Microstructures of TiN films grown by various physical vapour deposition techniques, *Surf. Coat. Technol*. **48**, 51–67 (1991).
39. B.-J. Kim, Y. C. Kim, and J.-J. Lee, The effect of NH_3 plasma pre-treatment on the adhesion property of $(Ti_{1-X}Al_X)N$ coatings deposited by plasma-enhanced chemical vapor deposition, *Surf. Coat. Technol*. **114**, 85–89 (1999).
40. D. B. Lewis, P. Eh. Hovsepian, and W.-D. Münz, Structure and stress of superlattice hard coatings deposited by a combined steered cathodic arc/unbalanced magnetron process, in *Proceedings of 7th Int. Symposium TAFT 2000*, Nancy, France, March 28–30, 2000, pp. 20–25.
41. C. Engström, J. Birch, L. Hultman, C. Lavoie, C. Cabral, J. L. Jordan-Sweet, and J. R. A. Carlson, Interdiffusion studies of single crystal TiN/NbN superlattice thin films, *J. Vac. Sci. Technol. A***17**(5), 2920–2927 (1999).
42. Z. Zhou, W. M. Rainforth, U. Falke, M. Falke, A. Bleloch, and P. Eh. Hovsepian, On the structure and composition of nanoscale TiAlN/VN multilayers, *Phil. Mag. A*, submitted.
43. B. Rother and H. A. Jehn, Calculations of industrial physical vapour deposition coating conditions examined in relation to (Cr, Ti)N deposition, *Surf. Coat. Technol*. **62**, 635–640 (1993).
44. B. Rother, G. Ebersbach, and H. M. Gabriel, Substrate-rotation systems and productivity of industrial PVD processes, *Surf. Coat. Technol*. **119**, 694–698 (1999).
45. J. Cawley, J. M. Titchmarsh, and L. A. Donohue, Investigation of elemental distributions in TiAlN–ZrN multi-layers using analytical transmission electron microscopy, *Surf. Coat. Technol*. **86**, 357–363 (1996).
46. H. Meidia, A. G. Cullis, C. Schönjahn, W.-D. Münz, and J. M. Rodenburg, Investigation of intermixing in TiAlN/VN nanoscale multilayer coatings by energy-filtered TEM, *Surf. Coat. Technol*. **151**, 209–213 (2002).
47. Z. Zhou, W. M. Rainforth, B. Rother, A. P. Ehiasarian, P. Eh. Hovsepian, and W.-D. Münz, Elemental distribution and substrate rotation in industrial TiAlN/VN superlattice hard coatings, *Surf. Coat. Technol*. **183**, 275–282 (2004).
48. D. B. Lewis, Q. Luo, P. Eh. Hovsepian, and W.-D. Münz, Interrelationship between atomic species, bias voltage, texture and microstructure of nano-scale multilayers, *Surf. Coat. Technol*. **184**, 225–232 (2004).

49. D. S. Rickerby, A. M. Jones, and B. A. Bellamy, X-ray-diffraction studies of physically vapour-deposited coatings, *Surf. Coat. Technol.* **37**(1), 111–137 (1989).
50. D. B. Lewis, I. P. Wadsworth, W.-D. Münz, R. Kuzel, Jr., and V. Valvoda, Structure and stress of TiAlN/CrN superlattice coatings as a function of CrN layer thickness, *Surf. Coat. Technol.* **119**, 284–291 (1999).
51. T. Hurkmans, D. B. Lewis, H. Paritong, J. S. Brooks, and W.-D. Münz, Influence of ion bombardment on structure and properties of unbalanced magnetron grown CrNx coatings, *Surf. Coat. Technol.* **114**, 52–59 (1999).
52. G. Farges, E. Beuprez, and M. C. Staine-Catherine, Preparation and characterization of V–N films deposited by reactive triode magnetron sputtering, *Surf. Coat. Technol.* **54**, 115–120 (1992).
53. J. Pelleg, L. Z. Zevin, and S. Lungo, Reactive-sputter-deposited TiN films on glass substrates, *Thin Solid Films* **197**, 117–128 (1991).
54. I. Wadsworth, D. B. Lewis, and G. Williams, Structural studies of TiN/ZrN multilayer coating deposited by physical vapour deposition, *J. Mater. Sci.* **31**, 5907–5914 (1996).
55. J. E. Greene, J.-E. Sundgren, L. Hultman, I. Petrov, and D. B. Bergstrom, Development of preferred orientation in polycrystalline TiN layers grown by ultrahigh-vacuum reactive magnetron sputtering, *Appl. Phys. Lett.* **67**, 2928–2930 (1995).
56. L. Hultman, J.-E. Sundgren, and J. E. Greene, Formation of polyhedral N_2 bubbles during reactive sputter deposition of epitaxial TiN(100) films, *J. Appl. Phys.* **66**, 536–544 (1989).
57. P. Eh. Hovsepian, and W.-D. Münz, Advanced application tailored PVD coatings utilizing nanoscale multilayer/superlattices, in *Proceedings of 45th Annual Technical Conference of Soc. of Vacuum Coaters SVC*, Lake Buena Vista, Florida, USA, April 2002, pp. 49–55. *Vacuum Technology & Coating*, November 2002, pp. 28–36.
58. P. Eh. Hovsepian, D. B. Lewis, W.-D. Münz, A. Rozaud, and P. Juliet, Chromium nitride/niobium nitride superlattice coatings deposited by combined cathodic-arc/unbalanced magnetron technique, *Surf. Coat. Technol.* **116–119**, 727–734 (1999).
59. S. Yang and D. G. Teer, Investigation of sputtered carbon and carbon/chromium multi-layered coatings, *Surf. Coat. Technol.* **131**, 412–416 (2000).
60. P. Eh. Hovsepian, D. B. Lewis, C. Constable, Q. Luo, Y. N. Kok, and W.-D. Münz, Combined steered cathodic arc/unbalanced magnetron grown C/Cr nanoscale multilayer coatings for tribological applications, *Surf. Coat. Technol.* **174**, 762–769 (2003).
61. W.-D. Münz, Titanium aluminium nitride films—A new alternative to TiN coatings, *J. Vac. Sci. Technol. A* **4**(6), 2717–2725 (1986).
62. M. I. Lembke, D. B. Lewis, W.-D. Münz, and J. M. Titchmarsh, Joint second prize—Significance of Y and Cr in TiAlN hard coatings for dry rich speed cutting, *Surf. Eng.* **17**(2), 153–158 (2001).
63. D. McIntyre, J. E. Greenne, G. Håkansson, J.-E. Sundgren, and W.-D. Münz, Oxidation of metastable single-phase polycrystalline $Ti_{0.5}Al_{0.5}N$ films: Kinetics and mechanisms, *J. Appl. Phys.* **67**, 1542–1553 (1990).
64. I. J. Smith, W.-D. Münz, L. A. Donohue, I. Petrov, and J. E. Greene, Improved $Ti_{1-x}Al_xN$ PCD coatings for dry high speed cutting operations, *Surf. Eng.* **14**(1), 37–41 (1998).
65. W.-D. Münz, M. I. Lembke, D. B. Lewis, and I. J. Smith, The role of yttrium incorporation into TiAlN coatings deposited on cemented carbide tools during dry high speed cutting, in *Paper presented at Industrial Tooling*, Southampton Institute Conference Centre, UK, September 5–6, 2001.
66. E. Pflüger, A. Schröer, P. Voumard, L. Donohue, and W.-D. Münz, Influence of incorporation of Cr and Y on the wear performance of TiAlN coatings at elevated temperatures, *Surf. Coat. Technol.* **115**, 17–23 (1999).
67. E. Zoestbergen, N. J. M. Carvalho, and J. T. M. DeHossen, Stress state or TiN/TiAlN PVD multilayers, *Surf. Eng.* **17**(1), 29–34 (2001).
68. R. R. Boyer, Titanium for aerospace: Rationale and applications, *Adv Perform. Mater.* **2**, 349–368 (1995).

69. C. Leyens, M. Peters, and W. A. Kaysser, Oxidation and embrittlement of near-α titanium alloys after long-term exposure to air, in *Proceedings of 4th European Conference on Advanced Materials and Processes*, Associaszione Italiana di Metallurgia, Italy, 1995.
70. C. Leyens, M. Peters, and W. A. Kaysser, Oxidation and protection of near-alpha titanium alloys, *Mater. Sci. Forum* **251–252**, 769–776 (1997).
71. M. Peters, J. Kumpfert, C. Leyens, D. Weinem, W. A. Kaysser, and Y. T. Lee, Structure and properties of titanium alloys for high temperature application, in *Proceedings of Second Pacific Rim International Conference on Advanced Materials and Processing (PRICM-2)*, The Korean Institute of Metals and Materials, Kyongju, Korea, 1995.
72. C. Leyens, Oxidationsverhalten und Oxidationsschutz von Titanlegierungen für den Hochtemperatureinsatz, in *Flugtriebwerken,* Dissertation RWTH Aachen (Verlag Shaker, Aachen, 1997).
73. C. Leyens, M. Peters, and W. A. Kaysser, Intermetallic Ti–Al coatings for protection of titanium alloys: Oxidation and mechanical behaviour, *Surf. Coat. Technol.* **94–95**, 34–40 (1997).
74. C. Leyens, M. Peters, and W. A. Kaysser, Influence of intermetallic Ti–Al coatings on the creep properties of TIMETAL 1100, *Scr. Mater.* **35**, 1423–1428 (1996).
75. C. Leyens, K.-H. Trautmann, M. Peters, and W. A. Kaysser, Influence of intermetallic Ti–Al coatings on the fatigue properties of TIMETAL 1100, *Scr. Mater.* **36**, 1309–1314 (1997).
76. C. Leyens, M. Schmidt, M. Peters, and W. A. Kaysser, Sputtered intermetallic Ti–Al–X coatings: Phase formation and oxidation behaviour, *Mater. Sci. Eng. A***239**/**240**, 680–687 (1997).
77. C. Leyens, M. Peters, P. Eh. Hovsepian, D. B. Lewis, Q. Luo, and W.-D. Münz, Novel coating systems produced by the combined cathodic arc/unbalanced magnetron sputtering for environmental protection of titanium alloys, *Surf. Coat. Technol.* **155**, 103–111 (2002).
78. C. Leyens, P. Eh. Hovsepian, W.-D. Münz, Protective Ti-Al-Cr-N coating. European Pat. EP 1 431 416 A1, Int CI.: C23C 28/02, 23.06.2004 Bulletin 2004/26 (2004).
79. K. Noguchi, N. Kitagava, H. Ohara, and H. Animoto, High speed drilling with coated carbide drills, in *Proceedings of 1stFrench and German Conf. on High Speed Machining*, University of Metz, France, 1997, pp. 407–413.
80. P. Eh. Hovsepian, D. B. Lewis, Q. Luo, W.-D. Münz, P. H. Mayrhofer, C. Mitterer, Z. Zhuo, and W. M. Rainforth, TiAlN based nanoscale multilayer PVD coatings designed to adapt their tribological properties at elevated temperatures, in *Invited paper presented at ICMCTF 2004*, San Diego, CA, 2004. *Thin Solid Films*, **485**, 160–168 (2005).
81. M. Voydt, A. Skopp, I. Dörfel, and K. Vitke, Wear engineering oxides/anti-wear oxides, *Wear* **218**, 84–95 (1998).
82. Q. Luo, P. Eh. Hovsepian, D. B. Lewis, W.-D. Münz, Y. N. Kok, J. Cockrem, M. Bolton, and A. Farinotti, Tribological properties of unbalanced magnetron sputtering nanoscale multilayer coatings TiAlN/VN and TiAlCrYN deposited on plasma nitrided steels, *Surf. Coat. Technol.*, **193**, 39–45 (2005).
83. C. P. Constable, J. Yarwood, P. Eh. Hovsepian, L. A. Donohue, D. B. Lewis, and W.-D. Münz, Structural determination of wear debris generated from sliding wear tests on ceramic coatings using Raman microscopy, *J. Vac. Sci. Technol. A***18**(4), 1681–1689 (2000).
84. P. H. Mayrhofer, P. Eh. Hovsepian, C. Mitterer, and W.-D. Münz, Calorimetric evidence for frictional self-adaptation of TiAlN/VN superlattice coatings, *Surf. Coat. Technol.* **177**, 341–347 (2004).
85. Z. Zhuo, W. M. Rainforth, D. B. Lewis, S. J. Creasey, J. J. Forsyth, F. Clegg, A. P. Ehiasarian, P. Eh. Hovsepian, and W.-D. Münz, Oxidation behaviour of nanoscale TiAlN/VN multilayer coatings, *Surf. Coat. Technol.* **177**/**178**, 198–203 (2004).
86. D.B. Lewis, S. Creasy, Z. Zhuo, J. J. Forsyth, A. P. Ehiasarian, P. Eh. Hovsepian, Q. Luo, W. M. Rainforth, and W.-D. Münz, The effect of (Ti+Al):V ratio on the structure and oxidation behaviour of TiAlN/VN nano-scale multilayer coatings, *Surf. Coat. Technol.* **177**, 252–259 (2004).
87. Y. Niguyi, L. Junuha, and L. Chenglu, Valence reduction process from sol–gel V_2O_5 to VO_2 thin films, *Appl. Surf. Sci.* **191**, 176–180 (2002).

88. S. Yang, X. Li, N. M. Renevier, and D. G. Teer, Tribological properties and wear mechanism of sputtered C/Cr coating, *Surf. Coat. Technol.* **142**, 85–93 (2001).
89. U. Wiklund, and M. Larsson, Low friction PVD titanium–carbon coatings, *Wear* **241**, 234–238 (2000).
90. D. G. Teer, D. Camino, and V. Bellido, UK Pat. Appl. GB 9725413 (1997).
91. J. Ullmann, K. Baba, H. Martin, and G. K. Wolf, Effect of deposition conditions on the growth and behaviour of thin carbon films prepared by ion-assisted evaporation, *Surf. Coat. Technol.* **74/75**, 746–753 (1995).
92. R. G. Lacerda, P. Hammer, F. L. Freire, Jr., F. Alvarez, and F. C. Marques, On the structure of argon assisted amorphous carbon films, *Diamond Relat. Mater.* **9**, 796–800 (2000).
93. V. V. Uglova, V. M. Anishchik, Y. Pauleau, A. K. Kuleshov, F. Thiery, J. Pelletier, S. N. Dub, and D. P. Rusalsky, Relations between deposition conditions, microstructure and mechanical properties of amorphous carbon-metal films, *Vacuum* **70**, 181–185 (2003).
94. I. Petrov, L. Hultman, U. Helmersson, J.-E. Sundgren, and J. E. Greene, Microstructure modification of TiN by ion bombardment during reactive sputter deposition, *Thin Solid Films* **169**, 299–314 (1989).
95. L. Hultman, W.-D. Münz, J. Musil, S. Kadlec, I. Petrov, and J. E. Greene, Low-energy (-100eV) ion irradiation during growth of TiN deposited by reactive magnetron sputtering—effects of ion flux on film microstructure, *J. Vac. Sci. Technol. A***9**(3), 434–438 (1991).
96. J. Neidhart, As. Czigany, I. F. Brunell, and L. Hultman, Growth of fullerene-like carbon nitride thin solid films by reactive magnetron sputtering; role of low-energy ion irradiation in determining microstructure and mechanical properties, *J. Appl. Phys.* **93**, 3002–3015 (2003).
97. B. Chapman, Sputtering and plasma etching, in *Glow Discharge Processes* (Wiley, New York, 1980).
98. P. Eh. Hovsepian, Y. N. Kok, A. P. Ehiasarian, A. Erdemir, J.-G. Wen, and I. Petrov, Structure and tribological behaviour of nanoscale multilayer C/Cr coatings deposited by the combined steered cathodic arc/unbalanced magnetron sputtering technique, *Thin Solid Films* **447**, 7–13 (2004).
99. Y. N. Kok, P. Eh. Hovsepian, Q. Luo, D. B. Lewis, and I. Petrov, Influence of the bias voltage on the structure and the tribological performance of nanoscale multilayer C/Cr PVD coatings, in *AEPSE*, Jeju, Korea, 2003. *Thin Solid Films,* **475**, 219–226 (2005).
100. G. L. Miller, *Tantalum and Niobium* (Butterworths Scientific, London, 1958).
101. W.-D. Münz, and P. Eh. Hovsepian, Final report of BRITE-EURAM project NEWCHROME, Report No. BE 96-3305, Sheffield Hallam University, UK, 2000.
102. M. Tomlinson, S. B. Lyon, P. Eh. Hovsepian, and W.-D. Münz, Corrosion performance of CrN/NbN superlattice coatings deposited by the combined cathodic arc/unbalanced magnetron technique, *Vacuum* **53**, 117–121 (1999).
103. P. Eh. Hovsepian, D. B. Lewis, W.-D. Münz, S. B. Lyon, and M. Tomlinson, Combined cathodic arc/unbalanced magnetron grown CrN/NbN superlattice coatings for corrosion resistant applications, *Surf. Coat. Technol.* **121**, 535–541 (1999).
104. E. E. Salagean, D. B. Lewis, J. S. Brooks, W.-D. Münz, I. Petrov, and J. E. Greene, Combined steered are-unbalanced magnetron grown niobium coatings for decorative and corrosion resistance applications, *Surf. Coat. Technol.* **82**, 57–64 (1996).
105. H. W. Wang, M. Stack, S. B. Lyon, P. Eh. Hovsepian, and W.-D. Münz, The corrosion behaviour of macroparticle defects in arc bond-sputtered CrN/NbN superlattice coatings, *Surf. Coat. Technol.* **126**, 279–287 (2000).
106. H. Paritong, I. Wadsworth, L. A. Donohue, and W.-D. Münz, Corrosion resistant Nb coatings grown by combined steered arc unbalanced magnetron deposition, *Trans. IMF* **76**, 144–148 (1998).
107. P. Eh. Hovsepian and W.-D. Münz, Properties of niobium based wear and corrosion resistant hard PVD coatings grown on various steels, in *Proceedings of EUROMAT 2001,* Rimini, Italy, June 10–14, 2001.

108. P. Eh. Hovsepian, and W.-D. Münz, Recent progress in large-scale production of nanoscale multilayer/superlattice hard coatings, *Vacuum* **69**, 27–36 (2003).
109. Y. Purandare, M. M. Stack, and P. Eh. Hovsepian, Impact angle effects on the erosion-corrosion of CrN/NbN superlattice PVD coatings, in *ICMCTF 2004*, San Diego, CA, USA. *Surf. Coat. Technol*., **188–189**, 556–565 (2004).
110. D. Reitz, and P. Eh. Hovsepian, Effect of coating texture on the tribological behaviour of low temperature CrN/NbN superlattice coatings, Placement report, SHU, Sheffield, UK, 2002.
111. P. Eh. Hovsepian, D. B. Lewis, Q. Luo, W.-D. Münz, and M. Meyer, High temperature performance of CrN/NbN superlattice coatings deposited on Ti alloy substrates, in *Surface Engineering, Euromat99,* Vol. 11, edited by H. Dimigen (Wiley-VCH, Weinheim, 1999), pp. 41–46. (ISBN 3-527-30196-8)
112. T. Gries, and B. Wulfhorst, Improvement of fatigue resistance of PVD thin films for textile machines by finite element analysis, *Surf. Coat. Technol.* **68**, 500–506 (1994).
113. K. Rodelsperger and H. J. Woittowitz, Airborne fibre concentrations and lung burden compared to the tumour response in rats and humans exposed to asbestos, *Anal. Occup. Hygiene* **39**(5), 715–725 (1995).
114. Th. Gries, PVD coatings for textile machine components, *Surf. Coat. Technol.* **62**, 443–447 (1993).
115. P. Eh. Hovsepian, W.-D. Münz, B. Schlömer, G. Gregory, and I. J. Smith, PVD CrN/NbN superlattice coatings to protect components used in the textile industry, in *Proceedings of 44th, Annual Conference of Soc. of Vacuum Coaters SVC*, Philadelphia, USA, April 2001, pp. 72–77.
116. P. Eh. Hovsepian, W.-D. Münz, A. Medlock, and G. Gregory, Low temperature CrN/NbN superlattice coatings deposited by combined cathodic arc/unbalanced magnetron technique for applications in cutlery industry, in *Proceedings of 12th International Colloquium on plasma processes*, Antibes-Juan-les-pins, France, June 1999, pp. 130–134.
117. P. Eh. Hovsepian, A. P. Ehiasarian, W.-D. Münz, D. B. Lewis, and G. Thompson, Performance of high-precision knife blades treated by plasma nitriding and PVD coating, in *Proceedings of 46th, Annual Conference of Soc. of Vacuum Coaters SVC*, San Francisco, USA, May 2003, pp. 61–66. *Vacuum Technology & Coating*, January 2004, pp. 47–52.

Index

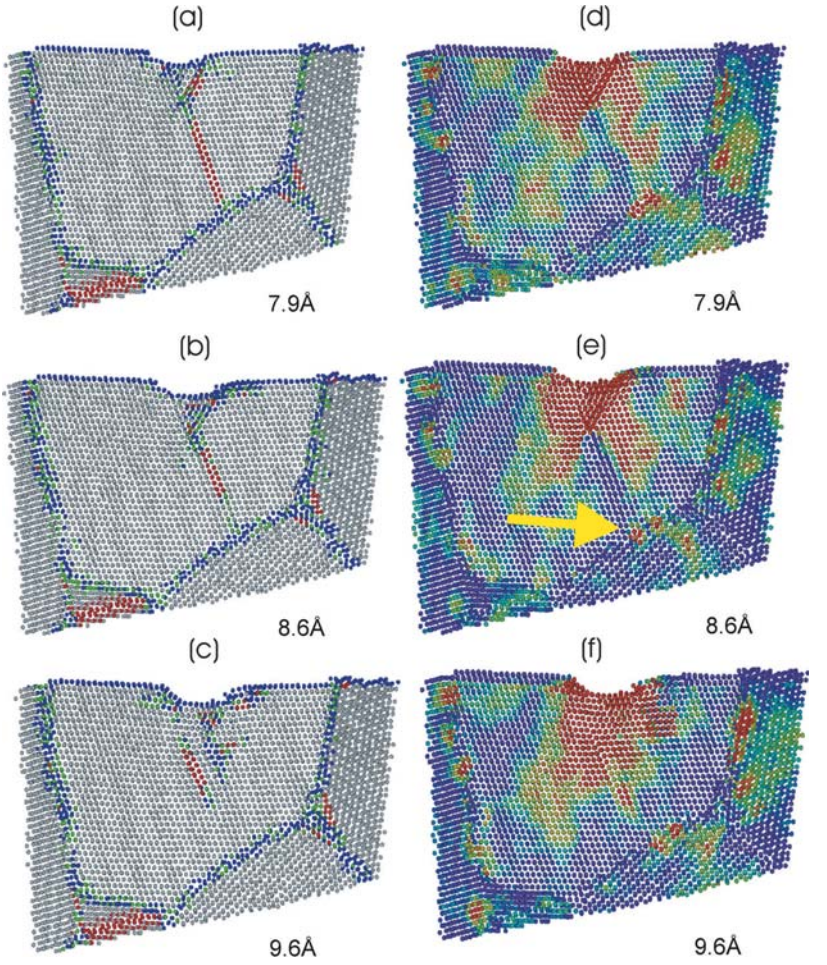

COLOR PLATE 1. Dislocation repelled at high stress region of the GB. (From Ref. 37.)

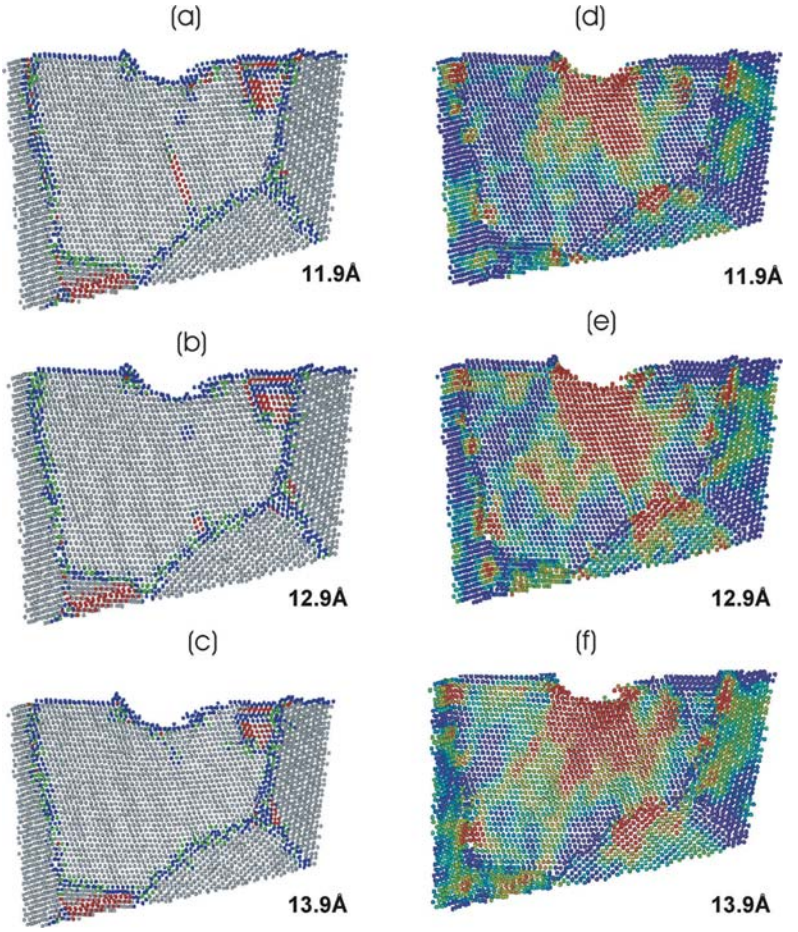

COLOR PLATE 2. Dislocation absorbed at low stress region of the GB. (From Ref. 37.)

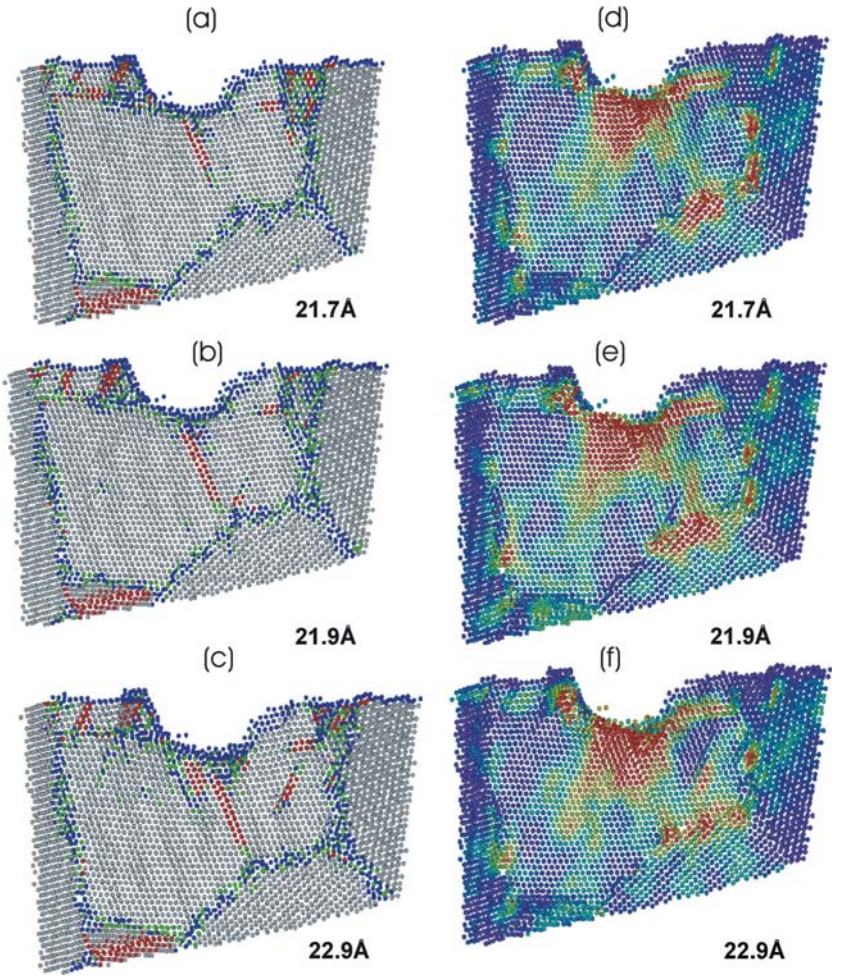

COLOR PLATE 3. Dislocation emitted by high stress region of the GB. (From Ref. 37.)